

# Gaseous Detonation Initiation via Wave Implosion

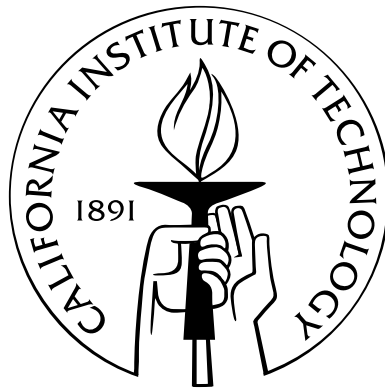
Thesis by

Scott Irving Jackson

In Partial Fulfillment of the Requirements

for the Degree of

Doctor of Philosophy



California Institute of Technology

Pasadena, California

2005

(Submitted April 15, 2005)

© 2005

Scott Irving Jackson

All Rights Reserved

# Abstract

Imploding shock geometries force shock-processed gas into an ever-decreasing area that creates high levels of compression and wave acceleration. A high-energy core results from this adiabatic compression, which may cause combustible gas mixtures to explode. If the blast wave created from this explosion is of sufficient strength, a detonation wave is initiated.

Toroidally imploding shock and detonation waves have been used to initiate detonations inside of a 76-mm-diameter tube filled with stoichiometric ethylene- and propane-oxygen-nitrogen mixtures. This research develops new techniques to efficiently detonate hydrocarbon-air mixtures, a topic that continues to plague pulse detonation engine development.

This experimental work is the first to detonate propane-air mixtures with an imploding-detonation wave and to detonate a gas mixture with a non-reflected, imploding shock. A unique device capable of generating an imploding toroidal detonation wave inside of a tube from a single ignition point without any obstruction to the tube flow path is presented. The development of a second device that creates a large-aspect-ratio planar detonation wave in a gas-phase explosive from a single ignition point is also discussed.

The minimum energy required to initiate detonations in hydrocarbon-oxygen-nitrogen mixtures inside of a tube with an imploding shock wave was determined to scale linearly with the induction-zone length, which is an indication of a planar initiation mode. The imploding toroidal detonation initiator was found to be more efficient at detonation initiation than the imploding shock initiator, using a comparable energy input to that of current initiator tubes.

# Acknowledgements

First and foremost, I would like to thank my advisor, Joe Shepherd, for his guidance, patience, and friendship. I have thoroughly enjoyed working with him and have been inspired by his amazing work ethic, as well as his enthusiasm for science and teaching. I would also like to thank Hans Hornung, whose direction, friendship, and help with AMRITA have been much appreciated during my time at GALCIT. I am also grateful to the other members of my doctoral committee, composed of Don Cohen, Tom Heaton, and Tony Leonard.

Past and present members of the Explosion Dynamics Laboratory group at Caltech have contributed to this work through discussion and experimental assistance including Eric Schultz, Joanna Austin, Eric Wintenberger, Tony Chao, Marcia Cooper, Florian Pintgen, Dan Lieberman, and Marty Grunthaner. In particular, I have enjoyed the late-night brainstorming sessions with Florian and have found Marcia's friendship indispensable, not to mention her proofreading skills. If any of the following chapters are coherent, it is in no small part due to her.

Additionally, I fear that I have been permanently spoiled by Suzy Dake, the administrative assistant of our group. Her organizational and proofreading skills have no peer and have greatly facilitated my work. Brad St. John, Joe Haggerty, and Ali Kiani have machined most of the experiments discussed herein. I also appreciate the time they have spent teaching me the basic machine shop skills that I had previously been (and according to them, am still) lacking.

Finally, I would like to thank my family, who has provided me with endless encouragement, support, motivation and advice for almost three decades. I have not forgotten the math lessons written at (and on) the kitchen table or the many hours

spent helping me practice for exams when I was younger.

This research was sponsored by the Department of Defense and Army Research Office through a National Defense Science and Engineering Graduate (NDSEG) Fellowship, by the Office of Naval Research Grants “*Pulse Detonation Engines: Initiation, Propagation and Performance*,” “*Multidisciplinary Study of Pulse Detonation Engine*,” and “*Detonation Initiation by Annular Jets and Shock Waves*,” by General Electric, and by the National Aeronautics and Space Administration and Marshall Space Flight Center through a Graduate Student Researchers Program (GSRP) Fellowship.

# Contents

<b>Abstract</b>	<b>iii</b>
<b>Acknowledgements</b>	<b>iv</b>
<b>List of Figures</b>	<b>xii</b>
<b>List of Tables</b>	<b>xxxii</b>
<b>Nomenclature</b>	<b>xxxiii</b>
<b>1 Introduction</b>	<b>1</b>
1.1 Motivation . . . . .	1
1.2 Detonation Initiation Mechanisms . . . . .	4
1.2.1 Direct Initiation from a Blast Wave . . . . .	4
1.2.1.1 Calculating Energy Required for Direct Initiation . . . . .	8
1.2.2 Deflagration-to-Detonation Transition . . . . .	10
1.2.3 Initiator Tubes . . . . .	12
1.2.3.1 Initiator Tubes with Confinement . . . . .	14
1.2.4 Obstacle Reflection . . . . .	15
1.2.5 The Importance of Temperature . . . . .	15
1.3 Previous Research on Imploding Waves . . . . .	16
1.3.1 Imploding Cylindrical and Spherical Shock Waves . . . . .	16
1.3.2 Imploding Cylindrical and Spherical Detonation Waves . . . . .	17
1.3.3 Imploding Toroidal Waves . . . . .	19
1.4 Outline . . . . .	21

<b>2</b>	<b>Detonation Propagation Through Small Tubes</b>	<b>23</b>
2.1	Introduction . . . . .	23
2.2	Previous Relevant Work . . . . .	23
2.2.1	Detonations and Sub-CJ Detonations . . . . .	24
2.2.2	Low-Velocity Detonations . . . . .	26
2.2.3	Galloping Detonations . . . . .	28
2.2.4	Shock Waves in Small Diameter Tubes . . . . .	29
2.3	Experimental Setup . . . . .	29
2.3.1	1.27 mm Inner Diameter Test Section . . . . .	30
2.3.2	6.35 mm Inner Diameter Test Section . . . . .	32
2.4	Analysis and Theory . . . . .	32
2.4.1	Boundary Layer Growth . . . . .	36
2.4.2	Quasi-One-Dimensional Analysis for the Velocity Deficit of a Detonation Wave . . . . .	39
2.4.2.1	One-Dimensional Waves with No Area Change . . . . .	40
2.4.2.2	One-Dimensional Waves with Area Change . . . . .	44
2.4.2.3	Solution Application in Fay (1959) . . . . .	46
2.4.2.4	Solution Application in Dupre et al. (1986) . . . . .	48
2.4.2.5	Limitations of the Model . . . . .	49
2.4.3	Lower Shock Velocity Limits . . . . .	50
2.4.3.1	Shock Tube Model . . . . .	50
2.4.3.2	Blowdown Analysis . . . . .	52
2.5	Summary . . . . .	53
<b>3</b>	<b>Static Detonation Initiator</b>	<b>57</b>
3.1	Introduction . . . . .	57
3.1.1	Toroidal Initiator . . . . .	57
3.1.2	Planar Initiator . . . . .	61
3.2	Experimental Facilities and Operation . . . . .	61
3.2.1	Planar Initiator . . . . .	61

3.2.2	Toroidal Initiator . . . . .	64
3.3	Results and Analysis . . . . .	68
3.3.1	Planar Initiator . . . . .	68
3.3.2	Toroidal Initiator . . . . .	68
3.3.2.1	AMRITA Simulations and Interpretation . . . . .	70
3.3.3	Pulsed Operation Considerations . . . . .	79
3.4	Summary . . . . .	81
<b>4</b>	<b>Dynamic Detonation Initiator</b>	<b>83</b>
4.1	Introduction . . . . .	83
4.2	Experimental Facilities and Operation . . . . .	83
4.2.1	Planar Initiator . . . . .	83
4.2.2	Toroidal Initiator . . . . .	86
4.2.2.1	Operation without Gas Injection . . . . .	86
4.2.2.2	Operation with Gas Injection . . . . .	86
4.3	Results and Analysis . . . . .	88
4.3.1	Planar Initiator with Gas Injection . . . . .	88
4.3.2	Toroidal Initiator without Gas Injection . . . . .	89
4.3.3	Toroidal Initiator with Gas Injection . . . . .	93
4.3.3.1	Example Data Traces . . . . .	95
4.3.3.2	Transmission Limits . . . . .	99
4.3.3.3	Initiation Attempts Using a Collapsing Shock Wave . . . . .	105
4.4	Summary . . . . .	108
<b>5</b>	<b>Imploding Shock Wave Initiator</b>	<b>111</b>
5.1	Introduction . . . . .	111
5.2	Experimental Facility . . . . .	112
5.2.1	GALCIT 6-Inch Shock Tube . . . . .	113
5.2.1.1	Diaphragm Selection for Shock Tube . . . . .	114
5.2.2	Test Section . . . . .	115
5.2.2.1	Diaphragm Selection for Test Section . . . . .	117

5.2.3	Basic Operation . . . . .	118
5.3	Results and Analysis . . . . .	119
5.3.1	Pressure Behind the Reflected Wave . . . . .	121
5.3.2	Classification of Data . . . . .	124
5.3.2.1	Prompt Detonation . . . . .	124
5.3.2.2	Deflagration-to-Detonation Transition . . . . .	126
5.3.2.3	Detonation after Reflection . . . . .	128
5.3.2.4	No Initiation . . . . .	128
5.3.3	Effect of Nitrogen Dilution . . . . .	128
5.4	Summary . . . . .	130
<b>6</b>	<b>Initiator Effectiveness</b>	<b>133</b>
6.1	Energy Input to the Shock Implosion Initiator . . . . .	136
6.2	Energy Input to the Toroidal Initiator . . . . .	142
6.3	Comparison of the Shock Implosion and Toroidal Initiators . . . . .	144
6.3.1	Comparison of the Toroidal Initiator Energy to Various Critical Energies . . . . .	147
6.3.2	Comparison with a Typical Initiator Tube . . . . .	148
6.4	Summary . . . . .	149
<b>7</b>	<b>Conclusions</b>	<b>151</b>
7.1	Future Work . . . . .	154
	<b>Bibliography</b>	<b>156</b>
<b>A</b>	<b>Detonation Models and Parameters</b>	<b>170</b>
A.1	CJ Theory . . . . .	170
A.2	ZND Theory . . . . .	172
A.3	Constant Volume Explosion Theory . . . . .	173
<b>B</b>	<b>The Similarity Solution for a Strong Blast Wave</b>	<b>177</b>
B.1	The Similarity Variable . . . . .	177

B.2	Self-Similar Equations . . . . .	179
B.3	Integration . . . . .	180
<b>C</b>	<b>Electronic Circuits</b>	<b>183</b>
<b>D</b>	<b>Small Tube Data</b>	<b>187</b>
D.1	Run Matrix . . . . .	188
D.2	Wave Arrival Times . . . . .	190
D.3	Velocity Data . . . . .	192
D.4	Pressure Traces . . . . .	194
<b>E</b>	<b>Planar Static Initiator Data</b>	<b>245</b>
E.1	Design Drawings . . . . .	246
E.2	Run Matrix . . . . .	251
E.3	Wave Arrival Times . . . . .	256
E.4	Selected Pressure Traces . . . . .	261
E.5	Chemiluminescence Images . . . . .	266
<b>F</b>	<b>Toroidal Static Initiator Data</b>	<b>317</b>
F.1	Drawings . . . . .	318
F.2	Run Matrix . . . . .	340
F.3	Pressure Traces . . . . .	342
F.4	Chemiluminescence Images . . . . .	349
<b>G</b>	<b>Planar Dynamic Initiator Data</b>	<b>359</b>
G.1	Design Drawings . . . . .	360
G.2	Run Matrix . . . . .	377
G.3	Wave Arrival Times . . . . .	379
G.4	Pressure Traces . . . . .	380
G.5	Chemiluminescence Images . . . . .	389

<b>H</b>	<b>Toroidal Dynamic Initiator Data</b>	<b>397</b>
H.1	Design Drawings . . . . .	398
H.2	Run Matrix: No Dynamic Injection . . . . .	421
H.3	Pressure Traces: No Dynamic Injection . . . . .	424
H.4	Chemiluminescence Images: No Dynamic Injection . . . . .	442
H.5	Run Matrix: Dynamic Gas Injection . . . . .	476
H.6	Measured Velocities: Dynamic Gas Injection . . . . .	479
H.7	Pressure Traces: Dynamic Gas Injection . . . . .	481
<b>I</b>	<b>Shock Implosion Initiator Data</b>	<b>533</b>
I.1	Drawings . . . . .	534
I.2	Run Matrix . . . . .	543
I.2.1	Shock-Tube Conditions . . . . .	543
I.2.2	Test-Section Conditions . . . . .	546
I.2.3	Energy Calculation . . . . .	549
I.3	Pressure Traces . . . . .	552

# List of Figures

1.1	Illustration of the PDE cycle. . . . .	2
1.2	The V-1 “Buzz Bomb. . . . .	3
1.3	Schematic of a detonation wave. . . . .	4
1.4	Direct initiation. . . . .	5
1.5	Critical blast wave parameters. . . . .	6
1.6	Images of the DDT process. . . . .	11
1.7	Detonation initiation from an initiator tube. . . . .	13
2.1	The 1.27 mm ID test section. . . . .	30
2.2	The pressure transducer station on the 1.27 mm ID test section. . . . .	31
2.3	The 6.35 mm ID test section. . . . .	32
2.4	Velocity data from the test sections. . . . .	34
2.5	Examples of pressure traces from both test sections. . . . .	35
2.6	Nondimensionalized velocity data from the test sections. . . . .	37
2.7	Boundary layer growth behind a shock wave. . . . .	38
2.8	The Hugoniot-Rayleigh representation of shock and detonation waves. . . . .	41
2.9	The difference between steady and unsteady expansions. . . . .	51
3.1	Initiator tube geometry. . . . .	58
3.2	Three geometries used to create imploding waves. . . . .	59
3.3	Schematic of the planar initiator. . . . .	62
3.4	Creation of a quasi-planar wave front. . . . .	63
3.5	The toroidal initiator design. . . . .	64
3.6	Rendering and cross-section of the toroidal initiator. . . . .	65

3.7	End flange with pressure transducers. . . . .	66
3.8	Composite imaging window. . . . .	67
3.9	Example pressure traces from the static planar initiator. . . . .	69
3.10	Chemiluminescence images from the planar initiator. . . . .	70
3.11	Pressure traces from the toroidal initiator. . . . .	71
3.12	Chemiluminescence images of the collapsing toroidal detonation wave. . . . .	72
3.13	The geometry of the toroidal detonation front. . . . .	74
3.14	Comparison of imploding detonation theories and experiment. . . . .	76
3.15	Simulation images of an imploding wave. . . . .	77
3.16	Simulation images and pressures of an imploding wave. . . . .	78
3.17	Simulation images and pressures of an imploding wave. . . . .	80
4.1	The dynamic planar initiator. . . . .	84
4.2	Schematic of the dynamic toroidal initiator. . . . .	87
4.3	The facility used for hydrocarbon-air initiation. . . . .	88
4.4	Chemiluminescence images from the dynamic planar initiator. . . . .	89
4.5	Chemiluminescence images of the implosion in ethylene-oxygen. . . . .	90
4.6	Chemiluminescence images of the implosion in ethylene-oxygen. . . . .	91
4.7	Implosion velocity in the toroidal initiator. . . . .	92
4.8	Chemiluminescence images of the implosion in propane-oxygen. . . . .	93
4.9	The initiator overfill concept. . . . .	94
4.10	Dynamic toroidal initiator calibration shot. . . . .	96
4.11	Dynamic toroidal initiator failed initiation attempt. . . . .	97
4.12	Dynamic toroidal initiator successful initiation attempt. . . . .	98
4.13	Implosion configurations. . . . .	100
4.14	Effect of overfill for implosion near wall in propane-air. . . . .	102
4.15	Effect of overfill for implosion near wall in ethylene-air. . . . .	103
4.16	Effect of overfill for implosion far from wall in propane-air. . . . .	104
4.17	Effect of overfill for implosion far from wall in ethylene-air. . . . .	105
4.18	Conventional driver length. . . . .	105

4.19	Pure symmetry. . . . .	106
4.20	Dynamic toroidal initiator shock wave initiation attempt. . . . .	107
4.21	Imploding shock wave configuration. . . . .	108
5.1	The shock implosion facility. . . . .	113
5.2	Diaphragm burst data. . . . .	115
5.3	Dimensions at the shock-tube test-section interface. . . . .	116
5.4	A schematic of the shock implosion initiator showing the locations of the pressure transducers and ionization probes relative to the inner face of the front test-section flange. Units are in decimeters (0.1 m). . . . .	117
5.5	The annular orifice and sliding gate. . . . .	118
5.6	AMRITA simulation of the shock implosion facility. . . . .	120
5.7	Comparison of pressure traces in the shock implosion initiator for reflected initiation. . . . .	122
5.8	Comparison of pressure traces in the shock implosion initiator for reflected initiation. . . . .	123
5.9	Prompt detonation initiation in $C_2H_4 + 3O_2$ with $M_s = 1.5$ . . . . .	125
5.10	DDT in $C_2H_4 + 3O_2 + 0.44N_2$ (10% $N_2$ by volume) with $M_s = 1.9$ . . . . .	126
5.11	Initiation behind reflected wave in $C_2H_4 + 3O_2 + 4N_2$ (50% $N_2$ by volume) with $M_s = 1.5$ . . . . .	127
5.12	No initiation in $C_2H_4 + 3O_2 + 6N_2$ (60% $N_2$ by volume) with $M_s = 1.7$ . . . . .	129
5.13	Initiation results from the imploding shock wave tests. . . . .	130
6.1	Reinitiation via Mach reflection. . . . .	134
6.2	Scaling criteria. . . . .	135
6.3	Critical energy for initiation from a blast wave inside a tube. . . . .	136
6.4	Control volume for the shock implosion tests. . . . .	137
6.5	Energy input to shock implosion for ethylene-oxygen-nitrogen. . . . .	140
6.6	Energy input to shock implosion for propane-oxygen-nitrogen. . . . .	141
6.7	Heat of reaction for acetylene-oxygen mixtures. . . . .	145
6.8	Energy input to the dynamic toroidal initiation. . . . .	145

6.9	Different pressure pulses. . . . .	146
A.1	Hugoniot-Rayleigh representation of shock and detonation waves. . . .	171
A.2	ZND structure. . . . .	174
A.3	The effect of shock speed on temperature and induction length. . . . .	175
C.1	The spark discharge circuit. . . . .	184
C.2	The ionization probe circuit. . . . .	185
D.1	Pressure history from small tube run 001. . . . .	194
D.2	Pressure history from small tube run 002. . . . .	195
D.3	Pressure history from small tube run 003. . . . .	196
D.4	Pressure history from small tube run 004. . . . .	197
D.5	Pressure history from small tube run 005. . . . .	198
D.6	Pressure history from small tube run 006. . . . .	199
D.7	Pressure history from small tube run 007. . . . .	200
D.8	Pressure history from small tube run 008. . . . .	201
D.9	Pressure history from small tube run 009. . . . .	202
D.10	Pressure history from small tube run 010. . . . .	203
D.11	Pressure history from small tube run 011. . . . .	204
D.12	Pressure history from small tube run 012. . . . .	205
D.13	Pressure history from small tube run 013. . . . .	206
D.14	Pressure history from small tube run 014. . . . .	207
D.15	Pressure history from small tube run 015. . . . .	208
D.16	Pressure history from small tube run 016. . . . .	209
D.17	Pressure history from small tube run 017. . . . .	210
D.18	Pressure history from small tube run 018. . . . .	211
D.19	Pressure history from small tube run 019. . . . .	212
D.20	Pressure history from small tube run 020. . . . .	213
D.21	Pressure history from small tube run 021. . . . .	214
D.22	Pressure history from small tube run 022. . . . .	215

D.23	Pressure history from small tube run 023. . . . .	216
D.24	Pressure history from small tube run 024. . . . .	217
D.25	Pressure history from small tube run 025. . . . .	218
D.26	Pressure history from small tube run 026. . . . .	219
D.27	Pressure history from small tube run 027. . . . .	220
D.28	Pressure history from small tube run 028. . . . .	221
D.29	Pressure history from small tube run 029. . . . .	222
D.30	Pressure history from small tube run 030. . . . .	223
D.31	Pressure history from small tube run 031. . . . .	224
D.32	Pressure history from small tube run 032. . . . .	225
D.33	Pressure history from small tube run 033. . . . .	226
D.34	Pressure history from small tube run 034. . . . .	227
D.35	Pressure history from small tube run 035. . . . .	228
D.36	Pressure history from small tube run 036. . . . .	229
D.37	Pressure history from small tube run 037. . . . .	230
D.38	Pressure history from small tube run 038. . . . .	231
D.39	Pressure history from small tube run 039. . . . .	232
D.40	Pressure history from small tube run 040. . . . .	233
D.41	Pressure history from small tube run 041. . . . .	234
D.42	Pressure history from small tube run 042. . . . .	235
D.43	Pressure history from small tube run 043. . . . .	236
D.44	Pressure history from small tube run 044. . . . .	237
D.45	Pressure history from small tube run 045. . . . .	238
D.46	Pressure history from small tube run 046. . . . .	239
D.47	Pressure history from small tube run 047. . . . .	240
D.48	Pressure history from small tube run 048. . . . .	241
D.49	Pressure history from small tube run 049. . . . .	242
D.50	Pressure history from small tube run 050. . . . .	243
E.1	Planar initiator design drawing - Top view. . . . .	247

E.2	Planar initiator design drawing - Side view. . . . .	248
E.3	Cover plate design drawing - Top view. . . . .	249
E.4	Modified planar initiator design drawing - Top view. . . . .	250
E.5	Pressure history from static planar initiator run 100. . . . .	261
E.6	Pressure history from static planar initiator run 105. . . . .	262
E.7	Pressure history from static planar initiator run 107. . . . .	263
E.8	Pressure history from static planar initiator run 108. . . . .	264
E.9	Pressure history from static planar initiator run 128. . . . .	265
E.10	Chemiluminescence image from static planar initiator run 013. . . . .	266
E.11	Chemiluminescence image from static planar initiator run 014. . . . .	267
E.12	Chemiluminescence image from static planar initiator run 015. . . . .	267
E.13	Chemiluminescence image from static planar initiator run 016. . . . .	268
E.14	Chemiluminescence image from static planar initiator run 017. . . . .	268
E.15	Chemiluminescence image from static planar initiator run 018. . . . .	269
E.16	Chemiluminescence image from static planar initiator run 019. . . . .	269
E.17	Chemiluminescence image from static planar initiator run 020. . . . .	269
E.18	Chemiluminescence image from static planar initiator run 021. . . . .	270
E.19	Chemiluminescence image from static planar initiator run 025. . . . .	270
E.20	Chemiluminescence image from static planar initiator run 027. . . . .	271
E.21	Chemiluminescence image from static planar initiator run 030. . . . .	271
E.22	Chemiluminescence image from static planar initiator run 031. . . . .	272
E.23	Chemiluminescence image from static planar initiator run 032. . . . .	272
E.24	Chemiluminescence image from static planar initiator run 033. . . . .	273
E.25	Chemiluminescence image from static planar initiator run 038. . . . .	273
E.26	Chemiluminescence image from static planar initiator run 039. . . . .	274
E.27	Chemiluminescence image from static planar initiator run 040. . . . .	275
E.28	Chemiluminescence image from static planar initiator run 041. . . . .	276
E.29	Chemiluminescence image from static planar initiator run 042. . . . .	277
E.30	Chemiluminescence image from static planar initiator run 043. . . . .	278
E.31	Chemiluminescence image from static planar initiator run 044. . . . .	279

E.32	Chemiluminescence image from static planar initiator run 045. . . . .	280
E.33	Chemiluminescence image from static planar initiator run 046. . . . .	281
E.34	Chemiluminescence image from static planar initiator run 050. . . . .	282
E.35	Chemiluminescence image from static planar initiator run 051. . . . .	283
E.36	Chemiluminescence image from static planar initiator run 052. . . . .	284
E.37	Chemiluminescence image from static planar initiator run 053. . . . .	284
E.38	Chemiluminescence image from static planar initiator run 054. . . . .	285
E.39	Chemiluminescence image from static planar initiator run 055. . . . .	285
E.40	Chemiluminescence image from static planar initiator run 056. . . . .	286
E.41	Chemiluminescence image from static planar initiator run 057. . . . .	286
E.42	Chemiluminescence image from static planar initiator run 058. . . . .	287
E.43	Chemiluminescence image from static planar initiator run 059. . . . .	287
E.44	Chemiluminescence image from static planar initiator run 060. . . . .	288
E.45	Chemiluminescence image from static planar initiator run 061. . . . .	288
E.46	Chemiluminescence image from static planar initiator run 062. . . . .	289
E.47	Chemiluminescence image from static planar initiator run 063. . . . .	289
E.48	Chemiluminescence image from static planar initiator run 064. . . . .	290
E.49	Chemiluminescence image from static planar initiator run 067. . . . .	290
E.50	Chemiluminescence image from static planar initiator run 068. . . . .	291
E.51	Chemiluminescence image from static planar initiator run 069. . . . .	291
E.52	Chemiluminescence image from static planar initiator run 070. . . . .	292
E.53	Chemiluminescence image from static planar initiator run 071. . . . .	292
E.54	Chemiluminescence image from static planar initiator run 072. . . . .	293
E.55	Chemiluminescence image from static planar initiator run 074. . . . .	293
E.56	Chemiluminescence image from static planar initiator run 075. . . . .	294
E.57	Chemiluminescence image from static planar initiator run 076. . . . .	294
E.58	Chemiluminescence image from static planar initiator run 077. . . . .	295
E.59	Chemiluminescence image from static planar initiator run 080. . . . .	295
E.60	Chemiluminescence image from static planar initiator run 081. . . . .	296
E.61	Chemiluminescence image from static planar initiator run 082. . . . .	296

E.62	Chemiluminescence image from static planar initiator run 083. . . . .	297
E.63	Chemiluminescence image from static planar initiator run 084. . . . .	297
E.64	Chemiluminescence image from static planar initiator run 085. . . . .	298
E.65	Chemiluminescence image from static planar initiator run 086. . . . .	298
E.66	Chemiluminescence image from static planar initiator run 087. . . . .	299
E.67	Chemiluminescence image from static planar initiator run 088. . . . .	299
E.68	Chemiluminescence image from static planar initiator run 089. . . . .	300
E.69	Chemiluminescence image from static planar initiator run 090. . . . .	300
E.70	Chemiluminescence image from static planar initiator run 091. . . . .	301
E.71	Chemiluminescence image from static planar initiator run 092. . . . .	301
E.72	Chemiluminescence image from static planar initiator run 095. . . . .	302
E.73	Chemiluminescence image from static planar initiator run 096. . . . .	302
E.74	Chemiluminescence image from static planar initiator run 097. . . . .	303
E.75	Chemiluminescence image from static planar initiator run 098. . . . .	303
E.76	Chemiluminescence image from static planar initiator run 099. . . . .	304
E.77	Chemiluminescence image from static planar initiator run 100. . . . .	304
E.78	Chemiluminescence image from static planar initiator run 101. . . . .	305
E.79	Chemiluminescence image from static planar initiator run 103. . . . .	305
E.80	Chemiluminescence image from static planar initiator run 104. . . . .	306
E.81	Chemiluminescence image from static planar initiator run 105. . . . .	306
E.82	Chemiluminescence image from static planar initiator run 107. . . . .	307
E.83	Chemiluminescence image from static planar initiator run 109. . . . .	307
E.84	Chemiluminescence image from static planar initiator run 110. . . . .	308
E.85	Chemiluminescence image from static planar initiator run 111. . . . .	308
E.86	Chemiluminescence image from static planar initiator run 112. . . . .	309
E.87	Chemiluminescence image from static planar initiator run 114. . . . .	309
E.88	Chemiluminescence image from static planar initiator run 115. . . . .	310
E.89	Chemiluminescence image from static planar initiator run 116. . . . .	310
E.90	Chemiluminescence image from static planar initiator run 117. . . . .	311
E.91	Chemiluminescence image from static planar initiator run 120. . . . .	311

E.92	Chemiluminescence image from static planar initiator run 122. . . . .	312
E.93	Chemiluminescence image from static planar initiator run 123. . . . .	312
E.94	Chemiluminescence image from static planar initiator run 124. . . . .	313
E.95	Chemiluminescence image from static planar initiator run 125. . . . .	313
E.96	Chemiluminescence image from static planar initiator run 127. . . . .	314
E.97	Chemiluminescence image from static planar initiator run 128. . . . .	314
E.98	Chemiluminescence image from static planar initiator run 129. . . . .	315
E.99	Chemiluminescence image from static planar initiator run 130. . . . .	315
F.1	Exploded view of the toroidal initiator assembly. . . . .	318
F.2	Assembled view of the toroidal initiator. . . . .	319
F.3	Initiator inner sleeve after assembly. . . . .	320
F.4	Adapter ring. . . . .	321
F.5	Focusing ring. . . . .	322
F.6	Initiator outer sleeve after assembly. . . . .	323
F.7	Spark plug port. . . . .	324
F.8	Gas fill port. . . . .	325
F.9	Blank end flange. . . . .	326
F.10	Setup for initiator assembly. . . . .	327
F.11	Initiator inner sleeve prior to assembly. . . . .	328
F.12	Initiator outer sleeve prior to assembly. . . . .	329
F.13	Alignment ring for assembly. . . . .	330
F.14	Handle assembly. . . . .	331
F.15	Handle. . . . .	332
F.16	Handle rod. . . . .	333
F.17	Handle plate. . . . .	334
F.18	Assembly stand. . . . .	335
F.19	Alignment pin. . . . .	336
F.20	Channel cut paths on outer diameter of inner sleeve. . . . .	337
F.21	View of the inner sleeve mapped to a planar surface. . . . .	338

F.22	Renderings of the inner sleeve with channels prior to assembly. . . . .	339
F.23	Pressure history from static planar initiator run 001. . . . .	342
F.24	Pressure history from static planar initiator run 002. . . . .	343
F.25	Pressure history from static planar initiator run 003. . . . .	344
F.26	Pressure history from static planar initiator run 004. . . . .	345
F.27	Pressure history from static planar initiator run 005. . . . .	346
F.28	Pressure history from static planar initiator run 006. . . . .	347
F.29	Pressure history from static planar initiator run 007. . . . .	348
F.30	Chemiluminescence image from static toroidal initiator run 018. . . . .	349
F.31	Chemiluminescence image from static toroidal initiator run 020. . . . .	350
F.32	Chemiluminescence image from static toroidal initiator run 021. . . . .	350
F.33	Chemiluminescence image from static toroidal initiator run 022. . . . .	351
F.34	Chemiluminescence image from static toroidal initiator run 023. . . . .	351
F.35	Chemiluminescence image from static toroidal initiator run 024. . . . .	352
F.36	Chemiluminescence image from static toroidal initiator run 030. . . . .	352
F.37	Chemiluminescence image from static toroidal initiator run 031. . . . .	353
F.38	Chemiluminescence image from static toroidal initiator run 032. . . . .	353
F.39	Chemiluminescence image from static toroidal initiator run 033. . . . .	354
F.40	Chemiluminescence image from static toroidal initiator run 035. . . . .	354
F.41	Chemiluminescence image from static toroidal initiator run 036. . . . .	355
F.42	Chemiluminescence image from static toroidal initiator run 037. . . . .	355
F.43	Chemiluminescence image from static toroidal initiator run 040. . . . .	356
F.44	Chemiluminescence image from static toroidal initiator run 041. . . . .	356
F.45	Chemiluminescence image from static toroidal initiator run 042. . . . .	357
F.46	Chemiluminescence image from static toroidal initiator run 043. . . . .	357
G.1	A view of the dynamic planar initiator assembly. . . . .	361
G.2	Isometric view of the dynamic planar initiator. . . . .	362
G.3	Outer dimension of the dynamic planar initiator. . . . .	363
G.4	Outer bolt dimensions on the dynamic planar initiator. . . . .	364

G.5	Outer o-ring dimensions on the dynamic planar initiator. . . . .	365
G.6	Bath tube dimensions on the dynamic planar initiator. . . . .	366
G.7	Inner bolt dimensions on the dynamic planar initiator. . . . .	367
G.8	Channel cutting path on the dynamic planar initiator. . . . .	368
G.9	Channel dimensions on the dynamic planar initiator. . . . .	369
G.10	Exit ramp dimensions on the dynamic planar initiator. . . . .	370
G.11	Isometric view of the dynamic planar initiator cover plate. . . . .	371
G.12	Outer dimension of the dynamic planar initiator cover plate. . . . .	372
G.13	Outer bolt dimensions on the dynamic planar initiator cover plate. . .	373
G.14	Bath tube dimensions on the dynamic planar initiator cover plate. . . .	374
G.15	Inner bolt dimensions on the dynamic planar initiator cover plate. . . .	375
G.16	Spark plug dimensions on the dynamic planar initiator cover plate. . . .	376
G.17	Pressure history from dynamic planar initiator run 001. . . . .	380
G.18	Pressure history from dynamic planar initiator run 003. . . . .	381
G.19	Pressure history from dynamic planar initiator run 004. . . . .	381
G.20	Pressure history from dynamic planar initiator run 005. . . . .	382
G.21	Pressure history from dynamic planar initiator run 006. . . . .	382
G.22	Pressure history from dynamic planar initiator run 007. . . . .	383
G.23	Pressure history from dynamic planar initiator run 008. . . . .	383
G.24	Pressure history from dynamic planar initiator run 010. . . . .	384
G.25	Pressure history from dynamic planar initiator run 011. . . . .	384
G.26	Pressure history from dynamic planar initiator run 012. . . . .	385
G.27	Pressure history from dynamic planar initiator run 014. . . . .	385
G.28	Pressure history from dynamic planar initiator run 015. . . . .	386
G.29	Pressure history from dynamic planar initiator run 016. . . . .	386
G.30	Pressure history from dynamic planar initiator run 017. . . . .	387
G.31	Pressure history from dynamic planar initiator run 018. . . . .	387
G.32	Pressure history from dynamic planar initiator run 019. . . . .	388
G.33	Pressure history from dynamic planar initiator run 020. . . . .	388
G.34	The dynamic toroidal initiator. . . . .	389

G.35	The dynamic toroidal initiator view for chemiluminescence imaging. . .	390
G.36	Chemiluminescence image from dynamic toroidal initiator run 001. . .	390
G.37	Chemiluminescence image from dynamic toroidal initiator run 002. . .	390
G.38	Chemiluminescence image from dynamic toroidal initiator run 003. . .	391
G.39	Chemiluminescence image from dynamic toroidal initiator run 004. . .	391
G.40	Chemiluminescence image from dynamic toroidal initiator run 005. . .	391
G.41	Chemiluminescence image from dynamic toroidal initiator run 006. . .	392
G.42	Chemiluminescence image from dynamic toroidal initiator run 007. . .	392
G.43	Chemiluminescence image from dynamic toroidal initiator run 008. . .	392
G.44	Chemiluminescence image from dynamic toroidal initiator run 009. . .	393
G.45	Chemiluminescence image from dynamic toroidal initiator run 011. . .	393
G.46	Chemiluminescence image from dynamic toroidal initiator run 012. . .	393
G.47	Chemiluminescence image from dynamic toroidal initiator run 013. . .	394
G.48	Chemiluminescence image from dynamic toroidal initiator run 014. . .	394
G.49	Chemiluminescence image from dynamic toroidal initiator run 015. . .	394
G.50	Chemiluminescence image from dynamic toroidal initiator run 016. . .	395
G.51	Chemiluminescence image from dynamic toroidal initiator run 017. . .	395
G.52	Chemiluminescence image from dynamic toroidal initiator run 018. . .	395
G.53	Chemiluminescence image from dynamic toroidal initiator run 019. . .	396
G.54	Chemiluminescence image from dynamic toroidal initiator run 020. . .	396
G.55	Chemiluminescence image from dynamic toroidal initiator run 021. . .	396
H.1	Exploded view of the toroidal initiator assembly. . . . .	398
H.2	Assembled view of the toroidal initiator. . . . .	399
H.3	Initiator inner sleeve after assembly. . . . .	400
H.4	Adapter ring. . . . .	401
H.5	Focusing ring. . . . .	402
H.6	Initiator outer sleeve after assembly. . . . .	403
H.7	Spark plug port. . . . .	404
H.8	Gas fill port. . . . .	405

H.9	Pressure transducer port. . . . .	406
H.10	Blank end flange. . . . .	407
H.11	Setup for initiator assembly. . . . .	408
H.12	Initiator inner sleeve prior to assembly. . . . .	409
H.13	Initiator inner sleeve prior to assembly. . . . .	410
H.14	Alignment ring for assembly. . . . .	411
H.15	Handle assembly. . . . .	412
H.16	Handle. . . . .	413
H.17	Handle rod. . . . .	414
H.18	Handle plate. . . . .	415
H.19	Assembly stand. . . . .	416
H.20	Alignment pin. . . . .	417
H.21	Channel paths mapped to a planar surface. . . . .	418
H.22	Unwrapped rendering of channels. . . . .	419
H.23	Channel geometry specifics. . . . .	420
H.24	Pressure history from dynamic toroidal initiator run 001. . . . .	424
H.25	Pressure history from dynamic toroidal initiator run 002. . . . .	425
H.26	Pressure history from dynamic toroidal initiator run 003. . . . .	426
H.27	Pressure history from dynamic toroidal initiator run 004. . . . .	427
H.28	Pressure history from dynamic toroidal initiator run 005. . . . .	428
H.29	Pressure history from dynamic toroidal initiator run 006. . . . .	429
H.30	Pressure history from dynamic toroidal initiator run 031. . . . .	430
H.31	Pressure history from dynamic toroidal initiator run 032. . . . .	431
H.32	Pressure history from dynamic toroidal initiator run 033. . . . .	432
H.33	Pressure history from dynamic toroidal initiator run 034. . . . .	433
H.34	Pressure history from dynamic toroidal initiator run 035. . . . .	434
H.35	Pressure history from dynamic toroidal initiator run 036. . . . .	435
H.36	Pressure history from dynamic toroidal initiator run 037. . . . .	436
H.37	Pressure history from dynamic toroidal initiator run 038. . . . .	437
H.38	Pressure history from dynamic toroidal initiator run 039. . . . .	438

H.39	Pressure history from dynamic toroidal initiator run 040. . . . .	439
H.40	Pressure history from dynamic toroidal initiator run 041. . . . .	440
H.41	Pressure history from dynamic toroidal initiator run 042. . . . .	441
H.42	Chemiluminescence image from dynamic toroidal initiator run 008. . .	442
H.43	Chemiluminescence image from dynamic toroidal initiator run 009. . .	443
H.44	Chemiluminescence image from dynamic toroidal initiator run 014. . .	443
H.45	Chemiluminescence image from dynamic toroidal initiator run 015. . .	444
H.46	Chemiluminescence image from dynamic toroidal initiator run 016. . .	444
H.47	Chemiluminescence image from dynamic toroidal initiator run 017. . .	445
H.48	Chemiluminescence image from dynamic toroidal initiator run 018. . .	445
H.49	Chemiluminescence image from dynamic toroidal initiator run 019. . .	446
H.50	Chemiluminescence image from dynamic toroidal initiator run 020. . .	446
H.51	Chemiluminescence image from dynamic toroidal initiator run 021. . .	447
H.52	Chemiluminescence image from dynamic toroidal initiator run 022. . .	447
H.53	Chemiluminescence image from dynamic toroidal initiator run 023. . .	448
H.54	Chemiluminescence image from dynamic toroidal initiator run 024. . .	448
H.55	Chemiluminescence image from dynamic toroidal initiator run 025. . .	449
H.56	Chemiluminescence image from dynamic toroidal initiator run 026. . .	449
H.57	Chemiluminescence image from dynamic toroidal initiator run 027. . .	450
H.58	Chemiluminescence image from dynamic toroidal initiator run 028. . .	450
H.59	Chemiluminescence image from dynamic toroidal initiator run 029. . .	451
H.60	Chemiluminescence image from dynamic toroidal initiator run 030. . .	451
H.61	Chemiluminescence image from dynamic toroidal initiator run 050. . .	452
H.62	Chemiluminescence image from dynamic toroidal initiator run 050. . .	452
H.63	Chemiluminescence image from dynamic toroidal initiator run 050. . .	453
H.64	Chemiluminescence image from dynamic toroidal initiator run 050. . .	453
H.65	Chemiluminescence image from dynamic toroidal initiator run 050. . .	454
H.66	Chemiluminescence image from dynamic toroidal initiator run 050. . .	454
H.67	Chemiluminescence image from dynamic toroidal initiator run 050. . .	455
H.68	Chemiluminescence image from dynamic toroidal initiator run 050. . .	455

H.69	Chemiluminescence image from dynamic toroidal initiator run 053.	. . .	456
H.70	Chemiluminescence image from dynamic toroidal initiator run 053.	. . .	456
H.71	Chemiluminescence image from dynamic toroidal initiator run 053.	. . .	457
H.72	Chemiluminescence image from dynamic toroidal initiator run 053.	. . .	457
H.73	Chemiluminescence image from dynamic toroidal initiator run 053.	. . .	458
H.74	Chemiluminescence image from dynamic toroidal initiator run 053.	. . .	458
H.75	Chemiluminescence image from dynamic toroidal initiator run 053.	. . .	459
H.76	Chemiluminescence image from dynamic toroidal initiator run 053.	. . .	459
H.77	Chemiluminescence image from dynamic toroidal initiator run 054.	. . .	460
H.78	Chemiluminescence image from dynamic toroidal initiator run 054.	. . .	460
H.79	Chemiluminescence image from dynamic toroidal initiator run 054.	. . .	461
H.80	Chemiluminescence image from dynamic toroidal initiator run 054.	. . .	461
H.81	Chemiluminescence image from dynamic toroidal initiator run 054.	. . .	462
H.82	Chemiluminescence image from dynamic toroidal initiator run 054.	. . .	462
H.83	Chemiluminescence image from dynamic toroidal initiator run 054.	. . .	463
H.84	Chemiluminescence image from dynamic toroidal initiator run 054.	. . .	463
H.85	Chemiluminescence image from dynamic toroidal initiator run 055.	. . .	464
H.86	Chemiluminescence image from dynamic toroidal initiator run 055.	. . .	464
H.87	Chemiluminescence image from dynamic toroidal initiator run 055.	. . .	465
H.88	Chemiluminescence image from dynamic toroidal initiator run 055.	. . .	465
H.89	Chemiluminescence image from dynamic toroidal initiator run 055.	. . .	466
H.90	Chemiluminescence image from dynamic toroidal initiator run 055.	. . .	466
H.91	Chemiluminescence image from dynamic toroidal initiator run 055.	. . .	467
H.92	Chemiluminescence image from dynamic toroidal initiator run 055.	. . .	467
H.93	Chemiluminescence image from dynamic toroidal initiator run 056.	. . .	468
H.94	Chemiluminescence image from dynamic toroidal initiator run 056.	. . .	468
H.95	Chemiluminescence image from dynamic toroidal initiator run 056.	. . .	469
H.96	Chemiluminescence image from dynamic toroidal initiator run 056.	. . .	469
H.97	Chemiluminescence image from dynamic toroidal initiator run 056.	. . .	470
H.98	Chemiluminescence image from dynamic toroidal initiator run 056.	. . .	470

H.99	Chemiluminescence image from dynamic toroidal initiator run 056. . .	471
H.100	Chemiluminescence image from dynamic toroidal initiator run 056. . .	471
H.101	Chemiluminescence image from dynamic toroidal initiator run 057. . .	472
H.102	Chemiluminescence image from dynamic toroidal initiator run 057. . .	472
H.103	Chemiluminescence image from dynamic toroidal initiator run 057. . .	473
H.104	Chemiluminescence image from dynamic toroidal initiator run 057. . .	473
H.105	Chemiluminescence image from dynamic toroidal initiator run 057. . .	474
H.106	Chemiluminescence image from dynamic toroidal initiator run 057. . .	474
H.107	Chemiluminescence image from dynamic toroidal initiator run 057. . .	475
H.108	Chemiluminescence image from dynamic toroidal initiator run 057. . .	475
H.109	Pressure history from gas injection toroidal initiator run 103. . . . .	482
H.110	Pressure history from gas injection toroidal initiator run 104. . . . .	483
H.111	Pressure history from gas injection toroidal initiator run 105. . . . .	484
H.112	Pressure history from gas injection toroidal initiator run 106. . . . .	485
H.113	Pressure history from gas injection toroidal initiator run 107. . . . .	486
H.114	Pressure history from gas injection toroidal initiator run 108. . . . .	487
H.115	Pressure history from gas injection toroidal initiator run 109. . . . .	488
H.116	Pressure history from gas injection toroidal initiator run 110. . . . .	489
H.117	Pressure history from gas injection toroidal initiator run 111. . . . .	490
H.118	Pressure history from gas injection toroidal initiator run 112. . . . .	491
H.119	Pressure history from gas injection toroidal initiator run 113. . . . .	492
H.120	Pressure history from gas injection toroidal initiator run 114. . . . .	493
H.121	Pressure history from gas injection toroidal initiator run 115. . . . .	494
H.122	Pressure history from gas injection toroidal initiator run 116. . . . .	495
H.123	Pressure history from gas injection toroidal initiator run 117. . . . .	496
H.124	Pressure history from gas injection toroidal initiator run 118. . . . .	497
H.125	Pressure history from gas injection toroidal initiator run 119. . . . .	498
H.126	Pressure history from gas injection toroidal initiator run 120. . . . .	499
H.127	Pressure history from gas injection toroidal initiator run 121. . . . .	500
H.128	Pressure history from gas injection toroidal initiator run 122. . . . .	501

H.129	Pressure history from gas injection toroidal initiator run 123. . . . .	502
H.130	Pressure history from gas injection toroidal initiator run 124. . . . .	503
H.131	Pressure history from gas injection toroidal initiator run 125. . . . .	504
H.132	Pressure history from gas injection toroidal initiator run 126. . . . .	505
H.133	Pressure history from gas injection toroidal initiator run 127. . . . .	506
H.134	Pressure history from gas injection toroidal initiator run 128. . . . .	507
H.135	Pressure history from gas injection toroidal initiator run 129. . . . .	508
H.136	Pressure history from gas injection toroidal initiator run 130. . . . .	509
H.137	Pressure history from gas injection toroidal initiator run 131. . . . .	510
H.138	Pressure history from gas injection toroidal initiator run 132. . . . .	511
H.139	Pressure history from gas injection toroidal initiator run 133. . . . .	512
H.140	Pressure history from gas injection toroidal initiator run 134. . . . .	513
H.141	Pressure history from gas injection toroidal initiator run 135. . . . .	514
H.142	Pressure history from gas injection toroidal initiator run 136. . . . .	515
H.143	Pressure history from gas injection toroidal initiator run 137. . . . .	516
H.144	Pressure history from gas injection toroidal initiator run 138. . . . .	517
H.145	Pressure history from gas injection toroidal initiator run 139. . . . .	518
H.146	Pressure history from gas injection toroidal initiator run 140. . . . .	519
H.147	Pressure history from gas injection toroidal initiator run 141. . . . .	520
H.148	Pressure history from gas injection toroidal initiator run 142. . . . .	521
H.149	Pressure history from gas injection toroidal initiator run 143. . . . .	522
H.150	Pressure history from gas injection toroidal initiator run 144. . . . .	523
H.151	Pressure history from gas injection toroidal initiator run 145. . . . .	524
H.152	Pressure history from gas injection toroidal initiator run 146. . . . .	525
H.153	Pressure history from gas injection toroidal initiator run 147. . . . .	526
H.154	Pressure history from gas injection toroidal initiator run 148. . . . .	527
H.155	Pressure history from gas injection toroidal initiator run 149. . . . .	528
H.156	Pressure history from gas injection toroidal initiator run 150. . . . .	529
H.157	Pressure history from gas injection toroidal initiator run 151. . . . .	530
H.158	Pressure history from gas injection toroidal initiator run 152. . . . .	531

H.159	Pressure history from gas injection toroidal initiator run 153. . . . .	532
I.1	Assembly drawing. . . . .	534
I.2	Flange for 6" Shock Tube - part 1. . . . .	535
I.3	Flange for 3" detonation tube - part 2. . . . .	536
I.4	Flange for 3" detonation tube - part 3. . . . .	537
I.5	End cap for 3" inner detonation tube - part 4. . . . .	538
I.6	3" inner detonation tube - part 5. . . . .	539
I.7	3" detonation tube with flange. . . . .	540
I.8	3" inner detonation tube with flange. . . . .	541
I.9	3" detonation tube. . . . .	542
I.10	Pressure and ionization data from shock initiator run 28. . . . .	552
I.11	Pressure and ionization data from shock initiator run 29. . . . .	553
I.12	Pressure and ionization data from shock initiator run 30. . . . .	554
I.13	Pressure and ionization data from shock initiator run 31. . . . .	555
I.14	Pressure and ionization data from shock initiator run 32. . . . .	556
I.15	Pressure and ionization data from shock initiator run 36. . . . .	557
I.16	Pressure and ionization data from shock initiator run 37. . . . .	558
I.17	Pressure and ionization data from shock initiator run 38. . . . .	559
I.18	Pressure and ionization data from shock initiator run 39. . . . .	560
I.19	Pressure and ionization data from shock initiator run 40. . . . .	561
I.20	Pressure and ionization data from shock initiator run 41. . . . .	562
I.21	Pressure and ionization data from shock initiator run 42. . . . .	563
I.22	Pressure and ionization data from shock initiator run 43. . . . .	564
I.23	Pressure and ionization data from shock initiator run 44. . . . .	565
I.24	Pressure and ionization data from shock initiator run 45. . . . .	566
I.25	Pressure and ionization data from shock initiator run 46. . . . .	567
I.26	Pressure and ionization data from shock initiator run 47. . . . .	568
I.27	Pressure and ionization data from shock initiator run 48. . . . .	569
I.28	Pressure and ionization data from shock initiator run 49. . . . .	570

I.29	Pressure and ionization data from shock initiator run 50. . . . .	571
I.30	Pressure and ionization data from shock initiator run 51. . . . .	572
I.31	Pressure and ionization data from shock initiator run 52. . . . .	573
I.32	Pressure and ionization data from shock initiator run 53. . . . .	574
I.33	Pressure and ionization data from shock initiator run 54. . . . .	575
I.34	Pressure and ionization data from shock initiator run 55. . . . .	576
I.35	Pressure and ionization data from shock initiator run 56. . . . .	577
I.36	Pressure and ionization data from shock initiator run 70. . . . .	578
I.37	Pressure and ionization data from shock initiator run 71. . . . .	579
I.38	Pressure and ionization data from shock initiator run 72. . . . .	580
I.39	Pressure and ionization data from shock initiator run 73. . . . .	581
I.40	Pressure and ionization data from shock initiator run 74. . . . .	582
I.41	Pressure and ionization data from shock initiator run 75. . . . .	583
I.42	Pressure and ionization data from shock initiator run 76. . . . .	584
I.43	Pressure and ionization data from shock initiator run 77. . . . .	585
I.44	Pressure and ionization data from shock initiator run 78. . . . .	586
I.45	Pressure and ionization data from shock initiator run 79. . . . .	587
I.46	Pressure and ionization data from shock initiator run 80. . . . .	588
I.47	Pressure and ionization data from shock initiator run 81. . . . .	589
I.48	Pressure and ionization data from shock initiator run 82. . . . .	590
I.49	Pressure and ionization data from shock initiator run 83. . . . .	591
I.50	Pressure and ionization data from shock initiator run 84. . . . .	592
I.51	Pressure and ionization data from shock initiator run 85. . . . .	593
I.52	Pressure and ionization data from shock initiator run 86. . . . .	594
I.53	Pressure and ionization data from shock initiator run 87. . . . .	595

# List of Tables

1.1	Critical detonation parameters for different geometries from Radulescu (1999). . . . .	10
2.1	Observed detonation propagation velocities. . . . .	24
4.1	Channel dimensions of the dynamic planar initiator. . . . .	85
4.2	Summary table of initiation results for propane mixtures with focus near the wall. . . . .	101
4.3	Summary table of initiation results for ethylene mixtures with focus near the wall. . . . .	101
4.4	Overfill required for detonation initiation. . . . .	103
4.5	Length required for conventional driver configuration. . . . .	104
6.1	Scaling data. . . . .	142
6.2	Critical energies for different types of initiation geometries. . . . .	147
6.3	Critical values for a initiator tube versus the toroidal initiator. . . . .	149
D.1	Experimental properties of each run. . . . .	188
D.2	Experimental properties of each run (continued). . . . .	189
D.3	Wave arrival times. . . . .	190
D.4	Wave arrival times (continued). . . . .	191
D.5	Wave velocities. . . . .	192
D.6	Wave velocities (continued). . . . .	193
E.1	Experimental properties of each static planar initiator run. . . . .	252
E.2	Experimental properties of each static planar initiator run (continued). . . . .	253

E.3	Experimental properties of each static planar initiator run (continued).	254
E.4	Experimental properties of each static planar initiator run (continued).	255
E.5	Wave arrival times for each static planar initiator run. . . . .	257
E.6	Wave arrival times for each static planar initiator run (continued). . . .	258
E.7	Wave arrival times for each static planar initiator run (continued). . . .	259
E.8	Wave arrival times for each static planar initiator run (continued). . . .	260
F.1	Experimental properties of each static toroidal initiator run. . . . .	340
F.2	Experimental properties of each static toroidal initiator run (continued).	341
G.1	Experimental properties of each static planar initiator run. . . . .	378
G.2	Wave arrival times for each static planar initiator run. . . . .	379
H.1	Experimental properties of each dynamic toroidal initiator run. . . . .	422
H.2	Experimental properties of each dynamic toroidal initiator run (continued). . . . .	423
H.3	Experimental properties of each dynamic toroidal initiator run. . . . .	477
H.4	Experimental properties of each dynamic toroidal initiator run. . . . .	478
H.5	Measured velocities for each dynamic toroidal initiator run. . . . .	479
H.6	Measured velocities for each dynamic toroidal initiator run. . . . .	480
I.1	6" Shock Tube run conditions for the shock initiator tests. . . . .	544
I.2	6" Shock Tube run conditions for the shock initiator tests (continued).	545
I.3	Test section conditions for the shock initiator tests. . . . .	547
I.4	Test section conditions for the shock initiator tests (continued). . . . .	548
I.5	Energy input calculation for the shock initiator tests. . . . .	550
I.6	Energy input calculation for the shock initiator tests (continued). . . .	551

# Nomenclature

## Roman characters

$\rho_0$	Initial density of the gas
$\rho_s$	Post-shock gas density
$\tau$	Shear force
$\tilde{R}$	Universal gas constant
$A$	Area
$a$	Sound speed
$A_{tube}$	Cross-sectional area of tube
$B$	Constant
$c$	Sound speed
$c_0$	Sound speed of undisturbed gas
$c_1$	Test-section mixture sound speed
$C_p$	Specific heat capacity at constant pressure
$c_p$	Specific heat at constant pressure
$c_p$	Specific heat of constant pressure combustion
$c_{CJ}$	Sound speed at Chapman-Jouguet conditions

$D$	Chapman-Jouguet detonation wave velocity
$d$	Main (test section) tube inner diameter
$d$	Tube diameter
$d_d$	Initiator tube inner diameter
$e$	Internal energy
$E_a$	Activation energy
$E_c$	Critical energy for initiation
$E_j$	Blast initiation energy (geometry specific)
$E_s$	Blast wave initiation energy
$E_s$	Blast wave source energy
$E_{cylindrical}^*$	Critical energy for cylindrical initiation
$E_{d,corr}$	Corrected initiator energy
$E_{d,uncorr}$	Uncorrected initiator energy
$E_{planar}^*$	Critical energy for planar initiation
$E_{spherical}^*$	Critical energy for spherical initiation
$E_{toroidal}$	Energy of toroidal initiator
$h$	Enthalpy
$h_0$	Total enthalpy
$j$	Geometry index (1 for planar, 2 for cylindrical, 3 for spherical)
$L$	Characteristic length of DDT
$L_d$	Initiator tube length

$M$	Mach number
$m$	Molecular weight
$M_s$	Mach number of shock wave
$M_s^*$	Critical shock Mach number
$M_{23}$	Average Mach number between ST2 and ST3
$M_{CJ}$	Chapman-Jouguet detonation wave Mach number
$P$	Pressure
$P$	Pressure
$P_0$	Initial pressure
$P_s$	Post-shock gas pressure
$P_{CJ}$	Pressure at Chapman-Jouguet condition
$Q$	Heat release
$R$	Gas constant
$R$	Instantaneous blast wave radius
$R$	Tube inner radius
$r$	Blast wave radius
$R_0$	Explosion length
$R_0$	Universal gas constant
$R_1$	Test-section tube radius
$R_i$	Wave radius at Chapman-Jouguet conditions
$R_s$	Varying wave radius

$R_s^*$	Critical shock radius
$R_s^*$	Instantaneous radius of shock wave
$R_{cylindrical}^*$	Critical shock radius for cylindrical initiation
$R_{planar}^*$	Critical shock radius for planar initiation
$R_{spherical}^*$	Critical shock radius for spherical initiation
$T$	Temperature
$T$	Traction force
$T_0$	Total temperature
$t_c$	Characteristic time for wave to implode
$t_c$	Chemical time-scale
$T_s$	Post-shock temperature
$U$	Velocity in the laboratory frame
$u$	Velocity, lab frame
$u$	Velocity
$u_r$	Radial velocity
$U_s$	Shock speed
$u_s$	Post-shock gas speed
$u_v$	Velocity of the control volume
$U_{23}$	Average wave speed between pressure transducers P2 and P3
$U_{34}$	Average wave speed between pressure transducers P3 and P4
$U_{45}$	Average wave speed between pressure transducers P4 and P5

$U_{AVG}$	Average wave velocity in the test section
$U_{CJ}$	Chapman-Jouguet detonation wave velocity
$V$	Control volume
$v$	Specific volume
$V_d$	Volume of simple tube initiator
$V_{toroidal}$	Volume of toroidal initiator
$W$	Molecular weight
$w$	Velocity in shock-fixed coordinates
$w$	Velocity, shock-fixed frame
$\hat{n}$	Normal vector

### **Greek characters**

$\alpha$	Intermediate variable used in imploding wave analysis
$\Delta h^0$	Effective heat of reaction of mixture
$\Delta t_{23}$	Duration between wave arrival at ST2 and ST3
$\Delta x_{23}$	Distance between ST2 and ST3
$\Delta$	Induction zone length
$\Delta$	Reaction zone thickness based on peak energy release
$\delta$	Boundary layer thickness
$\delta^*$	Displacement thickness
$\ell$	Length downstream of shock front
$\gamma$	Ratio of specific heats

$l_c$	Cell length
$\lambda$	Cell size
$\lambda$	Cell width
$\mu_e$	Viscosity of gas at the outer edge of the boundary layer
$\nu$	Intermediate variable in boundary layer model
$\partial V$	Control volume surface
$\Phi$	Equivalence ratio
$\rho$	Density
$\rho_0$	Initial density
$\tau$	Induction time
$\tau_{CJ}$	Induction time at Chapman-Jouguet conditions
$\theta$	Reduced activation energy
$\xi$	Blast wave dimensionless quantity
$\xi$	Stream-tube area divergence

## Acronyms

DDT Deflagration to Detonation Transition

HC Hydrocarbon

PDE Pulse Detonation Engine

## Subscripts

1 Driven section initial state

1 Upstream or initial state

- 2 State behind incident shock wave
- 2 State immediately downstream of the wave
- 5 State behind reflected shock wave
- CJ* Chapman-Jouguet state
- CV* Constant volume explosion state
- i* Initial or CJ conditions

# Chapter 1

## Introduction

### 1.1 Motivation

Imploding shock waves have intrigued researchers for decades. In any shock, gas processed by the wave is adiabatically compressed and accelerated in the direction of shock propagation. Imploding shock geometries force the shocked gas into an ever-decreasing area that creates additional compression when compared to that of planar geometries. The end result is a positive feedback cycle: The increased compression accelerates the shock, which, in turn, acts to further increase the post-shock pressure. This cycle continues throughout the implosion process and can result in extremely high post-shock pressures and temperatures as the wave radius approaches zero.

This positive feedback cycle allows for the creation of a precisely located, high-energy-density focal region that is used in many different applications today. For example, extracorporeal shock wave lithotripsy (ESWL) is a noninvasive procedure in which imploding shocks are used to fracture kidney stones. Shock waves, created outside a patient's body, are focused on the kidney stone, and the high focal pressures crush the stone into fragments that are small enough to pass through the urinary tract on their own. The shocks are relatively weak until focused, and, while they can damage tissue near focal regions (Sturtevant, 1998), ESWL typically causes less trauma than conventional surgical procedures.

Imploding shock waves are also used to create the supercritical mass of fissile material that is required for the large energy release in nuclear weapons. The fis-

sile material is stored in a subcritical state and the imploding shock wave rapidly compresses the material, increasing its density. Because the critical mass of the fissile material is inversely proportional to the square of its density, this compression renders the material supercritical.

In this work, imploding waves are used to create a high-energy core inside of a tube filled with a combustible gas mixture, with the expectation that the resulting explosion of this core will create a blast wave capable of initiating a detonation wave. This method of detonation initiation was originally proposed as a technique capable of efficiently generating detonations in hydrocarbon-air (HC-air) mixtures for use in air-breathing pulse detonation engines (Jackson and Shepherd, 2002, Jackson et al., 2003).

A pulse detonation engine (PDE) is an unsteady propulsive device in which a combustion chamber is filled with a reactive gas mixture, a detonation is initiated, the detonation propagates through the chamber, and the product gases are exhausted (Fig. 1.1). The resulting momentum flux out of the chamber generates thrust. Quasi-steady thrust levels can be achieved by repeating this cycle periodically. It is also possible to use more than one combustion chamber operating out of phase for additional thrust.

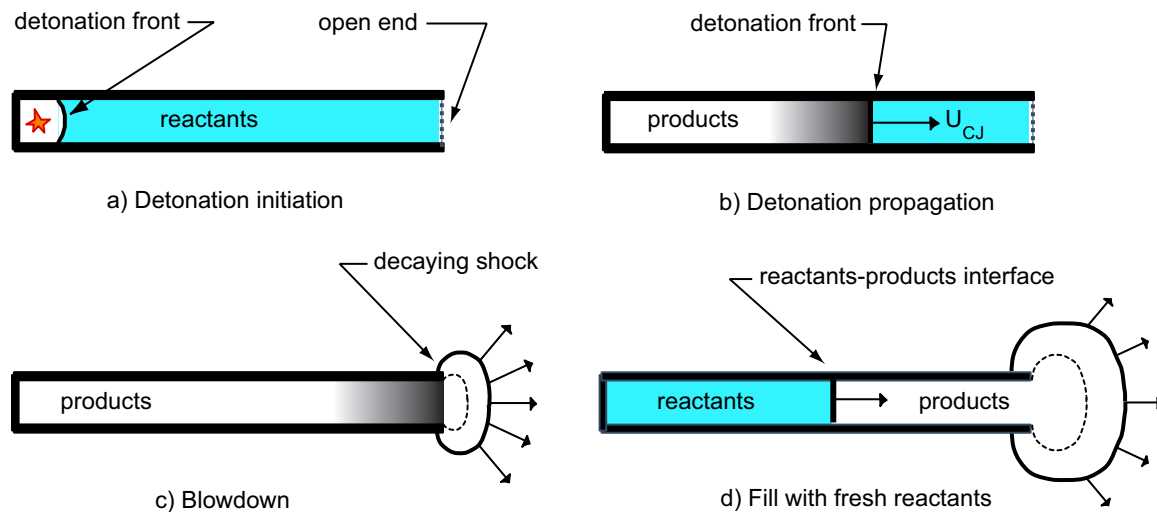


Figure 1.1: Illustration of the PDE cycle. The figure is adapted from Cooper (2004).

The concept of using pulsed combustion for propulsion was first developed over a century ago and has been used to power devices such as the V-1 “Buzz Bomb,” an early form of the cruise missile that was used in World War II (Fig. 1.2). Such devices were inefficient and loud, but were attractive due to their simple construction and low cost. Pulsed deflagration was used as the mode of combustion in early devices, as it was easily initiated in HC-air mixtures from a weak ignition source.



Figure 1.2: The V-1 “Buzz Bomb,” a World-War-II-era missile powered by a pulsed combustion engine.

Detonations are more appealing for use in a pulsed combustion engine due to the rapid reaction rate of the detonation mechanism, which enables much higher pressures and faster cycle times than are possible with a deflagration or flame. In a deflagration, diffusion of heat and species are responsible for flame propagation, resulting in maximum flame speeds of hundreds of meters per second. However, a detonation is composed of a coupled shock wave and reaction zone, resulting in detonation propagation speeds on the order of thousands of meters per second (Fig. 1.3). The shock generates sufficient post-shock pressures and temperatures to induce autoignition of the combustible mixture. The energy released in the resulting reactions then pushes the shock wave. Several detonation models and parameters are reviewed in Appendix A.

Initiating a self-sustaining detonation wave in a HC-air mixture requires significantly more energy (millijoules versus kilojoules) than initiation of a deflagration in the same mixture. For a flight system, this additional energy must be stored on-

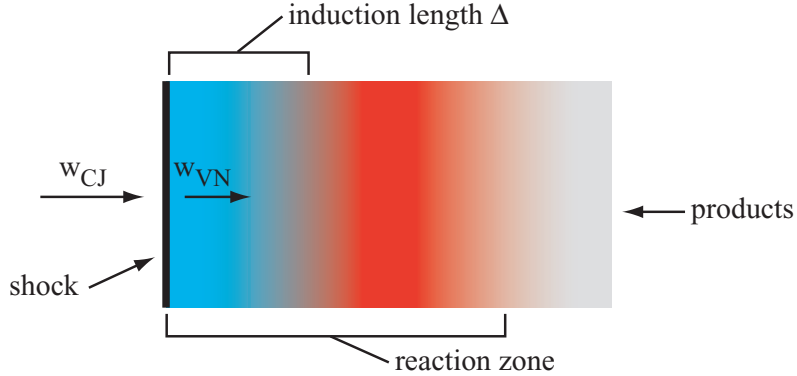


Figure 1.3: Schematic of a one-dimensional detonation wave.  $w_{CJ}$  and  $w_{VN}$  are the Chapman Jouguet and von Neumann states, respectively.

board either electrically (in batteries or capacitors) or thermodynamically (through combustion of a sensitive initiator mixture). Significant effort has been devoted to developing efficient methods of detonation initiation in HC-air mixtures. The main mechanisms of detonation initiation are discussed below, followed by a review of previous investigations on imploding shock and detonation waves that are relevant to this work.

## 1.2 Detonation Initiation Mechanisms

The literature on initiation of gaseous detonations identifies four main techniques currently used to detonate mixtures: direct initiation via a blast wave, deflagration-to-detonation transition, use of initiator tubes, and shock reflection from obstacles. The following section will briefly discuss each technique.

### 1.2.1 Direct Initiation from a Blast Wave

In direct initiation, rapid energy deposition into a mixture (e.g., via an exploding wire or high explosive) generates a strong blast wave that satisfies the condition  $(U_s/c_0)^2 \gg 1$ . The blast wave immediately begins to decay as it expands; however, for combustible mixtures, sufficiently strong blast waves will evolve into detonation

waves (Fig. 1.4). Blast waves that are too weak decay to shock waves trailed by a decoupled deflagration.

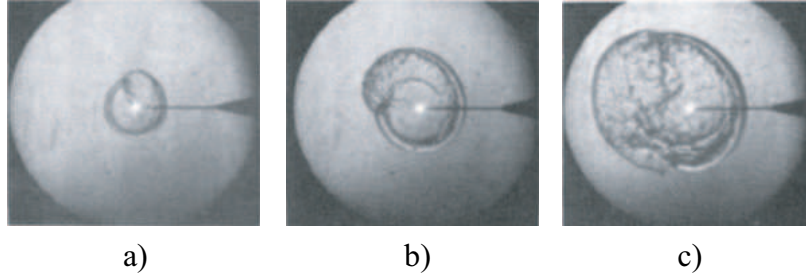


Figure 1.4: Direct initiation of a detonation wave in  $2\text{C}_2\text{H}_2 + 5\text{O}_2$  at 0.13 bar from a laser-induced spark (Bach et al., 1968). The case shown is critical: coupling occurs at the top of the blast wave in image (a) and spreads to the left, while the part of the blast wave expanding to the right of the image is a decoupled shock wave and reaction front.

Early work by Zel'dovich et al. (1956) proposed that in order for the blast wave to successfully transition to a detonation wave, adequate time must be available for the shocked gas to release its chemical energy before the wave decays too much. This led to the understanding that, for successful initiation to occur, the period from the instant of energy release until the blast wave decayed to the Chapman-Jouguet (CJ) detonation velocity  $U_{CJ}$  must be on the order of the induction time of the mixture. In terms of chemistry, blast waves that are too weak or decay too rapidly will not elevate the post-shock gas temperature for a sufficient length of time to allow the chain-branching reactions to build the necessary radical pool required for a self-sustaining detonation wave.

Expressing this coupling between the blast-wave decay and the detonation chemistry in terms of length-scales rather than time-scales leads to

$$\frac{\Delta_*}{R_*} \leq \beta_* \quad (1.1)$$

where  $R_*$  is the wave radius when it has decayed to some critical velocity  $U_*$ , and  $\Delta_*$  is the mixture-specific induction length for the wave at that velocity (Fig. 1.5). The value  $\beta_*$  is the critical ratio of reaction zone length to blast-wave radius required for

coupling of the chemical reactions to the shock wave. If the blast wave decays too rapidly or the mixture's chemical reaction is too slow, the detonation wave will fail to be created.

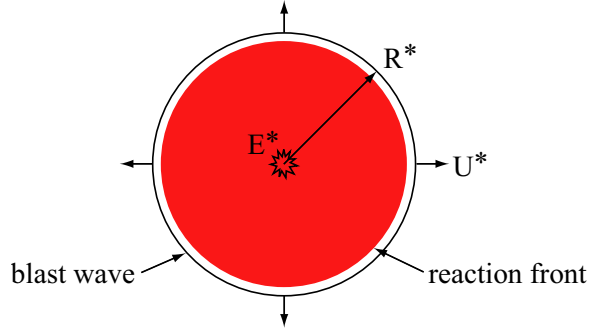


Figure 1.5: Critical blast wave parameters.

With the above criterion, the nonreactive blast wave solution (reviewed in Appendix B) can be used to solve for the source energy  $E_s$ . As discussed in Appendix B, for strong blast waves, the energy contained inside of a spherical control volume bounded by the blast wave is constant,

$$E_s = \int_V \left( e + \frac{|u|^2}{2} \right) \rho 4\pi r^2 dr = \text{constant}. \quad (1.2)$$

Nondimensionalizing this equation with characteristic dimensional parameters of initial gas density  $\rho_0$ , critical radius  $R_*$ , and critical velocity  $U_*$  leads to

$$E_s = \rho_0 U_*^2 R_*^3 \int_V \left( \hat{e} + \frac{|\hat{u}|^2}{2} \right) \hat{\rho} 4\pi \hat{r}^2 d\hat{r} = \text{constant} \quad (1.3)$$

or

$$\frac{E_s}{\rho_0 U_*^2 R_*^3} = B_1 \quad (1.4)$$

where  $B_1$  is a constant representing the nondimensionalized integral.

Solving for  $R_*$ , Eq. 1.4 can be rewritten as

$$R_* = B_2 \left( \frac{E_s}{\rho_0} \right)^{1/3} U_*^{-2/3} \quad (1.5)$$

where the constant  $B_2 = B_1^{-1/3}$ . Substituting  $R_*$  in Eq. 1.5 into Eq. 1.1 and solving for  $E_s$ ,

$$E_s \geq B_3 \frac{\rho_0 U_*^2 \Delta_*^3}{\beta_*^3} \quad (1.6)$$

where the constant  $B_3 = B_2^{-3}$ . Thus, the minimum energy  $E_{spherical}^*$  required for direct initiation of a spherical detonation wave

$$E_{spherical}^* \propto \frac{\rho_0 U_*^2 \Delta_*^3}{\beta_*^3} \quad (1.7)$$

scales with the initial density of the gas and inversely with the cube of the critical ratio  $\beta_*$ . Often, velocities on the order of  $U_{CJ}$  are chosen for  $U_*$  and either the CJ induction length  $\Delta_{CJ}$  or the cell size  $\lambda$  are used for  $\Delta_*$ . The constant of proportionality and critical ratio determined by Zel'dovich et al. (1956) were found to underpredict  $E_{spherical}^*$  by several orders of magnitude compared to experimental measurements; however, the cubic dependence of Eq. 1.7 was observed in the data.

Subsequently, a number of studies have examined this issue from experimental (Lee and Matsui, 1977, Benedick et al., 1985) and numerical (Eckett et al., 2000) points of view. Comparison of empirical models with the data by Benedick et al. (1985) showed agreement with the ‘‘surface energy model’’ (Lee et al., 1982):

$$E_{spherical}^* \cong 430 \rho_0 D^2 \lambda^3 . \quad (1.8)$$

The theoretical and numerical analysis of blast wave initiation by Eckett et al. (2000) used simplified kinetic models to find a similar expression using induction zone length

instead of cell size

$$E_{spherical}^* \cong B \rho_0 U_*^2 \theta^3 \Delta_*^3 \quad (1.9)$$

where their choice for  $U_*$  was slightly lower than the CJ value. The value  $\theta$  is the reduced-activation energy

$$\theta = \frac{E_a}{\tilde{R}T_s} \quad (1.10)$$

in which  $\tilde{R}$  is the universal gas constant and  $T_s$  is the post-shock temperature. Eckett et al. (2000) showed that this model was in reasonable quantitative agreement with experimental H<sub>2</sub>-air, C<sub>2</sub>H<sub>4</sub>-air, and CH<sub>4</sub>-O<sub>2</sub>-N<sub>2</sub> direct initiation data.

To date, most comparisons (Benedick et al., 1985, Vasilev, 1997, Eckett et al., 2000) between theory and experimental work have studied only spherical initiation into an unconfined volume. Due to lack of experimental data, limited comparison (Radulescu, 1999) between theory and experiment has been made for the planar and cylindrical geometries. A method for determination of the critical energy  $E^*$  required for initiation of the mixtures studied in Chapters 4 and 5 is now discussed.

### 1.2.1.1 Calculating Energy Required for Direct Initiation

Models for predicting critical energies of detonation initiation in spherical, cylindrical, and planar geometries can be developed from Eq. 1.7 by specifying values for  $R_*$ ,  $U_*$ , and  $\beta_*$  that are observed experimentally or that best re-create experimentally measured values for  $E^*$ . The values chosen by Radulescu et al. (2003) are used below.

In order to extend Eq. 1.7 to the planar and cylindrical geometries, consideration of the units of the  $E^*$  term is necessary. For spherical initiation energies,  $E_{spherical}^*$  has units of energy  $ML^2/T^2$ . However, for cylindrical initiation, the energy is per unit length, i.e.,  $E_{cylindrical}^*$  has units of  $ML/T^2$ . Finally, the planar initiation energy  $E_{planar}^*$  is per unit area and has units of  $M/T^2$ . To keep Eq. 1.7 dimensionally correct,

additional units of length are required such that

$$E_h^* R_*^h = A_h \rho_0 U_*^2 R_*^3 \quad (1.11)$$

where  $h = 2, 1,$  and  $0$  for planar, cylindrical, and spherical geometries, respectively.  $A_h$  accounts for both the constant of proportionality and  $1/\beta_*^3$  from Eq. 1.7. Collecting terms,

$$E_j^* = A_j \rho U_*^2 R_*^j \quad (1.12)$$

where  $j = 1, 2,$  and  $3$  for planar, cylindrical, and spherical geometries, respectively.

For a perfect gas,  $P = \rho \Re T$  and  $c^2 = \gamma \Re T$ , where  $\Re$  is the gas constant for a specific mixture. From these two relations,

$$\rho = \frac{\gamma P}{c^2}. \quad (1.13)$$

Substituting the above expression into Eq. 1.12,

$$E_j^* = A_j \gamma_0 P_0 M_*^2 R_*^j \quad (1.14)$$

where  $M_* = U_*/c_0$  is the critical Mach number.

Radulescu et al. (2003) notes that experimental work (Elsworth et al., 1984, Bull et al., 1978) in fuel-air mixtures has shown that for direct initiation in spherical geometries,

$$R_* \approx 10\lambda \quad (1.15)$$

is the approximate critical distance at which detonation initiation occurs and that the minimum shock Mach number  $M_*$  required for initiation is  $0.5 M_{CJ}$ .

With those parameters specified, it is possible to estimate the critical energy for any mixture and geometry as long as the cell size and CJ Mach number are known.

Table 1.1 summarizes the above results for the three geometries.

	Spherical	Cylindrical	Planar
j	3	2	1
$R_s^*$	$10\lambda$	$5.9\lambda$	$1.6\lambda$
$M_s^*$	$0.5M_{CJ}$	$0.5M_{CJ}$	$0.5M_{CJ}$
$E_c/\gamma P_0 M_{CJ}^2$	$1330\lambda^3$	$34.3\lambda^2$	$0.91\lambda$
$E_{s,C_3H_8-air}^*$	701.5 kJ	361.8 kJ/m	192.0 kJ/m <sup>2</sup>

Table 1.1: Critical detonation parameters for different geometries from Radulescu (1999). The bottom row shows the critical energy for a stoichiometric propane-air mixture with  $P_0 = 1$  bar,  $M_{CJ} = 5.49$ ,  $\lambda = 50$  mm, and  $\gamma = 1.4$ .

Radulescu (1999) observes that the critical energy estimate for spherical geometries agrees well with experimentally determined values (Benedick et al., 1985) for ethylene-air mixtures at atmospheric conditions. However, the predicted critical energy for stoichiometric propane-air mixtures at 1.0 bar initial pressure and 295 K initial temperature shown in Table 1.1 is more than twice the experimentally measured value (Kaneshige and Shepherd, 1997) of 283 kJ. Radulescu (1999) also notes that it is difficult to check the validity of the model for direct planar initiation since there is little experimental data available on critical energies for this geometry.

### 1.2.2 Deflagration-to-Detonation Transition

Deflagration-to-detonation transition (DDT) provides another mechanism for detonation initiation. During DDT, a weak flame or deflagration is accelerated by promoting turbulence at the flame front, often by placing obstacles in the flame path. Turbulence wrinkles the flame front, increasing its surface area. This increase results in a higher-energy release rate and sends compression waves ahead of the deflagration, which coalesce into a shock. The leading shock is strengthened by the compression wave sent from the trailing deflagration. The shocked fluid is then raised to a higher temperature, accelerating both combustion and compression wave generation.

Onset of detonation is characterized by the generation of local explosions that occur when a hot pocket of unburned gas located between the leading shock and a

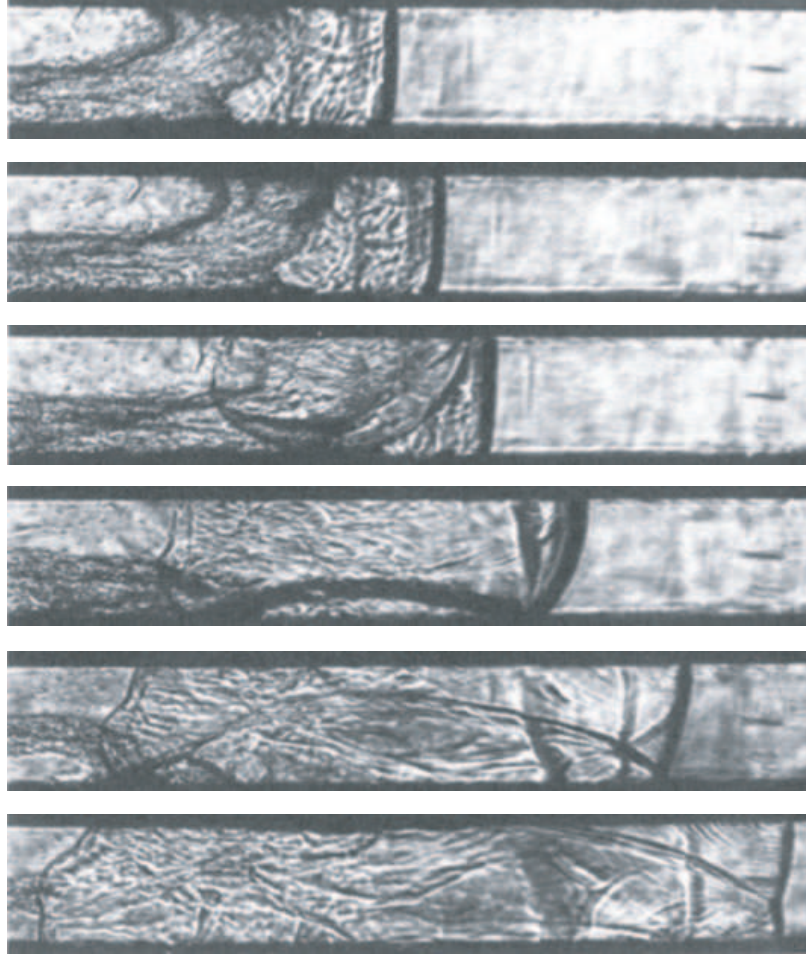


Figure 1.6: Images of the DDT process in  $2\text{H}_2 + \text{O}_2$  at 0.74 bar from Urtiew and Oppenheim (1966). In the first image, a shock wave propagates through a channel and is trailed by a flame brush. In the second image, an explosion inside the flame brush at the top of the image creates a blast wave, which couples the reaction front to the shock wave in the successive images.

trailing turbulent flame brush suddenly explodes. This explosion generates a blast wave that enables a fast flame to couple to the shock front, resulting in a detonation as shown in Fig. 1.6. Localized explosions have been found to be key in the DDT process.

Studies of DDT carried out at McGill University (Peraldi et al., 1988, Guirao et al., 1989) in tubes with obstacles have determined that, at the optimum blockage ratio  $BR = 0.43$ , the tube inner diameter  $d$  must be greater than the cell size of the mixture  $\lambda$  for a mixture to successfully undergo DDT in the tube. Subsequent work

(Lee et al., 1984, Teodorczyk et al., 1988, Kuznetsov et al., 1999) has confirmed that the ratio  $d/\lambda$  must be near or above 1. Dorofeev et al. (2000) note that the variations of this ratio can range from 0.8 to 5.1, depending on the blockage ratio.

Dorofeev et al. (2000) have examined DDT phenomena over a wide range of length-scales and mixtures in order to develop scaling parameters that characterize the onset of detonation. In particular, they suggest that the minimum distance (Dorofeev et al., 2000)  $L$  for detonation formation is dependent on the cell size of the mixture such that

$$L = 7\lambda . \tag{1.16}$$

For propane-air mixtures with cell sizes of 50 mm, this suggests a characteristic length  $L$  of 350 mm as the minimum length necessary for DDT to occur. However, this criterion appears to be necessary but not sufficient for the onset of detonation. Higgins et al. (2000) showed that even by enriching stoichiometric propane-air mixtures with oxygen and acetylene, the DDT distance could not be reduced to less than 1.5 m. Minimum DDT lengths of 1.5 m are impractical for engine technology. Caltech has also done previous work (Cooper et al., 2002) studying DDT for use with ethylene-air mixtures in short (less than 1 m) tubes and found that the DDT distance was too long to rely on DDT alone for detonation initiation.

### 1.2.3 Initiator Tubes

In practice, initiator tubes are often used to initiate detonations. An initiator tube is a tube filled with a sensitive mixture connected to a larger-diameter tube filled with a less-sensitive mixture. Low-energy ignition and DDT are used to create a detonation in the sensitive mixture. That detonation then propagates out into a larger main tube creating a decaying blast wave (Fig. 1.7). The initiation mechanism is similar to that of direct initiation described previously and the blast wave will become a detonation if it raises the mixture temperature for a sufficient length of time in order to successfully initiate a self-sustaining chemical reaction in the less-sensitive mixture.

Researchers (Mitrofanov and Soloukhin, 1965, Knystautas et al., 1982) have noticed that for situations where the initiator tube exhausts into a large, essentially unconfined volume, and both the initiator and unconfined volume contain the same mixture, the diameter of the initiator tube must exceed a certain “critical diameter” for the detonation to successfully transfer to the unconfined volume. The currently accepted value of the critical diameter  $d_c$  is

$$d_c = 13\lambda . \quad (1.17)$$

Schultz and Shepherd (2000a) have found that  $d_c$  can range from  $12\lambda$  to  $18\lambda$  when the unconfined volume contains a mixture with a cell size  $\lambda_2$  that is less sensitive than the initiator-mixture cell size  $\lambda_1$ .

In a short initiator tube, the Taylor wave will contribute to the decay of temperature and pressure behind the blast wave and can affect the initiation process. The Taylor wave is the expansion wave that brings the shocked gas to rest and originates due to boundary conditions at the far end of the initiator tube. The gradient in the Taylor wave can be reduced by extending the length of the initiator tube. This would allow the mixture in the main tube more time to release its chemical energy after it was processed by the shock wave. In addition, the pressure decay due to diffrac-

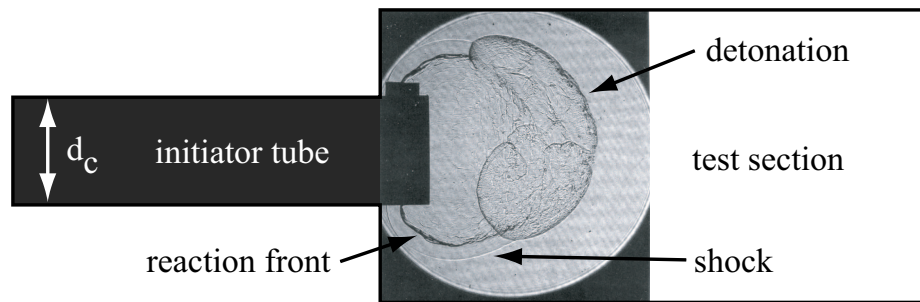


Figure 1.7: A critical case of detonation initiation in  $2\text{H}_2 + \text{O}_2$  at 1 bar from an initiator tube. The image is from Schultz and Shepherd (2000a). The portion of the wave along the tube axis is a detonation. The regions of the wave which have undergone more diffraction have decayed to a decoupled shock and reaction front.

tion and pressure increases due to reflection may play a significant role in initiator operation.

Kuznetsov et al. (1997) conducted experimental and numerical studies in an effort to correlate the transmitted wave overpressure and duration to the critical limits of initiation. They identified the ratio of the length of the initiator tube to the chemical length-scale of the mixture to be initiated as a key factor in initiator-tube effectiveness. The other important factor was the strength of the shock wave transmitted into the test section by the initiator tube. The results show that as initiator length is increased, the transmitted wave strength can be decreased to a lower limit and successful initiation can still occur. The critical strength of the transmitted wave increases with decreasing initiator length, implying that a higher reaction rate is necessary to initiate in a shorter time. Murray et al. (2003) have also recognized this effect and used experimental data to identify initiator length, transmitted wave strength, and initiator diameter as the key parameters in initiation. They found the same relationship as Kuznetsov et al. and also showed that increasing the initiator diameter decreases the necessary initiator length.

### **1.2.3.1 Initiator Tubes with Confinement**

When initiating a detonation inside of a larger-diameter tube (rather than an unconfined space), initiator tubes can take advantage of the proximity of the tube walls to enhance detonation transmission. The wave diffracting into the test section will reflect from the tube walls and generate regions of higher temperature and pressure than would occur were the tube walls not present. Often, the temperature and pressure in these regions are high enough to create a detonation kernel that then spreads throughout the tube. Thus, the confinement of the tube walls can reduce the minimum amount of energy required for initiation.

Work by Breitung et al. (2000) in hydrogen-air-steam mixtures has established critical Mach numbers for the shock waves propagating into the test section that predict if and how initiation will occur with initiator tubes. Transmitted shocks with Mach numbers greater than 1.4 are expected to cause ignition near obstacles

or tube walls. Shock waves with Mach numbers between 1.2 and 1.4 could cause flame ignition in reflections from obstacles or walls. Shock Mach numbers less than 1.2 are not thought to cause flame ignition, even when reflected off the tube walls or obstacles.

#### **1.2.4 Obstacle Reflection**

The reflection of shock waves from shock-tube end walls is a well-established method of initiation (Gilbert and Strehlow, 1966, Meyer and Oppenheim, 1971) and is the primary technique used to measure ignition delay times. Several studies have also shown that reflection of a planar incident shock wave from a concave end wall will focus the reflected wave (Sturtevant and Kulkarny, 1976, Nishida et al., 1986, Nishida, 1989, Isumi et al., 1994) and that the temperatures and pressures at the gas-dynamic focus can be sufficient for initiation of the post-shock mixture (Borisov et al., 1989, Chan et al., 1989, Gelfand et al., 1991, 1997, Bartenev et al., 2000, Gelfand et al., 2000).

#### **1.2.5 The Importance of Temperature**

In direct initiation, maintaining a sufficient chemical reaction rate for a sufficient duration was determined to be key to the success of detonation initiation. In geometries with confining walls, initiator tubes have been shown to be more effective at initiating detonations by utilizing shock reflection from tube walls to generate localized regions of high temperature that are capable of initiating detonations. In less-sensitive mixtures, these regions of high energy density are not always capable of directly initiating the mixture, but can accelerate the DDT process. Recent research (Jiang and Takayama, 1998, Murray et al., 2000, Gelfand et al., 2000) as well as this dissertation has focused on developing and enhancing the strength of these regions in an effort to initiate detonations in less-sensitive mixtures.

The toroidal and shock-implosion initiators, described in the following chapters, attempt to improve on previous initiation methods by using an imploding wave to

directly generate a volume of shock-heated gas with a high-temperature core. If heated sufficiently, the core then explodes, creating a blast wave that can initiate a detonation. It is expected that the success of the concept is directly dependent on the volume of gas and the temperature distribution inside this volume. These factors are difficult to quantify without detailed characterization of the focal region in each experimental configuration and are considered outside the scope of this work. However, the energy input to each initiator will be compared to the minimum energy required to initiate a detonation in the mixtures of interest.

### 1.3 Previous Research on Imploding Waves

This section reviews earlier work on imploding waves. For clarity, the literature has been separated into three sections: imploding shock waves, imploding detonation waves, and imploding toroidal waves.

#### 1.3.1 Imploding Cylindrical and Spherical Shock Waves

The imploding shock solution was first solved analytically in a self-similar fashion for cylindrical and spherical geometries by Guderley (1942) and later reworked by others (Butler, 1954, Sedov, 1959, Stanyukovich, 1960, Dyke and Guttman, 1982, Ponchaut, 2005) seeking to improve upon its accuracy. The solution assumes that the trajectory of the imploding and reflected shocks follow a power law. As the shock radius decreases to zero, the solution becomes singular. An approximate solution, referred to as the Chester-Chisnell-Whitham (CCW) theory, was found for shock-wave propagation in channels with varying cross-sectional areas by Chester (1954) and Chisnell (1955) and independently by Whitham (1958).

Perry and Kantrowitz (1951) first published experimental observations of the high-temperature focal region created by such an implosion. They (Perry and Kantrowitz, 1951) used a shock tube with a teardrop-shaped obstruction to shape a planar shock wave into a cylindrically imploding wave. While they did not obtain pressure measurements, they were able to image luminosity emitted from ionized argon at the

focus of the imploding shock, indicating the presence of high-temperature gas.

Since the work of Perry and Kantrowitz (1951), several similar experiments have been used to further characterize imploding shock waves. The facility of Wu et al. (1980) tested the ability of differently shaped teardrop obstructions to create symmetrical implosions. Out of the three obstructions tested (a logarithmic spiral, a five-element contraction, and a three-element conical contraction), the three-element conical contraction was found to provide the best performance, and the results agreed well with the CCW theory except when the imploding shock radius became very small. Matsuo and Nakamura (1981) used explosive cylindrical PETN shells to create imploding cylindrical shock waves in air. The shock waves created with this technique were of sufficient strength to ionize the air. Wave trajectories were measured with ionization probes and were found to agree with Guderley's work (Guderley, 1942). More recently, an annular vertical shock tube (Hosseini et al., 1998, 2000) was constructed that uses a rubber sheet under pressure to separate the driver gas from the driven gas. Instead of rupturing a diaphragm, the pressure supporting the rubber sheet is relaxed and the sheet retracts, creating an imploding, ring-shaped shock wave in the test section. The facility is intended to study the stability of imploding shock waves.

All previous experimental results on imploding shock waves (Perry and Kantrowitz, 1951, Wu et al., 1980, Matsuo and Nakamura, 1981, Takayama et al., 1987) have indicated that disturbances in the wave front (due to diaphragm opening or shock tube supports) become amplified as the wave implodes, resulting in growing nonuniformities at small radii. Numerical simulations of imploding shock waves (Sod, 1977, Fong and Ahlborn, 1979, Wang, 1982, Schwendeman, 2002) show growth of disturbances imposed on the boundary or initial conditions of the flow.

### 1.3.2 Imploding Cylindrical and Spherical Detonation Waves

Zel'dovich (1959) also observed that the implosion process would result in additional compression behind detonation waves, noting that the release of energy from the detonation reaction would eventually become negligible compared to the energy imparted

to the flow by shock processing in the final stages of the implosion process. Lee and Lee (1965) generated cylindrically imploding detonation waves in acetylene-oxygen mixtures and used pressure transducers and streak photographs to characterize the implosion process. They also extended the model of Whitham (1958) to detonation waves and found good agreement between their experiment and theory, measuring focal pressures of 18 times  $P_{CJ}$ .

Terao (1983), Terao and Wagner (1991), and Terao et al. (1995) have also performed studies on imploding detonation waves in spherical and cylindrical geometries with propane-oxygen mixtures and have characterized the imploding wave with ionization probes, pressure transducers, and soot foils. In their experiments, it was found that the experimentally measured wave acceleration was lower than that predicted by the theory of Guderley (1942), but that the post-detonation pressures were higher than theory. Terao and Wagner (1991) attributed such differences to the proximity of the experiment walls to the implosion.

A number of researchers have also attempted to measure the temperature near the focus of imploding detonation waves. Knystautas et al. (1969) inferred the temperature at the focus of a cylindrically imploding, acetylene-oxygen detonation wave using spectroscopic techniques and used Wein's Law to estimate that the maximum temperature was on the order of 200,000 K. Subsequent studies by Roberts and Glass (1971) and Roig and Glass (1977) measured focal temperatures of 4,500-6,000 K in hydrogen-oxygen mixtures. They (Roig and Glass, 1977) also suggested that Knystautas et al. (1969) may have incorrectly applied Wein's Law in arriving at such a large focal temperature. Further work by Saito and Glass (1982) with the apparatus of Roig and Glass (1977) measured peak temperatures of 10,000-13,000 K and also used PETN explosive shells around the periphery of the chamber to boost the measured temperature to 15,000-17,000 K. Matsuo et al. (1985) continued their previous experimental study, taking spectroscopic measurements of the temperature of cylindrically imploding waves in air. They found that the maximum temperature measured was approximately proportional to the square root of the initiation energy and they measured temperatures that ranged from 13,000-34,000 K, depending on the

initiation energy. They noted that these temperatures were 3,500-9,500 K lower than temperatures that would be estimated from the shock propagation speed alone. Terao et al. (1995) have also used a laser-light scattering method to measure temperatures of  $10^7$ - $10^8$  K at the focus of spherical imploding detonation waves in propane-oxygen mixtures from an initial wave radius of 500 mm.

Simulations of imploding detonation waves by Devore and Oran (1992) and Oran and Devore (1994) observed that, when disturbances were imposed on the wave from a tube support or similar obstacle, the imploding detonation became at least as unstable as shock waves under similar conditions, if not more so. This was in contrast to conclusions inferred from the experimental work of Knystautas and Lee (1971), who determined that imploding detonations were relatively stable.

### 1.3.3 Imploding Toroidal Waves

While all of the previously mentioned research was concerned with either cylindrically or spherically imploding shock waves, several studies have also been performed with toroidally imploding waves issuing from annular orifices. Simulations by Jiang and Takayama (1998) in air showed that a diffracting toroidal wave discharged from an annular gap created a region of intense shock-focusing when the toroidal waves merged at the axis of symmetry.

Murray et al. (2000) quantified the effectiveness of this geometry on detonation initiation while conducting experiments measuring the transfer of a detonation wave from a smaller-diameter initiator tube to a larger-diameter test-section tube. The initiator tube and test-section tube were both filled with a hydrogen-air mixture, and several different obstacles were placed between the two tubes. The effect of these obstacles on the detonation wave transmission was measured in terms of its transmission efficiency. Values of the transmission efficiency above unity represent situations where the obstacle allowed detonation transfer from the initiator tube to the test-section tube for mixtures with larger cell sizes than in the case where no obstacles were used. Conversely, values of the transmission efficiency below unity

required that smaller cell size mixtures be used (compared to the no-obstacle case) to transfer the detonation wave between the initiator tube and the test-section tube.

When using obstacles consisting of a circular plate, Murray et al. (2000) noted a substantial increase in the transmission efficiency. The obstacle created an annular orifice that generated an imploding toroidal shock wave downstream of the obstacle, which was trailed by a deflagration. Murray et al. (2000) demonstrated with numerical simulations that the focus of this imploding toroid was a region of high energy density, which was responsible for reinitiation of a self-sustaining detonation wave. Specifically, Murray et al. (2000) determined that the annular orifice allowed successful detonation transmission for tubes with diameters 2.2 times smaller than cases where no obstacles were located at the interface.

Improving on this concept, a detonation initiator has been developed (Jackson and Shepherd, 2002, Jackson et al., 2003) that successfully detonates propane-air mixtures inside a detonation tube using an imploding toroidal wave propagated into the propane-air mixture from the tube walls. In order to generate the imploding wave, the toroidal initiator uses a single spark plug and a small amount of acetylene-oxygen gas.

Recent numerical simulations (Li and Kailasanath, 2003b, 2005) proposed to improve upon this concept by using an imploding toroidal shock wave (instead of an imploding detonation wave) driven by jets of air or fuel. In particular, Li and Kailasanath (2005) computed that an imploding annular jet with a Mach number of unity, a pressure of 2.0 bar, and a temperature of 250 K (corresponding to a total pressure and temperature of 3.8 bar and 470 K, respectively) was able to initiate a detonation in a stoichiometric ethylene-air mixture inside of a tube. However, the subsequent experimental work of Jackson and Shepherd (2004) with a design similar to that specified by Li and Kailasanath (2005) was unable to initiate ethylene-air mixtures, even using sonic jets with total pressures and temperatures in excess (16.8 bar and 790 K) of those used in the numerical simulations (Li and Kailasanath, 2005). Simulations (Yu et al., 2004, Wang et al., 2005) have shown that the reflection of the primary explosion from the contact surface (separating the gas in the tube from

the gas driving the implosion) creates a secondary implosion that is responsible for creation of high-pressures and -temperatures leading to detonation initiation in this geometry.

## 1.4 Outline

This thesis contains descriptions of six related experimental studies and associated analysis that were intended to characterize the process of detonation initiation of gaseous mixtures inside tubes via imploding toroidal waves. More specifically, imploding detonation waves and imploding shock waves were used to initiate detonations in stoichiometric ethylene-oxygen-nitrogen and propane-oxygen-nitrogen mixtures with varying nitrogen dilutions inside of a 76 mm inner-diameter tube.

The design and testing of a device capable of initiating a toroidal detonation wave from a single spark, an array of small-diameter channels, and a small amount of acetylene-oxygen gas spans several chapters. Chapter 2 describes a study of detonation wave propagation through small-diameter tubing, where tube diameters on the order of the induction zone length of the detonation wave are considered small. By determining the minimum tube diameter that would support detonation propagation for a given mixture, the size of the channels used in the toroidal initiator could be appropriately sized to maintain a stable detonation wave without using an excessive amount of acetylene-oxygen gas.

Chapter 3 presents two prototypes, the static planar initiator and the static toroidal initiator, which are capable of creating large-aspect-ratio planar detonation waves and imploding toroidal detonation waves, respectively, in sensitive HC-oxygen-nitrogen mixtures. Both of these initiators were stepping-stone designs in the development of the dynamic planar and dynamic toroidal initiators (Chapter 4), which generated wave geometries that were identical to those of their static counterparts, but were able to do so in insensitive HC-air mixtures.

The effectiveness of toroidal imploding shock waves at detonation initiation is examined in Chapter 5. Imploding shock waves were created using a shock tube and

focused inside of a tube filled with HC-oxygen-nitrogen mixtures.

In Chapter 6, the minimum input energies to each device required to achieve a detonation inside the test-section tube are estimated for the dynamic toroidal initiator and the shock implosion initiator. These input energies are then compared to the energies required to directly initiate planar detonations inside of a tube and spherical detonations in an unconfined volume. Some conclusions are also drawn from the data about the enhancement of confinement on the process of detonation initiation from a blast wave.

Finally, Chapter 7 contains a summary of the work, reflections on the effectiveness of imploding toroidal waves as a form of detonation initiation, and also suggestions for continued research in this area. Several appendices, located at the end of this dissertation, contain design drawings of each facility, experimental parameters for each test, and all of the experimental data.

## Chapter 2

# Detonation Propagation Through Small Tubes

### 2.1 Introduction

This chapter presents an experimental study of detonation wave propagation in tubes with inner diameters (ID) comparable to the mixture cell size. Propane-oxygen mixtures were used in two test section tubes with inner diameters of 1.27 mm and 6.35 mm. For both test sections, the initial pressure of stoichiometric mixtures was varied to determine the effect on detonation propagation. For the 6.35 mm tube, the equivalence ratio  $\phi$  (where the mixture was  $\phi \text{ C}_3\text{H}_8 + 5\text{O}_2$ ) was also varied. Detonations were found to propagate in mixtures with cell sizes as large as five times the diameter of the tube. However, under these conditions, significant losses were observed, resulting in wave propagation velocities as slow as 40% of the CJ velocity  $U_{CJ}$ . A review of relevant literature is presented, followed by experimental details and data. Observed velocity deficits are predicted using models that account for boundary layer growth inside detonation waves.

### 2.2 Previous Relevant Work

In published literature, several different modes of detonation wave propagation below the CJ wave velocity have been observed including sub-CJ detonation waves, low-velocity detonation waves, and galloping waves. A brief description of each mode and

a summary of relevant literature is given below.

Mode	Propagation Velocity	Reference
Overdriven detonation	$> 1.00 U_{CJ}$	Sharpe (2001)
Typical detonation	$0.90 - 1.00 U_{CJ}$	Lewis and von Elbe (1961)
Sub-CJ detonation	$0.70 - 0.90 U_{CJ}$	Paillard et al. (1979)
Low-velocity detonation	$0.45 - 0.60 U_{CJ}$	Manzhalei (1999)
Galloping detonation	$0.50 - 1.50 U_{CJ}$	Lee et al. (1995)

Table 2.1: Observed detonation propagation velocities.

### 2.2.1 Detonations and Sub-CJ Detonations

Detonations and sub-CJ detonations propagate at velocities at or slightly below  $U_{CJ}$ , but are still thought to have a sonic surface behind the leading shock wave (Brailovsky and Sivashinsky, 2000). The sonic surface is a region of flow behind the reaction zone where the flow becomes locally sonic. Thus, the detonation wave is supersonic relative to products behind the sonic surface and disturbances behind the sonic surface cannot affect the wave propagation. However, disturbances in front of the sonic surface are expected to affect the detonation propagation.

Kistiakowsky et al. (1952a) experimentally observed that decreasing the tube diameter resulted in a decrease in detonation velocity in cyanogen-oxygen mixtures. Four different tube inner diameters were used (10, 5, 2.5, and 1.2 cm) with two different cyanogen-oxygen mixtures. The initial pressure was not reported but is assumed to be 1 atm. The smallest diameter tube exhibited a 3% detonation velocity decrease when compared to the largest diameter tube. Other studies by Kistiakowsky et al. (1952b) and Kistiakowsky and Zinman (1955) observed velocity deviations from CJ of up to 2% in acetylene-oxygen mixtures with varying tube diameters.

Fay (1959) attributed these velocity differences to boundary layer growth in the detonation wave resulting in flow divergence behind the shock wave. This flow divergence causes less energy to be released in the reaction zone before the sonic state is attained, underdriving the detonation wave and causing wave propagation at a

decreased velocity. Fay developed a model to quantify this boundary layer effect and found that the model agreed well with selected experimental data from Kistiakowsky and Zinman (1955).

Dove et al. (1974) extended Fay's model by computing velocity deficits in small diameter tubes using a quasi-one-dimensional ZND model with reaction kinetics and allowing for cross-sectional area changes in the flow. Hydrogen-oxygen gas mixtures were investigated and numerical results were compared with experimental data. It was found that the computational results underpredicted the measured velocity deficits.

Paillard et al. (1979) investigated hydrogen azide detonations in 1, 2, 5, and 10 mm ID tubes over a pressure range of 1-25 torr. Deficits of 30% were observed at the lowest pressures in the smallest diameter tubes. Wall heat fluxes were also recorded. For larger tubes and higher pressures, it was found that the CJ theory modeled the flow well; however, near propagation limits, the theory failed. They concluded that, in order to explain the velocity deficits, it was necessary to take into account kinetic parameters in the detonation structure.

Vasil'ev (1982) constructed an experiment capable of simultaneously measuring the detonation velocity in several differently sized rectangular channels. His study was primarily concerned with establishing detonation limits in stoichiometric hydrogen-oxygen and acetylene-oxygen mixtures, and detonation failure was assumed to occur at the onset of the galloping regime. However, one of his streak camera photographs appears to have captured a sub-CJ detonation, a low-velocity detonation, and a galloping wave propagating relative to each other in separate channels.

Dupre et al. (1986) studied the propagation of marginal detonations in lean hydrogen-air mixtures using a facility consisting of five tubes of decreasing diameter connected by 180° bends. The design was such that marginal waves propagating through the experiment would eventually fail as the wave propagated through increasingly smaller diameter tubing. Velocity deficits of up to 10% were observed. Dupre et al. (1986) attempted to fit the experimental data with a model based on the work of Fay (1959) and Dabora (1963) and found that the experimental data had a large amount of scatter but generally followed the same trend as the model. The scatter

in the data was probably due to the presence of 180° bends and short sections of Shchelkin spiral used in between tube diameter transitions.

In numerical work, Zel'dovich et al. (1987) added friction and heat loss terms to the equations of motion to model losses behind the detonation wave. Using the extended ZND theory, they calculated the effect of the friction on the flow. Their results were qualitative; however, they did note that detonation velocity decreased with increased friction. Frolov and Gelfand (1991) and Agafonov and Frolov (1994) also used frictional and heat losses to model tube size effects and predict detonation limits.

### 2.2.2 Low-Velocity Detonations

Low-velocity detonations have the lowest propagation velocity of any observed detonations and consist of a complex composed of a leading shock wave followed by a flame, which maintains a constant distance behind the shock front. While flame propagation velocities in quiescent gas are typically much slower (by several hundred meters per second) than the shock propagation velocity, the flame in the complex propagates into gas which has been accelerated by the shock wave. Thus, for the flame to remain a fixed distance behind the shock wave, the sum of the flame speed (in a quiescent mixture) and the post-shock flow velocity must equal the shock propagation velocity.

Manzhalei (1999) notes that in this situation, tube walls will induce a boundary layer in the post-shock flow. Discussed in detail in Section 2.4.1, the boundary layer growth removes mass from the freestream flow and forces it to expand as if the tube walls were diverging. This expansion results in decreasing post-shock flow velocity with increasing distance from the shock wave and allows the flame to stabilize some distance behind the wave. While low-velocity detonations are supersonic with respect to the reactant mixture, the post-shock flow is entirely subsonic. This is in contrast to the sonic condition present at the end of a CJ detonation wave.

Experiments by Manzhalei (1992, 1999) observed a low-velocity detonation regime while propagating detonations through capillary tubes with diameters of 0.6, 1.0, and

2.1 mm in stoichiometric acetylene-oxygen gas mixtures by using a photomultiplier to detect chemiluminescence. Wave velocities as low as  $0.50 U_{CJ}$  were measured for initial pressures of 0.05 atm in the 0.6 mm tube. These velocities were so low that he did not believe that ignition from adiabatic shock compression alone was possible and, instead, attributed the chemiluminescence to a deflagration or flame trailing behind the shock wave. The location of the luminous front was determined to exist at a constant value ranging from three to eight tube diameters behind the preceding shock wave.

Manzhalei also found that the low-velocity detonation regime and the more typically observed multifront detonation regime were separated by an additional regime characterized by galloping detonation waves. He observed that the boundary between the low-velocity regime and the galloping regime exists when the induction time of the shocked gas equals the time necessary for the gas to travel between the shock wave and flame front.

Numerical simulations by Brailovsky and Sivashinsky (2002, 2000) have used friction factors and heat loss terms to develop a model that solves for sub-CJ detonations, low-velocity detonations, and subsonic combustion. Their model solves for sub-CJ detonations using the ZND equations and a generalized CJ condition, which assumes that the solution remains nonsingular through the sonic surface. When, as in the case of the low-velocity detonation regime, the CJ criterion cannot be satisfied, Brailovsky and Sivashinsky (2002) instead assumed that the absolute particle velocity is zero at the end of the reaction zone in order to obtain a solution.

Simulations by Dionne et al. (2000) further investigated the effect of using a friction source term in the momentum equation. They solved the steady ZND structure with the generalized CJ criterion and used the criterion of Brailovsky and Sivashinsky (2000) to solve for the flow when the generalized CJ criterion could no longer be met. They also performed unsteady numerical simulations in the low-velocity detonation regime. Both Dionne et al. (2000) and Brailovsky and Sivashinsky (2000) determined the detonation velocity deficit as a function of flow friction, or drag, and found that multiple detonation velocities were possible for some unique values of friction.

Quasi detonations in tubes with dense obstacle fields along the tube wall have been experimentally measured to propagate as slowly as  $0.40 U_{CJ}$  (Teodorczyk et al., 1988). The detonation wave was observed to fail as it diffracted around each obstacle and then to reinitiate after reflecting from the tube wall. It was unclear whether the reinitiation was due to autoignition of gas behind the reflection of the failing wave or due to vortex mixing in this region; however, in experiments where this wave reflection was damped by wire mesh, reinitiation was not observed. Strictly speaking, it may not be valid to classify these results as low-velocity detonations or sub-CJ detonations since the wave continuously fails and reinitiates rather than propagating at a relatively constant, yet diminished, velocity. However, in a global sense, the waves in each experiment (Teodorczyk et al., 1988) were observed to propagate at average velocities below that of  $U_{CJ}$ .

### 2.2.3 Galloping Detonations

Galloping detonations are characterized by detonation propagation velocities that oscillate between a low ( $0.5 U_{CJ}$ ) and a high ( $1.5 U_{CJ}$ ) velocity. The end result is average wave speeds between  $0.8 - 1.0 U_{CJ}$ . The typical oscillation period is on the order of 100 tube diameters so it is possible for measurements with insufficient resolution to misidentify galloping detonations as underdriven stable detonations.

Edwards et al. (1970) used a microwave interferometer to observe propagation of such detonations in large-aspect-ratio rectangular channels ( $76 \text{ mm} \times 6.4 \text{ mm} \times 6 \text{ m}$  long). Using the wave velocity as a measure of stability, they found that it was necessary to observe the waves over long distances to ensure that they were stable and would not fail. In particular, their facility required about 100 tube widths to damp out the overdrive from their initiator and another 100 tube widths to determine the stability of the marginal wave. Edwards et al. (1971) continued the research, using the microwave interferometer in a rectangular ( $23 \text{ mm} \times 10 \text{ mm} \times 30 \text{ m}$ ) channel to obtain finely resolved velocity measurements of “cyclic-velocity” or galloping waves.

More detailed interferometry work on detonations was conducted by Lee et al.

(1995), who tested and characterized a large number of hydrocarbon mixtures using high-resolution velocity measurements in tubes. Several modes of detonation propagation were identified including stable detonations, rapidly fluctuating detonations, stuttering detonations (a mild form of galloping detonations), galloping detonations, low-velocity stable detonations, and failed detonations. Stable low-velocity, the slowest observed mode of detonation propagation, traveled at speeds as low as  $0.5 U_{CJ}$ . Similar low-velocity wave propagation ( $0.5 U_{CJ}$ ) was also observed in interferometry work by Haloua et al. (2000), who classified these waves as fast flames.

### 2.2.4 Shock Waves in Small Diameter Tubes

Work by Brouillette (2003) on shock wave propagation in small diameter tubes has shown that viscous and heat losses to the wall can significantly affect the flow. He developed shock jump conditions that included terms for shear stresses and heat flux at the wall and found that when solving the jump conditions for a given Mach number, accounting for momentum and heat losses resulted in higher post-shock pressures and lower particle velocities than flows with no losses. Experiments conducted in a small-scale shock tube qualitatively agreed with his model and demonstrated the importance of considering loss terms when working in such small scales.

## 2.3 Experimental Setup

The experiment consisted of an initiator tube attached to a smaller diameter test section tube. The initiator tube (Schultz, 2000) had a 38.1 mm ID and was 1.5 m long. One end flange of the detonation tube contained a spark plug connected to an electric-discharge system with 30 mJ stored energy. A 30.5 cm long section of Shchelkin spiral with a wire diameter of 4 mm and a coil spacing of 11 mm was located just downstream of the spark plug to promote DDT. The initiator tube contained two PCB pressure transducers (model 113A26) that were spaced 0.42 and 0.82 m from the ignition point in order to detect that a detonation was successfully initiated. The

transducer closest to the ignition point was referred to as P0 and the further one was referred to as P1.

The initiator-tube end flange opposite the spark plug was connected to the smaller diameter test section tube. Two different test section tubes (1.27 mm and 6.35 mm ID) were used and are described below. Each test section tube protruded some distance (given below) into the initiator tube in a cookie-cutter-style setup to mitigate the effects of wave reflection off the initiator tube end flange. Each test section tube was fitted with four PCB pressure transducers (model 113A26) to facilitate wave speed and pressure measurements. The transducers were labeled P2, P3, P4, and P5 with increasing distance from the spark point.

Prior to each run, the initiator and test section tubes were evacuated below a pressure of 0.2 mbar and then filled with the test mixture using the method of partial pressures. To ensure mixture homogeneity, the mixture was recirculated in the experiment for 15 minutes prior to each run using a bellows-style pump.

### 2.3.1 1.27 mm Inner Diameter Test Section

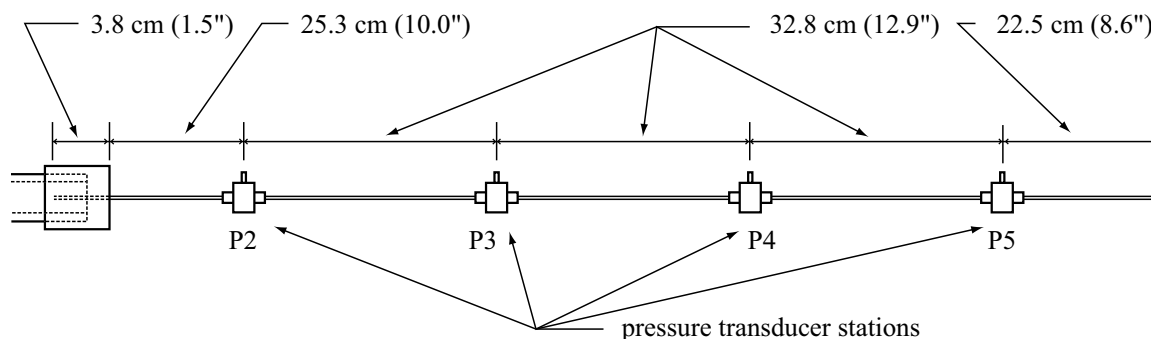


Figure 2.1: Relevant dimensions of the 1.27 mm ID test section are shown. The end of the initiator tube is shown on the left side of the figure. A more detailed drawing of the pressure transducer station is shown in Fig. 2.2.

A schematic of the 1.27 mm ID test section is shown in Fig. 2.1. It consisted of five sections of 1.27 mm ID stainless steel tubing (3.18 mm outer diameter) interrupted by pressure transducer stations. The total length of the test section was 1.50

m, corresponding to 1181 tube diameters. Each tube length was 25.4 cm long and connected to pressure transducer stations using Swagelok fittings. The total distance in between each pressure transducer, accounting for the length of the fittings, was 32.8 cm.

Each pressure transducer station was 25 mm long with an ID of 3.20 mm. A 0.76 mm diameter hole located in the middle of each section was connected to a pressure transducer. Due to machining constraints, there were other ID variations in the pressure transducer station that are illustrated in the enlarged view in Fig. 2.2. The 1.27 mm ID test section protruded 3.8 cm into the initiator tube.

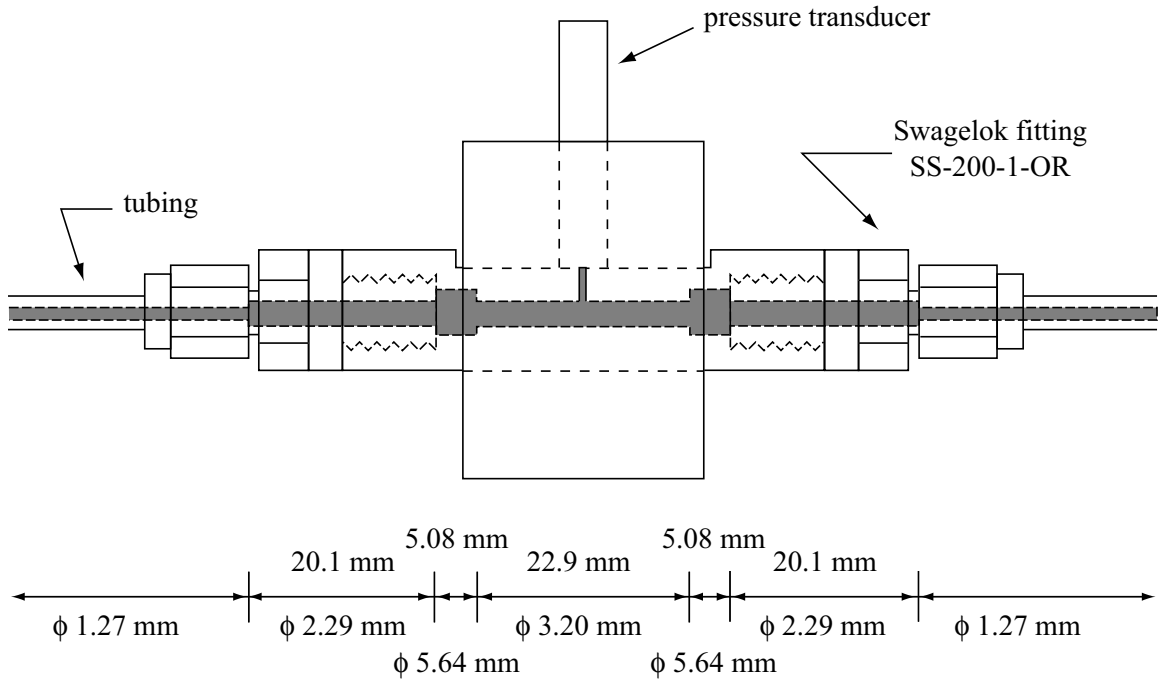


Figure 2.2: An enlarged drawing of the 1.27 mm ID tube pressure transducer station is shown. The volume filled with combustible mixture is shaded grey and the dimensions given correspond to this volume.

Stoichiometric propane-oxygen mixtures were used during testing of the 1.27 mm ID tube. Initial pressures of those mixtures ranged from 0.13 to 1.80 bar. Lower pressures were tested as well, but detonation initiation did not occur below 0.13 bar.

### 2.3.2 6.35 mm Inner Diameter Test Section

The 6.35 mm ID test section (Fig. 2.3) consisted of an uninterrupted length of steel tubing 1.82 m long (287 tube diameters). Four pressure transducers were spaced 0.508 m apart and measured the pressure through 1.5 mm diameter holes drilled in the tube wall. The 6.35 mm test section protruded about 10 cm into the initiator tube.

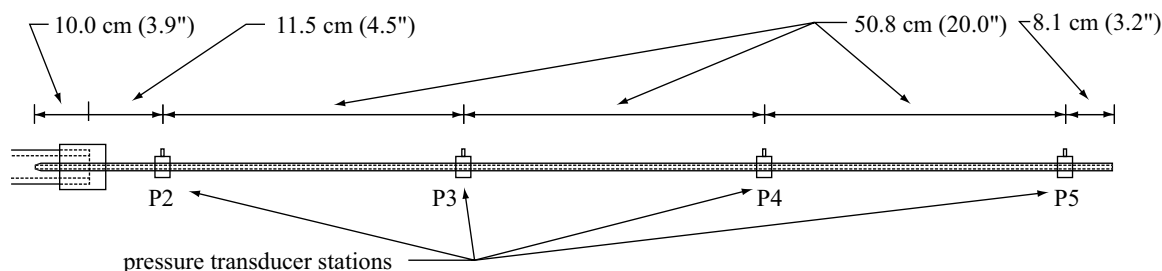


Figure 2.3: Relevant dimensions of the 6.35 mm ID test section are shown. The end of the initiator tube is on the left side of the figure. An enlarged view of the pressure transducer is not shown because there were no internal diameter changes in this test section.

Propane-oxygen mixtures were tested in the 6.35 mm test section. For stoichiometric mixtures, the pressure was varied from 0.15 to 1.00 bar. The equivalence ratio of the propane-oxygen mixture was also varied from 0.3 to 3.0 while keeping the initial pressure fixed at 1.00 bar.

## 2.4 Analysis and Theory

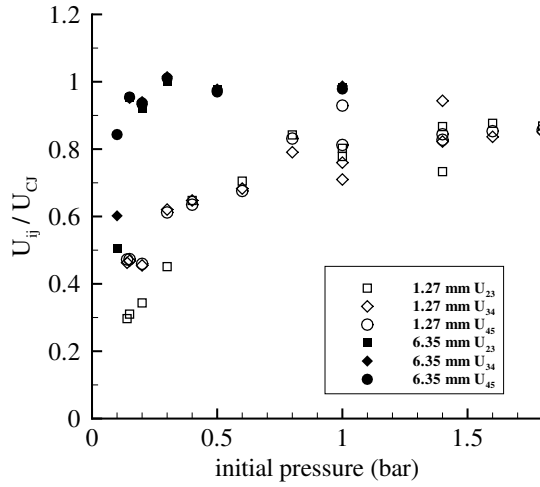
All experimental data, including tabulated run conditions, wave velocities, and pressure histories are available in Appendix D. The average wave velocity in between each pressure transducer station was calculated by dividing the distance between adjacent stations by the difference in the arrival times of the wave. Since there were four pressure transducer measurements in the test section, this technique yielded three velocity measurements in the test section for each run. These velocity data are normalized by  $U_{CJ}$  and appear in Fig. 2.4a for varying initial pressure and 2.4b for varying

equivalence ratio. Averaging these three velocity measurements for each experiment produced an average test section velocity  $U_{AVG}$  (Figs. 2.4c and 2.4d). Values of  $U_{CJ}$  were calculated using the equilibrium code STANJAN (Reynolds, 1986) and are listed in Appendix D.

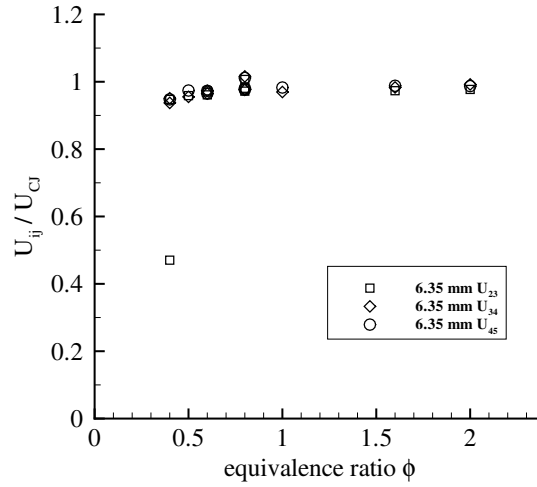
The data from varying equivalence ratio in the 6.35 mm ID tube (Figs. 2.4b and 2.4d) show small velocity deficits less than 10% as the mixture composition diverges from stoichiometric and the induction zone length  $\Delta$  (the distance between the shock front and the reaction zone) increases. As the initial pressure in the 6.35 mm ID tube is decreased (Fig. 2.4a and 2.4c), small velocity deficits are also observed until the initial pressure is decreased to 0.10 bar. At the lowest pressure tested (0.10 bar), a significant decrease in wave velocity ( $0.65 U_{CJ}$ ) exists. Experiments in the 1.27 mm ID tube display dramatic velocity deficits (up to 59%) as initial pressure is decreased. The detonation velocity smoothly decreases with decreasing pressure and the minimum wave propagation velocity measured was  $0.41 U_{CJ}$  for an initial pressure of 0.14 bar.

Examples of the pressure transducer histories are shown in Fig. 2.5a for the 6.35 mm tube with  $U_{AVG}/U_{CJ} = 1.01$  and in Fig. 2.5b for  $U_{AVG}/U_{CJ} = 0.42$ . Both sets of traces show the characteristic pressure signature of a detonation wave near the exit of the initiator tube. The actual presence of a detonation is difficult to verify, however, since no diagnostics were used to detect the reaction zone in these experiments and a combustion-driven shock wave could have a similar appearance. However, the velocity deficit smoothly increases as mixture sensitivity decreases, indicating that the detonation wave is experiencing increased losses rather than failure. Detonation failure at some limiting value would appear as a discontinuous decrease in the test-section velocity as a function of  $\Delta/R$ , which is not observed in the data.

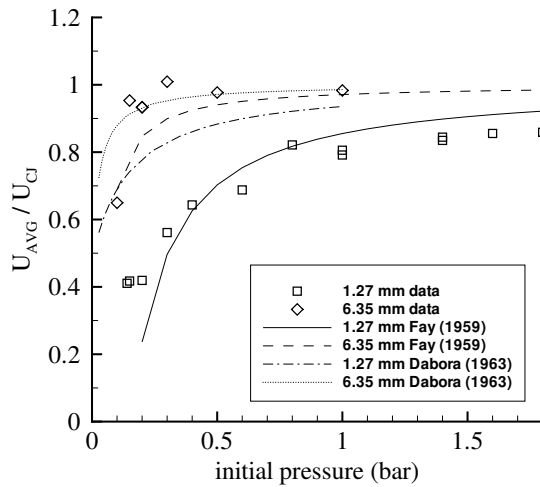
Fig. 2.4 indicates that the wave velocity deficits increase as  $\phi$  varies from unity, with decreasing initial pressure, and with decreasing tube diameter. Decreasing pressure and varying  $\phi$  from unity tend to increase  $\Delta$ . The dependence of the velocity deficits on  $\Delta$  and the tube diameter are more clearly illustrated by replotting all experimental data as a function of induction zone length normalized by the inner tube



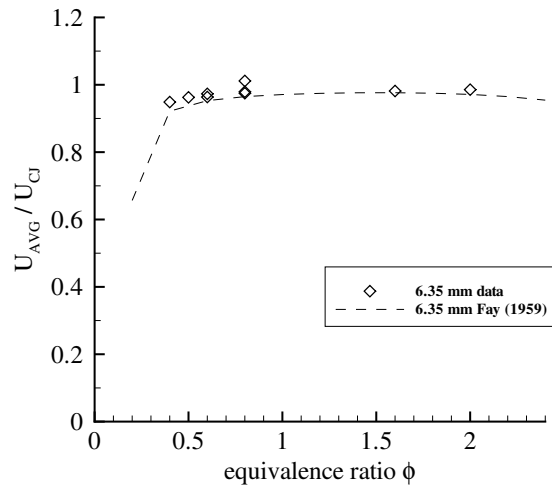
(a) Velocity in between each measurement station versus initial pressure.



(b) Velocity in between each measurement station versus equivalence ratio.

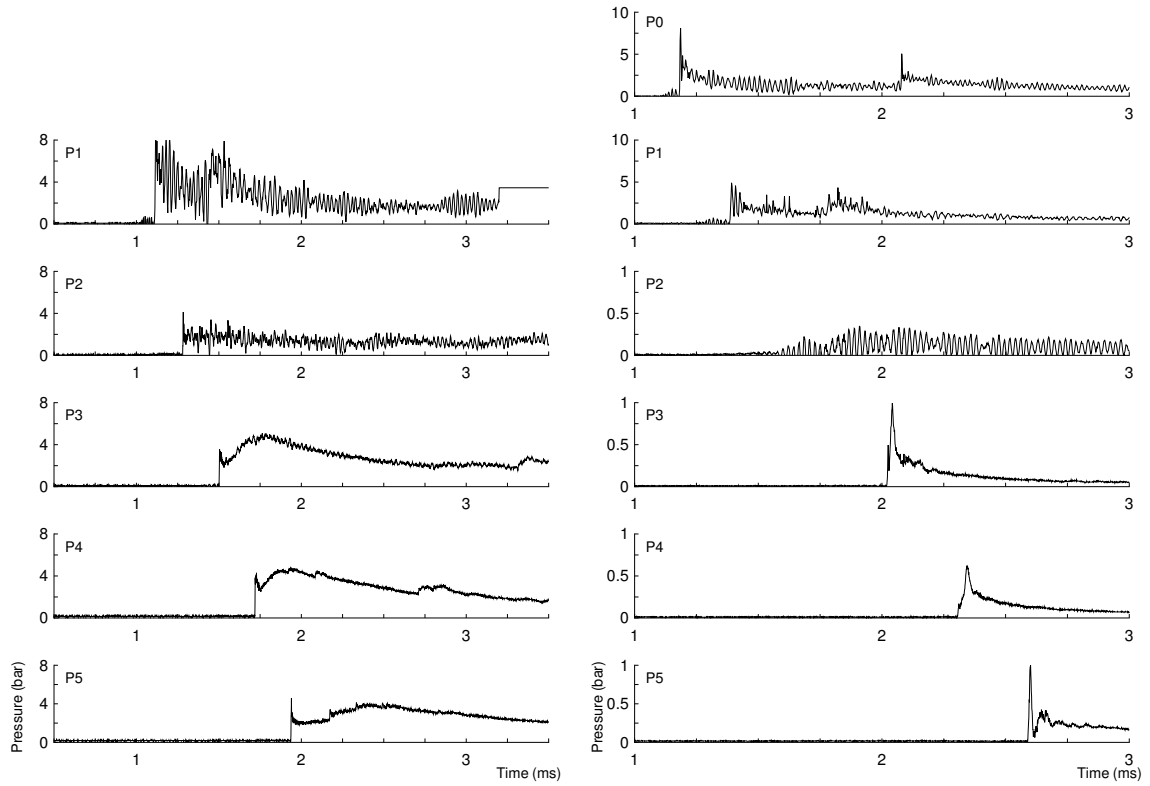


(c) Average test section velocity versus initial pressure.



(d) Average test section velocity versus equivalence ratio.

Figure 2.4: Test section velocity data: Average wave velocity in between each pressure measurement station is shown for (a) varying initial pressure and (b) varying equivalence ratio.  $U_{ij}$  is the average velocity between pressure transducers  $i$  and  $j$ . The individual wave speeds from each run in (a) and (b) have been averaged resulting in a single average test section velocity for each run as shown in (c) and (d). The lines correspond to the models in Fay (1959) and Dabora (1963) that account for boundary layer effects.



(a) Shot 016:  $C_3H_8+5O_2$  with  $P_1 = 0.30$  bar in 6.35 mm ID tube. Average test section velocity was  $1.01 U_{CJ}$ .

(b) Shot 045:  $C_3H_8+5O_2$  with  $P_1 = 0.15$  bar in 1.27 mm ID tube. Average test section velocity was  $0.42 U_{CJ}$ .

Figure 2.5: Examples of pressure traces from both test sections.

radius  $R$  (Fig. 2.6a).

The induction zone lengths for each data point were calculated by first assuming that mixtures were adiabatically compressed and accelerated by a shock wave propagating at the experimentally measured wave speed and then allowed to undergo constant volume combustion, as discussed in Appendix A.3. For all calculations, the induction zone length was defined as the product of the post-shock fluid velocity (in shock-fixed coordinates) and the time when the temporal temperature gradient was 90% of the peak value. The shock-jump conditions were numerically solved using the equilibrium code STANJAN (Reynolds, 1986) and the time for constant volume combustion was solved with the computer program CV (Shepherd, 1986) which uses the Chemkin package (Kee et al., 1989). The experimentally measured shock velocity  $U_{AVG}$  values used for the calculation and the resulting induction lengths are listed in Appendix D.

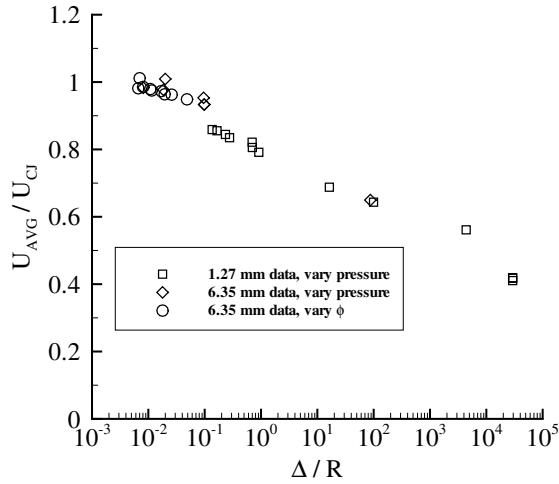
The data appear to collapse to a single relationship suggesting that

$$\frac{U}{U_{CJ}} = f\left(\frac{\Delta}{R}\right) \quad (2.1)$$

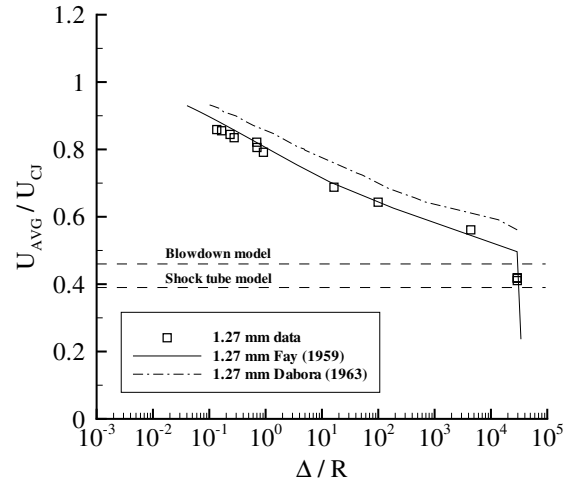
as shown in Fig. 2.6a, although closer examination shows a discontinuous step located near  $\Delta/R = 0.1$  that separates the 6.35 mm ID tube data (characterized by low-velocity deficits) and the 1.27 mm ID tube data (characterized by high-velocity deficits). However, one data point from the 6.35 mm ID tube is located among the 1.27 mm ID tube data near  $\Delta/R = 100$ .

### 2.4.1 Boundary Layer Growth

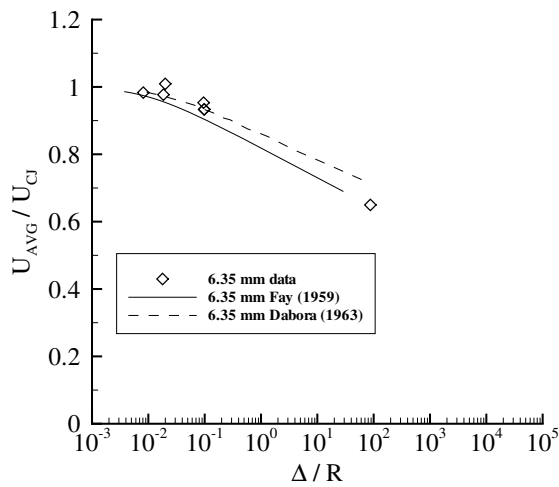
A shock wave propagating through a tube will impulsively accelerate the gas that it processes. If the post-shock gas velocity is different than that of the tube wall and the no-slip condition holds for the gas, viscous forces will accelerate the gas closest to the wall to match the wall velocity. The flow unaffected by the no-slip boundary condition is independent of the Reynolds number and is referred to as the freestream flow. The viscous or momentum boundary layer is defined as the region of gas that is affected



(a) All experimental velocity data.



(b) Data from varying pressure in the 1.27 mm ID tube.



(c) Data from varying pressure in the 6.35 mm ID tube.

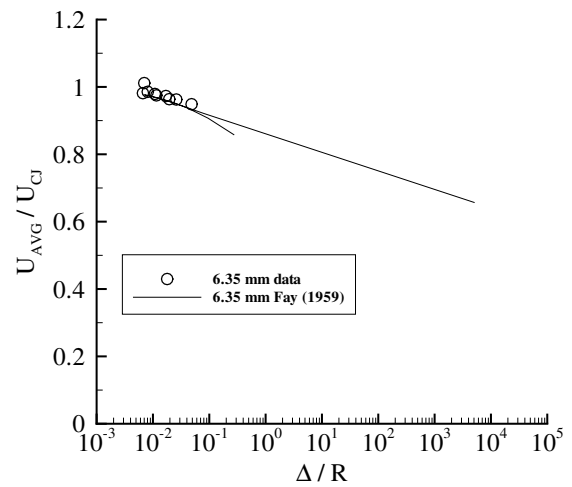
(d) Data from varying  $\phi$  in the 6.35 mm ID tube.

Figure 2.6: Experimental data presented as a function of induction zone length  $\Delta$  normalized by tube radius. The lines correspond to boundary layer models discussed in the text.

by the wall and will grow in size as the wall momentum diffuses into the freestream fluid. Thermal differences between the freestream fluid and the wall will also result in the growth of a thermal boundary layer. The momentum and thermal boundary layers typically grow at similar rates in gases due to their comparable diffusivities of momentum and heat transport.

Fig. 2.7 illustrates the velocity and temperature profiles behind a shock propagating in a tube filled with gas that is initially moving at the same velocity as the wall. As the flow enters the viscous boundary layer, it is accelerated towards the wall velocity. As the flow enters the thermal boundary layer, its temperature approaches the tube wall temperature. If the fluid and tube wall were initially at similar temperatures, the shock-processed gas would initially be much hotter than the tube wall and would cool isobarically (as there is no mechanism to support a pressure difference between the freestream and boundary layer flow) upon entering the thermal boundary layer. Thus, gas entering the boundary layer will increase in density, as per the ideal gas law.

These velocity and density changes cause gas entering the boundary layer to con-

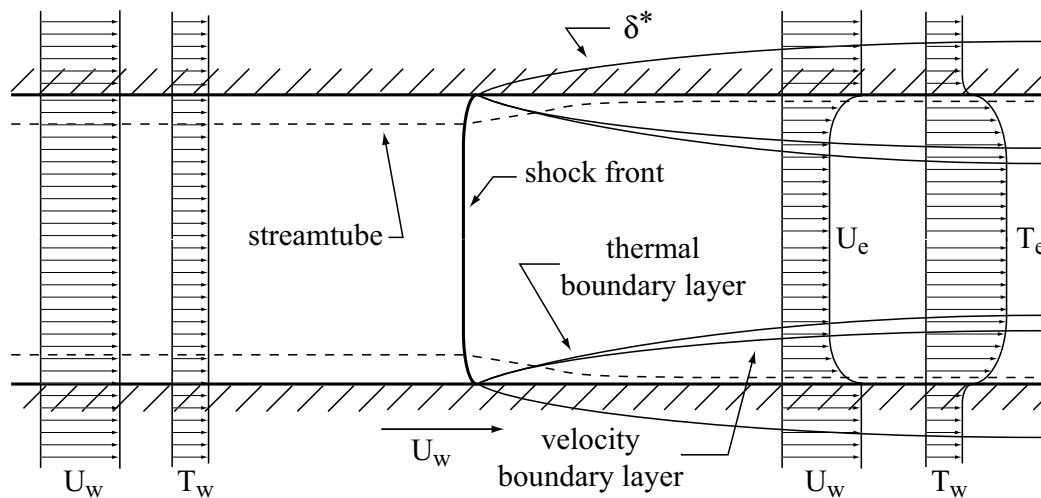


Figure 2.7: A shock wave propagating through a tube is shown in shock-fixed coordinates and illustrates the growth of the boundary layers and the displacement thickness. A streamtube, represented by the dashed line, illustrates the divergence of the flow behind the shock.

tract, forcing the freestream gas to expand to match the pressure at the interface between the boundary layer and the freestream fluid. The end result is that mass appears to be drawn from the flow into the tube wall or that the apparent flow area behind the shock front diverges. This apparent wall-sink effect can be modeled as a negative displacement thickness  $\delta^*$  growing behind the shock and is primarily due to the velocity change, although the density change contributes to the effect as well. The shock accounts for this effect by curving near the tube wall to direct flow radially into the wall.

The boundary layer growth can be important to detonation propagation. Shocked gas that enters the thermal boundary layer before autoigniting will undergo a significant temperature reduction that can delay or eliminate autoignition altogether. Furthermore, the flow divergence induced by the momentum boundary layer will expand the flow and slow the rate of energy release during combustion. As the energy release is slowed, more energy is released behind the sonic surface. Energy released behind this surface is not able to propagate upstream and does not contribute to the detonation wave propagation.

These thermal and momentum losses become more significant as the ratio of the mass of gas entering the boundary layer to the mass of gas remaining in the freestream increases. Two ways to increase this mass ratio are to decrease the pressure or decrease the tube radius. Decreasing pressure will enhance boundary layer growth while decreasing the tube radius will decrease the mass of the freestream gas so that the boundary layer growth is unaffected. A quantitative model designed to account for these effects is discussed below.

### **2.4.2 Quasi-One-Dimensional Analysis for the Velocity Deficit of a Detonation Wave**

The following derivation is taken from Dabora (1963) and presents a quasi-one-dimensional analysis for the velocity deficit of a detonation wave. First, the classical hydrodynamic formulation for the characteristics of a general, steady, one-dimensional

wave with no area divergence will be discussed. This theory will then be adapted to allow for situations where area divergence is present behind the shock front. A solution will be developed to determine the velocity deficit resulting from this divergence. Applications of this solution by Fay (1959) and Dupre et al. (1986) will then be presented. Finally, those techniques will be applied to the current data.

#### 2.4.2.1 One-Dimensional Waves with No Area Change

Modeling the wave as a one-dimensional planar discontinuity allows the conservation equations to be written in the following form:

$$\rho_1 w_1 = \rho_2 w_2 \quad (2.2)$$

$$\rho_1 w_1^2 + P_1 = \rho_2 w_2^2 + P_2 \quad (2.3)$$

$$\frac{w_1^2}{2} + h_1 = \frac{w_2^2}{2} + h_2 \quad (2.4)$$

where  $u$ ,  $\rho$ ,  $P$ , and  $h$  are the particle velocity, density, pressure, and enthalpy relative to the front. Conditions along the wave area are assumed to be uniform. The gases ahead and behind the wave can have different molecular weights  $m$  and ratios of specific heat  $\gamma$ ; however, both gases are assumed to be thermally and calorically perfect. Thus, the equation of state is

$$P = \rho \frac{R_0 T}{m} \quad (2.5)$$

where  $R_0$  is the universal gas constant and the enthalpy is defined as

$$h_1 = C_p T_1 = \frac{\gamma}{\gamma - 1} p_1 v_1 \quad (2.6)$$

$$h_2 = C_p T_2 - q = \frac{\gamma}{\gamma - 1} p_2 v_2 - q \quad (2.7)$$

where  $q$  is the heat release per unit mass due to chemical reaction.

Eqs. 2.2 and 2.3 can be combined to obtain the Rayleigh line:

$$\frac{\frac{P_2}{P_1} - 1}{\frac{v_2}{v_1} - 1} = -\frac{w_1^2}{P_1 v_1} = -\gamma_1 M_1^2 = -\frac{w_2^2 \rho_2^2}{P_1 \rho_1} \quad (2.8)$$

which forms a straight line with negative slope for any finite Mach number on a p-v diagram.

The Hugoniot relation can also be obtained by combining Eqs. 2.2, 2.3, 2.4, 2.6, and 2.7 and eliminating the velocity terms.

$$\left[ \frac{2q}{P_1 v_1} + \frac{\gamma_1 + 1}{\gamma_1 - 1} - \frac{\gamma_2 - 1}{\gamma_2 + 1} \right] \left[ \frac{\gamma_2 - 1}{\gamma_2 + 1} \right] = \left[ \frac{P_2}{P_1} + \frac{\gamma_2 - 1}{\gamma_2 + 1} \right] \left[ \frac{v_2}{v_1} - \frac{\gamma_2 - 1}{\gamma_2 + 1} \right] \quad (2.9)$$

On a p-v diagram, Eq. 2.9 represents a family of hyperbolas that are a function of the parameters  $q$  and  $\gamma$ .

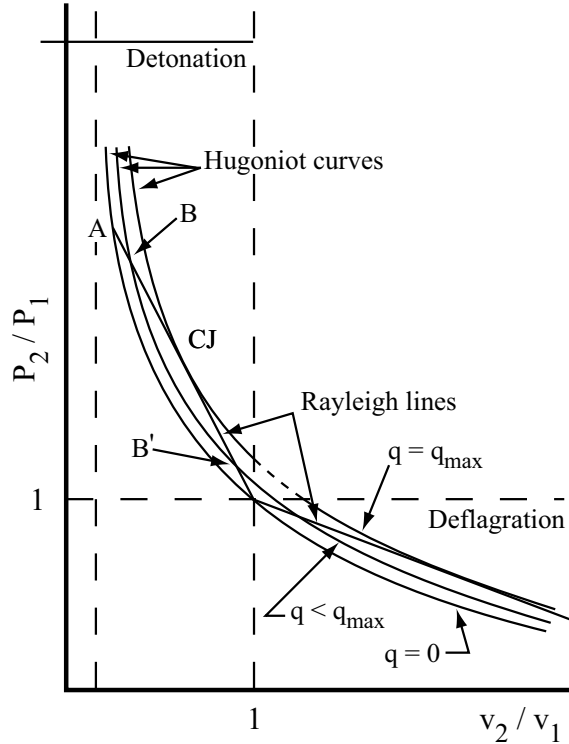


Figure 2.8: The Hugoniot-Rayleigh representation of shock and detonation waves.

Fig. 2.8 shows a schematic plot of Eq. 2.8 (two straight lines) and Eq. 2.9 for the

adiabatic case and for two cases with heat release. The lower branch of the Hugoniot curves, in conjunction with Rayleigh lines of absolute slope less than  $\gamma_1$ , represent the deflagration mode of combustion and are not considered in this study. The upper branch of the Hugoniot and Rayleigh lines of absolute slope greater than  $\gamma_1$  represent shock waves or detonation waves. In general, a Rayleigh line intersects the Hugoniot curve at two points, which represent the simultaneous solution of Eqs. 2.8 and 2.9. As an example, point A represents an adiabatic shock wave with  $P_2/P_1$  and  $\rho_2/\rho_1$  greater than unity. Point B is the solution for a strong detonation wave and point B' is that for a weak wave, both of which occur for values of  $q$  less than the limiting value. Points similar to B' are usually ruled out from entropy considerations if the detonation process is considered a shock followed by heat release. Finally, point CJ is the solution for the CJ wave and is realized at the limiting value of heat release. This is the type of wave observed in detonation tubes.

As can be seen from Fig. 2.8, at the CJ point, the Rayleigh line is tangent to the Hugoniot curve. Thus, it is possible to solve for this point by first differentiating Eqs. 2.8 and 2.9 to obtain

$$\frac{\partial \left( \frac{P_2}{P_1} \right)}{\partial \left( \frac{v_2}{v_1} \right)} = - \frac{w_2^2 \rho_2^2}{P_1 \rho_1} \quad (2.10)$$

and

$$\frac{\partial \left( \frac{P_2}{P_1} \right)}{\partial \left( \frac{v_2}{v_1} \right)} = - \frac{\frac{P_2}{P_1} + \frac{\gamma_2 - 1}{\gamma_2 + 1}}{\frac{\rho_1}{\rho_2} - \frac{\gamma_2 - 1}{\gamma_2 + 1}} \quad (2.11)$$

respectively.

Then, by equating Eqs. 2.10 and 2.11, substituting  $P_1$  from Eq. 2.3 and  $w_1$  from

Eq. 2.2, the solution of  $w_2$  for the CJ point is obtained:

$$w_2 = \sqrt{\frac{\gamma_2 P_2}{\rho_2}} = a_2 \quad (2.12)$$

which shows that for a CJ wave, the burned gas immediately behind the wave travels at the local sonic speed with respect to the wave.

With this CJ criterion, the jump conditions can be solved with the perfect gas relations to find the propagation velocity of the CJ detonation wave

$$M_{CJ} = \sqrt{\mathcal{H} + \frac{(\gamma_1 + \gamma_2)(\gamma_2 - 1)}{2\gamma_1(\gamma_1 - 1)}} + \sqrt{\mathcal{H} + \frac{(\gamma_2 - \gamma_1)(\gamma_2 + 1)}{2\gamma_1(\gamma_1 - 1)}} \quad (2.13)$$

where the non-dimensional heat of combustion  $\mathcal{H}$  is given by

$$\mathcal{H} = \frac{(\gamma_2 - 1)(\gamma_2 + 1)q}{2\gamma_1 R_1 T_1} \quad (2.14)$$

and is typically of order 10 (Thompson, 1988). Eq. 2.13 is referred to as the two- $\gamma$  CJ model.

The thermodynamic properties at the CJ surface can be determined by substitution into the conservation equations as well (Thompson, 1988)

$$\frac{P_2}{P_1} = \frac{\gamma_1 M_{CJ}^2 + 1}{\gamma_2 + 1} \quad (2.15)$$

$$\frac{\rho_2}{\rho_1} = \frac{\gamma_1 (\gamma_2 + 1) M_{CJ}^2}{\gamma_2 (1 + \gamma_1 M_{CJ}^2)} \quad (2.16)$$

$$\frac{T_2}{T_1} = \frac{R_1 P_2 \rho_1}{R_2 P_1 \rho_2}. \quad (2.17)$$

Thus, if the initial thermodynamic conditions, as well as the value of heat release and  $\gamma_2$  are known, the detonation velocity can be found. In general, however, finding  $q$  and  $\gamma_2$  requires a trial and error solution that involves chemical equilibrium behind the wave. The equilibrium code STANJAN (Reynolds, 1986) is used in the present work.

A one- $\gamma$  model is also available that uses a single specific heat ratio and perfect

gas constant for both the reactants and products

$$M_{CJ} = \sqrt{\mathcal{H} + 1} + \sqrt{\mathcal{H}}, \quad (2.18)$$

where  $\mathcal{H}$  is identical to Eq. 2.14 with  $\gamma_2 = \gamma_1$ . Similarly, the thermodynamic properties are given by Eqs. 2.15-2.17 with  $\gamma_2 = \gamma_1$  (Fickett and Davis, 2001).

### 2.4.2.2 One-Dimensional Waves with Area Change

For situations where there is an increase in stream-tube area between the shock wave and the CJ plane, a deficit in the propagation velocity will result. This type of situation occurs during boundary layer growth as well as in the presence of an expanding tube diameter or yielding walls. Under these conditions, it is necessary to modify the conservation equations to account for the change in stream-tube area.

Defining the change in stream-tube area as

$$\frac{A_2}{A_1} = 1 + \xi \quad (2.19)$$

where  $\xi$  is the average fractional change in the area of each stream tube, the conservation equations become

$$\rho_1 w_1 = \rho_2 w_2 (1 + \xi) \quad (2.20)$$

$$\rho_1 w_1^2 + P_1 = (\rho_2 w_2^2 + P_2) (1 + \xi) - \int_0^\xi P d\xi \quad (2.21)$$

$$\frac{w_1^2}{2} + h_1 + q = \frac{w_2^2}{2} + h_2. \quad (2.22)$$

The last term in Eq. 2.21 comes from considering the pressure force acting on the sides of the stream tube as it deforms behind the shock front. Evaluation of this term requires detailed knowledge of the pressure behind the shock front along the stream-tube boundary within the reaction zone. Fay (1959) chose to define the integral

as

$$\int_0^\xi P d\xi \equiv P_2 \epsilon \xi \quad (2.23)$$

and noted that for large  $M_1$ , the ratio  $P_2/P_1$  for a shock is about twice that for a detonation wave, so the value of  $\epsilon$  is between 2 and 1.

Using the same general assumptions as for the case involving no area increase, Eqs. 2.20, 2.21, 2.22, and 2.23, together with the definition of the speed of sound, can be combined to give

$$2 \left[ 1 + \frac{q}{c_{p1} T_1} \right] = \left[ \frac{\gamma_2}{\gamma_1} \right]^2 \left[ \frac{\gamma_1 - 1}{\gamma_2^2 - 1} \right] \left( \frac{1}{1 - \frac{\xi \epsilon}{(1+\gamma_2)(1+\xi)}} \right)^2 \frac{(\gamma_1 M_1^2 + 1)^2}{M_1^2} - (\gamma_1 - 1) M_1^2 . \quad (2.24)$$

Introducing a new function  $\psi$  defined by

$$1 + \psi \equiv \left( \frac{1}{1 - \frac{\xi \epsilon}{(1+\gamma_2)(1+\xi)}} \right)^2 \quad (2.25)$$

allows Eq. 2.24 to be reduced to

$$2 \left( \frac{q}{c_{p1} T_1} - \frac{\gamma_1 - \gamma_2}{\gamma_1 (\gamma_2 - 1)} \right) \frac{\gamma_2^2 - 1}{\gamma_1 - 1} = \frac{(M_1^2 - \frac{\gamma_2}{\gamma_1})^2}{M_1^2} + \frac{\psi \gamma_2^2 (M_1^2 + \frac{1}{\gamma_1})^2}{M_1^2} . \quad (2.26)$$

The last term of this equation represents the effect of area change. For large  $M_1$  (i.e.,  $M_1 \geq 5$ ), Eq. 2.26 can be reduced further:

$$2 \left( \frac{q}{c_{p1} T_1} - \frac{\gamma_1 - \gamma_2}{\gamma_1 (\gamma_2 - 1)} \right) \frac{\gamma_2^2 - 1}{\gamma_1 - 1} = M_1^2 (1 + \psi \gamma_2^2) . \quad (2.27)$$

If the heat release is assumed to remain the same whether there is an area change or not, the right-hand side of Eq. 2.27 remains essentially constant. Dabora (1963) notes that this is a reasonable assumption in that chemical equilibrium is expected to remain the same at the CJ plane whether there is an area change or not. This

is so because an area increase would decrease both pressure and temperature at that plane. The pressure decrease would increase the amount of radicals through increased dissociation and the lower temperature would slow the reaction rate. Thus, the pressure and temperature effects would tend to cancel each other, maintaining the amount of energy released in front of the sonic surface.

Noting that  $\psi = 0$  when  $\xi = 0$ , one can find, after making use of Eq. 2.27, that the decrease in Mach number from the case where there is no area change ( $\xi = 0$ ) to the case where  $\xi$  is finite can be written as:

$$\frac{M_1(\xi = 0) - M_1}{M_1(\xi = 0)} = \frac{\Delta M_1}{M_1(\xi = 0)} = 1 - \sqrt{\frac{1}{1 + \gamma_2^2 \psi}} \quad (2.28)$$

or in terms of  $\xi$ :

$$\frac{\Delta M_1}{M_1(\xi = 0)} = 1 - \sqrt{\frac{\left\{1 - \left[\frac{\epsilon}{1 + \gamma_2}\right] \left[\frac{\xi}{1 + \xi}\right]\right\}^2}{\left\{1 - \left[\frac{\epsilon}{1 + \gamma_2}\right] \left[\frac{\xi}{1 + \xi}\right]\right\}^2 + \gamma_2^2 \left\{2 \left[\frac{\epsilon}{1 + \gamma_2}\right] \left[\frac{\xi}{1 + \xi}\right] - \left[\frac{\epsilon}{1 + \gamma_2}\right]^2 \left[\frac{\xi}{1 + \xi}\right]^2\right\}}} \quad (2.29)$$

which for  $\xi \ll 1$  reduces to

$$\frac{\Delta M_1}{M_1(\xi = 0)} \cong \gamma_2^2 \left(\frac{\epsilon}{1 + \gamma_2}\right) \xi. \quad (2.30)$$

This expression predicts the wave velocity deficit dependence on  $\gamma_2$ ,  $\xi$ , and  $\epsilon$ . Application of the solution involves choosing the appropriate values of these parameters.

#### 2.4.2.3 Solution Application in Fay (1959)

Fay (1959) numerically calculated that for stoichiometric hydrogen-oxygen detonations at one atmosphere initial pressure,

$$\frac{\Delta M_1}{M_1(\xi = 0)} \cong 0.53 \epsilon \xi. \quad (2.31)$$

He then chose to express the fractional increase in stream-tube area  $\xi$  in terms of more convenient variables and approximated the increase in flow area as the displacement thickness times the tube circumference. Thus, the fractional area increase is approximately

$$\xi \simeq \frac{\pi d \delta^*}{\pi d^2/4} = \frac{4 \delta^*}{d} . \quad (2.32)$$

Substituting Eq. 2.32 into Eq. 2.31 and approximating  $\epsilon$  as 1, the expression for the velocity deficit becomes

$$\frac{\Delta M_1}{M_1} = \frac{\Delta U_1}{U_1} \simeq \frac{2.1 \delta^*}{d} \quad (2.33)$$

where  $\Delta U_1$  is the difference between the observed detonation wave velocity and is normalized by the wave velocity in the divergence-free case  $U_1$ . For a detonation wave,  $U_1$  is equal to the CJ velocity  $U_{CJ}$ . The equation used by Fay (1959) for displacement thickness was based on measurements (Gooderum, 1958) of turbulent boundary layers in shock tubes

$$\delta^* \simeq 0.22 \ell^{0.8} \left[ \frac{\mu_e}{\rho_1 U_{CJ}} \right]^{0.2} . \quad (2.34)$$

Gooderum (1958) initially reported the above expression for the growth of the turbulent boundary layer  $\delta$  behind a shock in a shock tube. Analytical work by Fay (1959) argued that the expression could also be used for the displacement thickness  $\delta^*$  behind the strong shock present in a detonation wave.

It is important to consider the value to use for the distance  $\ell$  behind the shock when evaluating  $\delta^*$ . Fay chose  $\ell$  to equal the detonation wave thickness and determined this value by deriving a transcendental equation based on an experimental parameter he referred to as the relaxation length, which was obtained from experimental measurements of the density profile within a detonation front or from schlieren pictures.

In applying this model to the current experimental data,  $\ell$  was set equal to the

induction zone length  $\Delta$  as calculated by CV (Shepherd, 1986), a resource not available to Fay in 1959. The initial gas density  $\rho_1$  was known and the velocity  $U_{CJ}$  was computed using STANJAN (Reynolds, 1986). The post-shock gas viscosity  $\mu_e$  was found not to vary significantly over the range of experimental conditions and was approximated as  $6.0 \times 10^{-5}$  Pa-s for the propane-oxygen mixtures tested.

The velocity predicted by this analysis is shown as a curve labeled ‘‘Fay’’ in Figs. 2.4c and 2.4d and in Figs. 2.6b, 2.6c and 2.6d. The predicted velocities agree very well with the experimental data in the 1.27 mm ID tube, but slightly under-predict the measured wave velocities in the 6.35 mm ID tube.

#### 2.4.2.4 Solution Application in Dupre et al. (1986)

Dabora (1963) used a value of  $\gamma_2 = 1.2$  for hydrogen-oxygen detonations to obtain a coefficient of 0.654 in Eq. 2.30 instead of the value of 0.53 numerically calculated by Fay (1959). However, Dabora (1963) also observed that in his applications,  $\xi$  could be as large as 0.25 and chose to use Eq. 2.29 instead of Eq. 2.30.

The model discussed in Dupre et al. (1986) used Eq. 2.29 with a definition for stream-tube area divergence developed by Murray (1984), which evaluated  $\delta^*$  at a distance of one detonation cell length  $l_c$  downstream of the shock:

$$\xi = 4 \frac{\delta_{l_c}^*}{d} . \quad (2.35)$$

The equation used for predicting velocity deficit was

$$\frac{\Delta U_1}{U_1} = 1 - \left[ \frac{(1 - \nu)^2}{(1 - \nu)^2 + \gamma_2^2 (2\nu - \nu^2)} \right]^{\frac{1}{2}} \quad (2.36)$$

where

$$\nu = \frac{\xi}{|(1 + \gamma_2)(1 + \xi)|} . \quad (2.37)$$

Eqs. 2.36 and 2.37 are identical to Eq. 2.29. Dupre et al. (1986) used Dabora’s choice

of  $\gamma_2 = 1.2$  for  $\text{H}_2\text{-O}_2$  mixtures and also chose  $\ell = \lambda/0.7$  in their analysis where  $\lambda$  was the detonation cell width.

This model was used to predict velocity deficits in the experimental data in the present work. Eq. 2.34 was first used to compute the displacement thickness behind the shock wave with downstream distance  $\ell = \lambda/0.7$ . The initial density was known and the velocity  $U_{CJ}$  was determined according to CJ theory by using the equilibrium code STANJAN (Reynolds, 1986). As before, the viscosity of the gas behind the shock wave  $\mu_e$  was approximated as  $6.0 \times 10^{-5}$  Pa-s.

Eq. 2.36 was then used with Eq. 2.35 and 2.37 to determine the expected velocity deficit. In this study, the value of  $\gamma_2 = 1.14$  was used for the propane-oxygen mixtures.

The result is the line labeled “Dabora” in Figs. 2.4c, 2.4d, 2.6b, 2.6c. This model fits the data well in the 6.35 mm ID tube, but underpredicts the velocity deficits observed in the 1.27 mm ID tube.

#### 2.4.2.5 Limitations of the Model

The quality of the fit can vary with the values of  $\gamma_2$  used in each analysis. For example, as mentioned above, the value of  $\gamma_2$  used in the “Dabora” line in Figs. 2.4 and 2.6 was  $\gamma_{2D} = 1.14$ . The value of  $\gamma_2$  used in the “Fay” line can be determined from setting the right-hand sides of Eqs. 2.30 and 2.31 equal to each other and solving for  $\gamma_2$ . The result is that  $\gamma_{2F} = 1.04$ . Since  $\gamma_2$  decreases with decreasing mixture pressure, it is possible that the model in Dupre et al. (1986) does not fit the high-deficit, low-pressure experimental data simply because the value of  $\gamma_2$  used in the model is too large. Similarly, the model of Fay (1959) does not fit the high-pressure, low-deficit data well, but the fit improves as the mixture pressure (and thus  $\gamma_2$ ) is decreased. Thus, it may be necessary to “tune” each model to a specific pressure range by selecting the appropriate value of  $\gamma_2$ .

A second factor to consider is that while the model generally predicts the velocity deficit trend, it does not fully account for the physics of boundary layer growing in the tube. For cases with low initial pressure, the boundary layer will completely close behind before the onset of the reaction zone. While it is not physically possible for

the boundary layer to continue to remove mass from the freestream flow after it has completely closed, the model continues to do so since it was not designed to account for such situations. While the model appears to accurately predict deficits when the boundary layer closure distance is shorter than the induction length, this is just luck and the model is reduced to an empirical fit. The models based on frictional flow in a tube (Zel'dovich et al., 1987, Frolov and Gelfand, 1991, Agafonov and Frolov, 1994) may be more appropriate for these cases.

### 2.4.3 Lower Shock Velocity Limits

The strength of the shock that would be created in the test section when a detonation is successfully initiated in the initiator tube but fails during the transition to the test section (for large values of  $\Delta/R$ ) is estimated below. Predicting the maximum possible shock speed would help interpret the experimental data since no reaction zone information was collected. This situation is analyzed using a shock tube model and a blowdown model.

#### 2.4.3.1 Shock Tube Model

The situation described above is modeled using a shock tube or unsteady wave analysis. Initially, the initiator and test-section tubes are filled with the same mixture at identical pressures. Assume the detonation wave in the initiator tube fails immediately upon entering the test-section tube. The pressure in the initiator tube will not be uniform as the reflections from the detonation wave from the tube end flanges interact with the Taylor wave; however, after the wave reflections have been allowed to run their course, the pressure in the detonation tube will be close to the constant volume combustion pressure  $P_{CV}$ .

The shock tube equation

$$\frac{P_{CV}}{P_1} = \frac{1 + \frac{2\gamma_1}{\gamma_1 + 1}(M_s^2 - 1)}{\left(1 - \frac{\gamma_{CV} - 1}{\gamma_1 + 1} \frac{a_1}{a_{CV}} \frac{M_s^2 - 1}{M_S}\right)^{\frac{2\gamma_{CV}}{\gamma_{CV} - 1}}} \quad (2.38)$$

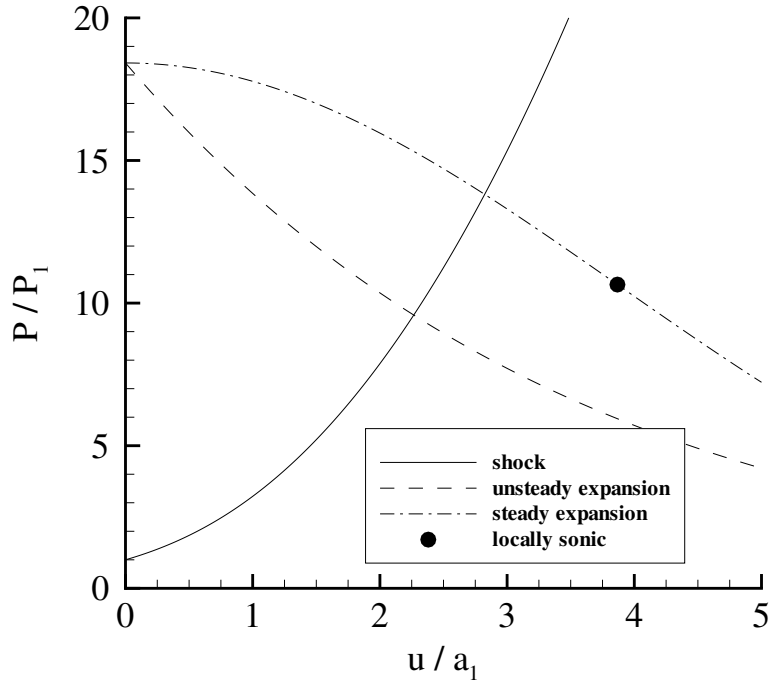


Figure 2.9: A graphical illustration of the difference between steady and unsteady expansion. The intersection of the shock and unsteady expansion lines represents the solution of the shock tube equation. The intersection of the shock and steady expansion lines represents the solution corresponding to quasi-steady flow expansion.

matches conditions across the shock wave and expansion fan to determine the Mach number  $M_s$  of the shock that is created in the test section. For stoichiometric propane-oxygen mixtures, the ratio of the constant volume explosion pressure to the initial pressure is approximately constant ( $P_{CV}/P_1 \approx 18$ ) and the ratio of the local sound speeds before and after combustion ( $a_{CV}/a_1 \approx 3.9$ ). The ratio of specific heats for a stoichiometric propane-oxygen mixture is  $\gamma_1 = 1.29$ , which changes after combustion to  $\gamma_{CV} \approx 1.12$  assuming equilibrium composition.

Substituting the aforementioned values into Eq. 2.38 yields  $M_s \approx 2.9$ . The typical initial test section sound speed  $a_1$  and  $U_{CJ}$  are approximately 308 m/s and 2300 m/s, respectively. This indicates that, neglecting boundary layer losses, a non-reacting shock wave would propagate through the test section at a wave speed  $U_s$  of 890 m/s, and a normalized velocity value  $U_{AVG}/U_{CJ}$  of 0.39. This velocity is slightly below the lowest velocities measured in the 1.27 mm ID tube (Fig. 2.6b).

### 2.4.3.2 Blowdown Analysis

If the driver tube has a significantly larger diameter than the test section tube (as in this experiment), the initial shock wave in the test section will be created by the unsteady phenomenon mentioned in the previous section, but will transition to a quasi-steady solution for longer times. The initial pressure difference between the initiator and test section tubes when the detonation reaches the end of the initiator tube drives fluid into the test section, creating a shock in the test section and expansion waves in the initiator. However, as the expansion waves diffract into the much larger initiator tube volume, they weaken significantly and the stagnation conditions inside the driver change slowly relative to the time-scale of interest, the propagation time of the shock wave in the test section tube. Thus, the process can be approximated as steady, and isentropic analysis can be used.

Assuming negligible heat losses, a steady flow accelerating the gas from the initiator tube into the test section can be modeled as adiabatic. Thus, the stagnation enthalpy is constant at the CV condition

$$h_{CV} = h(t) + \frac{u(t)^2}{2} . \quad (2.39)$$

For a perfect gas,

$$\Delta h = c_p \Delta T \quad (2.40)$$

making the temperature ratio

$$\frac{T(t)}{T_{CV}} = 1 - \frac{(\gamma - 1)}{2} \frac{u(t)^2}{a_{CV}^2} . \quad (2.41)$$

Assuming the flow is smoothly accelerated from the driver into the test section, the flow in the transition from the driver to the test section can be modeled as an isen-

tropic expansion and the pressure ratio can be computed as

$$\frac{P(t)}{P_{CV}} = \left( \frac{T(t)}{T_{CV}} \right)^{\frac{\gamma}{\gamma-1}} \quad (2.42)$$

$$\frac{P(t)}{P_{CV}} = \left[ 1 - \frac{(\gamma-1)u(t)^2}{2c_{CV}^2} \right]^{\frac{\gamma}{\gamma-1}} . \quad (2.43)$$

Eq. 2.43 represents the range of pressure-velocity values that may exist in the initiator tube due to isentropic expansion. In reality, the flow is not perfectly isentropic, resulting in lower pressures experimentally than predicted by isentropic theory.

In order to choose a specific set of pressure and velocity values, it is necessary to solve the intersection of Eq. 2.43 with the equation for the pressure increase across a shock wave:

$$\frac{P_2}{P_1} = 1 + \frac{2\gamma_1}{\gamma_1 + 1} (M_s^2 - 1) . \quad (2.44)$$

Doing so will match the pressure and velocity at the interface between the shocked test section gas and the expanding initiator tube flow.

This solution is illustrated graphically in Figs. 2.9. The steady expansion curve intersects the shock curve at a pressure of  $P_2/P_1 = 13.8$ . This corresponds to a shock Mach number of 3.5 and a shock speed of 1077 m/s. The intersection occurs before the expanded flow is locally sonic indicating that this is a valid solution. A shock interpreted as a detonation wave would have a  $U_{AVG}/U_{CJ}$  value of approximately 0.46 for the range of conditions investigated. Examination of the data (Fig. 2.6) shows that there is only one data point below this value, indicating that a reaction zone was most likely present in the test section for all other cases.

## 2.5 Summary

Detonation waves were propagated in propane-oxygen mixtures through tubes with diameters of 6.35 mm and 1.27 mm, which are on the order of the detonation cell size.

For experiments in the 6.35 mm ID tube, initial pressure and equivalence ratio were varied. Stoichiometric propane-oxygen mixtures were tested with initial pressures varying from 0.1 to 1 bar, and the mixture equivalence ratio  $\phi$  was varied from 0.3 to 3. For experiments in the 1.27 mm ID tube, the initial pressure of stoichiometric propane-oxygen mixtures was varied from 0.1 to 1.8 bar.

Wave speeds in the test section were found to decrease significantly below the CJ velocity as the initial pressure decreased. Minimum propagation velocities of  $0.4 U_{CJ}$  were observed for mixtures with initial pressures of 0.14 bar. Velocity deficits were also measured as  $\phi$  diverged from unity. The measured velocity data normalized by  $U_{CJ}$  appear to collapse to a single relationship dependent on induction zone length normalized by the tube radius. The induction zone length of each test mixture was calculated based on the initial state and the experimentally measured wave speed.

Deficits in the detonation wave velocity were attributed to boundary layer growth. A boundary layer model was used to quantitatively predict the decrease in detonation wave velocity as a function of a given tube diameter, initial gas properties and the parameters  $\gamma_2$ ,  $\xi$ , and  $\epsilon$ . Two versions of the model with different choices of parameters were used to predict the experimental data.

The first version from Fay (1959) substituted the induction zone length in place of Fay's original choice of relaxation length to calculate the displacement thickness and resulting stream-tube divergence. This model was found to agree well with the experimental data from the 1.27 mm ID tube where significant velocity deficits below  $0.9 U_{CJ}$  were present, but underpredicted the velocities measured in the 6.35 mm ID tube.

The second version presented in Dupre et al. (1986) was also based on Fay's model with contributions from Dabora (1963) and Murray (1984). This model was found to accurately predict velocities in the 6.35 mm ID tube, but overpredicted wave velocities in the 1.27 mm ID tube. Since data from the 6.35 mm ID tube typically had small velocity deficits (less than 10% of  $U_{CJ}$ ) and data from the 1.27 mm ID tube had larger velocity deficits (15% to 60% of  $U_{CJ}$ ), it seems that the version of Fay (1959) better predicts situations where large velocity losses are present, while the modified model

(Dupre et al., 1986) works better for smaller losses.

The choice of  $\gamma_2$  can significantly affect the fit of the model to the experimental data, and decreasing the value of  $\gamma_2$  as mixture pressure is decreased would improve the fit of each model. Additionally, it is important to be aware that the model does not account for situations where the boundary layer closes before the end of the reaction zone.

Experimental diagnostics such as ionization gauges were not present to measure the reaction zone trajectory in the tube, so it is possible that the detonation waves failed at the lowest speeds. This would have resulted in shock waves in the test section being interpreted as detonation waves with large velocity deficits. Unsteady and quasi-steady wave analyses were used to predict the maximum propagation velocity of a shock wave in this situation, assuming that pressure in the initiator tube corresponded to the constant volume explosion pressure. The maximum expected shock propagation velocity was calculated to be  $0.46 U_{CJ}$ , which was close to the slowest observed wave propagation velocities in the test section. The experiments showed that the wave velocities did not decay as the waves propagated through the test section. This suggests that it is unlikely that detonation failure in the test section was responsible for the observed velocity deficits.

Future experimental work should include a larger range of test section tube diameters to verify the effect of tube diameter on propagation velocity and enable further model development. Additionally, in future experiments, more care should be taken to ensure that the ID of each test section remains constant and free of obstacles that could enhance DDT or disrupt the detonation wave. Extending the length of each test section to several thousand tube diameters would help identify whether the observed velocity deficits were the result of a failing wave or a steady state process.

Also, the initiator tube should be modified to successfully initiate a detonation wave but not to act as a piston pushing on the test section gas. One way to do this would be to allow the initiator tube to vent pressure to the atmosphere behind the detonation wave. In the event of detonation failure in the test section, this would prevent a strong shock from being supported in the test section. Future experiments

should detect the location of the reaction zone relative to the shock wave. Photodiodes or ionization probes located at the same axial location as the pressure transducer would confirm the presence of combustion and would allow direct measurement of the distance between the shock wave and the reaction zone.

## Chapter 3

# Static Detonation Initiator

### 3.1 Introduction

This chapter discusses the development of the first-generation planar and toroidal initiators, which generate large-aspect-ratio planar detonation waves and toroidally imploding detonation waves, respectively. Both devices use a single spark and an array of small diameter channels filled with a small amount of hydrocarbon (HC) and oxygen initiator gas. This work sought to develop more compact and efficient methods of initiating detonations in insensitive HC-O<sub>2</sub>-N<sub>2</sub> mixtures, with a particular interest in detonating HC-air mixtures.

#### 3.1.1 Toroidal Initiator

Efficiently initiating detonations in insensitive HC-air mixtures (such as JP10-air or C<sub>3</sub>H<sub>8</sub>-air) is deemed essential to the success of PDEs. Existing PDEs (Brophy et al., 2002) use an initiator tube to initiate detonations in HC-air mixtures. The initiator tube contains a sensitive mixture such as propane-oxygen that transitions from a deflagration to a detonation sufficiently quickly after ignition by a weak spark. The fully developed detonation wave in the initiator then propagates into an insensitive hydrocarbon-air mixture. If the transmitted shock Mach number and the post-shock flow duration are sufficient (Murray et al., 2003), the detonation wave will be successfully transmitted into the HC-air mixture.

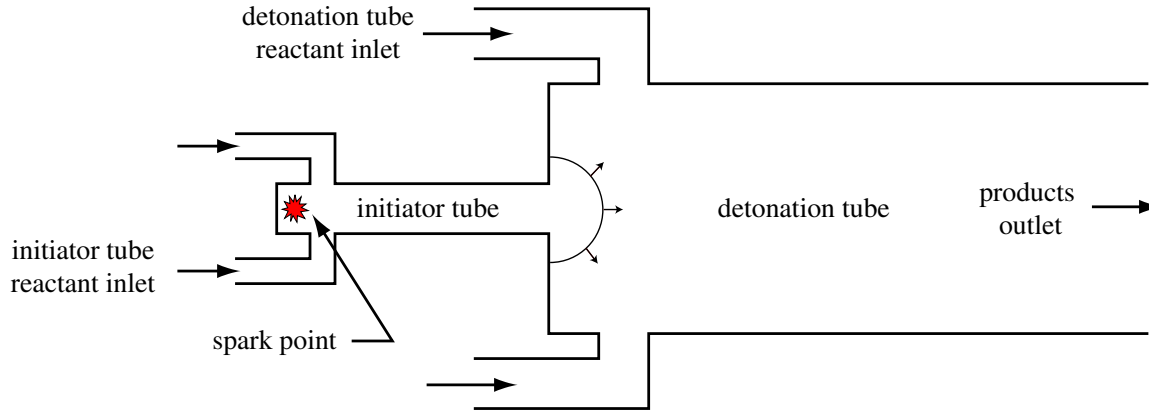


Figure 3.1: The geometry of a typical initiator tube. The detonation wave is created in the initiator tube and diffracts into the detonation tube.

Current initiator tube technology has several drawbacks. Typically, the initiator tube is located at the head of the main detonation tube (Fig. 3.1) on the central axis, resulting in drag as air flows into the main tube. Furthermore, use of a tube initiator requires an amount of energy to be stored on-board during flight. This energy can be stored either electrically in batteries and capacitors or thermodynamically in a sensitive initiator mixture. Given the state of current technology, it is more efficient to store the energy on-board in the form of an initiator mixture, carrying only enough battery power to periodically ignite the mixture with a weak spark. While the initiator mixture is lighter than large banks of batteries, the stored gas still takes up payload weight, decreasing engine performance. Therefore, the tube initiator should use as little gas as possible in order to maximize the engine performance. To reduce the amount of initiator gas, the efficiency of the initiator tube must be maximized by using advanced technologies such as shock focusing.

In shock focusing, a collapsing shock wave generates a high-pressure and high-temperature focal region by adiabatically compressing shocked gas as it flows into an ever-decreasing area (Whitham, 1958). This rapid gas compression generates regions of extremely high energy-density. The focusing of detonation waves also generates high-pressure and high-temperature regions similar to those generated by shock focusing (Lee and Lee, 1965, Jiang and Takayama, 1998, Takayama et al., 1987, Devore

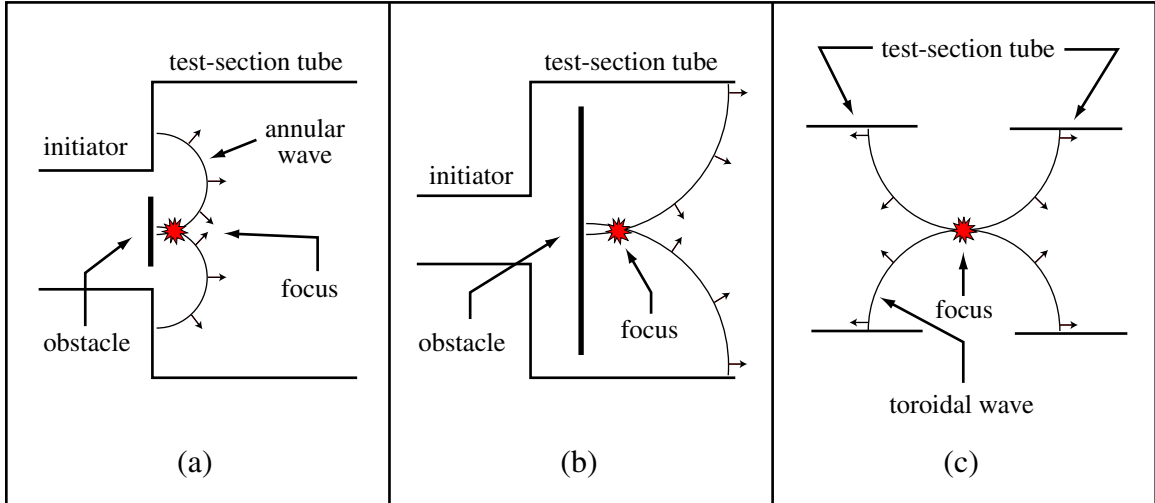


Figure 3.2: Shown are three different cross-sectional schematics of axisymmetric wave implosion experiments discussed in the text. (a) The setup tested by Murray et al. (2000). The wave enters the initiator tube from the left. (b) A similar setup tested at Caltech. As with the previous geometry, the wave enters the initiator tube from the left. (c) The concept of the toroidal initiator where an imploding toroidal wave is propagated into the test-section tube from an annular slot in the tube wall.

and Oran, 1992, Oran and Devore, 1994, Terao et al., 1995, Akbar, 1997). Compression of the detonation products generates post-detonation wave pressures in excess of the CJ pressure, resulting in an increasingly overdriven detonation wave. Thus, wave focusing can be used to increase the strength of the shock wave that is transmitted from the initiator section into the engine, facilitating more efficient detonation initiation.

Murray et al. (2000) noted that wave focusing could promote detonation initiation while conducting experiments measuring the transfer of a detonation wave from a smaller diameter initiator tube to a larger diameter test-section tube (Fig. 3.2a). The initiator tube and test-section tube were both filled with a hydrogen-air mixture and several different obstacles were placed at the interface between the two tubes. The effect of these obstacles on the detonation wave transmission was measured in terms of their transmission efficiency. Values of the transmission efficiency above unity represent situations where the obstacle allowed detonation transfer from the initiator tube to the test-section tube for mixtures with larger cell sizes than in the case where

no obstacles were used. Conversely, values of the transmission efficiency below unity required that smaller cell size mixtures be used (compared to the no-obstacle case) to transfer the detonation wave between the initiator tube and the test-section tube.

Murray et al. (2000) noted a substantial increase in the transmission efficiency when the obstacle was a circular plate. Such a geometry created an annular orifice that generated an imploding toroidal wave at the entrance of the test-section tube. The region of high energy-density at the focus of this imploding toroid was capable of evolving into a self-sustaining detonation wave. In particular, the annular orifice allowed successful detonation transmission for tubes with diameters 2.2 times smaller than cases where no obstacles were located at the interface (Murray et al., 2000).

Thus, the geometry of the wave emerging from the initiator tube has been shown to have a significant effect on the initiation process in the test-section tube (Murray et al., 2000). The appropriate wave geometry could dramatically increase the transmission efficiency and reduce the amount of initiator gas used during detonation initiation. Research at Caltech extended this concept by evaluating the transmission efficiency with a similar experimental design (Fig. 3.2b). Unlike the experiments of Murray et al. (2000), the initiator section was filled with a more sensitive gas than the gas in the test section. Using this technique, detonations were initiated in test section mixtures of  $C_3H_8$ -air at room temperature (298 K), but it was not possible to initiate detonations at elevated temperatures (373 K) in the  $C_3H_8$ -air or JP10-air mixtures. This loss in performance was attributed to the decrease in energy-density of the initiator- and test-gas mixtures due to gas expansion during heating.

The toroidal initiator was designed to create a stronger wave focus than the experimental setup of Murray et al. (2000). The device created an imploding toroidal detonation wave, which was propagated into the test-section tube from the tube wall in an effort to minimize the amount of diffraction that occurred prior to wave implosion. The toroidal initiator was intended to create the imploding wave in HC-air mixtures at elevated temperatures with a minimum amount of HC- $O_2$  initiator gas, and using only a single 46 mJ spark. In order to minimize the required amount of initiator gas, the internal volume of the initiator channels was minimized based on

the information presented in Chapter 2.

### 3.1.2 Planar Initiator

The design of the toroidal initiator involved applying wave focusing ideas to a cylindrical geometry. Such a geometry complicated visualization of its operation, so a planar version of each toroidal initiator, referred to as the planar initiator, was constructed and studied first. An optically transparent window enabled visualization of the detonation wave initiation and propagation processes within the initiator. The planar initiator was also found to be highly successful at generating a large-aspect-ratio planar detonation wave in a very short distance with a minimum amount of energy. This was an improvement over the previously established methods of generating large-aspect-ratio detonation waves such as using exploding wires or cylindrical expansion from a point initiation.

## 3.2 Experimental Facilities and Operation

### 3.2.1 Planar Initiator

The planar initiator design was based on a concept used for generating planar waves in solid-phase explosive research (Hill, 2000). The first-generation planar initiator consisted of a main channel with secondary channels that branch off of the main channel at  $90^\circ$  angles as shown in Fig. 3.3. All secondary channels terminated on a unique line, exhausting into a common test-section area. The channel geometry was such that all paths from the spark point to the secondary-channel-termination-line were equal. Thus, a detonation wave initiated in the main channel and traveling at a constant velocity would spread through the secondary channels to emerge simultaneously at the exit plane and coalesce to form a quasi-planar front as illustrated in Fig. 3.4.

The main channel had a  $9.53 \times 9.53$  mm square cross-section and a length of 0.431 m. The head of the main channel contained a gas fill port. Just downstream of the

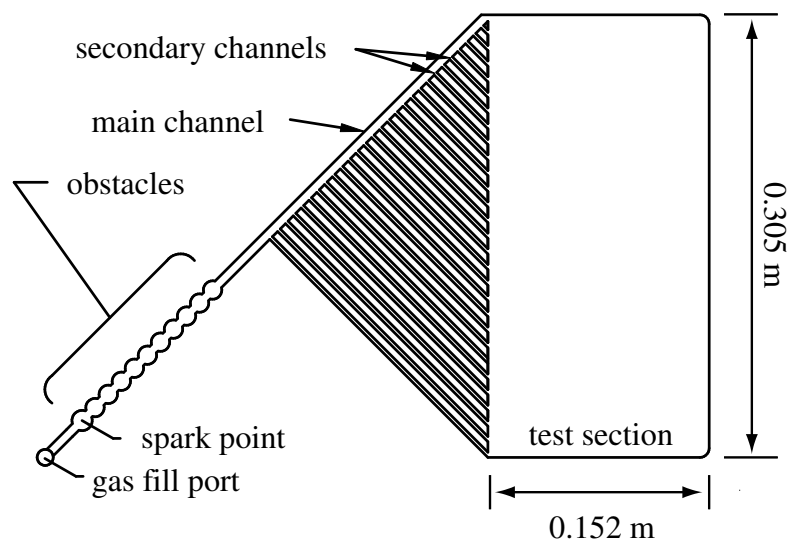


Figure 3.3: Schematic of the planar initiator.

fill port, a spark plug was located next to a series of obstacles that were milled into the main channel to promote DDT. The secondary channels each had a  $5.08 \times 5.08$  mm cross-section and were spaced 2.54 mm apart. Initially, the design had smaller-width channels and smaller obstacles; however, during testing, it became apparent that the channels were not large enough for propane-oxygen detonations to propagate in a regular and repeatable fashion. For this reason, all channels and obstacles were enlarged to the dimensions given above. Drawings of the initial and final dimensions of the facility are shown in Appendix E. In the experimental data discussed below, runs 001-097 were performed before this enlargement of the secondary channels.

The secondary channels exhausted into a  $0.152 \times 0.305$  m test section (Fig. 3.3). The test section contained a ramp near the secondary channel exhaust that enlarged the channel depth from 5.08 mm to 19.05 mm over a distance of 38.1 mm. The top surface of the planar initiator was sealed with two plates of optically transparent polycarbonate windows. A 28.6 mm thick plate provided structural support and a 3.2 mm sacrificial plate was sandwiched between the structural window and the planar initiator. During testing, the sacrificial window would become charred after a series

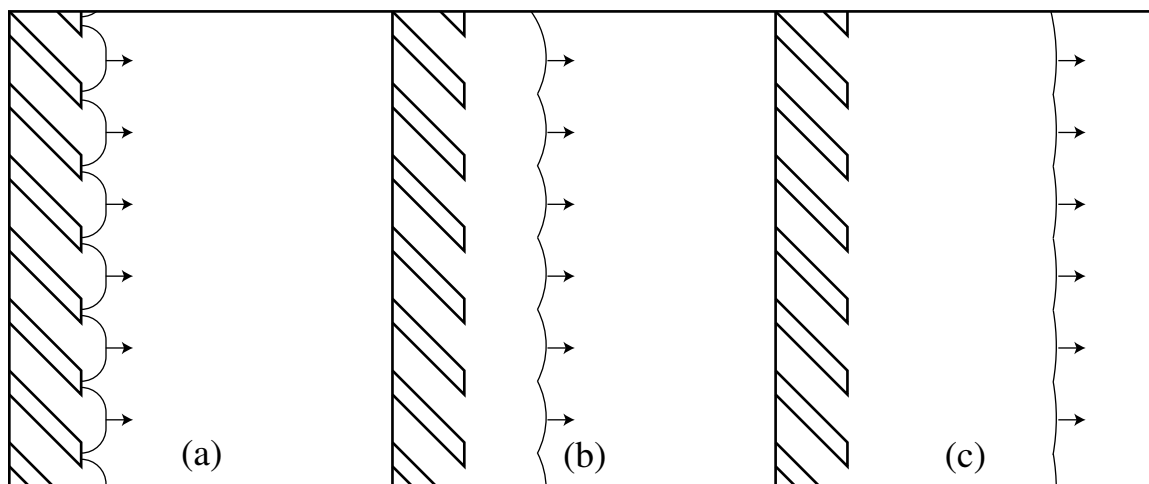


Figure 3.4: A series of sketches showing (a) the detonation wavelets emerging from the small channels of the initiator, (b) the merging of the wavelets, and (c) the generation of the quasi-planar wave.

of experiments and was replaced as needed.

During preliminary testing, it was apparent that insufficient mounting pressure on the windows resulted in a poor seal between the window and the top surface of the initiator. As a result, the detonation wave was able to jump from channel to channel and also propagate in the small gap between the top of the initiator and the window as shown in Fig. E.36 from Appendix E. After some experimentation, this problem was solved by placing a 1 mm thick sheet of Teflon in between the sacrificial window and the initiator. Both surfaces of the Teflon were covered with a thin layer of RTV silicone sealant. This solution created a reliable seal that was sufficient to contain the detonation wave propagation to the initiator channels.

The test section contained one row of four PCB 113A26 pressure transducers and two rows for ionization probes (Appendix C) that were used to detect the planarity of the detonation wave in the test section. Data from the pressure transducers and the ionization probes were collected using two Tektronics TDS 460 oscilloscopes and were processed using Labview software. The sampling rate of the oscilloscopes was 2.5 MHz. An intensified CCD (Princeton Instruments ITE/ICCD-576) camera recorded the chemiluminescence from the combustion for visual inspection of the wave shape.

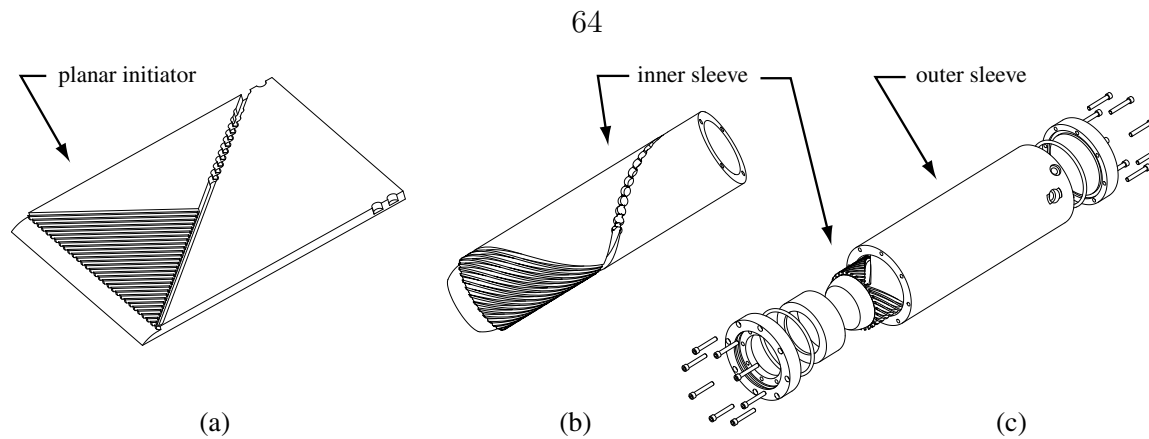


Figure 3.5: The planar geometry (a) is mapped to a cylindrical geometry (b) to create the inner sleeve. The inner sleeve is then inserted into the outer sleeve using shrink-fitting techniques (c).

The pressure transducers provided precise arrival time information for the shock wave in the test section. The CCD imaged the chemiluminescence behind the wave and provided an image of the wave planarity, and the two ionization probes (one was located in the center of each ionization row) allowed the wave velocity in the center of the test section to be determined.

During testing, the device was filled with stoichiometric propane-oxygen-nitrogen and ethylene-oxygen mixtures with initial pressures ranging from 0.20 to 1.50 bar. Gas mixtures were prepared using the method of partial pressures and then mixed for 15 minutes in a separate vessel. A Champion REJ-38 spark plug and associated discharge system (Appendix C) with 46 mJ of stored energy (Lieberman and Shepherd, 2005) was used to ignite the combustible mixture.

### 3.2.2 Toroidal Initiator

The toroidal initiator was created by mapping the geometry of the planar initiator to the surface of a cylinder so that the exit of each channel lies on a circle with the channels exhausting inward. The metal substrate of the planar initiator becomes a cylinder with the channels milled on its outer surface (Fig. 3.5). The inner surface of this cylinder had a diameter of 76.2 mm and formed the test-section tube. A second cylinder, constructed of aluminum, mated to the outer surface of the above

cylinder to seal the machined channels. Adding an additional ramp at the exhaust of the secondary channels turned the emerging wavelets inward toward the axis of the device. The channel dimensions remained the same as with the planar design. This design allows the initiator to be incorporated into the walls of a PDE, minimizing the drag losses by not obstructing the test section flow path in PDE applications. A sketch of the inner cylinder and accompanying schematic of the toroidal initiator is shown in Fig. 3.6 and design drawings with dimensions are shown in Appendix F.

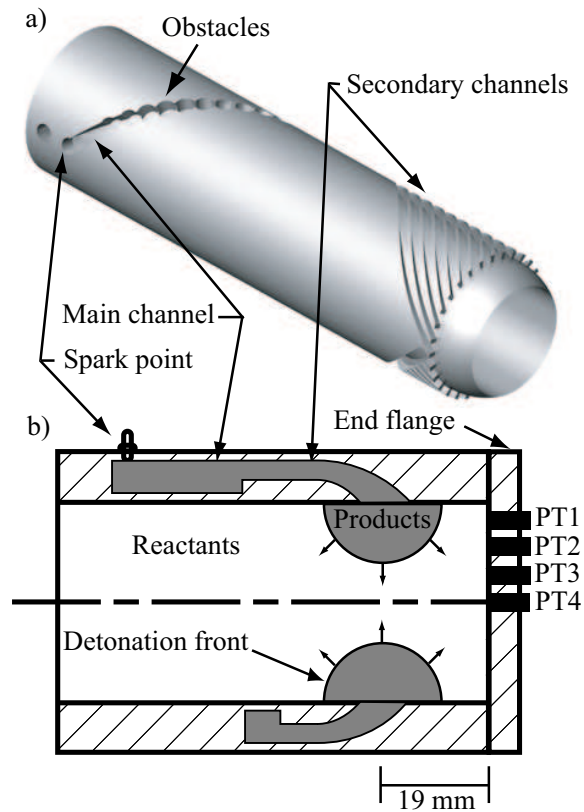


Figure 3.6: Toroidal initiator concept a) rendering and b) accompanying cut-away schematic. In the schematic, the gray areas are products, the white section is reactant, and the hatched areas are initiator walls. Pressure transducers are labeled PT1, PT2, PT3, and PT4.

The seal between the inner and outer sleeves was accomplished by a shrink fit. The outer diameter of the inner sleeve was slightly larger than the inner diameter of the outer sleeve. Prior to assembly, the inner sleeve was cooled in liquid nitrogen and the outer sleeve was kept at room temperature. The resulting thermal contraction

decreased the outer diameter of the inner sleeve so that it could be inserted into the outer sleeve. Once the temperature of the two pieces had equilibrated, the residual stress held the two sleeves together and maintained a tight seal at the interface. The details of this design, including design drawings, a parts description, assembly descriptions, and a discussion and example calculation of the shrink-fitting theory is presented in Grunthaler et al. (2001).

As with the planar initiator, pressure transducers and an intensified CCD camera observed the imploding wave. The end flange (shown in Fig. 3.6) could be instrumented with either pressure transducers or an optically clear window. When the experiment was set up to record pressure transducer measurements, the flange closest to the secondary channel exhaust was outfitted with four pressure transducers (PCB 113A series) spaced along a radial line (Fig. 3.7). The pressure transducers were spaced 10.7 mm apart and were mounted on a surface that was 19 mm from the center of the exit of the initiator as shown in Fig. 3.6. The central transducer was located at the centerline. The oscilloscopes and Labview system used with the planar initiator were also used to collect the toroidal initiator data at a sampling rate of 2.5 MHz.

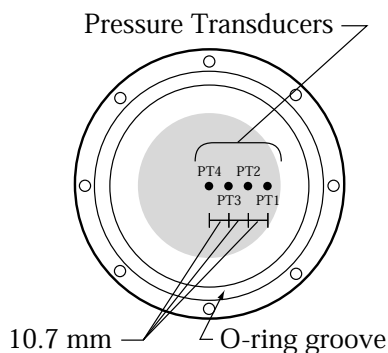


Figure 3.7: A drawing of the end flange with the pressure transducer locations shown. The central transducer was a PCB model 113A24 and all other transducers were PCB model 113A26. The shaded region denotes the wetted area when the focusing ring (Fig. F.5) is installed. Additional dimensions for this flange are shown in Fig. F.9.

When the experiment was set up to collect images of the imploding wave, the end flange consisted of a composite window with a thin sacrificial layer and a thicker

structural portion. The structural portion was 31.8 mm thick polycarbonate with a 6.35 mm thick aluminum ring containing bolt holes (Fig. 3.8) to protect the polycarbonate from the stress concentrations induced by the fastening bolts. The sacrificial layer was a 6.35 mm thick sheet of commercial glass sealed against the initiator via a 2.0 mm thick Viton gasket. Preliminary testing determined that glass windows were better able to withstand the heat generated by the combustion without charring (compared to polycarbonate windows). After approximately a dozen tests, the glass window would begin to develop cracks near the wave focus and would be replaced.

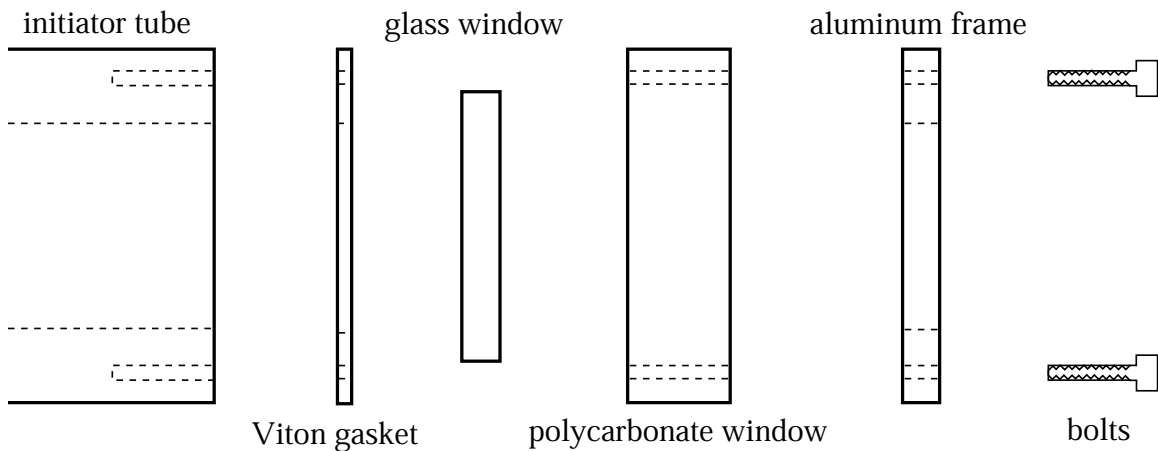


Figure 3.8: An exploded view of the composite window used for imaging the detonation wave.

For image acquisition, the same intensified CCD camera used with the planar initiator experiments was aligned with the centerline of the initiator and positioned a short distance outside the viewing window. The camera was initially (runs 1-24) triggered by the firing of the spark plug, but this technique did not accurately predict the wave arrival time in the test section due to slightly variable DDT times. For later tests (25-43), a pressure transducer was mounted at the exit of one of the secondary channels and used as the camera trigger. Since the pressure transducer was downstream of the DDT process, it provided a more reliable way to predict the wave arrival in the test section.

Testing was performed with stoichiometric propane-oxygen mixtures initially at 1 bar. The device was filled using the method of partial pressures and the mixture was

circulated using a bellows pump to ensure homogeneity. Combustion was initiated with the same spark plug and discharge system used for the planar initiator.

### 3.3 Results and Analysis

#### 3.3.1 Planar Initiator

After enlarging the channels and improving the seal between the initiator and the cover plate, images and pressure traces showed that the device produced planar waves with wave front deviations of less than 1 mm over the 30.5 cm test-section width. The device was consistently able to produce planar waves for initial pressures greater than 0.40 bar. A set of pressure traces are shown in Fig. 3.9 and chemiluminescence images of the detonation front from three different runs are shown in Fig. 3.10. Thus, the planar initiator was successful in generating planar detonation waves with large-aspect-ratios in a short distance. Pressure histories from selected tests and all imaging data are shown in Appendix E.

#### 3.3.2 Toroidal Initiator

A typical set of pressure traces is shown in Fig. 3.11. Transducers PT1-PT3 (Fig. 3.8) show a gradually decreasing post-shock pressure as the radius  $R_s$  (defined in Fig. 3.13) of the imploding torus decreases. However, the pressure appears to rapidly increase between gauges 3 and 4 where the central pressure transducer recorded a value above its maximum reliable operating range. This value was four times larger than the CJ pressure for the mixture. As discussed below, the pressure data differ significantly from idealized model predictions.

As mentioned, the camera was triggered by the detonation wave passing over a pressure transducer located at the end of one of the secondary channels. The wave produced was repeatable with the  $C_3H_8$  mixture, so by varying the delay between the trigger signal and the exposure, it was possible to image the imploding wave at different radii in the initiator test section. A series of images of the collapsing

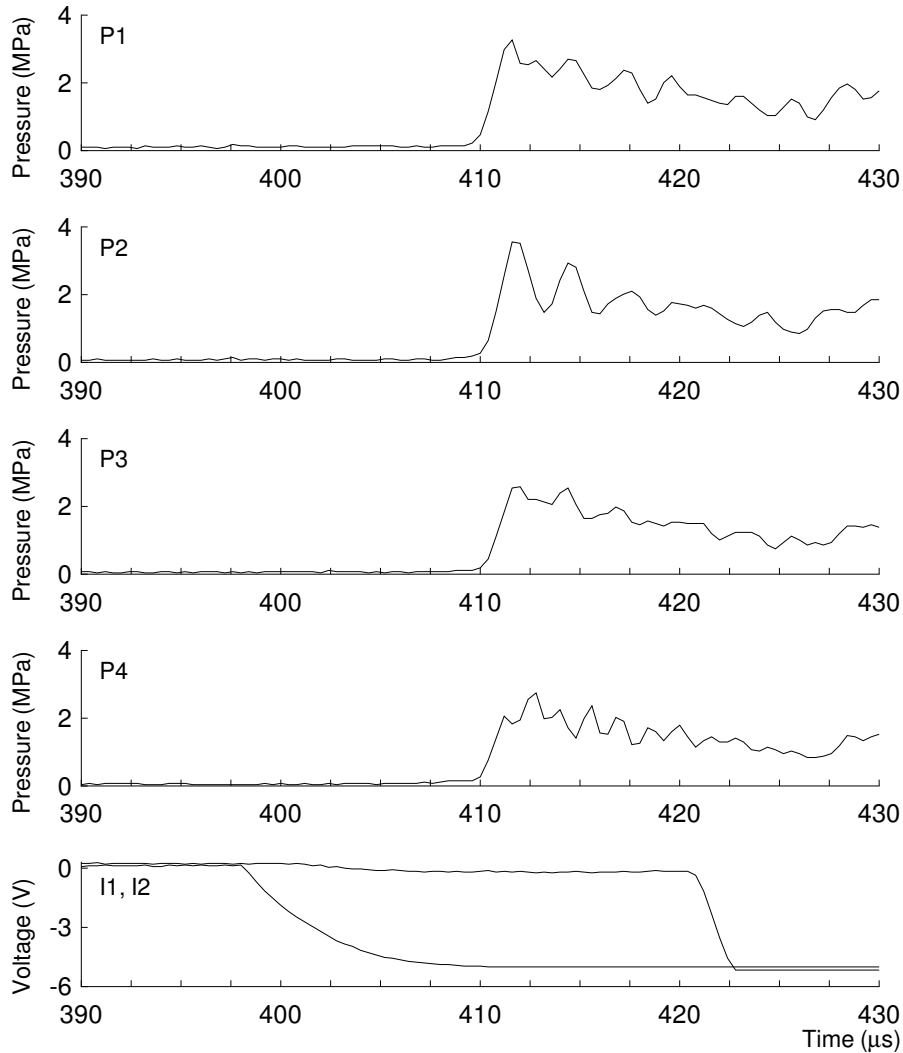


Figure 3.9: Pressure traces (P1-P4) and ionization probe traces (I1 and I2) from the static planar initiator (run 100). For this run, the difference in shock arrival times at each transducer station was not more than  $0.2 \mu\text{s}$  and the wave speed from the ionization probe data was  $2551 \text{ m/s}$ . The arrival time differences correspond to a wavefront deviation from planarity of  $0.5 \text{ mm}$ .

detonation wave is shown in Fig. 3.12.

The outermost black portion of each image is the initiator wall, which frames a  $76 \text{ mm}$  test-section diameter cross-section. In each image, the innermost circle corresponds to the collapsing detonation front. In some images, a “flower-shaped” structure behind the collapsing front (between the innermost circle and the initiator wall) is also visible. This structure is attributed to detonation wave reflection

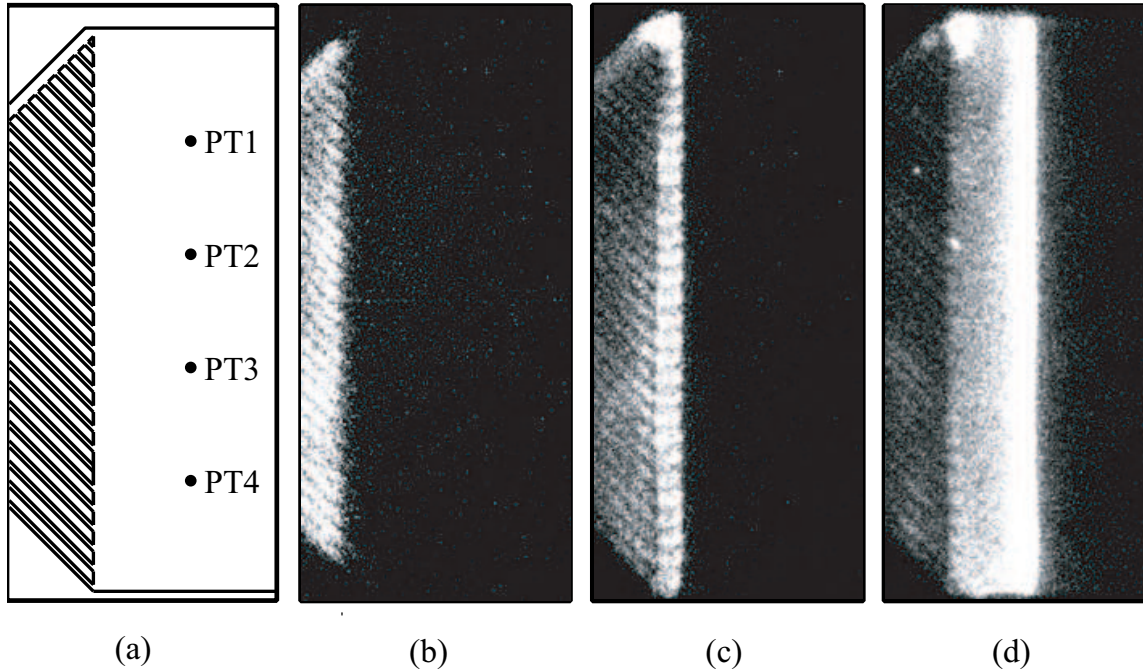


Figure 3.10: Planar initiator results showing: a) schematic of imaging area along with images taken b)  $360 \mu\text{s}$ , c)  $370 \mu\text{s}$ , and d)  $375 \mu\text{s}$  after ignition. Each image was taken during a separate experiment. Test mixture was stoichiometric propane-oxygen at 1 bar and CCD integration time was 100 ns.

from the imaging window. Experiment run conditions, selected pressure traces, and chemiluminescence images are located in Appendix F.

### 3.3.2.1 AMRITA Simulations and Interpretation

While little analysis has been published on imploding toroidal waves (Jiang and Takayama, 1998), much work has been done on cylindrical waves (Takayama et al., 1987, Devore and Oran, 1992, Oran and Devore, 1994, Terao et al., 1995, Akbar, 1997) due to the simplicity of the geometry. It is possible to imagine the focal region of an imploding toroidal wave being approximated by an imploding cylindrical wave. In the following analysis, this assumption is compared to an approximate solution that is developed for an imploding toroidal wave. Experimental results from the toroidal initiator are also compared with the cylindrical and toroidal solutions and a numerical simulation is used to help explain the differences between the experiment and

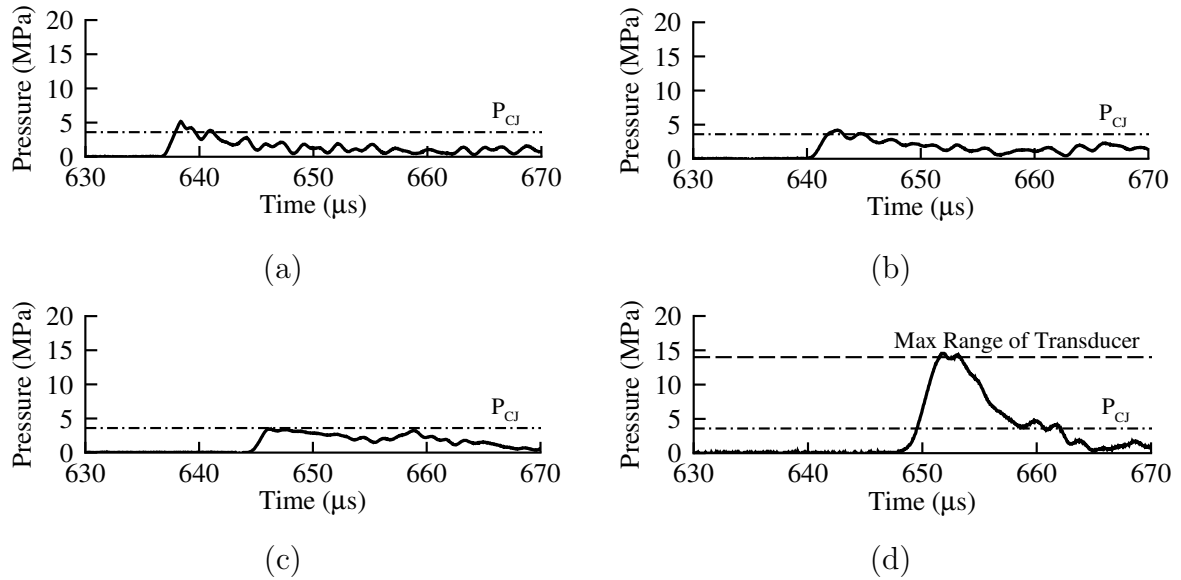


Figure 3.11: Typical pressure traces with a stoichiometric propane-oxygen test from pressure transducers (a) PT1, (b) PT2, (c) PT3, and (d) PT4. Initial pressure was 1.00 bar. Location of the pressure transducers is shown in Fig. 3.6b. The CJ pressure for the mixture is shown as a dashed line. Note that the pressure trace from PT4 exceeds the maximum reliable range of the transducer.

idealized models.

Early research on imploding cylindrical waves focused on shock waves. In 1958, Whitham developed a simple approximate solution to model the shock motion for a cylindrical-imploding-shock wave. His solution was based on an area-Mach number relationship for the wave and was derived by applying the equations of motion along a  $C^+$  characteristic behind the wave. The shock trajectory, pressure, and density were obtained using the shock-jump relations to show an inverse relationship between shock speed and shock area. As the area of the shock wave decreases, it becomes increasingly overdriven, generating elevated post-shock pressures and flow velocities.

Whitham's work was extended by Lee and Lee (1965) to cylindrically imploding detonation waves. Their model showed good agreement with their experiments, demonstrating that a collapsing cylindrical detonation wave is capable of producing pressures about 18 times higher than the normal CJ pressure.

For an imploding cylindrical detonation wave, Lee and Lee (1965) reduced the

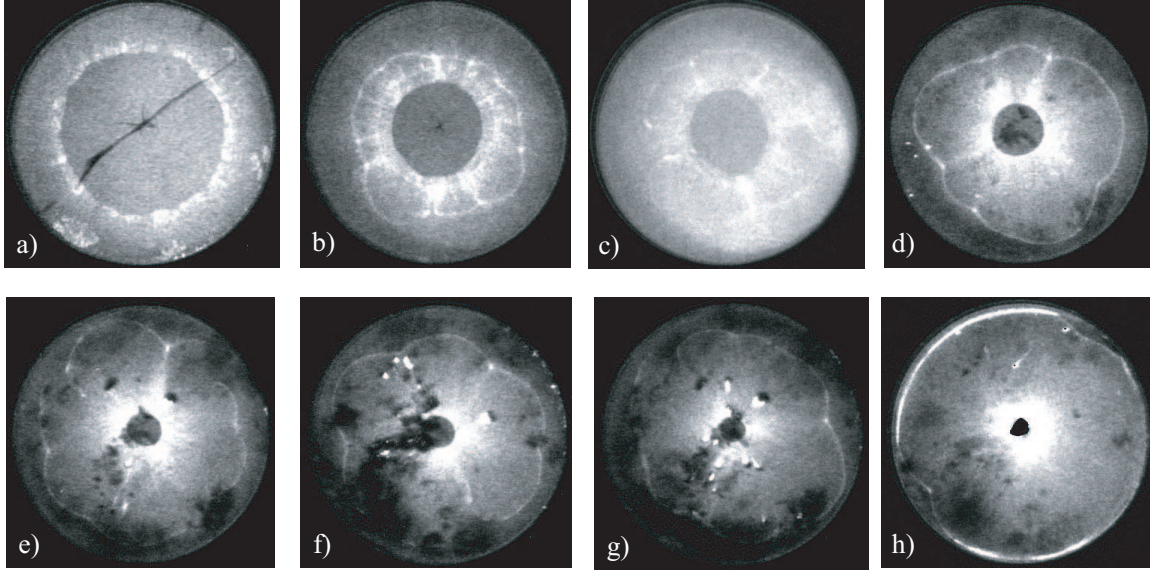


Figure 3.12: Chemiluminescence images of the collapsing toroidal detonation wave. Each image was taken during a separate experiment with a stoichiometric propane-oxygen mixture at 1 bar initial pressure. The period between arrival of the detonation front at the triggering pressure transducer and imaging was a)  $29 \mu\text{s}$ , b)  $34 \mu\text{s}$ , c)  $35 \mu\text{s}$ , d)  $37 \mu\text{s}$ , e)  $38 \mu\text{s}$ , f)  $38 \mu\text{s}$ , g)  $39 \mu\text{s}$ , h)  $42 \mu\text{s}$ . The dark splotches appearing in images (d) - (h) are due to charring of the polycarbonate window. CCD integration times were 100 ns. The diagonal black line in image (a) is a crack in the glass window.

Whitham model to

$$\frac{1 + \gamma\alpha + \gamma [(1 + \gamma)(1 - \alpha)]^{\frac{1}{2}}}{(1 - \gamma\alpha)(1 + \gamma)^2} \times \left[ 1 + \gamma\alpha + \left( \frac{1 + \gamma\alpha}{1 - \alpha} \right)^{\frac{1}{2}} \right] d\alpha + \frac{dA}{A} = 0, \quad (3.1)$$

where  $\alpha$  in Eq. (3.1) depends on the normalized wave speed,  $\dot{R}_s/D$  and  $\gamma$ :

$$\alpha = \left[ 1 - \left( D/\dot{R}_s \right)^2 \right]^{\frac{1}{2}} / \gamma. \quad (3.2)$$

$D$  is the CJ detonation wave velocity,

$$D = [2Q(\gamma^2 - 1)]^{\frac{1}{2}} \quad (3.3)$$

in the “strong-shock” limit.

It is necessary to solve Eq. (3.1) to determine the varying wave radius  $R_s$ . This can be done by relating the surface area of a collapsing cylindrical wave to the normalized shock radius  $R_s/R_i$  where  $R_i$  is the radius of the detonation wave at CJ conditions:

$$\frac{dA}{A} = d \frac{(R_s/R_i)}{(R_s/R_i)}. \quad (3.4)$$

Eq. 3.4 is then substituted into the last term of Eq. (3.1) resulting in a differential equation in which the shock radius can be solved as a function of  $\alpha$ . The initial condition

$$\frac{R_s}{R_i} = 1 \quad \text{at} \quad \alpha = 0 \quad (3.5)$$

can be used by assuming that the initial wave is a CJ detonation.

Solving Eq. (3.1) for  $\alpha$  as a function of  $R_s/R_i$  with the boundary condition allows the density, velocity, and pressure of the collapsing cylindrical detonation wave to be obtained as a function of  $R_s/R_i$  from the shock-jump conditions:

$$\frac{\rho}{\rho_i} = \frac{1}{1 - \alpha}, \quad (3.6)$$

$$\frac{u}{u_i} = \frac{1 + \gamma\alpha}{(1 - \gamma^2\alpha^2)^{\frac{1}{2}}}, \quad (3.7)$$

$$\frac{p}{p_i} = \frac{1}{1 - \gamma\alpha}. \quad (3.8)$$

It is also possible to modify the solution of Lee and Lee (1965) to approximate the motion of an imploding toroidal detonation wave using this method. Equations 3.1-3.3 and 3.6-3.8 remain valid as they are independent of geometry. However, Eq. 3.4 needs to be adapted to the toroidal geometry.

For the geometry in Fig. 3.13, the differential area of a central element of the imploding toroidal detonation wave front initiated at a circle of radius,  $R_i$ , can be represented as

$$\Delta A = 2\pi R_s \cdot \Delta\theta (R_i - R_s). \quad (3.9)$$

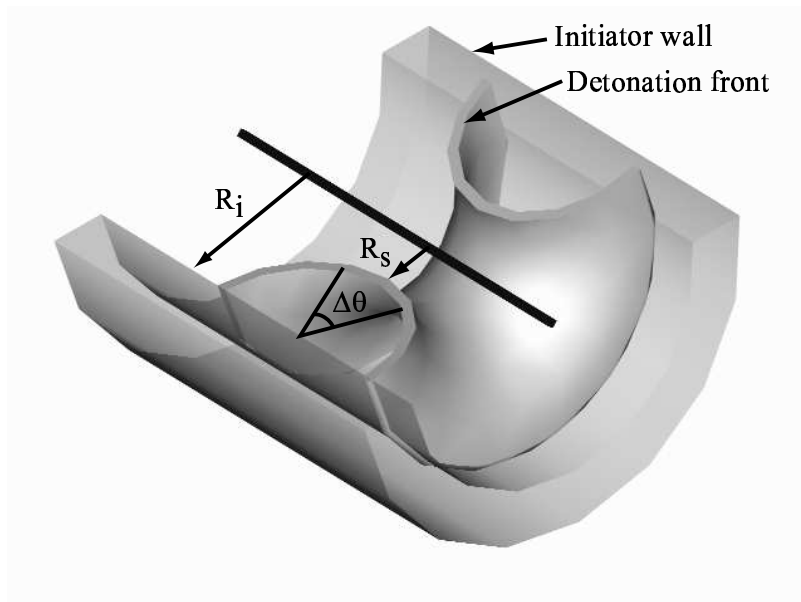


Figure 3.13: The geometry of the toroidal detonation front.

This is the equation for a parabola. Thus, as  $R_s$  decreases (corresponding to an increase of the radius of the torus), the differential surface area of a central element of the front first increases to a maximum at  $R_s = R_i/2$  and then decreases. With  $A$  represented as a function of  $R_s$ ,  $dA/A$  can be represented in terms of  $R_s/R_i$ . However, directly solving for the flow as was done in the cylindrical case is not possible without an additional assumption that the detonation wave remains at CJ conditions throughout that region of increasing area ( $R_s/R_i = 0 \rightarrow 0.5$ ). This is necessary since there are no solutions to the Whitham model (Eq. 3.1) when  $\dot{R}_s < D$ .

Experimentally, a CJ detonation wave emerging from the annulus at  $R_i$  could fail, becoming a non-reactive shock as its area increases. While it is possible that the resulting decoupled shock and reaction zone could reinitiate a detonation following the region of area increase, such analysis is beyond the scope of this discussion. Instead, it is assumed that the detonation is ideal and remains at the CJ condition throughout the area-expansion process. Whitham's method is applied only to the wave from  $R_s/R_i = 0.5 \rightarrow 1$ . In this regime, area is decreasing, resulting in an overdriven ( $\dot{R}_s > D$ ) detonation wave.

In practice, the likelihood of failure depends on the speed of the emerging detonation and the thickness of the detonation reaction zone as compared to the annular opening. While no results are available in the literature for diffraction of waves through an annulus in the side wall of a tube, the results of Murray et al. (2000) for an annular opening at the end of a tube should be a useful guide. If the detonation is propagating close to the CJ velocity, it will be transmitted as a detonation if the reaction zone length is sufficiently small compared to the width of the annular opening. If the reaction zone is too thick in comparison to the annular opening, failure of the detonation diffraction is anticipated. In the present case, the annular opening is about 12.7 mm, which is 423 times larger than the estimated reaction zone length of 30  $\mu\text{m}$  for a stoichiometric propane-oxygen mixture at an initial pressure of 1 atm (Schultz and Shepherd, 2000b). Based on previous diffraction experiments with slots (Benedick et al., 1984), this should be adequate to achieve successful detonation. In terms of the more conventional approach using detonation cell width to characterize the opening, the cell width is about 0.9 mm and the opening is, therefore, about 14 cell widths, greater than the six to ten cell widths previously observed to be needed for successful diffraction from planar slots (Benedick et al., 1984).

Experimental pressure data for the toroidal wave are plotted against previously discussed cylindrical and toroidal theories and shown in Fig. 3.14. As exhibited in the pressure history data in Fig. 3.11, the pressure of the toroidal detonation wave initially decays before increasing to more than four times  $P_{CJ}$  during the final stages of focusing. As expected, neither the cylindrical theory nor the toroidal theory exhibits a pressure decay at any point during the focusing process.

It is important to note that, as shown in Fig. 3.6, pressure was not actually measured along the central axis of the toroidal implosion, where the theoretical cylindrical and toroidal pressures were calculated. Thus, the measured pressures do not directly compare to the idealized calculations. Instead, they show effects of off-axis diffraction and shock interaction with the end flange. The peak pressures measured by the transducers on the end flange are significantly influenced by the angle the detonation wave makes with respect to the measurement surface. Only when the detonation front is

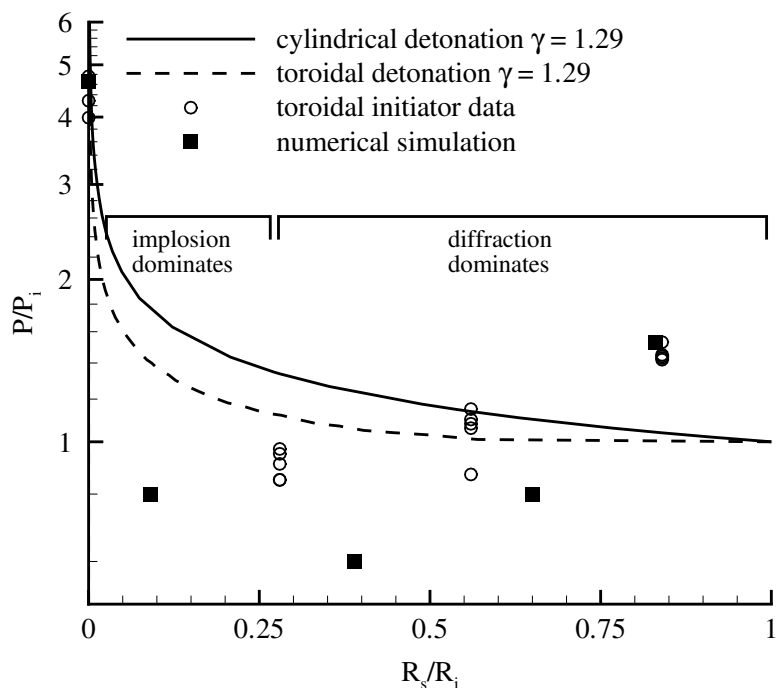


Figure 3.14: Comparison of imploding-cylindrical-detonation theory, imploding-toroidal-detonation theory, toroidal-initiator data and numerical simulations of an imploding shock from AMRITA.

normal to the wall can pressure be considered representative of the actual pressure in the undisturbed waves. The geometric considerations and the wave front shapes computed in the shock simulation of Fig. 3.15 (discussed below) indicate that a range of obliquities occurs. At the outer edge of the flange, the wave front is almost parallel to the end flange. As the wave proceeds inward, the front will rotate away from the wall. Previous work (Nettleton, 1987, Meltzer et al., 1993, Akbar, 1997) has shown that the reflection type will change from regular reflection to Mach reflection at the point where the included angle between the wave front and the wall is about  $55^\circ$ . For included angles between  $0^\circ$  and  $55^\circ$ , the peak pressure will be approximately  $2.5 P_{CJ}$ . Between  $55^\circ$  and  $90^\circ$ , the pressure decreases monotonically to  $P_{CJ}$ . This variation of pressure with wave angle is responsible for the peak pressure values greater than the CJ values as observed on the outer two transducers.

A computer simulation of the experiment was used to help clarify the pressure

wave interactions and focusing phenomena. Hornung (2002) computationally simulated a strong shock propagating through the geometry of the toroidal initiator with AMRITA (Quirk, 1998). Although the simulation is for non-reacting flow, it demonstrates how shock interaction with the pressure-sensing wall can result in the observed pressures. A series of images of the simulated shock geometry and pressure profile along the right wall is shown in Fig. 3.15. The simulation assumes an ideal gas in two-dimensional, axisymmetric flow; the lower edge of each image is the axis of symmetry.

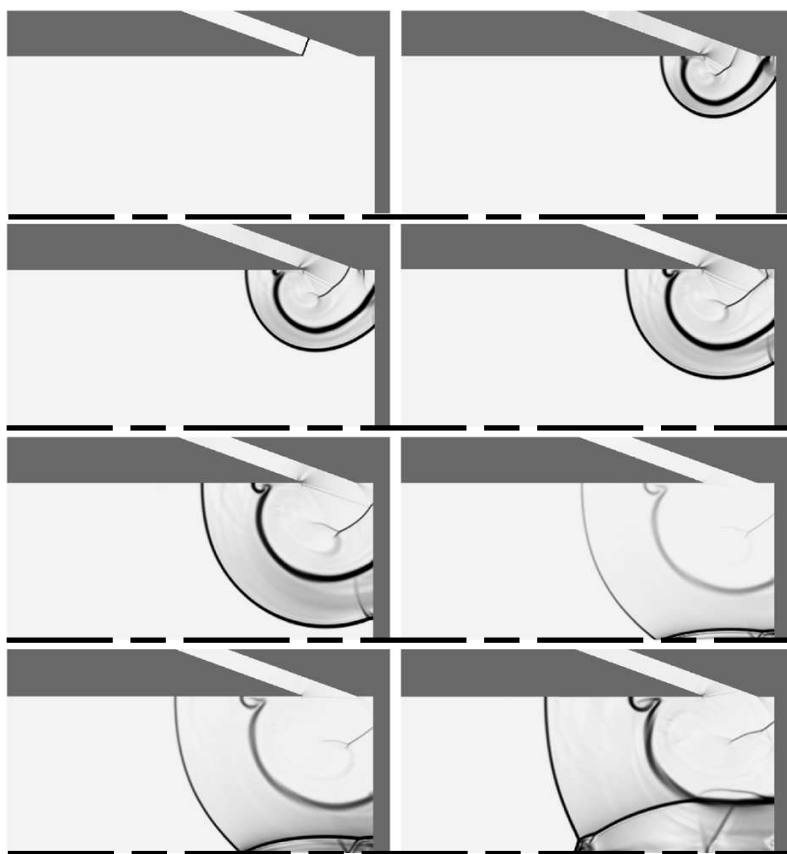


Figure 3.15: A series of images from numerical computations showing an imploding toroidal shock wave. The images are pseudo-schlieren visualizations showing density gradients in the flow. The initial conditions were a shock wave with  $P_2/P_1 = 15$  and  $T_2/T_1 = 10$ . Computations by Hornung (2002) using AMRITA (Quirk, 1998).

The simulation captures the experimental trend with initial pressure decay and the large increase in pressure toward the end of the focusing process. Figure 3.16 is

a composite of several images showing the leading shock at four different times along with the locations of the pressure transducers in the experiment. Segments of the pressure spatial distribution are shown for each of these times. Note the interaction of the shock with the wall at each location.

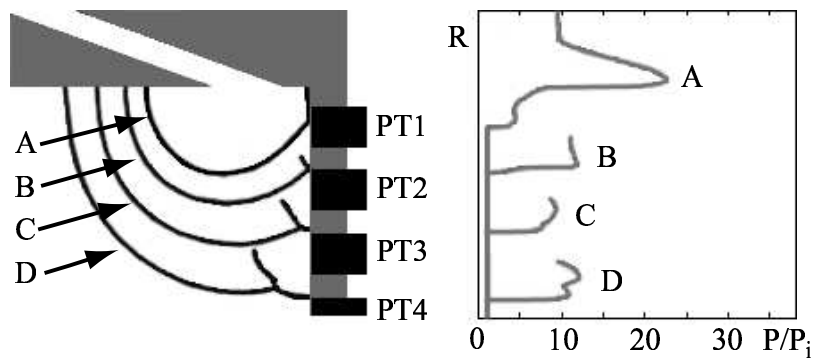


Figure 3.16: This composite image shows the shock front at four different times. The corresponding spatial pressure profiles are also plotted. Transducers not to scale.

Initially, near transducer PT1, the shock wave exhibits almost complete normal reflection from the wall. Correspondingly, the measured pressure at location PT1 is higher than the initial shock pressure. As the wave progresses, the reflection develops into a small Mach stem at location PT2, which results in a lower measured pressure than was recorded at PT1. As the Mach stem increases in size, the measured pressure at the wall decreases. Between locations PT3 and PT4, the focusing processes, initially weak, begin to dominate the system, and the pressure rises dramatically. The general trend from the four post-shock pressure histories (Fig. 3.16) follows that of the post-shock pressures measured in the toroidal initiator (Fig. 3.14).

The measured pressure evolution can be thought of as a combination of three processes: detonation-wall interaction, focusing effects, and diffraction. Initially, the detonation is not overdriven and focusing effects are weak. Detonation-wall interactions dominate the measured pressure, leading to the apparent pressure decay. Later on in the process after the Mach stem has developed, focusing processes significantly overdrive the wave and dramatically increase the pressure. It is important to note that the apparent pressure decay due to the wall reflection is not actually present

along the focal axis of the device, whereas the pressure increase due to focusing is present. However, since the toroidal wave is diffracting, some pressure decay is expected at any location off the implosion axis. Neither the diffraction nor the apparent wall reflection effects are present in the theoretical cylindrical wave solution as the wave is always assumed perpendicular to the pressure wall.

### 3.3.3 Pulsed Operation Considerations

In order to detonate the most insensitive mixtures possible in the test-section tube, the initiator channels were filled with a sensitive HC-O<sub>2</sub> initiator gas. Doing so ensured reliable detonation initiation and propagation in the small channels and sent the strongest possible wave into the test-section tube, promoting successful detonation transmission to the test-section mixture.

Filling different sections of the initiator with different mixtures required either a diaphragm or a dynamic injection system, such as the one used in Austin (2003), to generate the mixture gradients. A dynamic injection system was chosen for testing, since it would better simulate the operation of the device in a PDE.

During operation with the dynamic gas injection, the entire initiator volume would be filled with the insensitive mixture intended to be detonated in the test section. Then, sensitive initiator gas would be rapidly injected into the device at the gas injection port (Fig. 3.3). This initiator gas would displace the test-section gas, pushing it out of the small channels and into the test section. At the end of the gas injection, it was expected that the small channels would be completely filled with only the sensitive-initiator gas and the test section would contain only the insensitive test-section gas. Immediately after gas injection, the mixture could be initiated at the spark point.

Experimentation determined that the initiator design presented above was not suitable for rapid filling of the initiator channels. Different paths through the device had different flow resistance. The flow resistance variation with the path is attributed to (1) the difference in dimensions in the main and secondary channels and (2) the

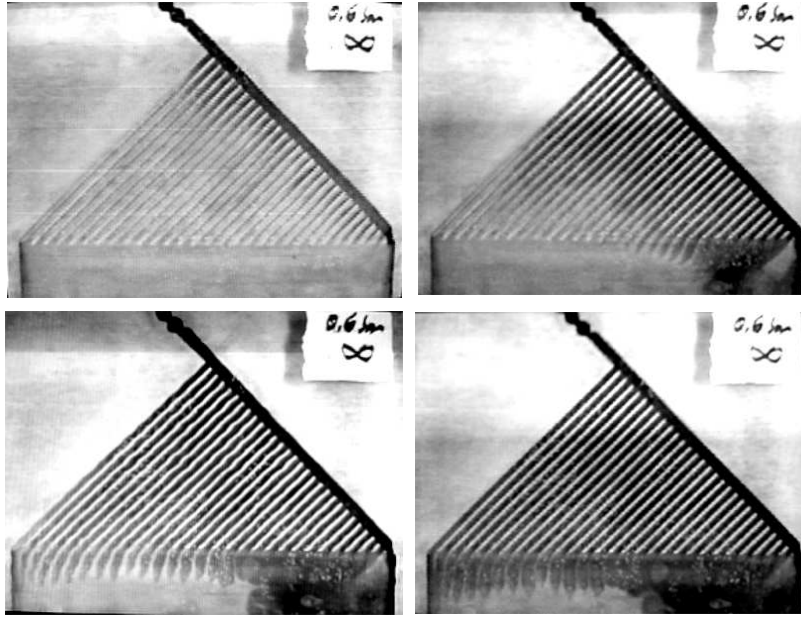


Figure 3.17: Water colored with dye was injected into the planar initiator from a 0.6 bar gauge source. Note how the injected fluid fills the main channel more quickly than the smaller channels. The planar initiator is oriented  $90^\circ$  clockwise compared to the schematic shown in Fig. 3.3. Images taken by F. Pintgen.

presence of the secondary channel entrances on the main channel wall. The result was that gas flowed through the main channel much more easily than through the secondary channels. This effect is illustrated by first filling the planar initiator with clear water and then injecting dyed water into the main channel as shown in Fig. 3.17.

During these experiments, the dyed water injected into the initiator traveled preferentially down the main channel. Small channels near the end of the main channel filled more quickly than those at the beginning and the dyed-water pools near the exhaust of the main channel. When using combustible gases instead of water, the detonation wave would travel more quickly and consistently through the more sensitive initiator gas (represented by the dyed water in Fig. 3.17), and would result in production of a non-planar wave. In order for the injected gas to uniformly fill the device, it was necessary to redesign the channel geometry such that the channel resistance was independent of path length.

The redesign of the channel geometry is discussed in the following chapter. The

initiator designs presented in this chapter are useful in creating large-aspect-ratio planar detonation waves and imploding toroidal detonation waves, as long as the entire initiator volume is filled with a single gas mixture sensitive enough to propagate a detonation through the small channels. As these initiator designs can not be used with dynamic gas injection systems, they are referred to as static initiators. The next generation of initiators with channel paths designed for uniform flow resistance are referred to as dynamic initiators.

### 3.4 Summary

Detonation initiators were developed that are capable of creating planar and toroidal detonation waves from a single spark and an array of small diameter channels. The planar detonation initiator develops a large-aspect-ratio planar detonation wave in shorter distances than is possible using exploding wires or by diffracting a wave from spherical initiation. Wavefronts produced by the planar initiator are planar to within 1 mm over the 30.5 cm test-section width.

The toroidal detonation initiator generates an imploding toroidal detonation wave inside of a detonation tube. Images of the imploding wave show that it is regular and repeatable. The pressure history measured near the focus of the imploding wave indicates the existence of pressures in excess of four times the  $P_{CJ}$ .

A model for the pressure in the central region of the imploding toroidal wave was developed using the work of Lee and Lee (1965) and was found to agree with the experimental data. Numerical simulations by Hornung (2002) were used to explain differences between the theory and experiment. The analysis indicates that for most of the evolution of the imploding wave, diffraction dominates. A significant pressure increase from the imploding geometry is evident only as the wave reaches the final stage of focusing.

Dye-injection experiments showed that the channels of the static initiators result in flow resistance that varies for different paths through the device. These varying flow resistances prevent the initiators from being used with dynamic injection. The

redesign of the channel geometry and initiator performance with dynamic gas injection are discussed in the following chapter.

## Chapter 4

# Dynamic Detonation Initiator

### 4.1 Introduction

As shown in Chapter 3, the channel geometry of the static initiator design was not acceptable for use with pulsed or dynamic operation. In this chapter a redesigned channel geometry is presented for the dynamic planar and toroidal initiators along with the results of testing each initiator. Both used a gas injection system that dynamically filled the initiator channels with equimolar acetylene-oxygen gas shortly before ignition to initiate less-sensitive test-section mixtures. In particular, the toroidal initiator was able to initiate stoichiometric propane-air mixtures and the planar initiator was able to initiate stoichiometric propane-oxygen diluted with 60% nitrogen by volume and stoichiometric ethylene-oxygen diluted with 72% nitrogen by volume (Austin, 2003). More extensive testing of the toroidal initiator was also performed with a static stoichiometric ethylene-oxygen gas mixture to better characterize the implosion process.

### 4.2 Experimental Facilities and Operation

#### 4.2.1 Planar Initiator

The dynamic planar initiator is shown in Fig. 4.1. Taking into account the design flaws discussed in Section 3.3.3, the new channel geometry ensures that all channel

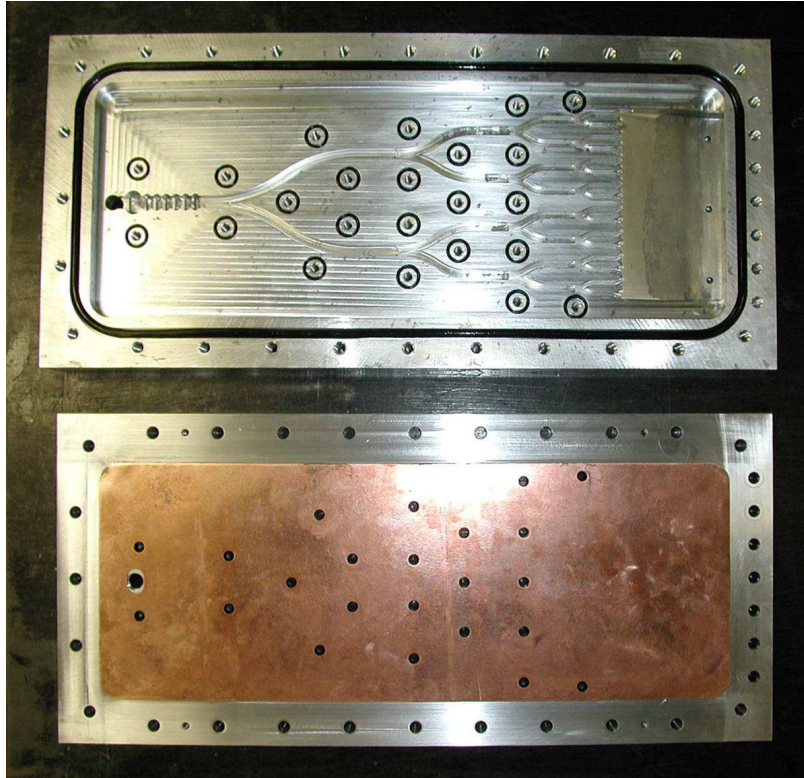


Figure 4.1: The dynamic planar initiator (top) and cover plate (bottom) are shown. The copper gasket sits on top of the cover plate. Note the symmetric channel design. Design drawings are available in Appendix G.

paths have equal lengths and flow resistances. Path lengths are identical due to the symmetry of the channel design along the horizontal axis (Fig. 4.1). This symmetry also lends itself to uniform flow resistance: At each channel intersection, the downstream channels branch out at similar angles (in opposite directions) and have similar channel widths. While more complicated to machine, the design also does not require detonations in the channels to turn sharp corners, which can often weaken the waves or cause them to fail.

The channel dimensions are shown in Table 4.1 and additional dimensions are available on the design drawings in Appendix G. As the design and operation are similar to the static planar initiator discussed in Chapter 3, only key differences between the static designs and the dynamic designs are discussed in this chapter.

A copper gasket was used instead of the Teflon gasket to seal the interface between

Series number	Number of channels	Channel width	Arc length per channel
1	1	10.2 mm	152.4 mm
2	2	8.5 mm	115.7 mm
3	4	7.2 mm	89.4 mm
4	8	6.1 mm	53.8 mm
5	16	5.1 mm	35.6 mm

Table 4.1: Channel dimensions of the dynamic planar initiator shown in Fig. 4.1.

the channels and the cover plate. Copper was more resistant to the combustion conditions and did not require frequent replacement. Several bolt holes (sealed with O-rings) in between the channels allowed the cover plate to be securely attached to the top of the initiator and ensured that the gasket sealed properly. The test section was 152 mm wide and the height gradually expanded from the initiator channel exit height (5.1 mm) to 18 mm. The test section connected to the Caltech Narrow Channel Facility, which is essentially an 18 mm  $\times$  152 mm rectangular channel that is several meters in length (Austin, 2003).

The test section contained three PCB model 113A26 pressure transducers, which were connected to a data acquisition system with a sampling rate of 1 MHz. For visualization of the wave chemiluminescence, the aluminum cover plate and copper gasket shown in Fig. 4.1 were replaced with an optically transparent polycarbonate cover plate and Teflon gasket. The dimensions of the cover plate and gasket were the same as their metal counterparts. The same ICCD camera described in Chapter 3 was used to image the experiment.

The gas injection system was driven by an interlocked timing circuit that controlled the injection of an equimolar acetylene-oxygen mixture into the initiator and the firing of the spark plug (Austin, 2003). With the system, it was possible to control two parameters, the duration of initiator gas injection and the delay between the end of gas injection and the firing of the spark plug discharge system (discussed in Chapter 3). For the planar initiator testing, the injection duration was about 0.8 s.

For all dynamic initiator tests discussed herein, the goal was to characterize the planarity of the waves produced by the dynamic initiator. Thus, the test section was

filled with air at an approximate initial pressure of 0.2 bar prior to injection system functioning. Specific testing parameters are given in Appendix G. The initiator was operated with insensitive HC-O<sub>2</sub>-N<sub>2</sub> mixtures in the test section in a separate study (Austin, 2003). As previously mentioned, Austin (2003) was able to initiate insensitive mixtures such as C<sub>3</sub>H<sub>8</sub> + 5O<sub>2</sub> + 9N<sub>2</sub> and C<sub>2</sub>H<sub>4</sub> + 3O<sub>2</sub> + 10.5N<sub>2</sub> using the dynamic planar initiator.

## 4.2.2 Toroidal Initiator

In all aspects except for the initiator channel geometry, the dynamic toroidal initiator was identical to the static toroidal initiator. An image and accompanying schematic of the initiator is shown in Fig. 4.2. The channel design was based on that of the dynamic planar initiator; however, a 180° turn was incorporated into the second series of channels in order to minimize the initiator length. Design drawings and dimensions are given in Appendix H.

### 4.2.2.1 Operation without Gas Injection

The dynamic toroidal initiator was initially tested without dynamic gas injection in order to verify that the new channel geometry was capable of creating an imploding wave. During testing without dynamic gas injection, the toroidal initiator was filled with stoichiometric propane-oxygen or ethylene-oxygen mixtures to 1.0 bar initial pressure using the method of partial pressures. A bellows pump was used to recirculate the gas to ensure homogeneity. After recirculation, the spark plug was discharged to ignite the mixture. As with previous experiments (Chapter 3), the end flange of the initiator was equipped with either pressure transducers or a window for imaging of the wave.

### 4.2.2.2 Operation with Gas Injection

For tests with the dynamic gas injection system, the initiator was attached to a longer tube, creating a test-section tube 1.0 m long, with 0.4 m made up by the

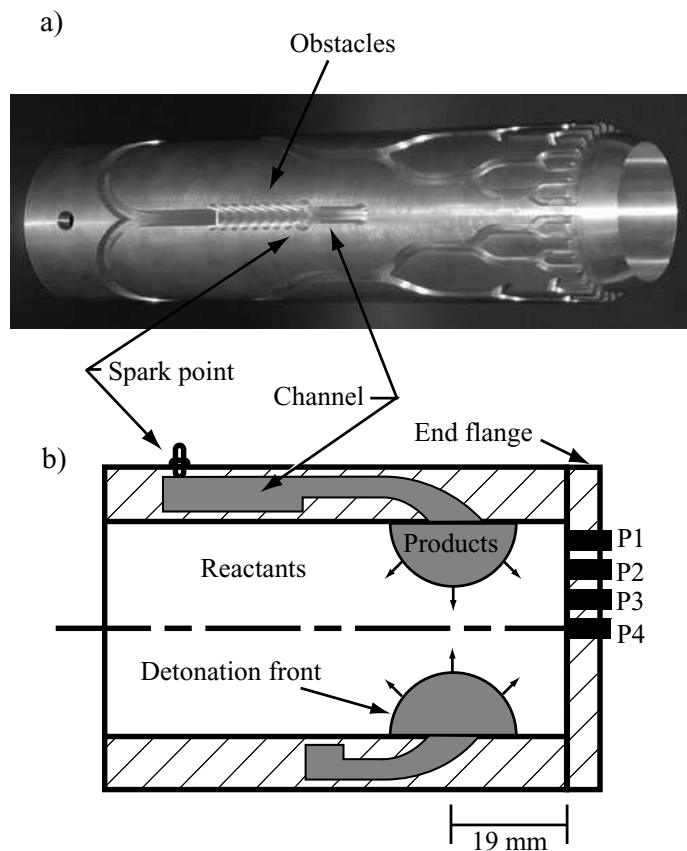


Figure 4.2: The dynamic toroidal initiator a) inner sleeve and b) accompanying schematic. In the schematic, the gray areas are products and the white area is reactants. Hatched sections indicate the initiator walls. Pressure transducers located on the end flange are labeled P1, P2, P3, and P4.

toroidal initiator. The facility was filled with stoichiometric ethylene-oxygen-nitrogen and propane-oxygen-nitrogen mixtures using the method of partial pressures. As before, mixture homogeneity was accomplished by gas circulation via a bellows pump. After mixing, the dynamic gas injection system (Austin, 2003) injected an equimolar acetylene-oxygen mixture into the initiator channels and discharged the spark plug. Pressure transducers and ionization probes located in the toroidal initiator and test section measured the resulting combustion front. The facility is shown in Fig. 4.3.

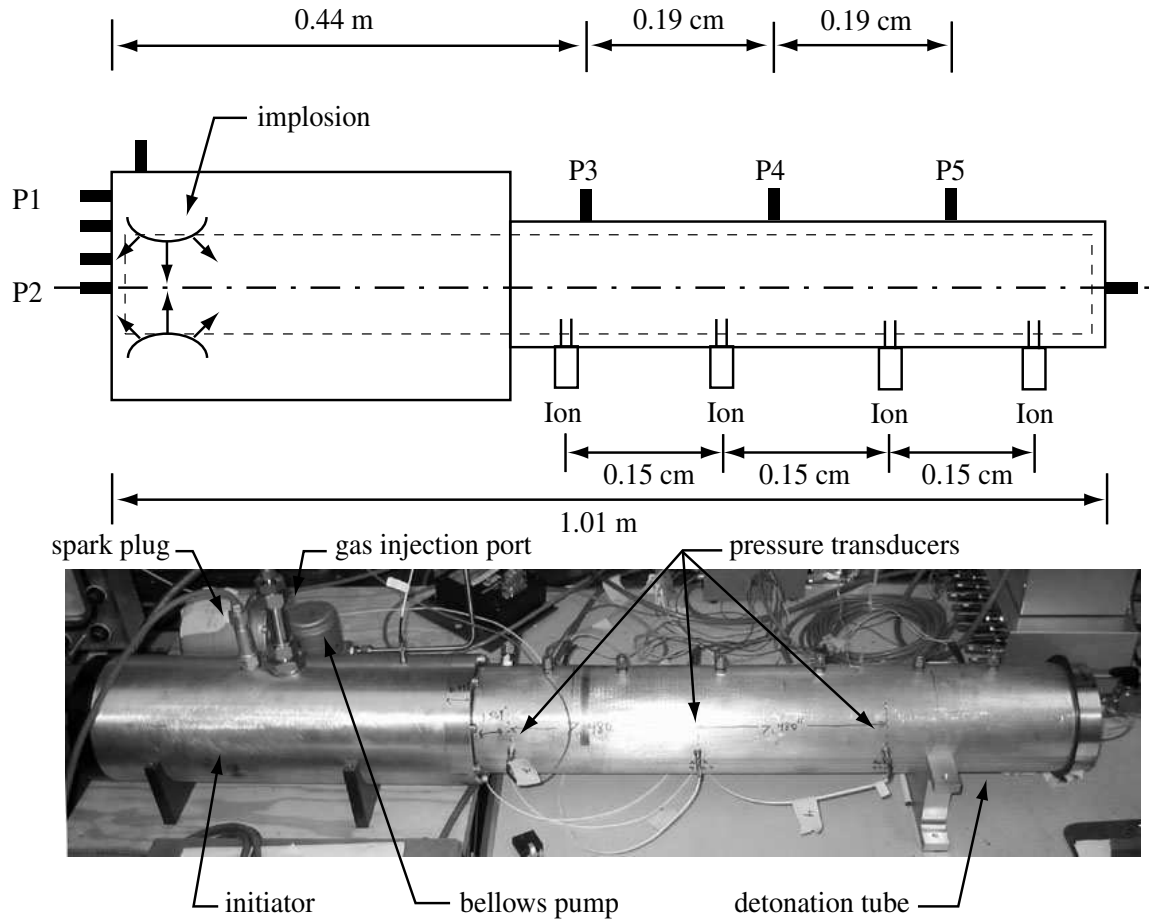


Figure 4.3: A schematic and accompanying picture of the experimental setup used for initiation of hydrocarbon-air mixtures. The initiator is on the left; the extension tube is on the right. PCBs P3-P5 are spaced 19.0 cm apart. Ion probes are spaced 15.0 cm apart.

## 4.3 Results and Analysis

### 4.3.1 Planar Initiator with Gas Injection

Figure 4.4 contains a series of images taken by an intensified CCD camera with exposure times of 100 ns. The channel orientation is the same as in Fig. 4.1. Chemiluminescence of the burning gas allows the progress of the detonation to be traced throughout the initiator channels. In the final image, the detonation wavelets in the channels have combined in the test section to form the planar detonation front. Pressure traces indicate that the resulting front in the test section is planar to within 6

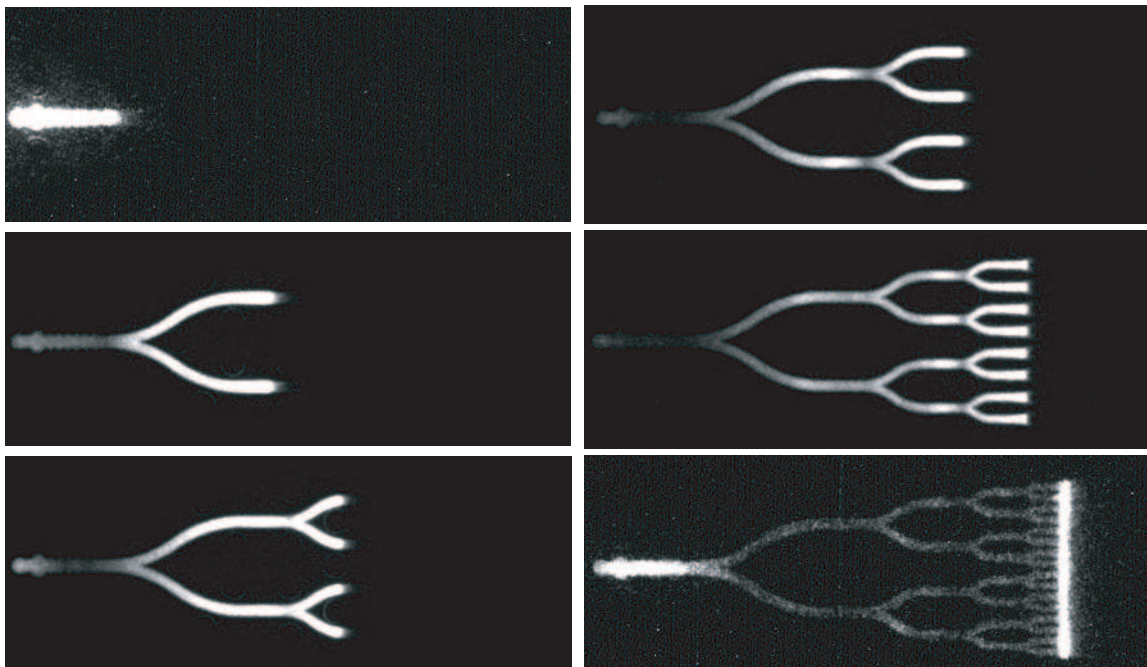


Figure 4.4: Chemiluminescence images from the dynamic planar initiator.

mm over a distance of 15 cm. Wave arrival times, pressure histories and chemiluminescence images are available in Appendix G.

### 4.3.2 Toroidal Initiator without Gas Injection

Run conditions and pressure data for the dynamic toroidal initiator tests with no gas injection is located in Appendix H. The pressure data collected from the transducers on the end flange were found to be similar in all aspects to the pressure data from the static toroidal initiator.

Images obtained from testing with stoichiometric ethylene-oxygen mixtures (Fig. 4.5) show a repeatable and regular collapsing circular front. The imaging view is the same as with the images in Section 3.3.2. While each image in Fig. 4.5 is from a separate experiment, multiple images of a single experiment were also recorded using a Cordin Model 220 gated, intensified camera that acquired an exposure every  $2.5 \mu\text{s}$  (Fig. 4.6). Those images were essentially identical to the single-run images (Fig. 4.5) and verified that with stoichiometric ethylene-oxygen mixtures at 1 bar initial pressure, the

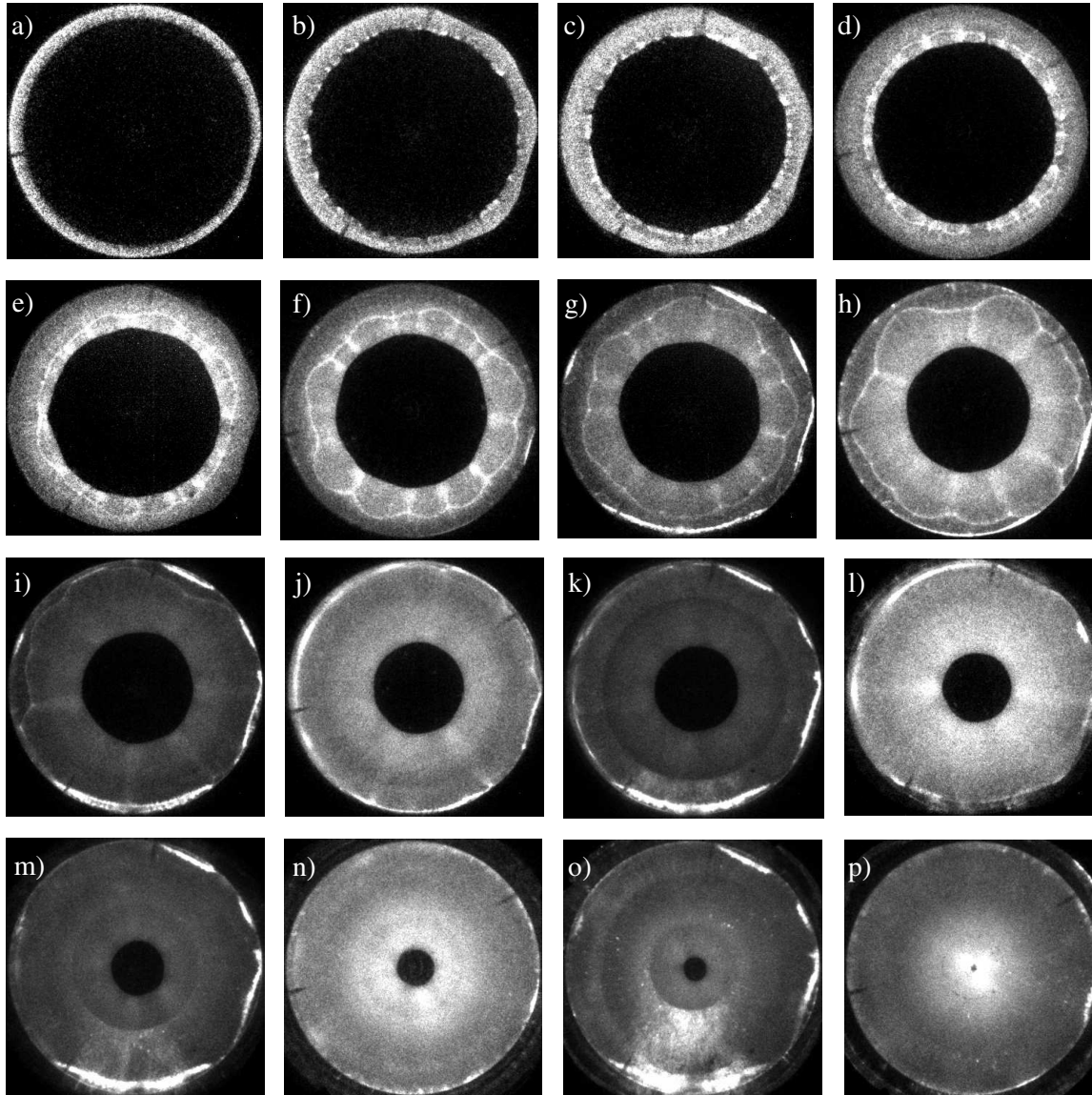


Figure 4.5: Chemiluminescence images of collapsing toroidal detonation wave in a stoichiometric ethylene-oxygen mixture at 1 bar initial pressure. Each image was acquired during a separate experiment and the period between the arrival of the detonation front at the triggering pressure transducer and imaging was a)  $18 \mu\text{s}$ , b)  $20 \mu\text{s}$ , c)  $21 \mu\text{s}$ , d)  $22 \mu\text{s}$ , e)  $23 \mu\text{s}$ , f)  $24 \mu\text{s}$ , g)  $25 \mu\text{s}$ , h)  $26 \mu\text{s}$ , i)  $27 \mu\text{s}$ , j)  $28 \mu\text{s}$ , k)  $29 \mu\text{s}$ , l)  $30 \mu\text{s}$ , m)  $31 \mu\text{s}$ , n)  $32 \mu\text{s}$ , o)  $33 \mu\text{s}$ , p)  $34 \mu\text{s}$ .

initiator operation is repeatable.

Using the series of images shown in Fig. 4.5, it is possible to infer the wave speed of the collapsing front. Fig. 4.7 contains a distance-time plot of wave radius against time. The data indicate that the wave is collapsing at a steady rate. The measured wave

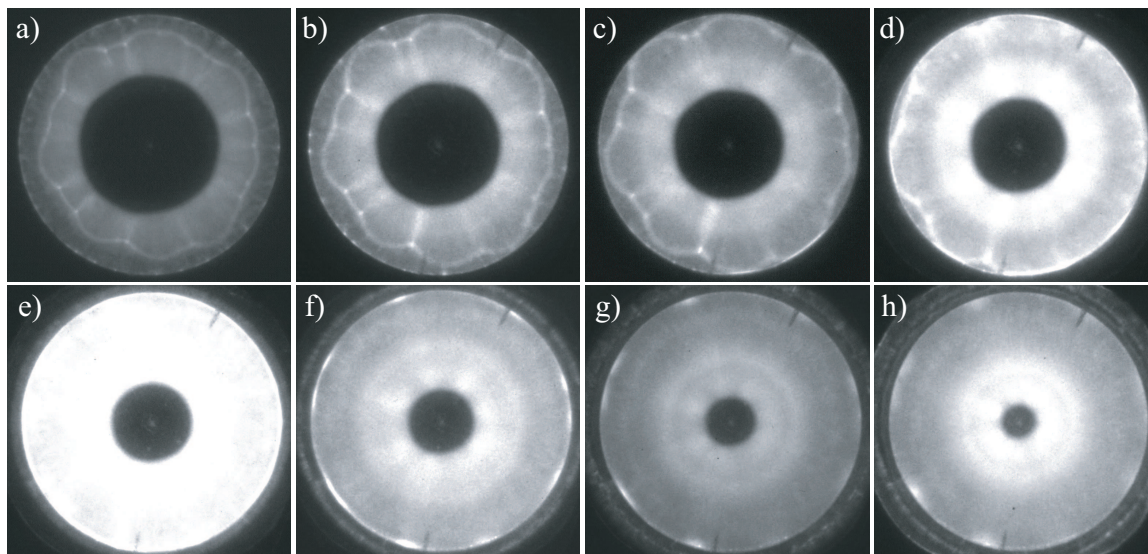


Figure 4.6: Chemiluminescence images of collapsing toroidal detonation wave in a stoichiometric ethylene-oxygen mixture at 1 bar initial pressure. Exposure times are 800 ns and all images were acquired during a single test. The period between the arrival of the detonation front at the triggering pressure transducer and imaging was a) 20.0  $\mu\text{s}$ , b) 21.0  $\mu\text{s}$ , c) 22.0  $\mu\text{s}$ , d) 23.0  $\mu\text{s}$ , e) 24.0  $\mu\text{s}$ , f) 25.0  $\mu\text{s}$ , g) 26.0  $\mu\text{s}$ , h) 27.0  $\mu\text{s}$ . Thanks to Cordin Scientific Imaging for use of the Model 220 camera and to N. Nebeker for assistance with the acquisition of these images.

velocity is 2200 m/s, which is 9% lower than the theoretical detonation wave speed of 2400 m/s predicted by the CJ theory. The velocity deficit can be explained by using Whitham's method to solve for the amount of overdrive present in the imploding wave. In Section 3.3.2.1, it was found that collapsing toroidal waves exhibit an initial period of velocity and pressure decay that is followed by a short period of overdrive due to wave focusing at the very end of the implosion process. In earlier work, velocity measurements of the collapsing wave were not available. The pressure of the imploding wave was observed to decay early on in the implosion process; however, this effect was attributed to wave decay and wall effects. The observed velocity deficit in recent experiments provides more direct evidence that the toroidal wave is underdriven for much of the implosion process.

While the initiator produces repeatable results with stoichiometric ethylene-oxygen mixtures, it produces irregular results with stoichiometric propane-oxygen mixtures

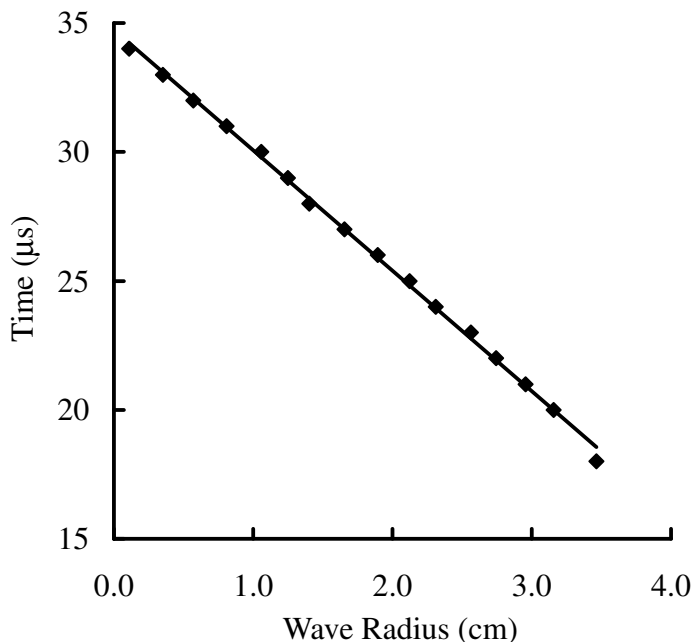


Figure 4.7: A plot of wave radius as a function of time. Data are measured from the images shown in Fig. 4.5. The slope of the line fit to the data corresponds to a velocity of 2200 m/s. The CJ wave speed  $U_{CJ}$  for the mixture is 2400 m/s.

at 1.0 bar initial pressure. Fig. 4.8 shows a series of eight images taken by the Cordin model 220 camera during a single experiment where the initiator was filled with stoichiometric propane-oxygen. In these experiments, the focus of the imploding wave was not aligned with the central axis of the initiator. Further investigation showed that the focal location of the imploding wave wanders from one experiment to another. When the “off-center” focus lined up with pressure transducers along the end flange, it was apparent that the device was still producing comparable focal pressures to tests where the focus was aligned in the center of the device.

While the cause of the off-axis implosions was not definitively determined, it is likely that they were the result of the detonation wave weakening and slowing as it propagated through one of the  $180^\circ$  turns in the initiator channels (shown at the left of Fig. 4.2a). In situations where the wave speed was slowed more in one  $180^\circ$  turn than in the other, the wavelets would emerge from each half of the initiator channels at different times, creating the observed off-axis effect. This hypothesis is

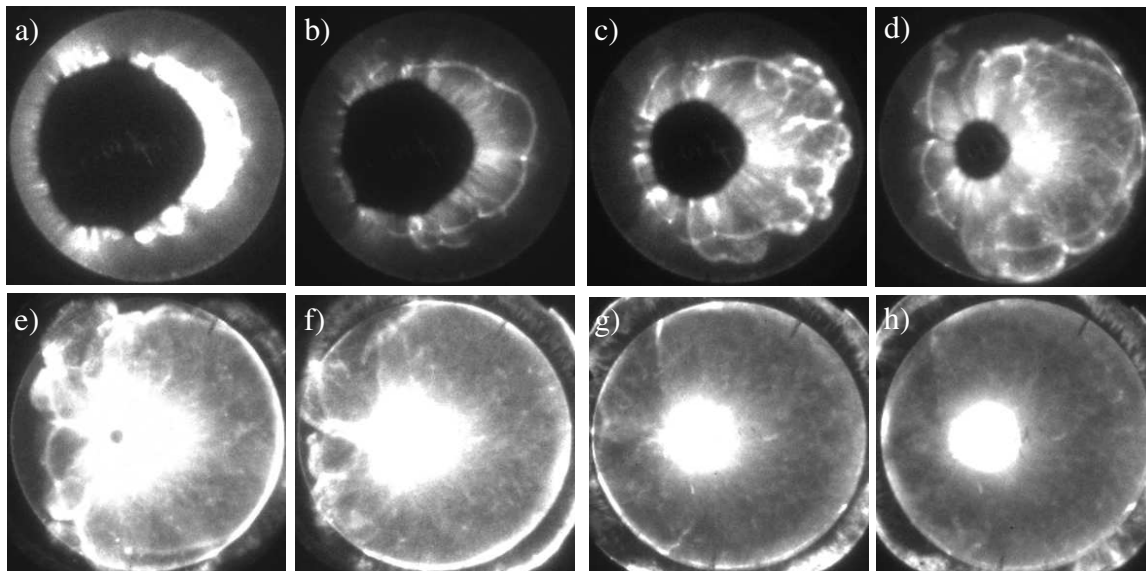


Figure 4.8: Chemiluminescence images of collapsing toroidal detonation wave in a stoichiometric propane-oxygen mixture at 1 bar initial pressure. Exposure times are 800 ns and all images were acquired during a single test. The period between the arrival of the detonation front at the triggering pressure transducer and imaging was a) 26.0  $\mu\text{s}$ , b) 28.5  $\mu\text{s}$ , c) 31.0  $\mu\text{s}$ , d) 33.5  $\mu\text{s}$ , e) 36.0  $\mu\text{s}$ , f) 38.5  $\mu\text{s}$ , g) 41.0  $\mu\text{s}$ , h) 43.5  $\mu\text{s}$ . Thanks to Cordin Scientific Imaging for use of the Model 220 camera and to N. Nebeker for assistance with the acquisition of these images.

further supported by two observations: (1) for the collection of the imaging data, the initiator was aligned such that the wavelets coming from one 180° turn would emerge on the left half of the image and the wavelets from the other 180° turn would emerge from the right half of the image and (2) all observed off-axis implosions were skewed to the left or right of the observation window.

### 4.3.3 Toroidal Initiator with Gas Injection

During testing, the amount of diluent in the test-section tube mixture and the amount of injected acetylene-oxygen gas were varied. The main criterion for successful initiation of the test-section mixture was that the wave speed be not more than 10% below the CJ detonation velocity  $U_{CJ}$  for the test-section mixture. If this criterion was met, the peak pressure of the wave was examined to ensure that it was on the order of  $P_{CJ}$  for the test-section mixture. Additionally, ionization probe traces were used to verify

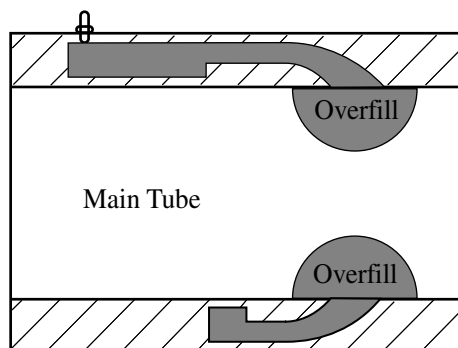


Figure 4.9: The overfilled initiator gas shown as semicircular volumes in the test-section tube.

that the shock wave measured by the pressure transducers was accompanied by a tightly-coupled reaction zone. It should be noted that the measured wave speed used in the above criterion was found by averaging the wave speeds measured between P3 and P4 and between P4 and P5. (PCB locations are shown in Fig. 4.3.)

The amount of acetylene-oxygen initiator gas used in each experiment is presented in terms of “initiator overfill.” This refers to the amount of gas injected into the experiment that was in excess of the volume of the initiator. A graphical interpretation of this concept is illustrated in Fig. 4.9. Negative values of initiator overfill correspond to the initiator not being completely filled with initiator gas. The effective volume of the initiator is 349 cc (21.6 in<sup>3</sup>), which accounts for the actual volume of the initiator (218 cc or 13.3 in<sup>3</sup>) and the volume of the tubing associated with the gas injection system (136 cc or 8.3 in<sup>3</sup>). The total system volume of the initiator assembly and the attached tube is 4980 cc (304 in<sup>3</sup>). An example of the overfill volume calculation is provided for clarity: An overfill volume of 37% corresponds to the effective initiator volume in addition to 37% of the actual initiator volume:

$$21.6 \text{ in}^3 + 0.37(13.3 \text{ in}^3) = 26.5 \text{ in}^3 .$$

Thus, immediately after injection, the initiator is completely filled and an additional 4.9 in<sup>3</sup> of acetylene-oxygen gas has spilled into the main tube volume.

#### 4.3.3.1 Example Data Traces

The result of each run was classified as either a successful initiation or a failed initiation depending on whether a detonation was initiated in the tube by the time the incident shock wave created in the test section by the implosion process reached the test-section end flange. To characterize the wave created in the test section by the initiator in the absence of combustion, calibration runs were also conducted with the test section filled with only nitrogen.

Fig. 4.10 shows several pressure transducer and ionization probe traces from a calibration run. The location of each pressure trace is labeled and corresponds to a transducer shown in Fig. 4.3. All ionization probe data are on the same data acquisition channel. It is assumed that the ionization probes were triggered sequentially from left to right as they are shown in Fig. 4.3. Pressure transducers P1 and P2 show data characteristic of the imploding wave and measure pressures on the order of 100 bar near the high-pressure focal region. The implosion generates a shock wave in the test section that decays as it propagates down the length of the tube. The flow behind the shock wave has an overpressure of 4 bar. This overpressure agrees with the measured shock velocity corresponding to a Mach 2 shock wave. The ionization probes measure no ionization, as would be expected from an inert mixture processed by a weak shock wave.

Fig. 4.11 shows data from a run with propane-air in the test section where a detonation was not successfully transmitted from the initiator to the test-section mixture. Initiator overfill in this experiment was 24% of the initiator volume. The data configuration is the same as with the previous example. Pressure transducer P1 shows a typical detonation wave that is overdriven to a very high pressure (200 bar) as it implodes near pressure transducer P2. Farther down the tube, a shock wave with an overpressure of 7 bar is present. As the wave propagates the length of the tube, it decays. The 7 bar overpressure is higher than the 4 bar overpressure measured in the calibration case where no combustion was present; however, it is far below the CJ pressure of 18.8 bar for stoichiometric propane-air mixtures. Inspection

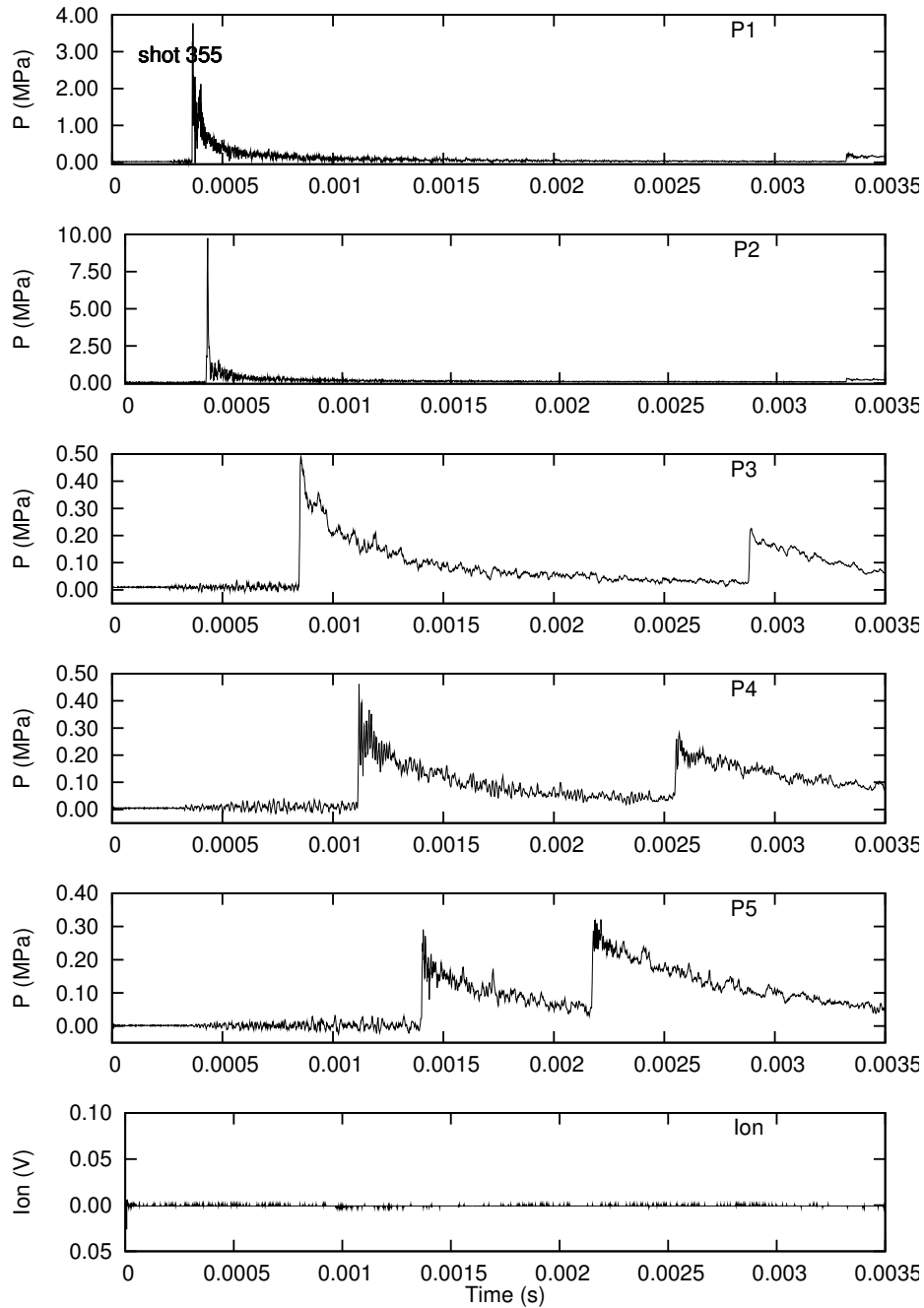


Figure 4.10: Pressure and ionization traces from shot 123, a typical calibration shot. Test-section mixture was nitrogen at 1 bar initial pressure. Traces are labeled and correspond to locations shown in Fig. 4.3.

of the ionization probe data shows the broad dips characteristic of a deflagration. Furthermore, the measured wave speeds are on the order of 800-1000 m/s, while CJ theory predicts  $U_{CJ}$  to be 1801 m/s. Thus, in this experiment, a detonation did not

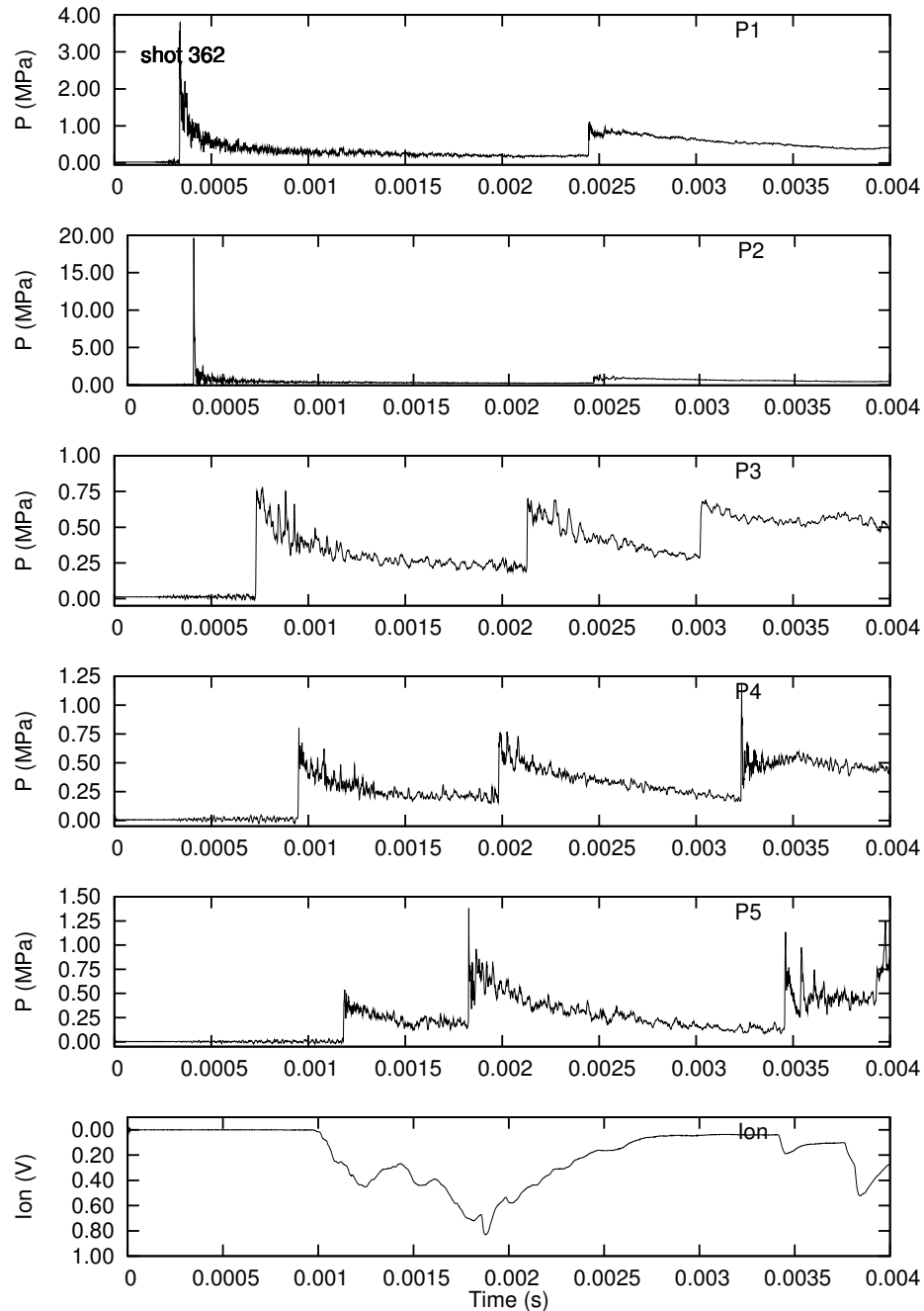


Figure 4.11: Pressure and ionization traces from shot 130, a typical failed initiation. Test-section mixture was stoichiometric propane-air at 1 bar initial pressure. Traces are labeled and correspond to locations shown in Fig. 4.3.

propagate down the length of the tube. Instead, a shock wave was present, followed by a deflagration.

Data from an experiment where a propane-air test-section mixture was success-

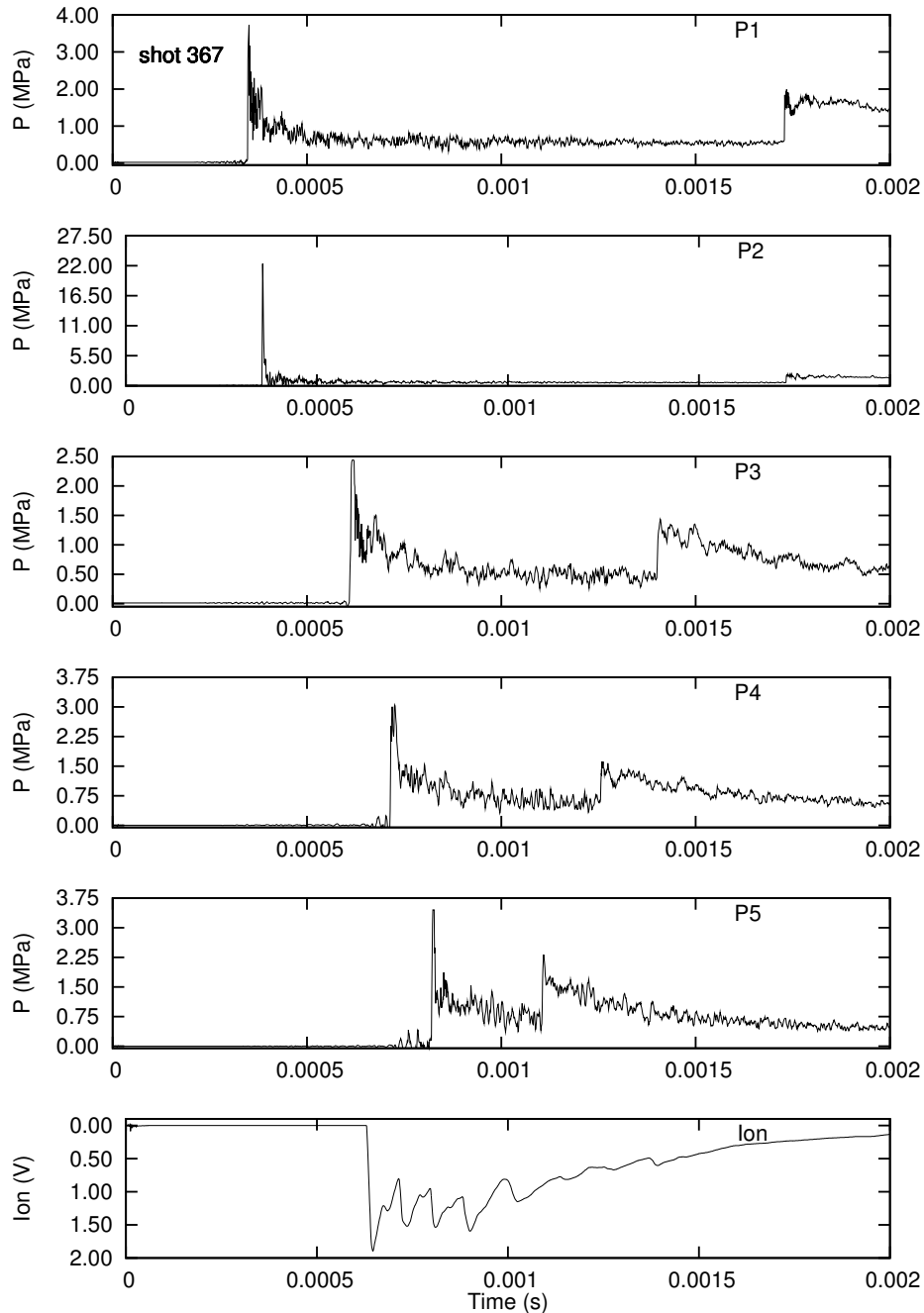


Figure 4.12: Pressure and ionization traces from shot 135, a typical successful initiation. Test-section mixture was stoichiometric propane-air at 1 bar initial pressure. Traces are labeled and correspond to locations shown in Fig. 4.3.

fully detonated are shown in Fig. 4.12. The initiator overfill in the experiment was 37% of the volume of the initiator. The data configuration is the same as in previous examples. Pressure transducers located near the implosion focus register the same

high-pressure focal region as in previous cases. This time, however, pressure transducer P3 records the passing of a wave with an overpressure of 25 bar which is 30% above  $P_{CJ}$ . This wave maintains its overpressure as it continues to propagate down the length of the tube. Measured wave speeds of 1811 m/s agree well with  $U_{CJ}$  (1801 m/s). Furthermore, the ionization probe traces show the sharp spike characteristic of a detonation wave and also indicate that the combustion front is coupled with the wave.

#### 4.3.3.2 Transmission Limits

During investigation of the transmission efficiency of the initiator, the amount of initiator gas injected into the device and the wall proximity to the implosion focus were varied. In order to vary the wall proximity to the focus, two experimental configurations were used. In the first, the focus was effectively at the end flange (Fig. 4.13a). It was thought that the end flange would enhance the focusing by providing an additional surface to reflect the waves. In order to remove this effect, separate tests were conducted with the initiator flipped around such that the focus was about 0.4 m from the end flange (Fig. 4.13b). In experiments with the focus at the end flange, stoichiometric propane-oxygen and ethylene-oxygen mixtures were used with varying amounts of nitrogen dilution. Experiments with no wall focusing effects involved only stoichiometric propane-air and ethylene-air mixtures. The results are separated into four categories according to wall proximity (wall focusing or no wall focusing) and fuel used in the test section (propane or ethylene).

**Propane Mixtures with Focus Near Wall:** Experimental results for the wave focus next to the end flange wall with propane fuel mixtures are shown in Table 4.2. The average wave velocity in the test section is compared to the amount of diluent present in the test-section mixture (by mole percent). The table clearly shows that as the amount of diluent is increased, it is necessary to inject more initiator gas in order to achieve a stronger initiation event. The minimum amount of initiator gas that was able to initiate stoichiometric propane-air was found to correspond to an

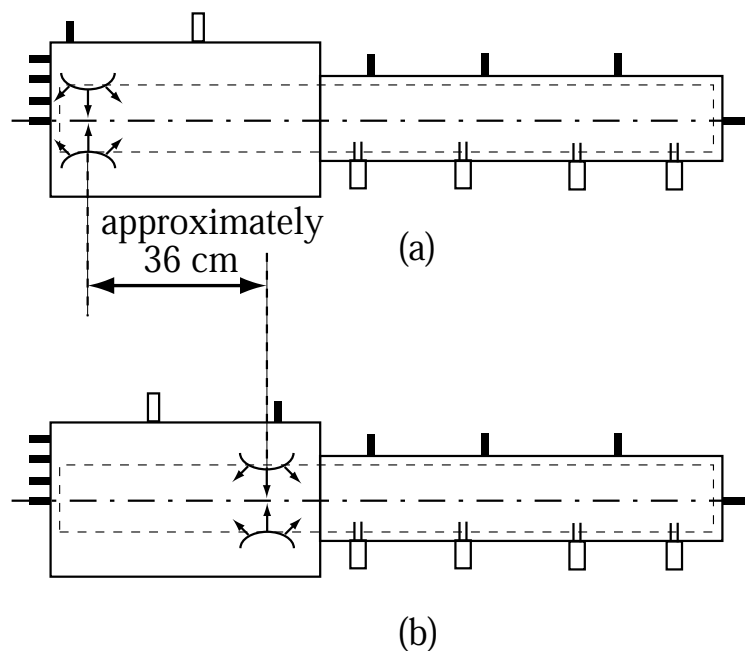


Figure 4.13: Schematics illustrating the difference in the focal location of the imploding wave when the focus was (a) near the end wall and (b) far from the end wall.

initiator overfill of 37%. Experiments with propane-air are presented on a separate plot (Fig. 4.14) in order to more clearly visualize the threshold. The wave appears to be overdriven near the initiation threshold, hinting at the presence of a galloping wave, a phenomenon that occurs in marginal detonations. Unfortunately, velocity measurements did not have sufficient resolution, and the tube was not of sufficient length to study this effect in detail. Assuming the critical amount of gas overfill was confined to a cylindrical slug with the same diameter as the inside of the tube (76 mm), the width of the cylinder would be 2.8 cm (1.1 in).

**Ethylene Mixtures with Focus Near Wall:** Results with ethylene fuel (Table 4.3) followed the same trend as the propane cases; however, due to the increased sensitivity of ethylene-oxygen mixtures, less initiator gas was required to initiate stoichiometric ethylene-air mixtures. The critical overfill value was determined to be 6%. Fuel-air cases are plotted alone in Fig. 4.15. No overdriven waves are present in this case. The critical amount of overfill corresponds to a disc of diameter 76 mm and

Initiator Overfill	Diluent (mole %)			
	50%	60%	70%	75.8%
6%	2080	940	810	X
15%	X	2000	850	X
24%	X	X	1890	840
32%	X	X	X	850
37%	X	X	X	2160
41%	X	X	X	1810
49%	X	X	X	1780
61%	X	X	X	1780
73%	X	X	X	1820
$U_{CJ}$	2062	1981	1879	1801

Table 4.2: Wave speed in the test-section tube as a function of test gas diluent and initiator overfill for stoichiometric propane-oxygen-nitrogen mixtures with the focus near the end wall. The second row denotes percent moles of nitrogen in the test-section tube mixture. The first column denotes initiator overfill. Values of  $U_{CJ}$  for each dilution listed on the bottom row. All other values are wave speeds (in m/s) measured in the test-section tube. Wave speeds within 10% of  $U_{CJ}$  are considered detonations. If a cell is filled with “X”, no experiment was performed at that condition.

width 0.45 cm (0.18 in).

Initiator Overfill	Diluent (mole %)			
	50%	60%	70%	73.8%
-30%	2050	1980	630	594
-7%	X	X	X	830
3%	X	X	X	850
5%	X	X	X	860
6%	X	X	X	1840
15%	X	X	X	1850
61%	X	X	X	1790
$U_{CJ}$	2060	1977	1874	1824

Table 4.3: Wave speed in the test-section tube as a function of test gas diluent and initiator overfill for stoichiometric ethylene-oxygen-nitrogen mixtures with the focus near the end wall. The second row denotes percent moles of nitrogen in the test-section tube mixture. The first column denotes initiator overfill. Values of  $U_{CJ}$  for each dilution listed on the bottom row. All other values are wave speeds (in m/s) measured in the test-section tube. Wave speeds within 10% of  $U_{CJ}$  are considered detonations. If a cell is filled with “X”, no experiment was performed at that condition.

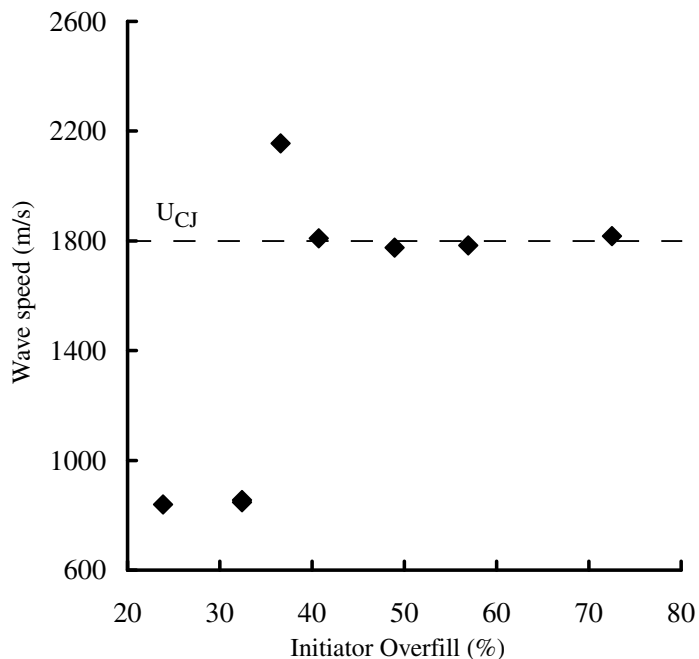


Figure 4.14: Wave speed in the test section as a function of initiator overfill for stoichiometric propane-air mixtures with the focus near the end wall.  $U_{CJ}$  is 1801 m/s.

**Propane Mixtures with Focus Far from Wall:** Increasing the distance of the end flange wall from the focusing event necessitated more initiator gas being injected to detonate propane-air mixtures. Fig. 4.16 shows steadily increasing test-section wave velocities as initiator overfill is increased. The critical amount of overfill required for initiation of the propane-air mixture was found to be 73%. It should be noted that while this is almost twice the critical overfill percent value for cases with the focus located next to the wall, twice the amount of gas was not injected. Instead, it means that only twice the amount of *overflow* gas was injected. The critical amount of overfill for this case corresponds to a cylinder of diameter 76 mm and a width of 5.5 cm (2.2 in).

**Ethylene Mixtures with Wave Focus Far from Wall:** As with the propane cases, distancing the end flange wall from the wave focus required more gas to be injected in order to initiate the ethylene-air mixture in the test section (Fig. 4.17).

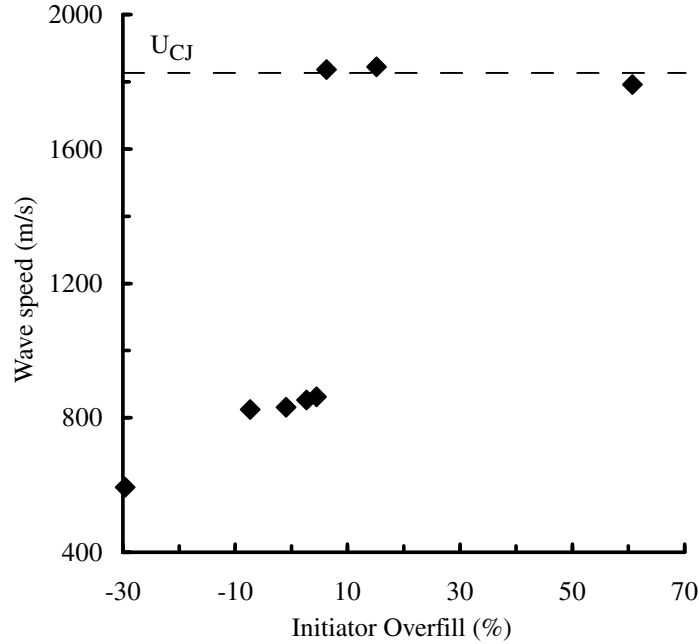


Figure 4.15: Wave speed in the test section as a function of initiator overfill for stoichiometric ethylene-air mixtures with the focus near the end wall.  $U_{CJ}$  is 1825 m/s.

The critical amount of overfill was found to be 20%, corresponding to a cylinder with a diameter of 76 mm and a width of 1.5 cm (0.59 in). Table 4.4 summarizes the above results, comparing the amount of overfill necessary for detonation transmission from the initiator to the test section with and without wall focusing for different fuels. Table 4.5 contains the length of the tube that the total amount of gas used in the *entire* initiation process would fill, were it injected directly into the test-section tube (Fig. 4.18), as would be done with a simple tube initiator.

	Near wall	Far from wall
$C_3H_8$ -air	37%	73%
$C_2H_4$ -air	6%	20%

Table 4.4: Critical amount of overfill necessary for detonation initiation with different experimental configurations.

The proximity of the end flange wall is thought to reduce the amount of gas required for initiation by creating symmetry and by promoting wave reflection. In

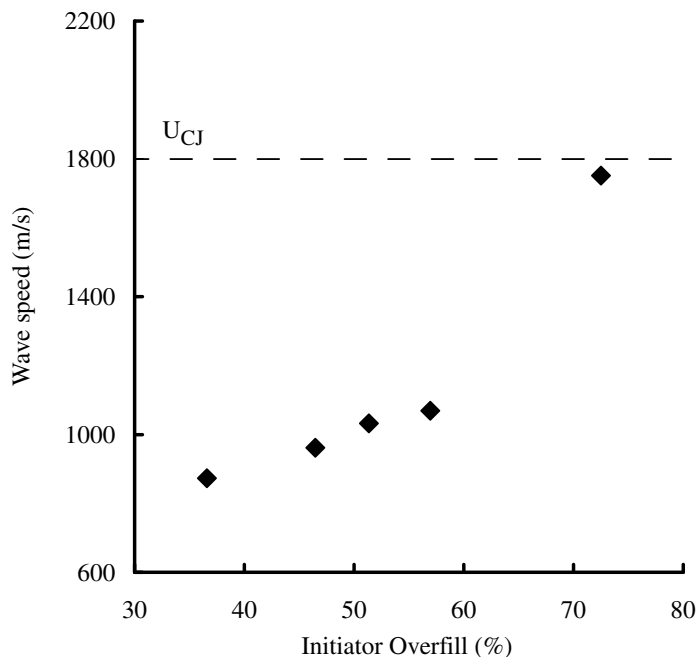


Figure 4.16: Wave speed in the test section as a function of initiator overfill for stoichiometric propane-air mixtures with the focus far from the wall.  $U_{CJ}$  is 1801 m/s.

	Near wall	Far from wall
$C_3H_8$ -air	9.3 cm	11.0 cm
$C_2H_4$ -air	7.8 cm	8.5 cm

Table 4.5: Length of 76 mm tube that would be filled by critical amount of initiator gas were the gas injected directly into the tube as is shown in Fig. 4.18.

a situation of perfect symmetry (Fig. 4.19), the wave focus would occur at the end flange wall and the overfill volume would be half of the case where no end wall was present. However, in the actual experiments with the wave focus near the end wall, the wave focus is still 19 mm away from the end wall, and only partial symmetry is achieved.

In addition to symmetry, the proximity of the end wall to the focus also enhances the initiation by providing an additional surface for the exploding waves to reflect from. This additional level of confinement further reduces the overfill volume. From Table 4.4, it can be seen that for propane-air mixtures, these two effects reduced the overfill volume by half when the focus was near the wall. For ethylene-air mixtures,

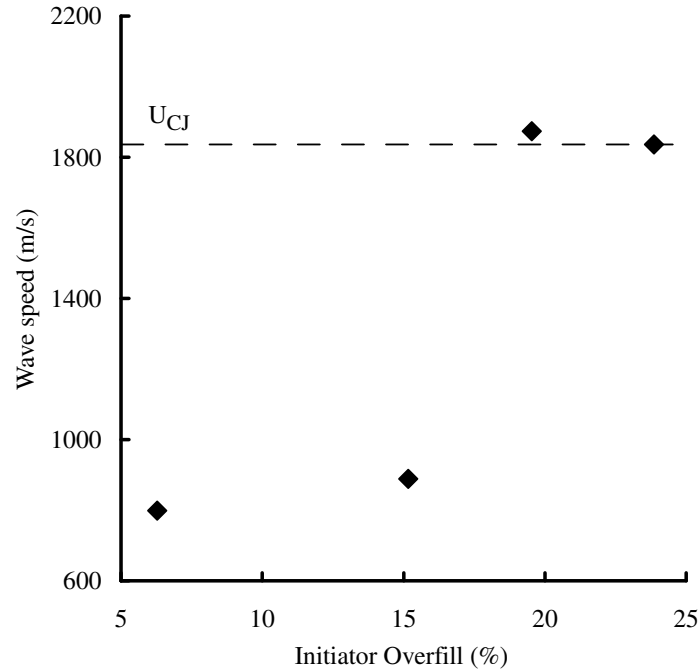


Figure 4.17: Wave speed in the test section as a function of initiator overfill for stoichiometric ethylene-air mixtures with the focus far from the wall.  $U_{CJ}$  is 1825 m/s.

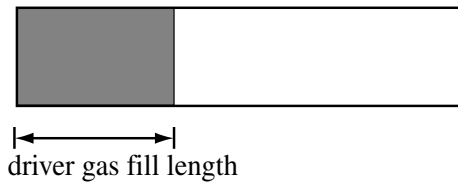


Figure 4.18: Accompanying schematic for Table 4.5, where critical amount of initiator gas (colored gray) is injected into the test-section tube directly.

the overfill reduction is even more dramatic; initiation near the wall requires only one-third the overfill volume compared to situations where the focus was far from the end wall.

#### 4.3.3.3 Initiation Attempts Using a Collapsing Shock Wave

The initiator was also used to generate an imploding shock wave in an attempt to initiate the test-section mixture. Recent computational simulations by Li and Kailasanath (2003b) have suggested that it is possible to initiate JP10-air mixtures using impul-

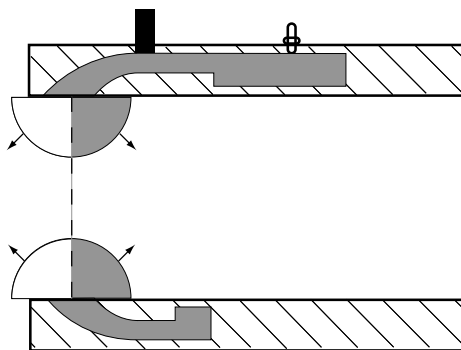


Figure 4.19: A schematic demonstrating the reduction in overfill volume due to symmetry. For pure symmetry, the end flange wall would be located at the dashed line. The volume of overfill gas would be reduced to the gas shaded gray, which is half of the volume required in the case where no end flange wall is present.

sively started jets of JP10 and air to create an annular shock wave.

A preliminary investigation of this notion was examined by conducting imploding shock experiments with the present setup. (More detailed experiments on this topic were performed with a different initiator and are discussed in the next chapter.) In order to generate an imploding shock wave, the initiator was partially filled (roughly 30%–40%) with initiator gas. Detonation of this gas propagated a shock wave followed by a deflagration through the channels of the device. This shock wave then implodes at the focus, creating an imploding shock wave in the fuel-air mixture.

This technique was unsuccessful at initiating stoichiometric ethylene-air mixtures. Pressure traces from an experiment where 41% of the initiator (and all of the plumbing) was filled with initiator mixture are shown in Fig. 4.20. The location of the pressure and ionization probe traces from Fig. 4.20 are shown in the schematic in Fig. 4.21. The test section mixture was ethylene-air.

Pressure transducer P2 shows a shock wave with an overpressure of 12 bar that is propagated into the test-section mixture from the initiator. As this wave implodes, the pressure measured near the focus is 100 bar. Farther down the tube, pressure transducers P4 and P5 show a shock with an overpressure of 4 bar. Measured wave speed in the test section is roughly 630 m/s while  $U_{CJ}$  is 1825 m/s. Initiation of the test section mixture was not successful. The pressure traces are similar to those pre-

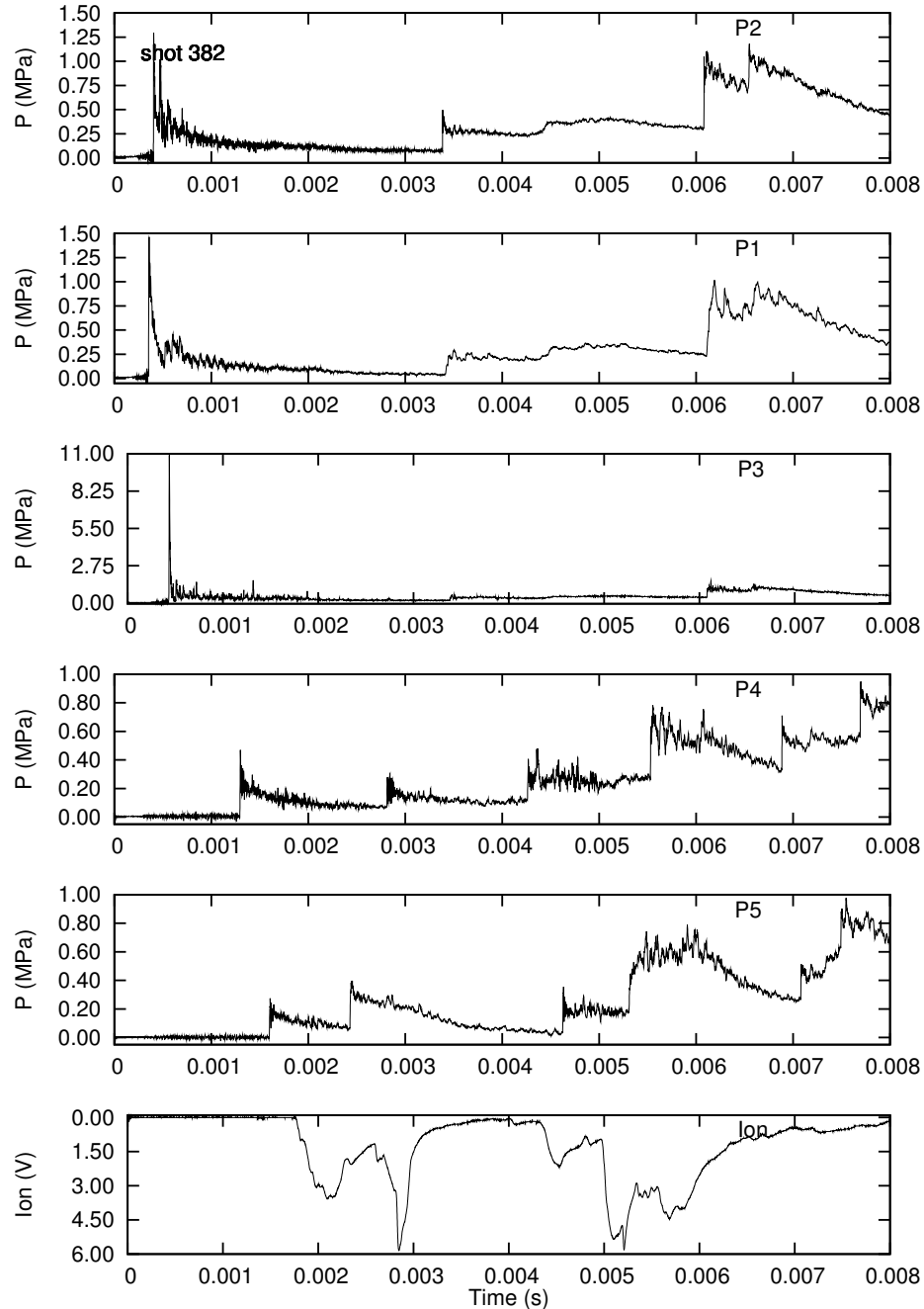


Figure 4.20: Pressure and ionization traces from shot 150, a typical shock initiation experiment. Test-section mixture was stoichiometric ethylene-air at 1 bar initial pressure. Traces are labeled and correspond to locations shown in Fig. 4.21.

viously presented for the “failed initiation” case where an imploding detonation wave (instead of a shock wave) was propagated into the test section. In these experiments, the imploding shock wave was not of sufficient Mach number and the post-shock flow

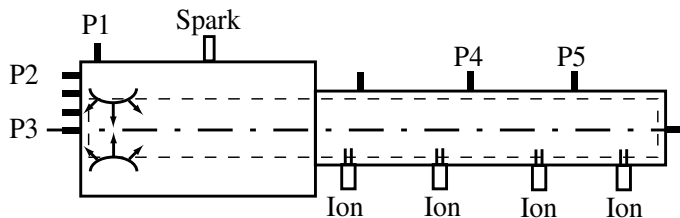


Figure 4.21: A schematic of the experimental setup used for attempted initiation of HC-air mixtures using an imploding shock wave.

was not of sufficient duration to initiate the ethylene-air mixture. This concept is addressed more extensively in the next chapter.

## 4.4 Summary

A dynamic planar initiator has been developed that is capable of producing a large-aspect-ratio planar-detonation-wave in insensitive mixtures. The planar initiator uses a single weak spark and a small amount of fuel-oxygen mixture to produce the planar wave in a short distance and is capable of initiating detonations in mixtures such as  $C_3H_8+5O_2+9N_2$  and  $C_2H_4+3O_2+10.5N_2$  (Austin, 2003). The device is currently in use on Caltech's Narrow Channel Facility.

A dynamic toroidal initiator has been developed that creates an imploding wave in an insensitive mixture using a small amount of hydrocarbon-oxygen gas and a weak spark. The imploding detonation wave initiates detonations in propane-air and ethylene-air mixtures with sufficient amounts of hydrocarbon-oxygen gas. The minimum volume of sensitive-initiator gas required for hydrocarbon-air detonation exceeded the volume of the initiator channels, causing some gas to spill into the test section. This "overflow volume" of initiator gas was found to increase as the mixture sensitivity decreased and increase as the implosion was moved away from the test-section end flange. It was thought that the proximity of the end flange to the wave focus reduced the critical overflow volume by creating symmetry and providing additional surfaces for wave reflection.

Imploding shock waves (instead of detonation waves) were also created by par-

tially filling the initiator channels. The imploding waves created in this fashion were not able to initiate the fuel-air mixtures for the single case tested. More rigorous experiments testing the effectiveness of imploding shock waves at detonation initiation are presented in the following chapter.



# Chapter 5

## Imploding Shock Wave Initiator

### 5.1 Introduction

In Chapter 4, the toroidal initiator results were characterized by the amount of acetylene-oxygen gas injected into the initiator channels during each test. In order to perform any type of gas-dynamical analysis, it is desirable to translate the amount of gas into a wave strength for the implosion. However, this conversion is not straightforward due to several undetermined factors in the experiment.

For example, while pressure measurements taken at the end flange could be used to infer the implosion strength, they were not aligned with the main axis of the implosion and were shown to be affected by both diffraction and reflection from the end flange itself. Furthermore, a contact surface separating the initiator gas and the test-section gas was created in the test section during the dynamic gas injection. The location of this contact surface was not measured and it varied with the amount of initiator gas used. The imploding detonation wave would have been affected by the contact surface in two ways. First, the density gradient at the interface would have affected the transmitted wave strength and created a reflected wave. Second, the test-section mixture was much less sensitive than the initiator gas, which could have caused the transmitted detonation wave to fail or substantially weaken. In an effort to create an experimental situation that would be simpler to analyze, a facility was designed to create an imploding annular shock wave (as opposed to the imploding detonation waves in previous chapters) that was used to initiate detonations in combustible

mixtures.

The facility was also designed to experimentally test the numerical work of Li and Kailasanath (2003b), who proposed that imploding shock waves could be used to initiate insensitive mixtures. Their numerical simulations (Li and Kailasanath, 2003a) found that detonations could be initiated in a 14 cm (5.5 in) diameter tube filled with stoichiometric ethylene-air using an imploding shock wave created from the injection of a converging annular jet of fuel or air from the outer diameter of the tube. At the injection point, the jet had a Mach number of 1, a pressure of 2.0 bar, and a temperature of 250 K. For a perfect gas with  $\gamma = 1.4$ , a jet with these properties could be generated from a reservoir with a total pressure of 3.8 bar and a total temperature of 470 K.

The concept of detonation initiation via a converging air jet is extremely appealing to designers of PDEs since it would eliminate the need for a spark plug and associated power supply or any sensitizer fuel. In flight, stagnation of the atmosphere would supply the hot, pressurized air needed to create the imploding wave.

The facility discussed in this chapter used a shock tube to create a reservoir of hot, pressurized air to generate imploding annular shock waves that were propagated into a 7.6 cm (3.0 in) diameter test-section tube filled with either stoichiometric ethylene-oxygen or propane-oxygen mixtures diluted with varying amounts of nitrogen. The strength of the imploding shock wave and the sensitivity of the test gas were varied in an effort to find the minimum shock strength required to initiate a detonation in each mixture. The total pressure of the air jet that was used to create the implosion ranged from 3.2 bar to 16.8 bar and the total temperature ranged from 420 K to 790 K. These jet properties were comparable to those proposed by Li and Kailasanath (2003a).

## 5.2 Experimental Facility

The experimental facility was a variation of the classical shock tunnel idea and consisted of a test-section tube with an annular orifice that protruded into the end of a

shock tube. A description of each component of the shock tunnel is included below and design drawings are available in Appendix I. The operation of the facility is also discussed.

### 5.2.1 GALCIT 6-Inch Shock Tube

The GALCIT 6-Inch Shock Tube (Smith and Coles, 1967) was used to create the primary shock wave in the experiment. The shock tube consists of a driver section with a 16.5 cm (6.50 in) ID and a driven section with a 15.2 cm (6.00 in) ID. During testing, the length of the driver section was 6.20 m (20.3 ft) and the length of the driven section was 11.3 m (37.0 ft). The end flange of the driven section contained a 10.8 cm (4.25 in) diameter hole through which the front of the test section was inserted into the rear of the driven section (Fig. 5.1).

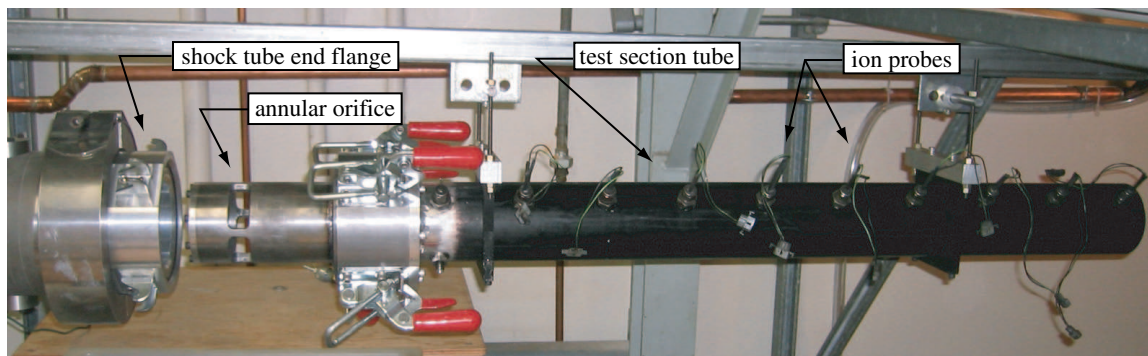


Figure 5.1: The test section is shown on the right. The end flange of the shock tube can be seen in the left side of the picture. The longer main tube is anodized black. The shorter extension containing the annular orifice and latch clamps is attached to the left side of the main tube.

The driver and driven sections were separated by a diaphragm held in place by a hydraulic clamp. The clamp was pressurized to 172 bar (2500 psi) during the experiment. The driver section was then pressurized with gas while the driven section pressure remained at atmospheric pressure. This pressure difference caused the diaphragm to bulge into the driven section and contact a cruciform blade cutting device similar to those described in Roshko and Baganoff (1961) and Liepmann et al. (1962), which was located immediately downstream of the diaphragm clamp. This

cutter ruptured the diaphragm and caused it to petal open. The diaphragm will burst without use of the cutters but previous experience (Smith and Coles, 1967, Roshko and Baganoff, 1961) has shown that use of the cutters results in a more repeatable rupture pressure and reduces the chance of the diaphragm fragmenting and traveling downstream. The burst pressure is dependent on the diaphragm properties (material and thickness) as well as the shape of the cutter. Two differently shaped cutting devices available for the shock tube were able to rupture diaphragms at approximately 50% (cutter 1) and 80% (cutter 2) of their free-burst pressure. Thus, three burst pressures were available for each diaphragm thickness by using cutter 1, cutter 2, or no cutter at all.

The driven section was equipped with four PCB 113A series piezoelectric pressure transducers, which were flush-mounted into the tube wall. Transducers ST1, ST2, ST3, and ST4 were located respectively at 3.85 m, 0.70 m, 0.20 m, and 0.10 m from the shock tube end flange (Fig. 5.4). The passage of the shock wave past transducer ST1 triggered the data acquisition system. The two intermediate transducers, ST2 and ST3, were used to record the shock arrival times in order to calculate the shock velocity. The transducer closest to the end flange provided pressure measurements near the annular orifice on the test section. Transducer data were recorded by a National Instruments data PCI-MIO-16E-1 acquisition card running at 250 kHz and processed by a Labview program.

#### **5.2.1.1 Diaphragm Selection for Shock Tube**

Different diaphragms were used in the shock tube to vary the shock strength. Diaphragms were made of dead-soft aluminum and two different alloys were used: Al 1100-0 and Al 2024-0. Each alloy and cutter combination yielded a different burst pressure. Burst pressure data for the 6-Inch Shock Tube are shown in Fig. 5.2 for the two diaphragm materials used in the experiments.

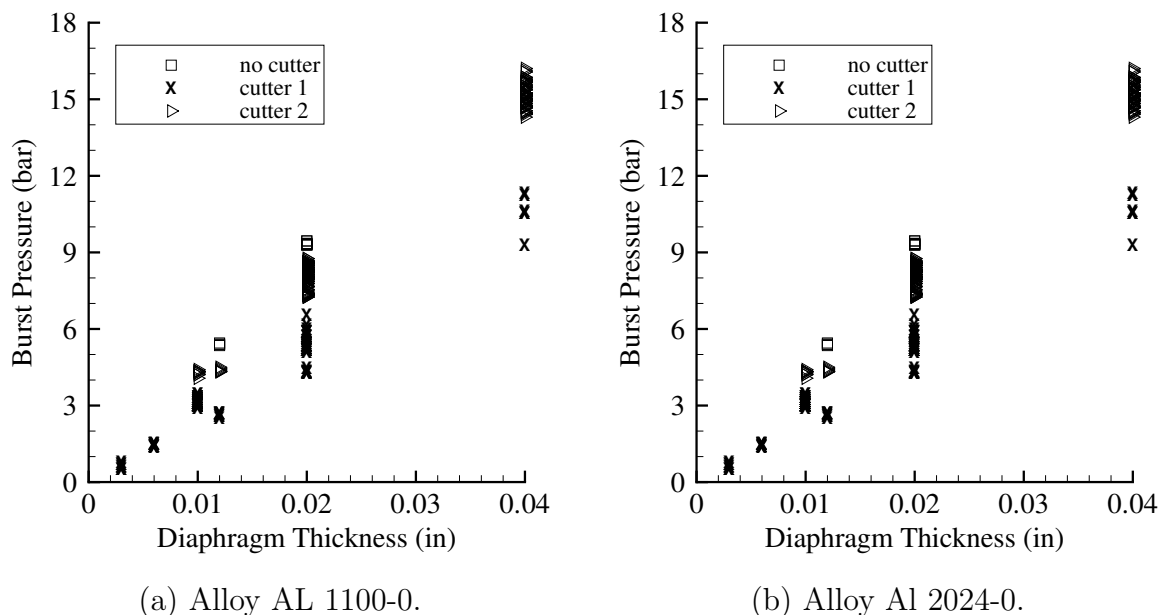


Figure 5.2: Burst data from the 6-Inch Shock Tube for diaphragm alloys used in the experiments. Burst pressure is defined as the pressure difference between the driver and driven section at the moment of diaphragm rupture.

### 5.2.2 Test Section

The test section consisted of a 1.0 m (40 in) long main tube attached to a shorter 0.25 m (10.0 in) long extension tube with an annular orifice (Fig. 5.1). Both components had a constant ID of 76 mm (3.0 in). The two sections combined to form a tube with an internal length of 1.25 m (49.4 in).

During the experiment, the extension tube was inserted 8.43 cm (3.32 in) into the driven section of the shock tube and fixed in place using four latch clamps. The upstream edge of the annular orifice was located 4.62 cm (1.82 in) behind the start of the test section. The orifice was 2.54 cm (1.00 in) wide and interrupted by four 1.0 cm (0.4 in) wide support struts. The region of the test section that protruded into the shock tube had a 10.2 cm (4.0 in) outer diameter. Further dimensional information for this section is shown in Fig. 5.3.

The test section was equipped with four pressure transducers and nine ionization probes. The ionization probes were spaced equidistantly 10.4 cm (4.10 in) apart (Fig. 5.4). The first ionization probe was located 38.4 cm (15.1 in) from the inner

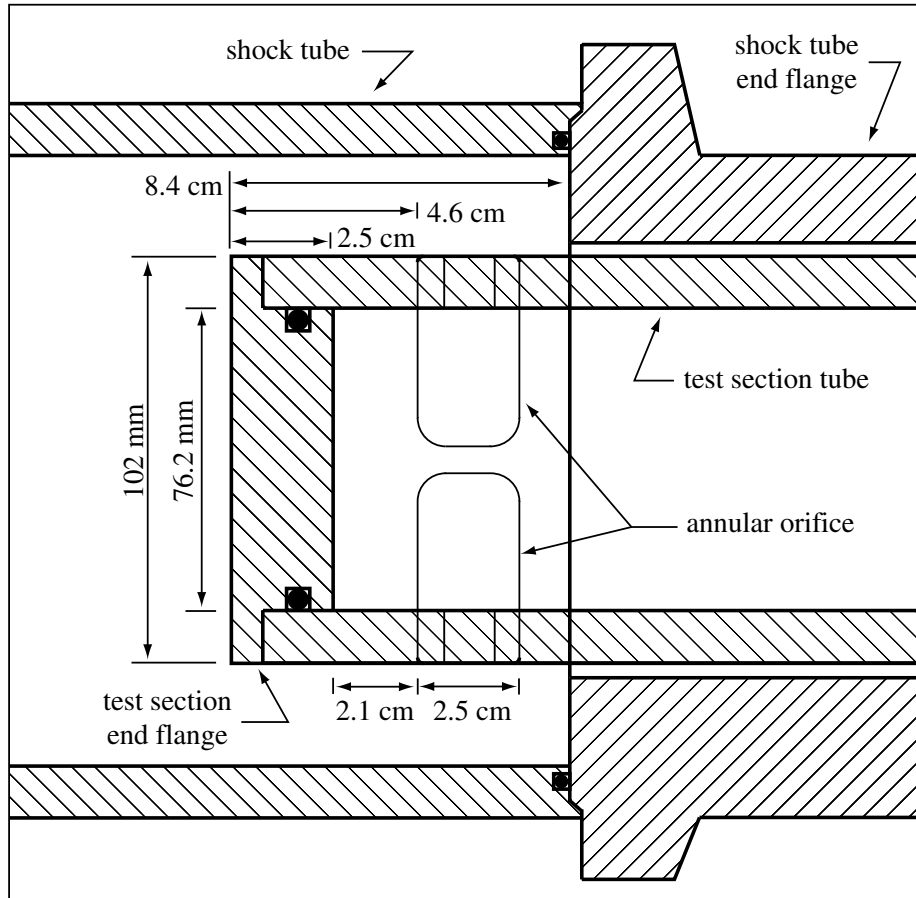


Figure 5.3: A sketch illustrating relevant dimensions of the test section while mated with the end flange of the shock tube.

face of the front test-section flange. Ionization probes were numbered I1 through I9 with the probe number increasing with increasing distance from the front test-section flange. The pressure transducers TS1, TS2, TS3, and TS4 were located respectively at 27.9 cm (11.0 in), 69.6 cm (27.4 in), 1.21 m (47.9 in), and 1.25 m (49.4 in) from the inner face of the front test-section flange (Fig. 5.4). Transducer and ionization probe data were recorded on two National Instruments PCI-6610 data acquisition cards running in master-slave configuration and processed with a Labview program. Recording of the test section data acquisition system was triggered by the arrival of the incident shock wave at the rearmost transducer ST4 in the shock tube. The data acquisition system for the test section recorded 20 ms of data at a sampling rate of 2.5 MHz.

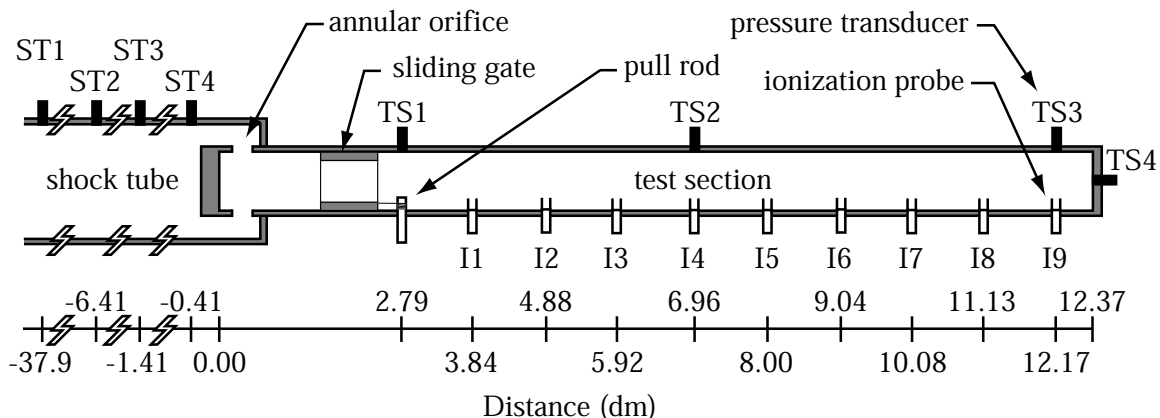


Figure 5.4: A schematic of the shock implosion initiator showing the locations of the pressure transducers and ionization probes relative to the inner face of the front test-section flange. Units are in decimeters (0.1 m).

### 5.2.2.1 Diaphragm Selection for Test Section

The annular orifice in the test section was originally intended to be sealed by a thin layer of Mylar or aluminum tape during gas evacuation and filling of the test section. This tape was then to be ruptured by the high-pressure gas behind the shock wave. However, testing determined that tape thick enough to reliably seal the annular orifice did not rupture promptly upon arrival of the incident shock wave. To make matters worse, all quadrants of the annular orifice did not rupture simultaneously. The delay between the first and last quadrant to rupture ranged from 40  $\mu\text{s}$  to 1 ms for diaphragms strong enough to maintain their integrity during the filling procedure.

To solve this problem, a short length of tube with two O-ring seals was inserted into the test section. This sliding gate was used to seal the annular orifice during test section evacuation and filling procedures but was moved to completely uncover the annular orifice before rupture of the shock tube diaphragm. Actuation of the slider gate was enabled by a wire connecting the slider gate to a rotatable pull rod. Turning the rod pulled the sliding gate along the tube axis. The sliding gate was 8.26 cm (3.25 in) long with an ID of 6.35 cm (2.50 in). It is shown in Fig. 5.5.

Use of the sliding gate to seal the annular orifice during gas evacuation and filling procedures allowed a much thinner diaphragm to be used to contain the test section

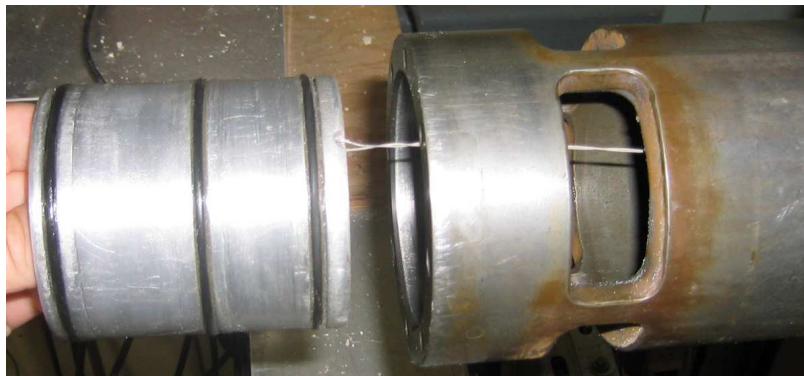


Figure 5.5: The sliding gate is shown removed from the test section. Note the wire connecting the sliding gate to the pull rod (not shown).

gas during pressurization of the shock tube driver section. Aluminum foil with a thickness of  $17.8 \mu\text{m}$  (0.7 mil) was used as the test section diaphragm for all data shown.

### 5.2.3 Basic Operation

During an experiment, the test-section slider gate was moved to seal the test section. Diaphragms were placed in the shock-tube hydraulic clamp and on the annular orifice of the test section. The test section was then secured to the end of the shock tube using the latch clamps. The test section was evacuated and then filled to 1 bar with the premixed combustible test mixture. Test-section gases were premixed for at least 15 minutes with a brushless fan suspended inside of a 9.25 liter mixture-preparation vessel. The desired composition was achieved by filling the mixture-preparation vessel using the method of partial pressures.

Once the test section was filled, the slider gate was retracted leaving only the test-section diaphragm to separate the test-section gas from air in the driven section. Both sections of the shock tube were filled with air at atmospheric pressure. The driver section was then filled with air from a compressed-air source until the shock-tube diaphragm ruptured.

Rupture of the diaphragm resulted in a shock wave that traveled along the long

axis of the shock tube to the end of the driven section. The shock reflected off the shock-tube end flange and created a region of slow moving test gas with elevated pressure and temperature. The increased pressure behind the shock wave ruptured the secondary diaphragm that covered the annular orifice and created an imploding shock wave, followed by a converging jet of air, into the test section. A matrix of the conditions tested is available in Appendix I.

### 5.3 Results and Analysis

Numerical calculations with AMRITA (Quirk, 1998) were conducted in order to gain an understanding of the type of implosion that would be created in the test section by the incident shock wave. The calculations did not model any combustion or the presence of the diaphragm covering the annular orifice. Fig. 5.6 shows several frames from the simulation. It can be seen that the facility does not create a single implosion inside the test section, but rather a series of closely spaced implosions. The first imploding wave results from the diffracting incident shock wave and enters the test section in frame 9. Part of the diffracting wave also reflects from the annular orifice (frame 10), propagating a second imploding wave into the test section. Finally, the incident shock wave reflects from the shock-tube end flange (frame 10) and the reflected wave also enters the test section (frame 14). This process creates two closely spaced implosions (frame 13) followed by a third one from the reflected wave (frame 17). By the end of the implosion process (frames 16-21), a standing normal shock wave is created just below the annular orifice. This normal shock wave indicates that the flow through the annular orifice is choked.

It is expected that this computed multiple-implosion structure was also present in the experiment, as the diaphragm covering the annular orifice was very thin and unable to support a pressure difference greater than 0.7 bar. Thus, it was likely to rupture soon after the passing of the incident shock wave and before the reflected shock returned to the orifice. Such a shock configuration enhances the possibility for interactions between the two imploding waves to promote initiation as discussed in

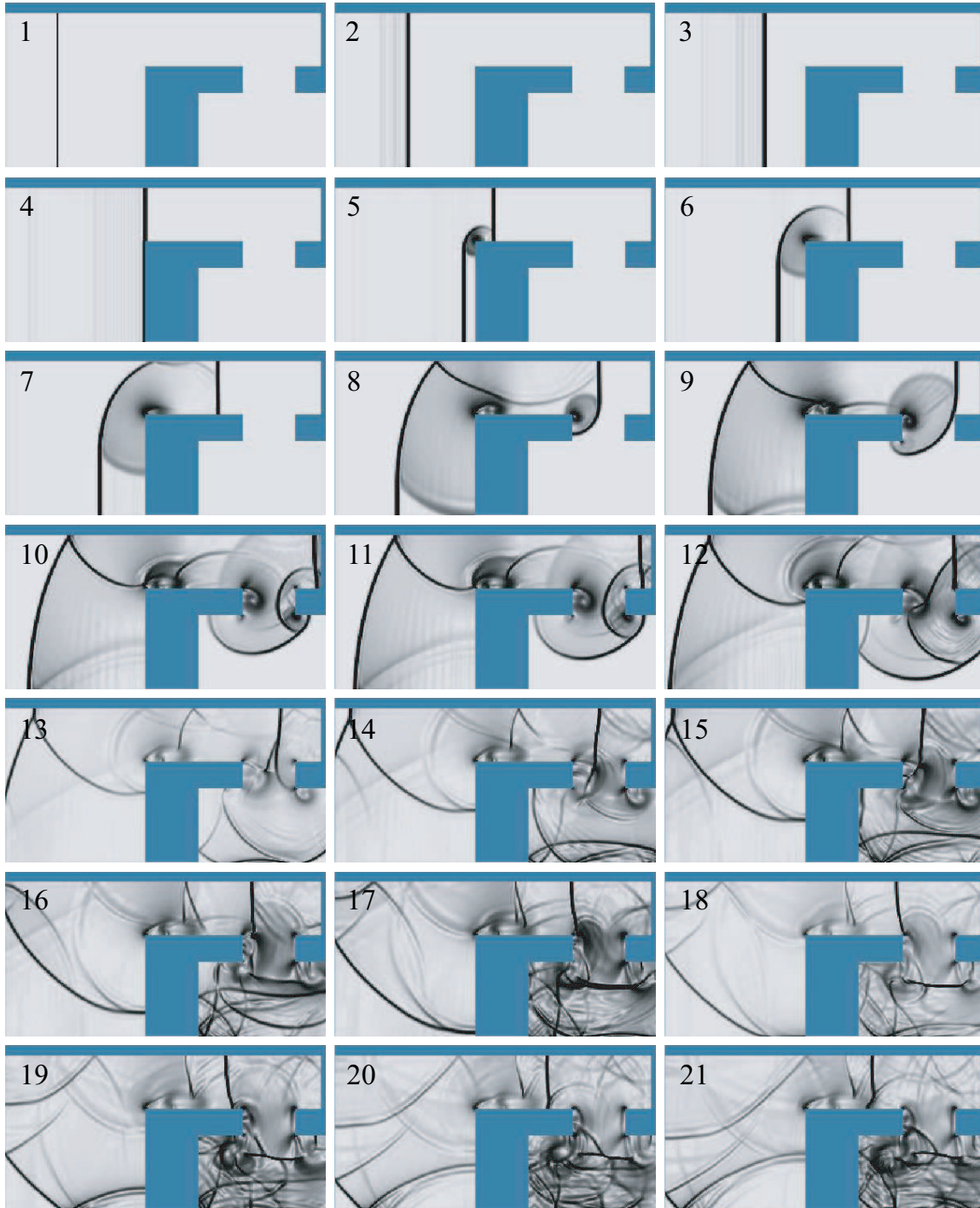


Figure 5.6: Pseudo-schlieren frames from an AMRITA simulation (Quirk, 1998) of the shock implosion facility. A Mach 1.5 incident wave is initially propagating to the right in the shock tube (frame 1). The simulations are axisymmetric and depict the region shown in Fig. 5.3. The lower edge of each image is the centerline of the tube.

Wang et al. (2005).

### 5.3.1 Pressure Behind the Reflected Wave

During each experiment, the Mach number of the incident shock wave was determined from the wave arrival times at pressure transducers ST2 and ST3 in the shock tube:

$$M_{23} = \frac{\Delta x_{23}}{\Delta t_{23} \sqrt{\gamma_1 R_1 T_1}} . \quad (5.1)$$

This allowed the post-shock conditions to be determined using the shock-jump equations for a perfect gas:

$$\frac{P_2}{P_1} = 1 + \frac{2\gamma}{\gamma + 1} (M^2 - 1) \quad (5.2)$$

$$\frac{T_2}{T_1} = 1 + \frac{2(\gamma - 1)(M^2 - 1)(1 + \gamma M^2)}{(\gamma + 1)M^2} \quad (5.3)$$

$$\frac{\Delta w}{a_1} = -\frac{2}{\gamma} \frac{M^2 - 1}{M} \quad (5.4)$$

where  $\Delta w = w_2 - w_1$  is the difference in flow velocity across the shock wave (Thompson, 1988).

For a shock tube with a closed end wall, the flow behind the reflected wave must have zero velocity:

$$u_5 = 0 . \quad (5.5)$$

Using this property and Eqs. 5.2-5.4, it is possible to determine the pressure ratio across the reflected shock as a function of the incident shock pressure ratio and Mach number.

$$\frac{P_5}{P_2} = \frac{(3\gamma - 1) \frac{P_2}{P_1} - (\gamma - 1)}{(\gamma - 1) \frac{P_2}{P_1} + (\gamma + 1)} \quad (5.6)$$

$$\frac{P_5}{P_1} = 1 + 2 \left( \frac{P_2}{P_1} - 1 \right) \frac{1 + \left( \frac{1}{2} + \frac{\gamma-1}{\gamma+1} \right) (M_{23}^2 - 1)}{1 + \frac{\gamma-1}{\gamma+1} (M_{23}^2 - 1)} \quad (5.7)$$

Thus, the pressure ratio across the reflected shock wave can be found as a function of the incident shock wave Mach number. This pressure ratio will be used below to approximate the reflected shock conditions in the experiments. The experimental flow behind the reflected shock wave will have a non-zero velocity (once the diaphragm ruptures) as it enters the test section, resulting in a lower  $P_5$  value.

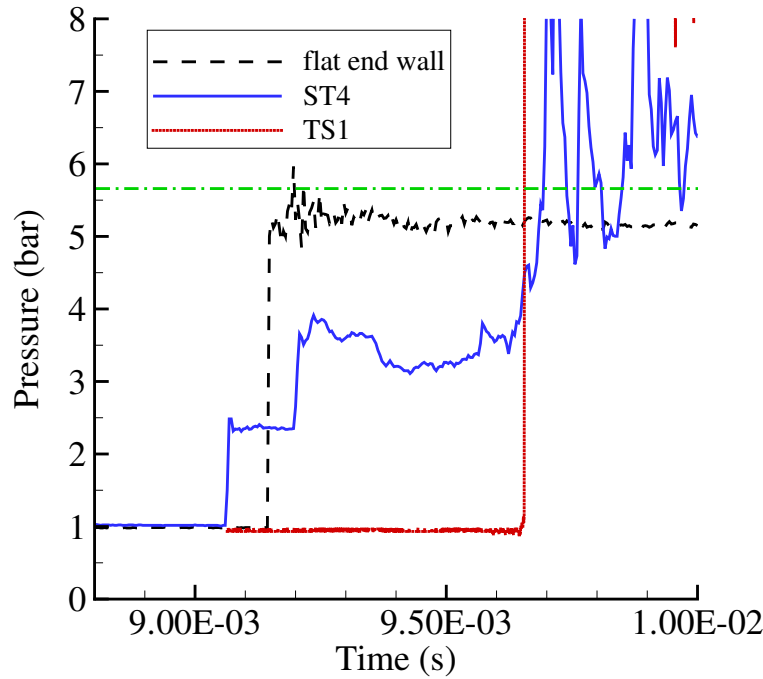


Figure 5.7: The gas flow into the initiator affects the pressure behind the reflected wave. The black, dashed line is the pressure measured by a transducer mounted in a flat end flange located at the end of the shock tube (when the shock initiator was not installed) during the reflection of a  $M = 1.52$  incident shock wave. The blue, solid line and the red, dotted line show the pressure measured by transducers ST4 and TS1, respectively, for a  $M = 1.52$  incident shock wave. The green, dashed-dotted line is the pressure predicted from theory (Eq. 5.7) for that shock wave. For this experiment (run 32), a detonation was initiated during the shock implosion process. The experimental  $P_5$  is significantly lower than the  $P_5$  values from theory and shock reflection from a flat, solid end wall.

The actual  $P_5$  value measured in the experiment is significantly lower than that

predicted by shock-tube theory, as is shown in Figs. 5.7 and 5.8. Data from tests where the shock tube contained a flat end flange are compared to data where the end flange was removed and replaced by the shock initiator and test section. The  $P_5$  value predicted from the Mach number measured in the shock tube is also plotted on the graphs. In both plots, the pressure behind the shock wave after it reflects off the flat end wall is about 20% lower than that predicted by the theory (Eq. 5.7). When the shock initiator is installed on the shock tube, the pressure behind the reflected wave is about 40% lower than theory. Thus, the movement of gas into the shock initiator significantly decreases the pressure behind the reflected wave.

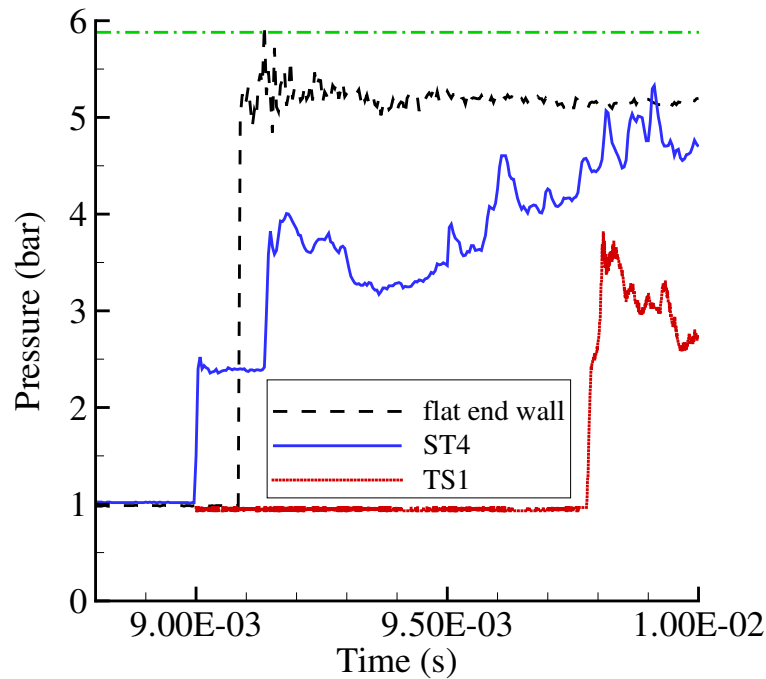


Figure 5.8: The gas flow into the initiator affects the pressure behind the reflected wave. The black, dashed line is the pressure measured by a transducer mounted in a flat end flange located at the end of the shock tube (when the shock initiator was not installed) during the reflection of a  $M = 1.52$  incident shock wave. The blue, solid line and the red, dotted line show the pressure measured by transducers ST4 and TS1, respectively, for a  $M = 1.53$  incident shock wave. The green, dashed-dotted line is the pressure predicted from theory (Eq. 5.7) for that shock wave. For this experiment (run 75), a detonation not initiated until the shock reflected from the end of the test section. The experimental  $P_5$  is significantly lower than the  $P_5$  values from theory and shock reflection from a flat, solid end wall.

### 5.3.2 Classification of Data

Each test was classified into one of four categories depending on the mode of combustion observed. The four categories were: prompt detonation, deflagration-to-detonation transition (DDT), reflected detonation, and no initiation. Examples of each category are shown in Figs. 5.9-5.12 and descriptions are presented below. All of the experimental data is contained in Appendix I.

The figures consist of combined pressure-time and space-time diagrams. The distance values correspond to the scale shown in Fig. 5.4. Zero distance on the vertical axis corresponds to the inner edge of the test-section front flange. Negative distances are located in the shock tube while positive distances are located in the test section. Pressure trace baselines (dotted line) indicate the location of the transducer relative to the zero distance. The square symbols connected by a dashed line are ionization probe data indicating the location of a strong reaction front.

A wave was considered to be a detonation if the average wave speed in between each pair of ionization probes or pressure transducers was within 10% of the CJ velocity  $U_{CJ}$  and the shock wave was closely coupled to the combustion front.

#### 5.3.2.1 Prompt Detonation

The classification of prompt detonation indicates that the first pressure transducer TS1 and ionization probe I1 in the test section detected a detonation wave. An example of a prompt detonation is shown in Fig. 5.9. In the combined pressure-time and space-time diagram, the lower three pressure traces are from ST2, ST3, and ST4 in the shock tube and show propagation of the incident shock wave with a Mach number of 1.52. Shortly after a time of 9 ms, the incident wave reflects from the shock-tube end flange and generates an imploding wave in the test section. The imploding wave initiates a detonation in the test section. The shock wave associated with the detonation is recorded by the pressure transducers and the arrival of the reaction zone is detected by the ionization probes. Ionization probe data show that the detonation is propagating at a constant speed that is within 10% of  $U_{CJ}$ . The

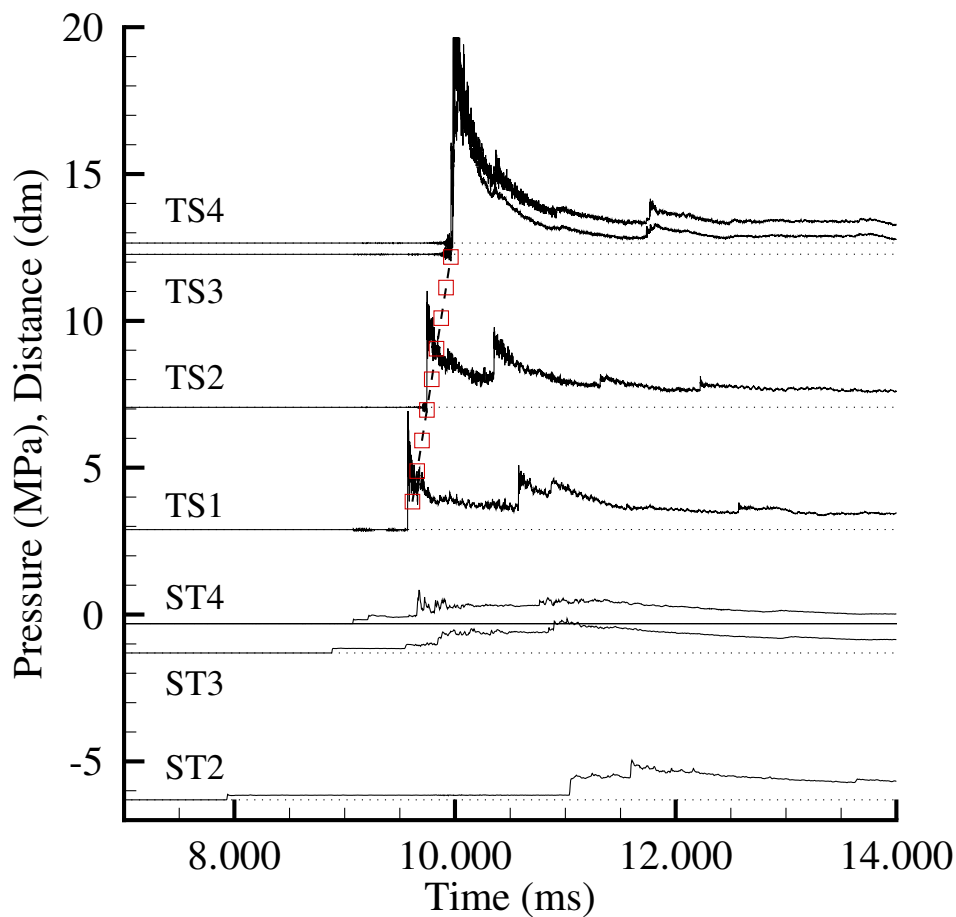


Figure 5.9: Prompt detonation initiation in  $\text{C}_2\text{H}_4 + 3\text{O}_2$  with incident Mach number  $M_s = 1.5$  in the shock tube (run 28). The y-intercept of the baseline of each trace corresponds to the transducer location in dm (0.1 m) as shown in Fig. 5.4.

coupling between the shock and the reaction front is evident in Fig. 5.9. Meanwhile, in the shock tube, the reflected shock wave travels back down the tube and is chased by a larger pressure wave from the detonation initiation in the test section. The larger wave eventually overtakes the reflected shock as can be seen in the lowermost pressure trace.

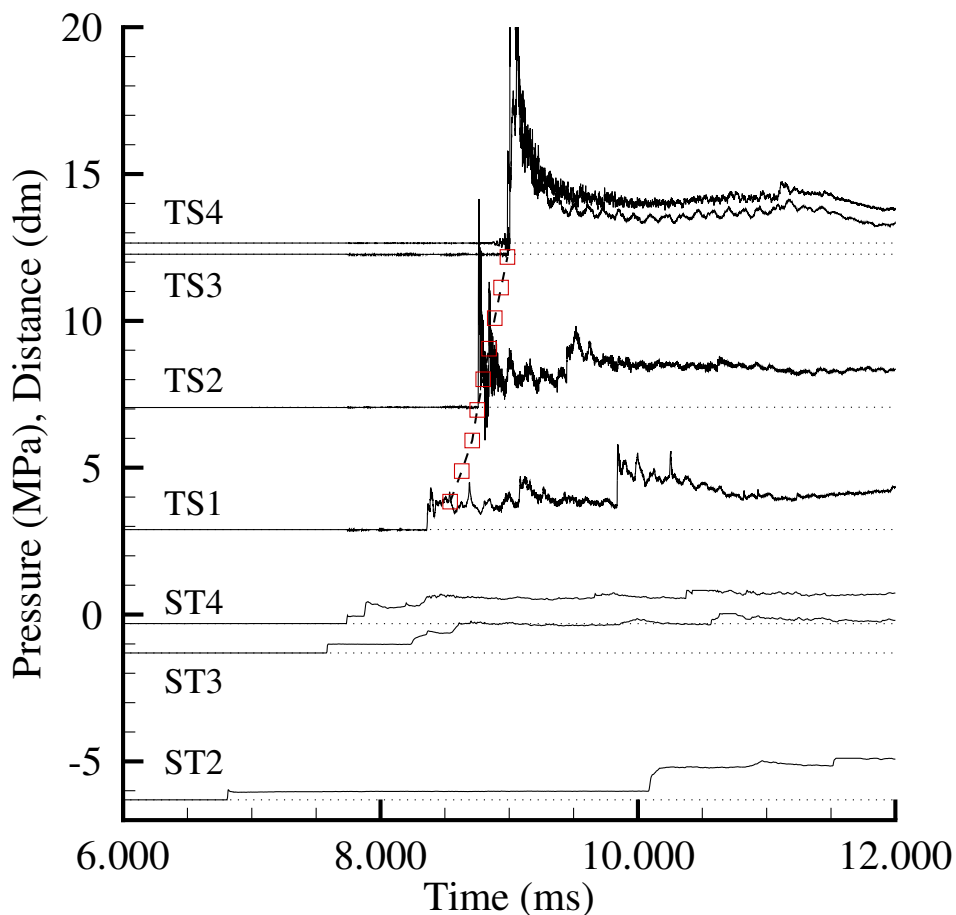


Figure 5.10: DDT in  $\text{C}_2\text{H}_4 + 3\text{O}_2 + 0.44\text{N}_2$  (10%  $\text{N}_2$  by volume) with incident Mach number  $M_s = 1.9$  in the shock tube (run 83). The y-intercept of the baseline of each trace corresponds to the transducer location in dm (0.1 m) as shown in Fig. 5.4.

### 5.3.2.2 Deflagration-to-Detonation Transition

An experiment was classified as DDT if the combustion mode was observed to transition from a deflagration to a detonation in the test section before the incident shock wave in the test section had reached the test-section end flange. The DDT process can be observed in Fig. 5.10. A shock wave ( $M = 1.88$ ) travels down the shock tube and reflects off the end flange as in the previous example. However, a detonation is not immediately initiated. The first wave recorded in the test section is a shock

wave. The ionization probes indicate that the shock is trailed by an accelerating deflagration. Near the middle of the test section (0.7 m), transition to an overdriven detonation ( $P = 7.0$  MPa,  $U = 2670$  m/s) occurs. The overdriven detonation relaxes as it travels down the test section and has a pressure and wave velocity characteristic of a CJ detonation wave shortly before it reflects off the test-section end wall.

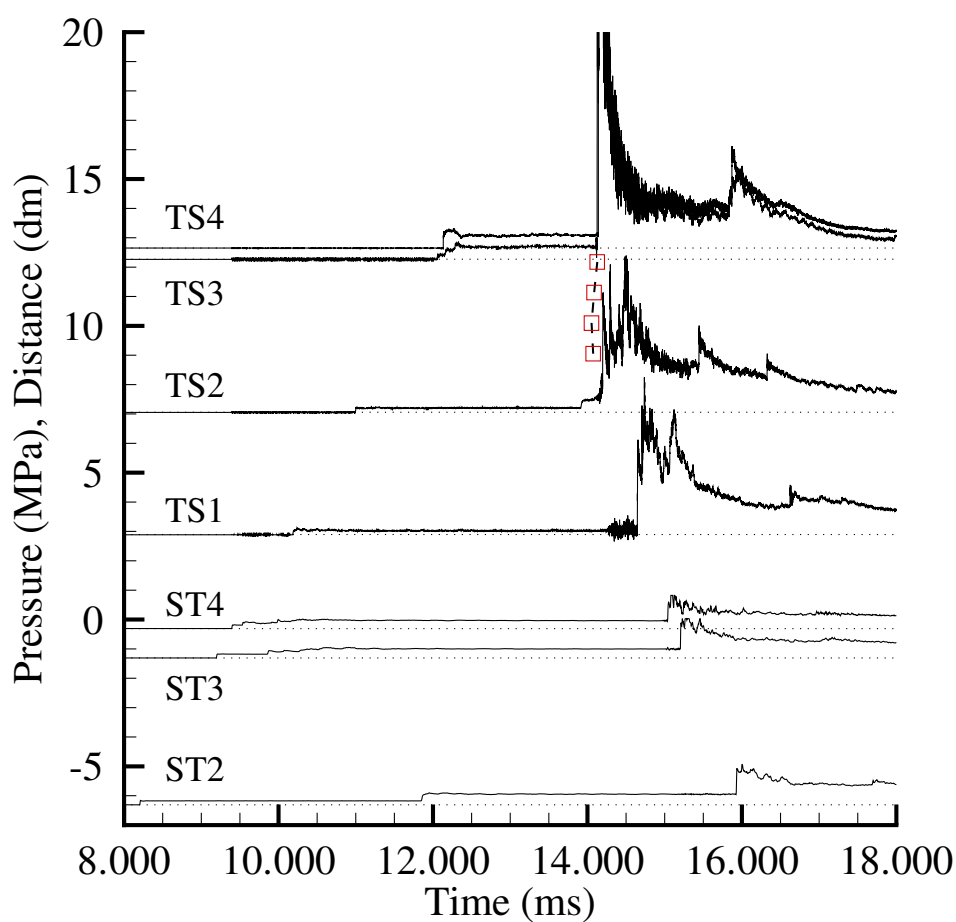


Figure 5.11: Initiation behind reflected wave in  $\text{C}_2\text{H}_4 + 3\text{O}_2 + 4\text{N}_2$  (50%  $\text{N}_2$  by volume) with incident Mach number  $M_s = 1.5$  in the shock tube (run 47). The y-intercept of the baseline of each trace corresponds to the transducer location in dm (0.1 m) as shown in Fig. 5.4.

### 5.3.2.3 Detonation after Reflection

The test-section mixture did not react behind the test-section incident shock wave. Instead, combustion initiated behind the reflected wave. In Fig. 5.11, a Mach 1.46 shock wave in the shock tube generated an implosion in the test section but failed to detonate the mixture. The implosion process propagated a shock wave through the test section, which reflected from the test-section end flange. A large explosion occurred near ionization probe I8 roughly 2 ms after the reflected wave had passed by. The closest pressure trace, TS4, measured the explosion pressure to be 26 MPa, which is more than eight times  $P_{CJ}$  for the test mixture. A significant ionization front was detected on only four of the nine transducers in the test section because the increased density behind the incident shock ( $M = 1.53$ ) compressed the combustible test mixture into the last half of the tube.

### 5.3.2.4 No Initiation

In some cases, low wave speeds and pressures were measured by the pressure transducers and no ionization was detected. Such experiments were labeled as failed to initiate. Data from a failure to initiate are shown in Fig. 5.12. A Mach 1.7 shock wave in the shock tube created a Mach 1.75 wave in the test section. The wave reflected from the test-section end wall and traveled back into the shock tube with no combustion occurring in the 20 ms data acquisition window.

## 5.3.3 Effect of Nitrogen Dilution

The experimental results are shown in Fig. 5.13 for stoichiometric ethylene-oxygen and propane-oxygen mixtures with varying nitrogen dilution. During the experiments, the incident shock strength varied from  $M = 1.31$  to 2.08. The Mach number of 2.08 generated a reflected shock pressure slightly above the maximum acceptable reflected-shock pressure in the facility and was tested only once.

Fig. 5.13 shows that for sufficiently small diluent concentration, a sufficiently large incident shock strength  $M$  resulted in prompt detonation in the test section. As  $M$

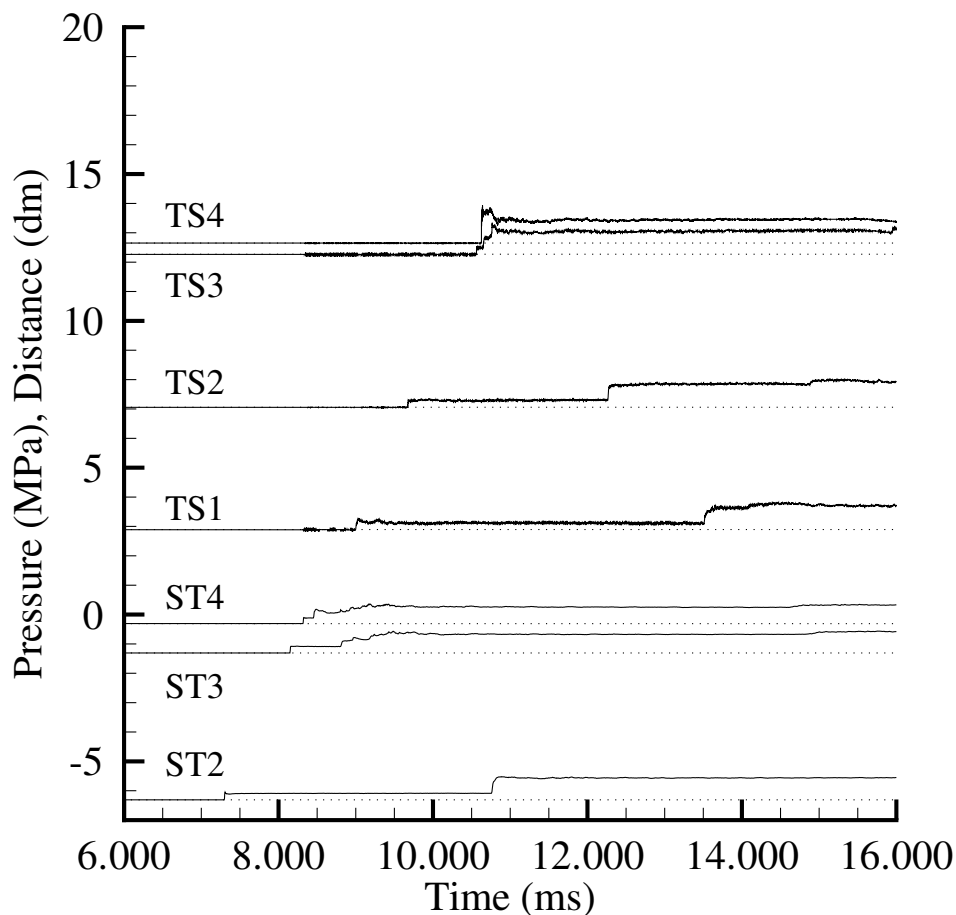
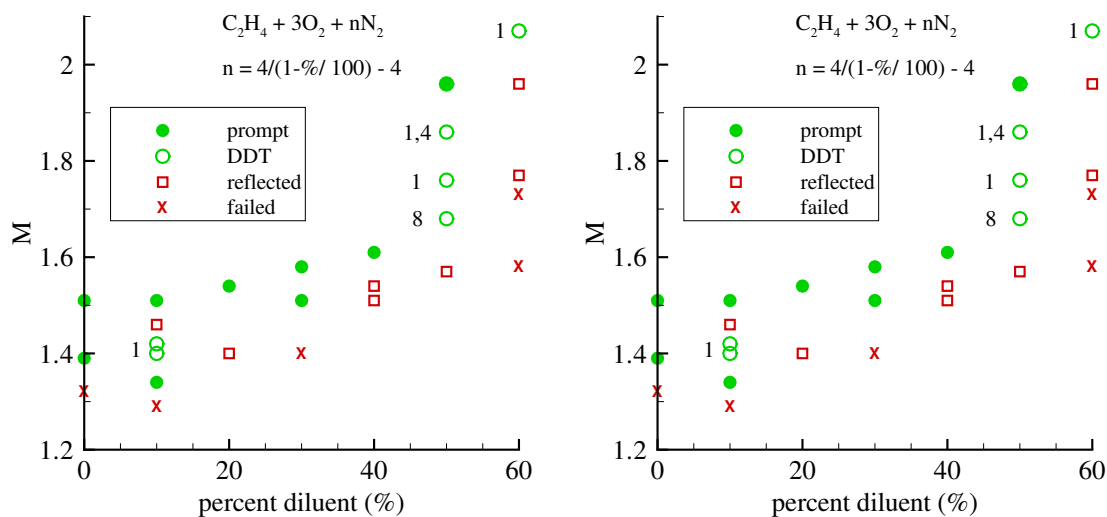


Figure 5.12: No initiation in  $\text{C}_2\text{H}_4 + 3\text{O}_2 + 6\text{N}_2$  (60%  $\text{N}_2$  by volume) with incident Mach number  $M_s = 1.7$  in the shock tube (run 43). The y-intercept of the baseline of each trace corresponds to the transducer location in dm (0.1 m) as shown in Fig. 5.4.

was decreased, prompt detonation no longer occurred, instead resulting in either DDT or detonation initiation behind the reflected shock. If  $M$  was too low, combustion no longer occurred during the data acquisition window.

Both hydrocarbon mixtures required increasing  $M$  to achieve detonation as the amount of dilution was increased. For the ethylene mixtures, this rate of increase jumped dramatically near dilution values of 50%. Propane mixtures exhibited a steeper rate of increase for low dilution values and reached the maximum test point at 40% nitrogen dilution before the presence of a similar trend could be investigated.



(a) Ethylene-oxygen-nitrogen data.

(b) Propane-oxygen-nitrogen data.

Figure 5.13: Initiation result classification for stoichiometric ethylene-oxygen and propane-oxygen test mixtures with varying nitrogen dilutions.  $M$  is the incident shock Mach number in the shock tube. Numbers to the left of the DDT data symbols indicate the number of the ionization probe that was closest to the DDT event.

Extrapolation of the data predicts that shock strengths in excess of  $M = 4$  and reflected-shock pressures  $P_5$  in excess of  $P_{CJ} = 19$  bar would be required to achieve successful initiation in fuel-air dilutions (73% by volume for ethylene and 75% by volume for propane) even using the most optimistic extrapolation technique. Additional analysis of the shock initiator data is discussed in the following chapter.

## 5.4 Summary

Imploding annular shock waves were propagated into a detonation tube filled with ethylene-oxygen-nitrogen and propane-oxygen-nitrogen mixtures to establish the minimum imploding shock strength necessary to successfully initiate detonations. The minimum shock strength required for initiation was found to increase with increasing dilution. The data indicate that initiating detonations in fuel-air mixtures would require shock driver pressures larger than the CJ pressure for the fuel-air mixtures. It should be noted, however, that the experiments used a converging jet of air to create

the imploding shock wave. Switching to a fuel-air driver gas could enhance the imploding shock initiation process by injecting a combustible mixture, rather than inert air, into the detonation tube. This could reduce the shock driver pressure required for initiation.

Increasing the diameter of the detonation tube to values used by Li and Kailasanath (2003a) could also enhance the initiation process as it would allow the imploding shock wave to achieve higher values of compression during the implosion process. However, an increased tube diameter would also reduce the amount of confinement, moving potential reflecting surfaces away from the implosion focus, which has been shown to be detrimental to the success of the implosion process (Chapter 4). Thus, it is not clear at this time what net effect changing the diameter would have on the initiation process.



## Chapter 6

# Initiator Effectiveness

To evaluate the effectiveness of each initiator type, the total energy input to each initiator should be compared to the minimum energy required for the detonation initiation process inside the tube. As previously mentioned, it is expected that the imploding wave creates a core of high-energy gas that then explodes, creating a blast wave. This blast wave then expands and reflects from the tube walls. The initial blast and subsequent reflections both contribute to the initiation process. If the blast wave is treated as ideal, then a specific quantity of energy can be associated with the creation of the blast. Furthermore, it can be expected that there will be a minimum or critical energy required for direct initiation.

While a substantial amount of data is available for the critical initiation energy for a spherical blast wave  $E_{spherical}^*$  in an unconfined volume, very few studies have been performed to determine the minimum energy required to initiate a detonation from a blast wave inside a tube. The minimum energy  $E^*$  is expected to be less than  $E_{spherical}^*$  due to confinement from the tube walls and greater than the minimum energy  $E_{tube}^*$  required for planar initiation:

$$E_{tube}^* < E^* < E_{spherical}^* . \quad (6.1)$$

The range between  $E_{tube}^*$  and  $E_{spherical}^*$  can be several orders of magnitude. For example, in stoichiometric propane-air, the work of Radulescu (1999) predicts that  $E_{spherical}^* = 702$  kJ while  $E_{tube}^* = E_{planar}^* \times A_{tube} = 0.87$  kJ for a 76 mm ID tube.

In an effort to further refine the comparison between the initiation energies, the confinement effect of the tube walls is considered in more detail. As previously mentioned, shock reflection from the tube walls can be responsible for initiation of a detonation kernel, which initiates the detonation wave in the tube. For this situation to occur, the blast wave must be of a sufficient strength such that its reflection from the tube walls generates a region of sufficiently high energy density that is capable of creating the detonation kernel. If the blast wave decays too rapidly, or conversely, if the tube diameter is too large, the reflection process will be too weak to have any effect on the detonation initiation. Under these conditions, the critical energy required to initiate a detonation inside the tube can be expected to scale with  $E_{spherical}^*$ , and the effects of confinement are minimal.

When the effects of confinement are significant, however, the critical energy will be less than  $E_{spherical}^*$ . It is proposed that the key requirement for successful initiation with confinement is that the blast wave be of a minimum strength  $M_s^*$  when it reflects from the tube wall.

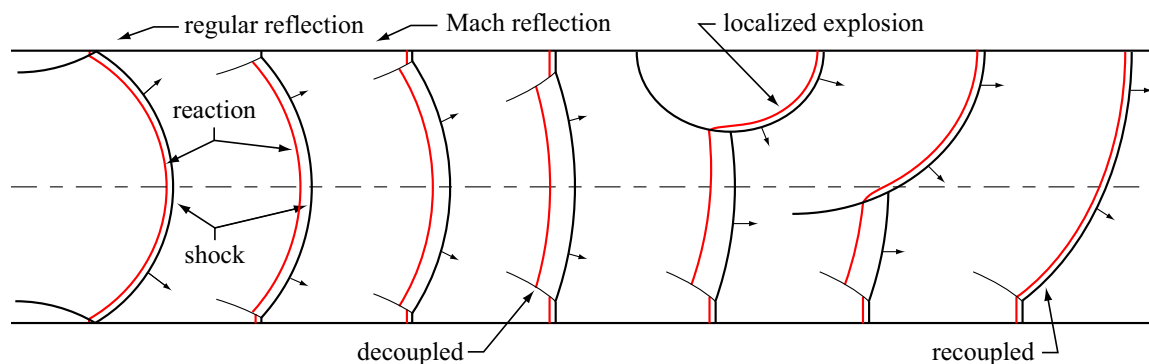


Figure 6.1: Reinitiation of the detonation wave from Mach reflection. The Mach reflection prevents the wave from failing near the wall and allows it to reinitiate a decoupled system.

At this minimum strength, the reaction front behind the incident wave will decouple and trail the shock front as the wave reflects from the wall. The reflection from the tube wall, initially regular, will transition into a Mach reflection. The Mach stem has been shown to be capable of reinitiation of the detonation wave (Murray et al.,

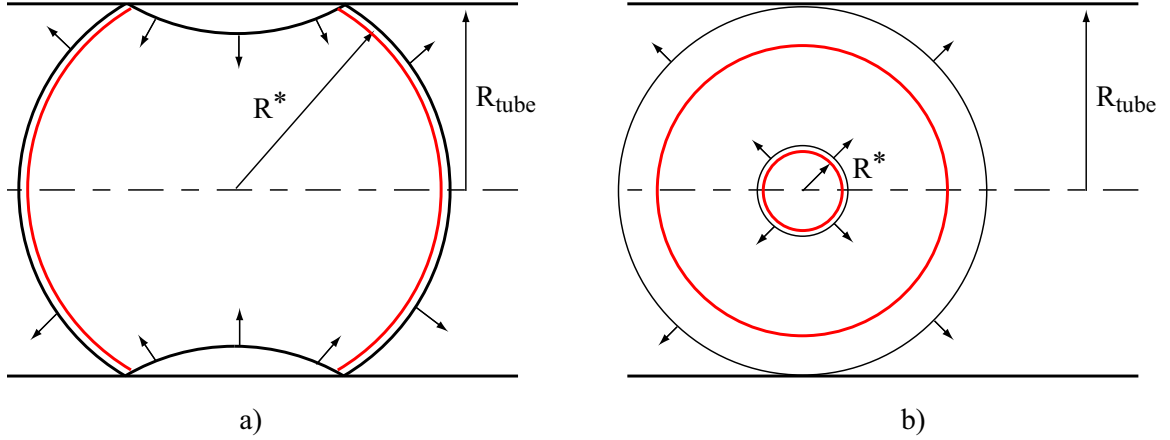


Figure 6.2: An illustration of the scaling criteria for the critical blast wave initiation energy inside a tube. (a) Blast waves that are of a critical strength  $M_s^*$  when they reflect from the tube wall will initiate detonations for  $E^*$  lower than  $E_{spherical}^*$ . (b) Blast waves that decay to less than  $M_s^*$  before reflecting from the tube walls will not create reflections of sufficient strength to result in detonation initiation.

2000, Brophy et al., 2003) as shown in Fig. 6.1.

It has been proposed that the reflected shock pressure and temperature must be on the order  $P_{CJ}$  and  $T_{CJ}$  in order for the detonation to succeed. The value of  $M_s^*$  required at the limiting condition is not currently known, and, as such, will be left arbitrary. Thus, the radius of the blast wave when it has decayed to  $M_s^*$  will be denoted by  $R_*$ .

Once the tube walls confine the flow, the blast wave no longer decays spherically, but, instead, will undergo a complex series of reflections and eventually transition to a planar wave propagating axially. If the initiation takes place after the transition to a planar wave, the critical energy will be that of the planar case:

$$E^* \propto E_{planar}^* A_{tube} \quad \text{for} \quad \frac{R_*}{R_{tube}} \geq 1 \quad (6.2)$$

$$E^* \propto E_{spherical}^* \quad \text{for} \quad \frac{R_*}{R_{tube}} \ll 1. \quad (6.3)$$

Figure 6.2 contains a sketch illustrating this concept. As  $R_{tube}$  increases for a given blast wave energy,  $E^*$  will transition from Eq. 6.2 to Eq. 6.3 (Fig. 6.3). Thus, confinement enhances the initiation process over only a finite range of tube diameters.

Solving for the intersection of  $E_{spherical}^*$  and  $E_{planar}^* \pi R_{tube}^2$  using the values of Radulescu (1999) yields that the transition occurs near  $R_{tube} = 21.6\lambda$ , which corresponds to approximately 1.0 m for propane-air mixtures at 1.0 bar and 295 K.

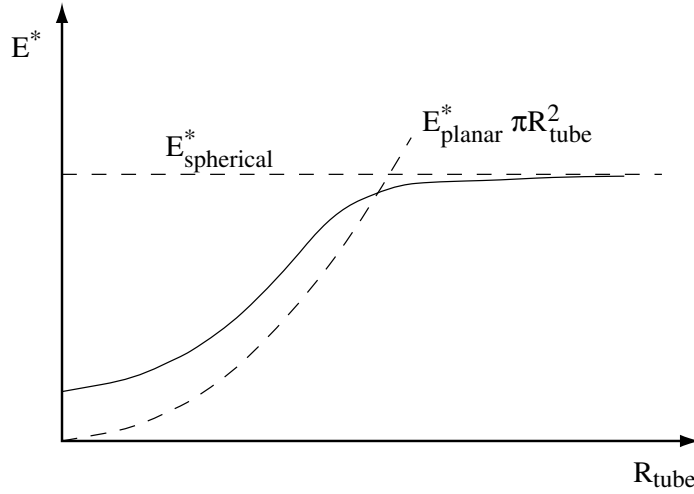


Figure 6.3: A sketch illustrating the predicted critical energy for a blast wave to initiate a detonation inside a tube. The dashed lines indicate the energies required for direct initiation of planar or spherical waves. The solid line indicates the relationship suggested by Eqs. 6.2 and 6.3.

## 6.1 Energy Input to the Shock Implosion Initiator

The unsteady energy-balance relation can be used to estimate the energy input to the shock implosion initiator. Setting a control volume around the test-section tube (Fig. 6.4) and assuming that there are no body forces or heat addition, the energy equation is

$$\frac{d}{dt} \int_V \rho \left( e + \frac{|u|^2}{2} \right) dV + \int_{\partial V} \rho \left( e + \frac{|u|^2}{2} \right) (u - u_v) \cdot \hat{n} dA = \int_{\partial V} T \cdot u dA \quad (6.4)$$

where surface forces on the control volume are represented by

$$T = -P\hat{n} + \tau \cdot \hat{n} . \quad (6.5)$$

For a stationary control volume with no shear forces, the equation can be reduced to

$$\frac{d}{dt} \int_V \rho \left( e + \frac{|u|^2}{2} \right) dV = - \int_{\partial V} \rho \left( h + \frac{|u|^2}{2} \right) u \cdot \hat{n} dA. \quad (6.6)$$

The left-hand side of the equation is the rate of energy change in the control volume. Applying the right-hand integral to the control volume and assuming that the flow is radially inward ( $u \cdot \hat{n} = -u_r$ ) and does not vary along the orifice, the equation becomes

$$\frac{d}{dt} \int_V \rho \left( e + \frac{|u|^2}{2} \right) dV = \left( h + \frac{|u|^2}{2} \right) \rho A u_r \quad (6.7)$$

where  $A$  is the area of the annular orifice. Note that since the control volume follows the inside of the test-section wall, all flow must enter the control volume through the annular orifice.

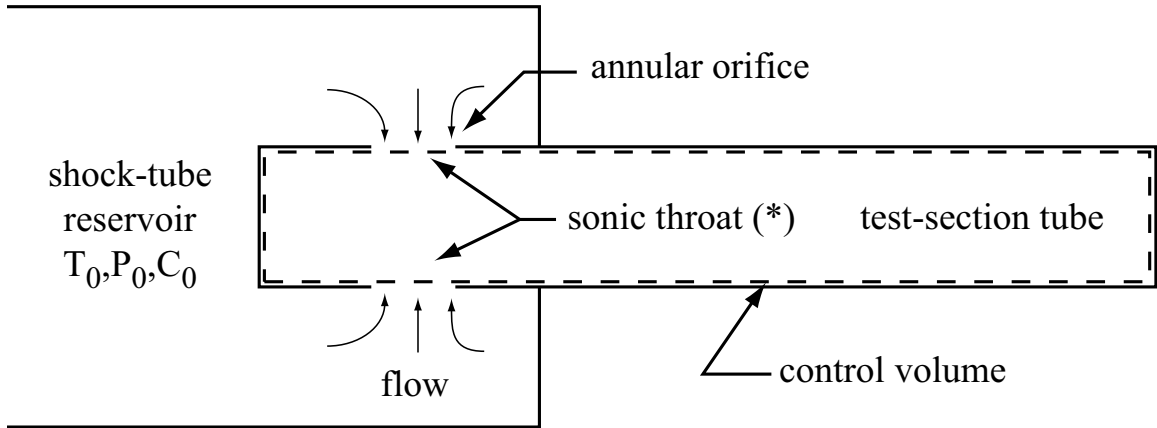


Figure 6.4: A sketch illustrating the control volume considered for the shock implosion tests. The control volume is indicated by the dashed line.

For steady adiabatic flow, the total enthalpy is conserved

$$h_0 = h + \frac{|u|^2}{2} \quad (6.8)$$

and for a constant heat capacity

$$h_0 = C_p T_0 + \text{constant} . \quad (6.9)$$

Substituting the previous two expressions into the energy equation and applying the perfect gas law

$$P = \rho R T , \quad (6.10)$$

the energy equation becomes

$$\frac{d}{dt} \int_V \rho \left( e + \frac{|u|^2}{2} \right) dV = C_p T_0 \frac{P}{RT} A u_r . \quad (6.11)$$

During the experiments, the pressure ratio across the annular orifice was high enough that the flow through the orifice can be assumed to be sonic or choked.

$$\frac{d}{dt} \int_V \rho \left( e + \frac{|u|^2}{2} \right) dV = \frac{C_p}{R} \frac{T_0}{T^*} P^* c^* A . \quad (6.12)$$

Since

$$C_p = C_v + R \quad (6.13)$$

and

$$\gamma = \frac{C_p}{C_v} \quad (6.14)$$

then

$$\frac{C_p}{R} = \frac{\gamma}{\gamma - 1} . \quad (6.15)$$

Additionally, from Eq. 6.8 and the speed of sound,

$$c = \sqrt{\gamma RT} , \quad (6.16)$$

it can be found that for adiabatic choked flow,

$$\frac{T_0}{T^*} = \frac{\gamma + 1}{2} \quad (6.17)$$

and for isentropic flow,

$$\frac{P_0}{P^*} = \left( \frac{T_0}{T^*} \right)^{\frac{\gamma}{\gamma-1}} = \left( \frac{\gamma + 1}{2} \right)^{\frac{\gamma}{\gamma-1}} . \quad (6.18)$$

Using these relations, the energy equation becomes

$$\frac{d}{dt} \int_V \rho \left( e + \frac{|u|^2}{2} \right) dV = \left( \frac{\gamma}{\gamma-1} \right) \left( \frac{\gamma+1}{2} \right) P^* c^* A , \quad (6.19)$$

or, in terms of the total reservoir properties,

$$\frac{d}{dt} \int_V \rho \left( e + \frac{|u|^2}{2} \right) dV = \left( \frac{\gamma}{\gamma-1} \right) \left( \frac{\gamma+1}{2} \right)^{\frac{\gamma}{1-\gamma}} P_0 c_0 A . \quad (6.20)$$

Eq. 6.20 provides an estimate of the energy input to the test section of the shock implosion initiator assuming that the stagnation values of the reservoir are known. In order to obtain an energy value, Eq. 6.20 must be integrated over time. Choosing a characteristic time  $t_c$ , based on the initial speed of sound  $c_1$  in the test section and the tube radius, yields

$$t_c = \frac{R_1}{c_1} \quad (6.21)$$

where  $R_1$  is the inner radius of the test-section tube.

During implosion, the inflow state is considered constant, an assumption which is valid only if the properties of the shocked-gas reservoir change slowly relative to the annular implosion process. In the experiment, this condition is likely not satisfied as

the mass of gas injected into the test section at time  $t_c$  is on the order of the mass of the gas processed by the reflected wave. Thus, the calculation will overpredict the actual energy input to the initiator.

With these considerations, the characteristic energy input can be estimated as

$$\int_V \rho \left( e + \frac{|u|^2}{2} \right) dV \approx \left( \frac{\gamma}{\gamma - 1} \right) \left( \frac{\gamma + 1}{2} \right)^{\frac{\gamma+1}{2(1-\gamma)}} P_0 c_0 (2\pi R_1 w) \frac{R_1}{c_1} \quad (6.22)$$

where  $2\pi R_1 w$  has been substituted for the inflow area  $A$ . The parameter  $w$  is the width of the annular orifice. For propane and ethylene mixtures, the value of  $\gamma \approx 1.37$  and the energy is approximately

$$\int_V \rho \left( e + \frac{|u|^2}{2} \right) dV \approx 10 w P_0 R_1^2 \frac{c_0}{c_1}. \quad (6.23)$$

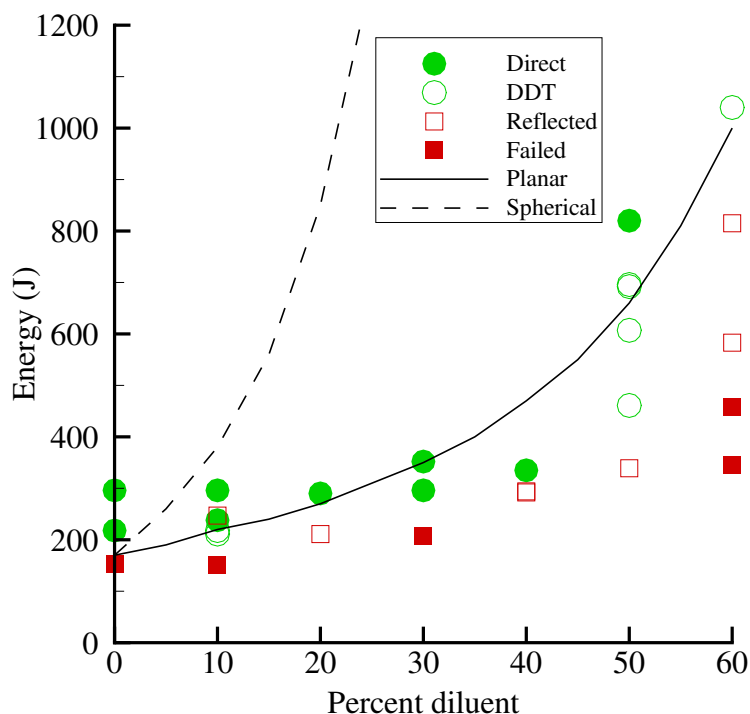


Figure 6.5: The energy input to the test-section tube for the shock implosion experiment for ethylene-oxygen-nitrogen data with  $m_1 = 0.79$  and  $m_3 = 8.3 \times 10^8$ .

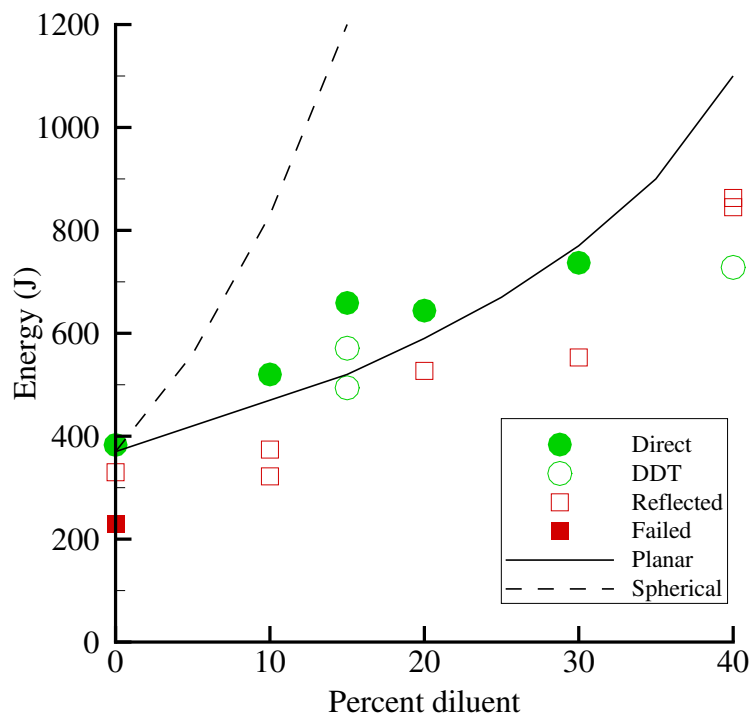


Figure 6.6: The energy input to the test-section tube for the shock implosion experiment for propane-oxygen-nitrogen data with  $m_1 = 1.6$  and  $m_3 = 1.8 \times 10^9$ .

Figures 6.5 and 6.6 show the energy calculated with Eq. 6.23 for the data from Fig. 5.13 as a function of diluent for each mixture. It can be seen that it takes roughly twice as much energy to achieve detonation in the propane mixtures compared to the ethylene mixtures.

Two curves are also plotted on each of the figures, which scale with the planar and spherical initiation energies using a form of Eq. 1.12,

$$E_j^* = m_j \rho_0 D^2 \Delta^j \quad (6.24)$$

where  $m_j$  is a scaling constant that was chosen such that the two curves coincide at 0% dilution. Over the range shown, the data agree better with the planar critical-energy trend rather than the spherical critical-energy trend for both the ethylene and propane mixtures. Induction distances for the scaling curves were computed with the

ZND program of Shepherd (1986) with the chemical kinetics mechanism of Konnov (1998). The data used to generate the scaling curves are shown in Table 6.1.

Diluent	Ethylene			Propane		
	$\rho_0$ (kg/m <sup>3</sup> )	$D$ (m/s)	$\Delta$ (mm)	$\rho_0$ (kg/m <sup>3</sup> )	$D$ (m/s)	$\Delta$ (mm)
0%	1.26	2376	0.031	1.39	2361	0.030
10%	1.25	2317	0.041	1.36	2306	0.040
20%	1.24	2259	0.054	1.34	2252	0.054
30%	1.23	2198	0.075	1.31	2195	0.076
40%	1.22	2132	0.107	1.29	2132	0.114
50%	1.20	2060	0.164	1.26	2062	0.187
60%	1.19	1977	0.282	1.24	1981	0.358
70%	1.18	1874	0.617	1.22	1879	0.916
73.8%	1.17	1824	0.963	1.20	1801	2.072
80%	1.17	1723	2.853	1.19	1728	4.809

Table 6.1: The scaling data used in Eq. 6.24 to generate the curves in Figs. 6.5 and 6.6.

## 6.2 Energy Input to the Toroidal Initiator

When determining the input energy calculation for the shock implosion initiator, it was assumed that all energy was from the converging jet of air. In the toroidal initiator, the implosion was created by detonating an equimolar acetylene-oxygen mixture. In calculating the input energy  $E_{inp}$  to the toroidal initiator, the chemical energy released will be assumed to be the dominant contribution to the initiation process and the energy input from mass flow will be neglected.

The toroidal initiator of Chapter 4 used a 434 cc (26.5 in<sup>3</sup>) volume of equimolar acetylene-oxygen gas initially at a temperature of 295 K and a pressure of 1 bar to initiate a detonation in a tube filled with stoichiometric propane-air. The effective heat of reaction  $\Delta h^0$  of the initiator gas mixture can be approximated in the following fashion.

The heat of reaction  $\Delta h^0$  is defined as the difference in enthalpy of the gas, ex-

trapolated from absolute zero temperature

$$h_1 = h^{01} + C_{p1}T_1 \quad (6.25)$$

$$h_2 = h^{02} + C_{p2}T_2 \quad (6.26)$$

$$h^{01} - h^{02} = \Delta h^0 \quad (6.27)$$

where the subscript 1 denotes the initial gas state and subscript 2 is the state which has been processed by the detonation wave.

Applying the above relations to the shock-jump condition for energy

$$h_1 + \frac{1}{2}w_1^2 = h_2 + \frac{1}{2}w_2^2 \quad (6.28)$$

yields

$$\Delta h^0 + C_{p1}T_1 + \frac{1}{2}w_1^2 = C_{p2}T_2 + \frac{1}{2}w_2^2. \quad (6.29)$$

Substituting

$$Pv = RT \quad (6.30)$$

and

$$C_p = \frac{\gamma}{\gamma - 1}R \quad (6.31)$$

into Eq. 6.29 and rearranging terms, the energy shock-jump condition for a perfect gas is obtained

$$\begin{aligned} \Delta h^0 + R_1T_1 \left( \frac{\gamma_1}{\gamma_1 - 1} \right) \left( 1 + \frac{\gamma_1 - 1}{2}M_1^2 \right) \\ = R_2T_2 \left( \frac{\gamma_2}{\gamma_2 - 1} \right) \left( 1 + \frac{\gamma_2 - 1}{2}M_2^2 \right). \end{aligned} \quad (6.32)$$

Evaluating the post-detonation flow at the CJ surface will set  $M_2 = 1$ . Solving for

$\Delta h^0$ , the heat of reaction is

$$\Delta h^0 = R_{CJ} T_{CJ} \left( \frac{\gamma_{CJ}}{\gamma_{CJ} - 1} \right) \left( 1 + \frac{\gamma_{CJ} - 1}{2} \right) - R_1 T_1 \left( \frac{\gamma_1}{\gamma_1 - 1} \right) \left( 1 + \frac{\gamma_1 - 1}{2} M_{CJ}^2 \right). \quad (6.33)$$

In this perfect gas,  $2-\gamma$ , CJ detonation model,  $\gamma_1$  and  $\gamma_{CJ}$  are the ratios of specific heats of the gas at the initial state and at the CJ surface respectively.  $T_{CJ}$  is the temperature at the CJ surface and  $M_{CJ}$  is the Mach number of the CJ detonation wave.

STANJAN (Reynolds, 1986) was used to perform the equilibrium calculations necessary to obtain the CJ parameters. For acetylene-oxygen mixtures, the effective heat of reaction is shown in Fig. 6.7 as a function of equivalence ratio  $\phi$ . For the equimolar ( $\phi = 2.5$ ) mixtures used in the toroidal initiator, the effective heat of reaction was determined to be  $\Delta h^0 = 7.07$  MJ/kg of initiator mixture. Thus, the energy released by detonation of the initiator gas mixture for propane-air was found to be

$$\begin{aligned} E_{toroidal} &= \Delta h^0 \rho_0 V_{initiator} \\ &= 3.62 \text{ kJ} . \end{aligned} \quad (6.34)$$

Applying this calculation to the dynamic initiator results given in Tables 4.2 and 4.3 yields the energy input to the dynamic initiators as a function of diluent and fuel (Fig. 6.8).

### 6.3 Comparison of the Shock Implosion and Toroidal Initiators

Comparison of the toroidal initiator energies (Fig. 6.8) with the shock implosion initiator data (Figs. 6.5 and 6.6) is not straightforward since the data ranges do

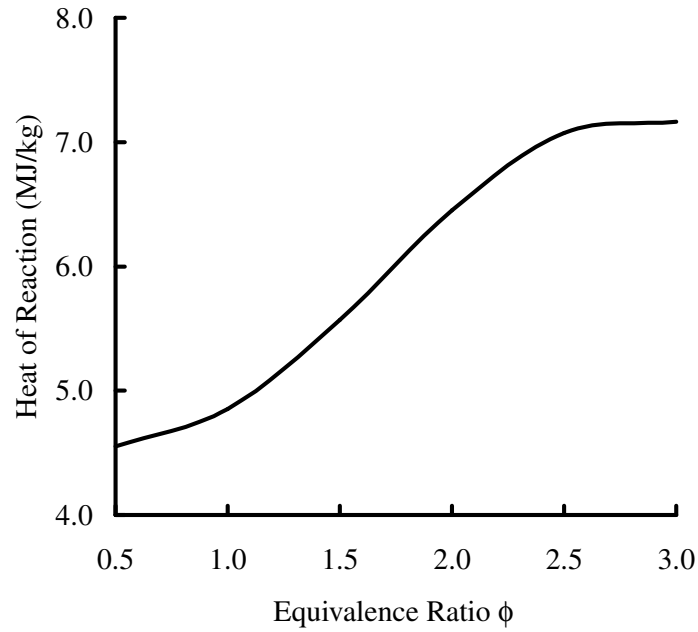


Figure 6.7: Effective heat of reaction of acetylene-oxygen mixtures as a function of equivalence ratio.

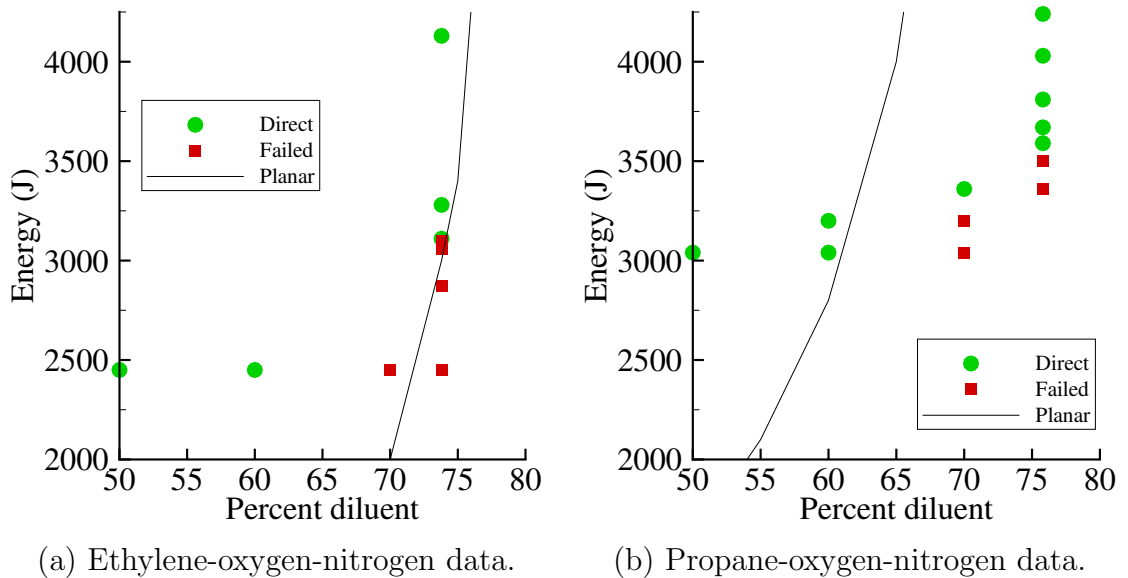


Figure 6.8: The energy input for the dynamic toroidal initiator. The curves shown are identical to those from Fig. 6.5 for ethylene and from Fig. 6.6 for propane.

not overlap. The maximum reflected shock pressure generated by the shock tube during the shock implosion tests was reached at relatively low diluent levels (60% for

ethylene mixtures and 40% for propane mixtures) and thus the conditions required for initiation of the higher dilutions that were used with the toroidal initiator could not be reached. However, the trend of the planar initiation energy curves in Figs. 6.5 and 6.6 predict that the toroidal initiator is at least as effective as the shock implosion initiator for ethylene-air mixtures and more effective for propane-air mixtures.

While comparing the critical energy input data from the two initiators, it was not possible to reduce the volume of initiator gas used in the toroidal initiator below a minimum limit. Approximately 30% of the initiator gas used by the toroidal initiator was required to fill the volume between the initiator and the gas injection system. This volume is not expected to have significantly contributed to the initiation process but was not subtracted when computing the initiation energy shown in Fig. 6.8.

The increased effectiveness of the toroidal initiator can be explained by several factors. First, the pressure pulses behind the imploding waves are different shapes for each facility. The toroidal initiator uses a detonation to generate the implosion, which initially has a high pressure and then decays to a much lower value. The shock implosion initiator, on the other hand, uses a high-pressure reservoir to create the implosion and provides a much longer constant-pressure pulse (Fig. 6.9). As discussed above, the longer-duration pulse can enhance the initiation process, but only if it is above a minimum value. Otherwise, a very strong blast wave will be more effective at initiation as it will induce locally higher-temperature values.

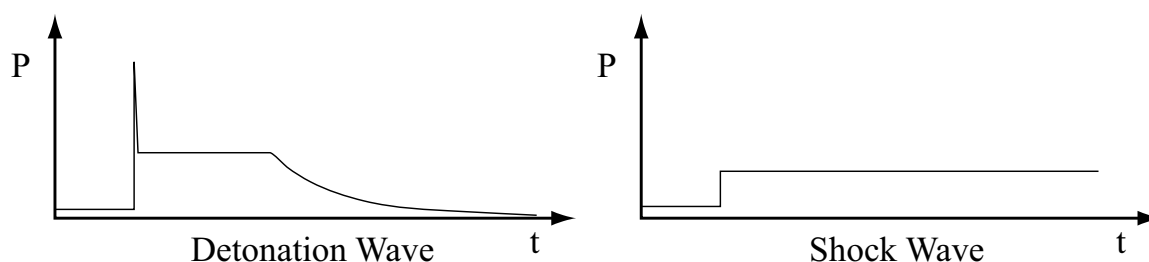


Figure 6.9: The different pressure pulses associated with each initiator.

Second, temperature of the gas injected into the test-section tube by the implosion process was much higher for the toroidal initiator than for the shock implosion

initiator. In the toroidal initiator, the injected gas just processed by the imploding detonation wave was at a temperature of approximately 4500 K. For the shock implosion initiator, the total temperature of the reservoir gas was approximately 500 degrees before acceleration through the sonic throat at the annular orifice. Since temperature plays a large role in generating the radicals essential for combustion, the hot gas from the toroidal initiator is expected to better facilitate detonation initiation compared to the cooler gas from the shock implosion initiator. It is even possible that the flow of lower-temperature gas into the test section could hinder the development of initiation by quenching nascent detonation kernels.

Finally, the shock implosion initiator relies on the implosion to ignite the test-section mixture, while the toroidal initiator introduces a reaction front into the test-section tube with the imploding wave, ensuring that prompt ignition will occur in the test section, even if transition to detonation does not.

### 6.3.1 Comparison of the Toroidal Initiator Energy to Various Critical Energies

Table 6.2 contains the critical energies from the toroidal initiator, spherical initiation experiments, and values obtained from the model of Radulescu (1999) for planar and spherical geometries. All table entries are normalized by the critical toroidal initiation energy (3.62 kJ). Thus, the normalized entries represent a sort of efficiency factor. It is clear that spherical initiation is far less efficient than toroidal initiation since it is intended to initiate a spherical detonation in an open space, while the toroidal initiator initiates a planar detonation wave in a 76 mm diameter tube.

Toroidal	Spherical (predicted)	Spherical (exp)	Planar (predicted)
1.0	190	78	0.24

Table 6.2: Critical energies for spherical and planar initiation compared to the toroidal initiator. The planar value is for a wave surface area of  $\pi(0.038)^2$  m<sup>2</sup>.

The energy required to initiate a planar detonation wave provides a more useful

comparison with the toroidal initiator critical energy as both initiation schemes generate a nominally planar detonation wave in a 76 mm diameter tube. As previously determined, the toroidal initiator uses 3.62 kJ of energy to initiate stoichiometric propane-air mixtures.

Using the modified blast wave model, the critical planar initiation energy per unit area was previously found to be 192.0 kJ/m<sup>2</sup>. Thus, the critical planar initiation energy required to initiate a planar detonation in a 76 mm diameter tube with a cross-sectional area of

$$A_{tube} = \pi \frac{d^2}{4} = 4.54 \times 10^{-3} \text{ m}^2 \quad (6.35)$$

is 192.0 kJ/m<sup>2</sup>  $\times$  (4.54  $\times$  10<sup>-3</sup> m<sup>2</sup>) = 0.87 kJ. The critical energy predicted for planar initiation appears to be about a quarter of the critical toroidal initiation energy. Unfortunately, experimental measurements of planar initiation energy are not currently available for comparison.

### 6.3.2 Comparison with a Typical Initiator Tube

Recent work by Murray et al. (2003) has resulted in a model based on an extensive data set that is capable of predicting the necessary initiator tube dimensions for stoichiometric acetylene-oxygen initiator mixtures. The model predicts that for an initiator tube diameter to main tube diameter ratio of  $d_d/d = 0.5$ , the initiator tube length  $L_d$  necessary to initiate a stoichiometric propane-air test-section mixture with a cell size of  $\lambda = 50$  mm (2 in) is approximately  $L_d/\lambda = 9$  or  $L_d = (45.7 \text{ cm})$  18 in. For main tube diameter of  $d = 76$  mm (3 in) used in the toroidal initiator experiments,

this corresponds to an initiator tube volume of

$$V_d = \frac{\pi d^2}{4} L_d \quad (6.36)$$

$$= \frac{\pi (0.75\lambda)^2}{4} 9\lambda \quad (6.37)$$

$$\approx 4\lambda^3 \quad (6.38)$$

$$= 32 \text{ in}^3 \text{ or } 524 \text{ cc.} \quad (6.39)$$

Since the Murray et al. model assumes a stoichiometric acetylene-oxygen initiator gas, the effective heat of reaction of the mixture using the perfect gas,  $2-\gamma$ , CJ detonation model is found to be  $\Delta h^0 = 4.85 \text{ MJ}$ . This corresponds to an energy release of

$$E_{d,uncorr} = \Delta h^0 \rho_0 V_{d,uncorr} \quad (6.40)$$

$$= 3.14 \text{ kJ} . \quad (6.41)$$

The amount of oxygen necessary for successful initiation is important in performance modeling as oxygen tanks will result in payload losses. The masses of fuel and oxygen initiator gas were also calculated and are shown in Table 6.3. Examination of the amount of initiator gas used by each initiator reveals that the toroidal initiator uses more fuel, but about half the amount of oxygen used by the model initiator tube.

	Toroidal Initiator	Tube
Energy	3.62 kJ	3.14 kJ
Mass $C_2H_2$	0.23 g	0.16 g
Mass $O_2$	0.28 g	0.49 g

Table 6.3: Critical values for a model initiator tube compared to the toroidal initiator.

## 6.4 Summary

Criteria predicting the effect of confinement on the scaling of the critical energy for detonation initiation from a blast wave in a tube were developed and were the basis of

a competition between the decay of the blast wave and the strength of the blast-wave reflection from the tube walls. The critical energy input to the shock implosion initiator and the toroidal initiator was calculated for the experimental conditions tested. For the shock implosion initiation, the dominant contributor to the input energy was assumed to be the fluid flux into the test section. The energy was calculated using the energy equation applied to the test section as a control volume. For the toroidal initiator, the fluid flux into the test section was neglected and the dominant energy source was attributed to the heat of reaction of the acetylene-oxygen initiator gas. This value was calculated using a two- $\gamma$ , perfect-gas, CJ detonation model.

Although a limited range of comparison was available, the toroidal initiator was determined to be more effective at initiating detonations for a given input energy than the shock implosion initiator. The increased effectiveness of the toroidal initiator was attributed to the higher strength of the toroidal initiator's imploding wave as well as the design's proficiency at injecting high-temperature products, accompanied by a reaction zone, into the test section. It was suggested that the longer-duration pressure pulse of the shock implosion initiator was not of sufficient strength to compete with the aforementioned attributes of the toroidal initiator.

The critical energy input required for the toroidal initiator to initiate stoichiometric propane-air mixtures was compared to direct initiation energies for spherical and planar geometries as well as the energy input to an initiator tube. As expected, the critical energy for the toroidal initiator was lower than that required for direct spherical initiation and higher than the energy required for direct planar initiation. The critical energy was also found to be comparable to that used by current initiator tubes.

# Chapter 7

## Conclusions

An experimental study has been conducted using toroidal imploding waves to initiate detonations inside of a 76 mm inner diameter test-section tube filled with stoichiometric ethylene-oxygen and propane-oxygen mixtures with varying amounts of nitrogen dilution. This work was motivated by recent interest in the development of efficient methods of detonation initiation for the HC-air mixtures used in air-breathing PDEs.

Two devices were developed to test the effectiveness of the toroidal imploding waves at detonation initiation. The first was the dynamic toroidal initiator, which uses a single spark, a series of small-diameter channels, and a small amount of acetylene-oxygen gas to create an imploding detonation wave in the test-section tube. This initiator was able to successfully initiate ethylene-air and propane-air mixtures, given a sufficient amount of acetylene-oxygen initiator gas.

During the design and testing of the toroidal initiator, the ability to use small detonation wavelets to create a shaped detonation front was demonstrated. Imaging of the toroidal detonation confirmed that the wave remained stable and uniform during the implosion process with HC-oxygen mixtures. Pressure measurements near the implosion indicate that focal pressures are in excess of  $4P_{CJ}$ . The pressures measured near the toroidal implosion were compared to AMRITA simulations as well as to previous experiments and calculations from cylindrical imploding detonations (Lee and Lee, 1965). It was concluded that the toroidally imploding wave initially experiences a period of diffraction that is not present in cylindrical implosions. This diffraction weakens the wave and competes with the pressure amplification from the imploding

geometry. As the wave radius decreases, the pressure amplification from the imploding geometry dominates. However, the diffraction could cause failure in marginal detonation waves. Successive distance-time measurements of the central portion of the toroidal imploding wave in HC-oxygen mixtures indicate that it maintains a constant velocity as it implodes, which is in contrast to the continuous acceleration of imploding waves in cylindrical and spherical geometries.

An intermediate step in the design process resulted in development of a device capable of creating large-aspect-ratio planar waves over shorter distances than used by current technologies such as exploding wires or initiation and expansion from a point source. This device is currently in use on Caltech's Narrow Channel Facility and is able to initiate mixtures as insensitive as  $C_3H_8+5O_2+9N_2$  and  $C_2H_4+3O_2+10.5N_2$  (Austin, 2003).

The second device, the shock implosion initiator, created an imploding shock wave in the test-section tube with a jet from a reservoir of high-pressure and -temperature air. This initiator was able to achieve detonations in ethylene-oxygen mixtures with 60% nitrogen dilution and in propane-oxygen mixtures with 40% nitrogen dilution before reaching the maximum allowable pressure of the facility. However, the data trends indicate that reservoir pressures in excess of  $P_{CJ}$  would be required to initiate detonations in ethylene-air and propane-air mixtures.

The energy input to each initiator was estimated. In the case of the toroidal initiator, the energy input was found by calculating the heat of reaction of the initiator gas mixture from a two- $\gamma$ , perfect-gas, CJ detonation model. The amount of acetylene-oxygen gas used was comparable to that used by current initiator tubes when detonating equivalent mixtures. However, since the toroidal initiator is incorporated into the walls of the tube, it does not obstruct the flow inside the tube in the same way as a conventional initiator tube and, thus, is an inherently lower-drag design with similar effectiveness.

For the shock implosion initiator, the energy input was determined from an energy-balance equation that accounted for the inflow of mass into the test-section tube. The critical input energy was found to scale linearly with the induction length of

the test-section mixture, indicating a planar-type of initiation mode. It was inferred from the data that the toroidal initiator is more effective at detonation initiation compared to the shock implosion initiator. The increased effectiveness was attributed to the stronger implosion, the reaction front, and the higher-temperature products introduced into the test section by the toroidal initiator. These three factors were found to be more significant for detonation initiation than the longer, but lower pressure, pulse supplied by the shock implosion initiator.

A study of detonation wave propagation through small-diameter tubes was also performed in an effort to determine the minimum tube diameter capable of detonation propagation. Tubes with IDs of 6.35 mm and 1.27 mm were used with propane-oxygen mixtures, and the initial pressure and equivalence ratio of the test mixtures were varied such that the induction length of the mixtures was similar to that of the tube diameter. From pressure transducer measurements, a smooth decrease in the wave velocity was observed as the induction length increased relative to the tube diameter. As the induction zone increased, velocities as low as  $0.4 U_{CJ}$  were observed before wave failure occurred in the test section and the mixture became too insensitive to detonate with the initiation system. The decrease in wave velocity was analyzed using a boundary layer model. Two models (Fay, 1959, Dabora, 1963) accounting for stream-tube divergence between the shock wave and the reaction front were compared to the data. While both models followed the trend of the data, the model of Fay (1959) better agreed with low-velocity data ( $0.4 U_{CJ}$ - $0.9 U_{CJ}$ ) and the model of Dabora (1963) better agreed the higher-velocity data ( $0.9 U_{CJ}$ - $1.0 U_{CJ}$ ). While no diagnostics were used to detect the presence of the reaction front in the small-diameter tube, its presence was inferred due to the fact that, without combustion, the highest wave speed possible in the small tubing was calculated to be  $0.46 U_{CJ}$  from unsteady and quasi-steady analyses.

The experimental results have shown that toroidal waves can successfully initiate detonations in insensitive combustible mixtures. While the imploding toroidal geometry has been shown to experience diffraction not present in imploding cylindrical and spherical geometries, it is also a more practical imploding geometry to achieve,

especially for engineering applications, since a toroidal imploding wave can be created from a short length of a cylindrically imploding source and no confining walls. The diffraction of the wave as it implodes then shapes the wave into a toroid. Initiating imploding cylindrical waves over long distances is impractical as a long source is needed and maintaining the cylindrical wave geometries requires the elimination of diffraction by using confining walls at each end of the wave. Initiating spherical implosions requires either a perfect spherical source shell (to initiate an entire imploding spherical wave) or a portion of a spherical source and confinement of the resulting wave to eliminate diffraction.

The results of this study have determined that, in terms of energy input derived from the detonation of acetylene-oxygen initiator gas, the effectiveness of the toroidal initiator at initiating detonations is similar to that of an initiator tube. The shock implosion initiator requires a higher-energy input, but uses only high-pressure air to drive the implosion. Thus, it may be more appealing for PDE design as no additional fuel, oxygen, or ignition source is required for the initiation process.

## 7.1 Future Work

Imploding waves were used to create regions of high energy density that are responsible for detonation initiation; however, no observations of the flow were obtained during the initiation of HC-air mixtures. Imaging of the imploding detonation wave traveling into HC-air mixtures could detect whether the detonation fails after passing through the contact surface into the less-sensitive test-section mixture and would locate high energy density regions in the flow. It stands to reason that at least one region of high energy density will be present at the focus of the implosion, but others may exist at subsequent secondary implosions or where the explosion reflects from the tube walls or the contact surface.

Visualizing the implosion in the shock implosion initiator would also locate these regions and identify the ignition source and the subsequent development of detonation, which is of interest since no reaction front is introduced by the imploding shock wave.

Additionally, it is recommended that further testing be carried out with the shock implosion initiator by modifying the facility to use fuel or oxygen mixtures to drive the imploding shock instead of air and to permit higher reservoir pressures to be achieved. Injecting a reactive gas instead of one composed primarily of nitrogen may facilitate more effective detonation initiation. Higher reservoir pressures would initiate less-sensitive test-section mixtures and allow direct comparison of the initiator effectiveness to that of the toroidal initiator. Knowledge of the critical input energy over a larger diluent range would also allow further comparison with the planar scaling criteria discussed in Chapter 6.

Finally, it is proposed that more detailed measurements be obtained for detonation propagation through small-diameter tubes. The detonation propagation should be observed over a longer distance to ensure that the wave is steady and not failing or galloping. Also, in future experiments, the location of the reaction zone relative to the shock wave should be identified with ionization probes or photodiodes. Such data would experimentally confirm that the wave inside the small-diameter tubing was indeed driven by a reacting front. Measurements of the distance between the shock front and the reaction front would make more detailed analysis and identification of the mode of wave propagation possible.

# Bibliography

- G.L. Agafonov and S.M. Frolov. Computation of the detonation limits in gaseous hydrogen-containing mixtures. *Combustion, Explosion, and Shock Waves*, 30(1): 91–100, 1994.
- R. Akbar. *Mach Reflection of Gaseous Detonations*. PhD thesis, Rensselaer Polytechnic Institute, Troy, New York, 1997.
- J. Austin. *The Role of Instability in Gaseous Detonation*. PhD thesis, California Institute of Technology, Pasadena, CA, 2003.
- G.G. Bach, R. Knystautas, and J.H. Lee. Direct initiation of spherical detonations in gaseous explosives. In *Proceedings of the 12th Symposium (International) on Combustion*, pages 853–867, Pittsburgh, PA, 1968.
- A.M. Bartenev, S.V. Khomik, B.E. Gelfand, H. Gronig, and H. Olivier. Effect of reflection type on detonation initiation at shock-wave focusing. *Shock Waves*, 10: 205–215, 2000.
- W.B. Benedick, C. Guirao, R. Knystautas, and J.H. Lee. Critical charge for the direct initiation of detonation in gaseous fuel-air mixtures. *Prog. Astro. Aero.*, 106: 181–202, 1985.
- W.B. Benedick, R. Knystautas, and J.H.S. Lee. Large scale experiments on the transmission of fuel-air detonations from two-dimensional channels. In *Dynamics of Detonations and Explosions*, volume 94 of *Prog. Astro. Aero.*, pages 546–555. AIAA, New York, 1984.

- A.A. Borisov, V.M. Zamanskii, V.V. Kosenkov, and V.V. Lisyanskii. Ignition of gaseous combustible mixtures in focused shock waves. In *Current Topics in Shock Waves, AIP Conference Proceedings*, volume 208, pages 696–701, 1989.
- I. Brailovsky and G. Sivashinsky. Hydraulic resistance and multiplicity of detonation regimes. *Combustion and Flame*, 122(1-2):130–138, 2000.
- I. Brailovsky and G. Sivashinsky. Effects of momentum and heat losses on the multiplicity of detonation regimes. *Combustion and Flame*, 128(1-2):191–196, 2002.
- W. Breitung, C.K. Chan, S.B. Dorofeev, A. Eder, B.E. Gelfand, M. Heitsch, I.R. Klein, A. Malliakos, J.E. Shepherd, E. Studer, and P. Thibault. Flame acceleration and deflagration to detonation transition in nuclear safety. State-of-the-Art Report by a Group of Experts NEA/CSNI/R(2000)7, OECD Nuclear Energy Agency, August 2000.
- C.M. Brophy, J.O. Sinibaldi, and P. Damphousse. Initiator performance for liquid-fueled pulse detonation engines. 40th AIAA Aerospace Sciences Meeting and Exhibit, January 14-17, 2002, Reno, NV, AIAA 02-0472, 2002.
- C.M. Brophy, J.O. Sinibaldi, D. Netzer, and K. Kailasanath. *Confined Detonations and Pulse Detonation Engines*, chapter Initiator Diffraction Limits in a Pulse Detonation Engine, pages 59–72. Torus Press, Moscow, Russia, 2003.
- M. Brouillette. Shock waves at microscales. *Shock Waves*, 13:3–12, 2003.
- D.C. Bull, J.E. Elsworth, and G. Hooper. Initiation of spherical detonation in hydrocarbon/air mixtures. *Acta Astro*, 5:997–1008, 1978.
- D.S. Butler. Converging spherical and cylindrical shocks. Technical report, Armament Research Establishment Report 54/54, 1954.
- C.K. Chan, D. Lau, P.A. Thibault, and J.D. Penrose. Ignition and detonation initiation by shock focusing. In *Current Topics in Shock Waves, AIP Conference Proceedings*, volume 208, pages 161–166, 1989.

- D.L. Chapman. On the rate of explosion in gases. *Philos. Mag.*, 47:90–104, 1899.
- W. Chester. The quasi-cylindrical shock tube. *Philosophical Magazine*, 45(371):1293–1301, 1954.
- R.F. Chisnell. The normal motion of a shock wave through a non-uniform one dimensional medium. *Proceedings of the Royal Society (London)*, 232(1190):350, 1955.
- M. Cooper, S. Jackson, J. Austin, E. Wintenberger, and J. E. Shepherd. Direct experimental impulse measurements for detonations and deflagrations. *Journal of Propulsion and Power*, 18(5):1033–1041, 2002.
- M.A. Cooper. *Impulse Generation by Detonation Tubes*. PhD thesis, California Institute of Technology, Pasadena, CA, 2004.
- E.K. Dabora. *The Influence of a Compressible Boundary on the Propagation of Gaseous Detonations*. PhD thesis, University of Michigan, Ann Arbor, Michigan, 1963.
- C.R. Devore and E.S. Oran. The stability of imploding detonations in the geometrical shock dynamics (ccw) model. *Physics of Fluids*, A4(4):835–844, 1992.
- J.P. Dionne, H.D. Ng, and J.H.S. Lee. Transient development of friction-induced low-velocity detonations. In *Proceedings of the Combustion Institute*, volume 28, pages 645–651. The Combustion Institute, 2000.
- W. Döring. On detonation processes in gases. *Ann. Phys.*, 43:421–436, 1943.
- S. Dorofeev, V. P. Sidorov, M. S. Kuznetzov, I. D. Matsukov, and V. I. Alekseev. Effect of scale on the onset of detonations. *Shock Waves*, 10:137–149, 2000.
- J.E. Dove, B.J. Scroggie, and H. Semerjian. Velocity deficit and detonability limits of hydrogen-oxygen detonations. *Acta Astronautica*, 1:345–359, 1974.
- G. Dupre, R. Knystautas, and J.H. Lee. Near-limit propagation of detonation tubes. *Progress in Astronautics and Aeronautics*, 106:244–259, 1986.

- M. Van Dyke and A.J. Guttman. The converging shock wave from a spherical or cylindrical implosion. *Journal of Fluid Mechanics*, 120:451–462, July 1982.
- C.A. Eckett, J.J. Quirk, and J.E. Shepherd. The role of unsteadiness in direct initiation of gaseous detonations. *Journal of Fluid Mechanics*, 421:147–183, 2000.
- D.H. Edwards, G. Hooper, and R.J. Meddins. Microwave velocity measurements of marginal detonation waves. *Journal of Physics D - Applied Physics*, 3(7):1130–1134, 1970.
- D.H. Edwards, G. Hooper, and J.M. Morgan. A study of unstable detonations using a microwave interferometer. *Journal of Physics D - Applied Physics*, 7:242–248, 1971.
- J.E. Elsworth, P.J. Shuff, and A. Ungut. Galloping gas detonations in the spherical mode. *Prog. Astro. Aero.*, 94:130–150, 1984.
- J.A. Fay. Two-dimensional gaseous detonations: Velocity deficit. *The Physics of Fluids*, 2(3):283–289, May-June 1959.
- W. Fickett and W.C. Davis. *Detonation Theory and Experiment*. Dover Publications Inc., Mineola, New York, 2001.
- K. Fong and B. Ahlborn. Stability of converging shock-waves. *Physics of Fluids*, 22(3):416–421, 1979.
- S.M. Frolov and B.E. Gelfand. Limit diameter of gas detonation propagation in tubes. *Combustion, Explosion, and Shock Waves*, 27(1):113–117, 1991.
- B.E. Gelfand, S.M. Frolov, S.P. Medev, and S.A. Tsyganov. Three cases of shock wave focusing in a two-phase combustible medium. In *Proceedings of the 18th International Symposium on Shock Waves*, pages 831–842, 1991.
- B.E. Gelfand, S.V. Khomik, A.M. Bartenev, S.P. Medvedev, H. Gronig, and H. Olivier. Detonation and deflagration initiation at the focusing of shock waves in a combustible mixture. *Shock Waves*, 10:197–204, 2000.

- B.E. Gelfand, S.P. Medvedev, A.N. Polenov, S.V. Khomik, and A.M. Bartenev. Basic self-ignition regimes and conditions for their realization in combustible mixtures. *Combustion, Explosion, and Shock Waves*, 33(2):127–133, 1997.
- R.B. Gilbert and R.A. Strehlow. Theory of detonation initiation behind reflected shock waves. *AIAA Journal*, 4(10), 1966.
- P.B. Gooderum. An experimental study of the turbulent boundary layer on a shock-tube wall. NACA Tech. Note 4243, NACA, 1958.
- M. Grunthaner, S.I. Jackson, and J.E. Shepherd. Design and construction of an annular detonation initiator. GALCIT Technical Report 2001.005, Graduate Aeronautical Laboratories, California Institute of Technology, Pasadena, CA, 2001.
- G. Guderley. Starke kugelige und zylindrische verdichtungsstöße in der nähe des kugelmittelpunktes bzw. der zylinderachse. *Luftfahrtforschung*, 19(9):302–312, 1942.
- C.M. Guirao, R. Knystautas, and J.H. Lee. A summary of hydrogen-air detonations for reactor safety. Report NUREG/CR-4961, Sandia National Laboratories/McGill University, Montreal, Canada, 1989.
- F. Haloua, M. Brouillette, V. Lienhart, and G. Dupre. Characteristics of unstable detonations near extinction limits. *Combustion and Flame*, 122:422–438, 2000.
- A.J Higgins, P. Yoshinaka, and J.H.S. Lee. Sensitization of fuel-air mixtures for deflagration to detonation transition. In *Proceedings of the International Colloquium on Control of Detonation Processes*, Moscow, Russia, July 4-7, 2000.
- L. Hill. Private communication, 2000.
- H. Hornung. Private communication, 2002.
- S.H.R. Hosseini, O. Onodera, and K. Takayama. Stability of converging cylindrical shock waves in a vertical annular co-axial diaphragmless shock tube. *Trans. Japan Soc. Aero. Space Sci.*, 42(135):19–26, 1998.

- S.H.R. Hosseini, O. Onodera, and K. Takayama. Characteristics of an annular vertical diaphragmless shock tube. *Shock Waves*, 10:151–158, 2000.
- K. Isumi, S. Aso, and M. Nishida. Experimental and computational studies focusing processes of shock waves reflected from parabolic reflectors. *Shock Waves*, 3:213–222, 1994.
- S.I. Jackson, M.P. Grunthaner, and J.E. Shepherd. Wave implosion as an initiation mechanism for pulse detonation engines. 39th AIAA/ASME/SAE/ASEE Joint Propulsion Conference and Exhibit, July 20-23, 2003, Huntsville, Alabama, AIAA 2003-4280, 2003.
- S.I. Jackson and J.E. Shepherd. Initiation systems for pulse detonation engines. 38th AIAA/ASME/SAE/ASEE Joint Propulsion Conference and Exhibit, July 7-10, 2002, Indianapolis, IN, AIAA 2002-3627, 2002.
- S.I. Jackson and J.E. Shepherd. Detonation initiation via imploding shock waves. 40th AIAA/ASME/SAE/ASEE Joint Propulsion Conference and Exhibit, July 11-14, 2004, Ft. Lauderdale, Florida AIAA 2004-3919, 2004.
- Z. Jiang and K. Takayama. Reflection and focusing of toroidal shock waves from coaxial annular shock tubes. *Computers and Fluids*, 27(5-6):553–562, 1998.
- E. Jouguet. On the propagation of chemical reactions in gases. *J. de Mathematiques Pures et Appliquees*, 1:347, 1905.
- M.J. Kaneshige and J.E. Shepherd. Detonation database. Technical Report FM97-8, Graduate Aeronautical Laboratories, California Institute of Technology, Pasadena, CA, 1997.
- R. J. Kee, F. M. Rupley, and James A. Miller. CHEMKIN-II: A Fortran chemical kinetics package for the analysis of gas-phase chemical kinetics. Technical Report SAND89-8009, Sandia National Laboratories, 1989.

- G.B. Kistiakowsky, H.T. Knight, and M.E. Malin. Gaseous detonations. III. Dissociation energies of nitrogen and carbon monoxide. *The Journal of Chemical Physics*, 20(5):876–883, May 1952a.
- G.B. Kistiakowsky, H.T. Knight, and M.E. Malin. Gaseous detonations. IV. The acetylene-oxygen mixtures. *The Journal of Chemical Physics*, 20(5):884–888, May 1952b.
- G.B. Kistiakowsky and W.G. Zinman. Gaseous detonations. vii. a study of thermodynamic equilibration in acetylene-oxygen waves. *The Journal of Chemical Physics*, 23(10):1889–1894, October 1955.
- R. Knystautas, B.H.K. Lee, and J.H.S. Lee. Diagnostic experiments on converging detonations. *Physics of Fluids*, 12(5P2S):I165, 1969.
- R. Knystautas and J.H. Lee. Experiments on stability of converging detonations. *Combustion and Flame*, 16(1):61, 1971.
- R. Knystautas, J.H.S. Lee, and C. Guirao. The critical tube diameter for detonation failure in hydrocarbon-air mixtures. *Combustion and Flame*, 48:63–83, 1982.
- A.A. Konnov. Detailed reaction mechanism for small hydrocarbons combustion, version 0.4. <http://homepages.vub.ac.be/~akonnov>, 1998.
- M.S. Kuznetsov, V.I. Alekseev, and S.B. Dorofeev. Comparisons of critical conditions for ddt in regular and irregular cellular detonation systems. In *Proceedings of the 22nd ISSW*, page 180, London, England, 1999.
- M.S. Kuznetsov, S.B. Dorofeev, A.A. Efimenko, V.I. Alekseev, and W. Breitung. Experimental and numerical studies on transmission of gaseous detonation to a less sensitive mixture. *Shock Waves*, 7(5):297–304, 1997.
- L.D. Landau and E.M. Lifshitz. *Fluid Mechanics*, volume 6 of *Course in Theoretical Physics*. Pergamon Press, London, 1959. Translated by J.B. Sykes and W.H. Reid.

- J.H. Lee, R. Knystautas, and C.K. Chan. Turbulent flame propagation in obstacle-filled tubes. In *Proceedings of the 20th Symposium (International) on Combustion*, pages 1663–1672, Pittsburgh, PA, 1984.
- J.H. Lee and B.H.K. Lee. Cylindrical imploding shock waves. *The Physics of Fluids*, 8(12):2148–2152, 1965.
- J.H. Lee and H. Matsui. A comparison of the critical energies for direct initiation of spherical detonations in acetylene-oxygen mixtures. *Combust. Flame*, 28:61–66, 1977.
- J.H.S. Lee, R. Knystautas, and C. Guirao. *Proceedings of the First Specialist Meeting on Fuel-Air Explosions*. University of Waterloo Press, Waterloo, Canada, 1982.
- J.J. Lee, G. Dupre, R. Knystautas, and L.H. Lee. Doppler interferometry study of unstable detonations. *Shock Waves*, 5(3):175–181, 1995.
- B. Lewis and G. von Elbe. *Combustion, Flames and Explosions of Gases*. Academic Press, Second Edition, 1961.
- C. Li and K. Kailasanath. Detonation initiation by annular-jet-induced imploding shocks. Technical note submitted to the *AIAA Journal of Propulsion and Power*, 2003a.
- C. Li and K. Kailasanath. Detonation initiation in pulse detonation engines. 41st AIAA Aerospace Sciences Meeting and Exhibit, January 6-9, 2003, Reno, NV, AIAA 2003-1170, 2003b.
- C. Li and K. Kailasanath. Detonation initiation by annular-jet-induced imploding shocks. *AIAA Journal of Propulsion and Power*, 21(1):183–186, 2005.
- D.H. Lieberman and J.E. Shepherd. Characterization of a corona discharge initiator using detonation tube impulse measurements. 43rd AIAA Aerospace Sciences Meeting and Exhibit, January 10-13, 2005, Reno, NV, AIAA 2005-24455, 2005.

- H. W. Liepmann, A. Roshko, D. Coles, and B. Sturtevant. A 17-inch diameter shock tube for studies in rarefied gasdynamics. *The Review of Scientific Instruments*, 33(6):625–631, 1962.
- V.I. Manzhalei. Detonation regime of gases in capillaries. *Combustion, Explosion and Shock Waves*, 28(3):296–302, 1992.
- V.I. Manzhalei. Low-velocity detonation limits of gaseous mixtures. *Combustion, Explosion, and Shock Waves*, 35(3):296–302, 1999.
- H. Matsuo, K. Ebihara, and Y. Ohya. Spectroscopic study of cylindrically converging shock waves. *Journal of Applied Physics*, 58(7):2487–2491, October 1985.
- H. Matsuo and U. Nakamura. Cylindrically converging blast waves in air. *Journal of Applied Physics*, 52(7):4350–4507, July 1981.
- J. Meltzer, J. E. Shepherd, R. Akbar, and A. Sabet. Mach reflection of detonation waves. In *Dynamics of Detonations and Explosions*, volume 153 of *Prog. Astro. Aero.*, pages 78–94. AIAA, New York, 1993.
- J.W. Meyer and A.K. Oppenheim. On the shock-induced ignition of explosive gases. In *13th Symposium on Combustion*, pages 1153–1163, 1971.
- V.V. Mitrofanov and R.I. Soloukhin. The diffraction of multi-front detonation waves. *Sov. Phys.-Dokl.*, 9:1055, 1965.
- S.B. Murray. *The Influence of Initial and Boundary Conditions on Gaseous Detonation Waves*. PhD thesis, McGill University, McGill, Canada, 1984.
- S.B. Murray, P.A. Thibault, F. Zhang, D. Bjerketvedt, A. Sulmistras, G.O. Thomas, A. Jenssen, and I.O. Moen. The role of energy distribution on the transmission of detonation. In *Proceedings of the International Colloquium on Control of Detonation Processes*, Moscow, Russia, July 4-7, 2000.

- S.B. Murray, D. Zhang, and K.B. Gerrard. Critical parameters for pulse detonation engine pre-detonator tubes. In *International Colloquium on the Dynamics of Explosions and Reactive Systems*, Hakone, Japan, July 27-August 14-7 2003.
- M. A. Nettleton. *Gaseous Detonations*. Chapman and Hall, 1987.
- M. Nishida. Focusing of reflected shock waves. In *Proceedings of the International Workshop on Shock Wave Focusing*, pages 140–153, Sendai, Japan, March 22-23 1989.
- M. Nishida, T. Nakagawa, and Y. Kikuyama. Focusing of reflected shock waves. *Transactions of the Japan Society for Aeronautics and Space Sciences*, 28(82):209–217, 1986.
- E.S. Oran and C.R. Devore. The stability of imploding detonations - results of numerical simulations. *Physics of Fluids*, 6(1):369–380, 1994.
- C. Paillard, G. Dupre, R. Lisbet, J. Combourieu, V.P. Fokeev, and L.G. Gvozdeva. A study of hydrogen azide detonation with heat transfer at the wall. *Acta Astronautica*, 6:227–242, 1979.
- O. Peraldi, R. Knystautas, and J.H. Lee. Criteria for transition to detonation in tubes. In *The 22nd International Symposium on Combustion*, pages 1629–1637, Pittsburgh, PA, 1988.
- R.W. Perry and A. Kantrowitz. The production and stability of converging shock waves. *Journal of Applied Physics*, 22(7):878–886, July 1951.
- N.F. Ponchaut. *Converging Shock Waves: Extension of the Guderley Solution*. PhD thesis, California Institute of Technology, Pasadena, CA, 2005.
- J. Quirk. Amrita - a computational facility (for cfd modelling). VKI 29th CFD Lecture Series, ISSN 0377-8312, 1998.
- M.I. Radulescu. Experimental investigation of direct initiation of quasi-cylindrical detonations. Master's thesis, McGill University, Montreal, Canada, 1999.

- M.I. Radulescu, A.J. Higgins, S.B. Murray, and J.H.S. Lee. An experimental investigation of the direct initiation of cylindrical detonations. *Journal of Fluid Mechanics*, 480:1–24, 2003.
- W. C. Reynolds. The element potential method for chemical equilibrium analysis: Implementation in the interactive program stanjan, version 3. Technical report, Dept. of Mechanical Engineering, Stanford University, Stanford, CA, 1986.
- D.E. Roberts and I.I. Glass. Spectroscopic investigation of combustion-driven spherical implosion waves. *Physics of Fluids*, 14(8):1662, 1971.
- R.A. Roig and I.I. Glass. Spectroscopic study of combustion-driven implosions. *Physics of Fluids*, 20(10):1651–1656, 1977.
- A. Roshko and D. Baganoff. A novel device for bursting shock-tube diaphragms. *Physics of Fluids*, 4(11):1445–1446, 1961.
- T. Saito and I.I. Glass. Temperature-measurements at an implosion focus. *Proc. Royal Soc. London, A*, 384(1786):217–231, 1982.
- E. Schultz. *Detonation Diffraction Through an Abrupt Area Expansion*. PhD thesis, California Institute of Technology, Pasadena, CA, 2000.
- E. Schultz and J.E. Shepherd. Detonation diffraction through a mixture gradient. GALCIT Technical Report FM00-1, Graduate Aeronautical Laboratories, California Institute of Technology, Pasadena, CA, 2000a.
- E. Schultz and J.E. Shepherd. Validation of detailed reaction mechanisms for detonation simulation. GALCIT Technical Report FM99-5, Graduate Aeronautical Laboratories, California Institute of Technology, Pasadena, CA, 2000b.
- D.W. Schwendeman. On converging shock waves of spherical and polyhedral form. *Journal of Fluid Mechanics*, 454:365–386, 2002.
- L.I. Sedov. *Similarity and Dimensional Methods in Mechanics*. Academic Press, New York, 1959. Translated by M. Holt.

- G.J. Sharpe. Numerical simulations of pulsating detonations: Ii. piston initiated detonations. *Combustion Theory and Modelling*, 5:623–638, 2001.
- J.E. Shepherd. Chemical kinetics and cellular structure of detonations in hydrogen sulfide and air. In *Prog. Astronaut. Aeronaut.*, volume 106, pages 294–320, 1986.
- J.A. Smith and D. Coles. A description of the GALCIT 6” shock tube. Technical Report FM-67-1, Graduate Aeronautical Laboratories, California Institute of Technology, June 1967.
- G.A. Sod. Numerical study of a converging cylindrical shock. *Journal of Fluid Mechanics*, 83:485–794, 1977.
- K.P. Stanyukovich. *Unsteady Motion of Continuous Media*. Pergamon Press, New York, 1960. Translated by M. Holt.
- B. Sturtevant. Shock wave effects in biomechanics. *Sādhanā - Academy Proceedings in Engineering Sciences*, 23(5-6):579–596, 1998.
- B. Sturtevant and V.A. Kulkarny. The focusing of weak shock waves. *Journal of Fluid Mechanics*, 73(4):651–671, 1976.
- K. Takayama, H. Kleine, and H. Gronig. An experimental investigation of the stability of converging cylindrical shock waves in air. *Experiments in Fluids*, 5(5):315–322, 1987.
- A. Teodorczyk, J.H.S. Lee, and R. Knystautas. Propagation mechanism of quasi-detonations. In *22nd Symposium (International) on Combustion*, pages 1723–1731. The Combustion Institute, 1988.
- K. Terao. Experimental study on cylindrical and spherical implosions. *Japanese Journal of Applied Physics*, 22(3):446–453, 1983.
- K. Terao, H. Akaba, and H. Shiraishi. Spherically imploding detonation waves initiated by 2-step divergent detonation. *Shock Waves*, 4(4):187–193, 1995.

- K. Terao and H.G. Wagner. Experimental study on spherically imploding detonation waves. *Shock Waves*, 1:27–34, 1991.
- P.A. Thompson. *Compressible-Fluid Dynamics*. McGraw-Hill, New York, 1988.
- P.A. Urtiew and A.K. Oppenheim. Experimental observations of the transition to detonation in an explosive gas. *Proceedings of the Royal Society of London Series A - Mathematical and Physical Sciences*, 295:13–28, 1966.
- A. Vasil'ev. Geometric limits of gas detonation propagation. *Combustion, Explosion, and Shock Waves*, 18(2):245–249, 1982.
- A.A. Vasilev. Gaseous fuels and detonation hazards. In *28th International Conference of ICT*, Karlsruhe, Germany, June 1997.
- J. von Neumann. *John von Neumann, Collected Works*, volume 6. Editions A. J. Taub, New York: Macmillan, 1942.
- B. Wang, H. He, and S.-T. Yu. Direct calculation of wave implosion for detonation initiation in pulsed detonation engines. 43rd AIAA Aerospace Sciences Meeting and Exhibit, January 10-13, 2005, Reno, NV, AIAA 2005-1306, 2005.
- J.T.C. Wang. On the theory of imploding shocks. *J. Appl. Math. Phys.*, 33:53–62, 1982.
- D.R. White. Turbulent structure of gaseous detonation. *Phys. Fluids*, 4:465–480, 1961.
- G.B. Whitham. On the propagation of shock waves through regions of non-uniform area or flow. *Journal of Fluid Mechanics*, 4:337–360, 1958.
- J.H.T. Wu, R.A. Neemeh, and P.P. Ostrowski. Experimental studies of the production of converging cylindrical shock waves. *AIAA Journal*, 18(1):47–48, 1980.
- S.-T. John Yu, B. Wang, and H. He. Direct calculation of wave implosion for detonation initiation in pulsed detonation engines. In G.D. Roy and A.F. Ghoniem,

editors, *Proceedings of the Seventeenth ONR Propulsion Meeting*, pages 169–180, Arlington, VA 22217, June 2004. Office of Naval Research.

Ia. B. Zel'dovich. On the theory of the propagation of detonation in gaseous systems. *Zh. Eksp. Teor. Fiz.*, 10:542–568, 1940.

Ia.B. Zel'dovich, S.M. Kogarko, and N.N. Simonov. An experimental investigation of spherical detonation of gases. *Soviet Physics-Technical Physics*, 1(8):1689–1713, 1956.

Y.B. Zel'dovich. Converging cylindrical detonation wave. *Soviet Physics JETP*, 9(3):550–557, 1959.

Y.B. Zel'dovich, B.E. Gelfand, Y.M. Kazhdan, and S.M. Frolov. Detonation propagation in a rough tube taking account of deceleration and heat transfer. *Combustion, Explosion, and Shock Waves*, 23(3):342–349, 1987.

# Appendix A

## Detonation Models and Parameters

This section briefly reviews the Chapman-Jouguet (CJ) and Zel'dovich-von Neumann-Döring (ZND) theories, which are used extensively to model detonation wave propagation. Both theories were developed before three-dimensional structures were detected in the detonation front (White, 1961) and, as such, approximate the detonation wave as one-dimensional. Even with this approximation, the detonation propagation velocities and thermodynamic conditions predicted by each model have been shown to agree well with experimental measurements. For a discussion of the three-dimensional structure observed in experiments, please refer to Fickett and Davis (2001).

### A.1 CJ Theory

The theory of Chapman (1899) and Jouguet (1905) considers a detonation as a shock wave and reaction zone contained inside a control volume. Application of the conservation equations to the control volume yields

$$\rho_1 w_1 = \rho_2 w_2 \tag{A.1}$$

$$\rho_1 w_1^2 + P_1 = \rho_2 w_2^2 + P_2 \tag{A.2}$$

$$\frac{w_1^2}{2} + h_1 = \frac{w_2^2}{2} + h_2 \tag{A.3}$$

where  $u$ ,  $\rho$ ,  $P$  and  $h$  are the particle velocity, density, pressure and enthalpy relative to the front. States 1 and 2 correspond to the reactant and products respectively.

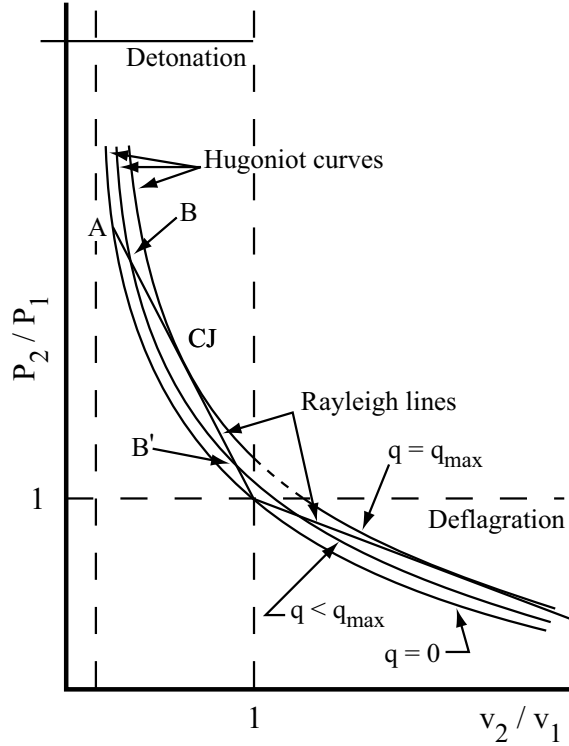


Figure A.1: The Hugoniot-Rayleigh representation of shock and detonation waves.

The Hugoniot line associated with the products and the Rayleigh line intersect at two points as shown in Fig A.1. (This solution is discussed in detail in Section 2.4.2.1.) At the upper point, referred to as the CJ point, the flow velocity is sonic

$$w_2 = a_2 . \quad (\text{A.4})$$

The presence of this sonic surface prevents information downstream of the wave from affecting the wave propagation. The theory allows calculation of the CJ detonation wave speed  $U_{CJ}$  and the post-detonation flow conditions (Section 2.4.2.1). The predicted wave speeds have been shown to be within 2% of experimentally-observed detonation velocities (Lewis and von Elbe, 1961) for cases where the presence of experiment walls have a minimal effect on wave propagation.

## A.2 ZND Theory

Zel'dovich (1940), von Neumann (1942), and Döring (1943) independently developed a more detailed theory for detonation wave propagation than had previously been available. In the previously-established CJ theory, the detonation was modeled as a discontinuity contained inside of a control volume and the conservation equations determined the inflow and outflow conditions to the control volume assuming only that the outflow was sonic. No assumptions were made as to the flow structure or chemical reaction rate inside the control volume.

The ZND theory extends the CJ theory by considering finite chemical reaction rates. In particular, the theory models the detonation as a planar shock propagating through reactants at the CJ detonation velocity. The shock compresses the reactants, increasing their temperature. The post-shock condition is referred to as the von-Neumann state and the elevated temperature of this state generates the radicals required for chain-branching reactions. After a thermally-neutral induction period, the reactions release energy, increasing the temperature and decreasing the pressure and density. This flow expansion drives the shock ahead.

The distance from the shock front to the location of maximum temperature gradient or heat release is defined as the induction distance  $\Delta$  and is dependent on the wave velocity and initial mixture conditions (Shepherd, 1986). The distance from the shock front to the end of the reaction zone is referred to as the reaction zone. The reaction zone is terminated by a region of sonic flow called the CJ surface.

In particular, the ZND model solves the steady and reactive Euler equations

$$w \frac{d\rho}{dx} = -\rho \frac{dw}{dx} \quad (\text{A.5})$$

$$w \frac{dw}{dx} = -\frac{1}{\rho} \frac{dP}{dx} \quad (\text{A.6})$$

$$\frac{de}{dx} = \frac{P}{\rho^2} \frac{d\rho}{dx} \quad (\text{A.7})$$

$$w \frac{dY_i}{dx} = \Omega_i \quad \text{where} \quad i = 1, \dots, N \quad (\text{A.8})$$

where  $w$ ,  $e$ ,  $Y_i$  and  $\Omega_i$  are the respective shock-fixed flow velocity, the specific internal energy, the mass fraction of species  $i$  and the production rate of species  $i$  as determined from a kinetic rate law.

Rewriting the equations as

$$w \frac{d\rho}{dx} = -\frac{\rho\dot{\sigma}}{1-M^2} \quad (\text{A.9})$$

$$w \frac{dw}{dx} = \frac{w\dot{\sigma}}{1-M^2} \quad (\text{A.10})$$

$$w \frac{dP}{dx} = -\frac{\rho w^2 \dot{\sigma}}{1-M^2} \quad (\text{A.11})$$

$$\dot{\sigma} = \sum_i^N \frac{\Omega_i}{\rho c^2} \left( \frac{\partial P}{\partial Y_i} \right)_{\rho, e, Y_{k \neq i}} \quad (\text{A.12})$$

where  $\dot{\sigma}$  is the thermicity as defined by (Fickett and Davis, 2001). The Mach number must approach unity as the thermicity approaches zero to avoid a singularity in the solution. Thus, chemical equilibrium occurs at the CJ surface.

For waves propagating at the CJ velocity, the ZND theory allows numerical solution of the thermodynamic conditions and chemical species throughout the detonation wave. An example of the wave structure that was calculated using the ZND program of Shepherd (1986) with the CHEMKIN II subroutines (Kee et al., 1989) is shown in Fig. A.2.

### A.3 Constant Volume Explosion Theory

When the detonation propagation velocity is below the CJ value (as is the case with the majority of results in Chapter 2), CJ theory will not yield a flow solution. In this situation, flow conditions can be determined by approximating the detonation process as adiabatic, constant volume combustion due to the adiabatic compression from shock processing. In addition to solving for the thermodynamic conditions, this calculation also allows estimation of the induction length.

In this situation, the induction length is defined to be the product of the induction

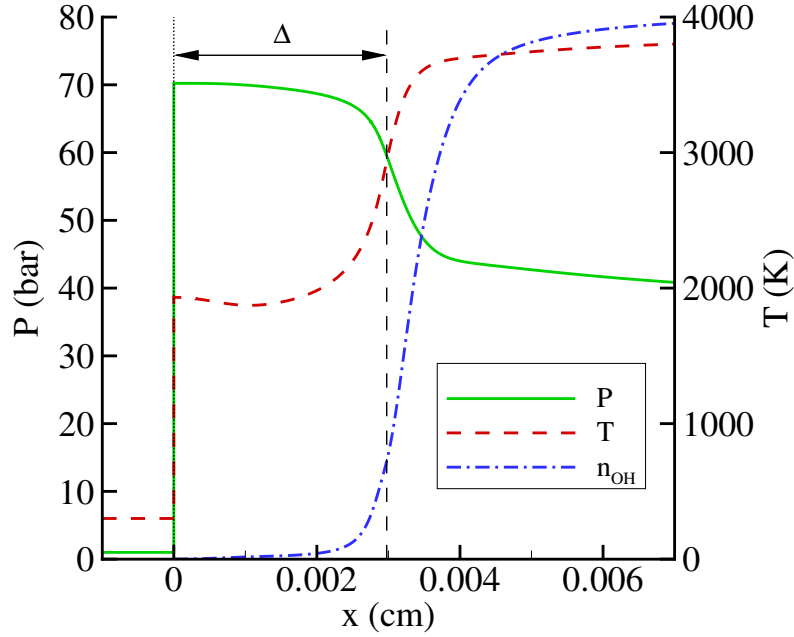


Figure A.2: Numerical solution of the ZND structure for a reactant mixture of  $\text{C}_3\text{H}_8 + 5\text{O}_2$  that is initially at 1 bar and 300 K. The solid green, dashed red and dashed-dotted blue lines show the pressure, temperature and OH concentration through the detonation wave respectively. The shock wave is located at  $x = 0$ . The OH concentration fraction ranges from 0.00-0.12 in the plot. This calculation was performed with the ZND code of Shepherd (1986) using the reaction mechanism of Konnov (1998).

time  $\tau$  and the post-shock velocity  $w_{VN}$ ,

$$\Delta = w_{VN} \tau . \quad (\text{A.13})$$

The induction time is dependent on the reactants, as well as the post-shock temperature and pressure and can be approximated by an Arrhenius expression of the form

$$\tau = C[\text{fuel}]^a[\text{oxidizer}]^b \frac{kR_g T_{VN}}{P_{VN}} \exp\left(\frac{E_a}{R_g T_{VN}}\right), \quad (\text{A.14})$$

where  $C$ ,  $a$ ,  $b$  and  $k$  are empirical constants,  $R_g$  is the mixture-specific gas constant and  $E_a$  is the activation energy. Due to the exponential term,  $\tau$  is most sensitive to

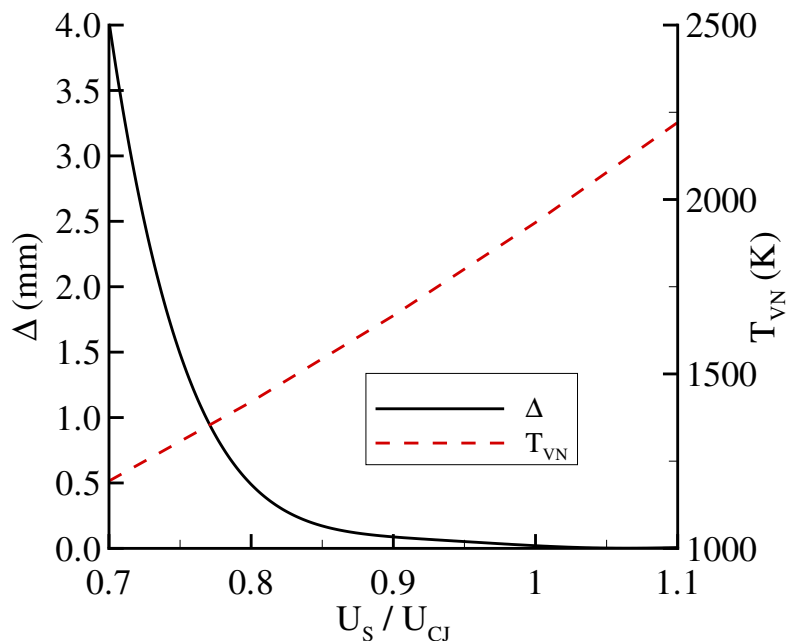


Figure A.3: The effect of shock speed on temperature and induction length for a reactant mixture of  $C_3H_8 + 5O_2$  that is initially at 1 bar and 300 K. The solid black and dashed red lines show the induction length and the temperature respectively as a function of shock velocity. The velocity and von Neumann temperature at the CJ condition are 2359 m/s and 1934 K respectively. This calculation was performed with the CV code of Shepherd (1986) using the reaction mechanism of Konnov (1998).

changes in temperature (Fig. A.3). In practice,  $\tau$  can be calculated from a computer program such as CV (Shepherd, 1986), which is part of the Chemkin II package (Kee et al., 1989) and uses detailed chemical kinetics mechanisms. In this work, the chemical kinetics mechanism of Konnov (1998) was used for all CV and ZND calculations.



## Appendix B

# The Similarity Solution for a Strong Blast Wave

Consider a large amount of energy  $E_s$  instantaneously released in a perfect-gas atmosphere that is initially at rest. The energy will substantially increase the kinetic and thermal energy of the gas, creating a strong shock wave that will expand into the perfect gas. At distances sufficiently far from the energy deposition, the source will appear as a point and the wave will be a spherical.

### B.1 The Similarity Variable

The solution for gas motion behind a strong blast wave is now presented. This is mostly taken from the work of Thompson (1988). For a strong shock [defined by the condition  $(U_s/c_0)^2 \gg 1$ ], the shock jump conditions become

$$P_s = \frac{2}{\gamma + 1} \rho_0 U_s^2 \quad (\text{B.1})$$

$$u_s = \frac{2}{\gamma + 1} U_s \quad (\text{B.2})$$

$$\rho_s = \frac{\gamma + 1}{\gamma - 1} \rho_0 \quad (\text{B.3})$$

where  $P_s$ ,  $u_s$  and  $\rho_s$  are the pressure, particle velocity and density immediately behind the shock.

Due to the high wave speed, the only gas initial property that affects the post-

shock conditions is the density  $\rho_0$ . Thus, for a strong shock and radially symmetric flow, the only dimensional and independent variables that affect the gas at a radius  $r$  and time  $t$  are  $E_s$  and  $\rho_0$ . Dependent variables are  $u$ ,  $P$ , and  $\rho$ . Only one dimensionless group is possible with the independent variables

$$\xi \equiv \frac{r}{\left(\frac{E_s}{\rho_0}\right)^{1/5} t^{2/5}} \quad (\text{B.4})$$

which constitutes the similarity variable for the blast wave solution.

Since the above expression is the only nondimensional combination that can be obtained from the variables, the expression for the shock position  $R$  in time is

$$\frac{R}{\left(\frac{E_s}{\rho_0}\right)^{1/5} t^{2/5}} = \xi_0 = \text{const} \quad (\text{B.5})$$

and it can be seen that  $R \propto t^{2/5}$ .

The shock velocity  $U_s$  can be found by solving for  $R$

$$R = \xi_0 \left(\frac{E_s}{\rho_0}\right)^{1/5} t^{2/5} \quad (\text{B.6})$$

and differentiating with respect to time to obtain

$$U_s = \frac{dR}{dt} = \frac{2}{5} \xi_0 \left(\frac{E_s}{\rho_0}\right)^{1/5} t^{-3/5} \quad (\text{B.7})$$

or more simply

$$U_s = \frac{2}{5} \frac{R}{t} . \quad (\text{B.8})$$

With these equations, the shock conditions can be readily determined as a function of  $E_s$ ,  $\rho_0$  and  $\xi_0$ . The parameter  $\xi_0$  is very close to unity and is a function of  $\gamma$ . A method for its determination is presented below.

## B.2 Self-Similar Equations

In order to solve for the value of  $\xi_0$ , the equations of motion are used to describe the flow behind the shock wave. These equations are nondimensionalized and reduced to a set of ordinary differential equations that can then be solved to obtain  $\xi_0 = f(\gamma)$ .

Nondimensionalization of the dependent variables requires scaling variables with dimensions of velocity and pressure; however the only constant variables in the problem that have been identified are  $\rho_0$  and  $E_s$ . Thus,  $r/t$  is chosen to normalize  $u$  and  $P$  is normalized by  $\rho_0 r^2/t^2$ :

$$\hat{u} \equiv \frac{5(\gamma+1)}{4} \frac{u}{r/t} \quad (\text{B.9})$$

$$\hat{P} \equiv \frac{25(\gamma+1)}{8} \frac{P}{\rho_0 r^2/t^2} \quad (\text{B.10})$$

$$\hat{\rho} \equiv \frac{\gamma-1}{\gamma+1} \frac{\rho}{\rho_0}. \quad (\text{B.11})$$

After normalization,  $\hat{u}$ ,  $\hat{P}$ , and  $\hat{\rho}$  are all functions of  $\xi$ . The coefficients of  $\gamma$  have been chosen with prior knowledge of the solution to simplify the boundary conditions.

In terms of these variables, the boundary conditions are

$$\begin{aligned} \hat{u} &= 1 \\ \hat{P} &= 1 \quad \text{at } \xi = \xi_0 \\ \hat{\rho} &= 1 \end{aligned} \quad (\text{B.12})$$

which apply to the shock front.

The equations of motion for centrally symmetric adiabatic gas flow are used to

describe the motion of the gas behind the shock front:

$$\frac{\partial u}{\partial t} + u \frac{\partial u}{\partial r} + \frac{1}{\rho} \frac{\partial P}{\partial r} = 0 \quad (\text{B.13})$$

$$\frac{\partial \rho}{\partial t} + \rho \frac{\partial u}{\partial r} + u \frac{\partial \rho}{\partial r} + \frac{2\rho u}{r} = 0 \quad (\text{B.14})$$

$$\left( \frac{\partial}{\partial t} + u \frac{\partial}{\partial r} \right) \ln \frac{P}{\rho^\gamma} = 0 \quad (\text{B.15})$$

where the last equation is the conservation of entropy in time for a particle in a perfect gas.

With the nondimensional variables, the above equations are reduced to a set of ordinary differential equations from Thompson (1988):

$$\hat{\rho} (2\hat{u} - \gamma - 1) \frac{d\hat{u}}{d\xi} + (\gamma - 1) \frac{d\hat{P}}{d\xi} = \frac{1}{2\xi} \left[ \hat{\rho} \hat{u} (5\gamma + 5 - 4\hat{u}) - 4(\gamma - 1) \hat{P} \right] \quad (\text{B.16})$$

$$\left( \hat{u} - \frac{\gamma + 1}{2} \right) \frac{1}{\hat{\rho}} \frac{d\hat{\rho}}{d\xi} + \frac{d\hat{u}}{d\xi} = -\frac{3\hat{u}}{\xi} \quad (\text{B.17})$$

$$\frac{d}{d\xi} \ln \frac{\hat{P}}{\hat{\rho}^\gamma} = \frac{1}{\xi} \frac{5(\gamma + 1) - 4\hat{u}}{2\hat{u} - (\gamma + 1)}. \quad (\text{B.18})$$

### B.3 Integration

Landau and Lifshitz (1959) show that the integration of the equations can be obtained from the argument that the total energy with the sphere bounded by the shock wave is equal to  $E_s$  and that any energy inside the gas before the addition of  $E_s$  can be considered negligible. They also note that the energy of the gas in any smaller sphere of radius  $r$  is constant as long as  $r$  increases in time such that  $\xi = \text{constant}$ . This is due to the similarity flow.

With this understanding, the energy equation applied to such a spherical surface becomes

$$4\pi r^2 \rho \left( u - \frac{2r}{5t} \right) \left( e + \frac{1}{2} u^2 \right) = -4\pi r^2 P u \quad (\text{B.19})$$

and with

$$e = \frac{1}{\gamma - 1} \frac{P}{\rho} \quad (\text{B.20})$$

is reduced to

$$\frac{\hat{P}}{\hat{\rho}} = \frac{\hat{u}^2 (\gamma + 1 - 2\hat{u})}{2\gamma\hat{u} - \gamma - 1}. \quad (\text{B.21})$$

Equation B.21 can be used in place of one of the differential equations Eqs. B.16-B.18. Substituting Eq. B.21 into eq. B.18 obtains a relation that is only a function of  $\hat{\rho}$  and  $\hat{u}$ . This relation can then be combined with Eq. B.17 to determine an equation only dependent on  $\hat{u}$  and its derivative. Integration with the boundary conditions (Eq. B.12) gives

$$\left(\frac{\xi_0}{\xi}\right)^5 = \hat{u}^2 \left[ \frac{5(\gamma + 1) - 2(3\gamma - 1)\hat{u}}{7 - \gamma} \right]^{k_1} \left[ \frac{2\gamma\hat{u} - \gamma - 1}{\gamma - 1} \right]^{k_2} \quad (\text{B.22})$$

$$\hat{\rho} = \left[ \frac{2\gamma\hat{u} - \gamma - 1}{\gamma - 1} \right]^{k_3} \left[ \frac{5(\gamma + 1) - 2(3\gamma - 1)\hat{u}}{7 - \gamma} \right]^{k_4} \left[ \frac{\gamma + 1 - 2\hat{u}}{\gamma - 1} \right]^{k_5} \quad (\text{B.23})$$

where

$$k_1 \equiv \frac{13\gamma^2 - 7\gamma + 12}{(3\gamma - 1)(2\gamma + 1)} \quad (\text{B.24})$$

$$k_2 \equiv \frac{-5(\gamma - 1)}{2\gamma + 1} \quad (\text{B.25})$$

$$k_3 \equiv \frac{3}{2\gamma + 1} \quad (\text{B.26})$$

$$k_4 \equiv \frac{13\gamma^2 - 7\gamma + 12}{(2 - \gamma)(3\gamma - 1)(2\gamma + 1)} \quad (\text{B.27})$$

$$k_5 \equiv \frac{2}{\gamma - 2}. \quad (\text{B.28})$$

Eq. B.21 can then be used to find the pressure  $\hat{P}$ .

Finally, the constant  $\xi_0$ , which corresponds to the position of the shock front, can

be found from the conservation of the explosion energy

$$E = \int_0^R \left( \frac{1}{2} \rho u^2 + \frac{P}{\gamma - 1} \right) 4\pi r^2 dr. \quad (\text{B.29})$$

The terms in the parenthesis correspond to the kinetic energy and the internal energy for the ideal gas inside of the spherical shock. Nondimensionalizing the conservation equation, the integral becomes

$$1 = \frac{32\pi\xi_0^5}{(25\gamma^2 - 1)} \int_0^1 \left( \hat{\rho} \hat{u}^2 + \hat{P} \right) \zeta^4 d\zeta \quad (\text{B.30})$$

where  $\zeta = \xi/\xi_0 = r/R$ . Evaluating this expression will determine  $\xi_0$  as a function of  $\gamma$ .

# Appendix C

## Electronic Circuits



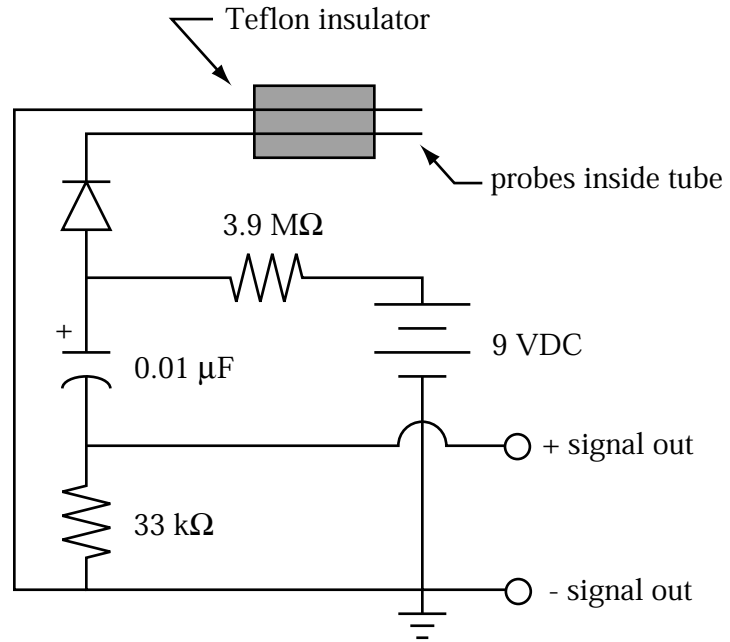


Figure C.2: The design of the ionization probe circuit.



# Appendix D

## Small Tube Data

## D.1 Run Matrix

Run	$\phi$	Pressure (bar)	Tube diameter (mm)	$P_{CJ}$ (bar)	$U_{CJ}$ (m/s)	Run classification
1	1.0	1.00	6.35	26.0	2360	detonation
2	1.0	0.50	6.35	17.6	2328	detonation
3	1.0	0.20	6.35	6.8	2287	detonation
4	1.0	0.10	6.35	3.3	2256	no data recorded
5	1.0	0.15	6.35	5.1	2274	detonation
6	0.8	1.00	6.35	32.6	2252	detonation
7	0.6	1.00	6.35	28.7	2122	detonation
8	0.5	1.00	6.35	26.5	2046	detonation
9	1.0	0.10	6.35	3.5	2256	detonation
10	0.4	1.00	6.35	24.1	1957	no data recorded
11	0.3	1.00	6.35	21.4	1848	DDT in test section
12	1.0	1.00	6.35	36.5	2360	no data recorded
13	1.0	0.50	6.35	17.8	2329	no data recorded
14	1.0	0.50	6.35	17.6	2328	detonation
15	1.0	0.20	6.35	6.8	2287	failed in test section
16	1.0	0.30	6.35	10.5	2306	detonation
17	1.0	0.20	6.35	6.8	2287	detonation
18	0.3	1.00	6.35	21.6	1848	DDT in test section
19	0.4	1.00	6.35	24.4	1957	detonation
20	0.8	1.00	6.35	32.6	2252	detonation
21	0.4	1.00	6.35	24.1	1957	detonation
22	0.6	1.00	6.35	29.1	2123	detonation
23	0.8	1.00	6.35	32.6	2252	detonation
24	2.0	1.00	6.35	45.0	2612	detonation

Table D.1: Experimental properties of each run.

Run	$\phi$	Pressure (bar)	Tube diameter (mm)	$P_{CJ}$ (bar)	$U_{CJ}$ (m/s)	Run classification
25	1.0	1.00	6.35	36.5	2360	detonation
26	2.4	1.00	6.35	44.3	2576	detonation
27	2.6	1.00	6.35	42.0	2532	DDT in test section
28	2.8	1.00	6.35	40.5	2471	DDT in test section
29	3.0	1.00	6.35	37.9	2395	failed driver
30	2.9	1.00	6.35	39.2	2435	failed driver
31	2.9	1.00	6.35	39.2	2435	DDT in test section
32	1.6	1.00	6.35	44.1	2571	detonation
33	1.0	1.00	1.27	36.0	2360	detonation
34	1.0	1.40	1.27	51.6	2376	detonation
35	1.0	1.60	1.27	59.4	2382	no data recorded
36	1.0	1.00	1.27	36.0	2360	detonation
37	1.0	1.40	1.27	51.6	2376	detonation
38	1.0	1.60	1.27	59.4	2382	detonation
39	1.0	0.80	1.27	29.0	2350	detonation
40	1.0	0.60	1.27	21.5	2337	detonation
41	1.0	0.40	1.27	14.1	2319	detonation
42	1.0	0.30	1.27	10.5	2306	detonation
43	1.0	0.20	1.27	6.9	2288	detonation
44	1.0	0.10	1.27	3.4	2257	no data recorded
45	1.0	0.15	1.27	5.1	2275	detonation
46	1.0	0.12	1.27	4.1	2265	failed in initiator
47	1.0	0.13	1.27	4.4	2269	failed in test section
48	1.0	0.14	1.27	4.8	2272	detonation
49	1.0	0.14	1.27	4.6	2271	failed in initiator
50	1.0	1.80	1.27	67.1	2387	detonation

Table D.2: Experimental properties of each run.

## D.2 Wave Arrival Times

Run	$t_0$ (s)	$t_1$ (s)	$t_2$ (s)	$t_3$ (s)	$t_4$ (s)	$t_5$ (s)
1	N/A	9.650E-04	1.134E-03	1.353E-03	1.571E-03	1.791E-03
2	N/A	N/A	1.248E-03	1.471E-03	1.694E-03	1.918E-03
3	N/A	N/A	1.397E-03	1.635E-03	1.873E-03	2.111E-03
4	N/A	N/A	N/A	N/A	N/A	N/A
5	N/A	N/A	1.540E-03	1.774E-03	2.009E-03	2.243E-03
6	N/A	1.060E-03	1.236E-03	1.466E-03	1.697E-03	1.927E-03
7	N/A	1.316E-03	1.506E-03	1.752E-03	1.998E-03	2.244E-03
8	N/A	N/A	1.800E-03	2.059E-03	2.319E-03	2.574E-03
9	N/A	N/A	1.679E-03	2.126E-03	2.500E-03	2.767E-03
10	N/A	N/A	2.444E-03	2.716E-03	2.987E-03	3.258E-03
11	N/A	N/A	8.857E-03	9.150E-03	9.419E-03	9.679E-03
12	N/A	N/A	N/A	N/A	N/A	N/A
13	N/A	N/A	N/A	N/A	N/A	N/A
14	N/A	1.065E-03	N/A	N/A	1.699E-03	1.924E-03
15	N/A	N/A	1.718E-03	2.248E-03	2.919E-03	7.356E-03
16	N/A	1.112E-03	1.282E-03	1.502E-03	1.719E-03	1.937E-03
17	N/A	1.284E-03	1.468E-03	1.709E-03	1.945E-03	2.182E-03
18	N/A	N/A	8.169E-03	8.572E-03	8.832E-03	9.088E-03
19	N/A	2.224E-03	2.432E-03	2.706E-03	2.979E-03	3.253E-03
20	N/A	9.720E-04	1.143E-03	1.367E-03	1.589E-03	1.812E-03
21	1.966E-03	2.182E-03	2.397E-03	2.949E-03	3.226E-03	N/A
22	1.136E-03	1.330E-03	1.522E-03	1.771E-03	2.019E-03	2.267E-03
23	8.840E-04	1.064E-03	1.245E-03	1.477E-03	1.708E-03	1.939E-03
24	1.298E-03	1.452E-03	1.603E-03	1.802E-03	1.998E-03	2.195E-03

Table D.3: Wave arrival times. N/A values indicate that wave front was either not recorded or could not be identified.

Run	$t_0$ (s)	$t_1$ (s)	$t_2$ (s)	$t_3$ (s)	$t_4$ (s)	$t_5$ (s)
25	7.640E-04	9.360E-04	N/A	1.105E-03	1.327E-03	1.546E-03
26	2.810E-03	2.966E-03	N/A	3.121E-03	3.326E-03	3.528E-03
27	5.295E-03	5.835E-03	N/A	6.480E-03	6.655E-03	6.862E-03
28	8.670E-03	9.580E-03	1.388E-02	1.416E-02	1.438E-02	1.459E-02
29	N/A	N/A	N/A	N/A	N/A	N/A
30	N/A	N/A	N/A	N/A	N/A	N/A
31	N/A	N/A	N/A	2.610E-02	2.672E-02	2.692E-02
32	8.220E-04	9.760E-04	1.135E-03	1.338E-03	1.539E-03	1.739E-03
33	7.660E-04	9.400E-04	1.175E-03	1.341E-03	1.523E-03	1.662E-03
34	7.100E-04	8.800E-04	1.105E-03	1.280E-03	1.416E-03	1.571E-03
35	N/A	N/A	N/A	N/A	N/A	N/A
36	8.060E-04	9.740E-04	1.211E-03	1.372E-03	1.542E-03	1.701E-03
37	7.300E-04	9.040E-04	1.135E-03	1.283E-03	1.439E-03	1.591E-03
38	6.920E-04	8.600E-04	1.087E-03	1.233E-03	1.386E-03	1.536E-03
39	8.020E-04	9.800E-04	1.221E-03	1.375E-03	1.539E-03	1.695E-03
40	8.260E-04	1.010E-03	1.295E-03	1.480E-03	1.671E-03	1.864E-03
41	9.600E-04	1.156E-03	1.446E-03	1.649E-03	1.852E-03	2.059E-03
42	1.010E-03	1.190E-03	1.395E-03	1.688E-03	1.901E-03	2.117E-03
43	1.060E-03	1.240E-03	1.473E-03	1.861E-03	2.154E-03	2.444E-03
44	N/A	N/A	N/A	N/A	N/A	N/A
45	1.180E-03	1.386E-03	1.590E-03	2.022E-03	2.308E-03	2.591E-03
46	N/A	N/A	N/A	N/A	N/A	N/A
47	1.770E-03	1.960E-03	N/A	N/A	N/A	N/A
48	2.510E-03	2.675E-03	2.820E-03	3.272E-03	3.562E-03	3.846E-03
49	1.630E-03	2.125E-03	2.565E-03	N/A	N/A	N/A
50	6.320E-04	7.940E-04	1.024E-03	1.171E-03	1.321E-03	1.470E-03

Table D.4: Wave arrival times. N/A values indicate that wave front was either not recorded or could not be identified.

### D.3 Velocity Data

Run	$\phi$	Pressure (bar)	$\Delta/R$	$\frac{U_{01}}{U_{CJ}}$	$\frac{U_{12}}{U_{CJ}}$	$\frac{U_{23}}{U_{CJ}}$	$\frac{U_{34}}{U_{CJ}}$	$\frac{U_{45}}{U_{CJ}}$	$\frac{U_{AVG}}{U_{CJ}}$
1	1.0	1.00	8.13E-03	N/A	1.2739	0.9831	0.9876	0.9786	0.9831
2	1.0	0.50	1.85E-02	N/A	N/A	0.9784	0.9784	0.9741	0.9770
3	1.0	0.20	9.80E-02	N/A	N/A	0.9333	0.9333	0.9333	0.9333
4	1.0	0.10	N/A	N/A	N/A	N/A	N/A	N/A	N/A
5	1.0	0.15	9.57E-02	N/A	N/A	0.9546	0.9505	0.9546	0.9532
6	0.8	1.00	1.08E-02	N/A	1.2815	0.9806	0.9764	0.9806	0.9792
7	0.6	1.00	1.69E-02	N/A	1.2598	0.9730	0.9730	0.9730	0.9730
8	0.5	1.00	2.60E-02	N/A	N/A	0.9589	0.9552	0.9739	0.9627
9	1.0	0.10	8.73E+01	N/A	N/A	0.5037	0.6020	0.8432	0.6496
10	0.4	1.00	N/A	N/A	N/A	N/A	N/A	N/A	N/A
11	0.3	1.00	N/A	N/A	N/A	N/A	N/A	N/A	N/A
12	1.0	1.00	N/A	N/A	N/A	N/A	N/A	N/A	N/A
13	1.0	0.50	N/A	N/A	N/A	N/A	N/A	N/A	N/A
14	1.0	0.50	N/A	N/A	N/A	N/A	N/A	0.9698	N/A
15	1.0	0.20	N/A	N/A	N/A	N/A	N/A	N/A	N/A
16	1.0	0.30	1.99E-02	N/A	1.2960	1.0014	1.0153	1.0106	1.0091
17	1.0	0.20	9.80E-02	N/A	1.2071	0.9216	0.9412	0.9372	0.9333
18	0.3	1.00	0	N/A	N/A	N/A	N/A	N/A	N/A
19	0.4	1.00	4.85E-02	N/A	1.2482	0.9476	0.9510	0.9476	0.9487
20	0.8	1.00	7.01E-03	N/A	1.3189	1.0069	1.0159	1.0114	1.0114
21	0.4	1.00	N/A	0.9464	0.9206	0.4703	0.9373	N/A	N/A
22	0.6	1.00	1.95E-02	0.9713	0.9502	0.9611	0.9649	0.9649	0.9637
23	0.8	1.00	1.15E-02	0.9866	0.9500	0.9721	0.9764	0.9764	0.9749
24	2.0	1.00	8.08E-03	0.9943	0.9819	0.9772	0.9922	0.9871	0.9855
25	1.0	1.00	N/A	0.9854	N/A	N/A	0.9696	0.9829	N/A

Table D.5: Calculated wave velocity.  $U_{ij}$  is the average velocity between stations  $i$  and  $j$ .  $U_{AVG}$  is the average of  $U_{23}$ ,  $U_{34}$ , and  $U_{45}$ .

Run	$\phi$	Pressure (bar)	$\Delta/R$	$\frac{U_{01}}{U_{CJ}}$	$\frac{U_{12}}{U_{CJ}}$	$\frac{U_{23}}{U_{CJ}}$	$\frac{U_{34}}{U_{CJ}}$	$\frac{U_{45}}{U_{CJ}}$	$\frac{U_{AVG}}{U_{CJ}}$
26	2.4	1.00	N/A	0.9954	N/A	N/A	0.9620	0.9763	N/A
27	2.6	1.00	N/A	N/A	N/A	N/A	N/A	N/A	N/A
28	2.8	1.00	N/A	N/A	N/A	N/A	N/A	N/A	N/A
29	3.0	1.00	N/A	N/A	N/A	N/A	N/A	N/A	N/A
30	2.9	1.00	N/A	N/A	N/A	N/A	N/A	N/A	N/A
31	2.9	1.00	N/A	N/A	N/A	N/A	N/A	N/A	N/A
32	1.6	1.00	6.63E-03	1.0103	0.9475	0.9734	0.9831	0.9880	0.9815
33	1.0	1.00	7.02E-01	0.9743	0.8703	0.7782	0.7097	0.9293	0.8057
34	1.0	1.40	2.76E-01	0.9905	0.9029	0.7332	0.9435	0.8278	0.8348
35	1.0	1.60	N/A	N/A	N/A	N/A	N/A	N/A	N/A
36	1.0	1.00	9.14E-01	1.0090	0.8630	0.8023	0.7598	0.8124	0.7915
37	1.0	1.40	2.34E-01	0.9677	0.8795	0.8670	0.8225	0.8441	0.8445
38	1.0	1.60	1.65E-01	0.9998	0.8927	0.8766	0.8365	0.8532	0.8555
39	1.0	0.80	6.96E-01	0.9562	0.8521	0.8422	0.7908	0.8314	0.8215
40	1.0	0.60	1.63E+01	0.9302	0.7245	0.7050	0.6828	0.6757	0.6878
41	1.0	0.40	9.95E+01	0.8801	0.7177	0.6475	0.6475	0.6350	0.6434
42	1.0	0.30	4.38E+03	0.9857	1.0210	0.4512	0.6206	0.6120	0.5612
43	1.0	0.20	2.93E+04	0.9714	0.9054	0.3434	0.4547	0.4594	0.4192
44	1.0	0.10	N/A	N/A	N/A	N/A	N/A	N/A	N/A
45	1.0	0.15	2.93E+04	0.8620	1.0400	0.3102	0.4685	0.4735	0.4174
46	1.0	0.12	N/A	N/A	N/A	N/A	N/A	N/A	N/A
47	1.0	0.13	N/A	0.9280	N/A	N/A	N/A	N/A	N/A
48	1.0	0.14	2.93E+04	1.0671	1.4650	0.2968	0.4626	0.4724	0.4106
49	1.0	0.14	N/A	N/A	N/A	N/A	N/A	N/A	N/A
50	1.0	1.80	1.36E-01	1.0345	0.8791	0.8687	0.8513	0.8570	0.8590

Table D.6: Calculated wave velocity.  $U_{ij}$  is the average velocity between stations  $i$  and  $j$ .  $U_{AVG}$  is the average of  $U_{23}$ ,  $U_{34}$ , and  $U_{45}$ .

## D.4 Pressure Traces

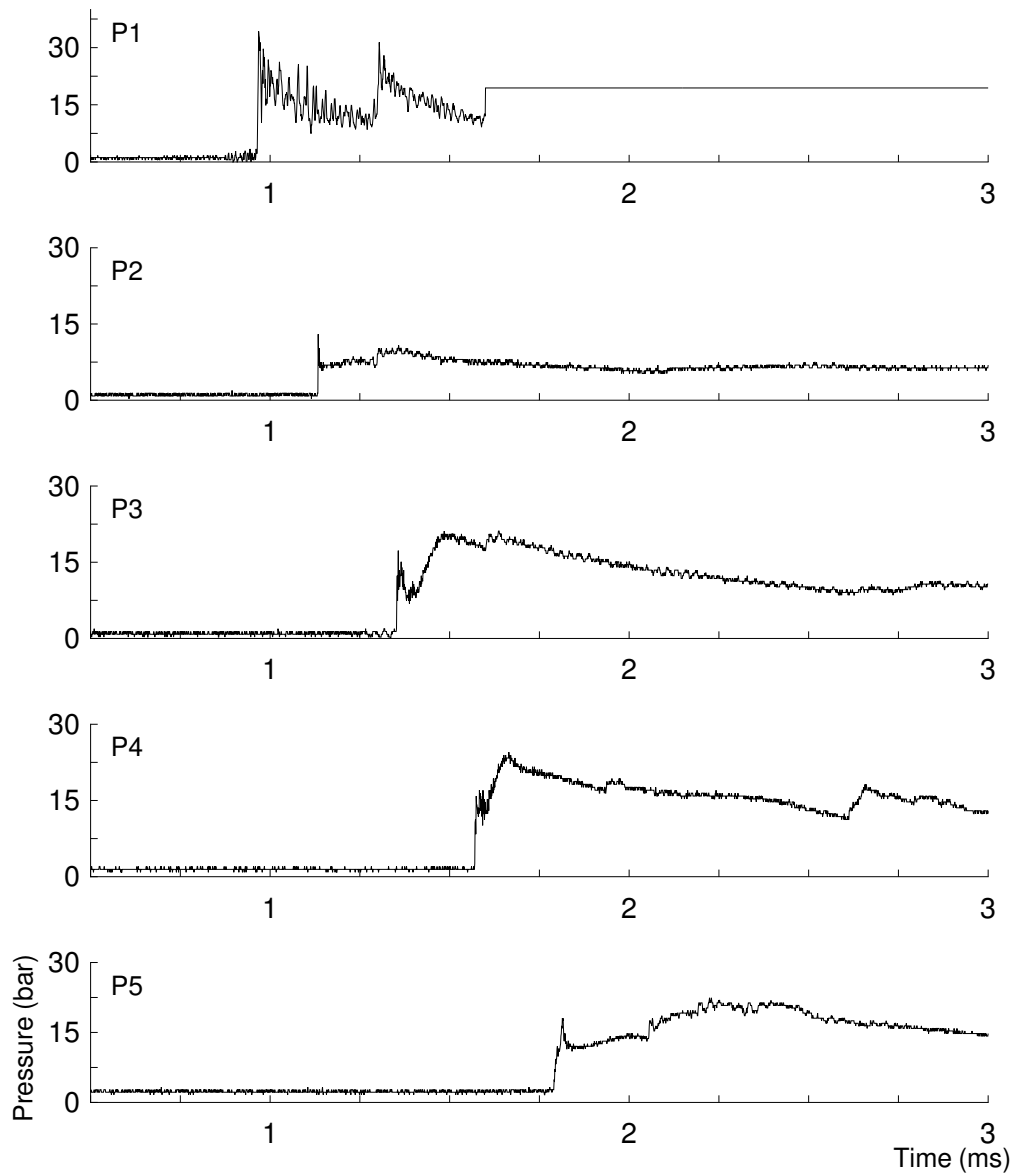


Figure D.1: Pressure history from run 001.

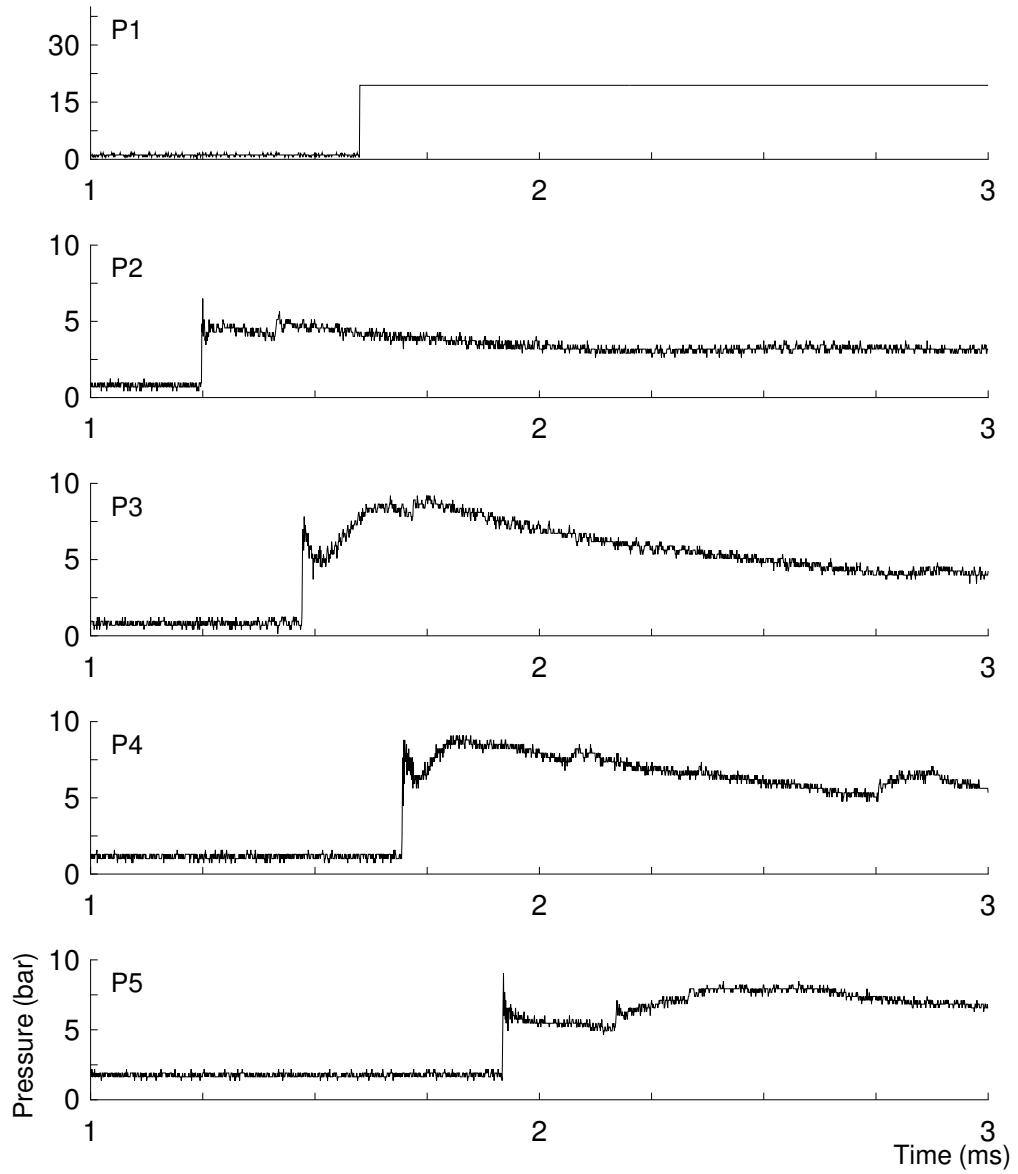


Figure D.2: Pressure history from run 002.

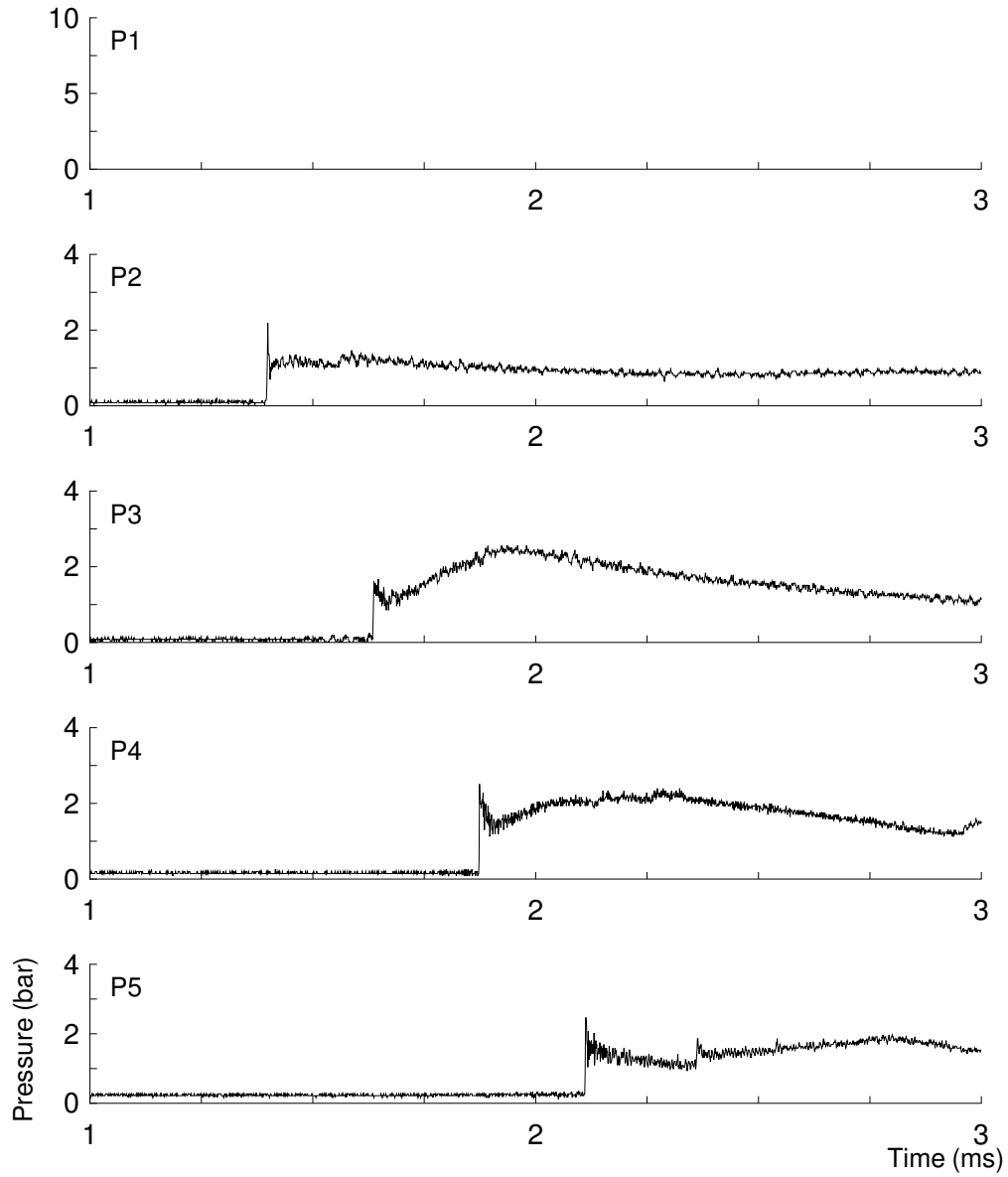


Figure D.3: Pressure history from run 003.

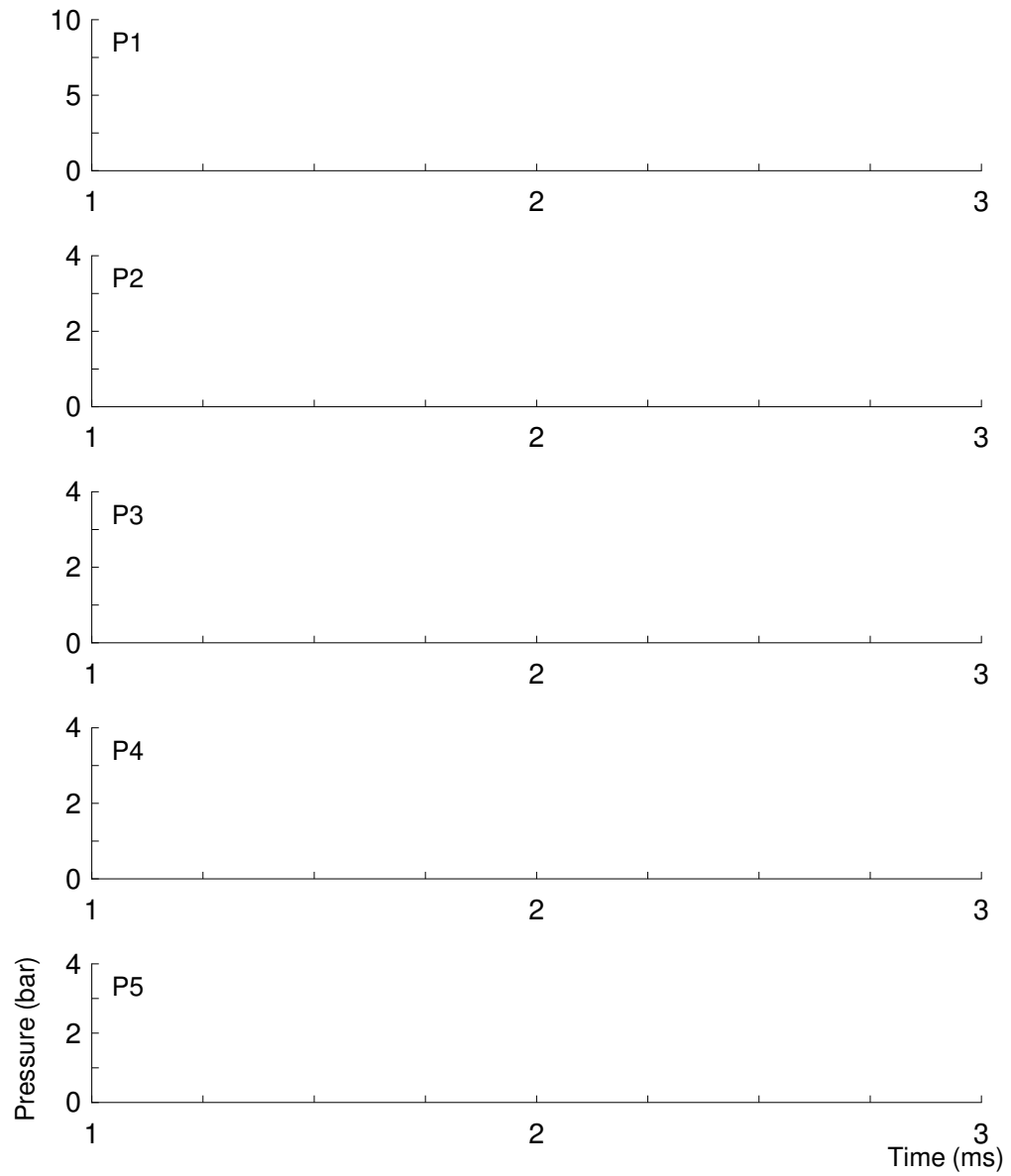


Figure D.4: Pressure history from run 004.

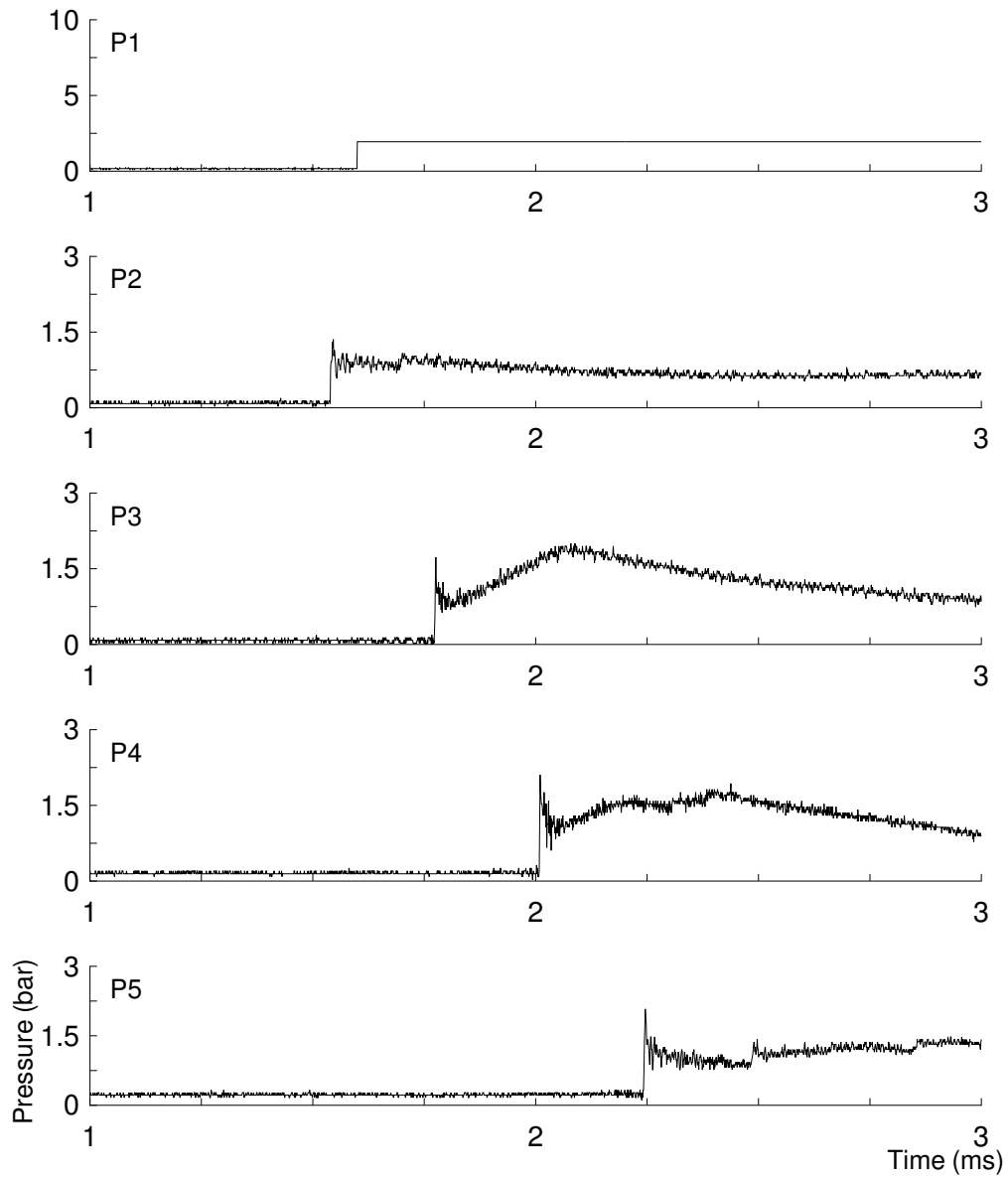


Figure D.5: Pressure history from run 005.

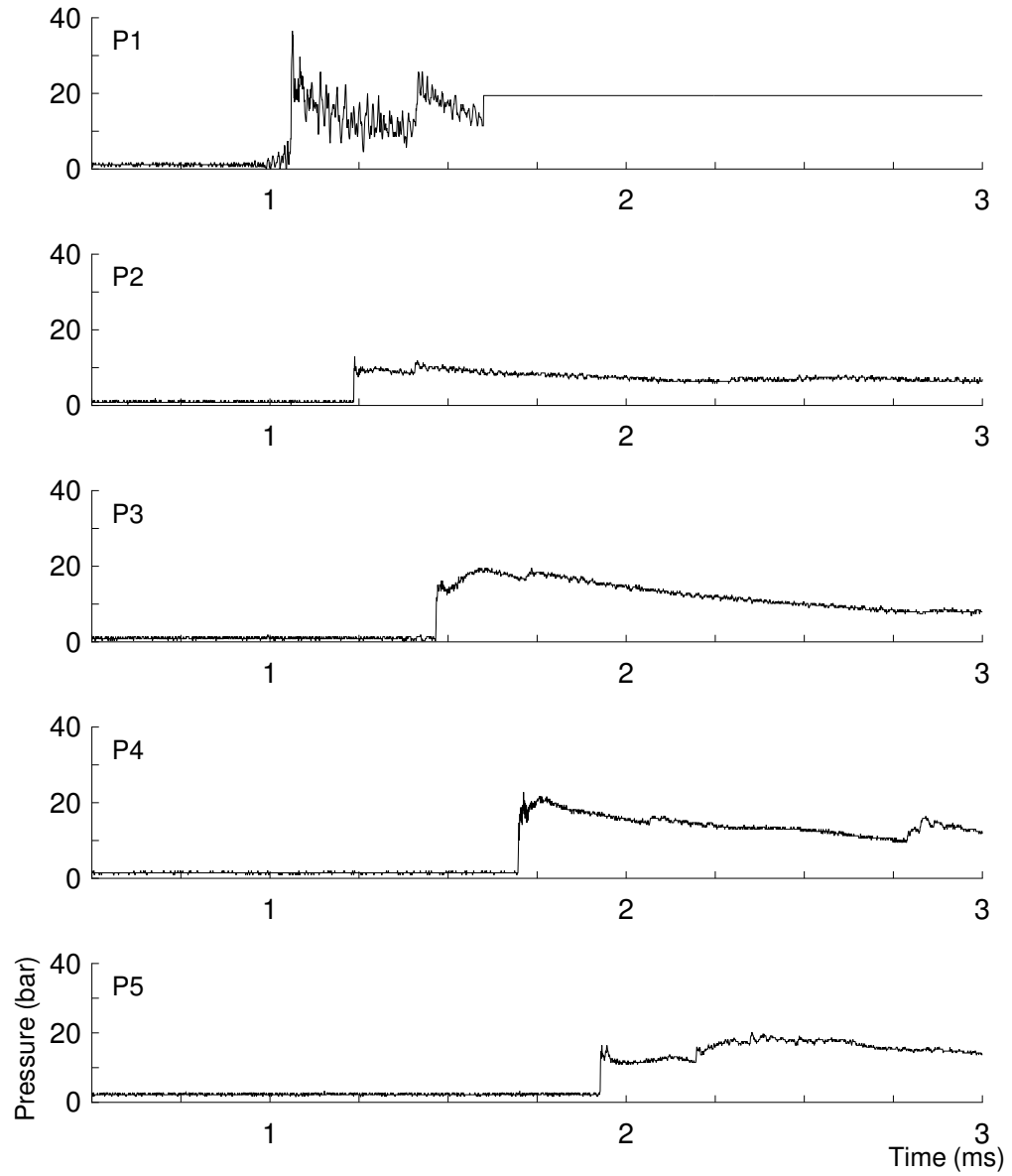


Figure D.6: Pressure history from run 006.

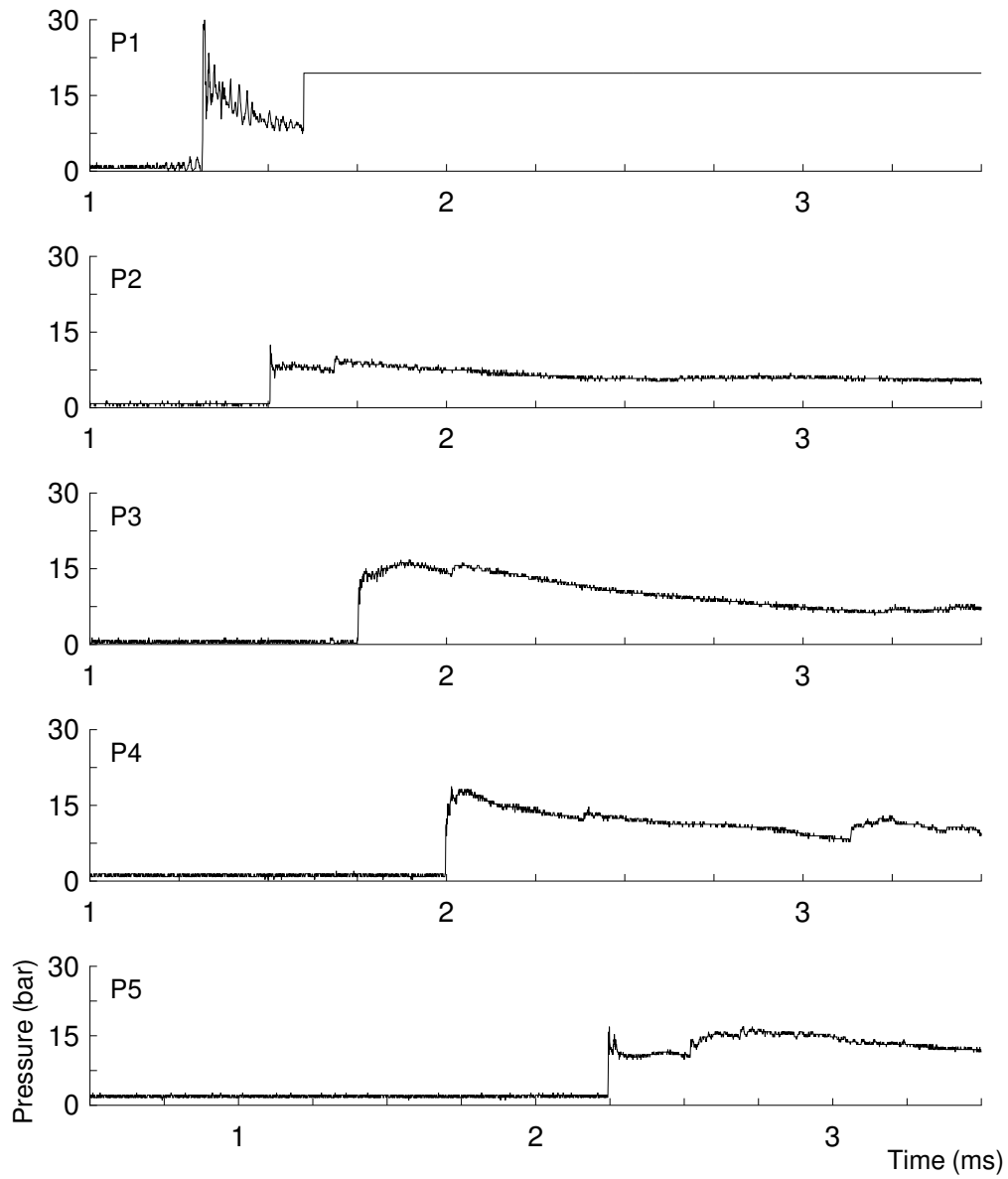


Figure D.7: Pressure history from run 007.

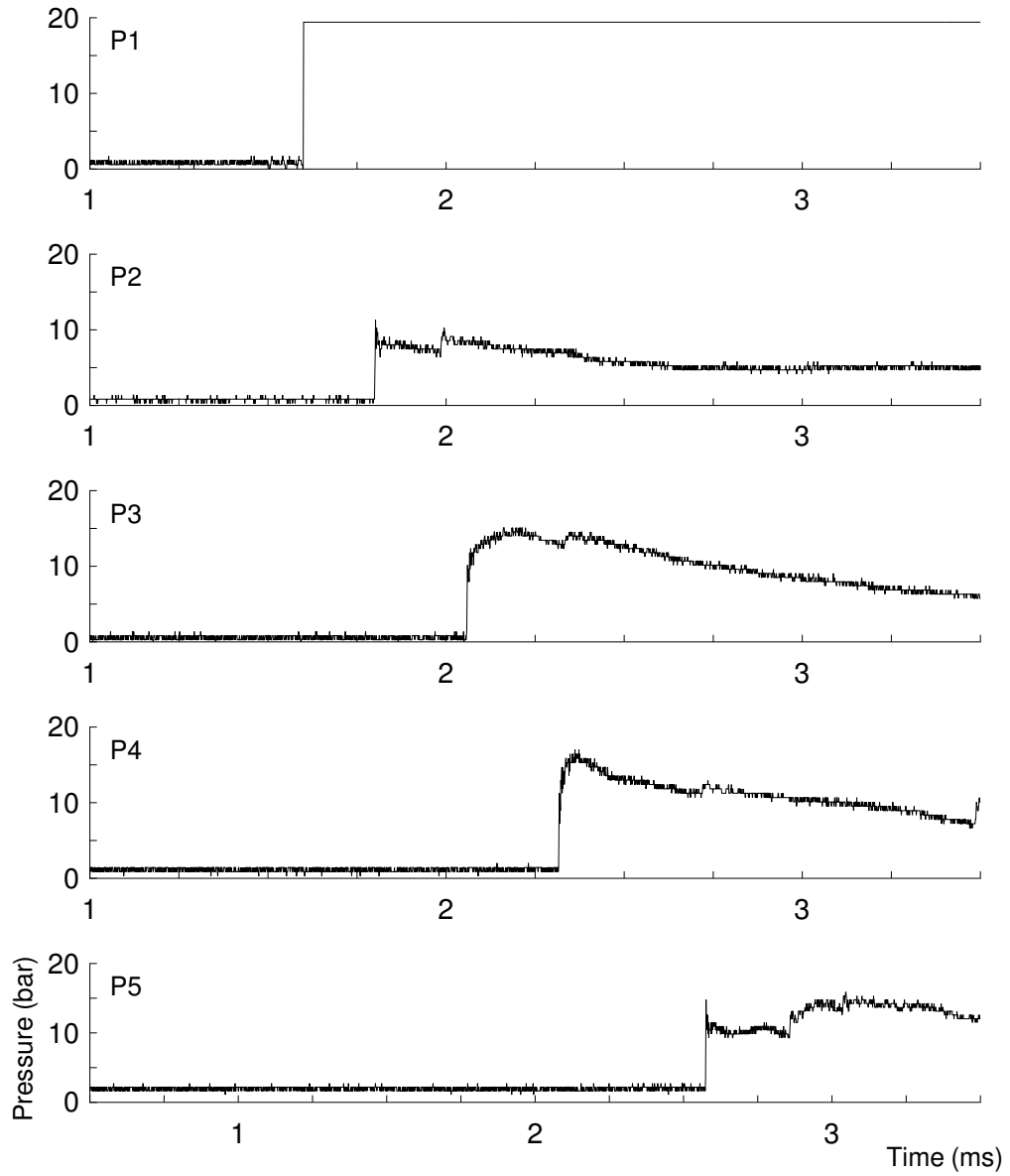


Figure D.8: Pressure history from run 008.

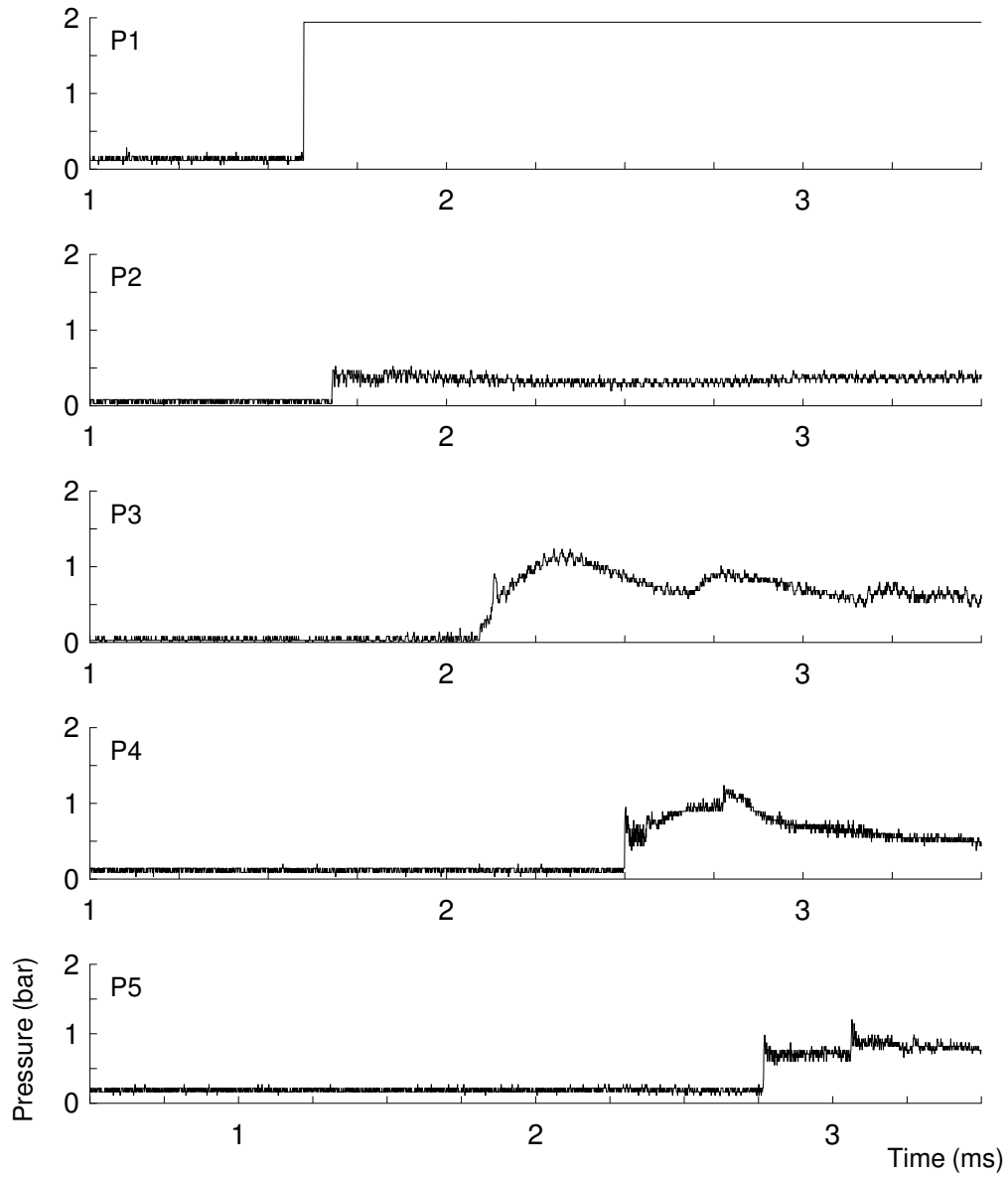


Figure D.9: Pressure history from run 009.

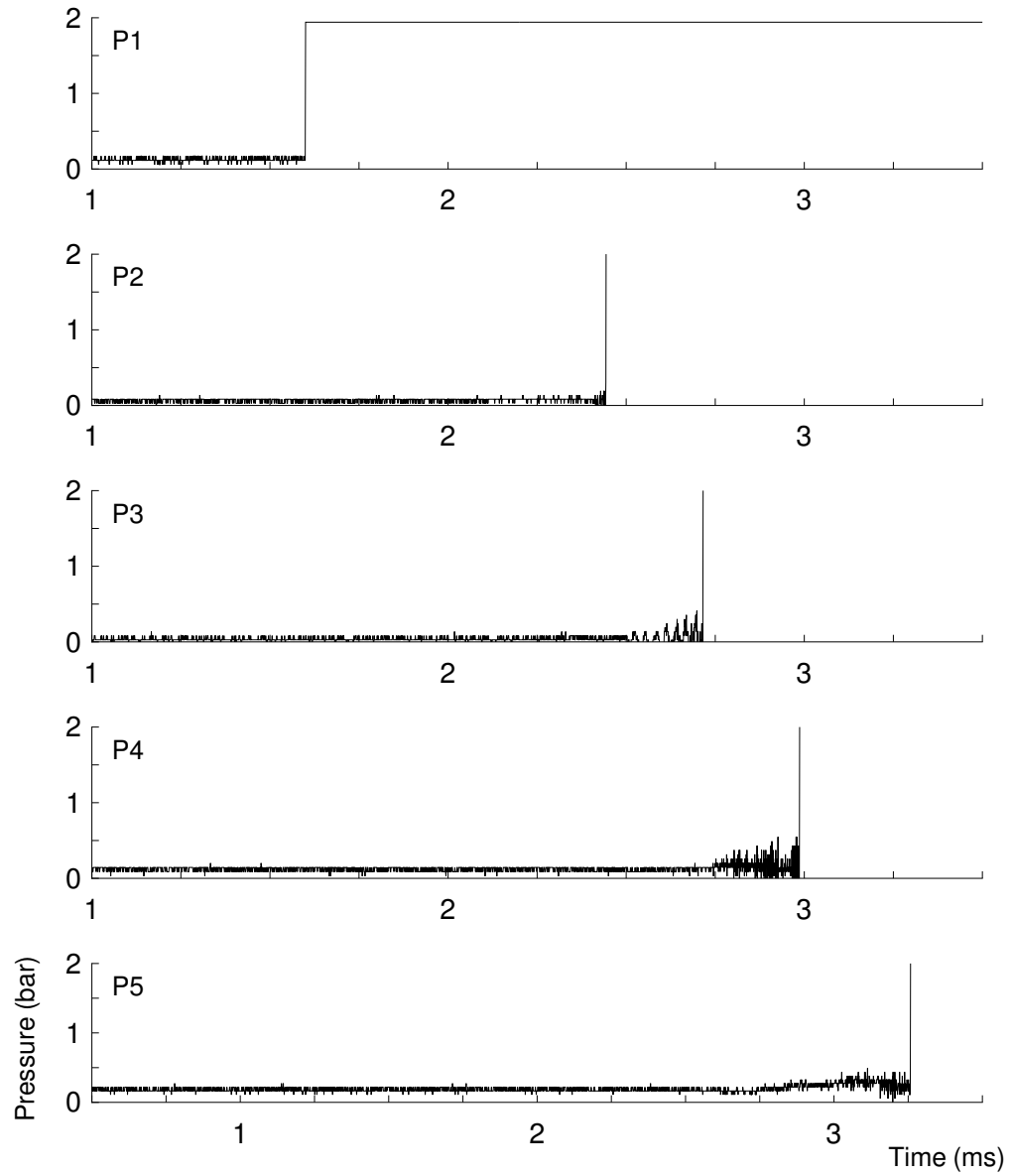


Figure D.10: Pressure history from run 010.

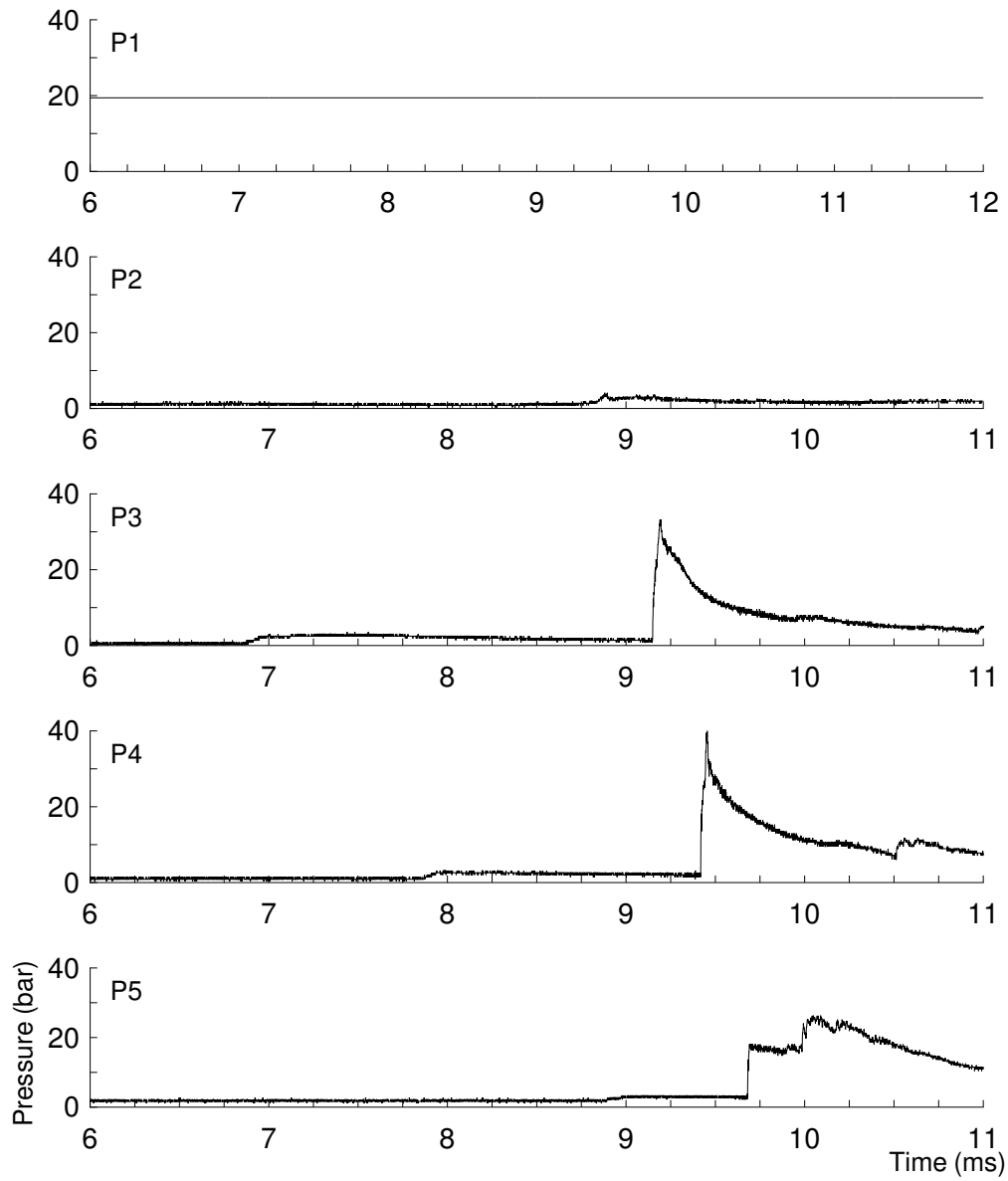


Figure D.11: Pressure history from run 011.

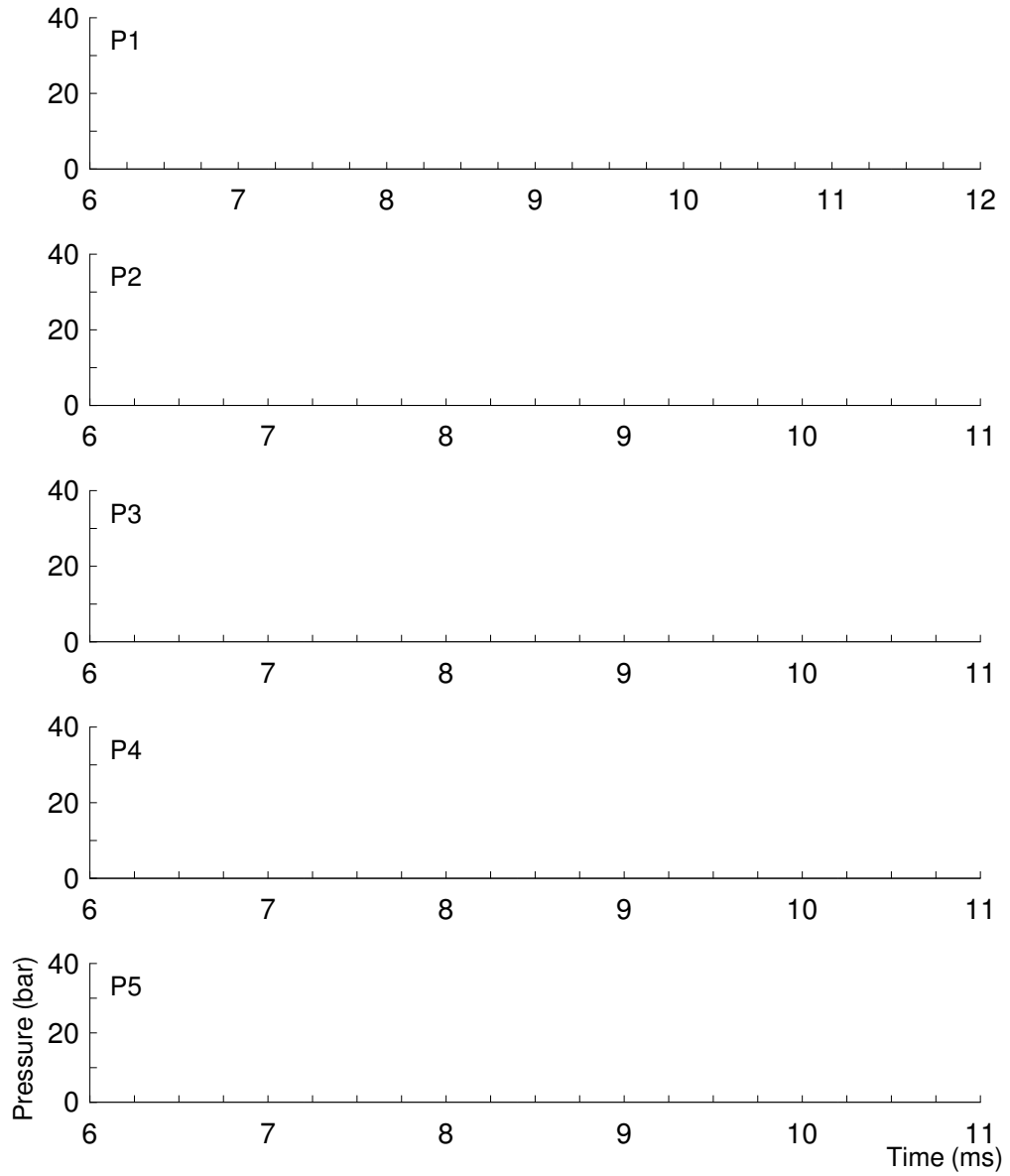


Figure D.12: Pressure history from run 012.

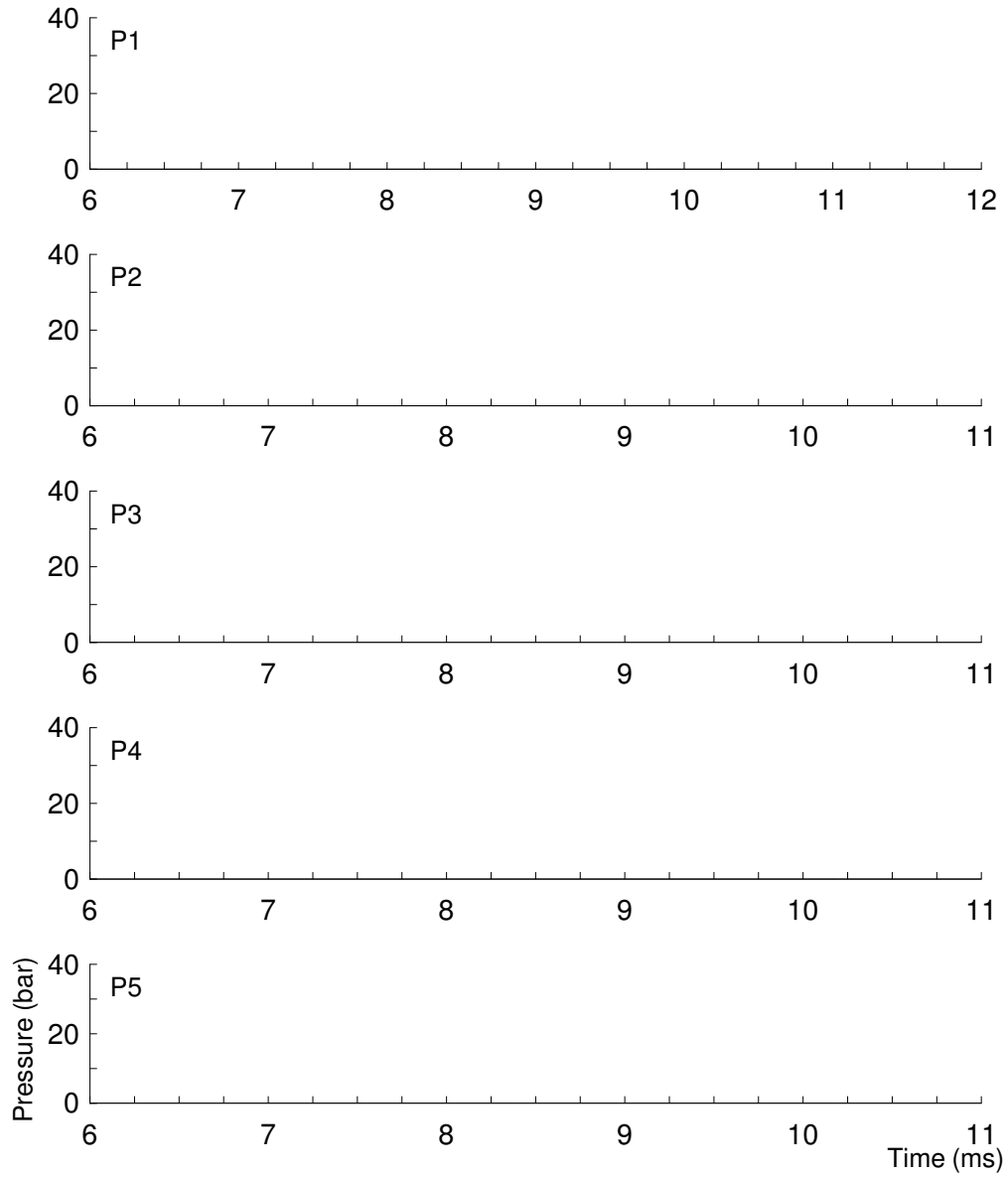


Figure D.13: Pressure history from run 013.

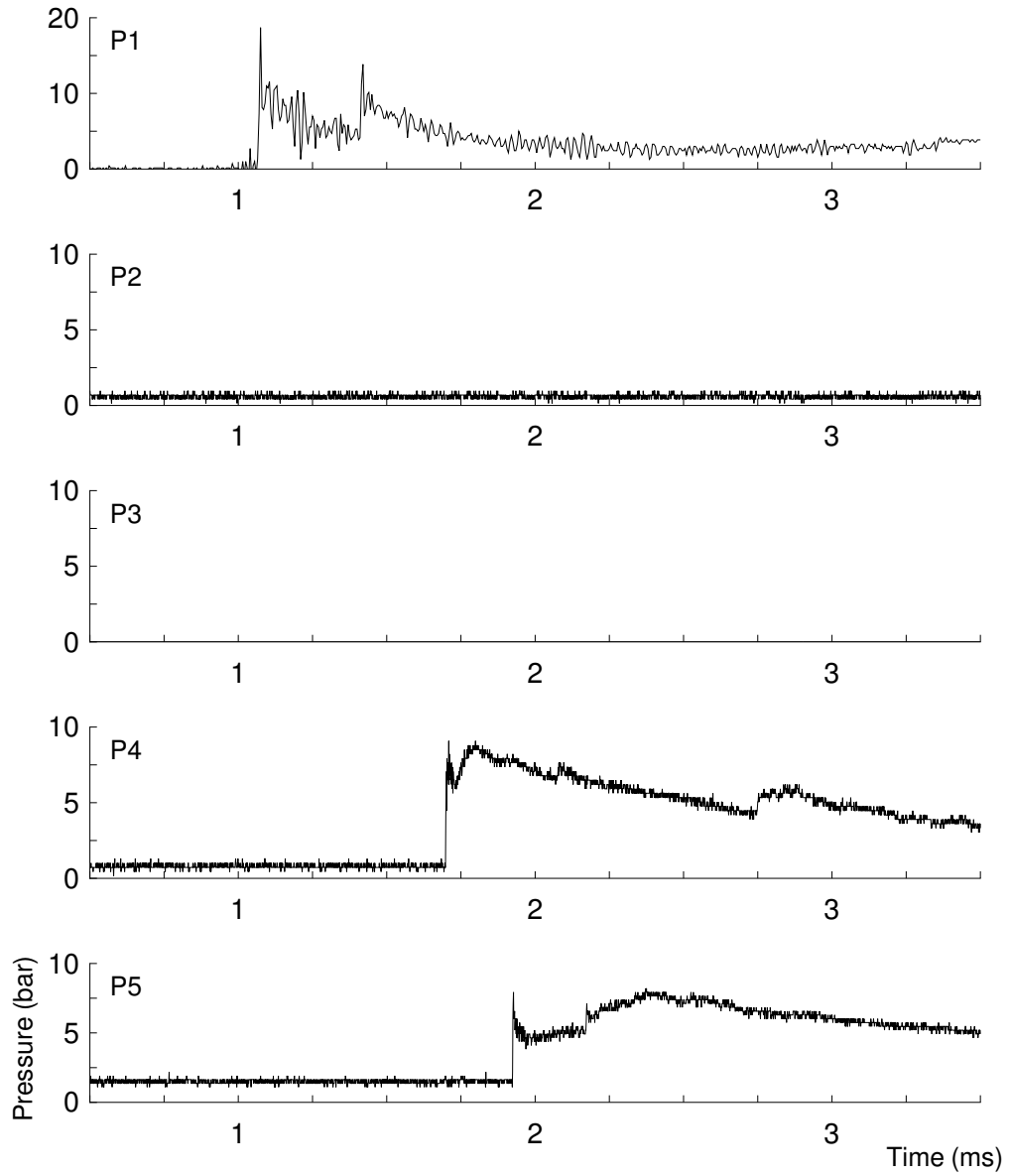


Figure D.14: Pressure history from run 014.

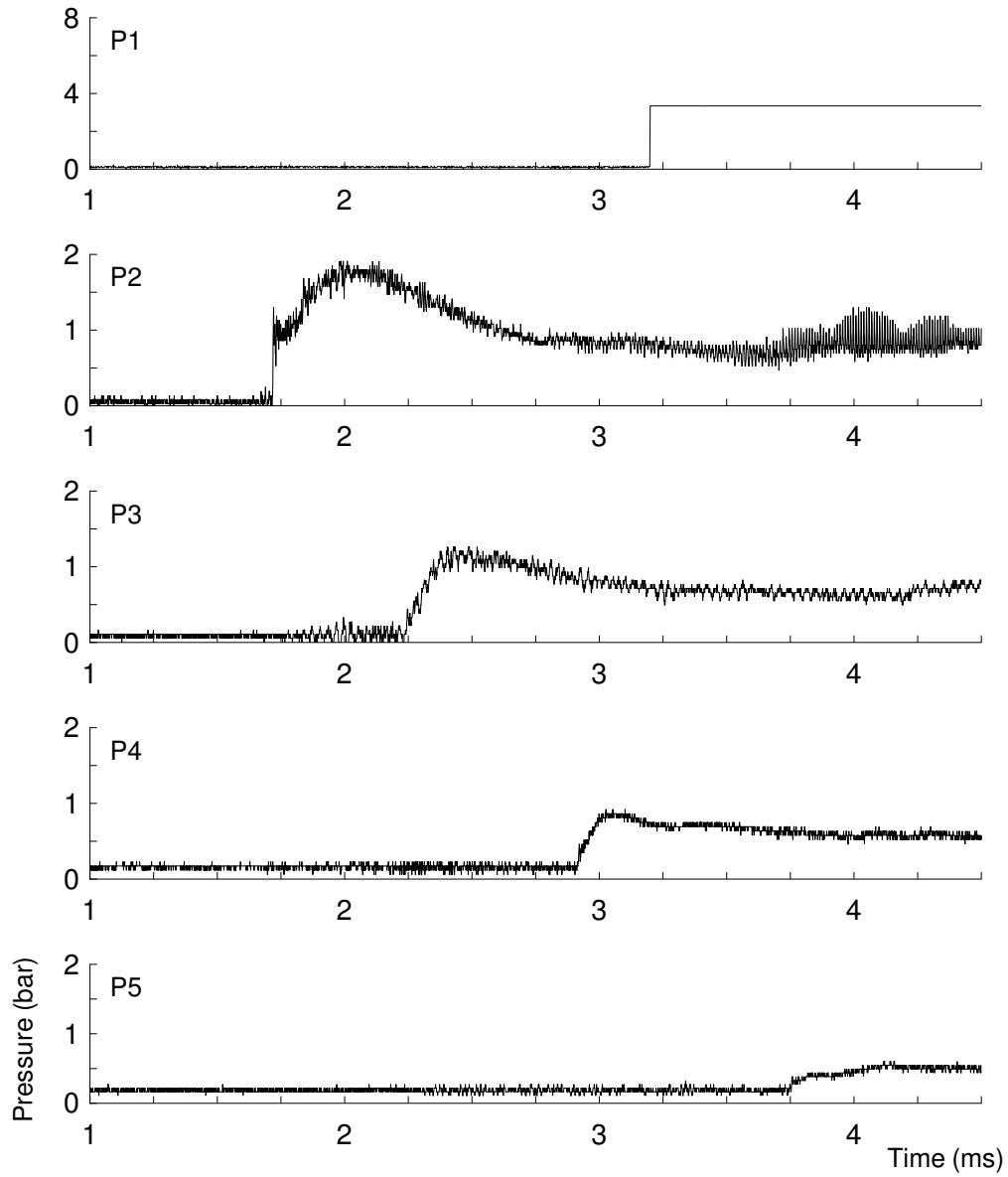


Figure D.15: Pressure history from run 015.

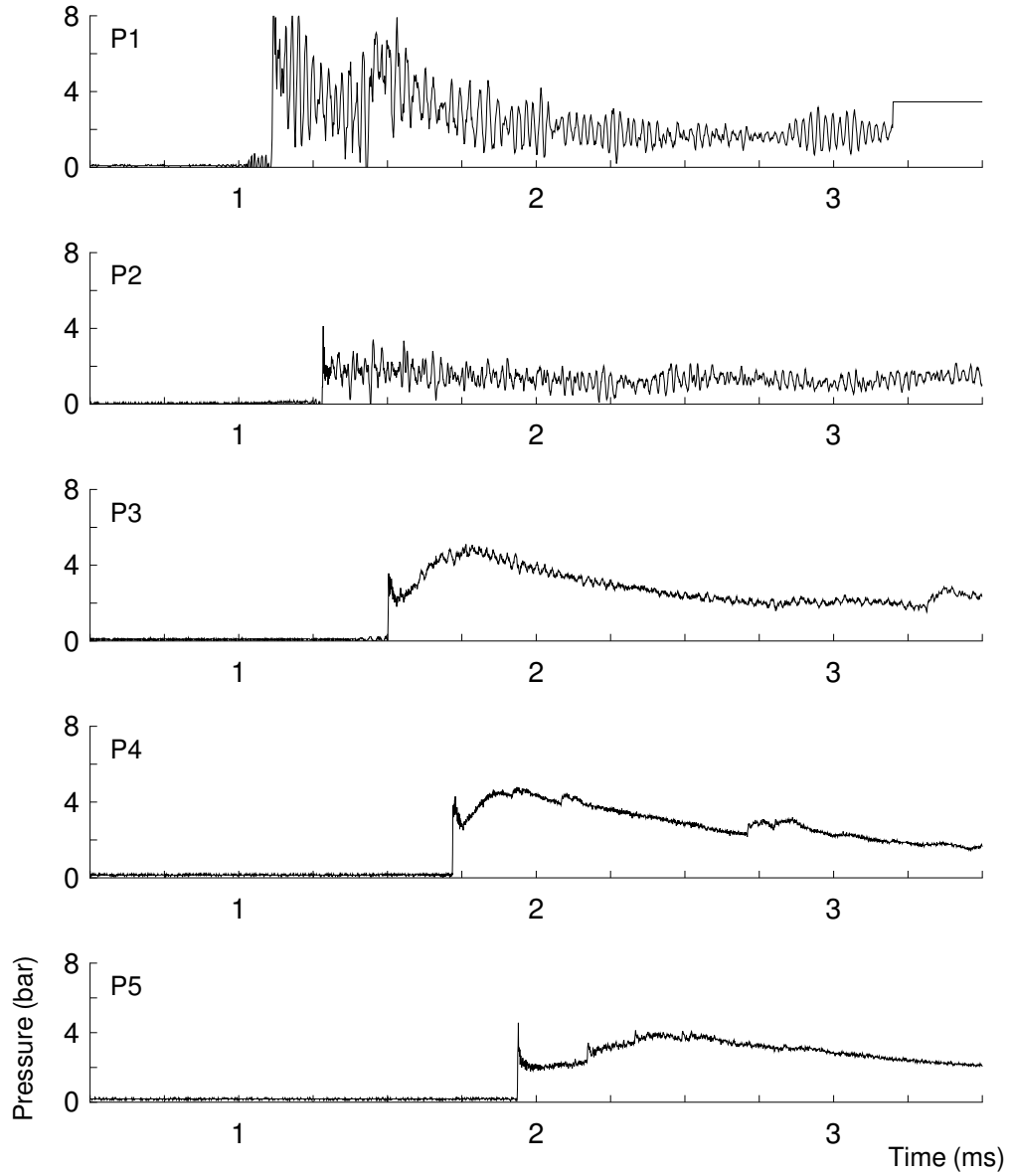


Figure D.16: Pressure history from run 016.

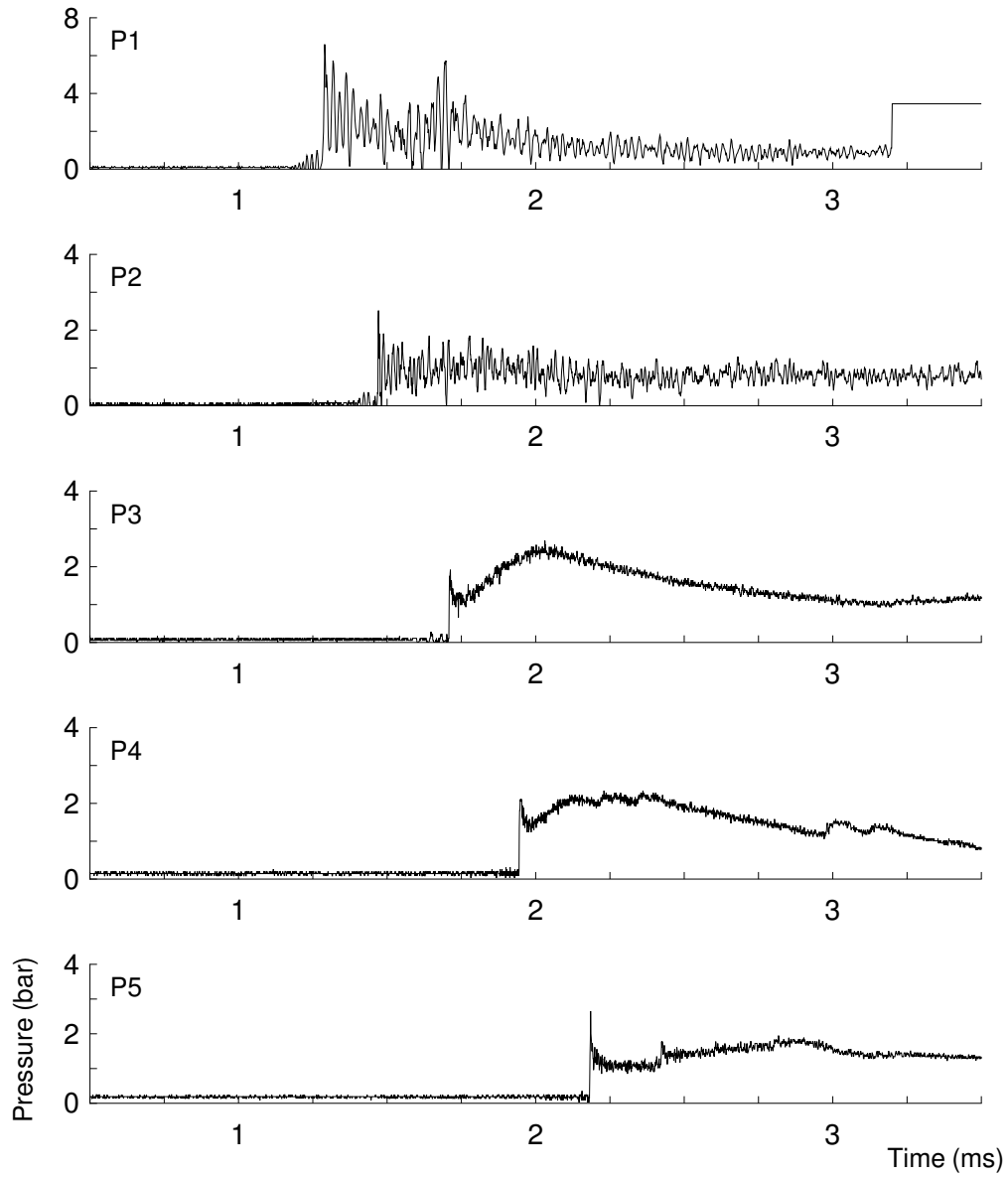


Figure D.17: Pressure history from run 017.

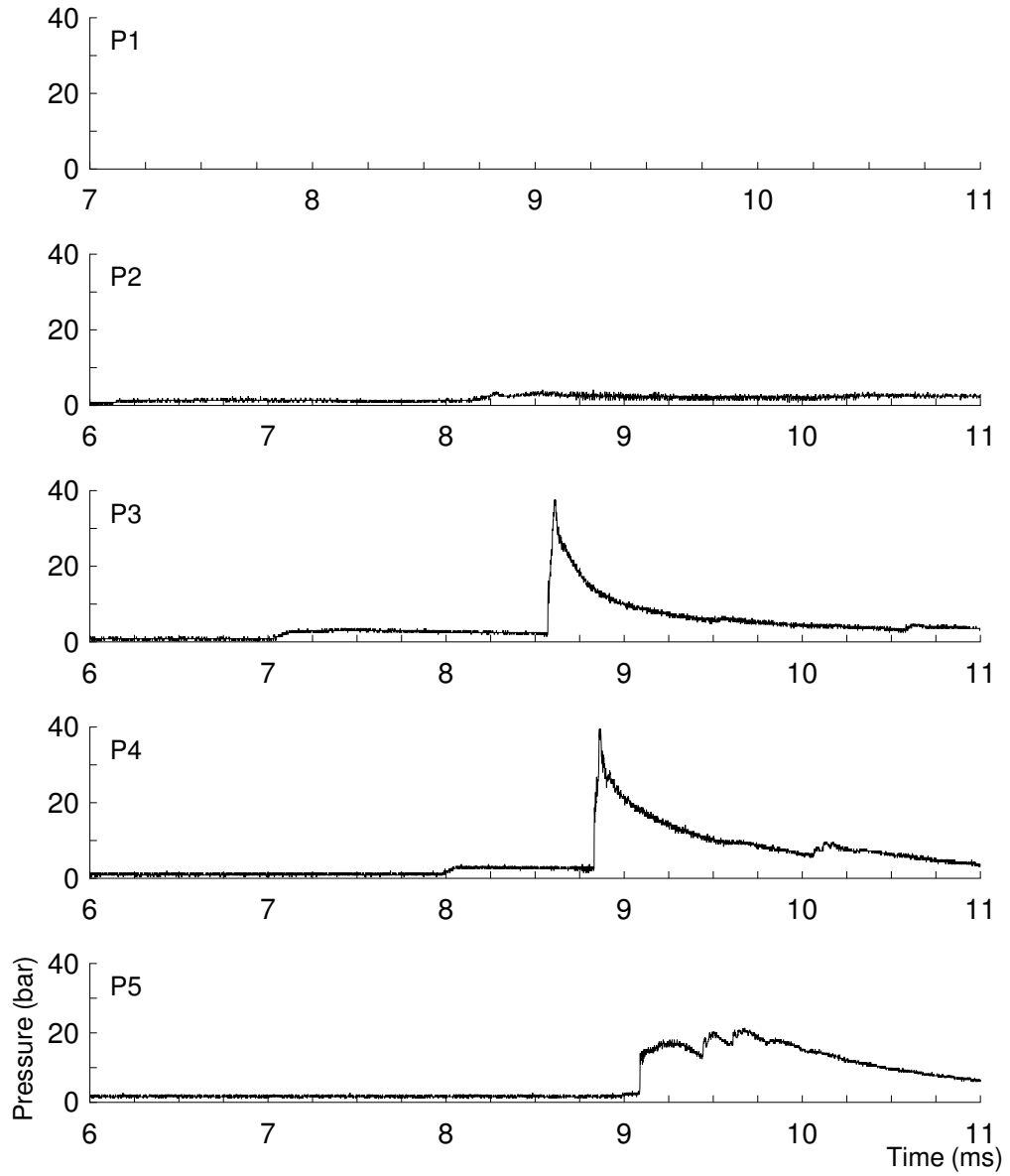


Figure D.18: Pressure history from run 018.

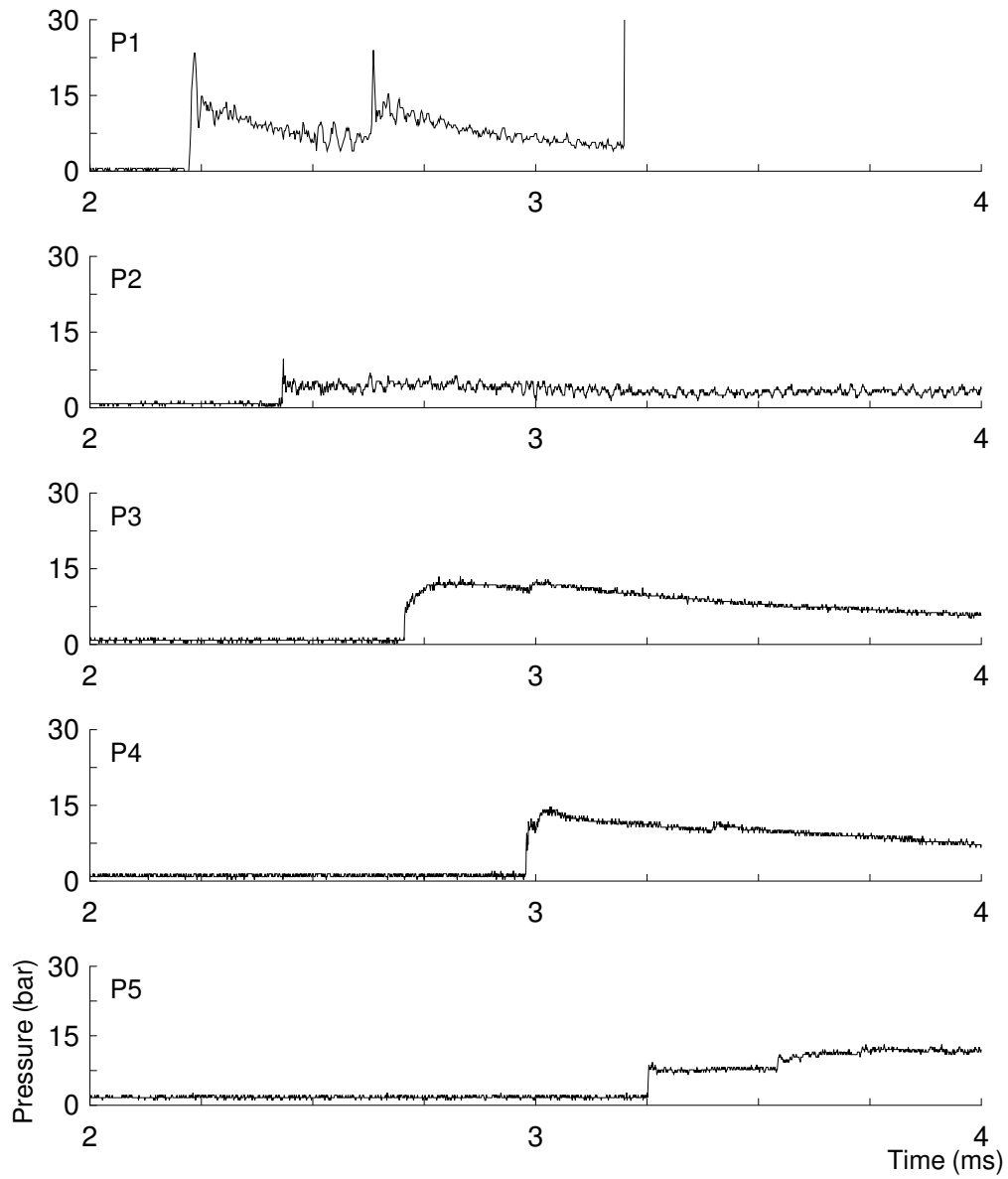


Figure D.19: Pressure history from run 019.

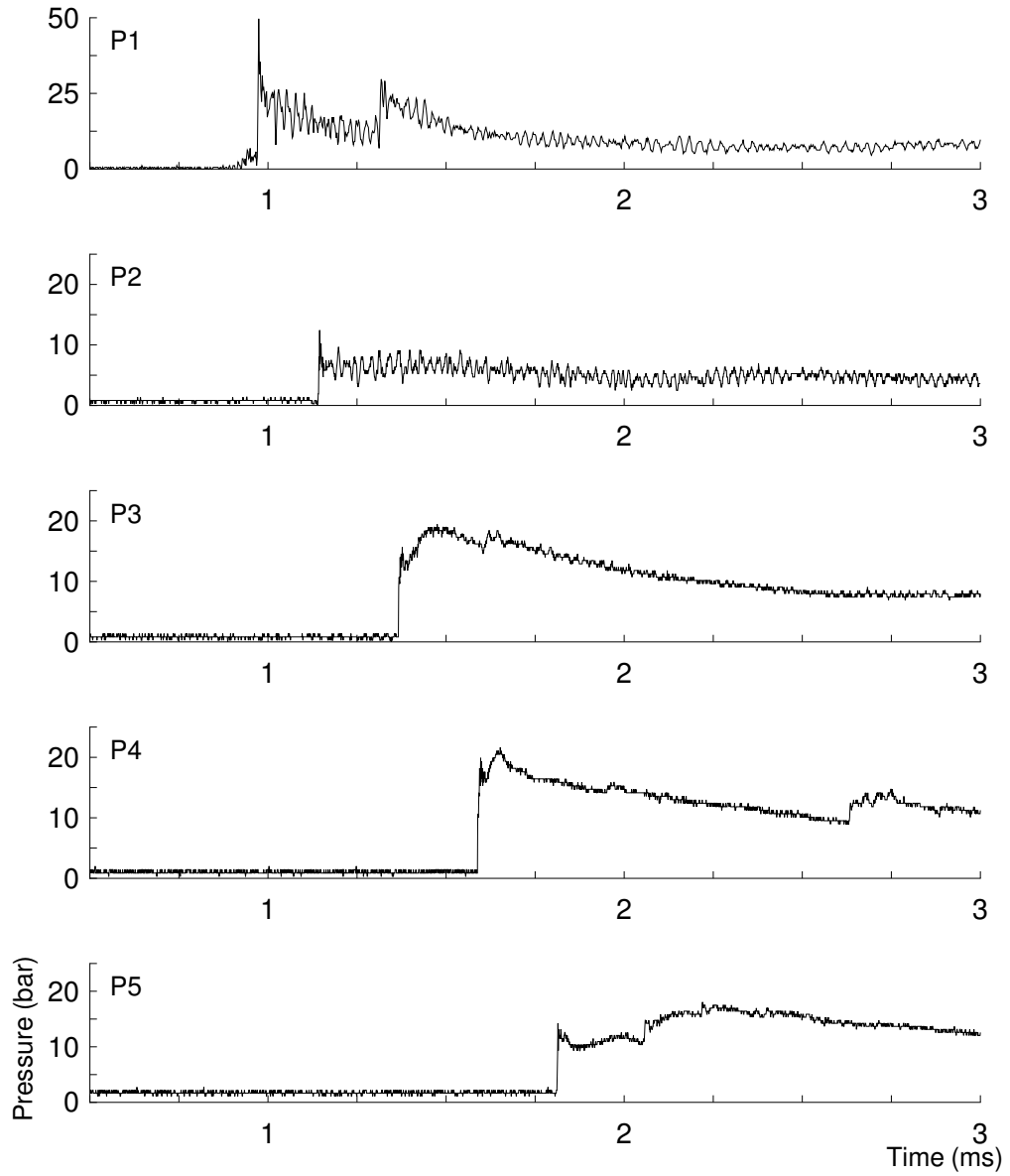


Figure D.20: Pressure history from run 020.

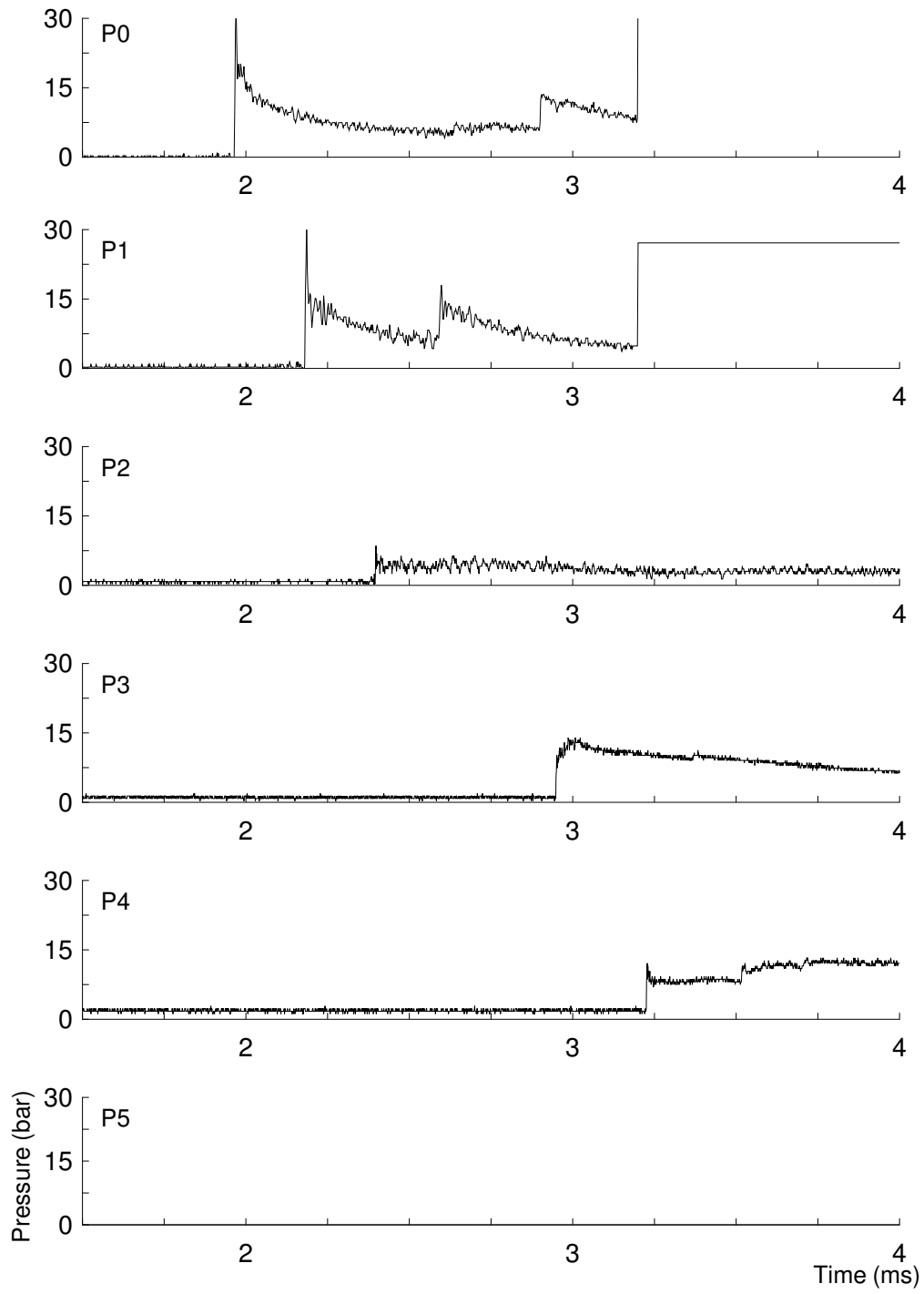


Figure D.21: Pressure history from run 021.

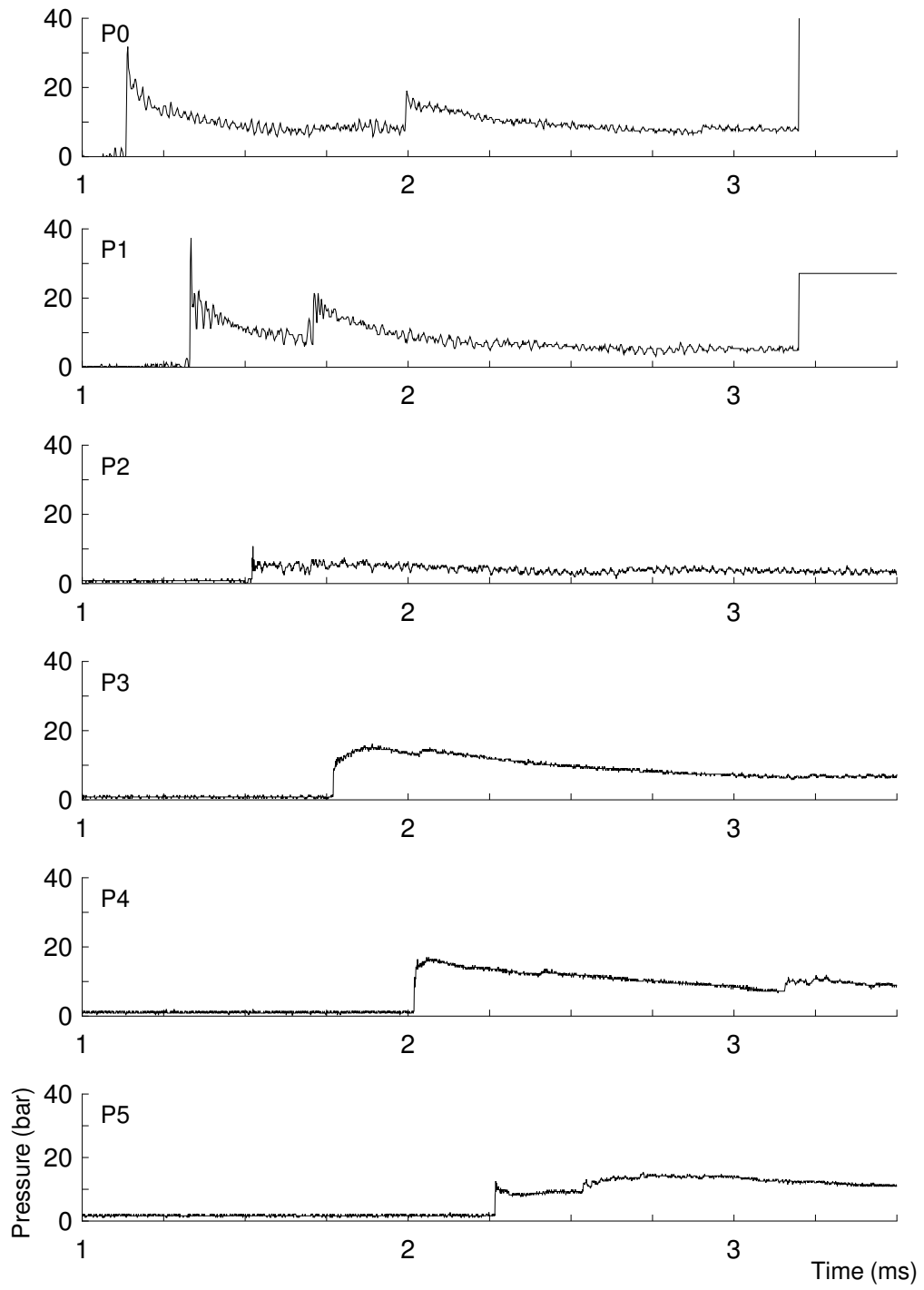


Figure D.22: Pressure history from run 022.

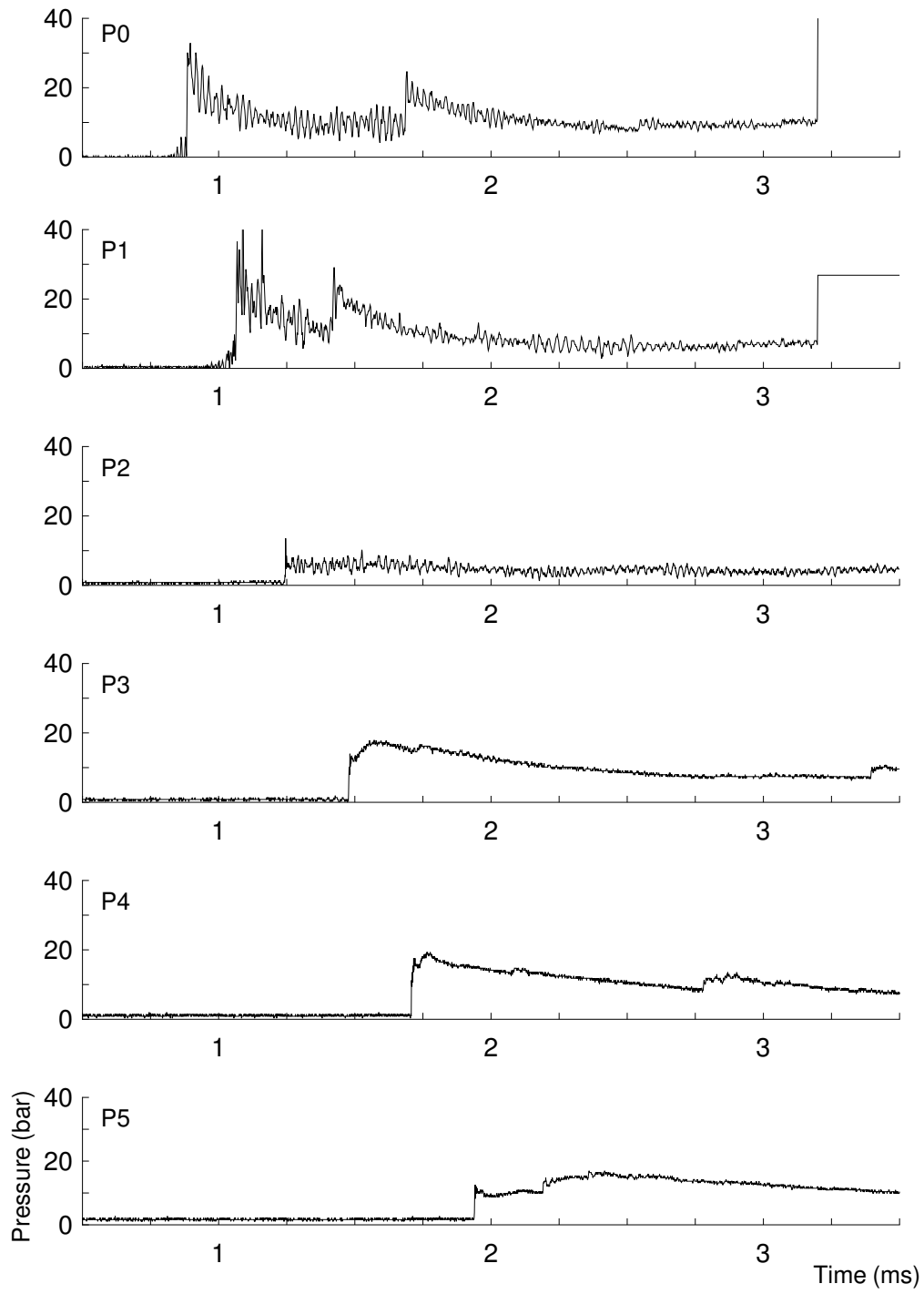


Figure D.23: Pressure history from run 023.

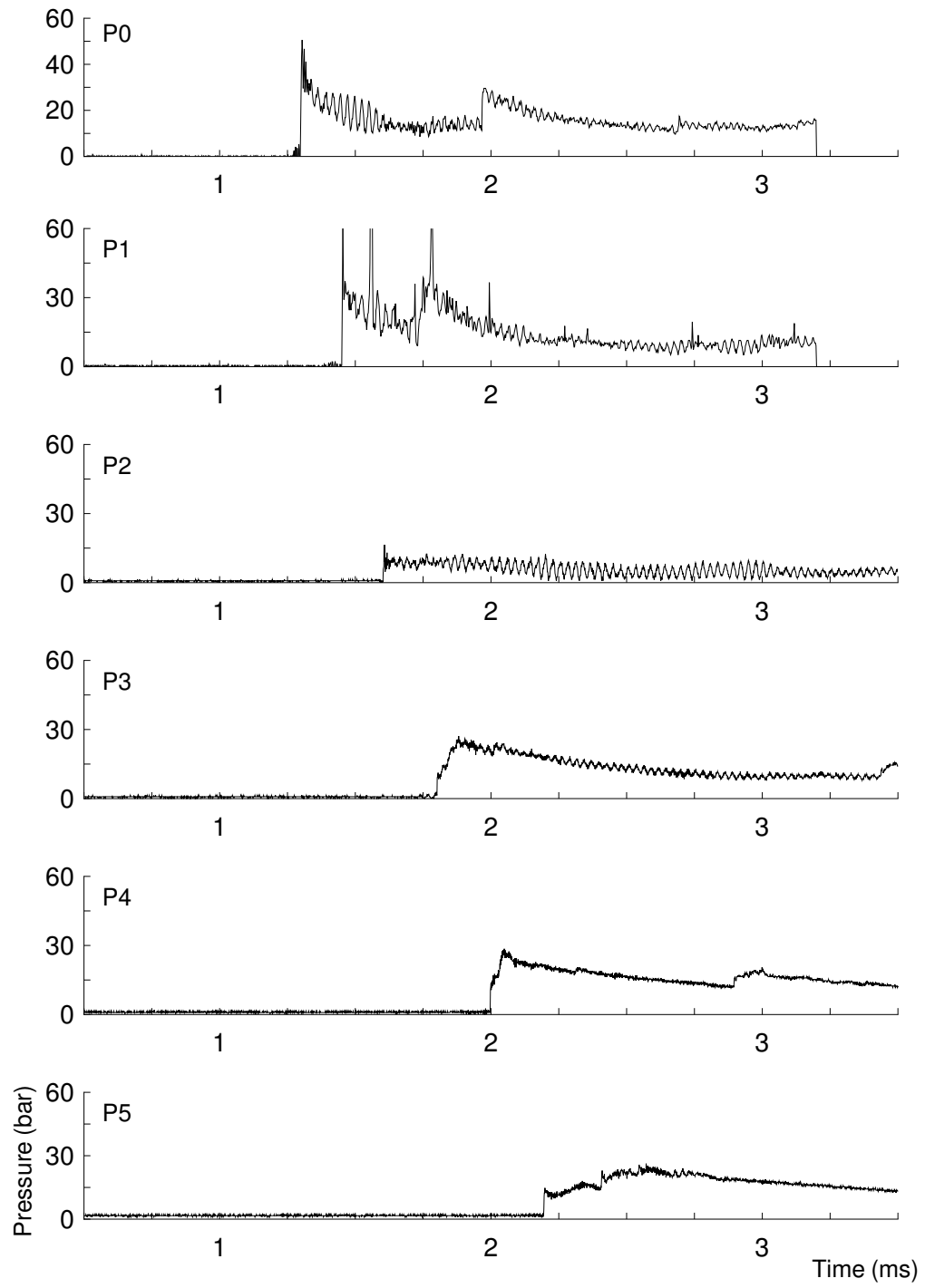


Figure D.24: Pressure history from run 024.

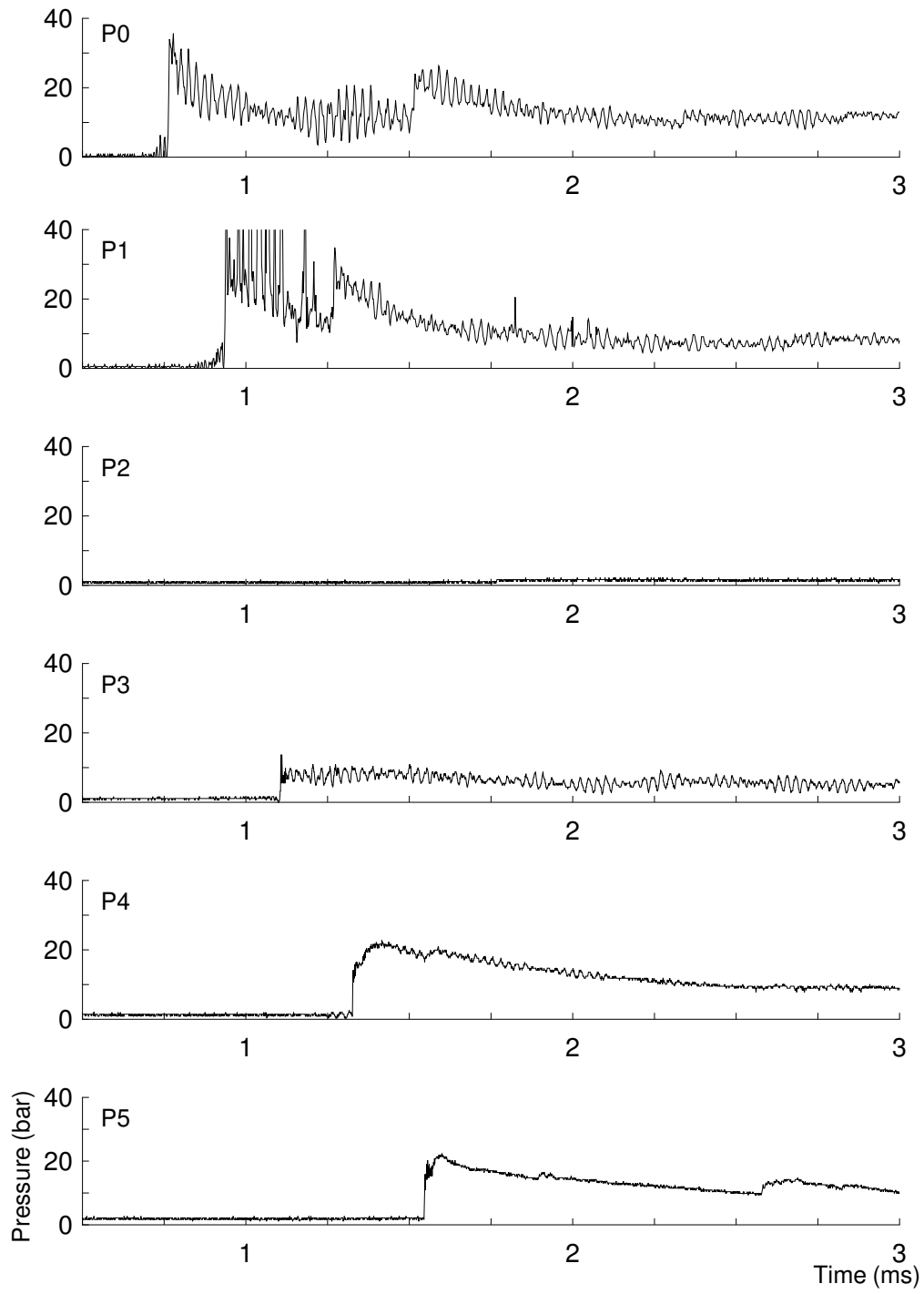


Figure D.25: Pressure history from run 025.

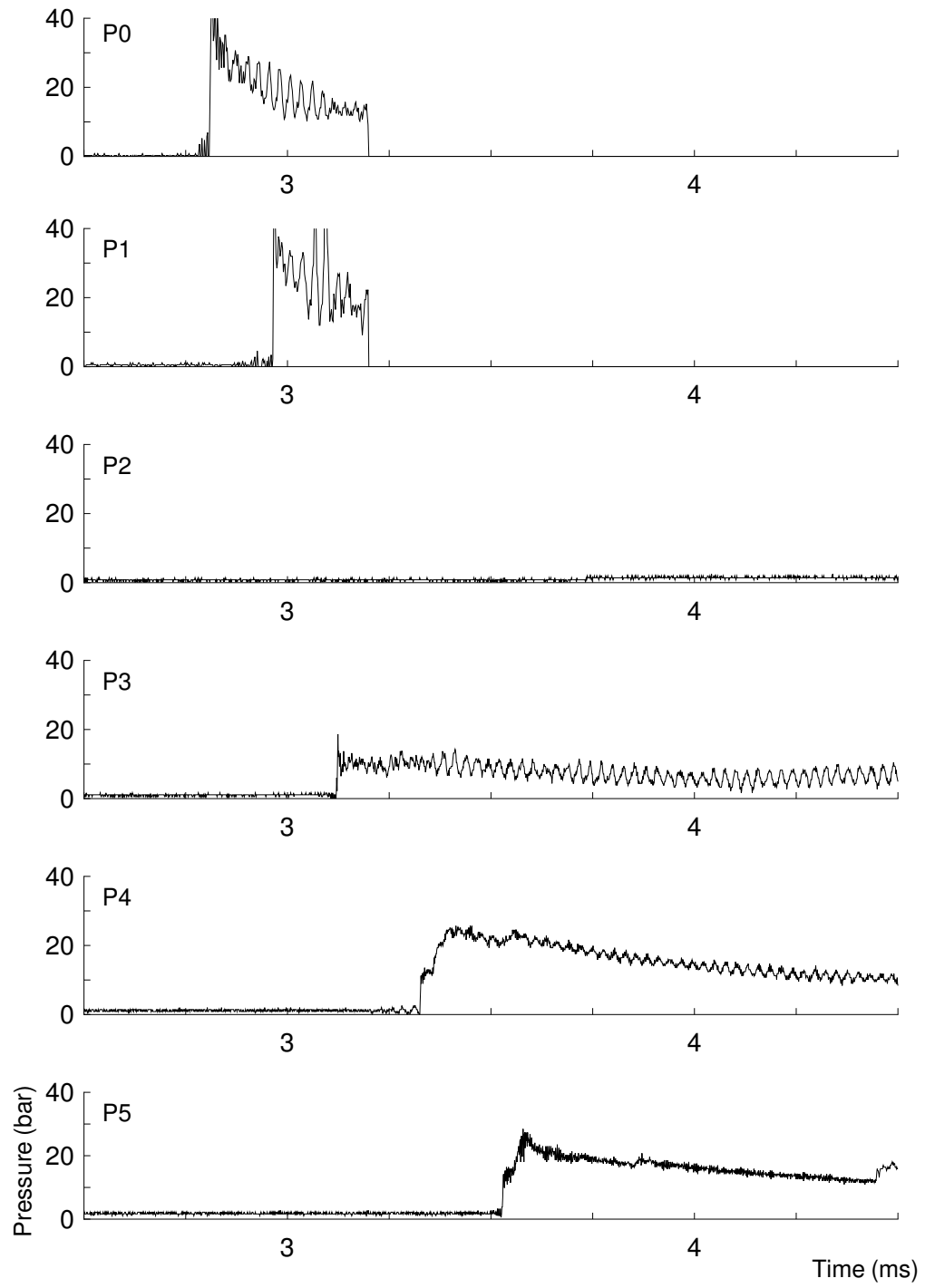


Figure D.26: Pressure history from run 026.

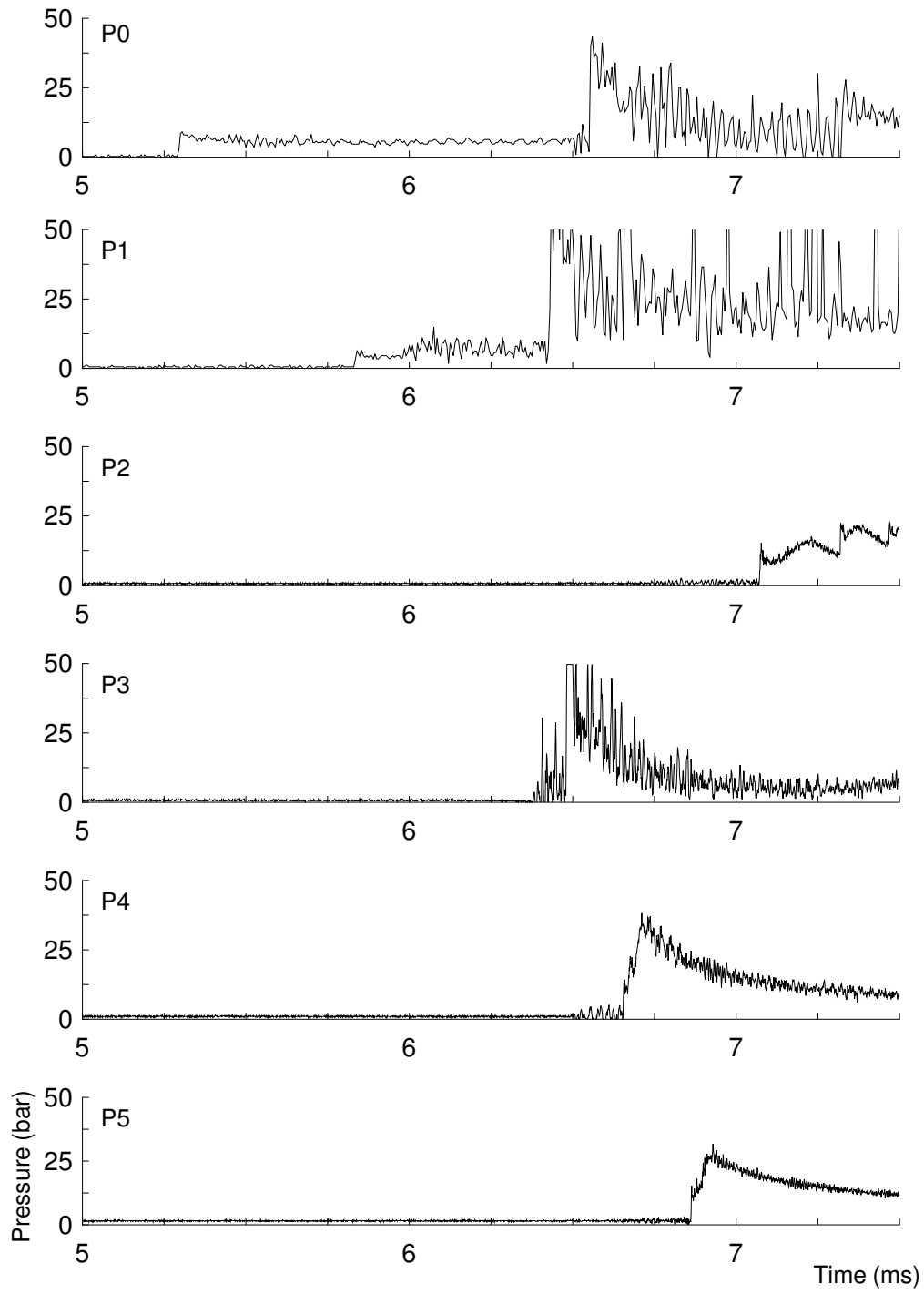


Figure D.27: Pressure history from run 027.

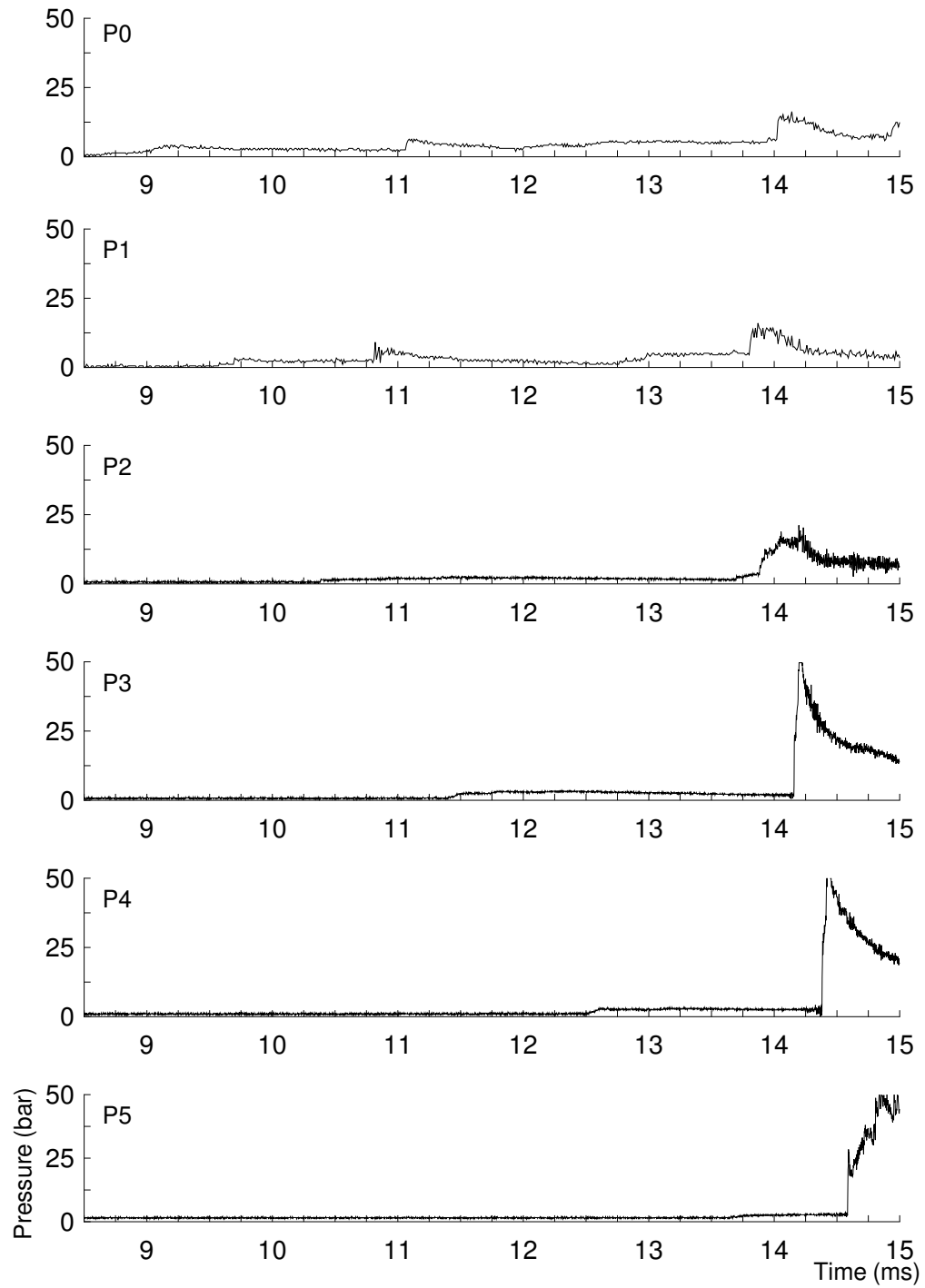


Figure D.28: Pressure history from run 028.

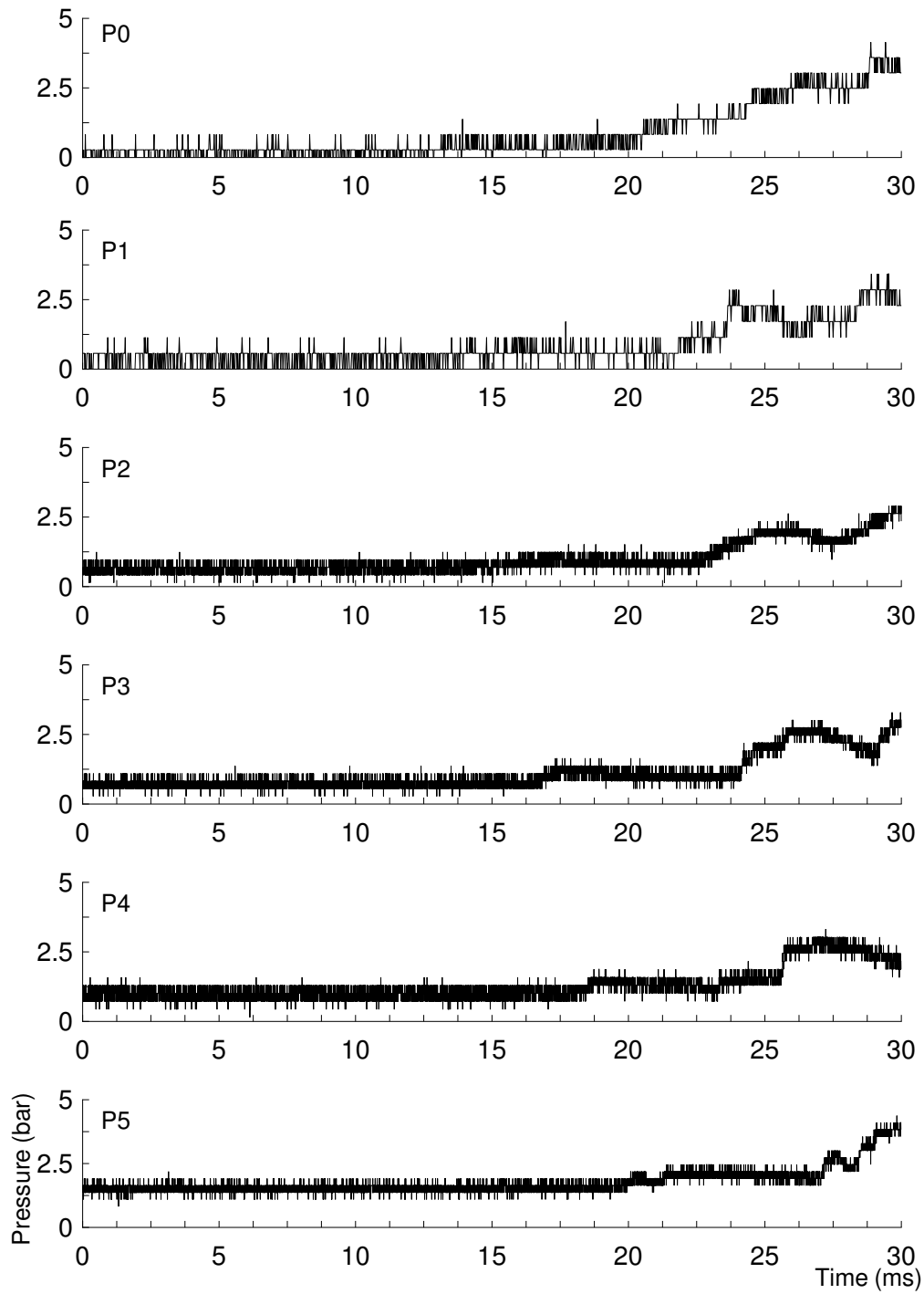


Figure D.29: Pressure history from run 029.

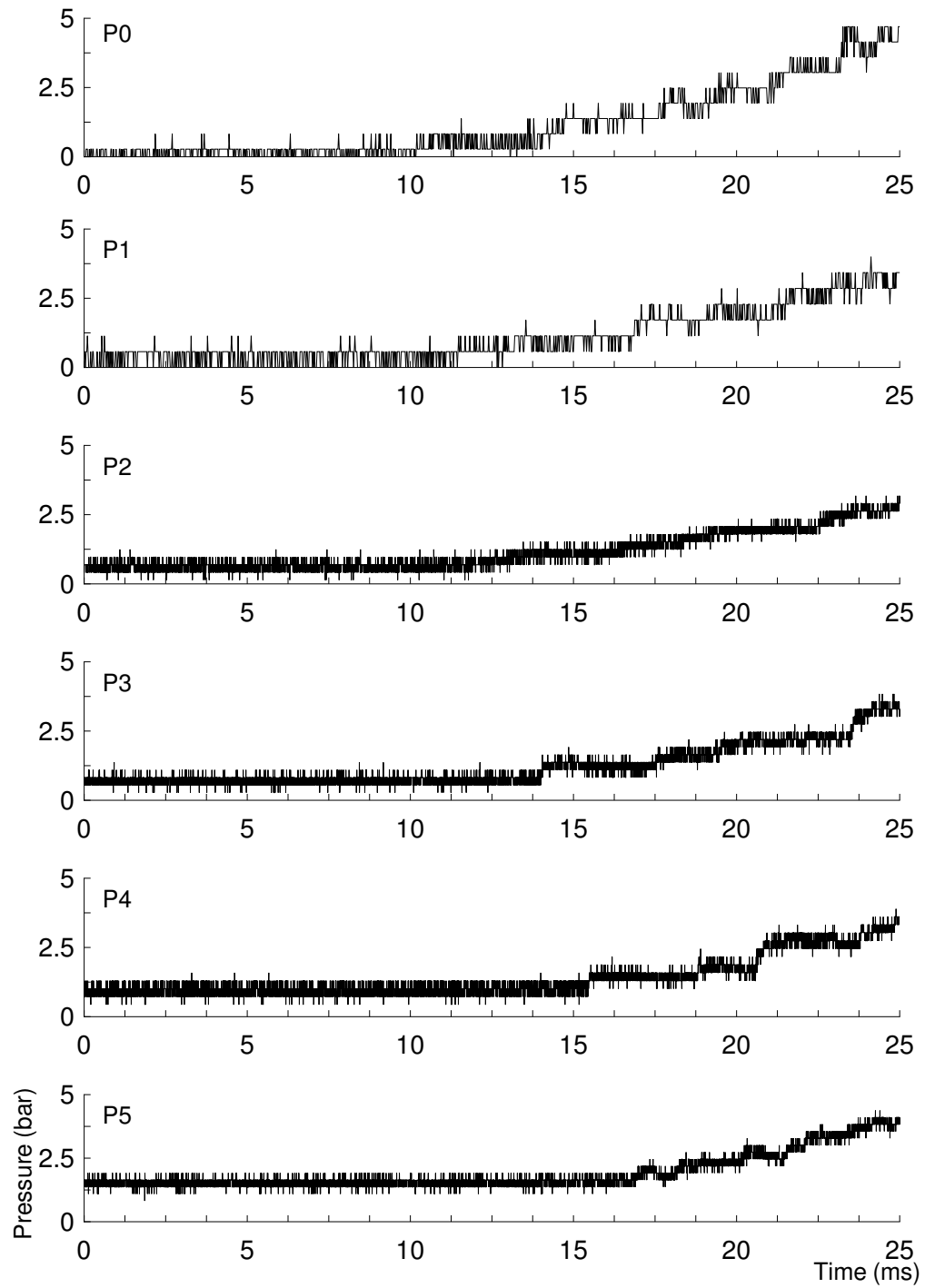


Figure D.30: Pressure history from run 030.

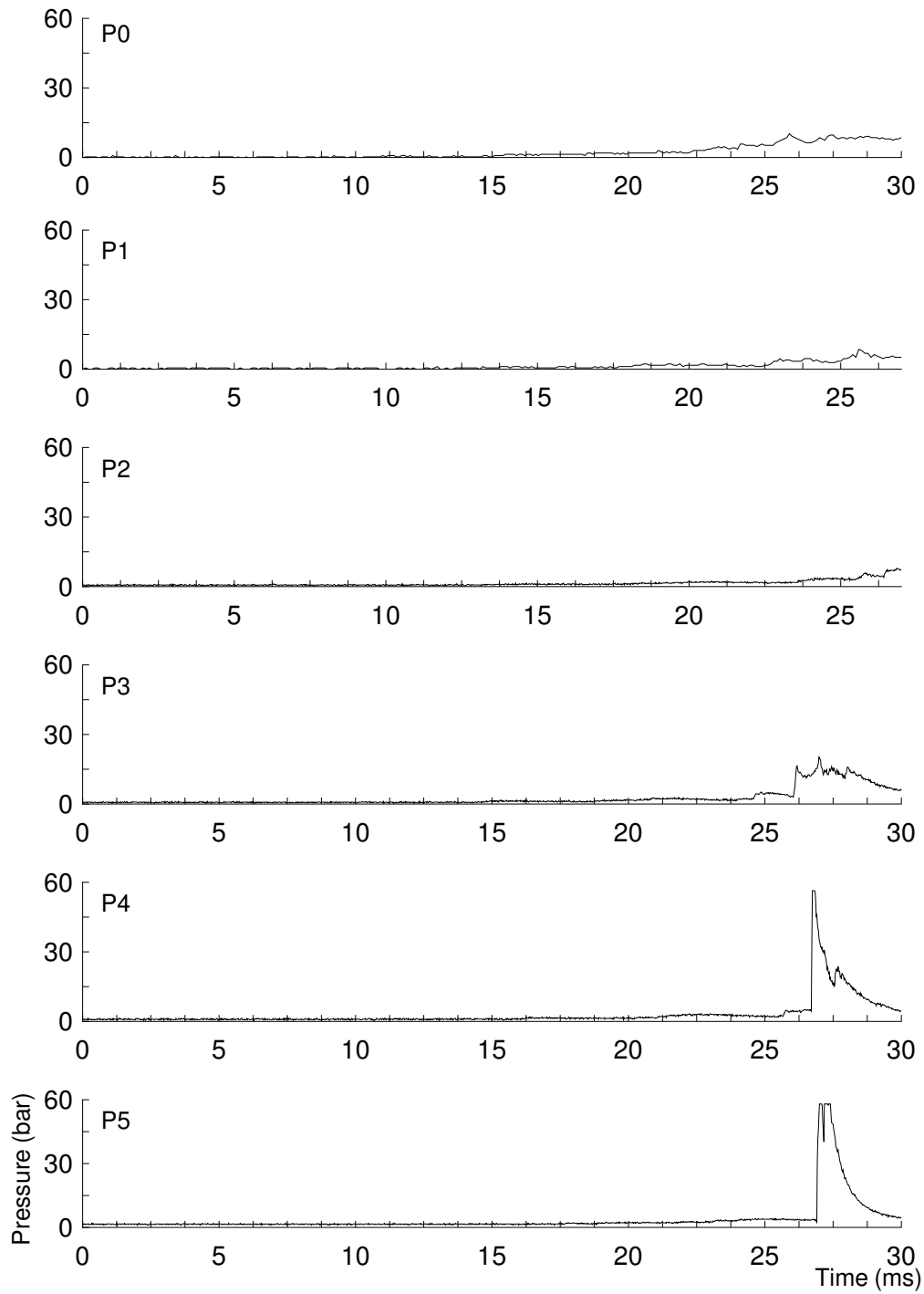


Figure D.31: Pressure history from run 031.

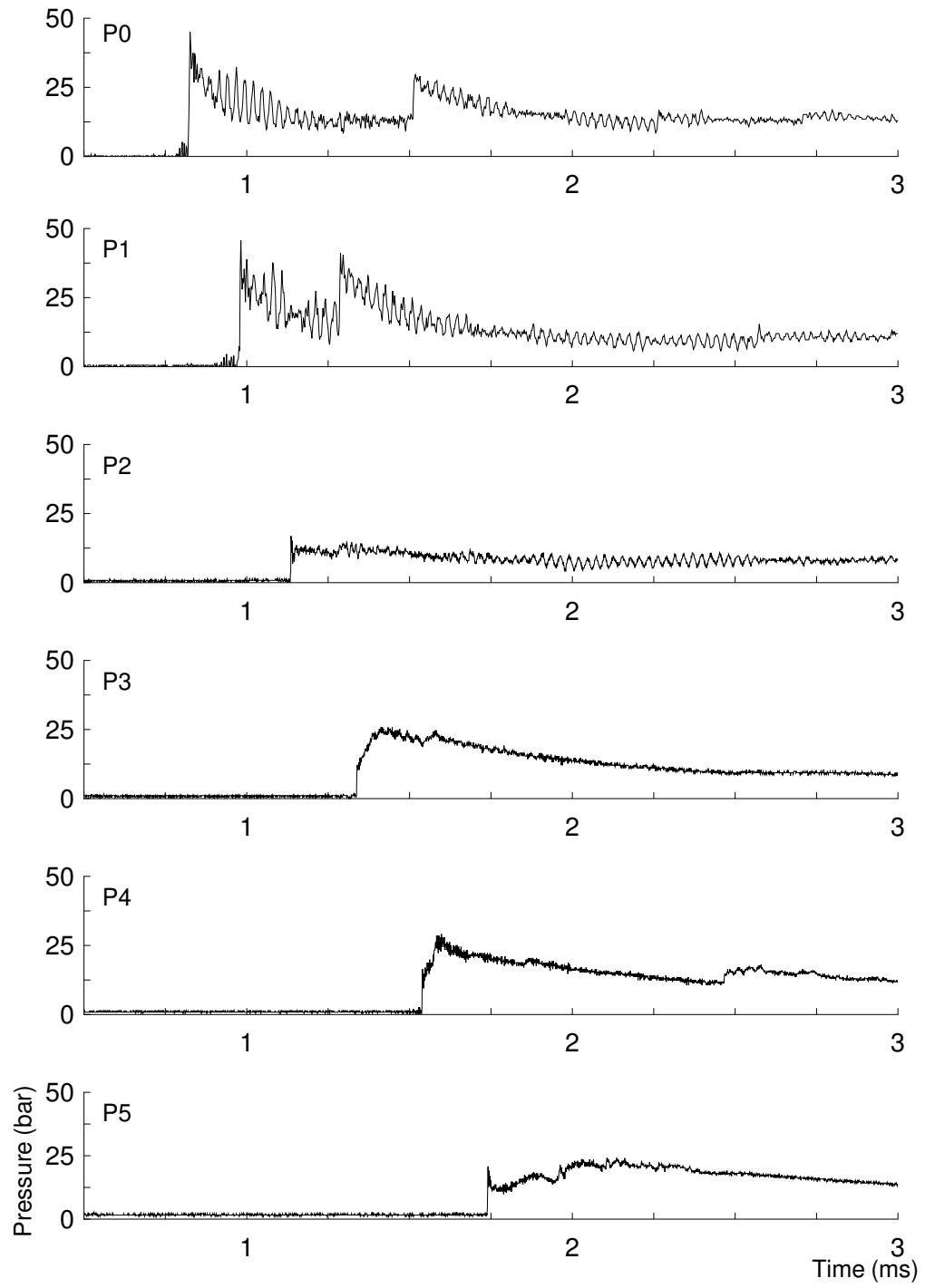


Figure D.32: Pressure history from run 032.

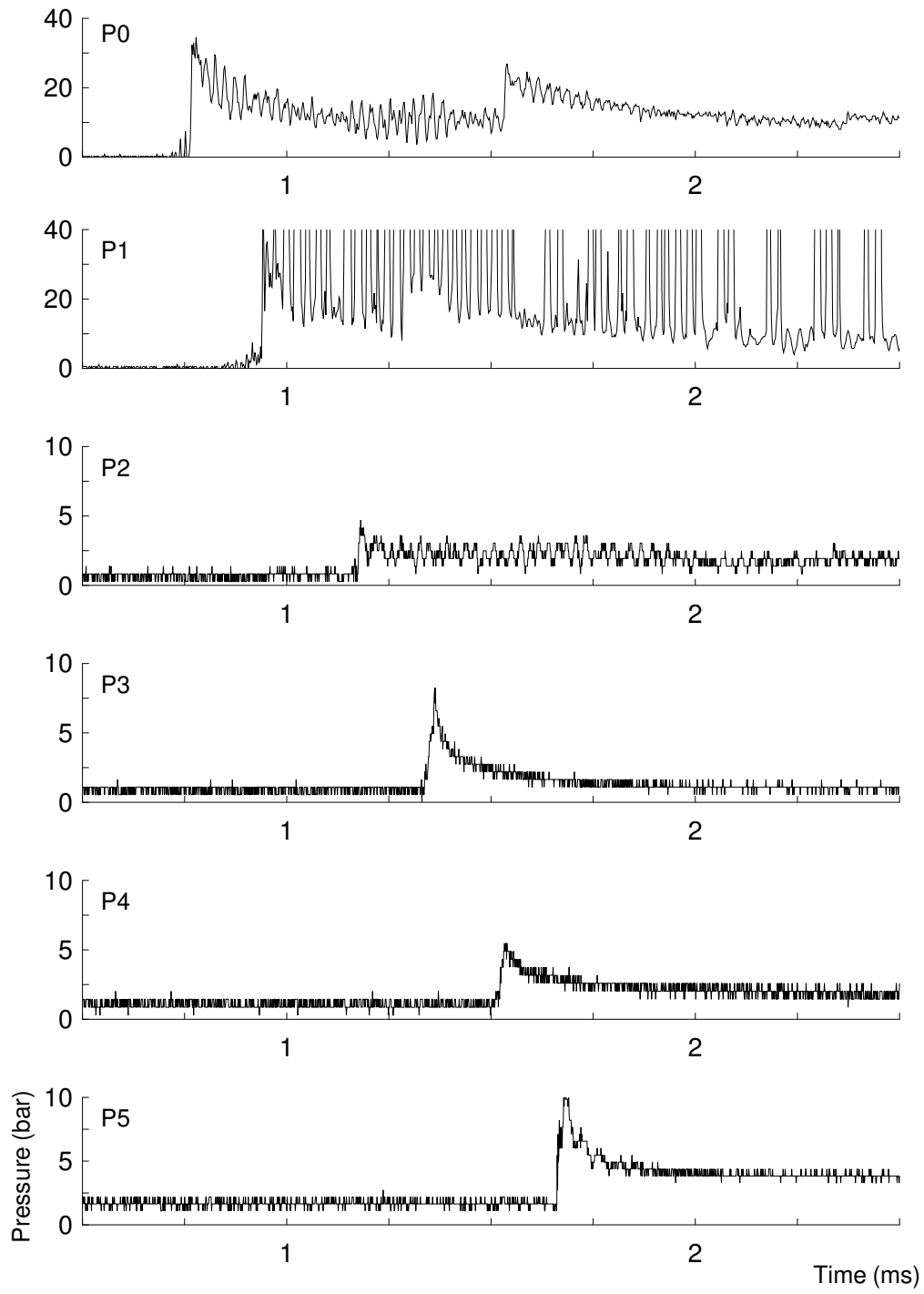


Figure D.33: Pressure history from run 033.

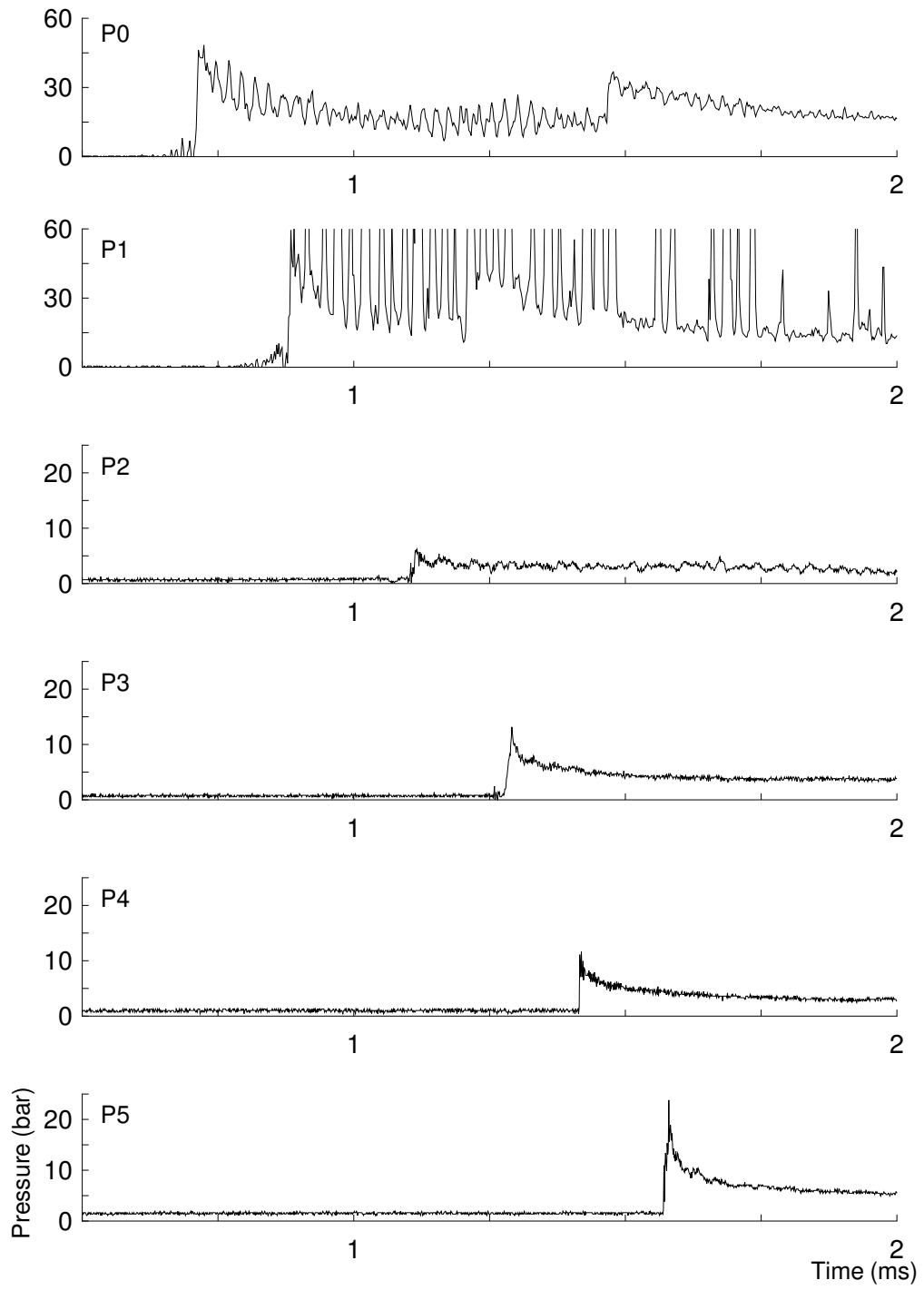


Figure D.34: Pressure history from run 034.

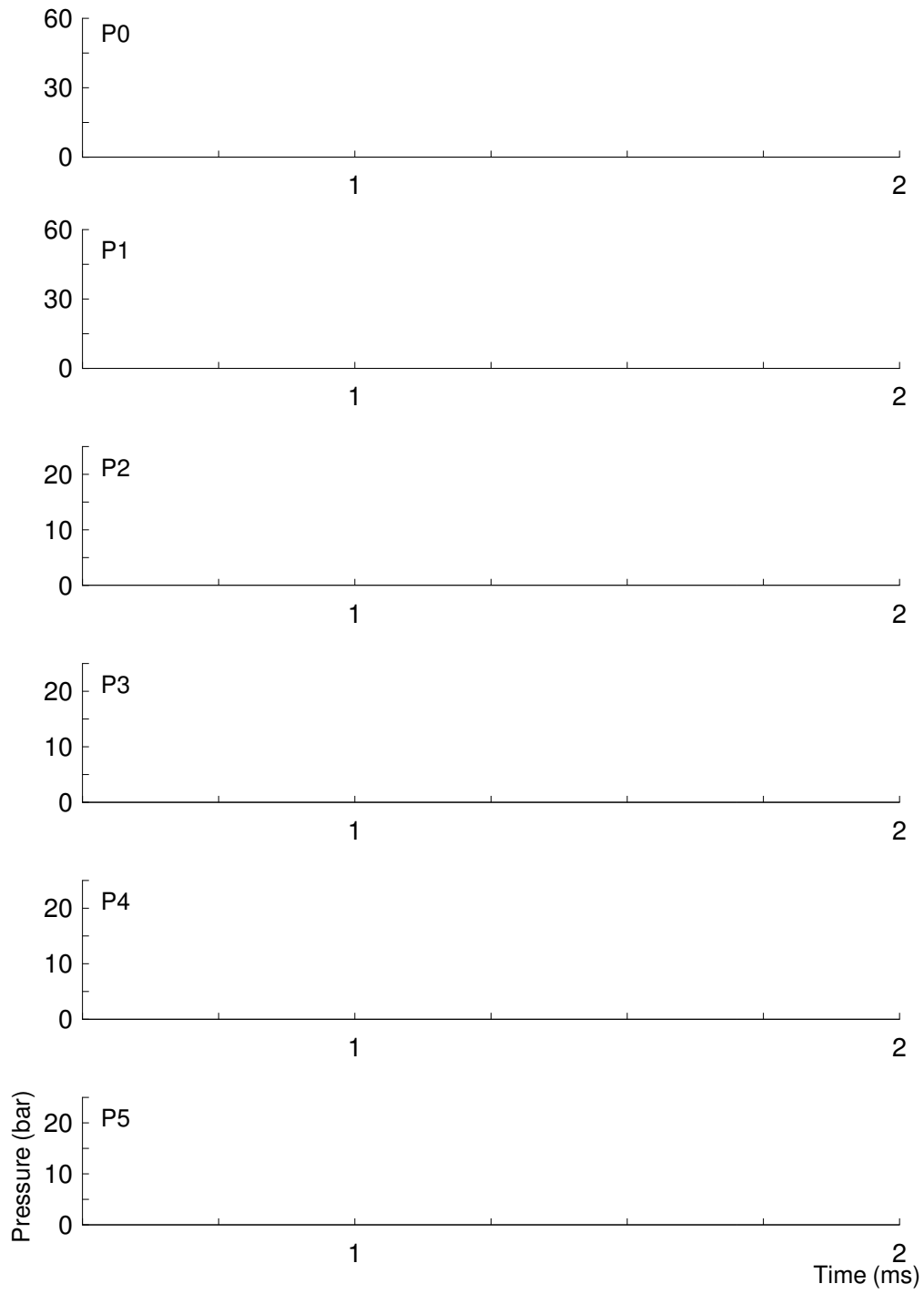


Figure D.35: Pressure history from run 035.

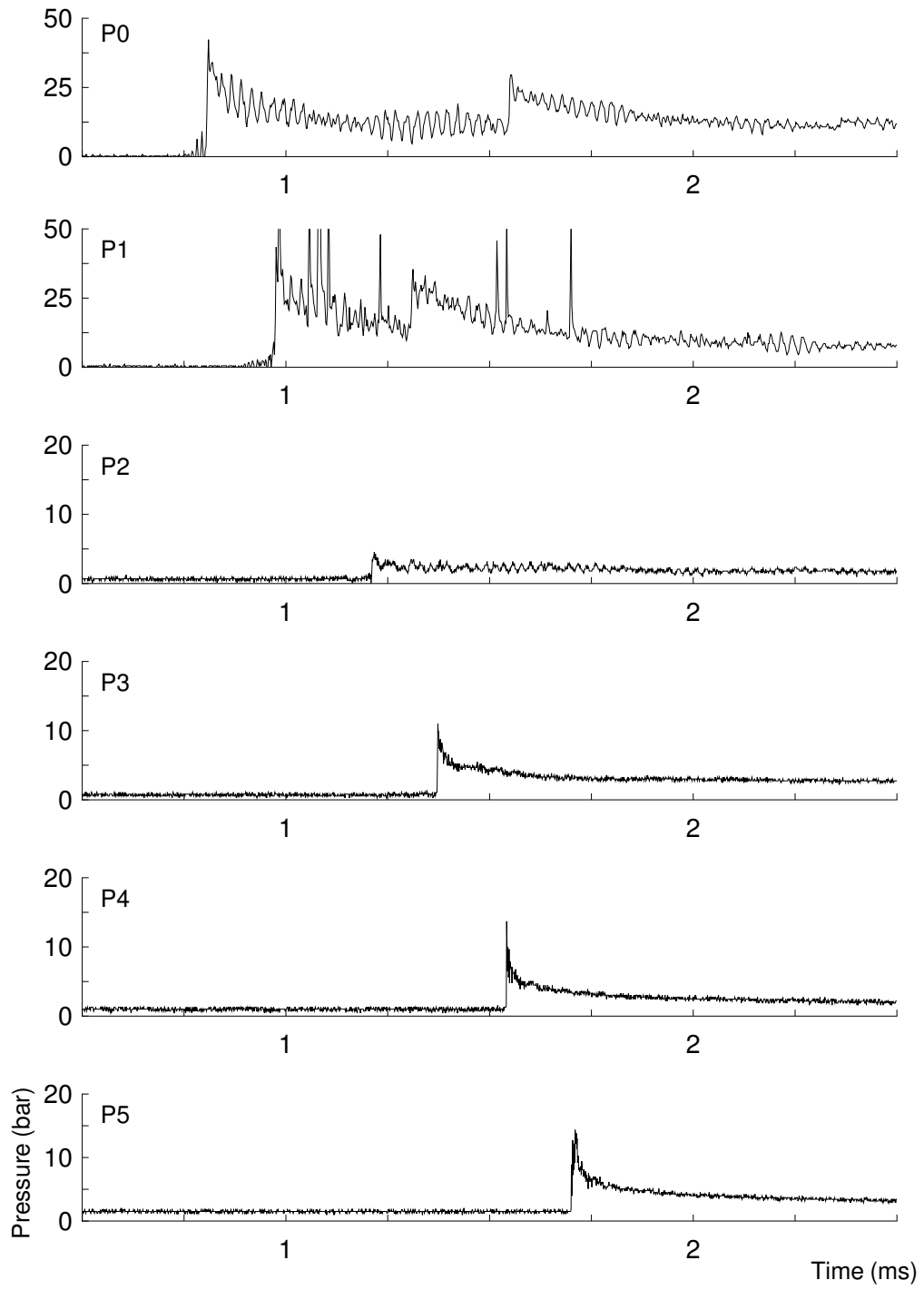


Figure D.36: Pressure history from run 036.

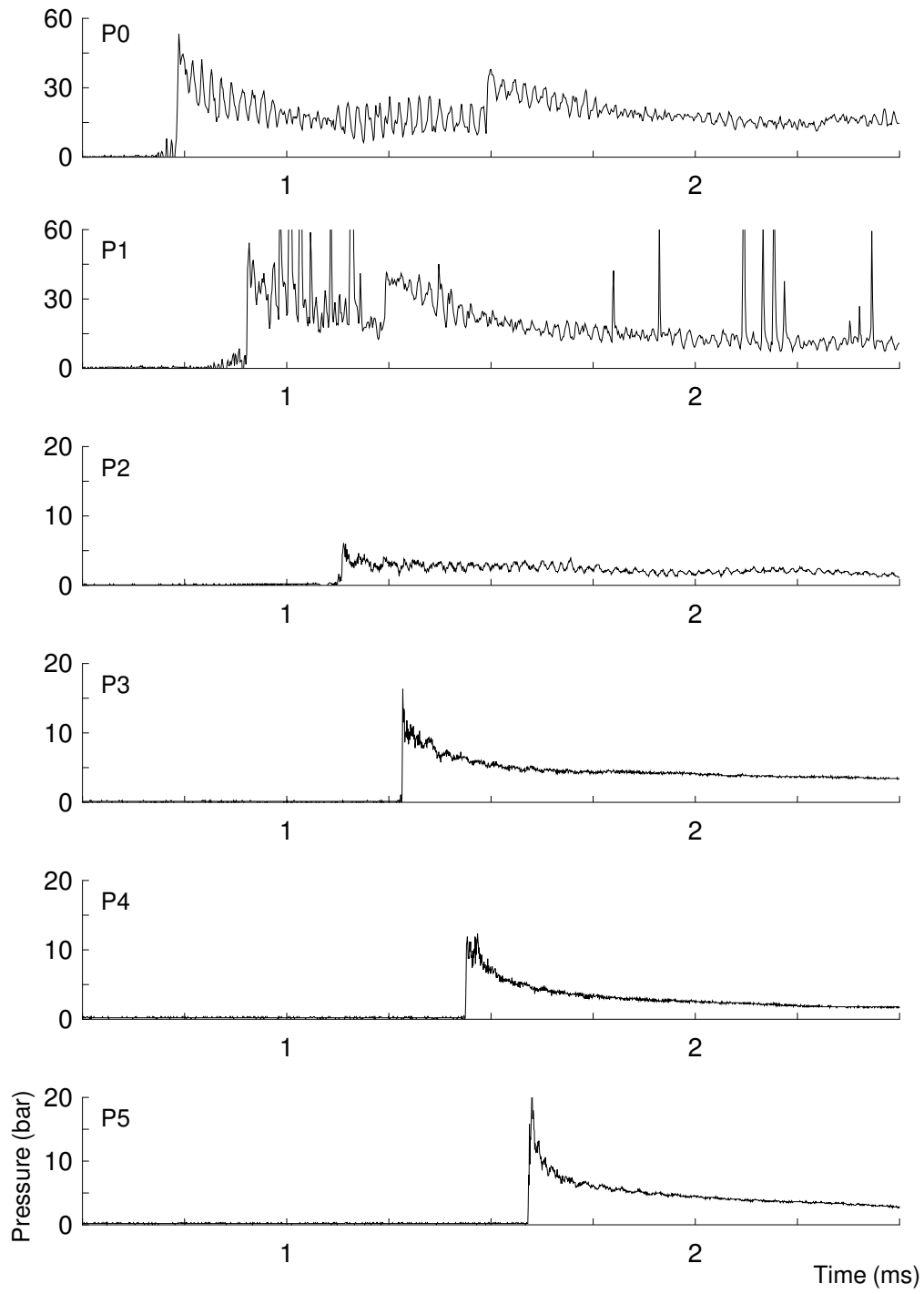


Figure D.37: Pressure history from run 037.

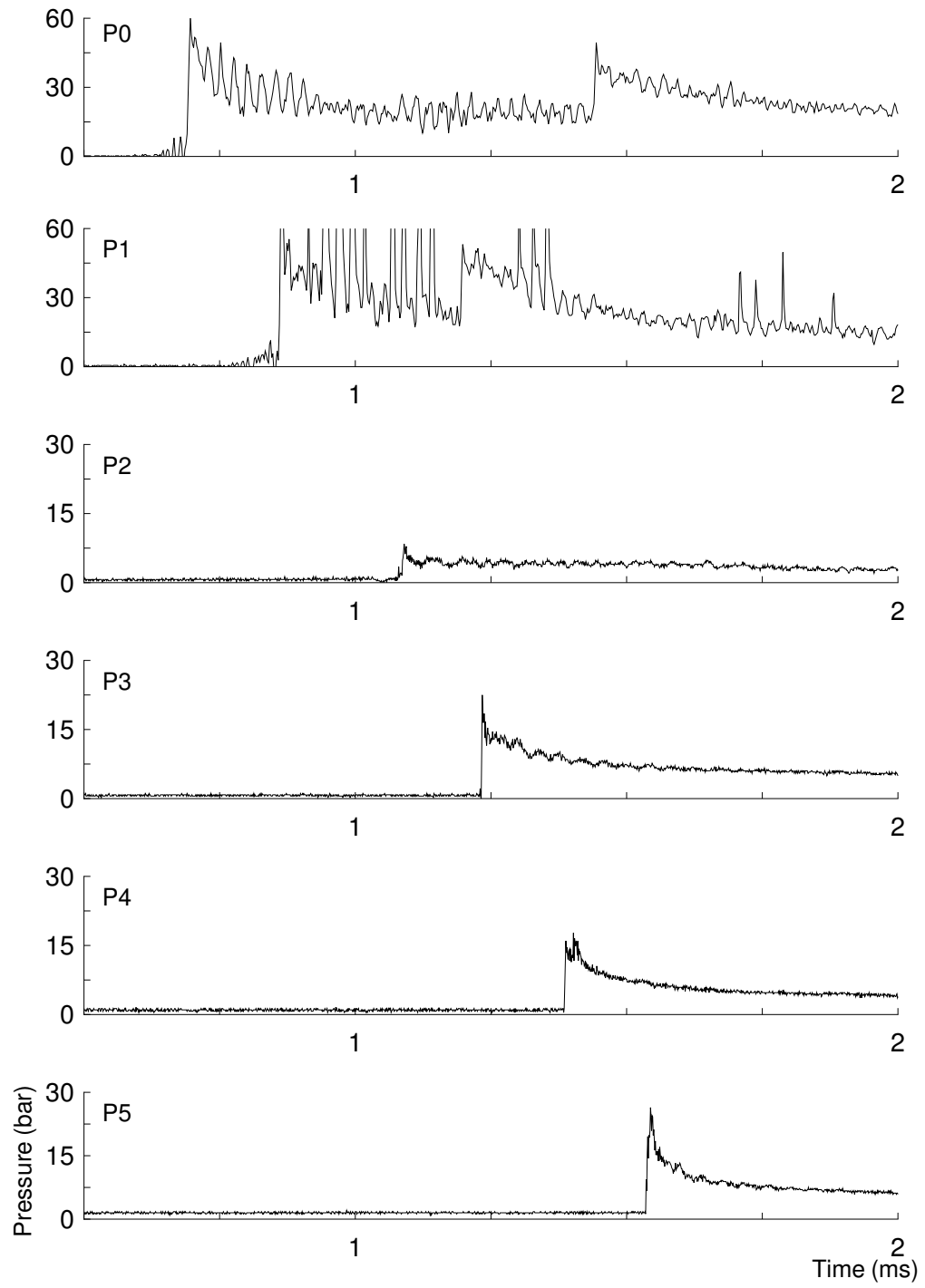


Figure D.38: Pressure history from run 038.

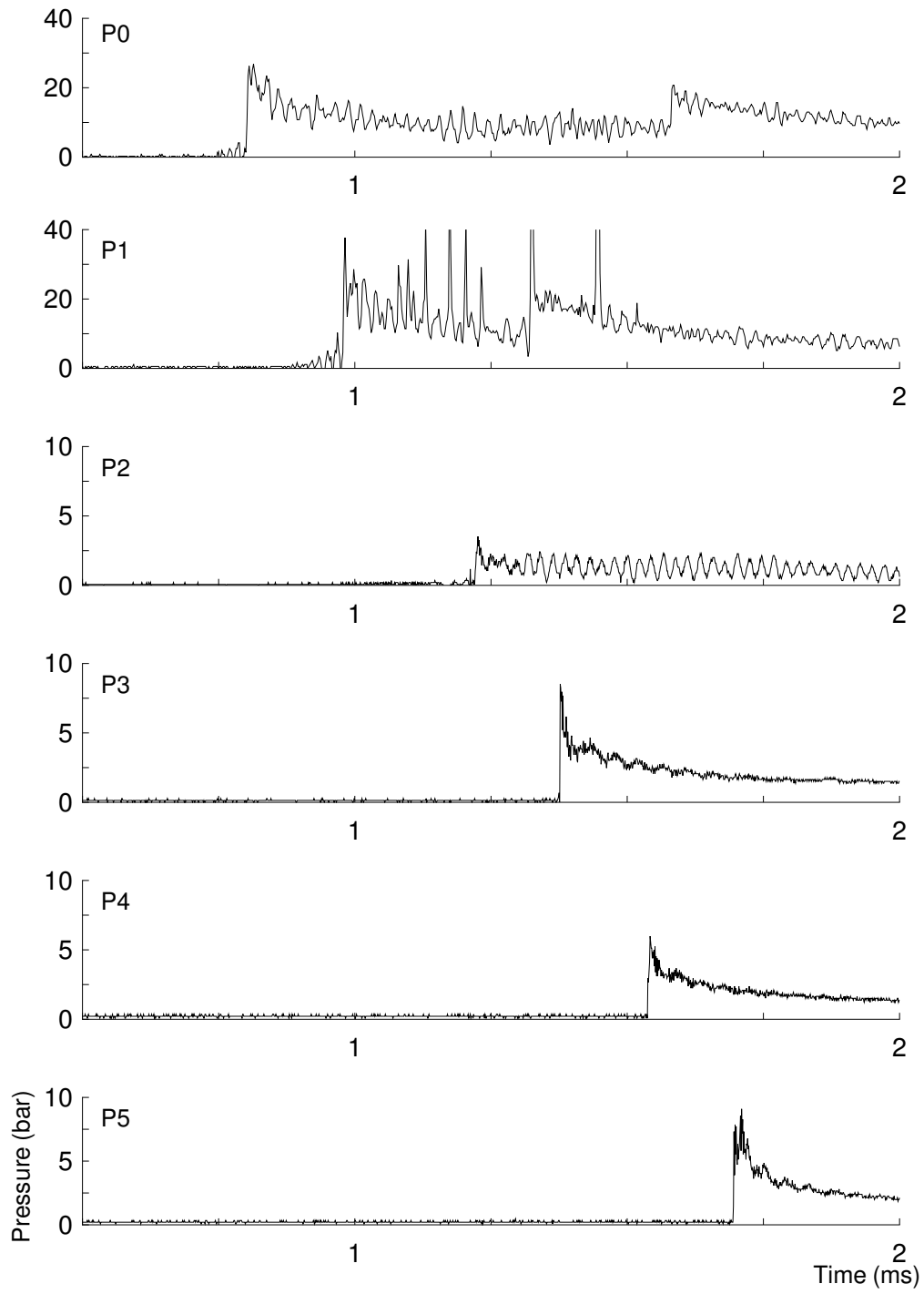


Figure D.39: Pressure history from run 039.

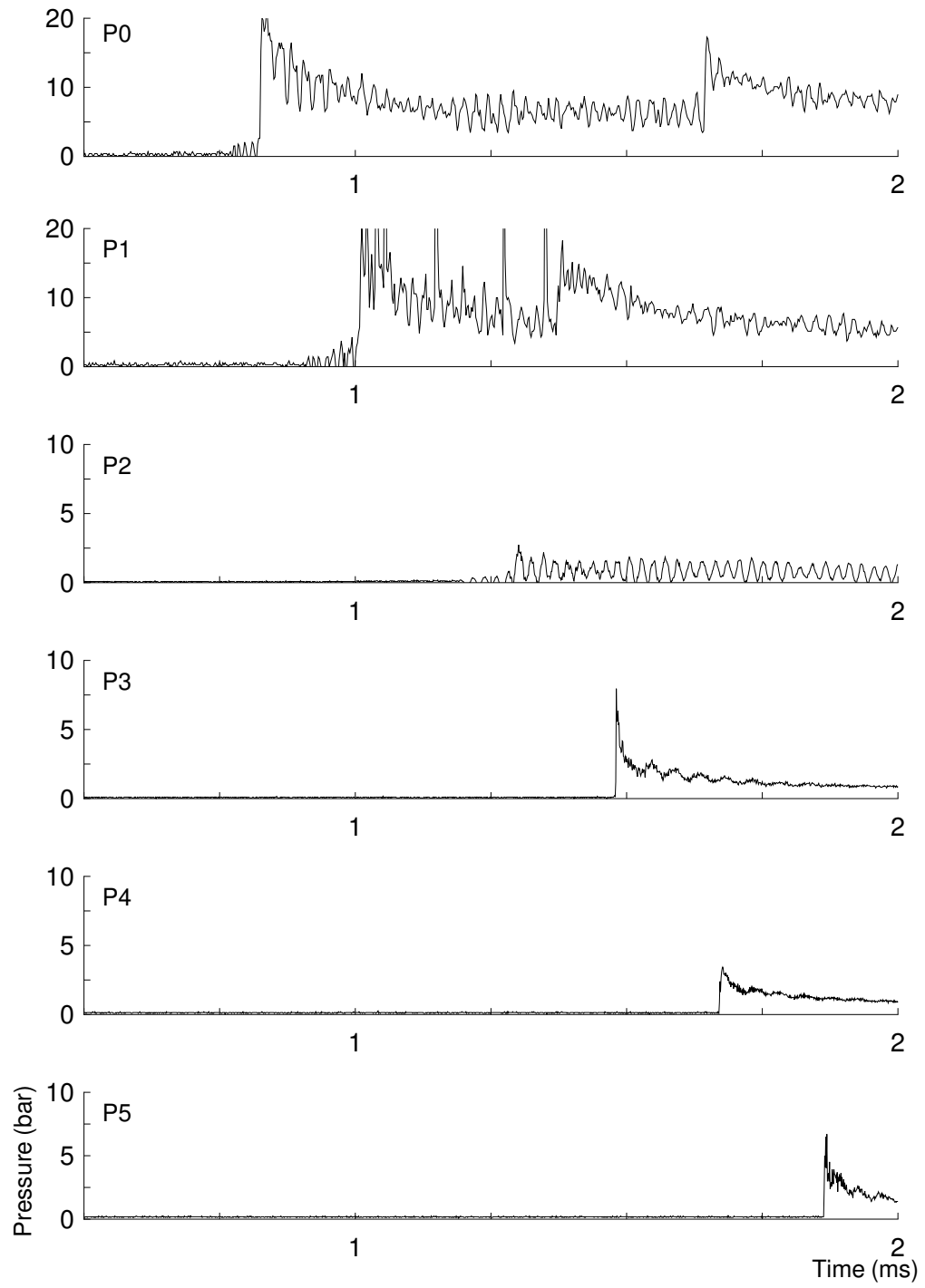


Figure D.40: Pressure history from run 040.

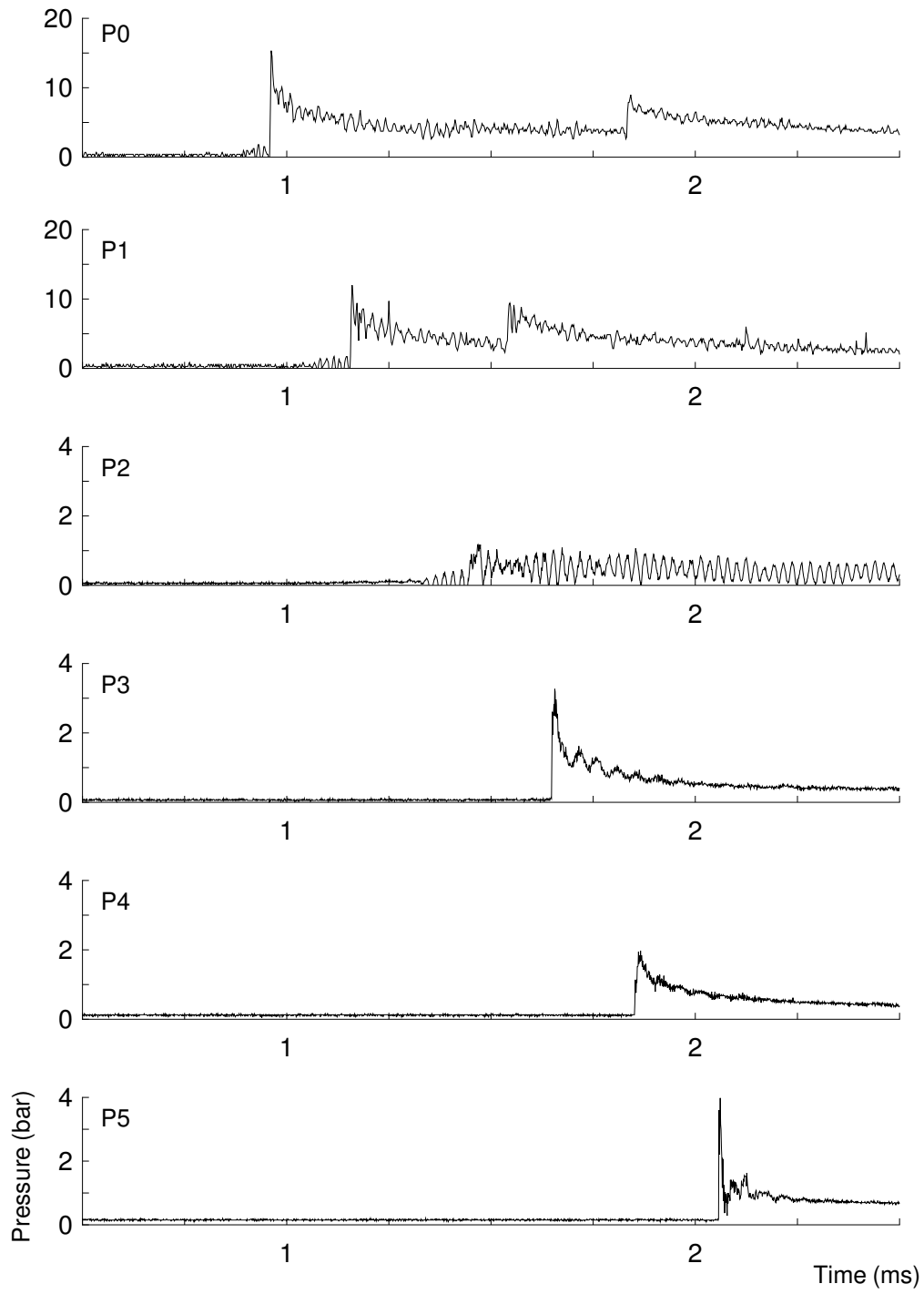


Figure D.41: Pressure history from run 041.

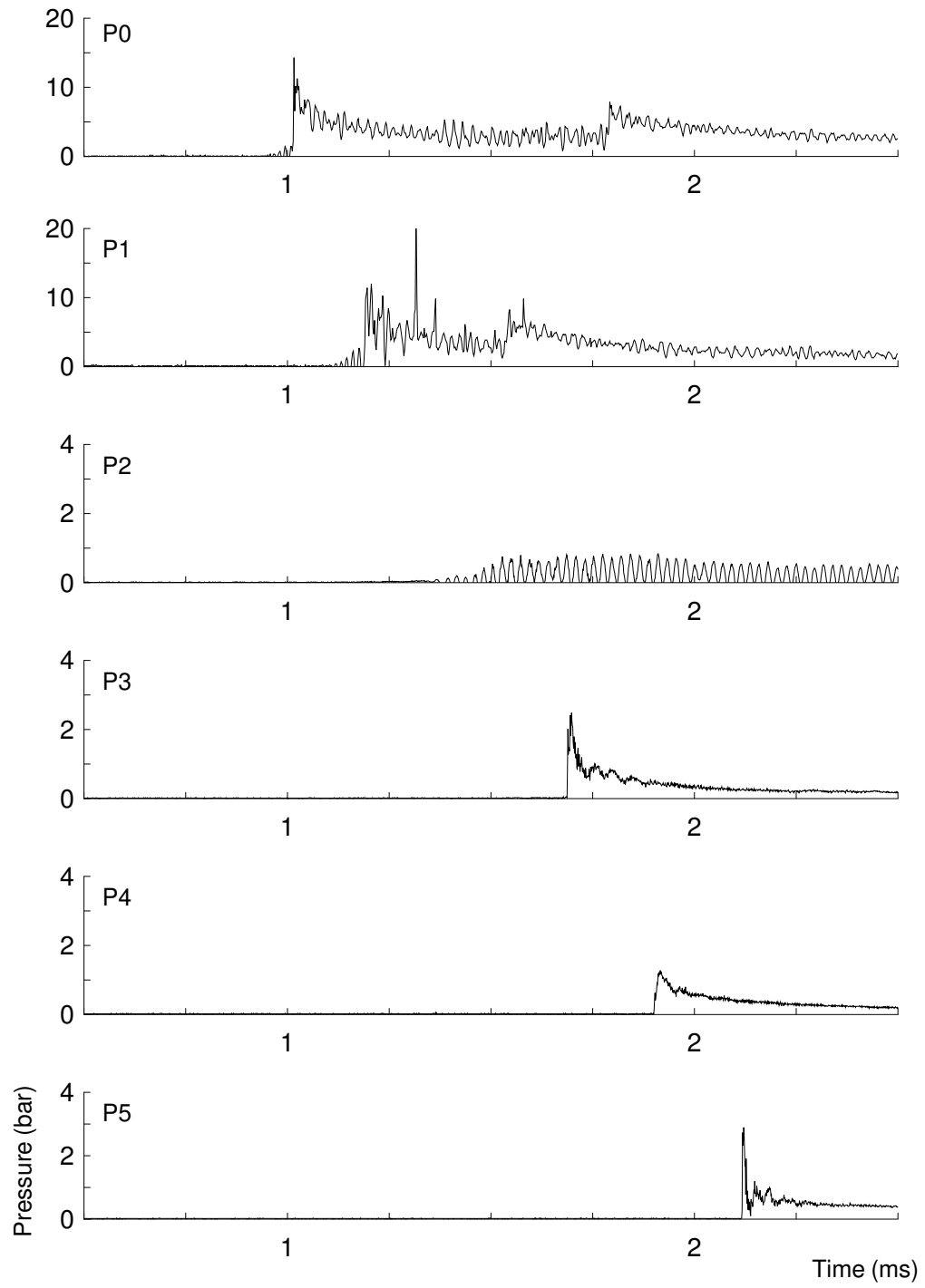


Figure D.42: Pressure history from run 042.

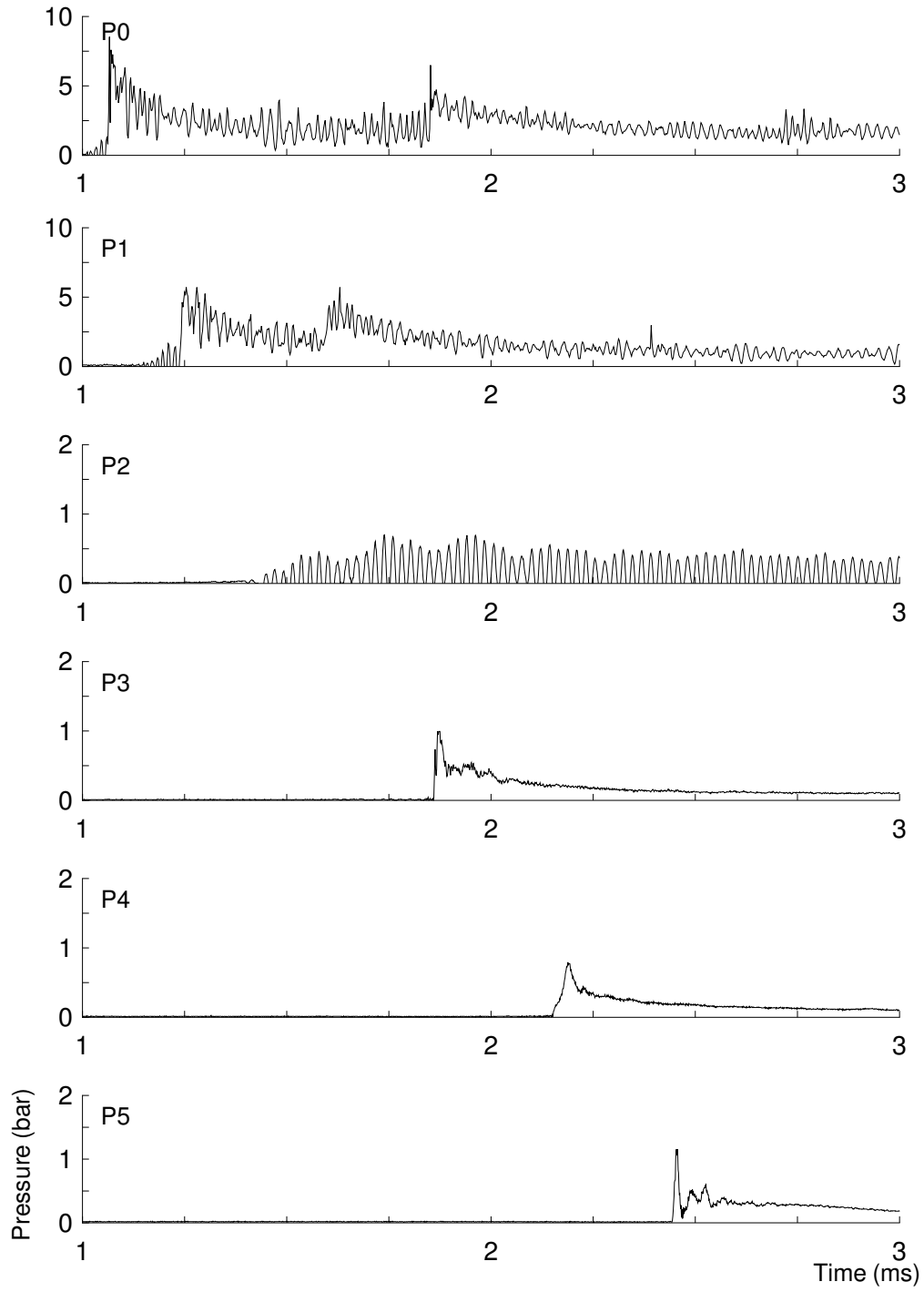


Figure D.43: Pressure history from run 043.

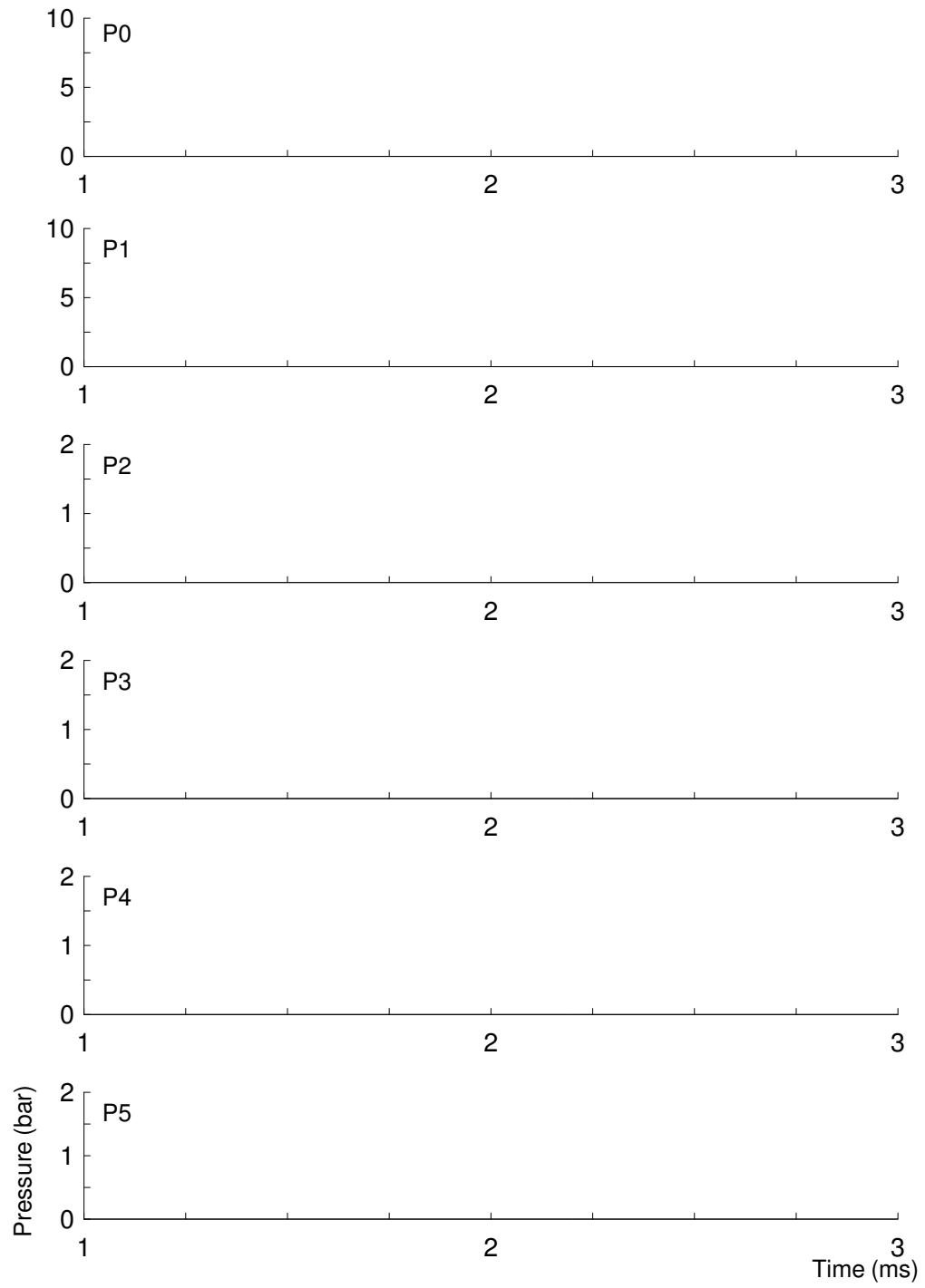


Figure D.44: Pressure history from run 044.

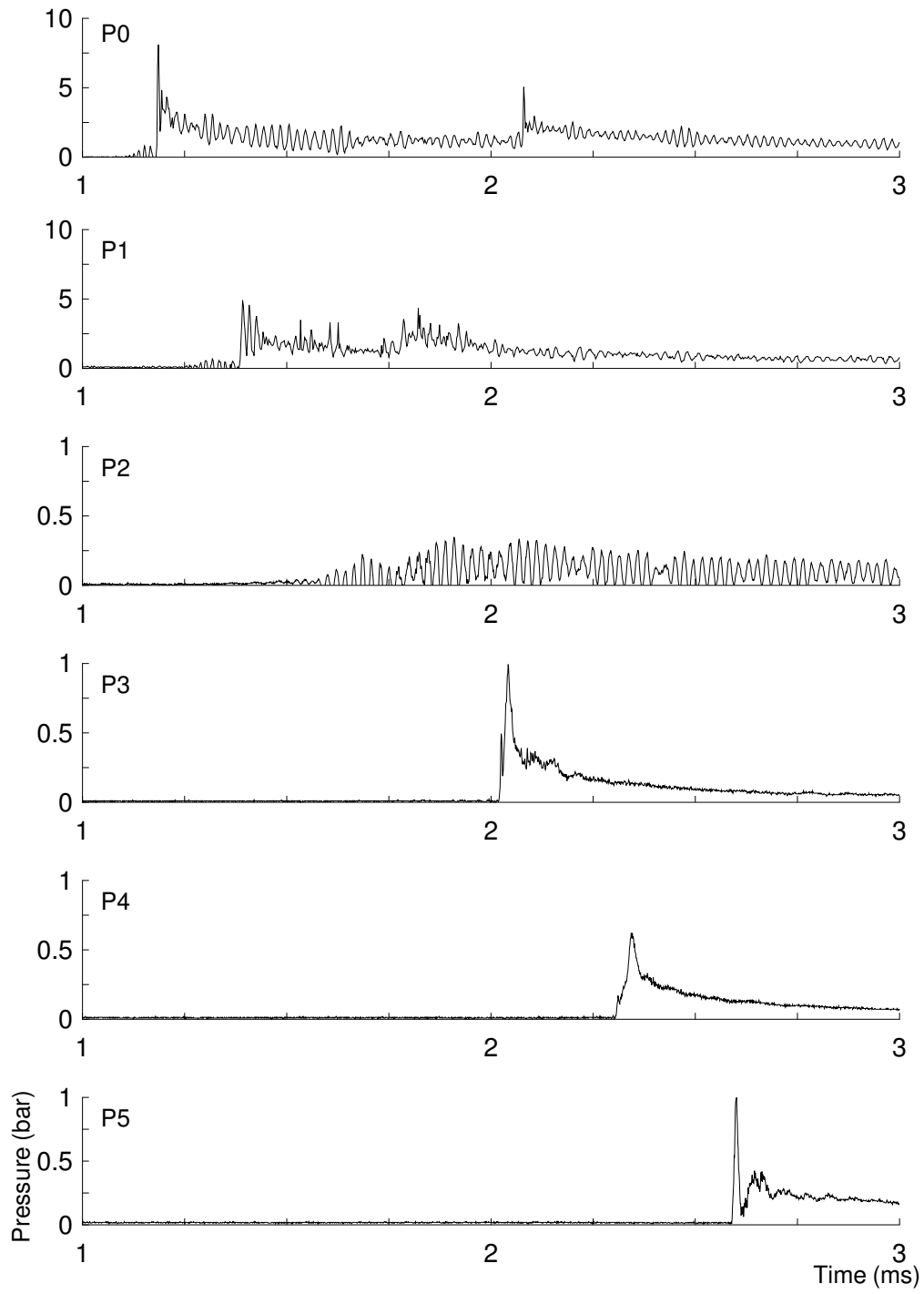


Figure D.45: Pressure history from run 045.

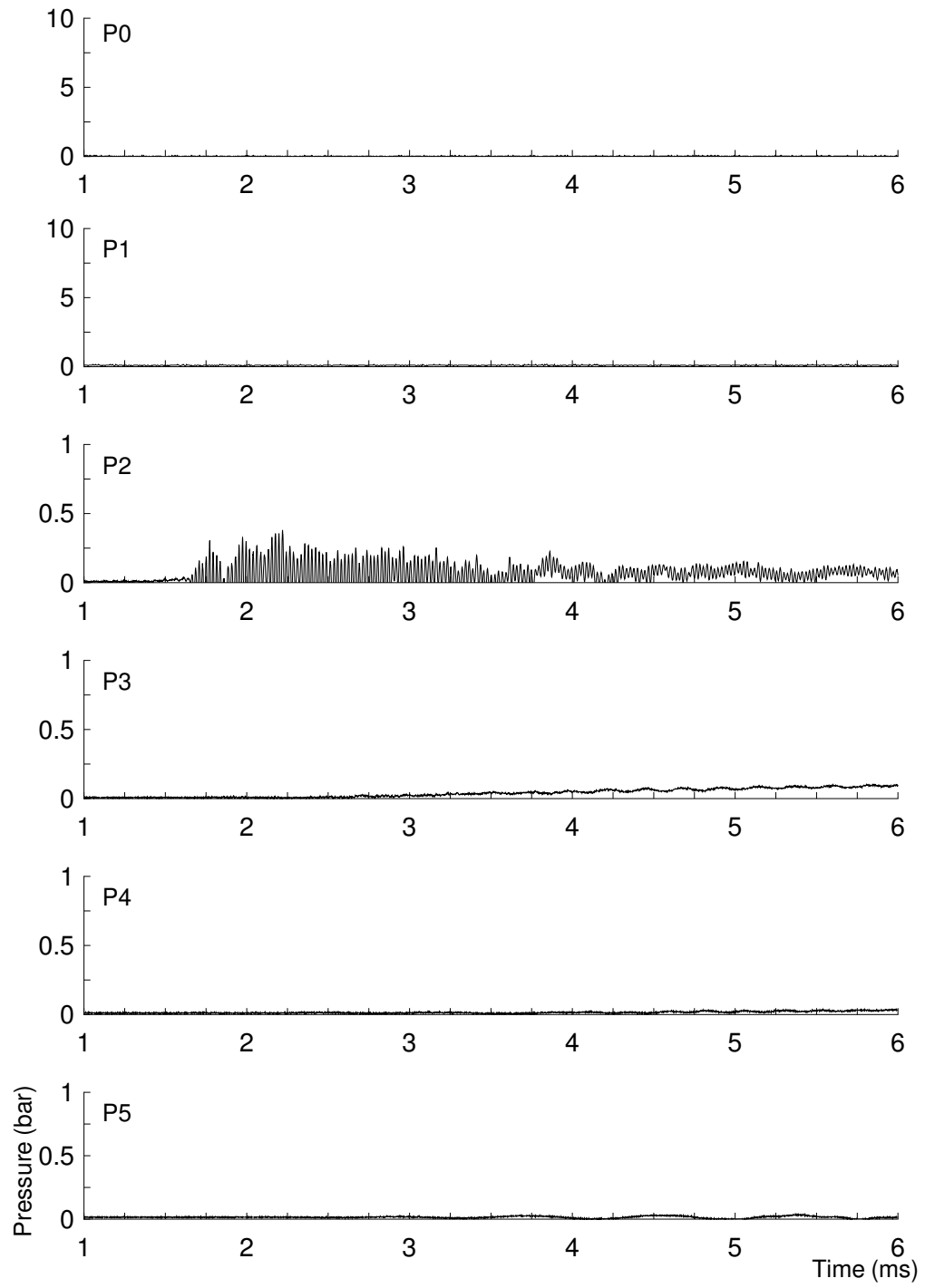


Figure D.46: Pressure history from run 046.

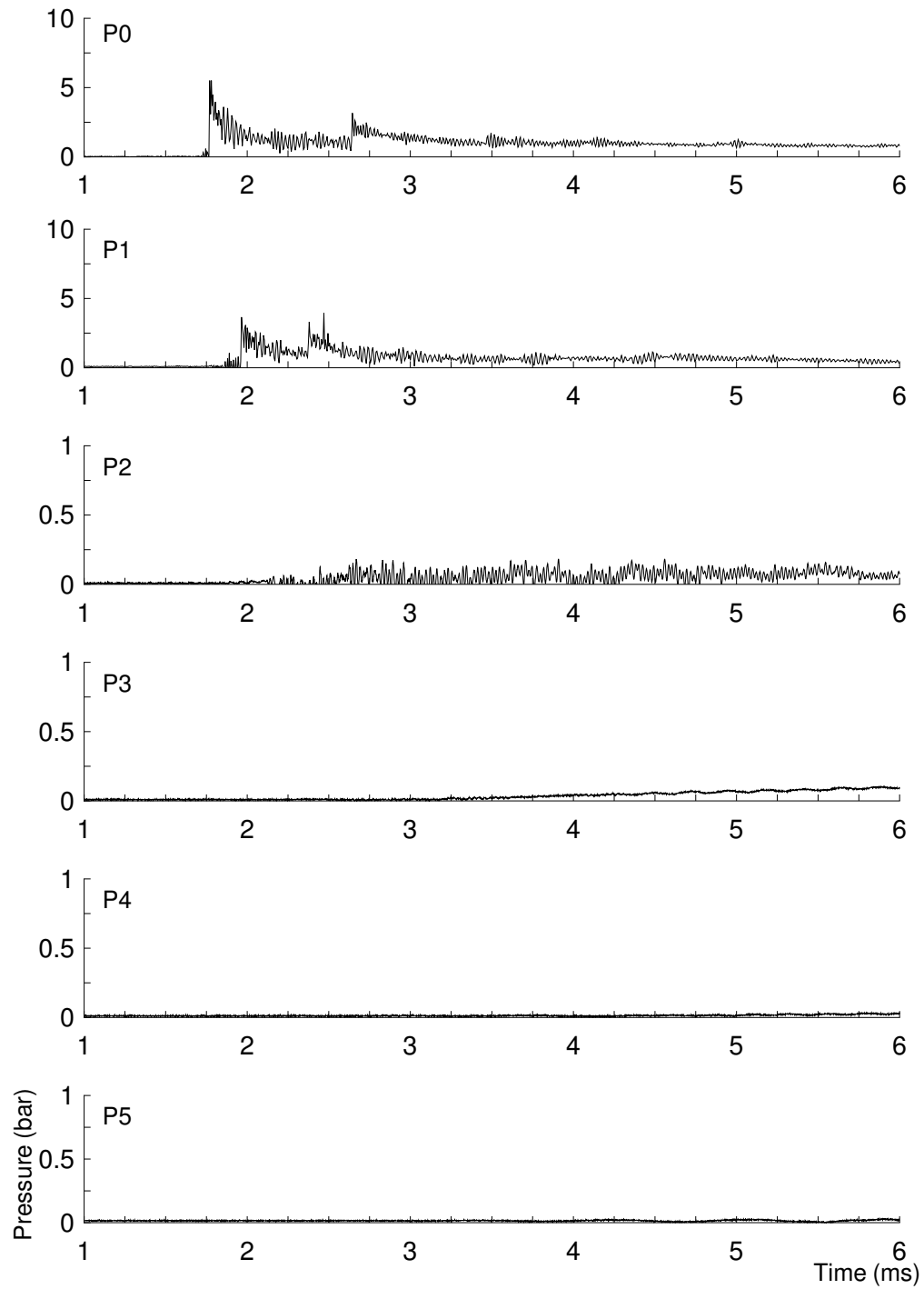


Figure D.47: Pressure history from run 047.

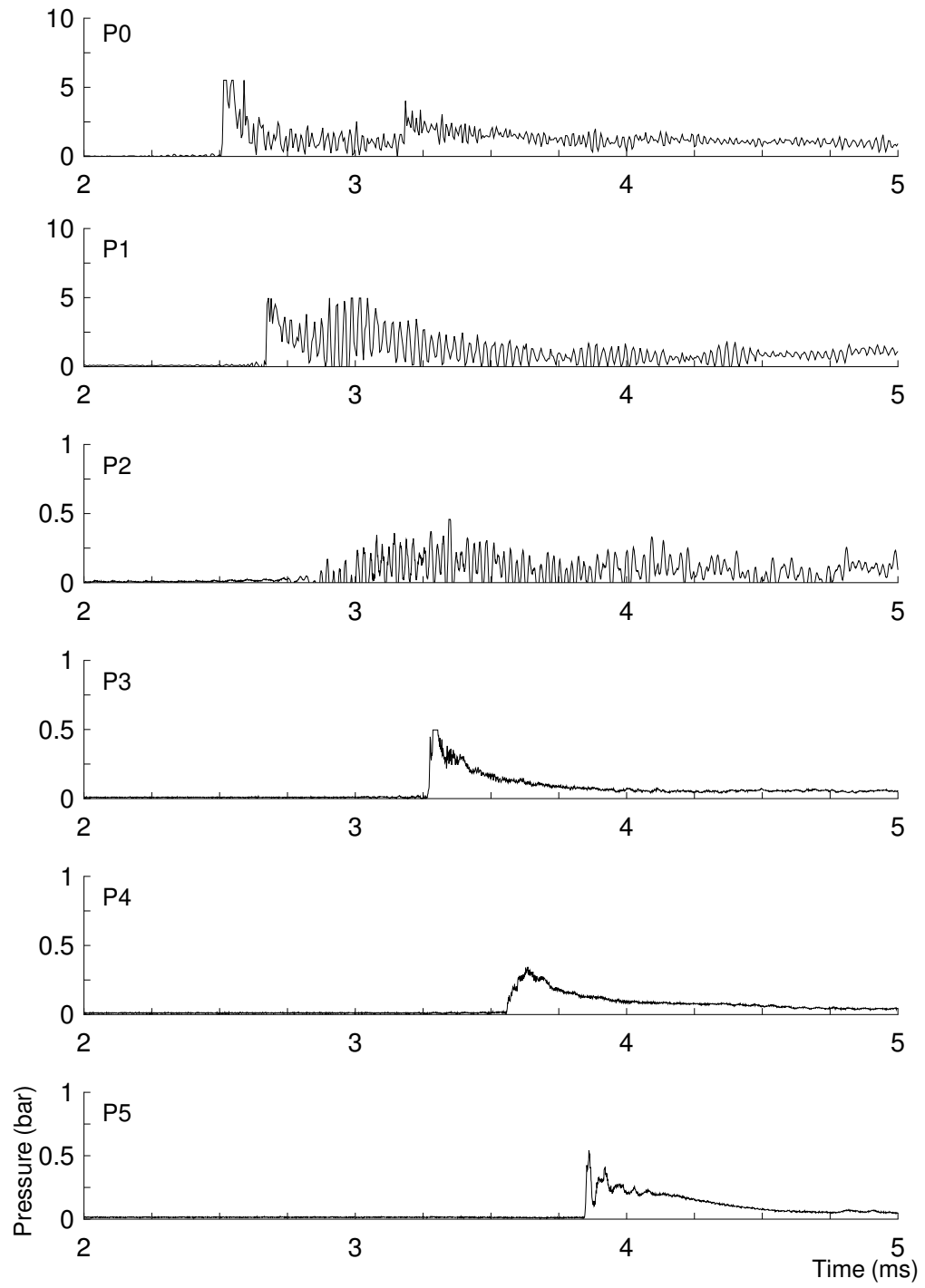


Figure D.48: Pressure history from run 048.

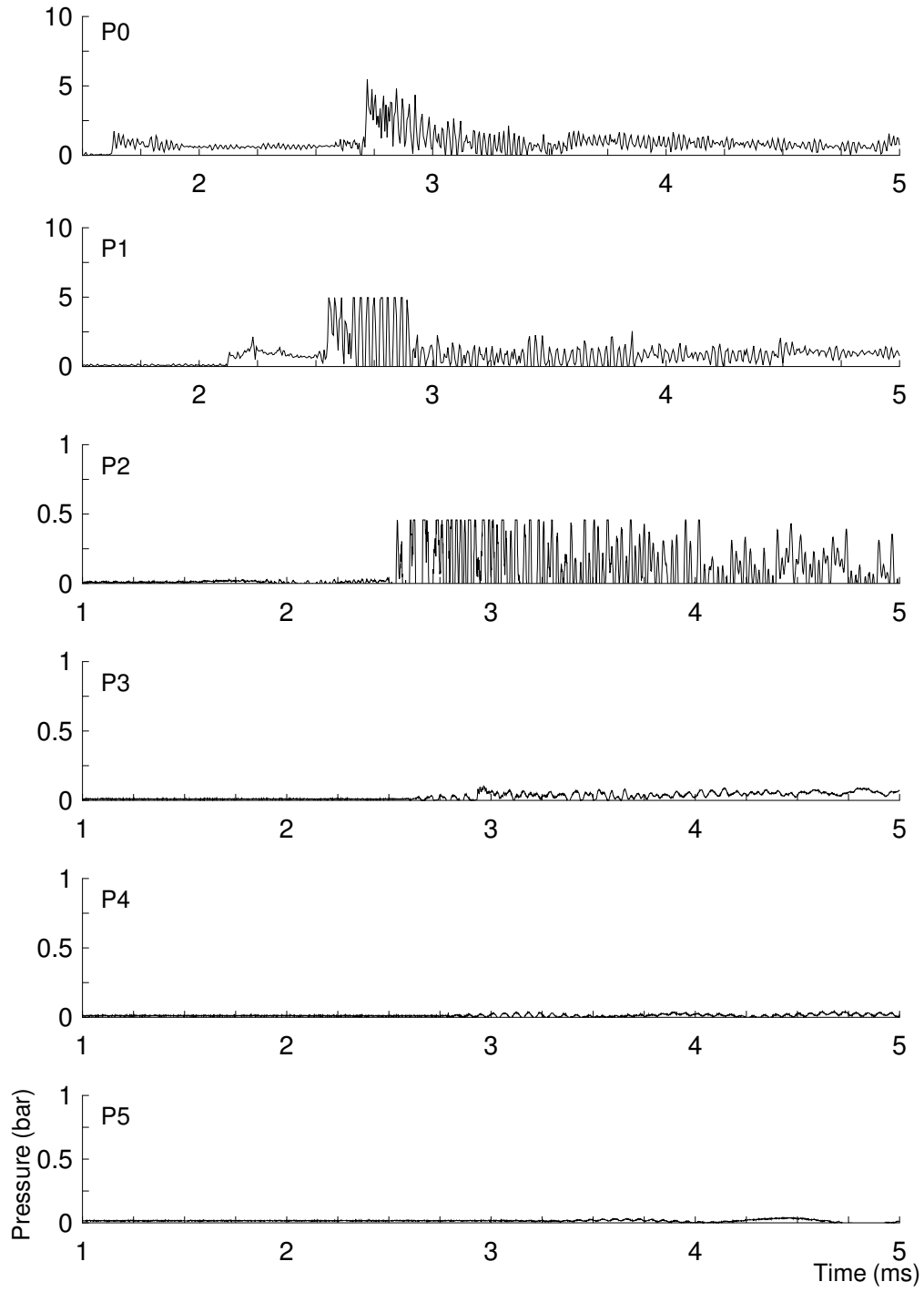


Figure D.49: Pressure history from run 049.

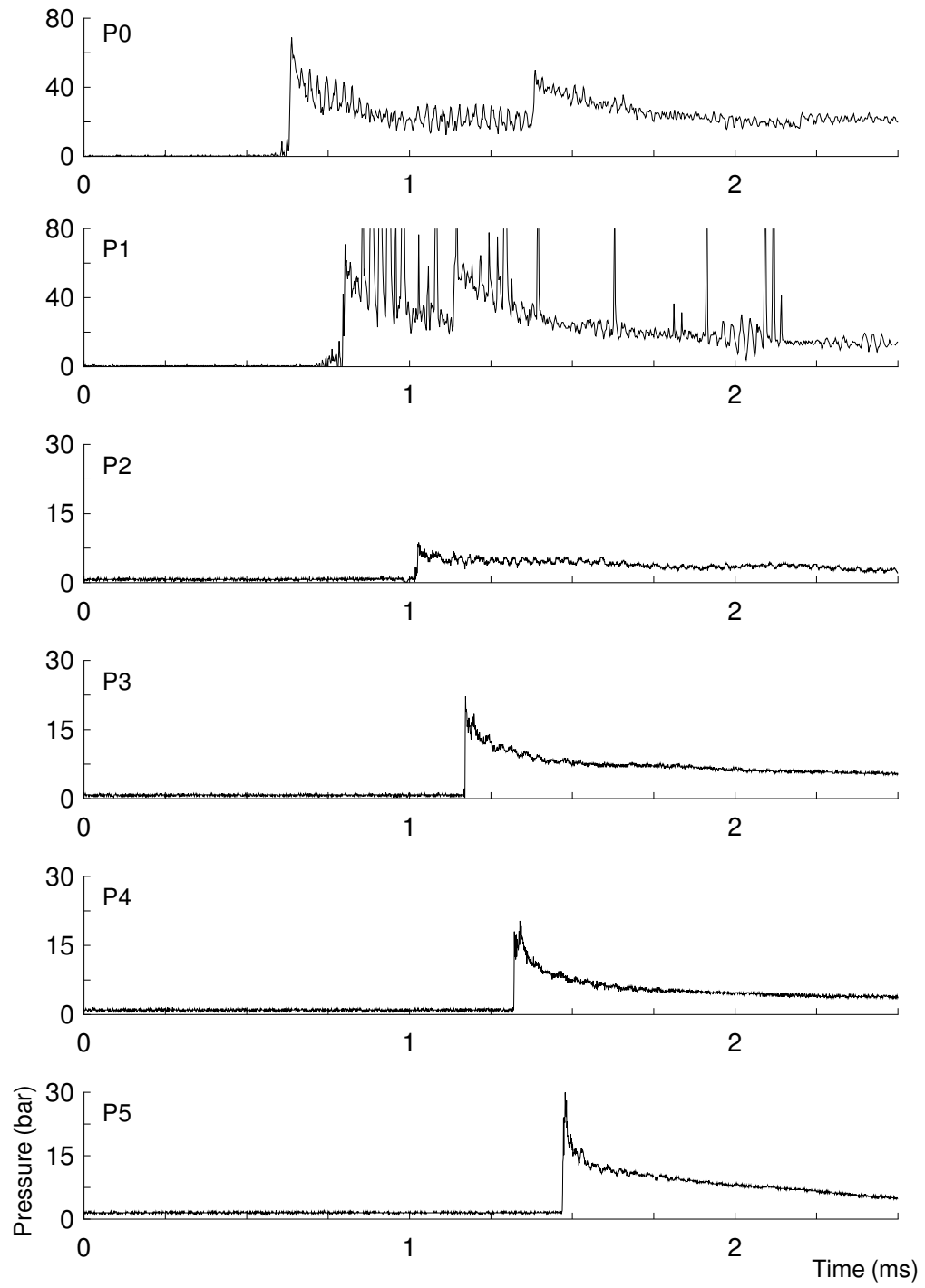


Figure D.50: Pressure history from run 050.

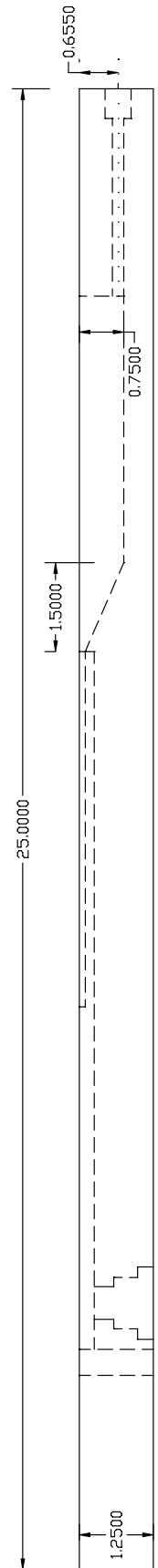


## Appendix E

### Planar Static Initiator Data

## E.1 Design Drawings





Bolt holes omitted for clarity

Figure E.2: Planar initiator design drawing - Side view.

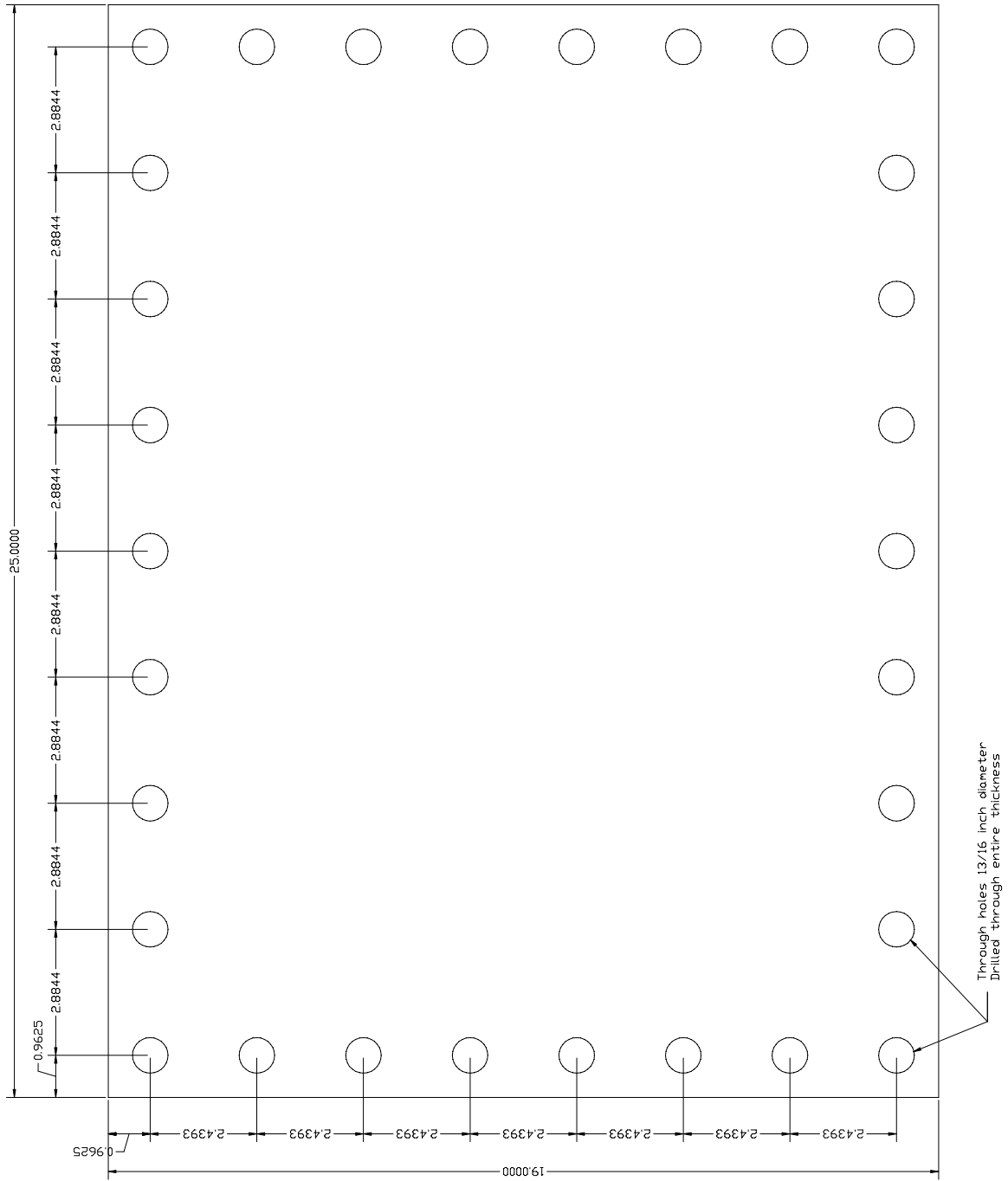


Figure E.3: Cover plate design drawing - Top view.



## E.2 Run Matrix

Run	Pressure (bar)	Fuel	N <sub>2</sub> fraction	Delay ( $\mu$ s)	Width (ns )	MCP (V)	F-ratio	Mode
11	1.000	C <sub>2</sub> H <sub>4</sub>	0.00	328	70	650	8	gated
12	1.000	C <sub>2</sub> H <sub>4</sub>	0.00	328	70	650	8	gated
13	1.000	C <sub>2</sub> H <sub>4</sub>	0.00	304	70	650	8	gated
14	1.000	C <sub>2</sub> H <sub>4</sub>	0.00	304	70	650	8	gated
15	1.000	C <sub>2</sub> H <sub>4</sub>	0.00	315	70	650	8	gated
16	1.000	C <sub>2</sub> H <sub>4</sub>	0.00	326	70	650	8	gated
17	1.000	C <sub>2</sub> H <sub>4</sub>	0.00	1210	70	650	8	gated
18	1.000	C <sub>2</sub> H <sub>4</sub>	0.00	397	70	650	8	gated
19	1.000	C <sub>3</sub> H <sub>8</sub>	0.00	378	70	650	8	gated
20	1.000	C <sub>3</sub> H <sub>8</sub>	0.00	388	70	650	8	gated
21	1.000	C <sub>3</sub> H <sub>8</sub>	0.00	398	70	650	8	gated
22	1.020	C <sub>3</sub> H <sub>8</sub>	0.00	398	70	650	11	gated
23	1.000	C <sub>3</sub> H <sub>8</sub>	0.00	395	70	650	11	gated
24	1.004	C <sub>3</sub> H <sub>8</sub>	0.00	410	70	650	8	gated
25	1.004	C <sub>3</sub> H <sub>8</sub>	0.00	398	70	650	8	gated
26	1.000	C <sub>3</sub> H <sub>8</sub>	0.00	10	70	550	32	gated
27	1.000	C <sub>3</sub> H <sub>8</sub>	0.00	10	20	500	32	gated
28	0.980	C <sub>3</sub> H <sub>8</sub>	0.00	10	10	700	5.6	gated
29	0.978	C <sub>3</sub> H <sub>8</sub>	0.00	370	10	550	5.6	gated
30	0.977	C <sub>3</sub> H <sub>8</sub>	0.00	390	70	650	2	gated
31	0.976	C <sub>3</sub> H <sub>8</sub>	0.00	365	70	650	2.8	gated
32	0.980	C <sub>3</sub> H <sub>8</sub>	0.00	365	70	700	2.8	gated
33	0.978	C <sub>3</sub> H <sub>8</sub>	0.00	340	70	700	2.8	gated
34	1.000	C <sub>3</sub> H <sub>8</sub>	0.00	385	70	700	32	shutter
35	1.002	C <sub>3</sub> H <sub>8</sub>	0.00	385	70	800	32	shutter
36	1.000	C <sub>3</sub> H <sub>8</sub>	0.00	375	70	900	11	shutter
37	1.000	C <sub>3</sub> H <sub>8</sub>	0.00	375	70	500	11	shutter
38	0.958	C <sub>3</sub> H <sub>8</sub>	0.00	375	5	500	32	shutter
39	1.000	C <sub>2</sub> H <sub>4</sub>	0.00	320	5	500	32	shutter
40	1.003	C <sub>2</sub> H <sub>4</sub>	0.00	300	5	500	32	shutter

Table E.1: Experimental properties of each run. All mixtures were stoichiometric fuel-oxygen. Some mixtures were diluted with nitrogen; “N<sub>2</sub> fraction is the volume fraction of nitrogen in the mixture. The last five columns are camera variables. “Delay” is the interval between either the firing of the spark plug (runs 1-24) or the wave exhaust from the small channels (runs 24-43) and time of image acquisition. “Width” is the integration time of the intensified CCD camera and “MCP” corresponds to the intensifier voltage setting.

Run	Pressure (bar)	Fuel	N <sub>2</sub> fraction	Delay ( $\mu$ s)	Width (ns )	MCP (V)	F-ratio	Mode
41	1.000	C <sub>2</sub> H <sub>4</sub>	0.00	310	5	500	32	shutter
42	0.999	C <sub>2</sub> H <sub>4</sub>	0.00	310	5	500	16	shutter
43	1.000	C <sub>2</sub> H <sub>4</sub>	0.00	310	50	500	16	shutter
44	1.000	C <sub>2</sub> H <sub>4</sub>	0.00	310	5	500	32	shutter
45	1.000	C <sub>2</sub> H <sub>4</sub>	0.00	310	5	500	32	shutter
46	1.002	C <sub>2</sub> H <sub>4</sub>	0.00	50	5	500	32	shutter
47	1.002	C <sub>2</sub> H <sub>4</sub>	0.00	310	10	500	32	shutter
48	1.002	C <sub>2</sub> H <sub>4</sub>	0.00	150	5	50	32	shutter
49	1.000	C <sub>2</sub> H <sub>4</sub>	0.00	310	50	630	32	shutter
50	1.000	C <sub>2</sub> H <sub>4</sub>	0.00	300	70	630	11	gated
51	1.000	C <sub>2</sub> H <sub>4</sub>	0.00	275	70	770	16	gated
52	1.000	C <sub>2</sub> H <sub>4</sub>	0.00	230	100	750	8	gated
53	1.000	C <sub>2</sub> H <sub>4</sub>	0.00	260	100	750	5.6	gated
54	1.000	C <sub>2</sub> H <sub>4</sub>	0.00	310	100	750	5.6	gated
55	1.010	C <sub>2</sub> H <sub>4</sub>	0.00	310	100	750	8	gated
56	0.804	C <sub>2</sub> H <sub>4</sub>	0.00	350	100	750	8	gated
57	0.603	C <sub>2</sub> H <sub>4</sub>	0.00	390	100	750	8	gated
58	0.801	C <sub>2</sub> H <sub>4</sub>	0.00	350	100	750	8	gated
59	1.000	C <sub>3</sub> H <sub>8</sub>	0.00	360	100	750	11	gated
60	1.003	C <sub>3</sub> H <sub>8</sub>	0.00	418	100	750	11	gated
61	0.996	C <sub>3</sub> H <sub>8</sub>	0.00	400	100	750	11	gated
62	1.002	C <sub>2</sub> H <sub>4</sub>	0.00	310	100	750	11	gated
63	1.002	C <sub>2</sub> H <sub>4</sub>	0.00	310	100	750	11	gated
64	1.000	C <sub>2</sub> H <sub>4</sub>	0.00	310	100	750	11	gated
65	1.000	C <sub>2</sub> H <sub>4</sub>	0.00	310	100	750	11	gated
66	1.000	C <sub>2</sub> H <sub>4</sub>	0.00	310	100	750	11	gated
67	1.100	C <sub>2</sub> H <sub>4</sub>	0.00	310	100	750	11	gated
68	1.001	C <sub>2</sub> H <sub>4</sub>	0.00	310	100	750	11	gated
69	1.001	C <sub>2</sub> H <sub>4</sub>	0.00	320	199	680	11	gated
70	1.000	C <sub>2</sub> H <sub>4</sub>	0.00	330	200	680	11	gated

Table E.2: Experimental properties of each run. All mixtures were stoichiometric fuel-oxygen. Some mixtures were diluted with nitrogen; “N<sub>2</sub> fraction is the volume fraction of nitrogen in the mixture. The last five columns are camera variables. “Delay” is the interval between either the firing of the spark plug (runs 1-24) or the wave exhaust from the small channels (runs 24-43) and time of image acquisition. “Width” is the integration time of the intensified CCD camera and “MCP” corresponds to the intensifier voltage setting.

Run	Pressure (bar)	Fuel	N <sub>2</sub> fraction	Delay ( $\mu$ s)	Width (ns )	MCP (V)	F-ratio	Mode
71	1.001	C <sub>2</sub> H <sub>4</sub>	0.00	340	100	750	11	gated
72	1.000	C <sub>2</sub> H <sub>4</sub>	0.00	350	100	750	11	gated
73	0.890	C <sub>2</sub> H <sub>4</sub>	0.00	300	100	750	11	gated
74	0.739	C <sub>2</sub> H <sub>4</sub>	0.00	350	100	750	11	gated
75	0.612	C <sub>2</sub> H <sub>4</sub>	0.00	450	100	750	11	gated
76	1.000	C <sub>3</sub> H <sub>8</sub>	0.00	410	100	750	11	gated
77	1.000	C <sub>3</sub> H <sub>8</sub>	0.00	410	100	750	11	gated
78	1.000	C <sub>3</sub> H <sub>8</sub>	0.00	410	100	750	11	gated
79	1.000	C <sub>3</sub> H <sub>8</sub>	0.00	410	100	750	11	gated
80	1.200	C <sub>3</sub> H <sub>8</sub>	0.00	410	100	750	11	gated
81	1.300	C <sub>3</sub> H <sub>8</sub>	0.00	400	100	750	11	gated
82	1.400	C <sub>3</sub> H <sub>8</sub>	0.00	385	100	750	11	gated
83	1.500	C <sub>3</sub> H <sub>8</sub>	0.00	380	100	750	11	gated
84	1.500	C <sub>3</sub> H <sub>8</sub>	0.00	365	100	750	11	gated
85	1.012	C <sub>3</sub> H <sub>8</sub>	0.00	450	100	750	11	gated
86	1.000	C <sub>2</sub> H <sub>4</sub>	0.00	340	100	750	11	gated
87	1.004	C <sub>2</sub> H <sub>4</sub>	0.00	330	100	750	11	gated
88	1.002	C <sub>2</sub> H <sub>4</sub>	0.00	340	100	750	11	gated
89	1.002	C <sub>2</sub> H <sub>4</sub>	0.00	320	100	750	11	gated
90	1.006	C <sub>2</sub> H <sub>4</sub>	0.00	315	100	750	11	gated
91	1.010	C <sub>2</sub> H <sub>4</sub>	0.00	305	100	750	11	gated
92	1.002	C <sub>2</sub> H <sub>4</sub>	0.00	300	100	750	11	gated
93	1.000	C <sub>2</sub> H <sub>4</sub>	0.00	295	100	750	11	gated
94	1.004	C <sub>2</sub> H <sub>4</sub>	0.00	295	100	750	11	gated
95	1.000	C <sub>2</sub> H <sub>4</sub>	0.00	297	100	750	11	gated
96	1.002	C <sub>2</sub> H <sub>4</sub>	0.00	296.5	100	750	11	gated
97	0.952	C <sub>2</sub> H <sub>4</sub>	0.00	300	100	750	11	gated
98	1.004	C <sub>3</sub> H <sub>8</sub>	0.00	460	100	750	11	gated
99	1.002	C <sub>3</sub> H <sub>8</sub>	0.00	400	100	750	11	gated
100	1.002	C <sub>3</sub> H <sub>8</sub>	0.00	400	100	750	11	gated

Table E.3: Experimental properties of each run. All mixtures were stoichiometric fuel-oxygen. Some mixtures were diluted with nitrogen; “N<sub>2</sub> fraction” is the volume fraction of nitrogen in the mixture. The last five columns are camera variables. “Delay” is the interval between the firing of the spark plug and time of image acquisition. “Width” is the integration time of the intensified CCD camera and “MCP” corresponds to the intensifier voltage setting.

Run	Pressure (bar)	Fuel	N <sub>2</sub> fraction	Delay ( $\mu$ s)	Width (ns)	MCP (V)	F-ratio	Mode
101	1.002	C <sub>3</sub> H <sub>8</sub>	0.00	390	100	750	11	gated
102	1.000	C <sub>3</sub> H <sub>8</sub>	0.00	375	100	750	11	gated
103	1.002	C <sub>3</sub> H <sub>8</sub>	0.00	375	100	750	11	gated
104	1.002	C <sub>3</sub> H <sub>8</sub>	0.00	360	100	750	11	gated
105	1.002	C <sub>3</sub> H <sub>8</sub>	0.00	370	100	750	11	gated
106	0.802	C <sub>3</sub> H <sub>8</sub>	0.00	420	100	750	11	gated
107	0.699	C <sub>3</sub> H <sub>8</sub>	0.00	435	100	750	11	gated
108	0.604	C <sub>3</sub> H <sub>8</sub>	0.00	450	100	750	11	gated
109	0.504	C <sub>3</sub> H <sub>8</sub>	0.00	460	100	750	11	gated
110	0.402	C <sub>3</sub> H <sub>8</sub>	0.00	470	100	750	11	gated
111	0.306	C <sub>3</sub> H <sub>8</sub>	0.00	485	100	750	11	gated
112	0.208	C <sub>3</sub> H <sub>8</sub>	0.00	600	100	750	11	gated
113	N/A	C <sub>3</sub> H <sub>8</sub>	0.00	N/A	N/A	N/A	N/A	gated
114	0.300	C <sub>3</sub> H <sub>8</sub>	0.00	545	100	750	11	gated
115	1.000	C <sub>3</sub> H <sub>8</sub>	0.20	435	100	750	11	gated
116	1.000	C <sub>3</sub> H <sub>8</sub>	0.20	488	100	750	11	gated
117	1.000	C <sub>3</sub> H <sub>8</sub>	0.30	540	100	750	11	gated
118	1.002	C <sub>3</sub> H <sub>8</sub>	0.40	570	100	750	11	gated
119	1.000	C <sub>3</sub> H <sub>8</sub>	0.50	605	100	750	11	gated
120	1.000	C <sub>3</sub> H <sub>8</sub>	0.50	710	100	750	11	gated
121	1.002	C <sub>3</sub> H <sub>8</sub>	0.00	410	100	750	11	gated
122	1.000	C <sub>3</sub> H <sub>8</sub>	0.00	410	100	750	11	gated
123	1.004	C <sub>3</sub> H <sub>8</sub>	0.00	200	100	800	11	gated
124	1.000	C <sub>3</sub> H <sub>8</sub>	0.00	250	100	800	16	gated
125	1.002	C <sub>3</sub> H <sub>8</sub>	0.00	300	100	800	22	gated
126	0.998	C <sub>3</sub> H <sub>8</sub>	0.00	100	100	800	22	gated
127	1.002	C <sub>3</sub> H <sub>8</sub>	0.00	150	100	800	8	gated
128	1.001	C <sub>3</sub> H <sub>8</sub>	0.00	330	100	800	8	gated
129	1.000	C <sub>3</sub> H <sub>8</sub>	0.00	100	100	800	2.8	gated
130	1.002	C <sub>3</sub> H <sub>8</sub>	0.00	275	100	800	8	gated

Table E.4: Experimental properties of each run. All mixtures were stoichiometric fuel-oxygen. Some mixtures were diluted with nitrogen; “N<sub>2</sub> fraction” is the volume fraction of nitrogen in the mixture. The last five columns are camera variables. “Delay” is the interval between the firing of the spark plug and time of image acquisition. “Width” is the integration time of the intensified CCD camera and “MCP” corresponds to the intensifier voltage setting.

## E.3 Wave Arrival Times

Run	$t_{P1}$ ( $\mu\text{s}$ )	$t_{P2}$ ( $\mu\text{s}$ )	$t_{P3}$ ( $\mu\text{s}$ )	$t_{P4}$ ( $\mu\text{s}$ )	$t_{I1}$ ( $\mu\text{s}$ )	$t_{I2}$ ( $\mu\text{s}$ )	$U_{ion}$ (m/s)	$U_{CJ}$ (m/s)
11	N/A	N/A	N/A	N/A	N/A	N/A	N/A	2376
12	N/A	N/A	N/A	N/A	N/A	N/A	N/A	2376
13	N/A	N/A	N/A	N/A	N/A	N/A	N/A	2376
14	N/A	N/A	N/A	N/A	N/A	N/A	N/A	2376
15	N/A	N/A	N/A	N/A	N/A	N/A	N/A	2376
16	N/A	N/A	N/A	N/A	N/A	N/A	N/A	2376
17	N/A	N/A	N/A	N/A	N/A	N/A	N/A	2376
18	N/A	N/A	N/A	N/A	N/A	N/A	N/A	2376
19	N/A	N/A	N/A	N/A	N/A	N/A	N/A	2360
20	N/A	N/A	N/A	N/A	N/A	N/A	N/A	2360
21	N/A	N/A	N/A	N/A	N/A	N/A	N/A	2360
22	N/A	N/A	N/A	N/A	N/A	N/A	N/A	2361
23	N/A	N/A	N/A	N/A	N/A	N/A	N/A	2360
24	N/A	N/A	N/A	N/A	N/A	N/A	N/A	2360
25	396.0	386.0	386.0	389.0	374.0	396.0	2598	2360
26	372.0	376.0	378.0	382.0	365.0	388.0	2485	2360
27	353.0	356.0	359.0	362.0	342.0	368.0	2198	2360
28	385.0	384.0	386.0	387.0	371.0	395.0	2381	2359
29	389.0	387.0	389.0	389.0	375.0	397.0	2598	2359
30	385.0	383.0	383.0	385.0	372.0	393.0	2721	2359
31	393.0	384.0	385.0	398.0	372.0	394.0	2598	2359
32	388.0	384.0	388.0	397.0	376.0	398.0	2598	2359
33	385.0	386.2	386.4	390.0	374.0	396.0	2598	2359
34	373.0	376.8	378.4	381.6	365.6	388.0	2551	2360
35	368.0	370.8	374.0	378.4	360.4	383.2	2507	2360
36	377.6	380.8	384.0	388.0	370.8	393.6	2507	2360
37	370.6	372.2	375.0	378.6	362.4	384.0	2646	2360
38	438.0	425.4	410.8	394.4	410.8	426.8	3572	2358
39	N/A	N/A	N/A	N/A	N/A	N/A	N/A	2376
40	N/A	N/A	N/A	N/A	N/A	N/A	N/A	2376

Table E.5: For each run, the wave arrival times at each pressure transducer (P1, P2, P3, P4) and ionization probe (I1, I2) are given. A wave arrival time of zero corresponds to the instant the spark plug was fired.  $U_{ion}$  is the average wave velocity in between the two ion probes.

Run	$t_{P1}$ ( $\mu\text{s}$ )	$t_{P2}$ ( $\mu\text{s}$ )	$t_{P3}$ ( $\mu\text{s}$ )	$t_{P4}$ ( $\mu\text{s}$ )	$t_{I1}$ ( $\mu\text{s}$ )	$t_{I2}$ ( $\mu\text{s}$ )	$U_{ion}$ (m/s)	$U_{CJ}$ (m/s)
41	N/A	N/A	N/A	N/A	N/A	N/A	N/A	2376
42	N/A	N/A	N/A	N/A	N/A	N/A	N/A	2376
43	N/A	N/A	N/A	N/A	N/A	N/A	N/A	2376
44	N/A	N/A	N/A	N/A	N/A	N/A	N/A	2376
45	N/A	N/A	N/A	N/A	N/A	N/A	N/A	2376
46	N/A	N/A	N/A	N/A	N/A	N/A	N/A	2376
47	N/A	N/A	N/A	N/A	N/A	N/A	N/A	2376
48	N/A	N/A	N/A	N/A	N/A	N/A	N/A	2376
49	N/A	N/A	N/A	N/A	N/A	N/A	N/A	2376
50	N/A	N/A	N/A	N/A	N/A	N/A	N/A	2376
51	N/A	N/A	N/A	N/A	N/A	N/A	N/A	2376
52	N/A	N/A	N/A	N/A	N/A	N/A	N/A	2376
53	N/A	N/A	N/A	N/A	N/A	N/A	N/A	2376
54	N/A	N/A	N/A	N/A	N/A	N/A	N/A	2376
55	320.4	320.4	321.4	319.6	308.0	308.0	N/A	2377
56	341.4	353.8	350.8	339.0	350.2	366.4	3528	2365
57	396.4	375.6	356.0	339.6	N/A	N/A	N/A	2352
58	N/A	N/A	N/A	N/A	N/A	N/A	N/A	2365
59	403.6	418.2	418.2	401.8	408.8	429.6	2748	2360
60	384.8	387.0	400.6	391.0	382.4	402.4	2858	2360
61	415.4	411.6	410.2	394.0	N/A	N/A	N/A	2360
62	N/A	N/A	N/A	N/A	N/A	N/A	N/A	2376
63	N/A	N/A	N/A	N/A	N/A	N/A	N/A	2376
64	N/A	N/A	N/A	N/A	N/A	N/A	N/A	2376
65	N/A	N/A	N/A	N/A	N/A	N/A	N/A	2376
66	N/A	N/A	N/A	N/A	N/A	N/A	N/A	2376
67	N/A	N/A	N/A	N/A	N/A	N/A	N/A	2376
68	N/A	N/A	N/A	N/A	N/A	N/A	N/A	2376
69	336.2	338.8	336.2	335.2	324.4	346.8	2551	2376
70	347.4	348.6	346.2	346.6	334.2	357.0	2507	2376

Table E.6: For each run, the wave arrival times at each pressure transducer (P1, P2, P3, P4) and ionization probe (I1, I2) are given. A wave arrival time of zero corresponds to the instant the spark plug was fired.  $U_{ion}$  is the average wave velocity in between the two ion probes.

Run	$t_{P1}$ ( $\mu\text{s}$ )	$t_{P2}$ ( $\mu\text{s}$ )	$t_{P3}$ ( $\mu\text{s}$ )	$t_{P4}$ ( $\mu\text{s}$ )	$t_{I1}$ ( $\mu\text{s}$ )	$t_{I2}$ ( $\mu\text{s}$ )	$U_{ion}$ (m/s)	$U_{CJ}$ (m/s)
71	345.8	349.4	347.6	346.8	335.0	357.8	2507	2376
72	339.0	343.0	340.4	339.8	328.2	350.8	2529	2376
73	342.0	341.2	340.4	352.4	326.8	349.8	2485	2371
74	390.6	408.0	407.6	389.6	410.0	423.6	4202	2362
75	382.8	400.8	415.6	396.0	403.4	417.4	4082	2325
76	425.4	416.4	415.2	427.2	401.4	424.8	2442	2360
77	440.0	457.6	462.0	444.0	460.6	474.6	4082	2360
78	460.6	472.6	460.6	442.2	462.6	476.6	4082	2360
79	443.8	461.0	470.0	459.0	464.2	478.2	4082	2360
80	414.8	409.8	408.8	421.0	395.2	418.4	2463	2368
81	393.4	396.2	410.8	408.4	393.4	412.2	3040	2372
82	385.8	384.0	383.8	387.4	371.8	394.8	2485	2375
83	356.4	356.6	354.8	356.8	343.4	366.0	2529	2378
84	378.6	379.0	376.4	376.8	N/A	N/A	N/A	2378
85	423.6	342.0	425.0	408.8	426.4	441.2	3861	2360
86	343.4	345.0	345.0	344.6	N/A	N/A	N/A	2376
87	338.6	338.2	340.2	338.4	326.0	348.8	2507	2376
88	331.0	330.4	331.2	331.8	319.6	342.0	2551	2376
89	341.0	341.6	342.2	342.2	329.4	352.2	2507	2376
90	328.4	328.4	328.2	328.2	316.4	339.2	2507	2376
91	336.6	336.2	336.4	336.2	324.8	347.4	2529	2377
92	332.4	332.4	333.4	333.0	320.6	343.2	2529	2376
93	339.2	339.8	339.0	339.0	327.6	350.4	2507	2376
94	336.6	336.4	335.8	336.0	324.4	347.2	2507	2376
95	332.2	331.6	331.4	331.2	320.0	342.8	2507	2376
96	329.6	328.8	330.0	329.2	317.4	340.2	2507	2376
97	344.0	343.6	344.0	343.8	332.2	354.8	2529	2374
98	400.8	401.2	401.2	401.4	388.3	411.2	2496	2360
99	N/A	N/A	N/A	N/A	N/A	N/A	N/A	2360
100	410.4	410.6	410.6	410.4	398.4	420.8	2551	2360

Table E.7: For each run, the wave arrival times at each pressure transducer (P1, P2, P3, P4) and ionization probe (I1, I2) are given. A wave arrival time of zero corresponds to the instant the spark plug was fired.  $U_{ion}$  is the average wave velocity in between the two ion probes.

Run	$t_{P1}$ ( $\mu\text{s}$ )	$t_{P2}$ ( $\mu\text{s}$ )	$t_{P3}$ ( $\mu\text{s}$ )	$t_{P4}$ ( $\mu\text{s}$ )	$t_{I1}$ ( $\mu\text{s}$ )	$t_{I2}$ ( $\mu\text{s}$ )	$U_{ion}$ (m/s)	$U_{CJ}$ (m/s)
101	402.0	402.2	402.2	402.4	390.0	412.4	2551	2360
102	406.0	406.0	406.8	406.8	398.0	420.4	2551	2360
103	397.6	397.8	398.0	398.0	385.4	408.0	2529	2360
104	412.0	412.0	412.4	412.2	400.0	422.4	2551	2360
105	N/A	4072.0	407.4	407.2	395.0	417.6	2529	2360
106	423.0	422.6	422.8	422.2	410.2	433.2	2485	2350
107	441.0	440.6	440.8	440.4	428.0	451.0	2485	2344
108	441.2	440.8	440.8	440.4	428.0	451.0	2485	2337
109	464.0	463.6	464.0	463.8	451.0	474.2	2463	2329
110	489.8	487.8	489.0	488.4	475.4	498.6	2463	2319
111	549.4	541.0	545.2	544.0	528.0	551.0	2485	2306
112	623.0	618.0	622.4	623.4	519.8	651.2	435	2288
113	N/A	N/A	N/A	N/A	N/A	N/A	N/A	N/A
114	531.6	530.4	529.0	527.4	521.6	542.6	2721	2306
115	488.0	488.0	488.6	488.6	475.6	499.6	2381	2252
116	482.6	482.4	483.2	483.2	469.6	493.8	2362	2252
117	526.8	526.2	527.0	527.2	514.0	538.2	2362	2194
118	570.0	568.8	569.4	568.2	556.8	581.6	2304	2132
119	708.8	708.8	704.4	704.4	698.8	720.6	2622	2060
120	725.2	706.4	492.2	491.0	686.8	709.0	2574	2060
121	414.8	414.4	415.0	415.2	402.4	425.2	2507	2360
122	406.6	406.2	406.6	406.4	394.0	416.8	2507	2360
123	383.8	383.8	384.4	384.2	372.0	394.6	2529	2360
124	399.4	399.4	399.8	399.8	387.6	410.0	2551	2360
125	396.0	396.0	396.8	396.6	384.0	406.8	2507	2360
126	399.6	399.6	400.2	400.2	387.8	410.4	2529	2360
127	N/A	N/A	N/A	N/A	N/A	N/A	N/A	2360
128	405.6	405.8	406.0	405.8	393.2	416.0	2507	2360
129	N/A	N/A	N/A	N/A	N/A	N/A	N/A	2360
130	398.4	398.2	398.8	398.8	386.4	409.0	2529	2360

Table E.8: For each run, the wave arrival times at each pressure transducer (P1, P2, P3, P4) and ionization probe (I1, I2) are given. A wave arrival time of zero corresponds to the instant the spark plug was fired.  $U_{ion}$  is the average wave velocity in between the two ion probes.

## E.4 Selected Pressure Traces

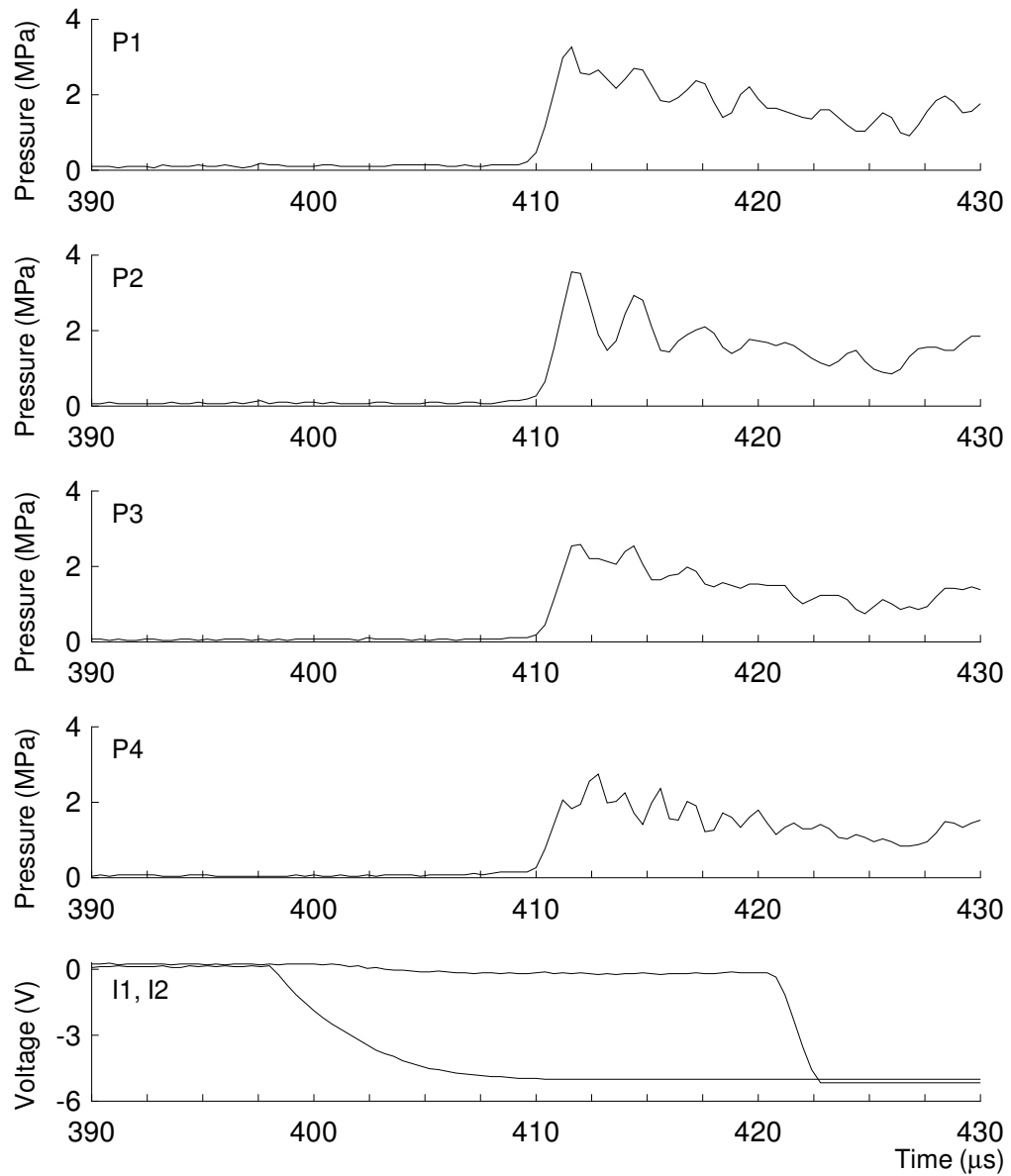


Figure E.5: Pressure history from run 100.

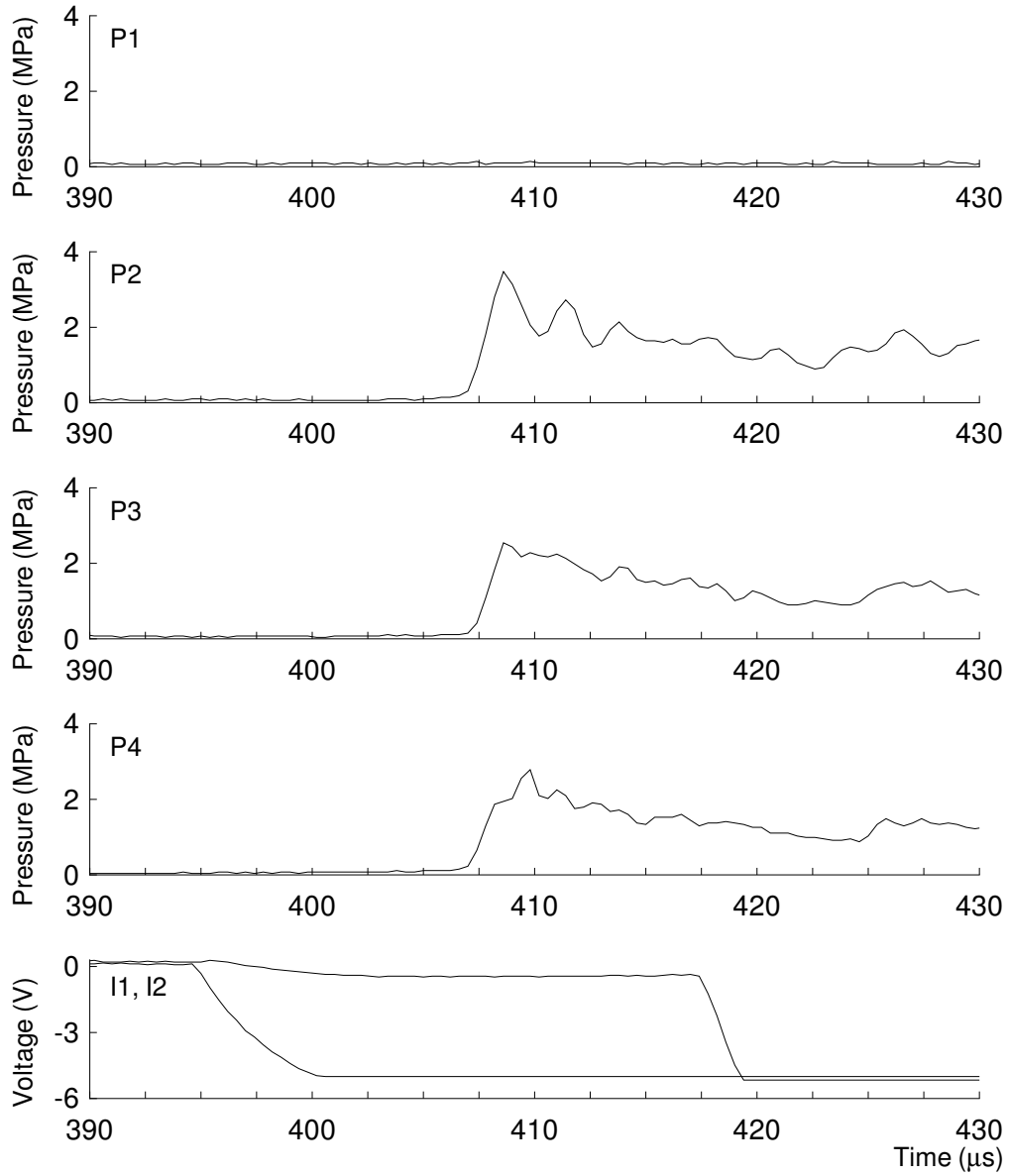


Figure E.6: Pressure history from run 105.

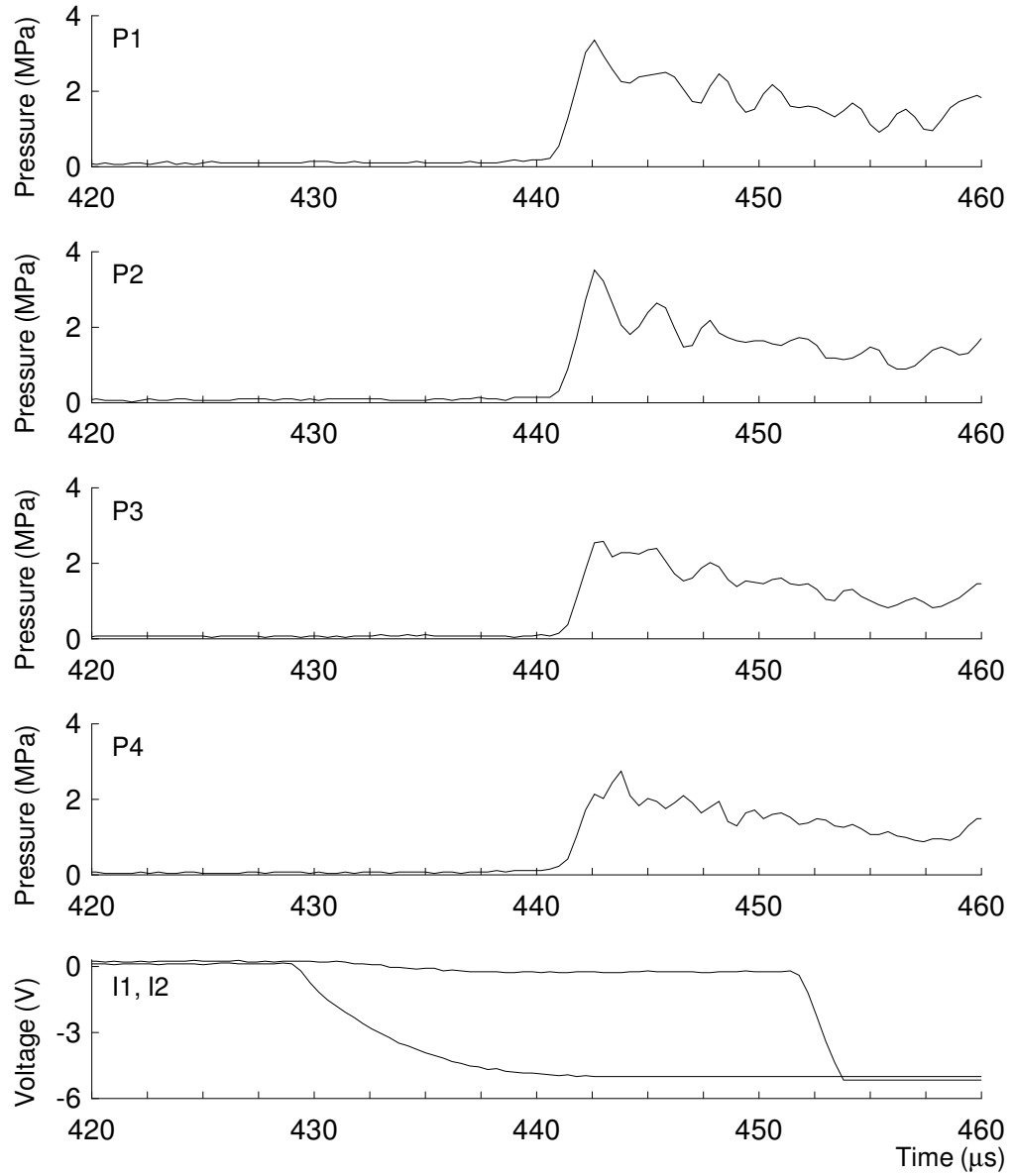


Figure E.7: Pressure history from run 107.

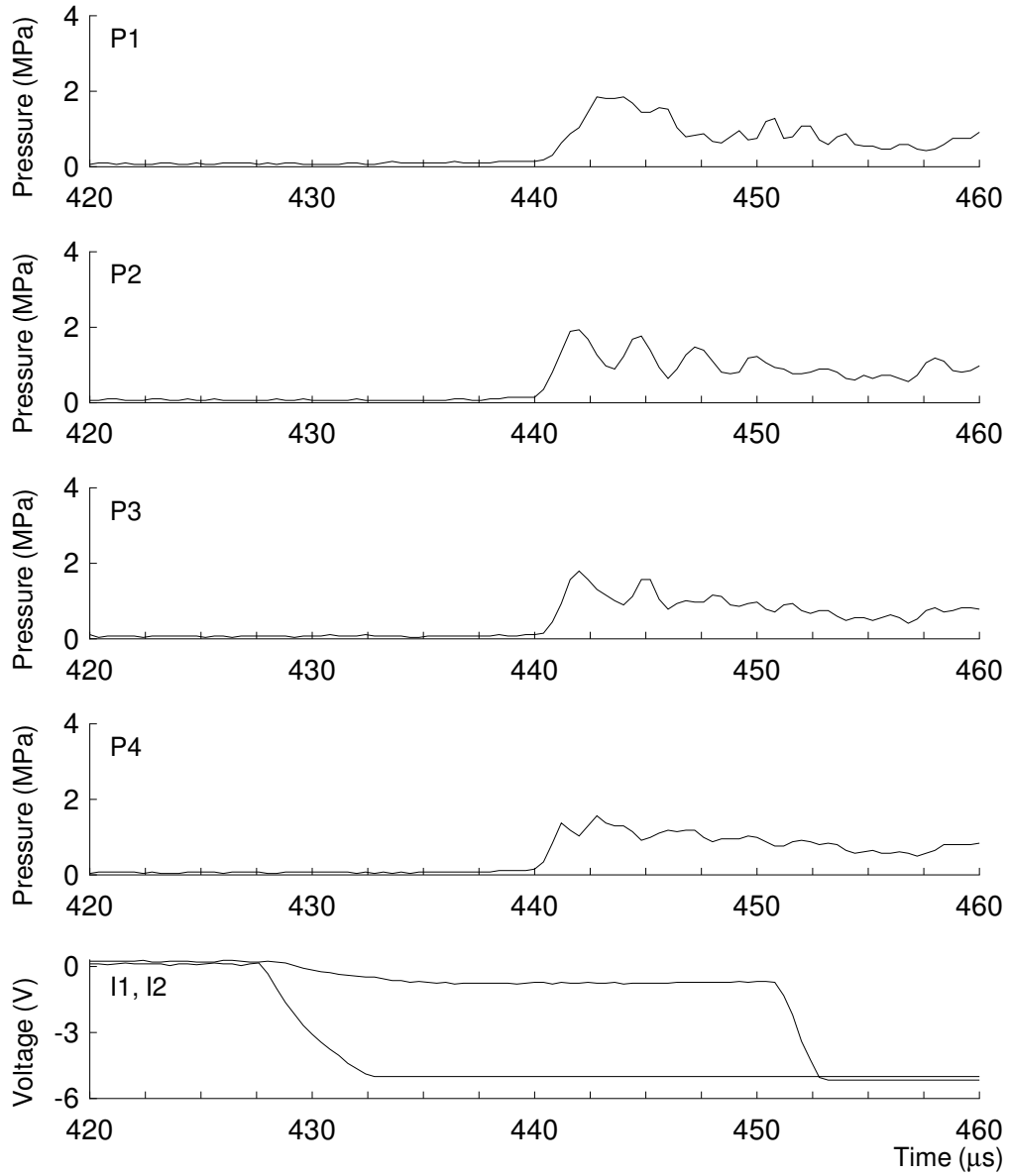


Figure E.8: Pressure history from run 108.

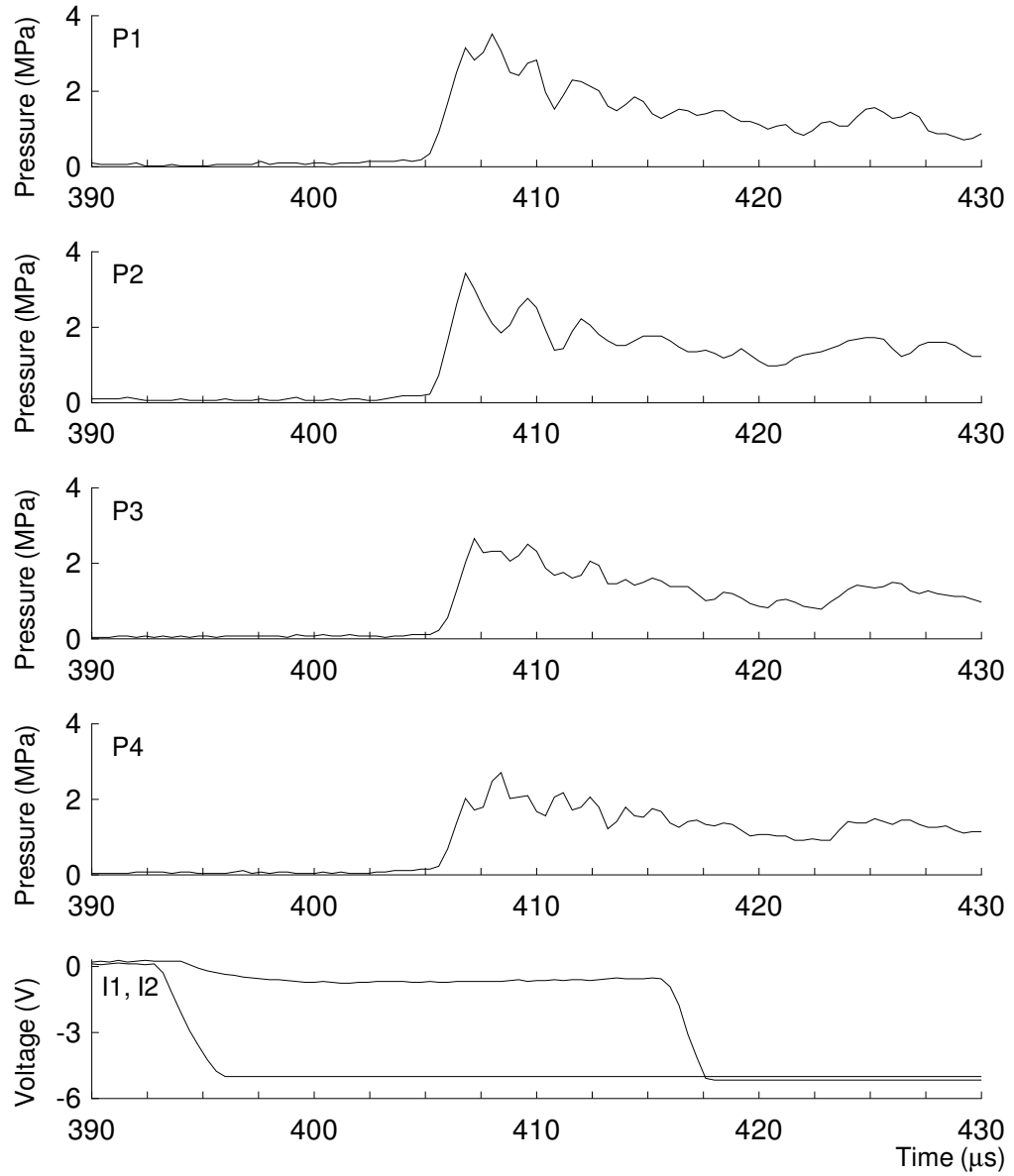


Figure E.9: Pressure history from run 128.

## E.5 Chemiluminescence Images

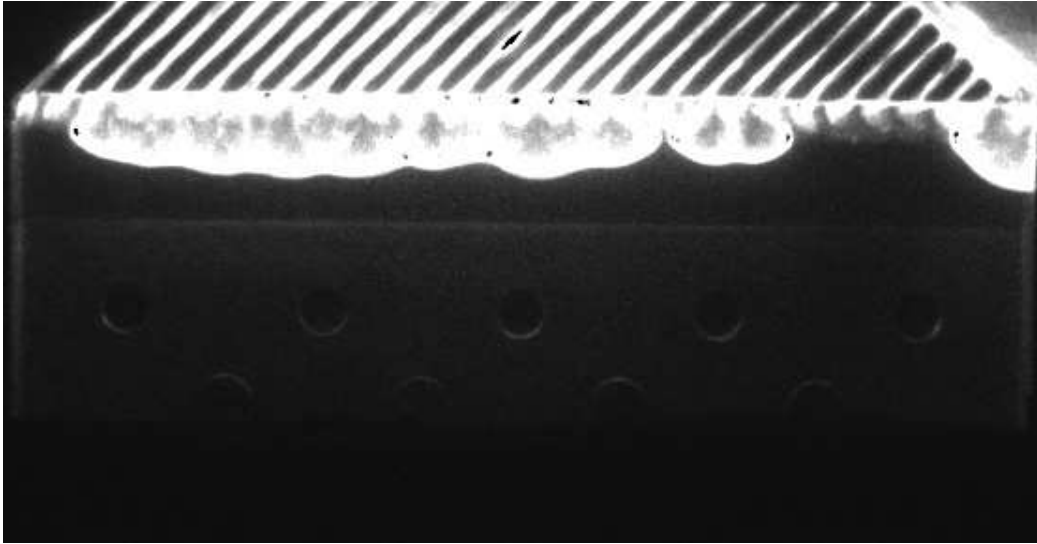


Figure E.10: Chemiluminescence from run 013.

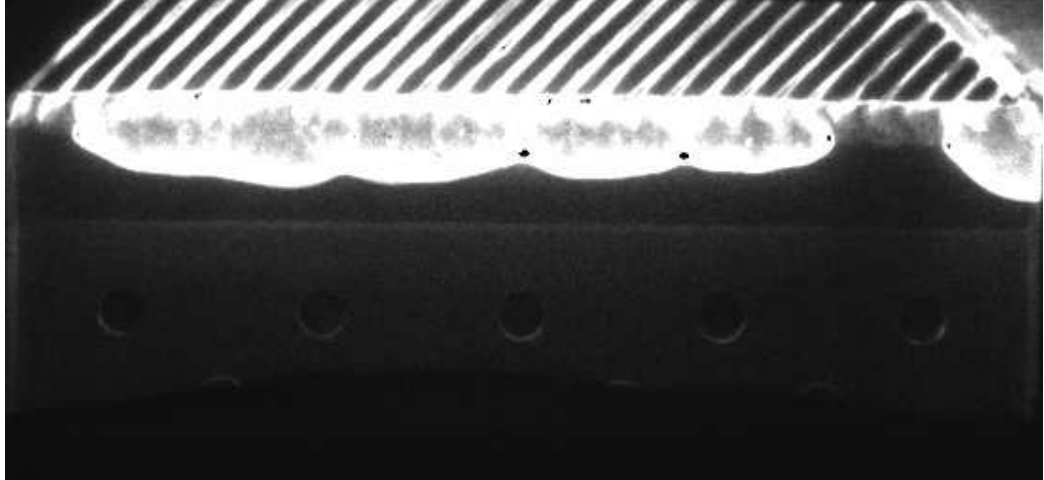


Figure E.11: Chemiluminescence from run 014.

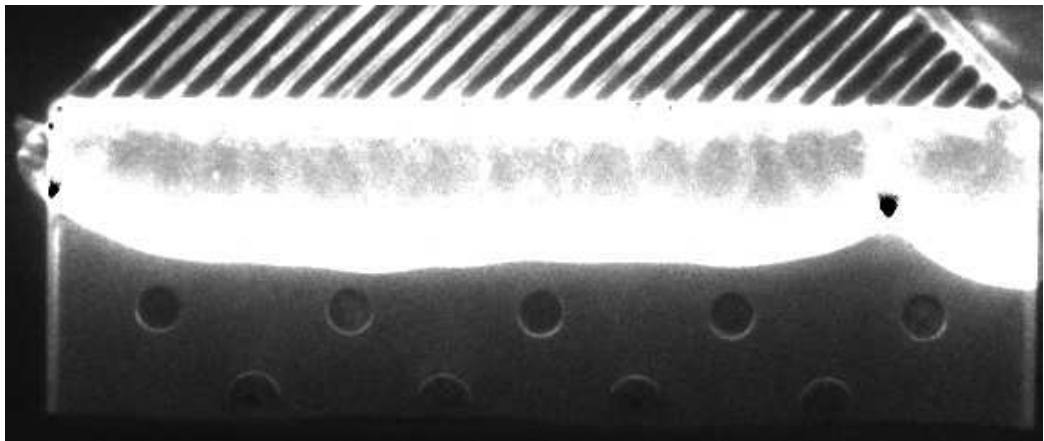


Figure E.12: Chemiluminescence from run 015.

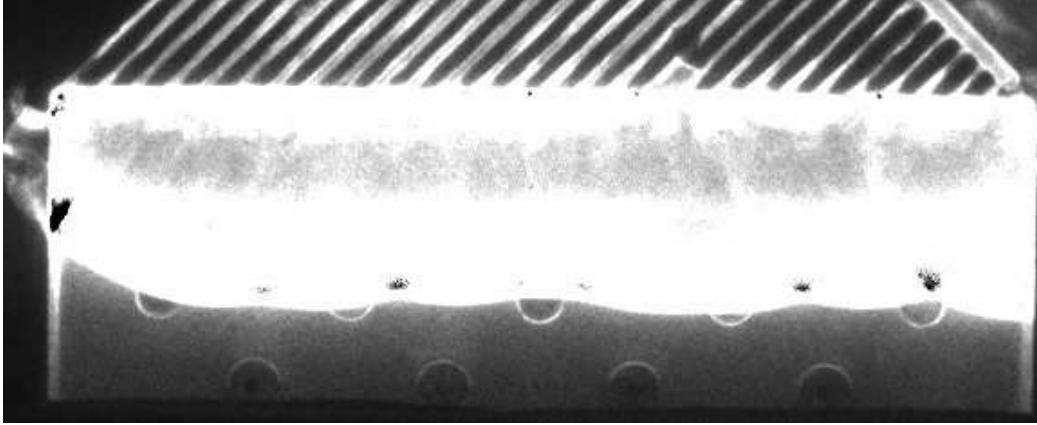


Figure E.13: Chemiluminescence from run 016.

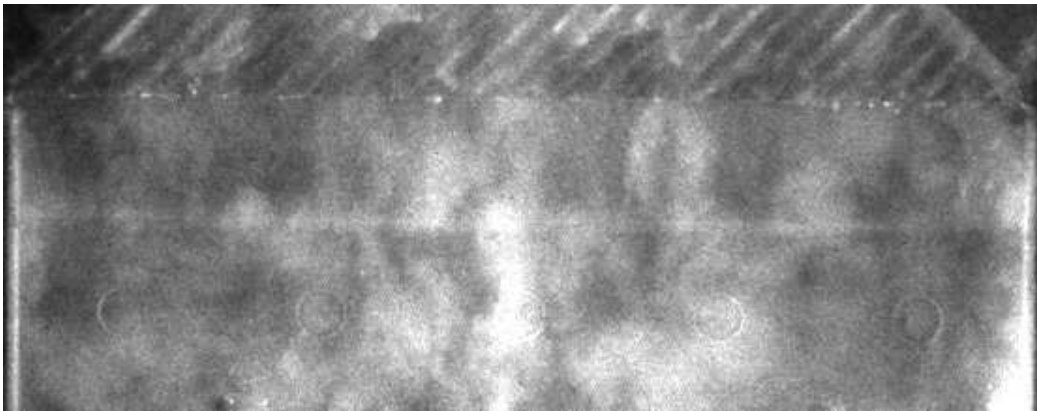


Figure E.14: Chemiluminescence from run 017.

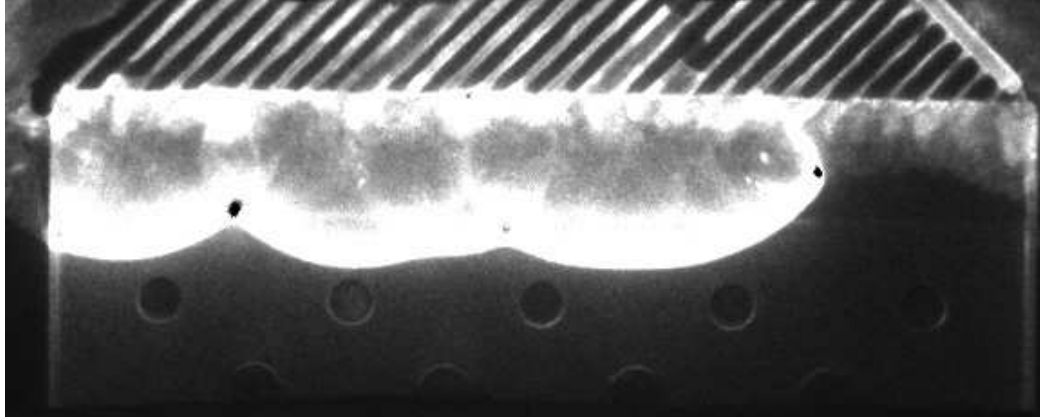


Figure E.15: Chemiluminescence from run 018.

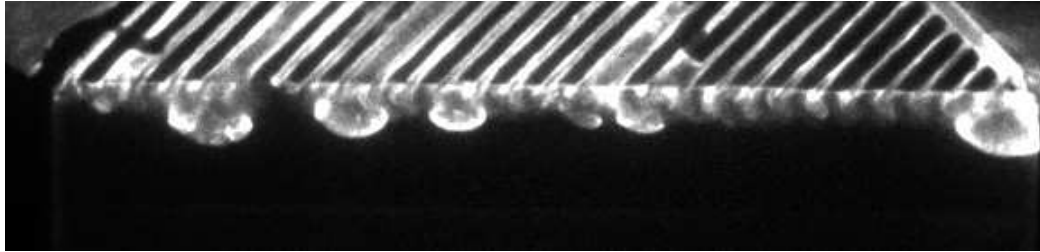


Figure E.16: Chemiluminescence from run 019.

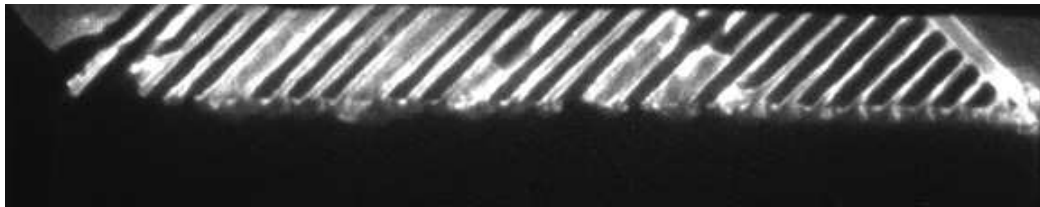


Figure E.17: Chemiluminescence from run 020.

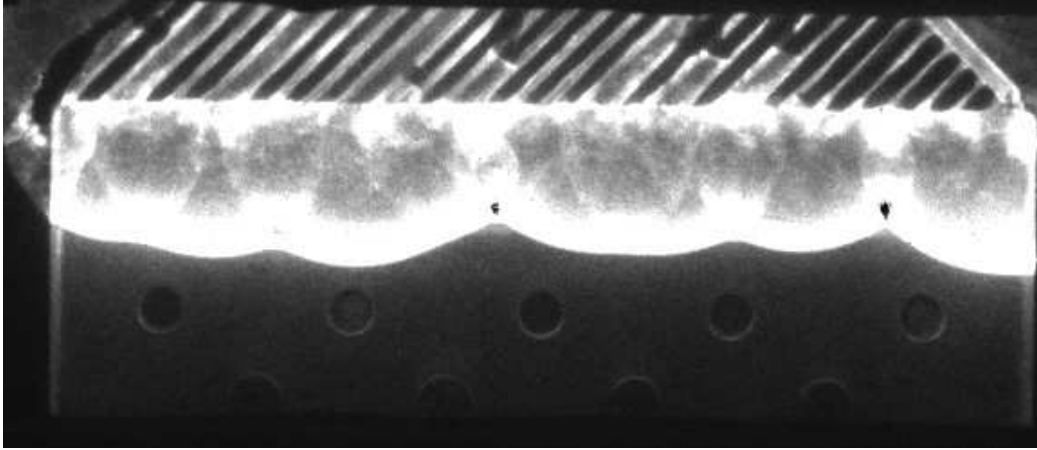


Figure E.18: Chemiluminescence from run 021.

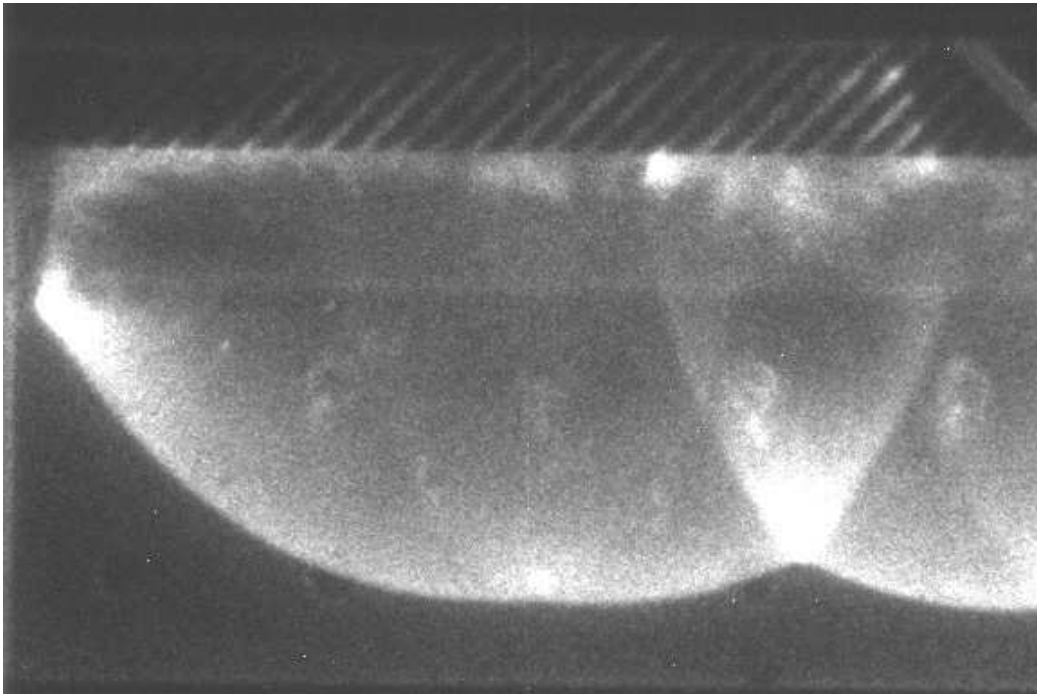


Figure E.19: Chemiluminescence from run 025.



Figure E.20: Chemiluminescence from run 027.

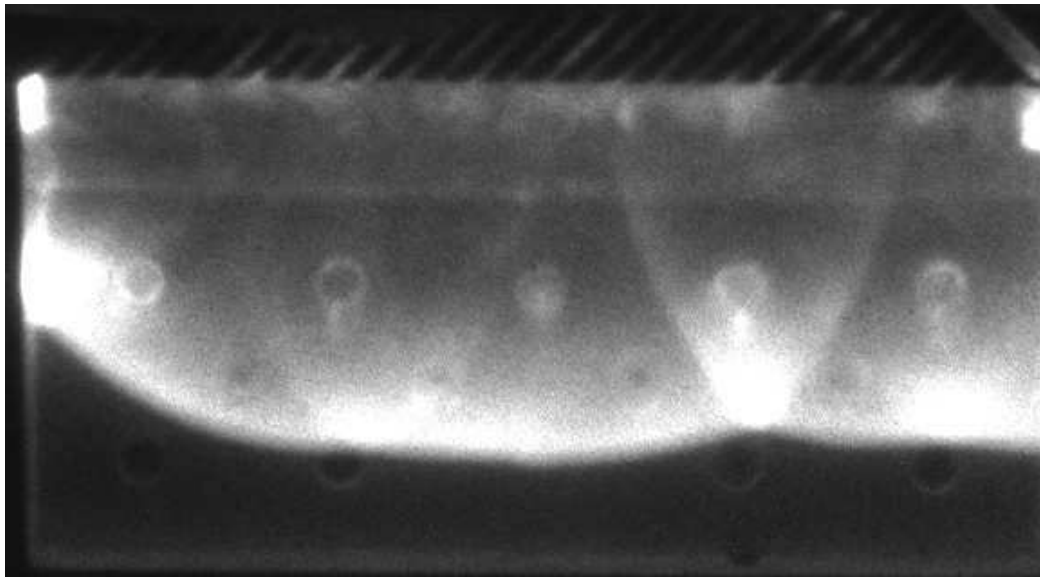


Figure E.21: Chemiluminescence from run 030.

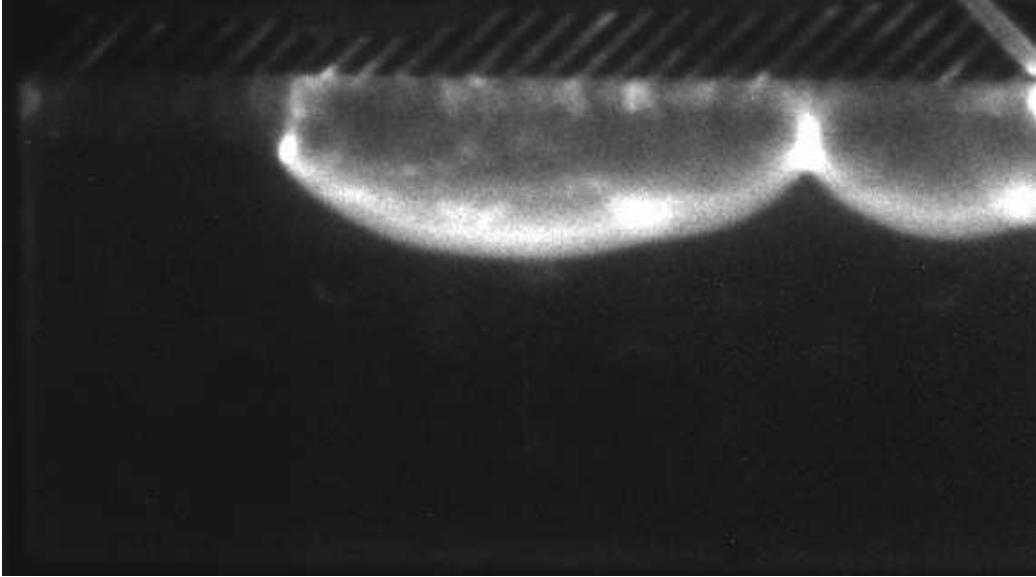


Figure E.22: Chemiluminescence from run 031.

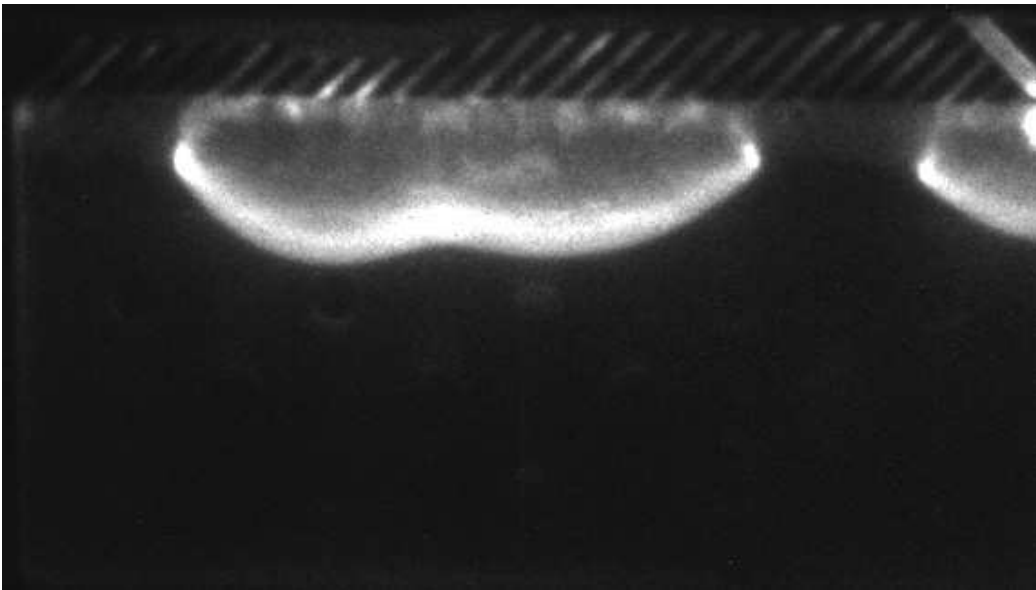


Figure E.23: Chemiluminescence from run 032.

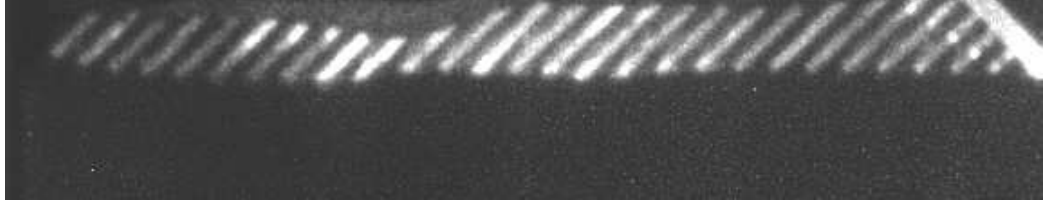


Figure E.24: Chemiluminescence from run 033.

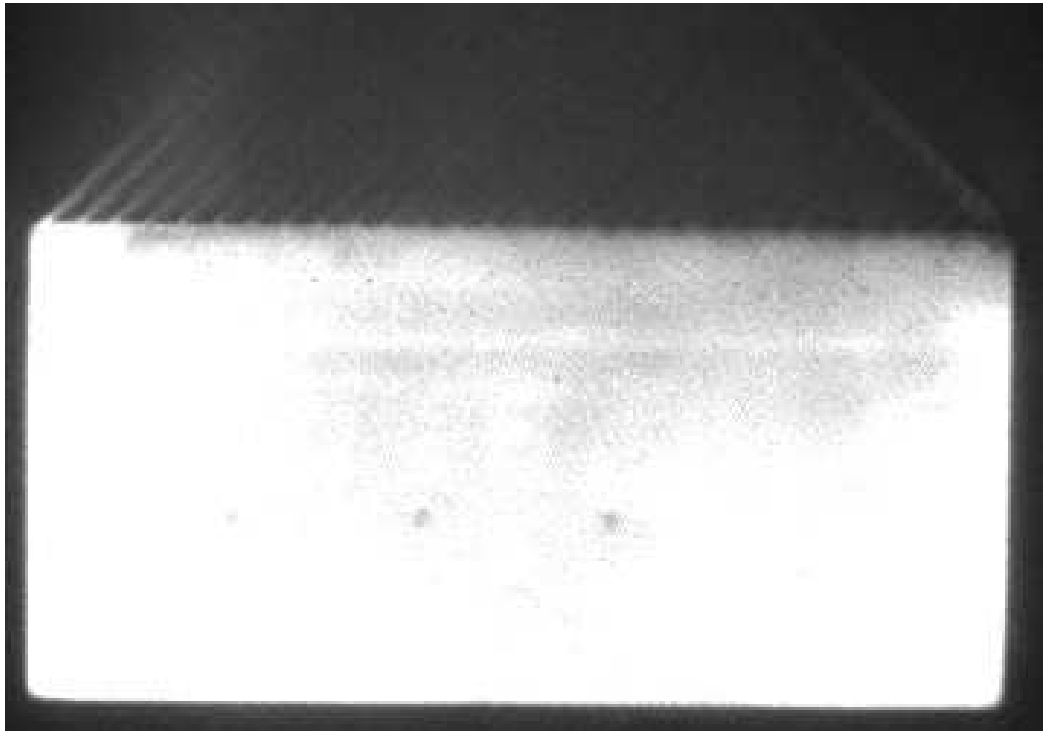


Figure E.25: Chemiluminescence from run 038.

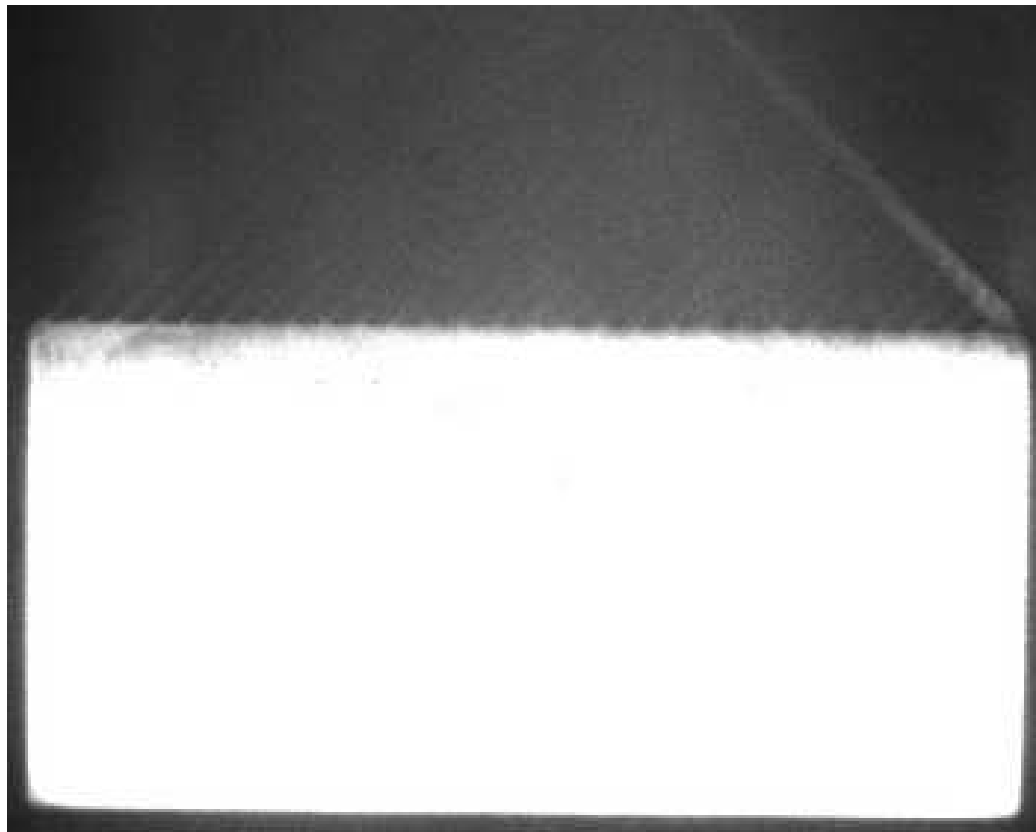


Figure E.26: Chemiluminescence from run 039.

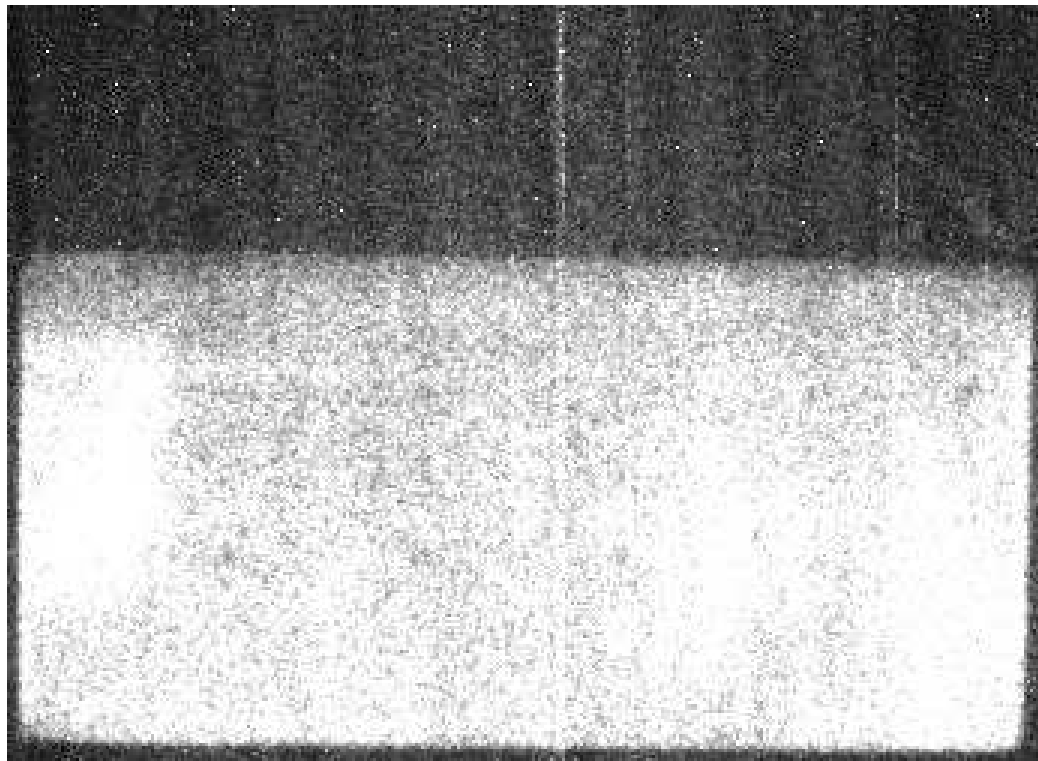


Figure E.27: Chemiluminescence from run 040.

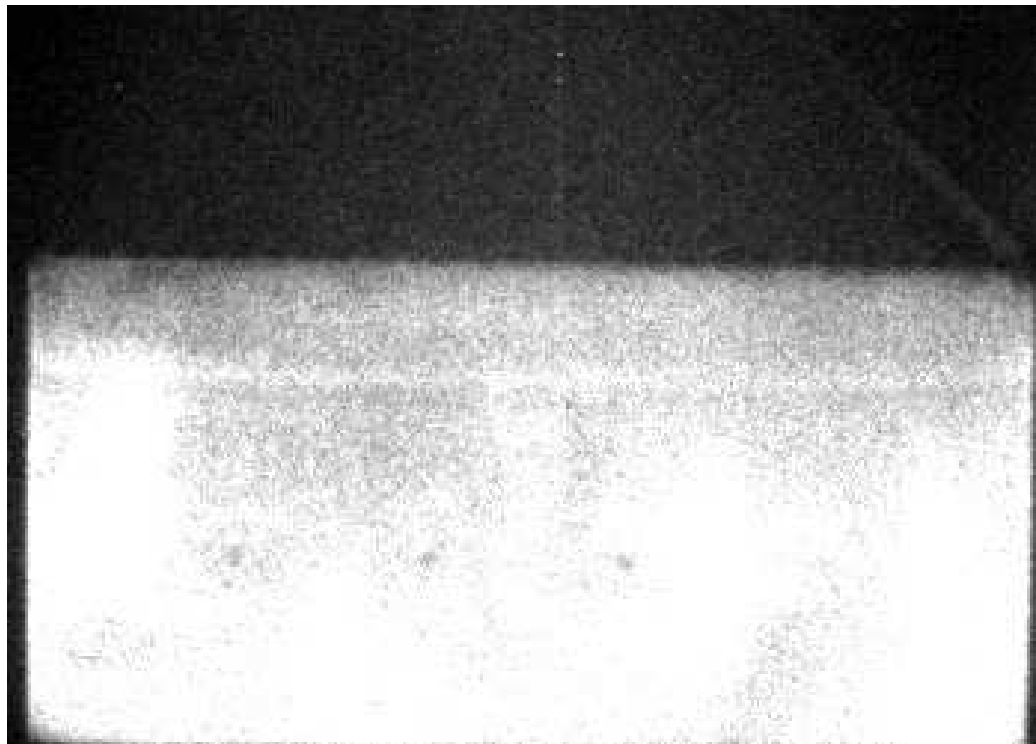


Figure E.28: Chemiluminescence from run 041.

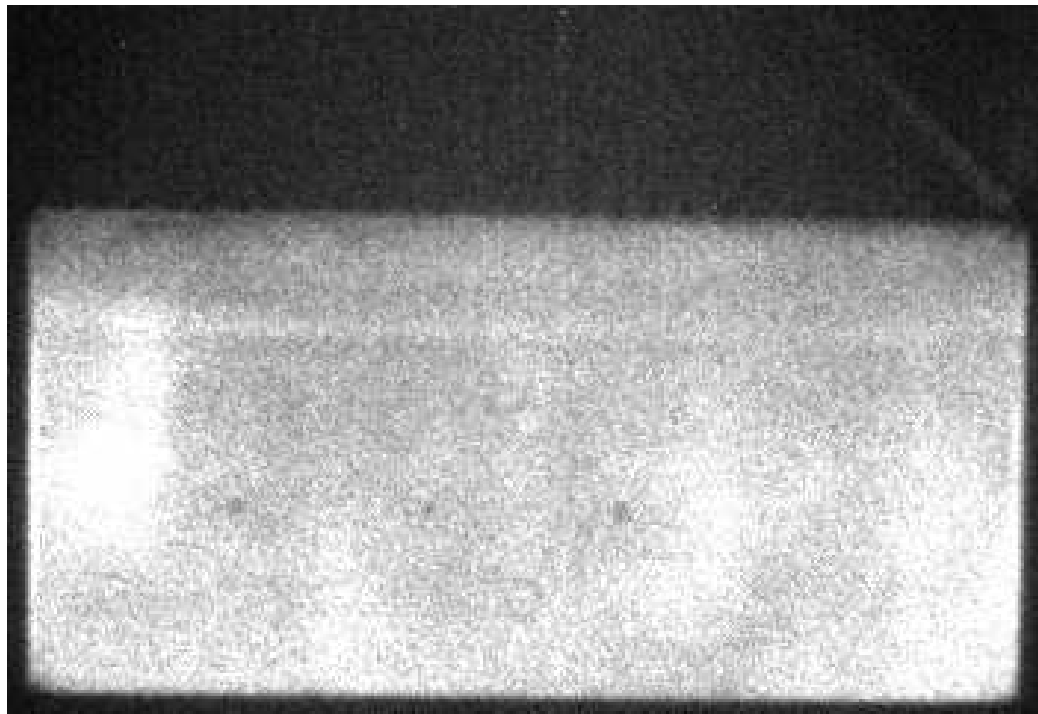


Figure E.29: Chemiluminescence from run 042.

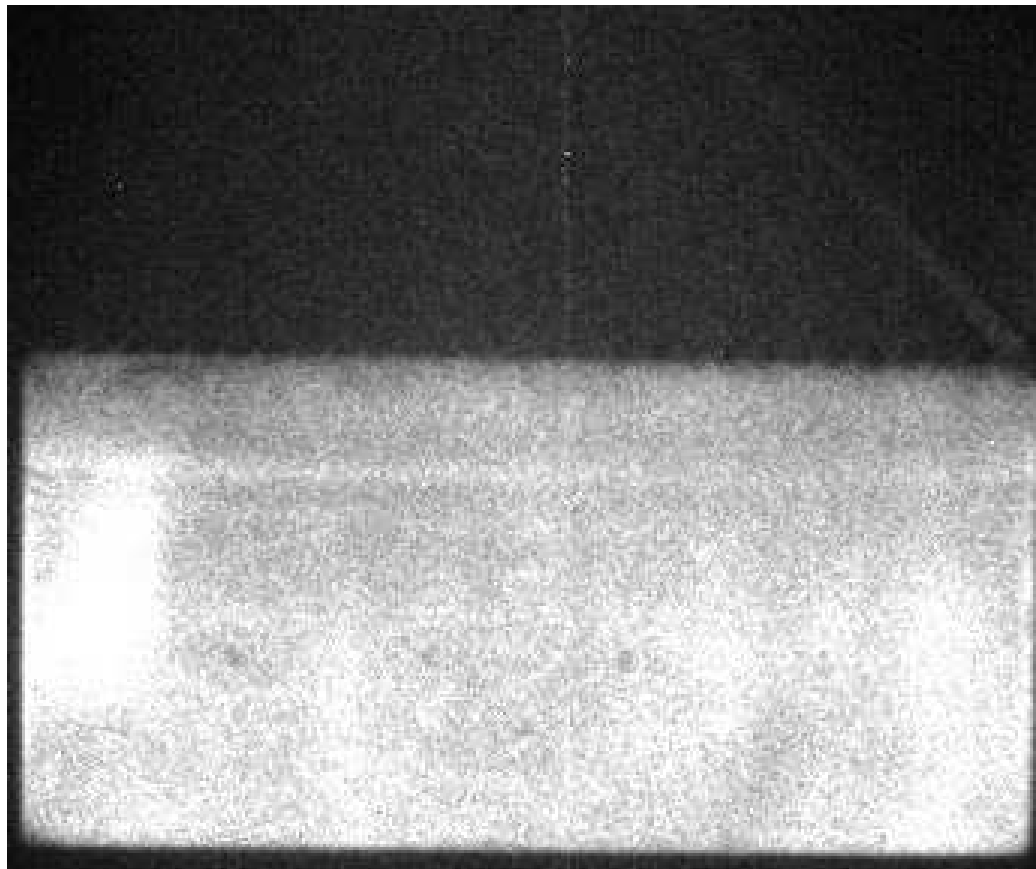


Figure E.30: Chemiluminescence from run 043.

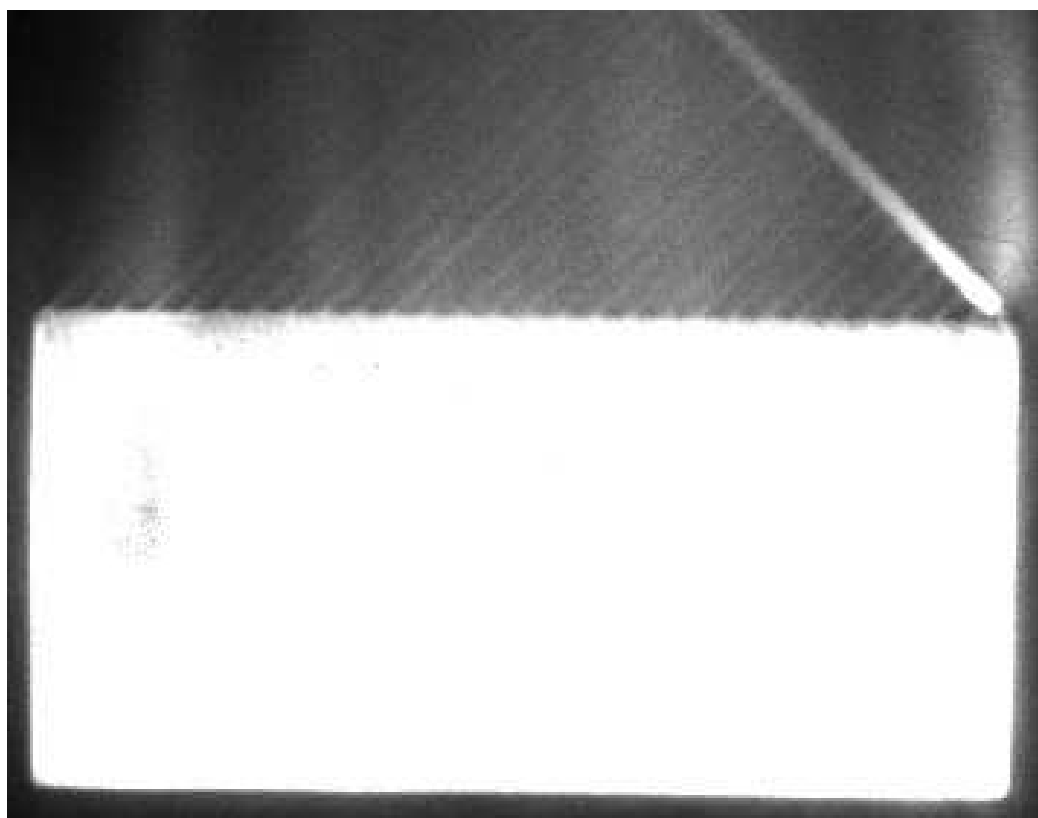


Figure E.31: Chemiluminescence from run 044.

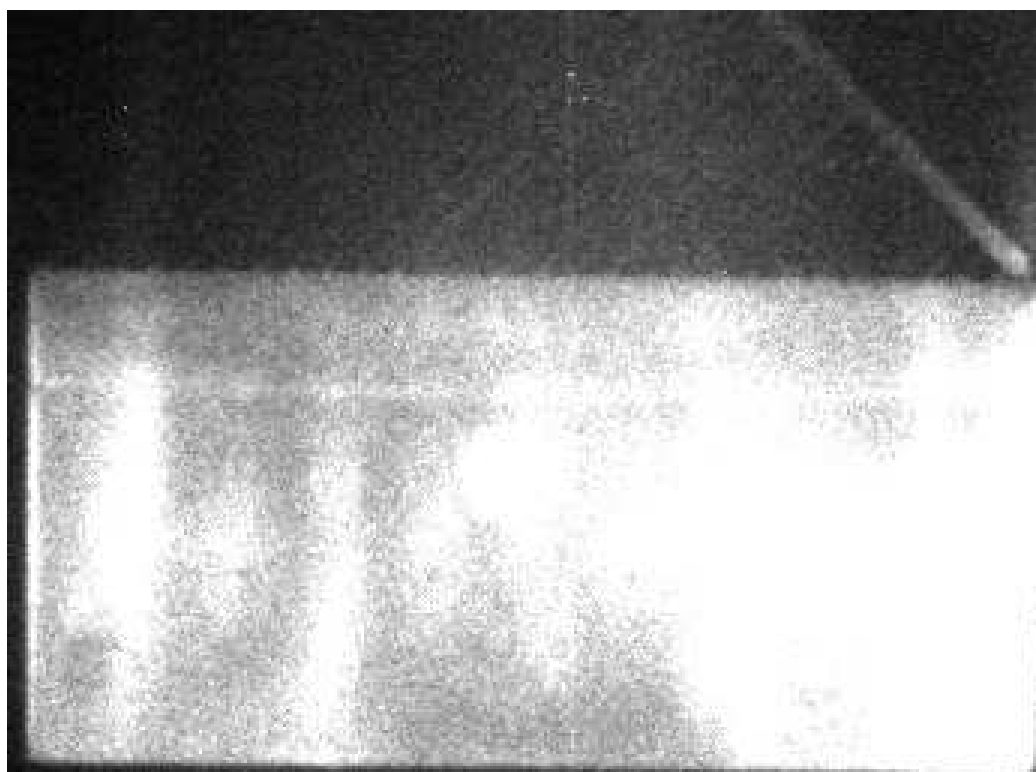


Figure E.32: Chemiluminescence from run 045.

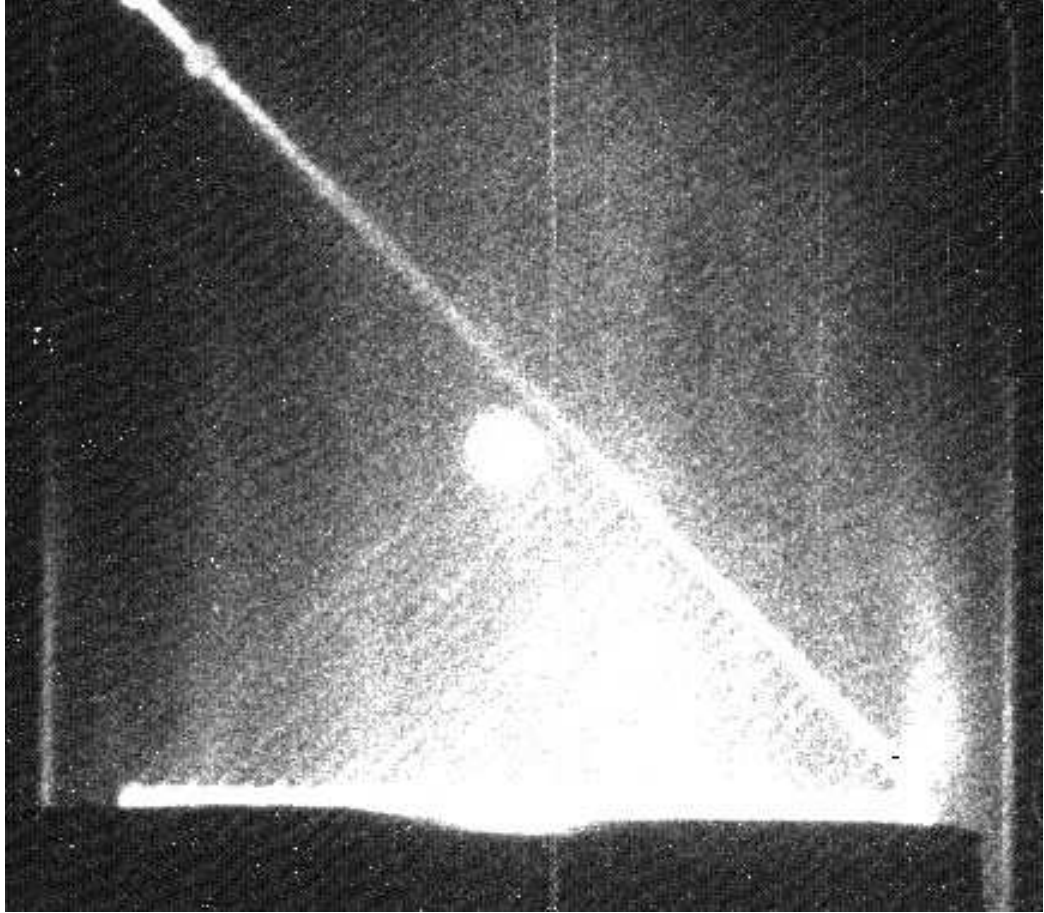


Figure E.33: Chemiluminescence from run 046.

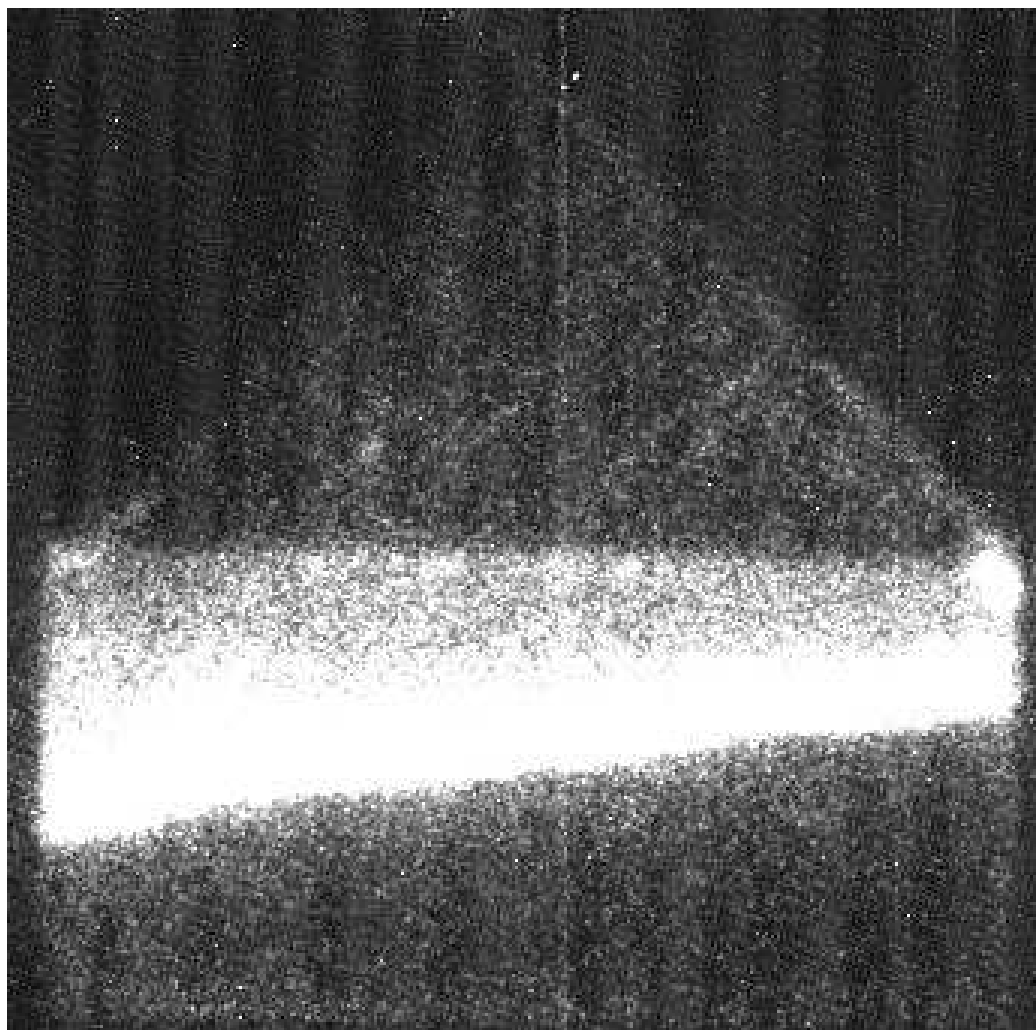


Figure E.34: Chemiluminescence from run 050.

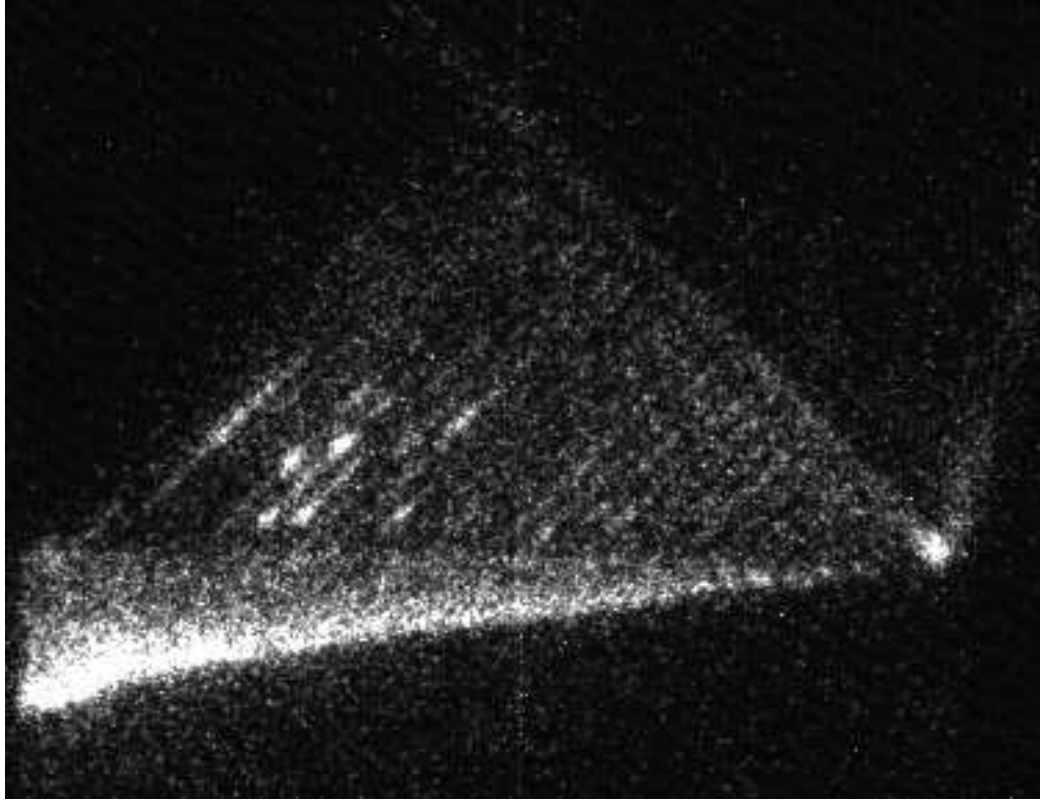


Figure E.35: Chemiluminescence from run 051.

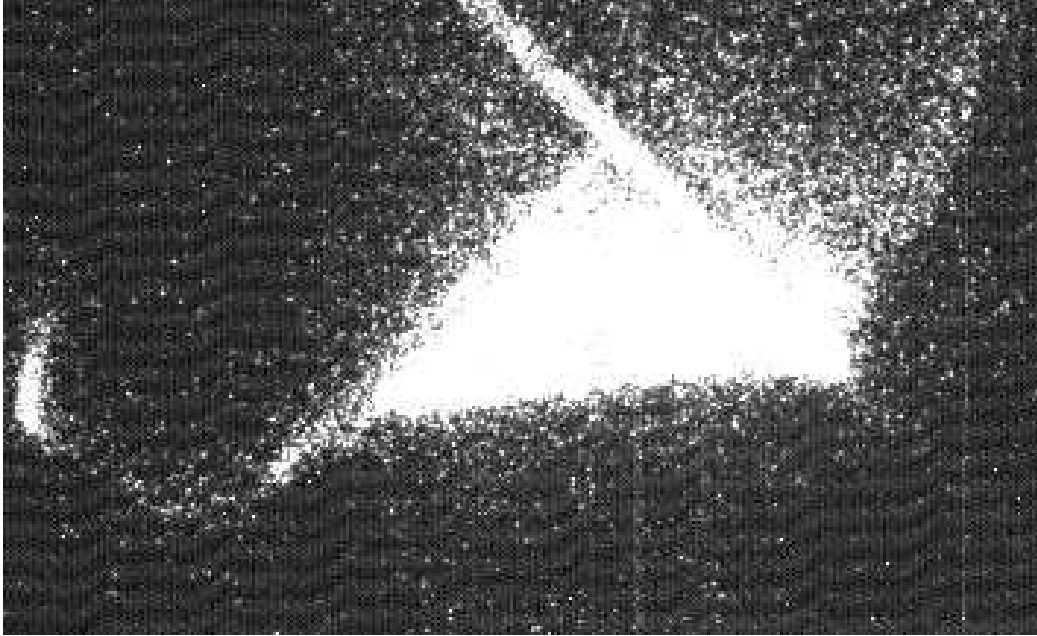


Figure E.36: Chemiluminescence from run 052.

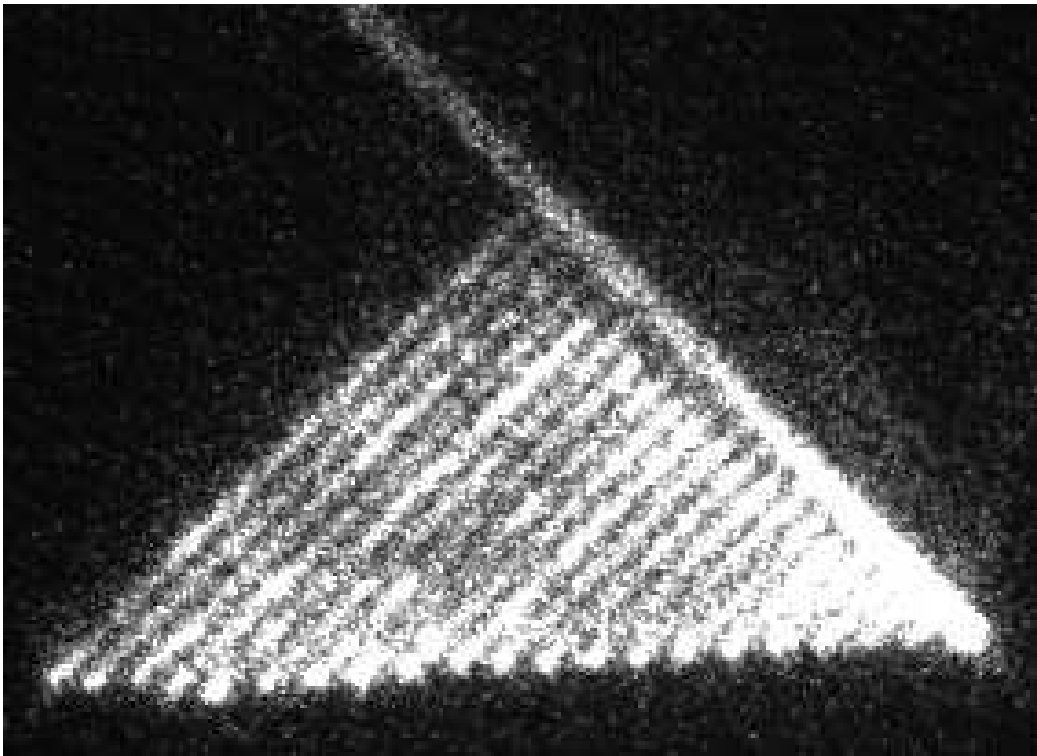


Figure E.37: Chemiluminescence from run 053.

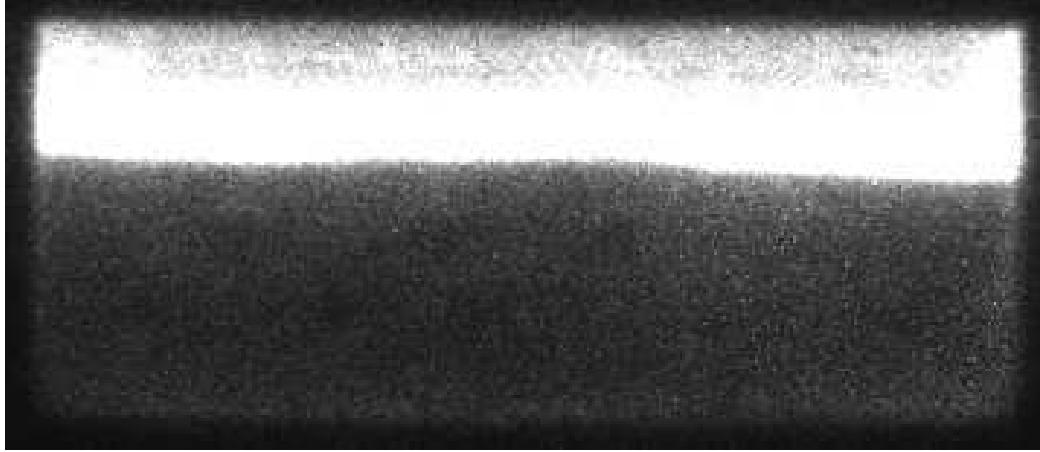


Figure E.38: Chemiluminescence from run 054.

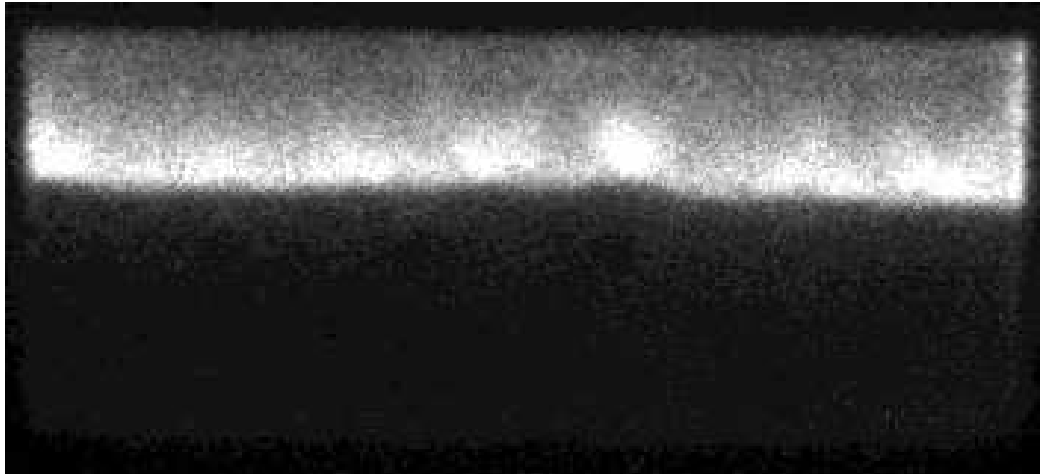


Figure E.39: Chemiluminescence from run 055.

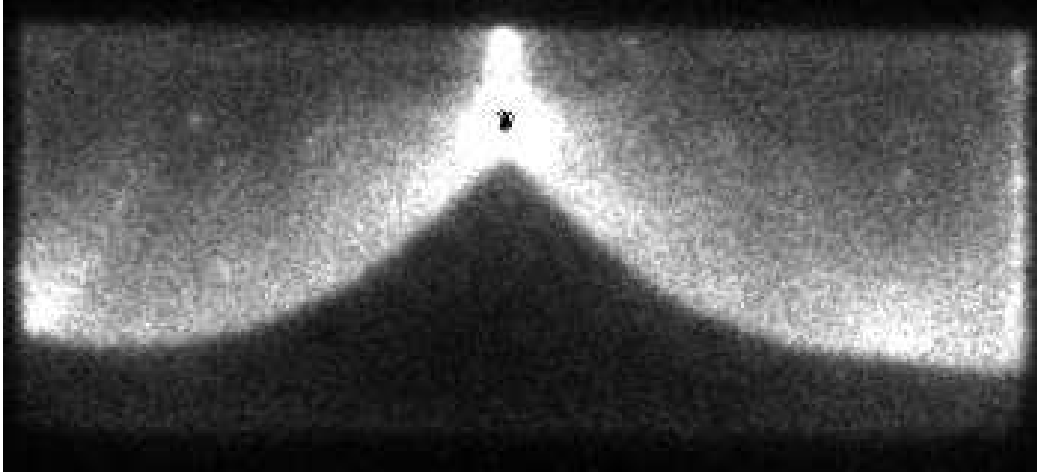


Figure E.40: Chemiluminescence from run 056.

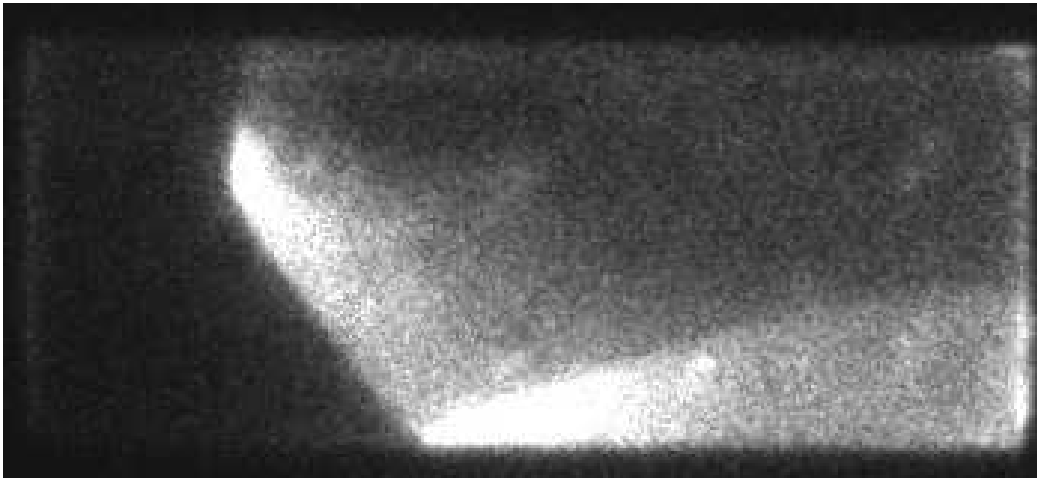


Figure E.41: Chemiluminescence from run 057.



Figure E.42: Chemiluminescence from run 058.

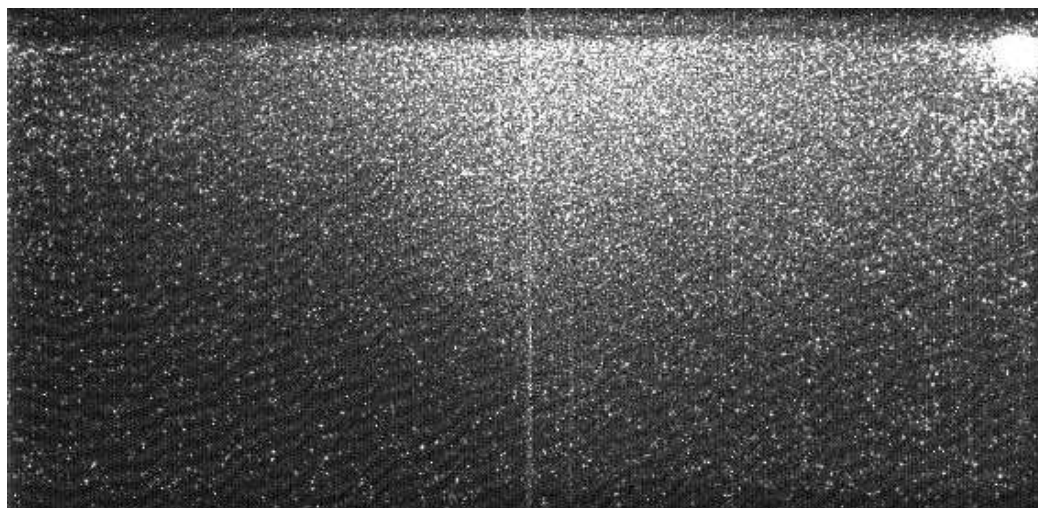


Figure E.43: Chemiluminescence from run 059.

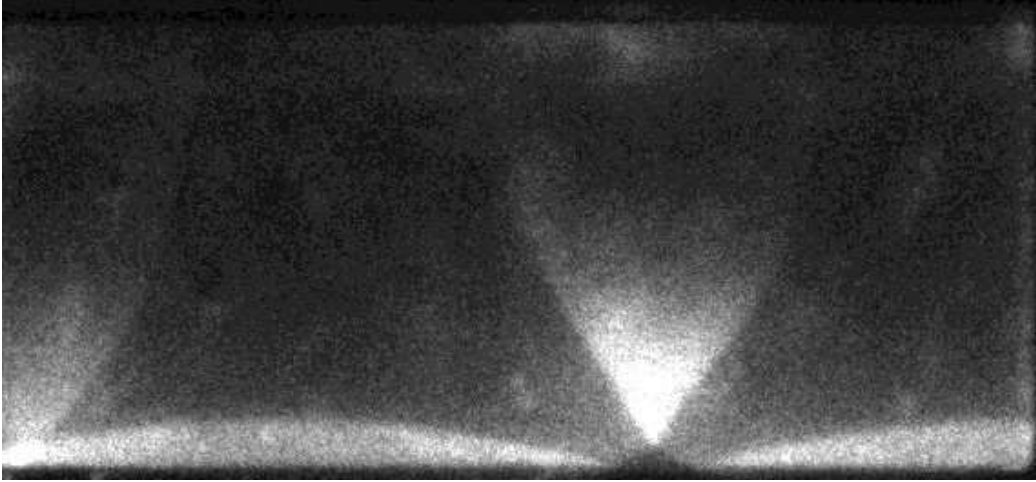


Figure E.44: Chemiluminescence from run 060.



Figure E.45: Chemiluminescence from run 061.

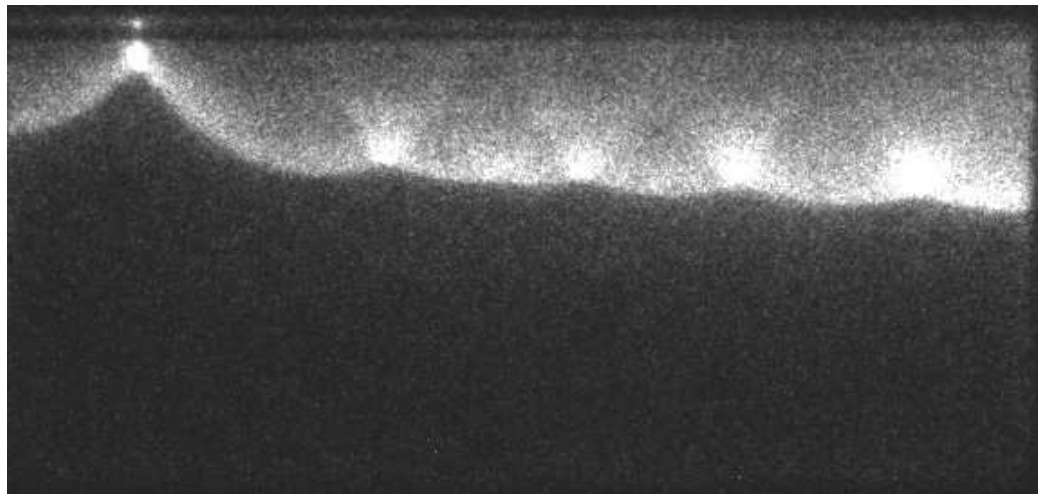


Figure E.46: Chemiluminescence from run 062.



Figure E.47: Chemiluminescence from run 063.



Figure E.48: Chemiluminescence from run 064.

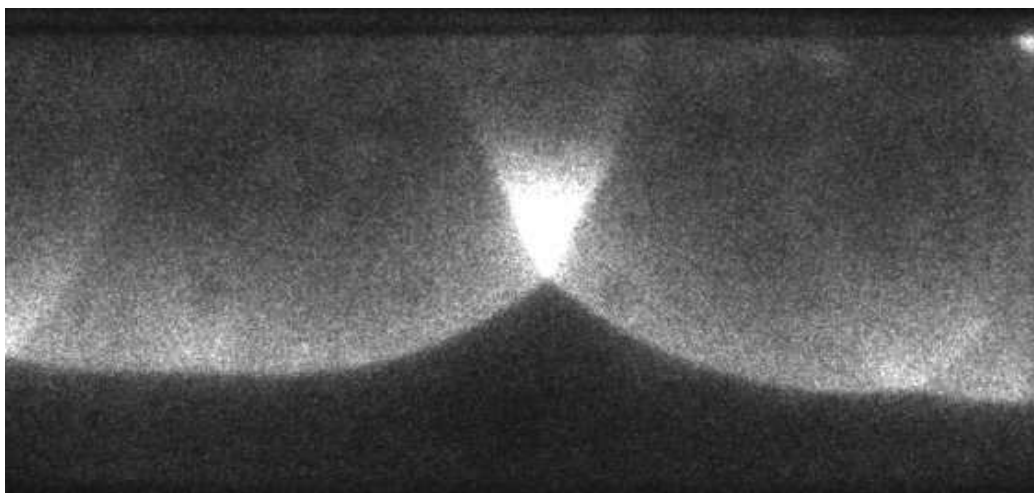


Figure E.49: Chemiluminescence from run 067.

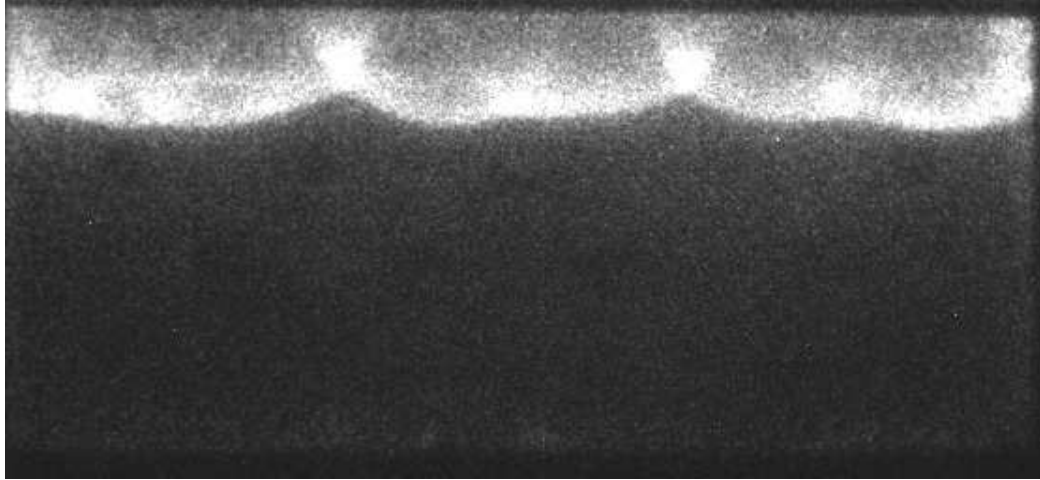


Figure E.50: Chemiluminescence from run 068.

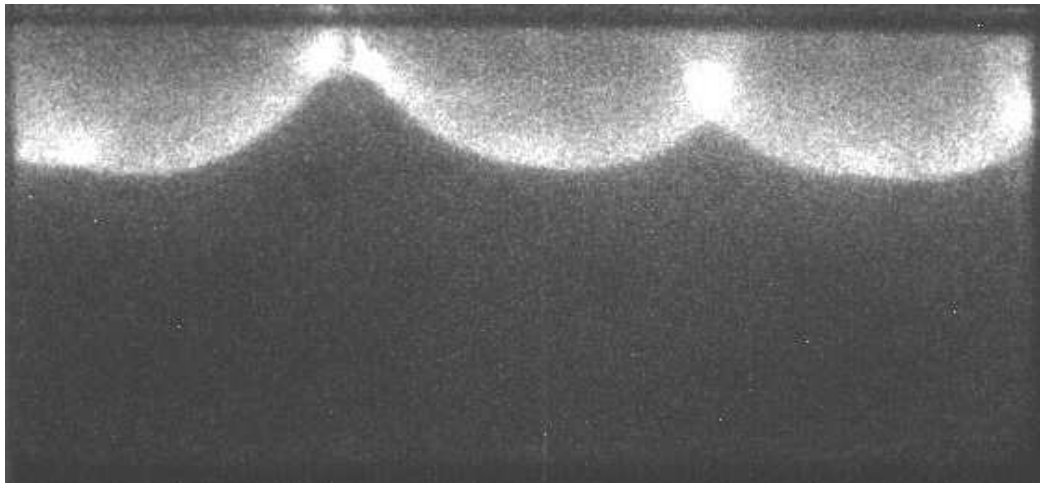


Figure E.51: Chemiluminescence from run 069.

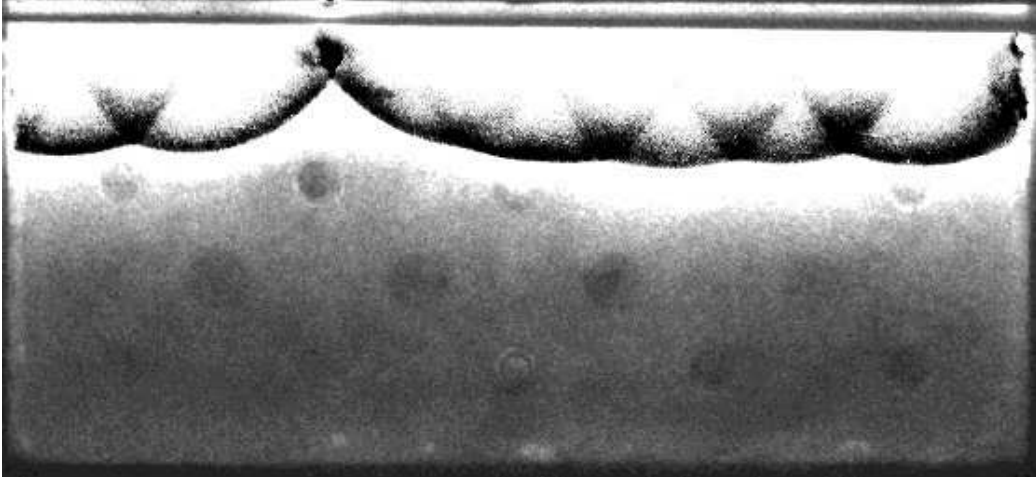


Figure E.52: Chemiluminescence from run 070.

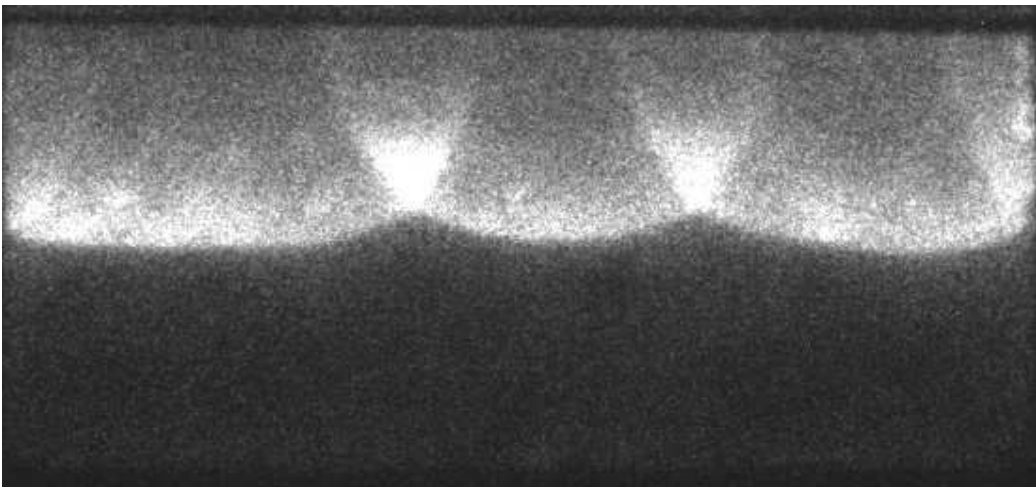


Figure E.53: Chemiluminescence from run 071.

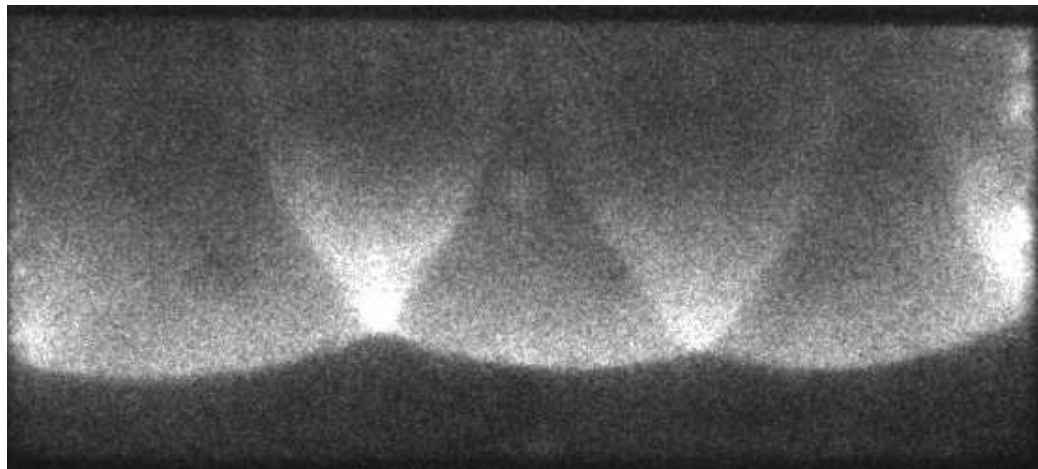


Figure E.54: Chemiluminescence from run 072.

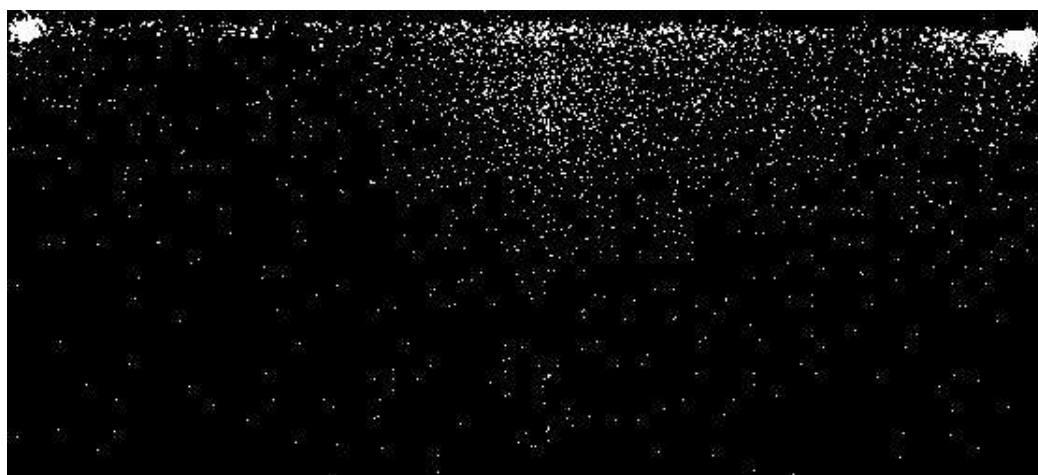


Figure E.55: Chemiluminescence from run 074.

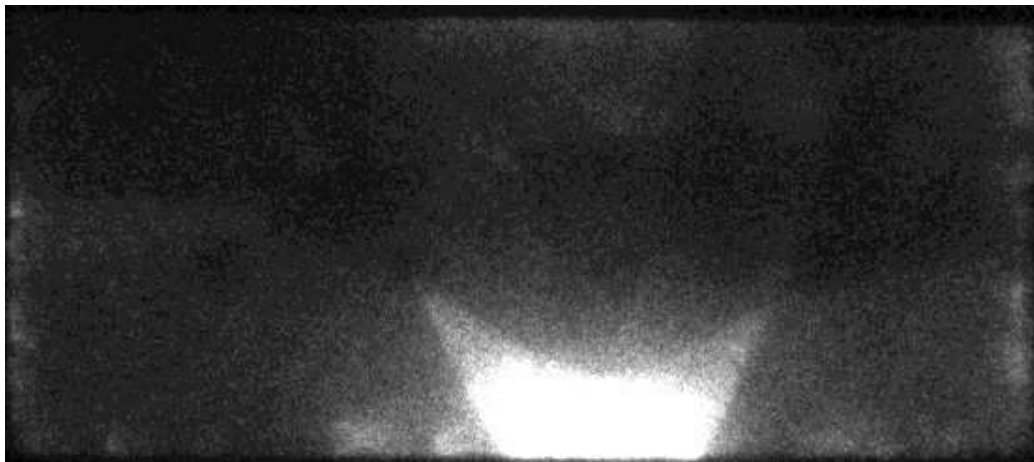


Figure E.56: Chemiluminescence from run 075.

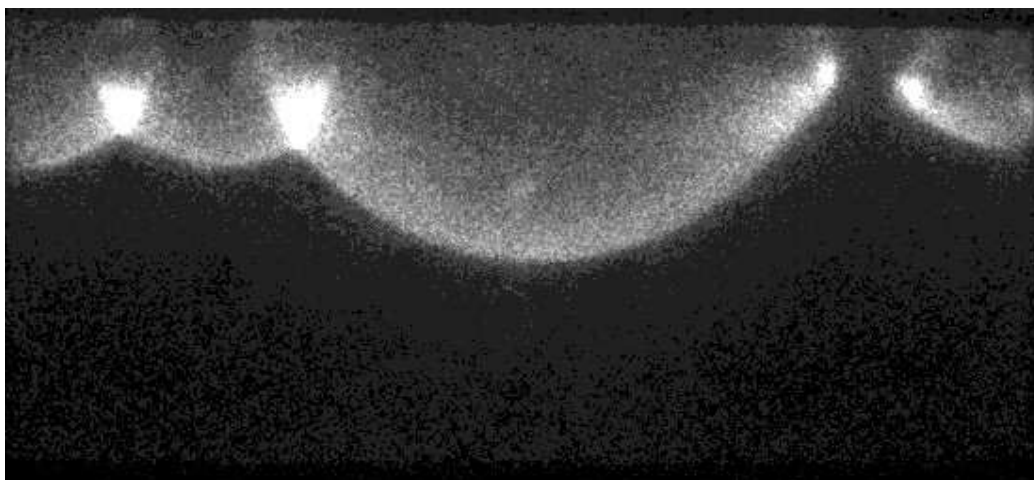


Figure E.57: Chemiluminescence from run 076.

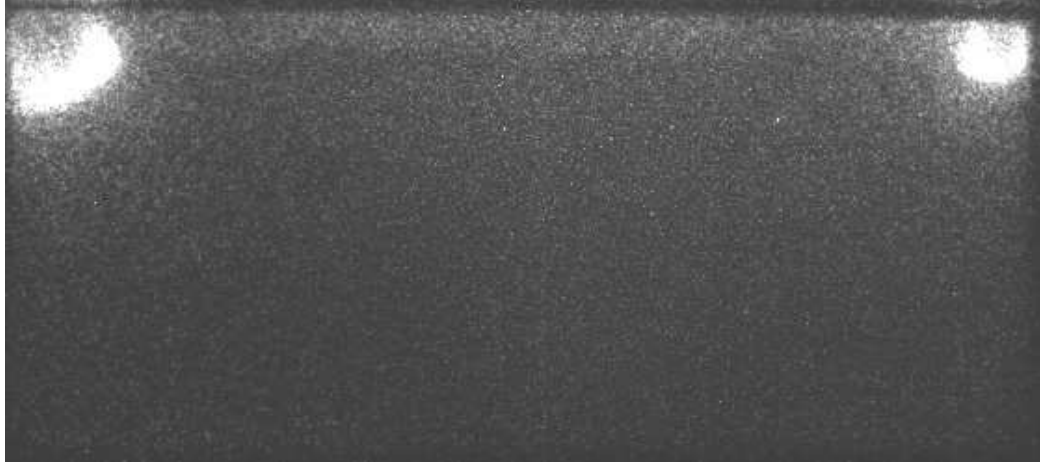


Figure E.58: Chemiluminescence from run 077.

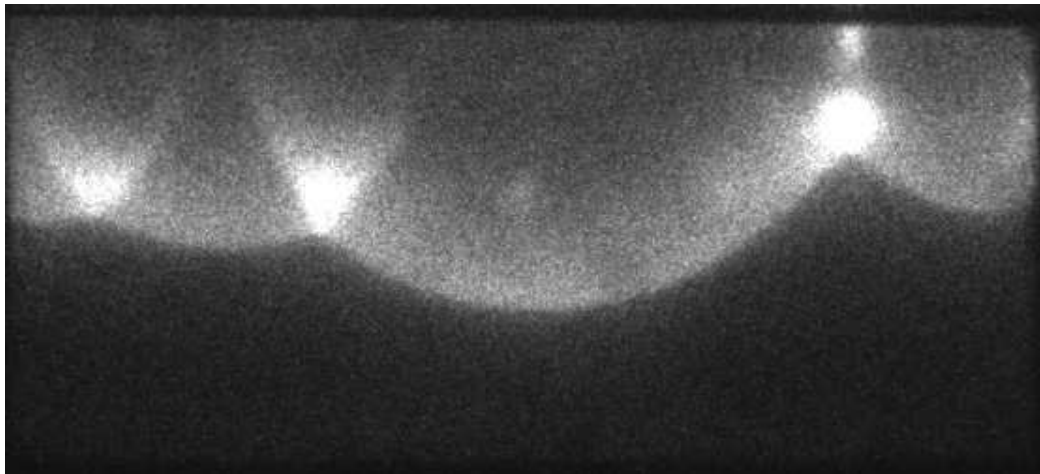


Figure E.59: Chemiluminescence from run 080.



Figure E.60: Chemiluminescence from run 081.

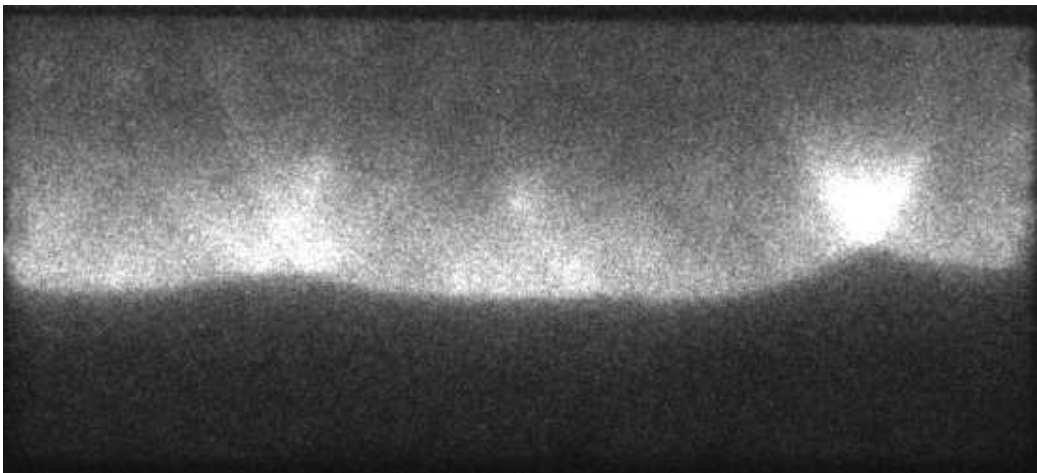


Figure E.61: Chemiluminescence from run 082.

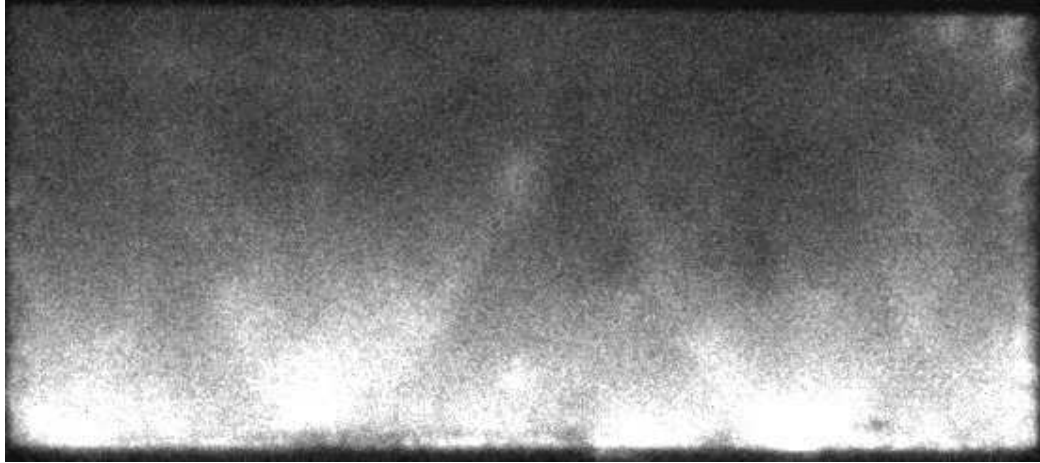


Figure E.62: Chemiluminescence from run 083.

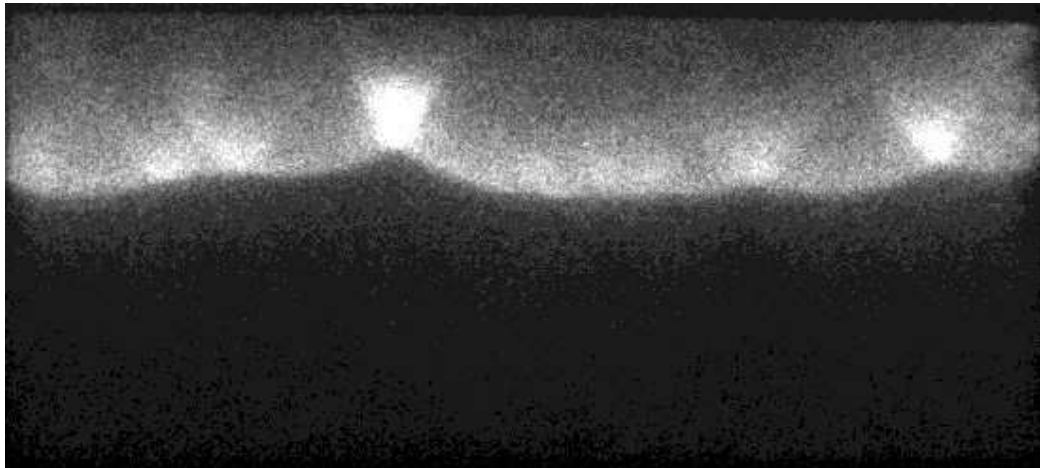


Figure E.63: Chemiluminescence from run 084.



Figure E.64: Chemiluminescence from run 085.



Figure E.65: Chemiluminescence from run 086.



Figure E.66: Chemiluminescence from run 087.

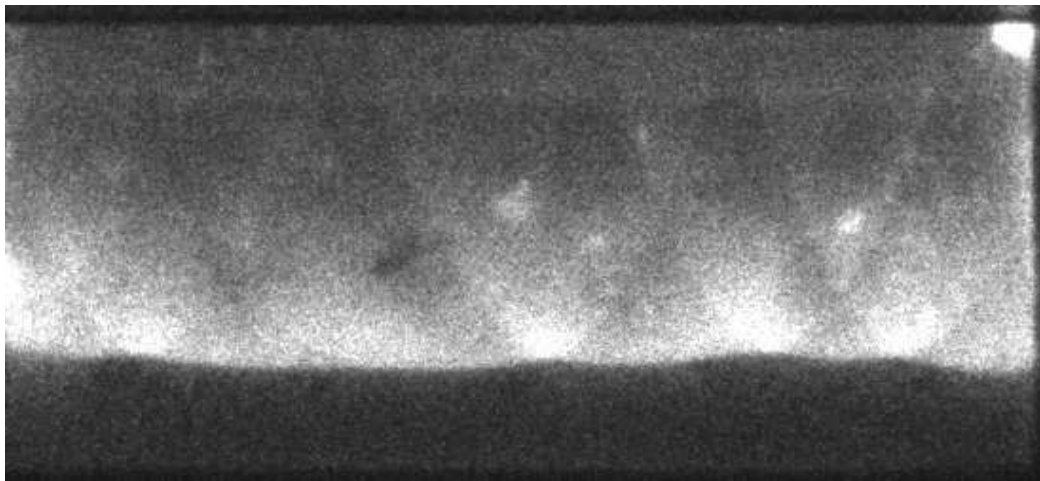


Figure E.67: Chemiluminescence from run 088.

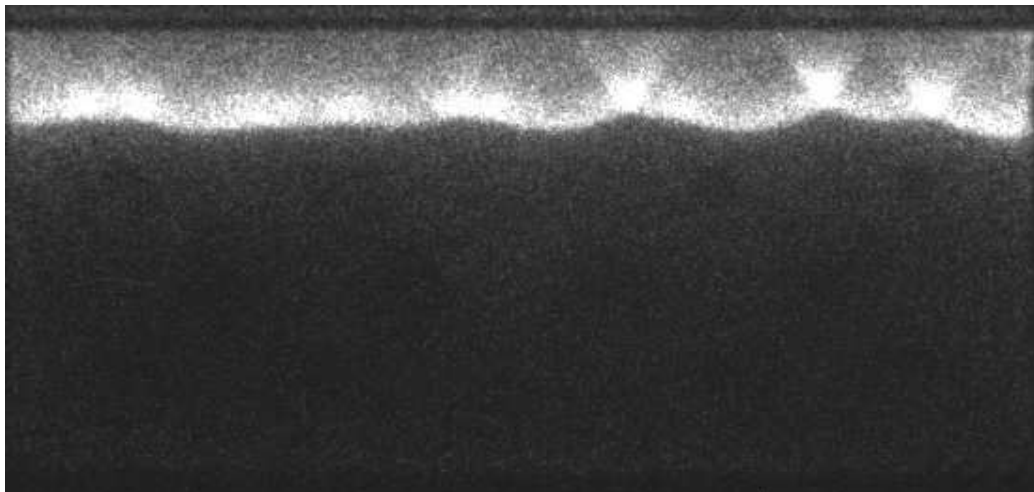


Figure E.68: Chemiluminescence from run 089.

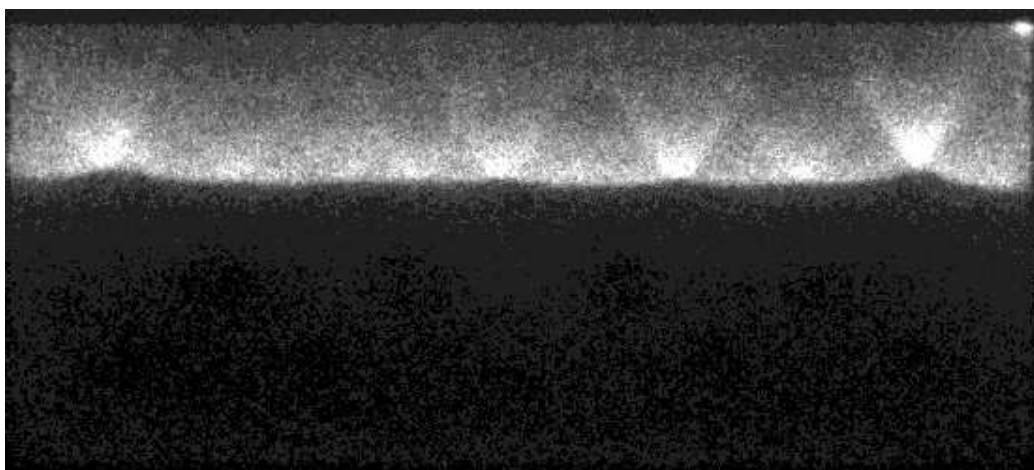


Figure E.69: Chemiluminescence from run 090.

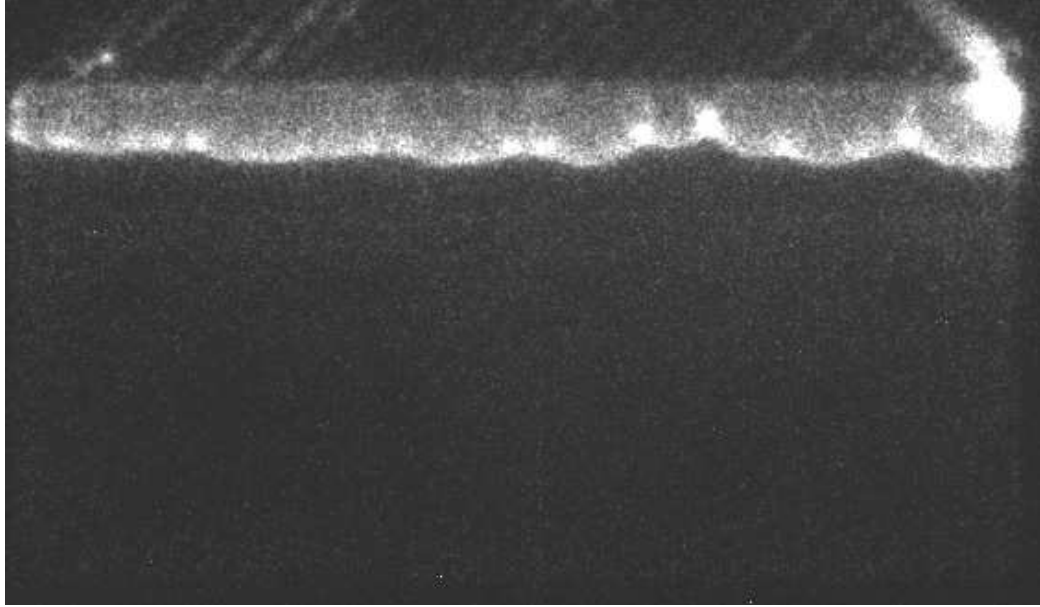


Figure E.70: Chemiluminescence from run 091.

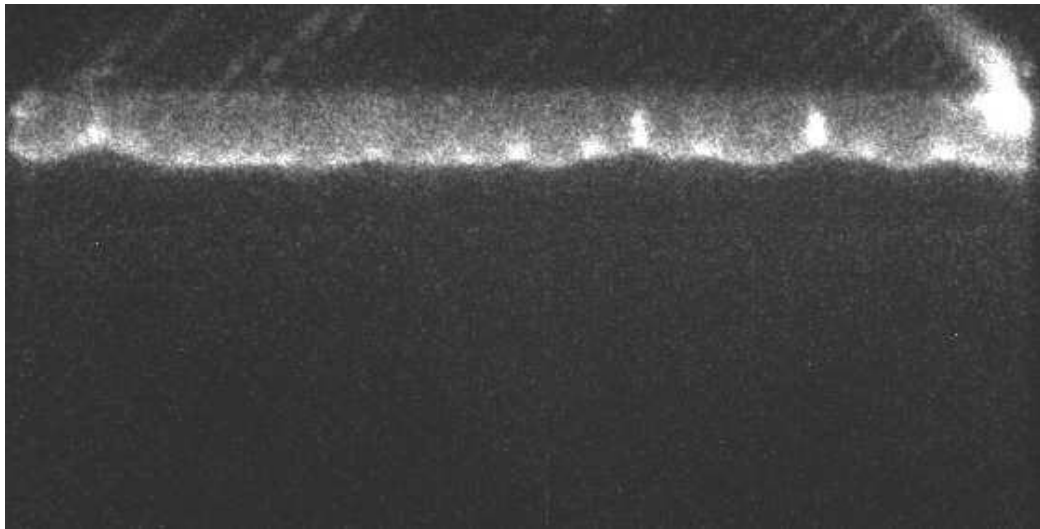


Figure E.71: Chemiluminescence from run 092.

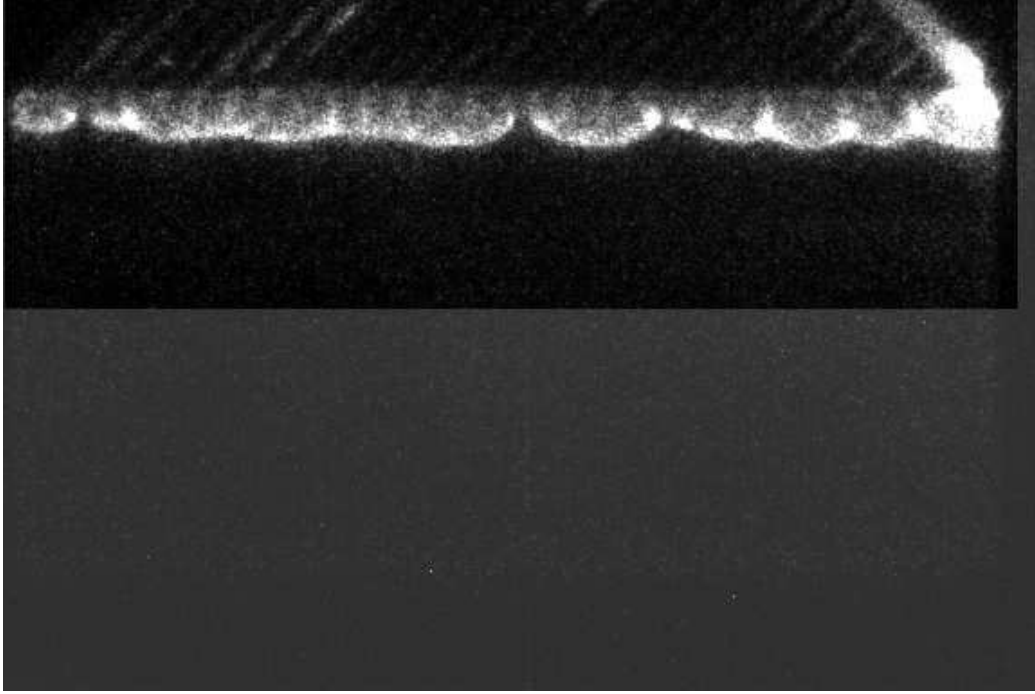


Figure E.72: Chemiluminescence from run 095.

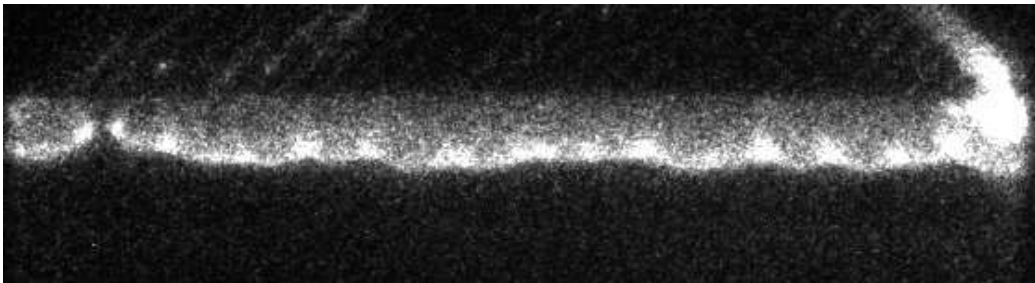


Figure E.73: Chemiluminescence from run 096.

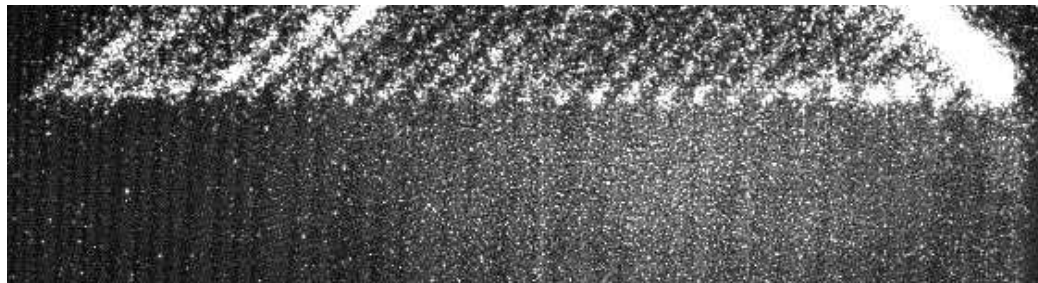


Figure E.74: Chemiluminescence from run 097.

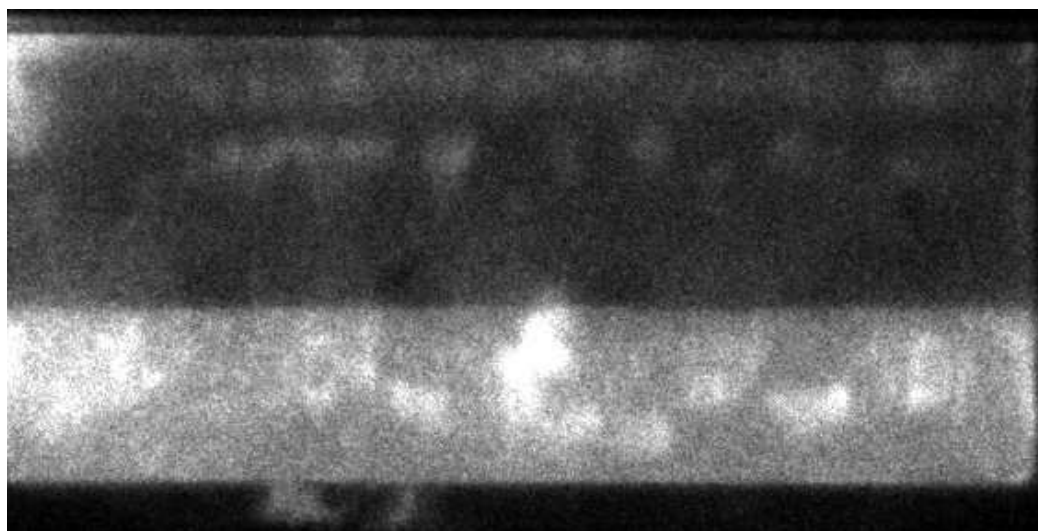


Figure E.75: Chemiluminescence from run 098.

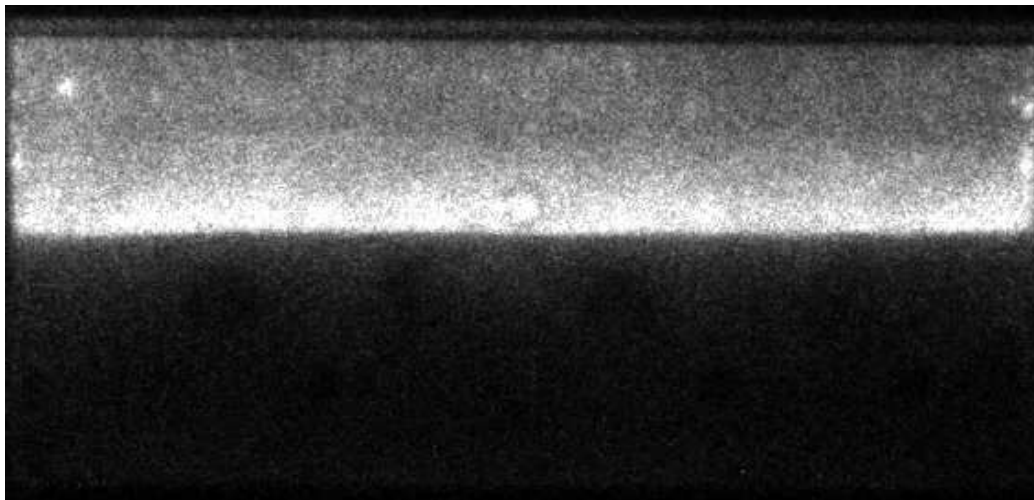


Figure E.76: Chemiluminescence from run 099.

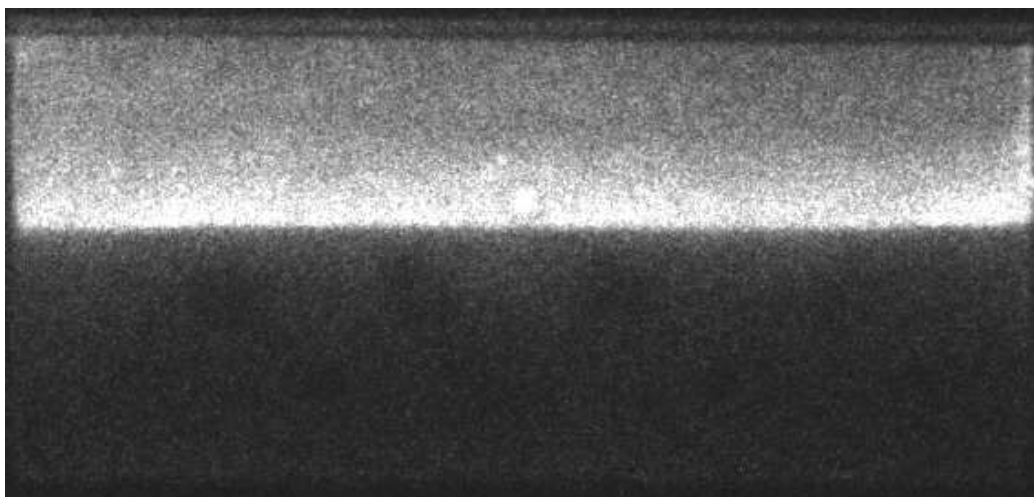


Figure E.77: Chemiluminescence from run 100.

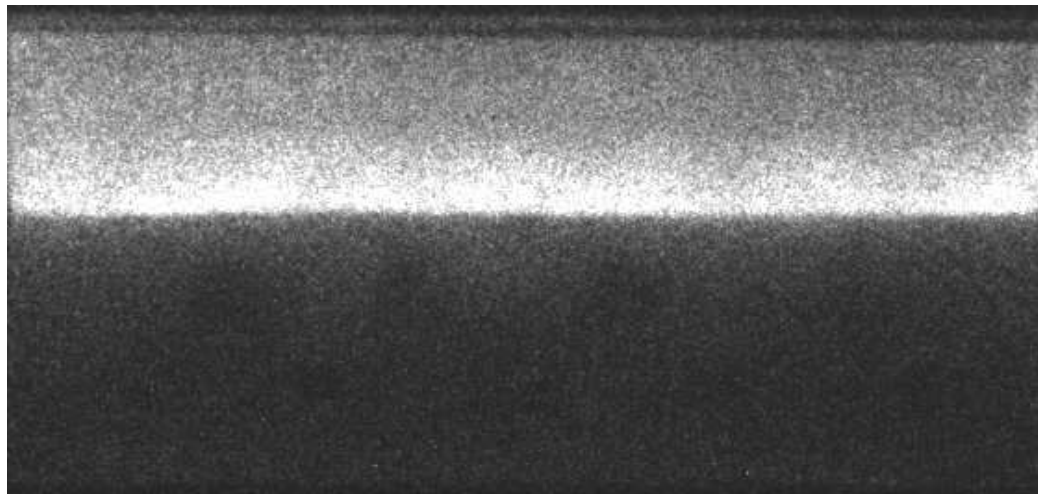


Figure E.78: Chemiluminescence from run 101.

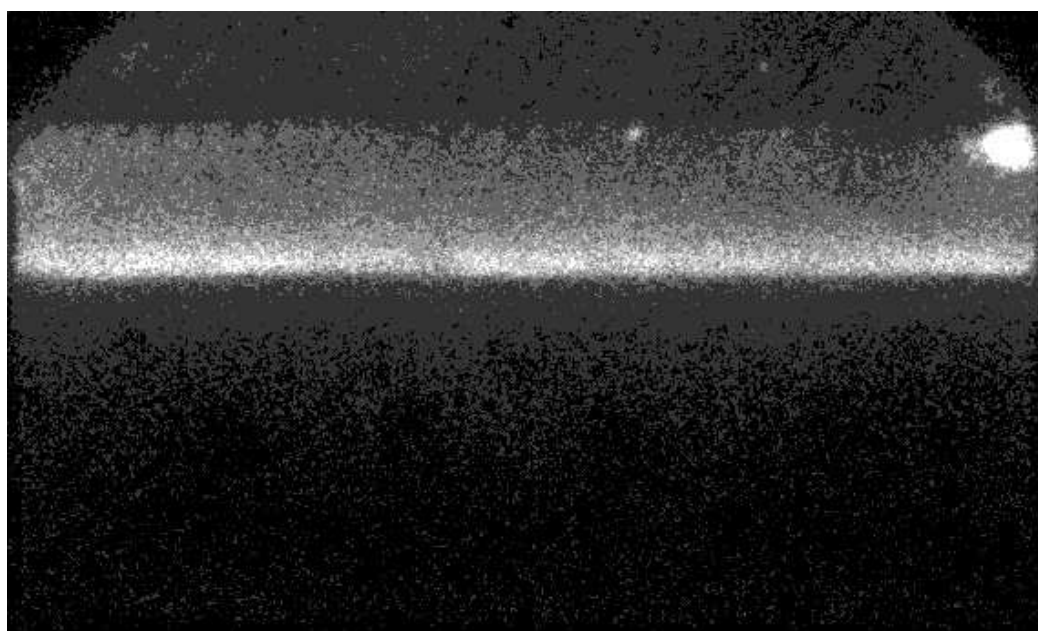


Figure E.79: Chemiluminescence from run 103.

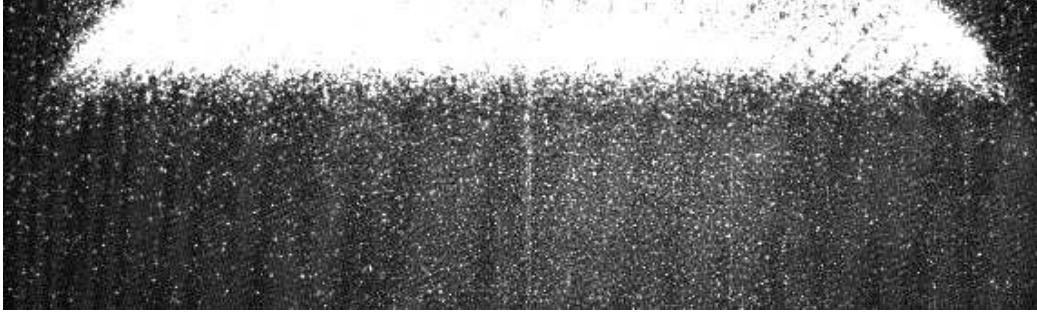


Figure E.80: Chemiluminescence from run 104.

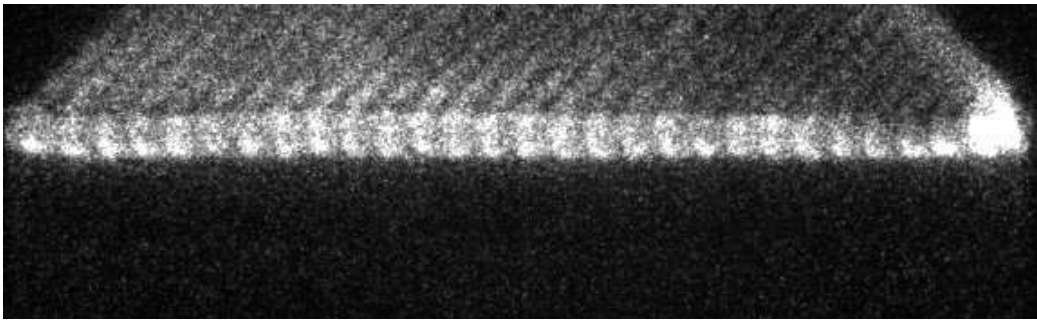


Figure E.81: Chemiluminescence from run 105.

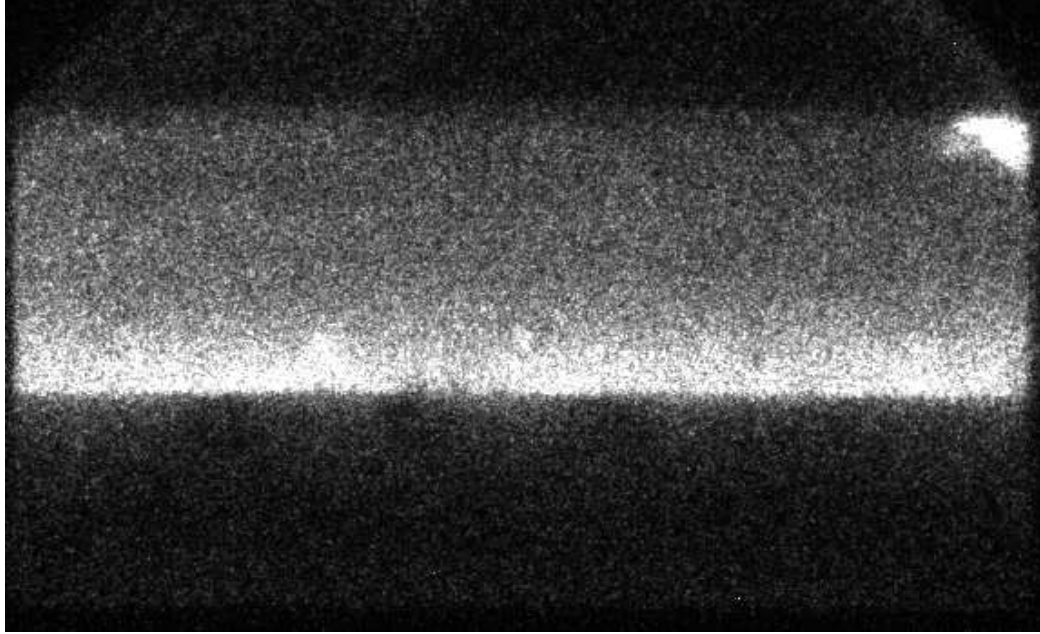


Figure E.82: Chemiluminescence from run 107.

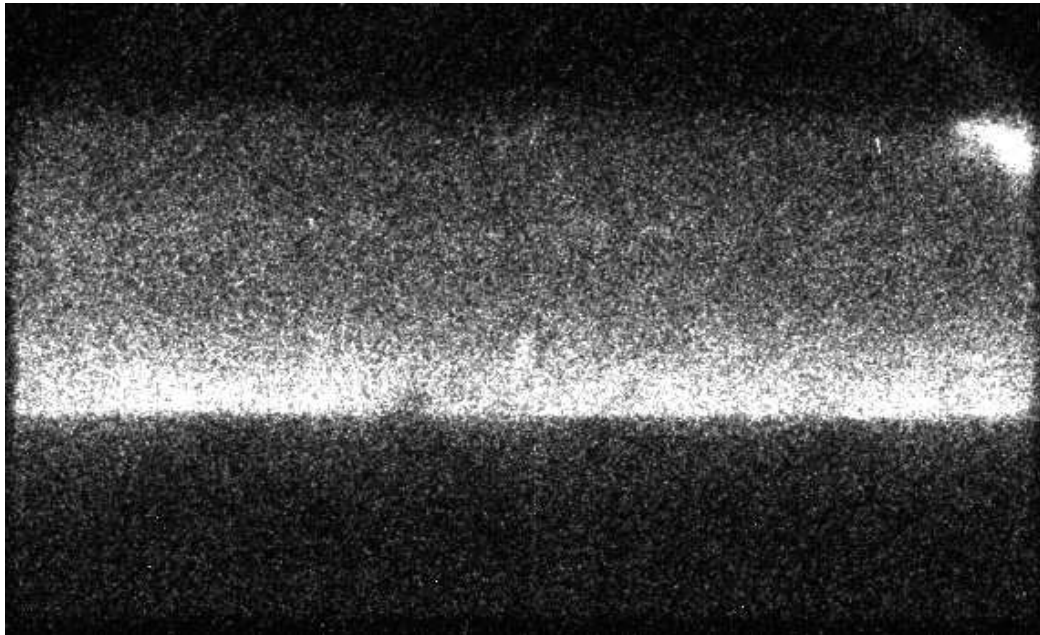


Figure E.83: Chemiluminescence from run 109.

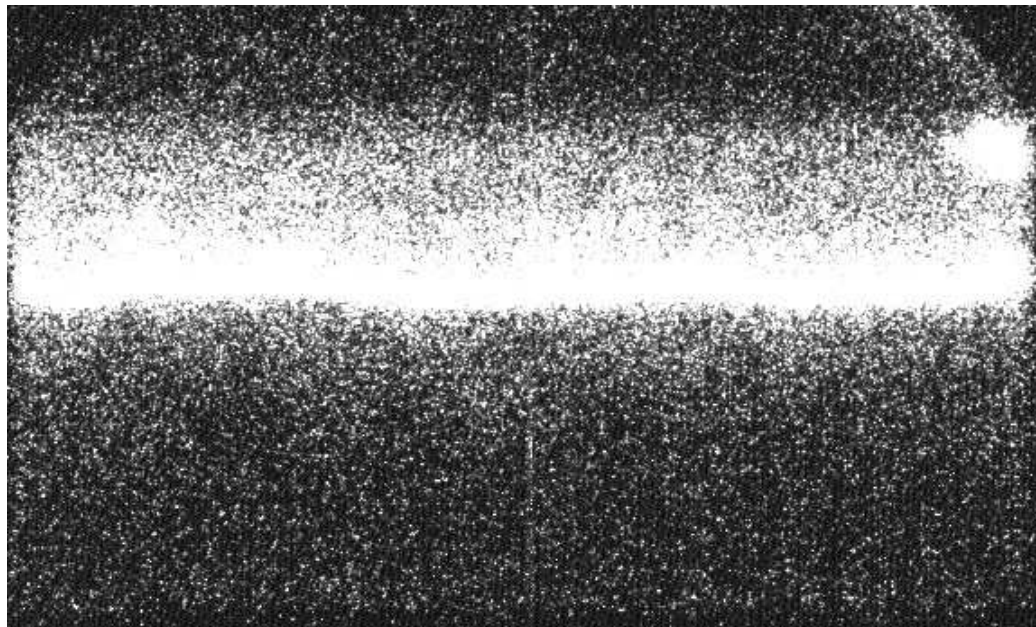


Figure E.84: Chemiluminescence from run 110.

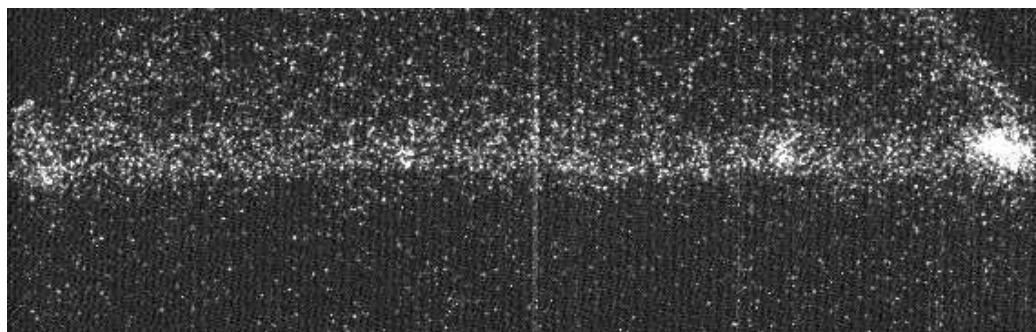


Figure E.85: Chemiluminescence from run 111.

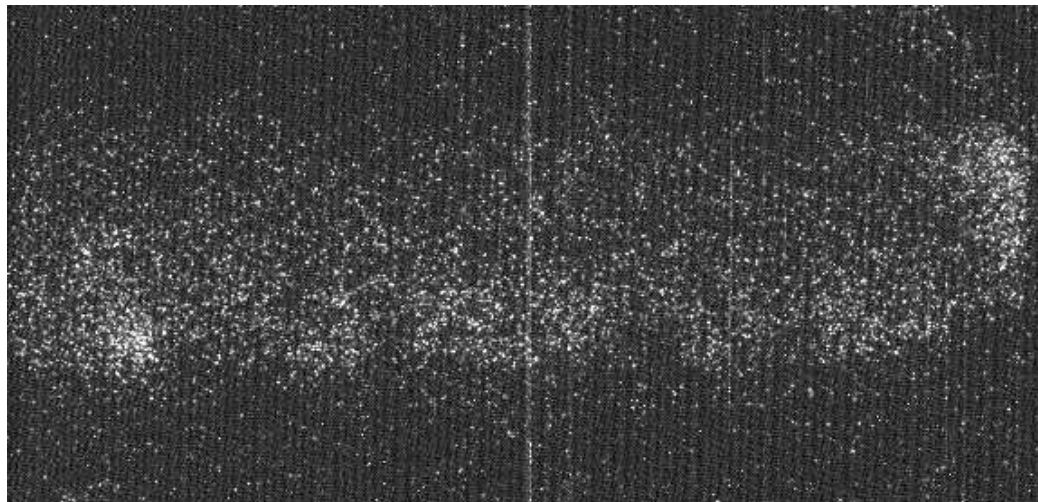


Figure E.86: Chemiluminescence from run 112.

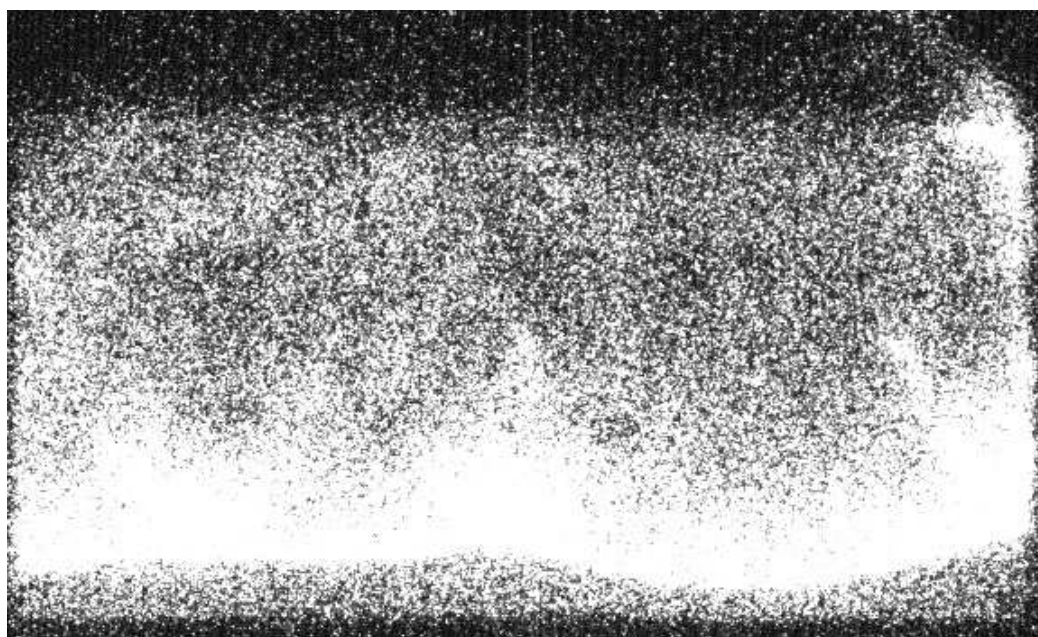


Figure E.87: Chemiluminescence from run 114.

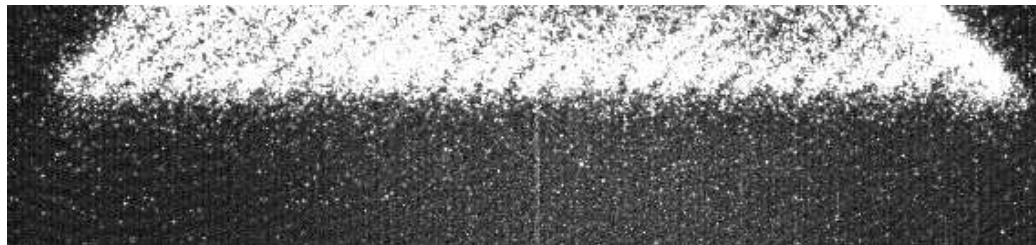


Figure E.88: Chemiluminescence from run 115.

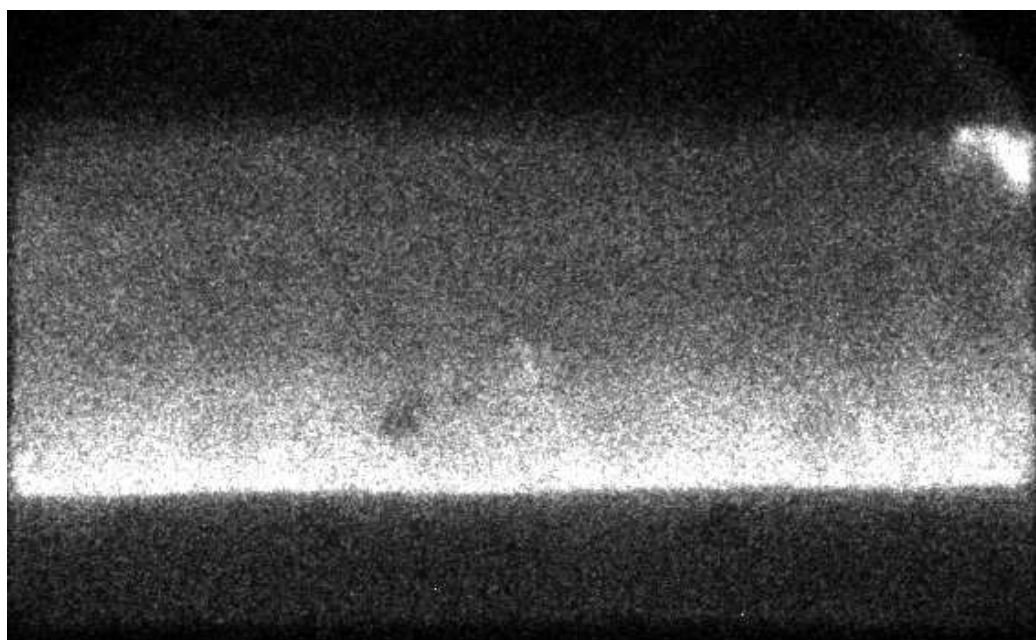


Figure E.89: Chemiluminescence from run 116.

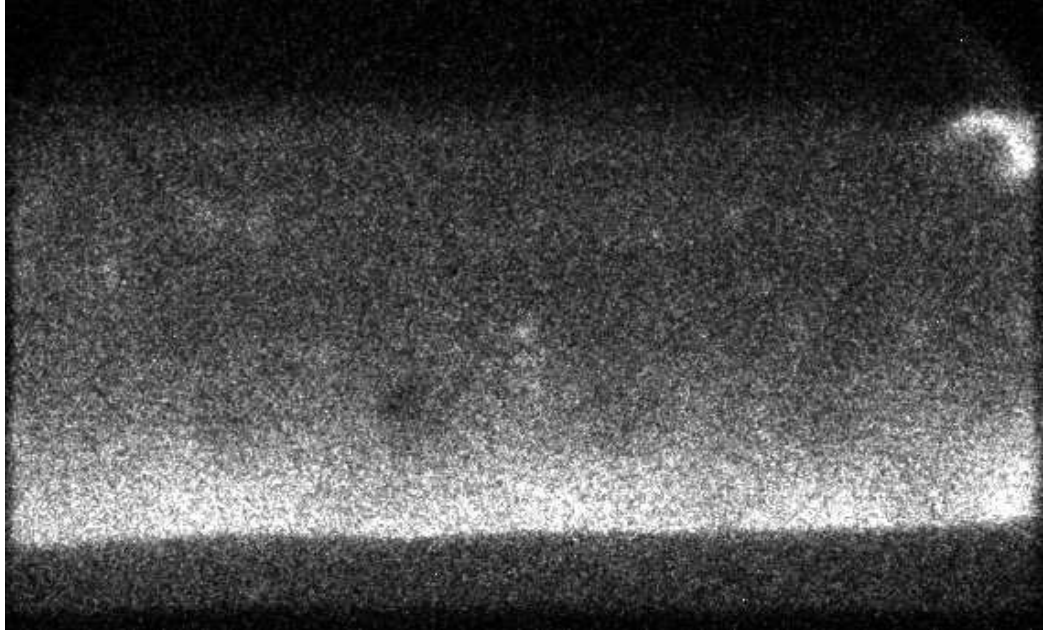


Figure E.90: Chemiluminescence from run 117.

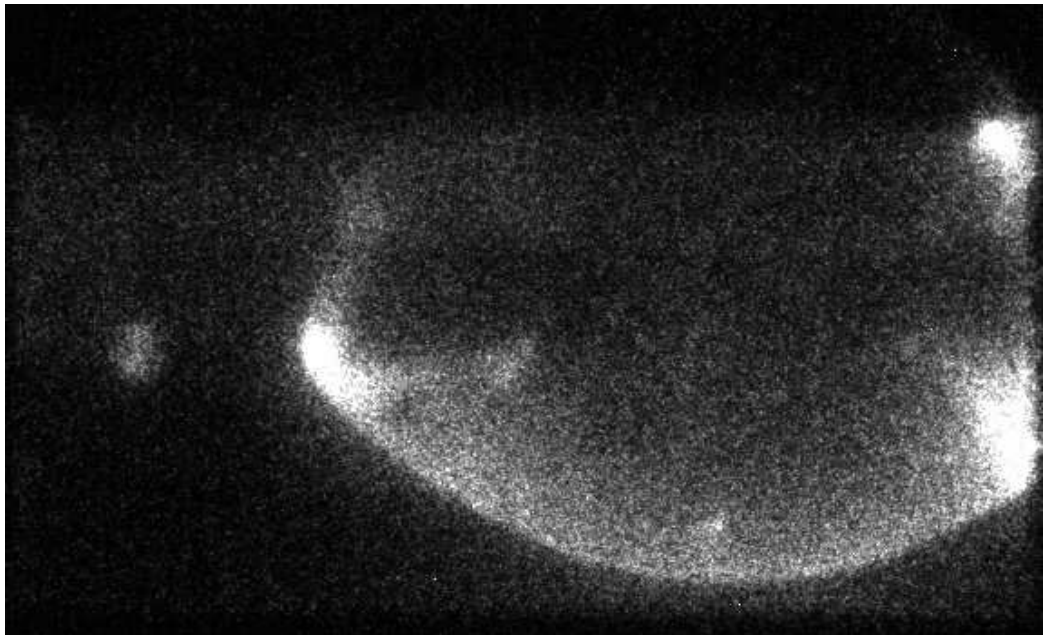


Figure E.91: Chemiluminescence from run 120.

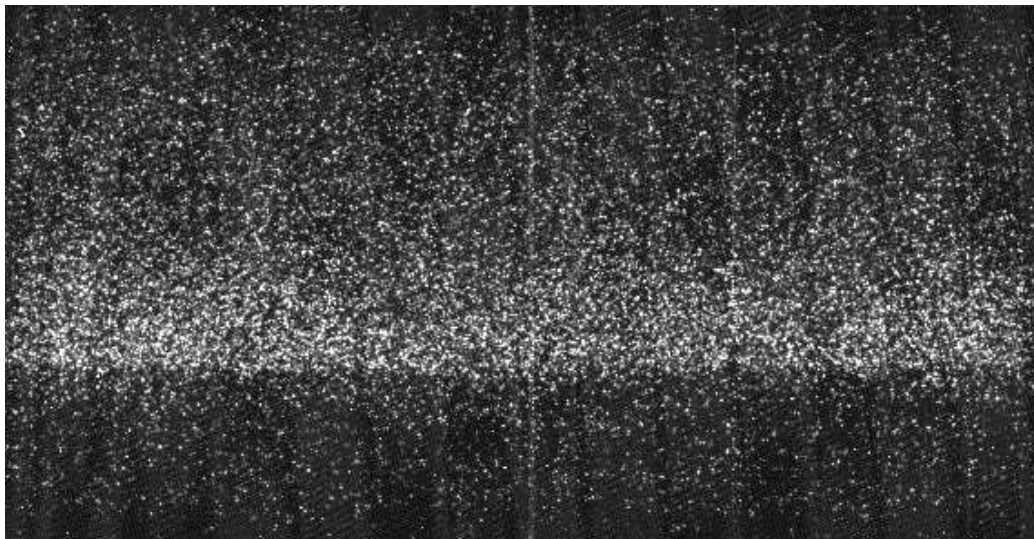


Figure E.92: Chemiluminescence from run 122.

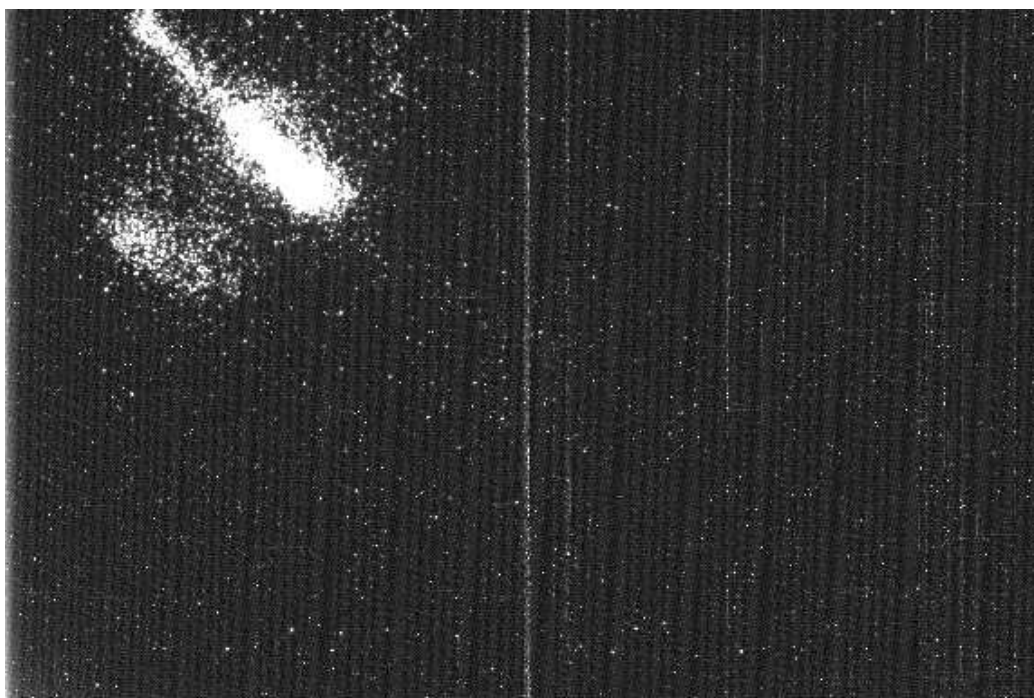


Figure E.93: Chemiluminescence from run 123.

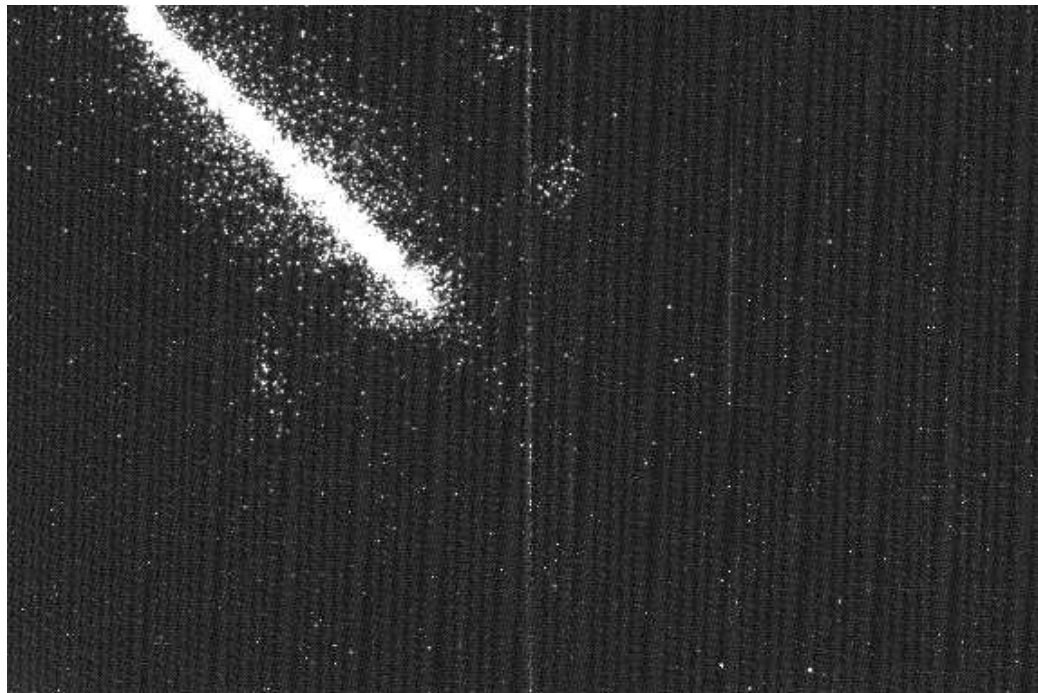


Figure E.94: Chemiluminescence from run 124.

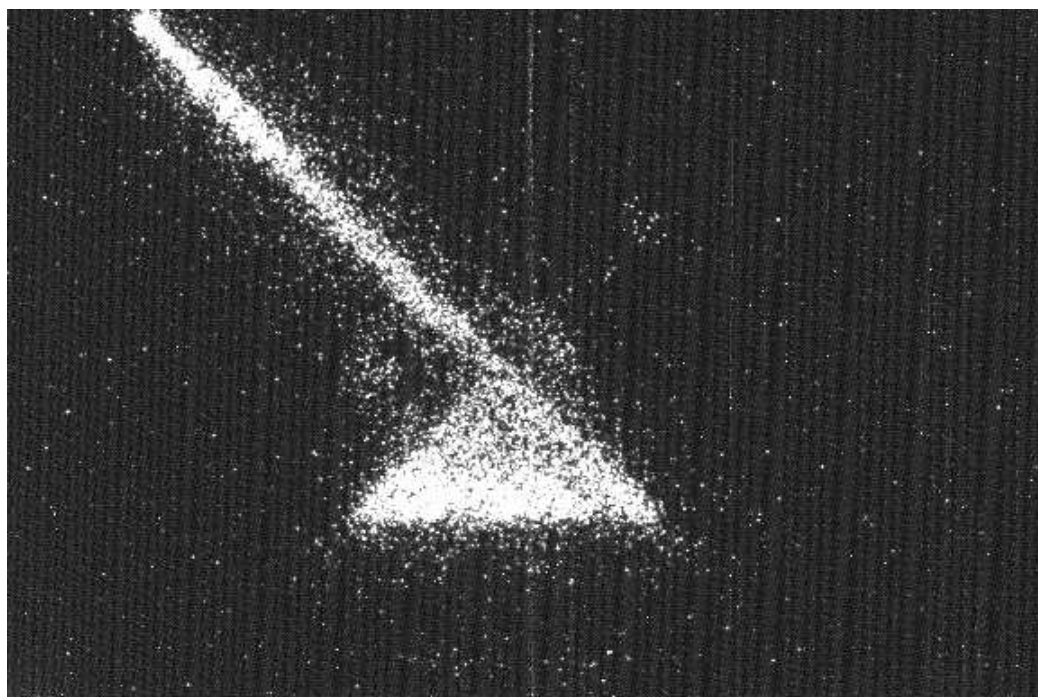


Figure E.95: Chemiluminescence from run 125.

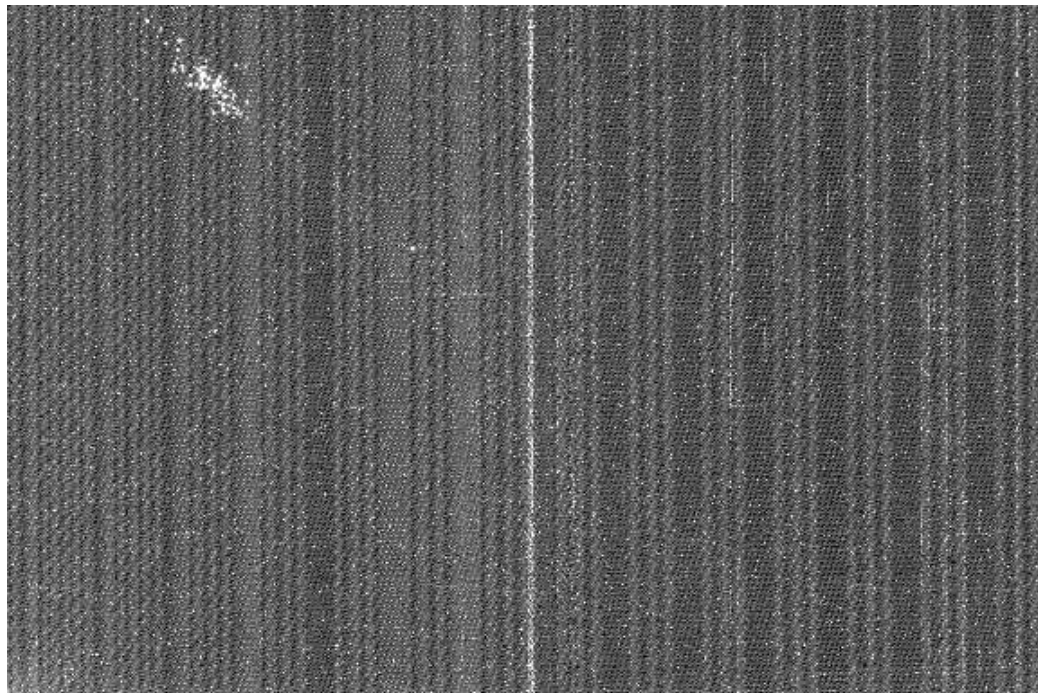


Figure E.96: Chemiluminescence from run 127.

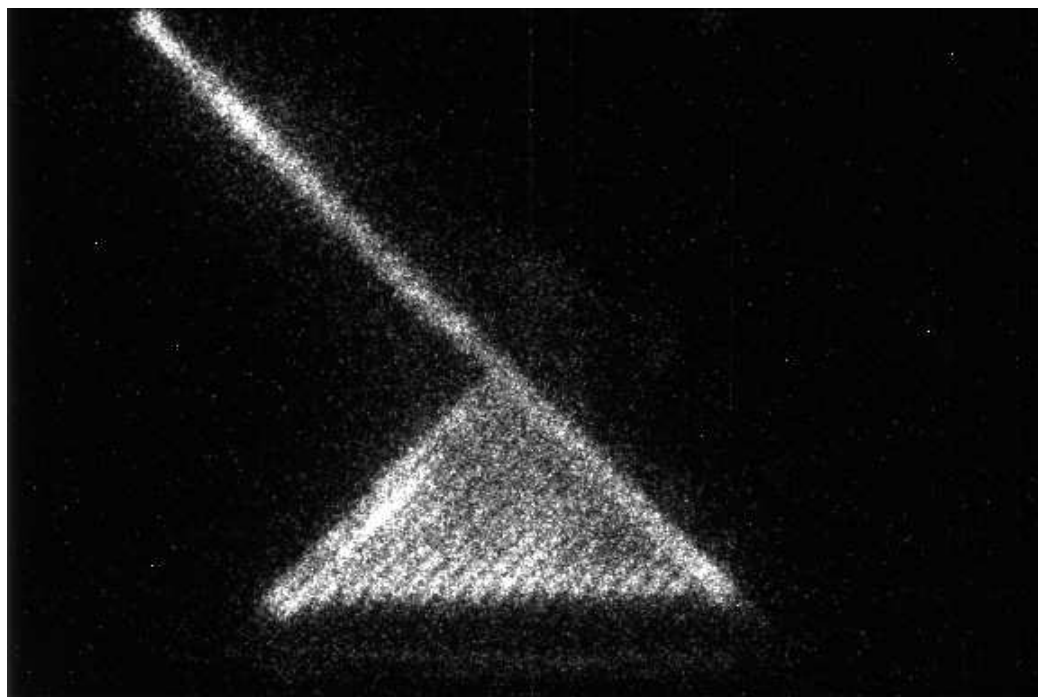


Figure E.97: Chemiluminescence from run 128.

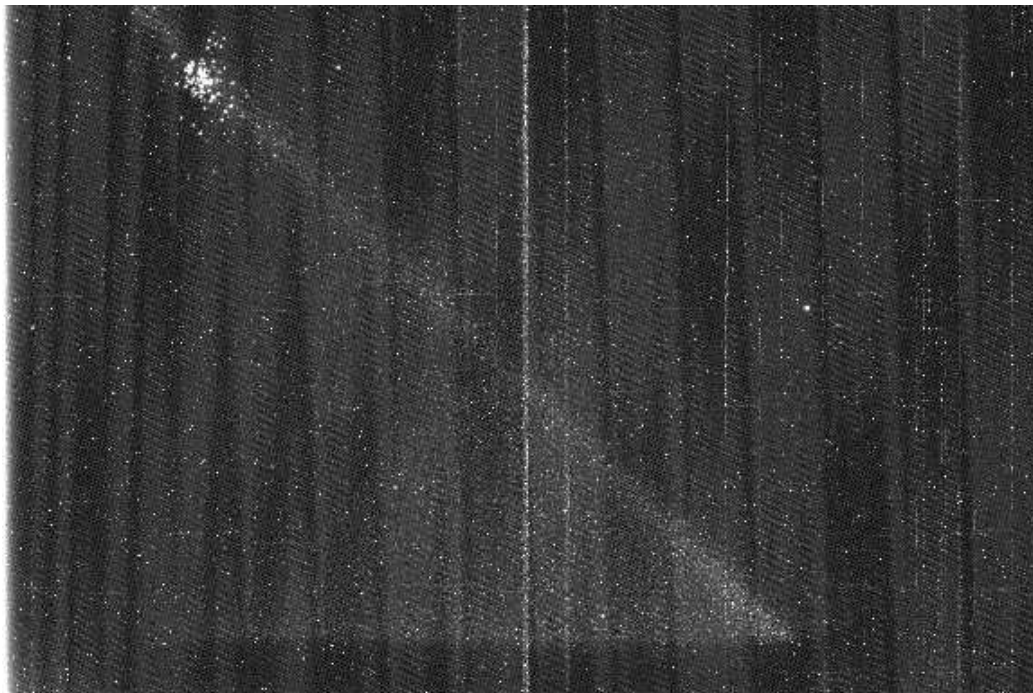


Figure E.98: Chemiluminescence from run 129.

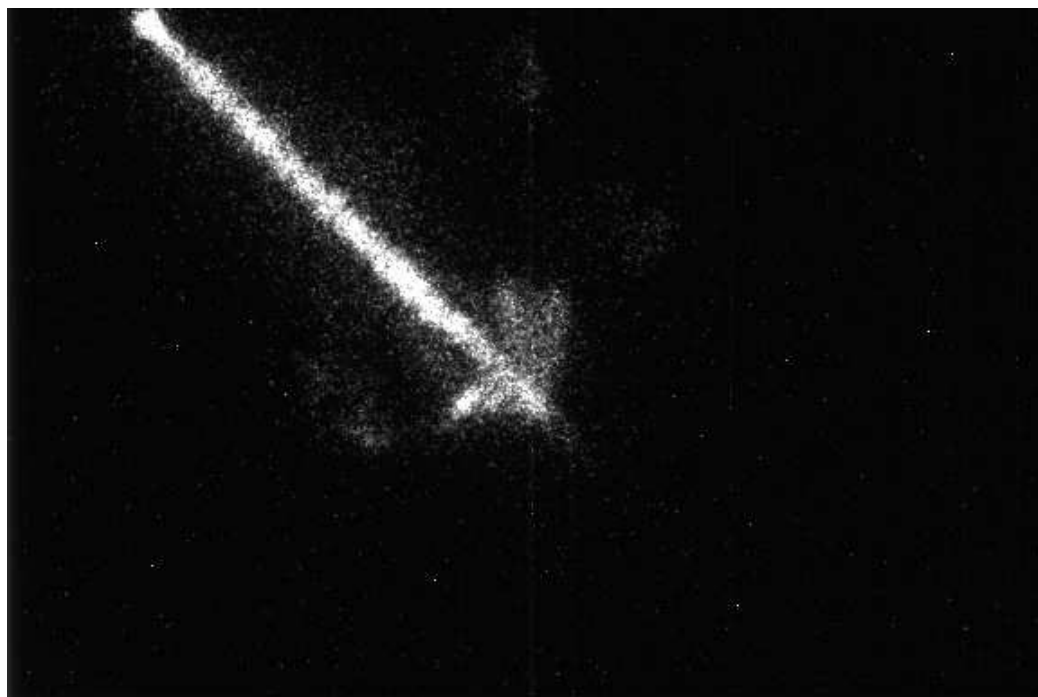


Figure E.99: Chemiluminescence from run 130.



## Appendix F

### Toroidal Static Initiator Data

# F.1 Drawings

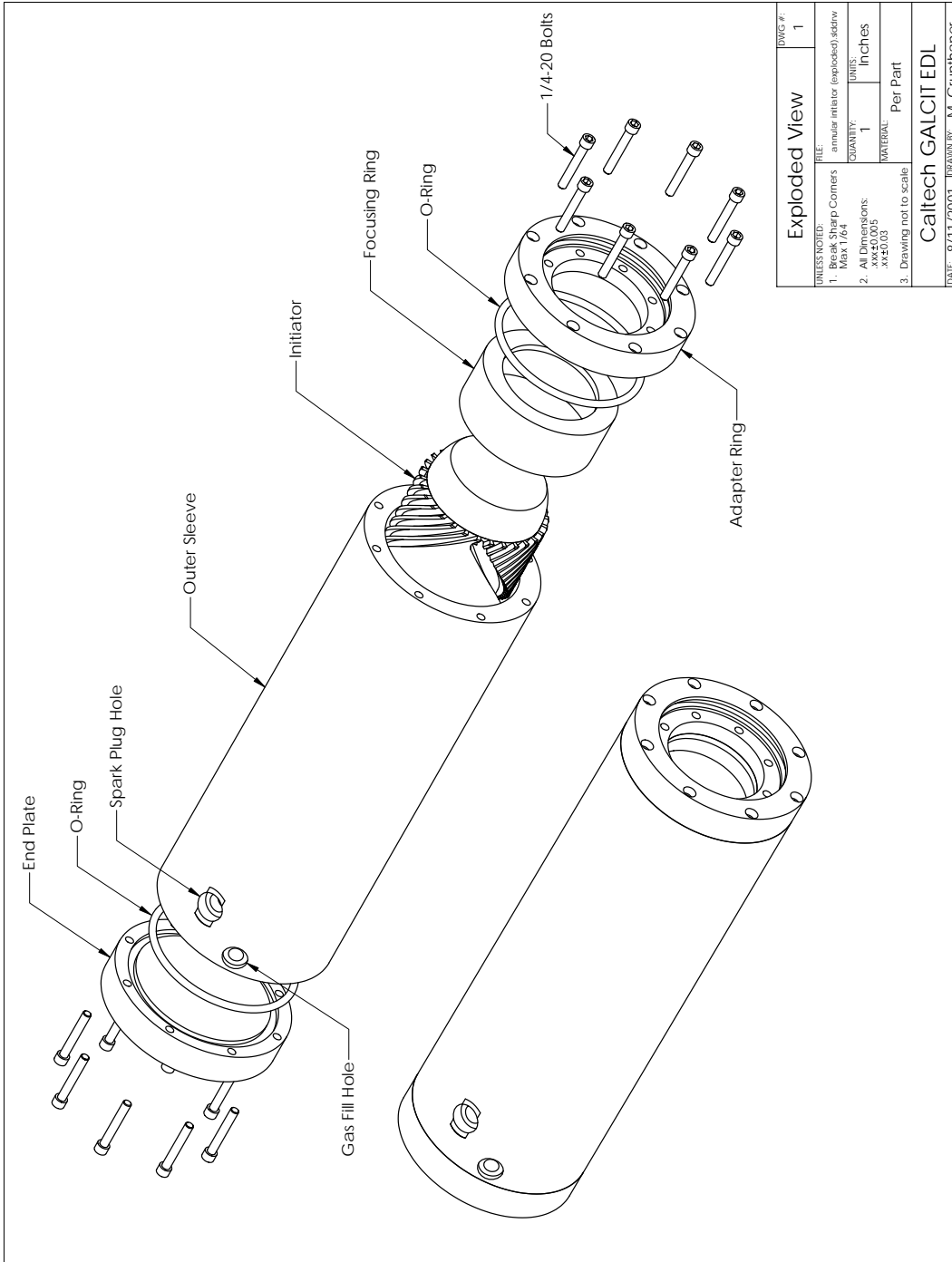


Figure F.1: Exploded view of the toroidal initiator assembly.

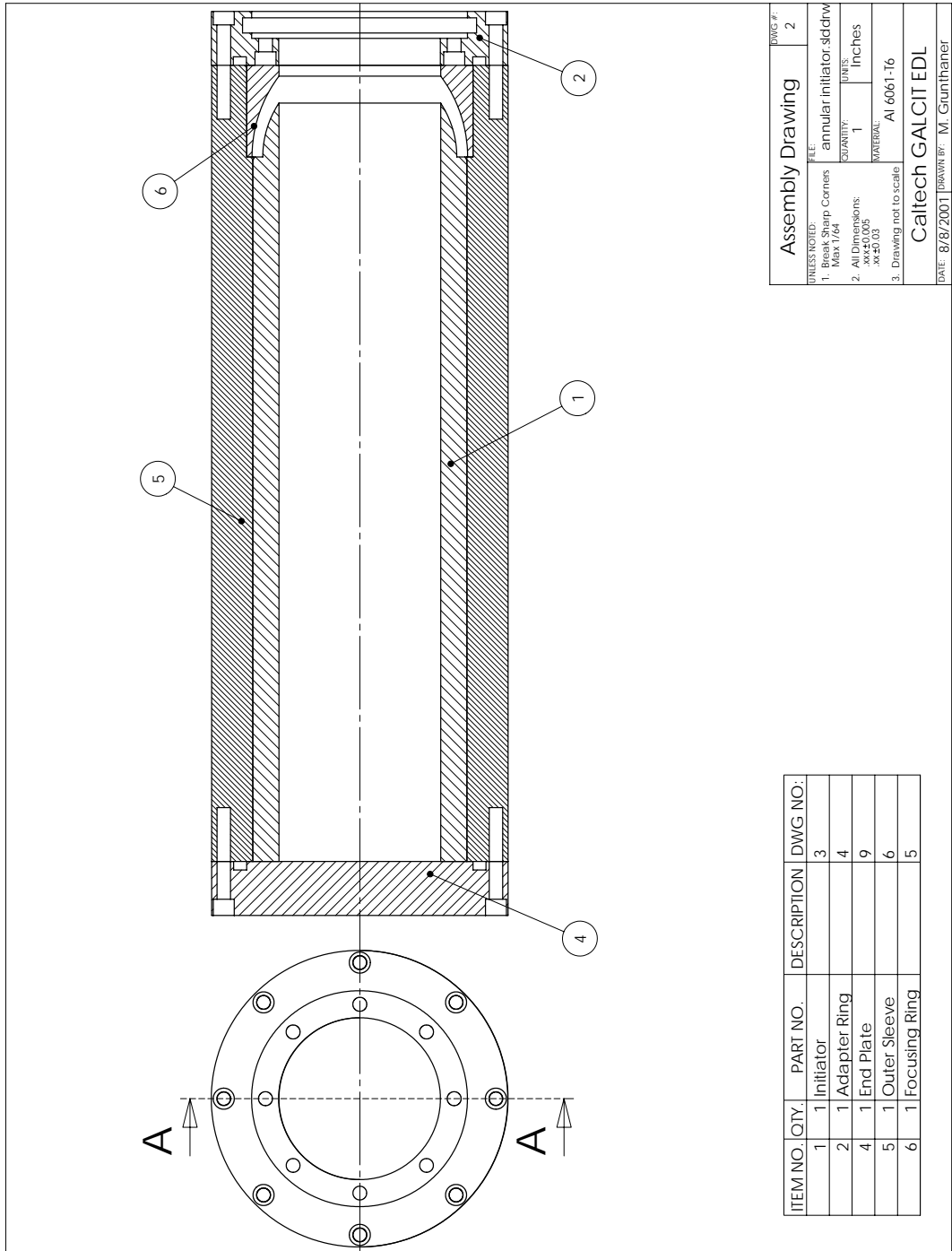


Figure F.2: Assembled view of the toroidal initiator.

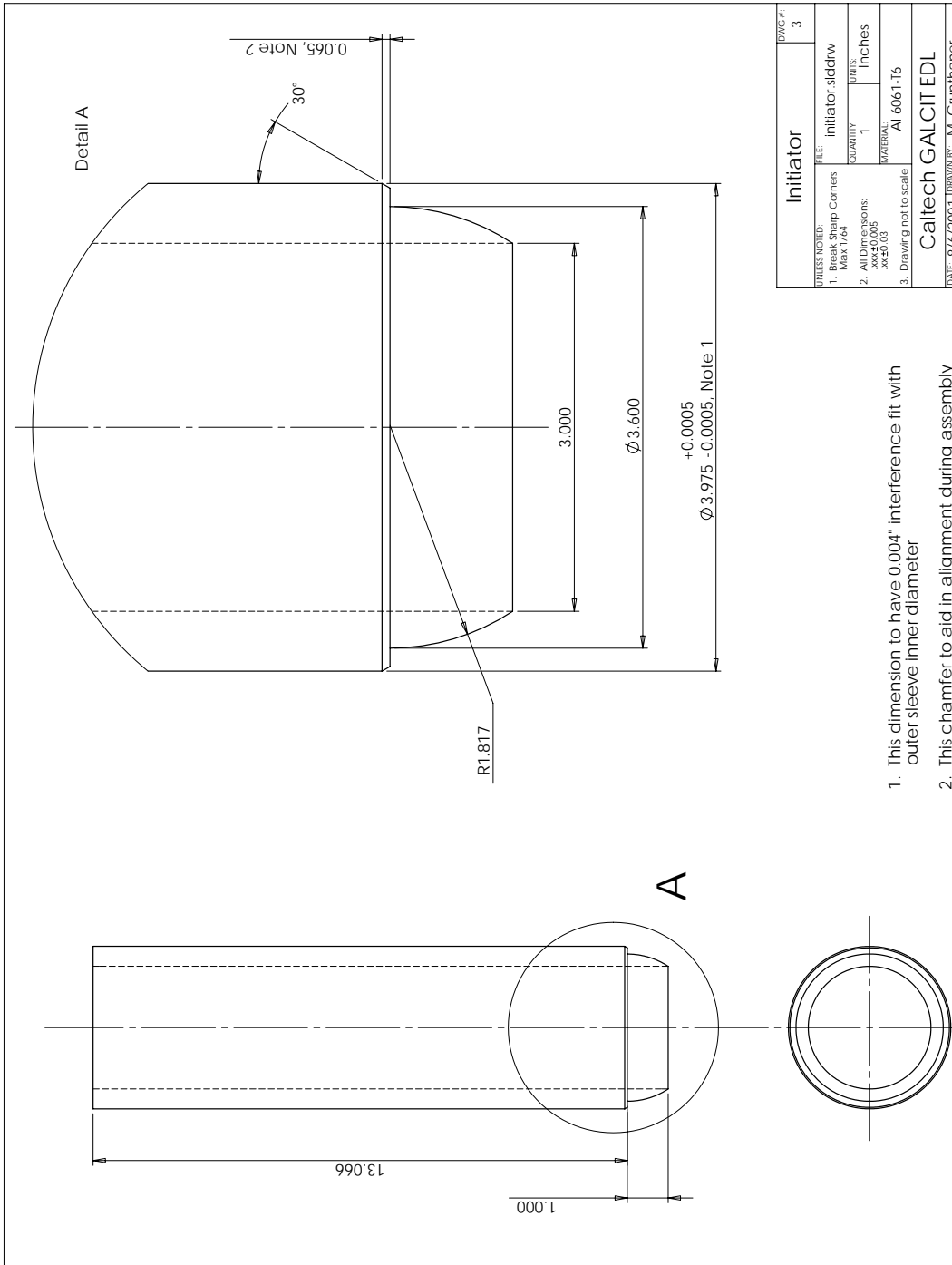


Figure F.3: Initiator inner sleeve after assembly.

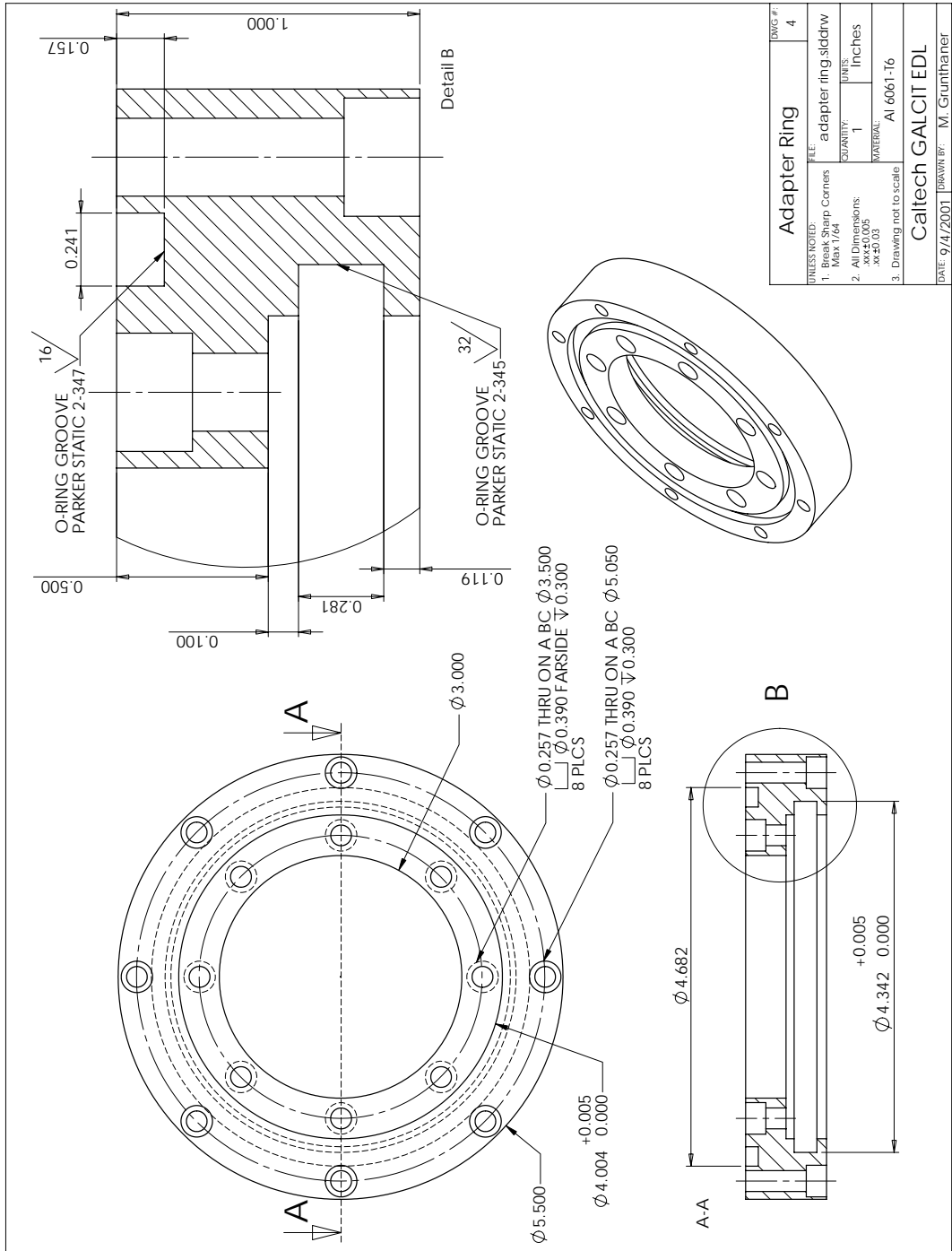


Figure F.4: Adapter ring.

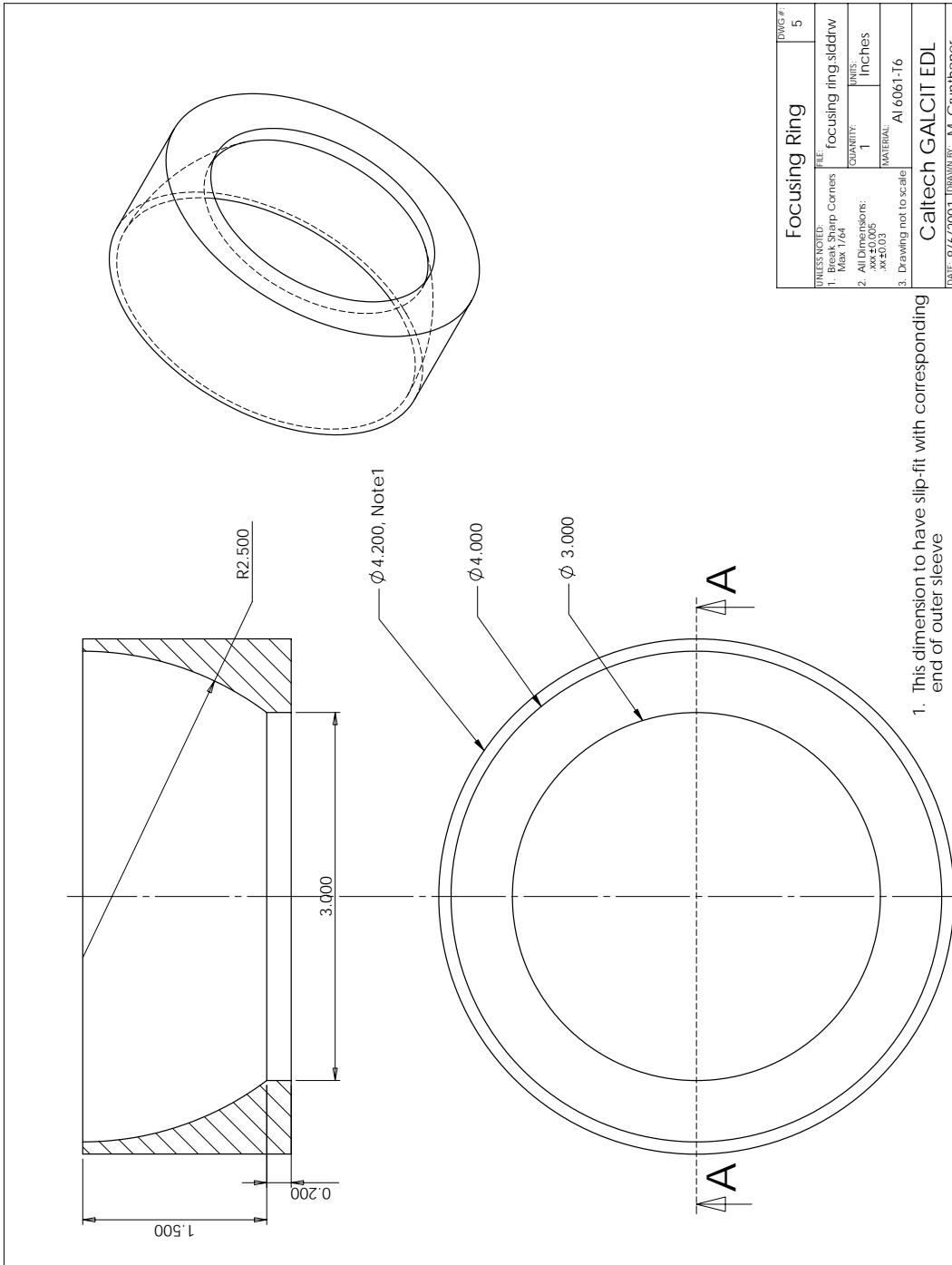


Figure F.5: Focusing ring.

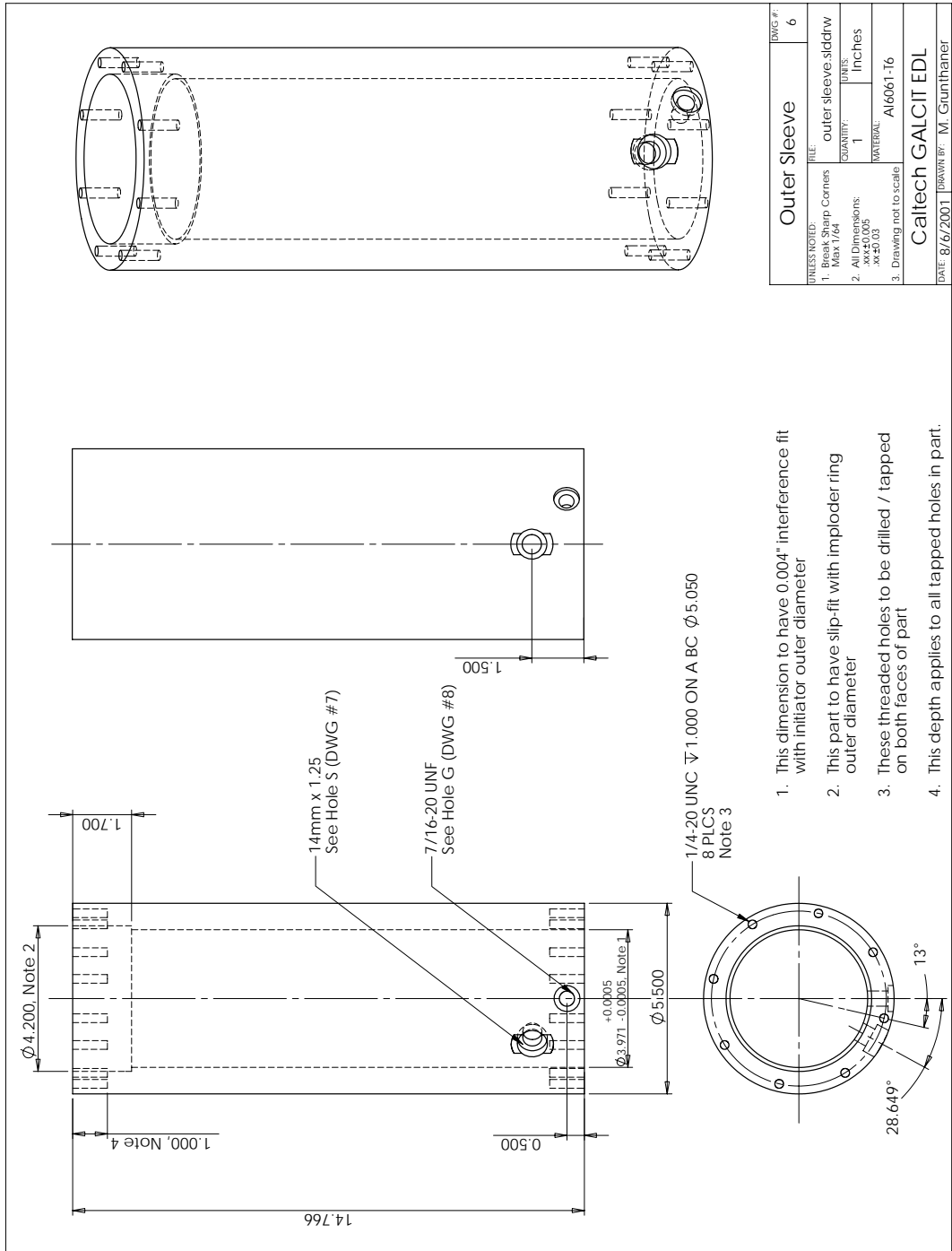


Figure F.6: Initiator outer sleeve after assembly.

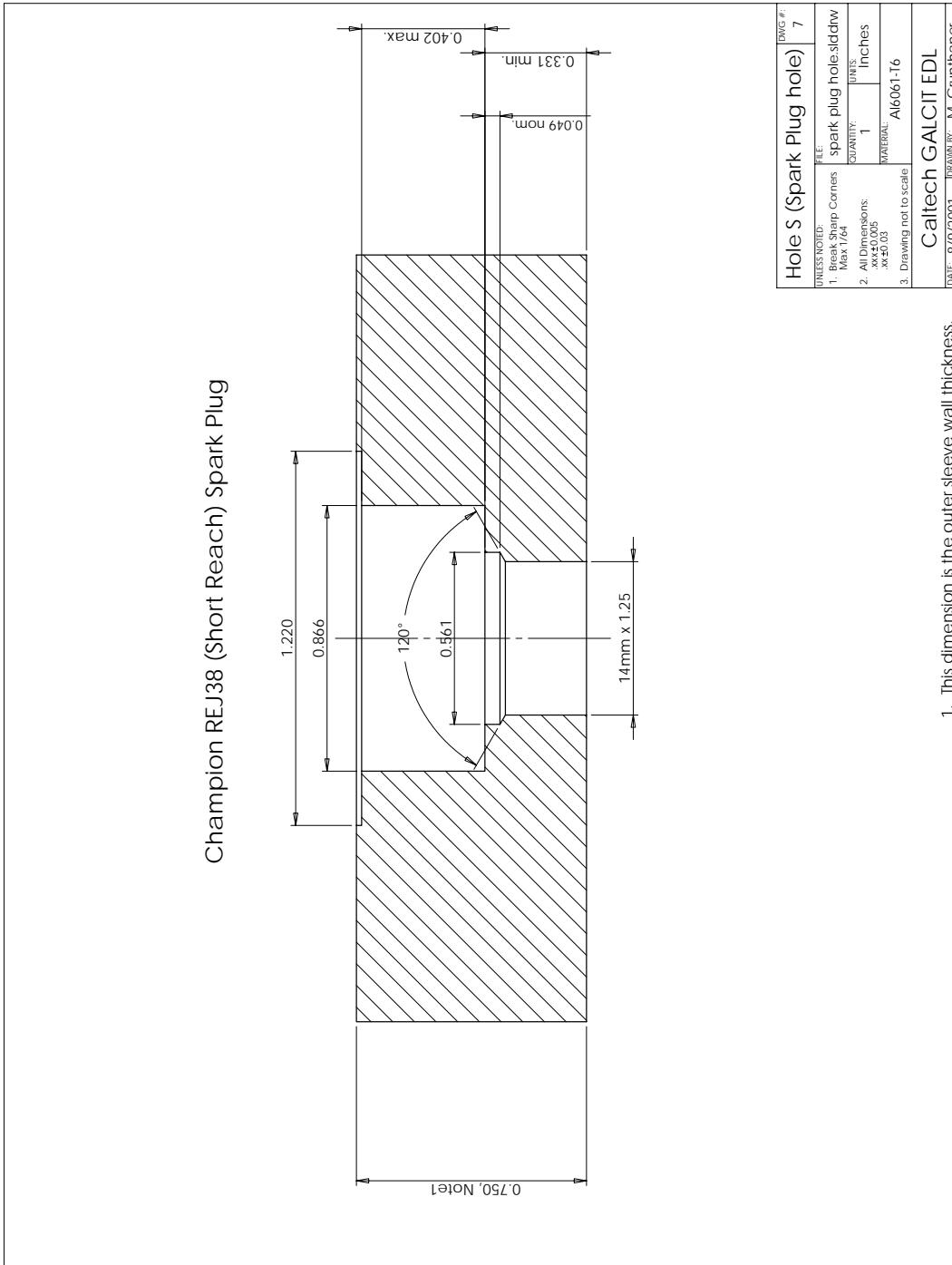


Figure F.7: Spark plug port.

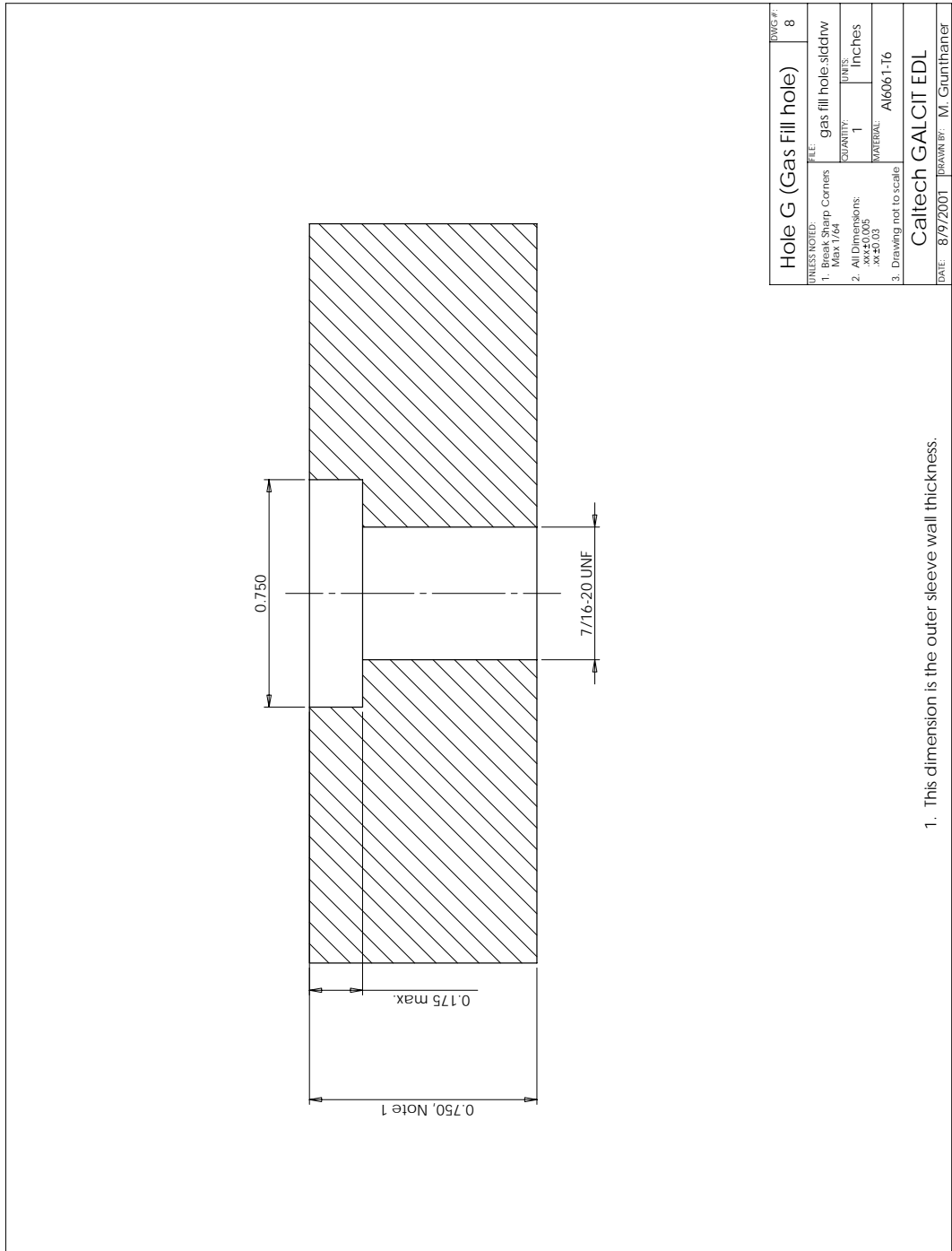


Figure F.8: Gas fill port.

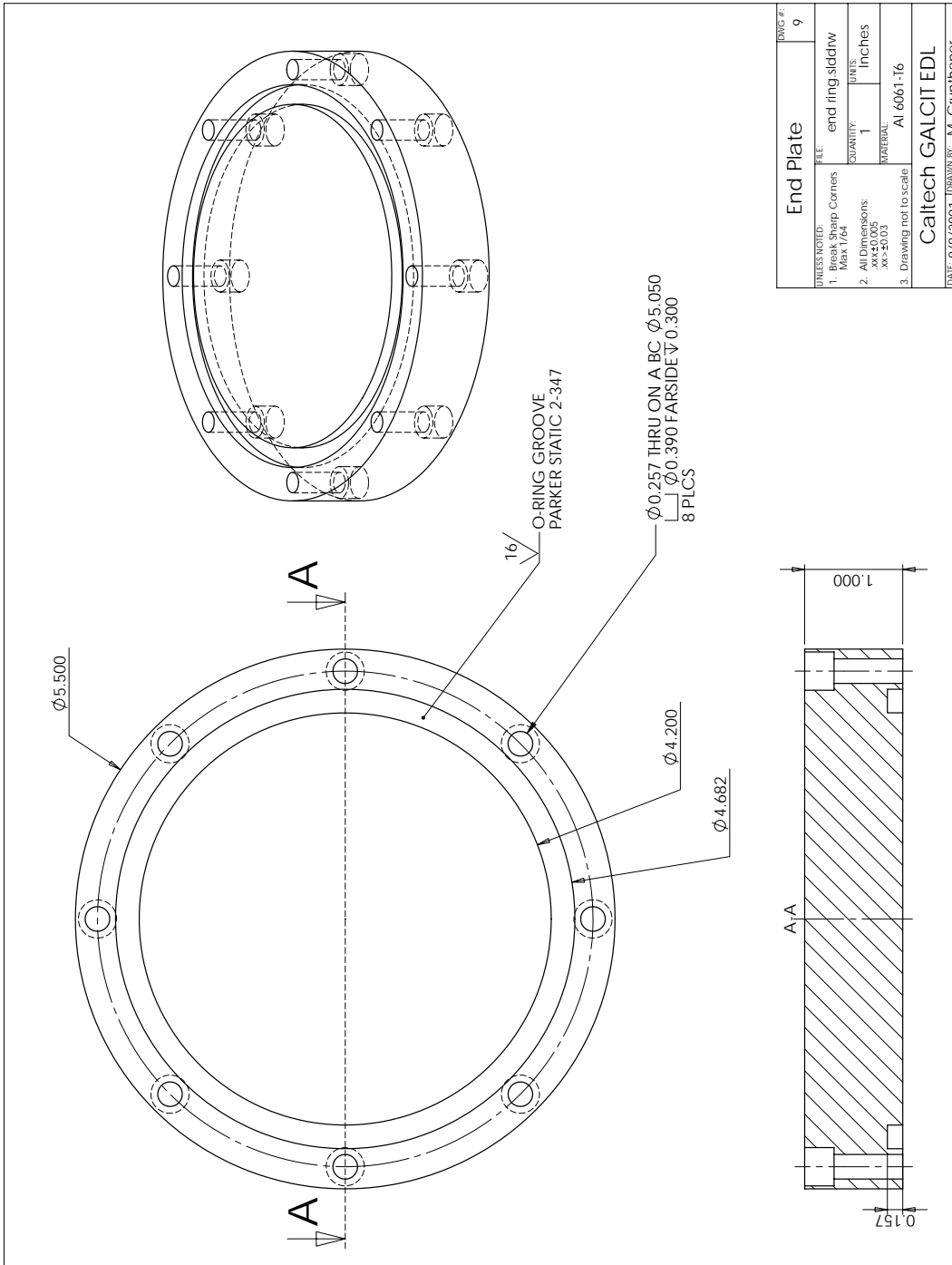


Figure F.9: Blank end flange.

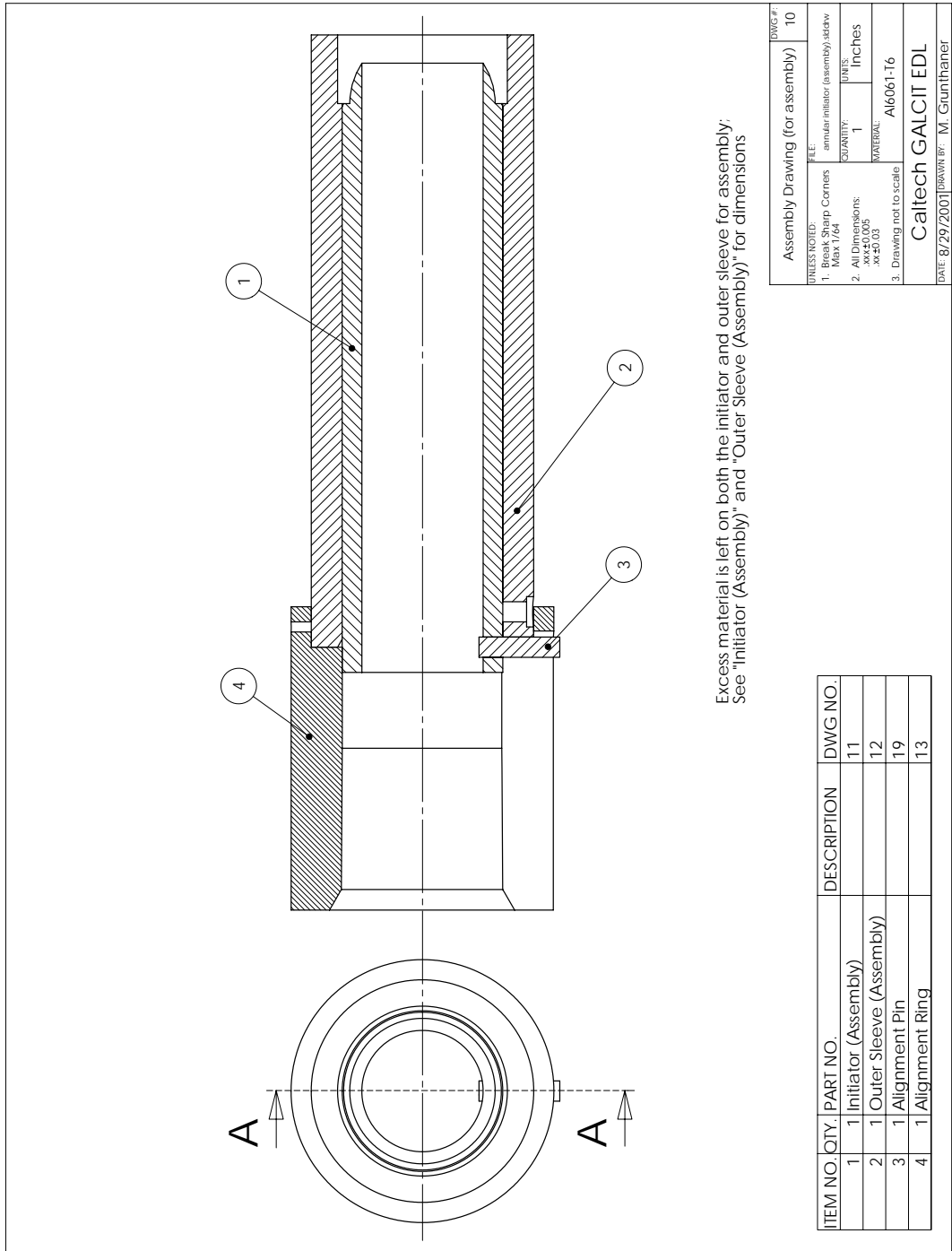


Figure F.10: Setup for initiator assembly.

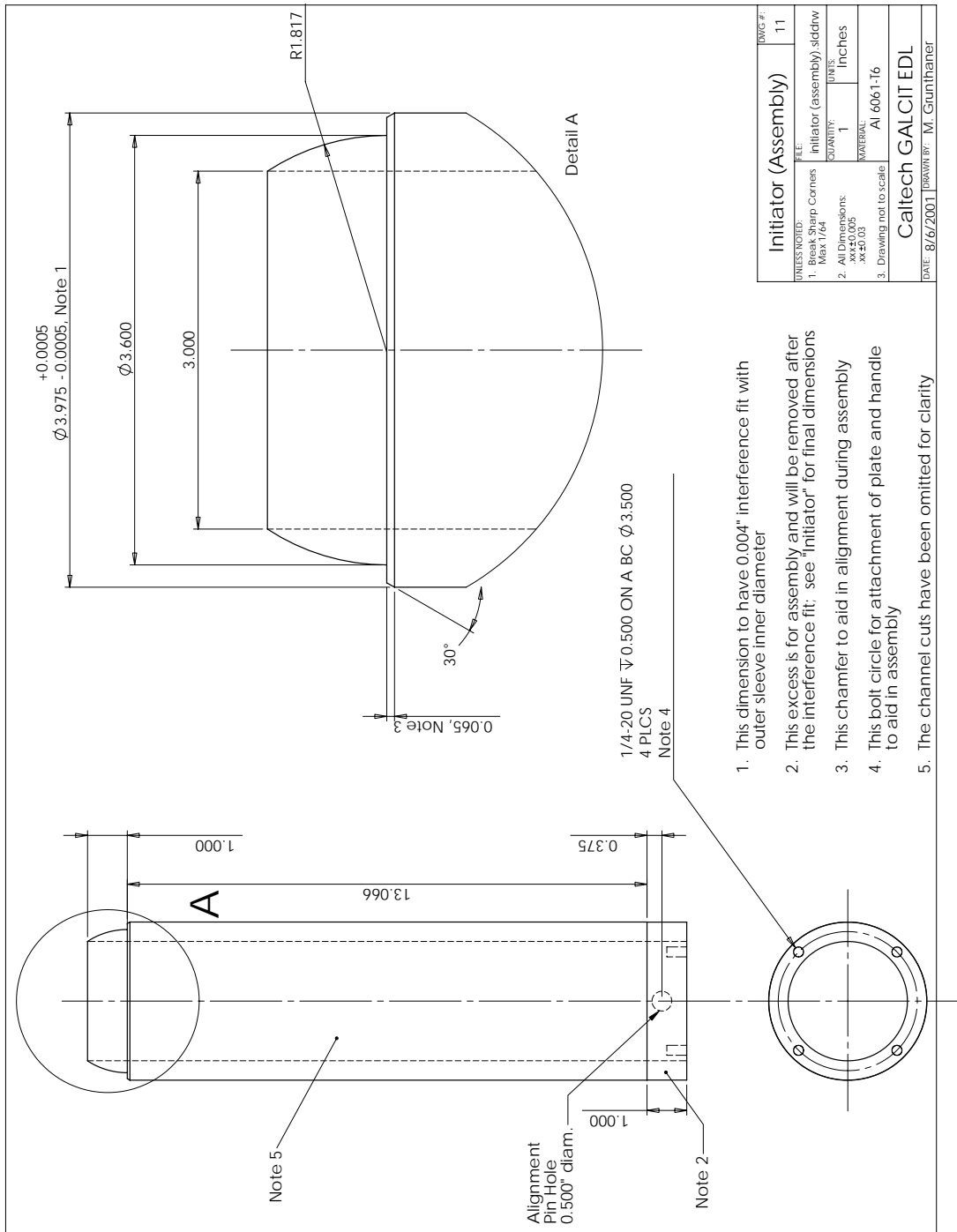


Figure F.11: Initiator inner sleeve prior to assembly.

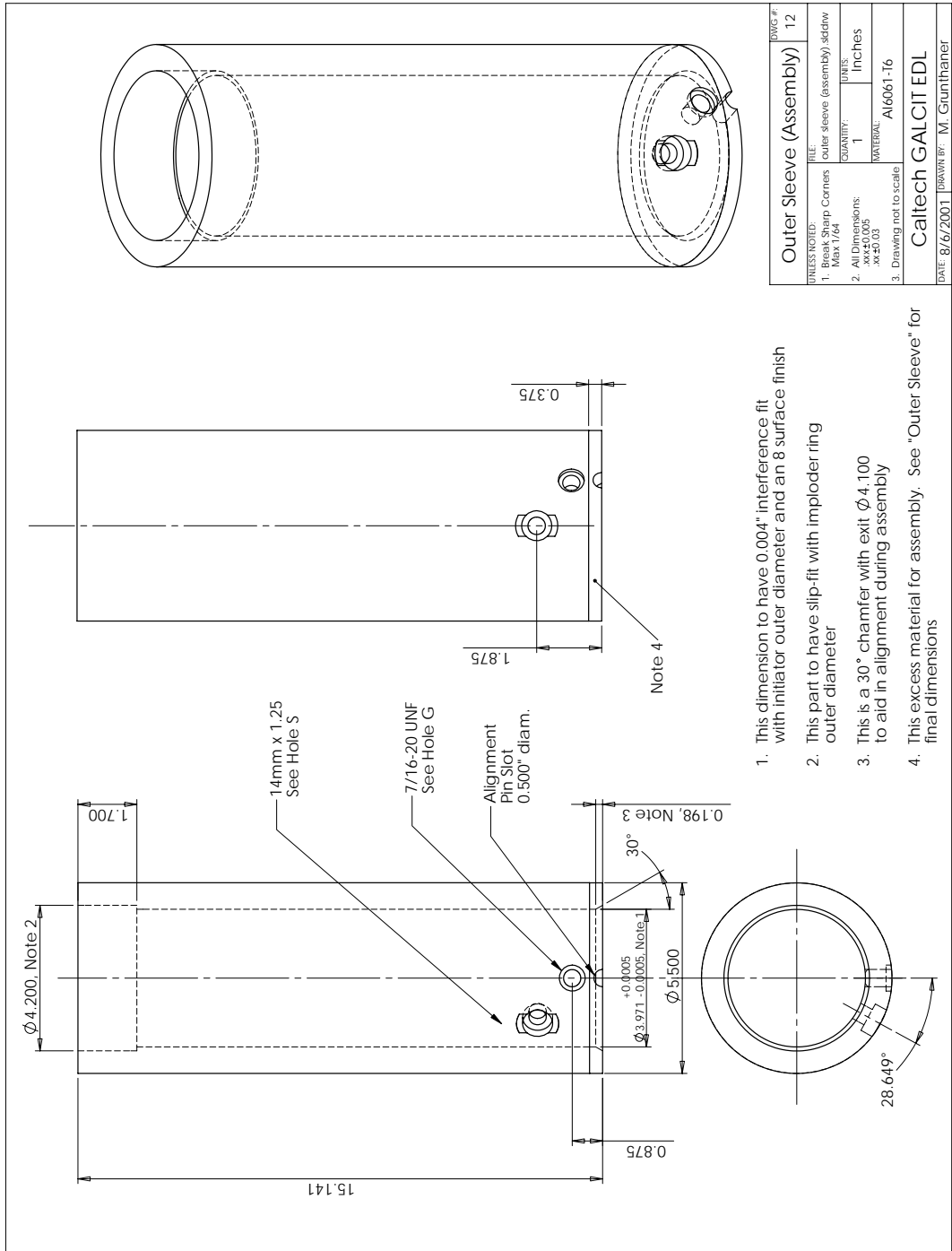


Figure F.12: Initiator outer sleeve prior to assembly.

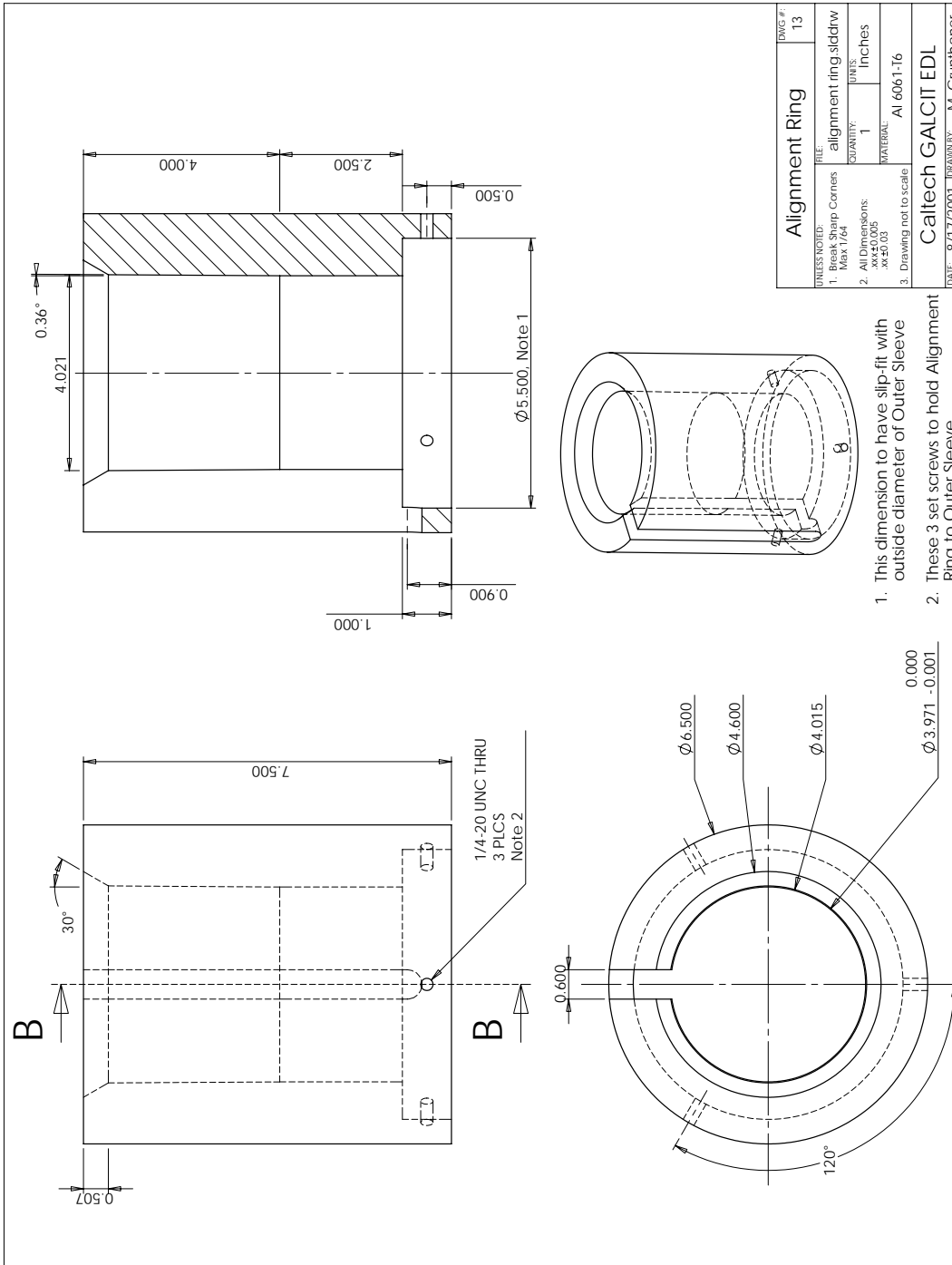
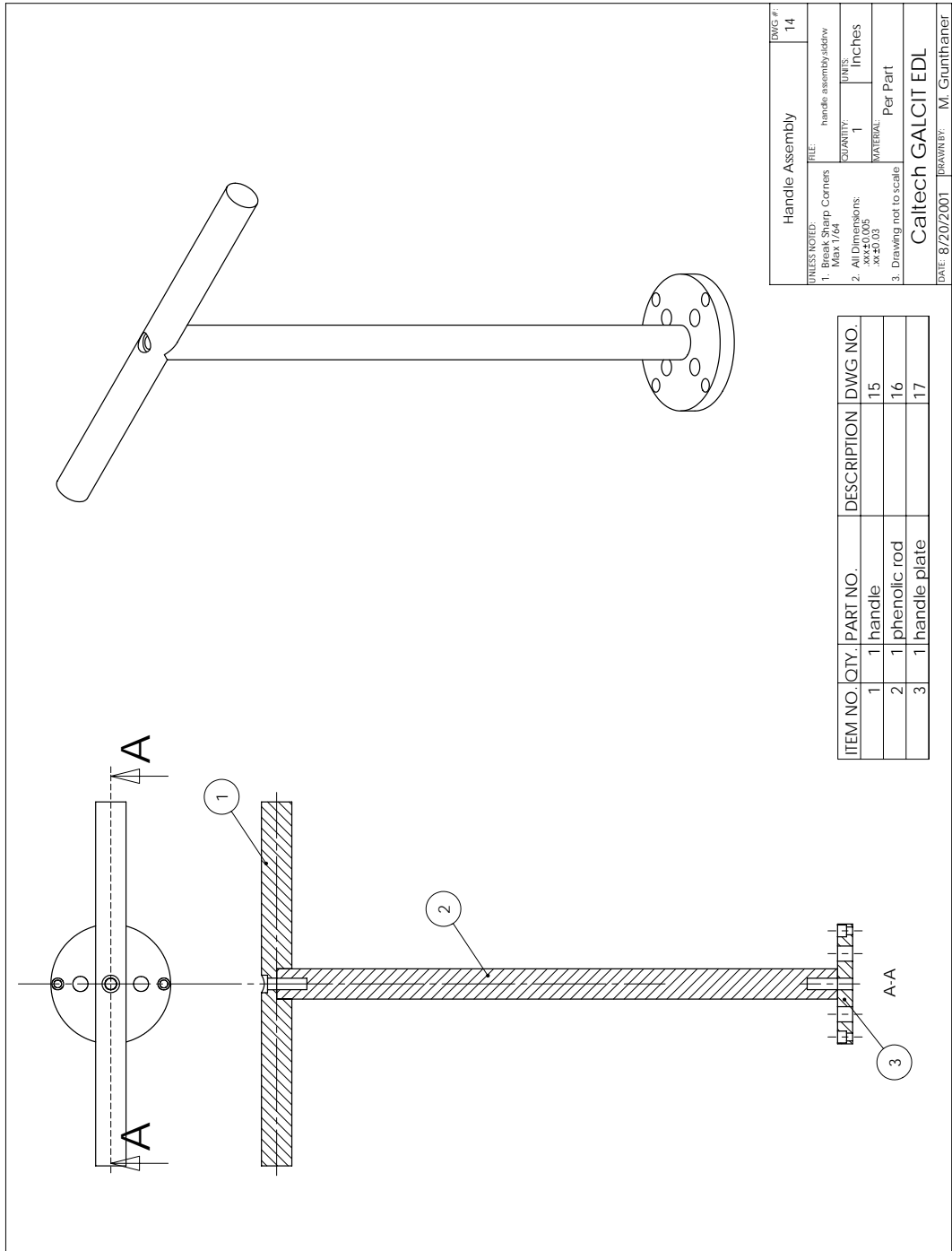


Figure F.13: Alignment ring for assembly.



Handle Assembly		DWG #:	14
UNLESS NOTED:			
FILE:	handle assembly.dsdw	QUANTITY:	1
1. Break Sharp Corners Max 1/64		UNITS:	Inches
2. All Dimensions: .xx±0.005 .xx±0.03		MATERIAL:	Per Part
3. Drawing not to scale		Caltech GALCIT EDL	
DATE: 8/20/2001		DRAWN BY: M. Grunthaner	

ITEM NO.	QTY.	PART NO.	DESCRIPTION	DWG NO.
1	1	handle		15
2	1	phenolic rod		16
3	1	handle plate		17

Figure F.14: Handle assembly.

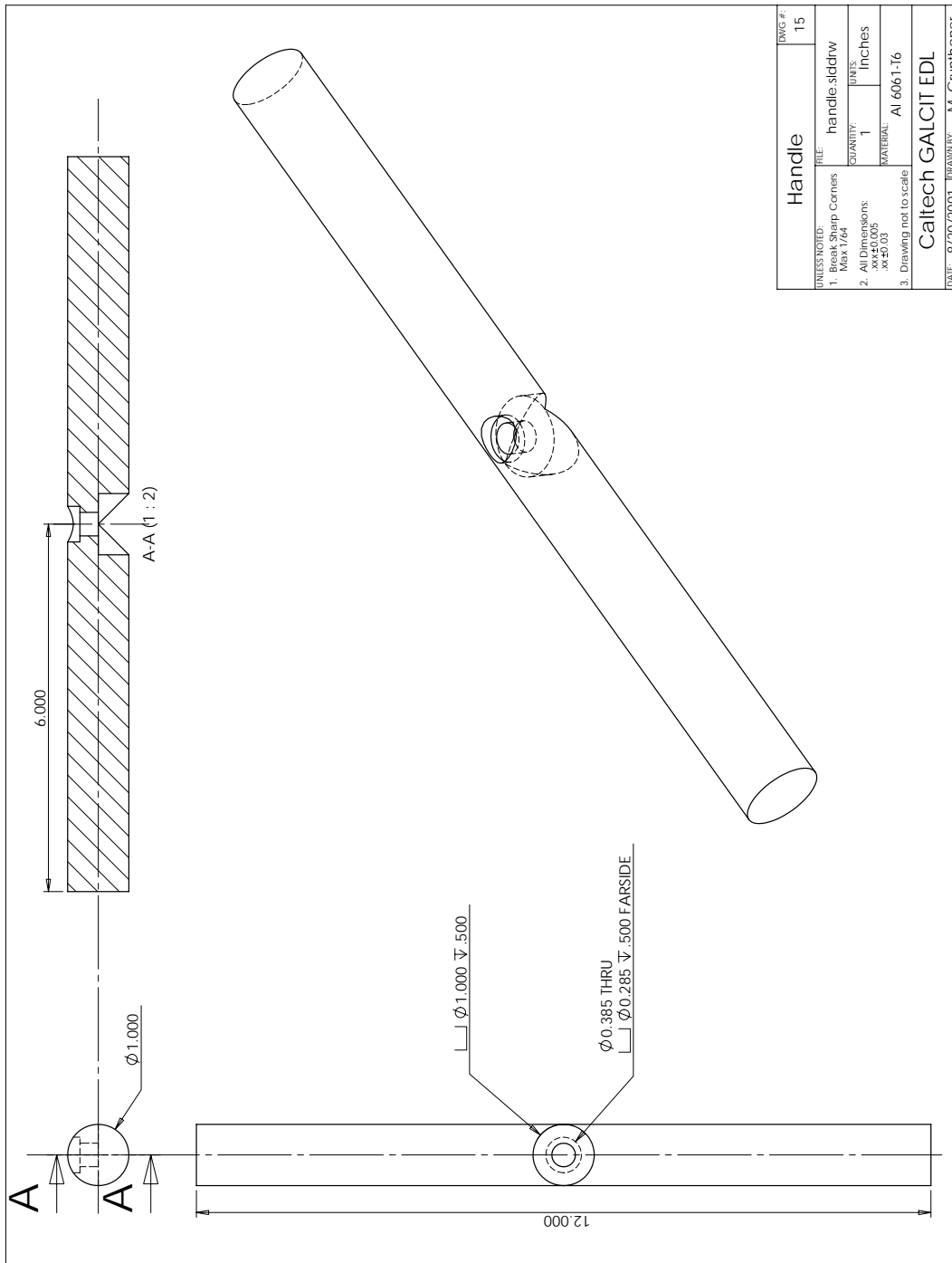


Figure F.15: Handle.

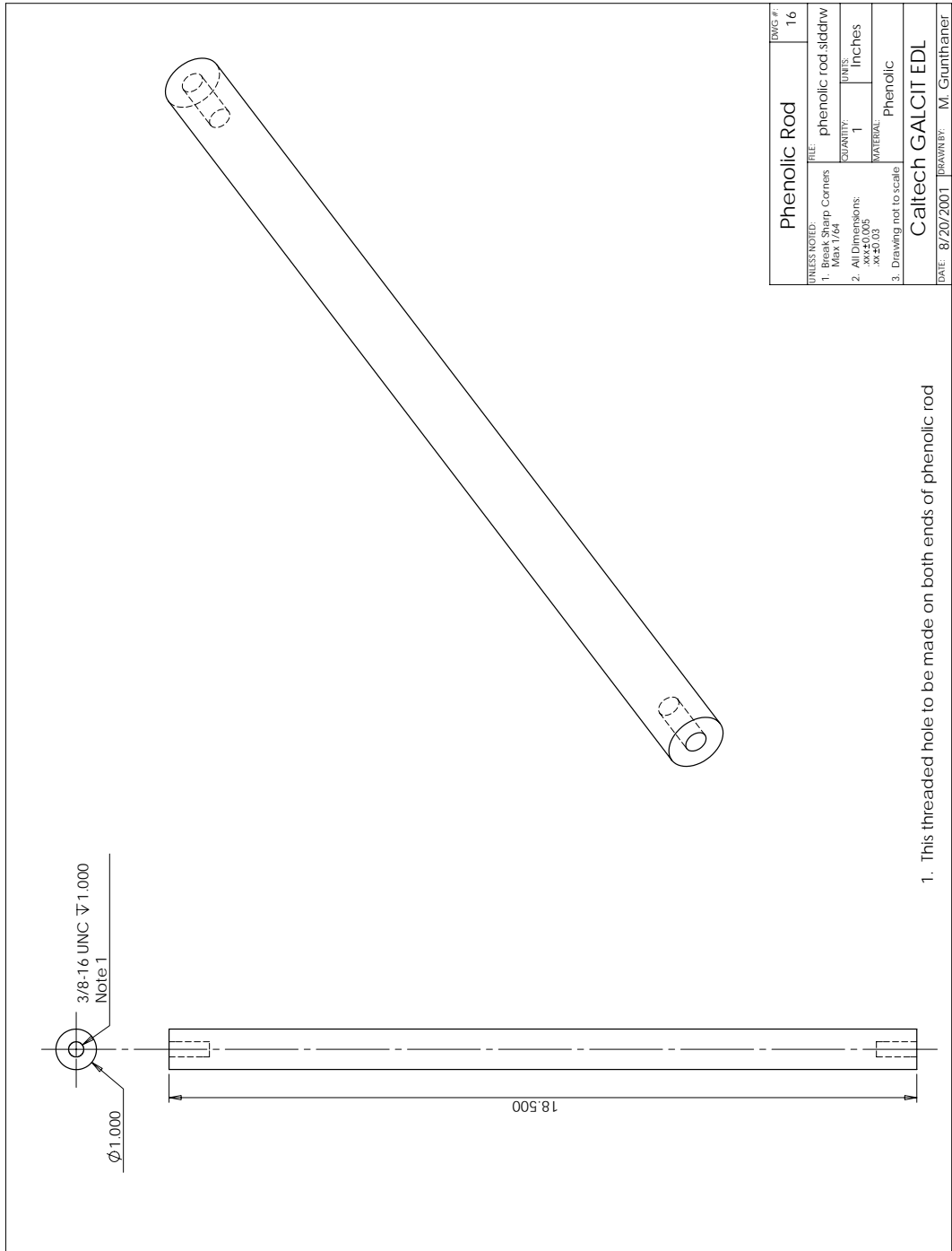


Figure F.16: Handle rod.

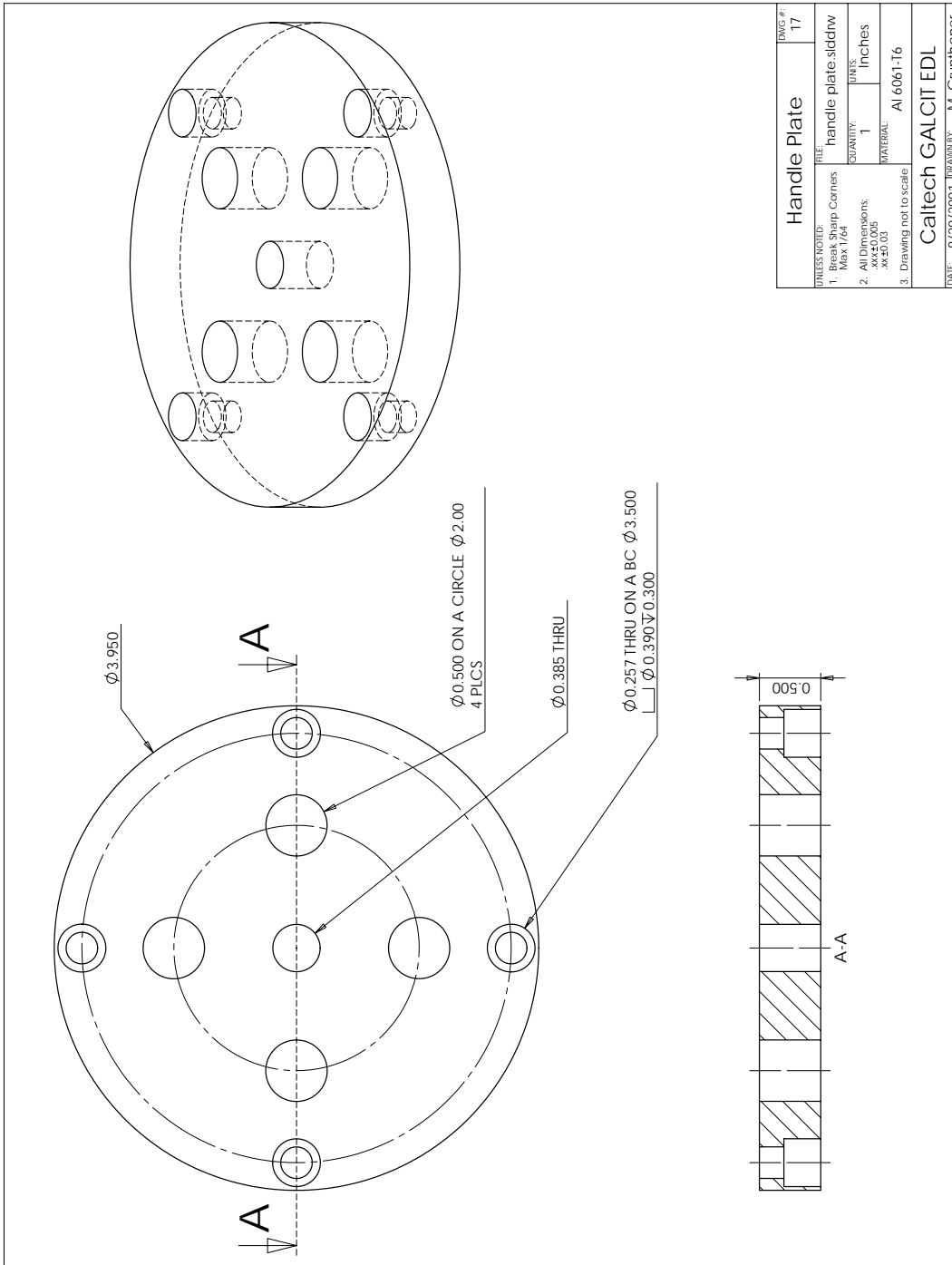


Figure F.17: Handle plate.

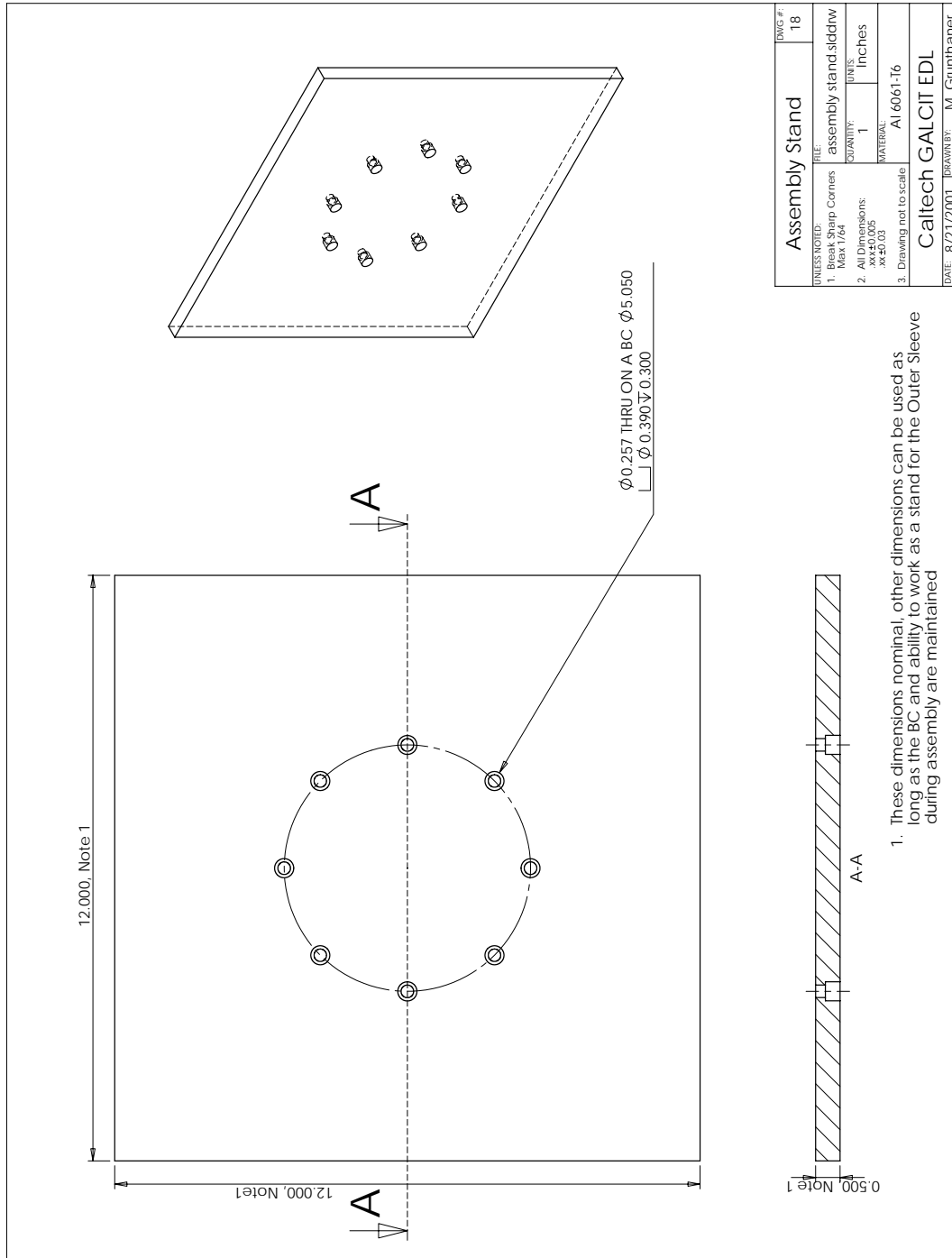


Figure F.18: Assembly stand.

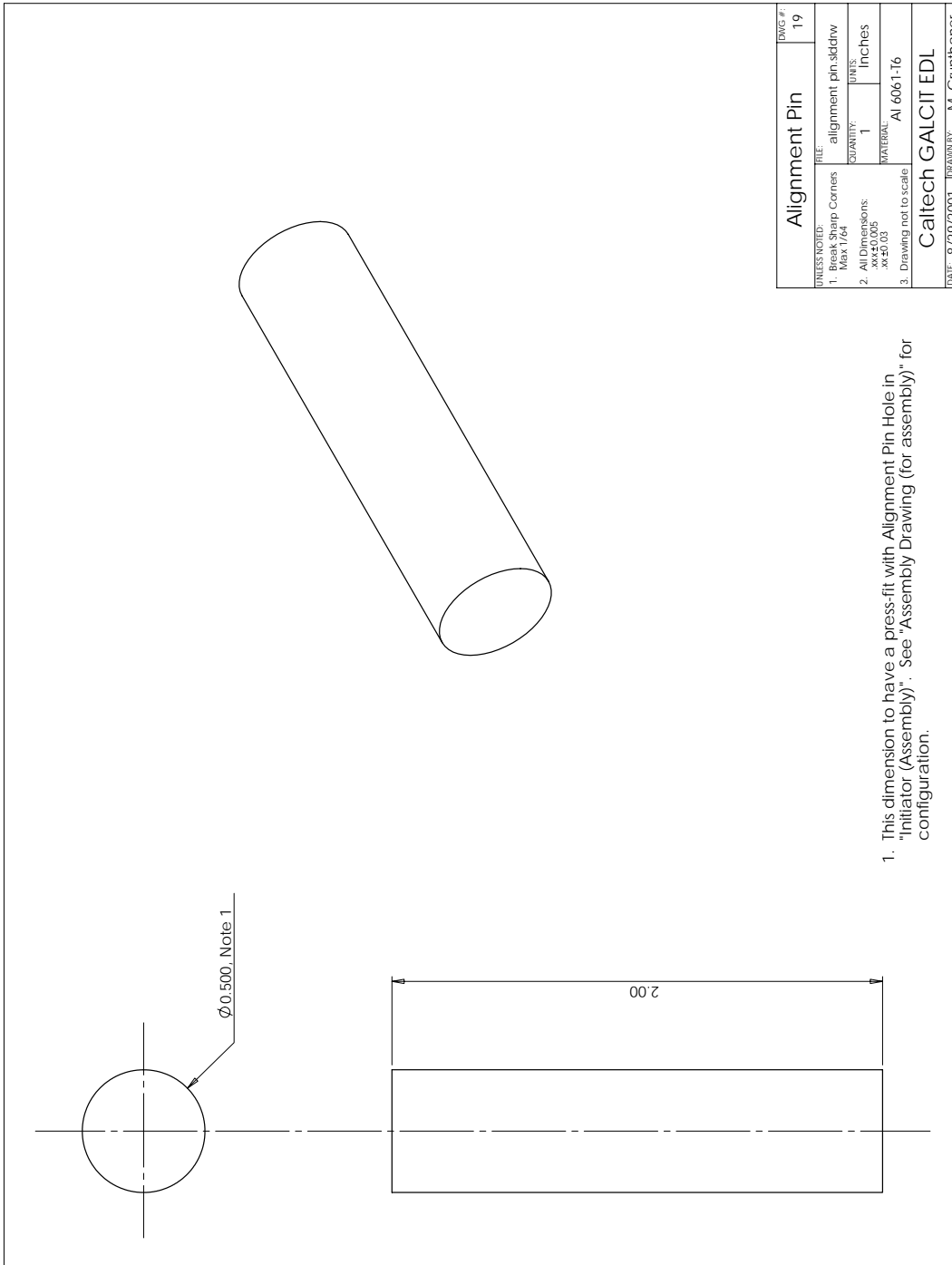


Figure F.19: Alignment pin.

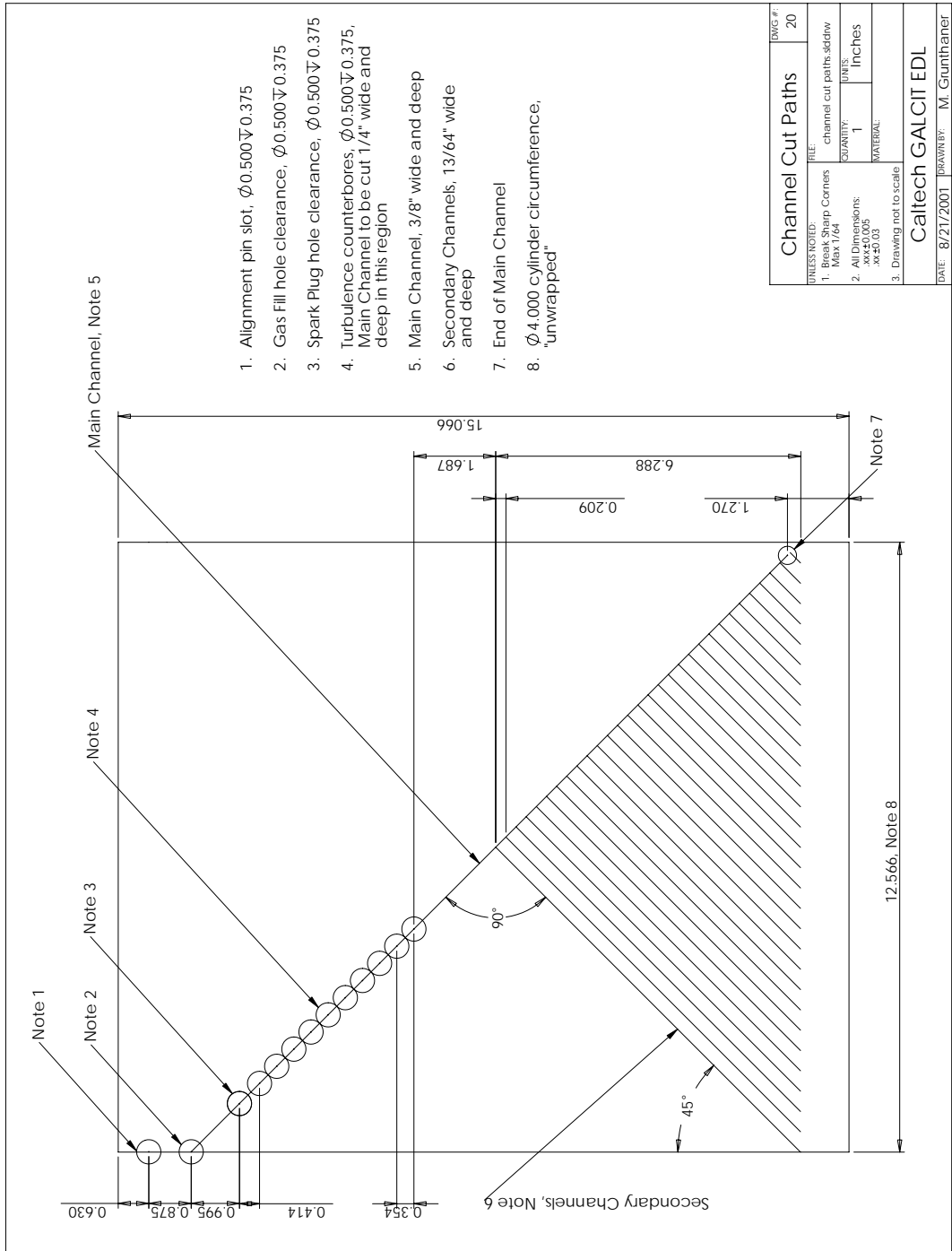


Figure F.20: Channel cut paths on outer diameter of inner sleeve.

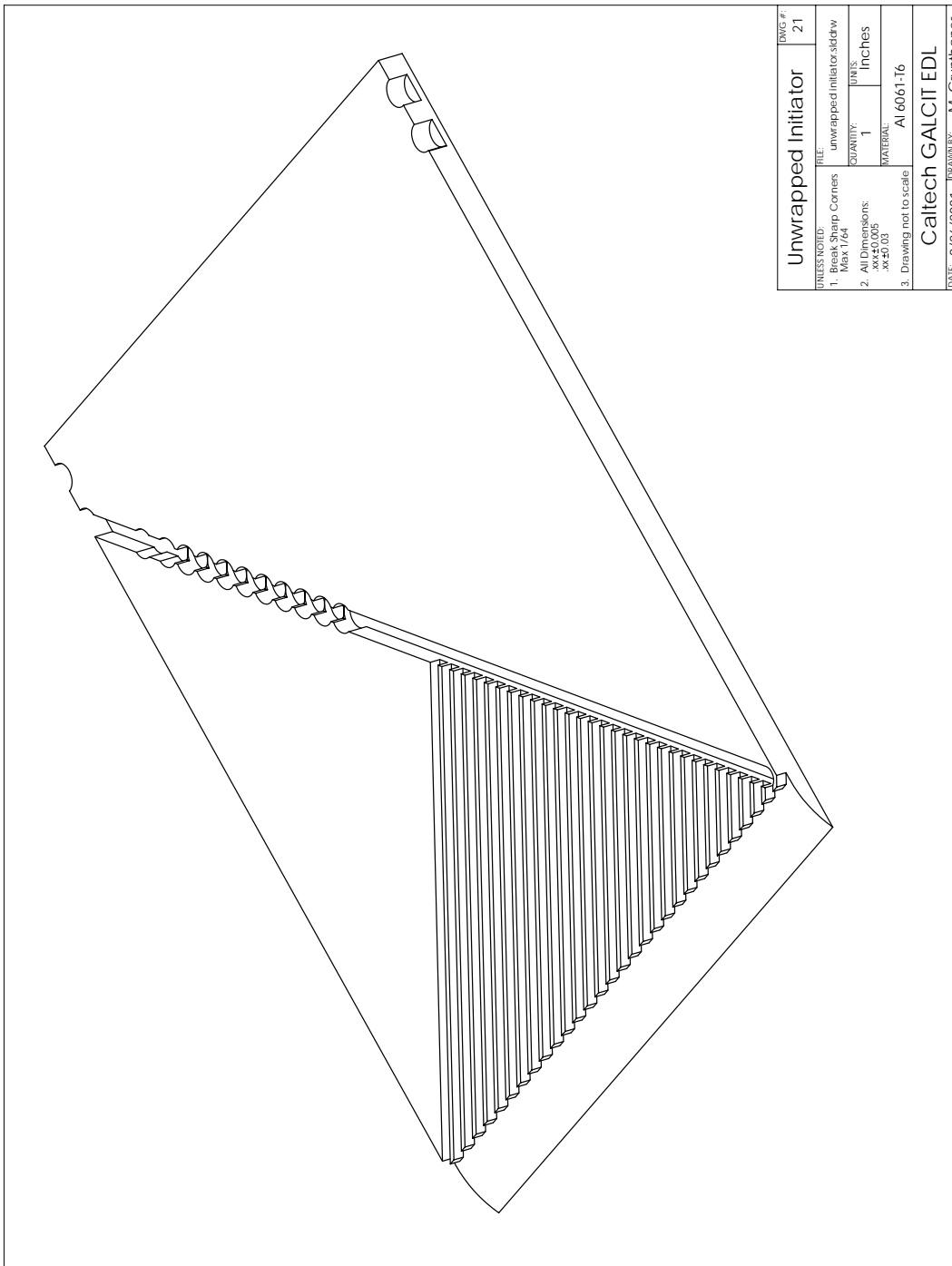


Figure F.21: View of the inner sleeve mapped to a planar surface.

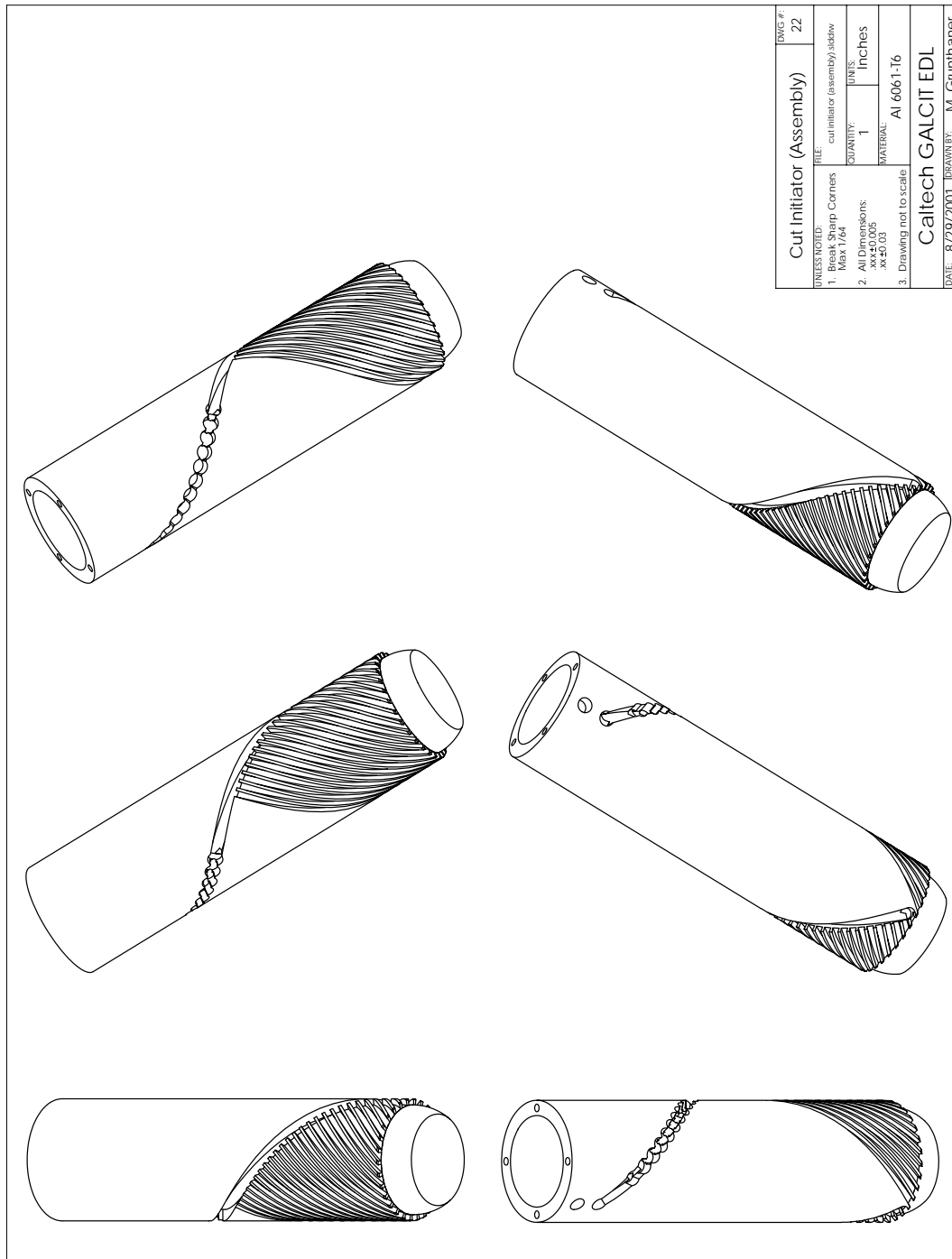


Figure F.22: Renderings of the inner sleeve with channels prior to assembly.

## F.2 Run Matrix

Run	Type	Delay ( $\mu$ s)	Width (ns)	F-ratio	MCP (V)	Mode
1	pressure	N/A	N/A	N/A	N/A	N/A
2	pressure	N/A	N/A	N/A	N/A	N/A
3	pressure	N/A	N/A	N/A	N/A	N/A
4	pressure	N/A	N/A	N/A	N/A	N/A
5	pressure	N/A	N/A	N/A	N/A	N/A
6	pressure	N/A	N/A	N/A	N/A	N/A
7	pressure	N/A	N/A	N/A	N/A	N/A
8	image	640	100	11	750	gated
9	image	640	100	16	600	gated
10	image	640	100	32	500	gated
11	image	640	100	22	570	gated
12	image	645	100	22	580	gated
13	image	0	100	22	580	gated
14	image	600	100	22	580	gated
15	image	500	100	22	580	gated
16	image	475	100	22	580	gated
17	image	482	100	22	580	gated
18	image	489	100	22	580	gated
19	image	494	100	22	590	gated
20	image	494	100	22	580	gated
21	image	500	100	16	580	gated

Table F.1: Experimental properties of each run. All mixtures were stoichiometric propane-oxygen. The initial pressure on all runs was 1.00 bar except for runs 1 and 2 where the initial pressure was 0.70 bar. “Type” indicates if the experiment was set to acquire pressure history data or to image the imploding wave. The last five columns are camera variables. “Delay” is the interval between the firing of the spark plug and time of image acquisition. “Width” is the integration time of the intensified CCD camera and “MCP” corresponds to the intensifier voltage setting.

Run	Type	Delay ( $\mu$ s)	Width (ns)	F-ratio	MCP (V)	Mode
22	image	500	100	16	580	gated
23	image	500	100	16	580	gated
24	image	510	100	16	580	gated
25	image	15	100	22	580	gated
26	image	15	100	22	580	gated
27	image	35	100	22	580	gated
28	image	35	100	22	580	gated
29	image	35	100	22	580	gated
30	image	35	100	22	580	gated
31	image	42	100	22	750	gated
32	image	38	100	22	680	gated
33	image	32	100	22	750	gated
34	image	30	100	22	800	gated
35	image	37	100	22	680	gated
36	image	38.1	100	22	680	gated
37	image	38.9	100	22	680	gated
38	image	24	100	22	800	gated
39	image	27	100	22	800	gated
40	image	35	100	22	680	gated
41	image	34	100	22	680	gated
42	image	33	100	22	680	gated
43	image	29	100	22	680	gated

Table F.2: Experimental properties of each run. All mixtures were stoichiometric propane-oxygen. The initial pressure on all runs was 1.00 bar except for runs 1 and 2 where the initial pressure was 0.70 bar. “Type” indicates if the experiment was set to acquire pressure history data or to image the imploding wave. The last five columns are camera variables. “Delay” is the interval between the firing of the spark plug and time of image acquisition. “Width” is the integration time of the intensified CCD camera and “MCP” corresponds to the intensifier voltage setting.

### F.3 Pressure Traces

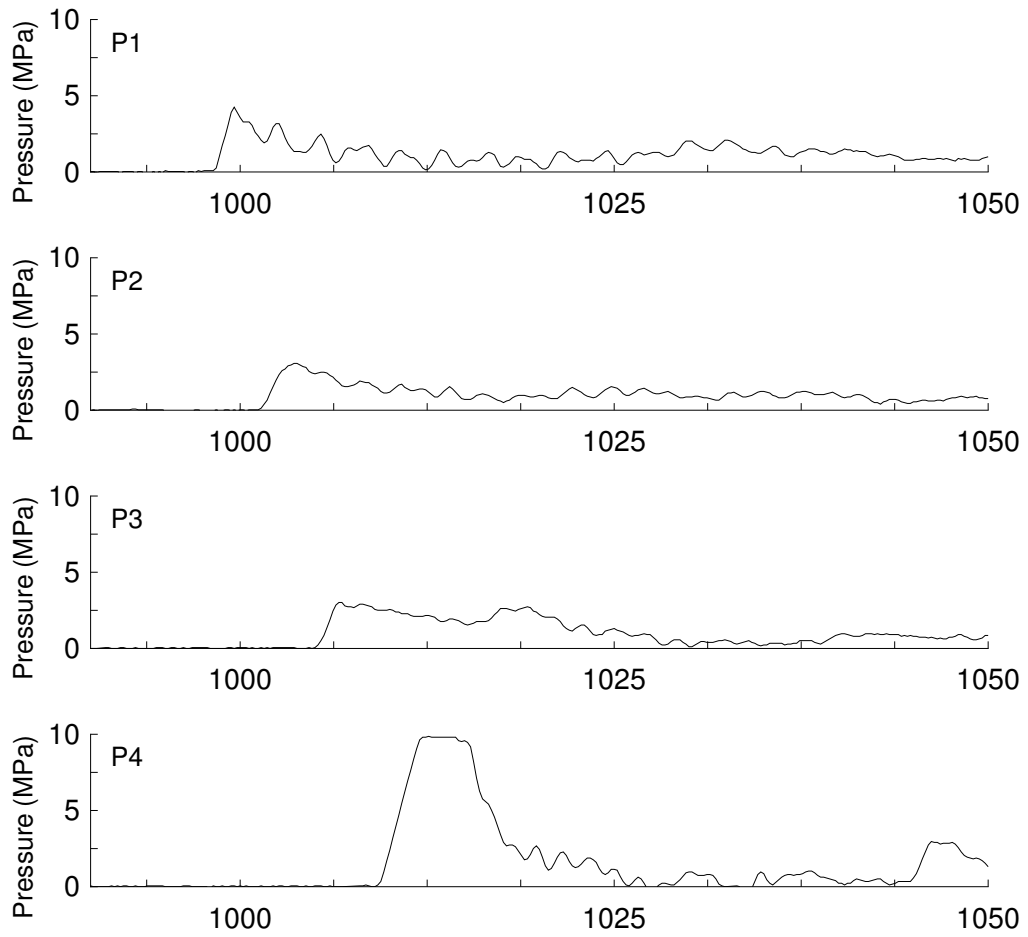


Figure F.23: Pressure history from run 001.

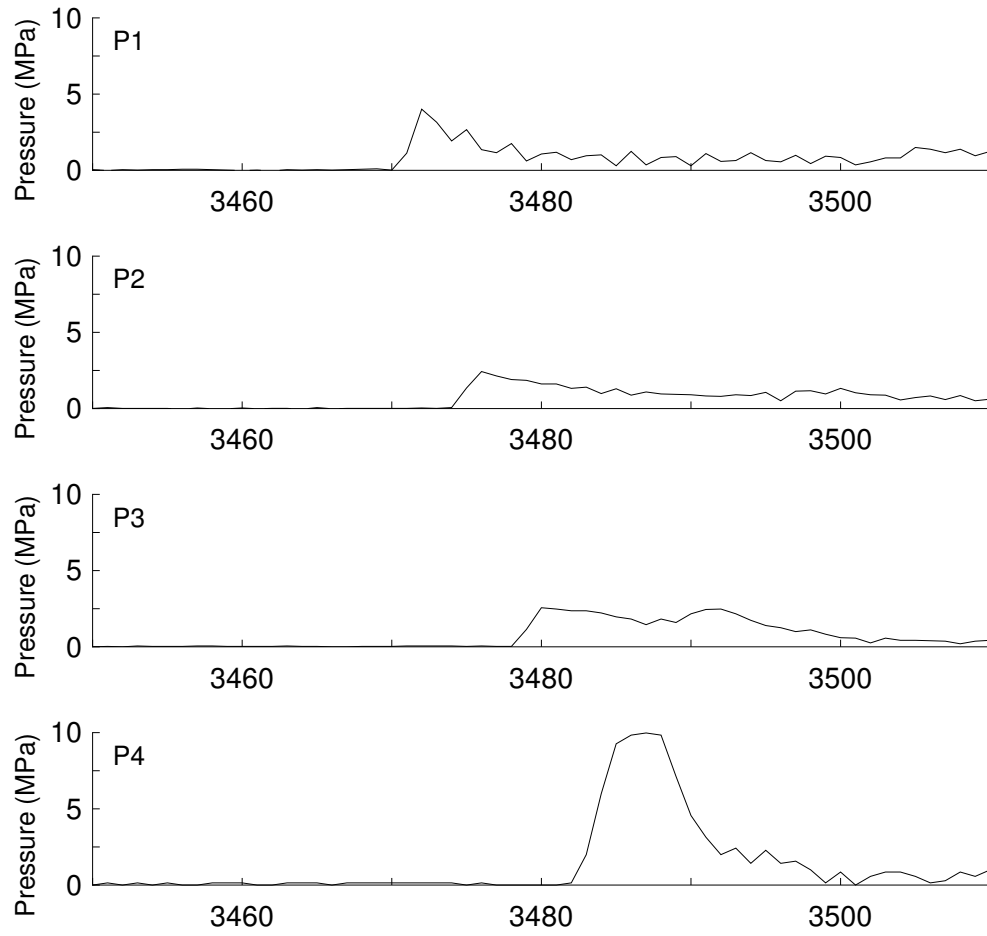


Figure F.24: Pressure history from run 002.

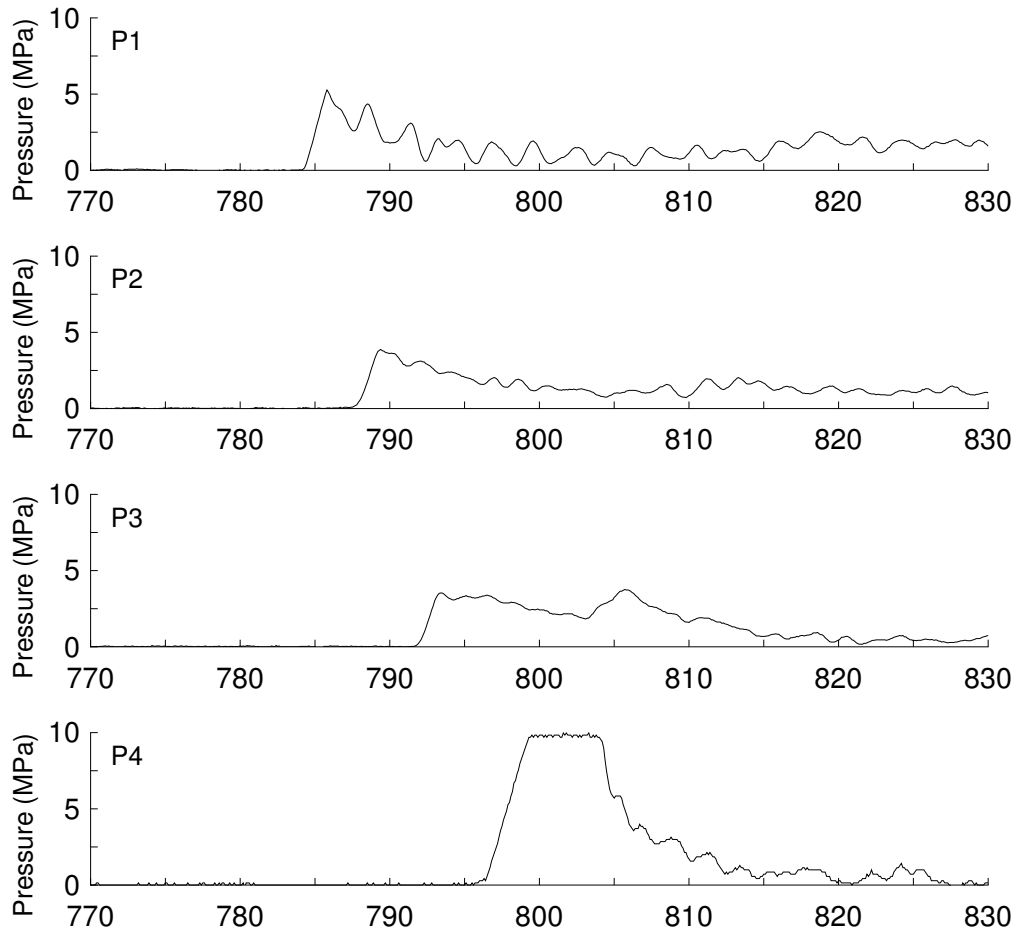


Figure F.25: Pressure history from run 003.

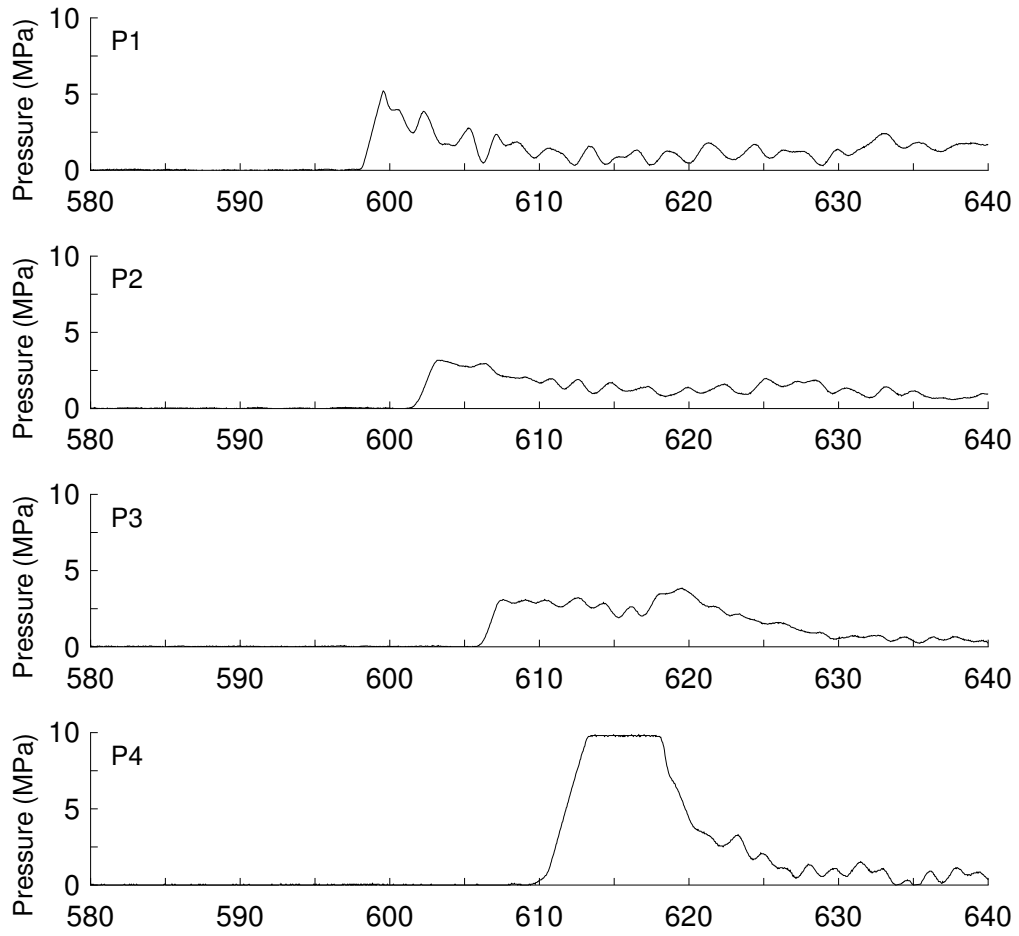


Figure F.26: Pressure history from run 004.

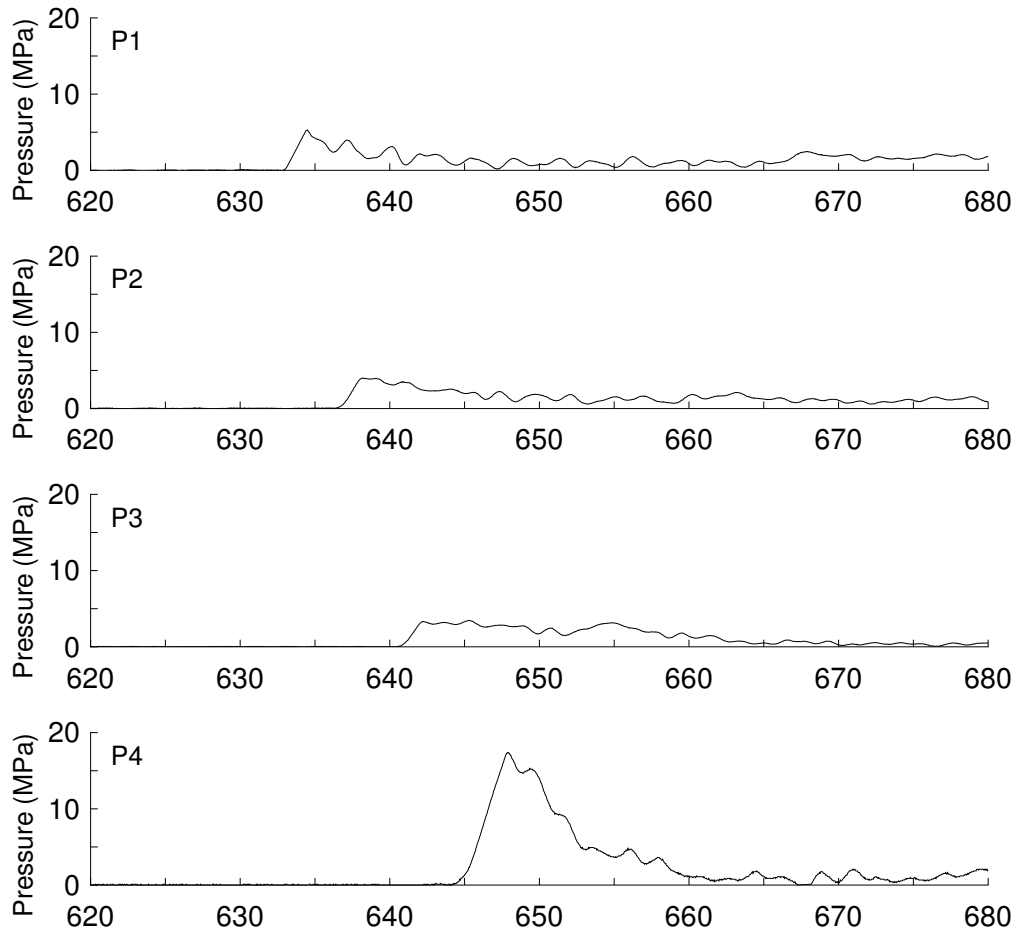


Figure F.27: Pressure history from run 005.

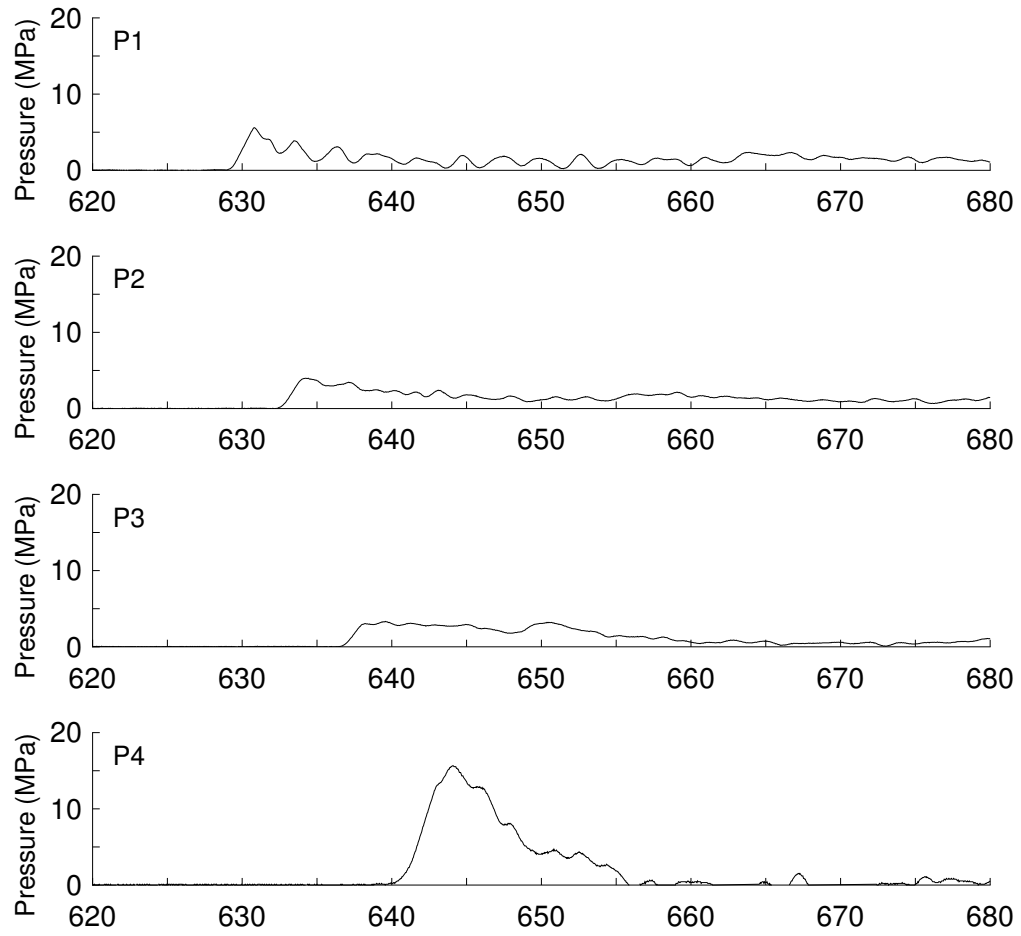


Figure F.28: Pressure history from run 006.

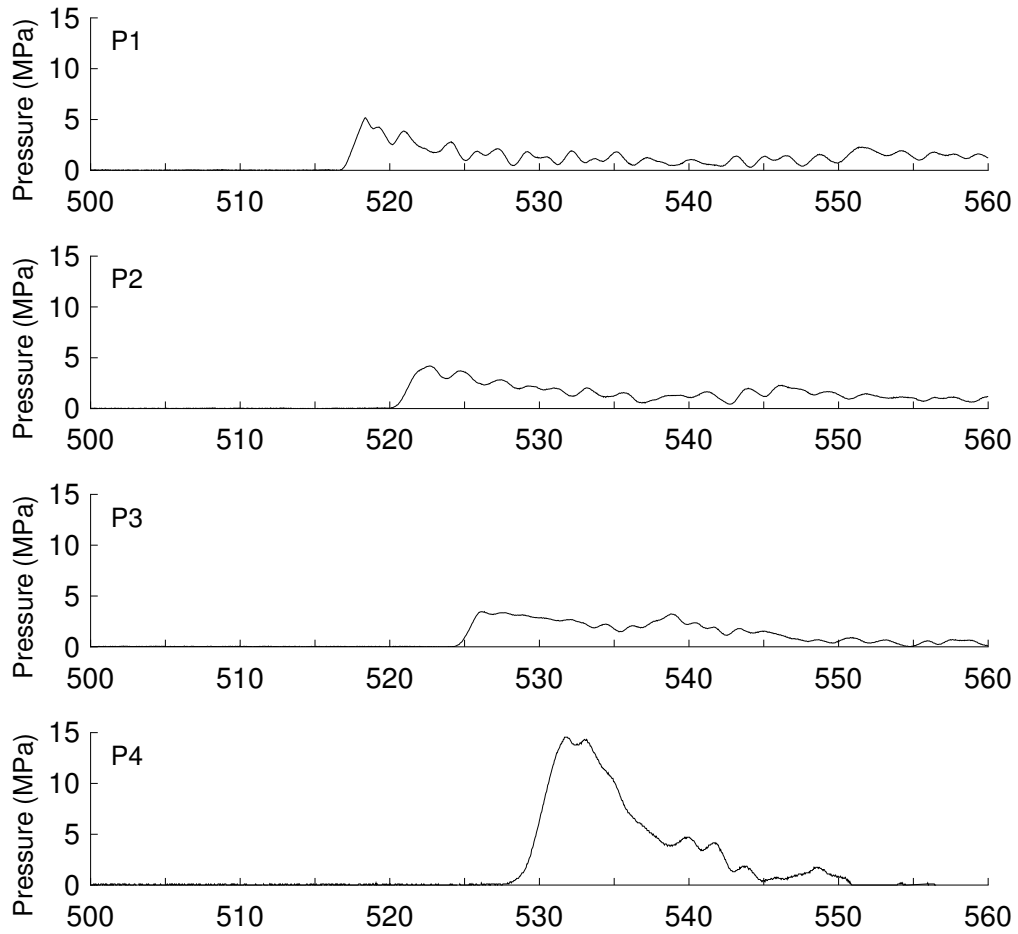


Figure F.29: Pressure history from run 007.

## F.4 Chemiluminescence Images

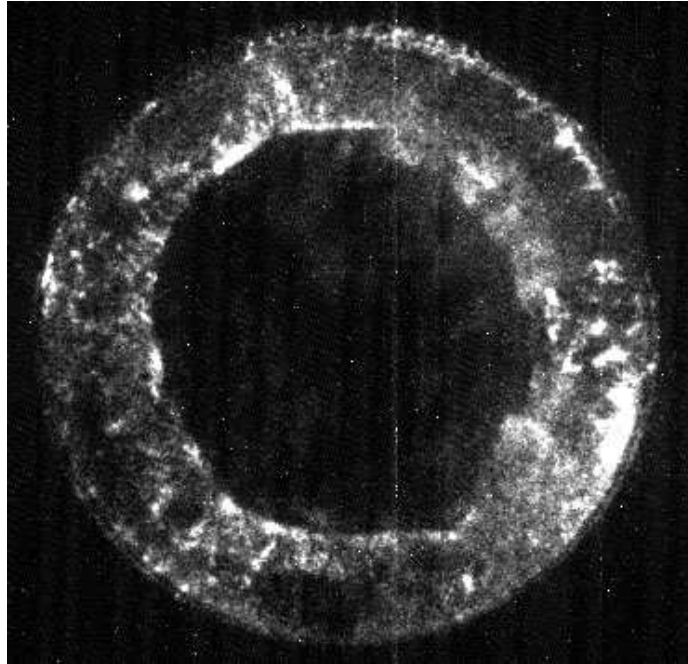


Figure F.30: Chemiluminescence from run 018.

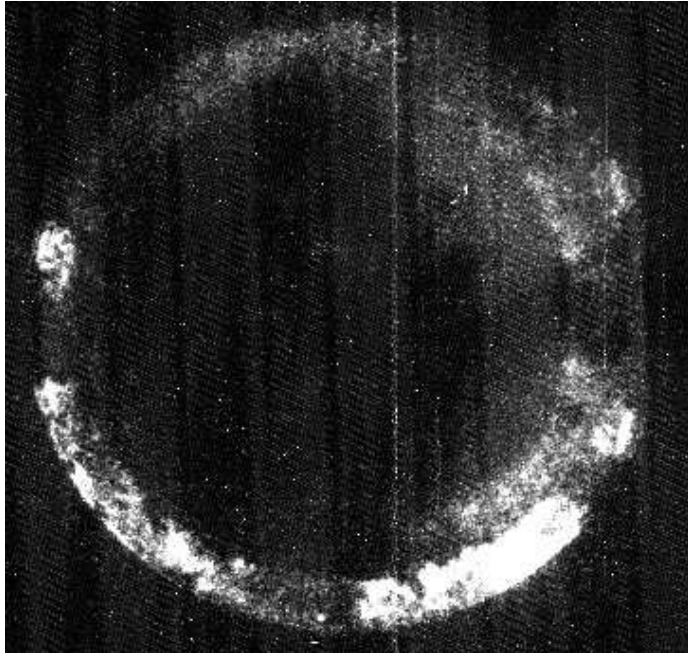


Figure F.31: Chemiluminescence from run 020.

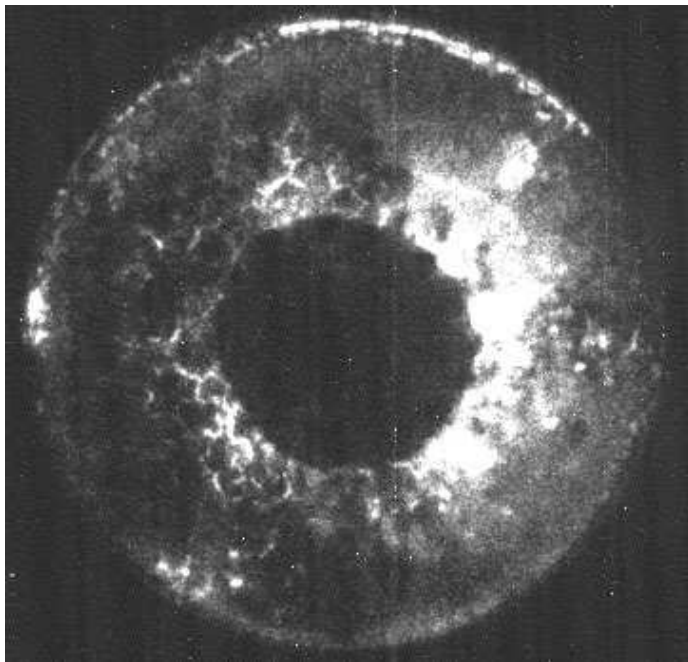


Figure F.32: Chemiluminescence from run 021.

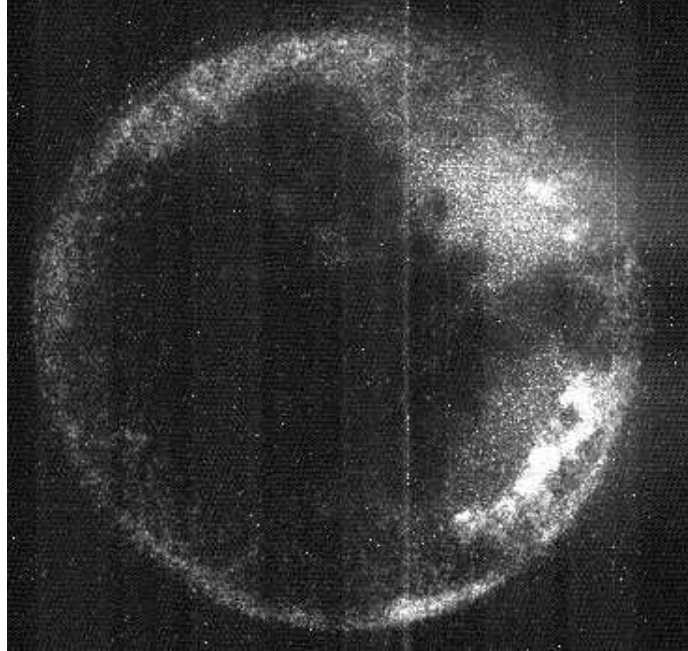


Figure F.33: Chemiluminescence from run 022.

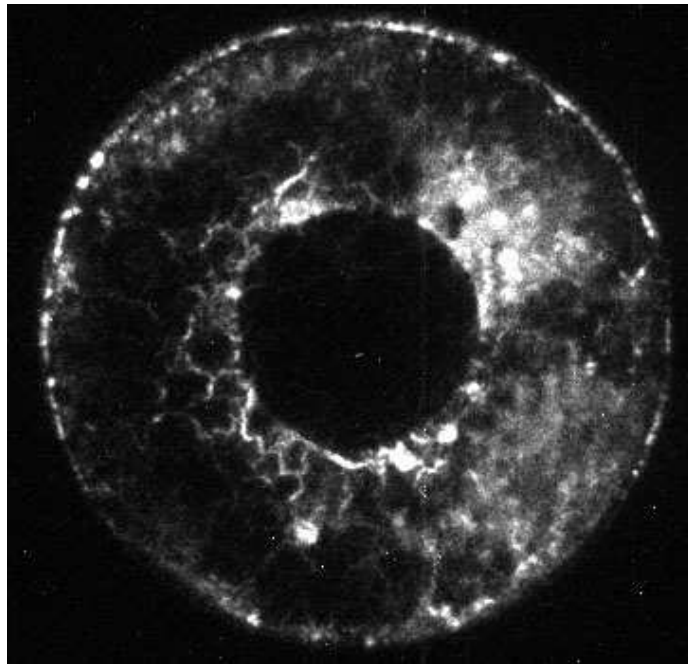


Figure F.34: Chemiluminescence from run 023.

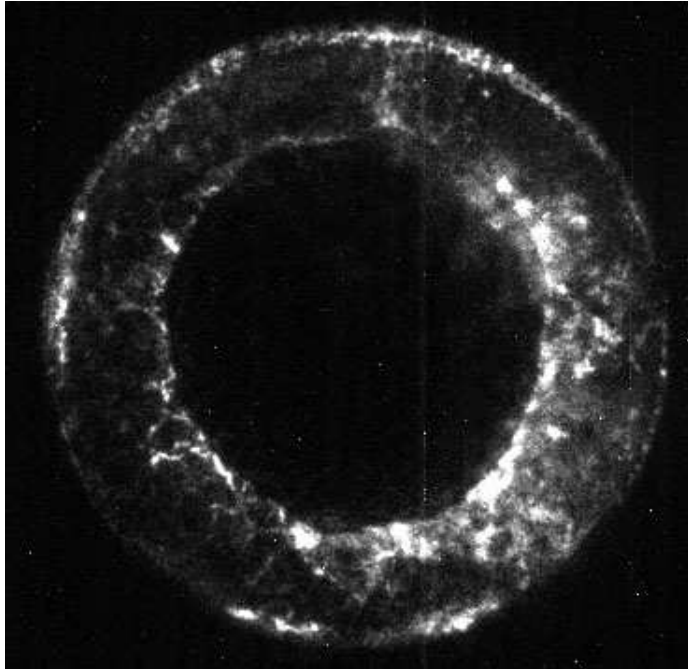


Figure F.35: Chemiluminescence from run 024.

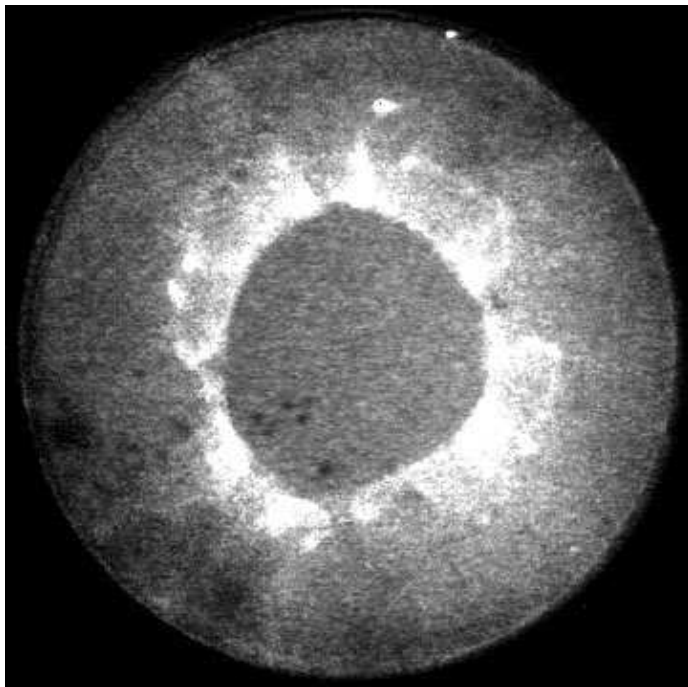


Figure F.36: Chemiluminescence from run 030.

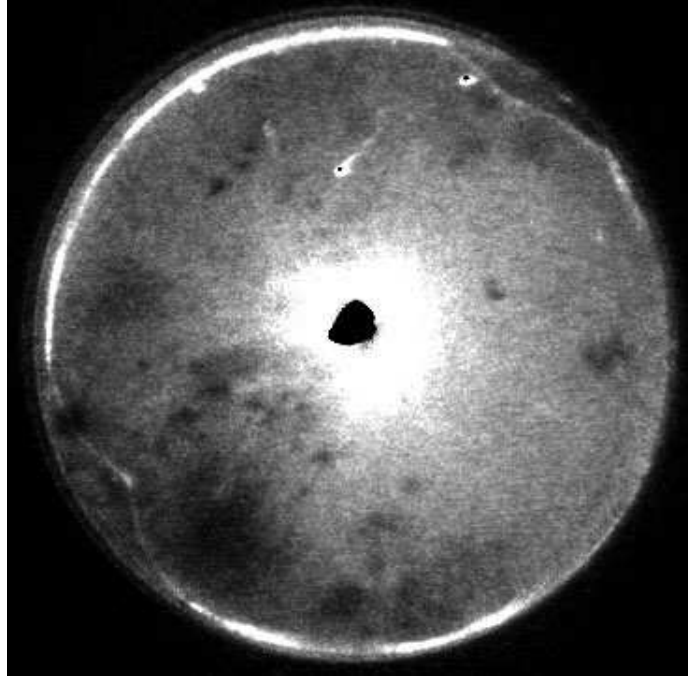


Figure F.37: Chemiluminescence from run 031.

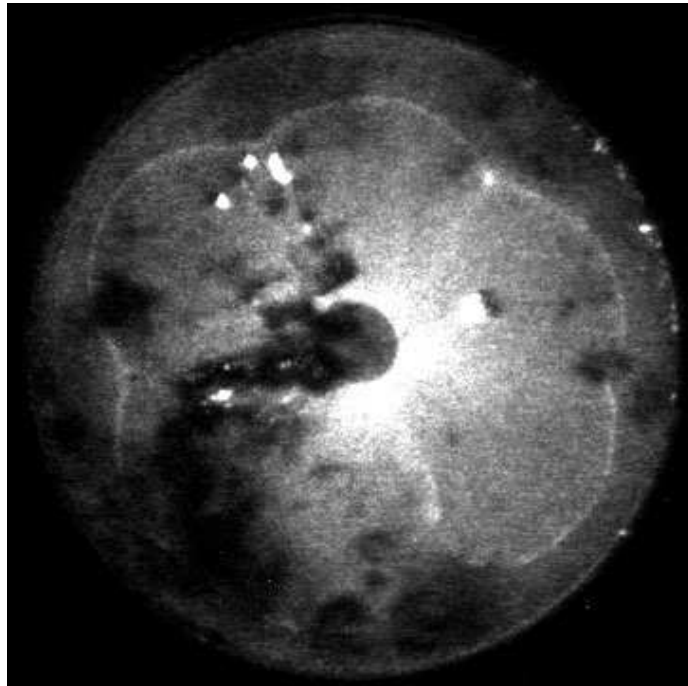


Figure F.38: Chemiluminescence from run 032.

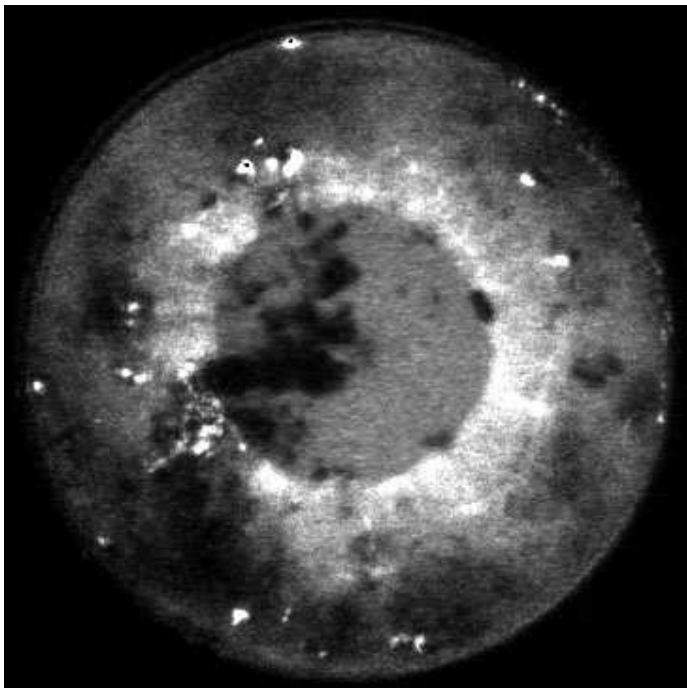


Figure F.39: Chemiluminescence from run 033.

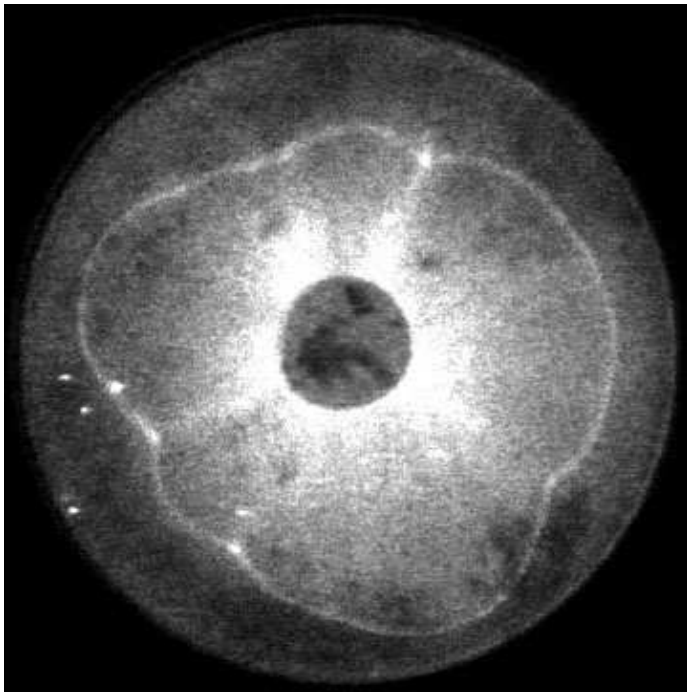


Figure F.40: Chemiluminescence from run 035.

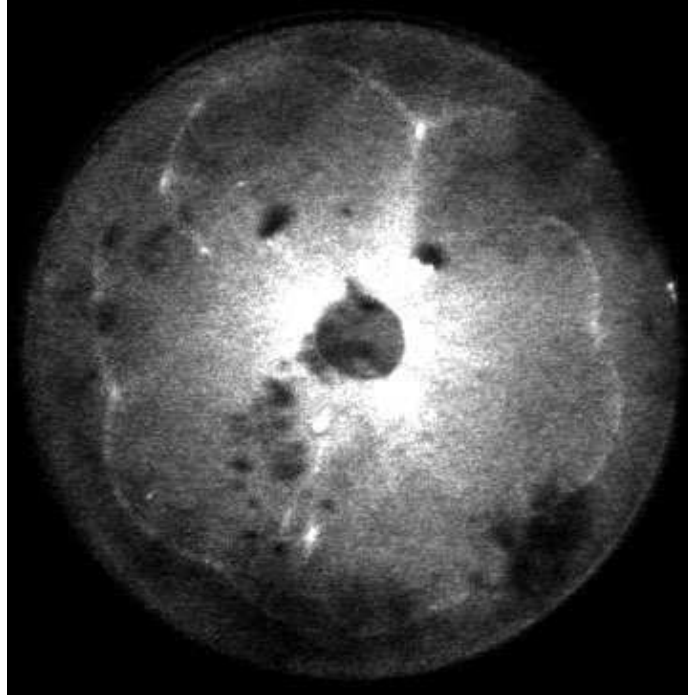


Figure F.41: Chemiluminescence from run 036.

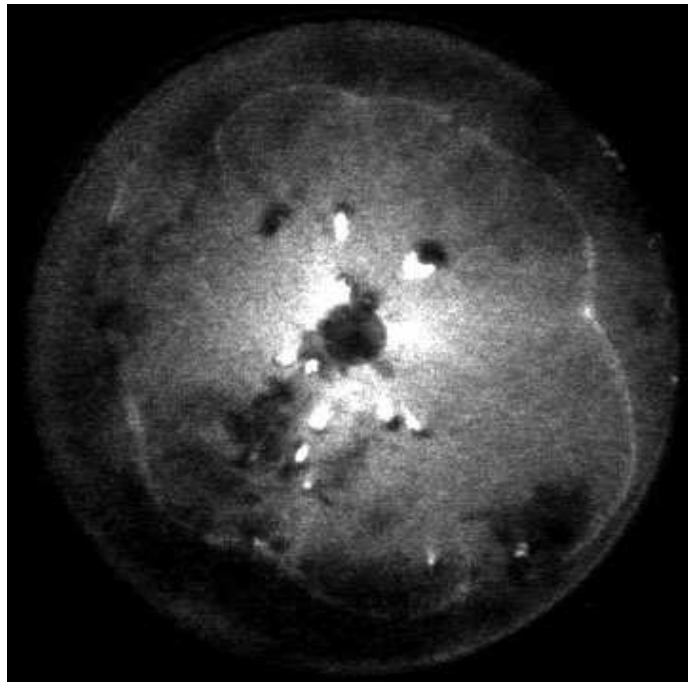


Figure F.42: Chemiluminescence from run 037.

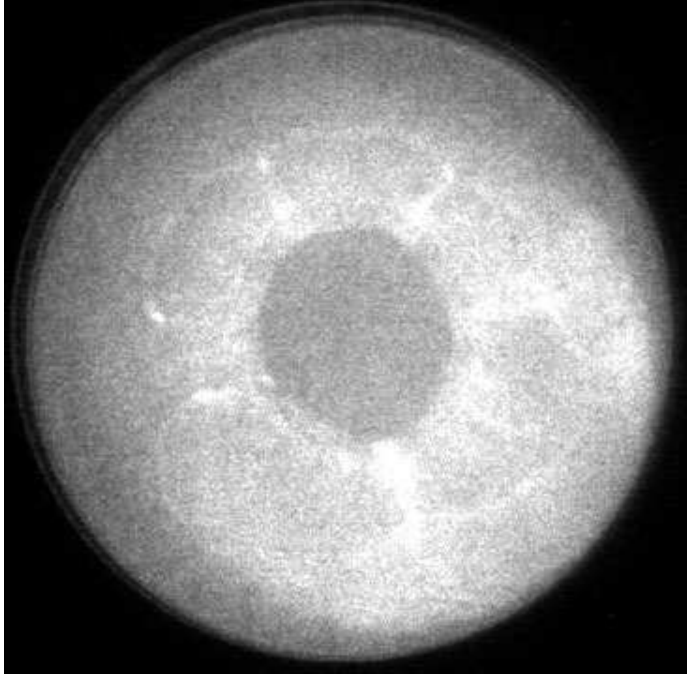


Figure F.43: Chemiluminescence from run 040.

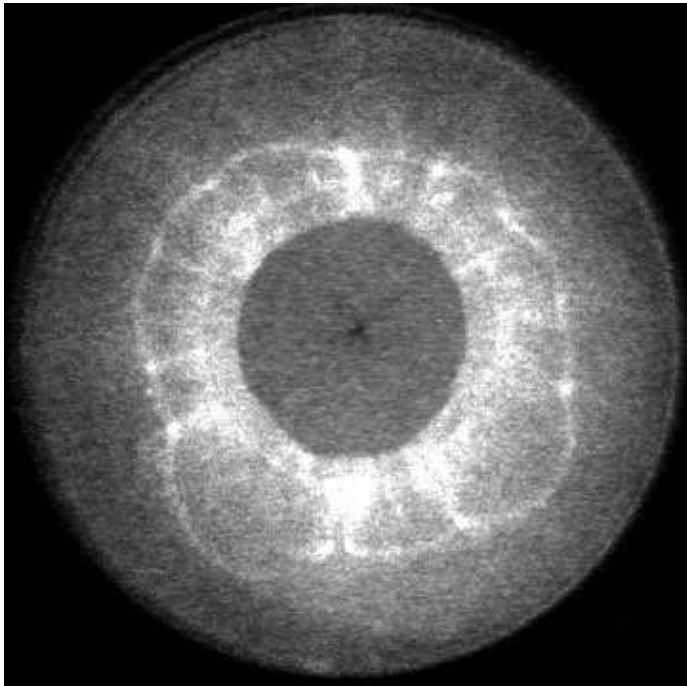


Figure F.44: Chemiluminescence from run 041.

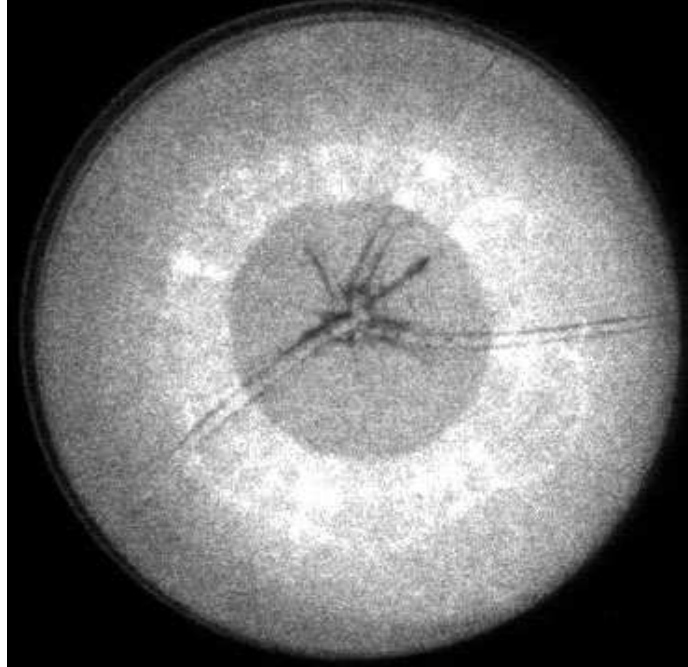


Figure F.45: Chemiluminescence from run 042.

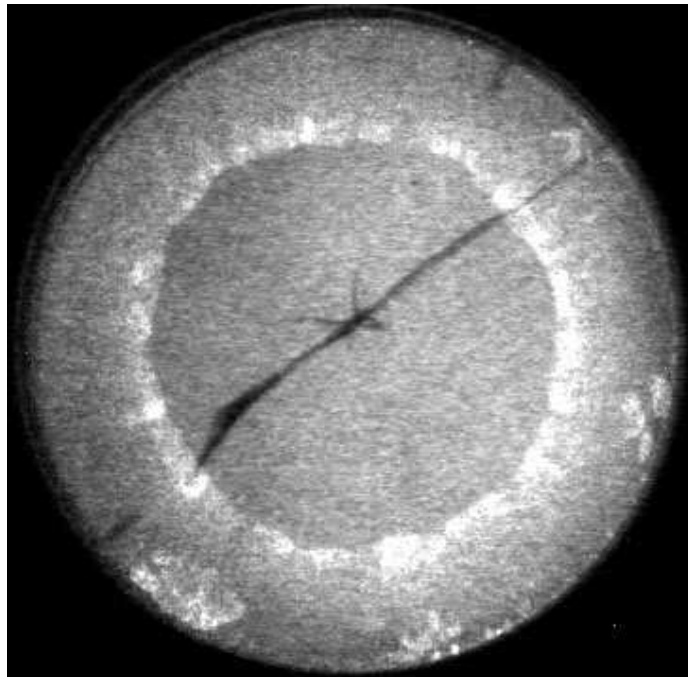


Figure F.46: Chemiluminescence from run 043.



## Appendix G

# Planar Dynamic Initiator Data

## G.1 Design Drawings

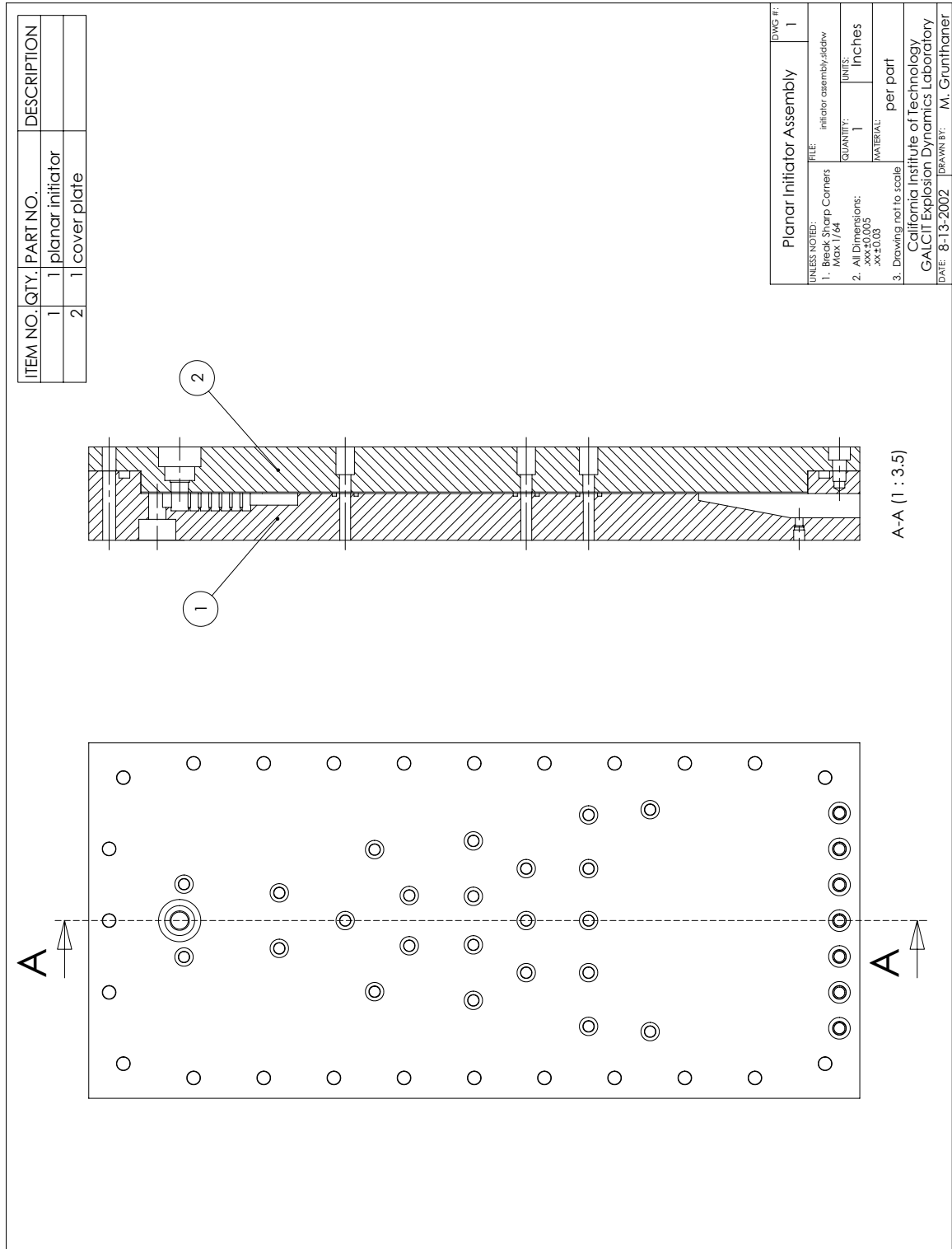


Figure G.1: A view of the dynamic planar initiator assembly.

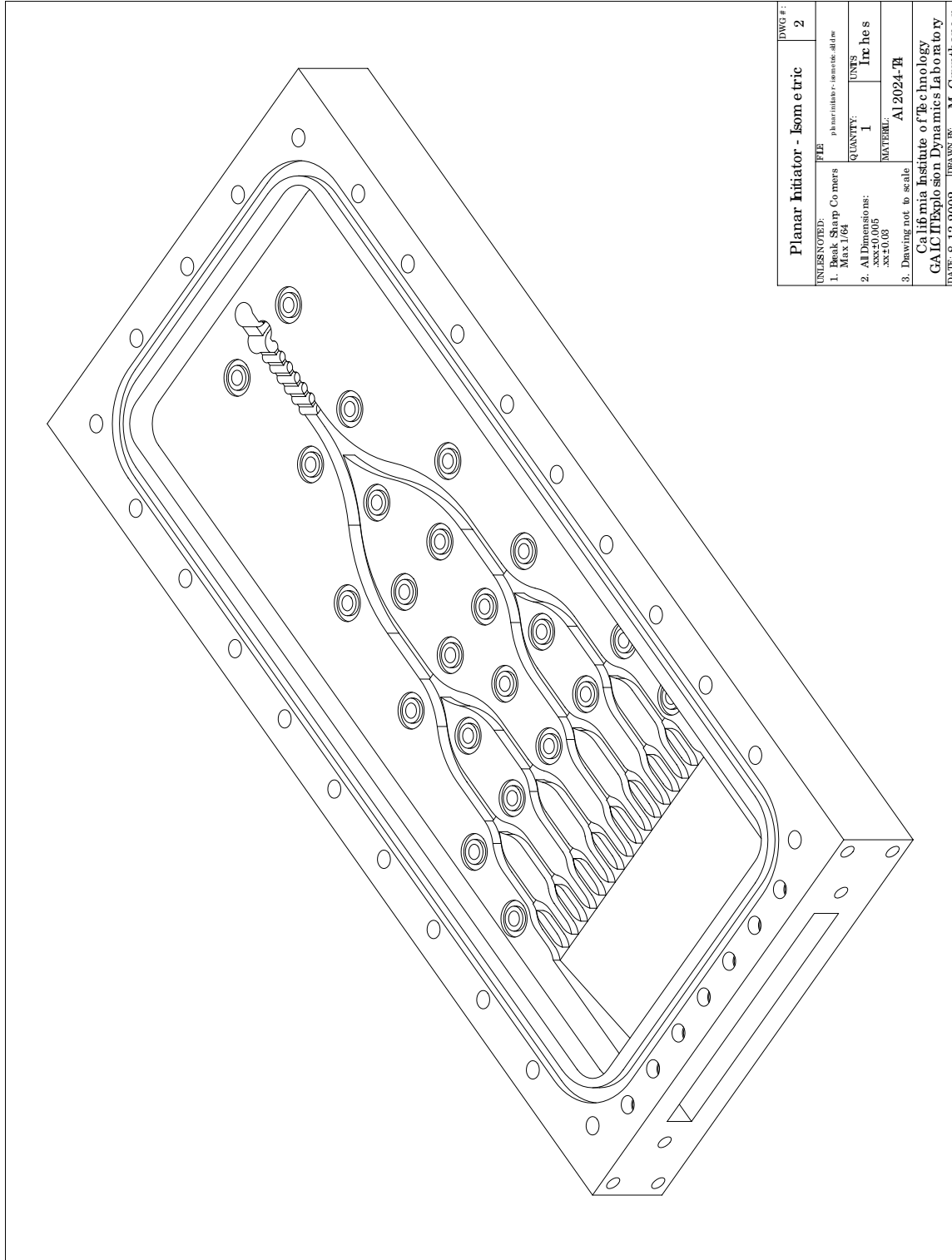


Figure G.2: Isometric view of the dynamic planar initiator.

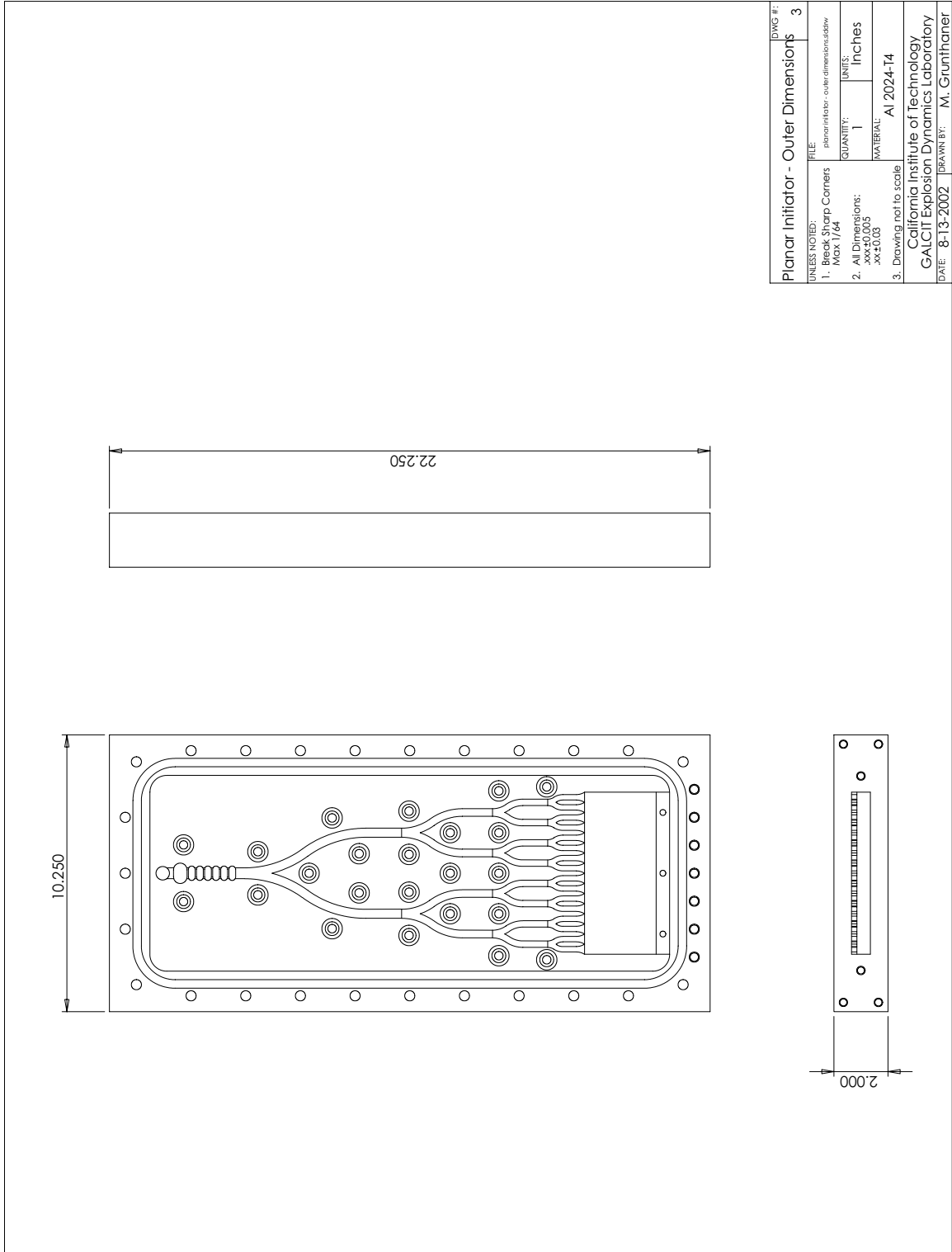


Figure G.3: Outer dimension of the dynamic planar initiator.

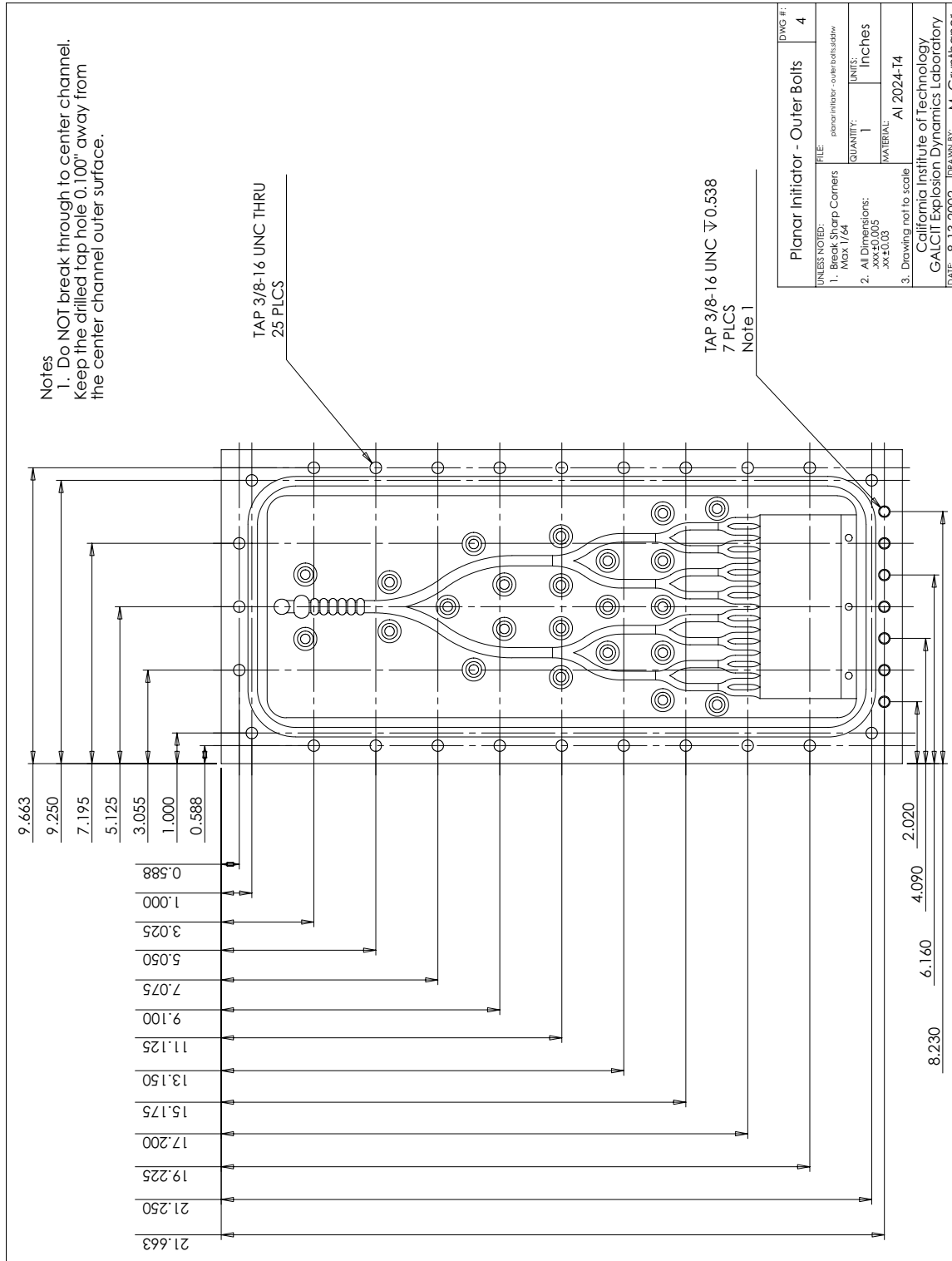


Figure G.4: Outer bolt dimensions on the dynamic planar initiator.

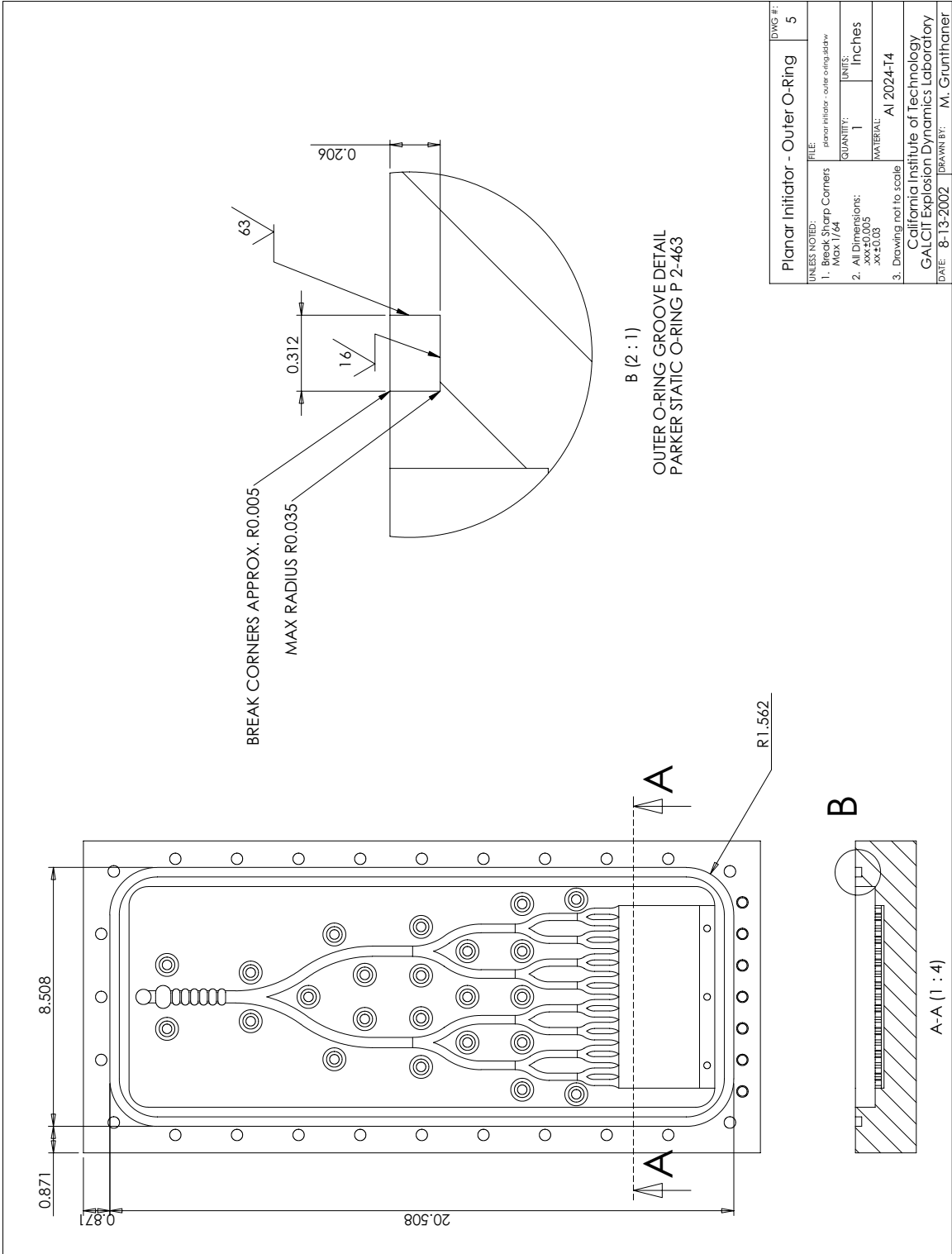


Figure G.5: Outer o-ring dimensions on the dynamic planar initiator.

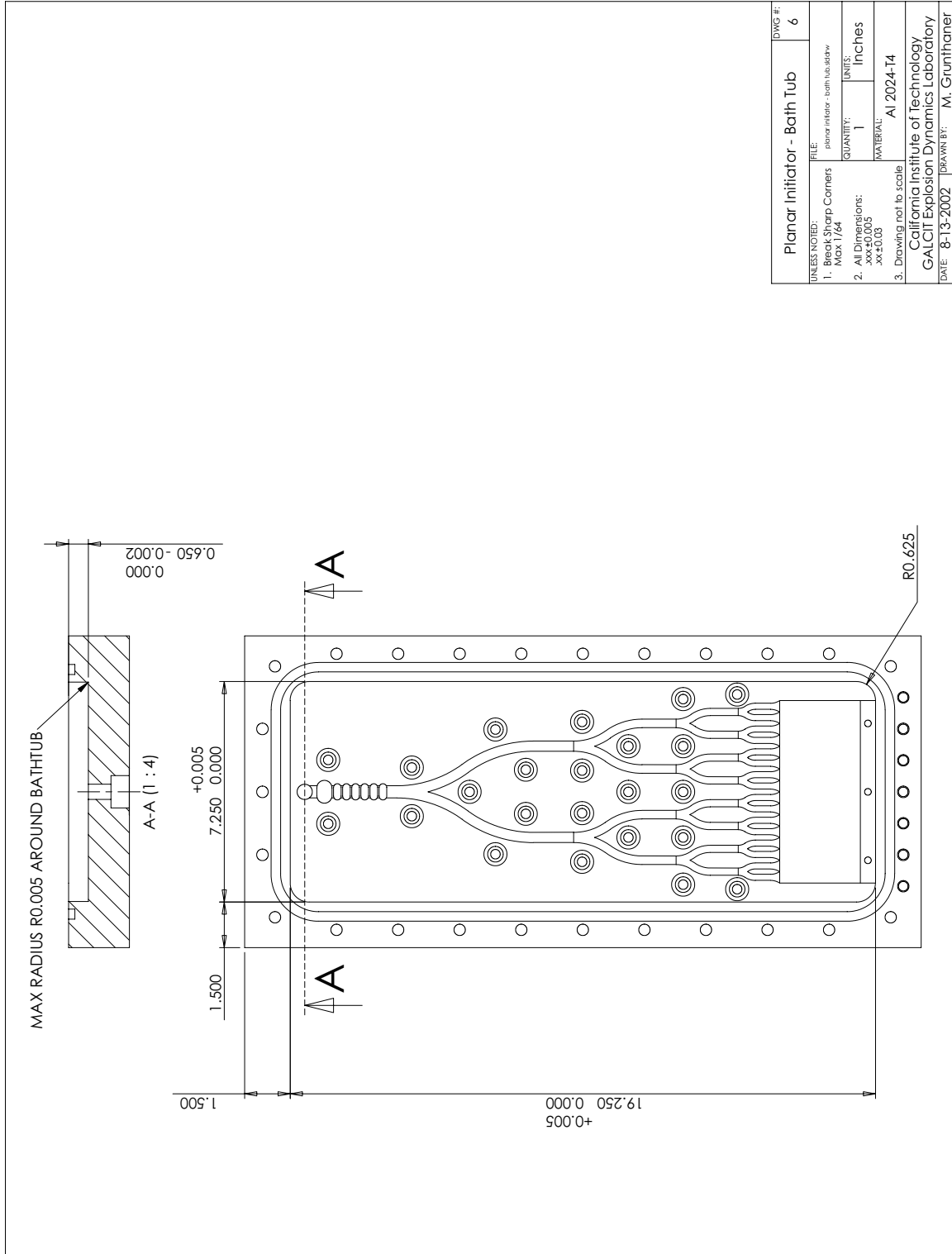


Figure G.6: Bath tube dimensions on the dynamic planar initiator.

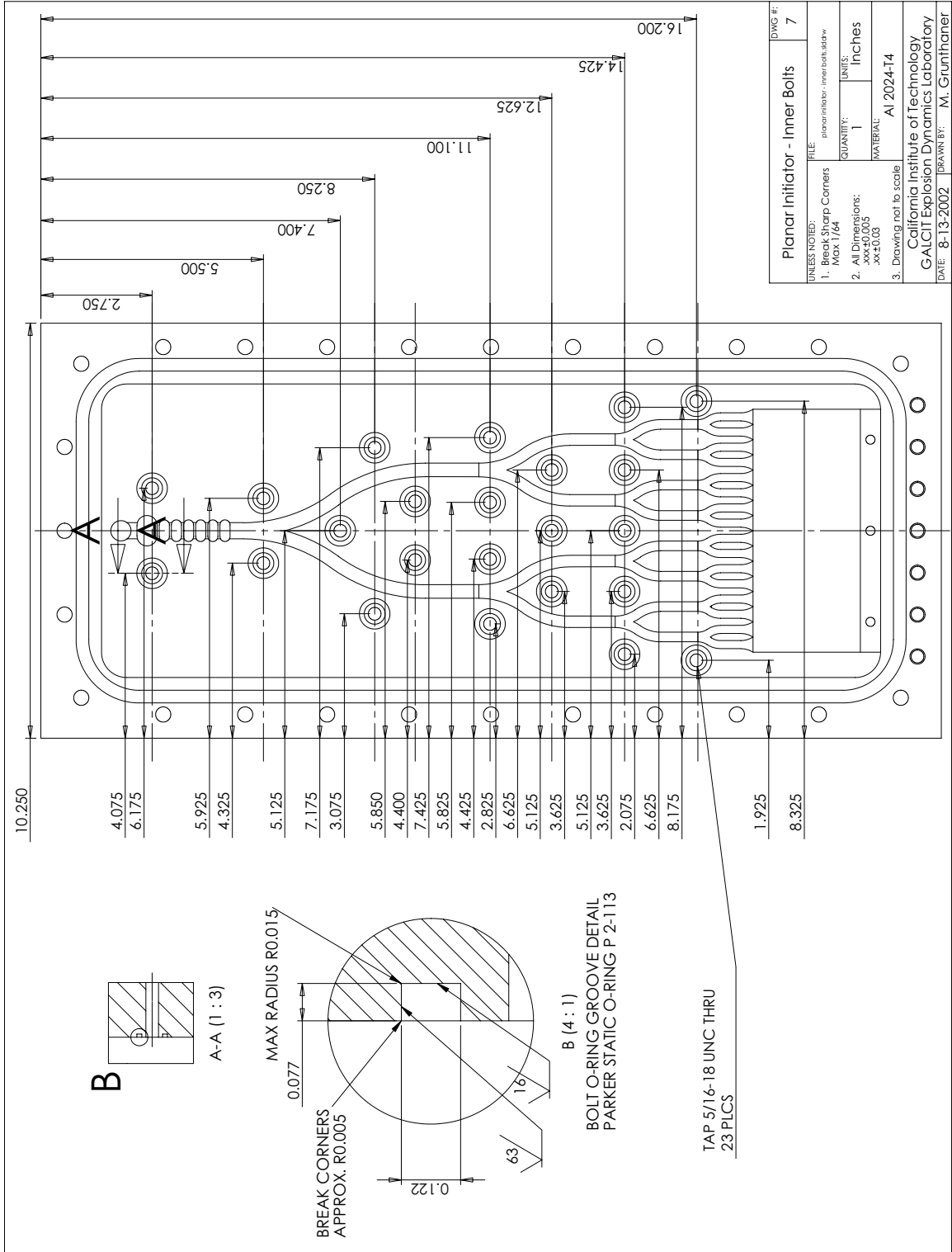


Figure G.7: Inner bolt dimensions on the dynamic planar initiator.

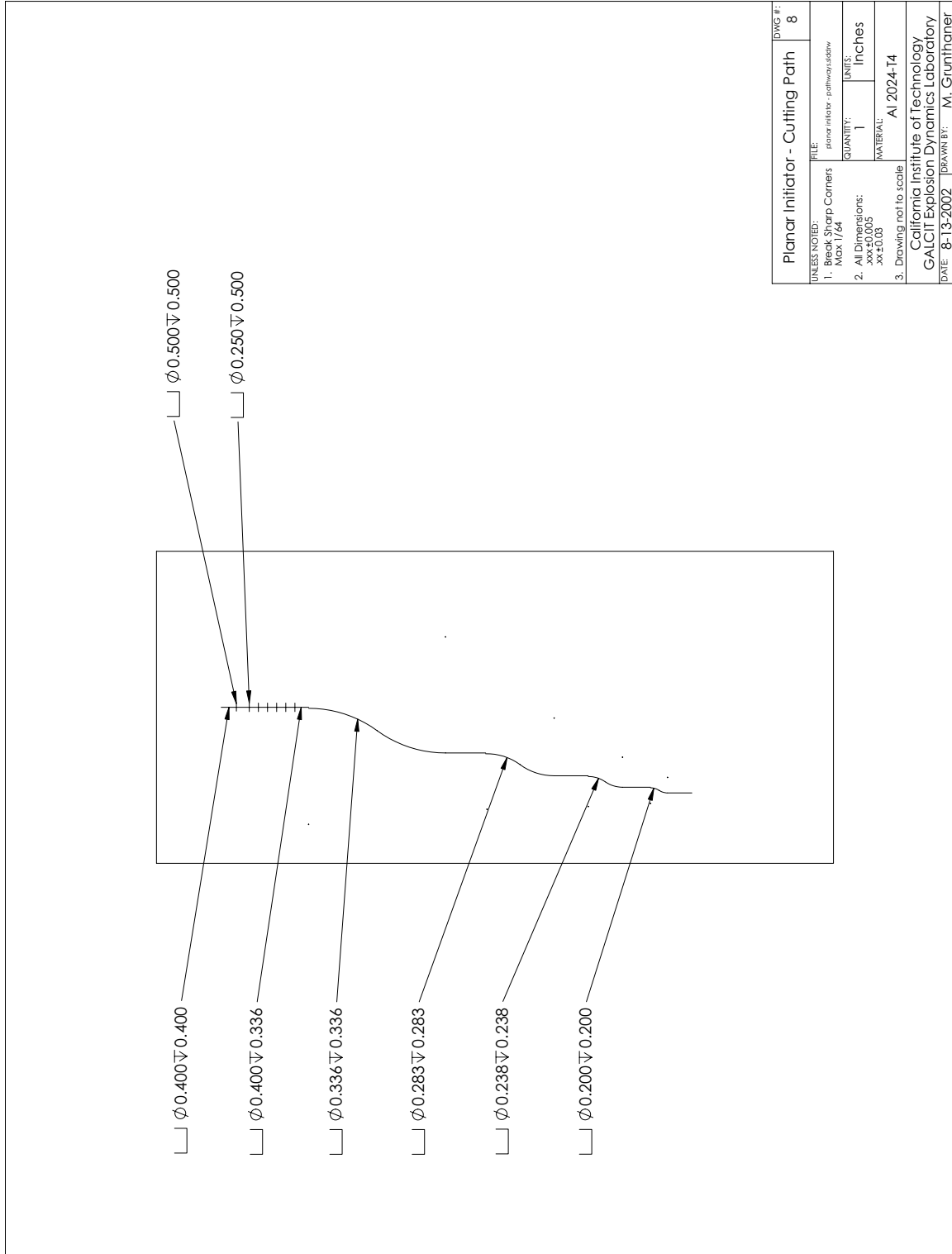


Figure G.8: Channel cutting path on the dynamic planar initiator.

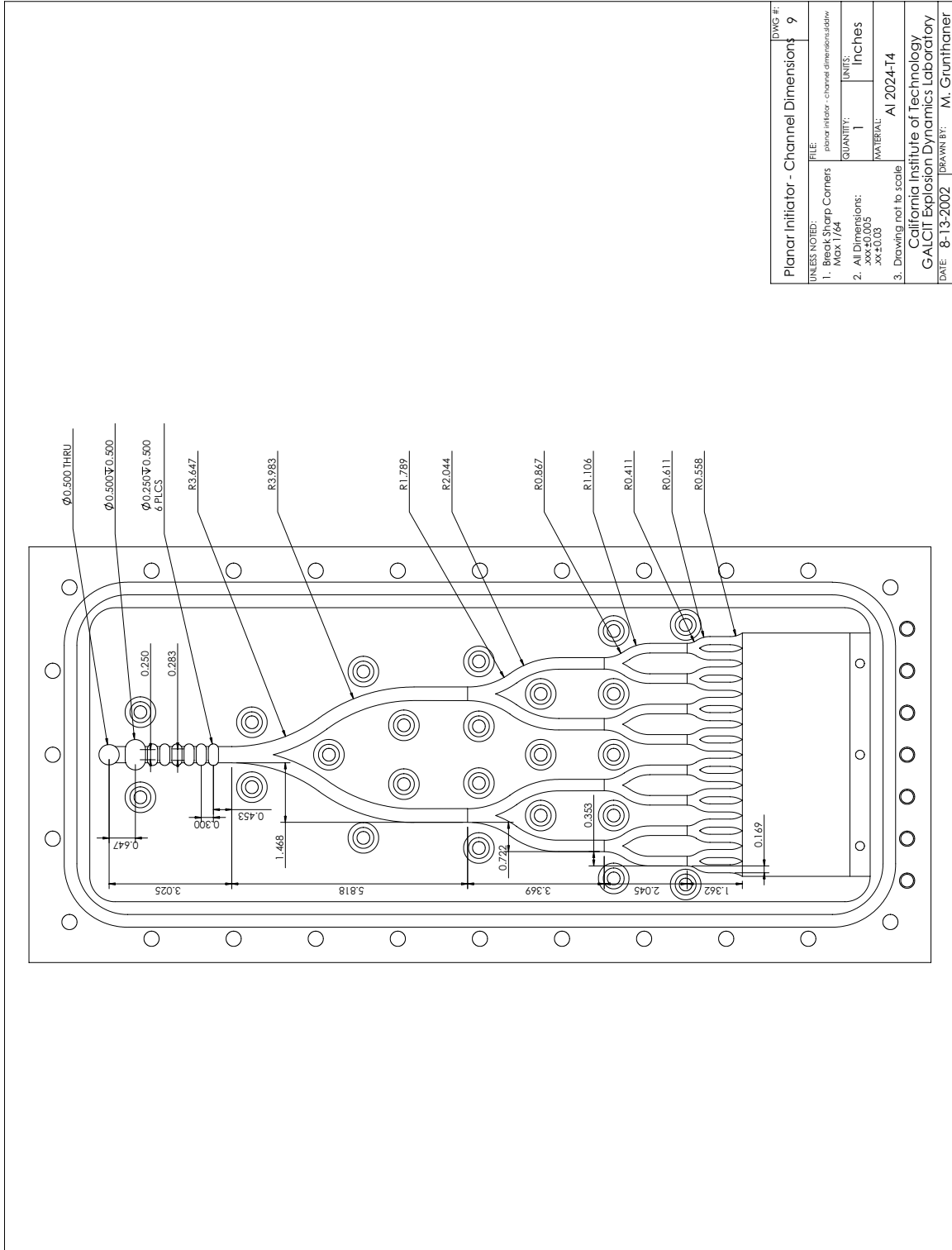


Figure G.9: Channel dimensions on the dynamic planar initiator.

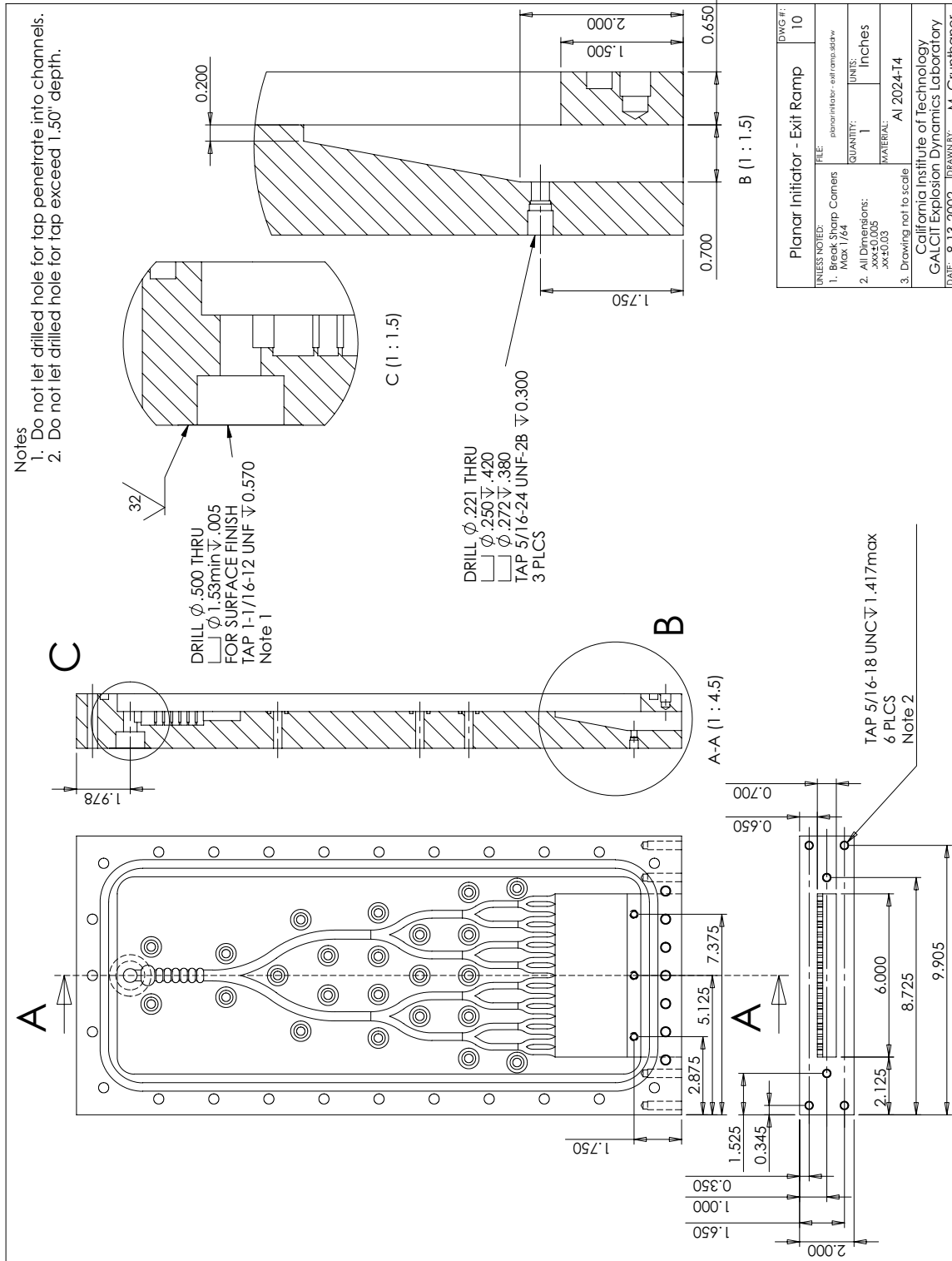
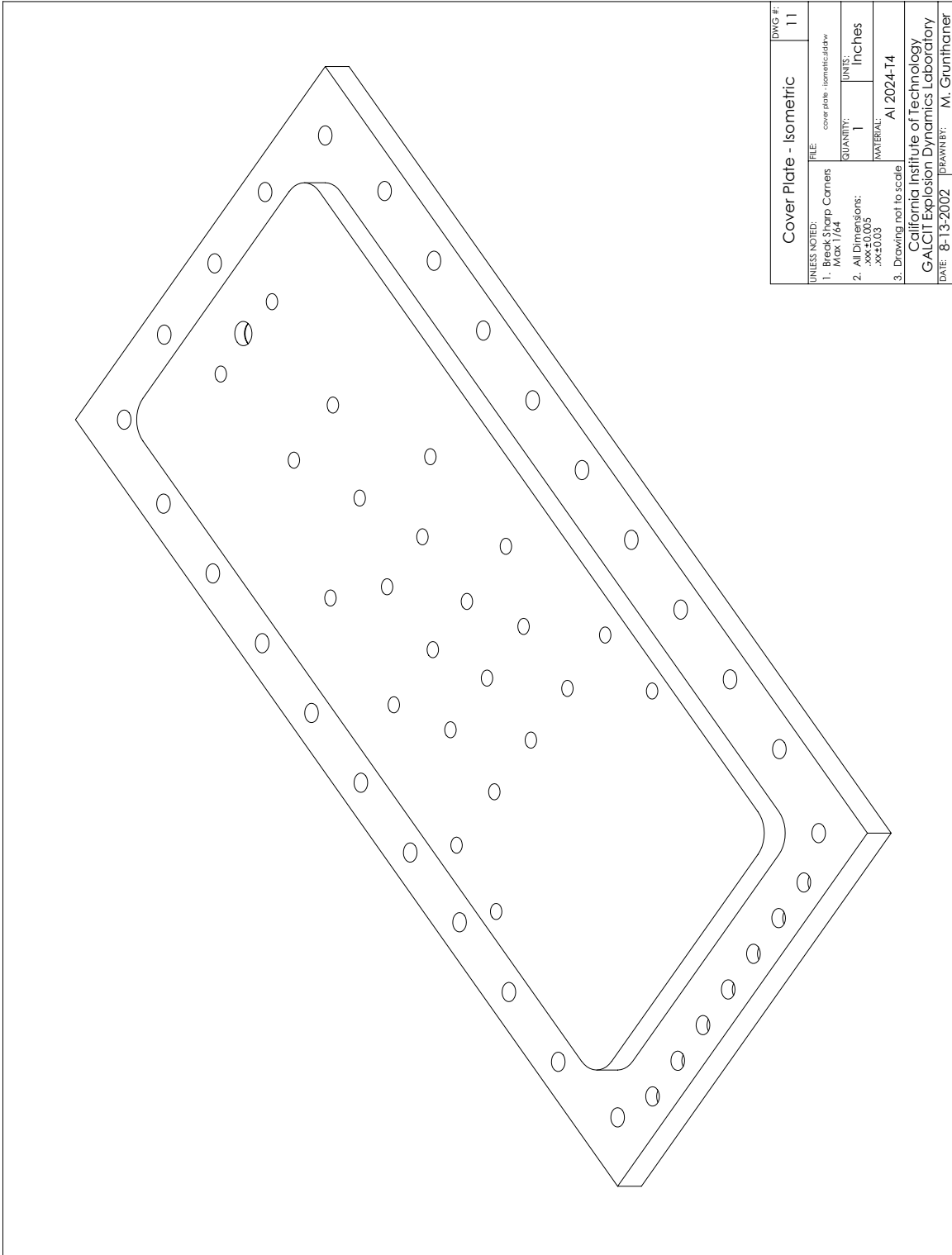


Figure G.10: Exit ramp dimensions on the dynamic planar initiator.



Cover Plate - Isometric		DWG #:	11
UNLESS NOTED:	FILE:	cover plate - isometric.dwg	
1. Break Sharp Corners Max 1/64	QUANTITY:	1	UNITS: Inches
2. All Dimensions: .xxx±0.005 .xx±0.03	MATERIAL:	Al 2024-T4	
3. Drawing not to scale	California Institute of Technology CALCI Explosion Dynamics Laboratory DATE: 8-13-2002 DRAWN BY: M. Grunthaner		

Figure G.11: Isometric view of the dynamic planar initiator cover plate.

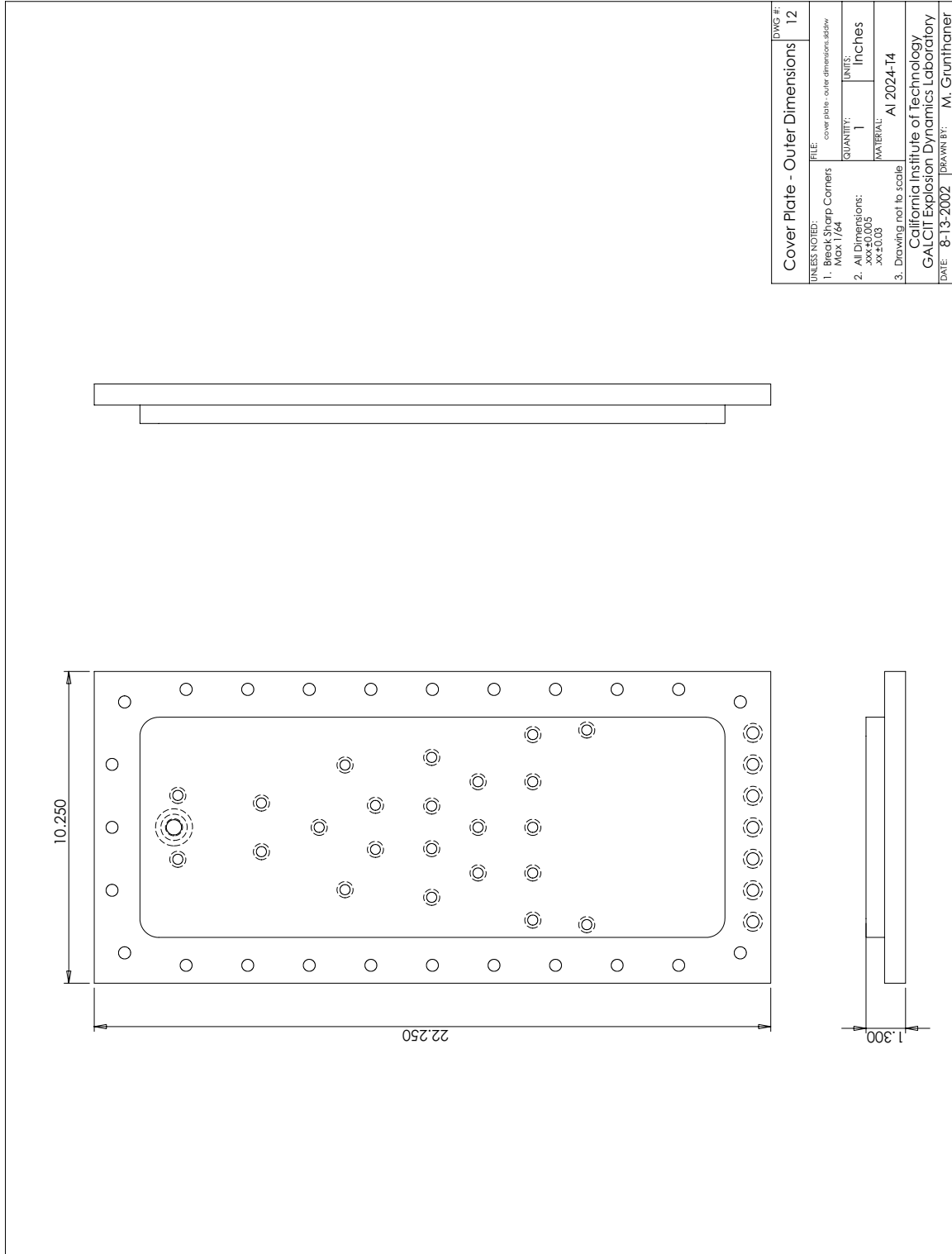


Figure G.12: Outer dimension of the dynamic planar initiator cover plate.

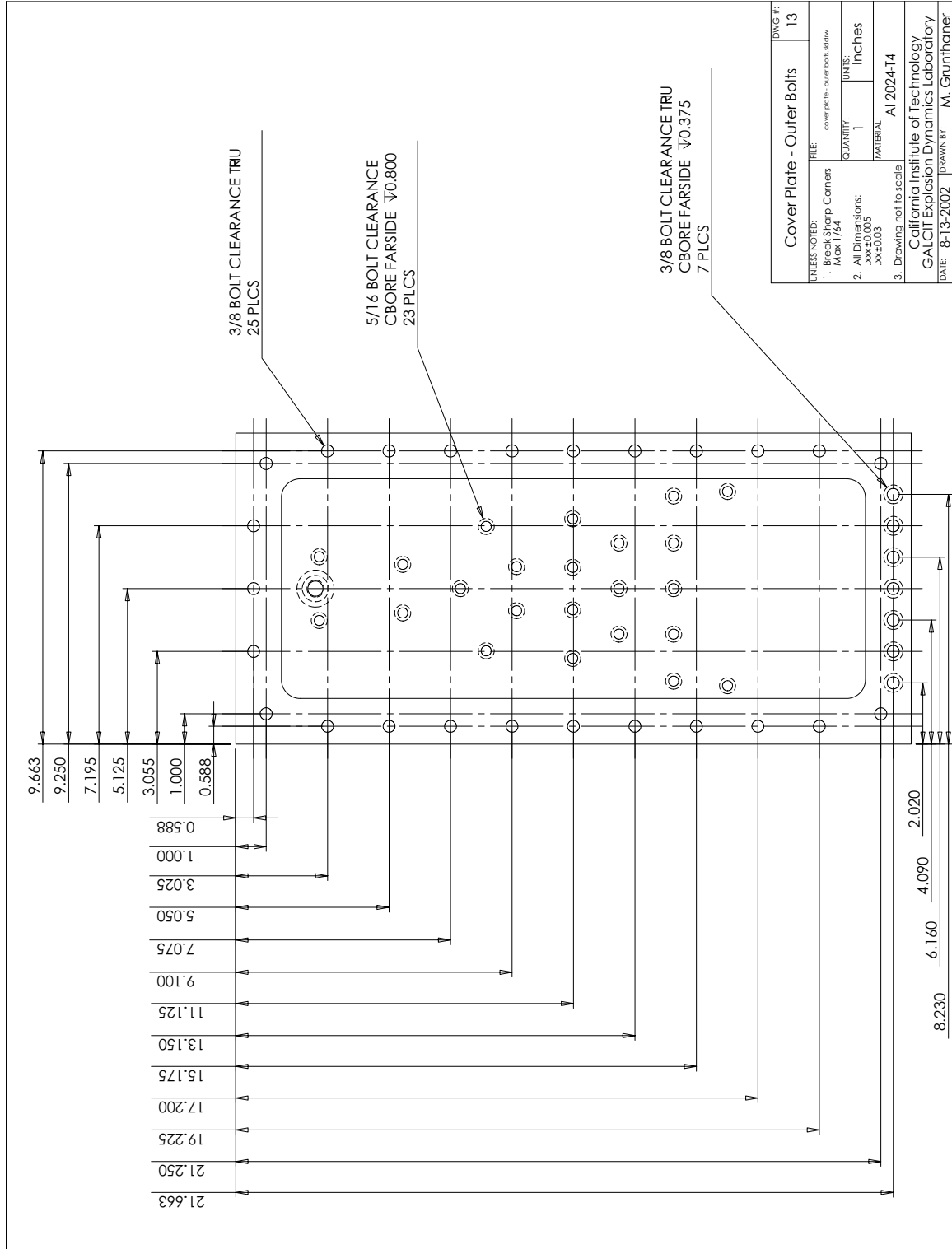


Figure G.13: Outer bolt dimensions on the dynamic planar initiator cover plate.

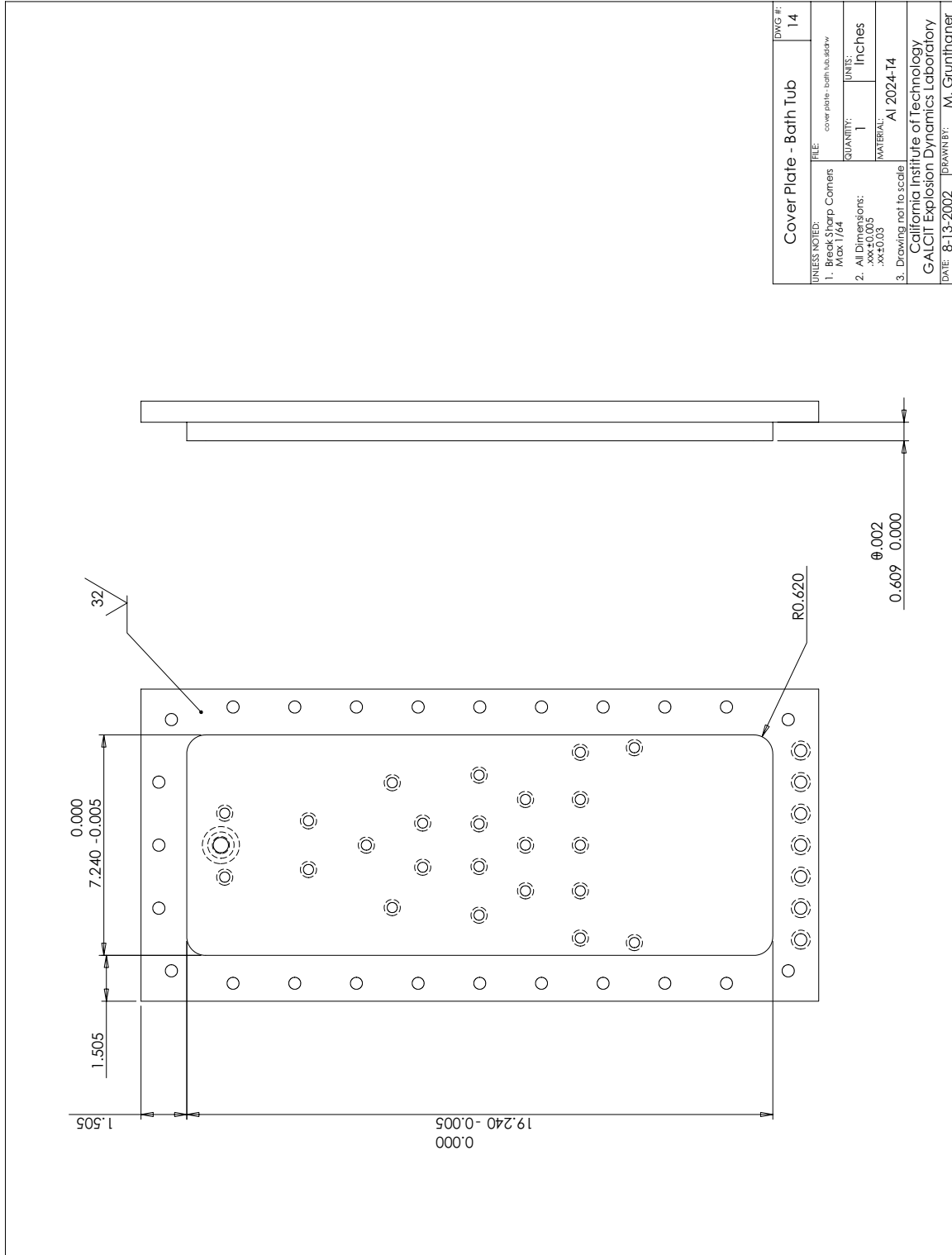


Figure G.14: Bath tube dimensions on the dynamic planar initiator cover plate.

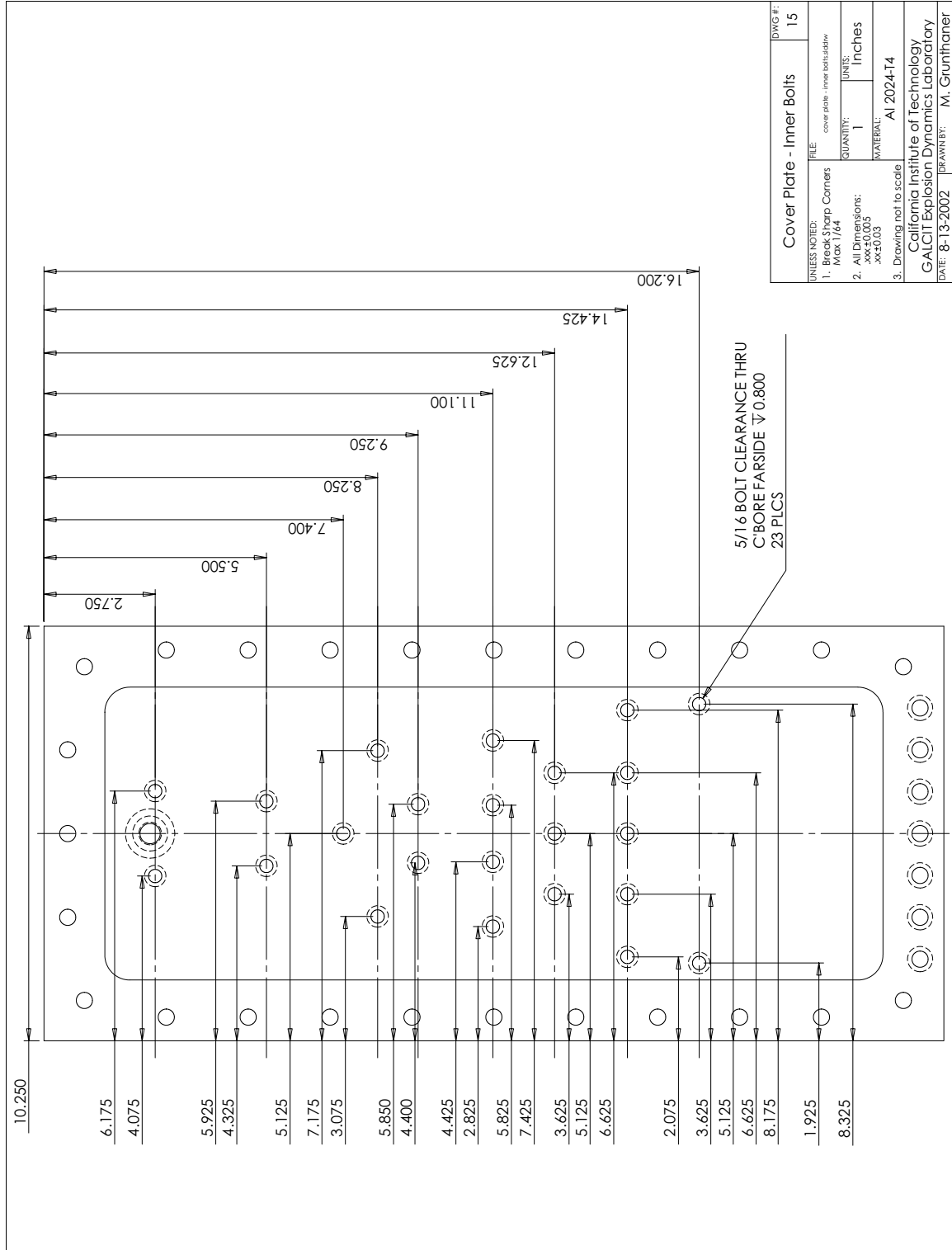


Figure G.15: Inner bolt dimensions on the dynamic planar initiator cover plate.

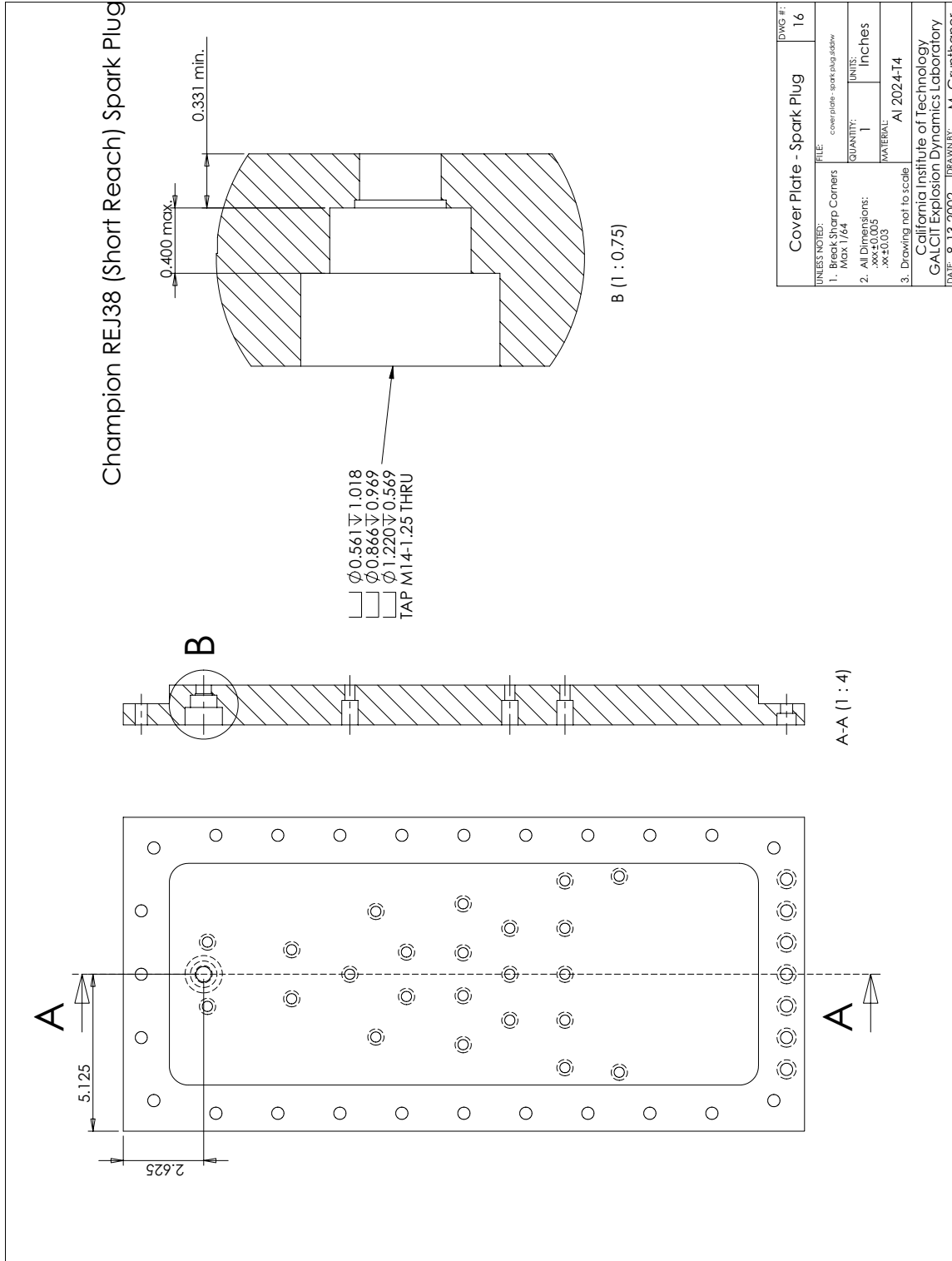


Figure G.16: Spark plug dimensions on the dynamic planar initiator cover plate.

## G.2 Run Matrix

Imaging Run	NCF Run	Injection Pressure (bar)	Injector Duration	Injector Delay	Camera Delay ( $\mu\text{s}$ )	MCP (V)
1	269	0.261	40	250	400	800
2	N/A	0.211	40	250	400	800
3	270	0.219	40	250	400	680
4	271	0.219	40	250	400	680
5	272	0.219	40	250	350	680
6	273	0.219	40	375	350	680
7	274	0.219	40	375	350	680
8	275	0.219	40	375	360	680
9	N/A	0.238	70	375	360	680
10	277	0.223	70	375	360	600
11	278	0.223	70	375	370	600
12	279	0.223	70	375	380	600
13	N/A	0.238	70	375	390	600
14	281	0.223	70	375	400	600
15	282	0.223	70	375	410	600
16	283	0.223	70	375	420	600
17	284	0.223	70	375	430	600
18	285	0.223	70	375	425	600
19	286	0.223	70	375	430	600
20	287	0.223	70	375	435	600
21	288	0.223	70	375	435	600

Table G.1: Experimental properties of each run. The initiator and narrow channel facility (NCF) were initially filled with air. Shortly before ignition, an equimolar  $\text{C}_2\text{H}_2\text{-O}_2$  mixture was injected into the initiator channels. “Imaging Run” refers to the run number taken with the CCD camera. “NCF Run” refers to the run number in the NCF facility. “Injection duration” corresponds to the dial setting on the injection system controlling the initiator gas injection duration. “Injector delay” corresponds to the dial setting on the injection system controlling the length of time between the end of initiator gas injection and the firing of the spark plug. “Camera delay” refers to the time interval between the firing of the spark plug and when the CCD image was acquired and the “MCP” value refers to the intensifier setting. For all runs, the camera was in gated mode with an integration width of 100 ns. The camera lens has an F-ratio of 20.

### G.3 Wave Arrival Times

Imaging Run	NCF Run	t1 ( $\mu\text{s}$ )	t2 ( $\mu\text{s}$ )	t3 ( $\mu\text{s}$ )
1	269	441	454	445
2	N/A	N/A	N/A	N/A
3	270	432	434	432
4	271	402	406	401
5	272	506	511	505
6	273	422	436	421
7	274	404	409	404
8	275	387	390	387
9	N/A	N/A	N/A	N/A
10	277	477	479	477
11	278	489	490	489
12	279	484	486	484
13	N/A	N/A	N/A	N/A
14	281	467	469	467
15	282	510	513	510
16	283	465	467	465
17	284	433	434	433
18	285	488	489	488
19	286	504	507	505
20	287	501	502	500
21	288	N/A	N/A	N/A

Table G.2: For each run, the wave arrival times are given for each pressure transducer in the initiator test section (P1, P2, P3). A wave arrival time of zero corresponds to the instant the spark plug was fired.

## G.4 Pressure Traces

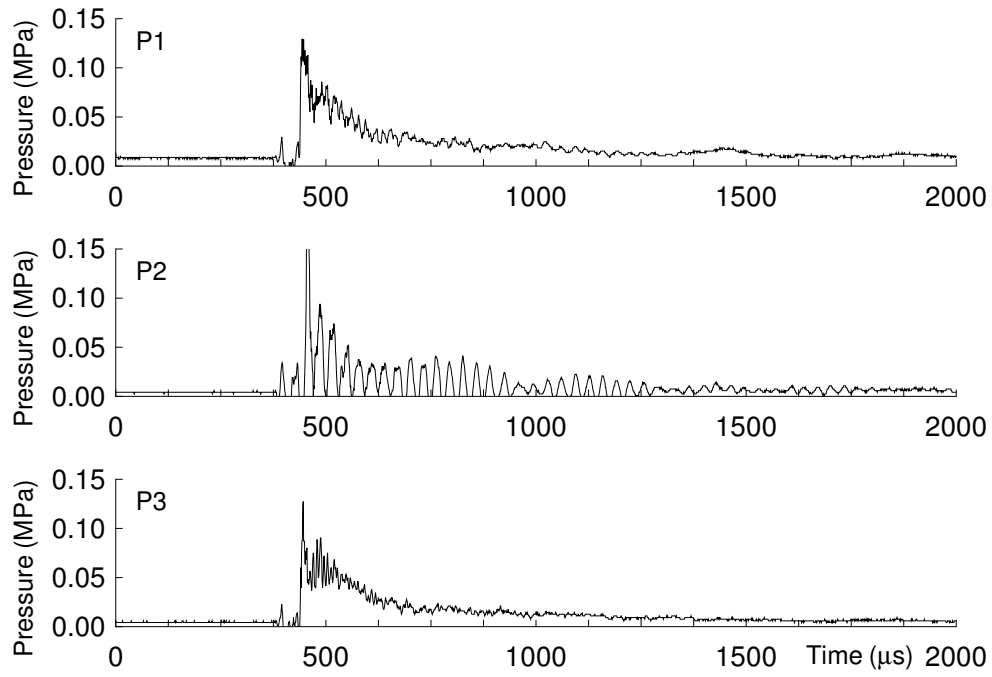


Figure G.17: Pressure history from run 001.

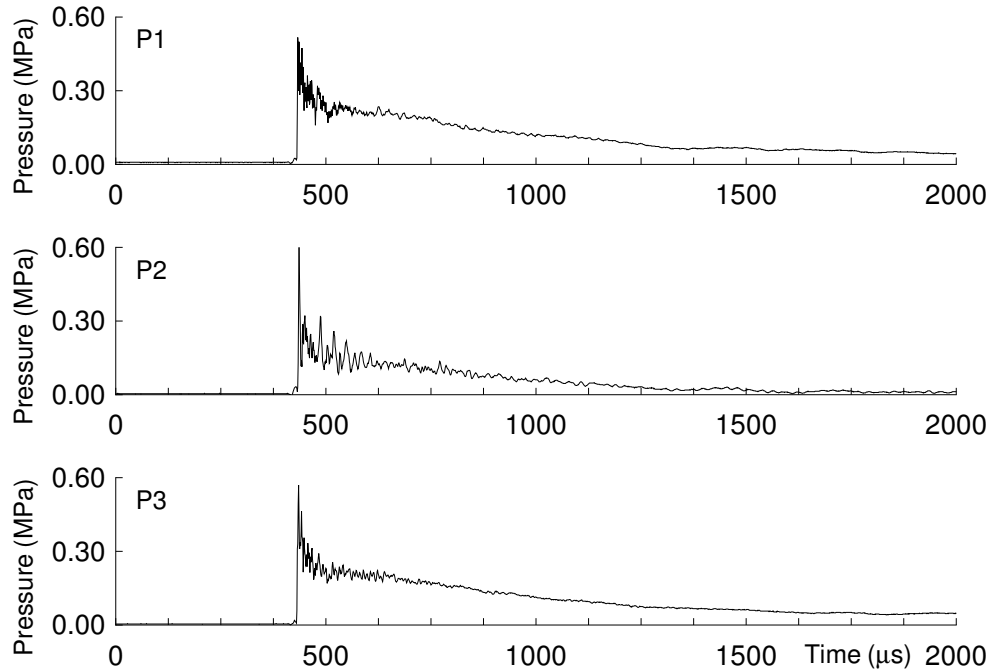


Figure G.18: Pressure history from run 003.

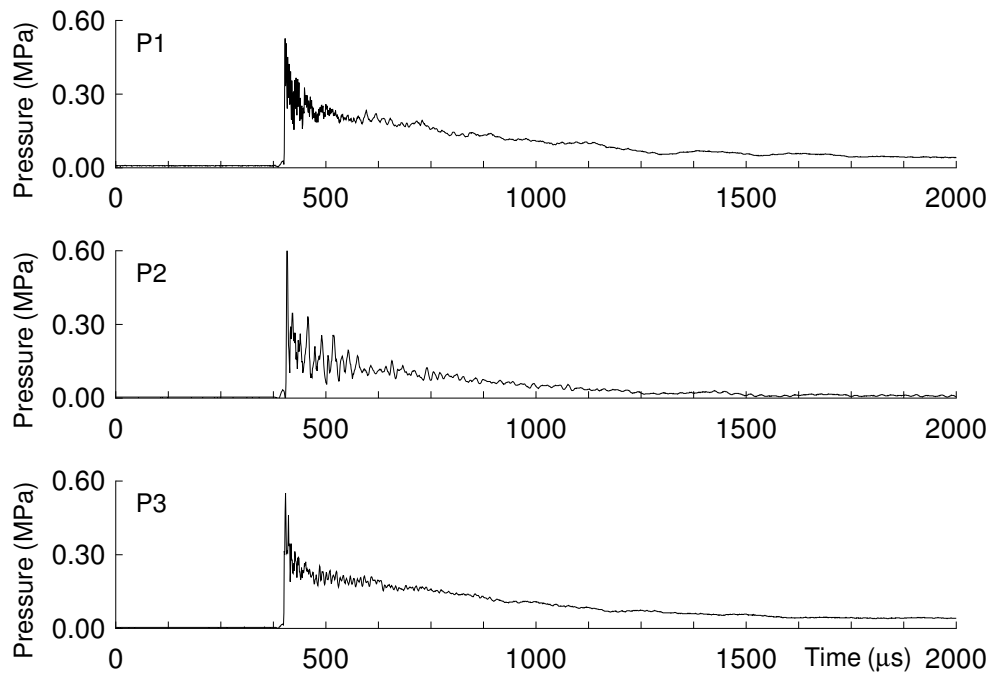


Figure G.19: Pressure history from run 004.

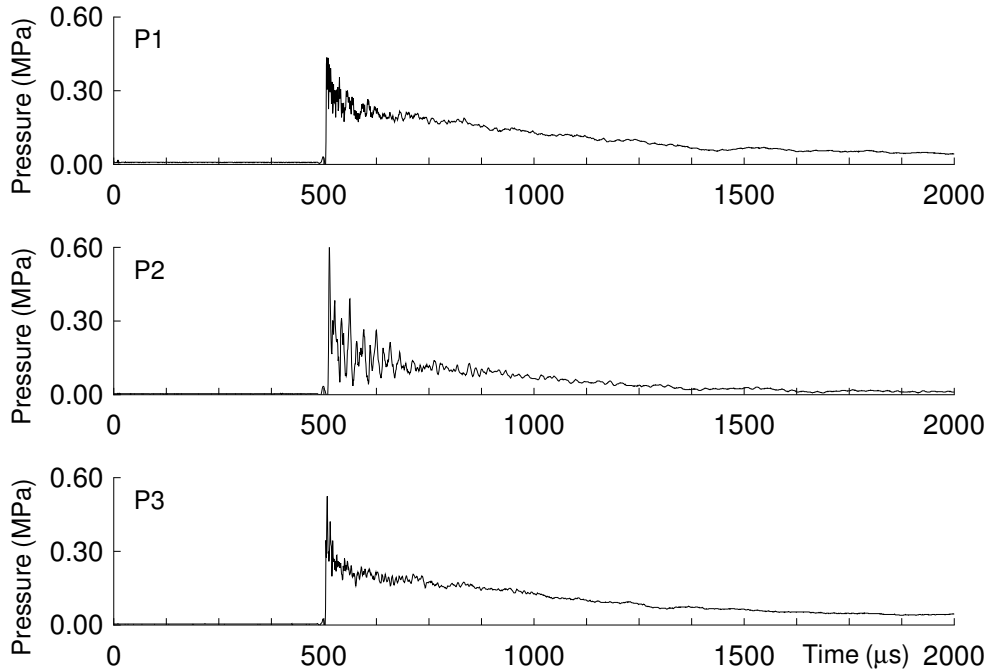


Figure G.20: Pressure history from run 005.

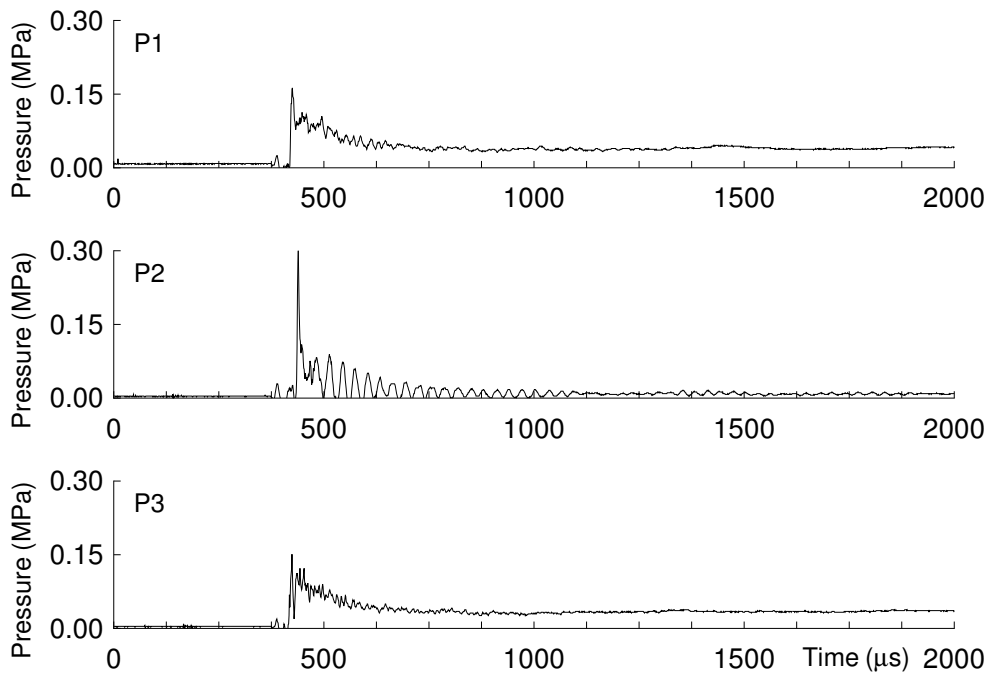


Figure G.21: Pressure history from run 006.

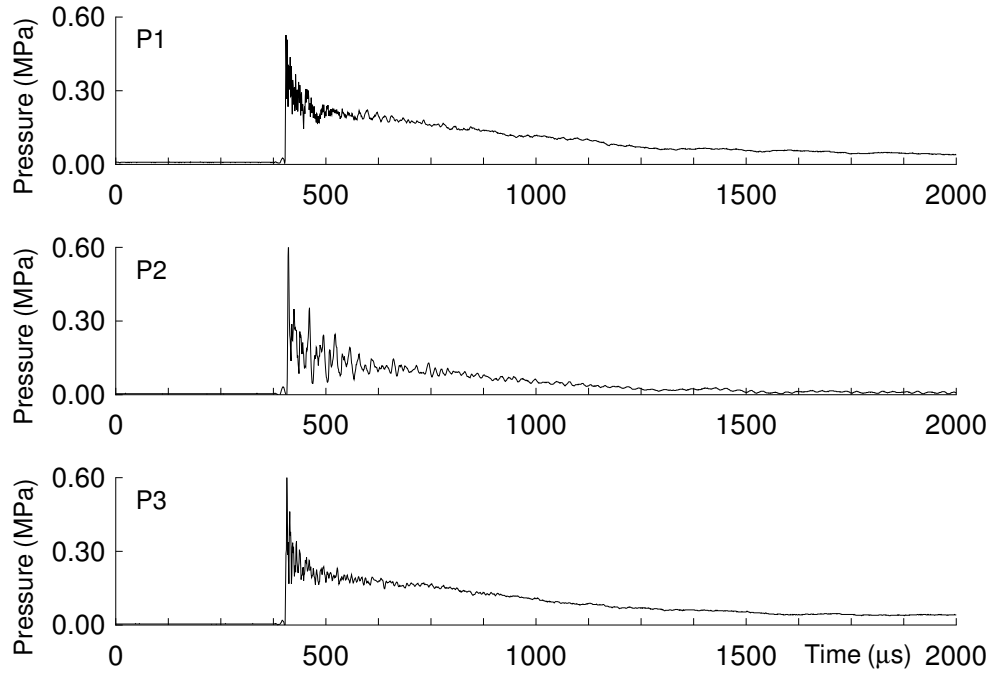


Figure G.22: Pressure history from run 007.

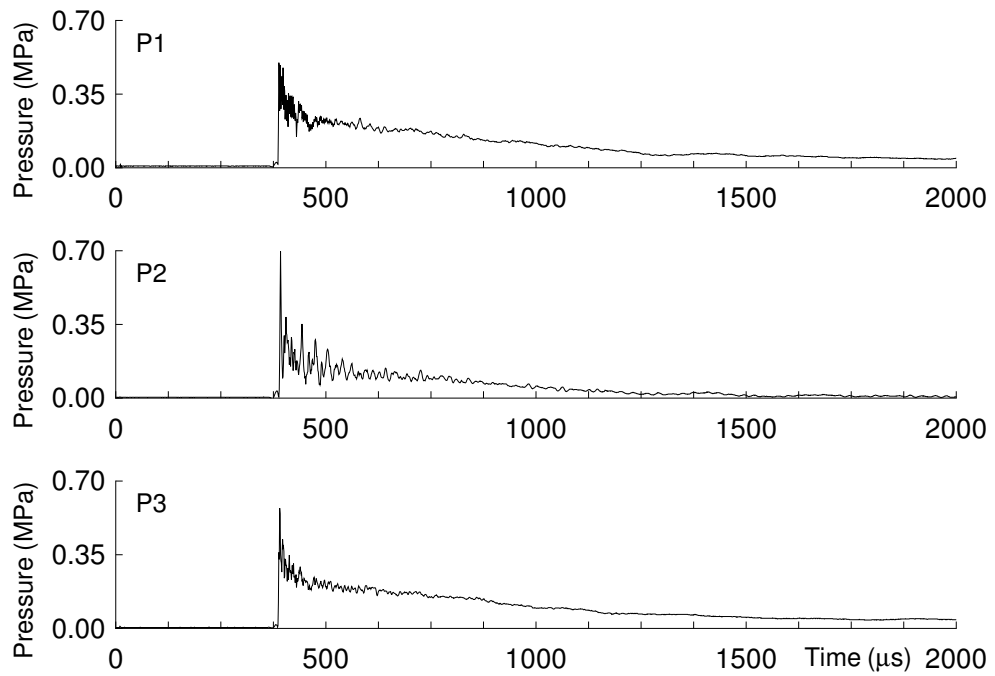


Figure G.23: Pressure history from run 008.

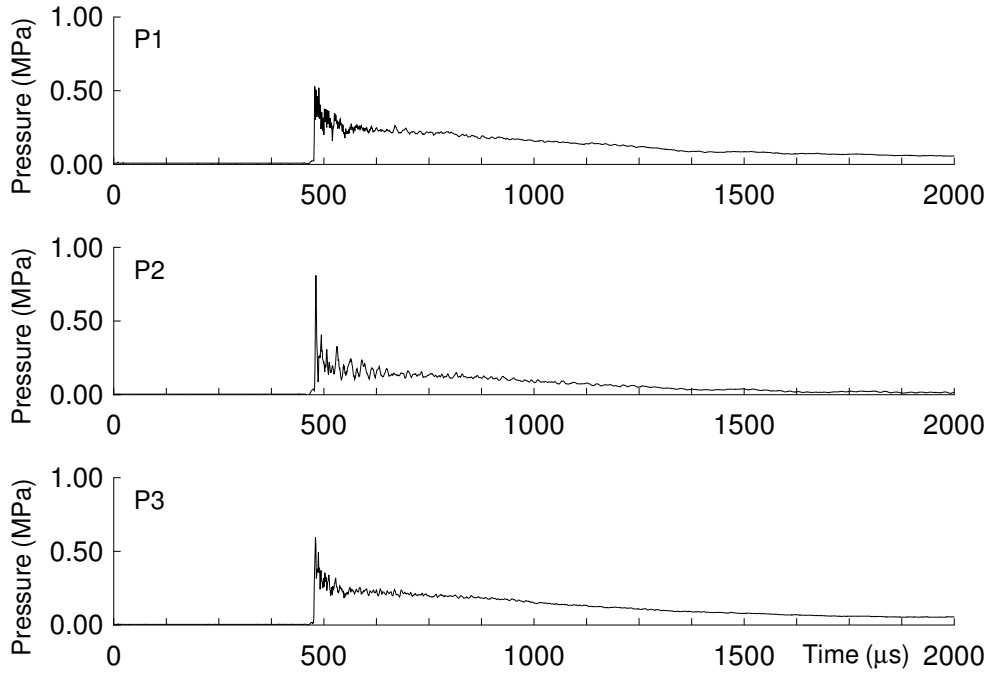


Figure G.24: Pressure history from run 010.

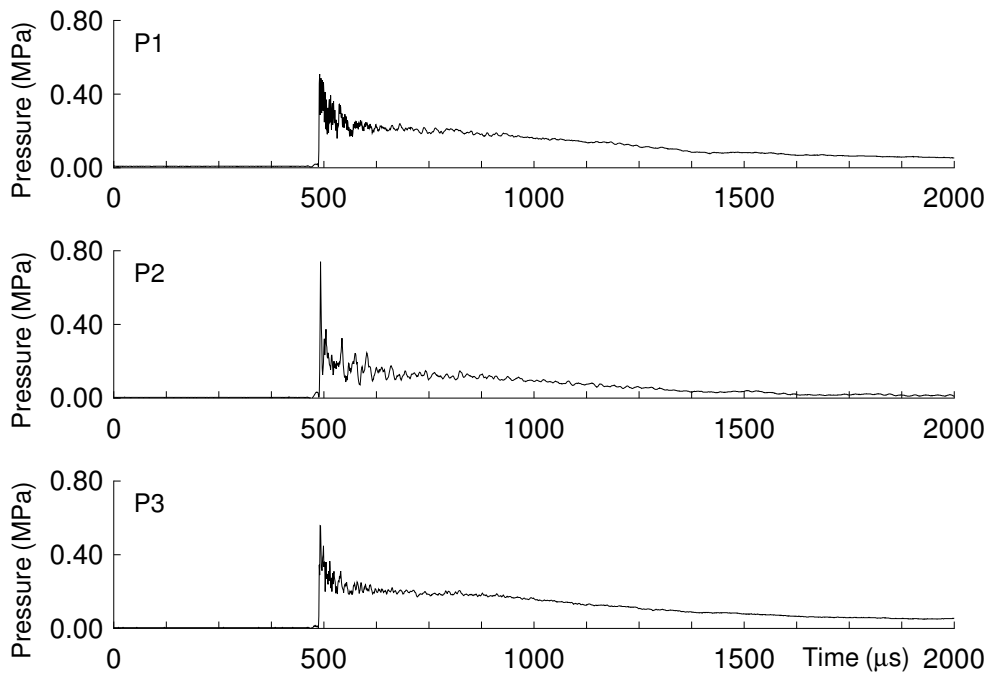


Figure G.25: Pressure history from run 011.

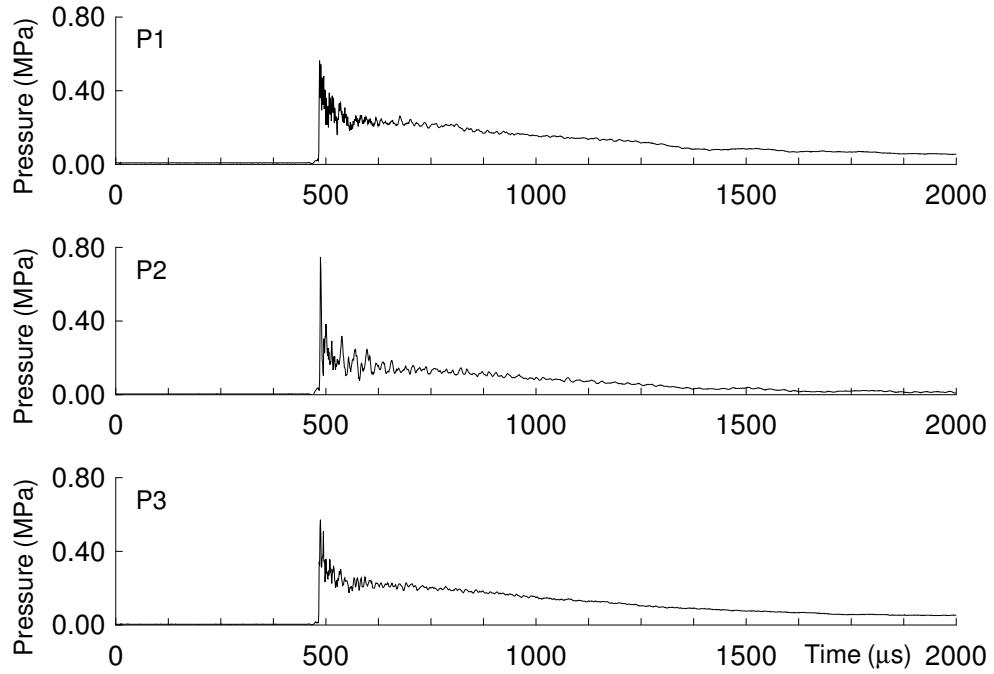


Figure G.26: Pressure history from run 012.

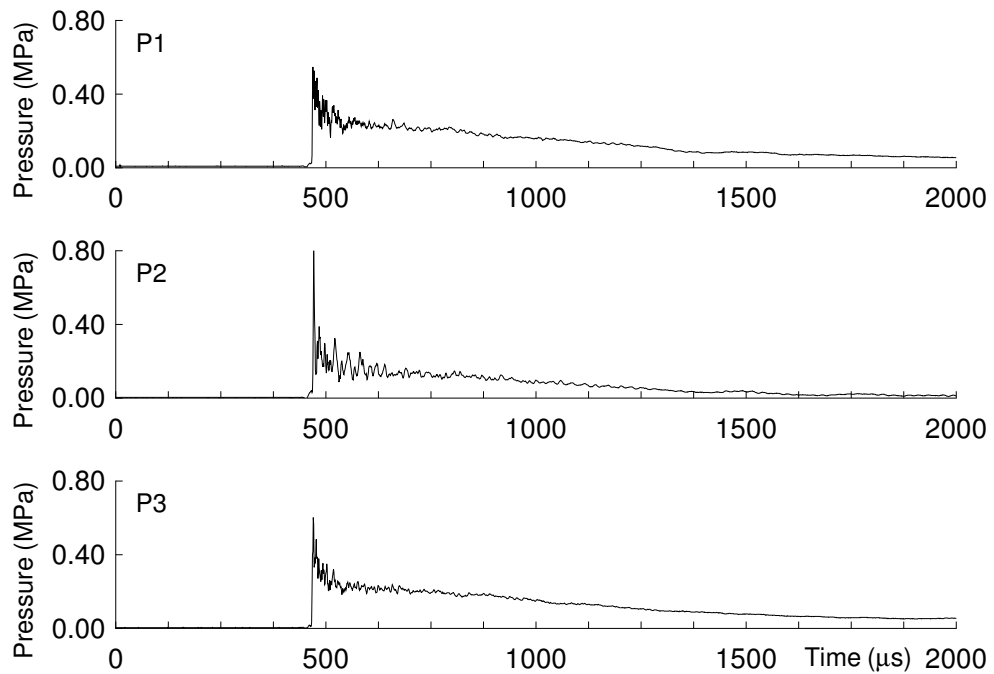


Figure G.27: Pressure history from run 014.

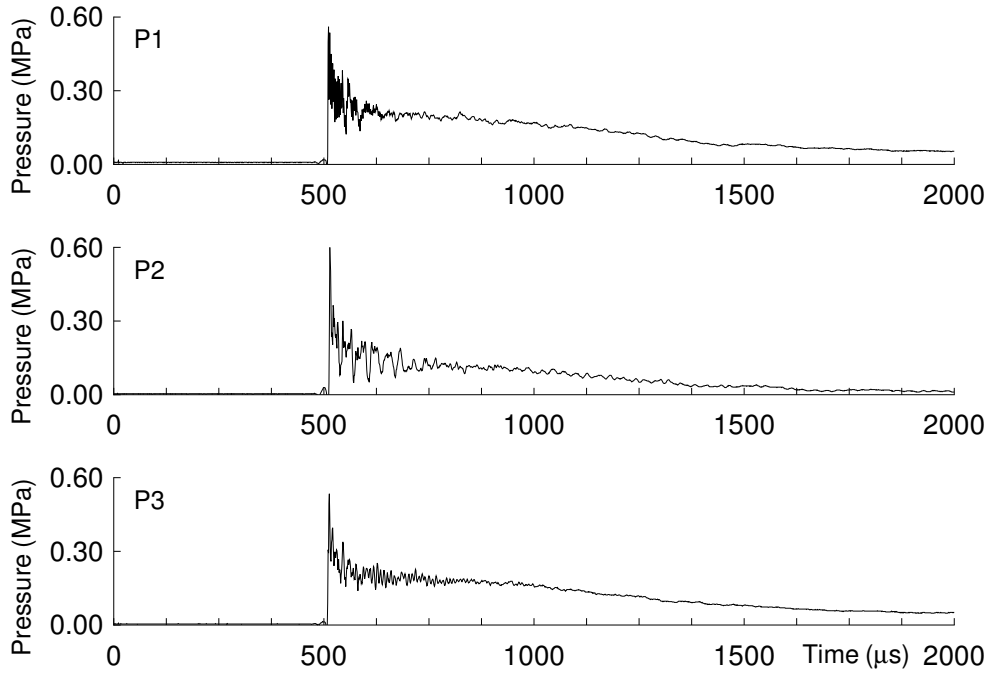


Figure G.28: Pressure history from run 015.

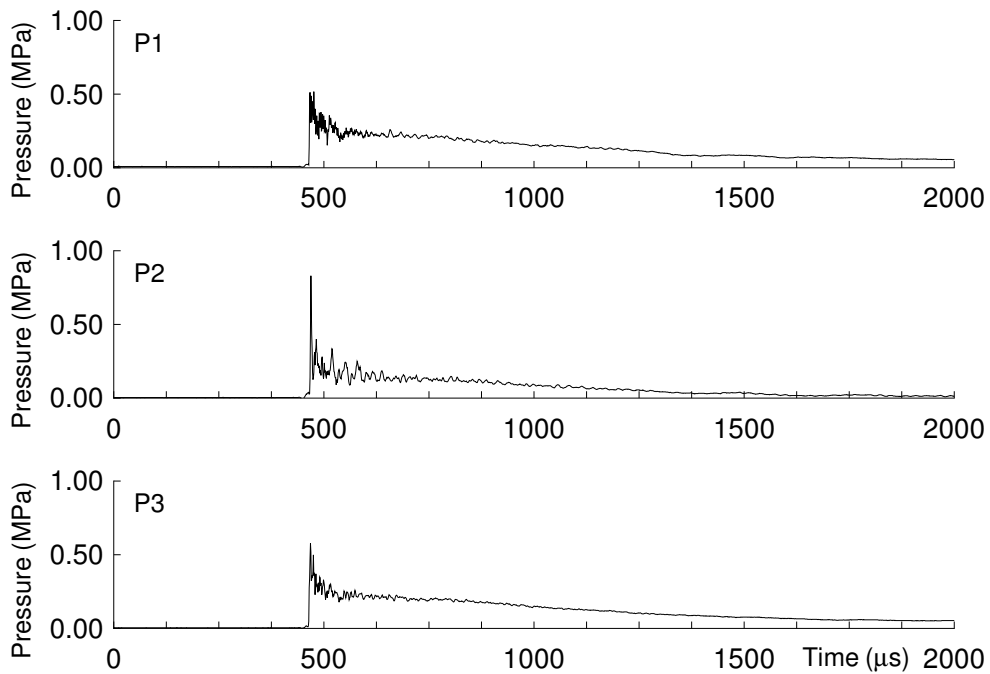


Figure G.29: Pressure history from run 016.

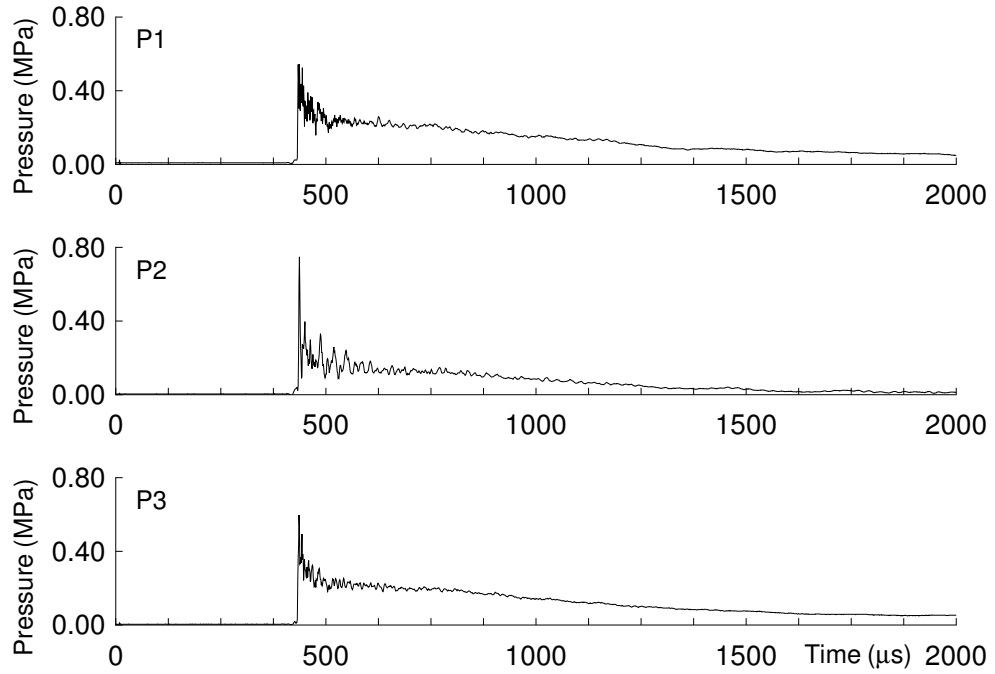


Figure G.30: Pressure history from run 017.

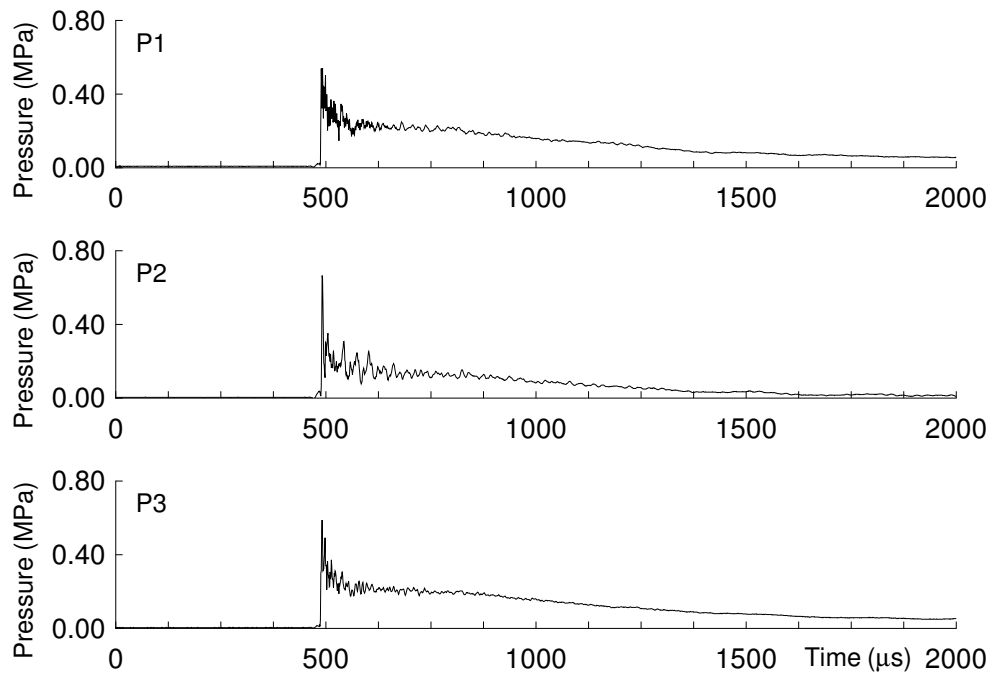


Figure G.31: Pressure history from run 018.

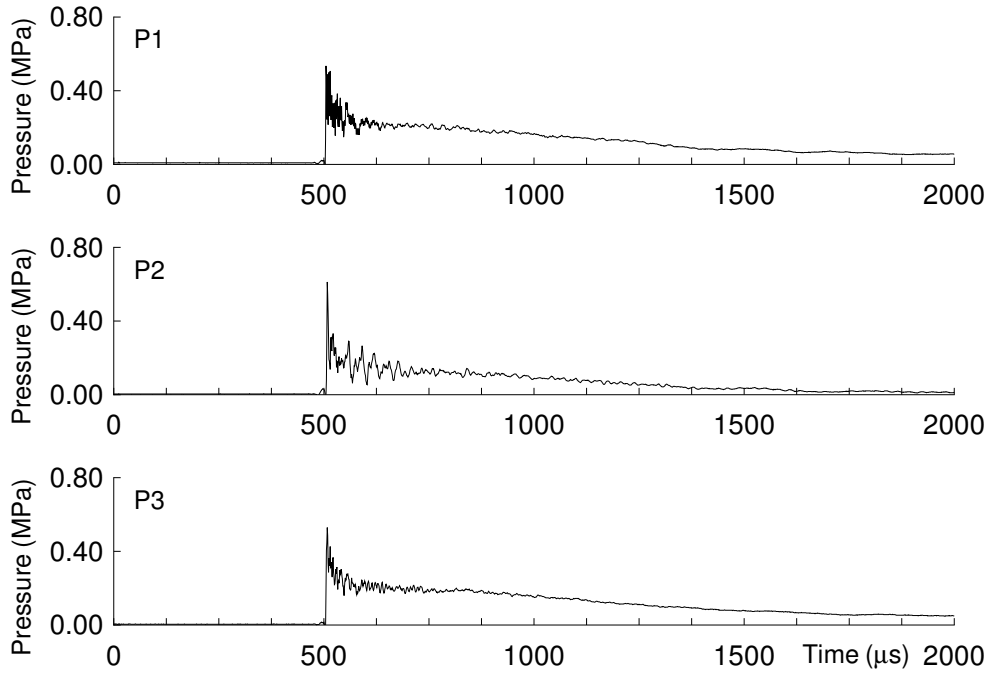


Figure G.32: Pressure history from run 019.

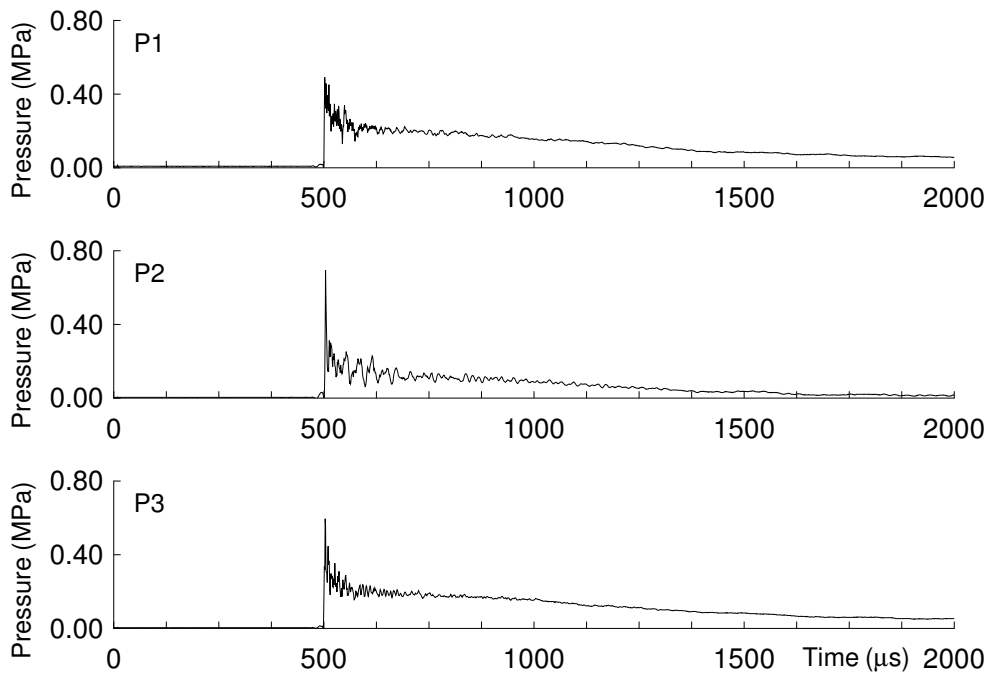


Figure G.33: Pressure history from run 020.

## G.5 Chemiluminescence Images

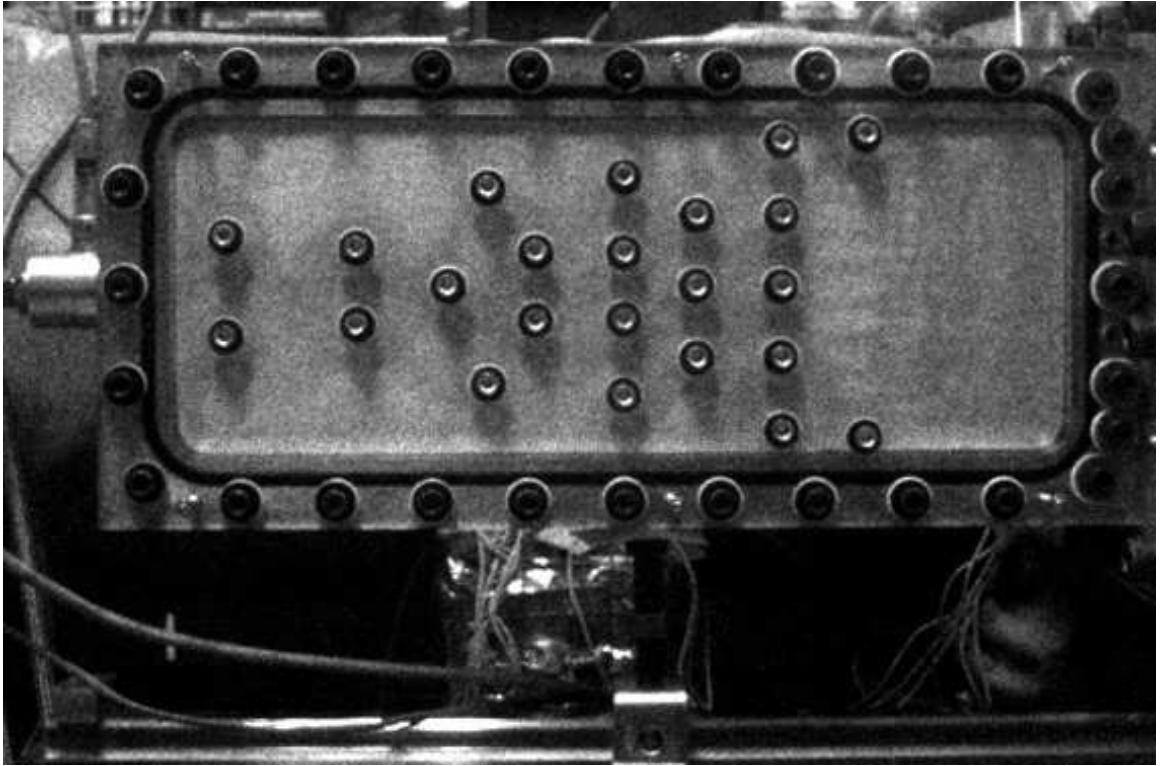


Figure G.34: The dynamic toroidal initiator is shown. The test section is on the right and the injection and ignition points are on the left.

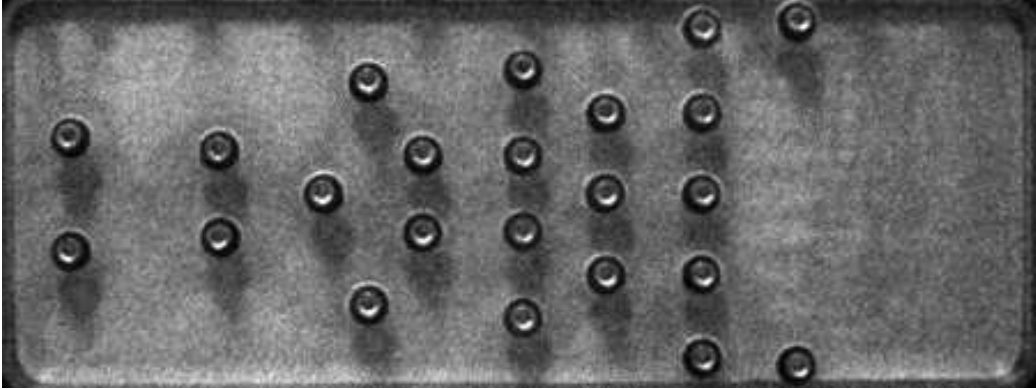


Figure G.35: The dynamic toroidal initiator view for chemiluminescence images G.36 - G.55.

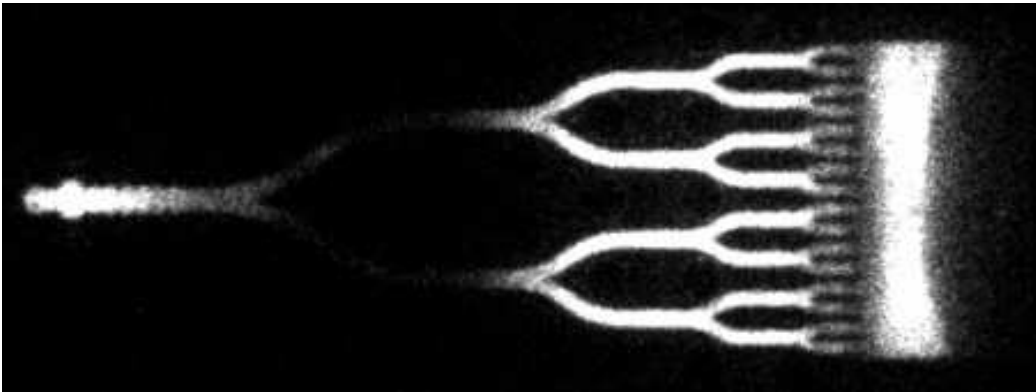


Figure G.36: Chemiluminescence from run 001.

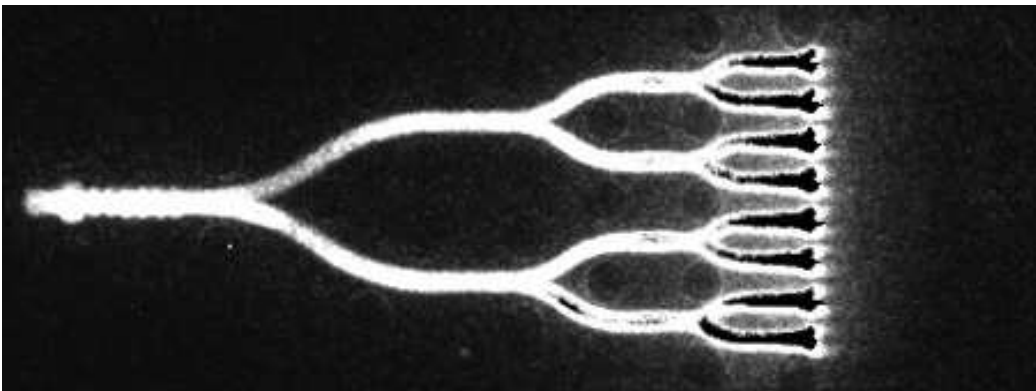


Figure G.37: Chemiluminescence from run 002.

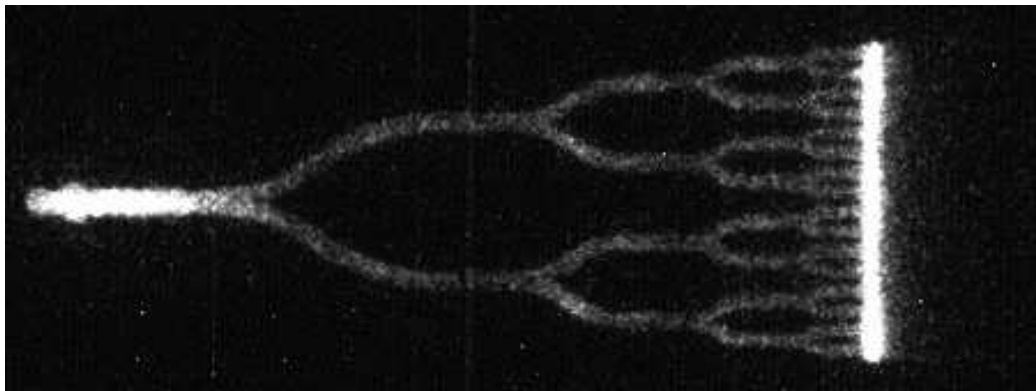


Figure G.38: Chemiluminescence from run 003.



Figure G.39: Chemiluminescence from run 004.



Figure G.40: Chemiluminescence from run 005.



Figure G.41: Chemiluminescence from run 006.



Figure G.42: Chemiluminescence from run 007.



Figure G.43: Chemiluminescence from run 008.

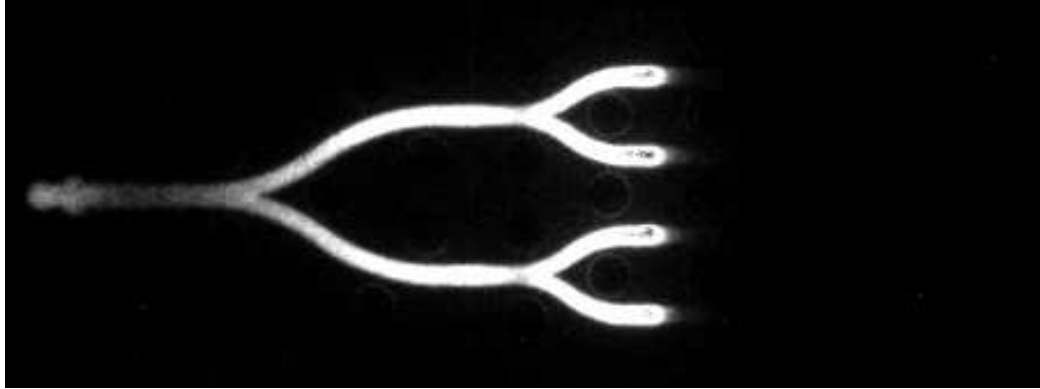


Figure G.44: Chemiluminescence from run 009.

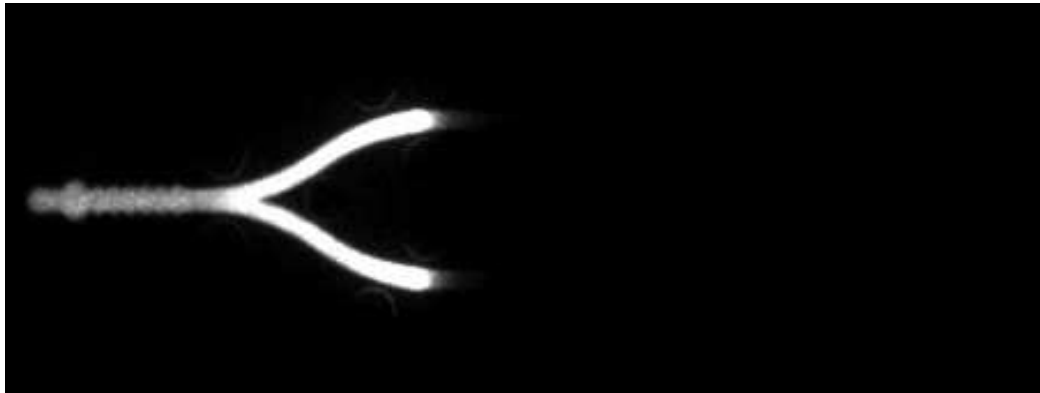


Figure G.45: Chemiluminescence from run 011.



Figure G.46: Chemiluminescence from run 012.

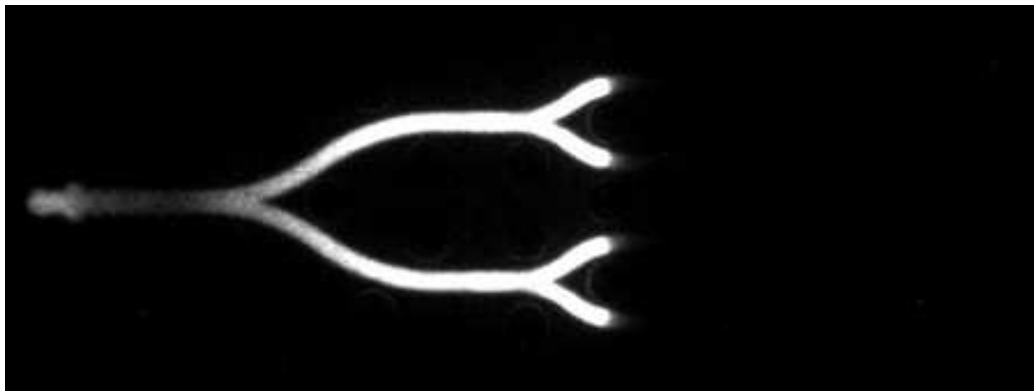


Figure G.47: Chemiluminescence from run 013.

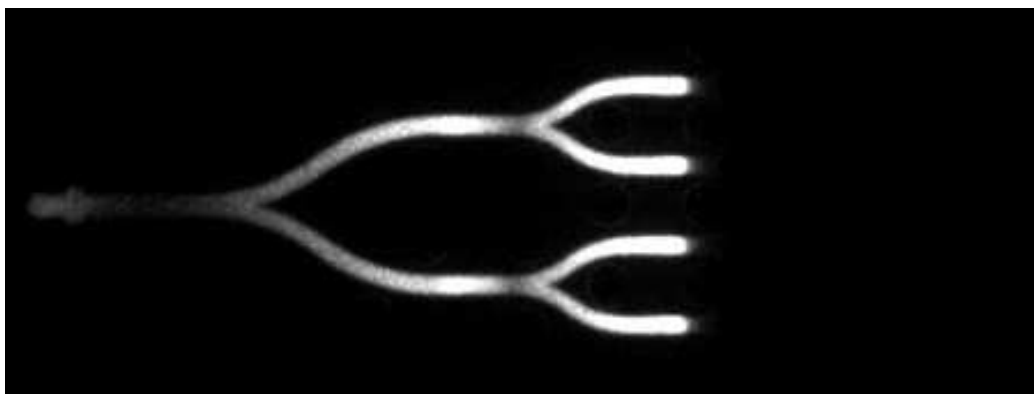


Figure G.48: Chemiluminescence from run 014.

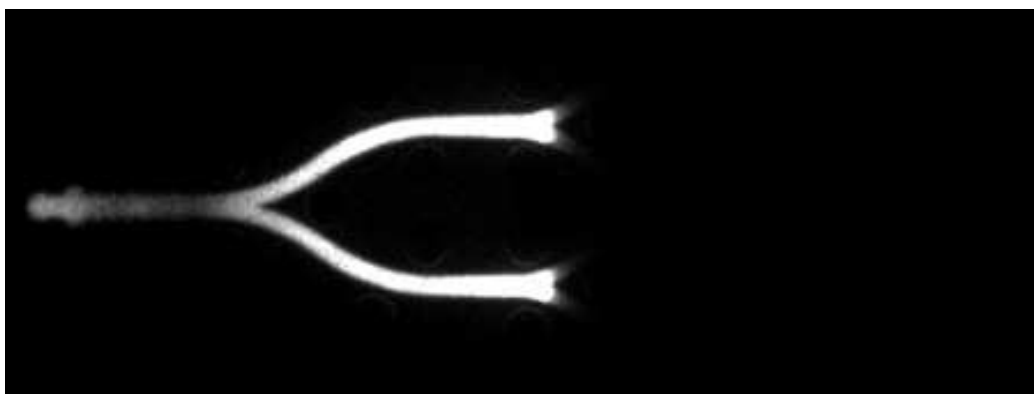


Figure G.49: Chemiluminescence from run 015.

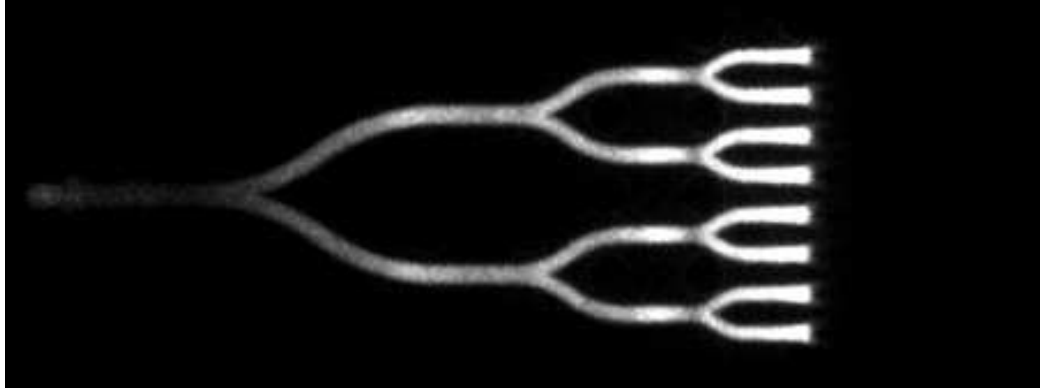


Figure G.50: Chemiluminescence from run 016.

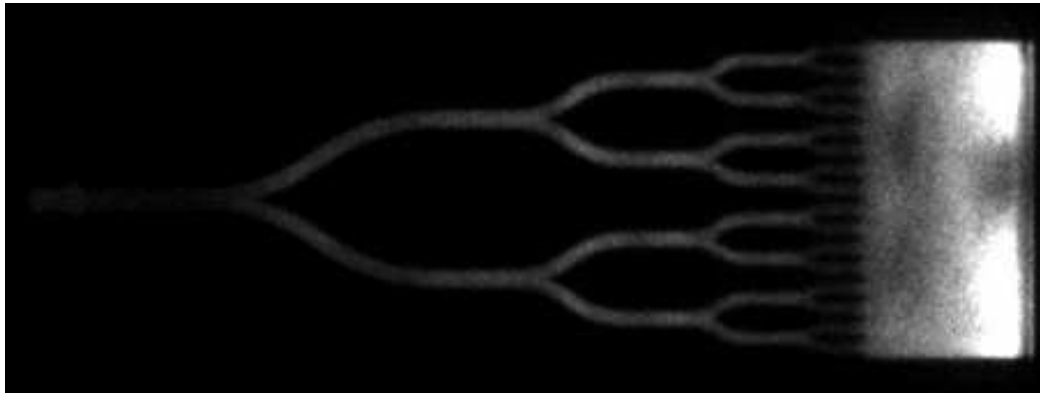


Figure G.51: Chemiluminescence from run 017.

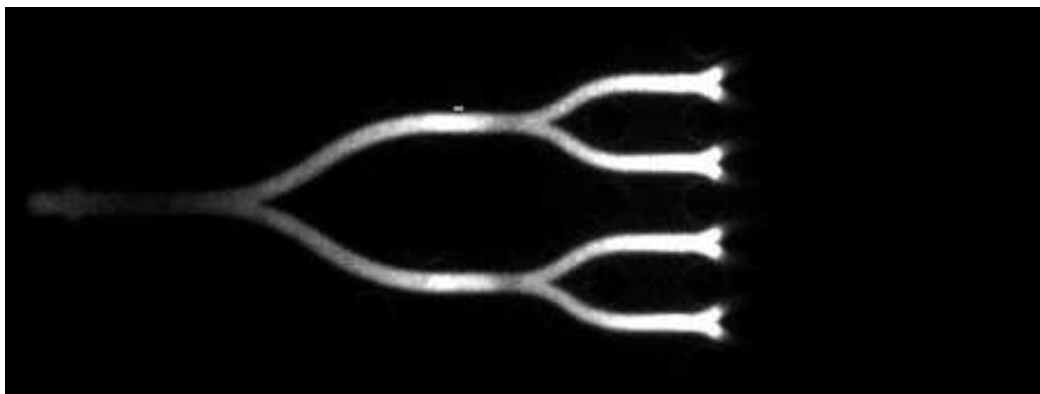


Figure G.52: Chemiluminescence from run 018.

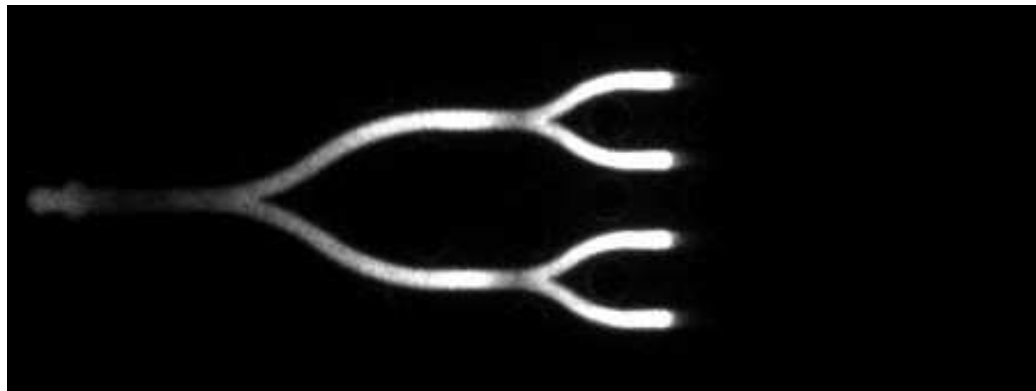


Figure G.53: Chemiluminescence from run 019.

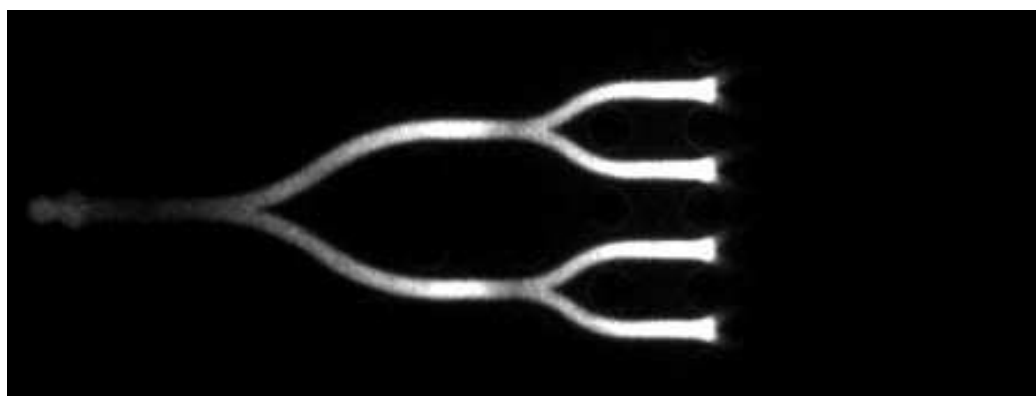


Figure G.54: Chemiluminescence from run 020.

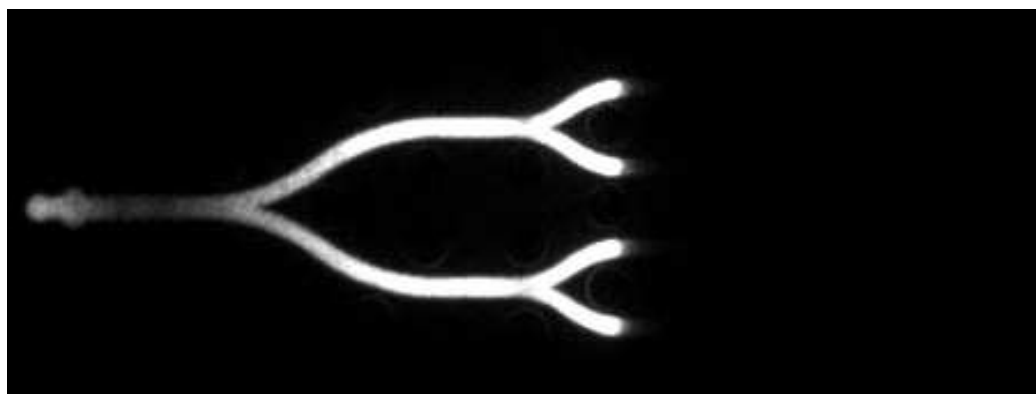


Figure G.55: Chemiluminescence from run 021.

## Appendix H

# Toroidal Dynamic Initiator Data

# H.1 Design Drawings

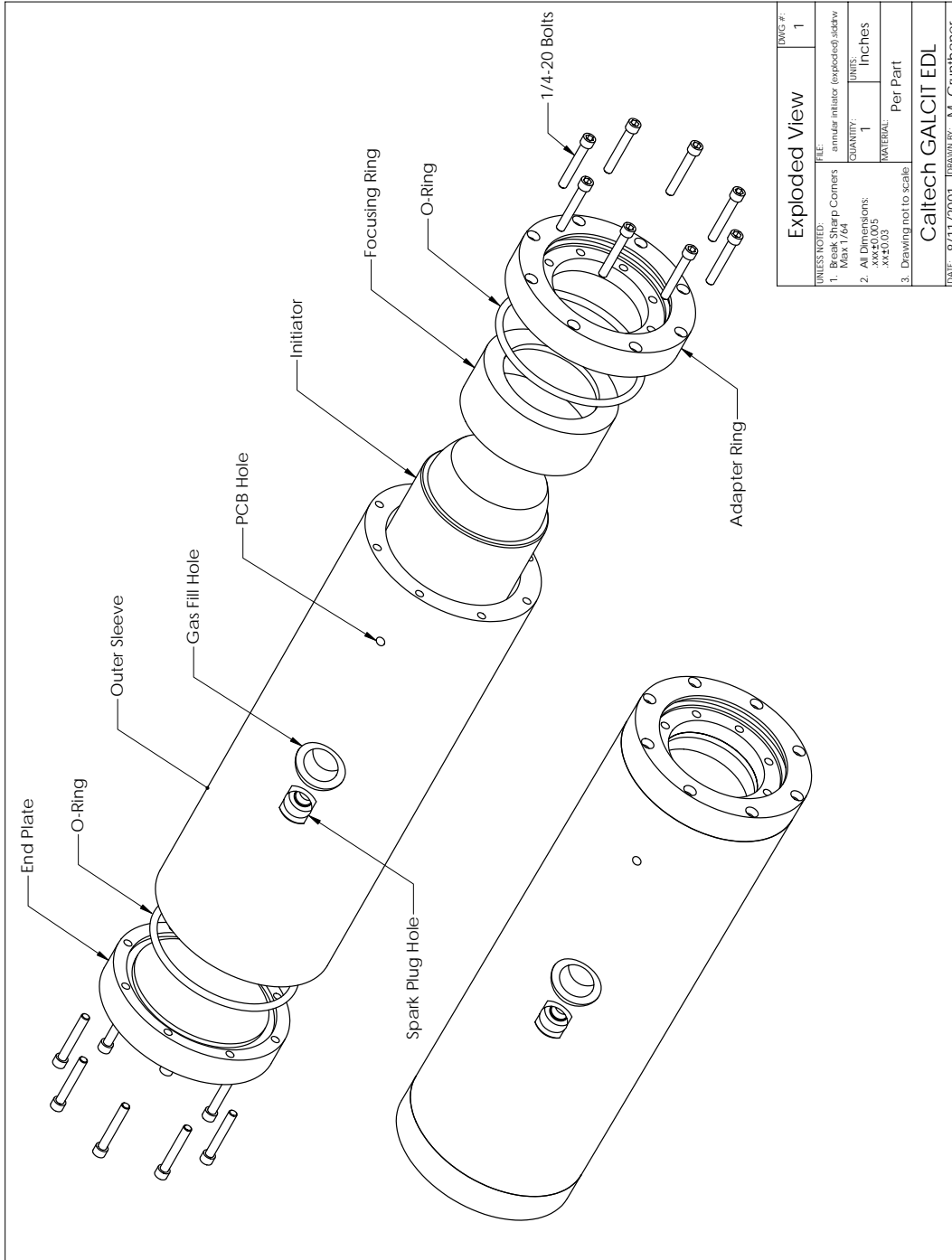


Figure H.1: Exploded view of the toroidal initiator assembly.

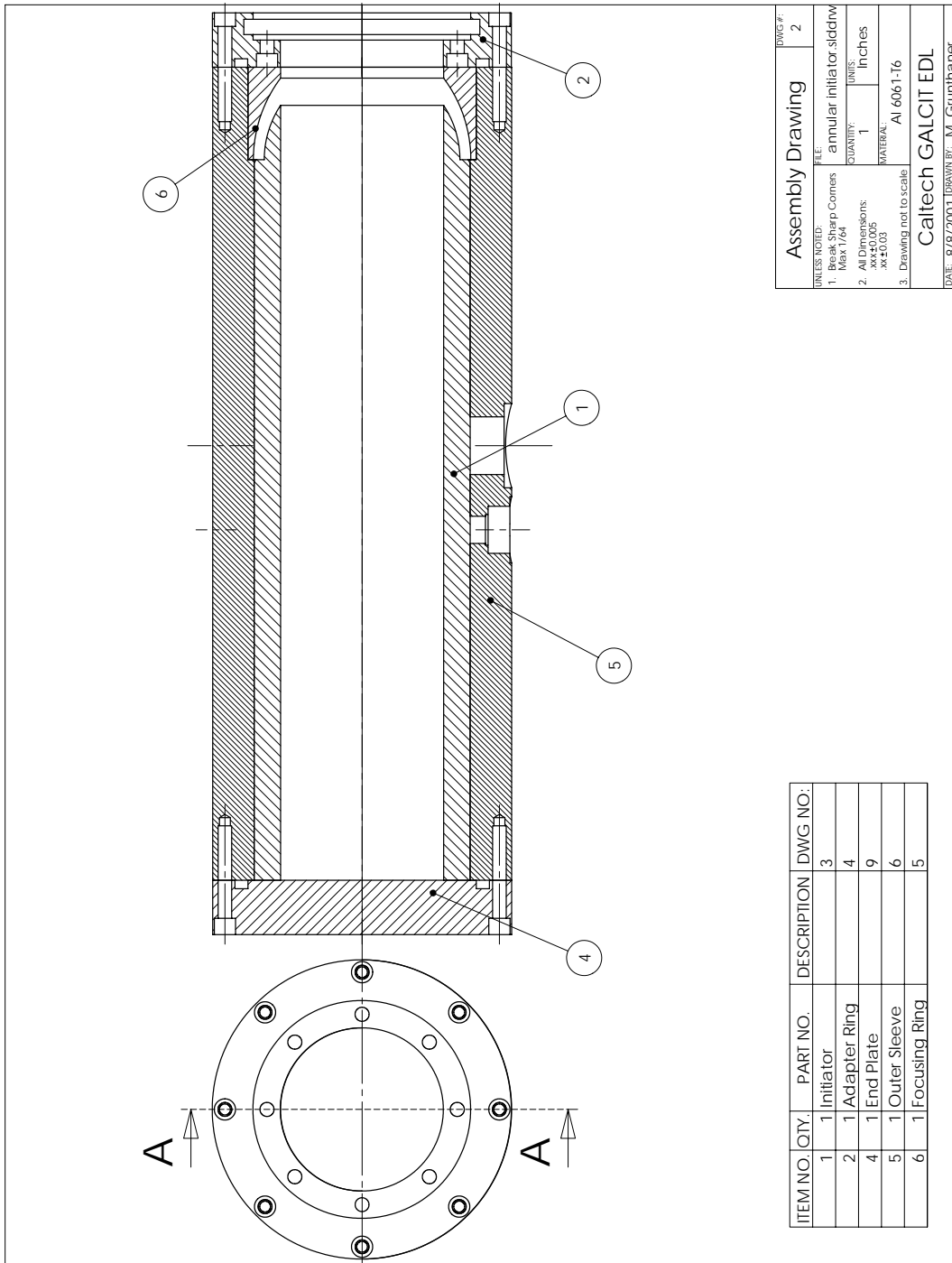


Figure H.2: Assembled view of the toroidal initiator.

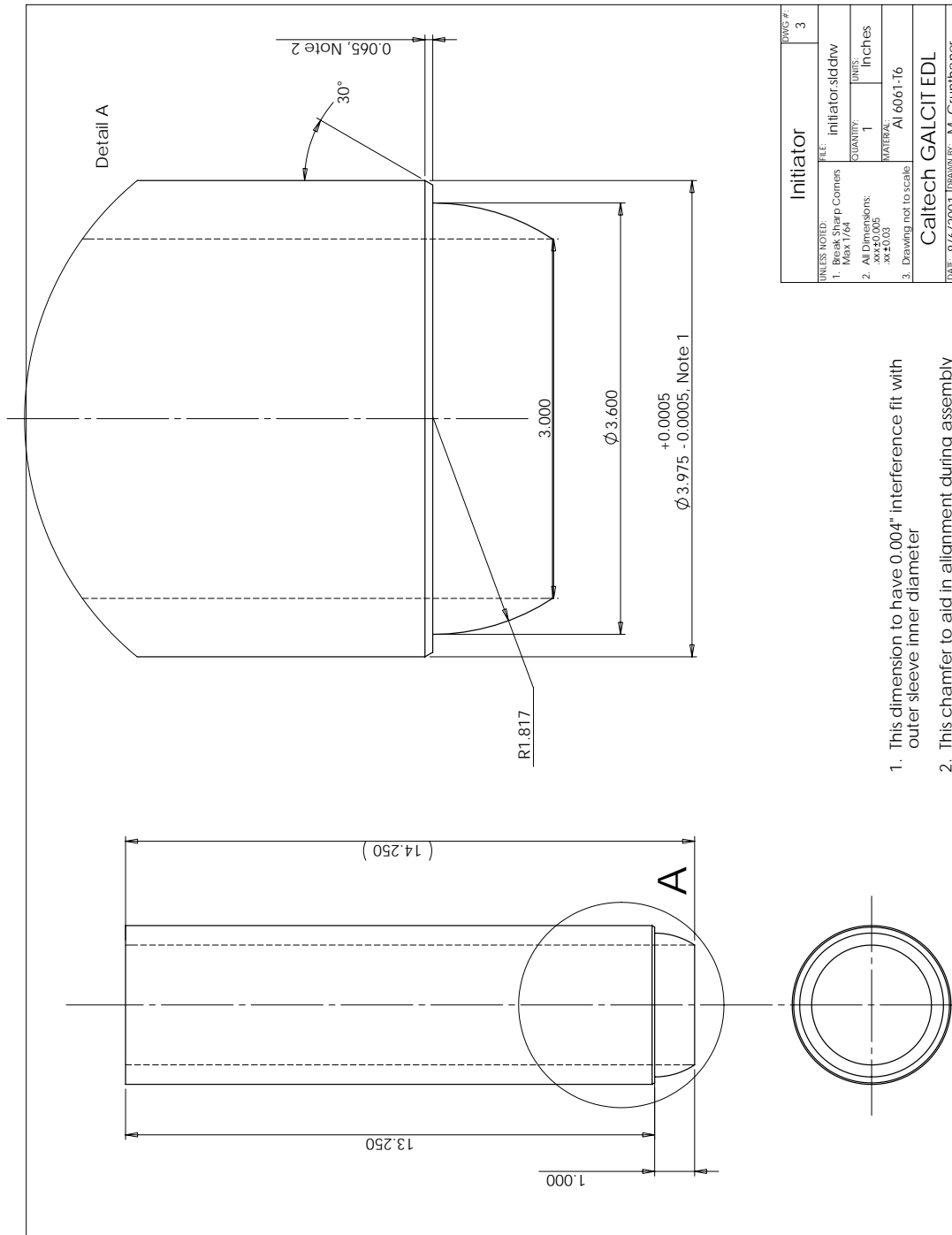


Figure H.3: Initiator inner sleeve after assembly.

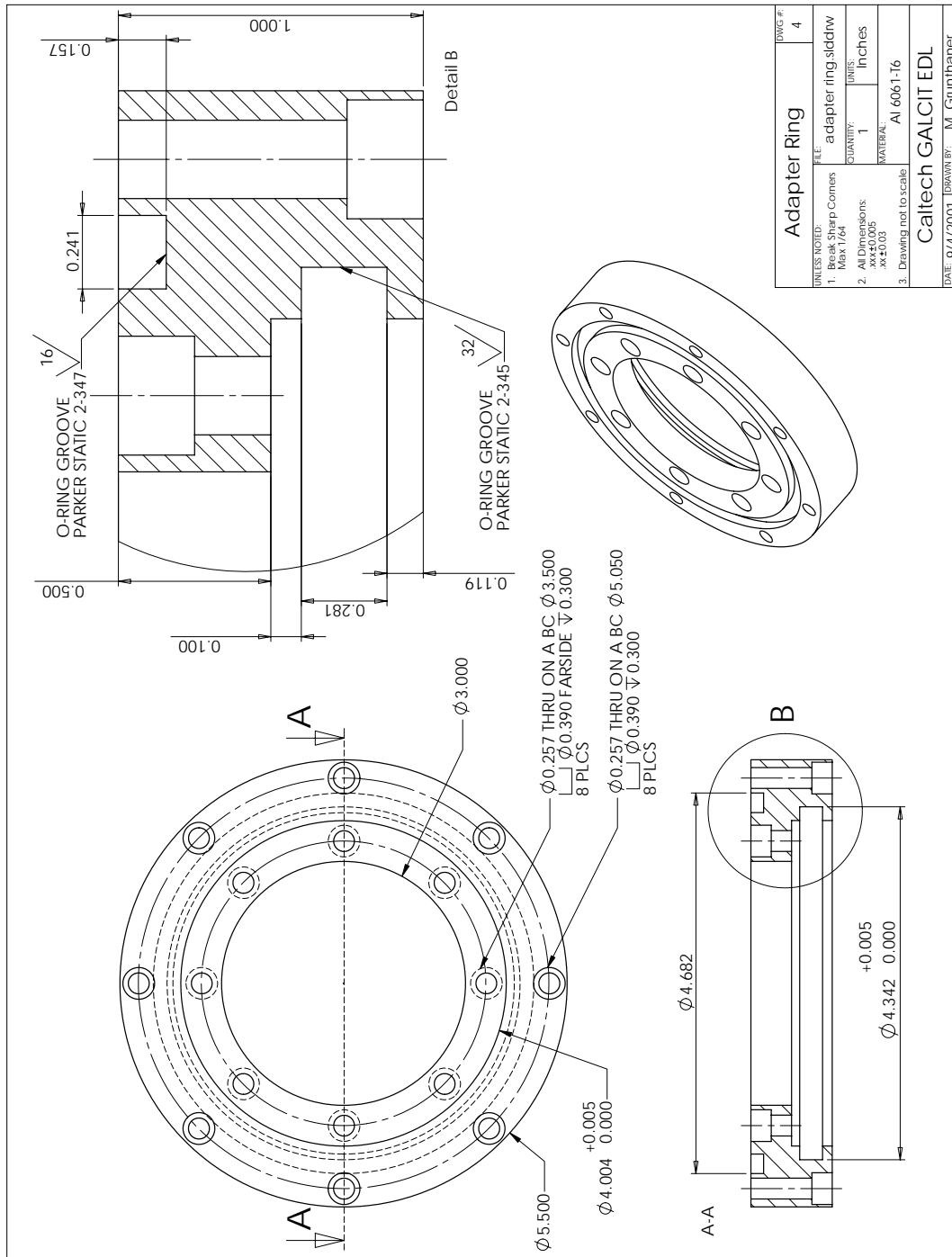


Figure H.4: Adapter ring.

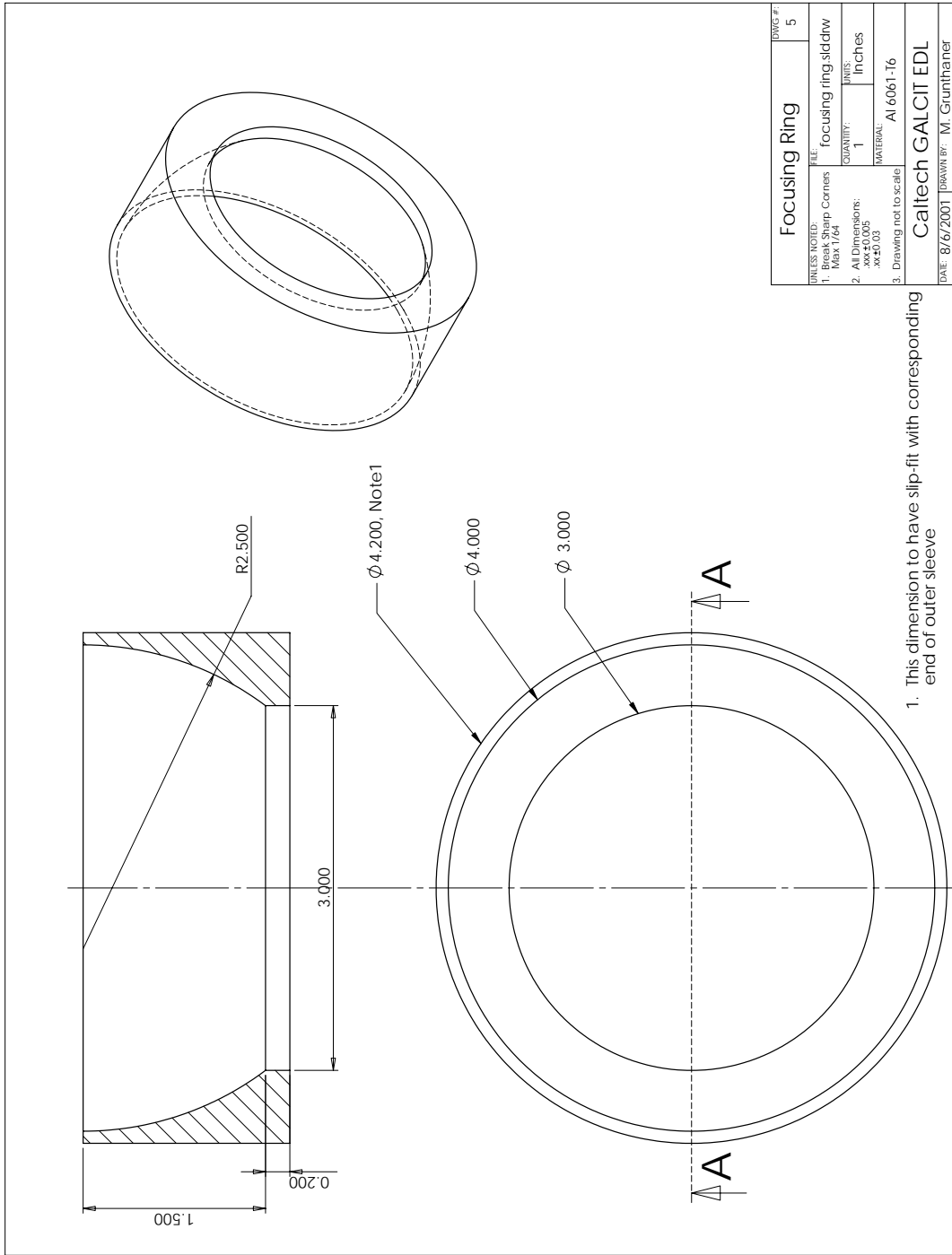


Figure H.5: Focusing ring.

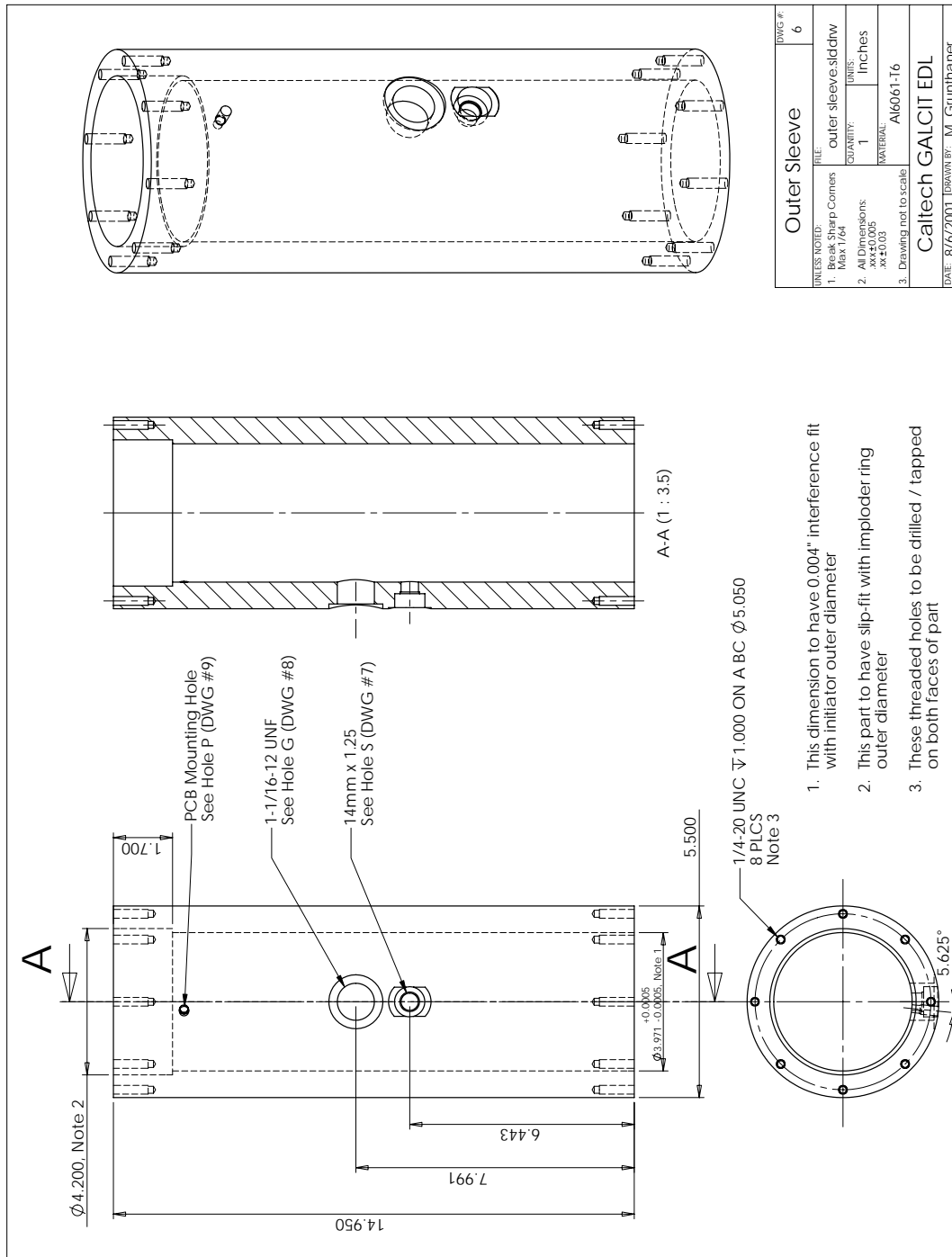


Figure H.6: Initiator outer sleeve after assembly.

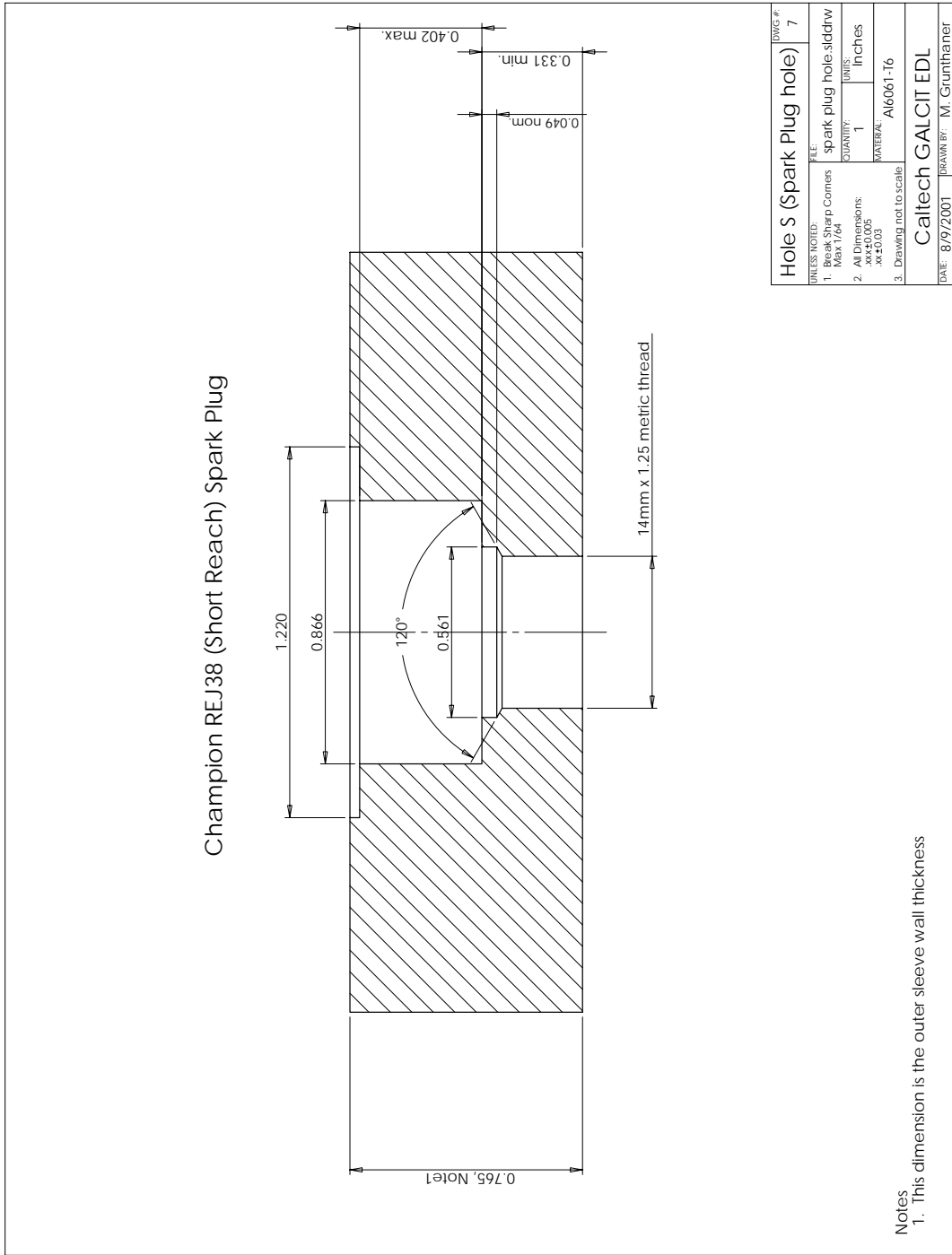


Figure H.7: Spark plug port.

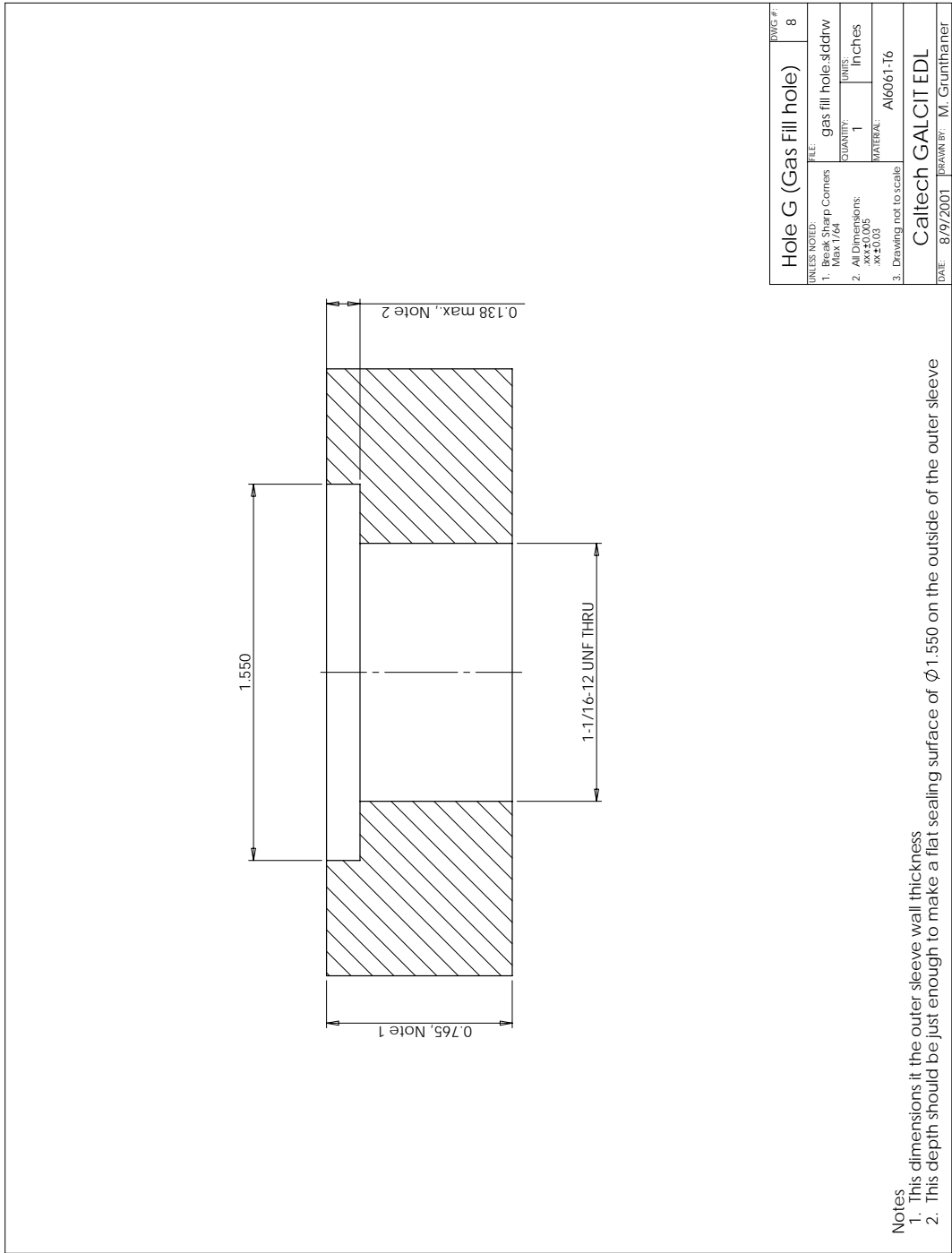


Figure H.8: Gas fill port.

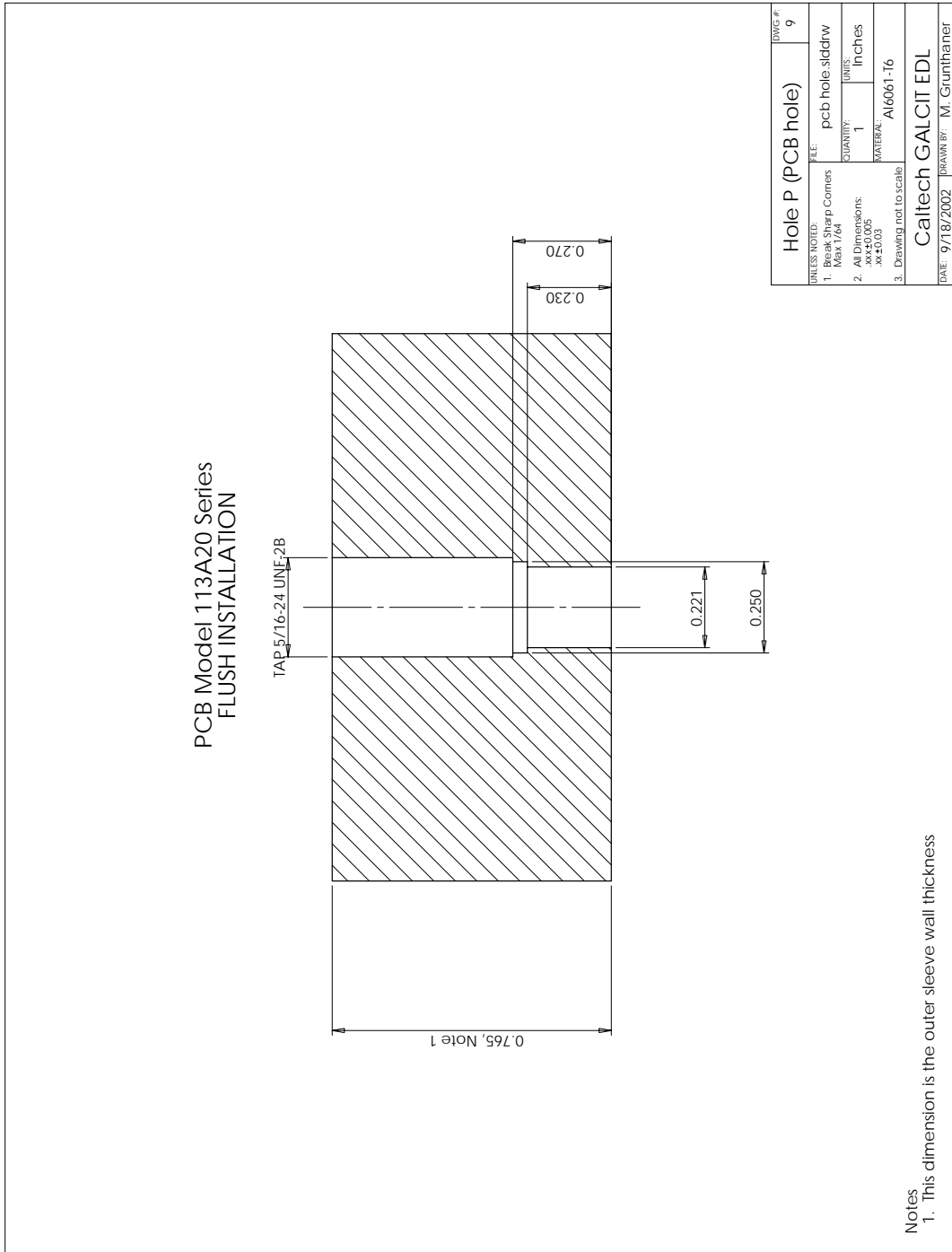
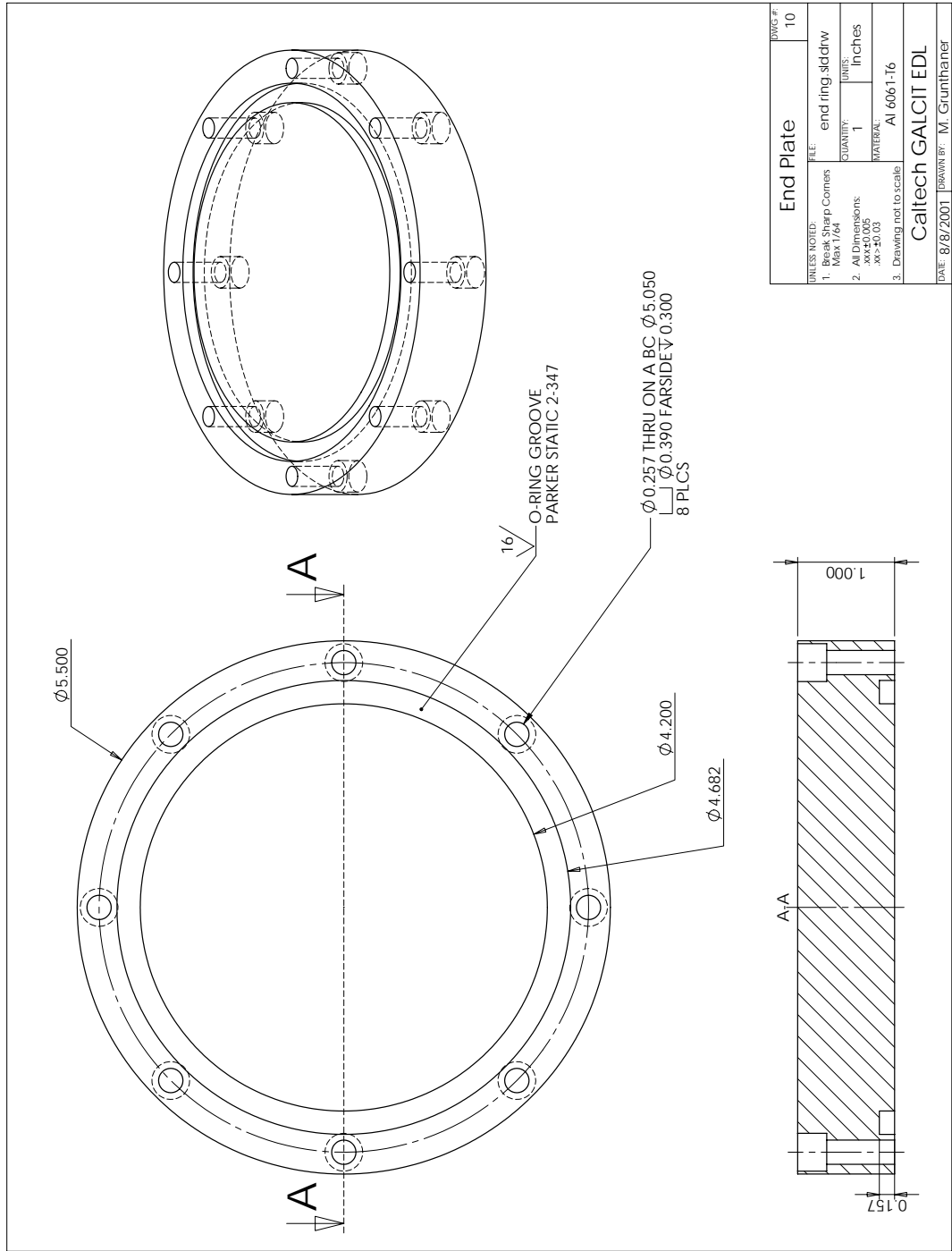


Figure H.9: Pressure transducer port.



UNLESS NOTED:		DWG #:	10
1. Break Sharp Corners Max 1/64		FILE:	end ring.slddrw
2. All Dimensions: .xx±0.005 .xx±0.03		QUANTITY:	1
3. Drawing not to scale		UNITS:	Inches
		MATERIAL:	Al 6061-T6
		Caltech GALCIT EDL	
		DATE:	8/8/2001
		DRAWN BY:	M. Grunthaler

Figure H.10: Blank end flange.

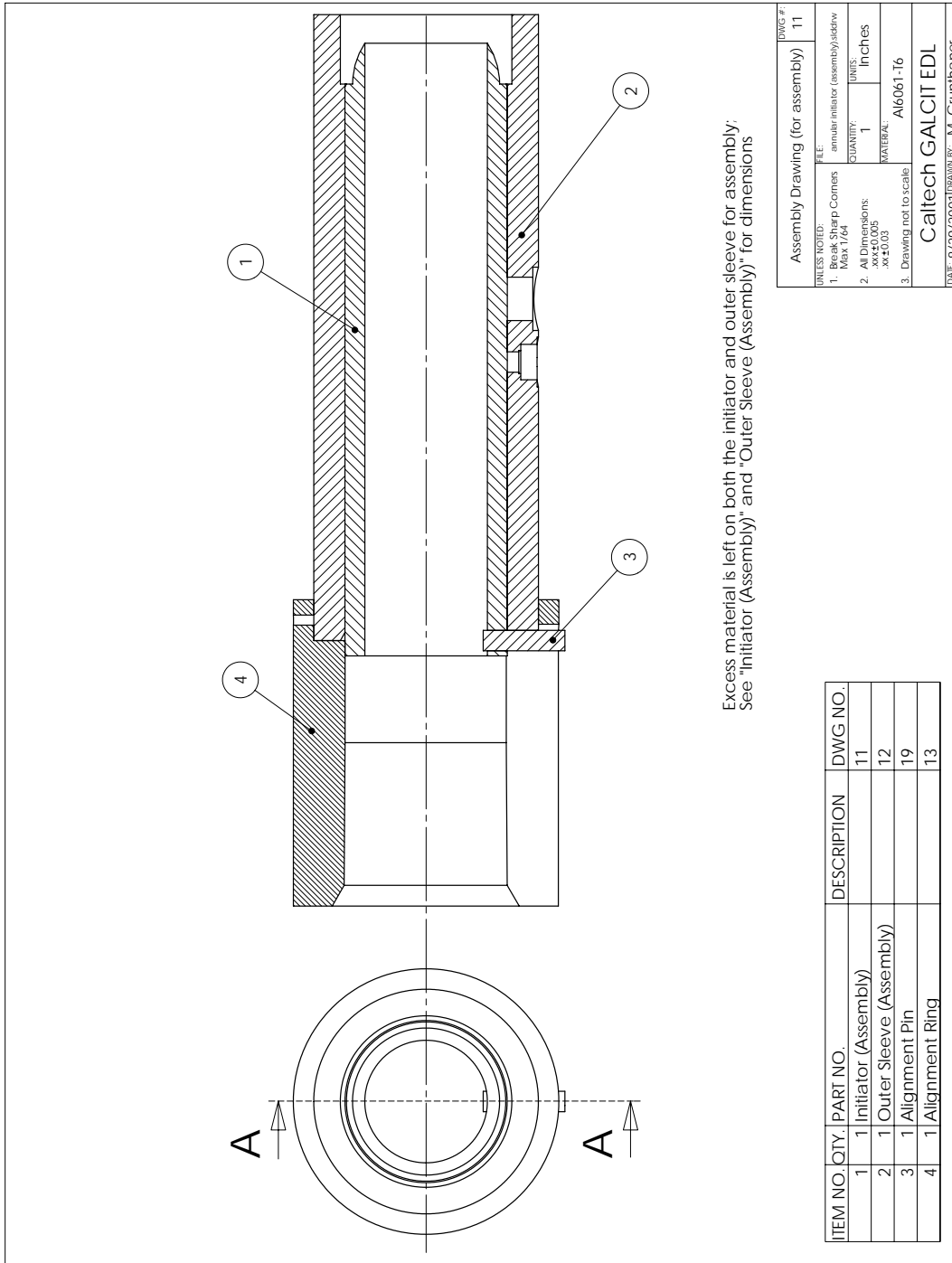


Figure H.11: Setup for initiator assembly.

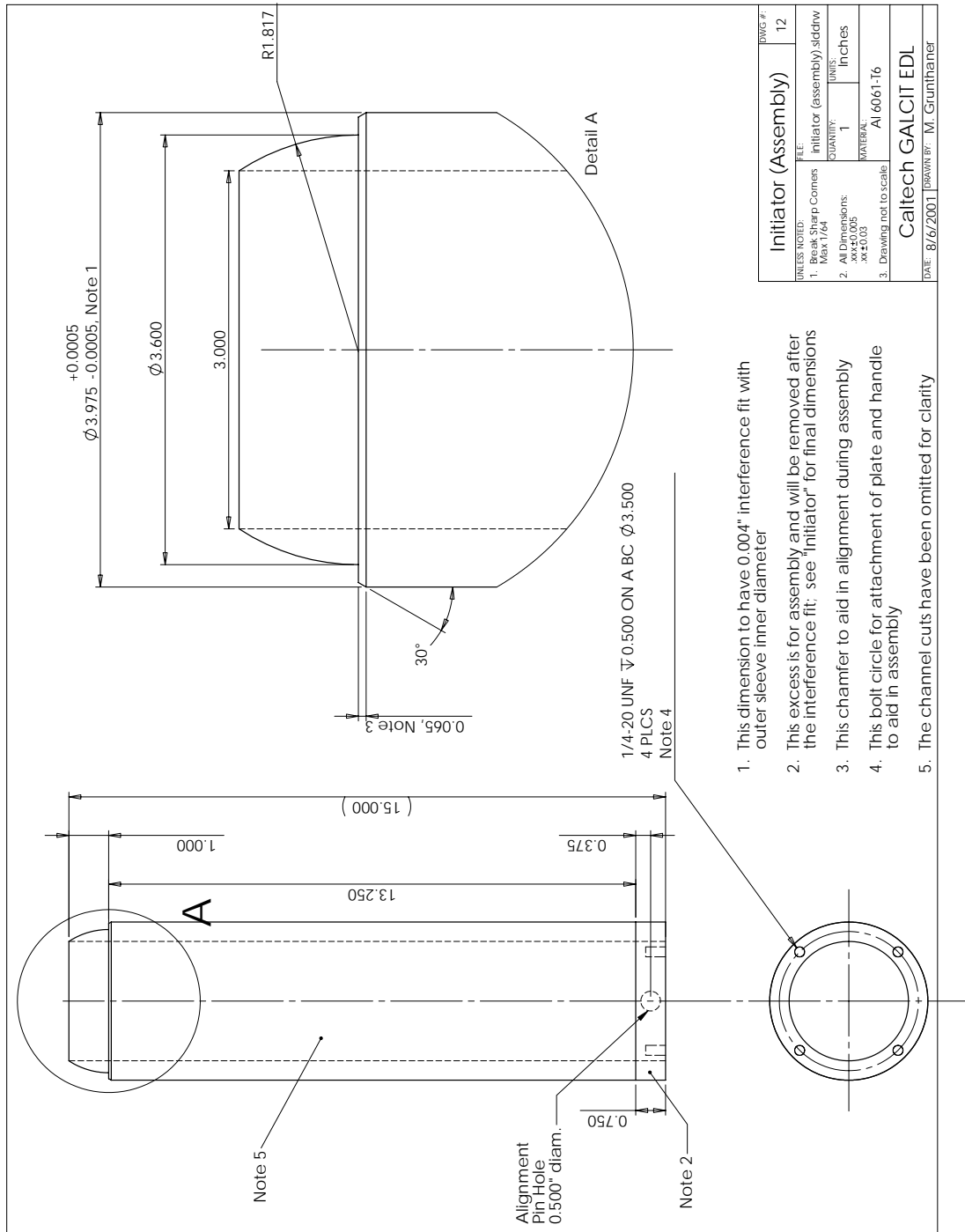


Figure H.12: Initiator inner sleeve prior to assembly.

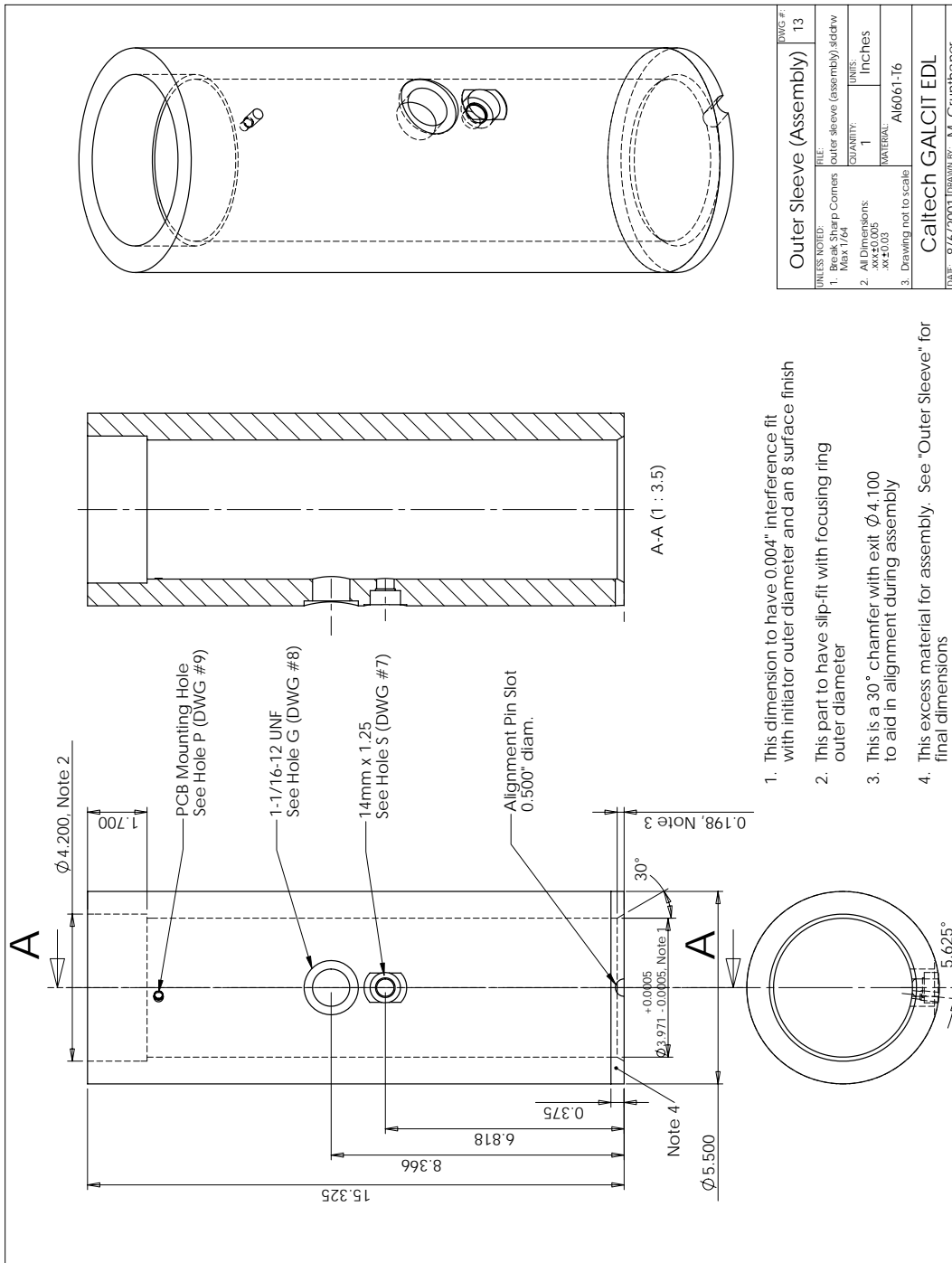


Figure H.13: Initiator inner sleeve prior to assembly.

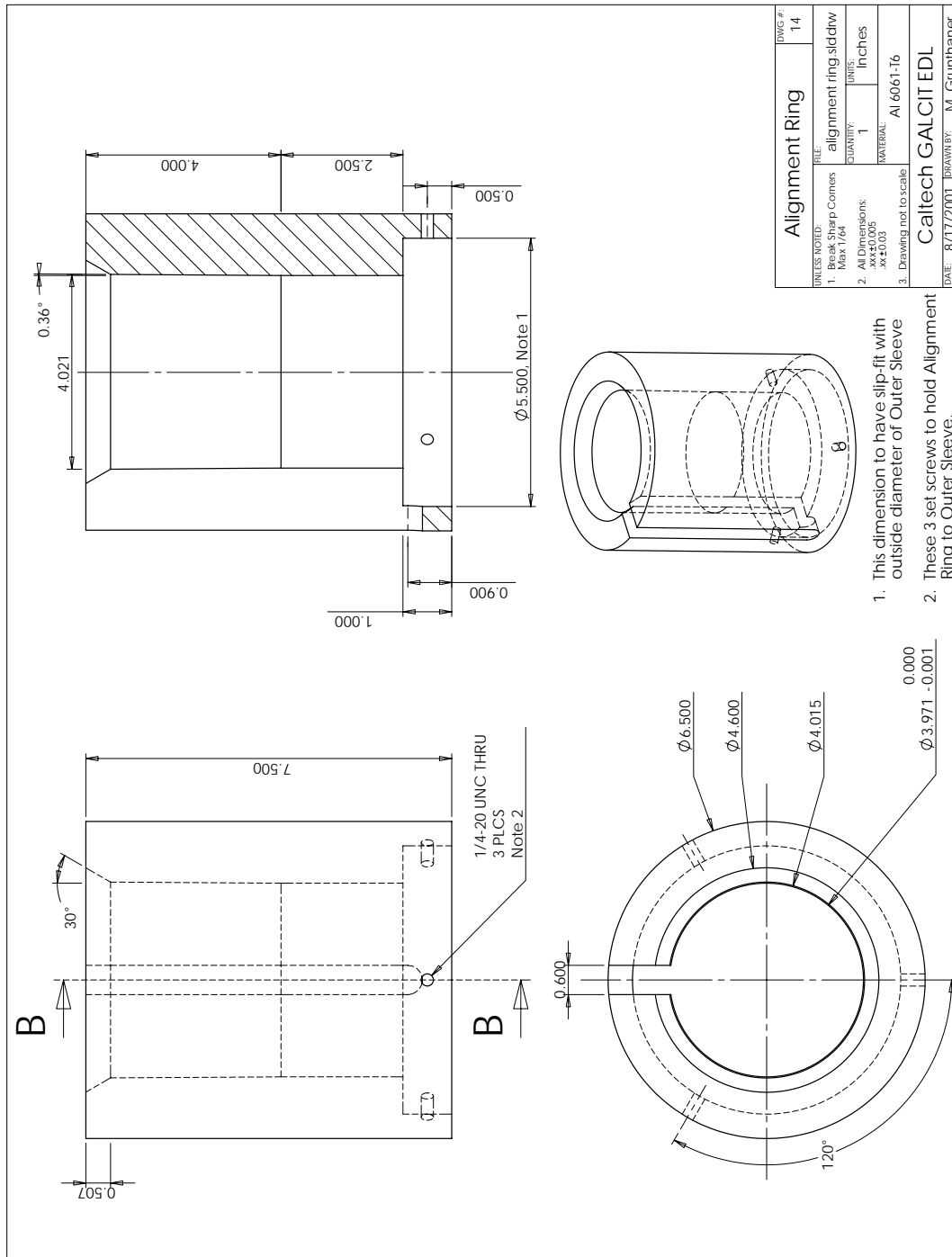


Figure H.14: Alignment ring for assembly.

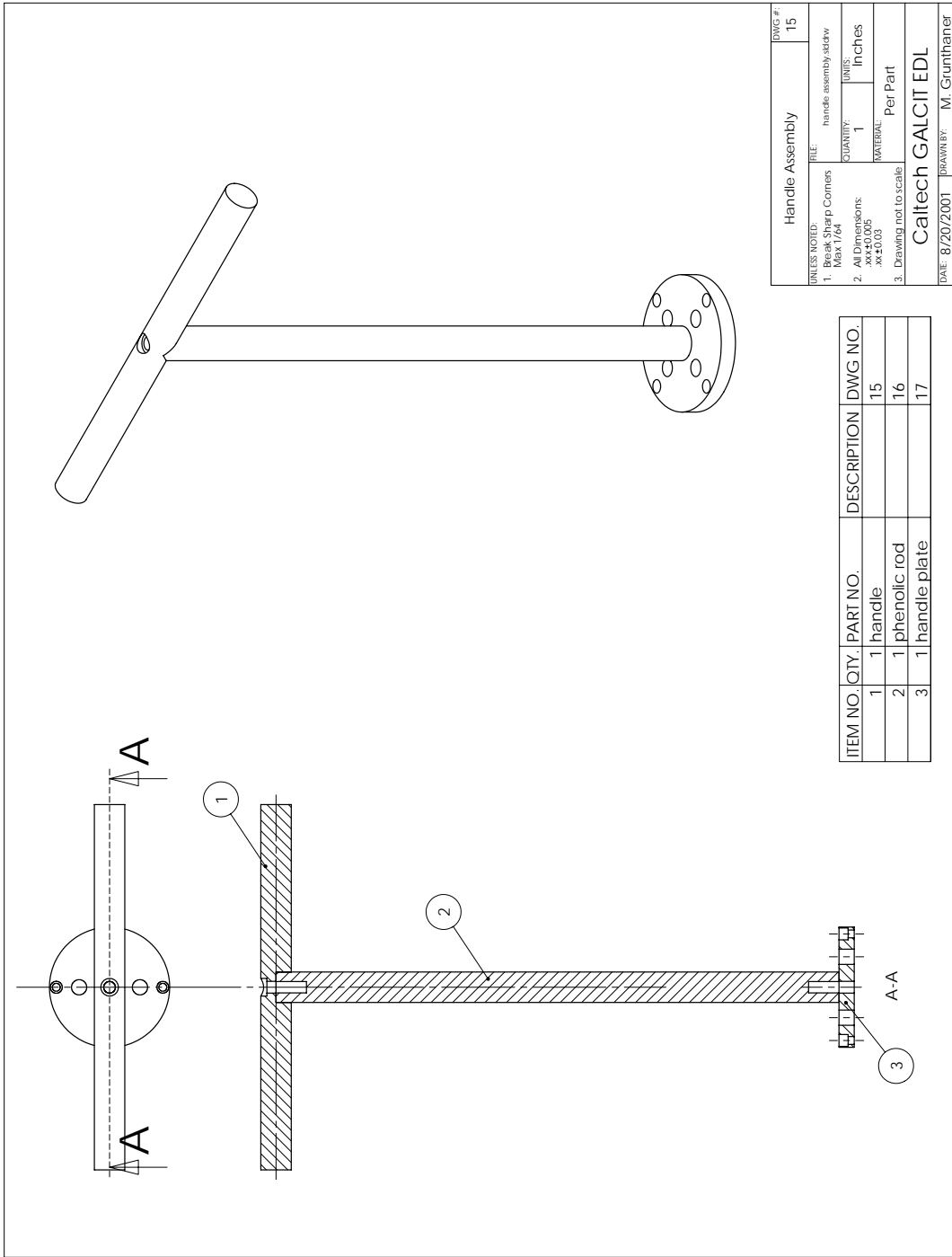
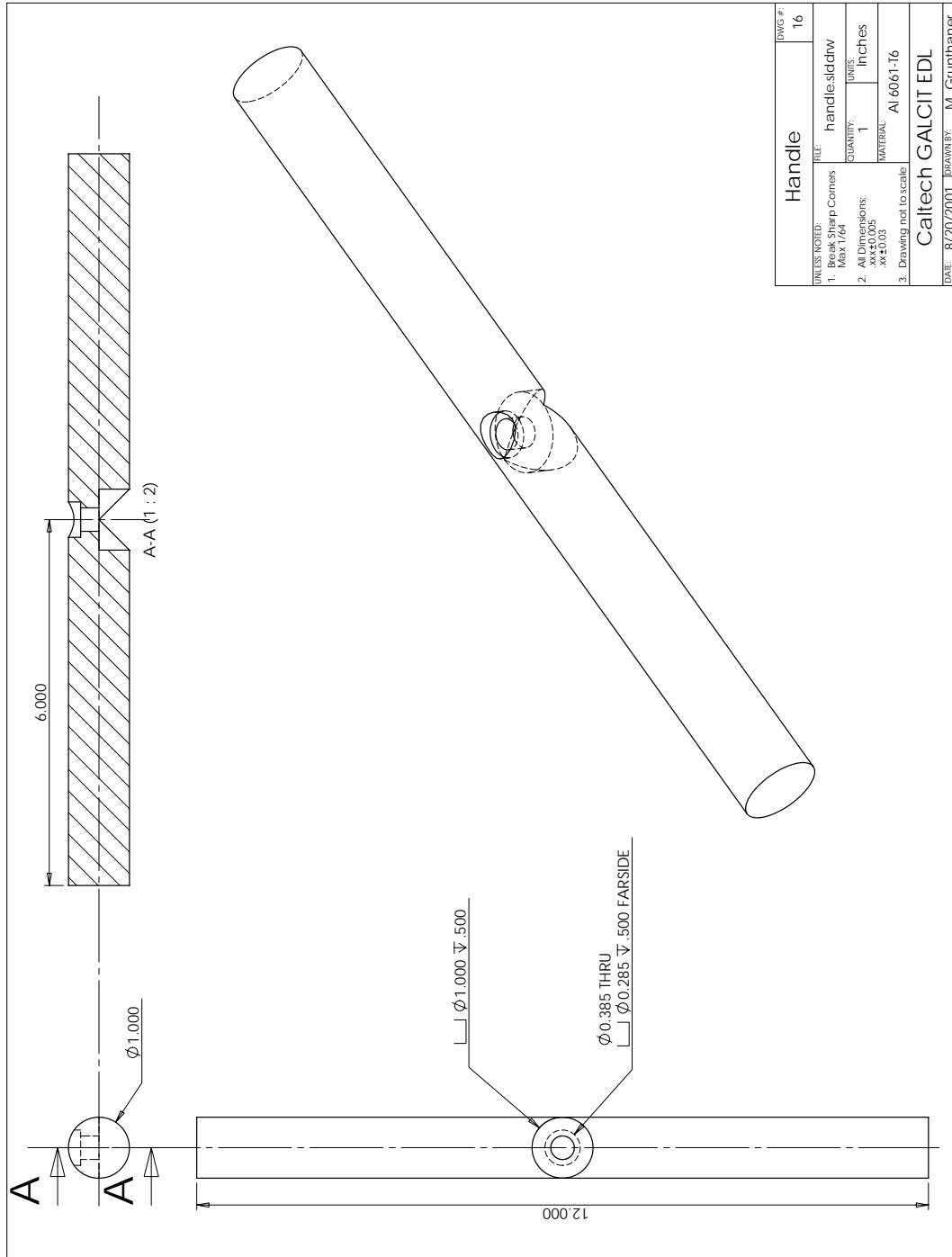


Figure H.15: Handle assembly.



DWG #:	16
Handle	
UNLESS NOTED:	
1. Break Sharp Corners	Max 1/64
2. All Dimensions:	.xx+0.005 .xx-0.03
3. Drawing not to scale	
FILE:	handle.sladdw
QUANTITY:	1
UNITS:	Inches
MATERIAL:	Al 6061-T6
DATE:	8/20/2001
DRAWN BY:	M. Grunthaler
<b>Caltech GALCIT EDL</b>	

Figure H.16: Handle.

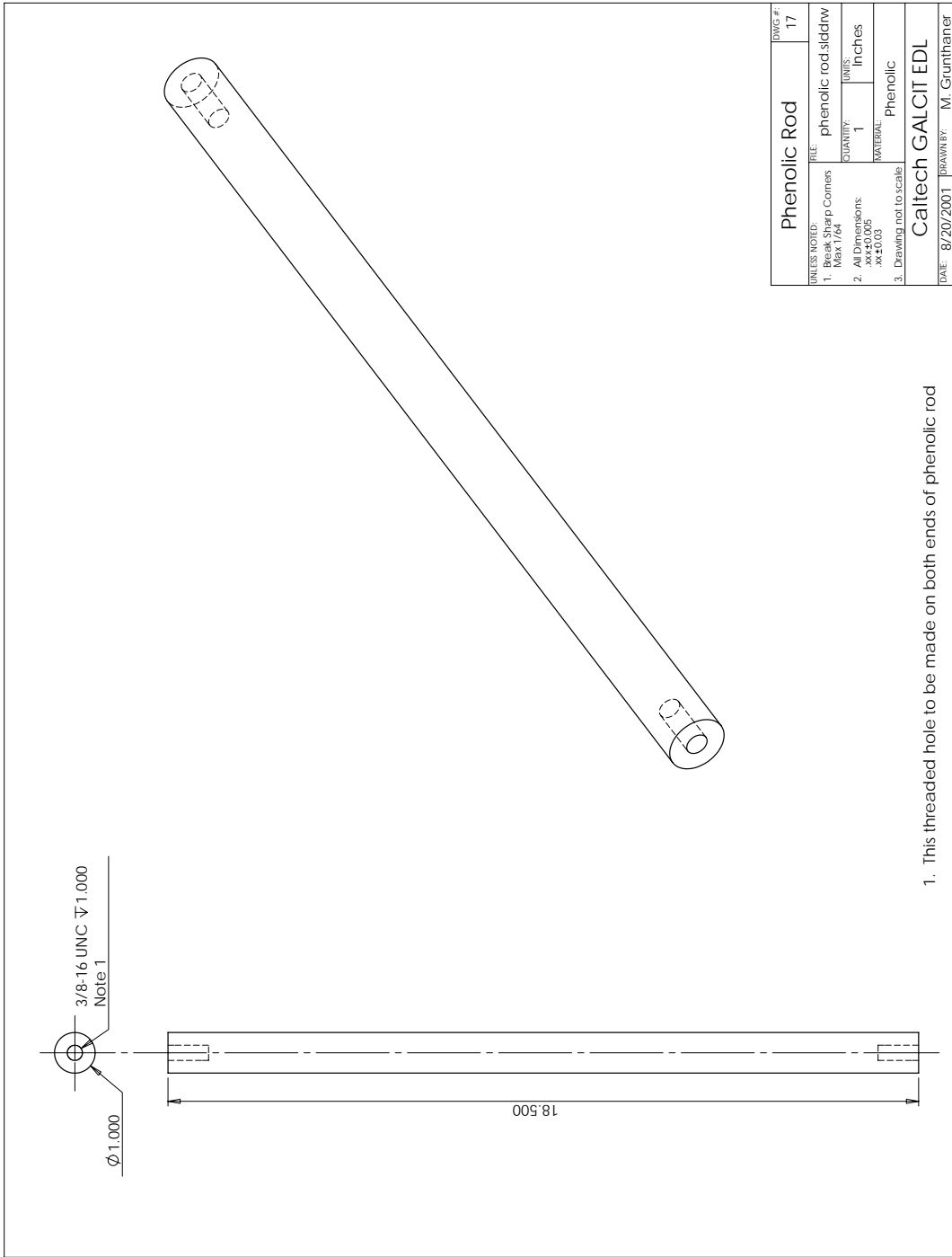


Figure H.17: Handle rod.

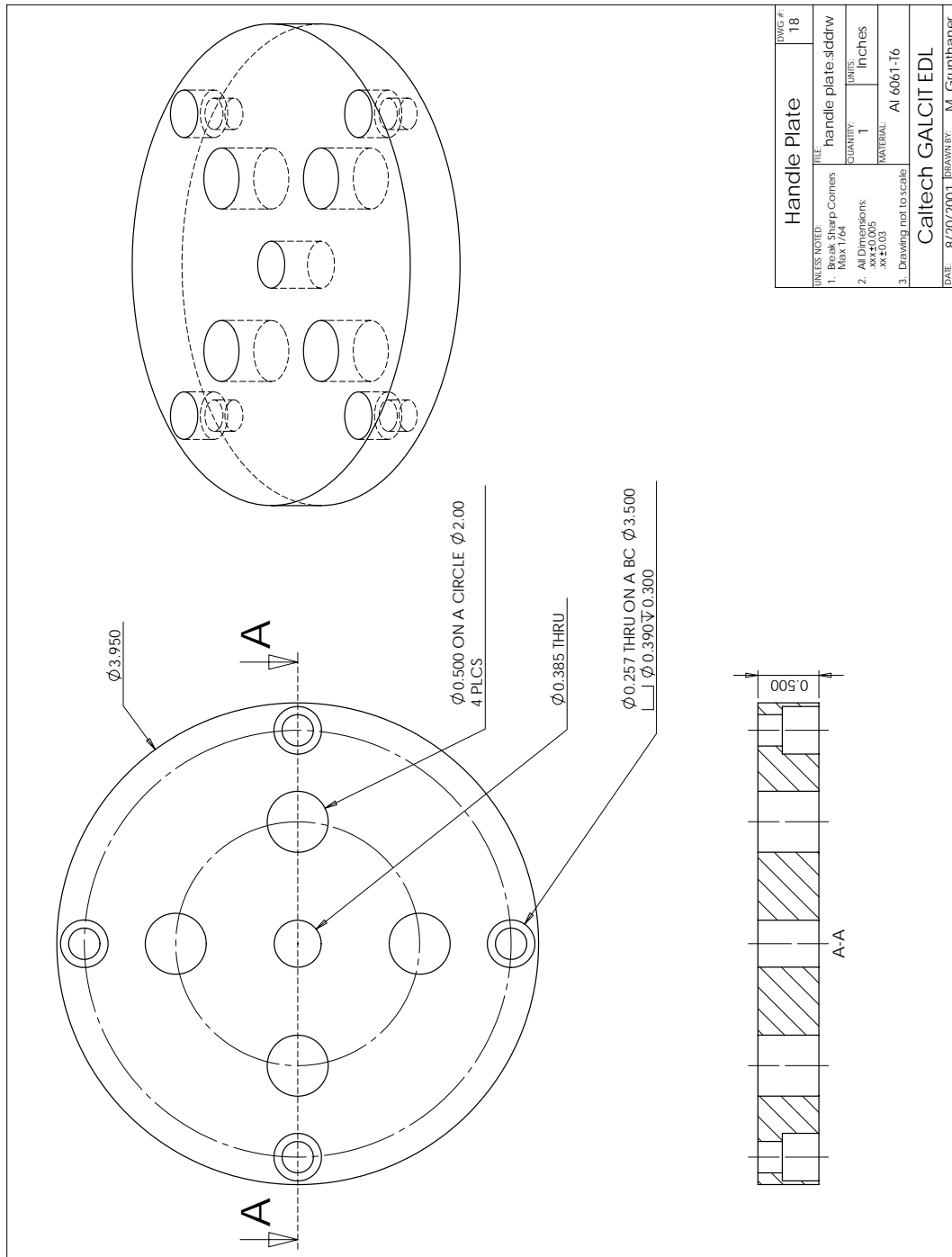


Figure H.18: Handle plate.

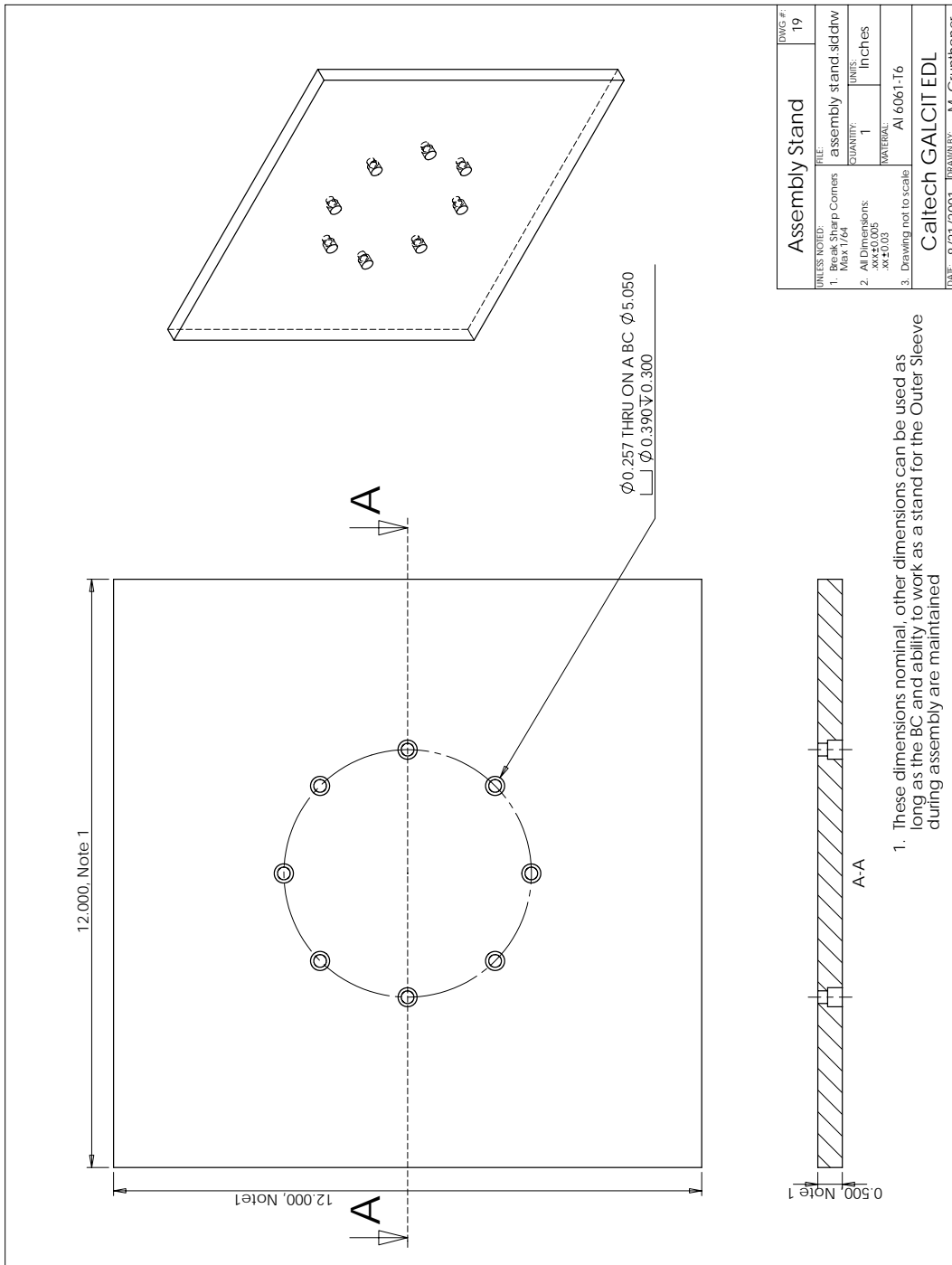


Figure H.19: Assembly stand.

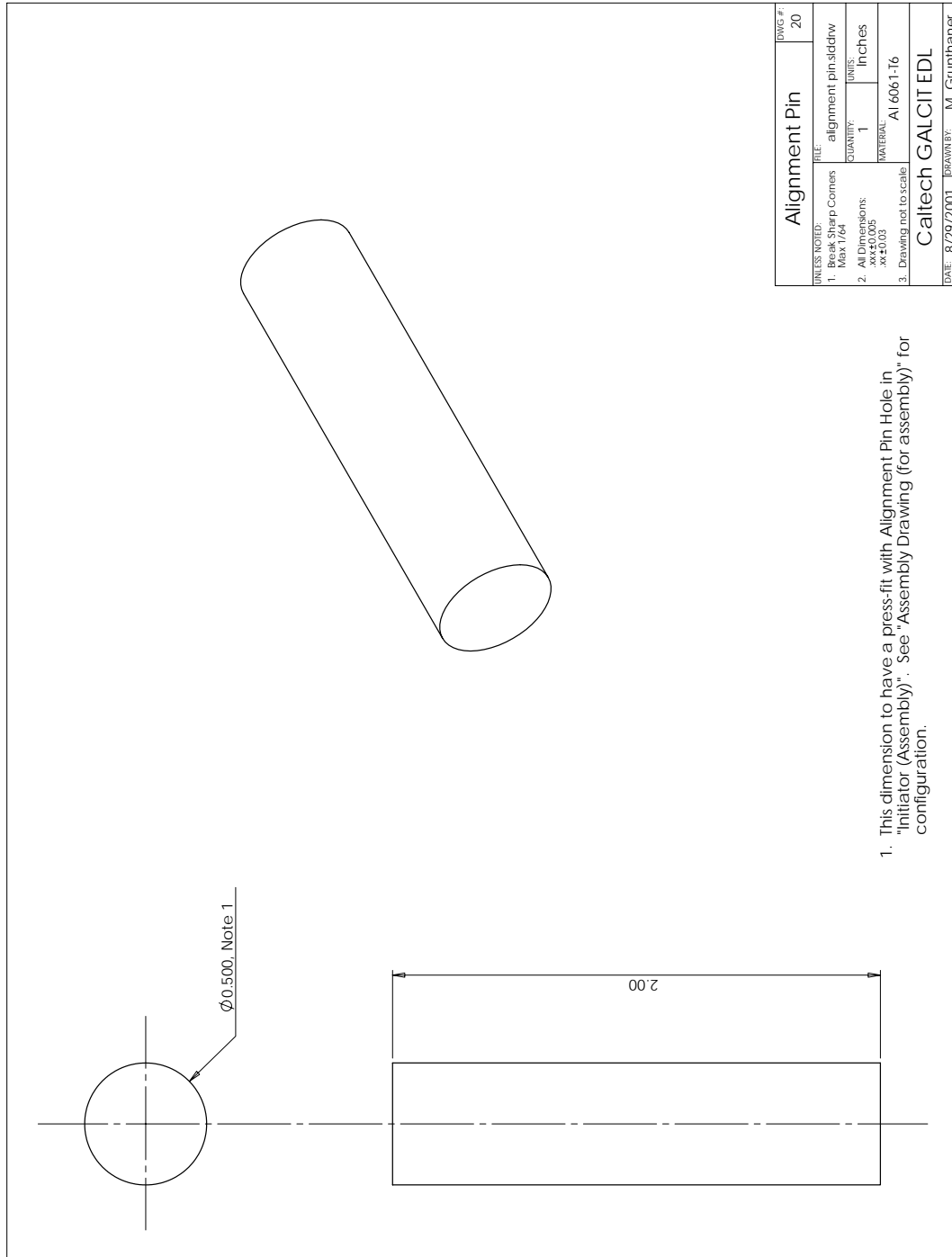


Figure H.20: Alignment pin.

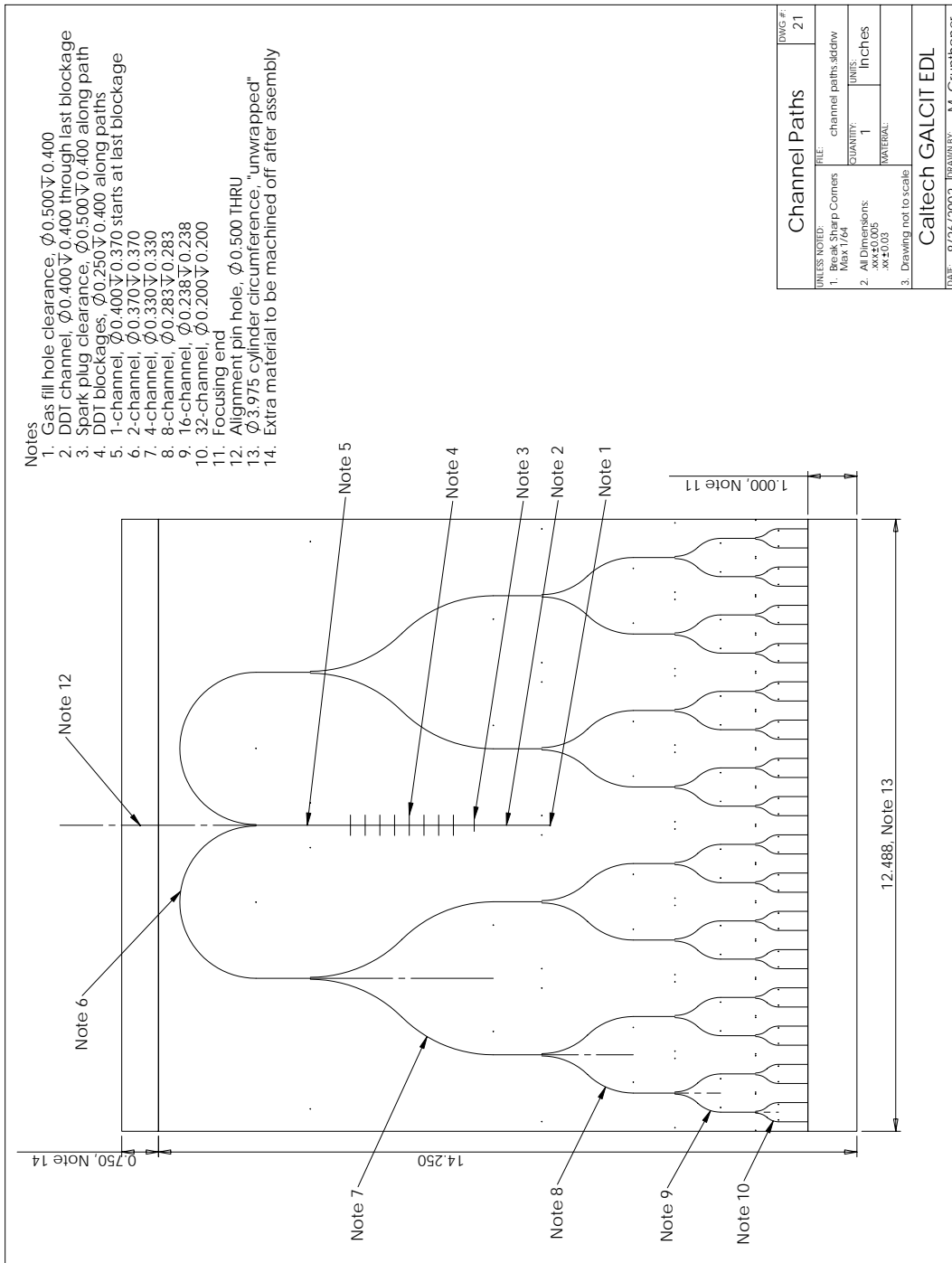


Figure H.21: Channel paths mapped to a planar surface.

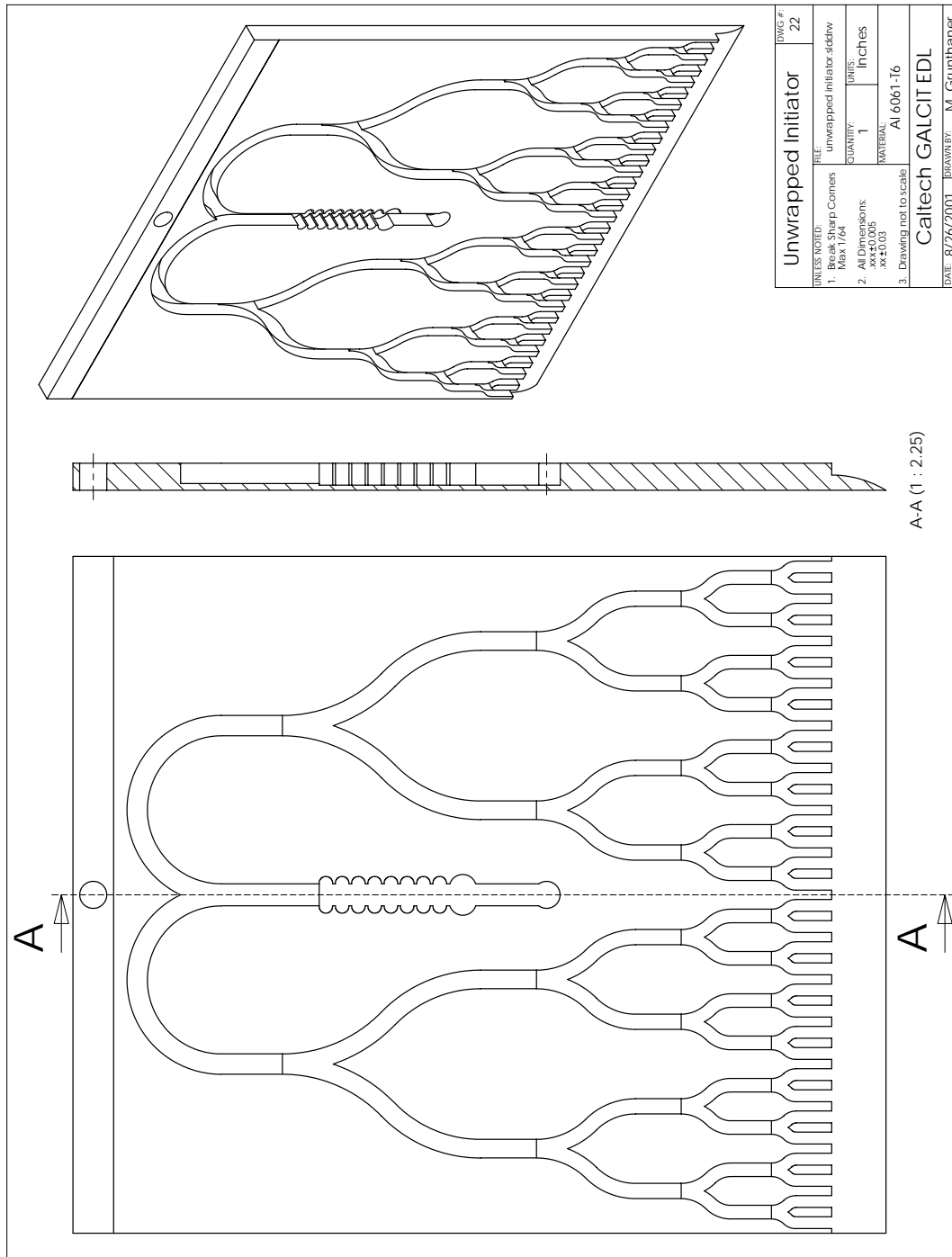


Figure H.22: Unwrapped rendering of channels.

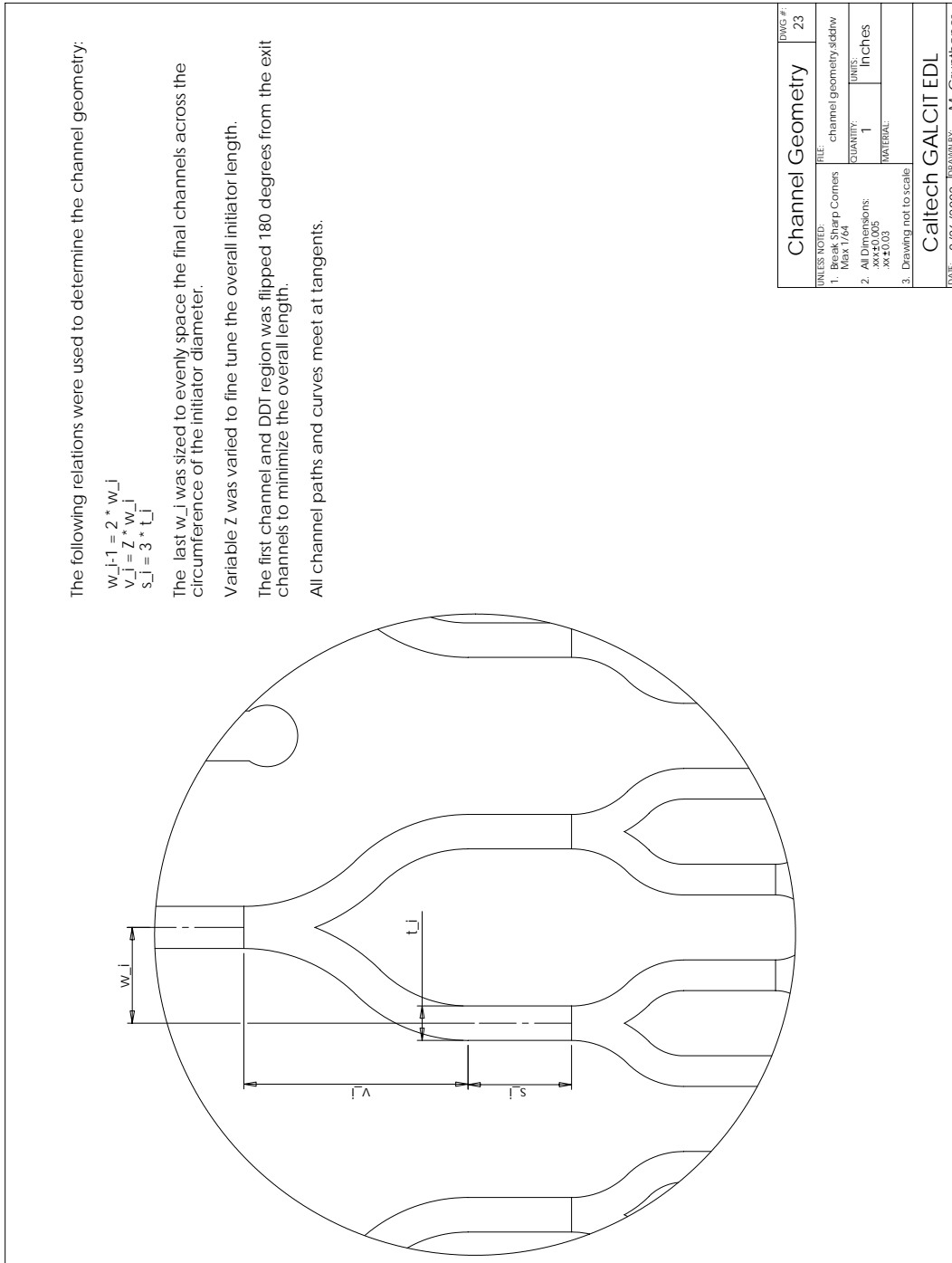


Figure H.23: Channel geometry specifics.

## H.2 Run Matrix: No Dynamic Injection

Run	fuel	Type	Delay ( $\mu$ s)	Width (ns)	F-ratio	MCP (V)	$d_{wave}/d_0$
1	H <sub>2</sub>	pressure	N/A	N/A	N/A	N/A	N/A
2	H <sub>2</sub>	pressure	N/A	N/A	N/A	N/A	N/A
3	H <sub>2</sub>	pressure	N/A	N/A	N/A	N/A	N/A
4	H <sub>2</sub>	pressure	N/A	N/A	N/A	N/A	N/A
5	H <sub>2</sub>	pressure	N/A	N/A	N/A	N/A	N/A
6	H <sub>2</sub>	pressure	N/A	N/A	N/A	N/A	N/A
7	H <sub>2</sub>	pressure	N/A	N/A	N/A	N/A	N/A
8	H <sub>2</sub>	pressure	N/A	N/A	N/A	N/A	N/A
9	H <sub>2</sub>	pressure	N/A	N/A	N/A	N/A	N/A
10	H <sub>2</sub>	image	22	100	16	610	N/A
11	H <sub>2</sub>	image	20	100	22	610	N/A
12	H <sub>2</sub>	image	20	100	22	610	N/A
13	N/A	N/A	N/A	N/A	N/A	N/A	N/A
14	C <sub>2</sub> H <sub>4</sub>	image	30	100	22	680	0.278
15	C <sub>2</sub> H <sub>4</sub>	image	35	100	22	680	0.000
16	C <sub>2</sub> H <sub>4</sub>	image	33	100	22	680	0.092
17	C <sub>2</sub> H <sub>4</sub>	image	31	100	22	670	0.213
18	C <sub>2</sub> H <sub>4</sub>	image	29	100	22	670	0.328
19	C <sub>2</sub> H <sub>4</sub>	image	27	100	22	670	0.434
20	C <sub>2</sub> H <sub>4</sub>	image	25	100	22	670	0.558
21	C <sub>2</sub> H <sub>4</sub>	image	23	100	22	670	0.672
22	C <sub>2</sub> H <sub>4</sub>	image	21	100	22	750	0.776
23	C <sub>2</sub> H <sub>4</sub>	image	20	100	22	800	0.827
24	C <sub>2</sub> H <sub>4</sub>	image	28	100	22	690	0.368
25	C <sub>2</sub> H <sub>4</sub>	image	26	100	22	750	0.497
26	C <sub>2</sub> H <sub>4</sub>	image	34	100	22	670	0.029
27	C <sub>2</sub> H <sub>4</sub>	image	18	100	22	800	0.909
28	C <sub>2</sub> H <sub>4</sub>	image	24	100	22	750	0.607
29	C <sub>2</sub> H <sub>4</sub>	image	22	100	22	750	0.72
30	C <sub>2</sub> H <sub>4</sub>	image	32	100	22	720	0.149

Table H.1: Experimental properties of each run. All mixtures were stoichiometric fuel-oxygen at 1.00 bar initial pressure. “Type” indicates if the experiment was set to acquire pressure history data or to image the imploding wave. All images were acquired in gated mode. “Delay” is the interval between the firing of the spark plug and time of image acquisition. “Width” is the integration time of the intensified CCD camera and “MCP” corresponds to the intensifier voltage setting. The variable “ $d_{wave}/d_0$ ” is the diameter of the wave during imaging, normalized by the diameter of the test section.

Run	fuel	Type	Delay ( $\mu$ s)	Width (ns)	F-ratio	MCP (V)	Interval ( $\mu$ s)
31	C <sub>2</sub> H <sub>4</sub>	pressure	N/A	N/A	N/A	N/A	N/A
32	C <sub>2</sub> H <sub>4</sub>	pressure	N/A	N/A	N/A	N/A	N/A
33	C <sub>2</sub> H <sub>4</sub>	pressure	N/A	N/A	N/A	N/A	N/A
34	C <sub>2</sub> H <sub>4</sub>	pressure	N/A	N/A	N/A	N/A	N/A
35	C <sub>2</sub> H <sub>4</sub>	pressure	N/A	N/A	N/A	N/A	N/A
36	C <sub>2</sub> H <sub>4</sub>	pressure	N/A	N/A	N/A	N/A	N/A
37	C <sub>3</sub> H <sub>8</sub>	pressure	N/A	N/A	N/A	N/A	N/A
38	C <sub>3</sub> H <sub>8</sub>	pressure	N/A	N/A	N/A	N/A	N/A
39	C <sub>3</sub> H <sub>8</sub>	pressure	N/A	N/A	N/A	N/A	N/A
40	C <sub>3</sub> H <sub>8</sub>	pressure	N/A	N/A	N/A	N/A	N/A
41	C <sub>3</sub> H <sub>8</sub>	pressure	N/A	N/A	N/A	N/A	N/A
42	C <sub>3</sub> H <sub>8</sub>	pressure	N/A	N/A	N/A	N/A	N/A
43	C <sub>3</sub> H <sub>8</sub>	image	24	100	N/A	N/A	2.0
44	C <sub>3</sub> H <sub>8</sub>	image	24	100	N/A	N/A	2.0
45	C <sub>3</sub> H <sub>8</sub>	image	24	100	N/A	N/A	2.0
46	C <sub>3</sub> H <sub>8</sub>	image	N/A	N/A	N/A	N/A	N/A
47	C <sub>3</sub> H <sub>8</sub>	image	N/A	N/A	N/A	N/A	N/A
48	C <sub>3</sub> H <sub>8</sub>	image	N/A	N/A	N/A	N/A	N/A
49	C <sub>3</sub> H <sub>8</sub>	image	N/A	N/A	N/A	N/A	N/A
50	C <sub>3</sub> H <sub>8</sub>	image	24	100	N/A	N/A	2.0
51	C <sub>3</sub> H <sub>8</sub>	image	N/A	N/A	N/A	N/A	N/A
52	C <sub>3</sub> H <sub>8</sub>	image	15	800	4	N/A	3.0
53	C <sub>3</sub> H <sub>8</sub>	image	20	800	4	N/A	2.5
54	C <sub>3</sub> H <sub>8</sub>	image	26	800	4	N/A	2.5
55	C <sub>2</sub> H <sub>4</sub>	image	18	800	4	N/A	2.0
56	C <sub>2</sub> H <sub>4</sub>	image	12	800	4	N/A	1.0
57	C <sub>2</sub> H <sub>4</sub>	image	N/A	N/A	N/A	N/A	N/A

Table H.2: Experimental properties of each run. All mixtures were stoichiometric fuel-oxygen at 1.00 bar initial pressure. “Type” indicates if the experiment was set to acquire pressure history data or to image the imploding wave. All images were acquired in gated mode. “Delay” is the interval between the firing of the spark plug and time of image acquisition. “Width” is the integration time of the intensified CCD camera and “MCP” corresponds to the intensifier voltage setting. For runs 1-42, a single image was taken during each experiment using the Princeton Instruments ITE/ICCD-576 camera. For runs 43-57, up to eight images were acquired during a single run using the Cordin Model 220 CCD camera. For runs with the Cordin camera, the variable “Interval” corresponds to time interval between images.

### H.3 Pressure Traces: No Dynamic Injection

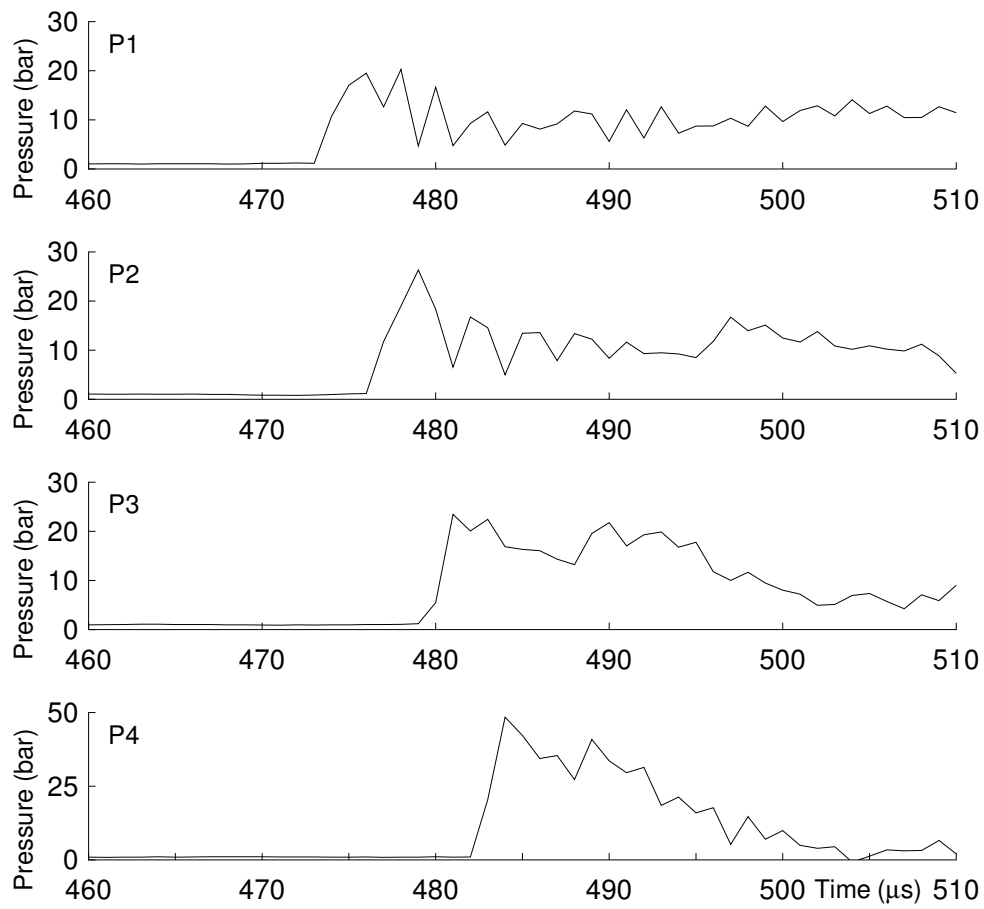


Figure H.24: Pressure history from run 001 with no initiator gas injection.

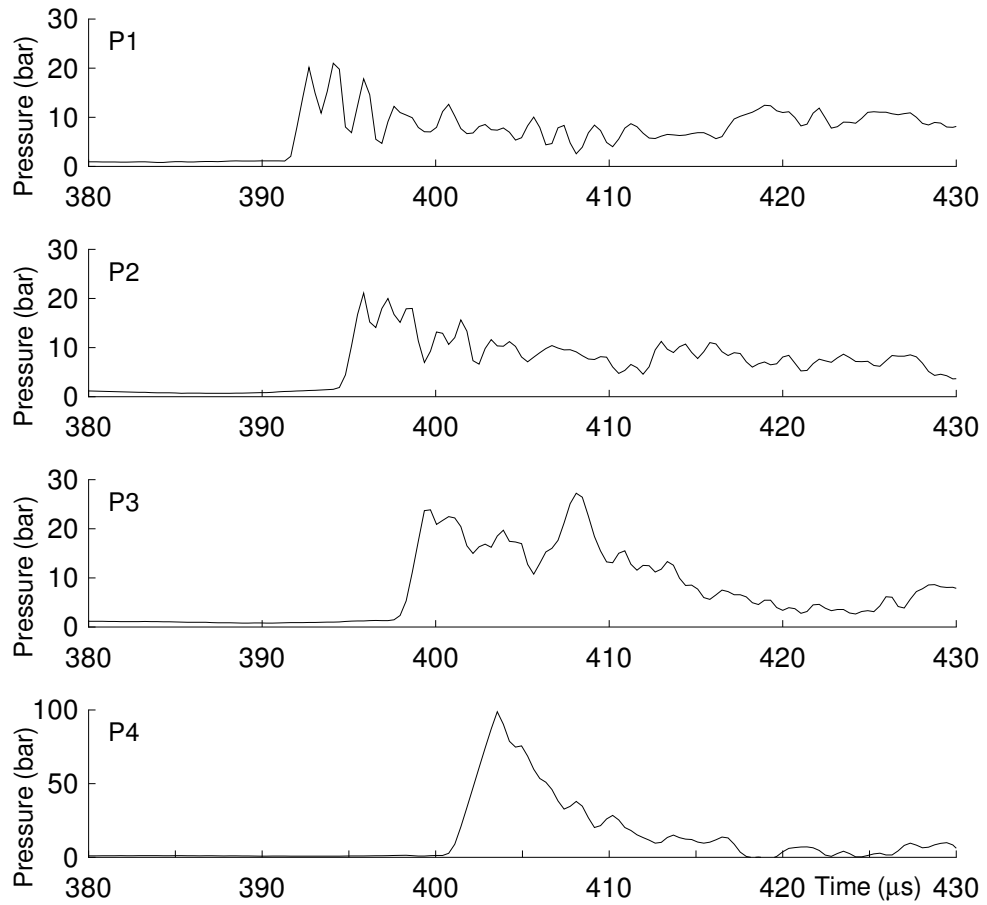


Figure H.25: Pressure history from run 002 with no initiator gas injection.

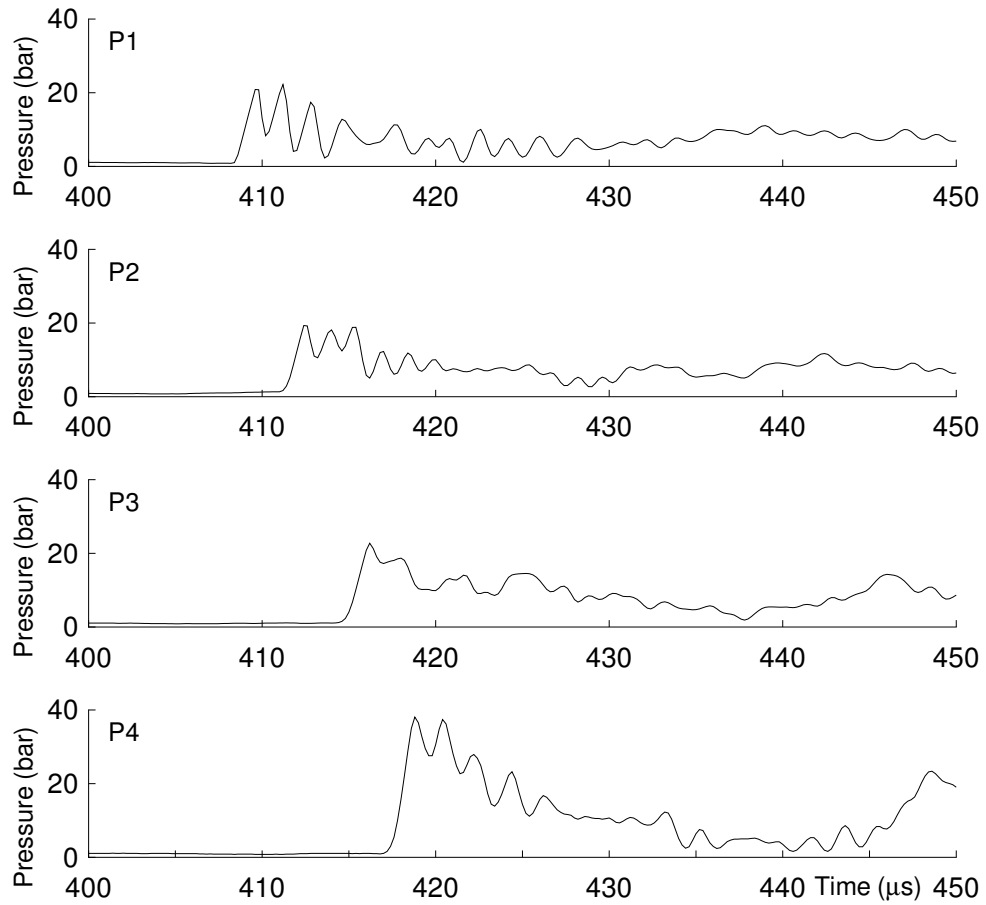


Figure H.26: Pressure history from run 003 with no initiator gas injection.

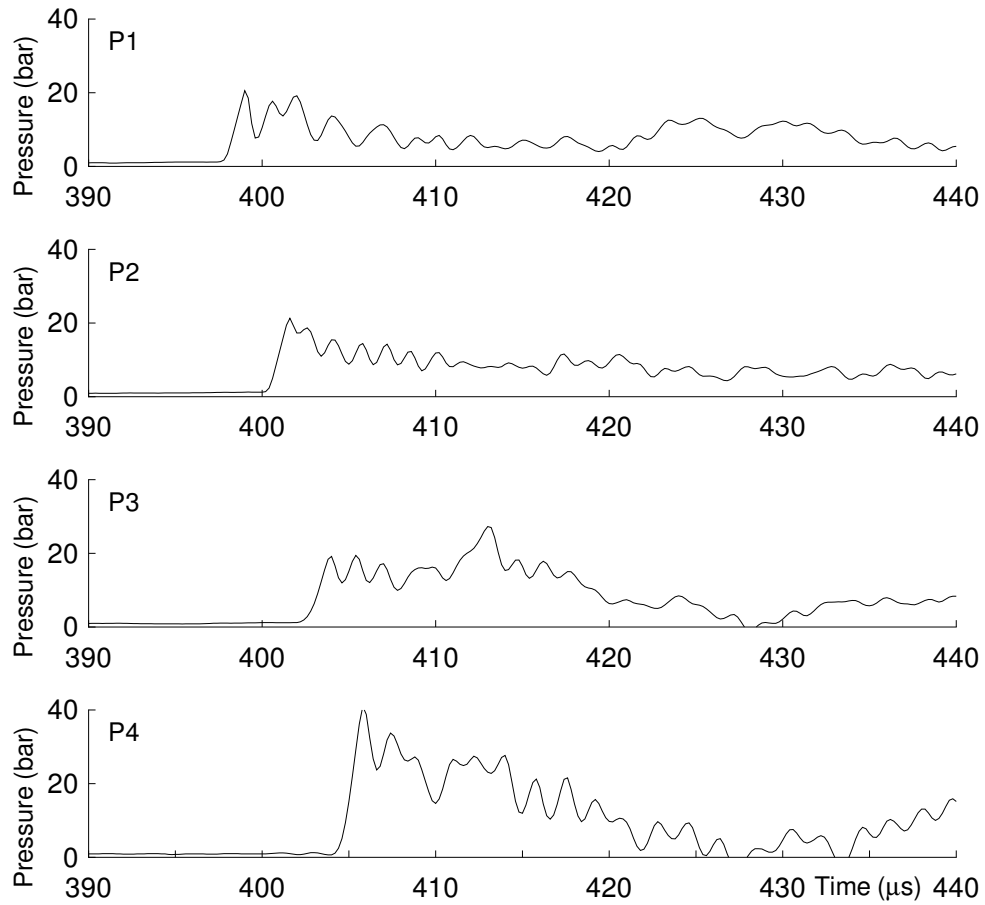


Figure H.27: Pressure history from run 004 with no initiator gas injection.

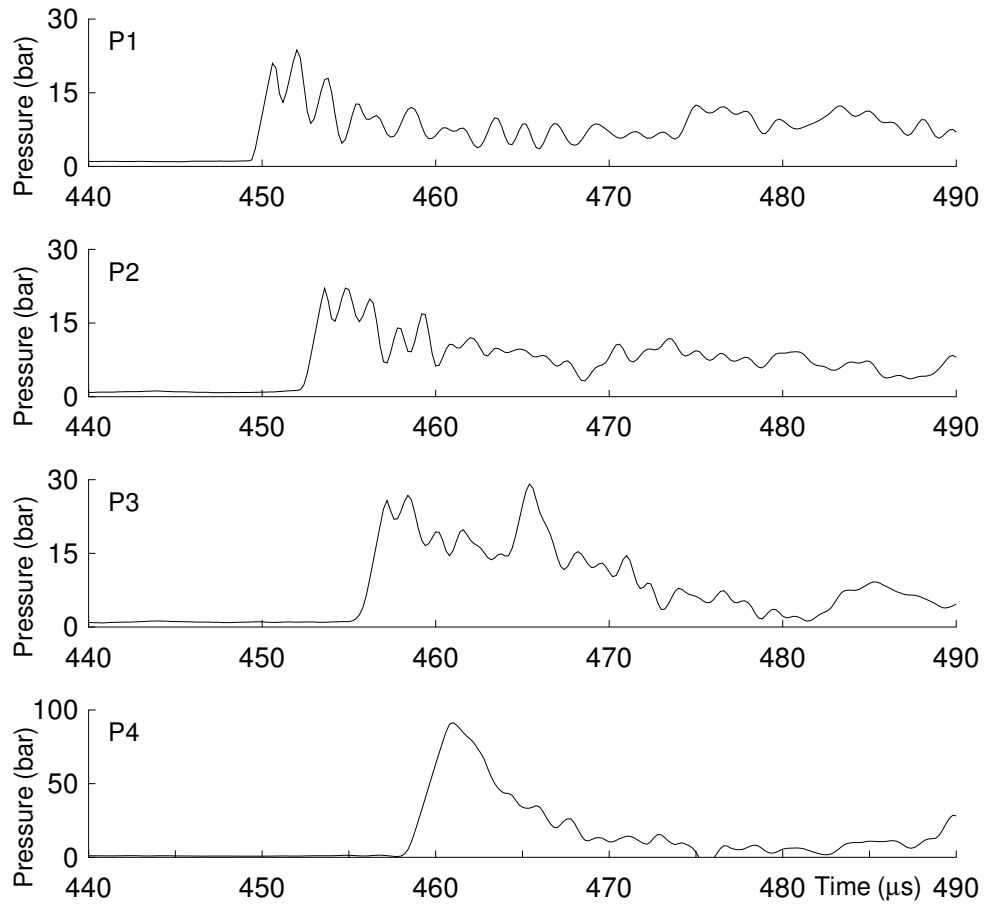


Figure H.28: Pressure history from run 005 with no initiator gas injection.

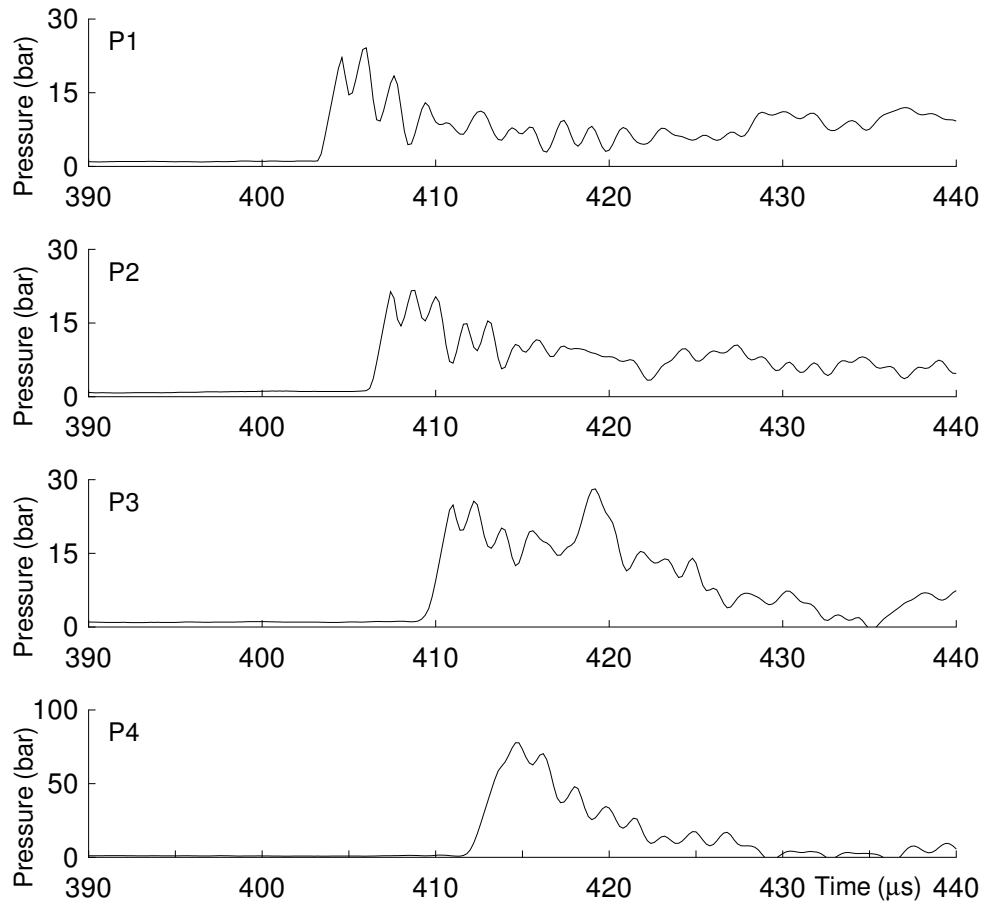


Figure H.29: Pressure history from run 006 with no initiator gas injection.

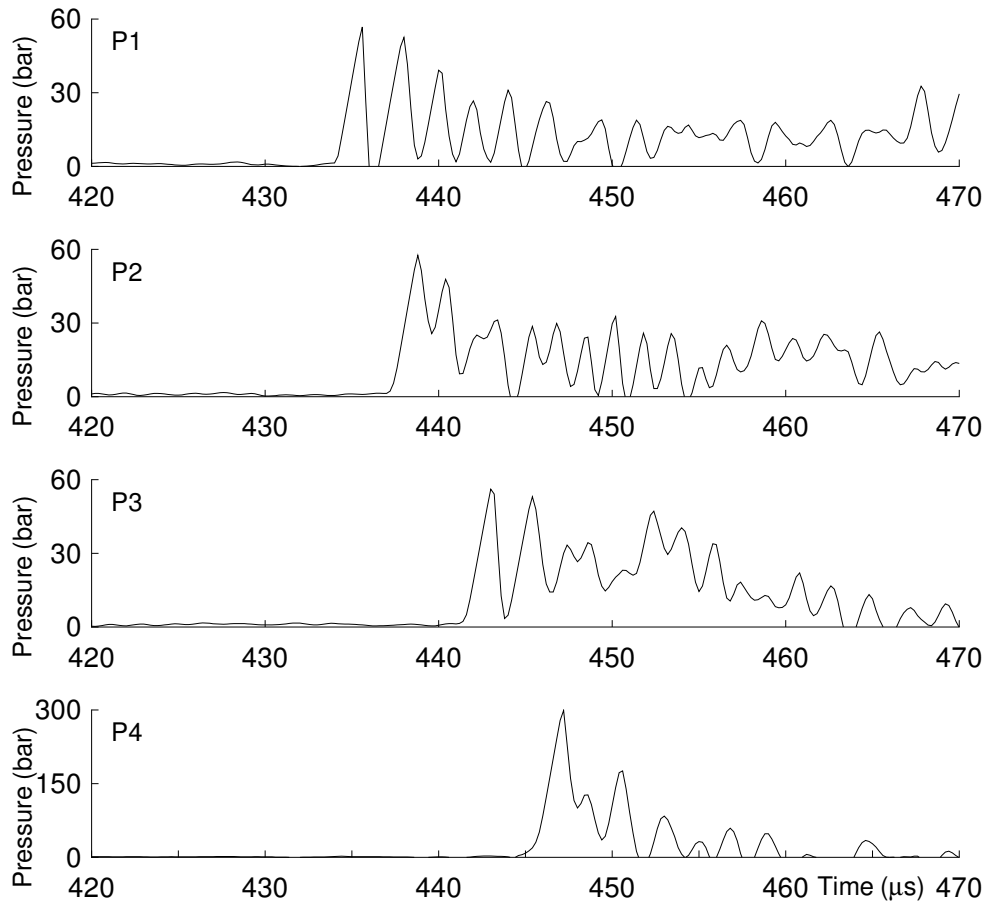


Figure H.30: Pressure history from run 031 with no initiator gas injection.

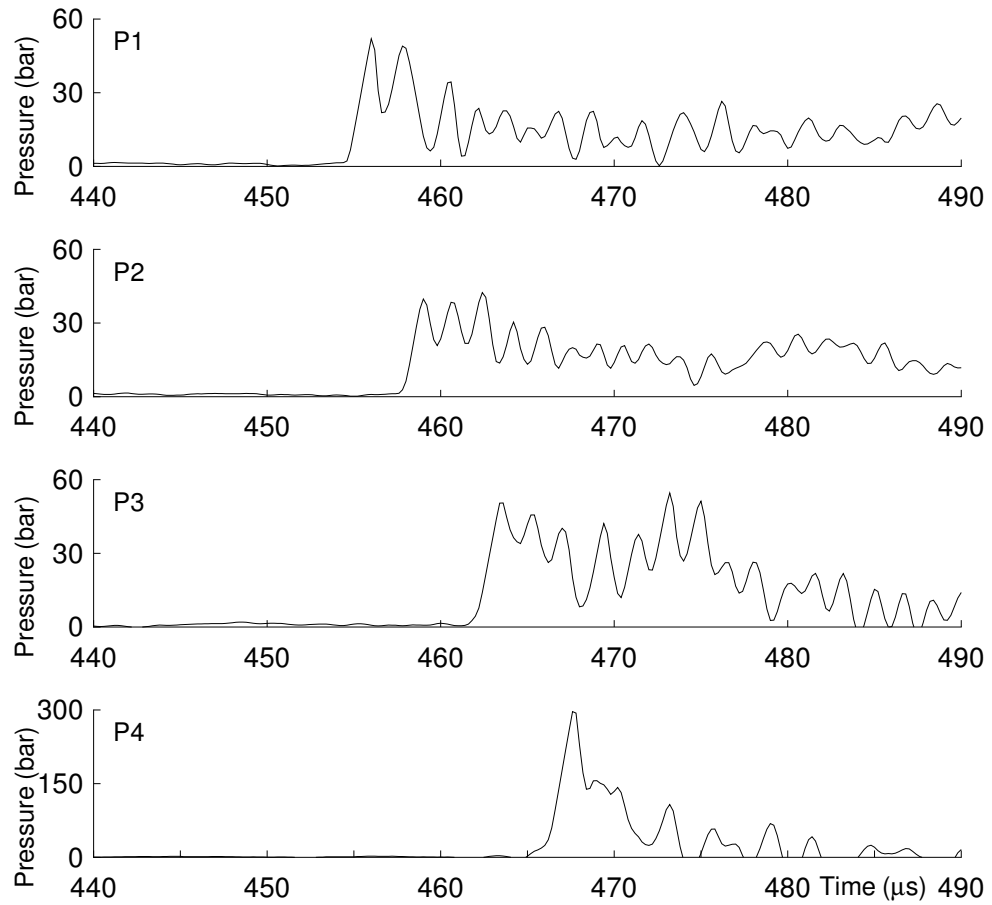


Figure H.31: Pressure history from run 032 with no initiator gas injection.

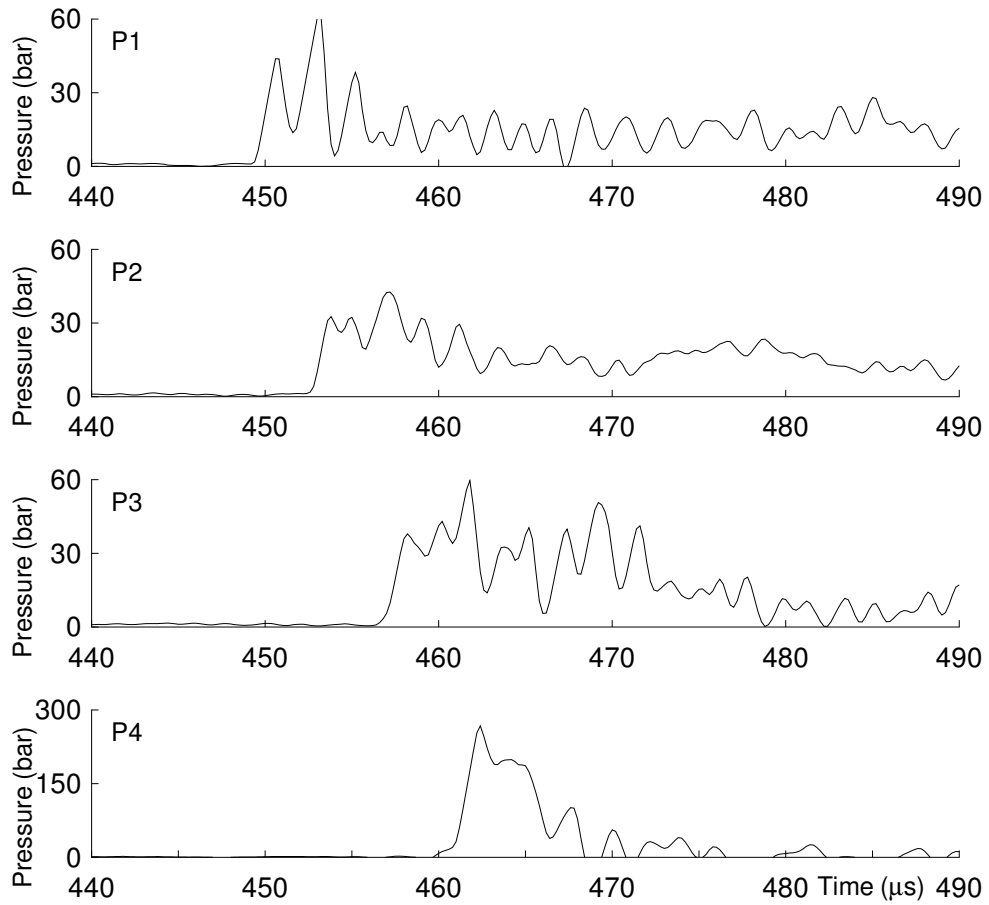


Figure H.32: Pressure history from run 033 with no initiator gas injection.

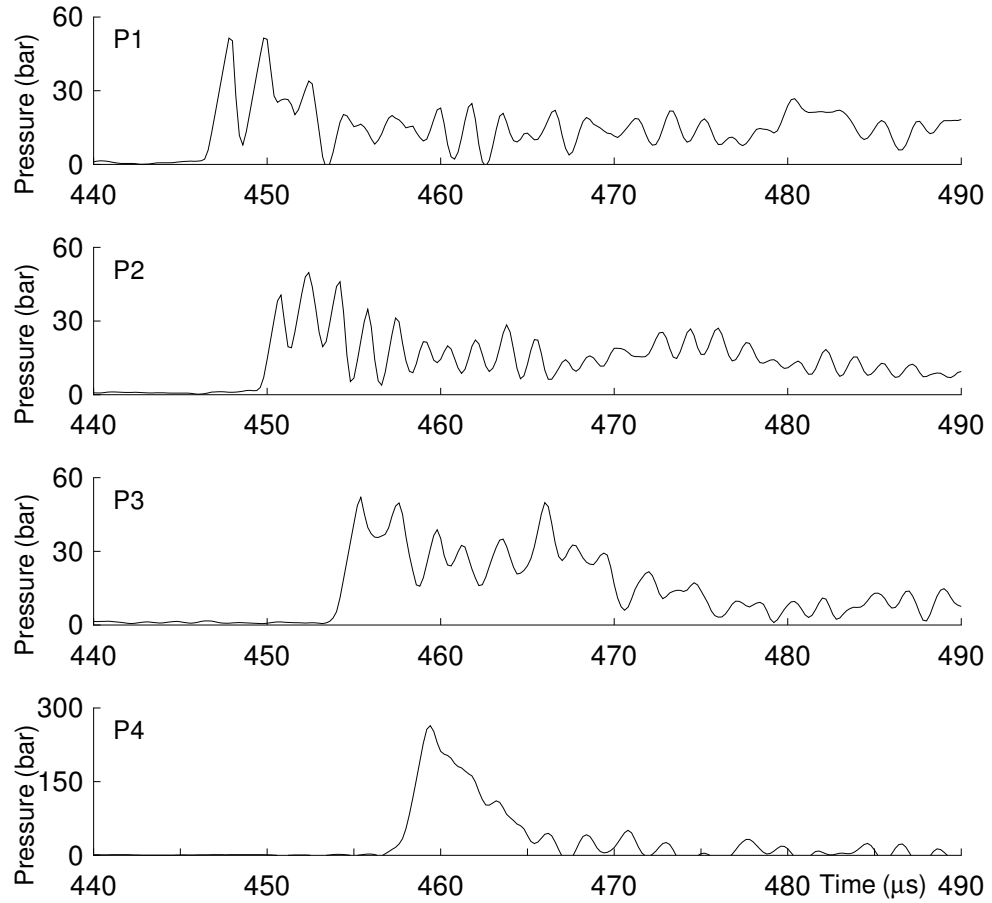


Figure H.33: Pressure history from run 034 with no initiator gas injection.

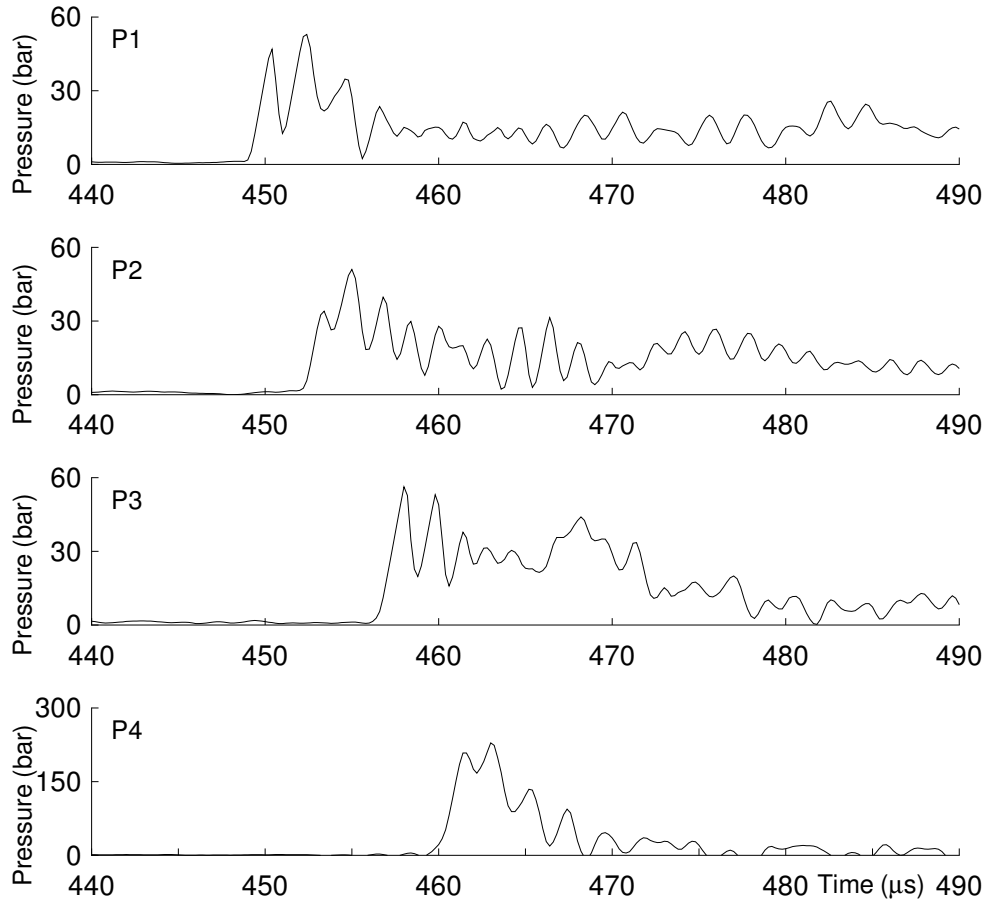


Figure H.34: Pressure history from run 035 with no initiator gas injection.

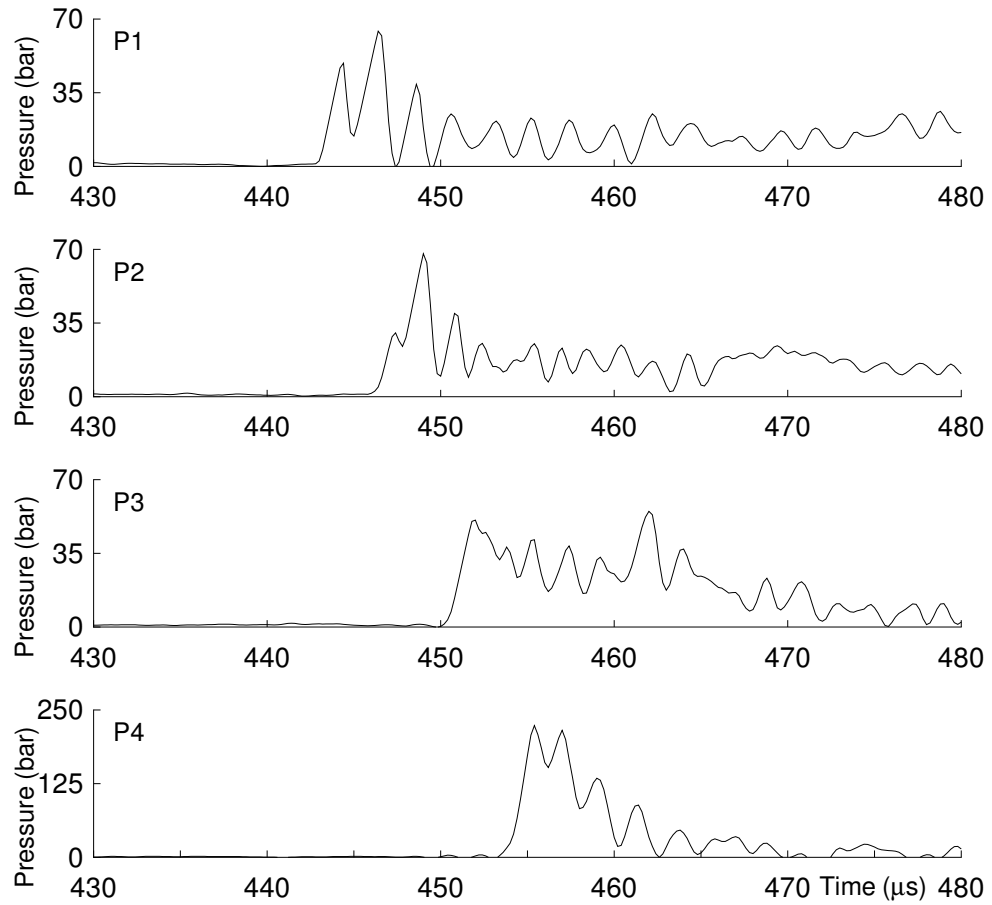


Figure H.35: Pressure history from run 036 with no initiator gas injection.

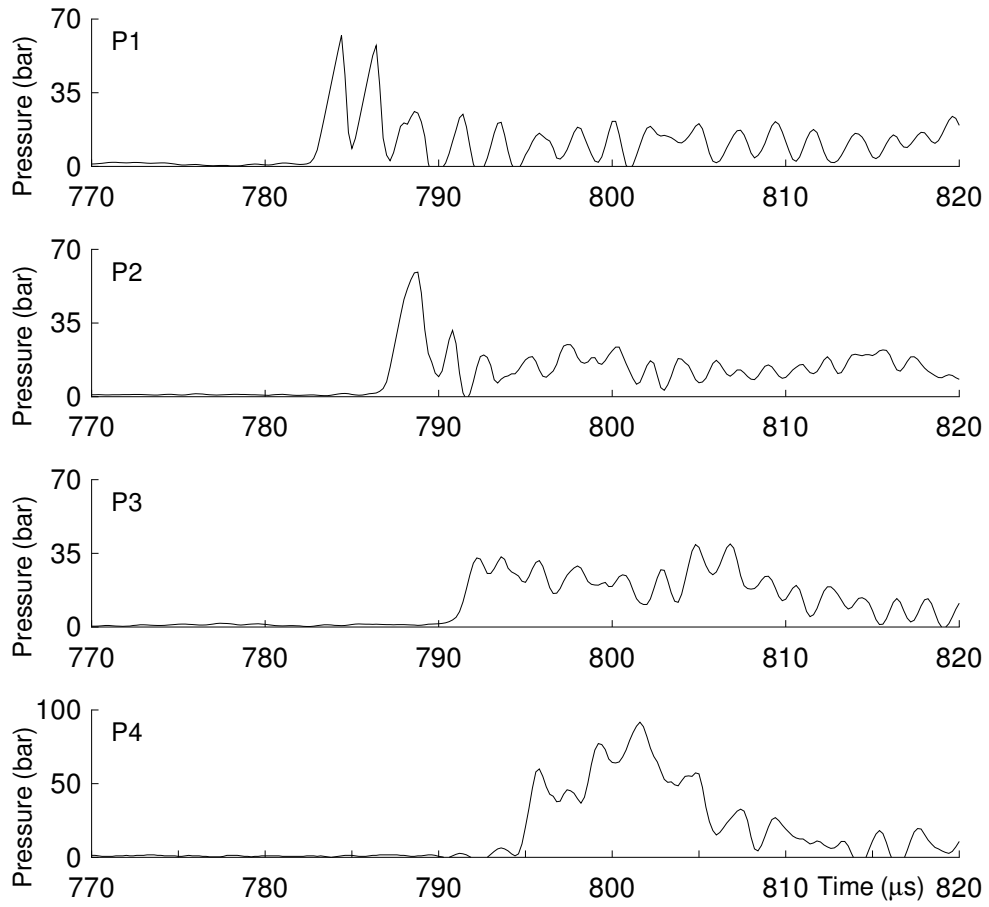


Figure H.36: Pressure history from run 037 with no initiator gas injection.

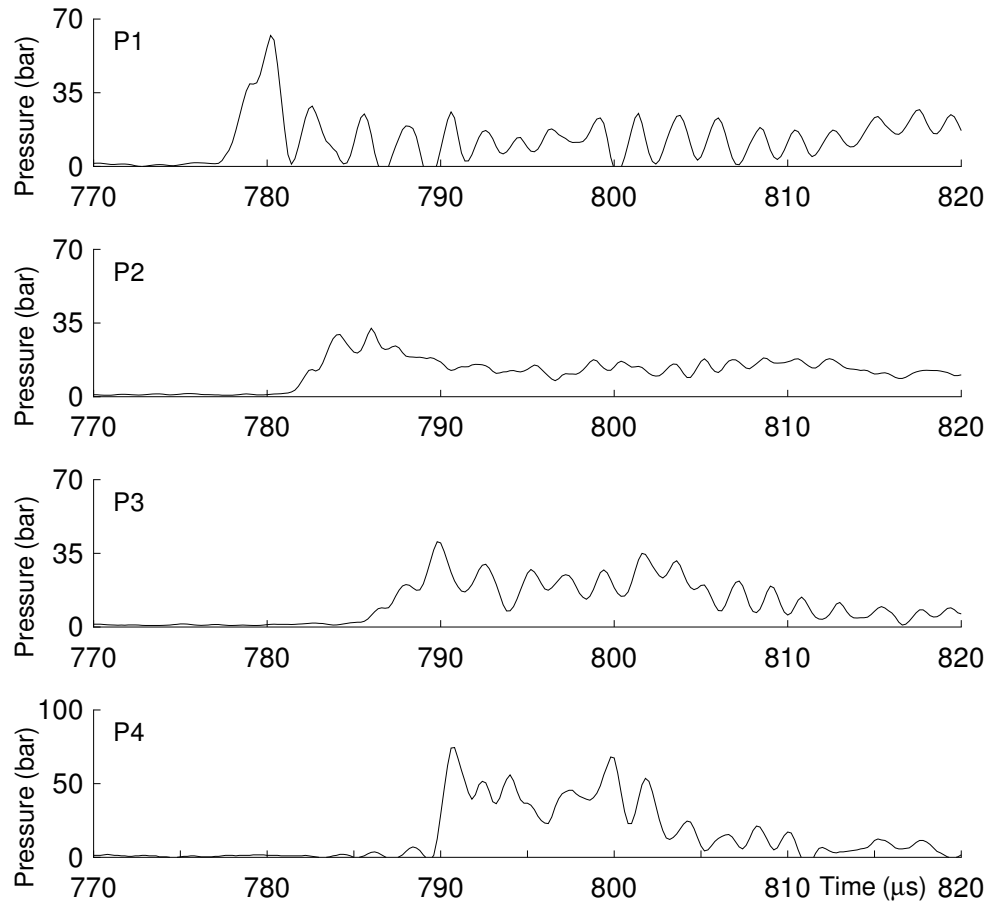


Figure H.37: Pressure history from run 038 with no initiator gas injection.

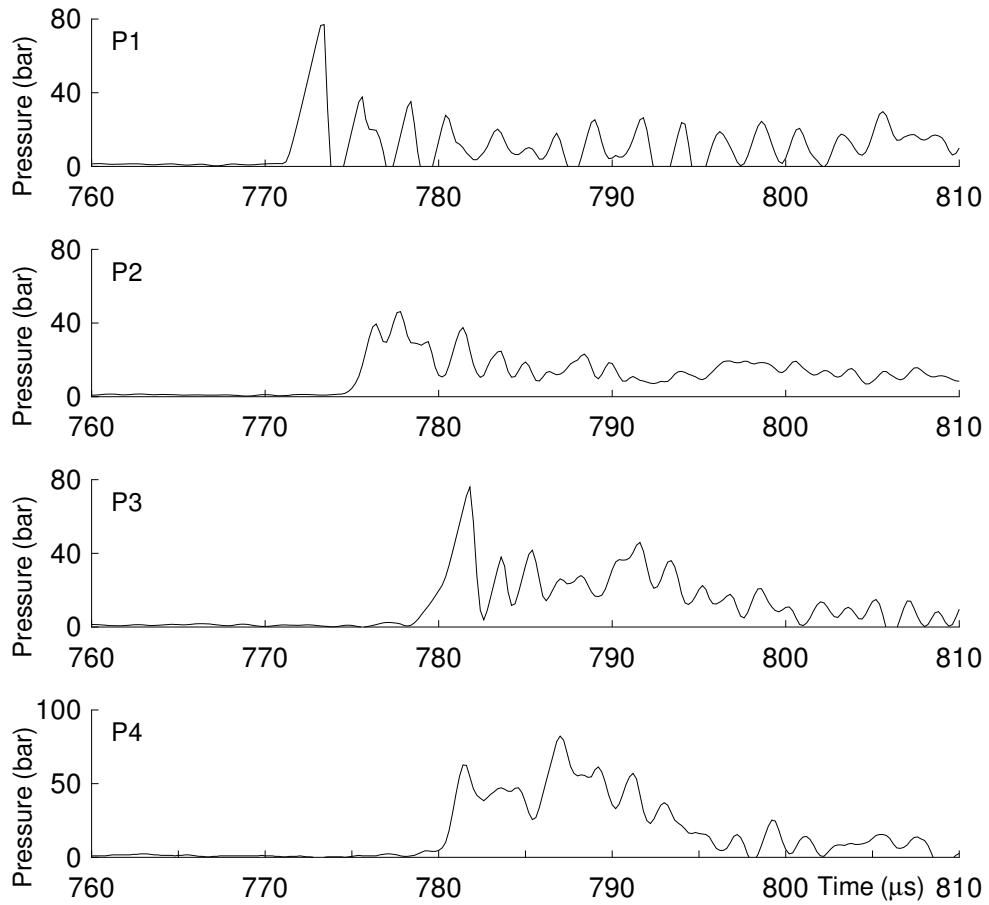


Figure H.38: Pressure history from run 039 with no initiator gas injection.

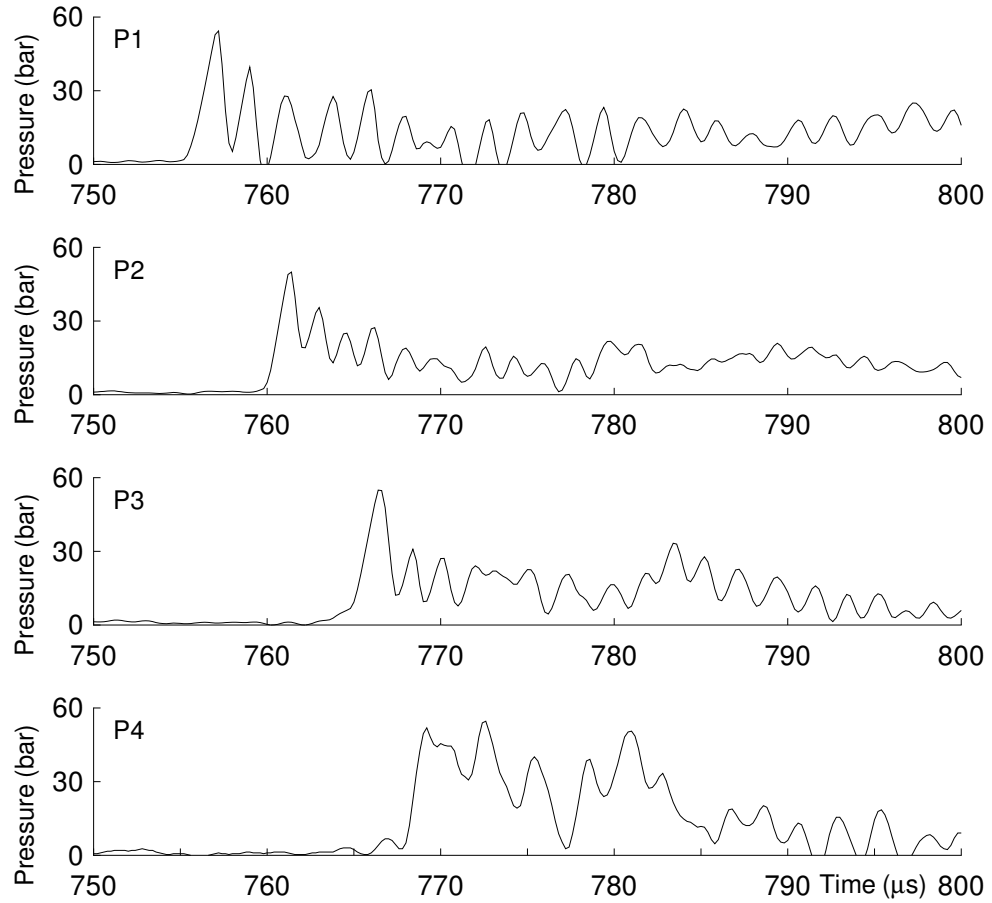


Figure H.39: Pressure history from run 040 with no initiator gas injection.

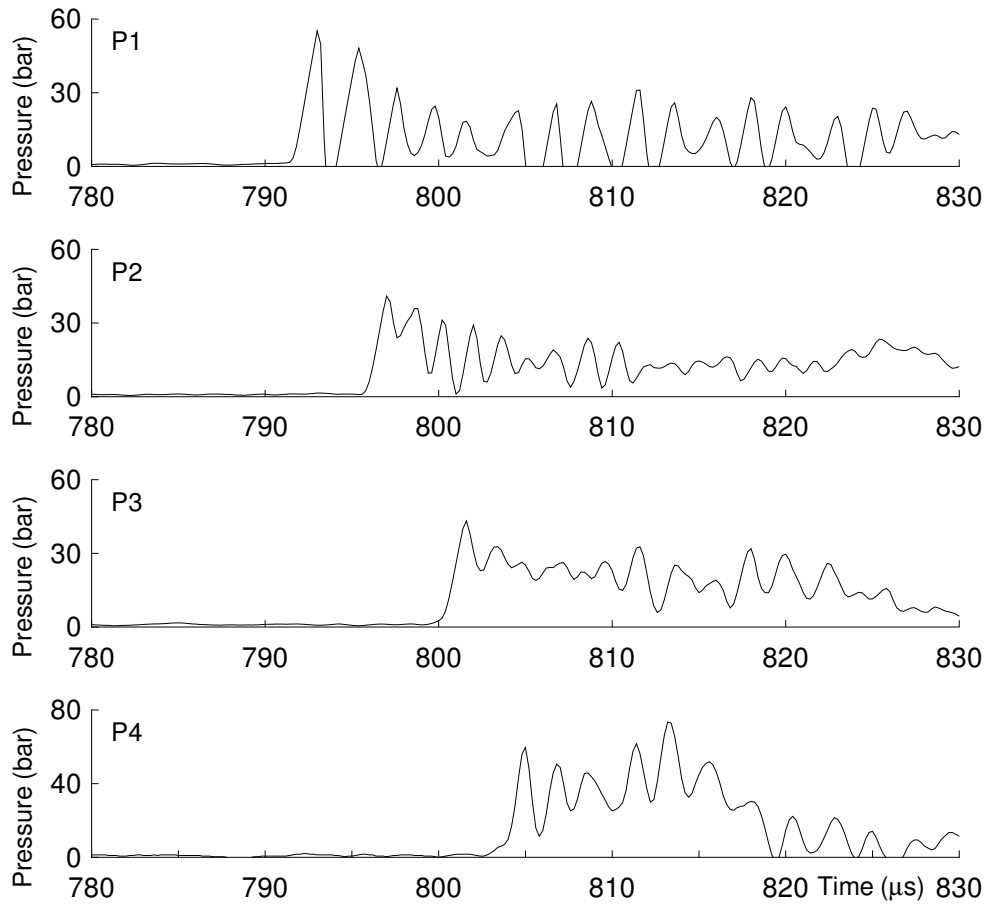


Figure H.40: Pressure history from run 041 with no initiator gas injection.

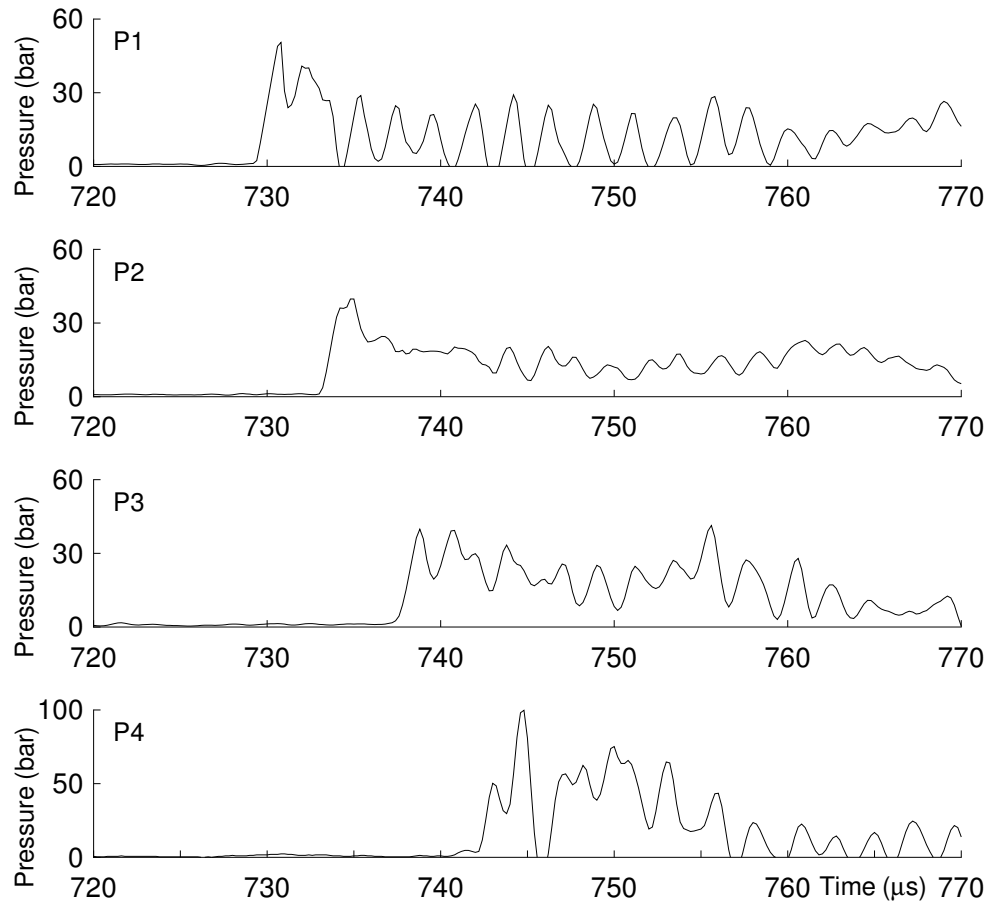


Figure H.41: Pressure history from run 042 with no initiator gas injection.

## H.4 Chemiluminescence Images: No Dynamic Injection

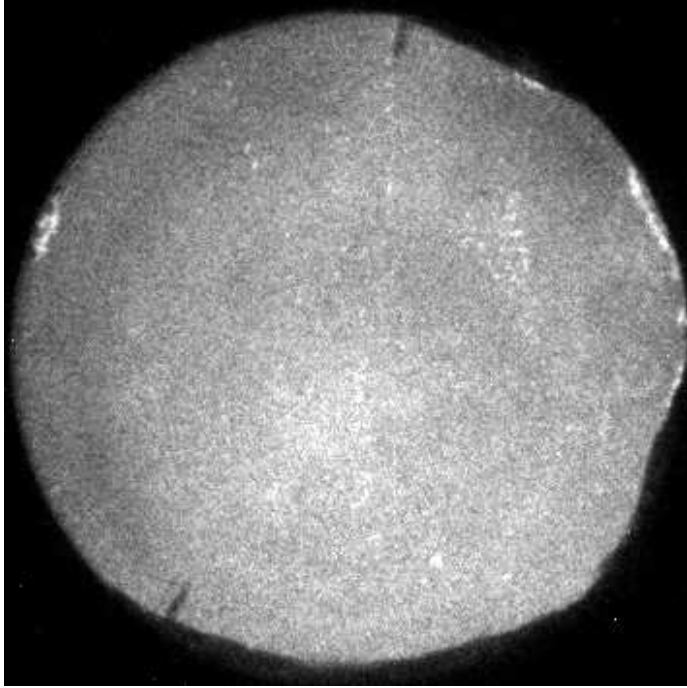


Figure H.42: Chemiluminescence from run 008 with no initiator gas injection.

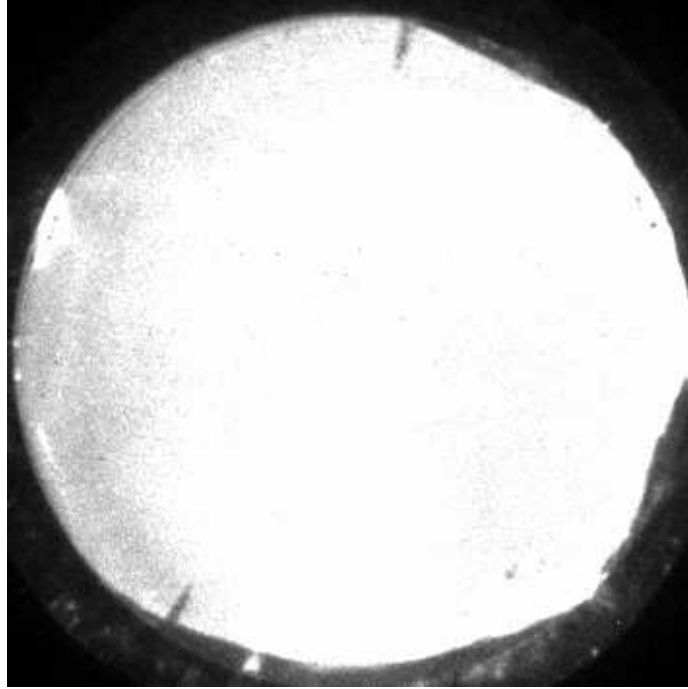


Figure H.43: Chemiluminescence from run 009 with no initiator gas injection.

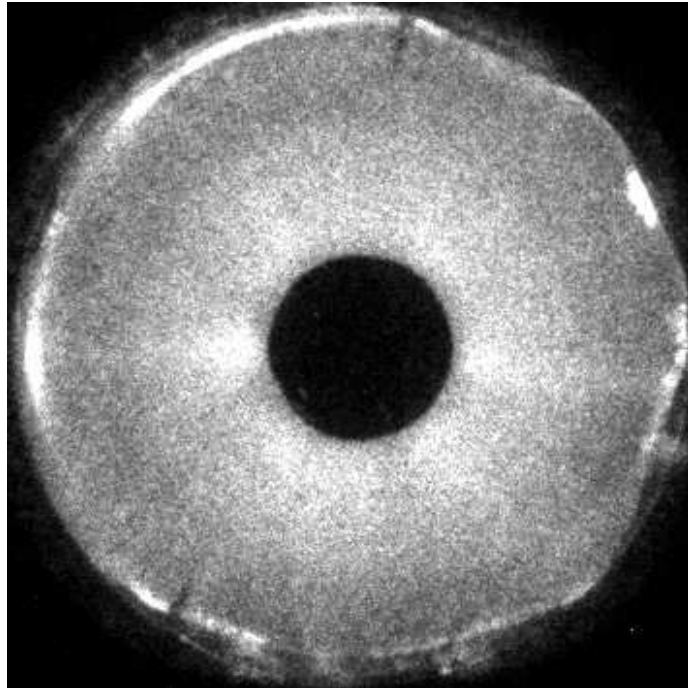


Figure H.44: Chemiluminescence from run 014 with no initiator gas injection.

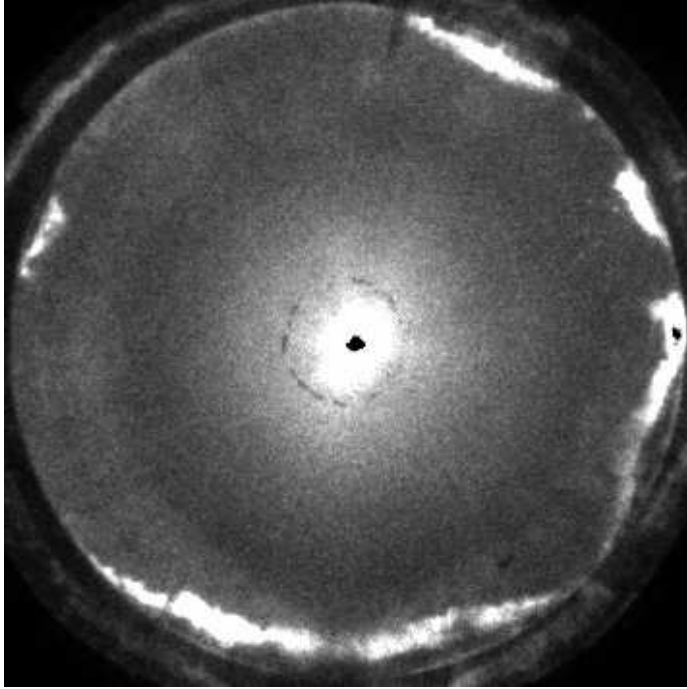


Figure H.45: Chemiluminescence from run 015 with no initiator gas injection.

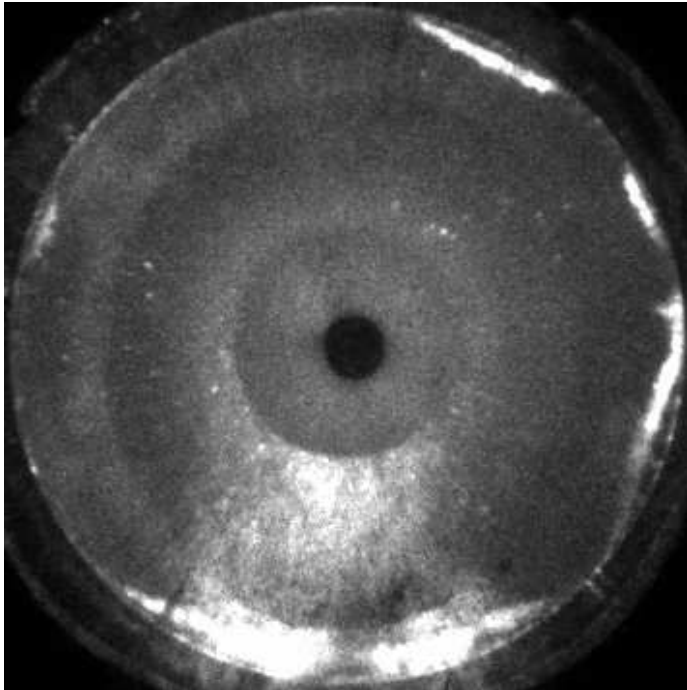


Figure H.46: Chemiluminescence from run 016 with no initiator gas injection.

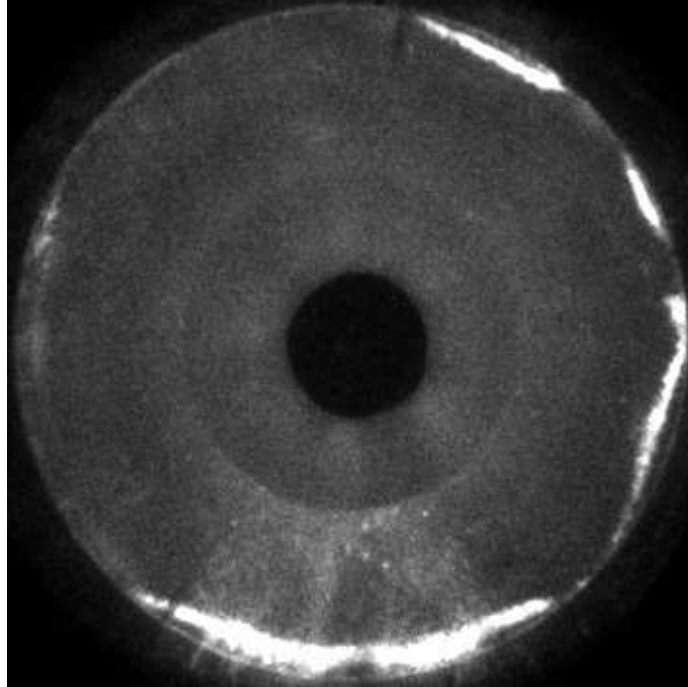


Figure H.47: Chemiluminescence from run 017 with no initiator gas injection.

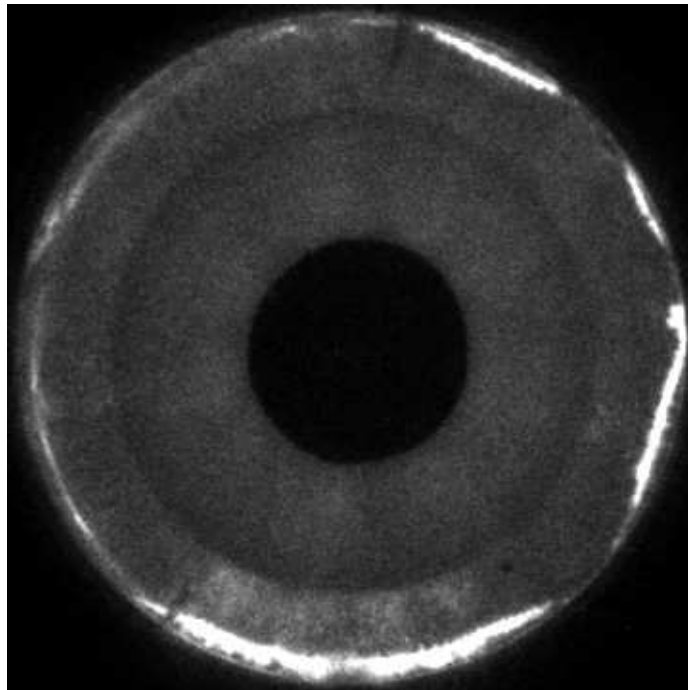


Figure H.48: Chemiluminescence from run 018 with no initiator gas injection.

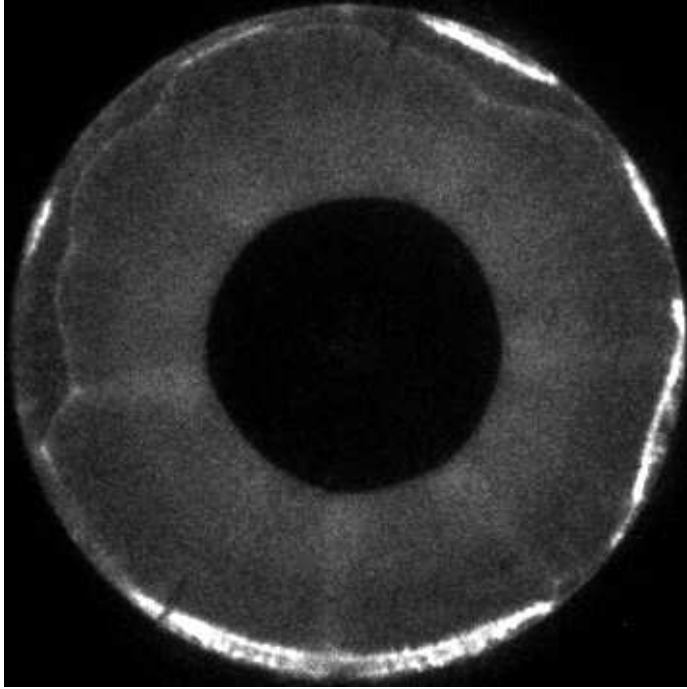


Figure H.49: Chemiluminescence from run 019 with no initiator gas injection.

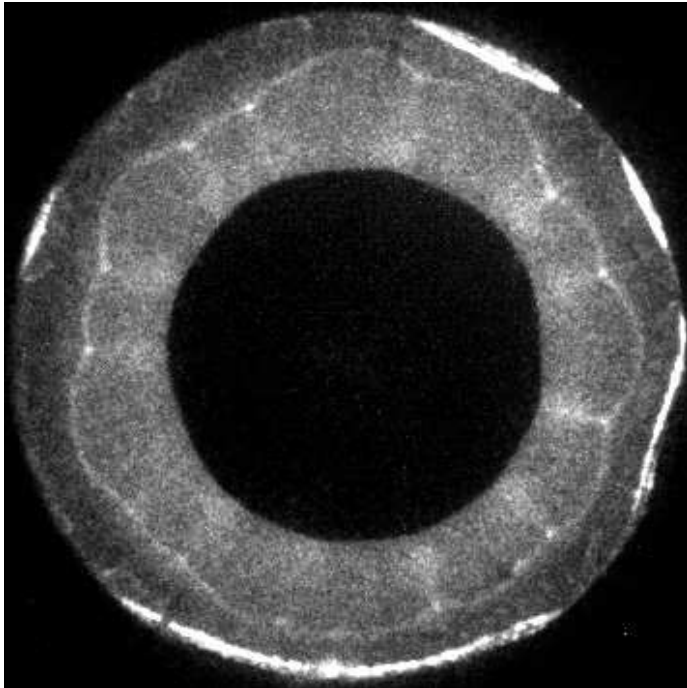


Figure H.50: Chemiluminescence from run 020 with no initiator gas injection.

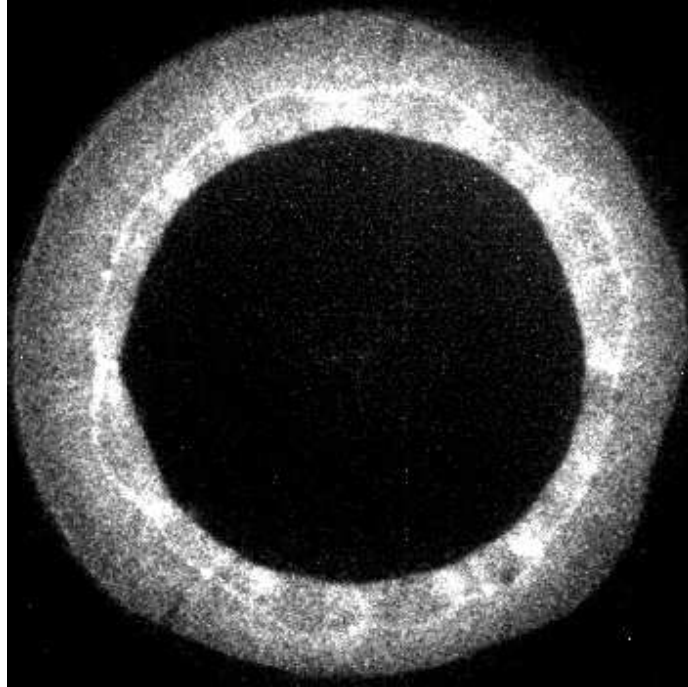


Figure H.51: Chemiluminescence from run 021 with no initiator gas injection.

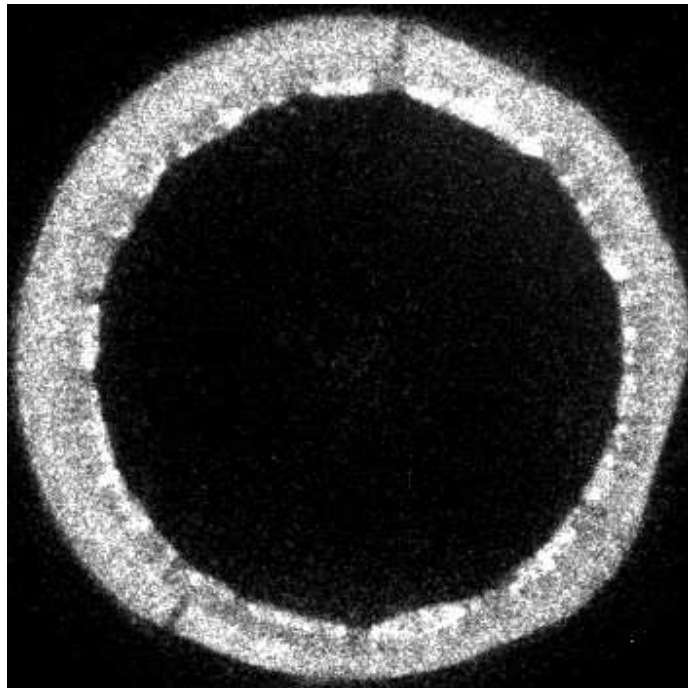


Figure H.52: Chemiluminescence from run 022 with no initiator gas injection.

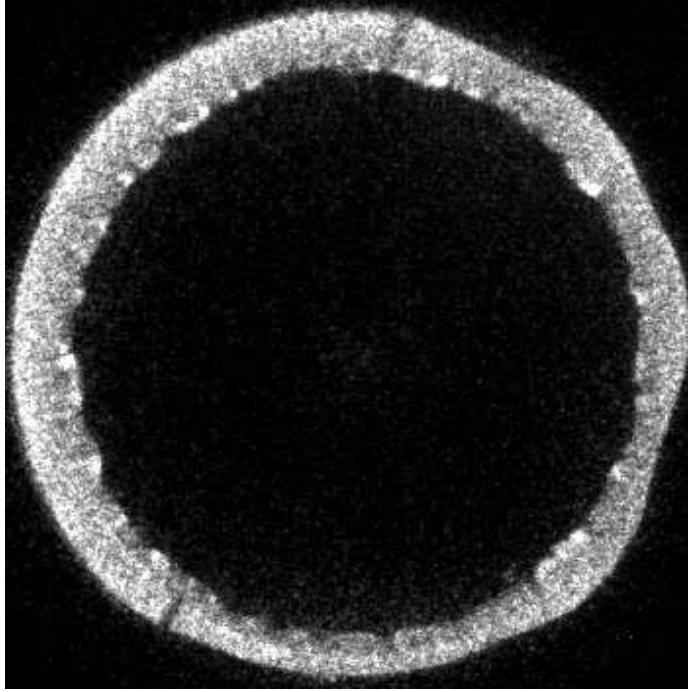


Figure H.53: Chemiluminescence from run 023 with no initiator gas injection.

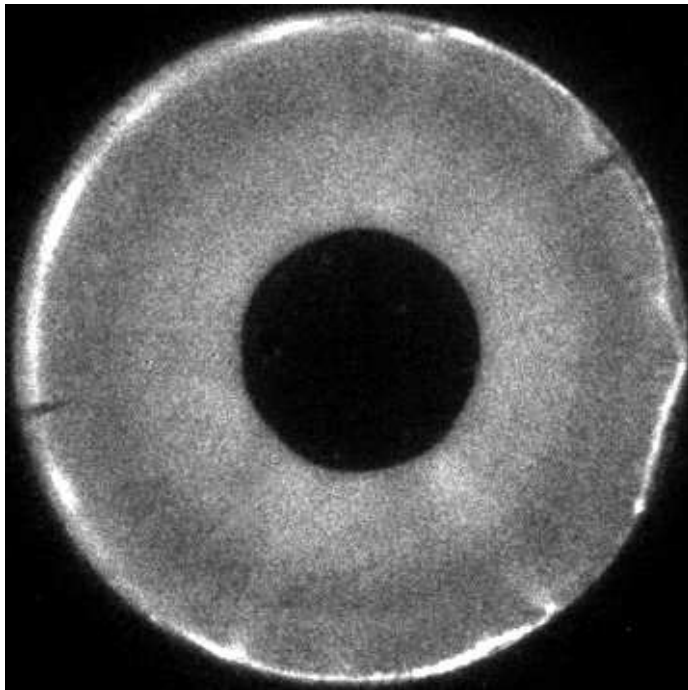


Figure H.54: Chemiluminescence from run 024 with no initiator gas injection.

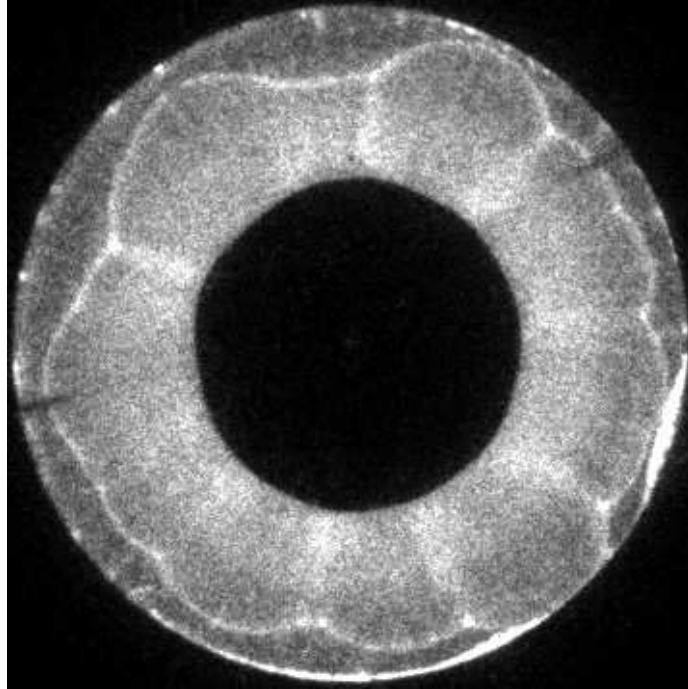


Figure H.55: Chemiluminescence from run 025 with no initiator gas injection.

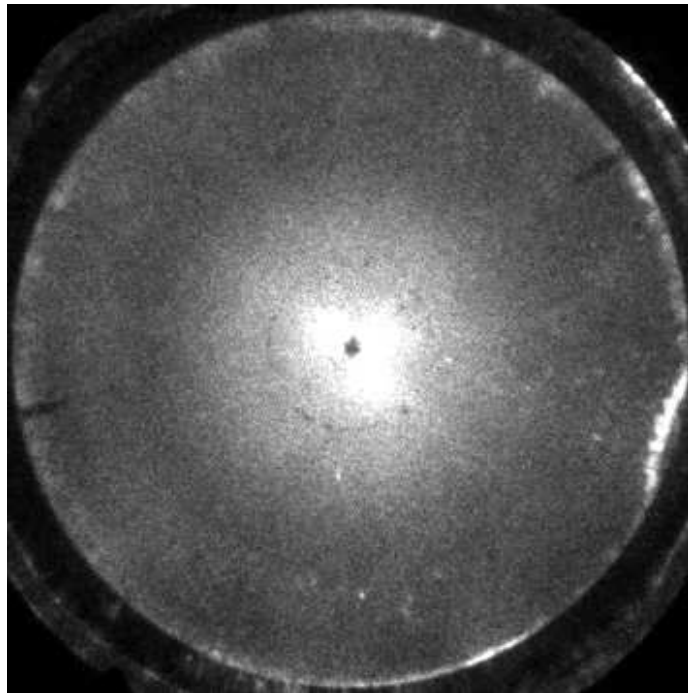


Figure H.56: Chemiluminescence from run 026 with no initiator gas injection.

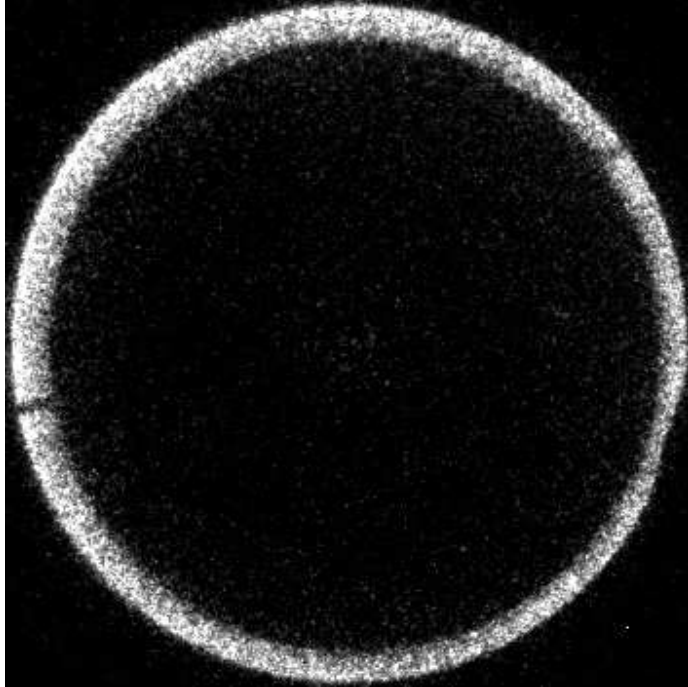


Figure H.57: Chemiluminescence from run 027 with no initiator gas injection.

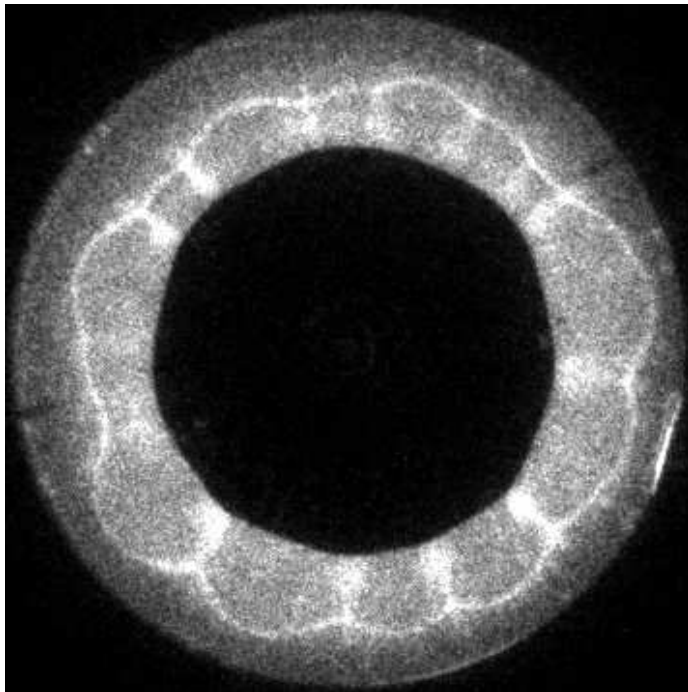


Figure H.58: Chemiluminescence from run 028 with no initiator gas injection.

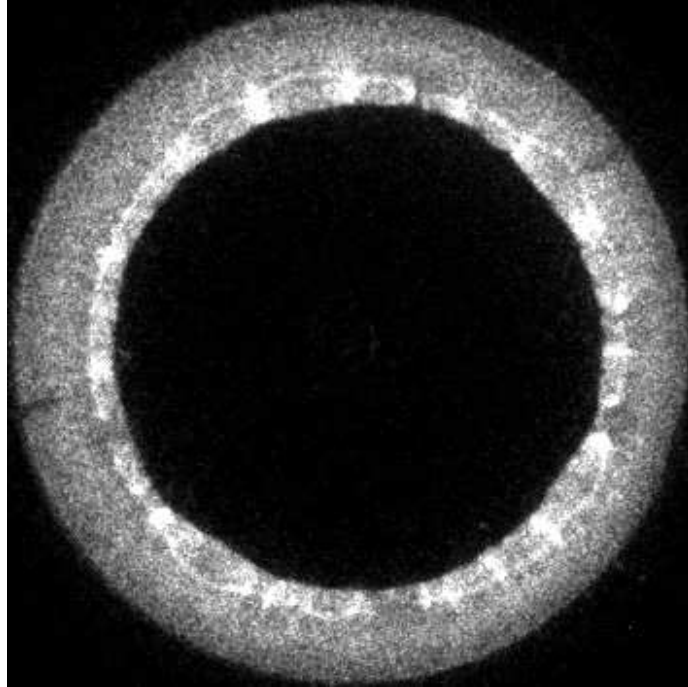


Figure H.59: Chemiluminescence from run 029 with no initiator gas injection.

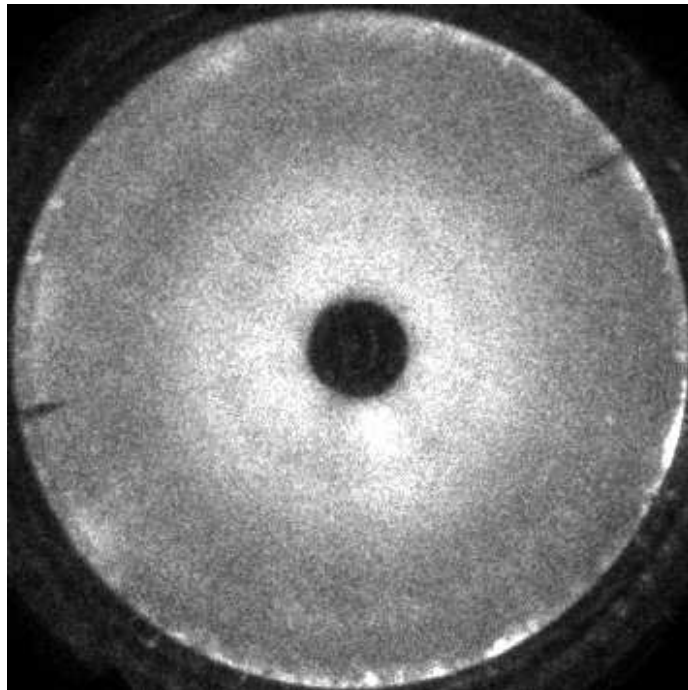


Figure H.60: Chemiluminescence from run 030 with no initiator gas injection.

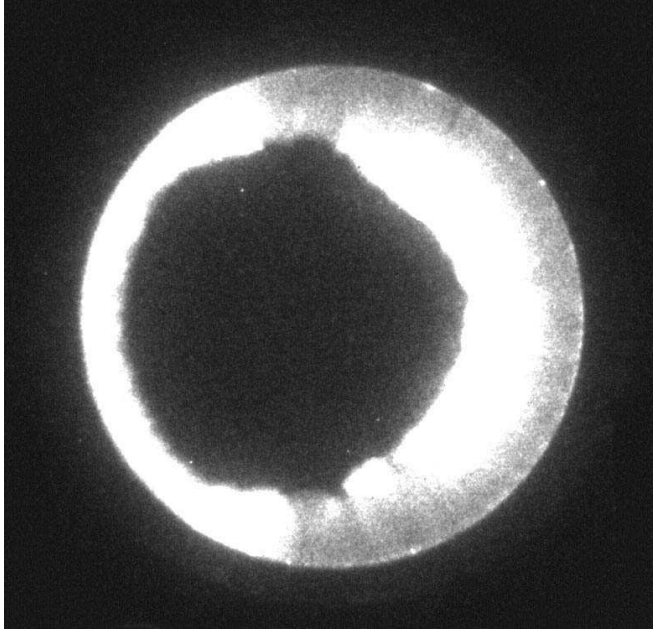


Figure H.61: Chemiluminescence from run 050, image 1 of 8, with no initiator gas injection.

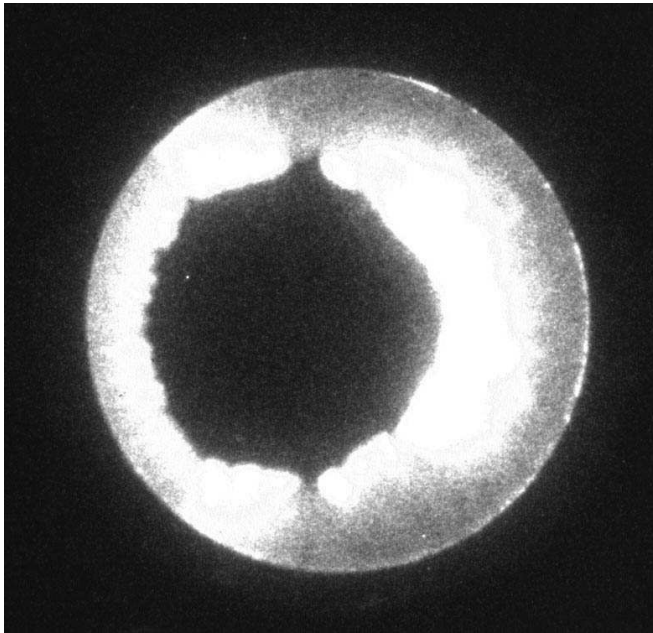


Figure H.62: Chemiluminescence from run 050, image 2 of 8, with no initiator gas injection.

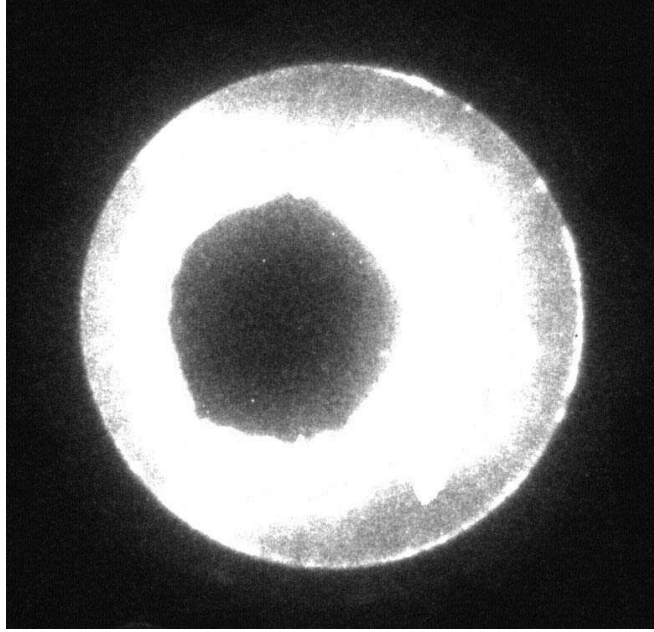


Figure H.63: Chemiluminescence from run 050, image 3 of 8, with no initiator gas injection.

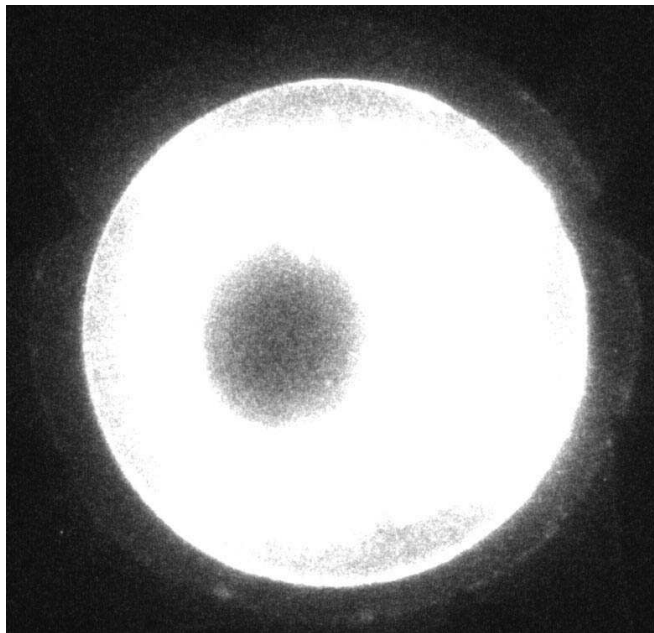


Figure H.64: Chemiluminescence from run 050, image 4 of 8, with no initiator gas injection.

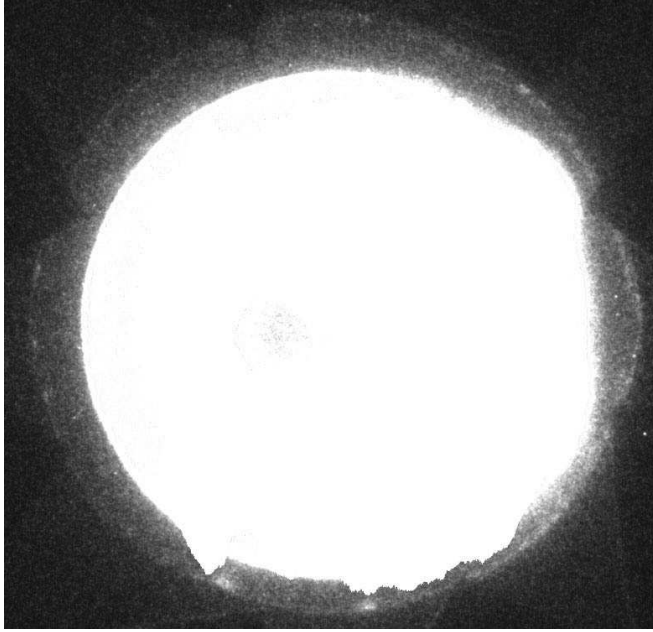


Figure H.65: Chemiluminescence from run 050, image 5 of 8, with no initiator gas injection.

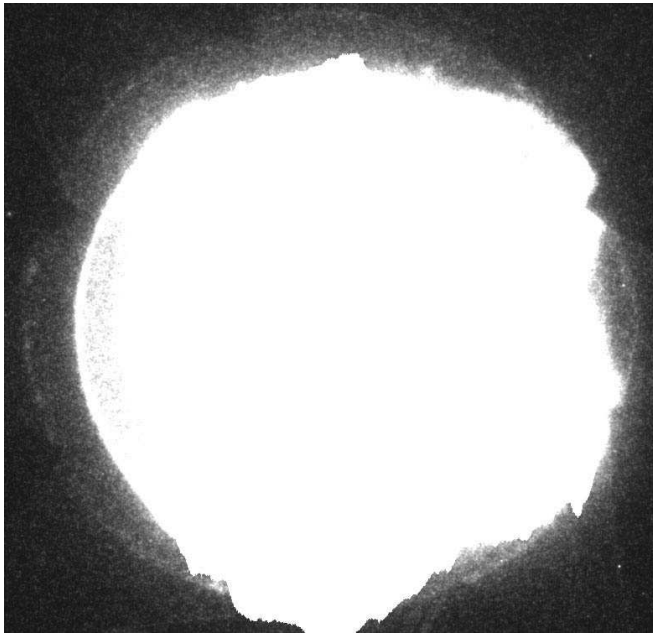


Figure H.66: Chemiluminescence from run 050, image 6 of 8, with no initiator gas injection.

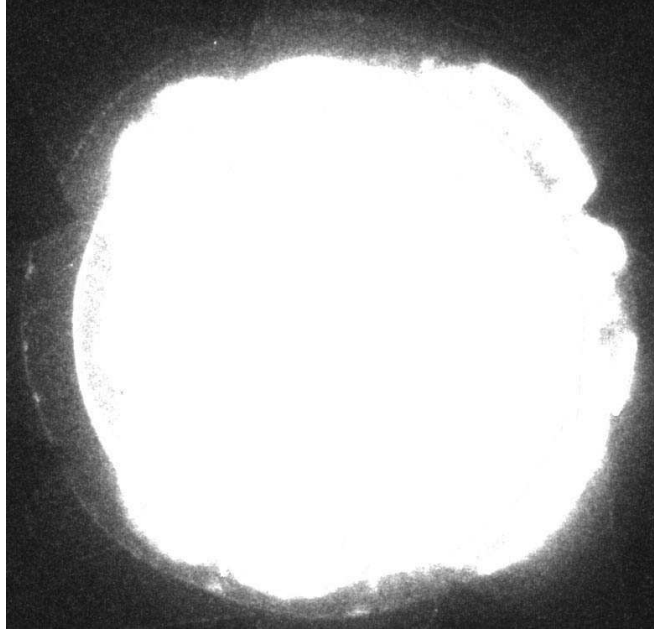


Figure H.67: Chemiluminescence from run 050, image 7 of 8, with no initiator gas injection.

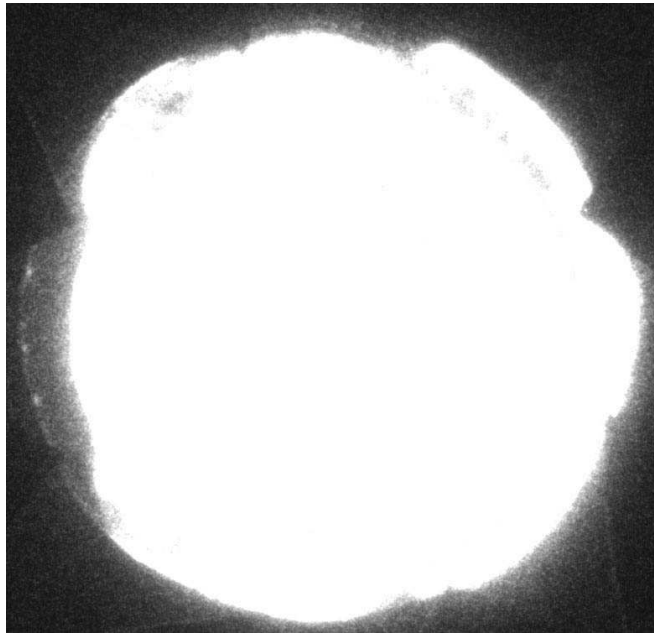


Figure H.68: Chemiluminescence from run 050, image 8 of 8, with no initiator gas injection.

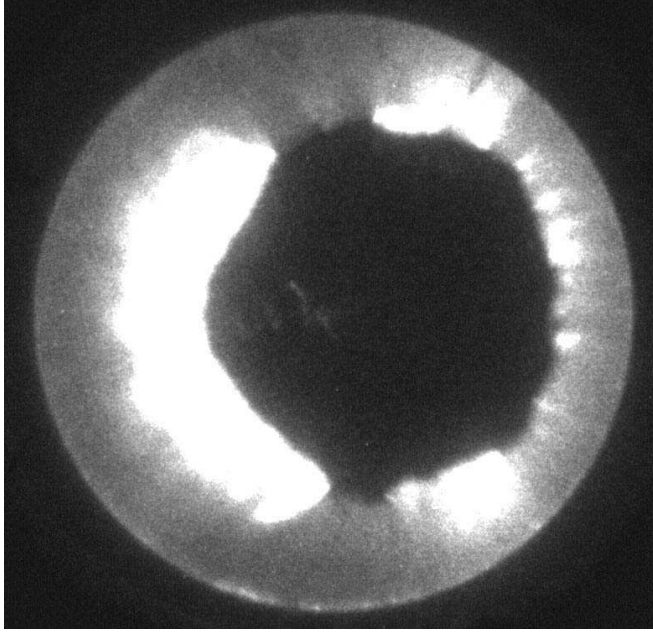


Figure H.69: Chemiluminescence from run 053, image 1 of 8, with no initiator gas injection.

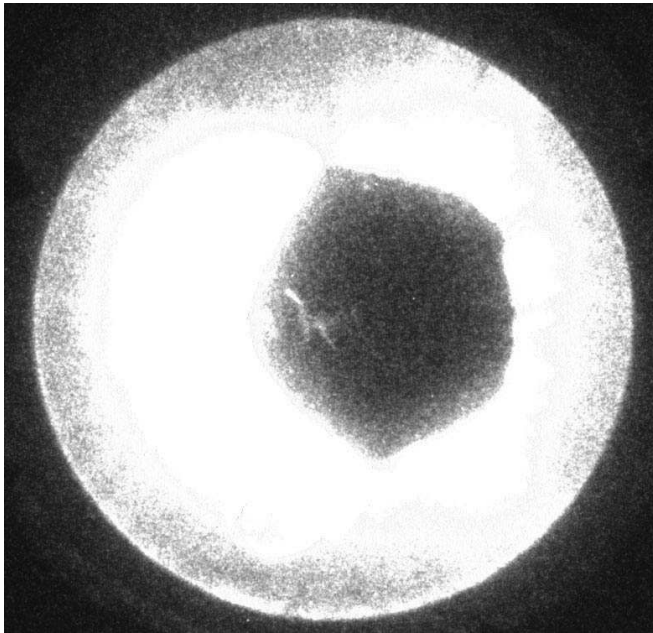


Figure H.70: Chemiluminescence from run 053, image 2 of 8, with no initiator gas injection.

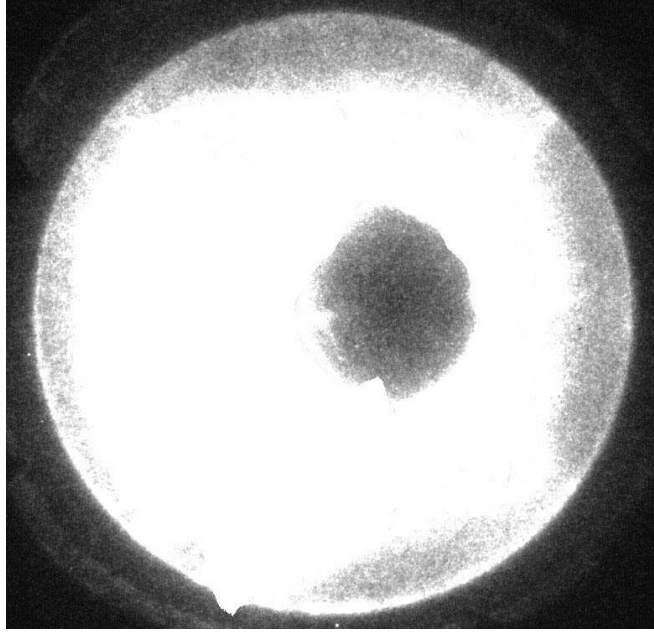


Figure H.71: Chemiluminescence from run 053, image 3 of 8, with no initiator gas injection.

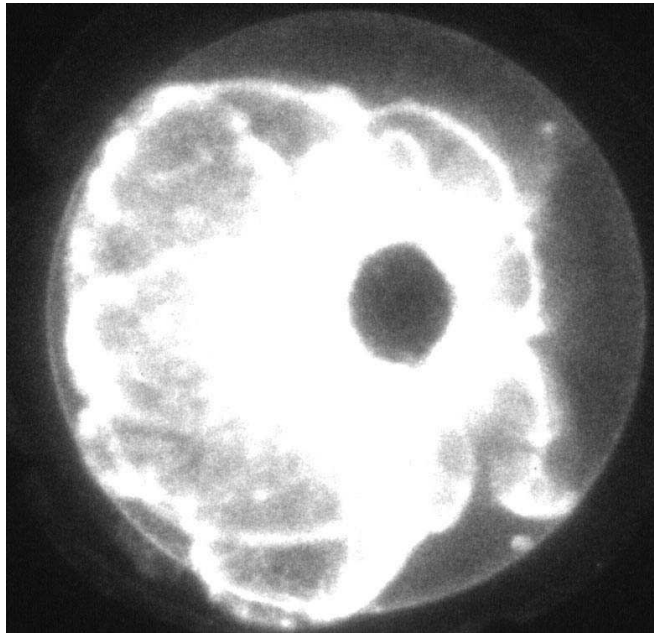


Figure H.72: Chemiluminescence from run 053, image 4 of 8, with no initiator gas injection.

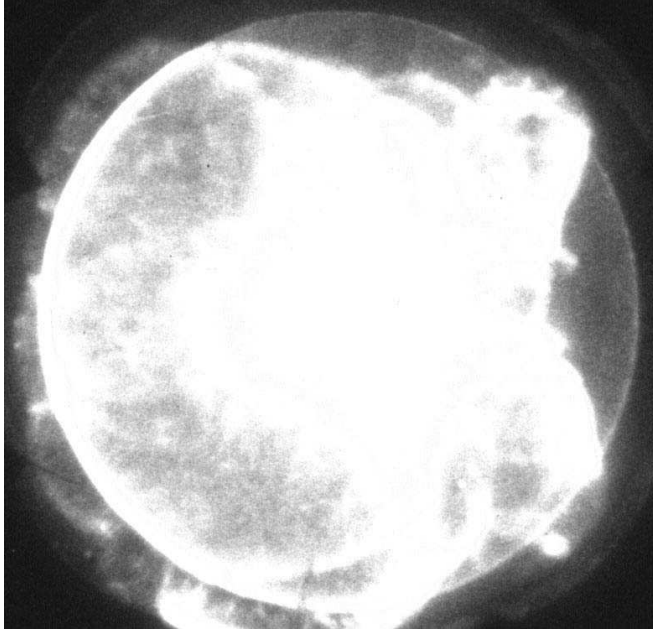


Figure H.73: Chemiluminescence from run 053, image 5 of 8, with no initiator gas injection.

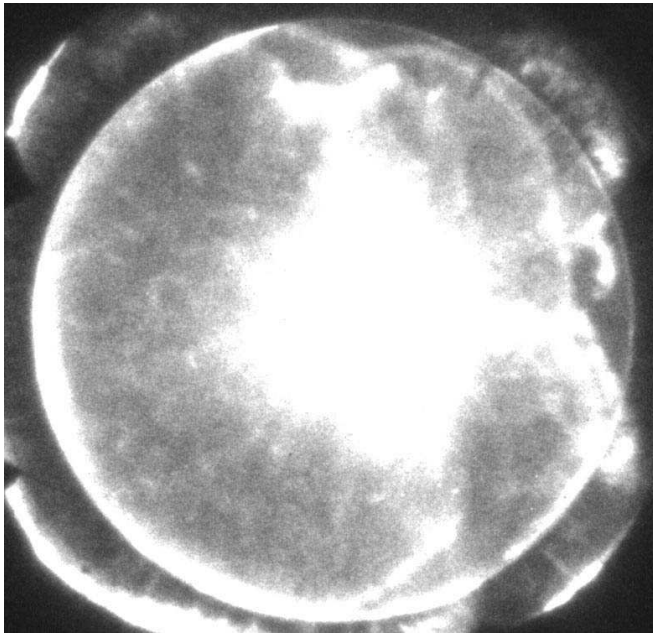


Figure H.74: Chemiluminescence from run 053, image 6 of 8, with no initiator gas injection.

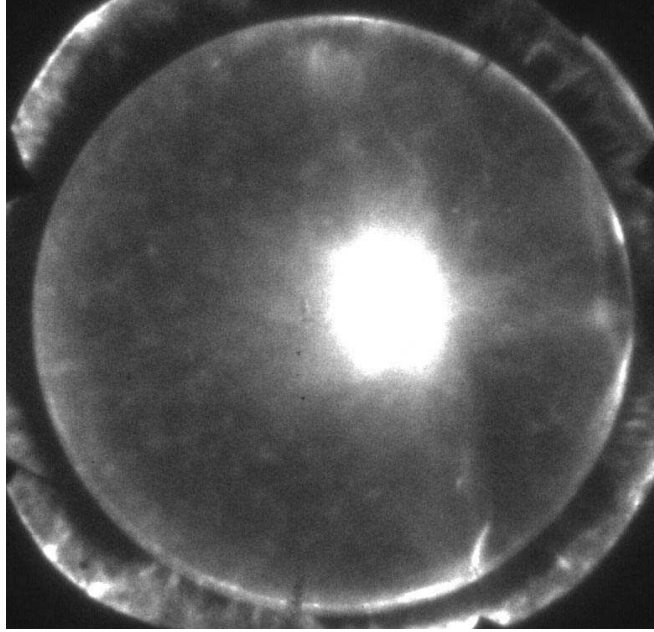


Figure H.75: Chemiluminescence from run 053, image 7 of 8, with no initiator gas injection.

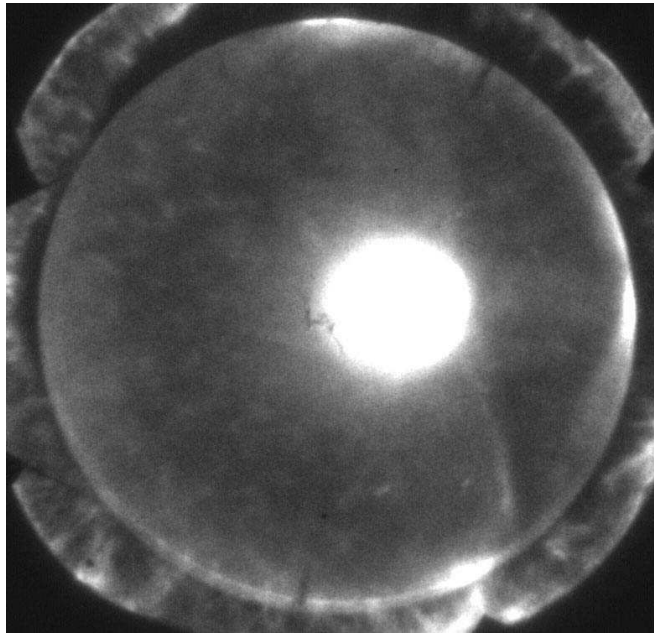


Figure H.76: Chemiluminescence from run 053, image 8 of 8, with no initiator gas injection.

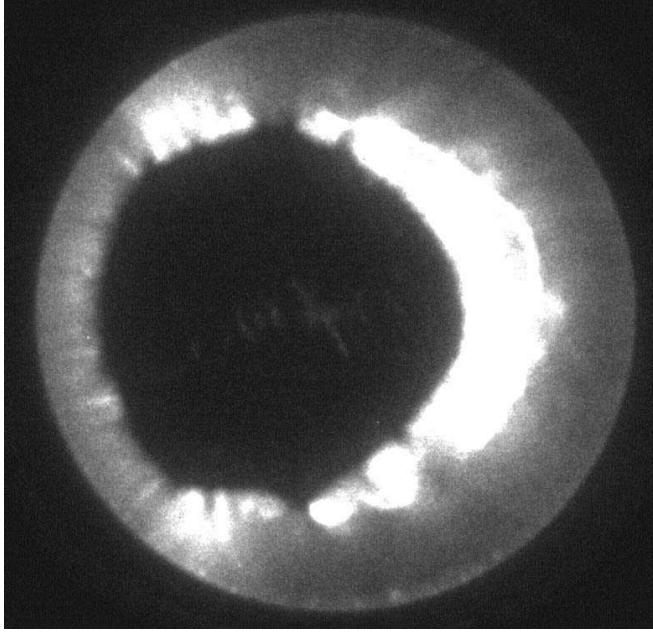


Figure H.77: Chemiluminescence from run 054, image 1 of 8, with no initiator gas injection.

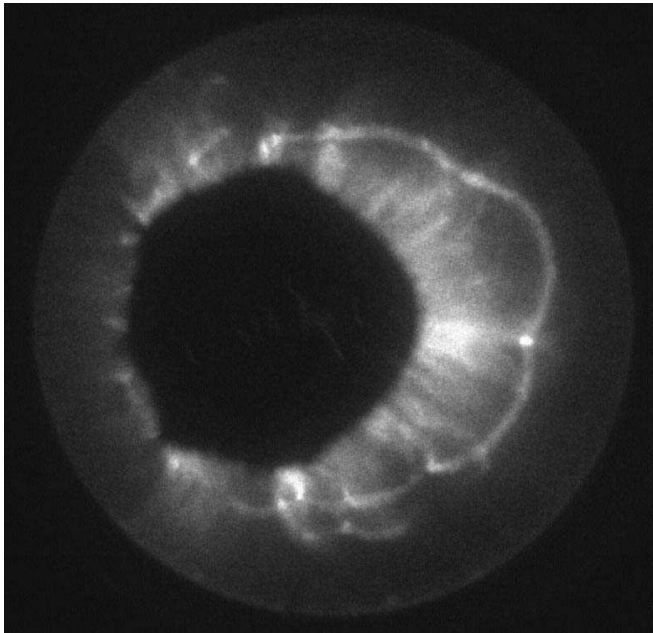


Figure H.78: Chemiluminescence from run 054, image 2 of 8, with no initiator gas injection.

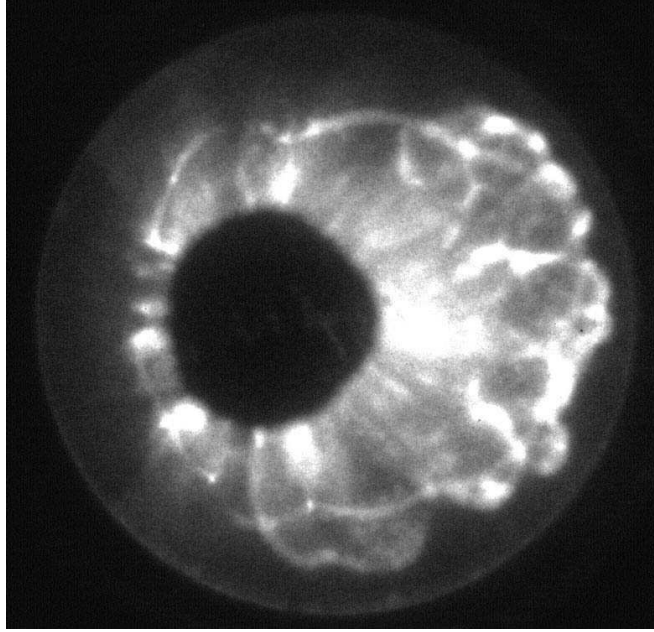


Figure H.79: Chemiluminescence from run 054, image 3 of 8, with no initiator gas injection.

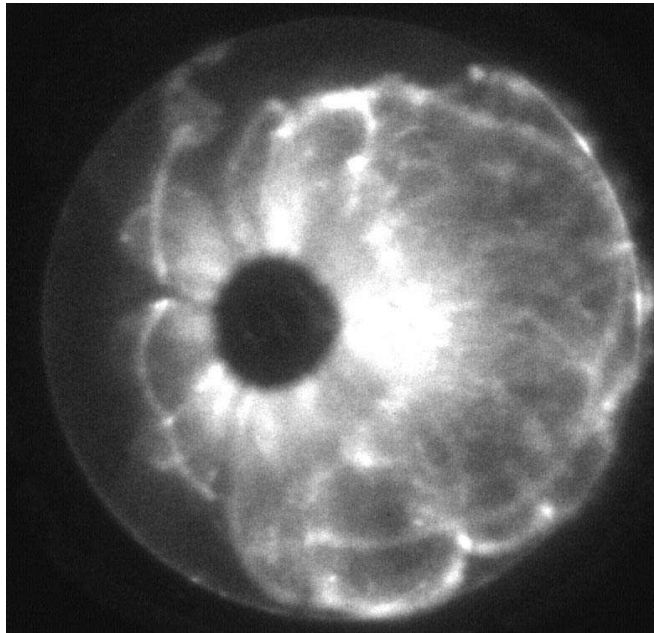


Figure H.80: Chemiluminescence from run 054, image 4 of 8, with no initiator gas injection.

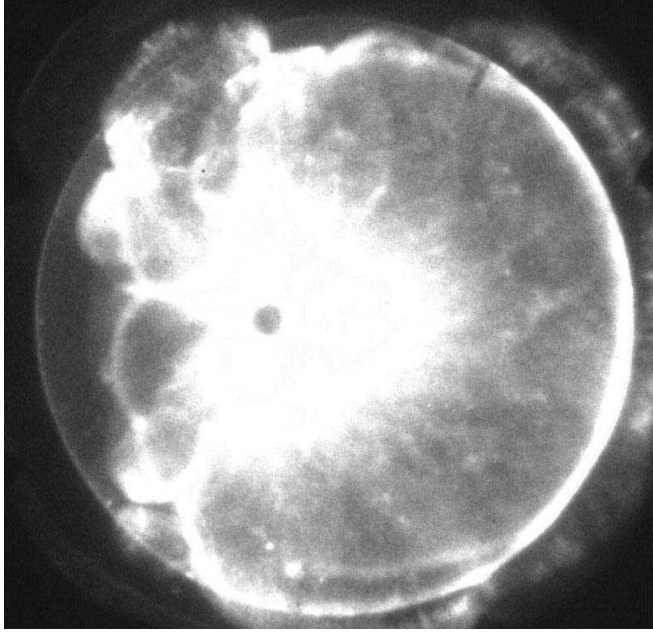


Figure H.81: Chemiluminescence from run 054, image 5 of 8, with no initiator gas injection.

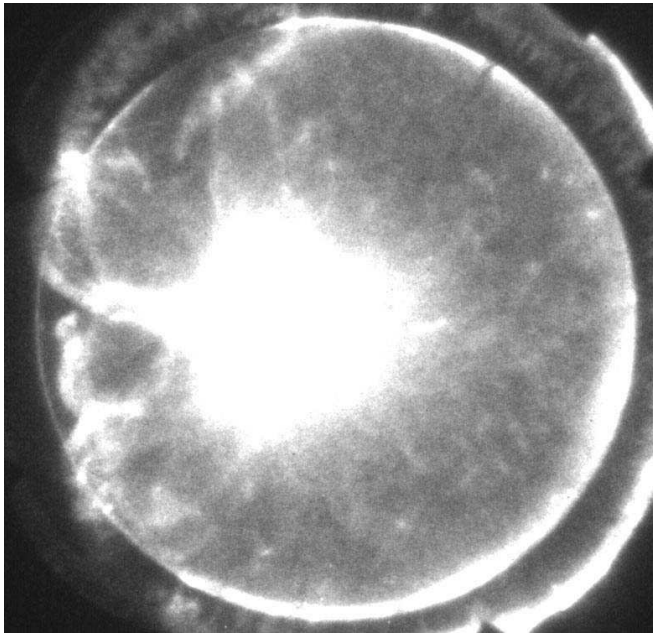


Figure H.82: Chemiluminescence from run 054, image 6 of 8, with no initiator gas injection.

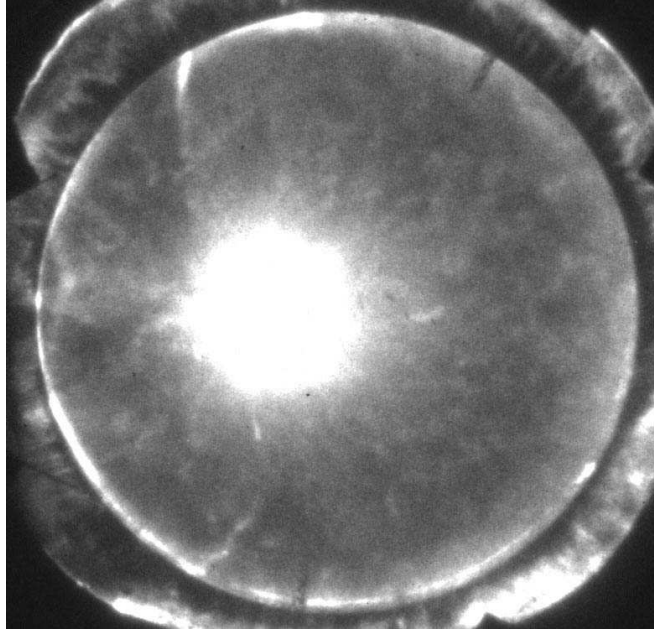


Figure H.83: Chemiluminescence from run 054, image 7 of 8, with no initiator gas injection.

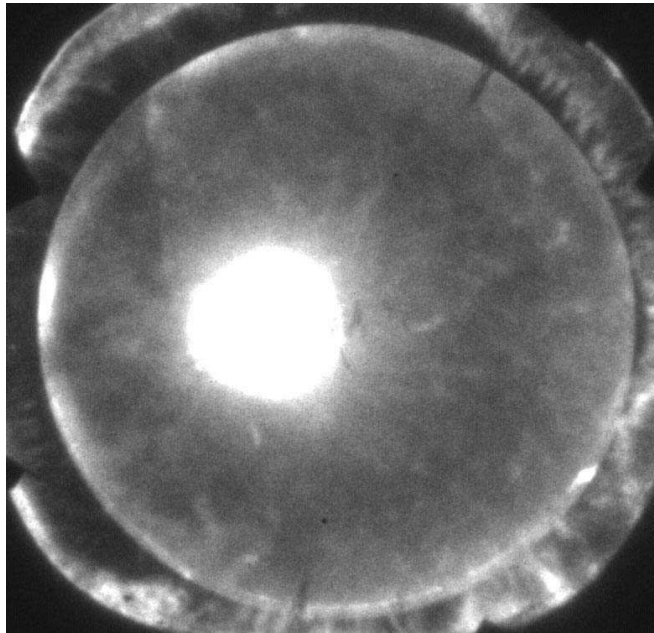


Figure H.84: Chemiluminescence from run 054, image 8 of 8, with no initiator gas injection.

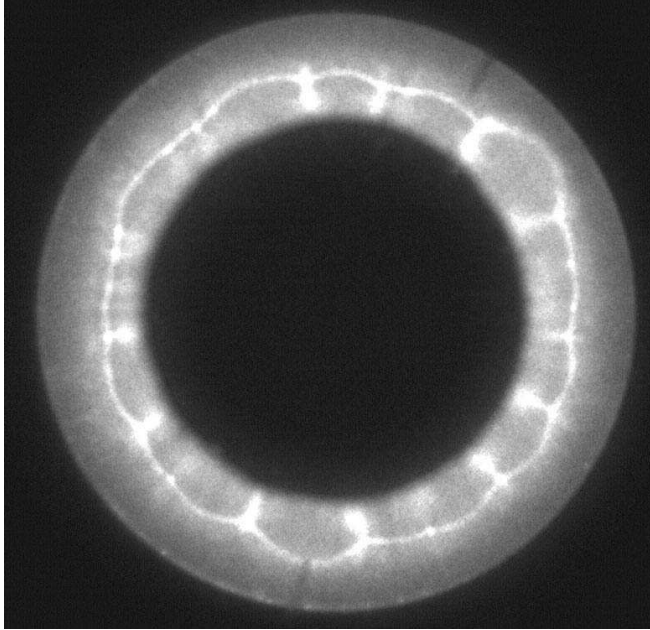


Figure H.85: Chemiluminescence from run 055, image 1 of 8, with no initiator gas injection.

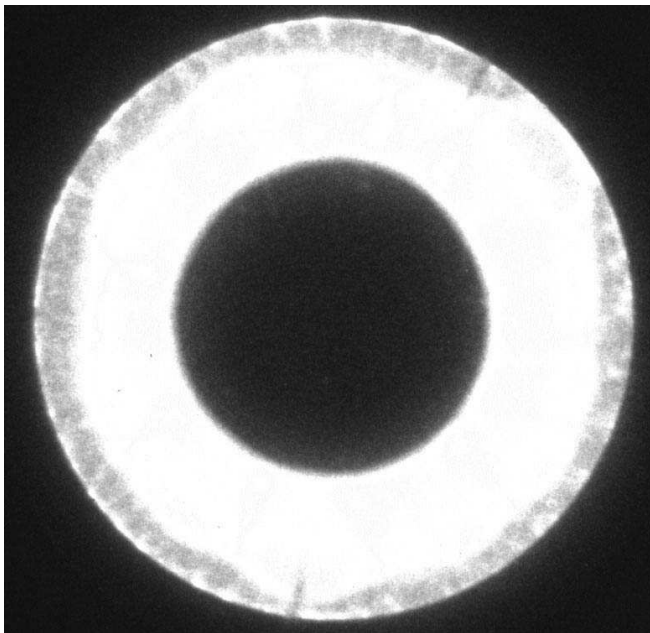


Figure H.86: Chemiluminescence from run 055, image 2 of 8, with no initiator gas injection.

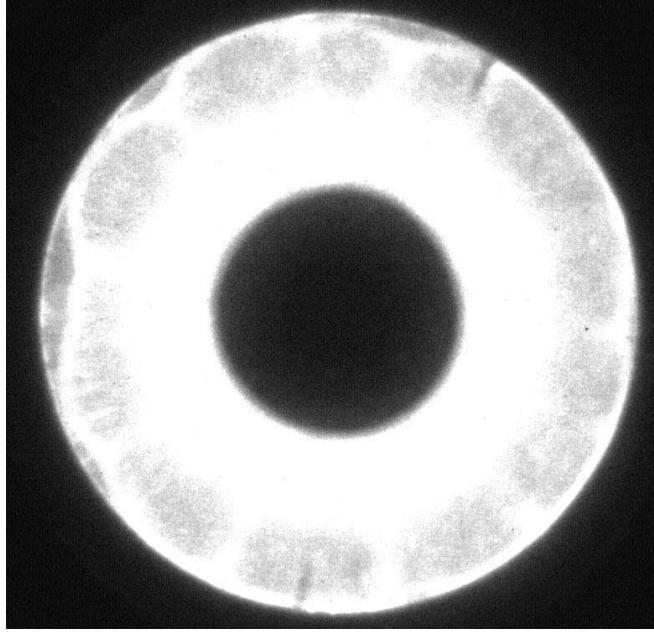


Figure H.87: Chemiluminescence from run 055, image 3 of 8, with no initiator gas injection.

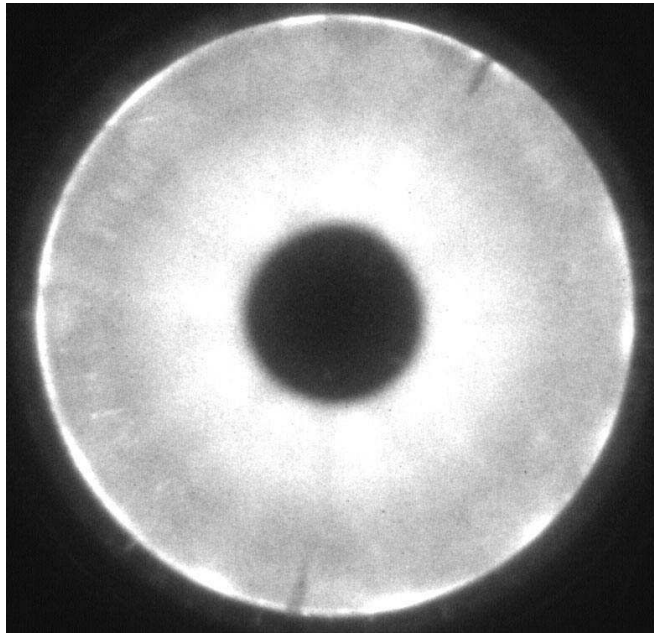


Figure H.88: Chemiluminescence from run 055, image 4 of 8, with no initiator gas injection.

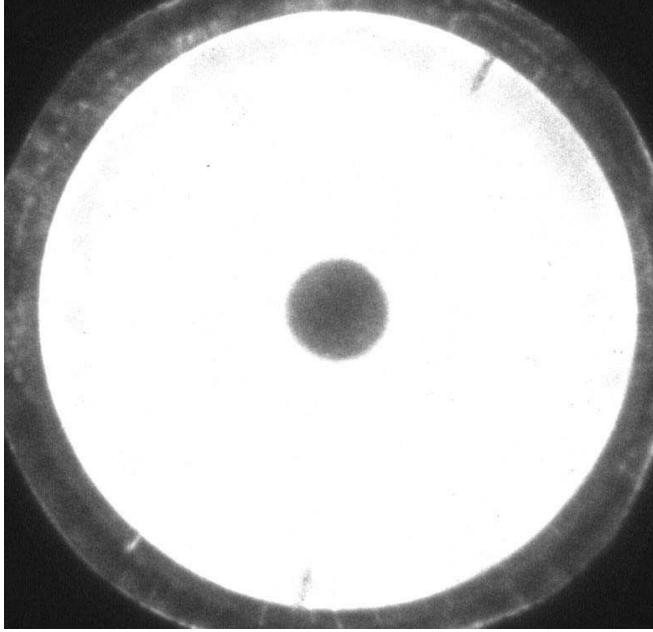


Figure H.89: Chemiluminescence from run 055, image 5 of 8, with no initiator gas injection.

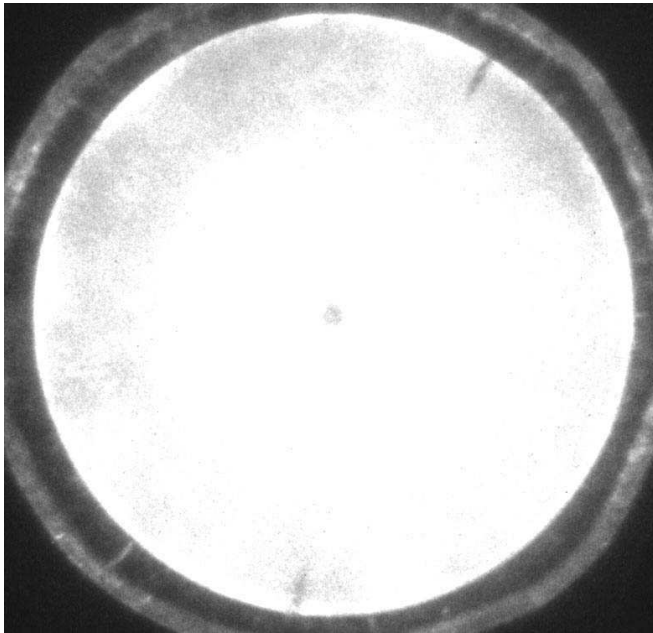


Figure H.90: Chemiluminescence from run 055, image 6 of 8, with no initiator gas injection.

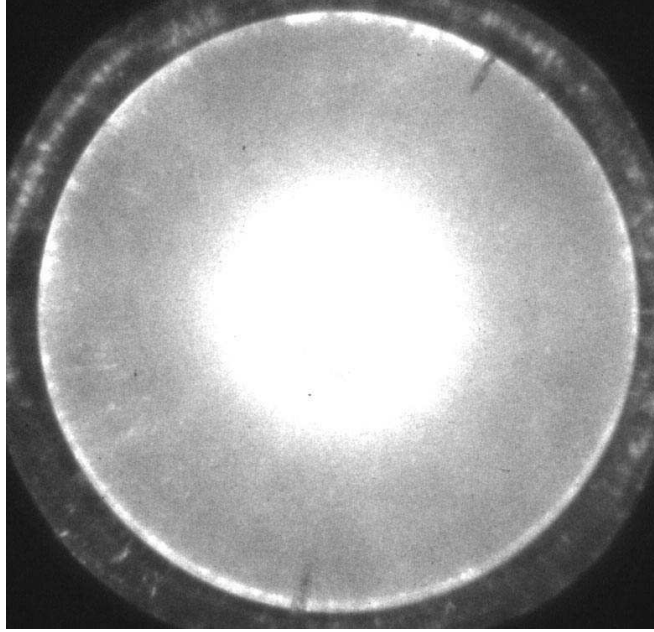


Figure H.91: Chemiluminescence from run 055, image 7 of 8, with no initiator gas injection.

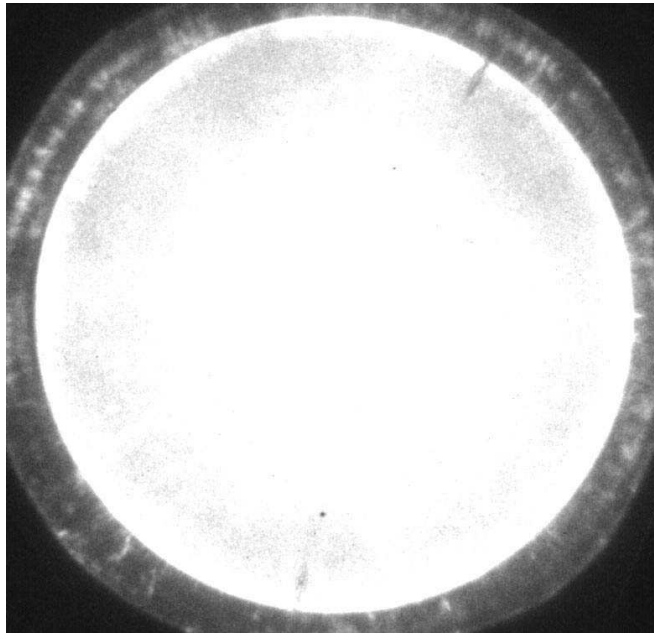


Figure H.92: Chemiluminescence from run 055, image 8 of 8, with no initiator gas injection.

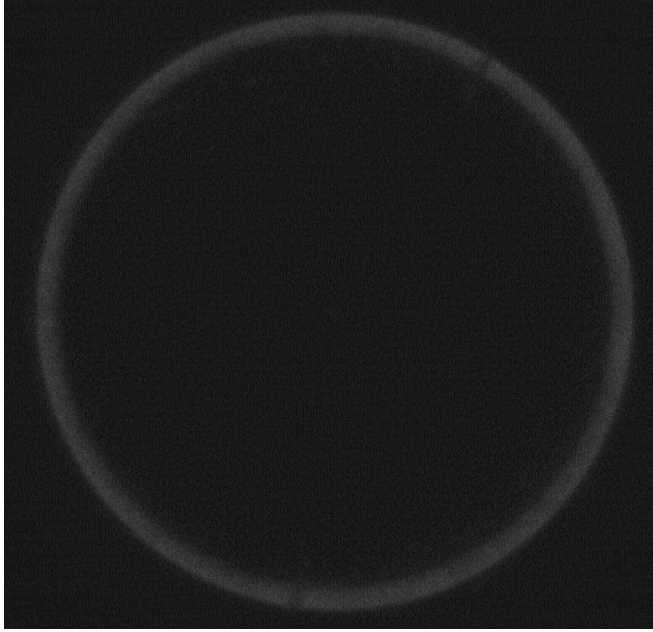


Figure H.93: Chemiluminescence from run 056, image 1 of 8, with no initiator gas injection.

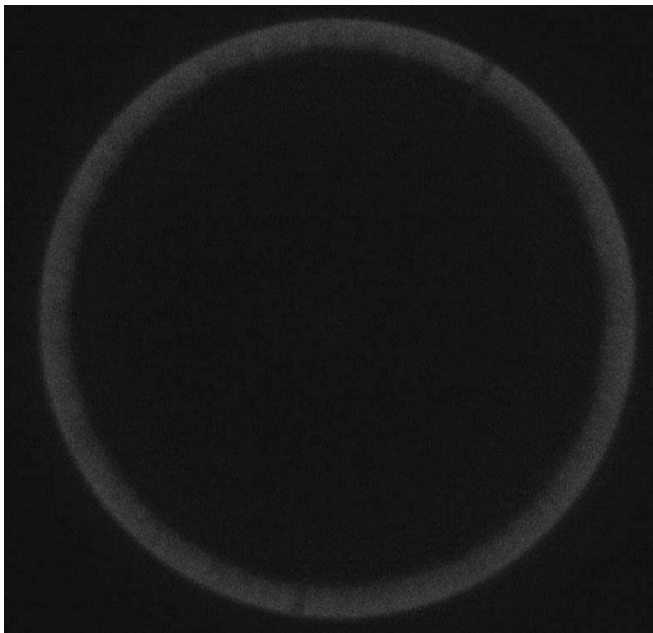


Figure H.94: Chemiluminescence from run 056, image 2 of 8, with no initiator gas injection.

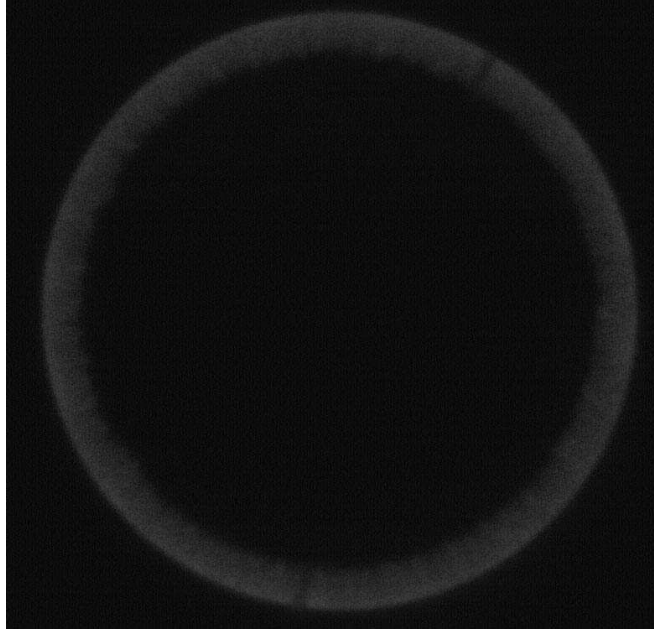


Figure H.95: Chemiluminescence from run 056, image 3 of 8, with no initiator gas injection.

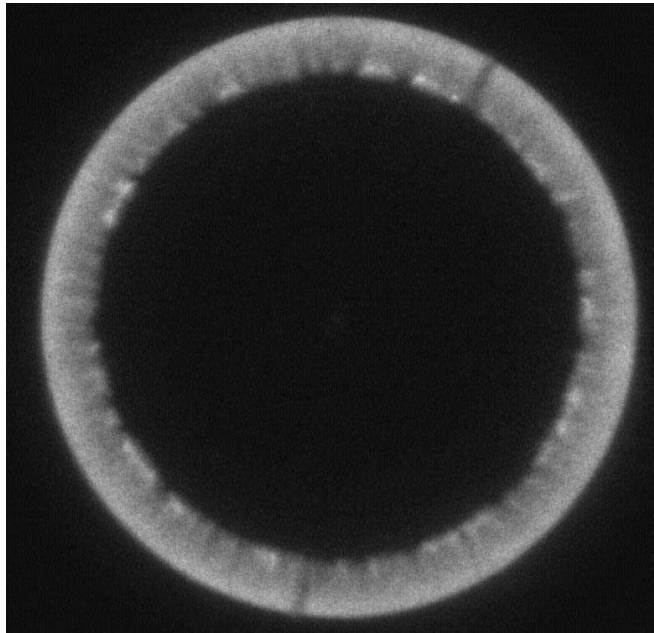


Figure H.96: Chemiluminescence from run 056, image 4 of 8, with no initiator gas injection.

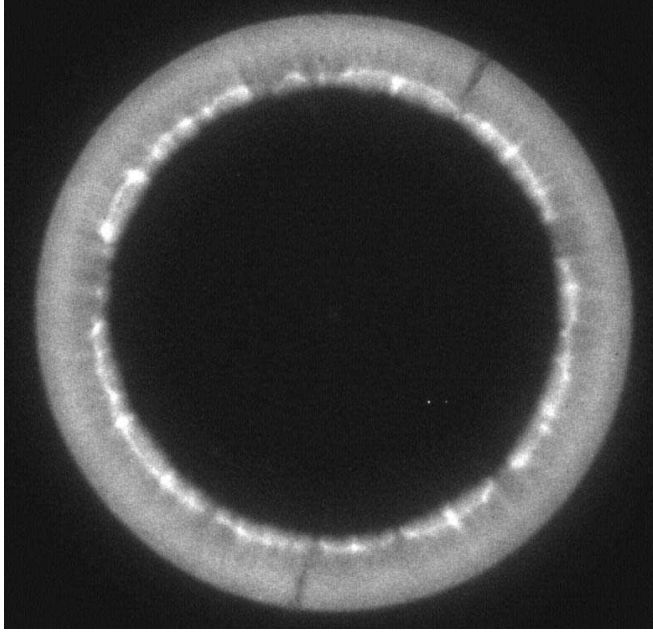


Figure H.97: Chemiluminescence from run 056, image 5 of 8, with no initiator gas injection.

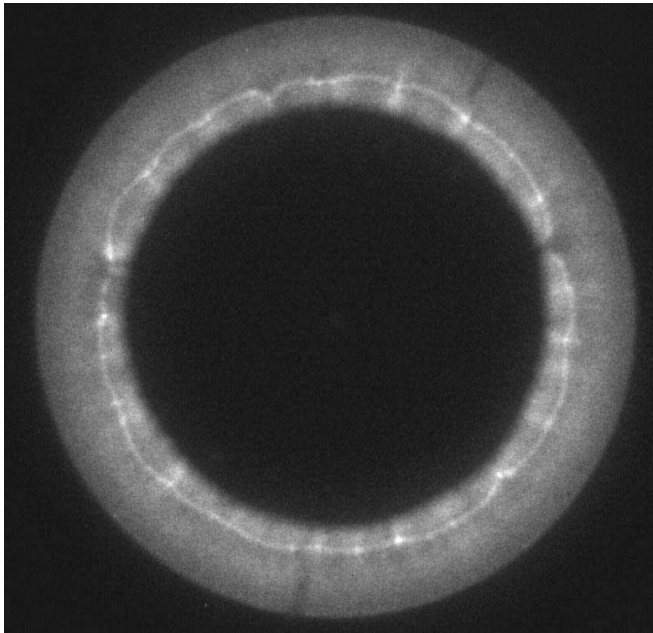


Figure H.98: Chemiluminescence from run 056, image 6 of 8, with no initiator gas injection.

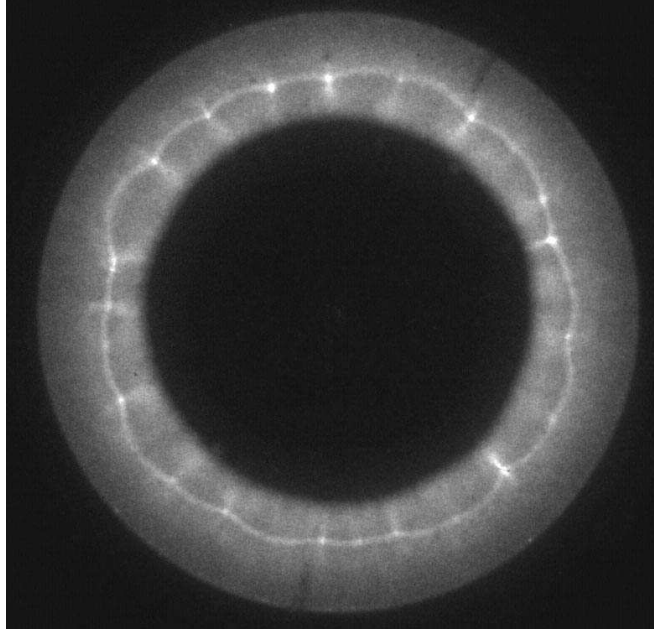


Figure H.99: Chemiluminescence from run 056, image 7 of 8, with no initiator gas injection.

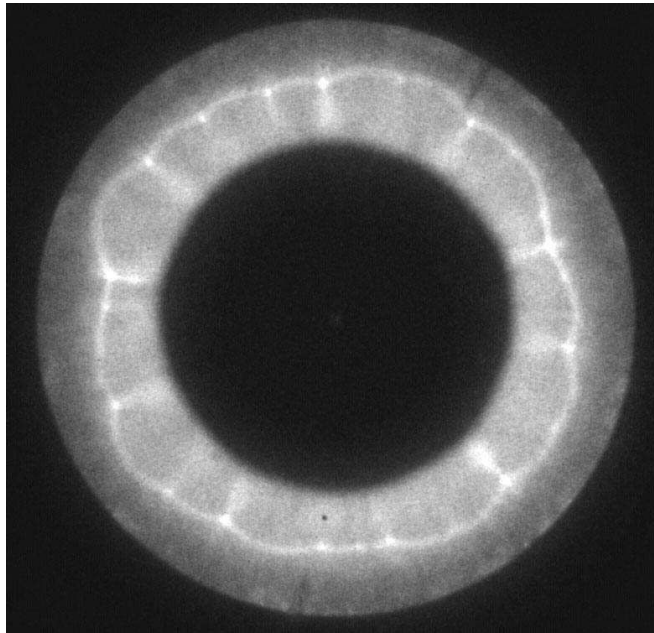


Figure H.100: Chemiluminescence from run 056, image 8 of 8, with no initiator gas injection.

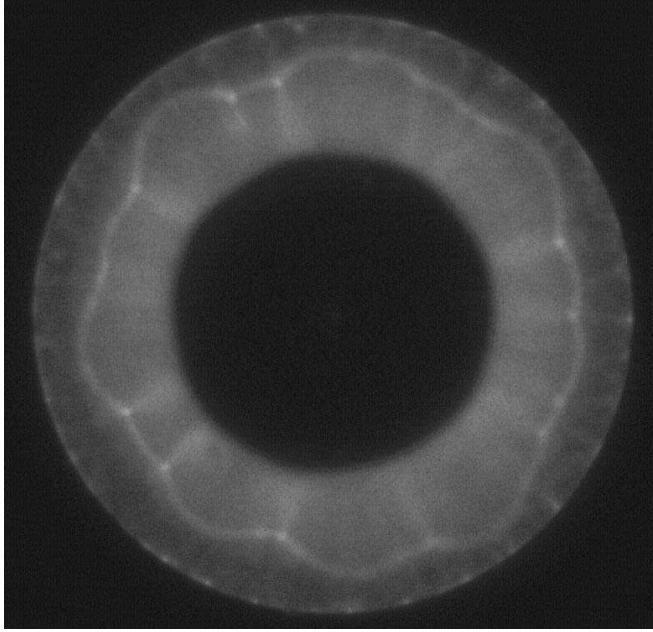


Figure H.101: Chemiluminescence from run 057, image 1 of 8, with no initiator gas injection.

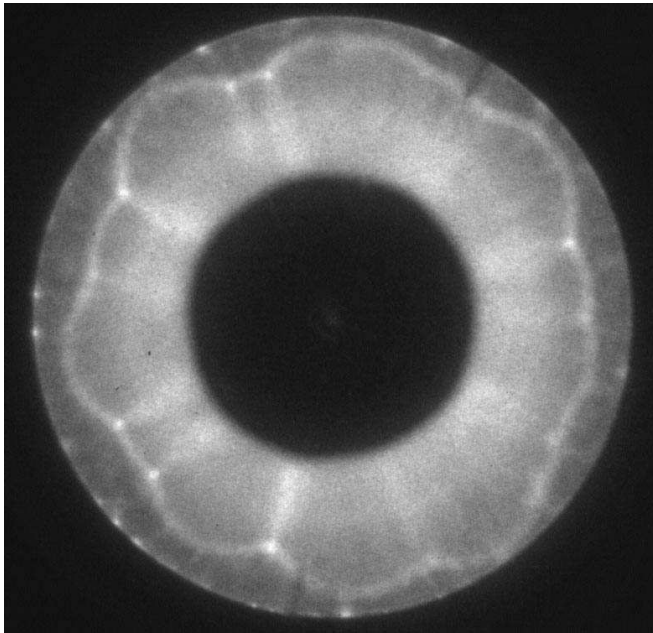


Figure H.102: Chemiluminescence from run 057, image 2 of 8, with no initiator gas injection.

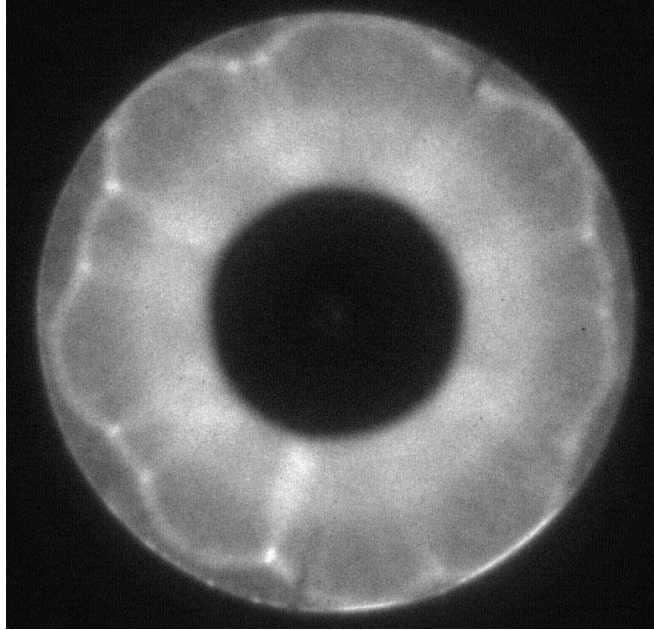


Figure H.103: Chemiluminescence from run 057, image 3 of 8, with no initiator gas injection.

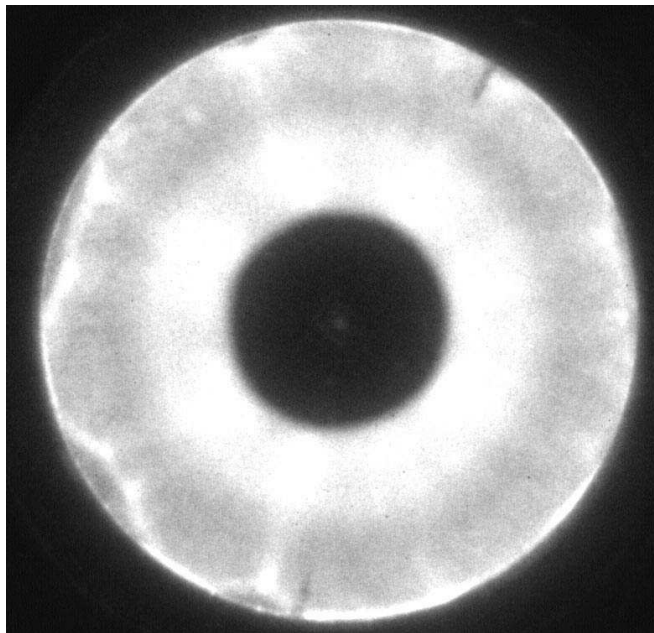


Figure H.104: Chemiluminescence from run 057, image 4 of 8, with no initiator gas injection.

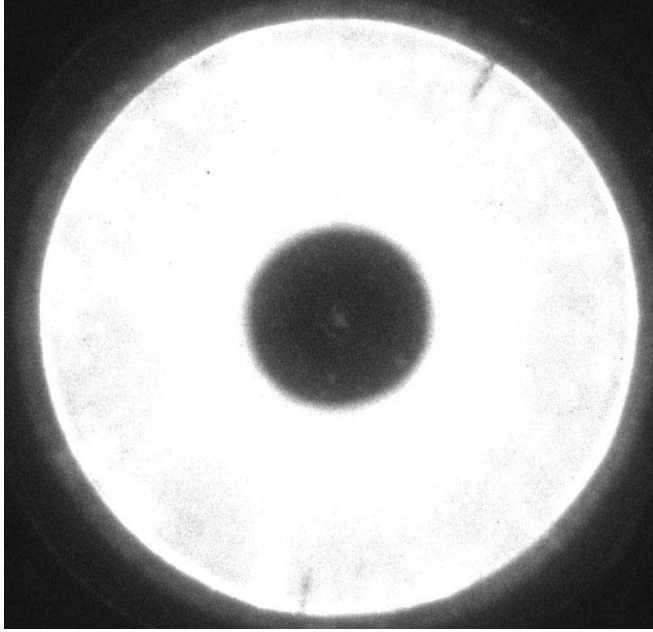


Figure H.105: Chemiluminescence from run 057, image 5 of 8, with no initiator gas injection.

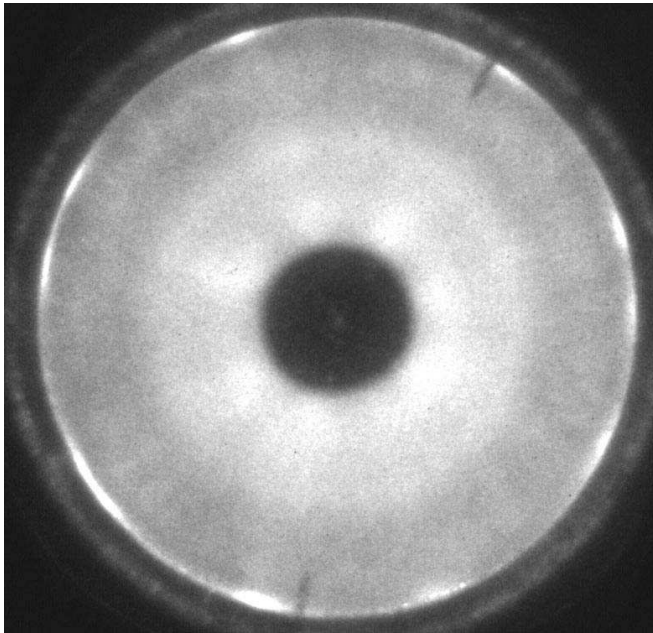


Figure H.106: Chemiluminescence from run 057, image 6 of 8, with no initiator gas injection.

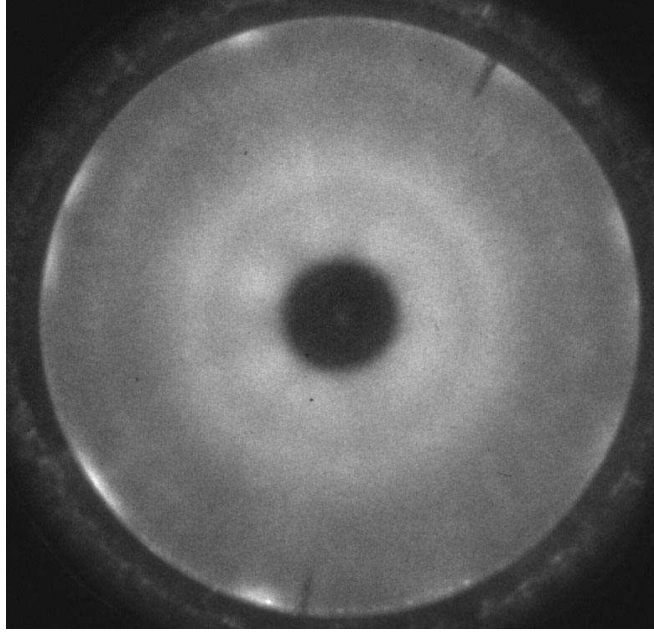


Figure H.107: Chemiluminescence from run 057, image 7 of 8, with no initiator gas injection.

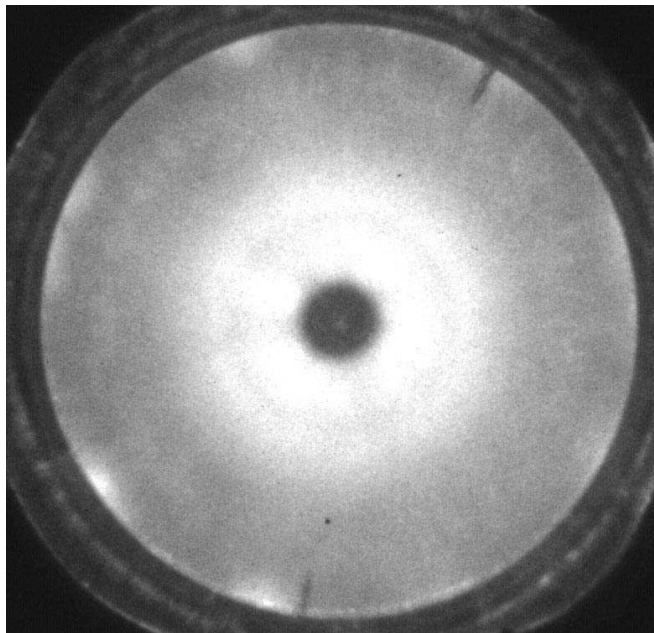


Figure H.108: Chemiluminescence from run 057, image 8 of 8, with no initiator gas injection.

## H.5 Run Matrix: Dynamic Gas Injection

DTI Run	NCF Run	Fuel	N <sub>2</sub> fraction	Focus	P <sub>1</sub> (bar)	Initiator overfill	Mode of initiation
103	335	C <sub>2</sub> H <sub>4</sub>	1.000	near	1.05	-29.6	no detonation
104	336	C <sub>2</sub> H <sub>4</sub>	0.300	near	1.05	-29.6	detonation
105	337	C <sub>2</sub> H <sub>4</sub>	0.300	near	1.05	-29.6	detonation
106	338	C <sub>2</sub> H <sub>4</sub>	0.300	near	1.05	-29.6	detonation
107	339	C <sub>2</sub> H <sub>4</sub>	0.738	near	1.05	-29.6	no detonation
108	340	C <sub>2</sub> H <sub>4</sub>	0.500	near	1.05	-29.6	detonation
109	341	C <sub>2</sub> H <sub>4</sub>	0.600	near	1.05	-29.6	detonation
110	342	C <sub>2</sub> H <sub>4</sub>	0.700	near	1.05	-29.6	no detonation
111	343	C <sub>2</sub> H <sub>4</sub>	0.700	near	1.10	60.7	detonation
112	344	C <sub>2</sub> H <sub>4</sub>	0.738	near	1.10	60.7	detonation
113	345	C <sub>2</sub> H <sub>4</sub>	1.000	near	1.10	60.7	detonation
114	346	C <sub>2</sub> H <sub>4</sub>	0.738	near	1.05	-31.1	no detonation
115	347	C <sub>2</sub> H <sub>4</sub>	0.738	near	1.08	15.2	detonation
116	348	C <sub>2</sub> H <sub>4</sub>	0.738	near	1.06	-7.4	no detonation
117	349	C <sub>2</sub> H <sub>4</sub>	0.738	near	1.07	-0.9	no detonation
118	350	C <sub>2</sub> H <sub>4</sub>	0.738	near	1.07	6.3	detonation
119	351	C <sub>2</sub> H <sub>4</sub>	0.738	near	1.07	2.7	DDT
120	352	C <sub>2</sub> H <sub>4</sub>	0.738	near	1.07	4.5	DDT
121	353	C <sub>2</sub> H <sub>4</sub>	0.800	near	1.07	6.3	no detonation
122	354	C <sub>2</sub> H <sub>4</sub>	0.800	near	1.08	15.2	no detonation
123	355	C <sub>2</sub> H <sub>4</sub>	1.000	near	1.07	6.3	no detonation
124	356	C <sub>3</sub> H <sub>8</sub>	0.700	near	1.07	6.3	no detonation
125	357	C <sub>3</sub> H <sub>8</sub>	0.500	near	1.07	6.3	detonation
126	358	C <sub>3</sub> H <sub>8</sub>	0.600	near	1.07	6.3	DDT

Table H.3: Experimental properties of each run. “DTI Run” is for the dynamic toroidal initiator run number and “NCF Run” is the narrow channel facility run number. All mixtures were stoichiometric fuel-oxygen diluted with nitrogen. The “Focus” location was either near the end wall or far from it, as described in the text. The initial pressure before initiator gas injection on all runs was 0.99 bar.  $P_1$  was the pressure at the instant of spark ignition. “Initiator overfill” is the volume of the initiator channels filled with acetylene-oxygen initiator gas.

DTI Run	NCF Run	Fuel	N <sub>2</sub> fraction	Focus	P <sub>1</sub> (bar)	Initiator overfill	Mode of initiation
127	359	C <sub>3</sub> H <sub>8</sub>	0.600	near	1.08	15.2	detonation
128	360	C <sub>3</sub> H <sub>8</sub>	0.700	near	1.08	15.2	no detonation
129	361	C <sub>3</sub> H <sub>8</sub>	0.700	near	1.08	23.9	detonation
130	362	C <sub>3</sub> H <sub>8</sub>	0.758	near	1.08	23.9	no detonation
131	363	C <sub>3</sub> H <sub>8</sub>	0.758	near	1.08	32.4	no detonation
132	364	C <sub>3</sub> H <sub>8</sub>	0.758	near	1.10	56.9	detonation
133	365	C <sub>3</sub> H <sub>8</sub>	0.758	near	1.11	72.5	detonation
134	366	C <sub>3</sub> H <sub>8</sub>	0.758	near	1.09	48.9	detonation
135	367	C <sub>3</sub> H <sub>8</sub>	0.758	near	1.09	40.7	detonation
136	368	C <sub>3</sub> H <sub>8</sub>	0.758	near	1.09	36.6	detonation
137	369	C <sub>3</sub> H <sub>8</sub>	0.758	near	1.08	32.4	no detonation
138	370	C <sub>3</sub> H <sub>8</sub>	0.758	far	1.10	56.9	detonation
139	371	C <sub>3</sub> H <sub>8</sub>	1.000	far	1.10	56.9	no detonation
140	372	C <sub>3</sub> H <sub>8</sub>	0.758	far	1.09	36.6	no detonation
141	373	C <sub>3</sub> H <sub>8</sub>	0.758	far	1.09	46.5	no detonation
142	374	C <sub>3</sub> H <sub>8</sub>	0.758	far	1.09	51.3	detonation
143	375	C <sub>3</sub> H <sub>8</sub>	0.758	far	1.11	72.5	detonation
144	376	C <sub>3</sub> H <sub>8</sub>	1.000	far	1.11	72.5	no detonation
145	377	C <sub>2</sub> H <sub>4</sub>	0.738	far	1.07	6.3	no detonation
146	378	C <sub>2</sub> H <sub>4</sub>	0.738	far	1.08	23.9	detonation
147	379	C <sub>2</sub> H <sub>4</sub>	0.738	far	1.08	15.2	no detonation
148	380	C <sub>2</sub> H <sub>4</sub>	0.738	far	1.08	19.5	detonation
149	381	C <sub>2</sub> H <sub>4</sub>	0.738	far	1.04	-61.1	no detonation
150	382	C <sub>2</sub> H <sub>4</sub>	0.738	far	1.04	-61.1	no detonation
151	383	C <sub>2</sub> H <sub>4</sub>	0.738	far	1.03	-71.6	no detonation
152	384	C <sub>2</sub> H <sub>4</sub>	0.738	far	1.03	-71.6	no detonation
153	385	C <sub>2</sub> H <sub>4</sub>	0.738	far	1.03	-82.2	no detonation

Table H.4: Experimental properties of each run. “DTI Run” is for the dynamic toroidal initiator run number and “NCF Run” is the narrow channel facility run number. All mixtures were stoichiometric fuel-oxygen diluted with nitrogen. The “Focus” location was either near the end wall or far from it, as described in the text. The initial pressure before initiator gas injection on all runs was 0.99 bar.  $P_1$  was the pressure at the instant of spark ignition. “Initiator overfill” is the volume of the initiator channels filled with acetylene-oxygen initiator gas.

## H.6 Measured Velocities: Dynamic Gas Injection

DTI Run	Fuel	N <sub>2</sub> fraction	Initiator overfill	Mode of initiation	U <sub>3,4</sub> (m/s)	U <sub>4,5</sub> (m/s)	U <sub>AVG</sub> (m/s)
103	C <sub>2</sub> H <sub>4</sub>	1.000	-29.6	no detonation	599	568	584
104	C <sub>2</sub> H <sub>4</sub>	0.300	-29.6	detonation	1844	1844	1844
105	C <sub>2</sub> H <sub>4</sub>	0.300	-29.6	detonation	2603	2375	2489
106	C <sub>2</sub> H <sub>4</sub>	0.300	-29.6	detonation	2184	2794	2489
107	C <sub>2</sub> H <sub>4</sub>	0.738	-29.6	no detonation	601	586	594
108	C <sub>2</sub> H <sub>4</sub>	0.500	-29.6	detonation	2065	2043	2054
109	C <sub>2</sub> H <sub>4</sub>	0.600	-29.6	detonation	1979	1979	1979
110	C <sub>2</sub> H <sub>4</sub>	0.700	-29.6	no detonation	648	614	631
111	C <sub>2</sub> H <sub>4</sub>	0.700	60.7	detonation	1845	1863	1854
112	C <sub>2</sub> H <sub>4</sub>	0.738	60.7	detonation	1792	1792	1792
113	C <sub>2</sub> H <sub>4</sub>	1.000	60.7	detonation	805	754	780
114	C <sub>2</sub> H <sub>4</sub>	0.738	-31.1	no detonation	785	745	765
115	C <sub>2</sub> H <sub>4</sub>	0.738	15.2	detonation	1845	1845	1845
116	C <sub>2</sub> H <sub>4</sub>	0.738	-7.4	no detonation	830	819	825
117	C <sub>2</sub> H <sub>4</sub>	0.738	-0.9	no detonation	856	808	832
118	C <sub>2</sub> H <sub>4</sub>	0.738	6.3	detonation	1845	1827	1836
119	C <sub>2</sub> H <sub>4</sub>	0.738	2.7	DDT	888	819	854
120	C <sub>2</sub> H <sub>4</sub>	0.738	4.5	DDT	905	819	862
121	C <sub>2</sub> H <sub>4</sub>	0.800	6.3	no detonation	792	742	767
122	C <sub>2</sub> H <sub>4</sub>	0.800	15.2	no detonation	848	785	817
123	C <sub>2</sub> H <sub>4</sub>	1.000	6.3	no detonation	714	657	686
124	C <sub>3</sub> H <sub>8</sub>	0.700	6.3	no detonation	844	782	813
125	C <sub>3</sub> H <sub>8</sub>	0.500	6.3	detonation	2088	2065	2077
126	C <sub>3</sub> H <sub>8</sub>	0.600	6.3	DDT	964	905	935

Table H.5: Test-section wave velocities for each run. “DTI Run” is the dynamic toroidal initiator run number. All mixtures were stoichiometric fuel-oxygen diluted with nitrogen.  $U_{i,j}$  is the average velocity between stations  $i$  and  $j$ , respectively.  $U_{AVG}$  is the average of  $U_{3,4}$  and  $U_{4,5}$ .

DTI Run	Fuel	N <sub>2</sub> fraction	Initiator overfill	Mode of initiation	U <sub>3,4</sub> (m/s)	U <sub>4,5</sub> (m/s)	U <sub>AVG</sub> (m/s)
127	C <sub>3</sub> H <sub>8</sub>	0.600	15.2	detonation	2000	2000	2000
128	C <sub>3</sub> H <sub>8</sub>	0.700	15.2	no detonation	876	819	848
129	C <sub>3</sub> H <sub>8</sub>	0.700	23.9	detonation	1881	1900	1891
130	C <sub>3</sub> H <sub>8</sub>	0.758	23.9	no detonation	868	812	840
131	C <sub>3</sub> H <sub>8</sub>	0.758	32.4	no detonation	880	830	855
132	C <sub>3</sub> H <sub>8</sub>	0.758	56.9	detonation	1776	1792	1784
133	C <sub>3</sub> H <sub>8</sub>	0.758	72.5	detonation	1809	1827	1818
134	C <sub>3</sub> H <sub>8</sub>	0.758	48.9	detonation	1792	1759	1776
135	C <sub>3</sub> H <sub>8</sub>	0.758	40.7	detonation	1827	1792	1810
136	C <sub>3</sub> H <sub>8</sub>	0.758	36.6	detonation	1743	2567	2155
137	C <sub>3</sub> H <sub>8</sub>	0.758	32.4	no detonation	868	826	847
138	C <sub>3</sub> H <sub>8</sub>	0.758	56.9	detonation	1158	979	1069
139	C <sub>3</sub> H <sub>8</sub>	1.000	56.9	no detonation	775	686	731
140	C <sub>3</sub> H <sub>8</sub>	0.758	36.6	no detonation	927	819	873
141	C <sub>3</sub> H <sub>8</sub>	0.758	46.5	no detonation	1000	922	961
142	C <sub>3</sub> H <sub>8</sub>	0.758	51.3	detonation	1124	941	1033
143	C <sub>3</sub> H <sub>8</sub>	0.758	72.5	detonation	1743	1759	1751
144	C <sub>3</sub> H <sub>8</sub>	1.000	72.5	no detonation	798	701	750
145	C <sub>2</sub> H <sub>4</sub>	0.738	6.3	no detonation	841	757	799
146	C <sub>2</sub> H <sub>4</sub>	0.738	23.9	detonation	1863	1809	1836
147	C <sub>2</sub> H <sub>4</sub>	0.738	15.2	no detonation	945	833	889
148	C <sub>2</sub> H <sub>4</sub>	0.738	19.5	detonation	1939	1809	1874
149	C <sub>2</sub> H <sub>4</sub>	0.738	-61.1	no detonation	N/A	N/A	N/A
150	C <sub>2</sub> H <sub>4</sub>	0.738	-61.1	no detonation	713	615	664
151	C <sub>2</sub> H <sub>4</sub>	0.738	-71.6	no detonation	698	603	651
152	C <sub>2</sub> H <sub>4</sub>	0.738	-71.6	no detonation	N/A	N/A	N/A
153	C <sub>2</sub> H <sub>4</sub>	0.738	-82.2	no detonation	N/A	N/A	N/A

Table H.6: Test-section wave velocities for each run. “DTI Run” is the dynamic toroidal initiator run number. All mixtures were stoichiometric fuel-oxygen diluted with nitrogen.  $U_{i,j}$  is the average velocity between stations  $i$  and  $j$ , respectively.  $U_{AVG}$  is the average of  $U_{3,4}$  and  $U_{4,5}$ .

## H.7 Pressure Traces: Dynamic Gas Injection

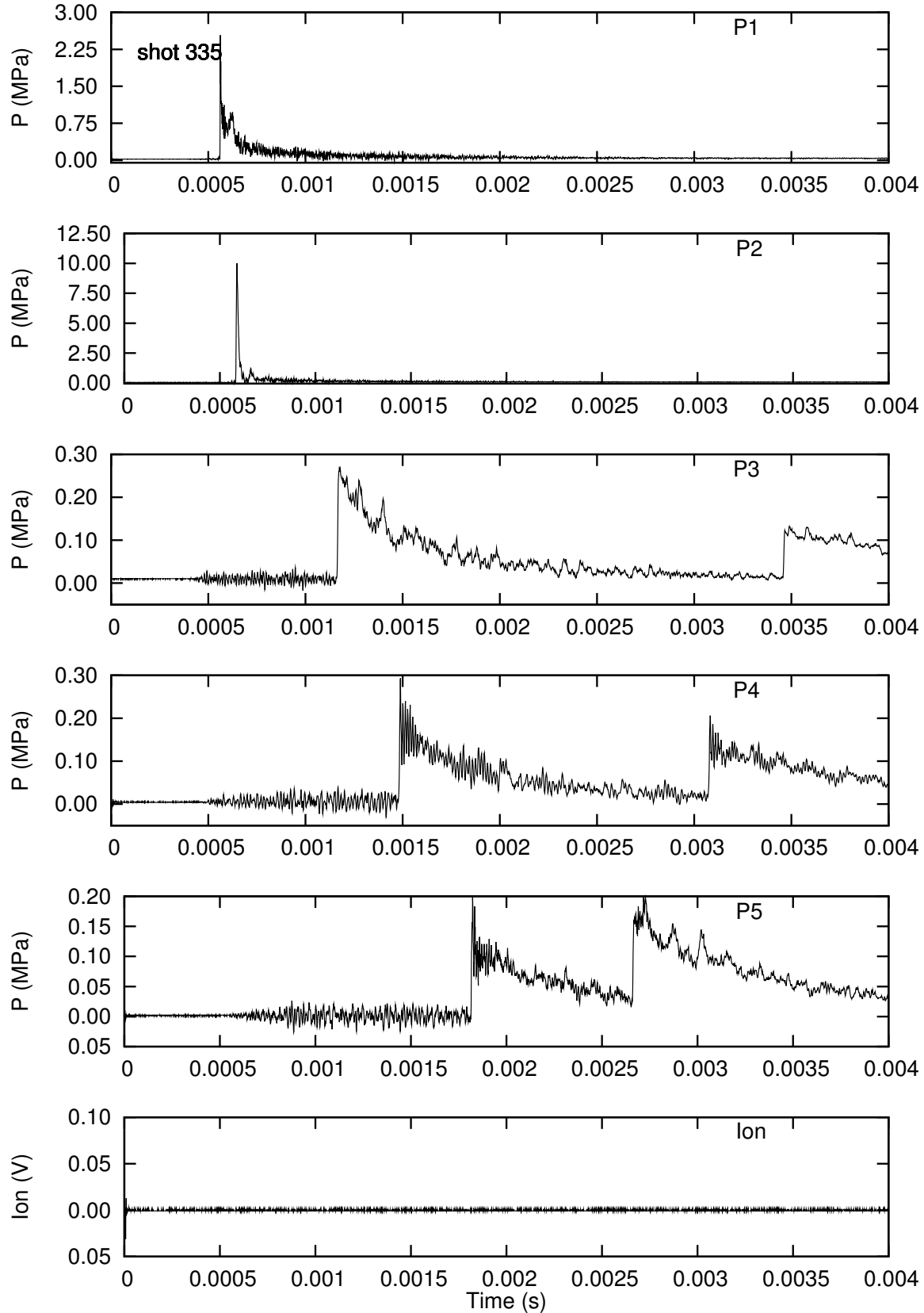


Figure H.109: Pressure history from run 103 with initiator gas injection.

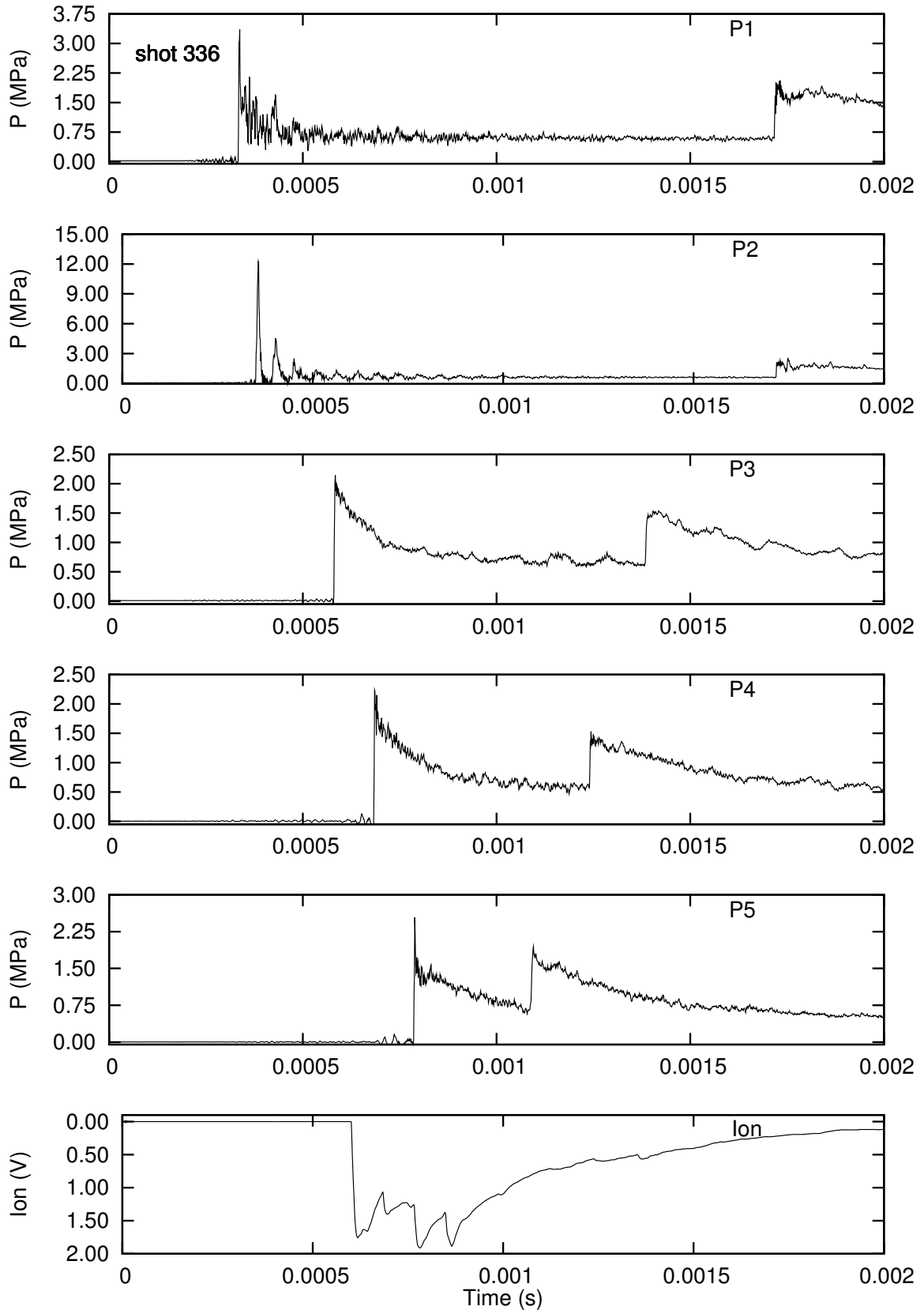


Figure H.110: Pressure history from run 104 with initiator gas injection.

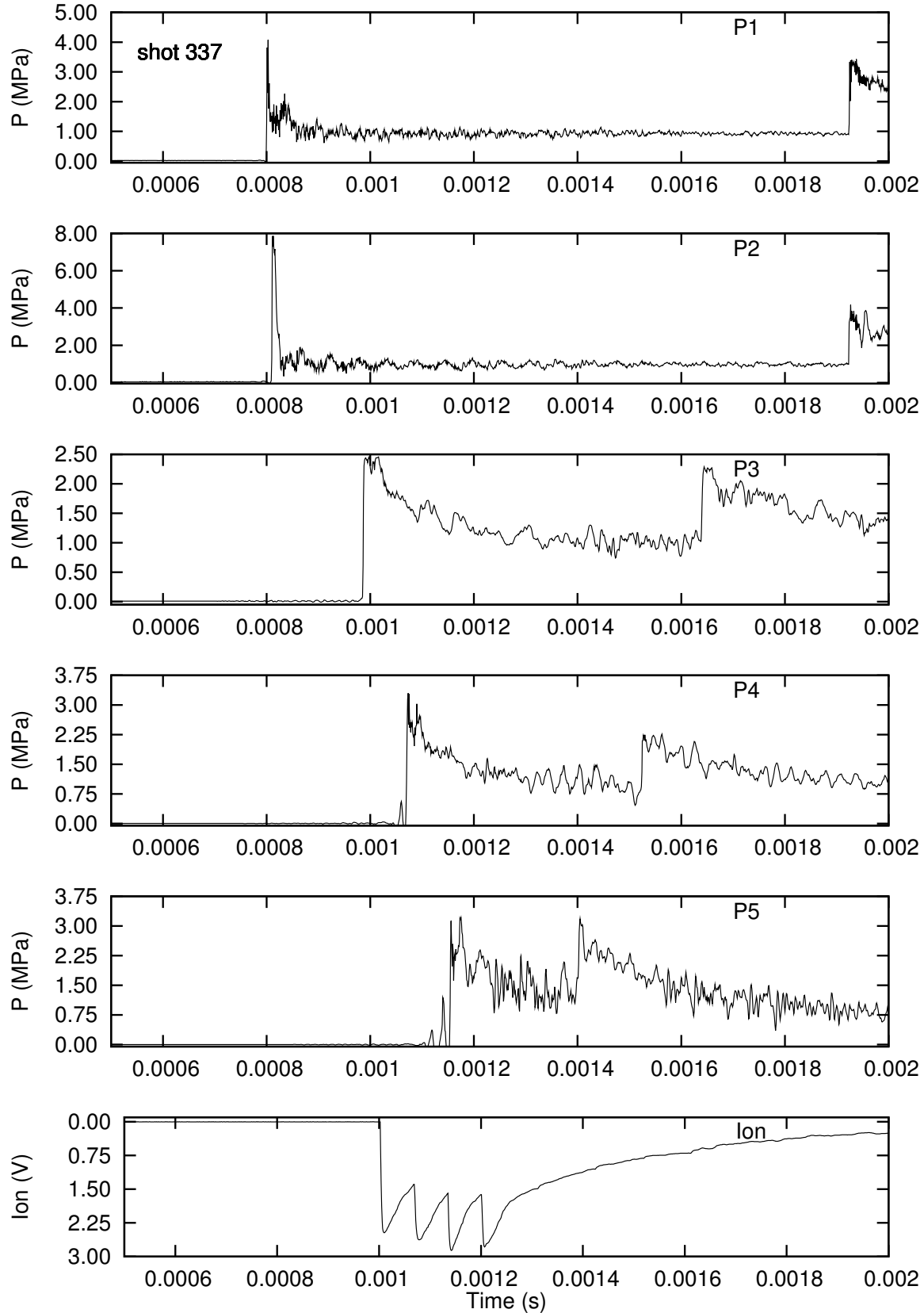


Figure H.111: Pressure history from run 105 with initiator gas injection.

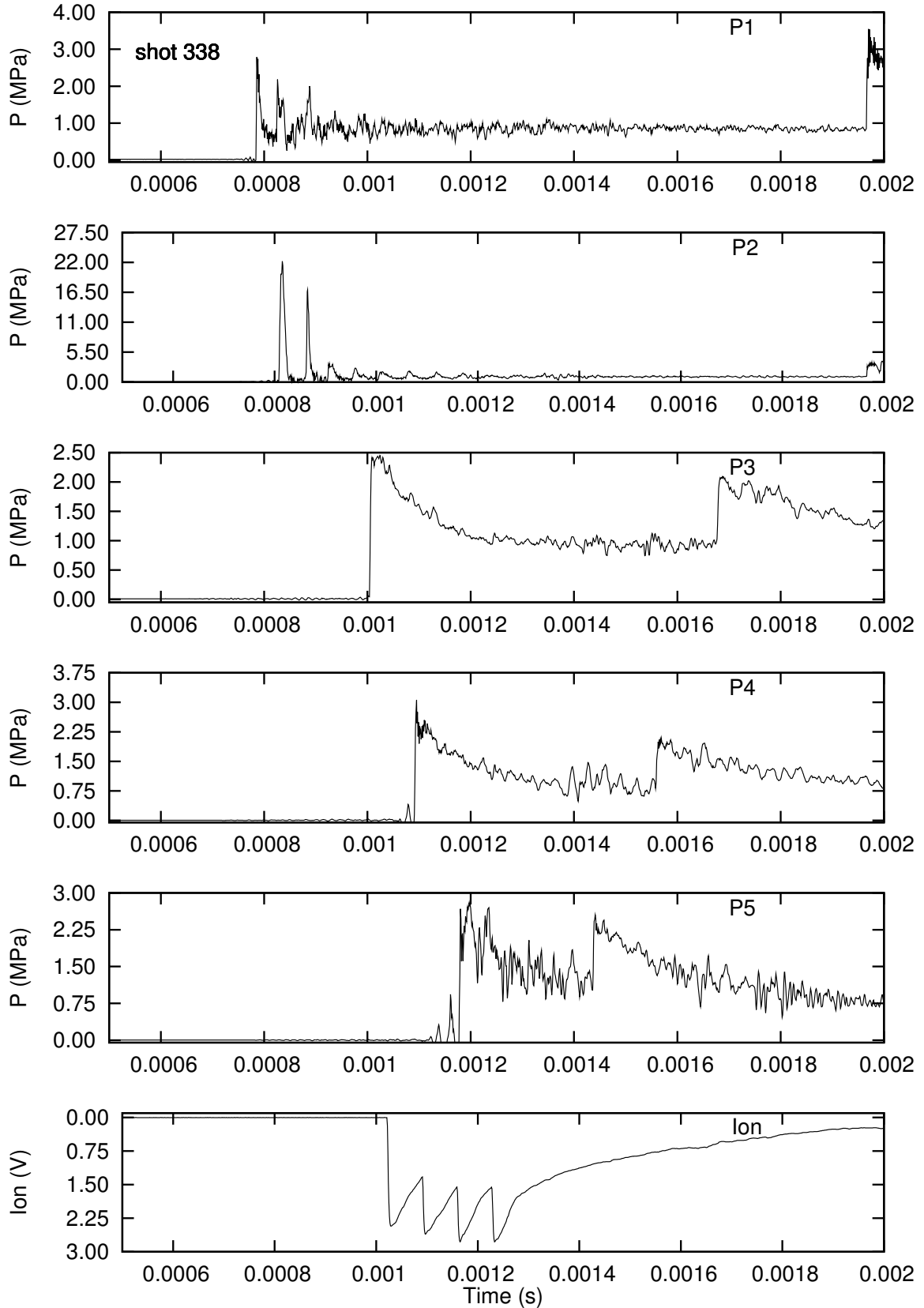


Figure H.112: Pressure history from run 106 with initiator gas injection.

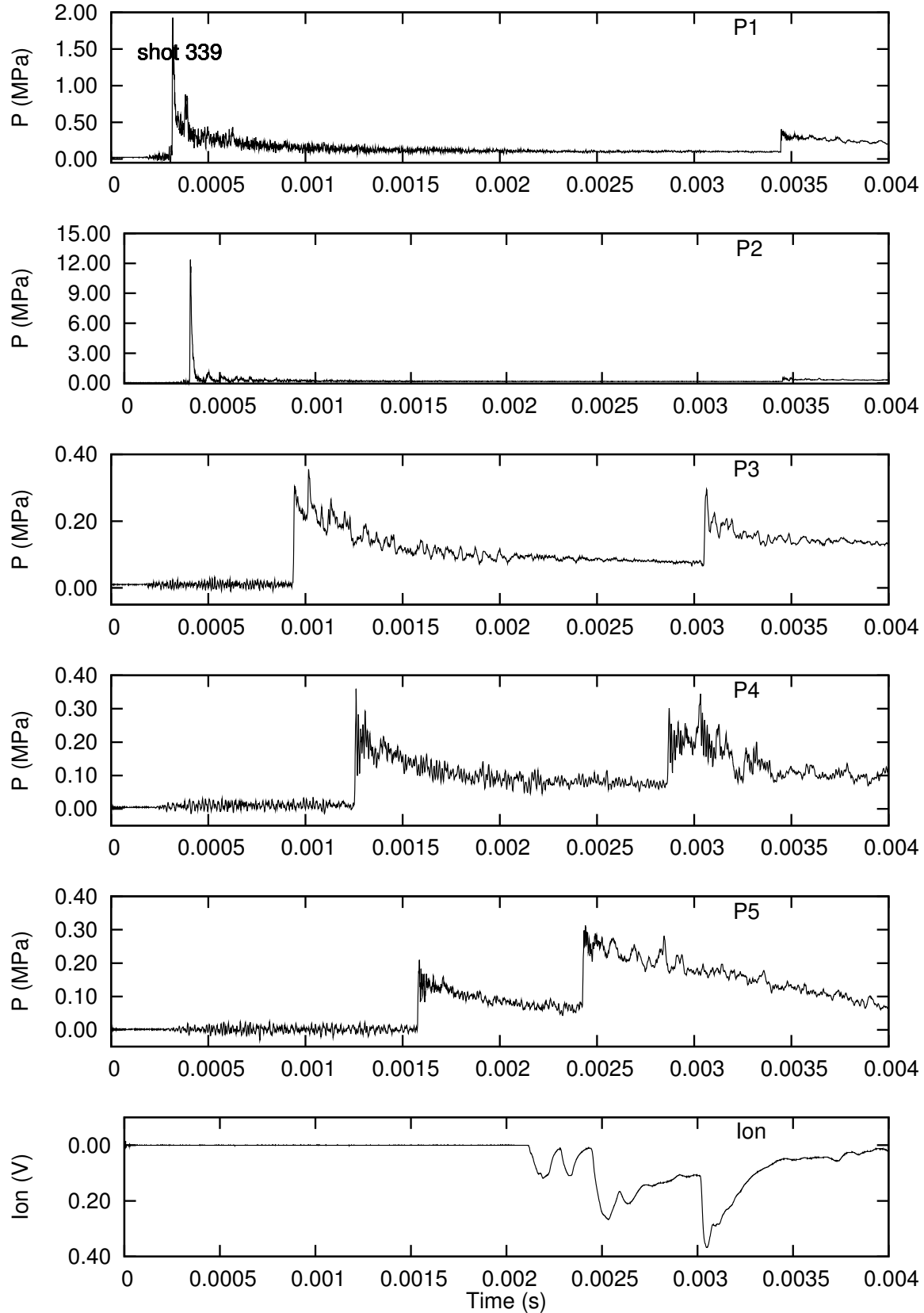


Figure H.113: Pressure history from run 107 with initiator gas injection.

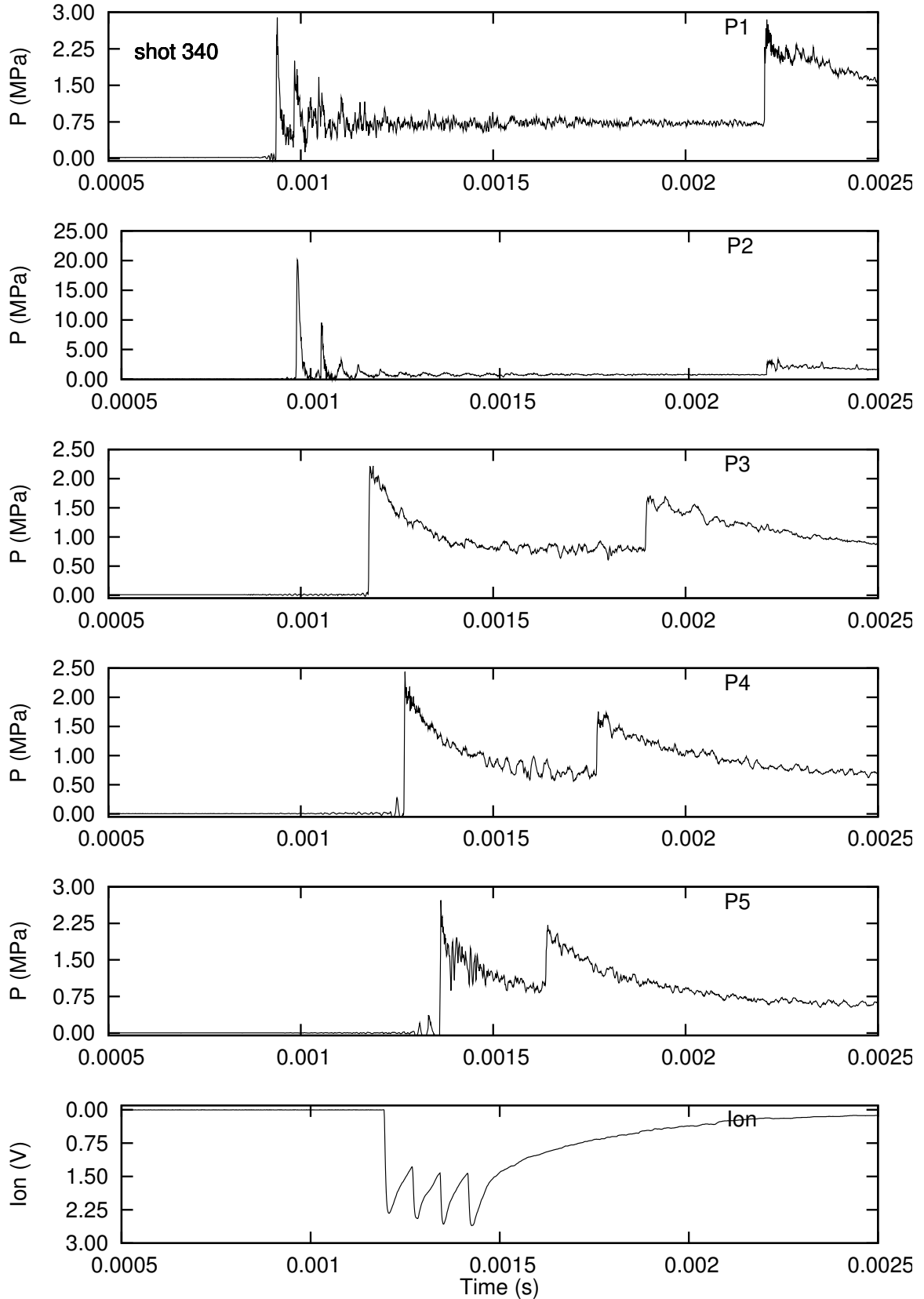


Figure H.114: Pressure history from run 108 with initiator gas injection.

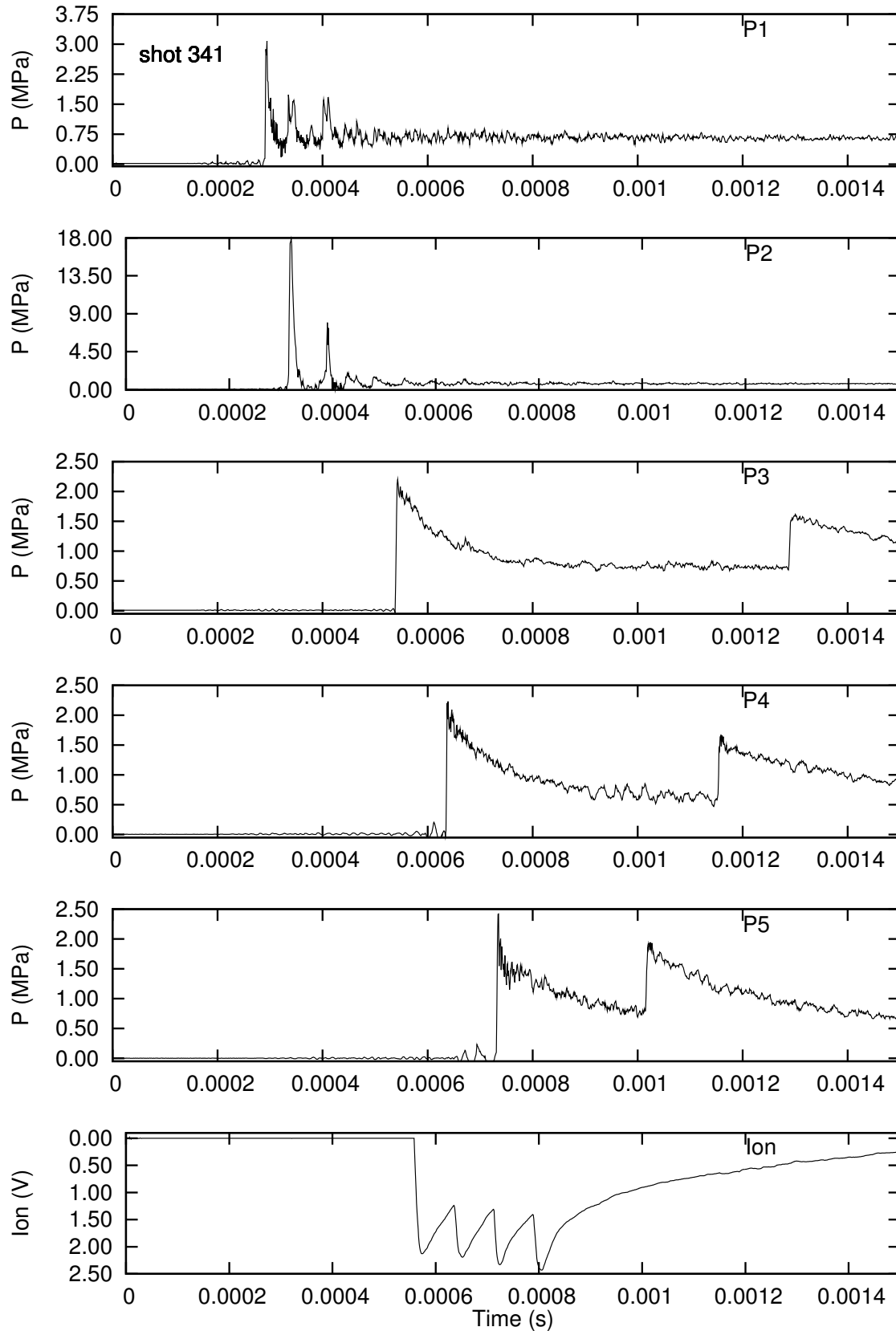


Figure H.115: Pressure history from run 109 with initiator gas injection.

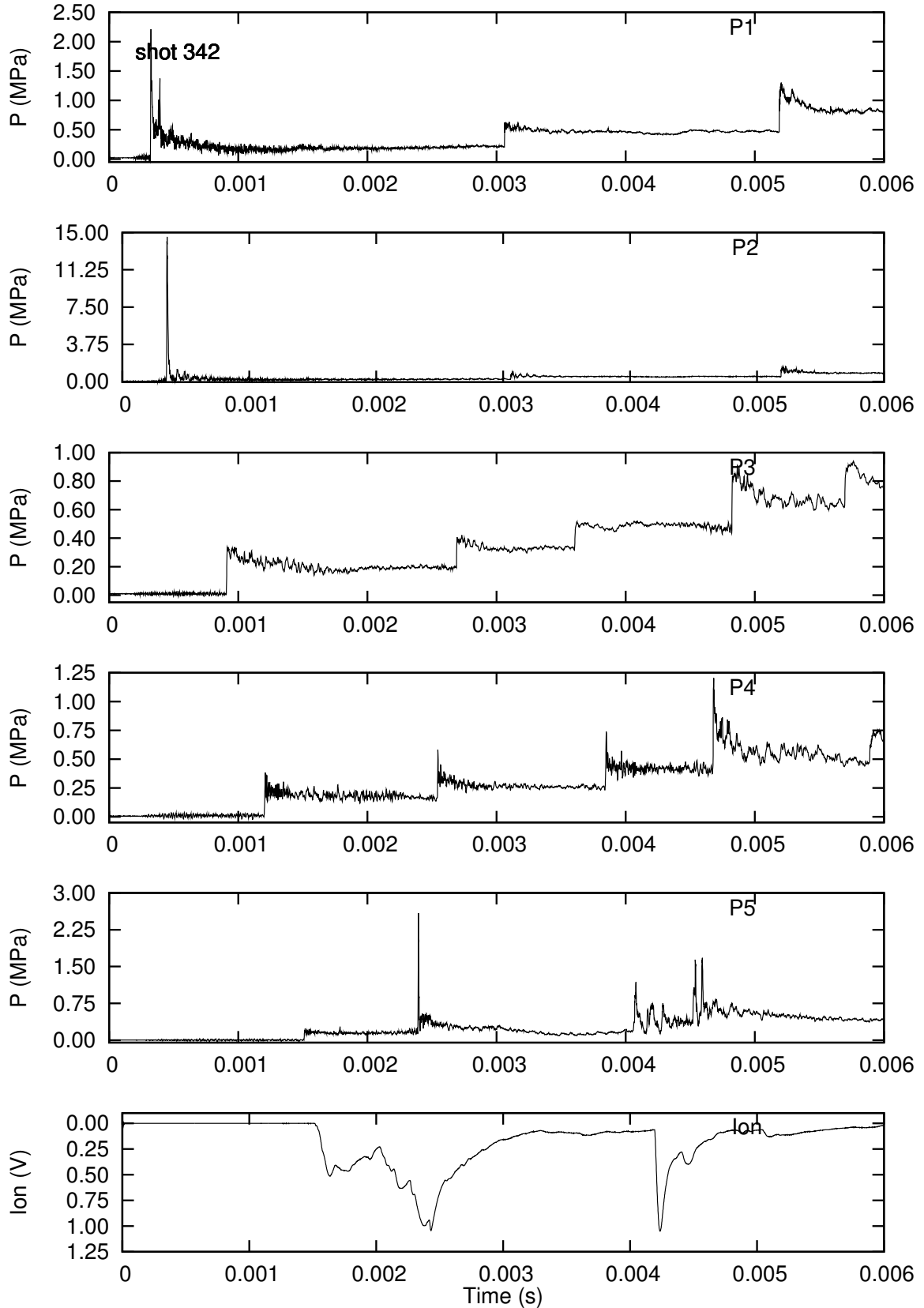


Figure H.116: Pressure history from run 110 with initiator gas injection.

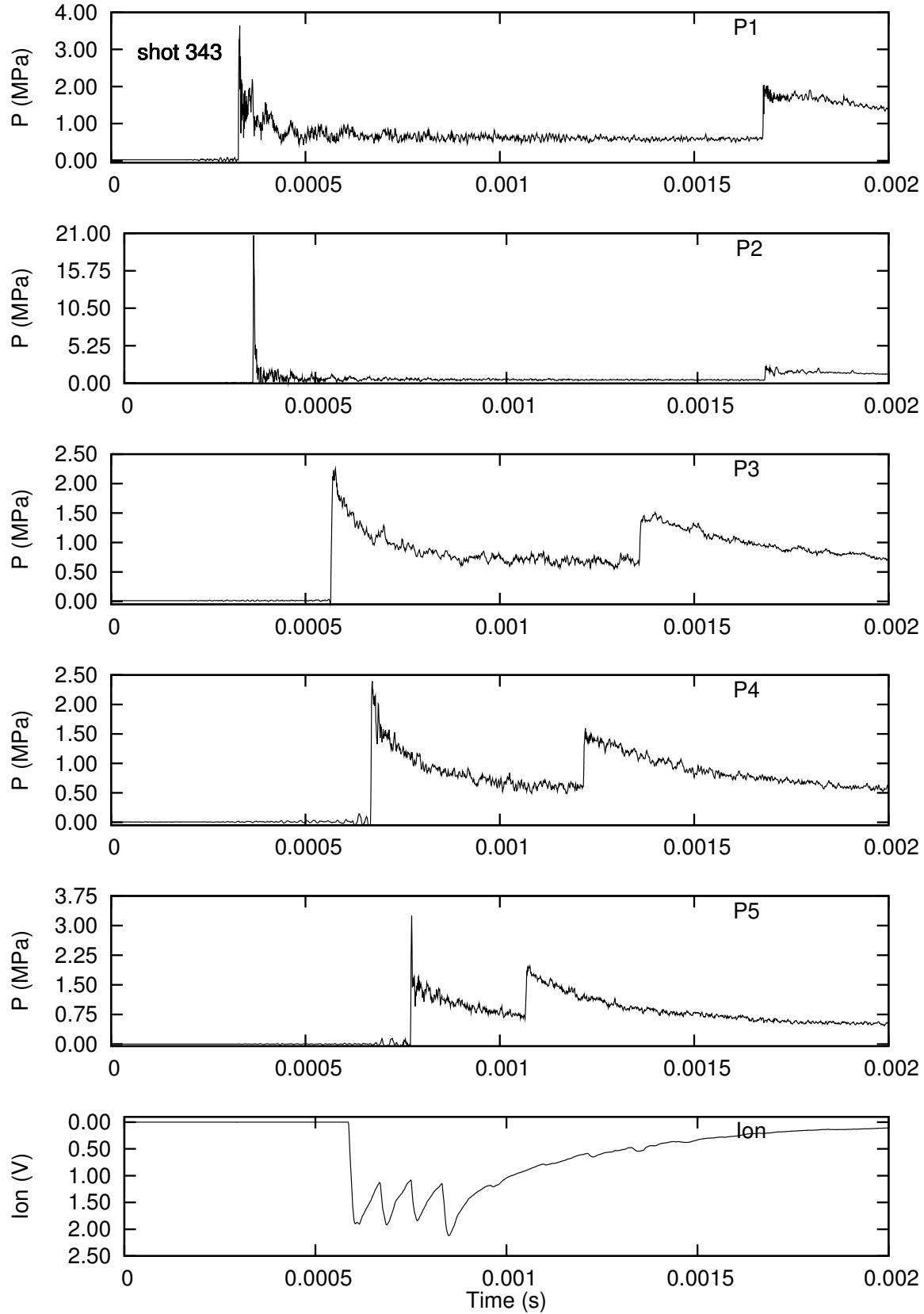


Figure H.117: Pressure history from run 111 with initiator gas injection.

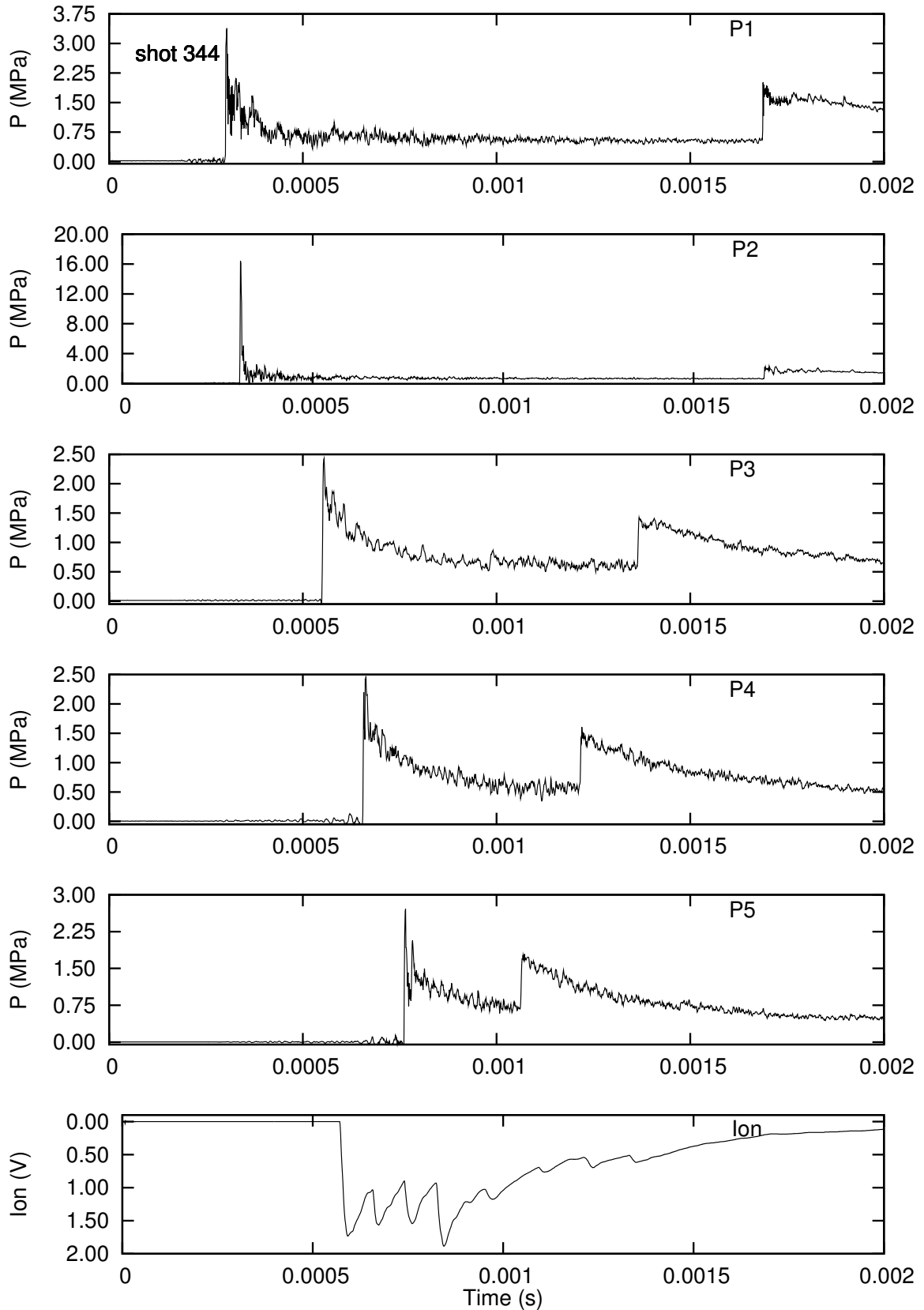


Figure H.118: Pressure history from run 112 with initiator gas injection.

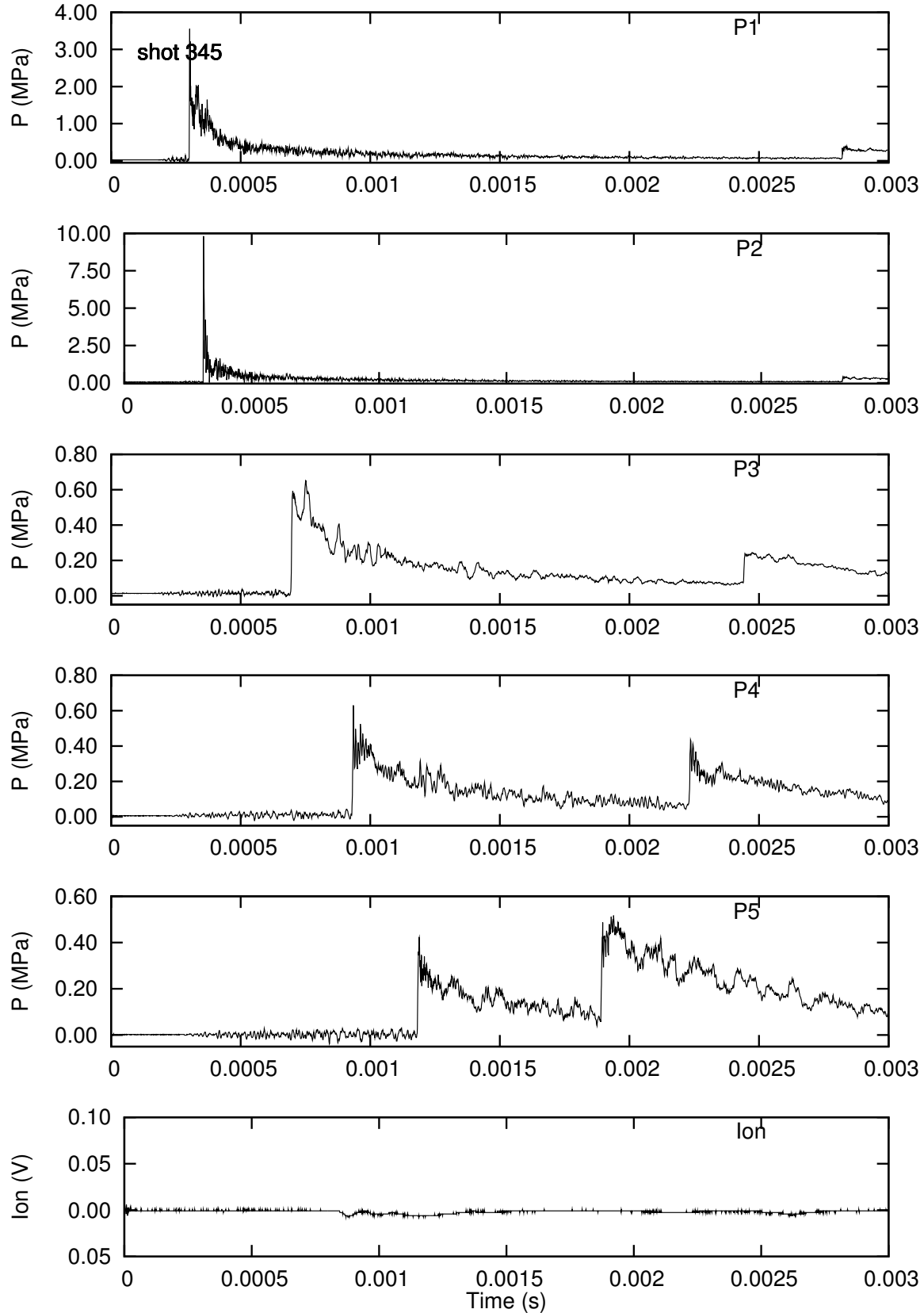


Figure H.119: Pressure history from run 113 with initiator gas injection.

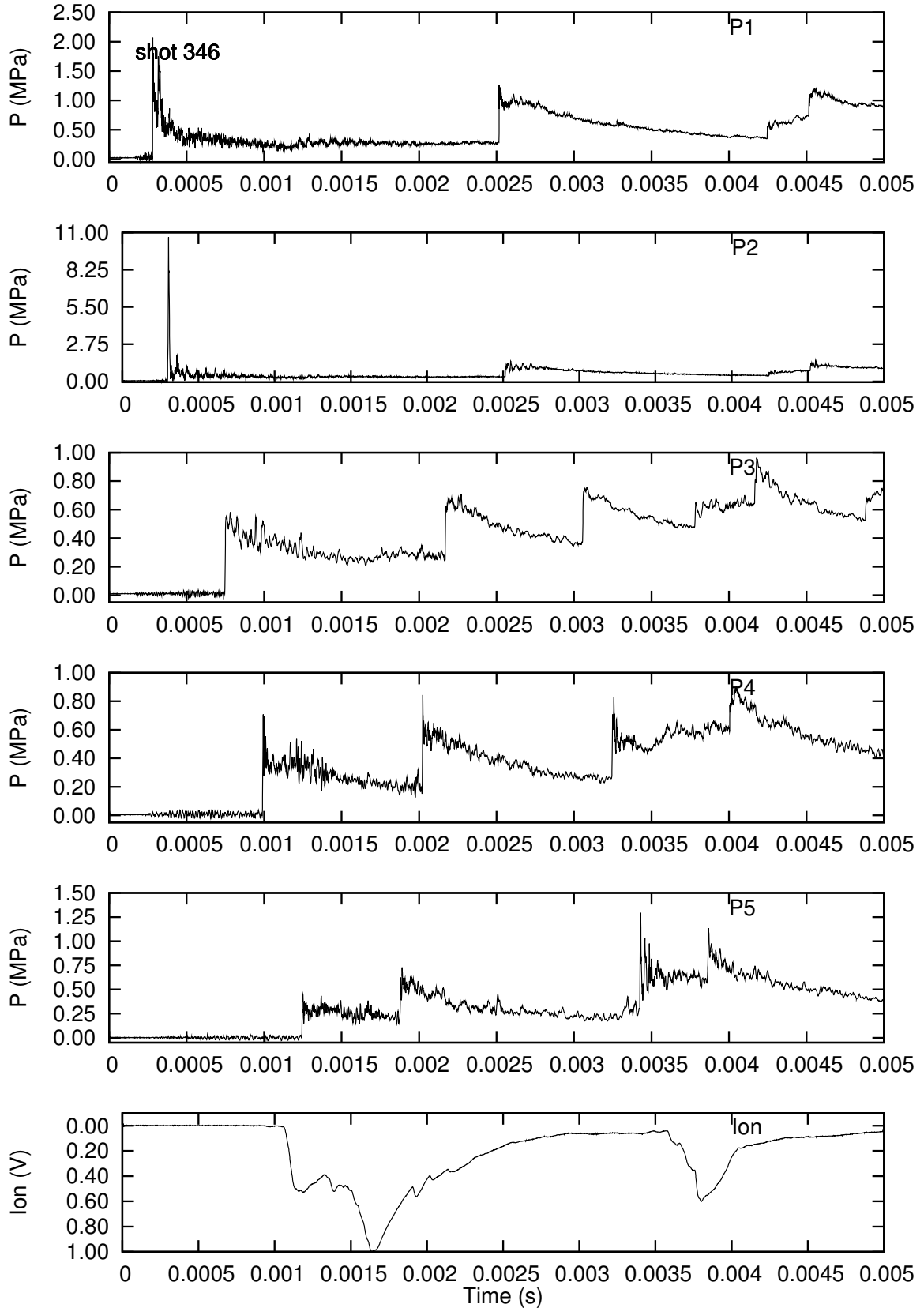


Figure H.120: Pressure history from run 114 with initiator gas injection.

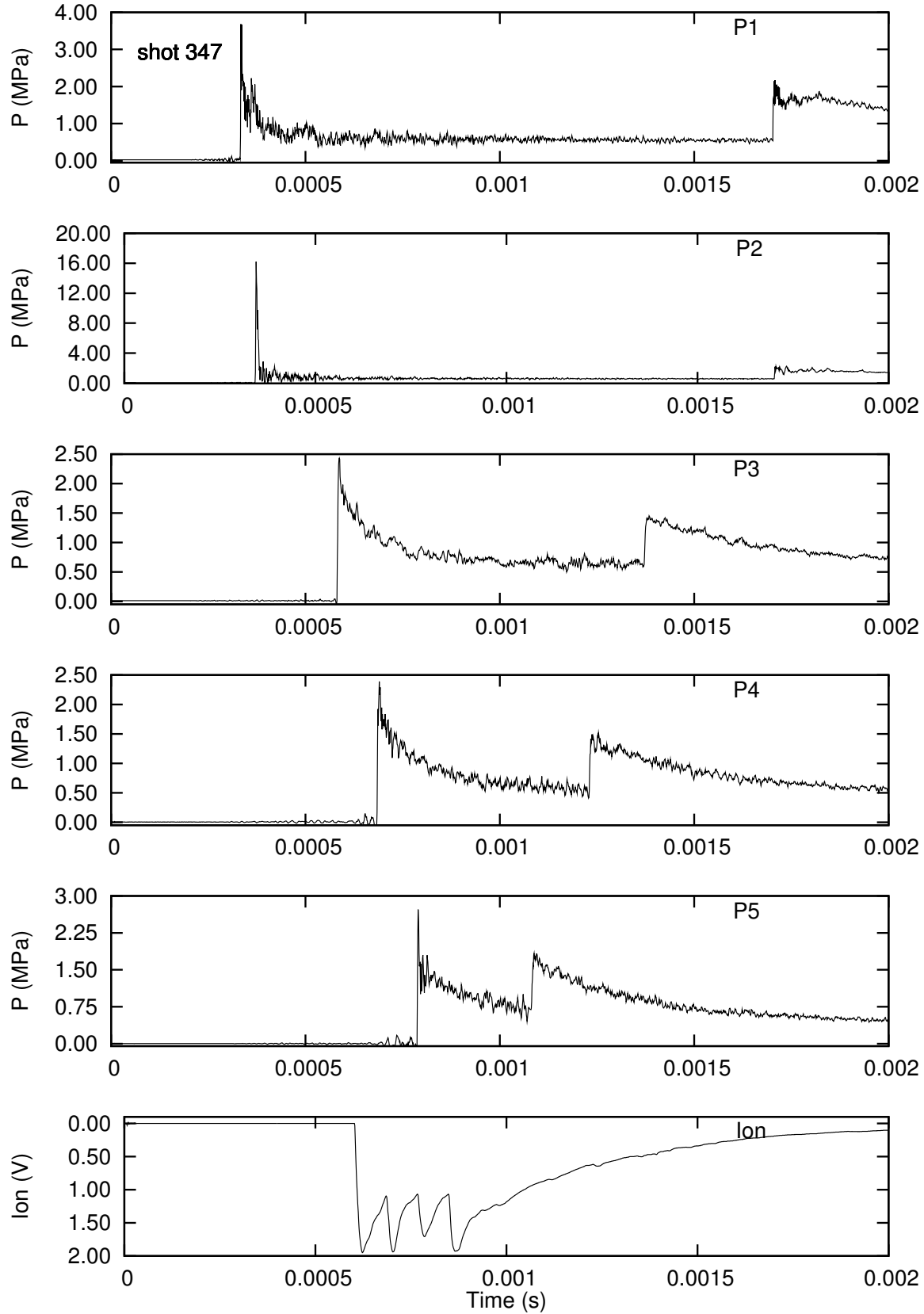


Figure H.121: Pressure history from run 115 with initiator gas injection.

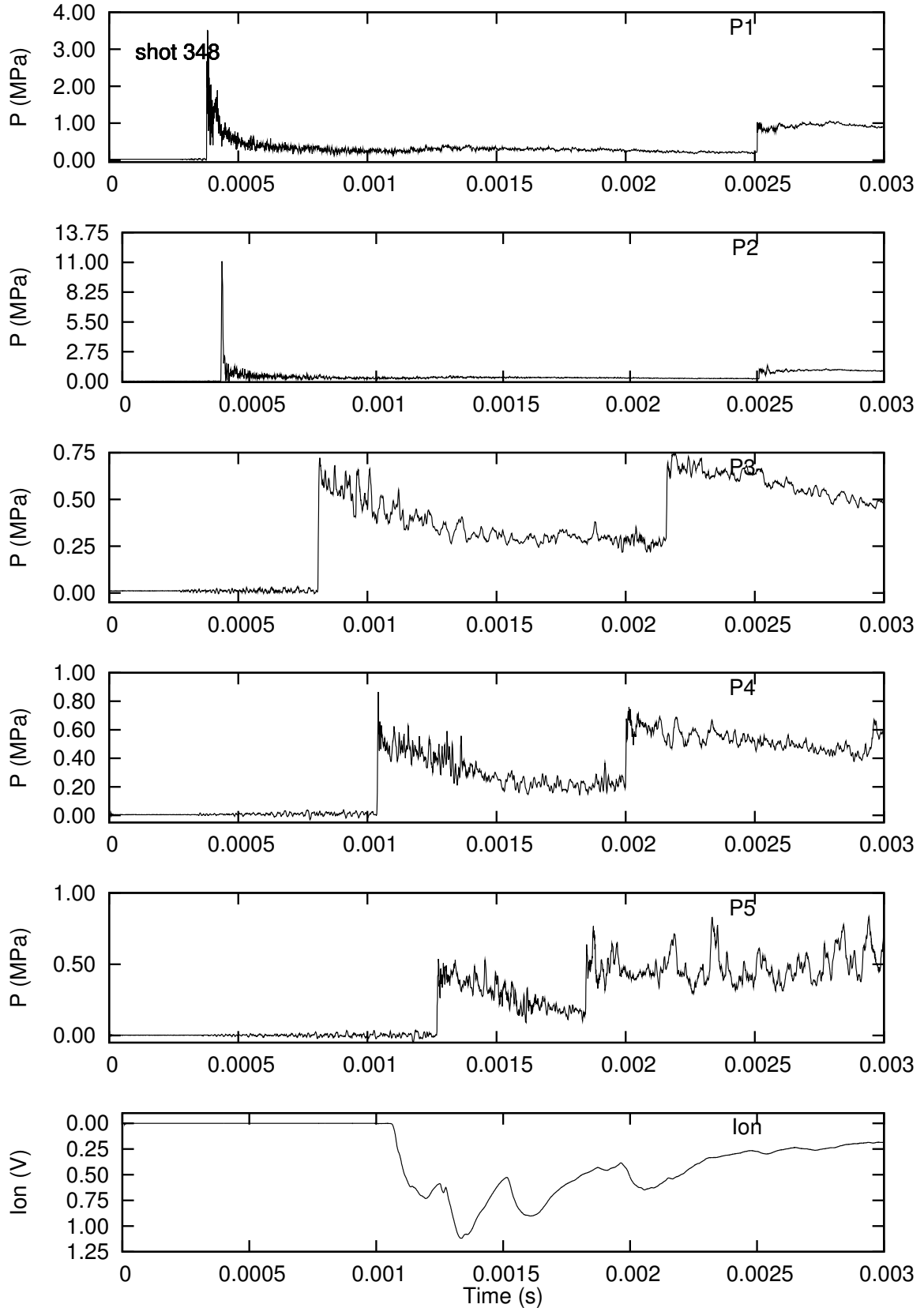


Figure H.122: Pressure history from run 116 with initiator gas injection.

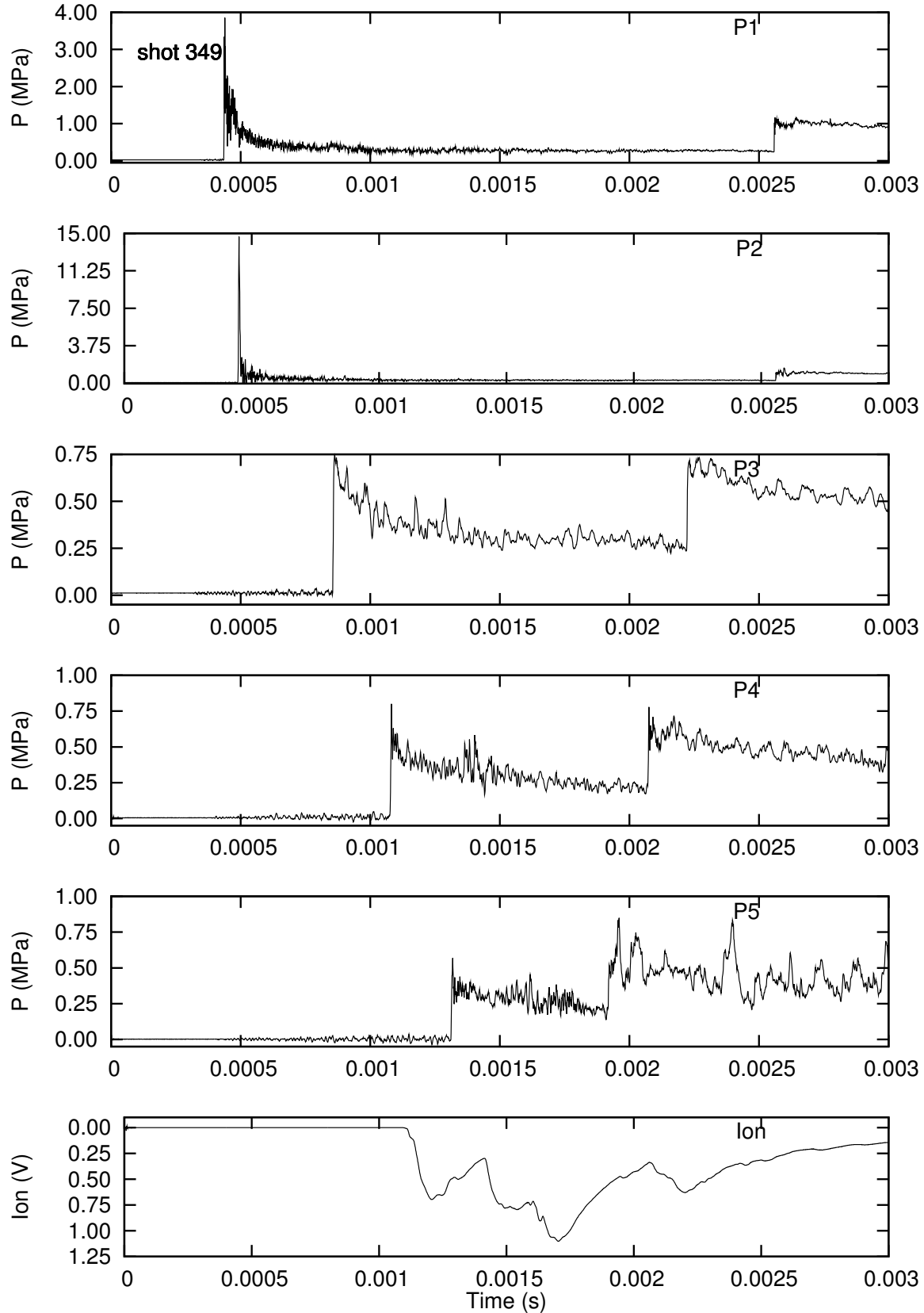


Figure H.123: Pressure history from run 117 with initiator gas injection.

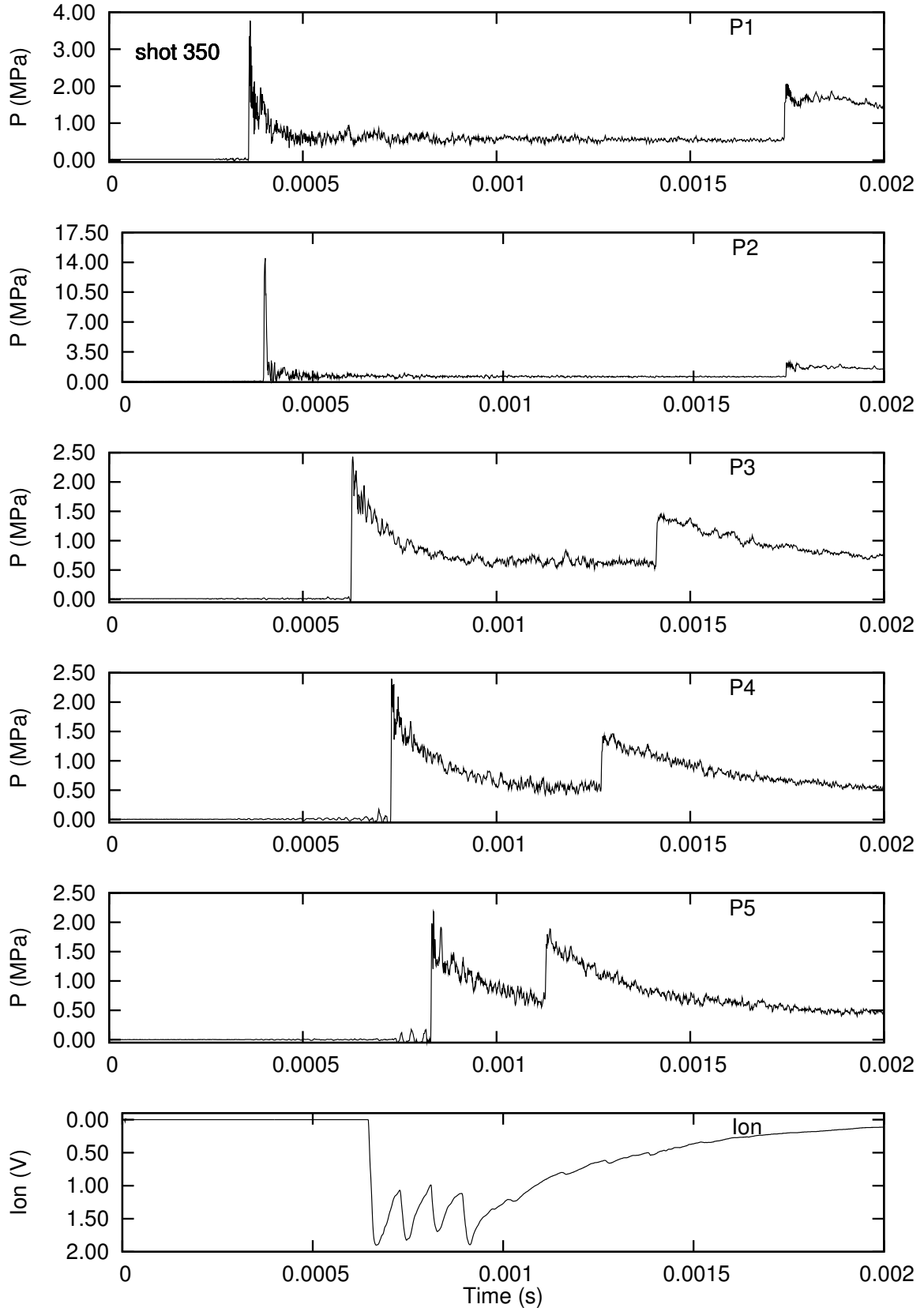


Figure H.124: Pressure history from run 118 with initiator gas injection.

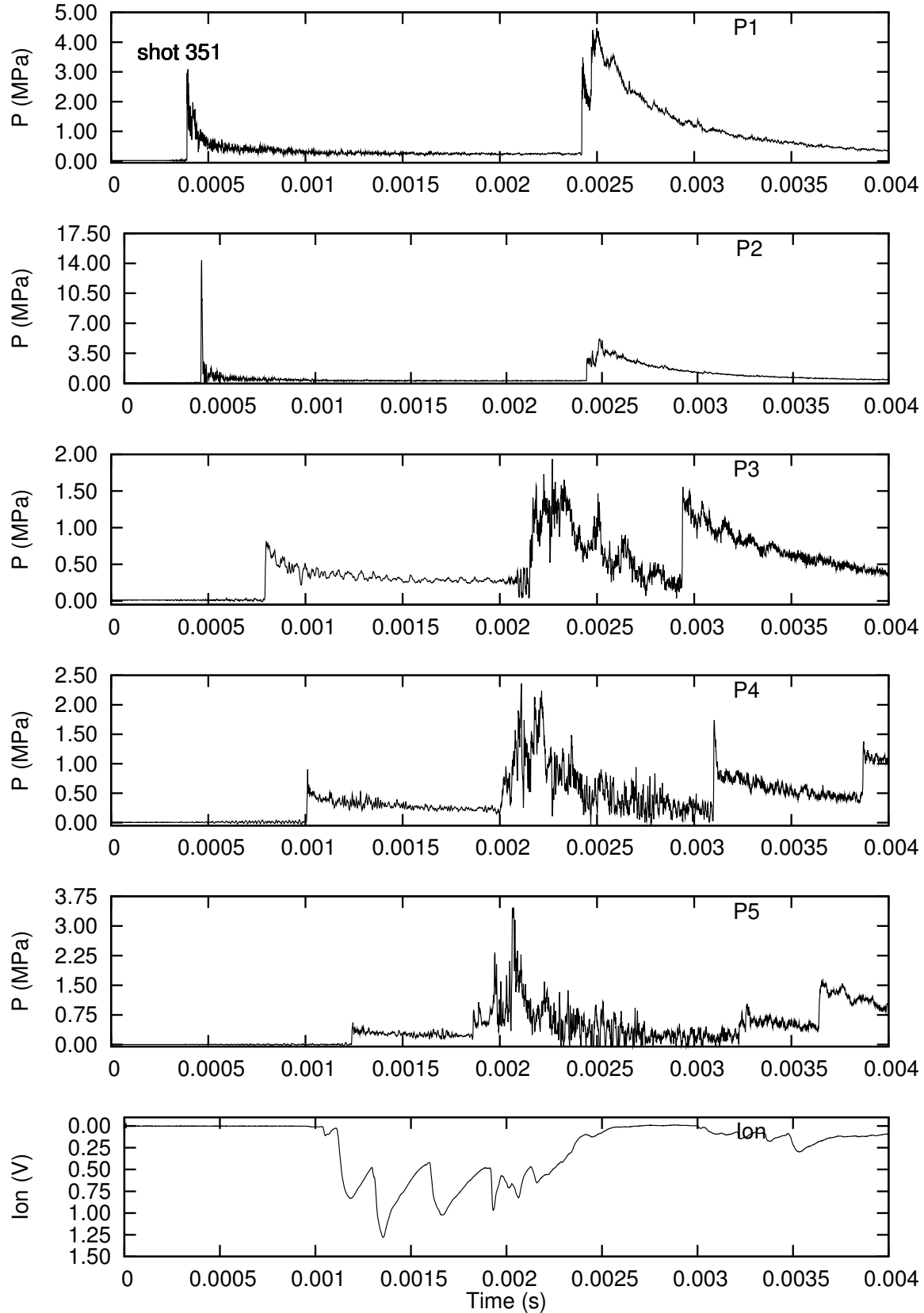


Figure H.125: Pressure history from run 119 with initiator gas injection.

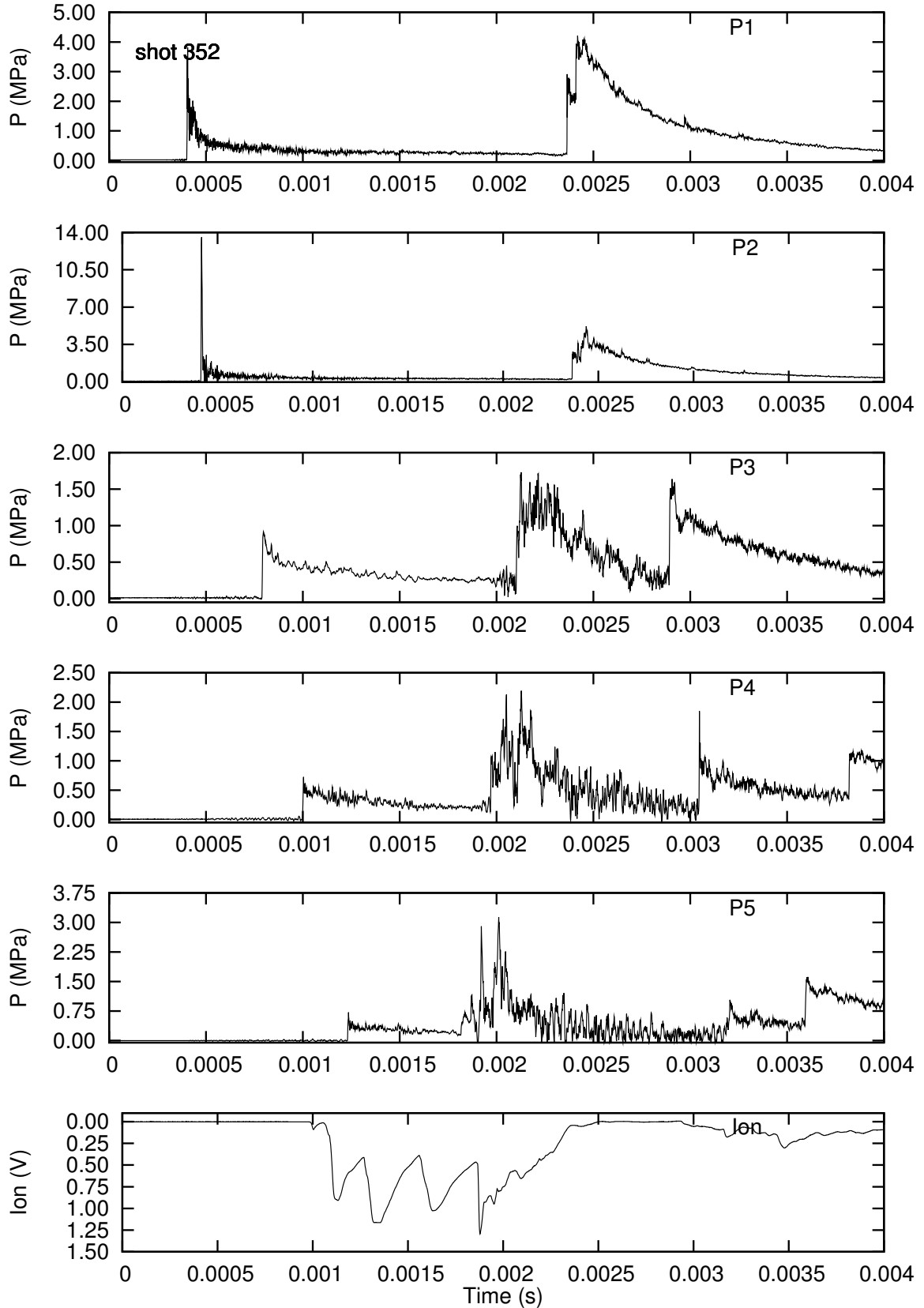


Figure H.126: Pressure history from run 120 with initiator gas injection.

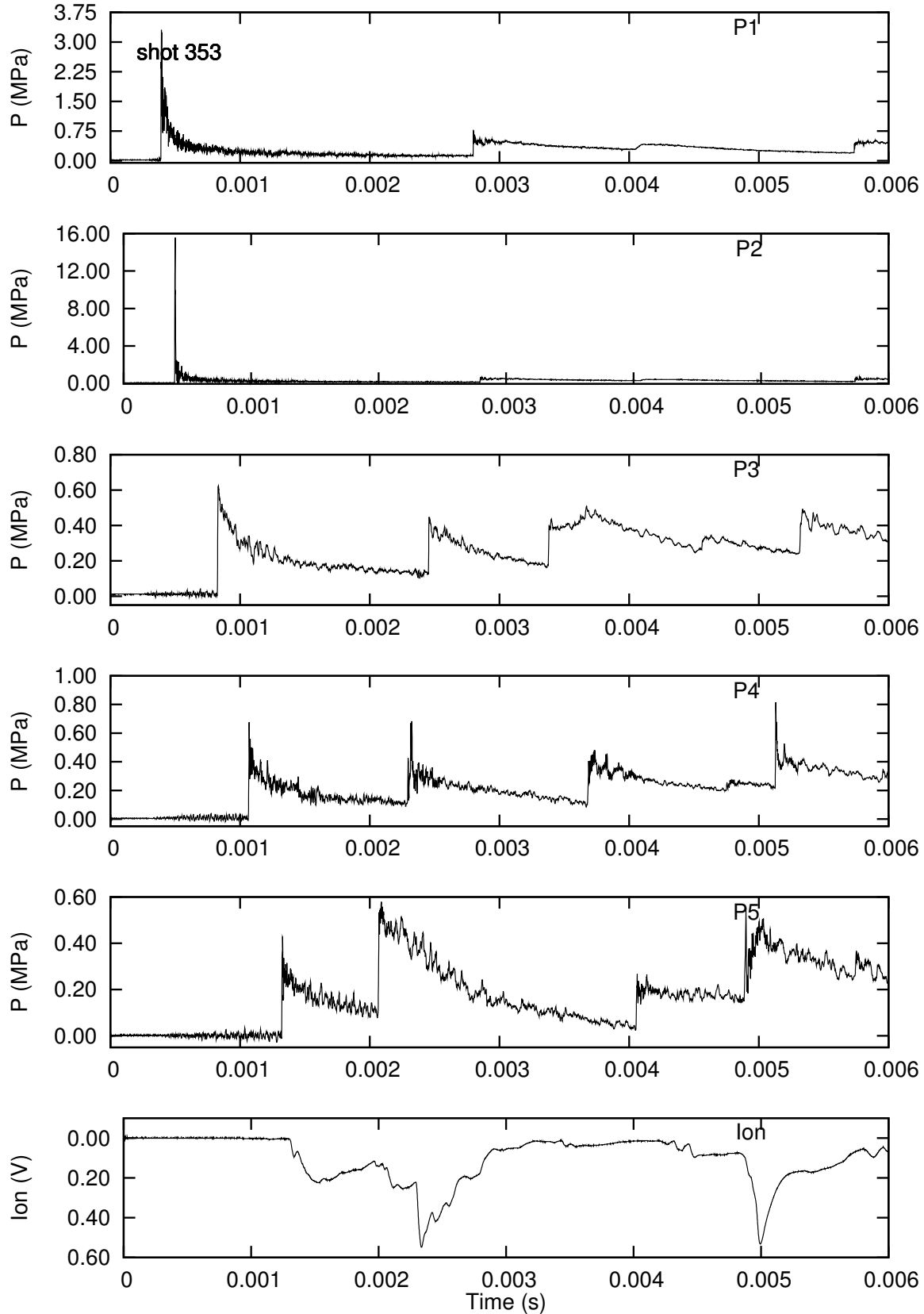


Figure H.127: Pressure history from run 121 with initiator gas injection.

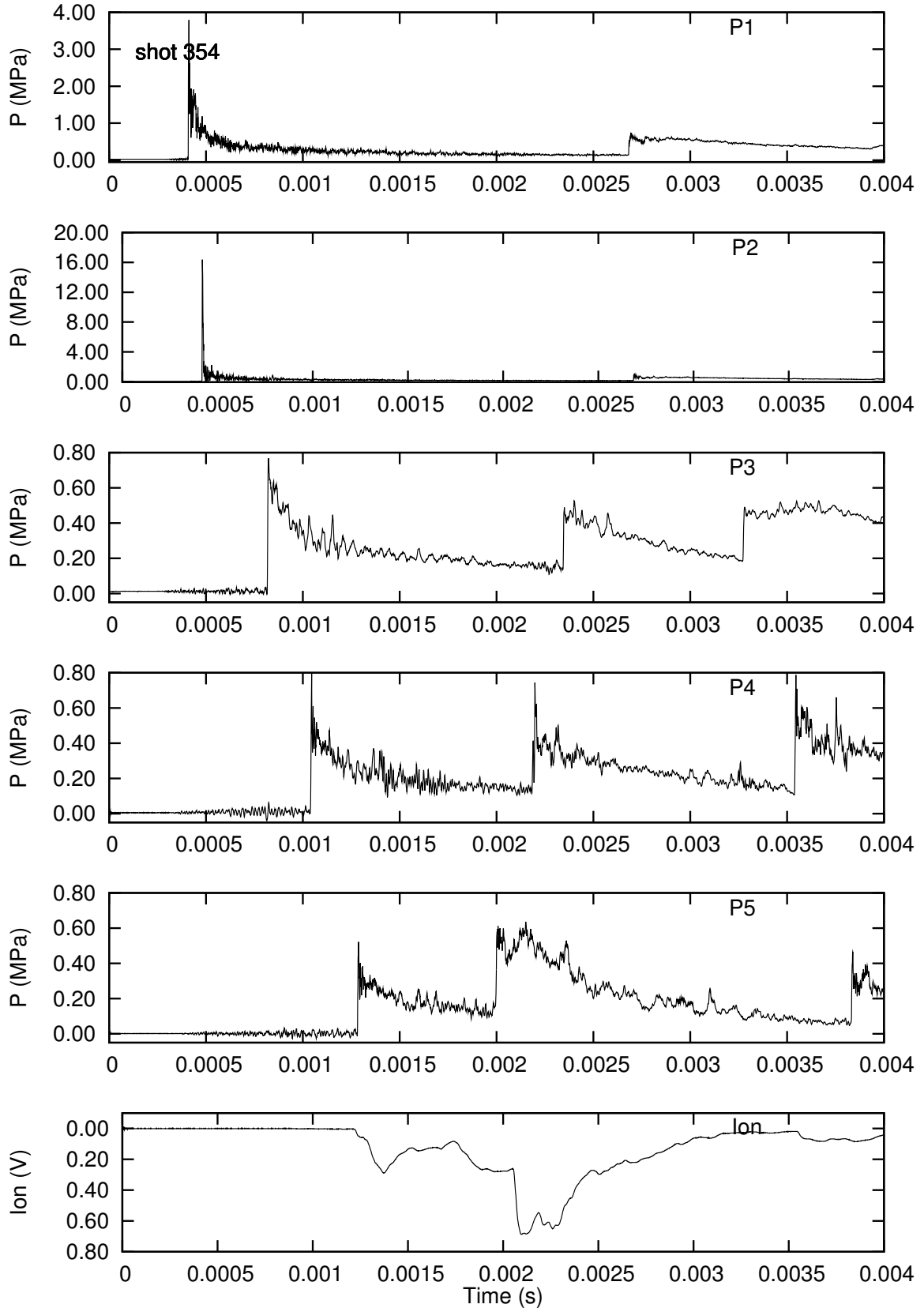


Figure H.128: Pressure history from run 122 with initiator gas injection.

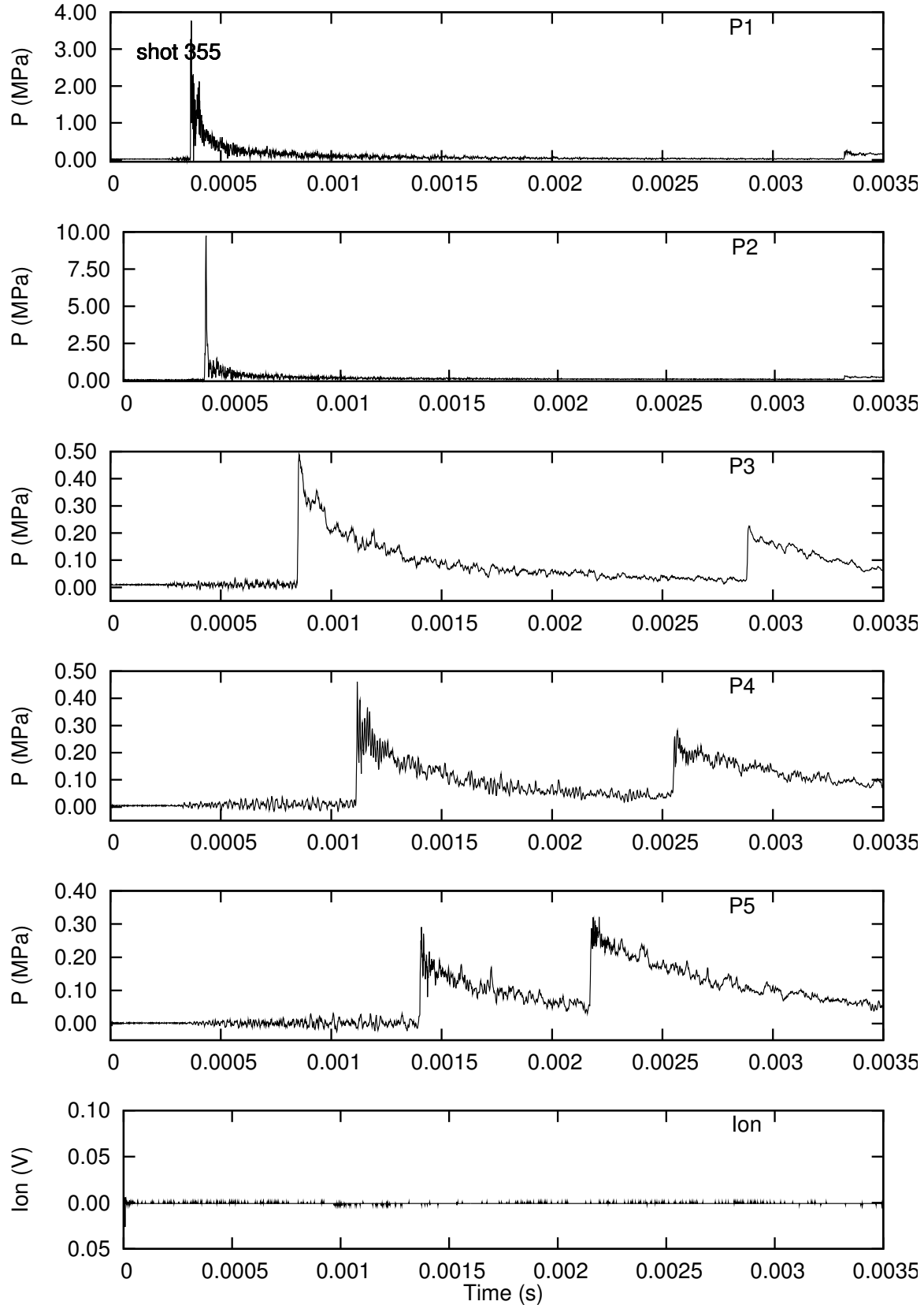


Figure H.129: Pressure history from run 123 with initiator gas injection.

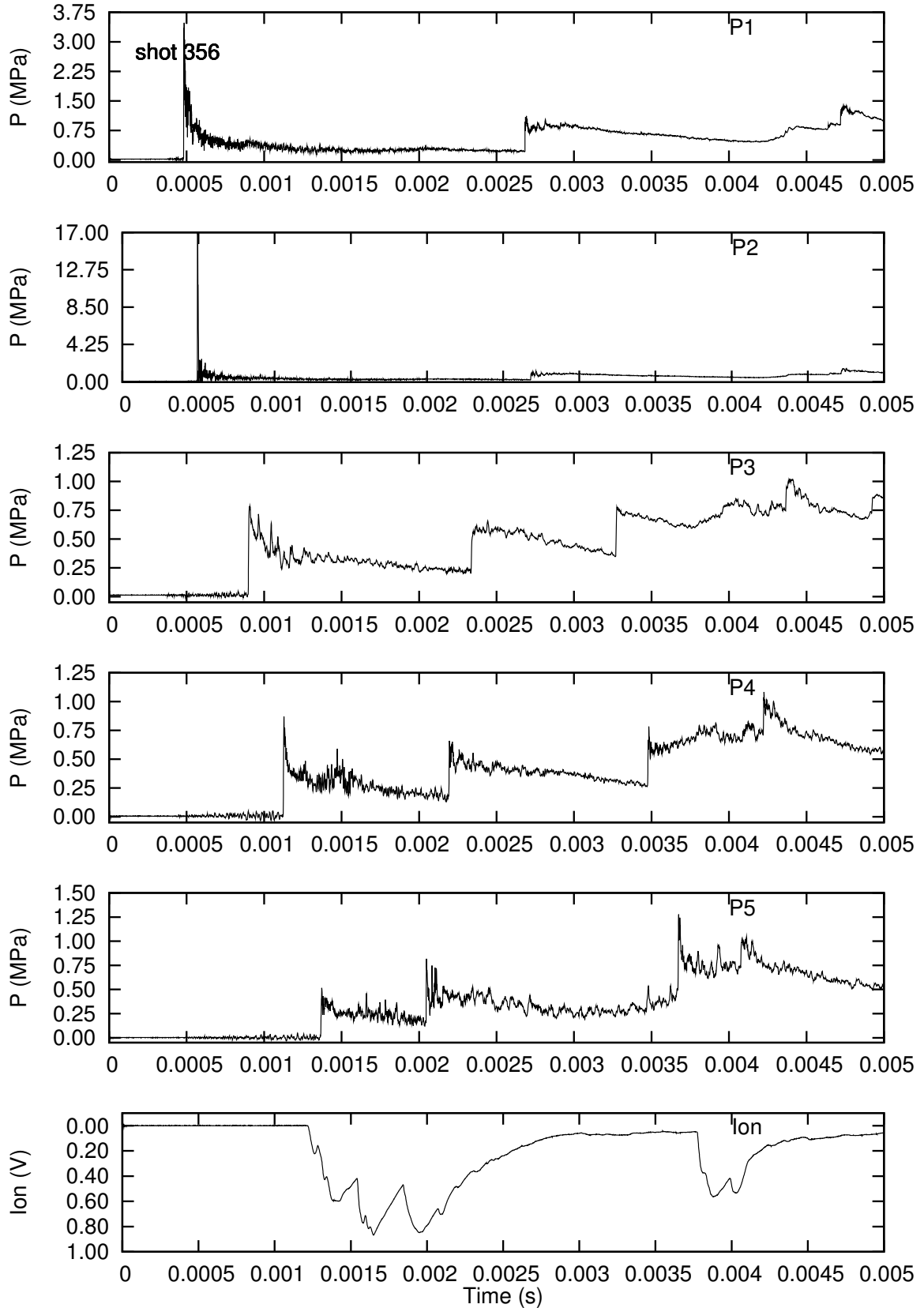


Figure H.130: Pressure history from run 124 with initiator gas injection.

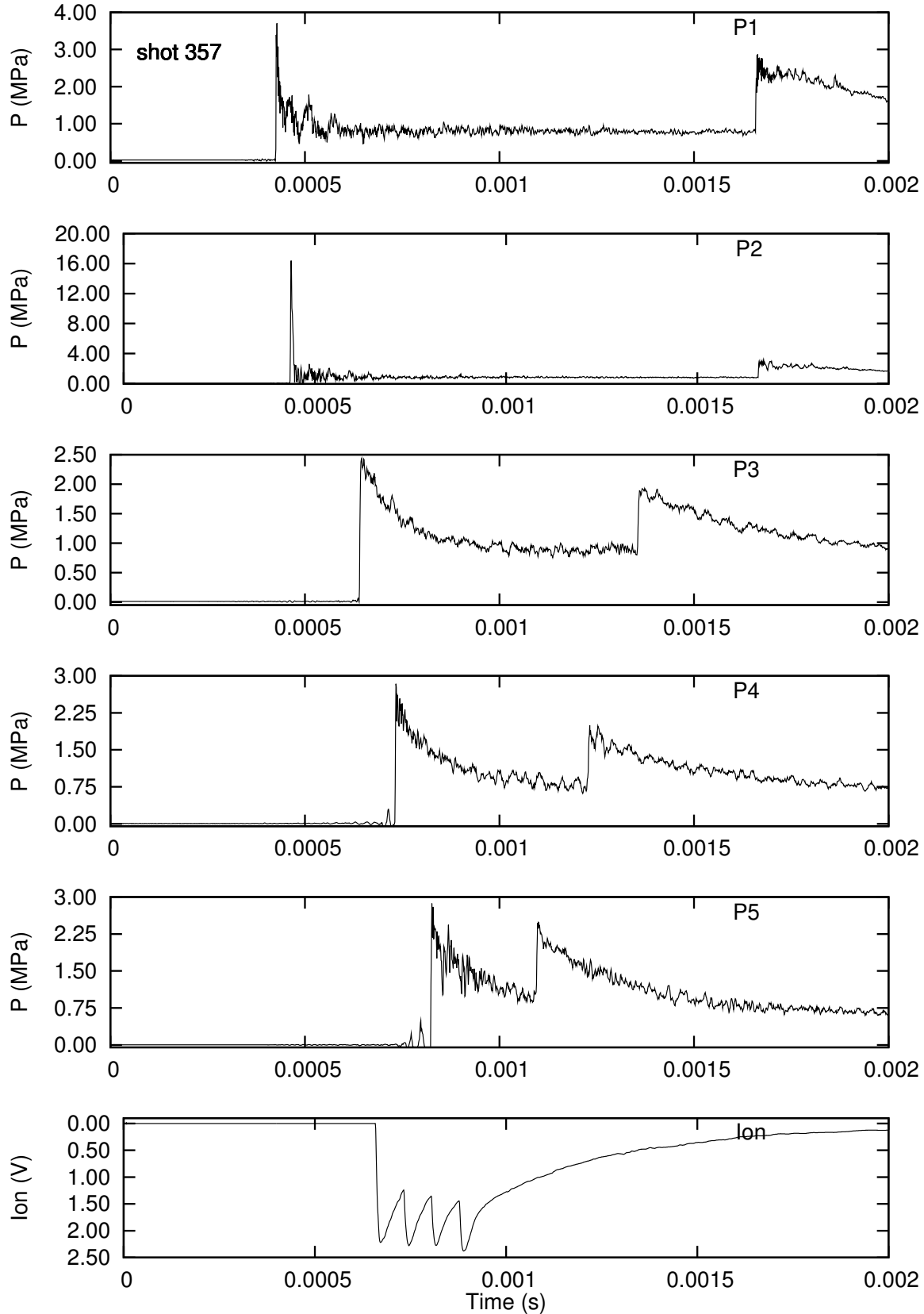


Figure H.131: Pressure history from run 125 with initiator gas injection.

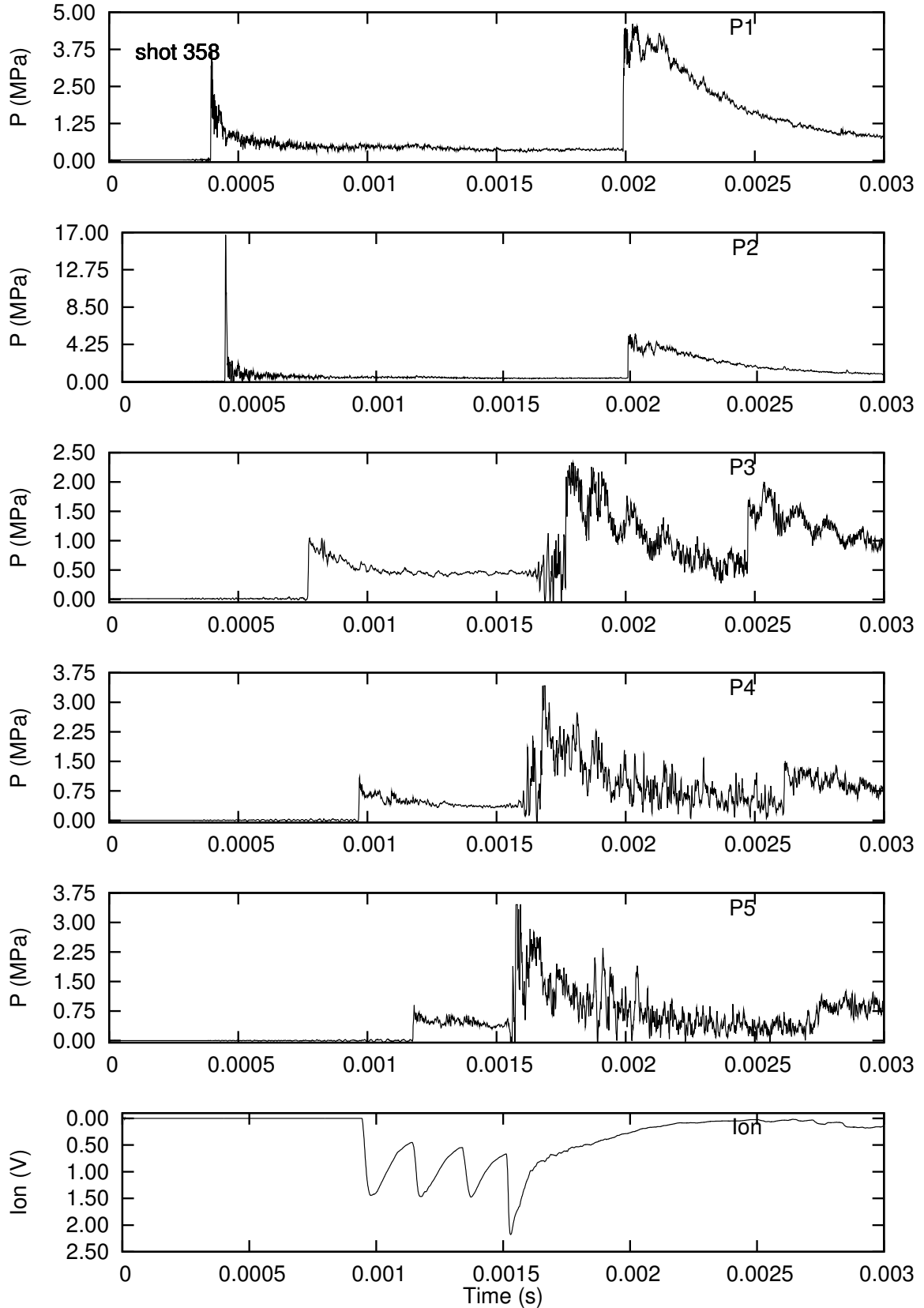


Figure H.132: Pressure history from run 126 with initiator gas injection.

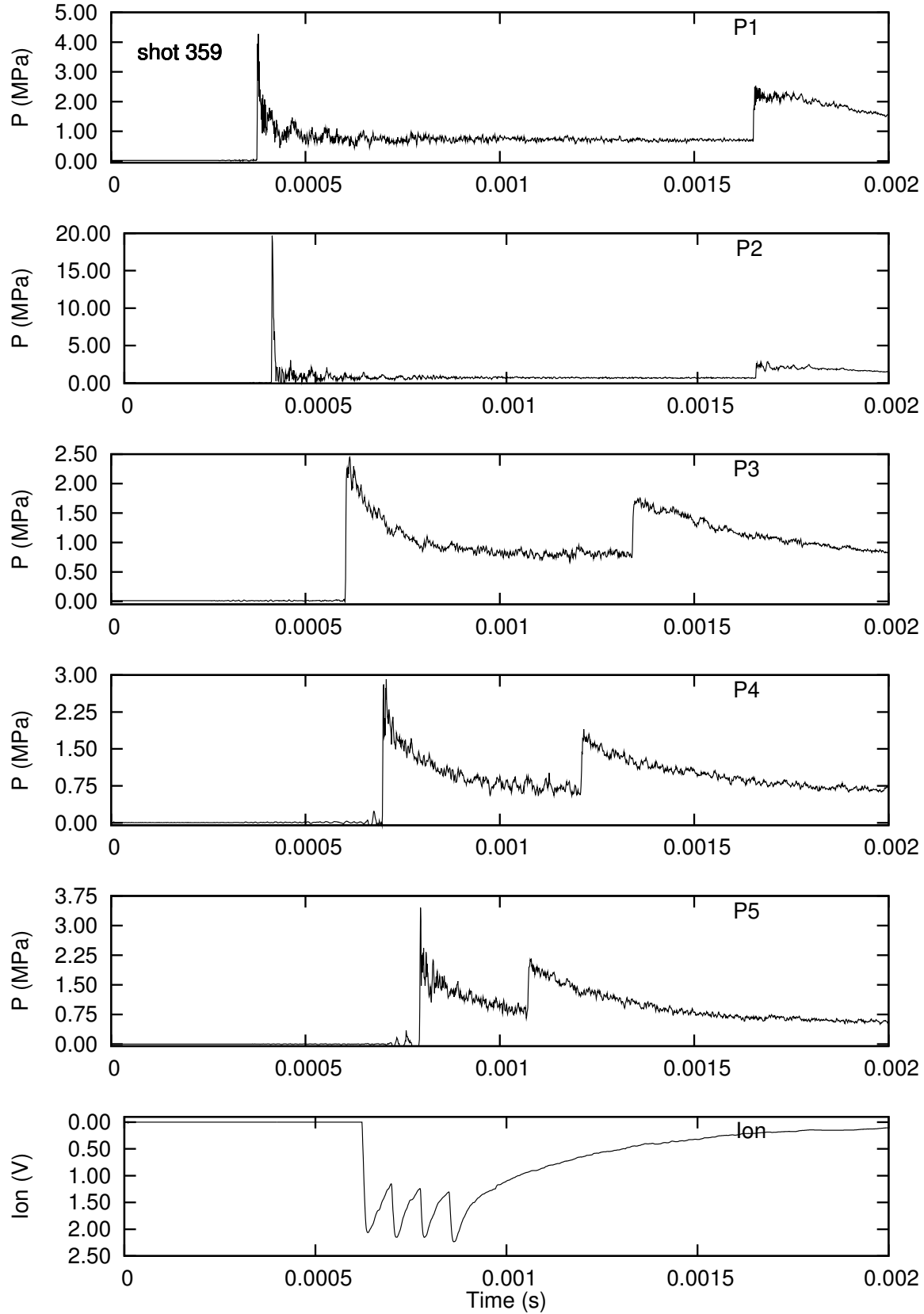


Figure H.133: Pressure history from run 127 with initiator gas injection.

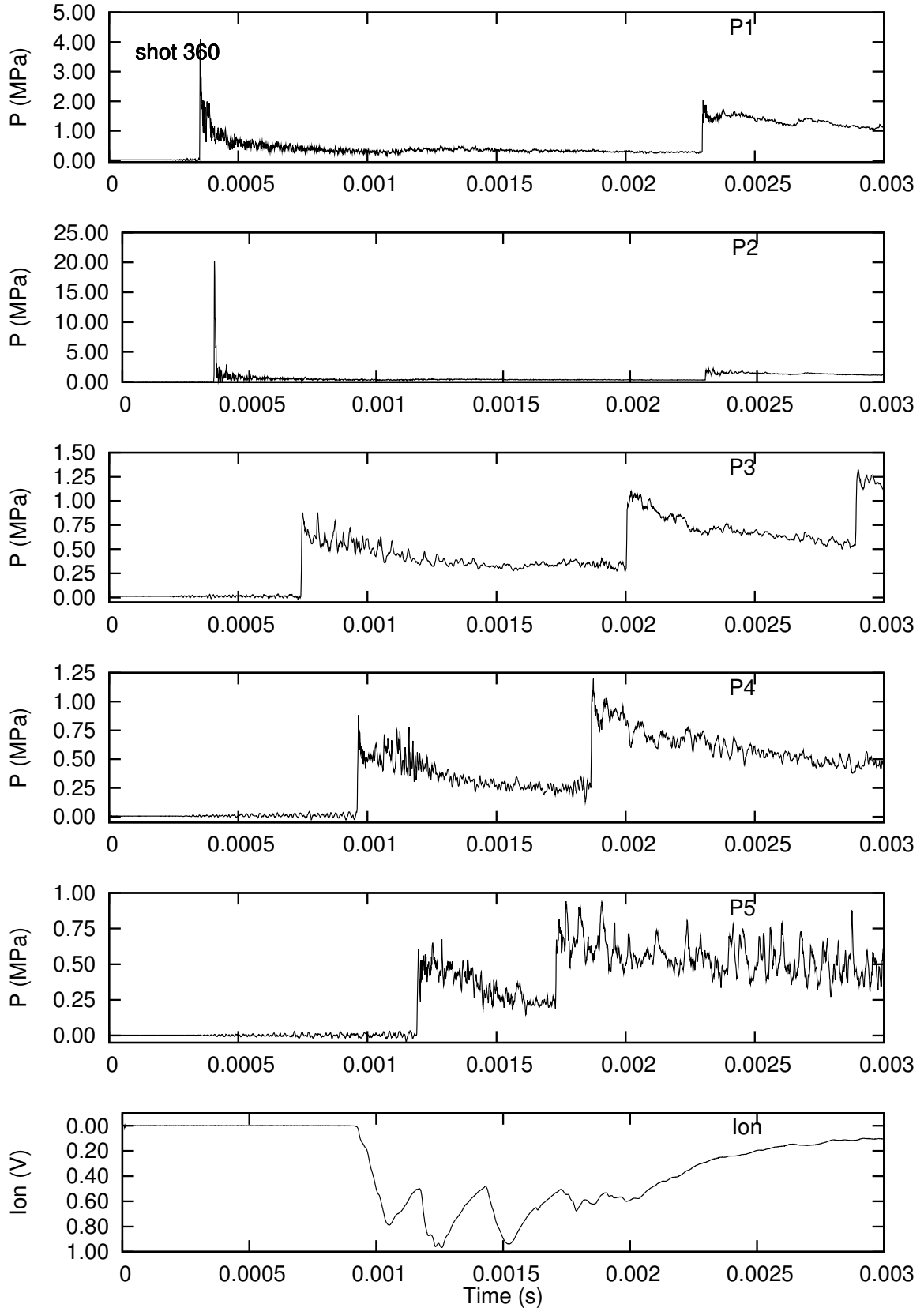


Figure H.134: Pressure history from run 128 with initiator gas injection.

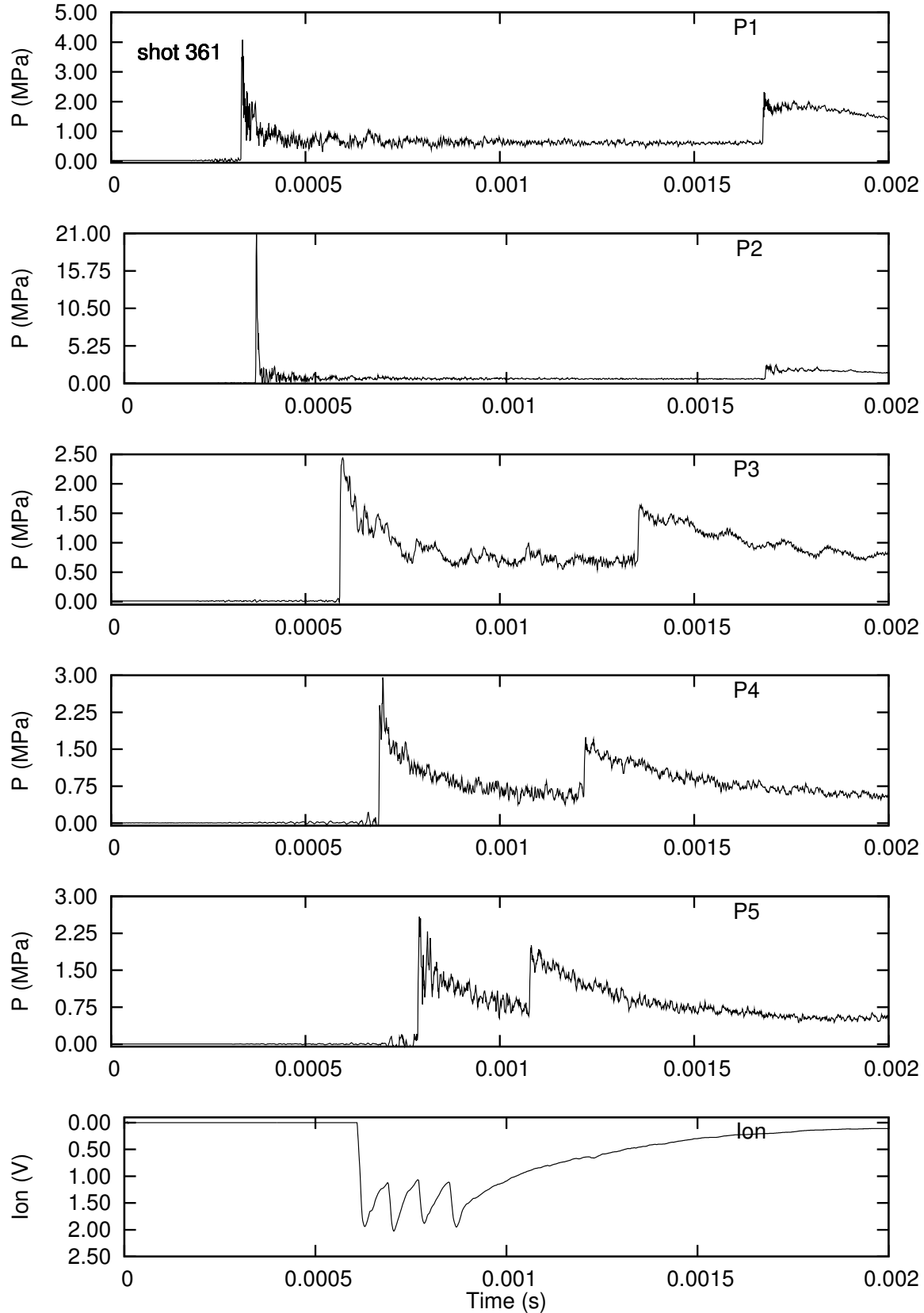


Figure H.135: Pressure history from run 129 with initiator gas injection.

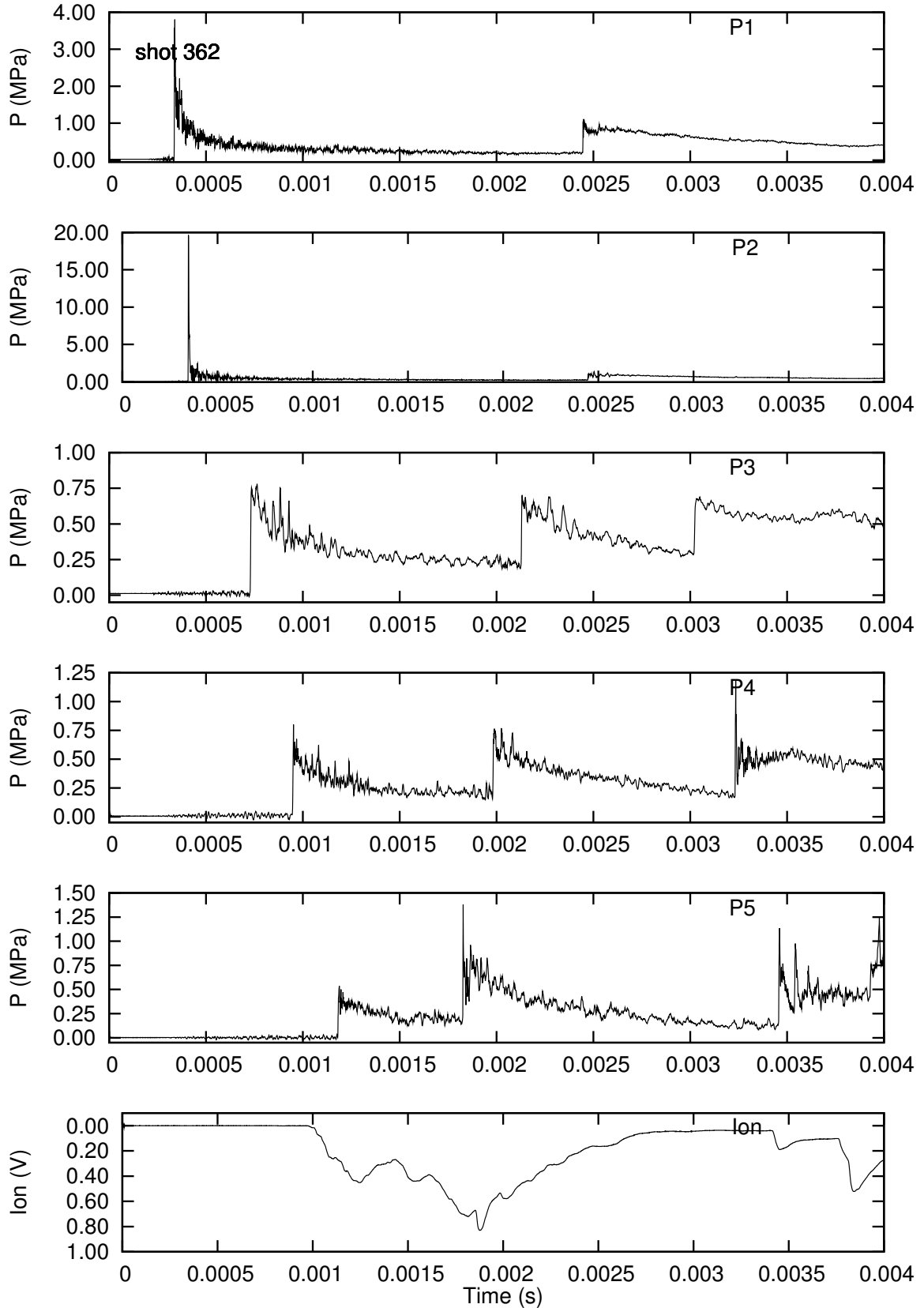


Figure H.136: Pressure history from run 130 with initiator gas injection.

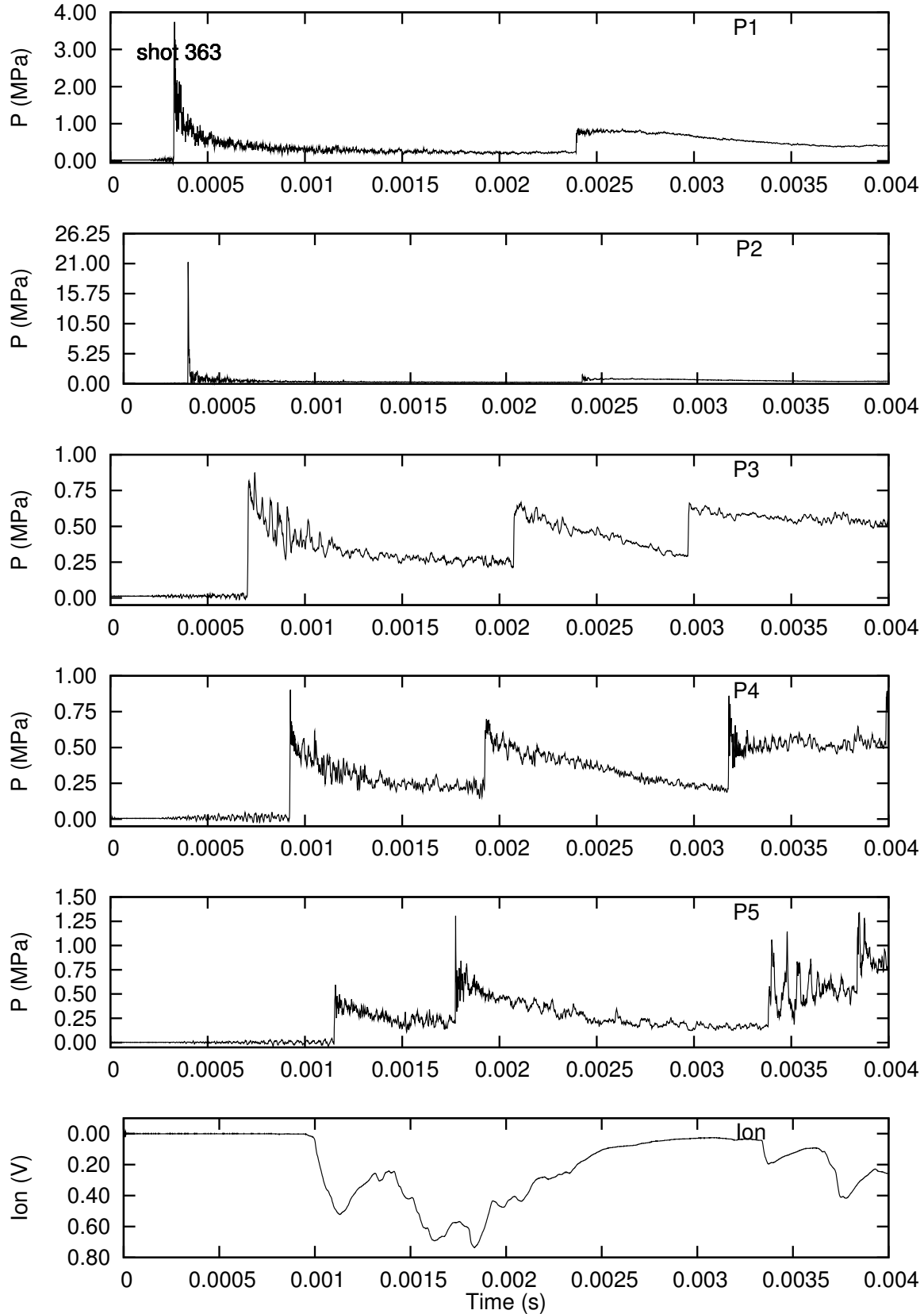


Figure H.137: Pressure history from run 131 with initiator gas injection.

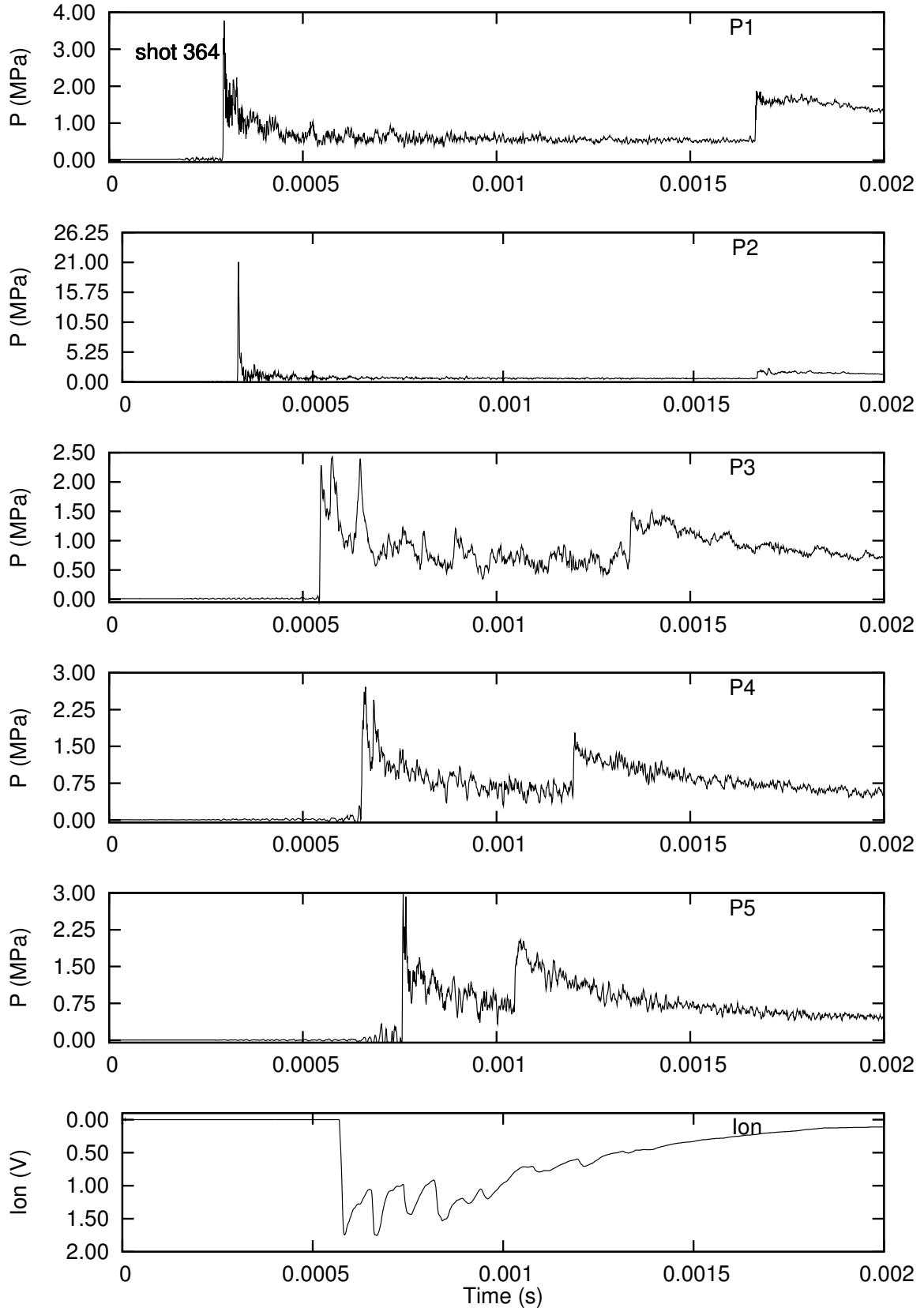


Figure H.138: Pressure history from run 132 with initiator gas injection.

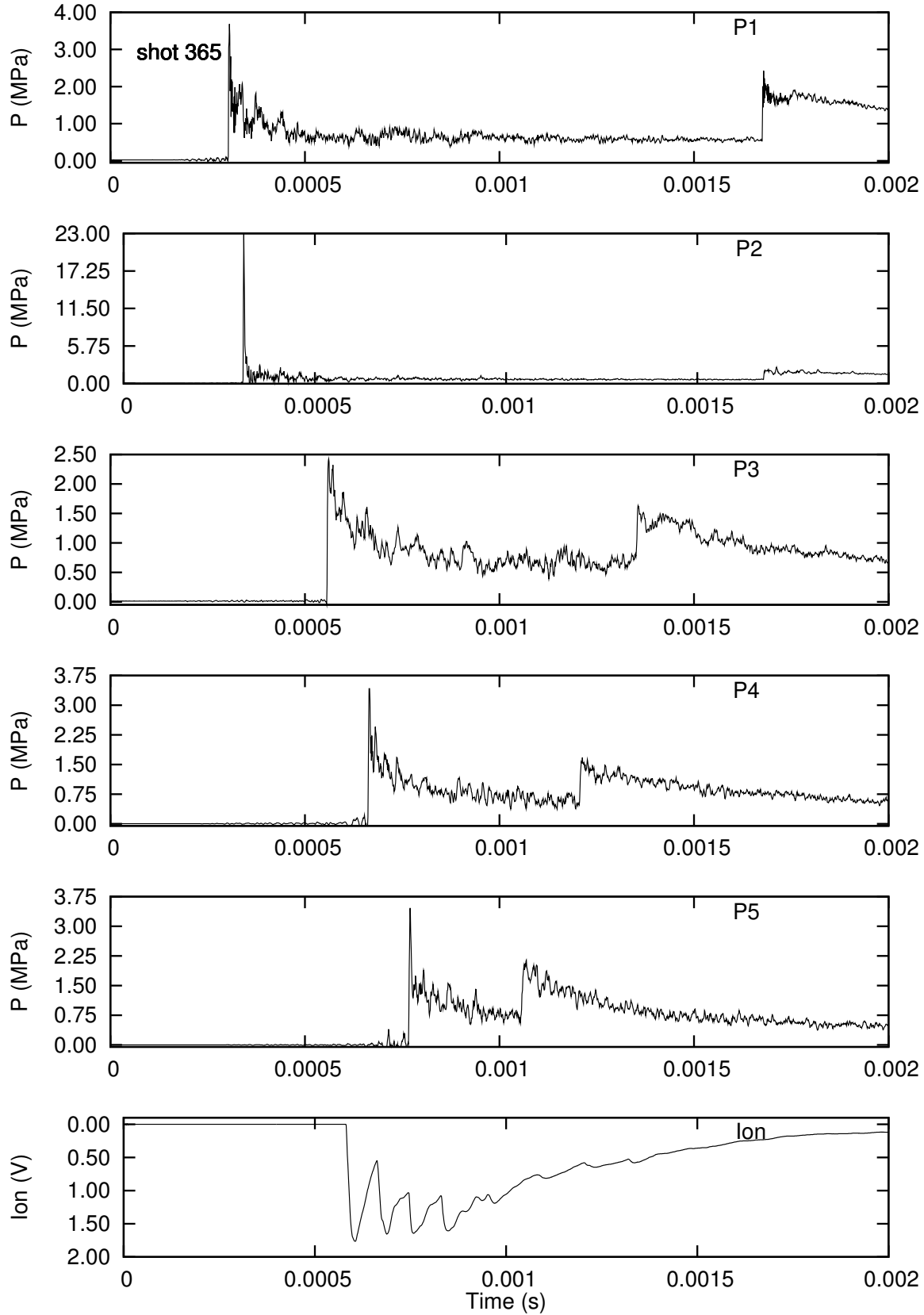


Figure H.139: Pressure history from run 133 with initiator gas injection.

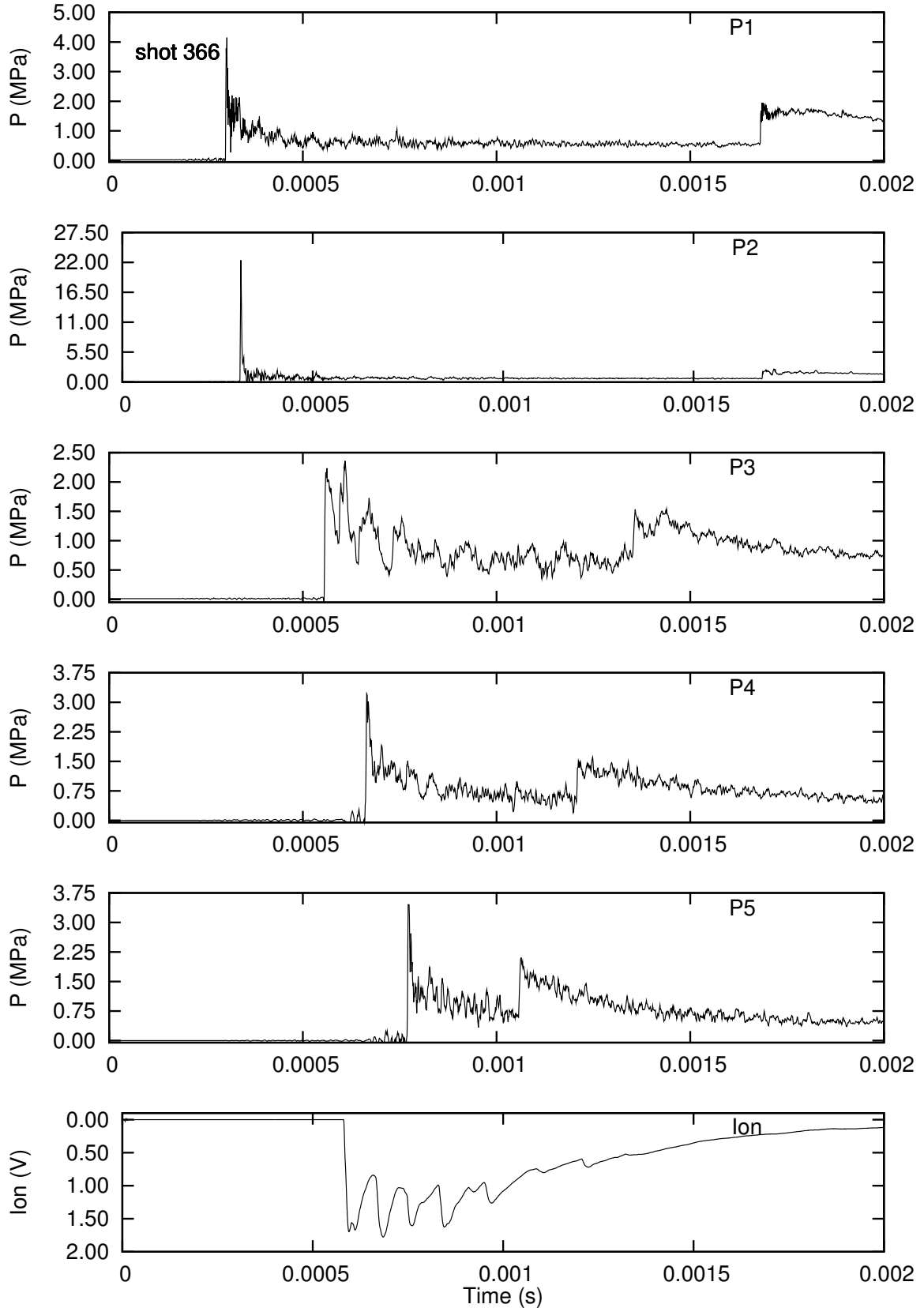


Figure H.140: Pressure history from run 134 with initiator gas injection.

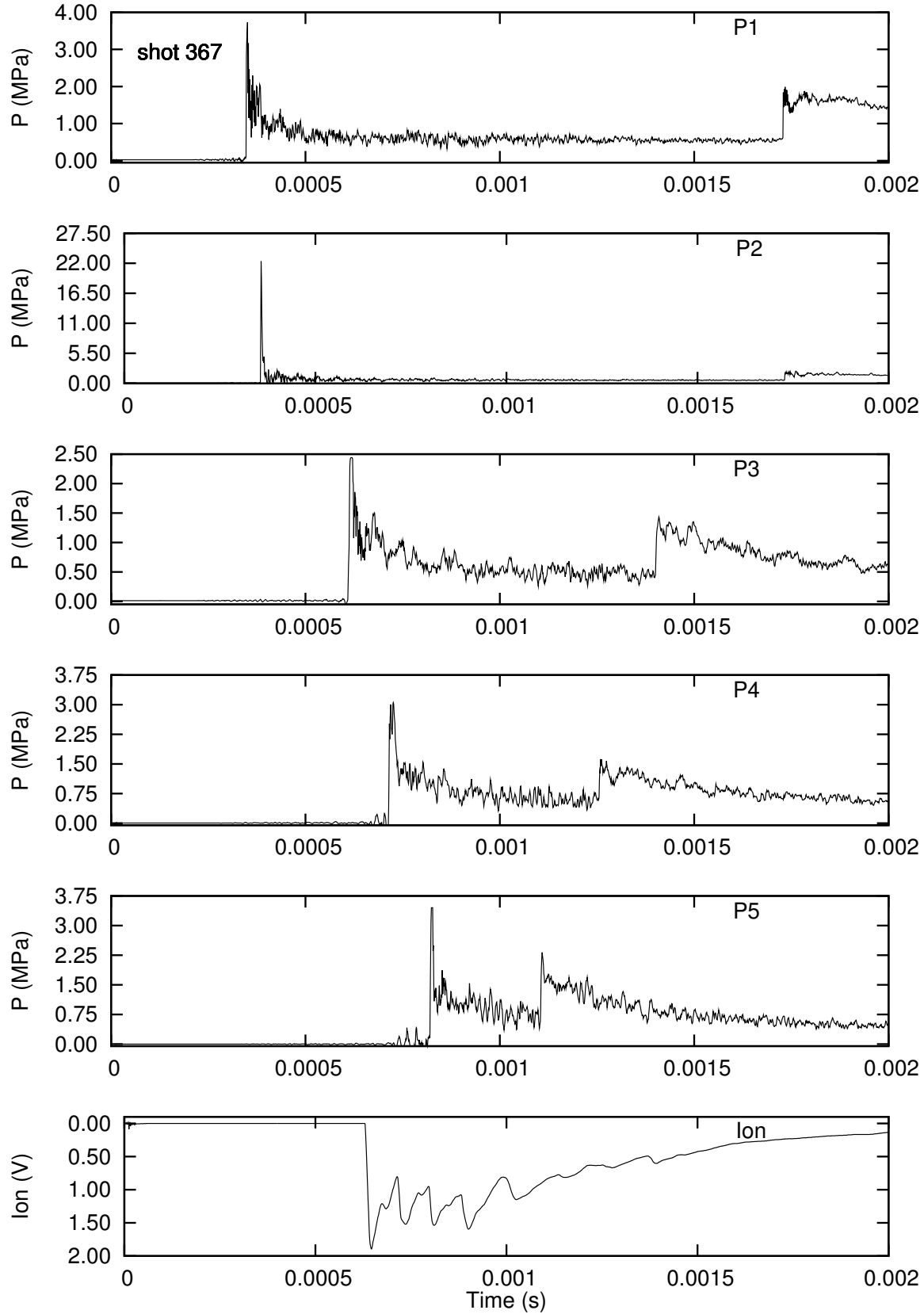


Figure H.141: Pressure history from run 135 with initiator gas injection.

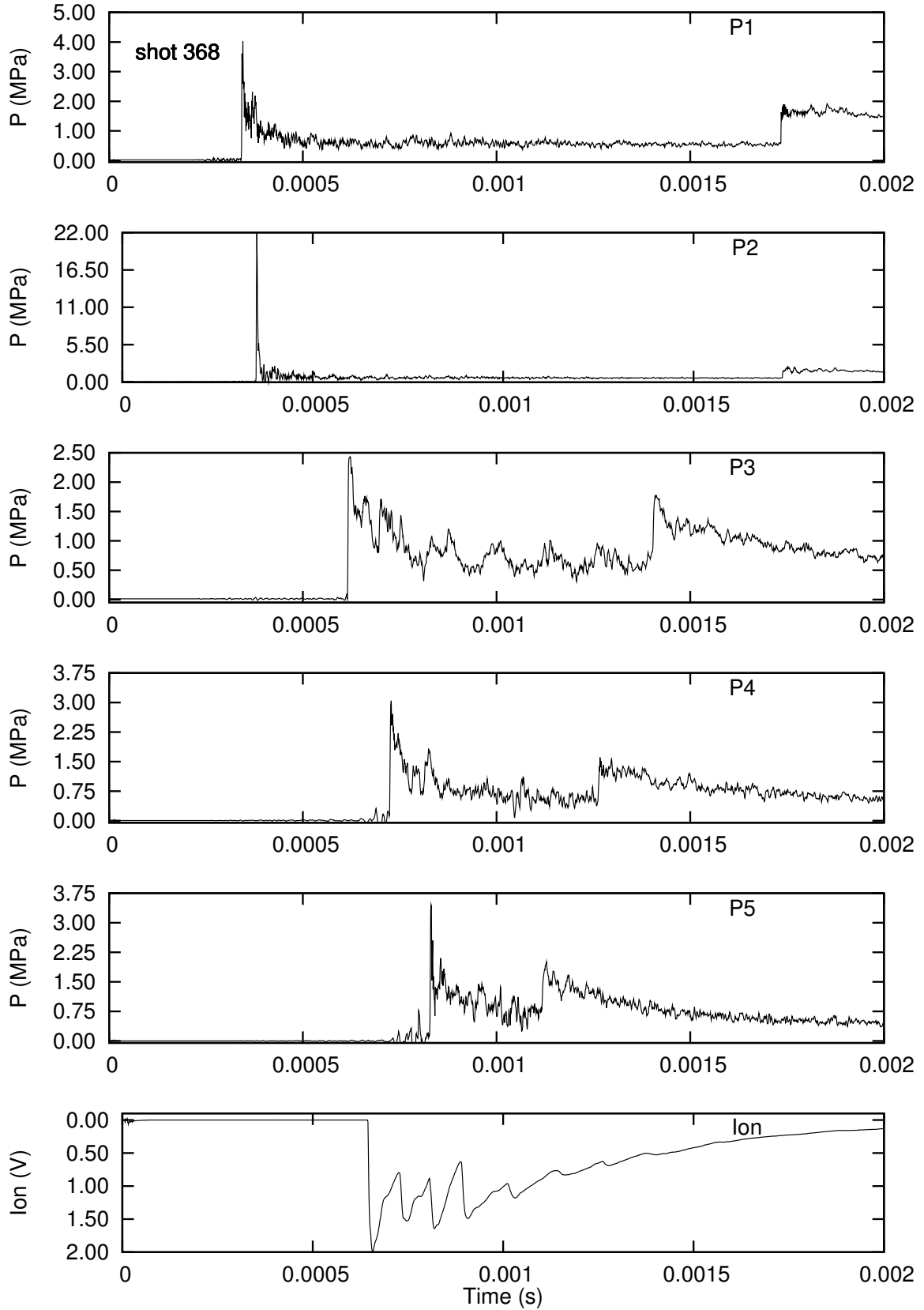


Figure H.142: Pressure history from run 136 with initiator gas injection.

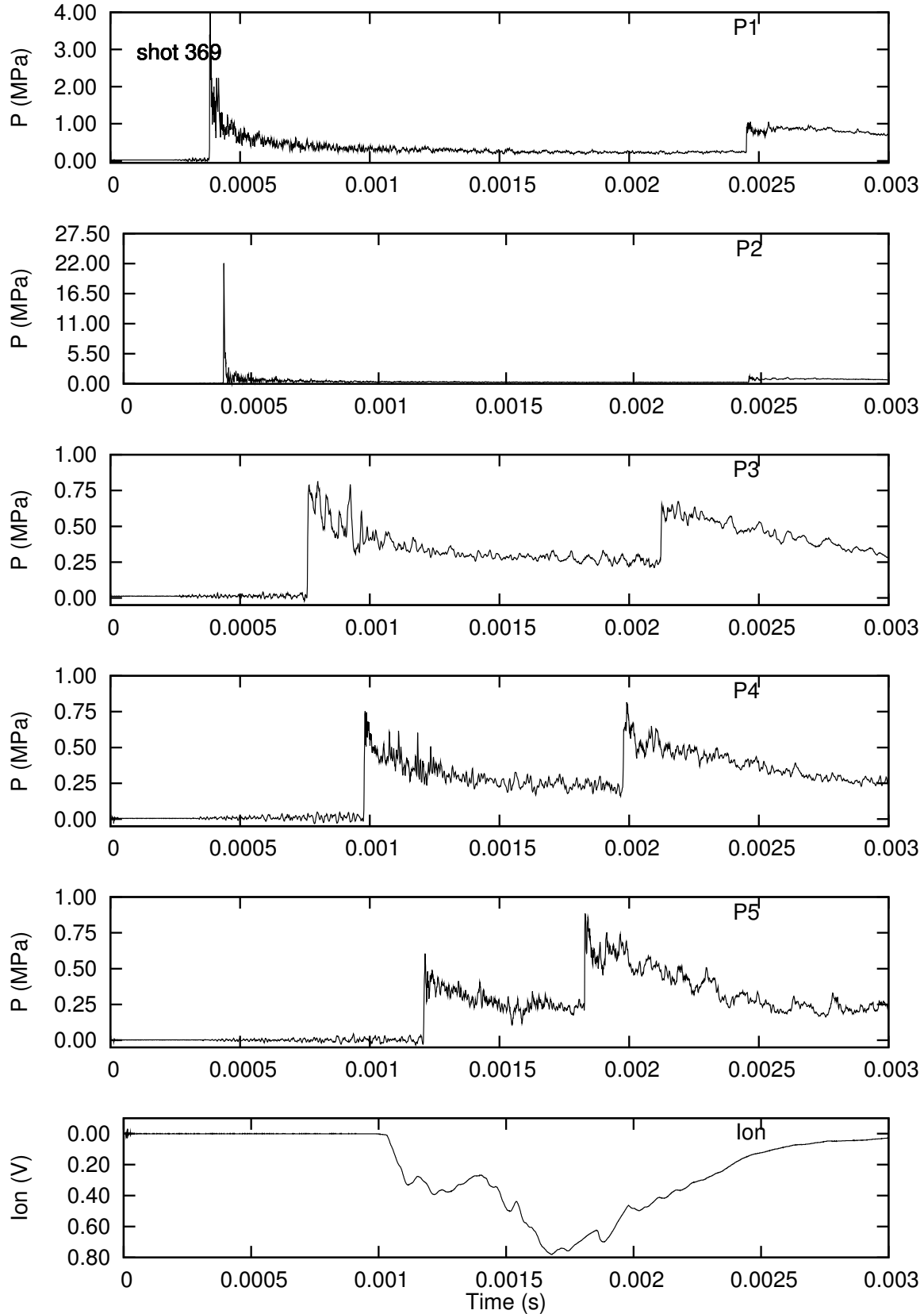


Figure H.143: Pressure history from run 137 with initiator gas injection.

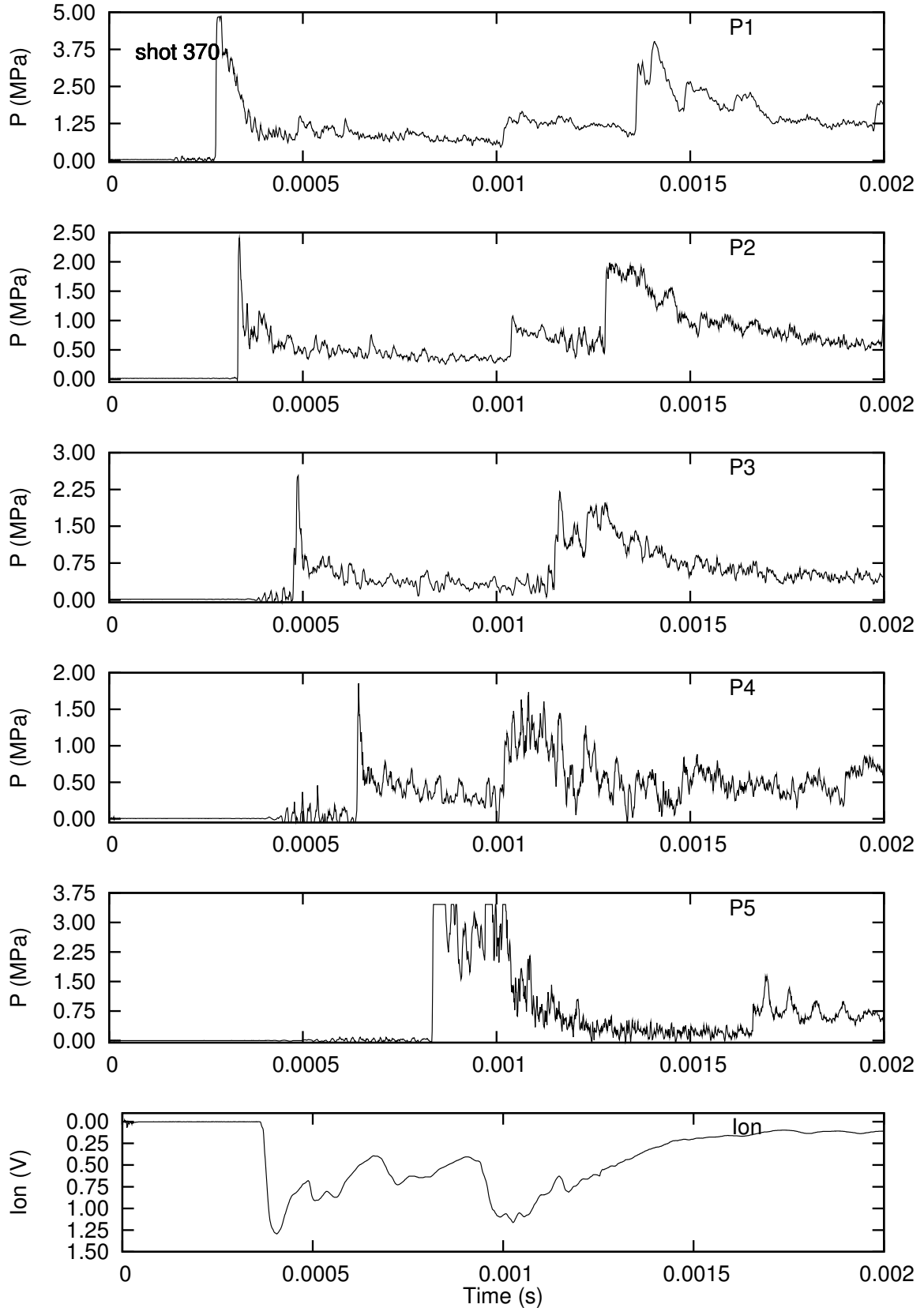


Figure H.144: Pressure history from run 138 with initiator gas injection.

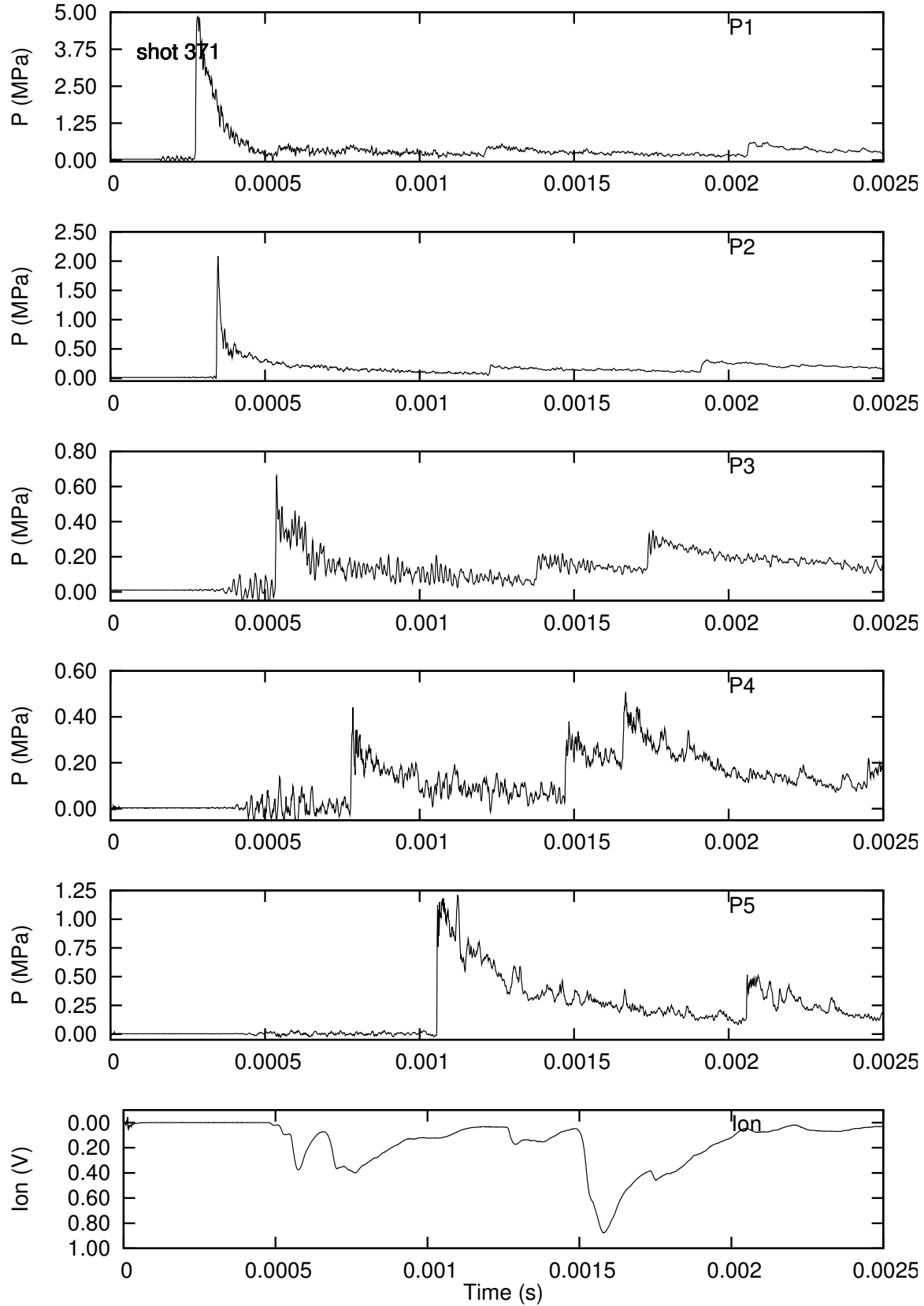


Figure H.145: Pressure history from run 139 with initiator gas injection.

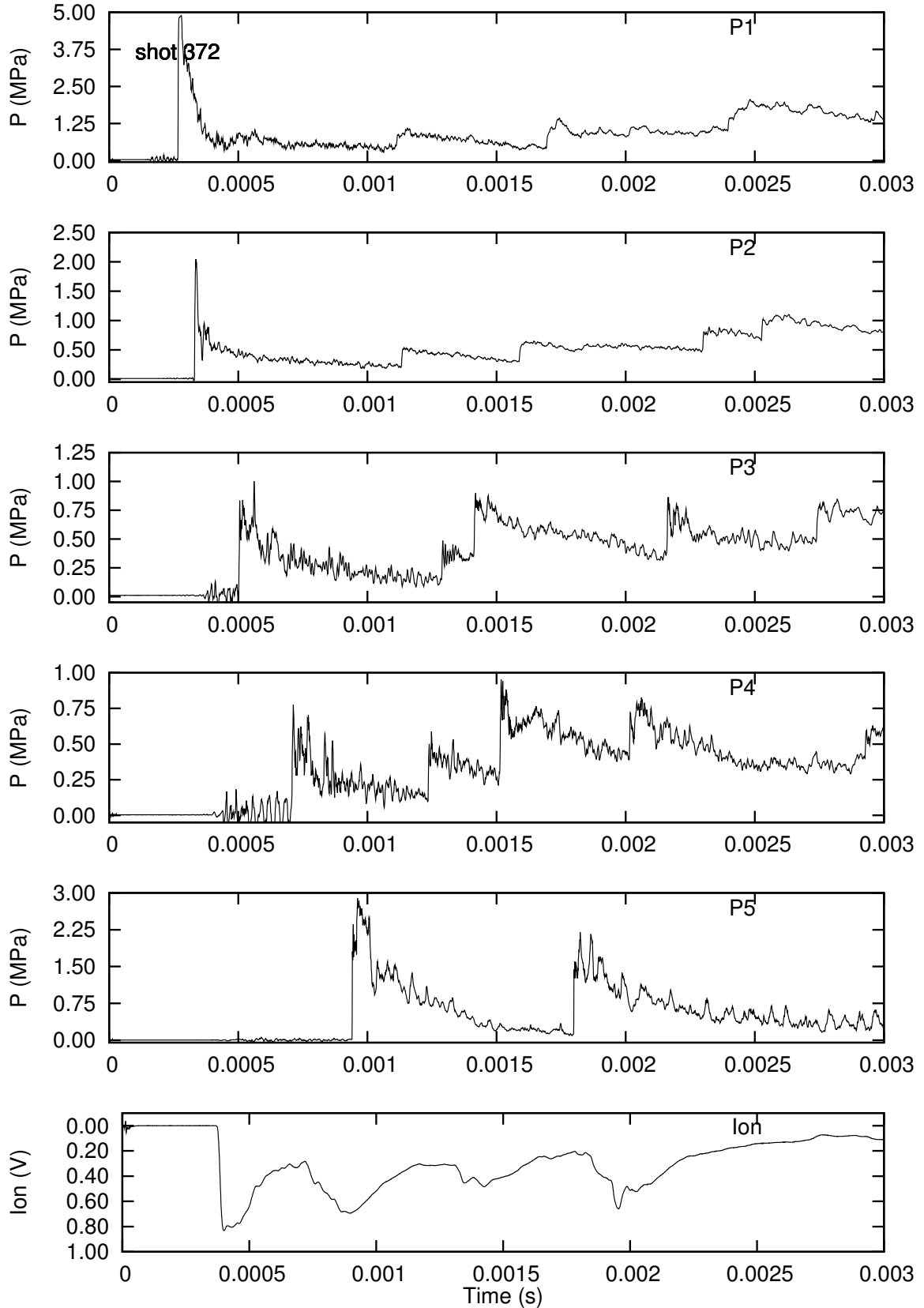


Figure H.146: Pressure history from run 140 with initiator gas injection.

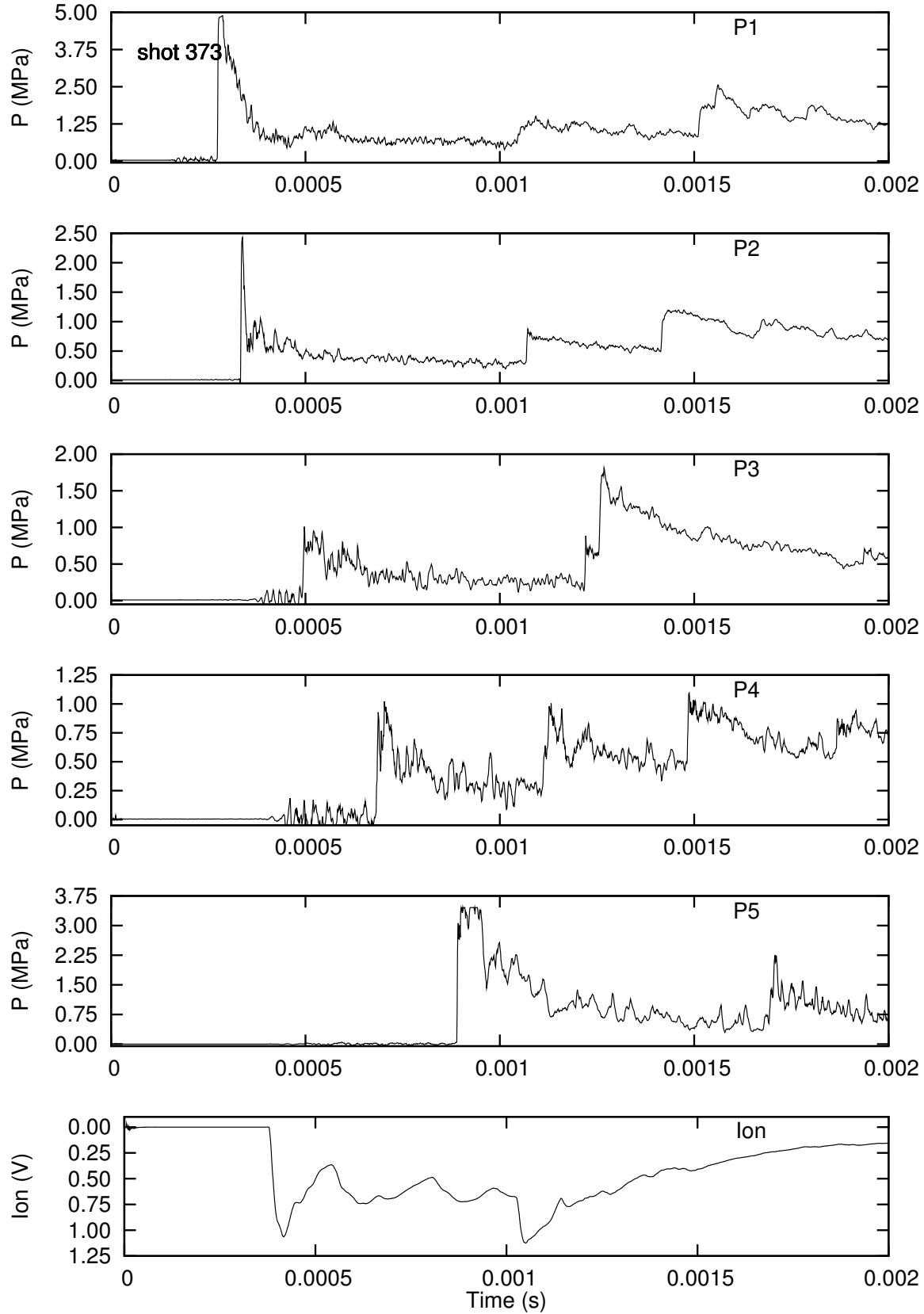


Figure H.147: Pressure history from run 141 with initiator gas injection.

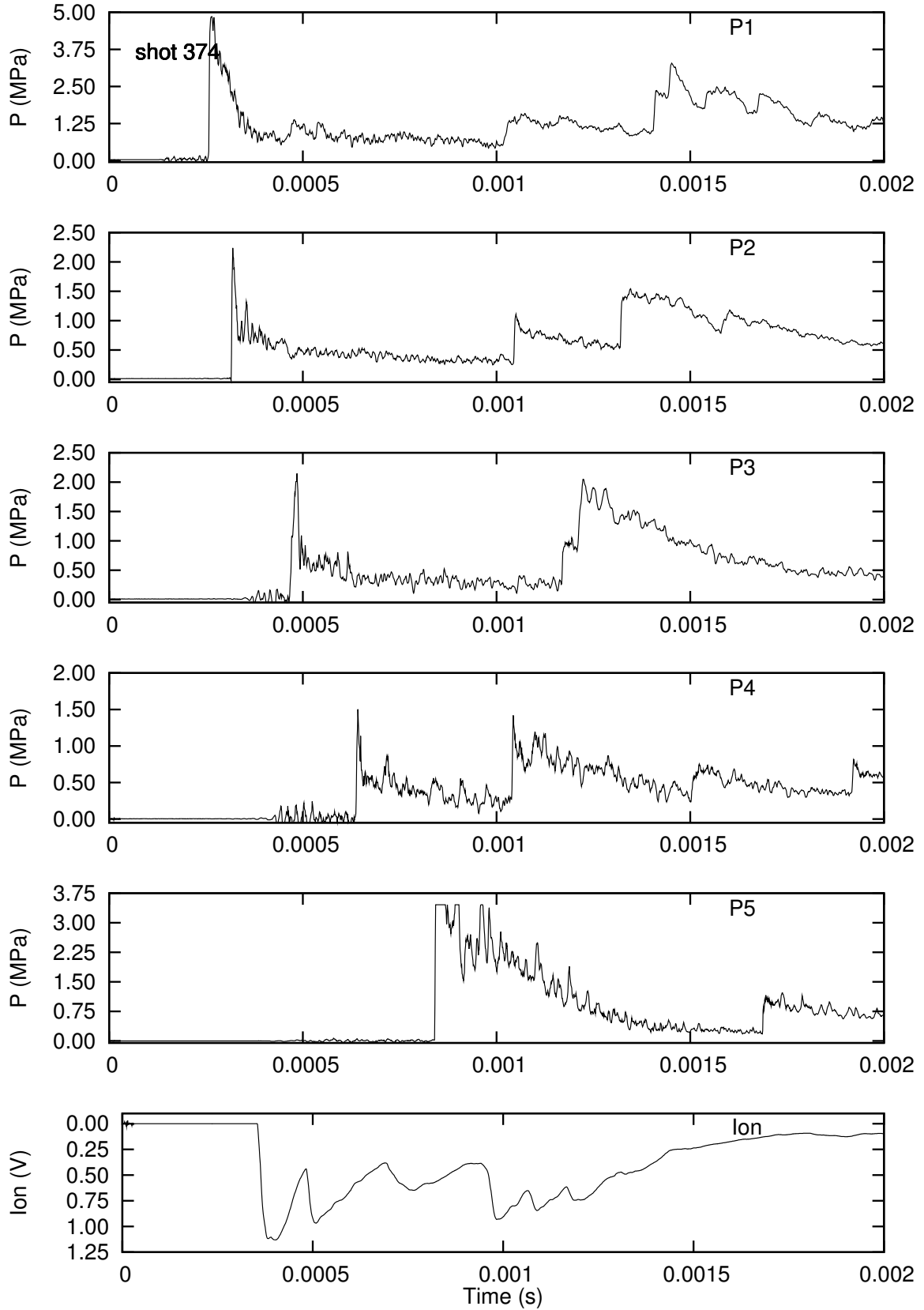


Figure H.148: Pressure history from run 142 with initiator gas injection.

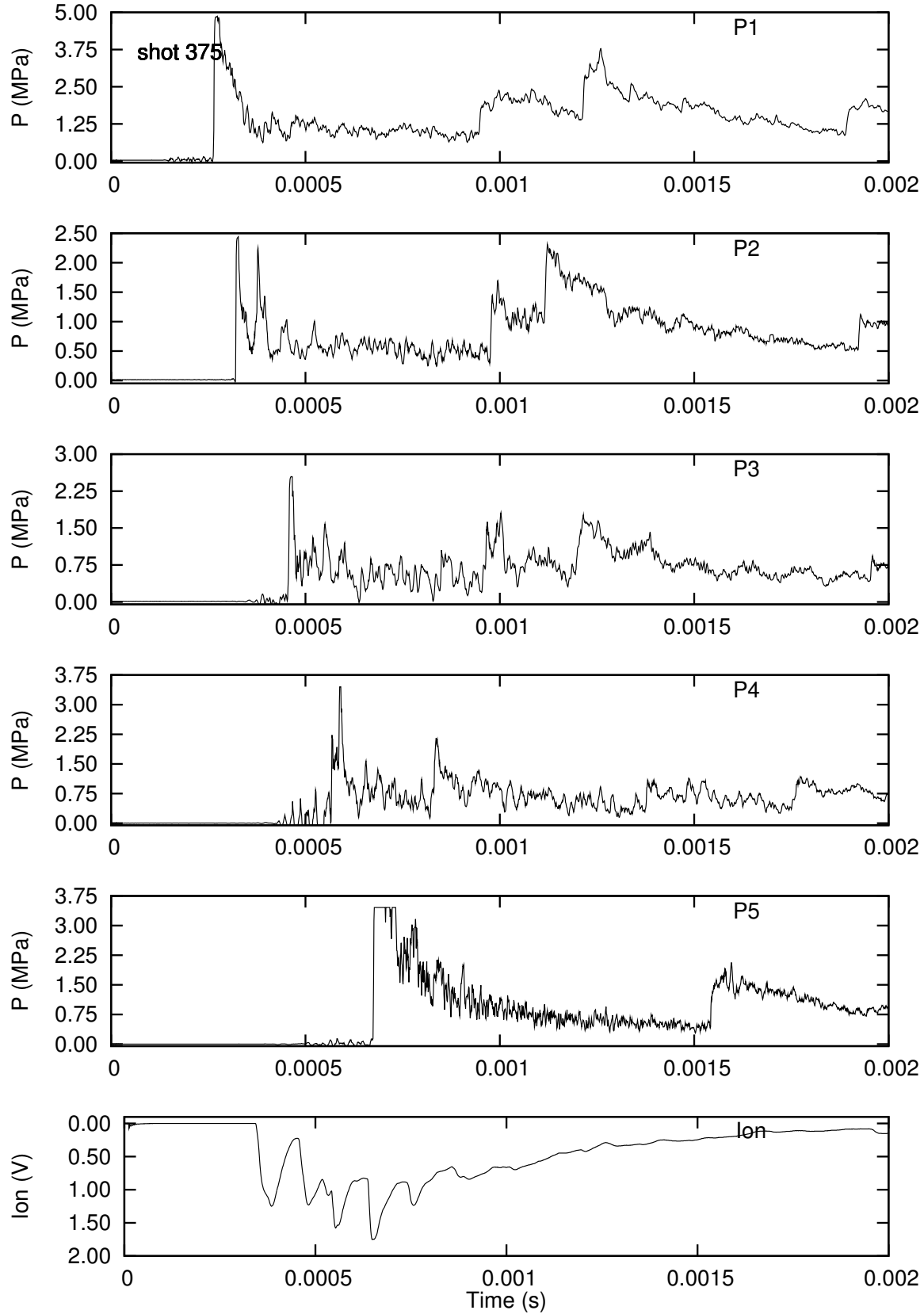


Figure H.149: Pressure history from run 143 with initiator gas injection.

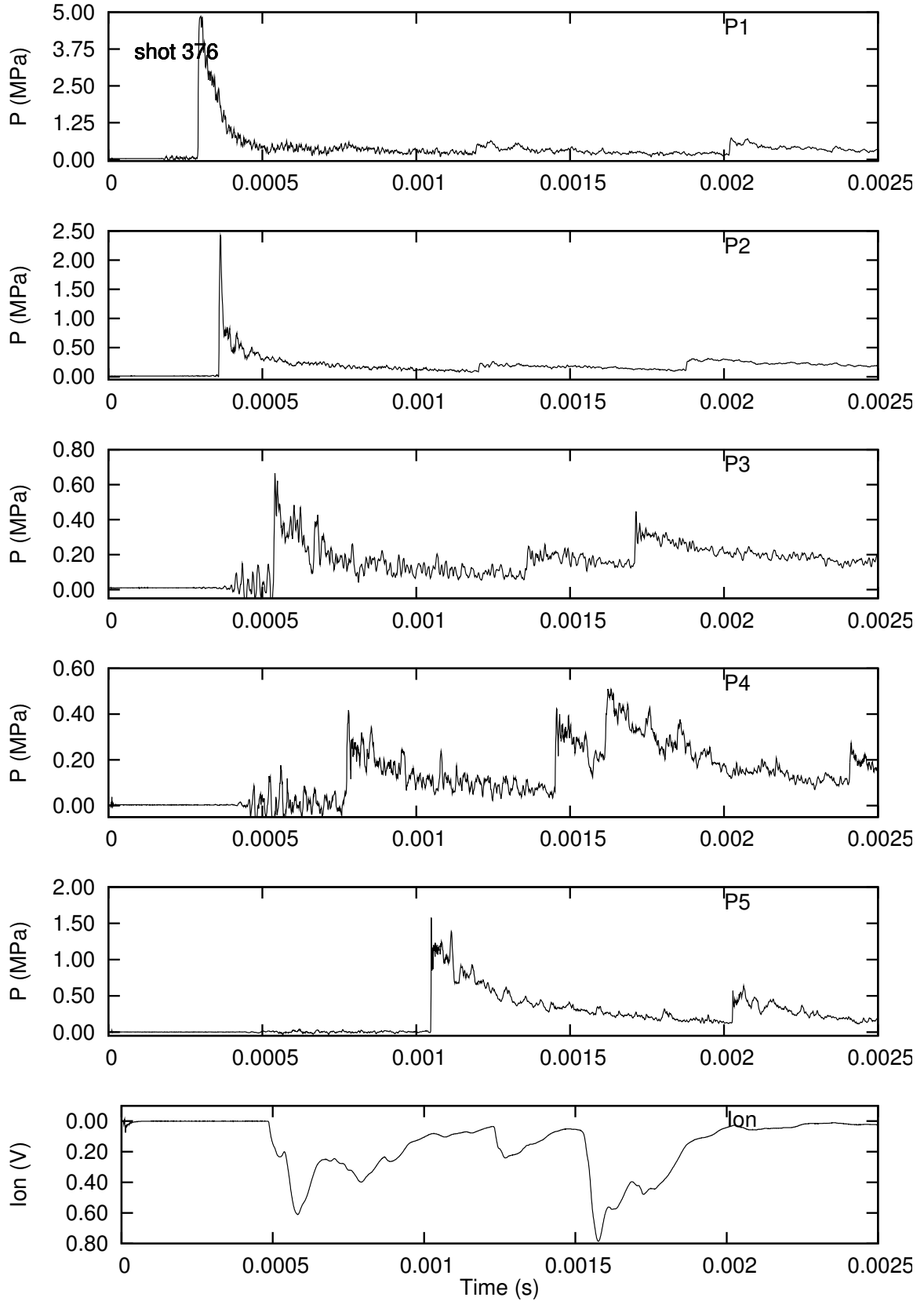


Figure H.150: Pressure history from run 144 with initiator gas injection.

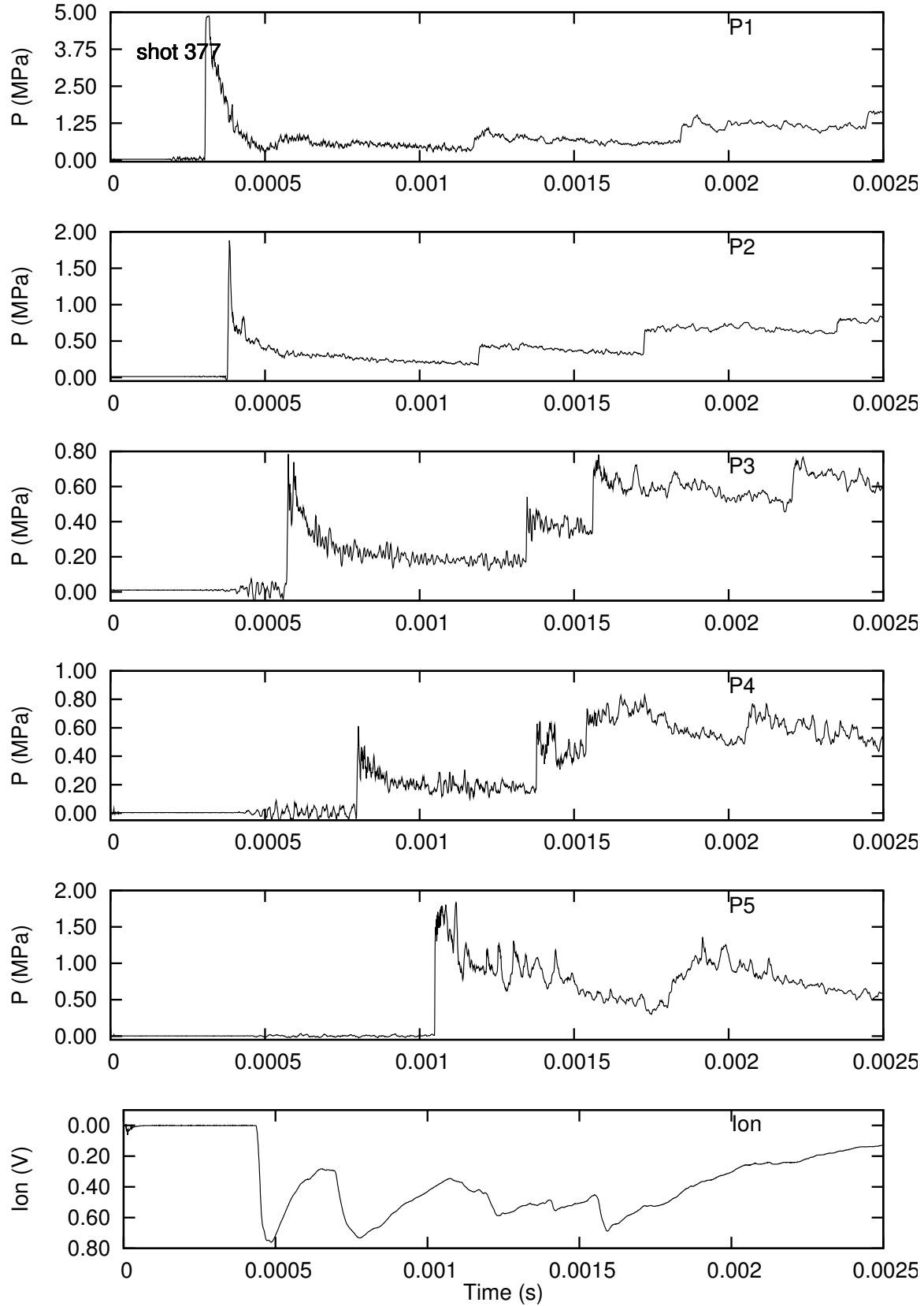


Figure H.151: Pressure history from run 145 with initiator gas injection.

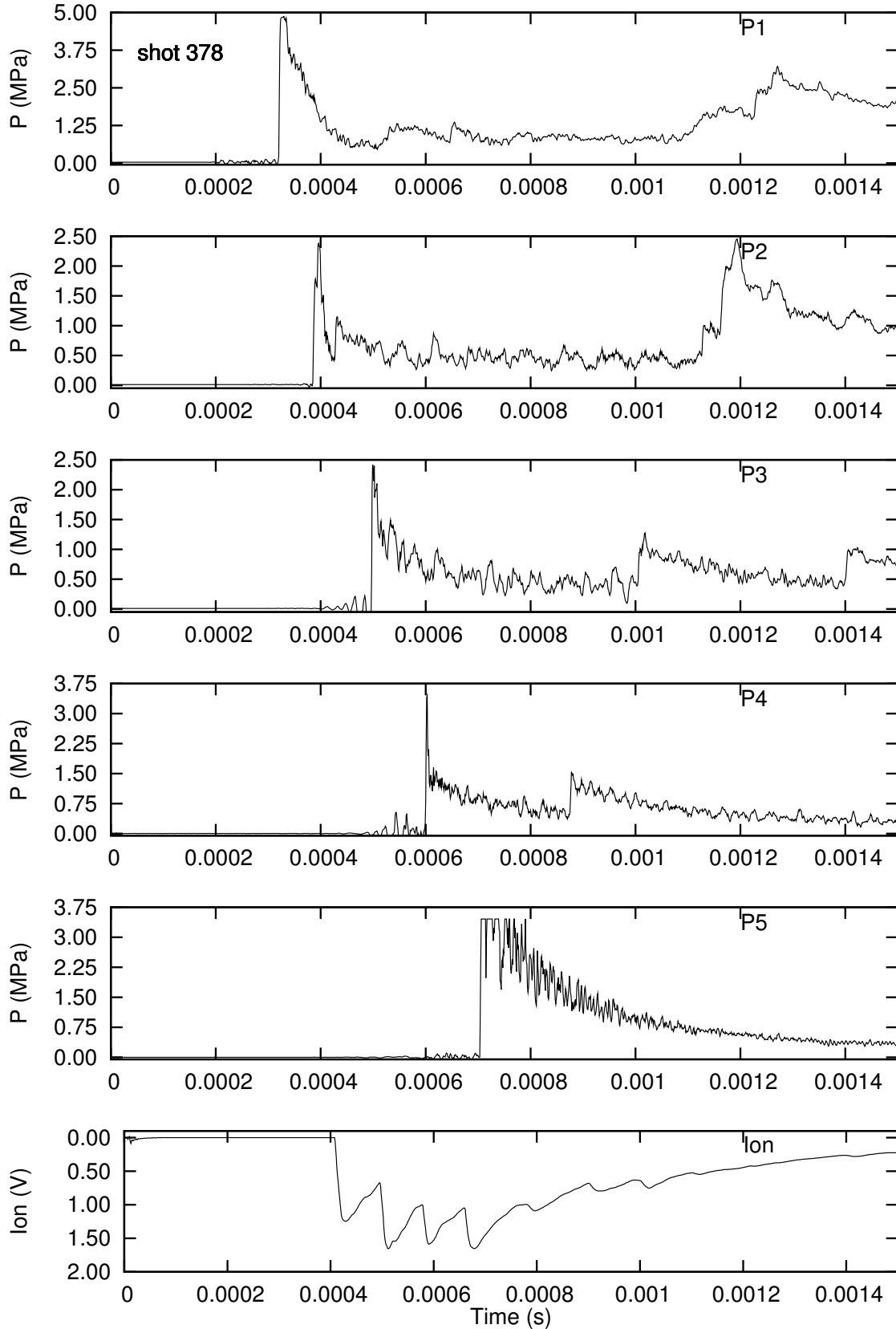


Figure H.152: Pressure history from run 146 with initiator gas injection.

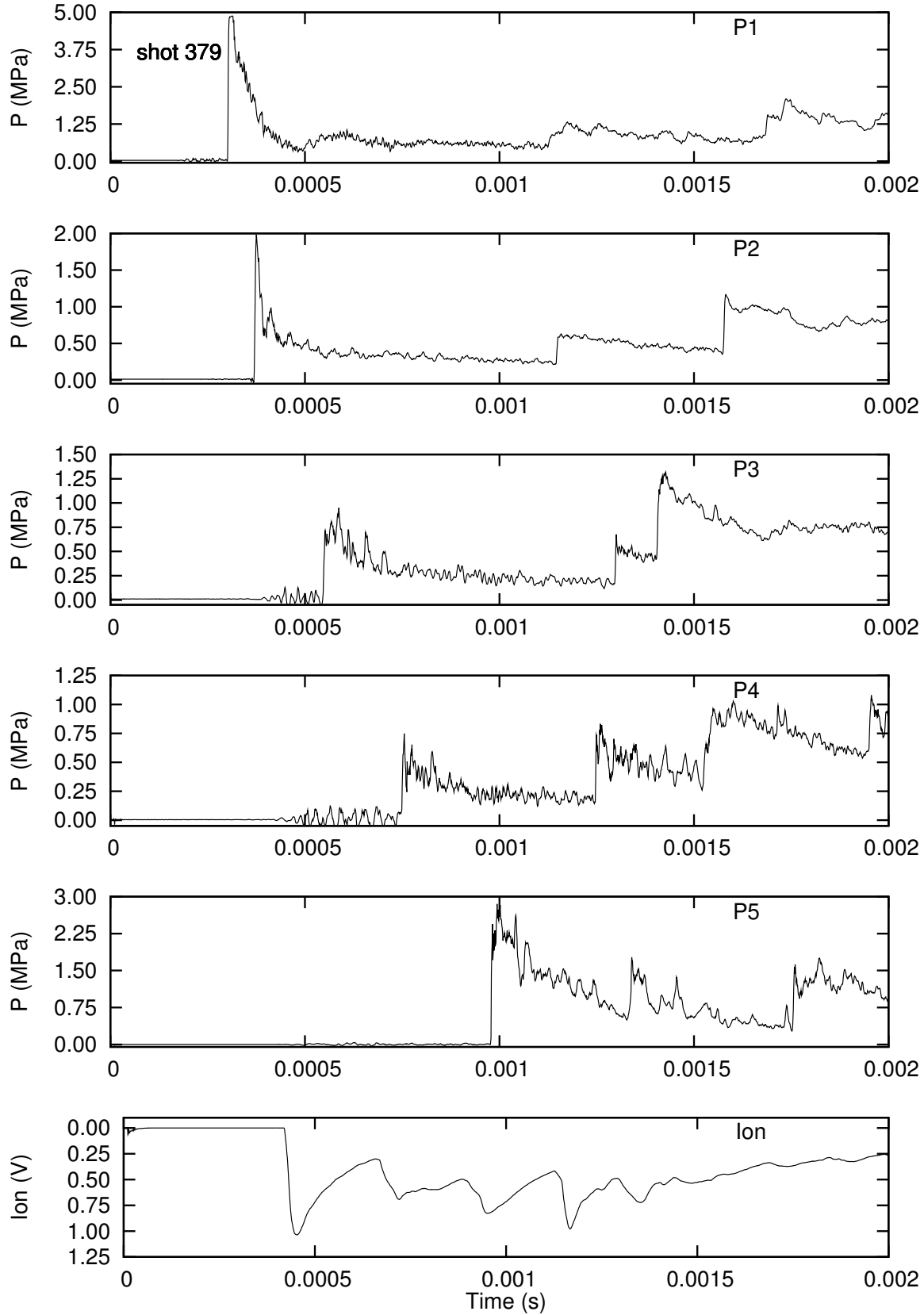


Figure H.153: Pressure history from run 147 with initiator gas injection.

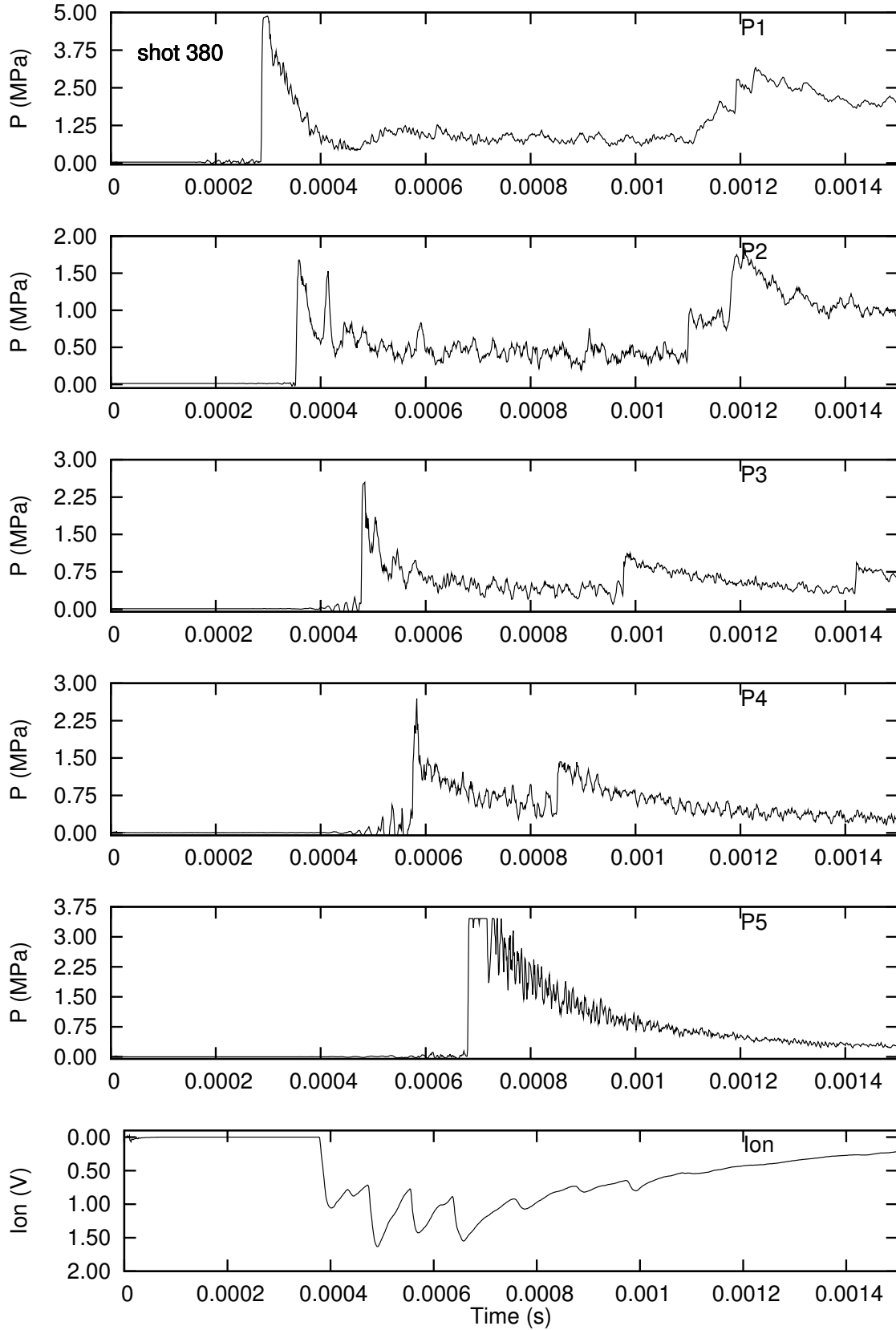


Figure H.154: Pressure history from run 148 with initiator gas injection.

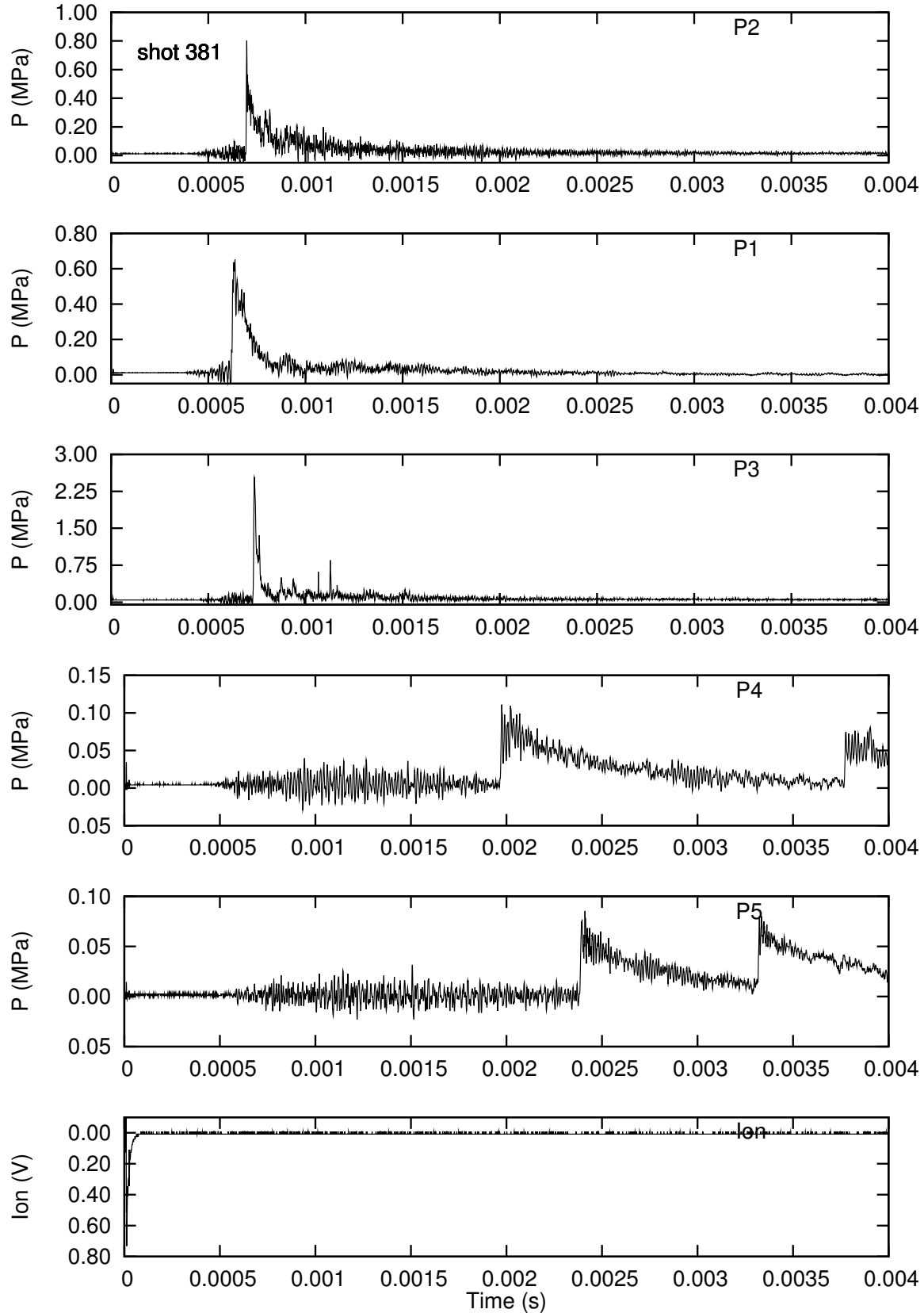


Figure H.155: Pressure history from run 149 with initiator gas injection.

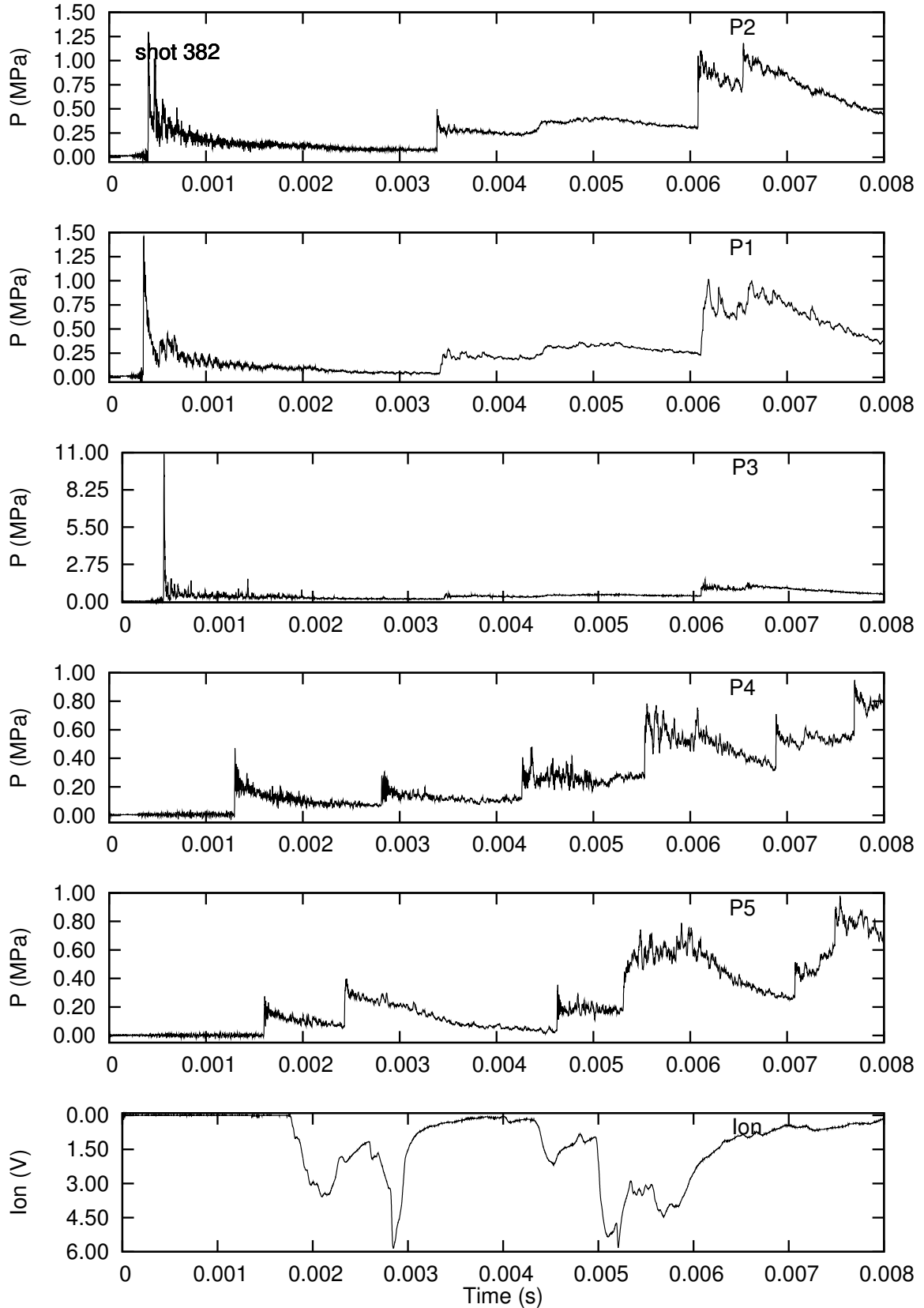


Figure H.156: Pressure history from run 150 with initiator gas injection.

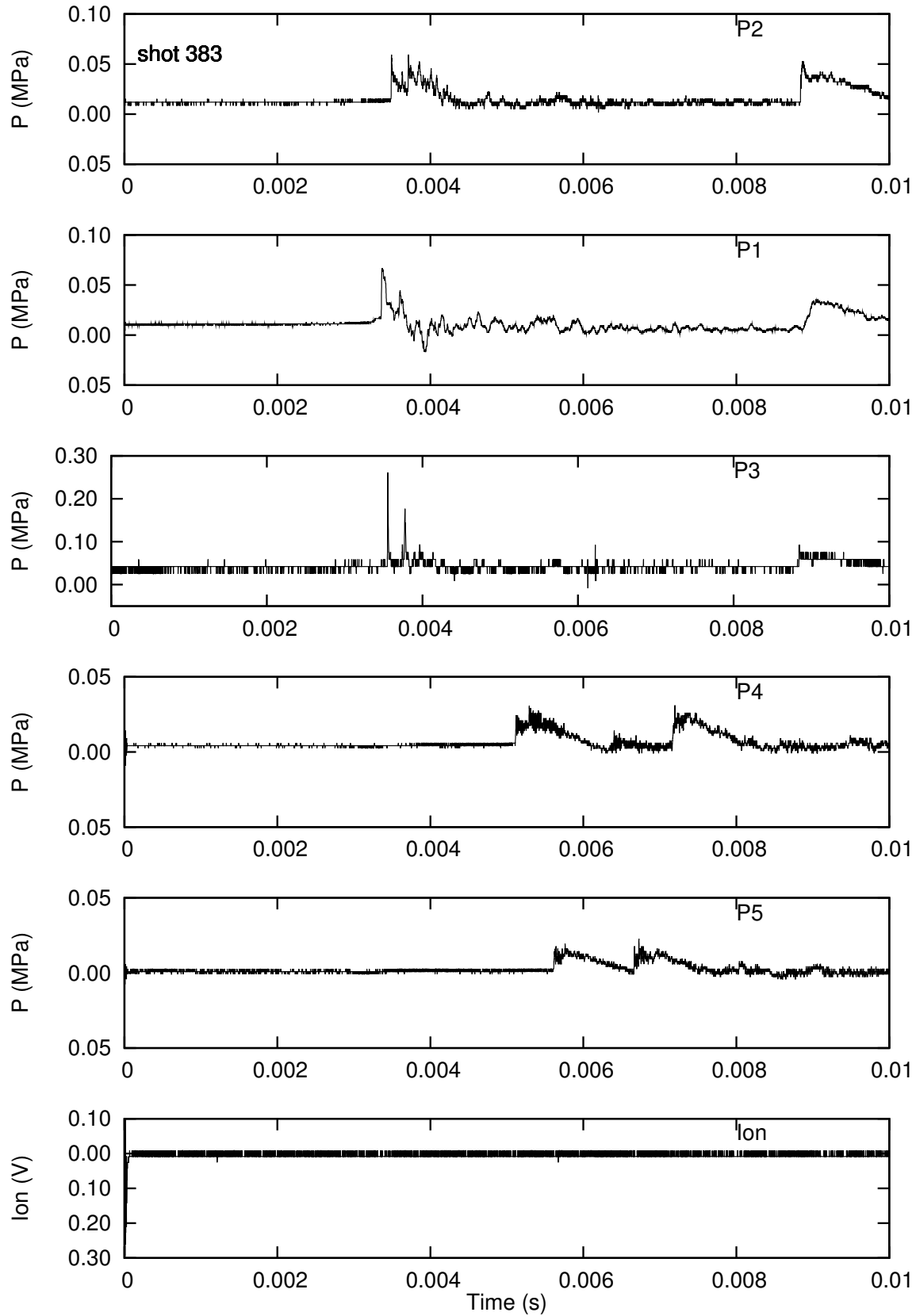


Figure H.157: Pressure history from run 151 with initiator gas injection.

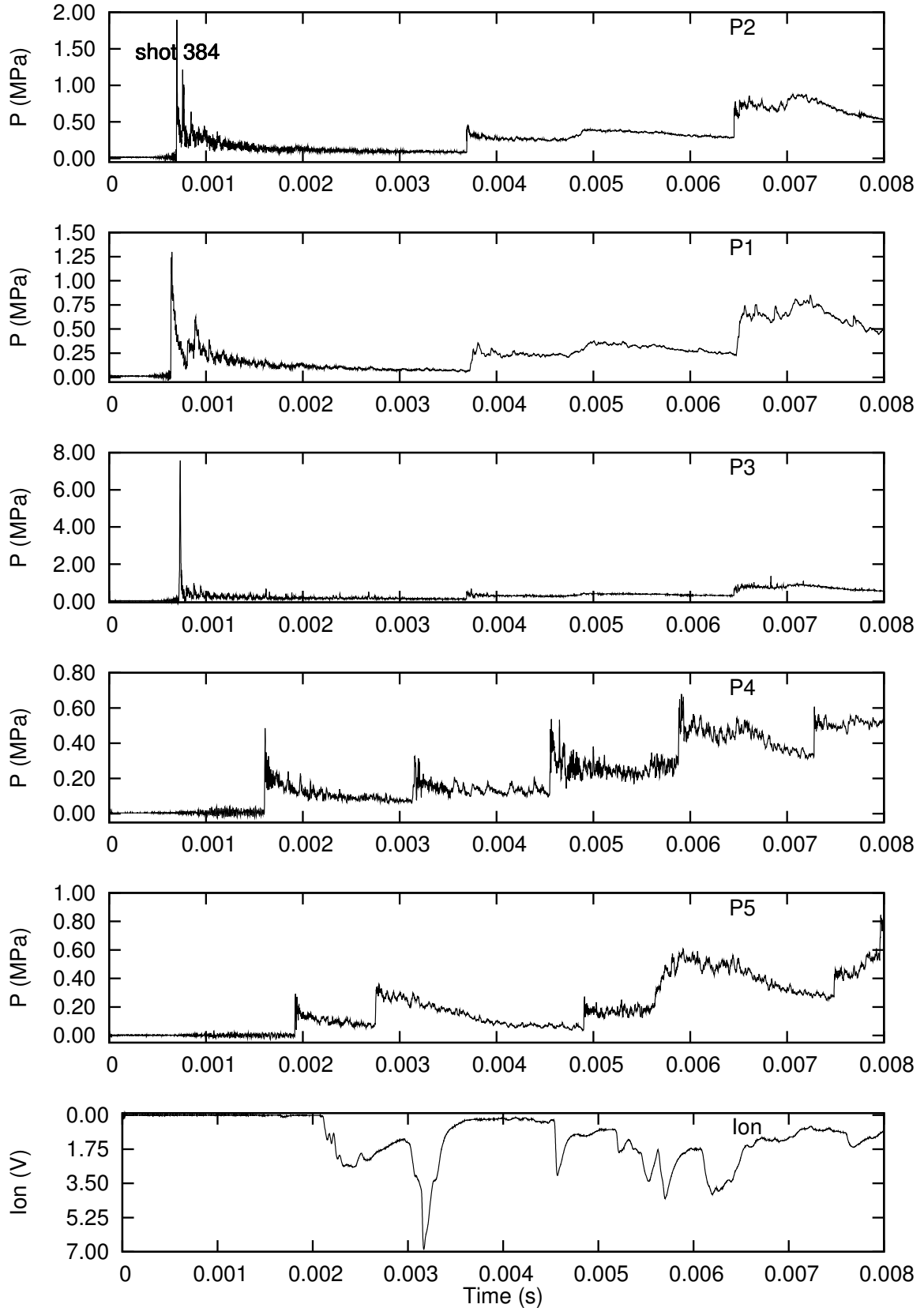


Figure H.158: Pressure history from run 152 with initiator gas injection.

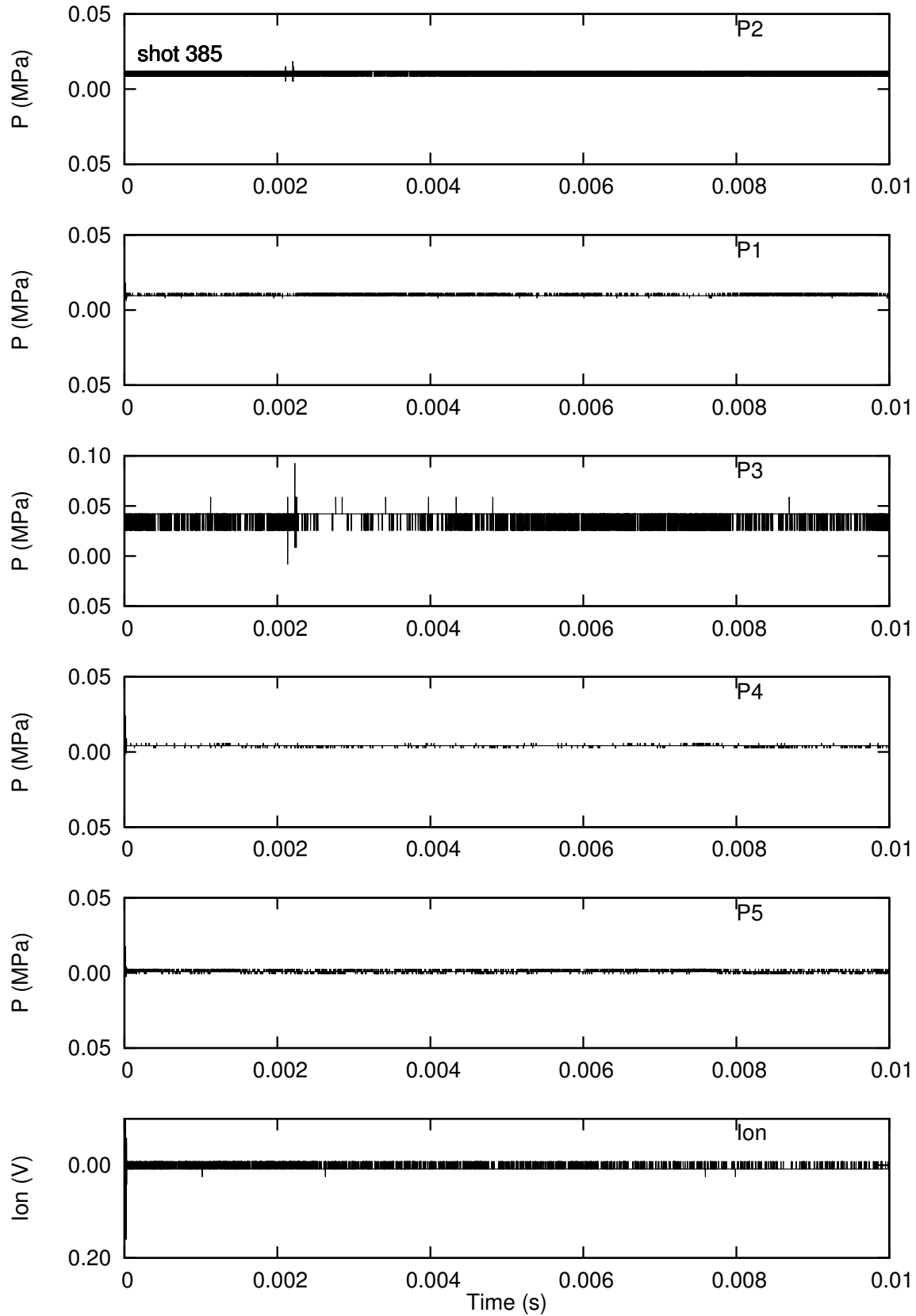
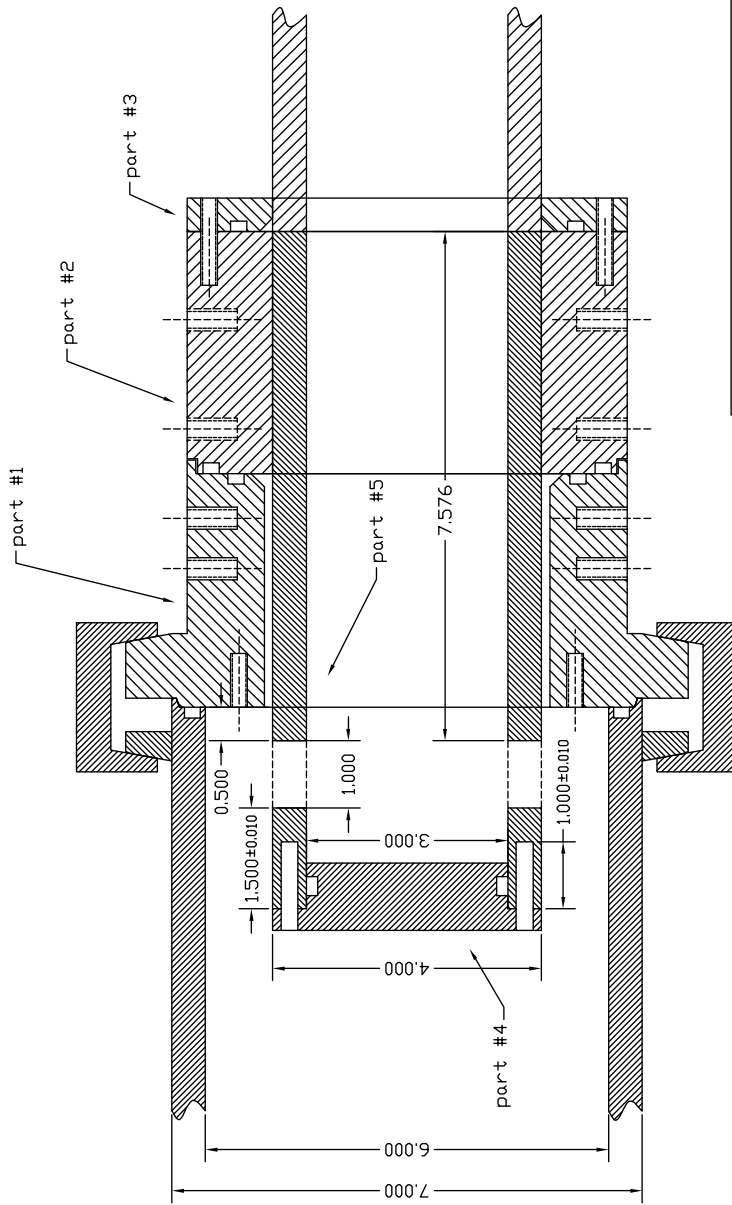


Figure H.159: Pressure history from run 153 with initiator gas injection.

# Appendix I

## Shock Implosion Initiator Data

# I.1 Drawings



Assembly drawing			
FILE:	rys2.dwg		
QUANTITY:	1	UNITS:	inches
MATERIAL:	P. Buraczewski pbura@galcit.caltech.edu ext: 4744		
DATE:	12/10/03		

Figure I.1: Assembly drawing.

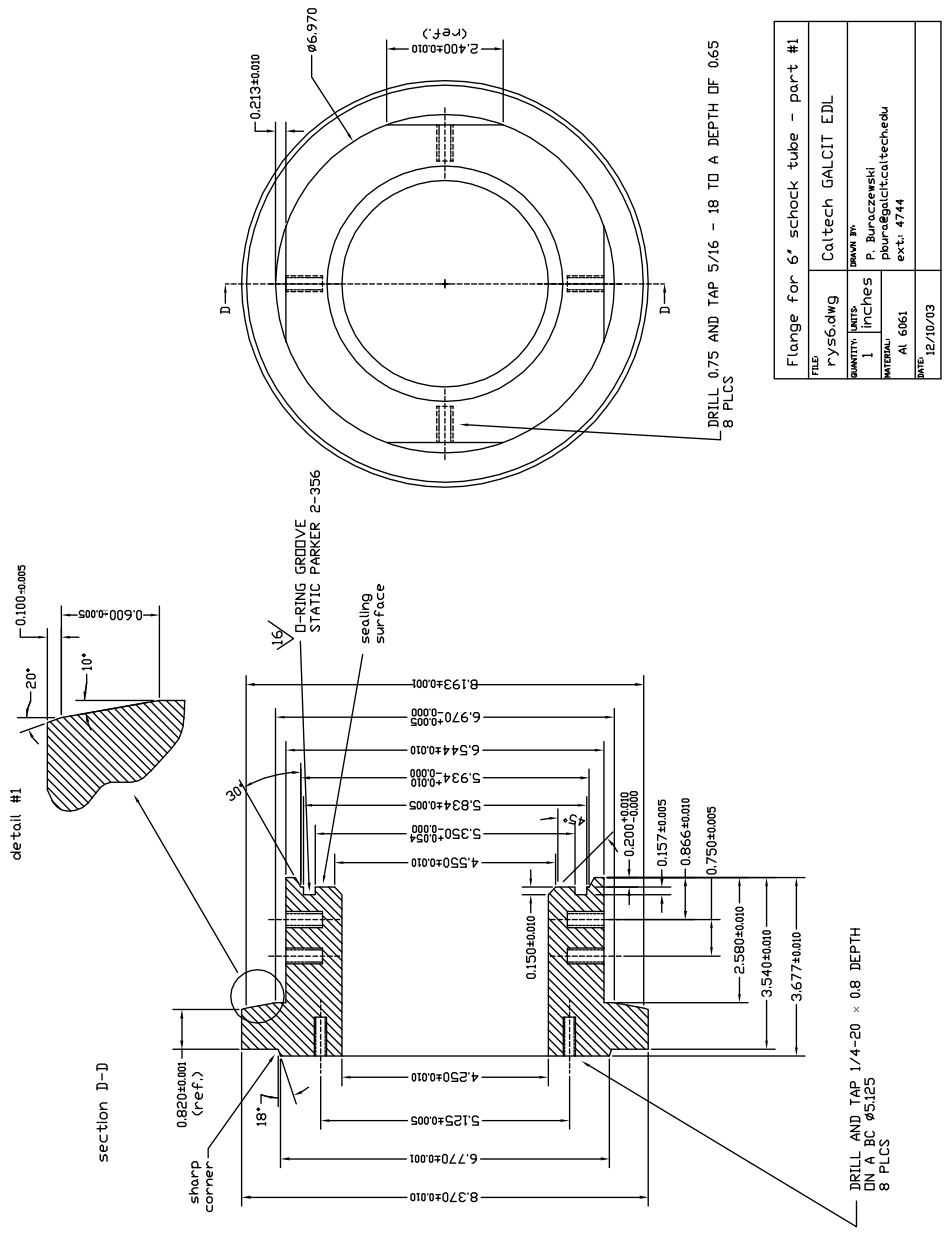
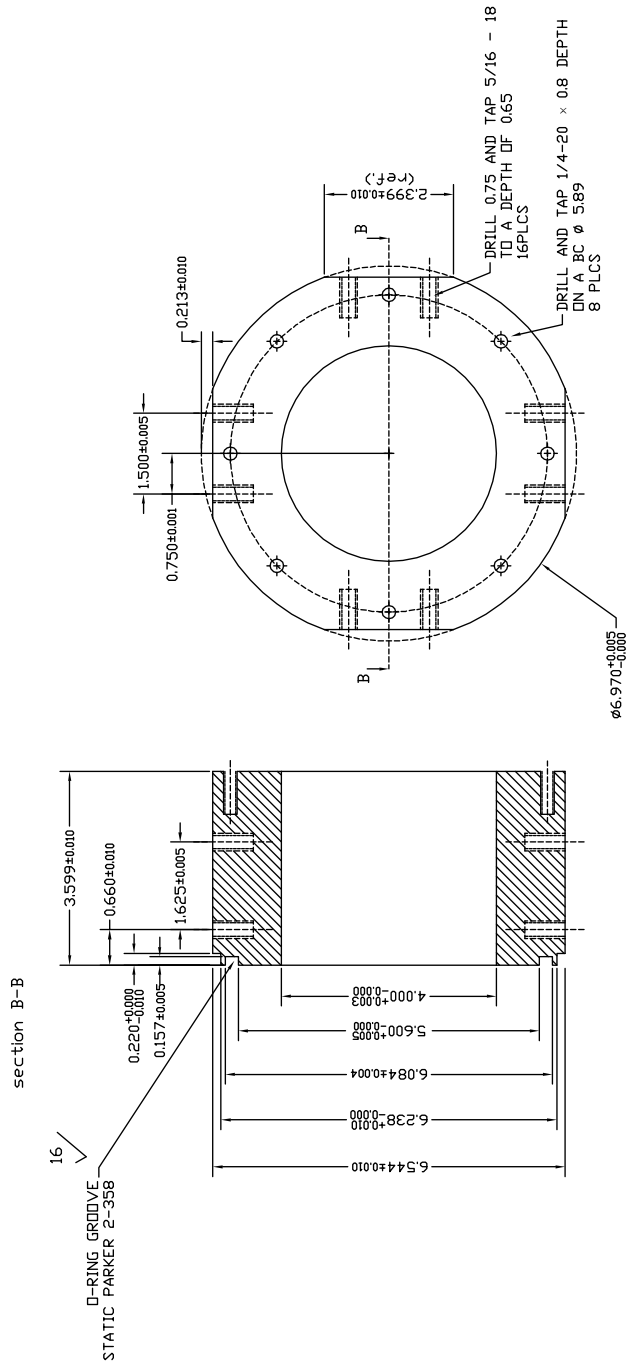
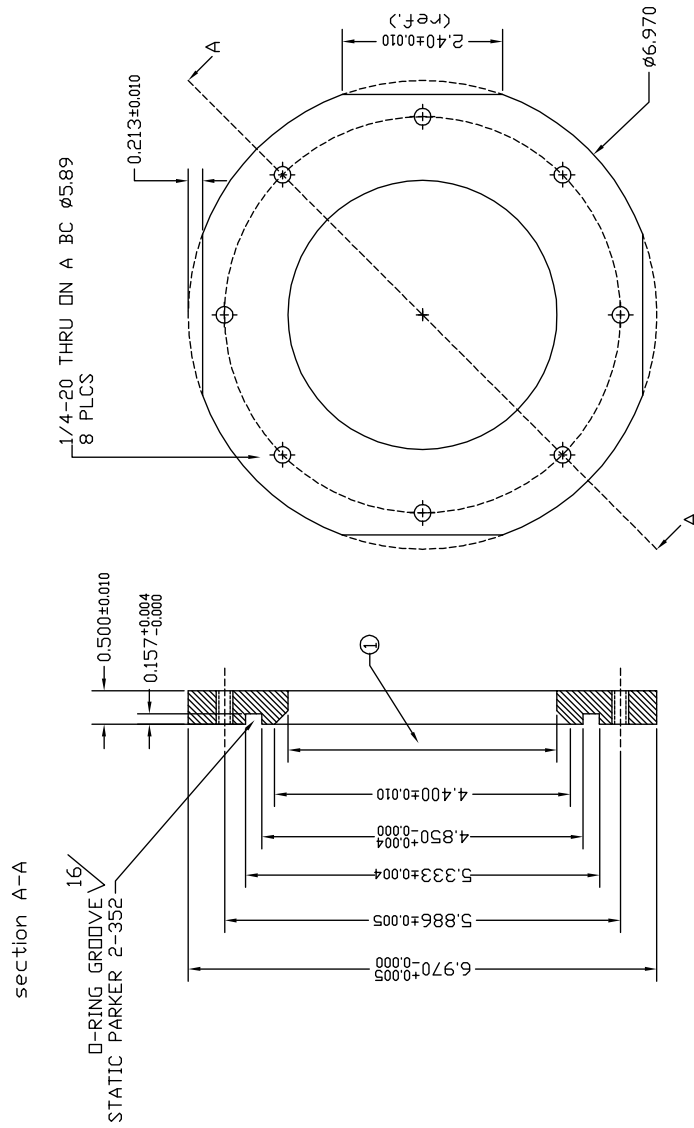


Figure I.2: Flange for 6" Shock Tube - part 1.



Flange for 3" inner det. tube - part #2	
FILE:	rly2.dwg
QUANTITY:	1
UNITS:	inches
DRAWN BY:	P. Buraczewski
MATERIAL:	mild steel 1020
DATE:	12/10/03
	ext.: 4744
	plura@galcit.caltech.edu
	Caltech GALCIT EDL

Figure I.3: Flange for 3" detonation tube - part 2.



Flange for 3" det. tube - part #3			
FILE:	Pys2.dwg		
QUANTITY:	1	UNITS:	inches
MATERIAL:	Al 6061		
DATE:	12/10/03		
	DRAWN BY: P. Buraczewski pburac@galcit.caltech.edu ext.: 4744		
	CALTECH GALCIT EDL		

Figure I.4: Flange for 3" detonation tube - part 3.

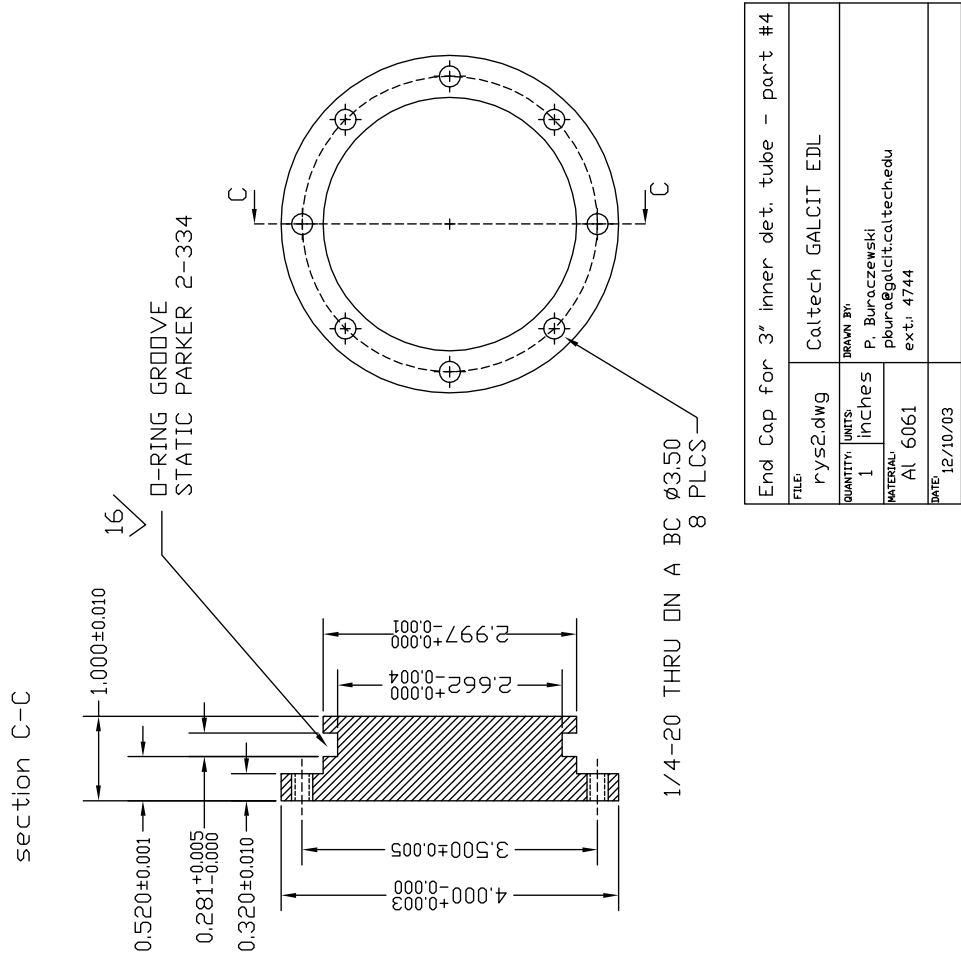


Figure I.5: End cap for 3" inner detonation tube - part 4.



1. remove 1" of anodized surface for weld flange
2. machine flange and tube flat after welding, clean up o-ring groove
3. ID of flange fixed for slip fit on tube w/anodizing removed

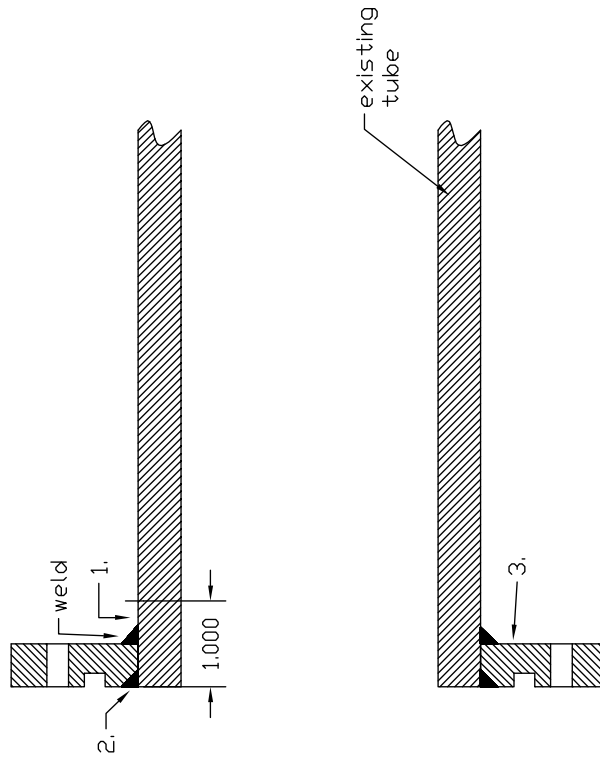
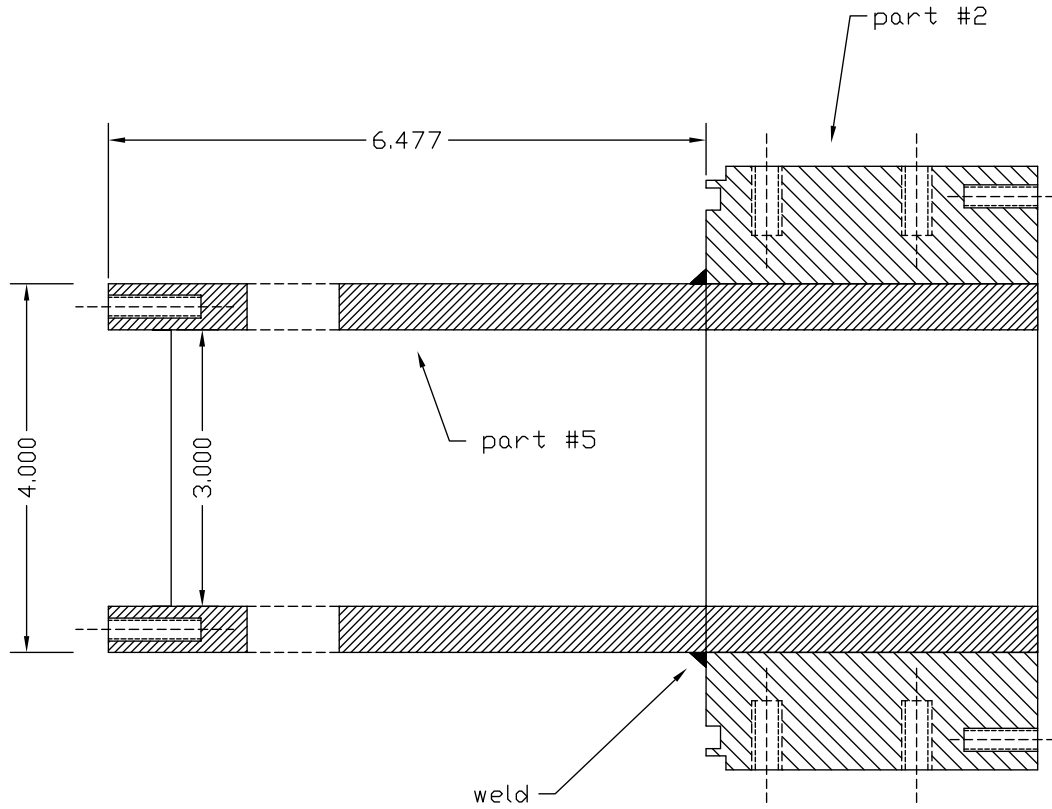


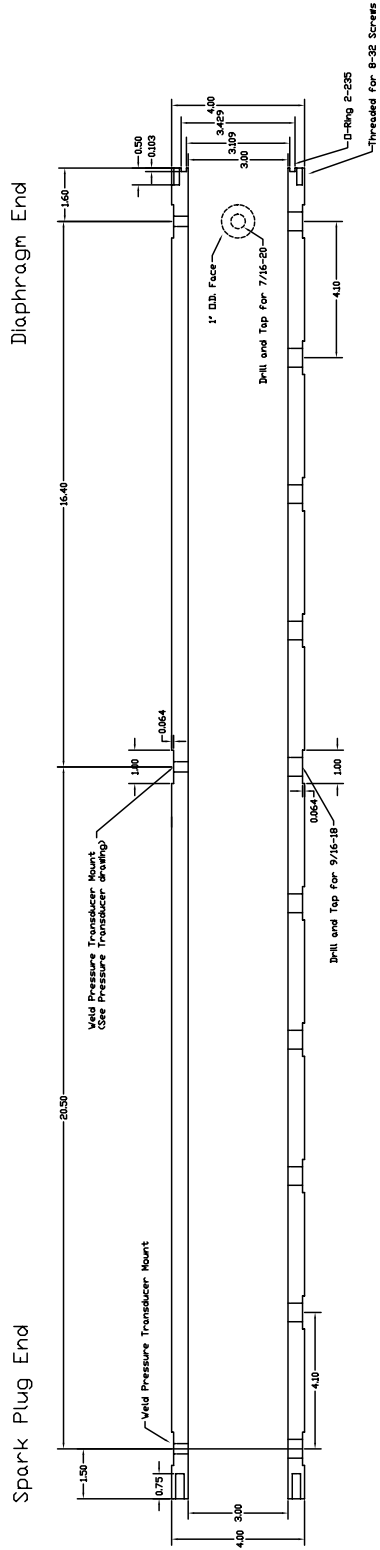
Figure I.7: 3" detonation tube with flange.

3" det. tube with flange	
FILE:	rys2.dwg
QUANTITY:	1
UNITS:	inches
MATERIAL:	AL 6061
DATE:	12/10/03
DRAWN BY:	P. Buraczewski pbura@galcit.caltech.edu ext.: 4744
	Caltech GALCIT EDL
	drawing not to scale



3" inner det. tube with flange		
FILE: rys2.dwg		Caltech GALCIT EDL
QUANTITY: 1	UNITS: inches	DRAWN BY: P. Buraczewski pbura@galcit.caltech.edu ext.: 4744
MATERIAL: Al 6061		
DATE: 12/10/03		drawing not to scale

Figure I.8: 3" inner detonation tube with flange.



3" det. tube	
FILE:	rys2.dwg
QUANTITY:	1
UNITS:	inches
MATERIAL:	Al
DATE:	03/22/00
drawing to scale	

Figure I.9: 3" detonation tube.

## I.2 Run Matrix

### I.2.1 Shock-Tube Conditions

SI Run	ST Run	$T_1$ (K)	$c_{1,ST}$ (m/s)	$M_{2,3}$	$T_5$ (K)	$P_5$ (bar)	$c_5$ (m/s)
28	2004-085	296.7	335	1.52	503.9	5.69	448
29	2004-086	297.2	335	1.57	526.7	6.47	458
30	2004-087	297.7	335	1.53	506.7	5.78	449
31	2004-088	297.2	337	1.53	507.2	5.75	449
32	2004-089	297.7	337	1.52	504.5	5.66	448
33	2004-090	297.7	337	1.53	507.2	5.75	449
34	2004-091	298.2	337	1.58	533.1	6.63	460
35	2004-092	297.7	337	1.40	455.5	4.16	427
36	2004-093	297.2	335	1.31	418.1	3.21	409
37	2004-094	296.7	335	1.42	461.7	4.38	430
38	2004-095	294.7	334	1.41	456.1	4.30	427
39	2004-096	295.7	334	1.41	456.6	4.28	427
40	2004-097	296.7	335	1.53	506.7	5.78	449
41	2004-098	296.2	334	1.59	532.0	6.72	460
42	2004-099	296.2	334	1.59	532.0	6.72	460
43	2004-100	296.7	335	1.70	582.2	8.54	480
44	2004-101	296.7	335	1.80	628.6	10.48	498
45	2004-102	295.9	334	1.42	461.1	4.41	429
46	2004-103	295.7	334	1.41	456.6	4.28	427
47	2004-104	295.7	334	1.46	477.6	4.90	437
48	2004-105	295.7	334	1.52	503.4	5.73	448
49	2004-106	295.7	334	1.45	472.8	4.76	435
50	2004-107	296.2	334	1.31	415.7	3.18	408
51	2004-108	297.2	335	1.58	529.7	6.57	459
52	2004-109	297.2	335	1.70	582.2	8.54	480
53	2004-110	297.7	337	1.82	637.6	10.78	501
54	2004-111	297.7	337	1.42	462.2	4.35	430
55	2004-112	297.7	337	1.54	512.8	5.93	452
56	2004-113	297.7	337	1.59	536.3	6.75	462
57	2004-114	297.7	N/A	1.59	N/A	N/A	N/A
58	2004-115	297.7	N/A	1.54	N/A	N/A	N/A

Table I.1: 6” Shock Tube run conditions for the shock initiator tests. “SI Run” is the number of the shock implosion initiator run and “ST Run” is the number of the shock tube run.  $T_1$  is the initial temperature of air in the shock tube and  $c_{1,ST}$  is the calculated initial sound speed.  $M_{2,3}$  is the average Mach number of the wave between ST2 and ST3.  $T_5$ ,  $P_5$  and  $c_5$  are the respective temperature, pressure and sound speed behind the reflected shock, which have been calculated by STANJAN (Reynolds, 1986) based on the Mach number.

SI Run	ST Run	$T_1$ (K)	$c_{1,ST}$ (m/s)	$M_{2,3}$	$T_5$ (K)	$P_5$ (bar)	$c_5$ (m/s)
59	2004-116	297.2	N/A	1.55	N/A	N/A	N/A
60	2004-117	297.2	N/A	1.53	N/A	N/A	N/A
61	2004-118	297.7	N/A	1.58	N/A	N/A	N/A
62	2004-119	296.7	N/A	1.46	N/A	N/A	N/A
63	2004-120	297.2	N/A	1.59	N/A	N/A	N/A
64	2004-121	296.9	N/A	1.45	N/A	N/A	N/A
65	2004-122	297.2	N/A	1.71	N/A	N/A	N/A
66	2004-123	297.7	N/A	1.71	N/A	N/A	N/A
67	2004-124	297.2	N/A	1.59	N/A	N/A	N/A
68	2004-125	296.2	N/A	1.71	N/A	N/A	N/A
69	2004-126	297.7	N/A	1.81	N/A	N/A	N/A
70	2004-127	297.7	337	1.70	582.8	8.49	481
71	2004-128	297.2	335	1.76	608.4	9.61	490
72	2004-129	296.9	335	1.82	637.4	10.86	501
73	2004-130	296.9	335	1.72	589.4	8.83	483
74	2004-131	296.7	335	1.59	532.5	6.67	460
75	2004-132	297.2	335	1.53	509.5	5.88	450
76	2004-133	295.7	334	1.73	592.4	9.03	484
77	2004-134	295.7	334	1.81	632.1	10.72	499
78	2004-135	295.7	334	1.88	663.1	12.12	511
79	2004-136	295.7	334	1.75	603.9	9.51	488
80	2004-137	295.7	334	1.88	663.1	12.12	511
81	2004-138	296.2	334	1.95	697.0	13.73	523
82	2004-139	295.7	334	1.96	702.3	13.99	525
83	2004-140	296.4	334	1.88	663.1	12.12	511
84	2004-141	296.7	335	1.96	702.9	13.91	525
85	2004-142	296.7	335	1.88	663.8	12.05	511
86	2004-143	297.2	335	1.96	702.9	13.91	525
87	2004-144	297.4	335	2.08	764.5	17.04	546

Table I.2: 6” Shock Tube run conditions for the shock initiator tests. “SI Run” is the number of the shock implosion initiator run and “ST Run” is the number of the shock tube run.  $T_1$  is the initial temperature of air in the shock tube and  $c_{1,ST}$  is the calculated initial sound speed.  $M_{2,3}$  is the average Mach number of the wave between ST2 and ST3.  $T_5$ ,  $P_5$  and  $c_5$  are the respective temperature, pressure and sound speed behind the reflected shock, which have been calculated by STANJAN (Reynolds, 1986) based on the Mach number.

## I.2.2 Test-Section Conditions

SI Run	Fuel	N <sub>2</sub> fraction	$c_{1,TS}$ (m/s)	$P_{CJ}$ (bar)	Initiation type
28	C <sub>2</sub> H <sub>4</sub>	0.00	318	33.7	Direct
29	C <sub>2</sub> H <sub>4</sub>	0.40	326	26.2	Direct
30	C <sub>2</sub> H <sub>4</sub>	0.40	326	26.2	Reflected
31	C <sub>2</sub> H <sub>4</sub>	0.40	326	26.2	Reflected
32	C <sub>2</sub> H <sub>4</sub>	0.20	322	30	Direct
33	N/A	N/A	N/A	N/A	N/A
34	N/A	N/A	N/A	N/A	N/A
35	N/A	N/A	N/A	N/A	N/A
36	C <sub>2</sub> H <sub>4</sub>	0.00	318	33.7	Failed
37	C <sub>2</sub> H <sub>4</sub>	0.00	318	33.7	Direct
38	C <sub>2</sub> H <sub>4</sub>	0.20	322	30	Reflected
39	C <sub>2</sub> H <sub>4</sub>	0.30	324	28.2	Failed
40	C <sub>2</sub> H <sub>4</sub>	0.30	324	28.2	Direct
41	C <sub>2</sub> H <sub>4</sub>	0.30	324	28.2	Direct
42	C <sub>2</sub> H <sub>4</sub>	0.60	330	22.1	Failed
43	C <sub>2</sub> H <sub>4</sub>	0.60	330	22.1	Failed
44	C <sub>2</sub> H <sub>4</sub>	0.60	330	22.1	Reflected
45	C <sub>2</sub> H <sub>4</sub>	0.10	320	31.8	DDT
46	C <sub>2</sub> H <sub>4</sub>	0.10	320	31.8	DDT
47	C <sub>2</sub> H <sub>4</sub>	0.10	320	31.8	Reflected
48	C <sub>2</sub> H <sub>4</sub>	0.10	320	31.8	Direct
49	C <sub>2</sub> H <sub>4</sub>	0.10	320	31.8	Direct
50	C <sub>2</sub> H <sub>4</sub>	0.10	320	31.8	Failed
51	C <sub>2</sub> H <sub>4</sub>	0.50	328	24.3	Reflected
52	C <sub>2</sub> H <sub>4</sub>	0.50	328	24.3	DDT
53	C <sub>2</sub> H <sub>4</sub>	0.50	328	24.3	DDT
54	C <sub>3</sub> H <sub>8</sub>	0.00	300	36.5	Failed
55	C <sub>3</sub> H <sub>8</sub>	0.00	300	36.5	Reflected
56	C <sub>3</sub> H <sub>8</sub>	0.00	300	36.5	Direct
57	N/A	N/A	N/A	N/A	N/A
58	N/A	N/A	N/A	N/A	N/A

Table I.3: Test section conditions for the shock initiator tests. “SI Run” is the number of the shock implosion initiator run. “Fuel” is the type of fuel used in the test-section. All test-section mixtures were stoichiometric and diluted with nitrogen to the “N<sub>2</sub> fraction” listed.  $c_{1,TS}$  and  $P_{CJ}$  are the initial sound speed and the CJ detonation pressure for the test-section mixture, respectively. “Initiation type” is the initiation mode observed in each run as discussed in the text.

SI Run	Fuel	N <sub>2</sub> fraction	$c_{1,TS}$ (m/s)	$P_{CJ}$ (bar)	Initiation type
59	N/A	N/A	N/A	N/A	N/A
60	N/A	N/A	N/A	N/A	N/A
61	N/A	N/A	N/A	N/A	N/A
62	N/A	N/A	N/A	N/A	N/A
63	N/A	N/A	N/A	N/A	N/A
64	N/A	N/A	N/A	N/A	N/A
65	N/A	N/A	N/A	N/A	N/A
66	N/A	N/A	N/A	N/A	N/A
67	N/A	N/A	N/A	N/A	N/A
68	N/A	N/A	N/A	N/A	N/A
69	N/A	N/A	N/A	N/A	N/A
70	C <sub>3</sub> H <sub>8</sub>	0.15	304.5	33.2	DDT
71	C <sub>3</sub> H <sub>8</sub>	0.15	304.5	33.2	DDT
72	C <sub>3</sub> H <sub>8</sub>	0.15	304.5	33.2	Direct
73	C <sub>3</sub> H <sub>8</sub>	0.10	303	34.3	Direct
74	C <sub>3</sub> H <sub>8</sub>	0.10	303	34.3	Reflected
75	C <sub>3</sub> H <sub>8</sub>	0.10	303	34.3	Reflected
76	C <sub>3</sub> H <sub>8</sub>	0.20	306	32.2	Reflected
77	C <sub>3</sub> H <sub>8</sub>	0.20	306	32.2	Direct
78	C <sub>3</sub> H <sub>8</sub>	0.30	310	30	Direct
79	C <sub>3</sub> H <sub>8</sub>	0.30	310	30	Reflected
80	C <sub>3</sub> H <sub>8</sub>	0.40	314	27.8	DDT
81	C <sub>3</sub> H <sub>8</sub>	0.40	314	27.8	Reflected
82	C <sub>3</sub> H <sub>8</sub>	0.40	314	27.8	Reflected
83	C <sub>2</sub> H <sub>4</sub>	0.50	328	24.3	DDT
84	C <sub>2</sub> H <sub>4</sub>	0.50	328	24.3	Direct
85	C <sub>2</sub> H <sub>4</sub>	0.50	328	24.3	DDT
86	C <sub>2</sub> H <sub>4</sub>	0.60	330	22.1	Reflected
87	C <sub>2</sub> H <sub>4</sub>	0.60	330	22.1	DDT

Table I.4: Test section conditions for the shock initiator tests. “SI Run” is the number of the shock implosion initiator run. “Fuel” is the type of fuel used in the test-section. All test-section mixtures were stoichiometric and diluted with nitrogen to the “N<sub>2</sub> fraction” listed.  $c_{1,TS}$  and  $P_{CJ}$  are the initial sound speed and the CJ detonation pressure for the test-section mixture, respectively. “Initiation type” is the initiation mode observed in each run as discussed in the text.

### I.2.3 Energy Calculation

SI Run	Fuel	N <sub>2</sub> fraction	$\rho_1$ (kg/m <sup>3</sup> )	$U_{CJ}$ (m/s)	$\Delta$ (mm)	Energy (J)
28	C <sub>2</sub> H <sub>4</sub>	0.00	1.264	2376	0.0308	296
29	C <sub>2</sub> H <sub>4</sub>	0.40	1.215	2132.4	0.1072	335
30	C <sub>2</sub> H <sub>4</sub>	0.40	1.215	2132.4	0.1072	294
31	C <sub>2</sub> H <sub>4</sub>	0.40	1.215	2132.4	0.1072	292
32	C <sub>2</sub> H <sub>4</sub>	0.20	1.240	2259	0.0545	290
33	N/A	N/A	N/A	N/A	N/A	N/A
34	N/A	N/A	N/A	N/A	N/A	N/A
35	N/A	N/A	N/A	N/A	N/A	N/A
36	C <sub>2</sub> H <sub>4</sub>	0.00	1.264	2376	0.0308	152
37	C <sub>2</sub> H <sub>4</sub>	0.00	1.264	2376	0.0308	218
38	C <sub>2</sub> H <sub>4</sub>	0.20	1.240	2259	0.0545	211
39	C <sub>2</sub> H <sub>4</sub>	0.30	1.228	2198	0.0747	208
40	C <sub>2</sub> H <sub>4</sub>	0.30	1.228	2198	0.0747	296
41	C <sub>2</sub> H <sub>4</sub>	0.30	1.228	2198	0.0747	352
42	C <sub>2</sub> H <sub>4</sub>	0.60	1.191	1977	0.2815	345
43	C <sub>2</sub> H <sub>4</sub>	0.60	1.191	1977	0.2815	458
44	C <sub>2</sub> H <sub>4</sub>	0.60	1.191	1977	0.2815	583
45	C <sub>2</sub> H <sub>4</sub>	0.10	1.252	2316.6	0.0407	218
46	C <sub>2</sub> H <sub>4</sub>	0.10	1.252	2316.6	0.0407	211
47	C <sub>2</sub> H <sub>4</sub>	0.10	1.252	2316.6	0.0407	247
48	C <sub>2</sub> H <sub>4</sub>	0.10	1.252	2316.6	0.0407	296
49	C <sub>2</sub> H <sub>4</sub>	0.10	1.252	2316.6	0.0407	238
50	C <sub>2</sub> H <sub>4</sub>	0.10	1.252	2316.6	0.0407	150
51	C <sub>2</sub> H <sub>4</sub>	0.50	1.203	2060	0.1641	339
52	C <sub>2</sub> H <sub>4</sub>	0.50	1.203	2060	0.1641	461
53	C <sub>2</sub> H <sub>4</sub>	0.50	1.203	2060	0.1641	607
54	C <sub>3</sub> H <sub>8</sub>	0.00	1.387	2360	0.0301	230
55	C <sub>3</sub> H <sub>8</sub>	0.00	1.387	2360	0.0301	330
56	C <sub>3</sub> H <sub>8</sub>	0.00	1.387	2360	0.0301	383
57	N/A	N/A	N/A	N/A	N/A	N/A
58	N/A	N/A	N/A	N/A	N/A	N/A

Table I.5: Energy input calculation for the shock initiator tests. “SI Run” is the number of the shock implosion initiator run. “Fuel” is the type of fuel used in the test-section. All test-section mixtures were stoichiometric and diluted with nitrogen to the “N<sub>2</sub> fraction” listed. The values  $\rho_1$  and  $U_{CJ}$  are the initial density and the CJ detonation wave speed for the test-section mixture, respectively. The induction length  $\Delta$  has been calculated for each mixture using the program ZND (Shepherd, 1986). The calculated input energy to the shock implosion initiator is listed under “Energy.”

SI Run	Fuel	N <sub>2</sub> fraction	$\rho_1$ (kg/m <sup>3</sup> )	$U_{CJ}$ (m/s)	$\Delta$ (mm)	Energy (J)
59	N/A	N/A	N/A	N/A	N/A	N/A
60	N/A	N/A	N/A	N/A	N/A	N/A
61	N/A	N/A	N/A	N/A	N/A	N/A
62	N/A	N/A	N/A	N/A	N/A	N/A
63	N/A	N/A	N/A	N/A	N/A	N/A
64	N/A	N/A	N/A	N/A	N/A	N/A
65	N/A	N/A	N/A	N/A	N/A	N/A
66	N/A	N/A	N/A	N/A	N/A	N/A
67	N/A	N/A	N/A	N/A	N/A	N/A
68	N/A	N/A	N/A	N/A	N/A	N/A
69	N/A	N/A	N/A	N/A	N/A	N/A
70	C <sub>3</sub> H <sub>8</sub>	0.15	1.350	2278.9	0.0460	494
71	C <sub>3</sub> H <sub>8</sub>	0.15	1.350	2278.9	0.0460	571
72	C <sub>3</sub> H <sub>8</sub>	0.15	1.350	2278.9	0.0460	659
73	C <sub>3</sub> H <sub>8</sub>	0.10	1.362	2305.5	0.0402	520
74	C <sub>3</sub> H <sub>8</sub>	0.10	1.362	2305.5	0.0402	374
75	C <sub>3</sub> H <sub>8</sub>	0.10	1.362	2305.5	0.0402	322
76	C <sub>3</sub> H <sub>8</sub>	0.20	1.338	2251.7	0.0542	527
77	C <sub>3</sub> H <sub>8</sub>	0.20	1.338	2251.7	0.0542	644
78	C <sub>3</sub> H <sub>8</sub>	0.30	1.314	2194.3	0.0761	737
79	C <sub>3</sub> H <sub>8</sub>	0.30	1.314	2194.3	0.0761	553
80	C <sub>3</sub> H <sub>8</sub>	0.40	1.289	2132	0.1139	728
81	C <sub>3</sub> H <sub>8</sub>	0.40	1.289	2132	0.1139	845
82	C <sub>3</sub> H <sub>8</sub>	0.40	1.289	2132	0.1139	863
83	C <sub>2</sub> H <sub>4</sub>	0.50	1.203	2060	0.1641	696
84	C <sub>2</sub> H <sub>4</sub>	0.50	1.203	2060	0.1641	820
85	C <sub>2</sub> H <sub>4</sub>	0.50	1.203	2060	0.1641	692
86	C <sub>2</sub> H <sub>4</sub>	0.60	1.191	1977	0.2815	815
87	C <sub>2</sub> H <sub>4</sub>	0.60	1.191	1977	0.2815	1039

Table I.6: Energy input calculation for the shock initiator tests. “SI Run” is the number of the shock implosion initiator run. “Fuel” is the type of fuel used in the test-section. All test-section mixtures were stoichiometric and diluted with nitrogen to the “N<sub>2</sub> fraction” listed. The values  $\rho_1$  and  $U_{CJ}$  are the initial density and the CJ detonation wave speed for the test-section mixture, respectively. The induction length  $\Delta$  has been calculated for each mixture using the program ZND (Shepherd, 1986). The calculated input energy to the shock implosion initiator is listed under “Energy.”

### I.3 Pressure Traces

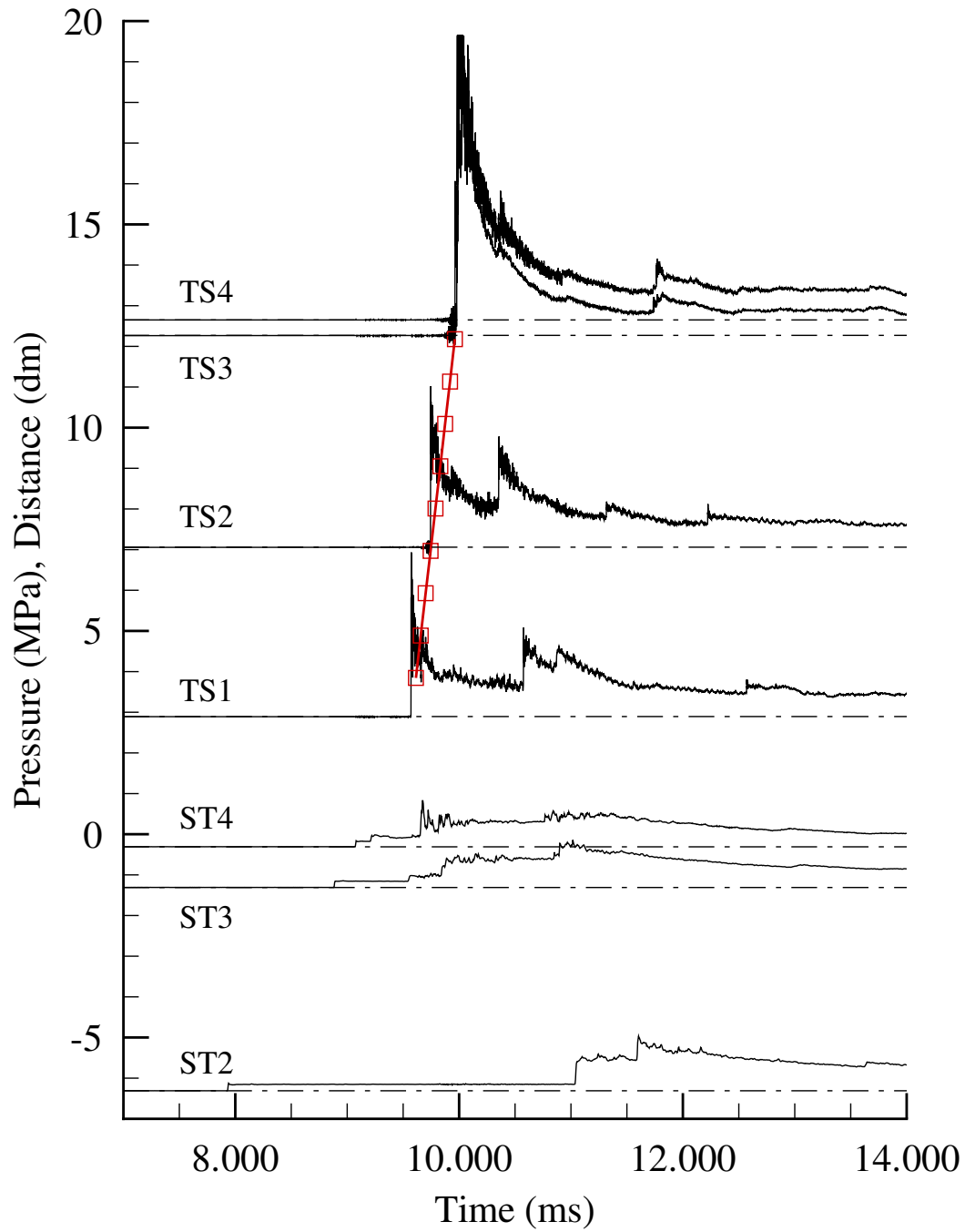


Figure I.10: Pressure and ionization data from shock initiator run 28.

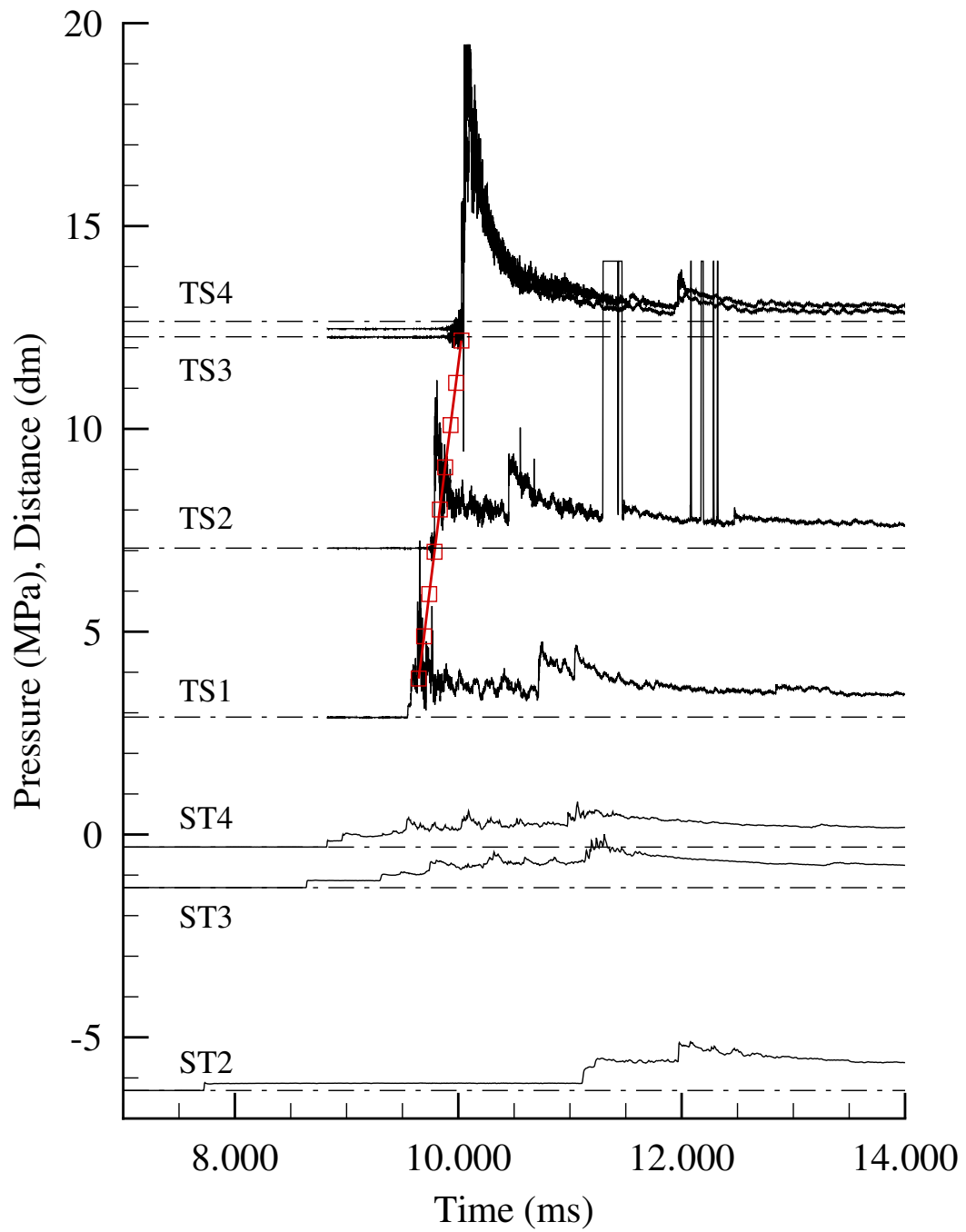


Figure I.11: Pressure and ionization data from shock initiator run 29.

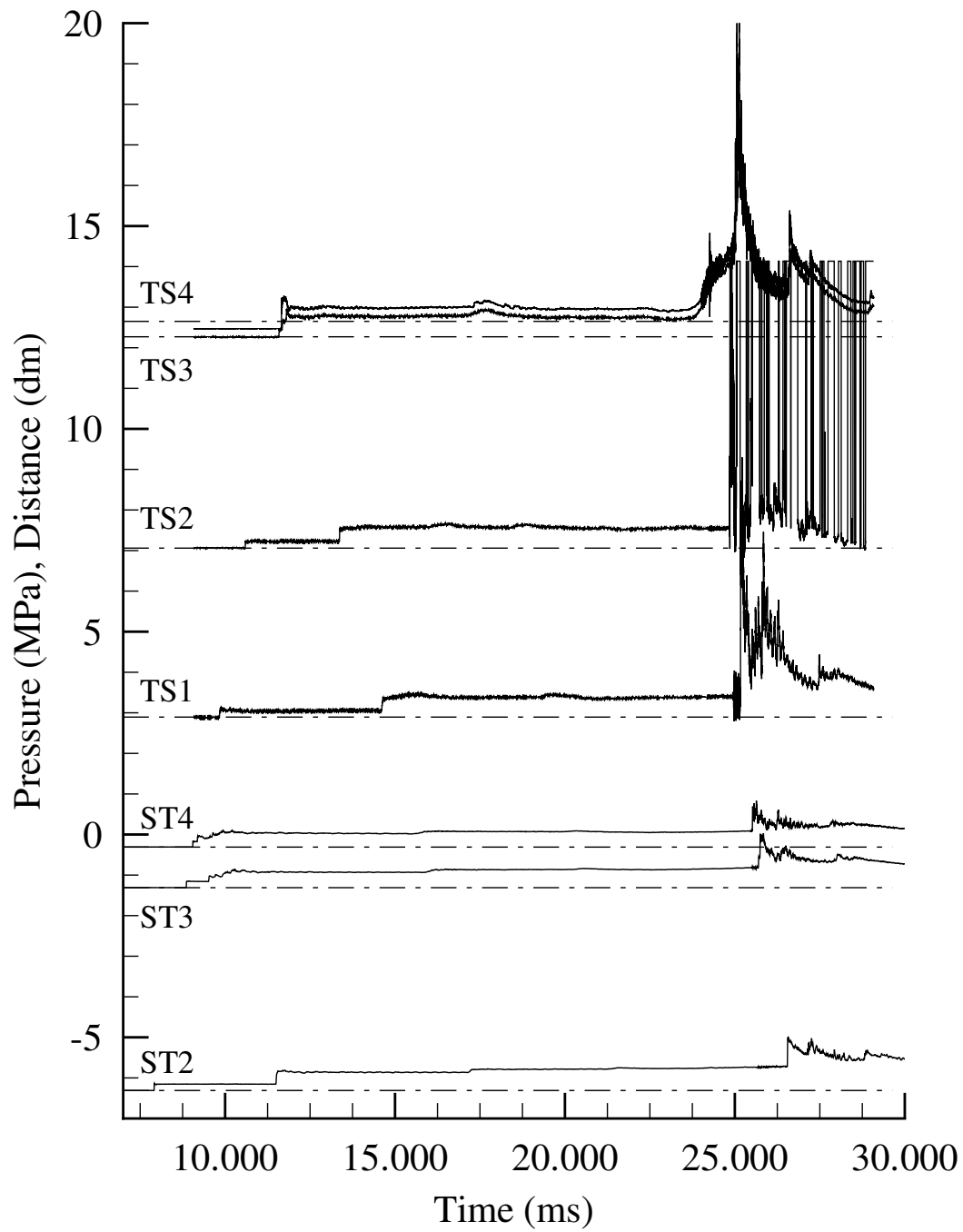


Figure I.12: Pressure and ionization data from shock initiator run 30.

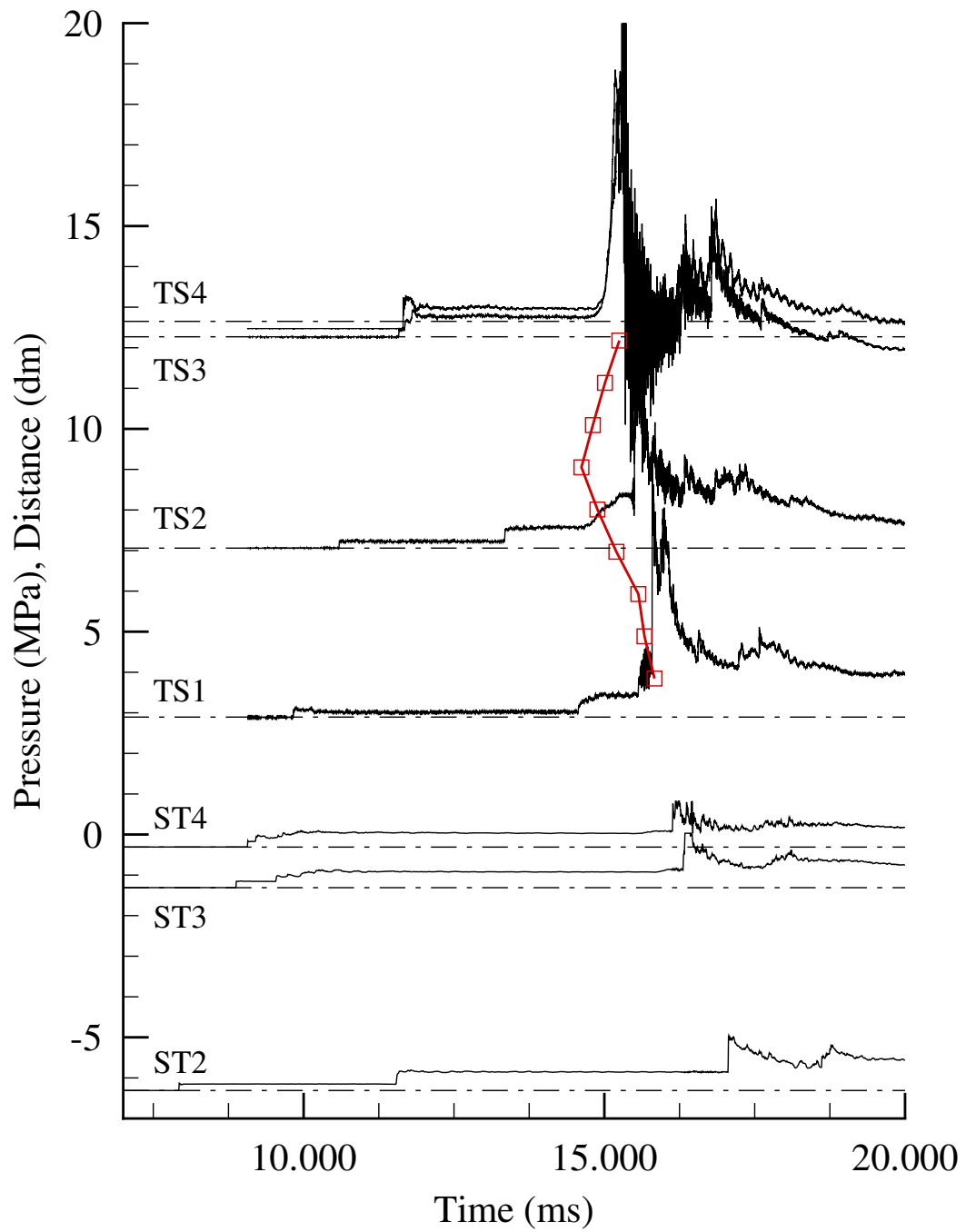


Figure I.13: Pressure and ionization data from shock initiator run 31.

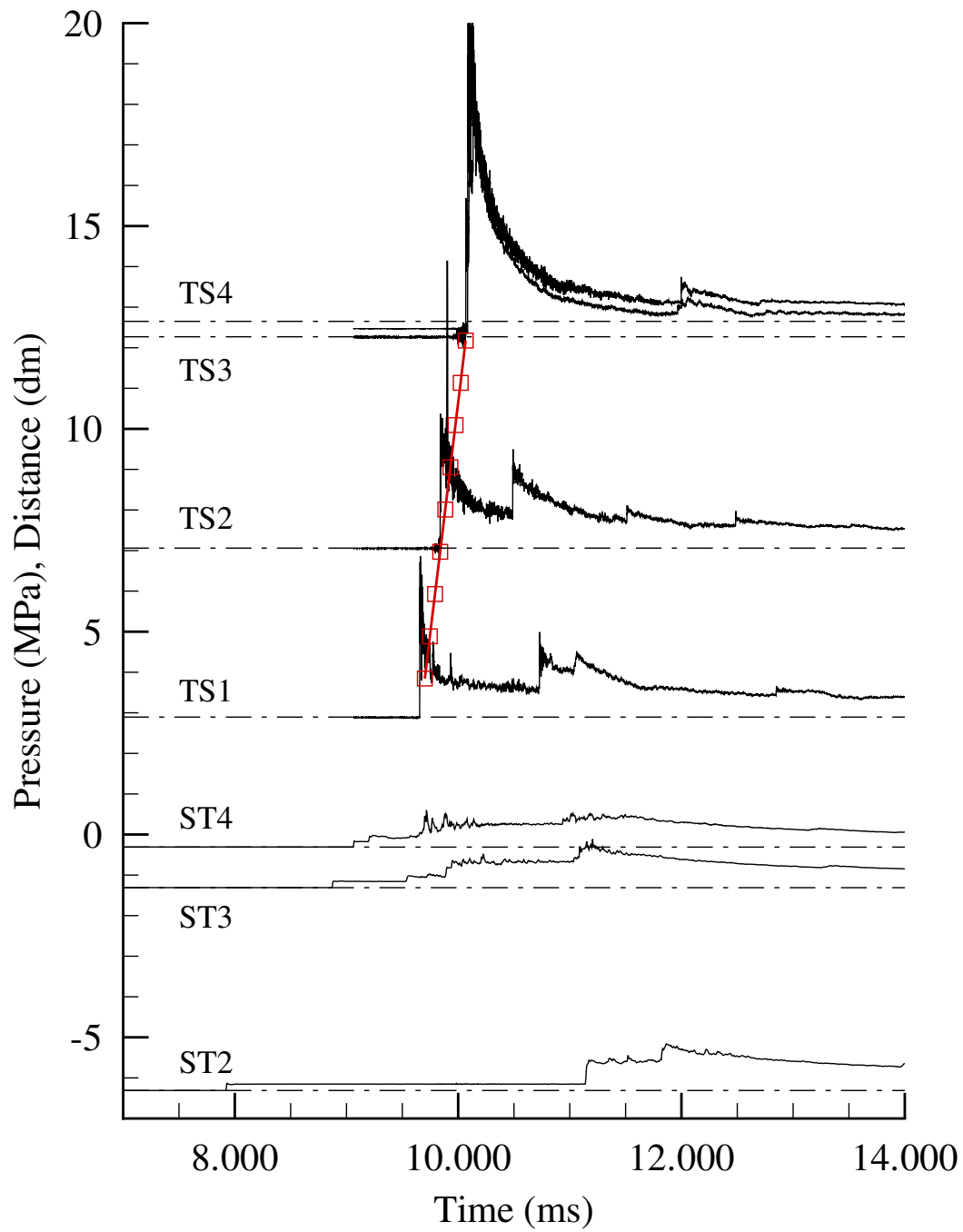


Figure I.14: Pressure and ionization data from shock initiator run 32.

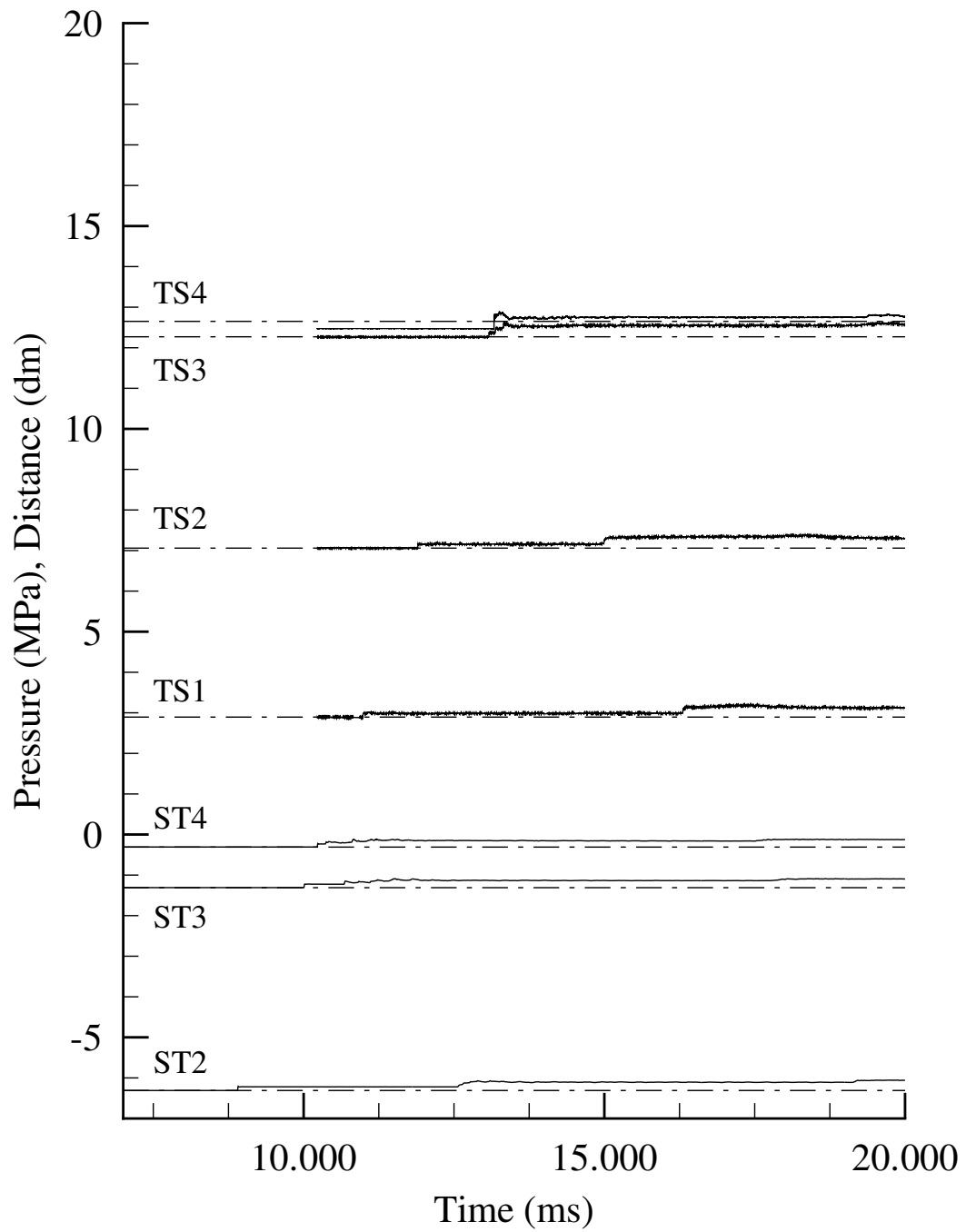


Figure I.15: Pressure and ionization data from shock initiator run 36.

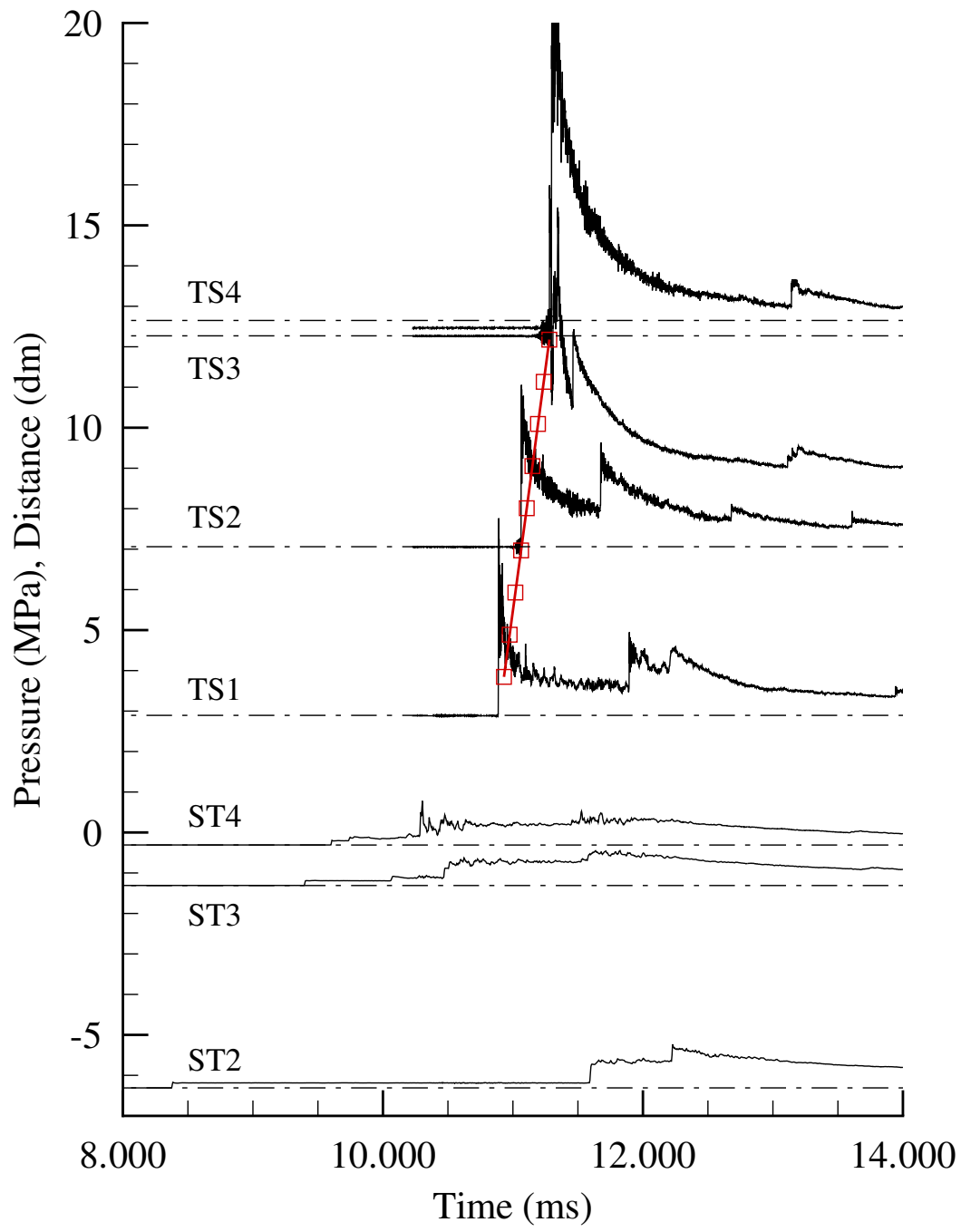


Figure I.16: Pressure and ionization data from shock initiator run 37.

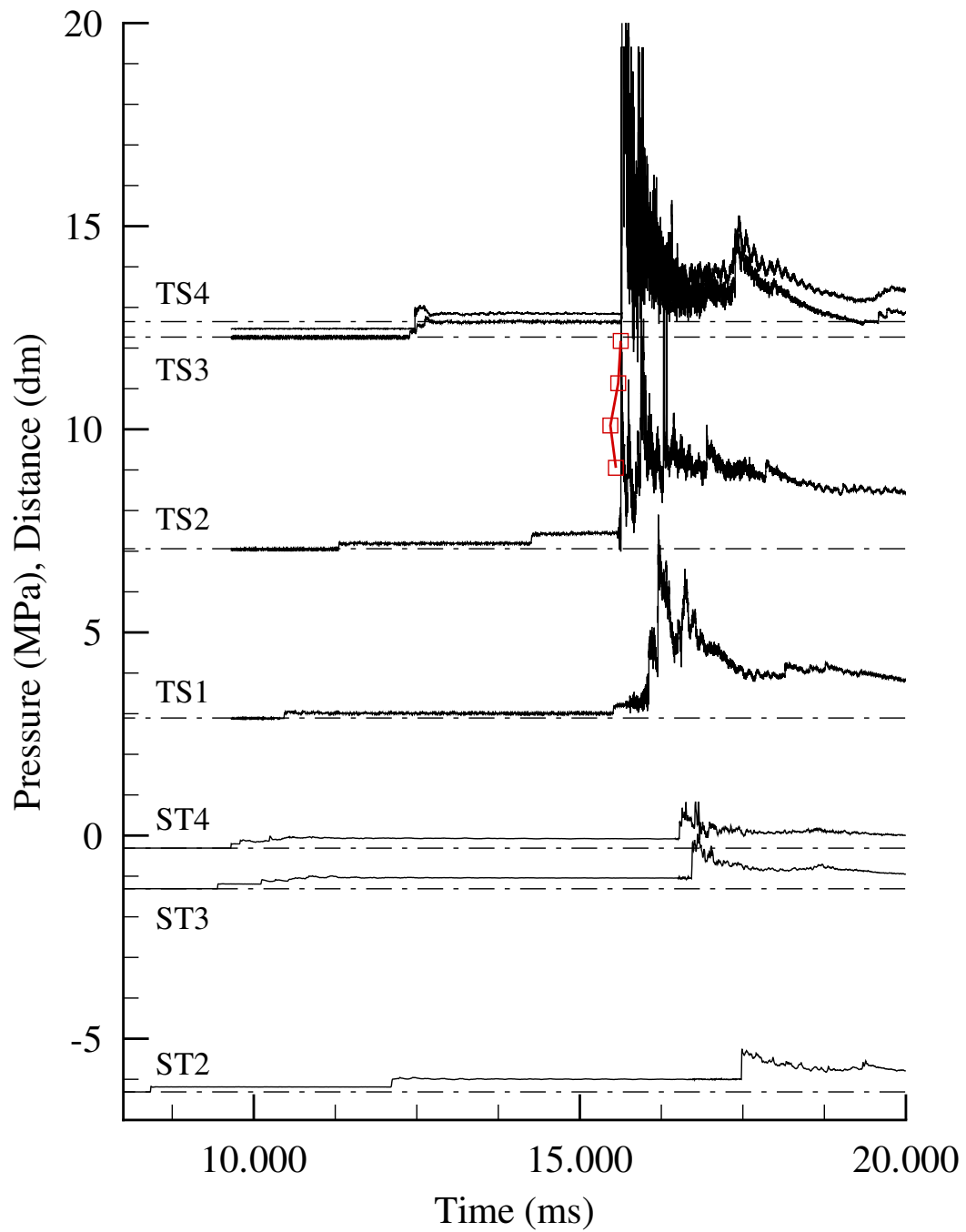


Figure I.17: Pressure and ionization data from shock initiator run 38.

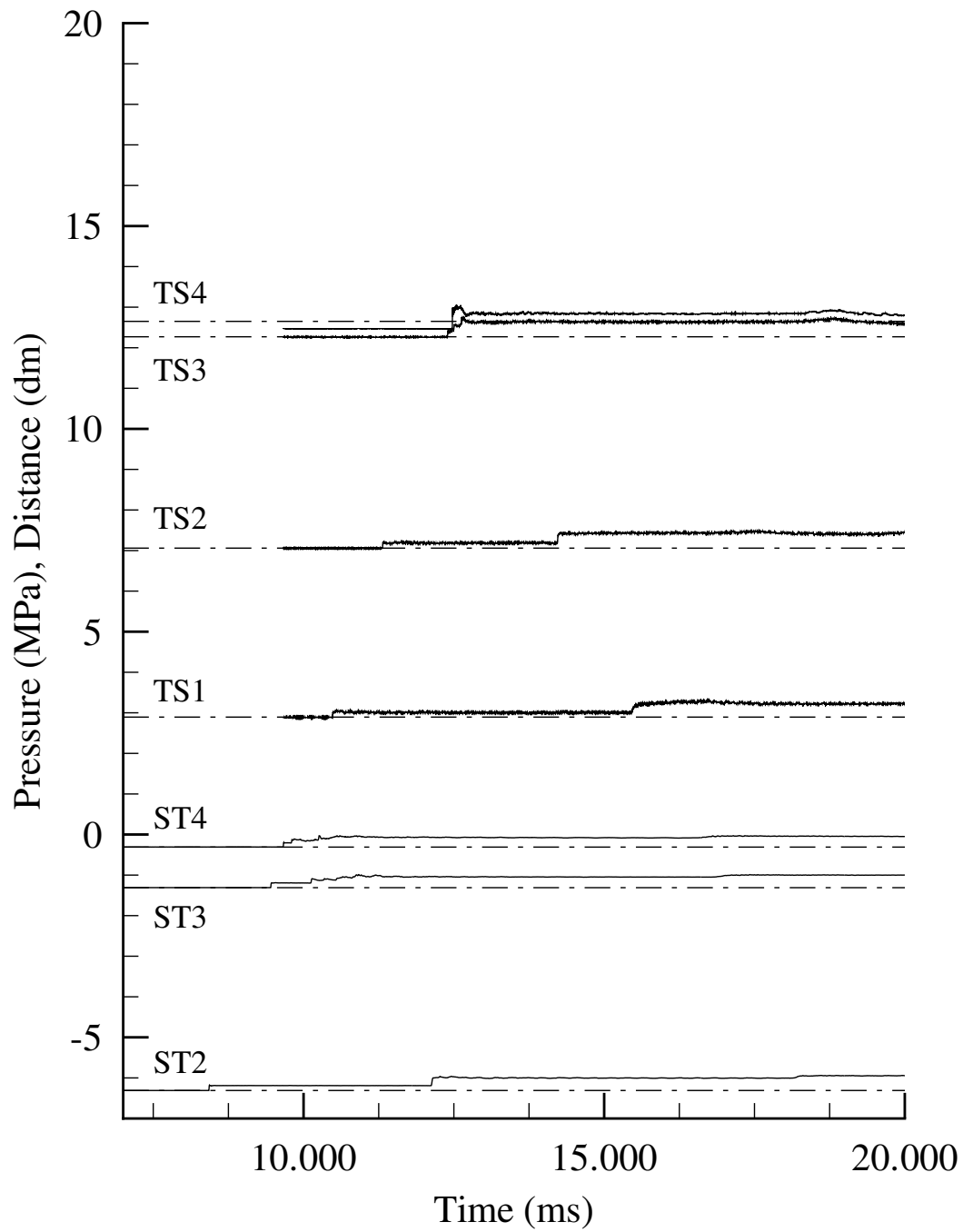


Figure I.18: Pressure and ionization data from shock initiator run 39.

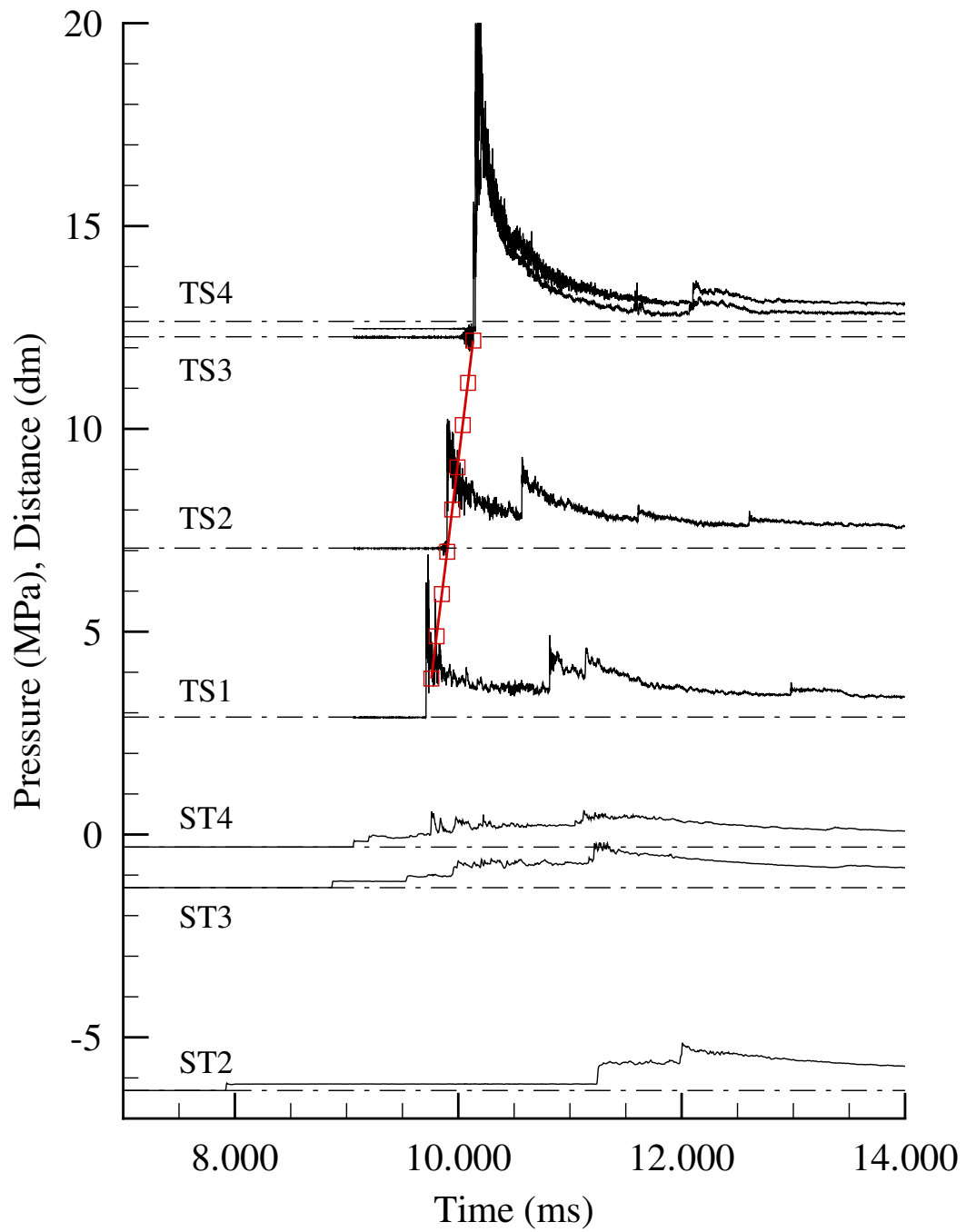


Figure I.19: Pressure and ionization data from shock initiator run 40.

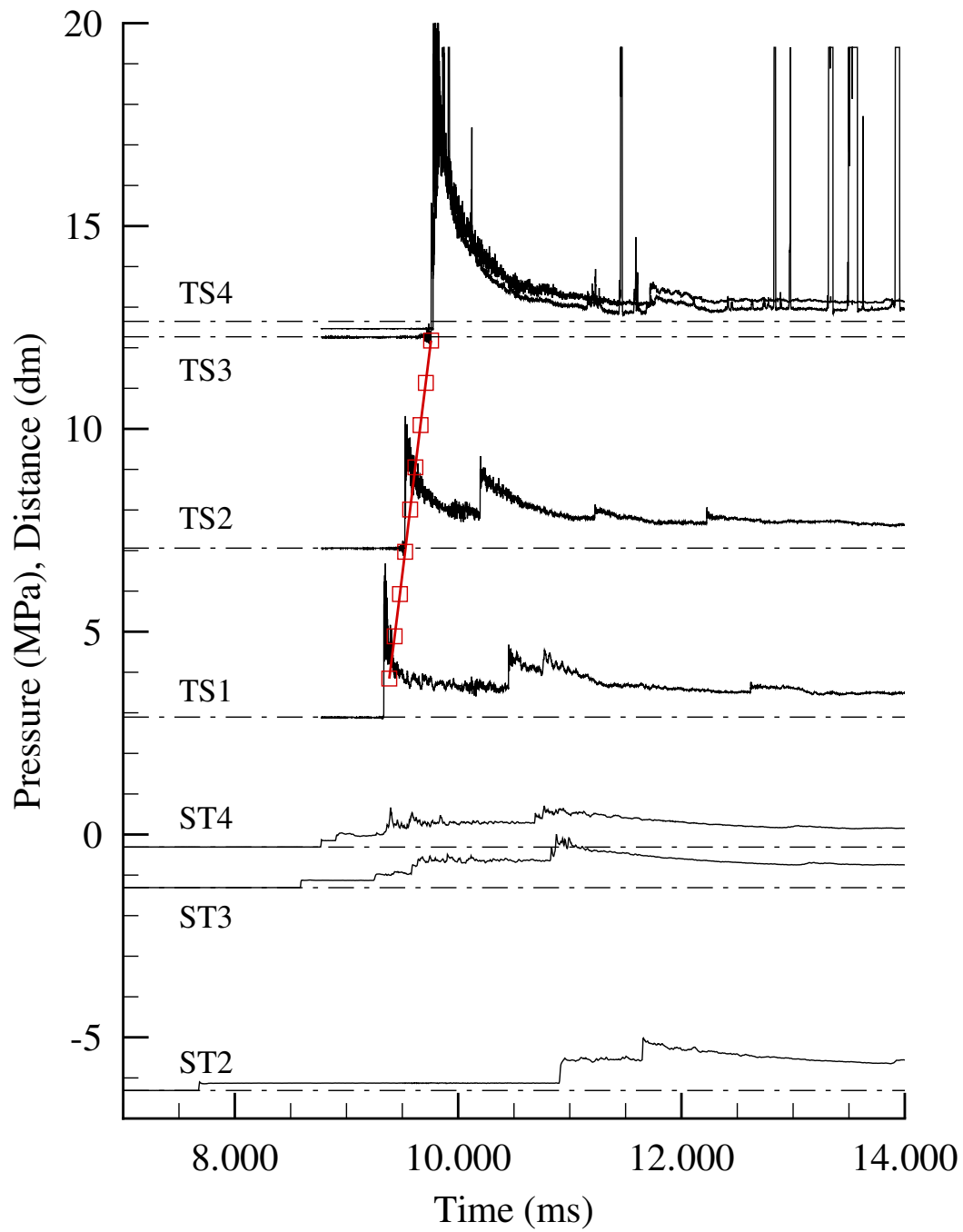


Figure I.20: Pressure and ionization data from shock initiator run 41.

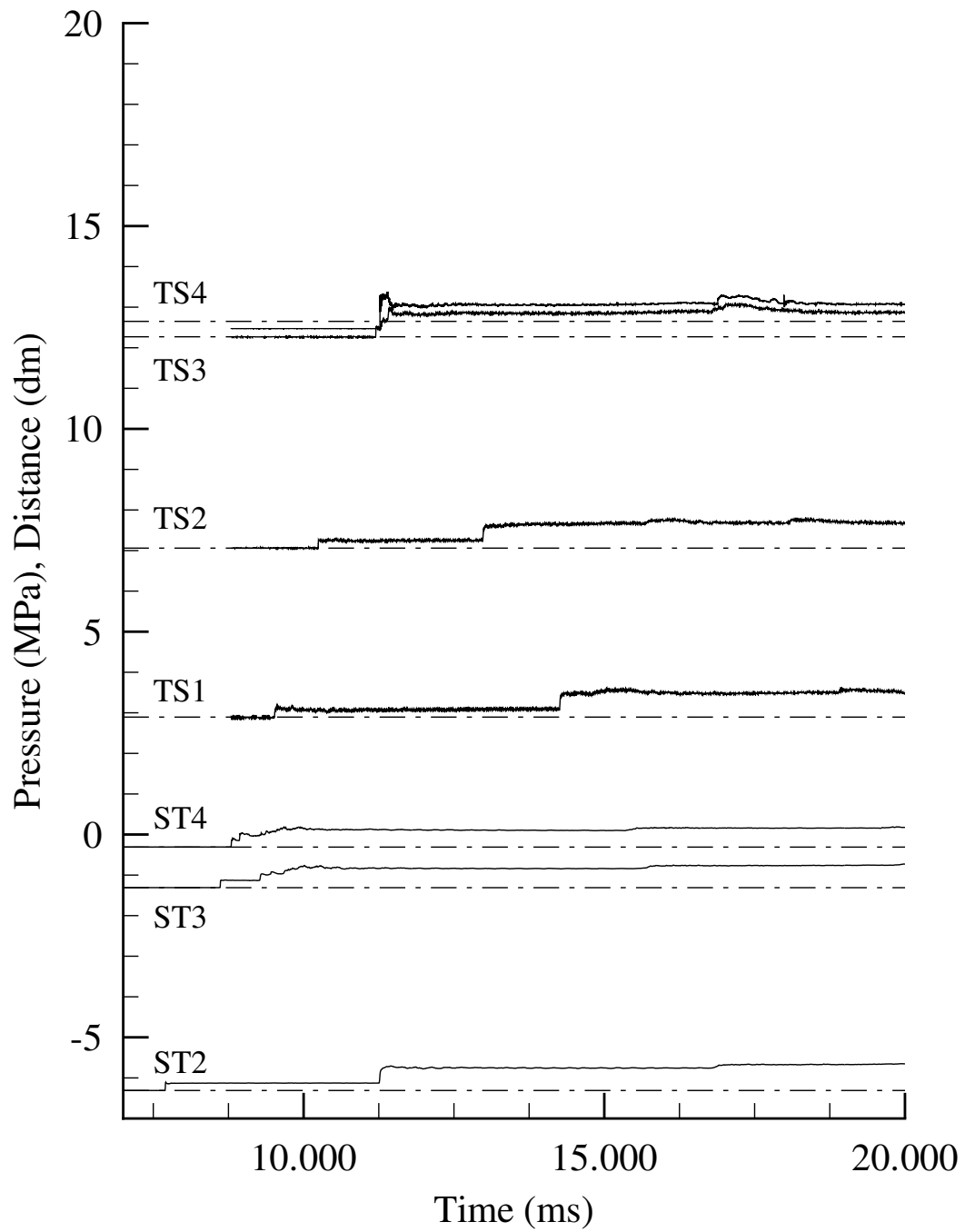


Figure I.21: Pressure and ionization data from shock initiator run 42.

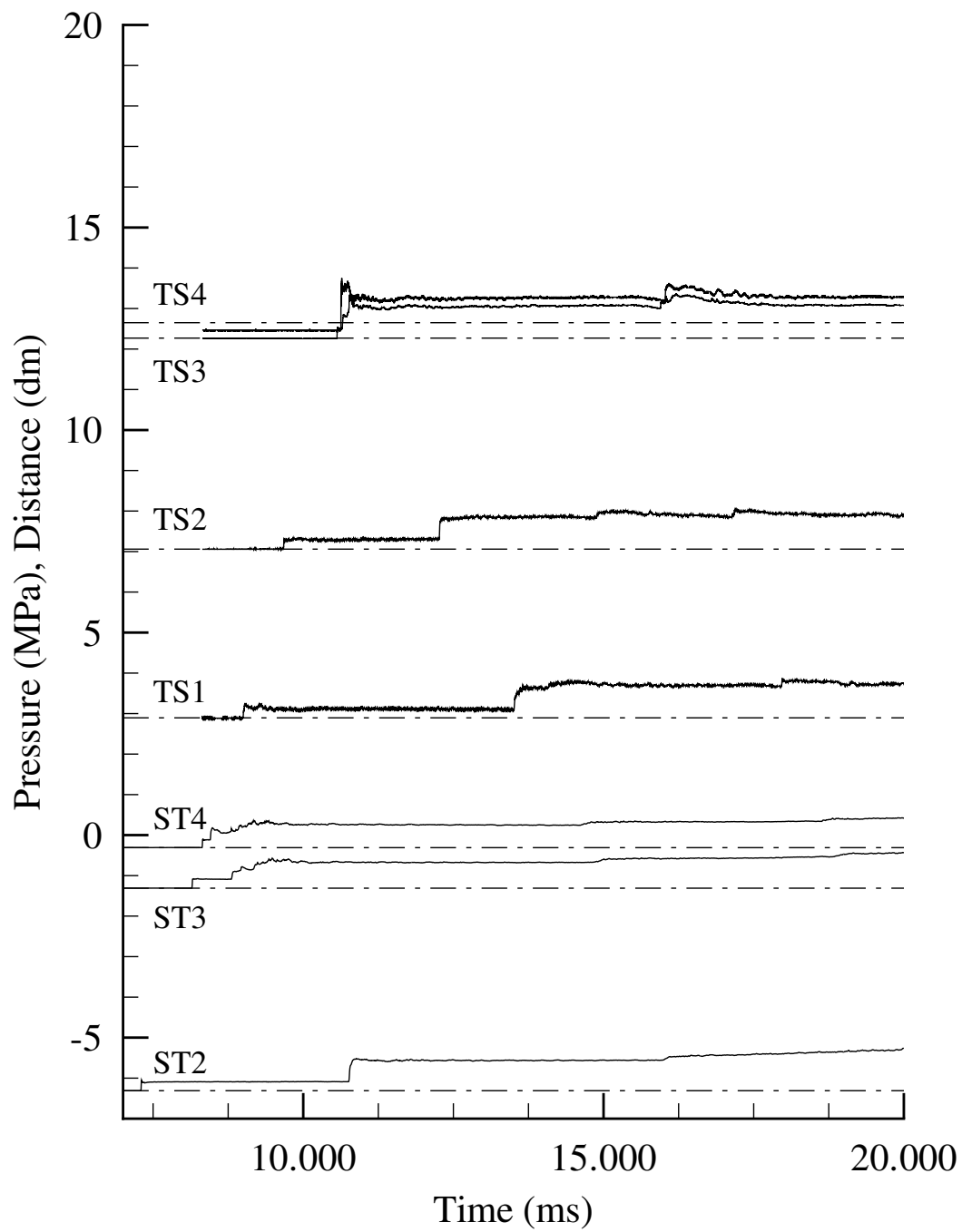


Figure I.22: Pressure and ionization data from shock initiator run 43.

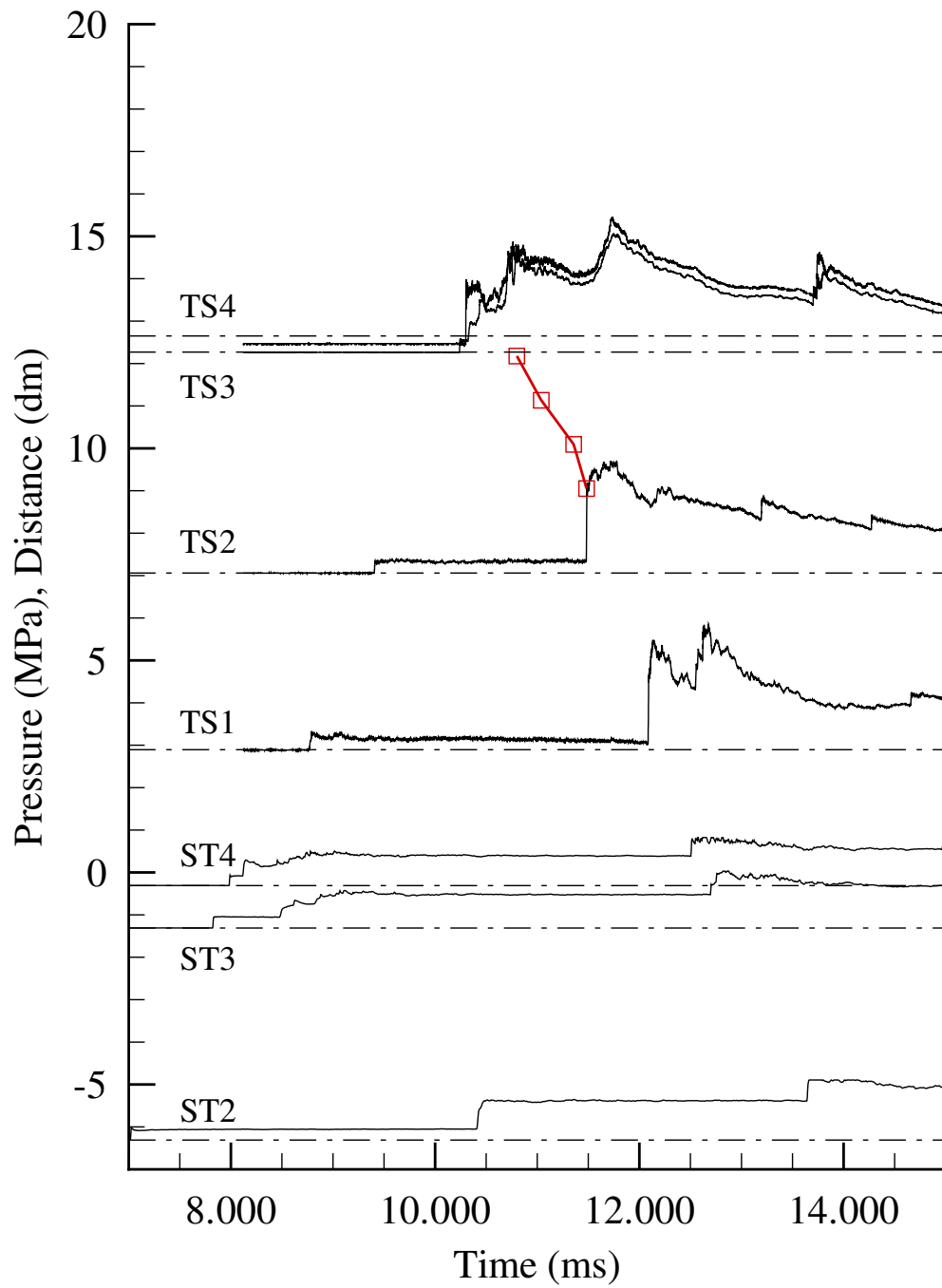


Figure I.23: Pressure and ionization data from shock initiator run 44.

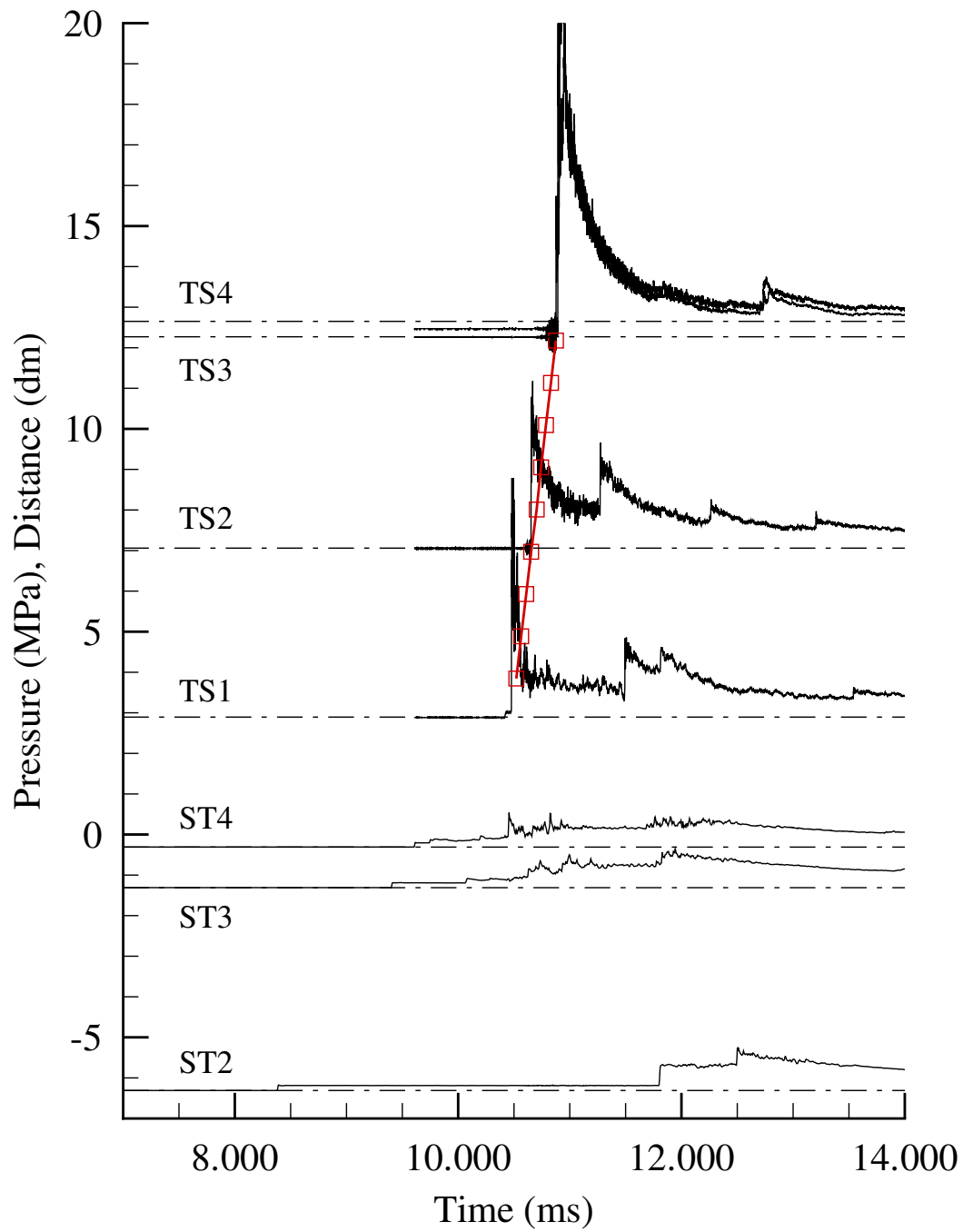


Figure I.24: Pressure and ionization data from shock initiator run 45.

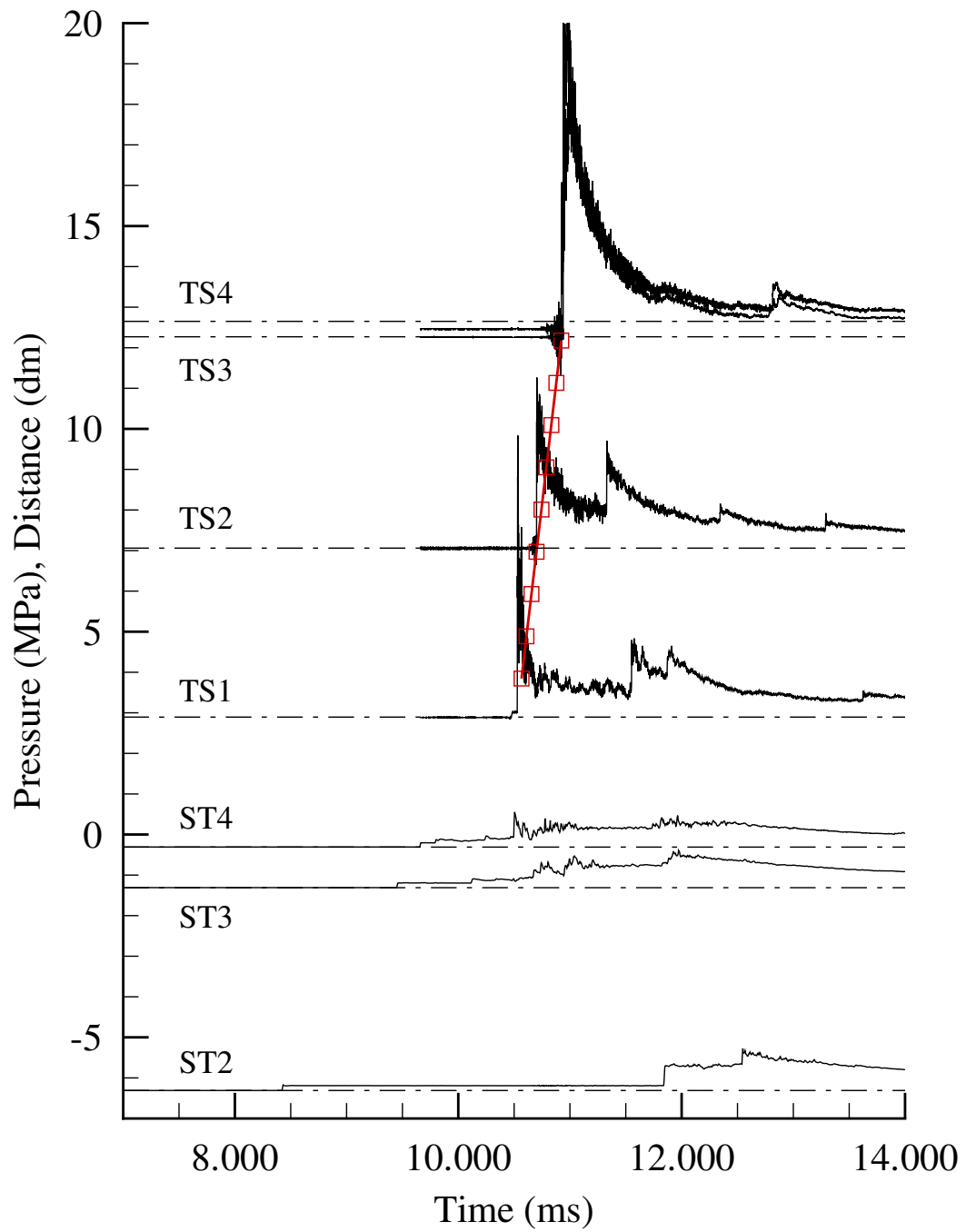


Figure I.25: Pressure and ionization data from shock initiator run 46.

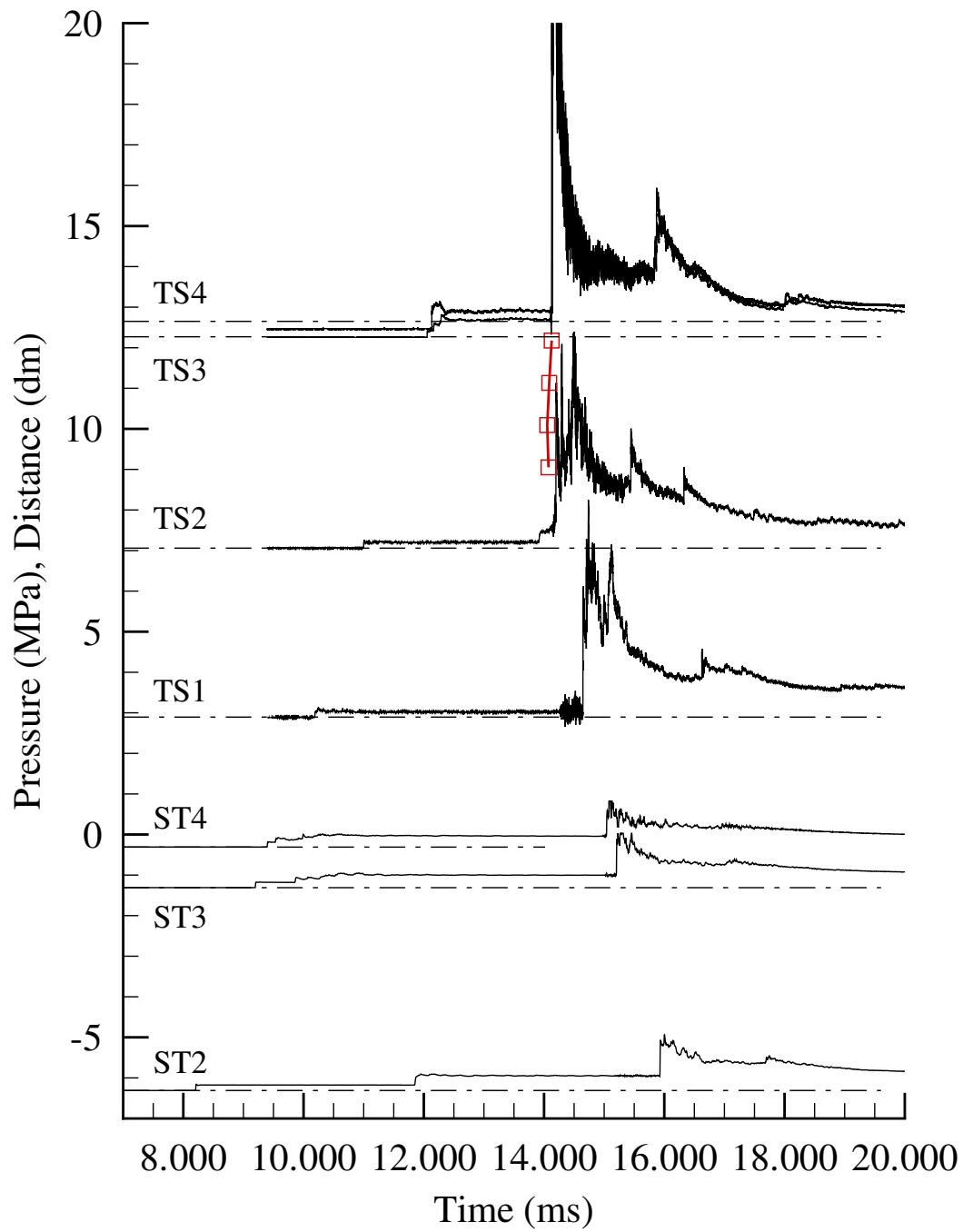


Figure I.26: Pressure and ionization data from shock initiator run 47.

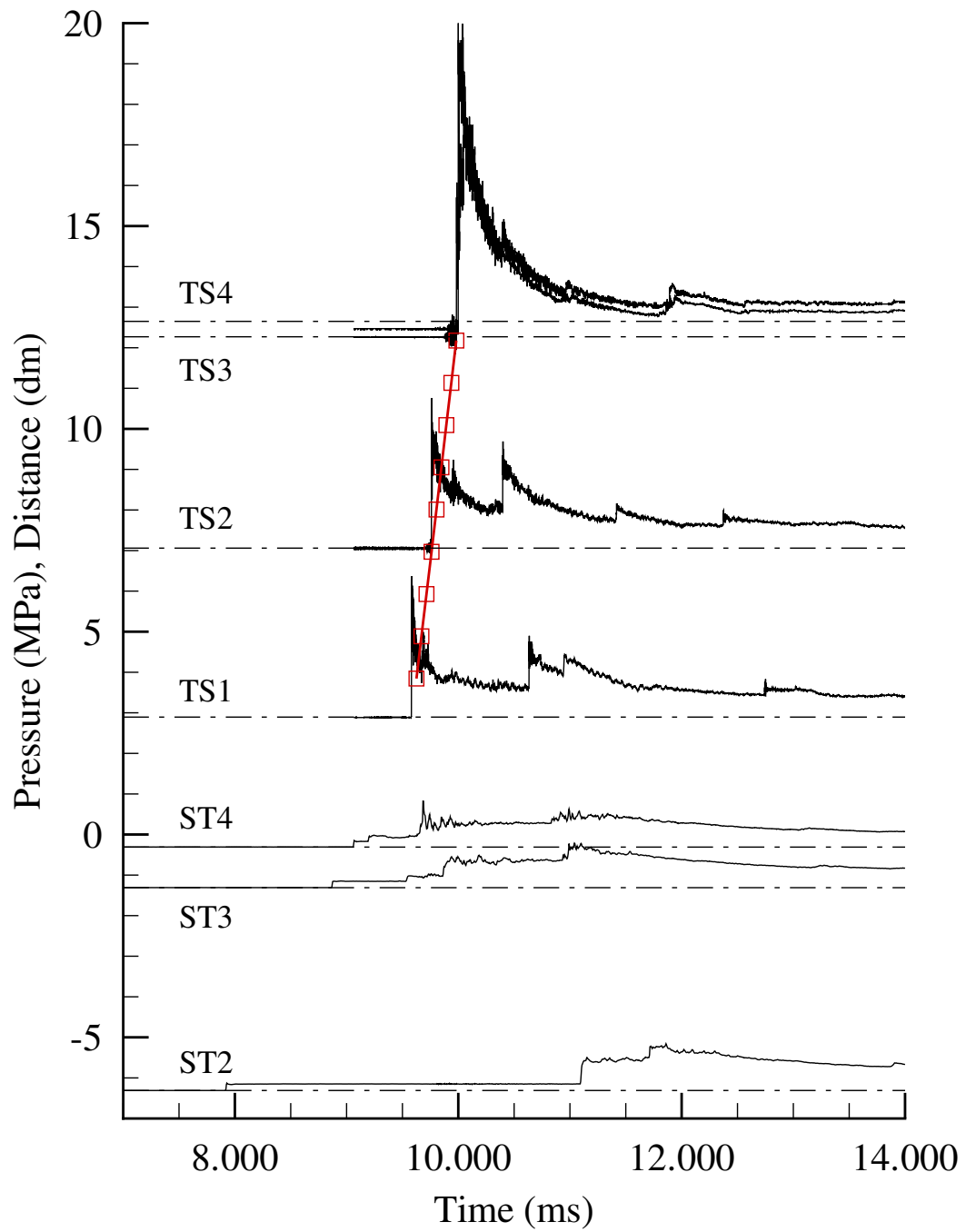


Figure I.27: Pressure and ionization data from shock initiator run 48.

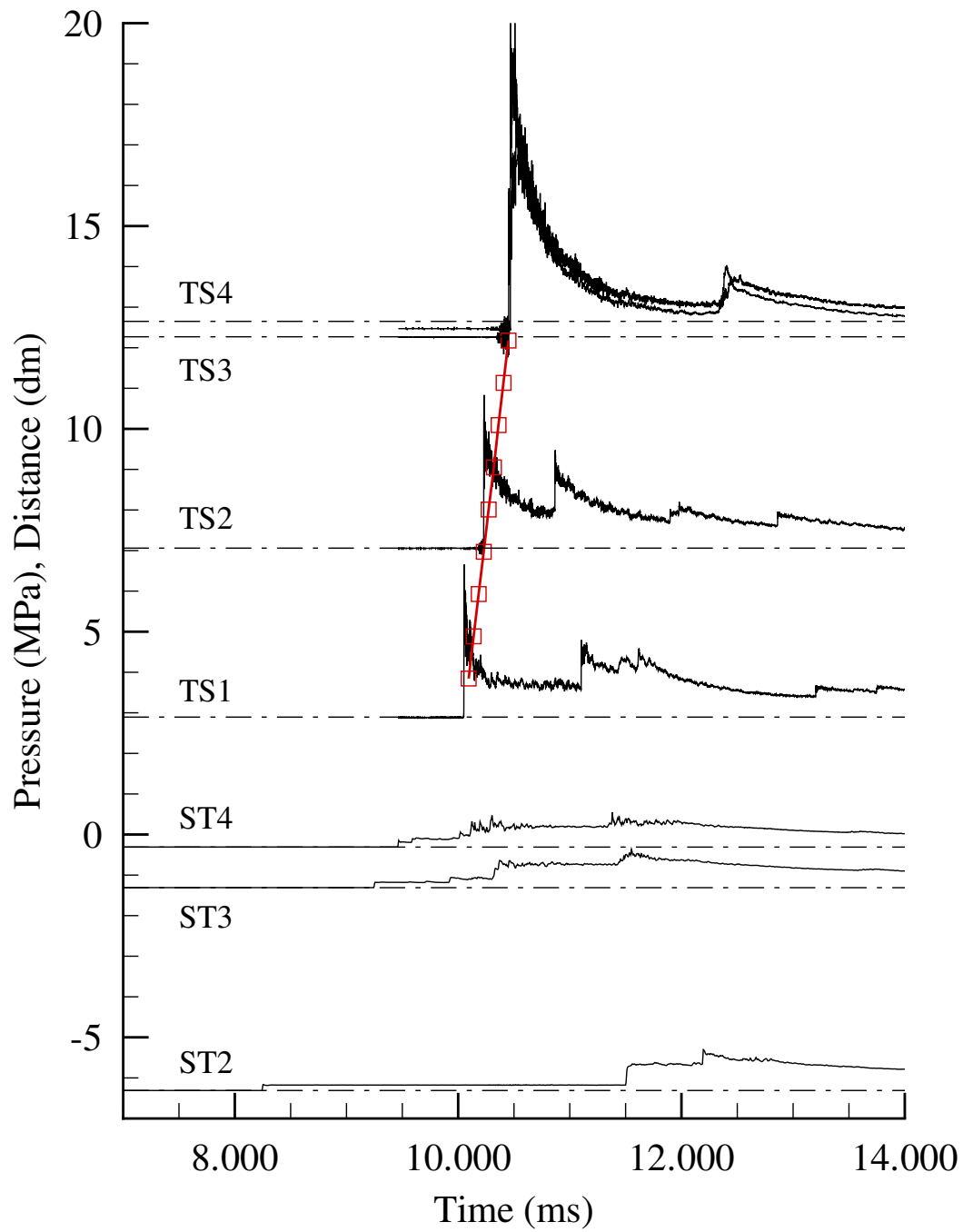


Figure I.28: Pressure and ionization data from shock initiator run 49.

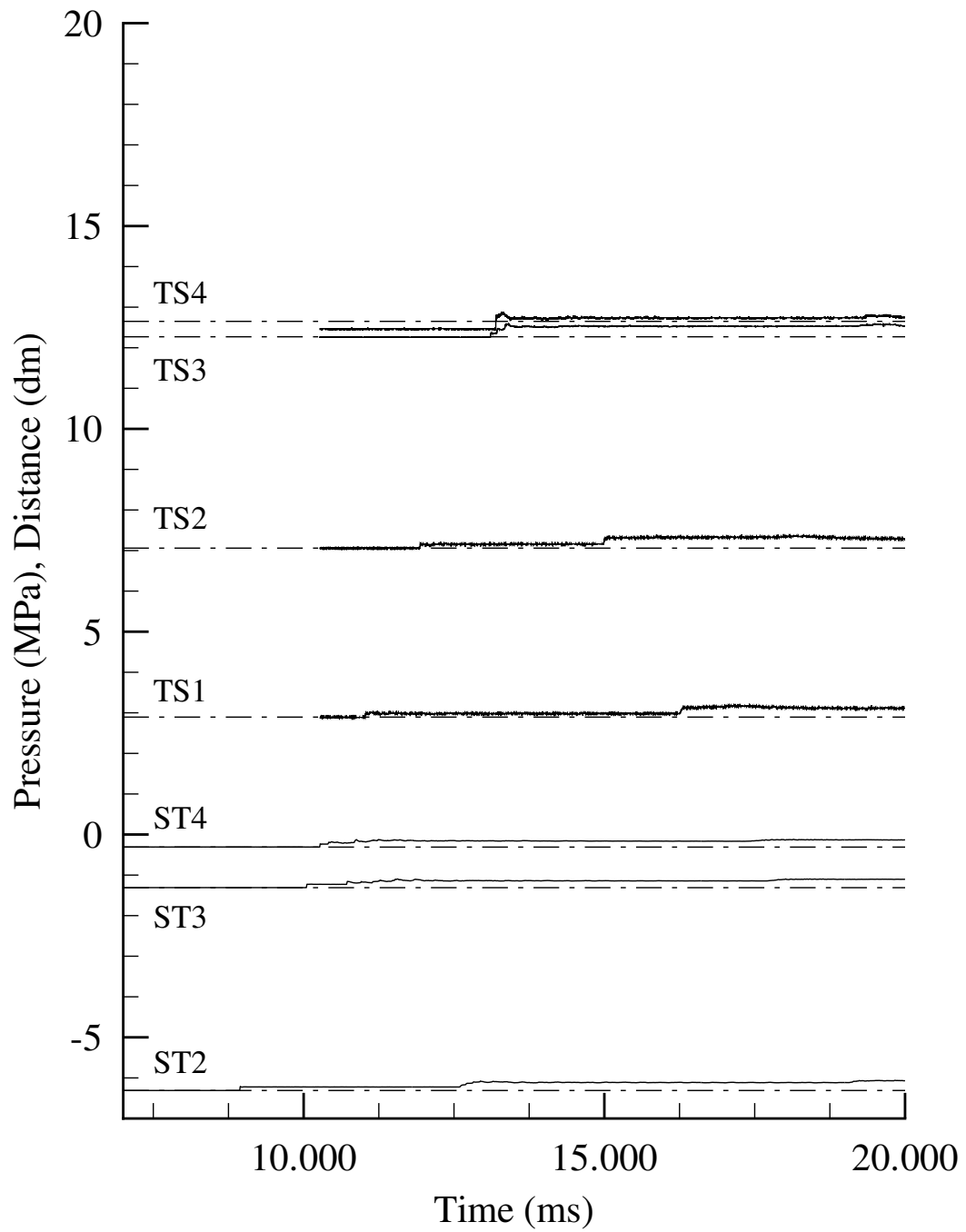


Figure I.29: Pressure and ionization data from shock initiator run 50.

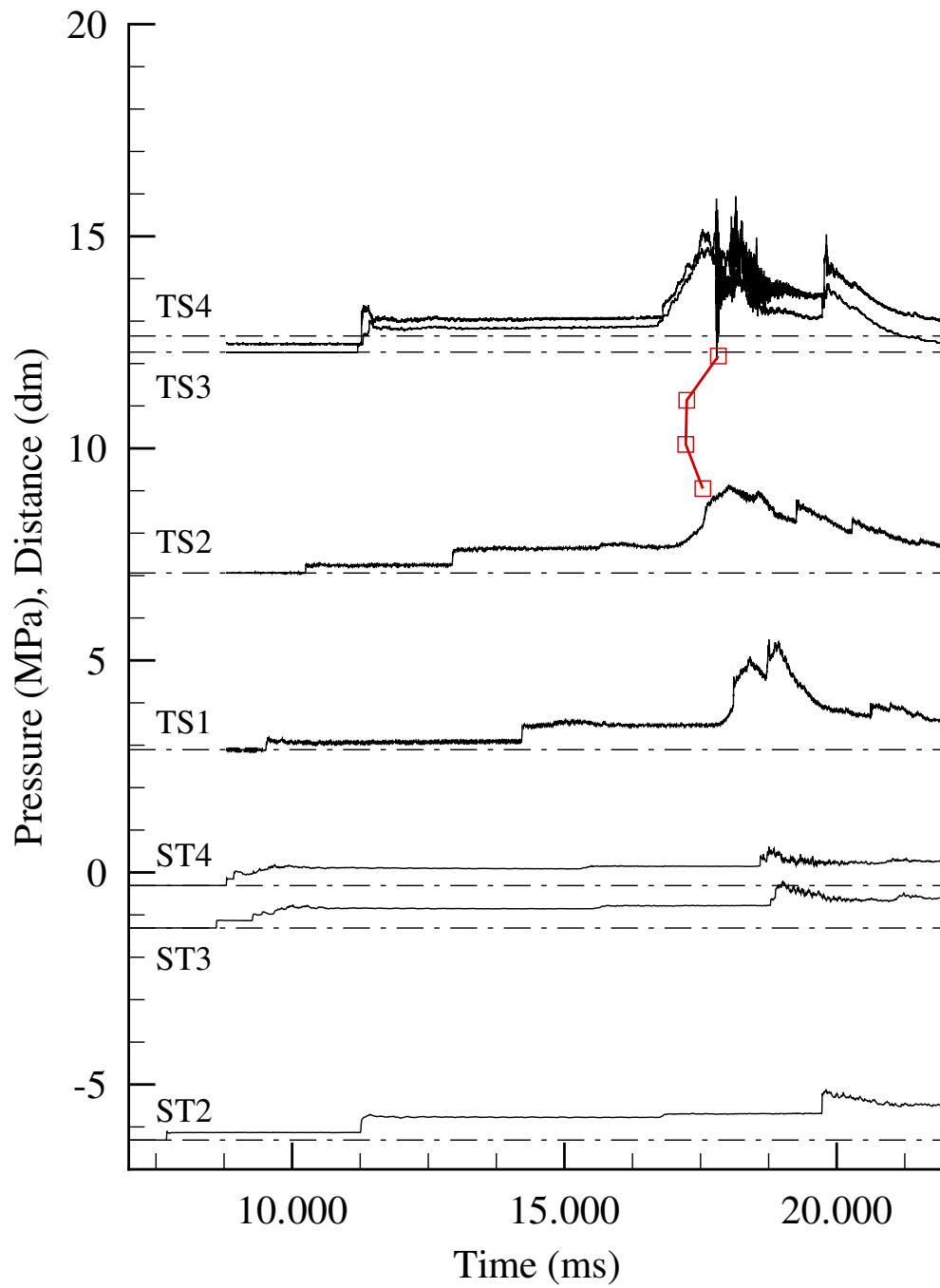


Figure I.30: Pressure and ionization data from shock initiator run 51.

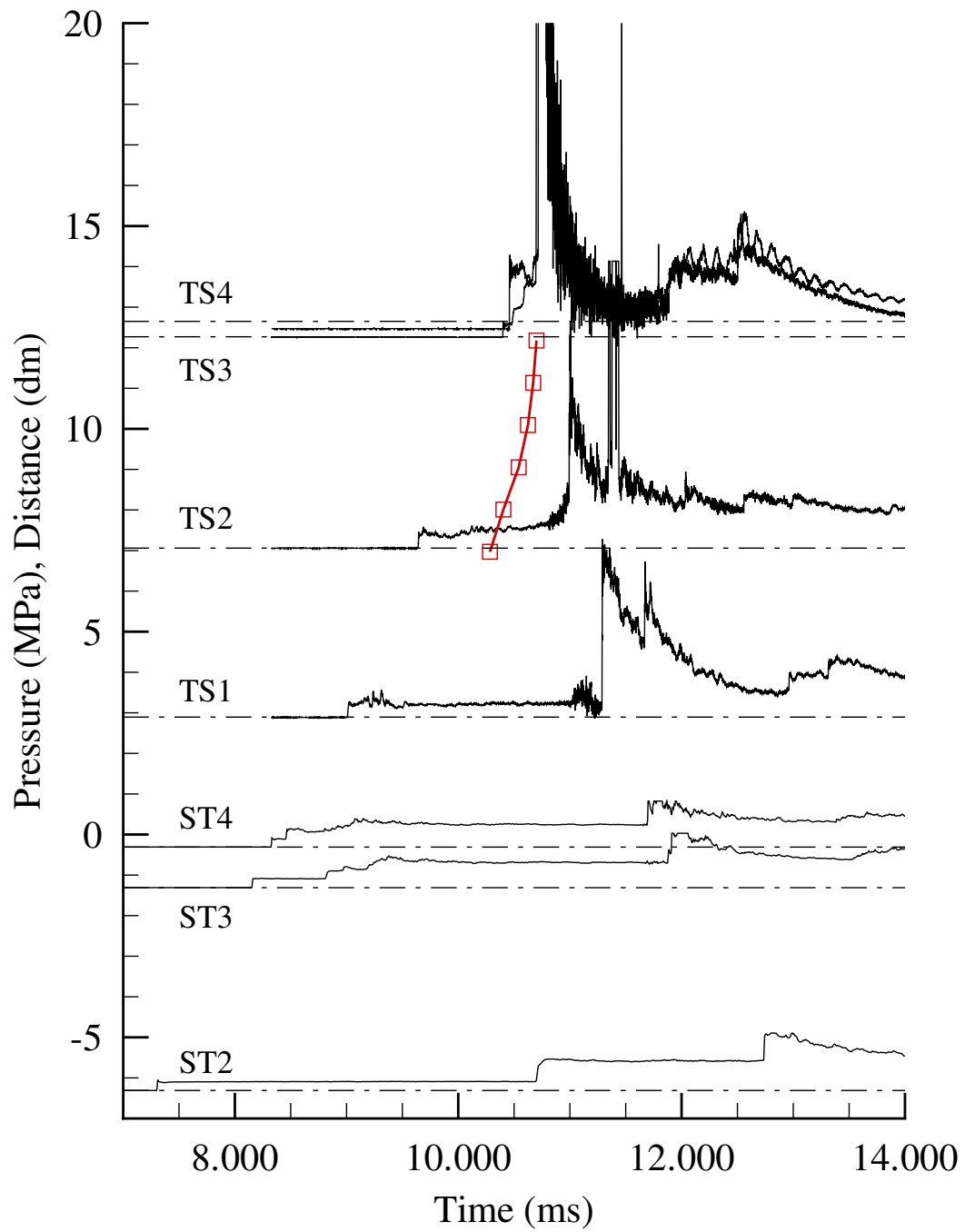


Figure I.31: Pressure and ionization data from shock initiator run 52.

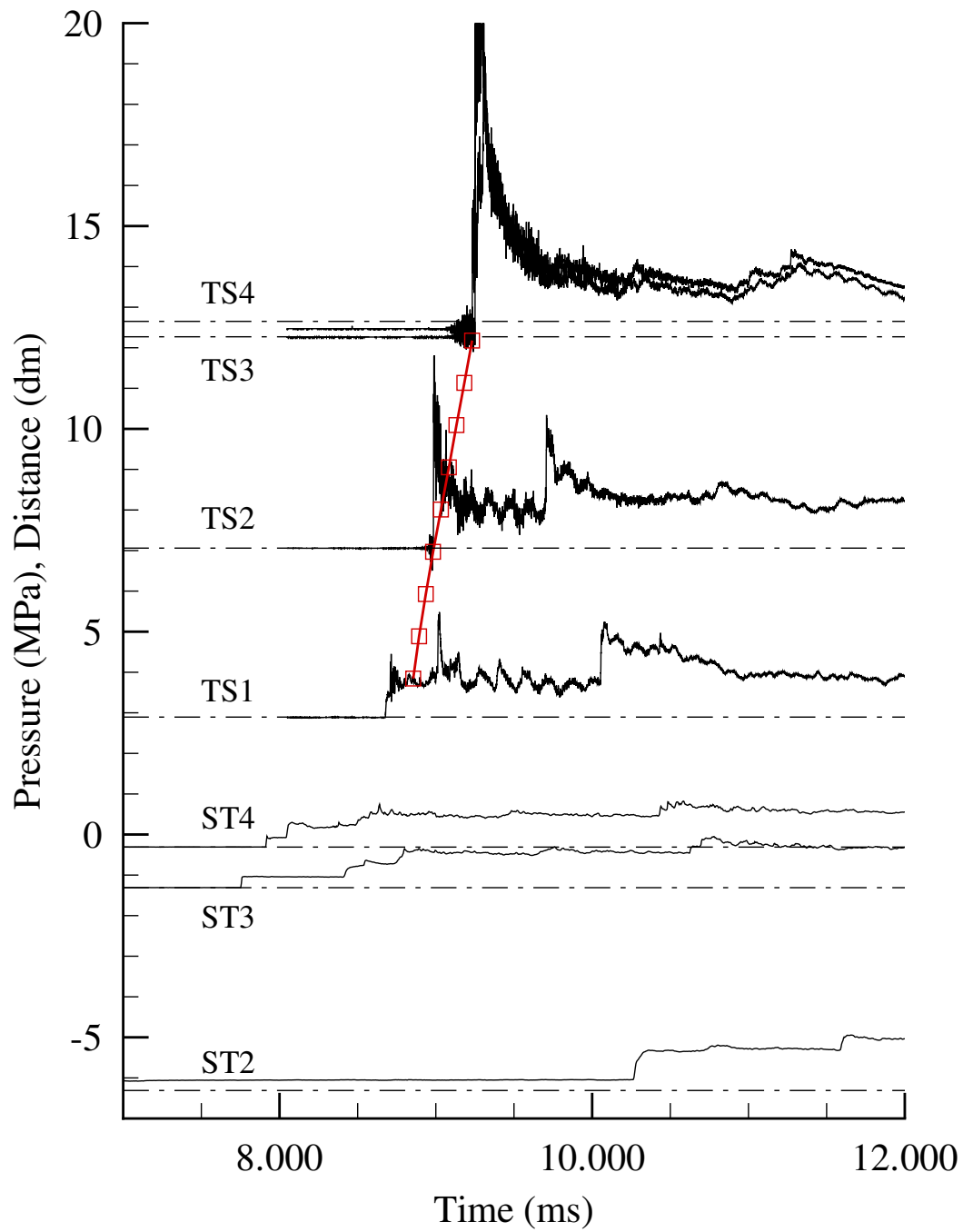


Figure I.32: Pressure and ionization data from shock initiator run 53.

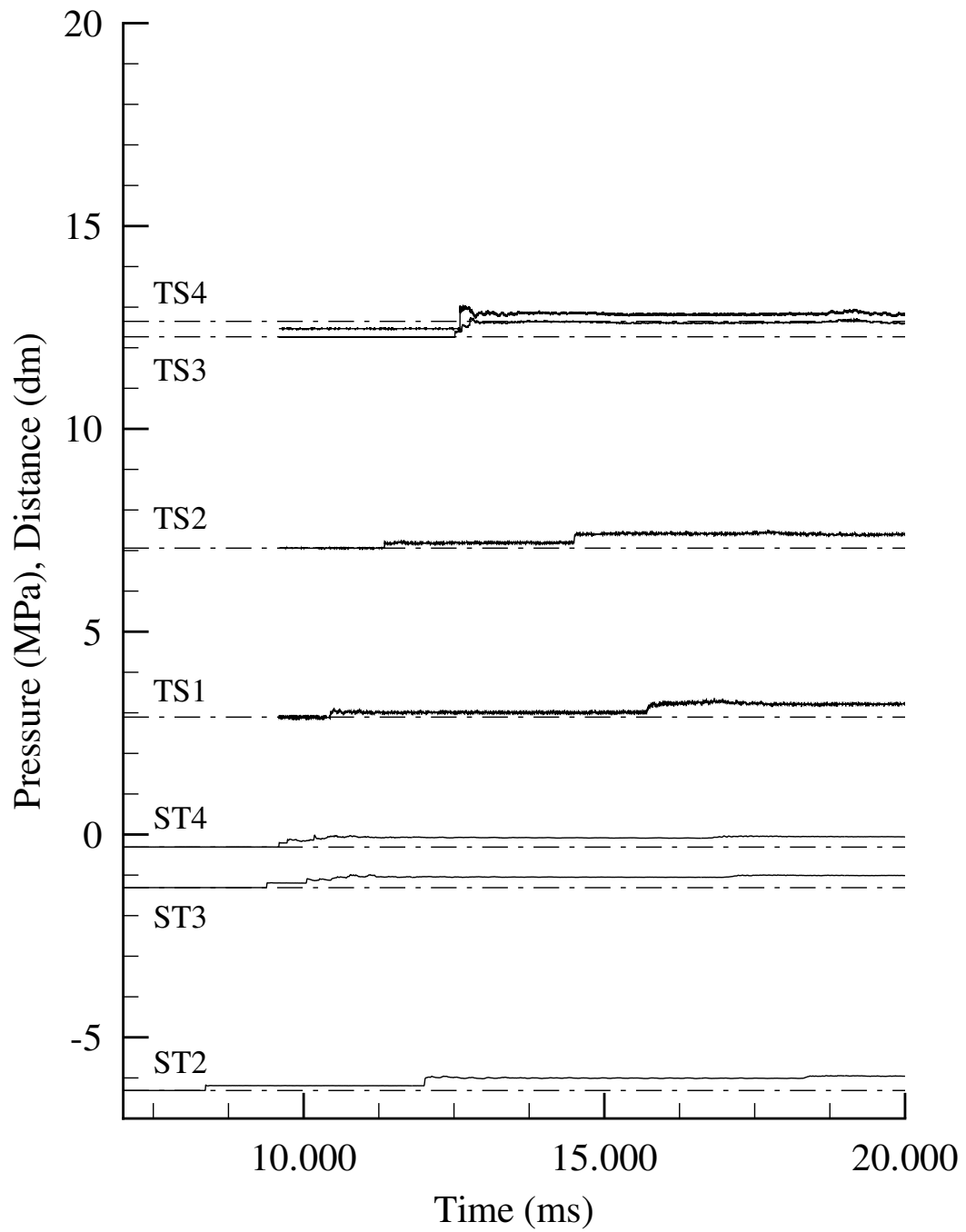


Figure I.33: Pressure and ionization data from shock initiator run 54.

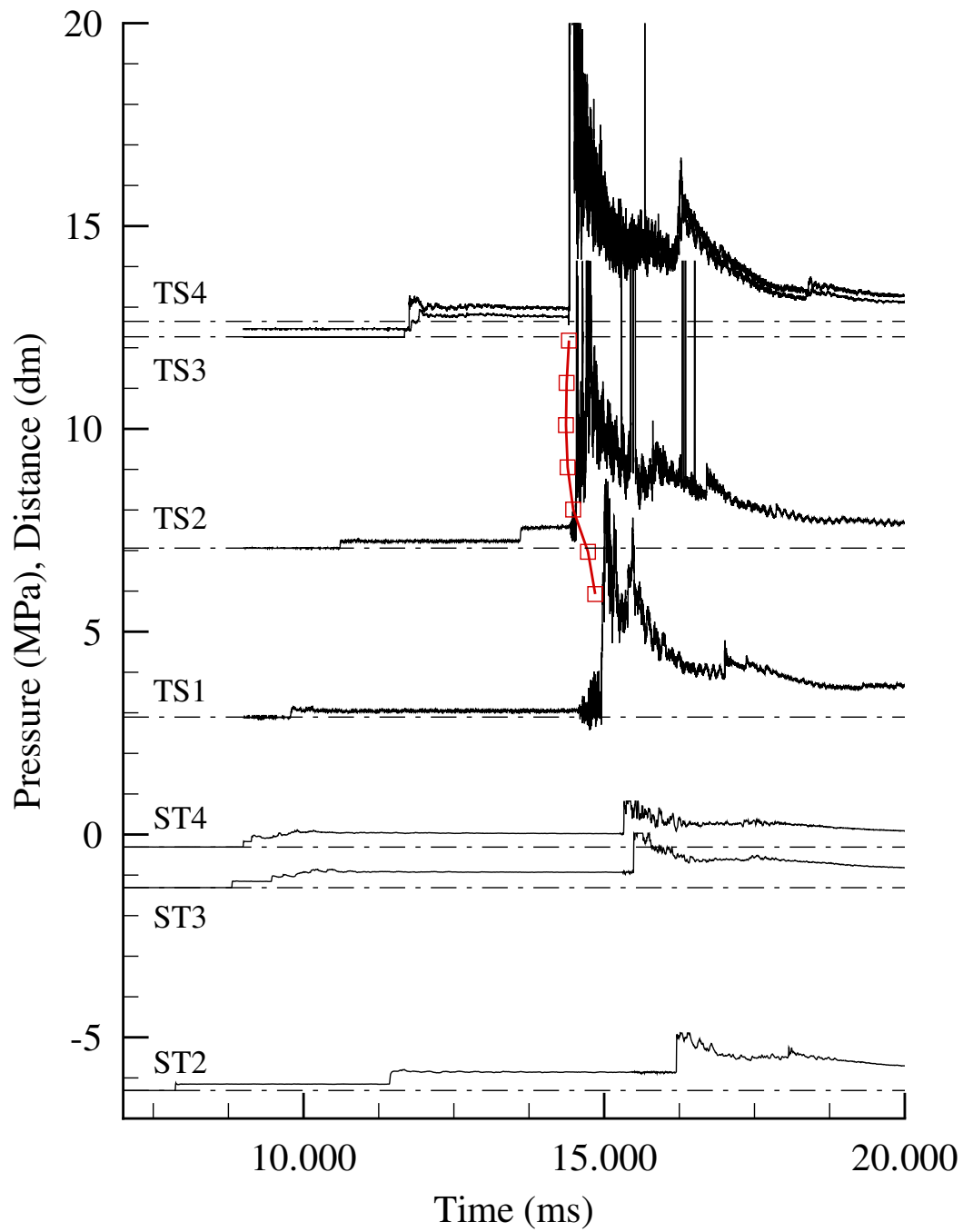


Figure I.34: Pressure and ionization data from shock initiator run 55.

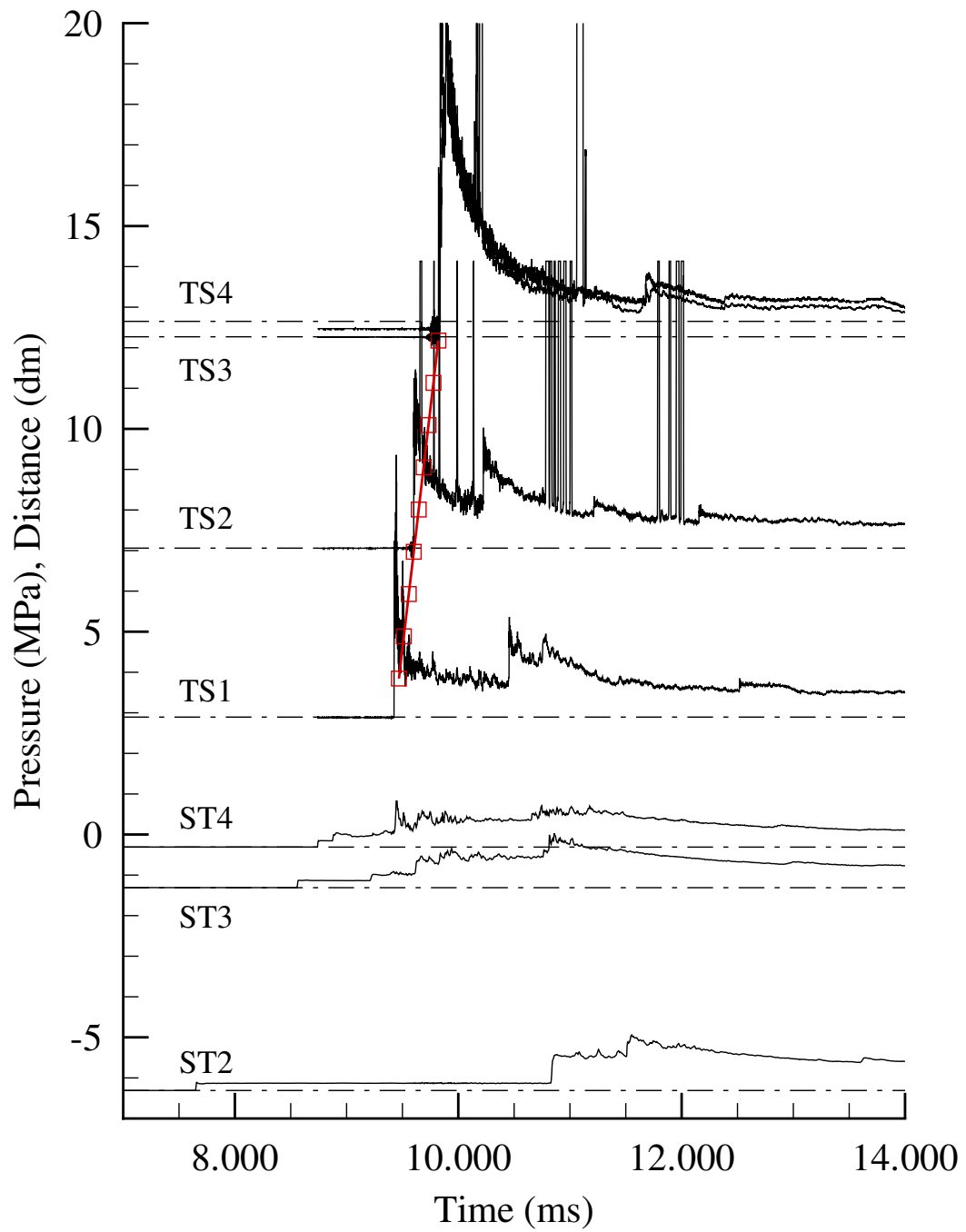


Figure I.35: Pressure and ionization data from shock initiator run 56.

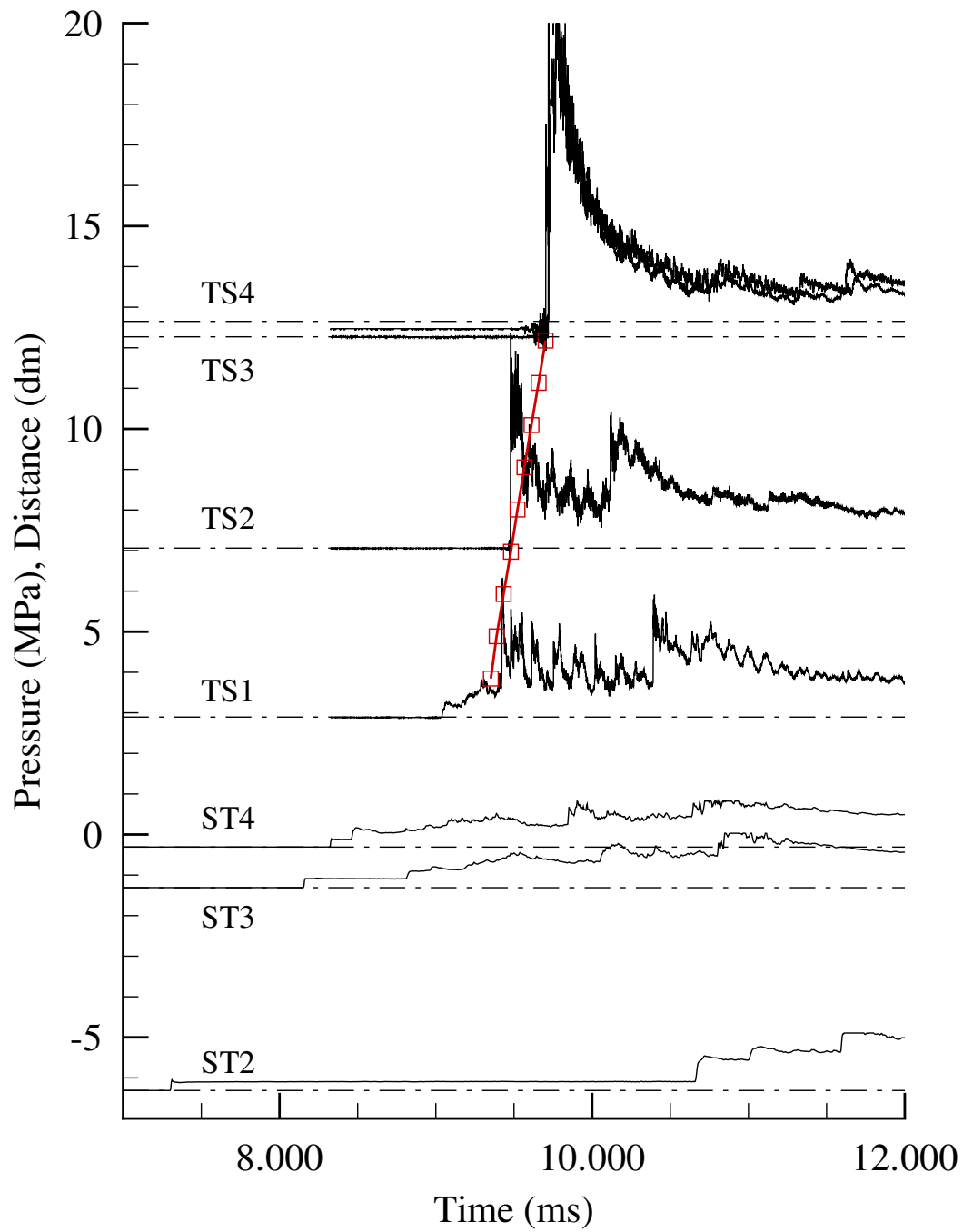


Figure I.36: Pressure and ionization data from shock initiator run 70.

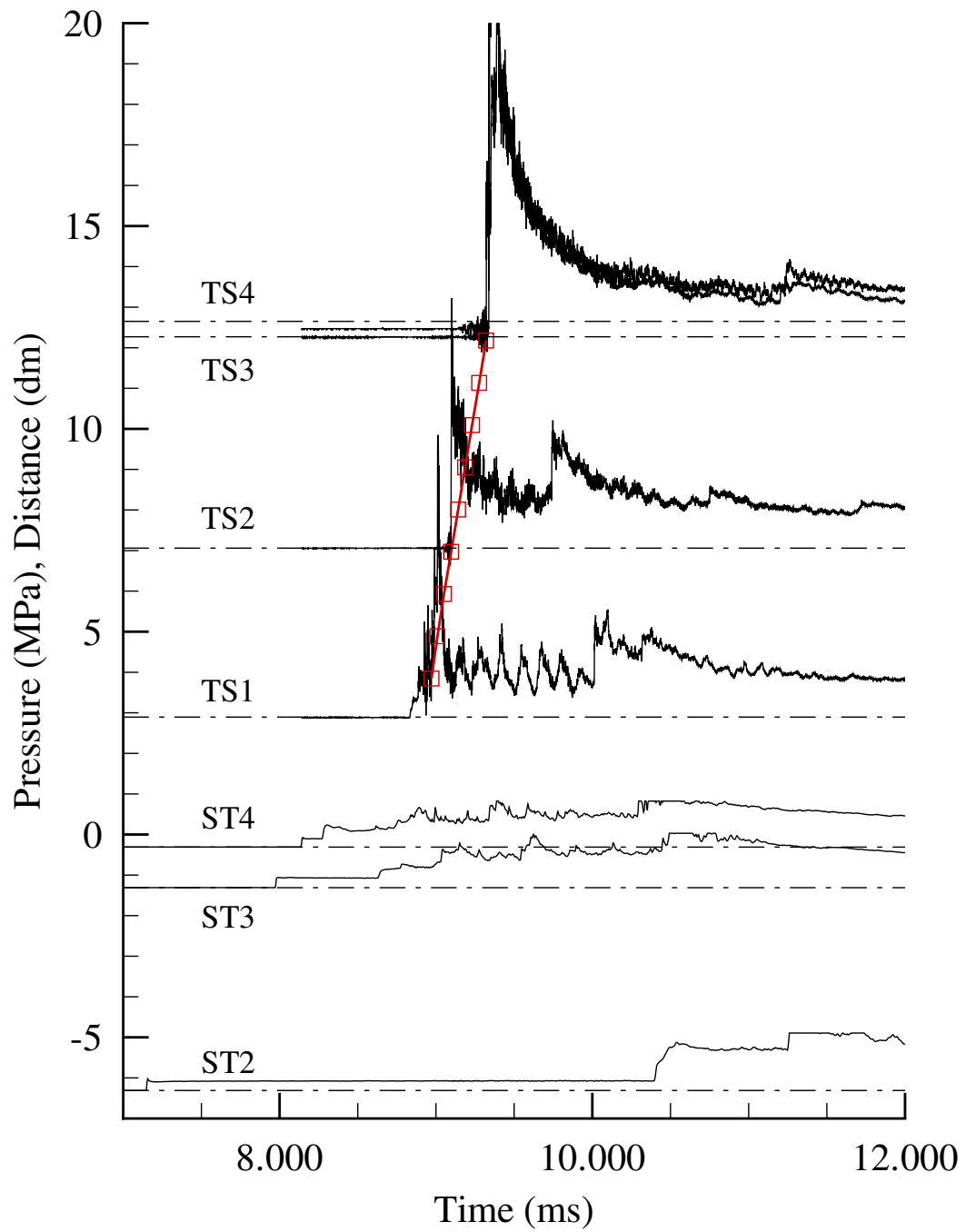


Figure I.37: Pressure and ionization data from shock initiator run 71.

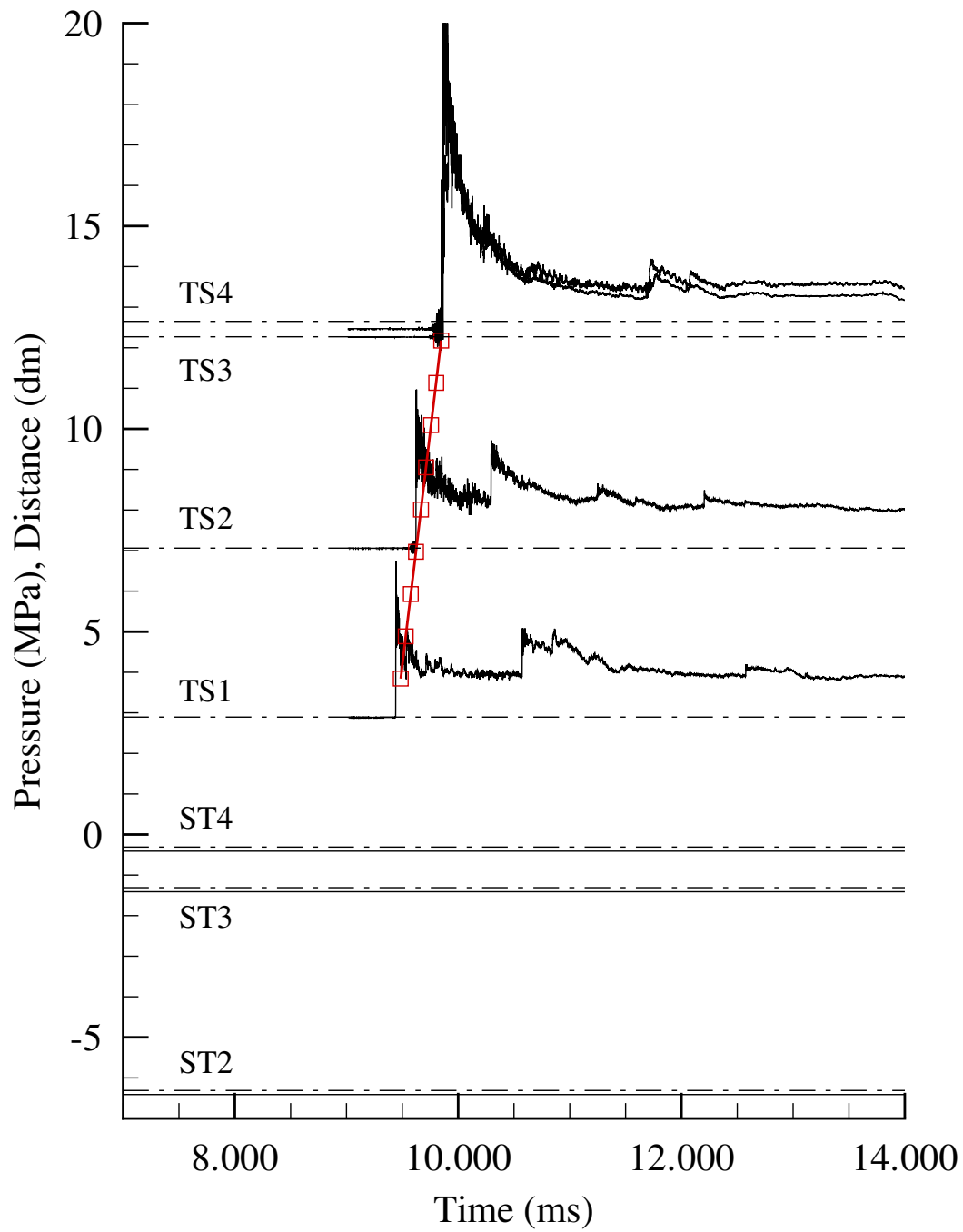


Figure I.38: Pressure and ionization data from shock initiator run 72.

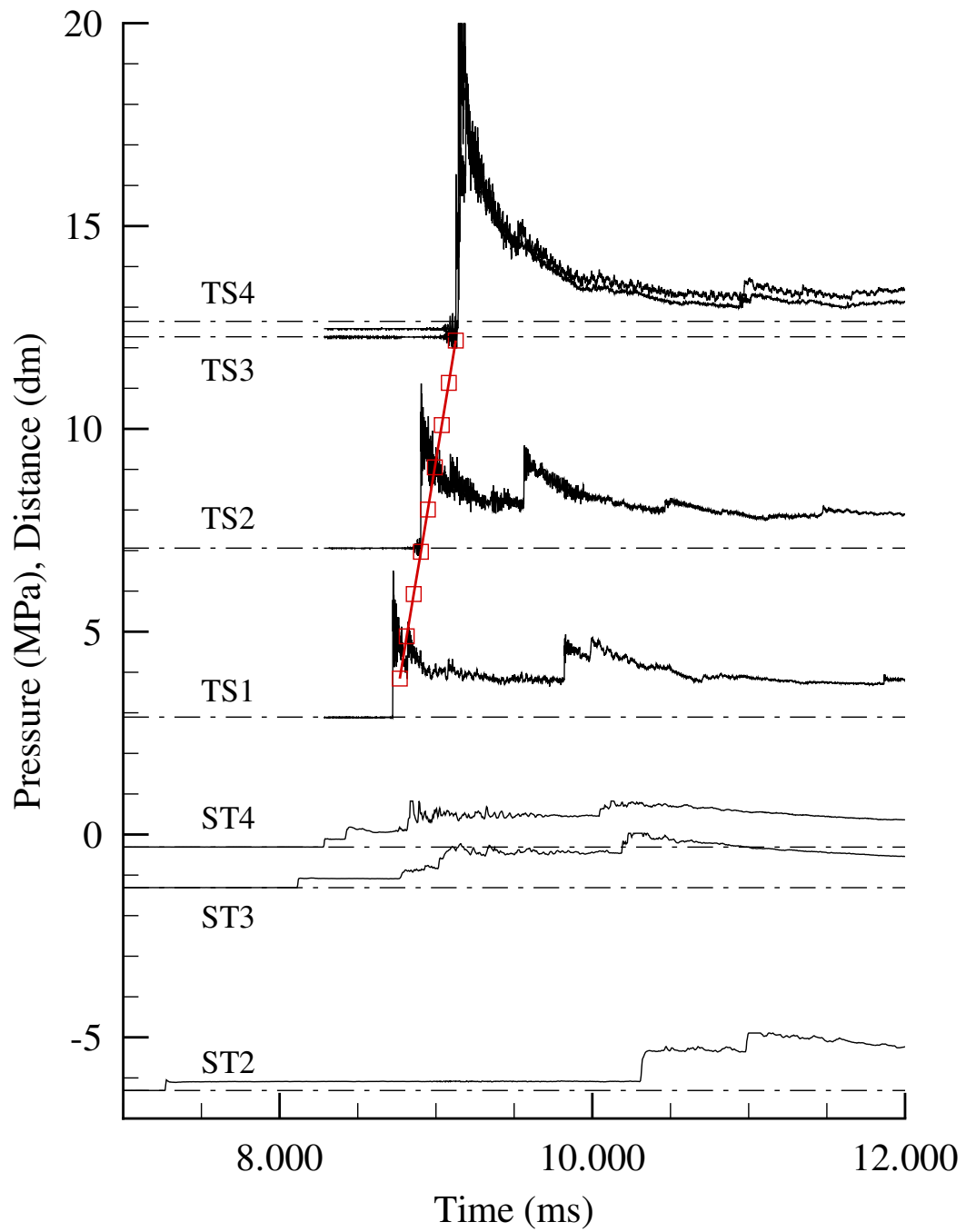


Figure I.39: Pressure and ionization data from shock initiator run 73.

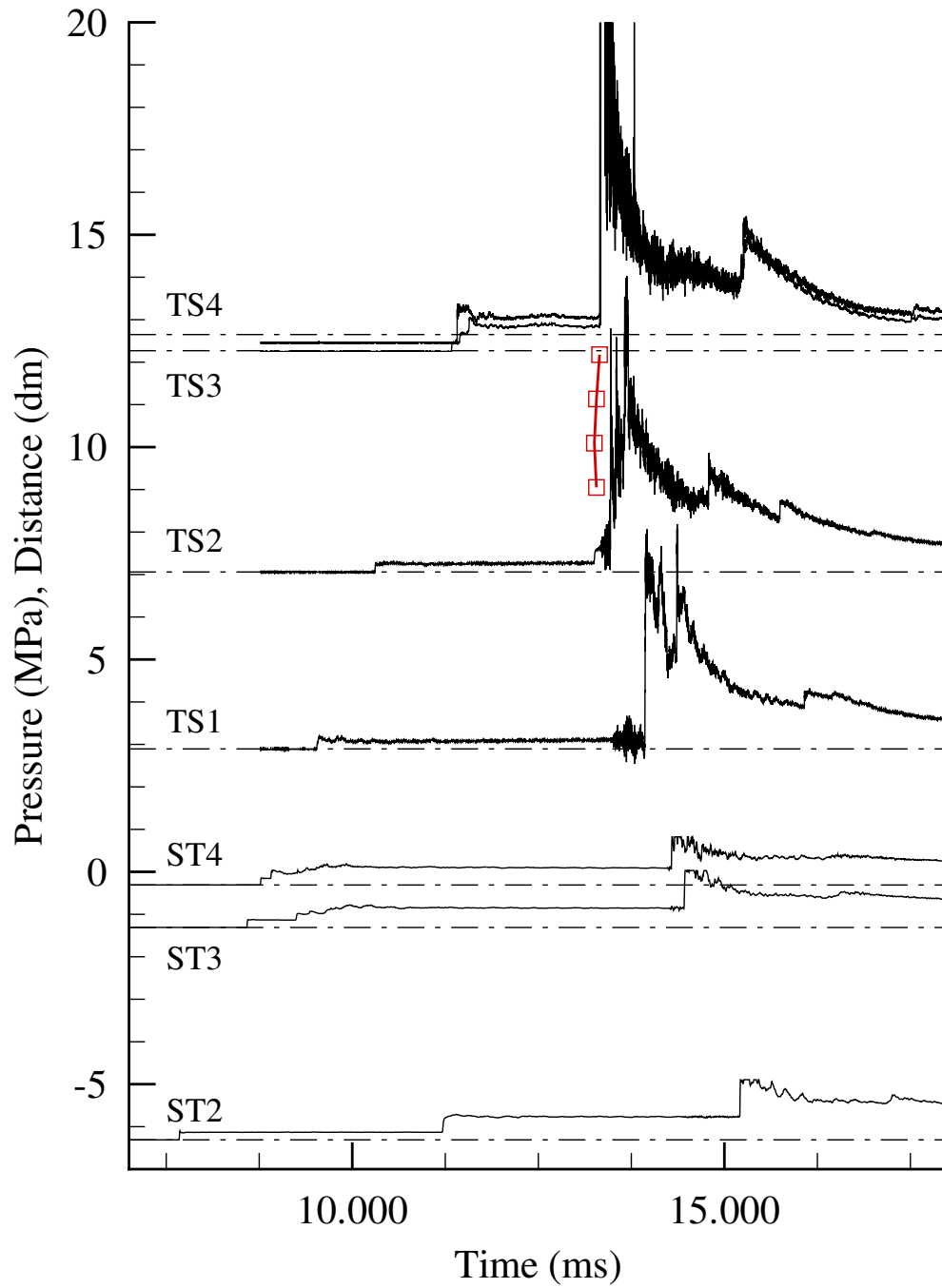


Figure I.40: Pressure and ionization data from shock initiator run 74.

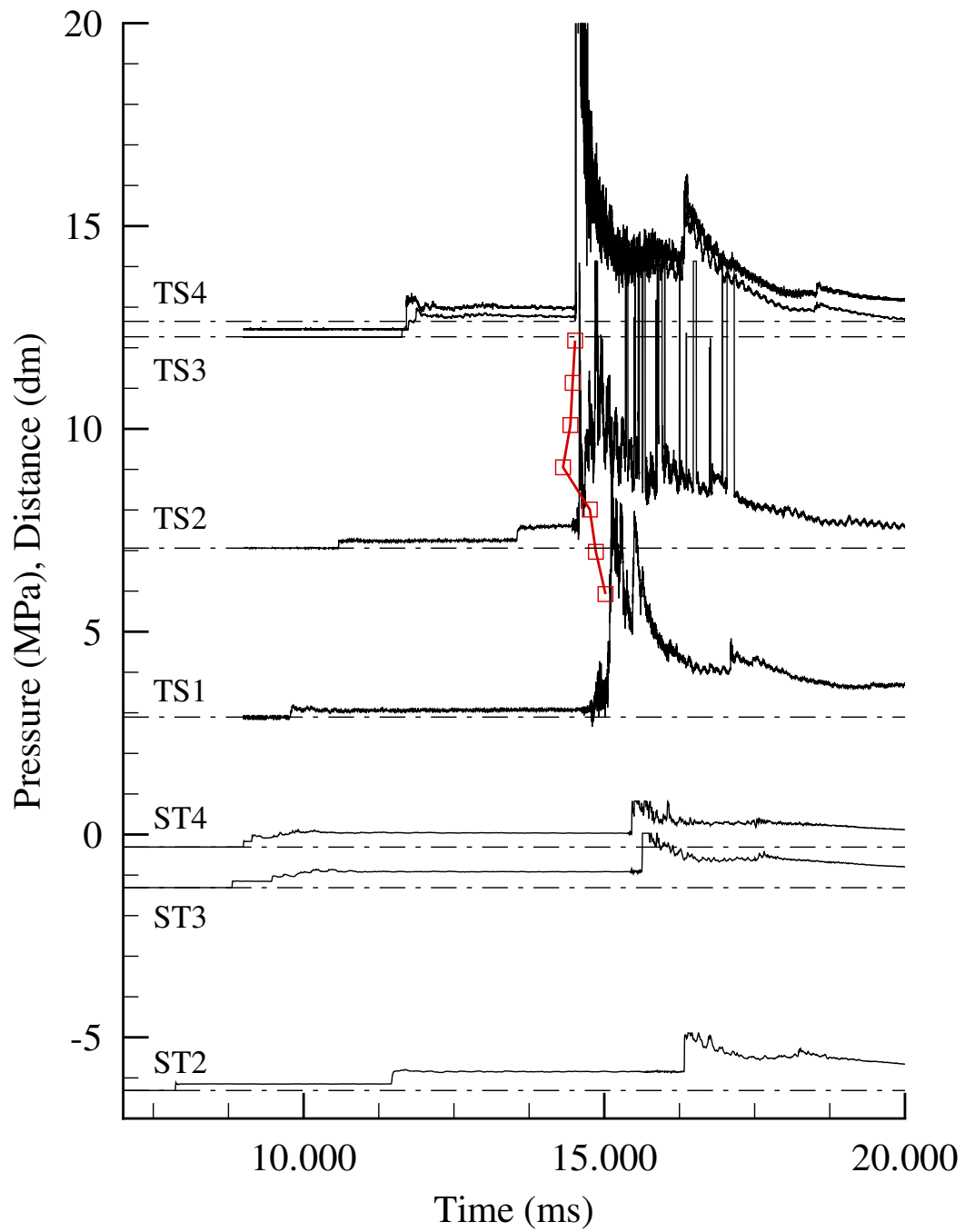


Figure I.41: Pressure and ionization data from shock initiator run 75.

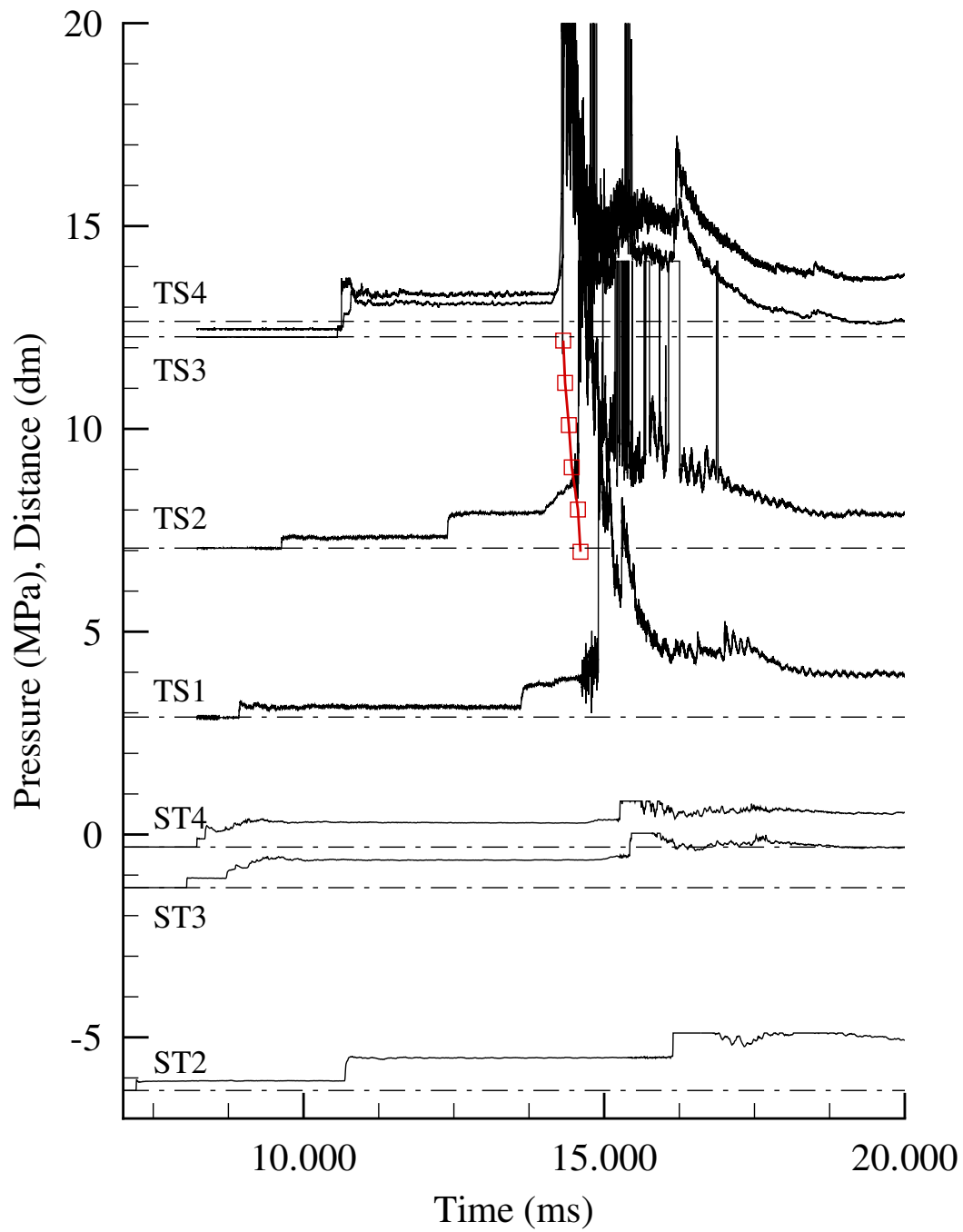


Figure I.42: Pressure and ionization data from shock initiator run 76.

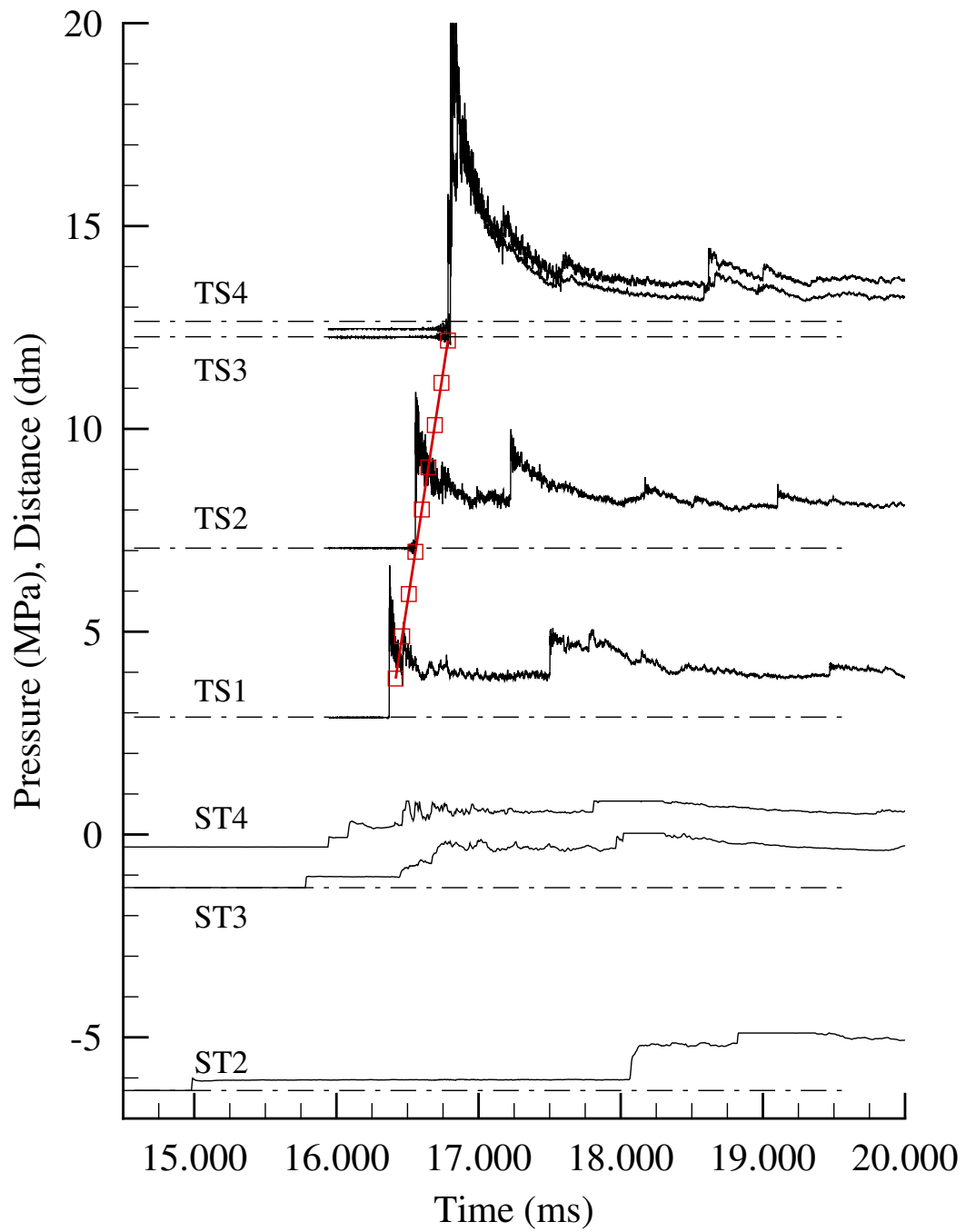


Figure I.43: Pressure and ionization data from shock initiator run 77.

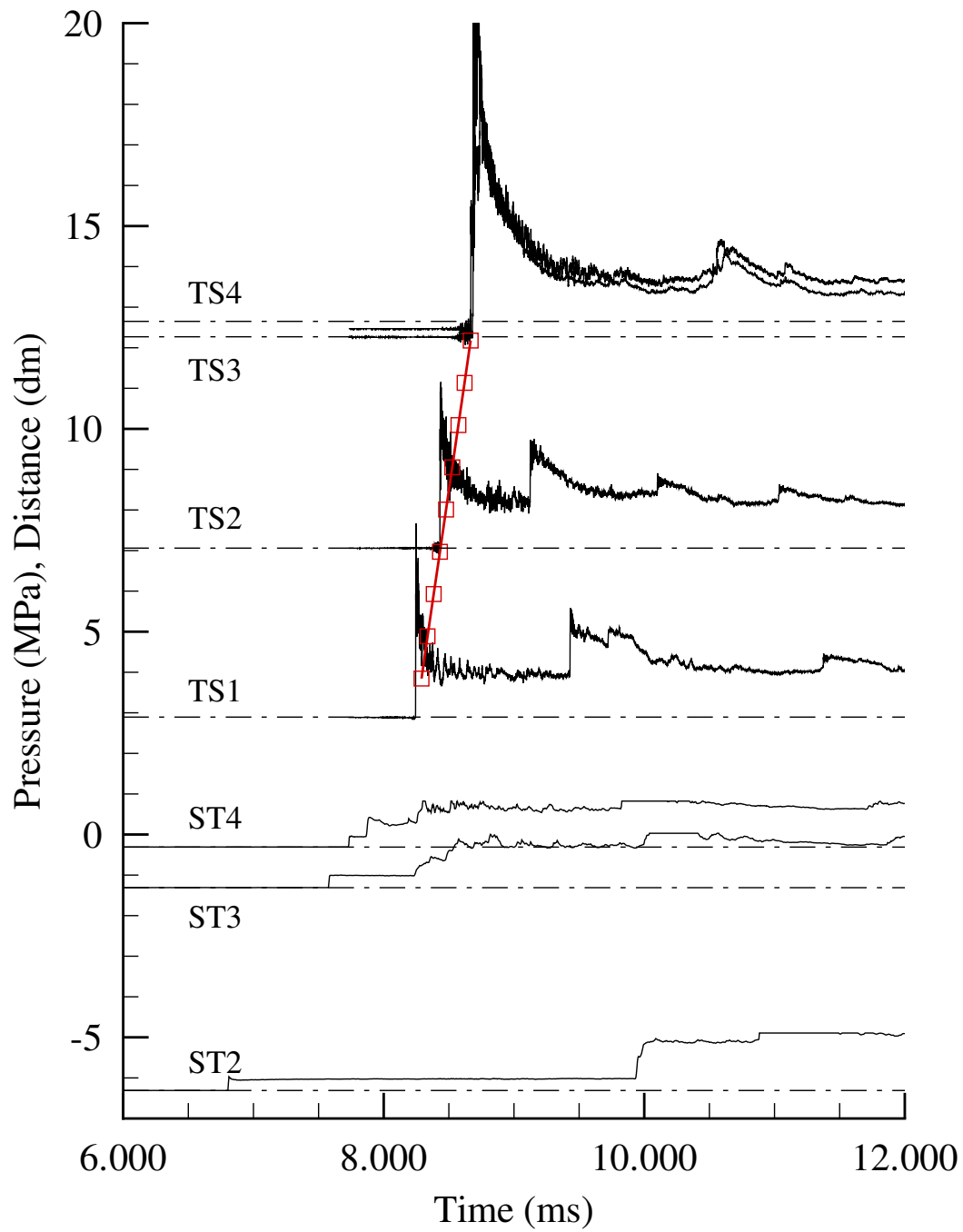


Figure I.44: Pressure and ionization data from shock initiator run 78.

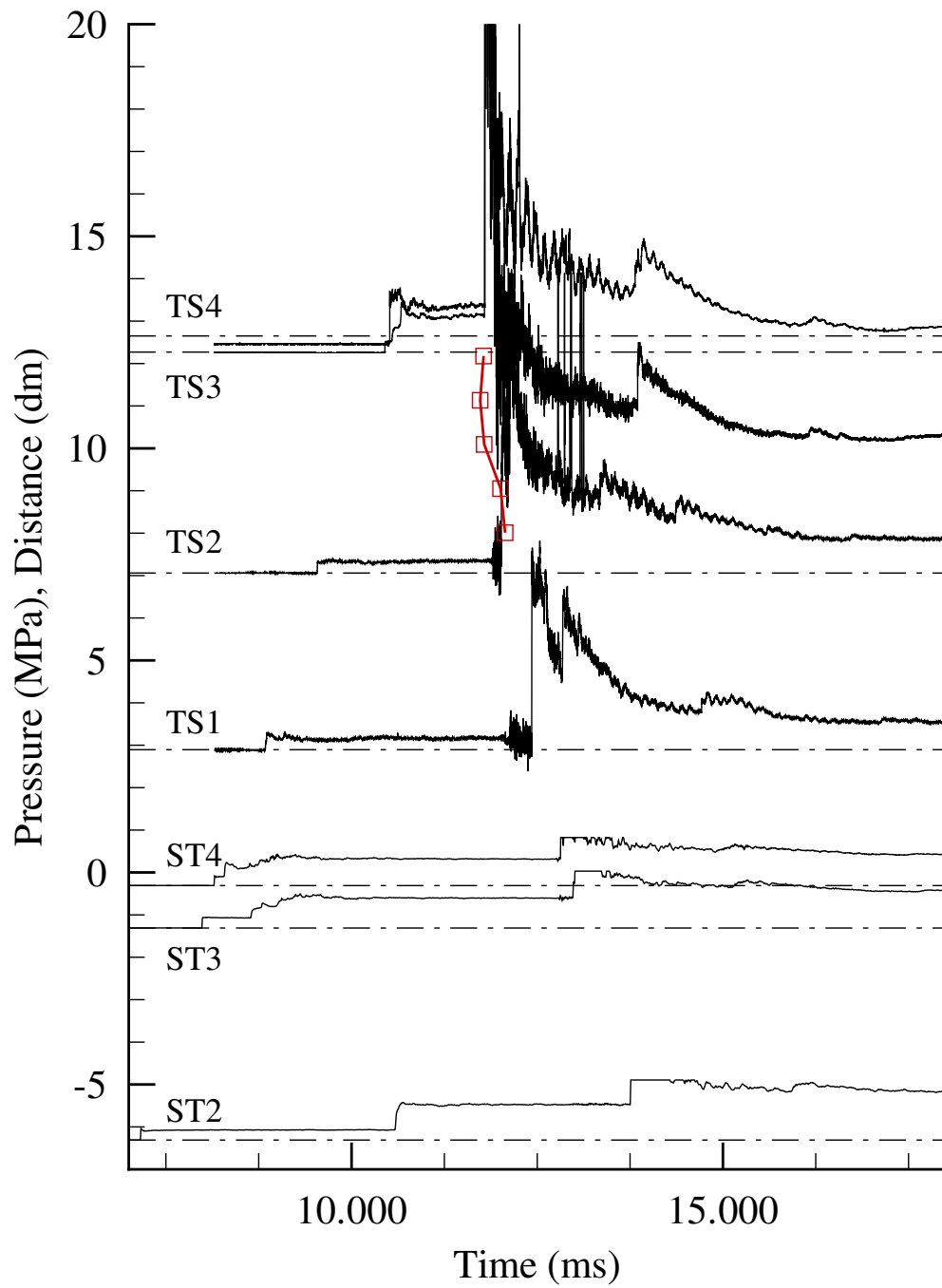


Figure I.45: Pressure and ionization data from shock initiator run 79.

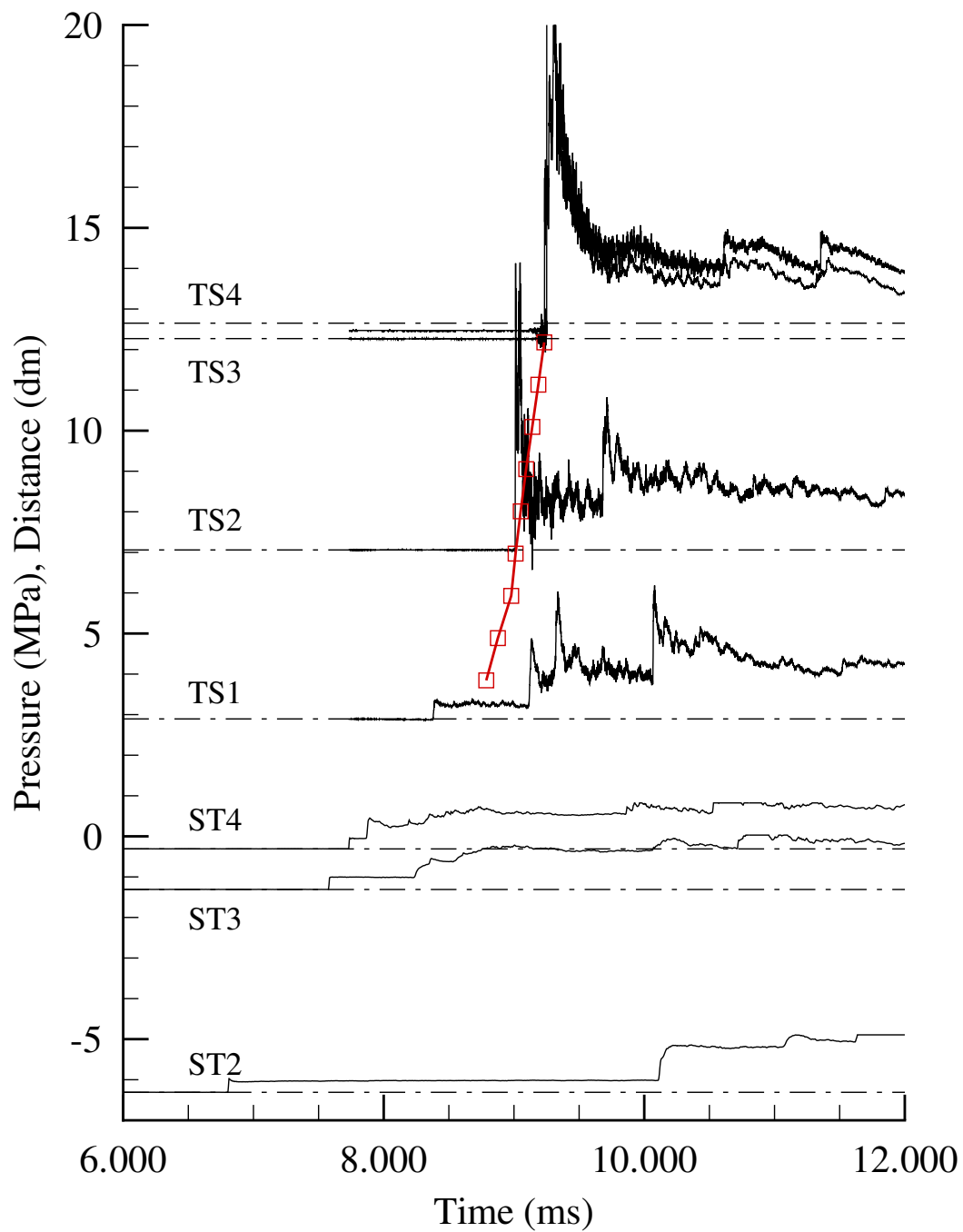


Figure I.46: Pressure and ionization data from shock initiator run 80.

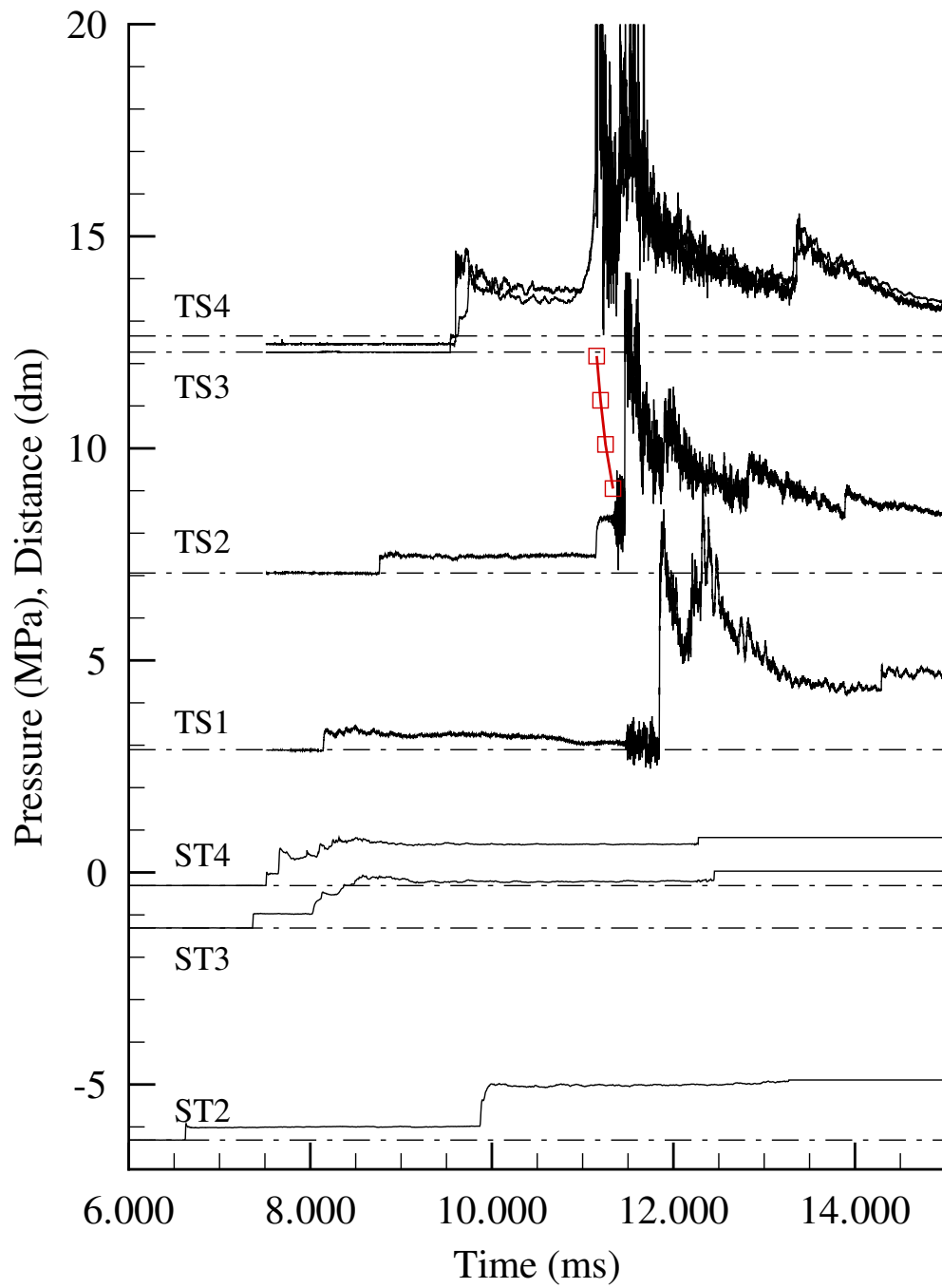


Figure I.47: Pressure and ionization data from shock initiator run 81.

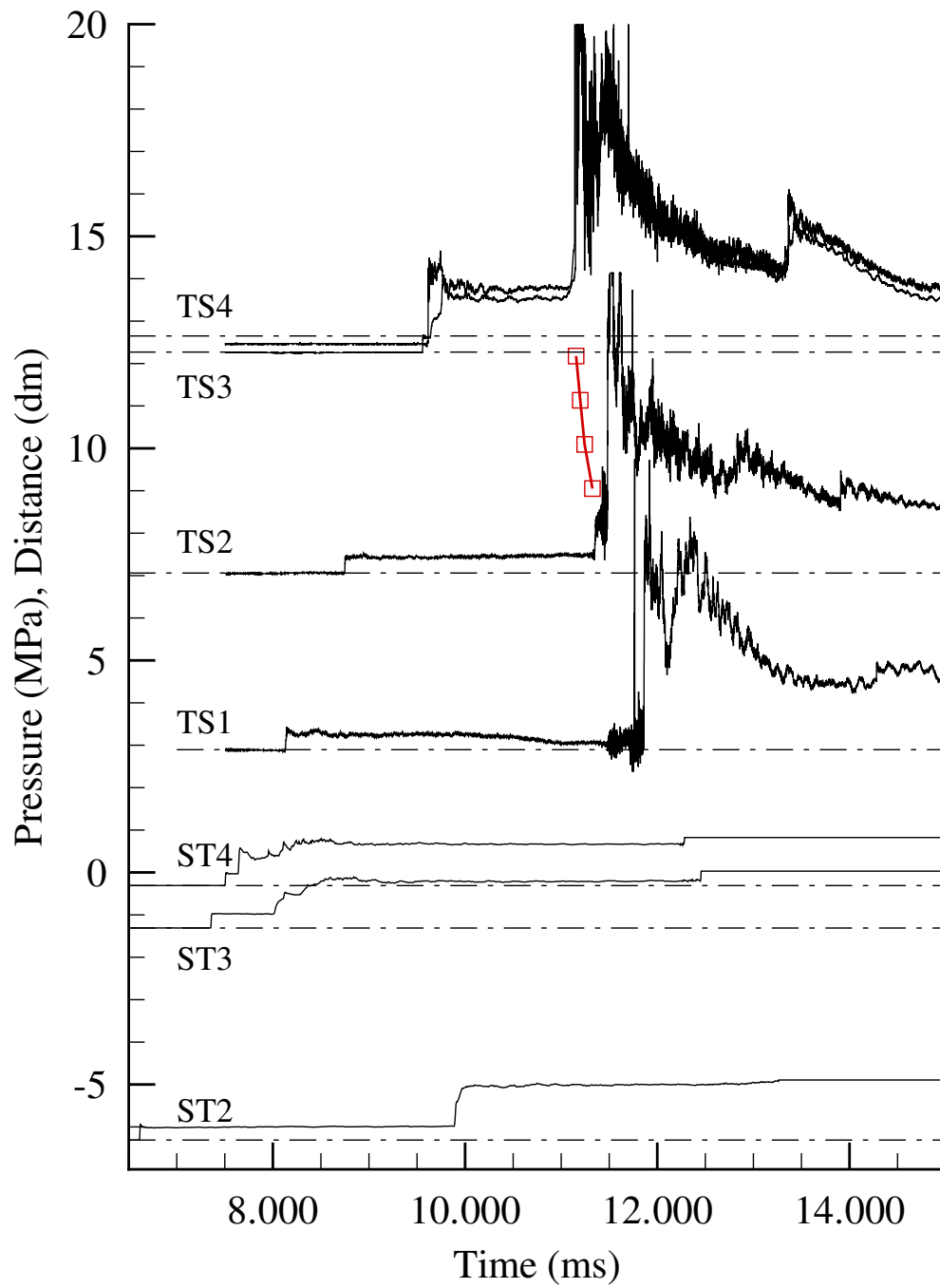


Figure I.48: Pressure and ionization data from shock initiator run 82.

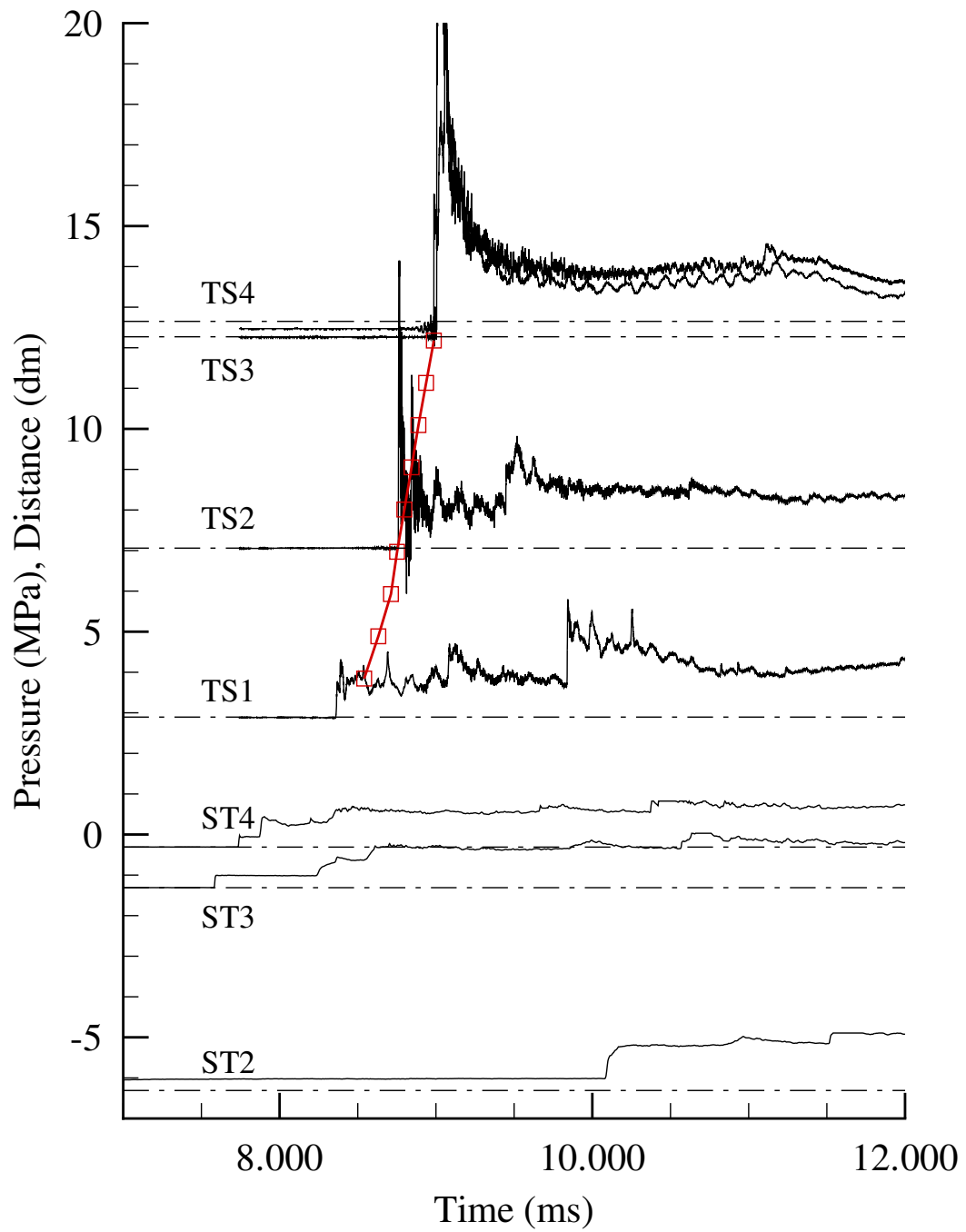


Figure I.49: Pressure and ionization data from shock initiator run 83.

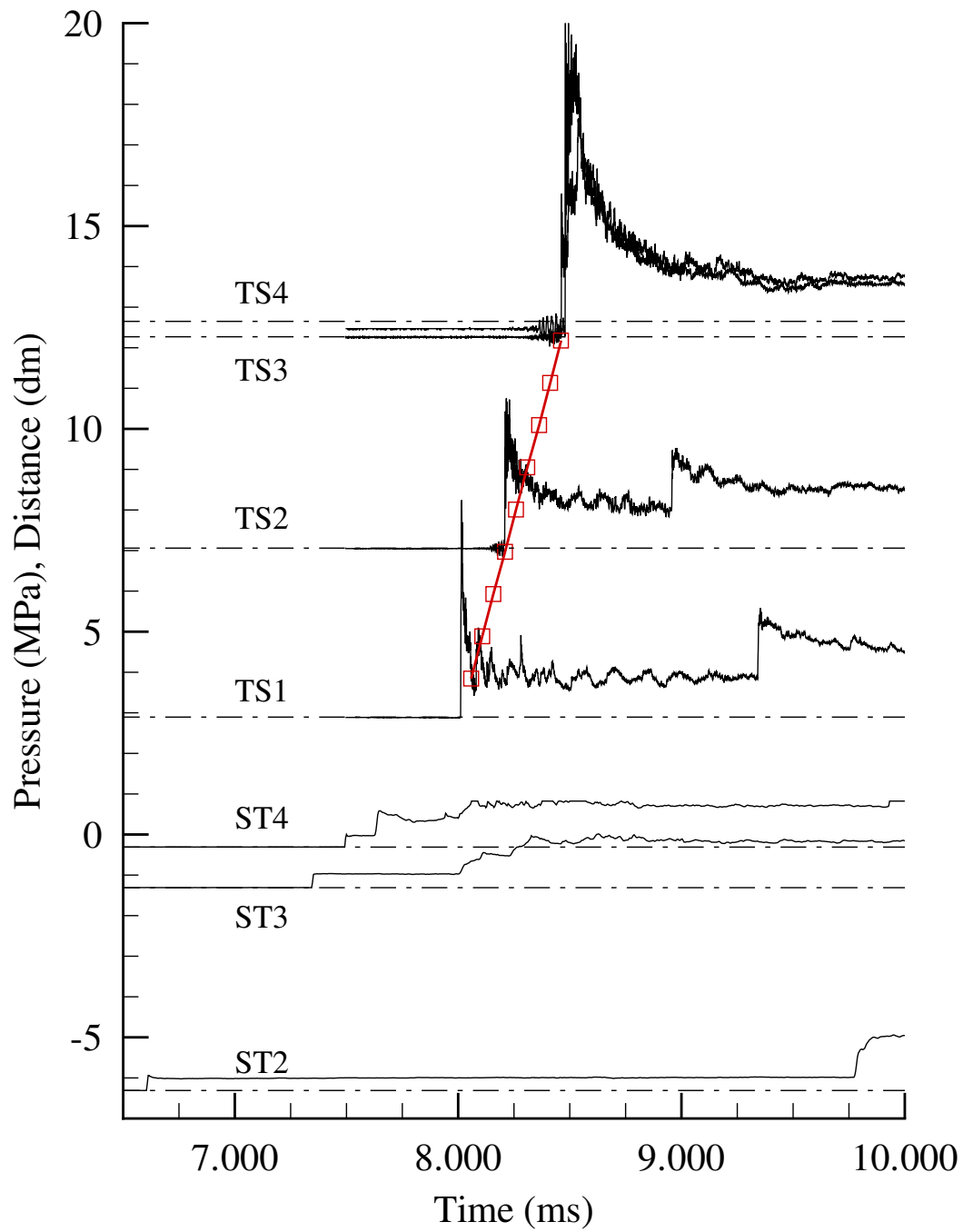


Figure I.50: Pressure and ionization data from shock initiator run 84.

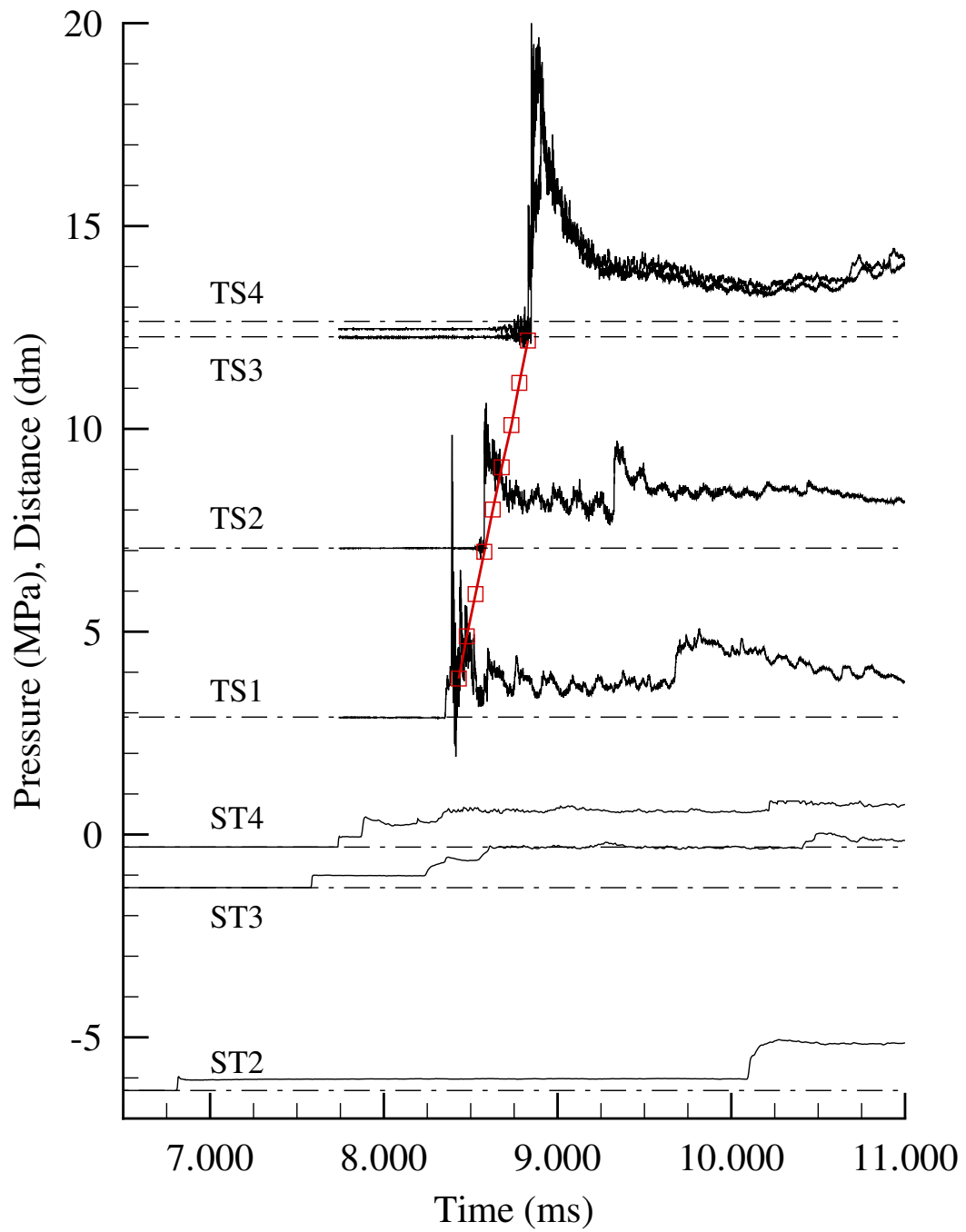


Figure I.51: Pressure and ionization data from shock initiator run 85.

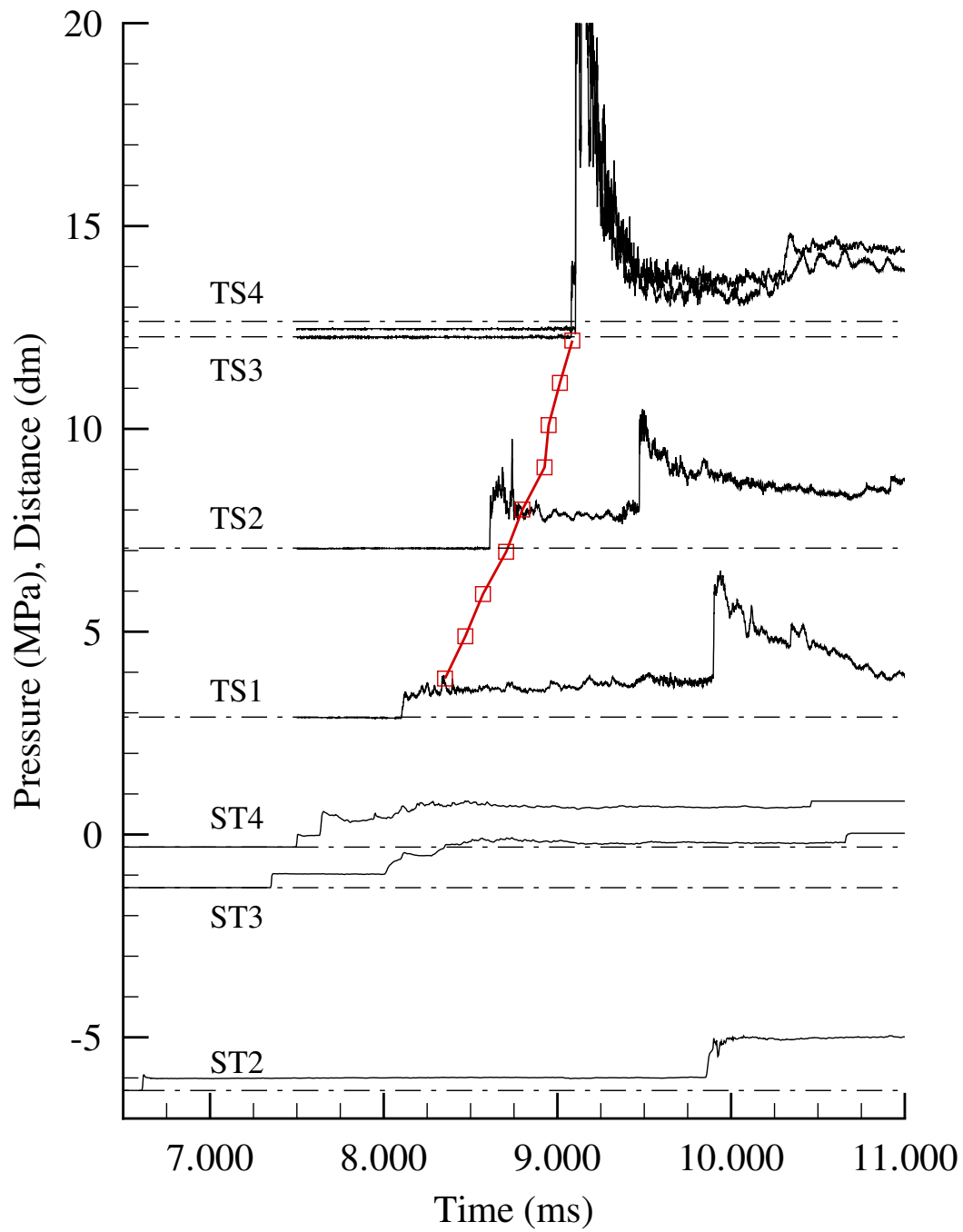


Figure I.52: Pressure and ionization data from shock initiator run 86.

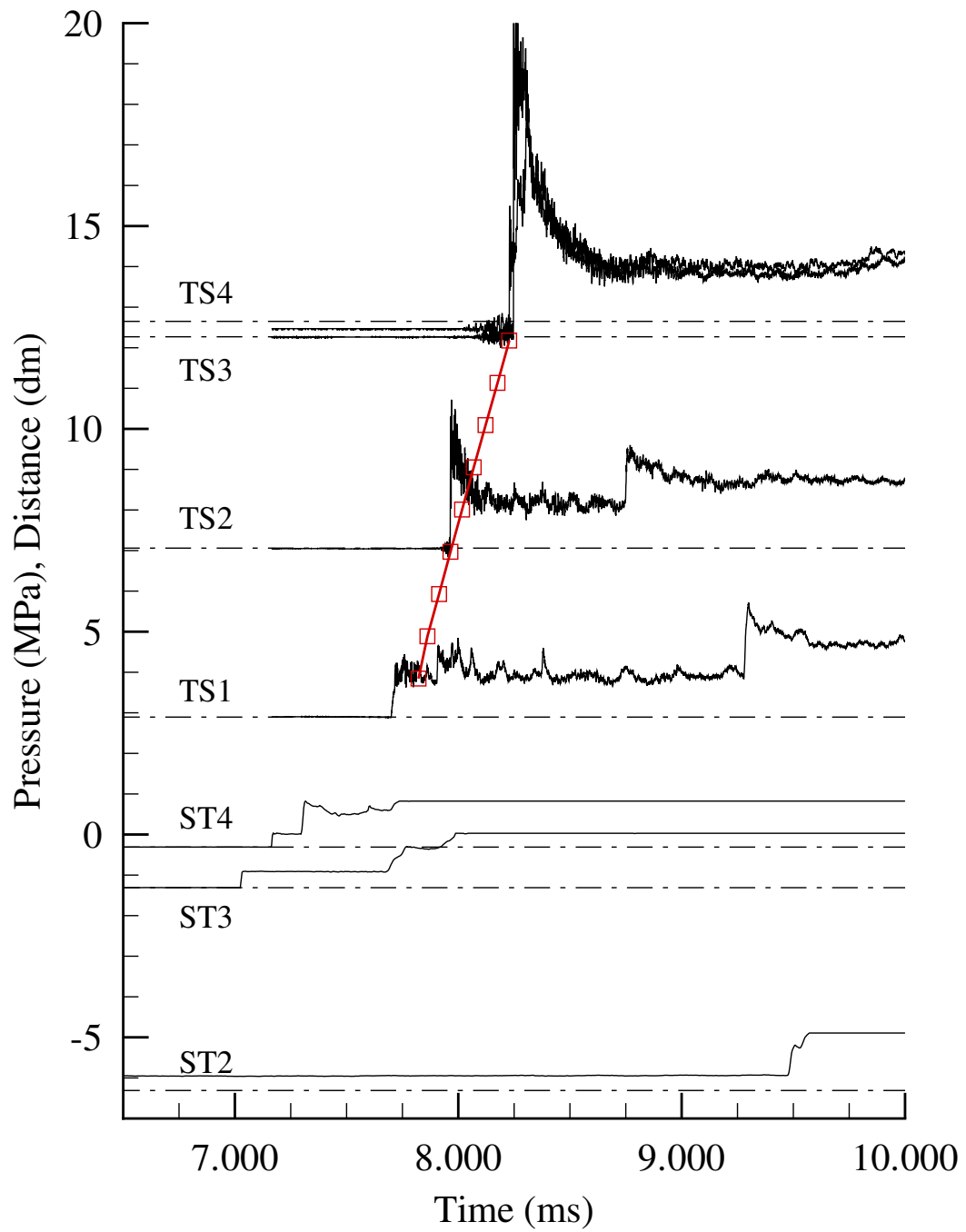


Figure I.53: Pressure and ionization data from shock initiator run 87.

